CODEN: JASMAN 4966

THE JOURNAL of the Acoustical Society of America

Vol. 105, No. 1 January 1999

MEETING PROGRAM SUMMARY **BERLIN MEETING** **14–19 MARCH 1999**
(see p. 51–55)

SOUNDINGS SECTION

SELECTED RESEARCH ARTICLES [10]

GENERAL LINEAR ACOUSTICS [20]

(Continued)

CONTENTS—*Continued from preceding page*

UNDERWATER SOUND [30]

TRANSDUCTION [38]

STRUCTURAL ACOUSTICS AND VIBRATION [40]

ARCHITECTURAL ACOUSTICS [55]

ACOUSTICAL MEASUREMENTS AND INSTRUMENTATION [58]

ACOUSTIC SIGNAL PROCESSING [60]

PHYSIOLOGICAL ACOUSTICS [64]

(Continued)

CONTENTS—*Continued from preceding page*

PSYCHOLOGICAL ACOUSTICS [66]

SPEECH PRODUCTION [70]

SPEECH PERCEPTION [71]

SPEECH PROCESSING AND COMMUNICATION SYSTEMS [72]

MUSIC AND MUSICAL INSTRUMENTS [75]

(Continued)

CONTENTS—*Continued from preceding page*

NOTES CONCERNING ARTICLE ABSTRACTS

1. The number following the abstract copyright notice is a Publisher Item Identifier (PII) code that provides a unique and concise identification of each individual published document. This PII number should be included in all document delivery requests for copies of the article.
2. PACS numbers are for subject classification and indexing. See June and December issues for detailed listing of acoustical classes and subclasses.
3. The initials in brackets following the PACS numbers are the initials of the JASA Associate Editor who accepted the paper for publication.

SOUNDINGS

Section Editor: Richard Stern

This front section of the *Journal* includes acoustical news, views, reviews, and general tutorial or selected research articles chosen for wide acoustical interest and written for broad acoustical readership.

ACOUSTICAL NEWS—USA

Elaine Moran
Acoustical Society of America, 500 Sunnyside Boulevard, Woodbury, New York 11797

Editor's Note: *Readers of this Journal are asked to submit news items on awards, appointments, and other activities about themselves or their colleagues. Deadline dates for news items and notices are 2 months prior to publication.*

New Fellows of the Acoustical Society of America

Robert P. Carlyon—For contributions to the understanding of perceptual grouping processes and pitch perception.

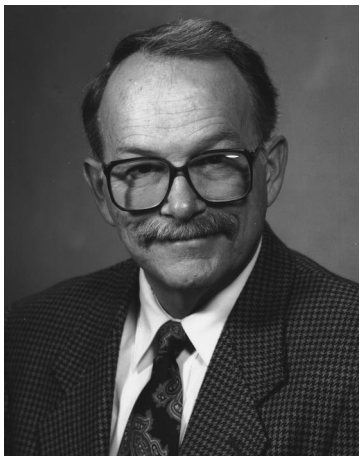

James F. Greenleaf—For contributions to medical ultrasound.

Daniel Juve—For contributions to understanding sound generation by turbulent flow and propagation in inhomogeneous media.

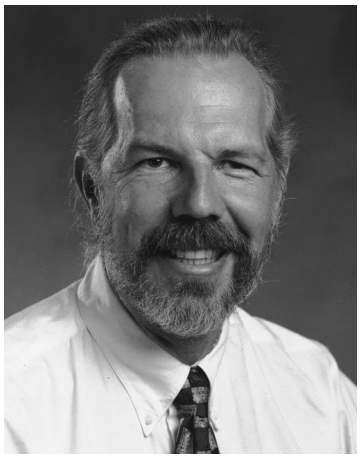

John C. Middlebrooks—For contributions to the psychophysics and physiology of spatial hearing.

Edward C. Monahan—For contributions to the acoustics of the air–sea interface.

Oleg V. Rudenko—For contributions to nonlinear acoustics.

 0001-4966/99/105(1)/1/5/$15.00

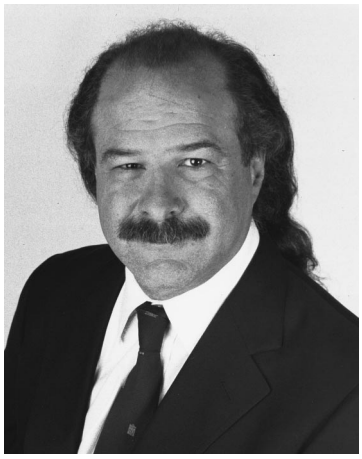

Neil A. Shaw—For contributions to architectural acoustics and audio design.

Yohichi Tohkura—For contributions to cross-language speech perception and production.

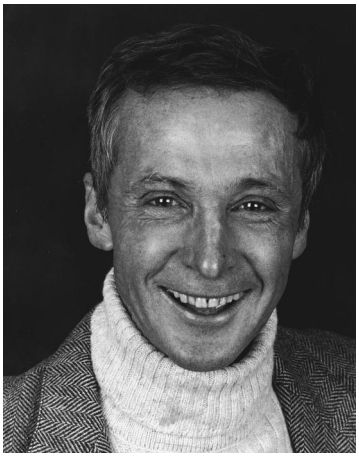

Barry Uscinski—For contributions to the understanding of wave propagation in random media.

ICA/ASA '98: The Joint meeting of the 16th International Congress on Acoustics and the 135th meeting of the Acoustical Society of America held in Seattle, Washington

ICA/ASA '98 was held 20–26 June 1998 in Seattle, Washington. Technical and social meeting events were organized at a variety of locations in and nearby Seattle including the Seattle Sheraton Hotel and Towers, the Westin Hotel, the Pacific Science Center, The Fifth Avenue Theatre, and Tillicum Village on Blake Island. This was the second time an International Congress was held in the United States, the first occurred in 1956 in Cambridge, Massachusetts and the third time the Acoustical Society has met in Seattle, the previous meetings were held in 1962 and 1988.

The meeting drew a total of 2124 registrants. Attesting to the importance of this international event, this meeting drew attendees from 42 countries. There were 36 from Australia, 11 from Austria, 15 from Belgium, 12 from Brazil, 75 from Canada, 2 from Chile, 1 from Columbia, 3 from the Czech Republic, 17 from Denmark, 1 from Egypt, 2 from Estonia, 7 from Finland, 95 from France, 49 from Germany, 1 from Greece, 4 from Hong Kong, 1 from Hungary, 9 from India, 3 from Ireland, 3 from Israel, 28 from Italy, 173 from Japan, 33 from Korea, 8 from Mexico, 27 from the Netherlands, 9 from New Zealand, 18 from Norway, 12 from Poland, 47 from the Republic of China, 27 from Russia, 3 from Singapore, 1 from the Slovak Republic, 3 from South Africa, 13 from Spain, 25 from Sweden, 7 from Switzerland, 1 from Turkey, 2 from Venezuela, 77 from the United Kingdom, 1066 from the United States, and 3 from Yugoslavia.

This meeting provided a host of opportunities for technical and social exchange, both formal and informal. A welcome reception was held on Saturday, 20 June, at the Pacific Science Center, one of the top science museums in the United States. Attendees were able to enjoy hors d'oeuvres while exploring the hands-on and interactive exhibits featured at the museum. On Sunday, 21 June, Opening Ceremonies were held at The Fifth Avenue Theatre, which included welcoming remarks from members of the ICA/ASA '98 Executive Committee and the Chair of the International Commission on Acoustics. The ceremonies opened with a presentation on Native American drumming by Ralph Bennett as well as prototypically America musical presentations by Susan Pascal Quartet, a jazz ensemble, and The Total Experience Gospel Choir.

A total of 1504 papers organized into 170 sessions covered the areas of interest of all 12 Technical Committees and 1 Technical Group. Technical Sessions began on Monday morning, 22 June and were held each day until Friday evening. Sixteen Plenary Lectures were presented by recognized experts in the field and were well attended. The Technical Program included over 90 special sessions. An ''Opera House Design Student Competition,'' memorial sessions honoring Manfred Heckl, Isadore Rudnick, and Hugh Flynn and a short course on ''Nonlinear System Techniques and Applications'' were also part of the technical program.

A meeting proceedings on CD-ROM containing two-page manuscripts of presentations was provided to registrants and a printed version was available at an extra charge.

An equipment exhibition was held from Monday through Wednesday and included over 30 exhibits on active noise control systems, computer-based instrumentation, sound level systems, signal processing systems, sound intensity systems, devices for noise control, and acoustical materials.

The Technical Committees/Technical Specialty Group all held meetings of their committees to which all meeting attendees were invited. The meeting also included 18 different meetings dealing with standards, indicating a healthy level of activity in this area of our endeavors. Technical tours were arranged to the Boeing Aerodynamics, Noise and Propulsion Laboratories, and to the new Seattle concert hall, Benaroya Hall.

A social was held on Monday evening at the Sheraton Hotel, to give all attendees an opportunity to get together with colleagues. On Wednesday and Thursday, participants enjoyed boat cruises to Tillicum Village on Blake Island. The visit to this Northwest native village included a salmon dinner followed by a presentation of ''Dance on the Wind'' featuring songs and dances from Northwest Native American tribes. Participants were treated to the beautiful Seattle nighttime skyline on the return cruise.

On Thursday a banquet and closing ceremonies were held at the Westin Hotel and included musical entertainment by Northwest Choral Arts.

Other social events included lunches and receptions for students where

FIG. 1. 1999 Gold Medal recipient Floyd Dunn (l–r, Vice President Ilene Busch-Vishniac, Elsa Dunn, Floyd Dunn, President Lawrence Crum)

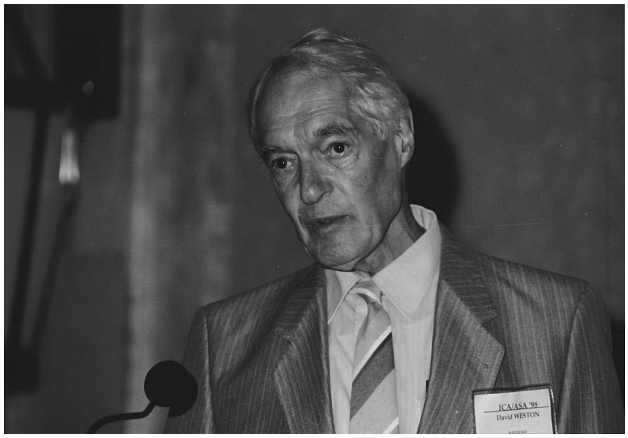

FIG. 2. 1999 Helmholtz–Rayleigh Interdisciplinary Silver Medal recipient David E. Weston.

FIG. 4. 1999 R. Bruce Lindsay Award recipient Robert L. Clark (l–r Vice President Ilene Busch-Vishniac, Chris Fuller, Robert Clark, President Lawrence Crum).

they could meet with other students and with senior members of the acoustics community.

The Women in Acoustics Committee sponsored a luncheon that was especially well-attended by a number of foreign guests. The Committee welcomed Patricia Kuhl, the next President of ASA, who made some remarks concerning the increasing role of women in the ASA.

The plenary session included the presentation of Acoustical Society awards and announcement of newly elected Fellows of the Society.

The ASA President and Vice President presented four Society awards (see Figs. 1 through 4) and announced the election of 17 new Fellows (see Fig. 5). The Gold Medal was presented to Floyd Dunn ''for creative contributions to fundamental knowledge of ultrasonic propagation in, and interactions with, biological media.'' The Helmholtz–Rayleigh Interdisciplinary Silver Medal in Acoustical Oceanography and Underwater Acoustics was presented to David E. Weston ''for seminal work on the physics of explosive sources, scattering, and the horizontal refraction of sound.'' Honorary Fellowship was conferred upon Carleen M. Hutchins ''for her unique role in combining the art of violin making with the science of acoustics.'' The R. Bruce Lindsay Award was presented to Robert L. Clark ''for contributions to active adaptive noise control.'' Election of the following persons to Fellow grade was announced: Xavier Boutillon, Armand Dancer, C. J. Darwin, Robert Dooling, Jos J. Eggermont, Kenneth G. Foote, Juan A. Gallego-Juarez, Charles F. Greenlaw, Timothy Leighton, Jacques Reisse, Edwin W. Rubel, Ronald Schusterman, John P. Seiler, Kawan Soetanto, Quetin Summerfield, Harvey Sussman, and Kevin L. Williams.

President-Elect James West presented the traditional President's Tuning Fork to Lawrence Crum whose term as President of ASA ended at the close of ICA/ASA '98 (see Fig. 6).

The International Congress on Acoustics (ICA) is held every three years under the authority of the International Commission on Acoustics. A special event during ICA/ASA '98 was the first general assembly of the reorganized International Commission on Acoustics. The main agenda items for the General Assembly were the election of the Board for the next three years, agreement on the budget, adoption of the by-laws, and discussion of other items that may be suggested by member societies. The General Assembly elected ASA members Gilles Daigle as General Secretary and Lawrence Crum as President. Indeed it is a compliment to the ASA that the overwhelming majority of the Board of the ICA are also members of the ASA.

The President expressed the Society's thanks to the Local Committee for the excellent execution of the meeting, which clearly required meticulous planning. Local committee members were: Michael Bailey, Steven Kargl, Audio-Visual; Thomas Matula, Peter Kaczkowski, Computer Access/ Paper Copying Service; Charles Schmid, Evan Davis, Entertainment; Will Cady, Peter Chang, Exhibits; Nancy Penrose, Facilities; Pierre Mourad, Food Service; James Angerer, James Mercer, Fundraising; Kirk Beach, Housing; Kevin Williams, Medals and Awards Plenary Session; Rex Andrew, Marilee Andrew, Opening Ceremonies; Susan Norton, John Reid, Plenary Sessions; Monty Bolstad, Thomas Matula, Public Relations; Brian Dushaw, Registration; Iona Park, Belur Shivrashankara; Signs and Posters; Bruce Howe, Dajun Tang, Darrell Jackson, Jeffrey Nystuen, Socials and Receptions; Tyrone Porter, Student Participation; Peter Dahl, Robert Dougherty, Michalakis Averkiou, Technical Tours; Jane Crum, Jennifer Clesceri, Marilyn Matula, Visitors' Program; Professional meeting services provided by Jan Kvamme and Sarah Cook of Engineering Professional Services (see Fig. 7).

The President also extended thanks to the members of the Technical Program Organizing Committee and the Scientific Advisory Committee. Members of the Technical Program Organizing Committee were: Patricia K. Kuhl, Scientific Program Chair; Anthony A. Atchley, Vice Chair; Brian

FIG. 3. Honorary Fellow Carleen M. Hutchins (l–r Vice President Ilene Busch-Vishniac, Robert Schumacher, Carleen Hutchins, President Lawrence Crum).

FIG. 5. ASA President and Vice President congratulate the newly elected Fellows of ASA who attended the meeting.

FIG. 6. Presentation of the ASA President's Tuning Fork (l–r President-Elect James West, President Lawrence Crum).

Dushaw, Darrell R. Jackson, Acoustical Oceanography; Whitlow W. L. Au, Animal Bioacoustics; Michael R. Yantis, Architectural Acoustics; Ronald A. Roy, Michael R. Bailey, Bioresponse to Vibration/Biomedical Ultrasound; Harry Simpson, Thomas R. Howarth, Engineering Acoustics; Victor W. Sparrow, Education in Acoustics; Douglas H. Keefe, Edward M. Burns, Musical Acoustics; Iona Park, Richard Peppin, Noise; Thomas R. Matula, Steven Kargl, Physical Acoustics; Donna L. Neff, Lynne Werner, Susan Norton, Psychological and Physiological Acoustics; Gary R. Wilson, David I. Havelock, Signal Processing in Acoustics; Terrance M. Nearey, Paul Iverson, Speech Communication; Jerry H. Ginsberg, David Feit, Structural Acoustics and Vibration; George V. Frisk, Dajun Tang, Underwater Acoustics.

Members of the Scientific Advisory Committee were: Acoustical Oceanography: Darrell R. Jackson, Chair; Tokou Yamamoto, Peter F. Worcester, Timothy K. Stanton; Animal Bioacoustics: Whitlow W. L. Au, Chair; Bertel Mohl, Uli Schnitzler; Architectural Acoustics: Dana S. Hougland, Chair; Mendel Kleiner, David Lubman, Ewart A. Wetherill, Jerry G. Lilly; Bioresponse to Vibration/Biomedical Ultrasound: Ronald A. Roy, Chair; Floyd Dunn, Shira L. Broschat, Anthony J. Brammer; Engineering Acoustics: Thomas R. Howarth, Chair; James M. Powers; Musical Acoustics: Douglas H. Keefe, Chair; Juergen Meyer, Thomas D. Rossing, Uwe J. Hansen; Noise: Richard J. Peppin, Chair; Leo L. Beranek, Louis C. Sutherland; Physical Acoustics: James M. Sabatier, Chair; David T. Blackstock, Henry E. Bass, Werner H. Lauterborn. Psychological and Physiological Acoustics: Donna L. Neff, Chair; William A. Yost, Nathaniel I. Durlach, Peter Dallos, Ervin R. Hafter; Signal Processing in Acoustics: David I. Havelock, Chair; J. Stuart Bolton; Speech Communication: Terrance M. Nearey, Chair; Kenneth N. Stevens, John J. Ohala; Structural Acoustics and Vibration: Jerry H. Ginsberg, Chair; Sabih I. Hayek, Scott D. Sommerfeldt, Jean-Louis Guyader; Underwater Acoustics: George V. Frisk, Chair; Ralph R. Goodman, Anatoliy N. Ivakin, William M. Carey.

The excellent international response to this meeting in terms of the attendance and representation from the various acoustical societies of the world speak strongly of the leadership role that the ASA plays in international acoustics. The President encourages everyone to continue to support such a role for the ASA by their attendance at the joint meeting of the ASA and the European Acoustics Association in Berlin in March.

LAWRENCE A. CRUM
President 1997–1998

FIG. 7. Members of the Local Organizing Committee.

Mie Kim Najita summer fellowship for undergraduates with interests in hearing research

The Parmly Hearing Institute of Loyola University Chicago may support one or more undergraduate fellows for the summer of 1999 to work at the institute on projects involving basic neuro- and behavioral-science in hearing.

A stipend of approximately $2500.00 will be provided for the 11-week position (the exact time for the 11-week position will be coordinated with the student's schedule, but the time must be between 17 May and 20 August 1999). The student(s) will participate in one or more on-going research projects.

Funding for this year's award is made possible by the Parmly Hearing Institute and by funds contributed in memory of a former Loyola student, Mie Kim Najita, who worked at the institute as a research subject in 1982–83 and on a hearing research project for her honors degree in psychology.

Interested current undergraduate students should apply by submitting a 500-word statement describing why they wish to receive this position, two letters of reference, and a letter containing: grade point average (certified either by the school's registrar or by the student's advisor), major, and a list of all the science courses in which the student has received a ''B'' (or equivalent) or higher grade.

Please send the application material (with the student's complete address and phone number) to:

William A. Yost, Ph.D., Director
Parmly Hearing Institute
Loyola University Chicago
6525 North Sheridan Road
Chicago, IL 60626
Tel: (773) 508-2712
Fax: (773) 508-2719

Complete application materials must be received by 15 March 1999.

Call for papers and presentations for the International Clarinet Association Clarinetfest Ostend, Belgium, 6–11 July 1999

The International Clarinet Association will hold its 1999 ClarinetFest, a symposium and festival devoted to the clarinet, in Ostend, Belgium 6–11 July 1999. The festival host is Guido Six. The program for the conference will include a series of scholarly papers and presentations, as well as poster presentations to be displayed. The Association solicits proposals for presentations (such as papers or lecture-recitals) and proposals for poster presentations on any topic related to the clarinet. For the live presentations, the use of live or recorded performance is acceptable; however, presentations whose sole aim is performance are discouraged. Presentations should be designed to be no more than 25 minutes in length. Proposals which are not selected for presentation may be invited for the poster session.

Prizes will be offered as follows: First place paper, $300 and guaranteed publication in *The Clarinet* journal (subject to editing); and second place paper, $200.

Six copies of an abstract, one page only, describing the content of papers, lecture-recitals, or poster presentations must be submitted to Dr. Keith Koons, ICA Research Presentation Committee Chair, Music Department, University of Central Florida, P.O. Box 161354, Orlando, FL 32816-1354. No name or identification of the author should appear on the proposal. The postmark deadline for proposals is 31 January 1999. For more information, write or call Keith Koons at (407) 823-5116 or by electronic mail: ⟨kkoons@pegasus.cc.ucf.edu⟩.

USA Meetings Calendar

Listed below is a summary of meetings related to acoustics to be held in the U.S. in the near future. The month/year notation refers to the issue in which a complete meeting announcement appeared.

1999

25–27 Feb. 24th Annual Conference, National Hearing Conservation Association, Atlanta, GA [National Hearing Conservation Association, 9101 E. Kenyon Ave., Suite 3000, Denver, CO 80237, Tel.: 303-224-9022; Fax: 303-770-1812; E-mail: nhca@gwami.com].

15–19 March Joint meeting: 137th meeting of the Acoustical Society of America/2ndConvention of the European Acoustics Association: Forum Acusticum, integrating the 25th Anniversary DAGA conference, Berlin, Germany [Acoustical Society of America, 500 Sunnyside Blvd., Woodbury, NY 11797, Tel.: 516-576-2360; Fax: 516-576-2377; E-mail: asa@aip.org; WWW:asa.aip.org].

10–12 May AIAA/CEAS Aeroacoustics Conference, Bellevue, WA [Belur Shivashankara, The Boeing Company, P.O. Box 3707, MS 67-ML, Seattle, WA 98124-2207; Tel.: 425-234-9551, Fax: 425-237-5247; E-mail: belur.n.shivashankara@boeing.com].

6–7 June 1999 SEM Spring Conference, Cincinnati, OH [Katherine M. Ramsay, Conference Manager, Society for Experimental Mechanics, Inc., 7 School St., Bethel, CT 06801; Tel.: 203-790-6373; Fax: 203-790-4472; E-mail: meetings@seml.com].

27–30 June ASME Mechanics and Materials Conference, Blacksburg, VA [Norma Guynn, Dept. of Engineering Science and Mechanics, Virginia Tech, Blacksburg, VA 24061-0219; Fax: 540-231-4574; E-mail: nguynn@vt.edu; WWW:http://www.esm.vt.edu/mmconf/]. Deadline for receipt of abstracts: 15 January 1999.

6–11 July 1999 Clarinetfest, Ostend, Belgium [International Clarinet Association, Keith Koons, Music Dept., Univ. of Central Florida, P.O. Box 161354, Orlando, FL 32816-1354]. Deadline for receipt of abstracts: 31 January 1999.

1–5 Nov. 138th meeting of the Acoustical Society of America, Columbus, OH [Acoustical Society of America, 500 Sunnyside Blvd., Woodbury, NY 11797, Tel.: 516-576-2360; Fax: 516-576-2377; E-mail: asa@aip.org; WWW:asa.aip.org].

2–4 Dec. ACTIVE 99, Fort Lauderdale, FL [Institute of Noise Control Engineering, P.O. Box 3206, Arlington Branch, Poughkeepsie, NY 12603, Tel.: 914-462-4006; Fax: 914-463-020; E-mail: INCEUSA@aol.com; WWW:users.aol.com/inceusa/ince.html].

6–8 Dec. INTER-NOISE 99, Fort Lauderdale, FL [Institute of Noise Control Engineering, P.O. Box 3206, Arlington Branch, Poughkeepsie, NY 12603, Tel.: 914-462-4006; Fax: 914-463-020; E-mail: INCEUSA@aol.com; WWW:users.aol.com/inceusa/ince.html].

REPORTS OF RELATED MEETINGS

This Journal department provides concise reports of meetings that have been held by other organizations concerned with acoustical subjects; and of meetings co-sponsored by the Acoustical Society but planned primarily by other co-sponsors.

NHCA's 23rd Annual Hearing Conservation Conference

Albuquerque, NM, 19–21 February 1998

On 19–21 February 1998 in Albuquerque, NM, the National Hearing Conservation Association (NHCA) held its 23rd Annual Hearing Conservation Conference, chaired by Theresa Y. Schulz, Vice-President of NHCA. This highly successful event attended by approximately 240 hearing conservation professionals included four concurrent half-day workshops, from which attendees could select two. The workshops covered application of ANSI S3.44, education and motivation, marketing hearing conservation programs to customers and to society at large, and the audiologist as a knowledgeable informant in litigation issues. The program also included 12 platform presentations, 20 posters, four forums, a film series featuring four films and an audio demonstration CD, a number of allied committee and ANSI working group meetings, a change-of-pace luncheon lecture by the well-known author, professor, composer, R. Murray Schafer who spoke on soundscapes for acoustical ecology, and enjoyable social events and exhibitor receptions.

The lectures covered topics such as the effects of NIHL on speech perception, hearing requirements for truck drivers, hearing conservation in high-school shop classes, shooting habits and demographics of recreational shooters, otoacoustic emissions and hearing loss prevention, a new ANSI hearing protector standard, and a survey of judgments on hearing-loss compensation cases. The posters were equally as diverse, covering hearing loss in the farming community, design of effective emergency alarm systems, 3-D audio displays, financial costs of hearing conservation programs, problems of noisy toys, and other related issues. Although primarily drawing on a U.S. and Canadian audience, speakers and attendees arrived from around the world, including countries such as the Netherlands, Australia, and Brazil.

The prestigious NHCA-sponsored awards were presented at the Saturday luncheon. Susan Cooper Megerson received the Michael Beall Threadgill Award for Outstanding Service to NHCA, and ASA Fellow, Julia D. Royster received the Outstanding Hearing Conservationist Award for her contributions towards evaluating the efficacy of hearing conservation programs, and for her fundamental research and contributions to acoustical standards.

For those who missed this exciting event, the technical information can be recaptured in the loose-leaf proceedings available from the NHCA Executive Offices in Denver, CO (303-224-9022, e-mail: nhca@gwami.com), or the abstracts can be reviewed on the NHCA website at http://www.hearingconservation.org. Better yet, plan to join us next year in Atlanta from 25–27 February 1999 for another extraordinary event.

ELLIOTT H. BERGER
Senior Scientist, Auditory Research
E-A-R Hearing Protection Products
7911 Zionsville Rd.
Indianapolis, IN 46268-1657

 0001-4966/99/105(1)/17/1/$15.00

BOOK REVIEWS

James F. Bartram
94 Kane Avenue, Middletown, Rhode Island 02842

These reviews of books and other forms of information express the opinions of the individual reviewers and are not necessarily endorsed by the Editorial Board of this Journal.

Editorial Policy: *If there is a negative review, the author of the book will be given a chance to respond to the review in this section of the Journal and the reviewer will be allowed to respond to the author's comments. [See ''Book Reviews Editor's Note,'' J. Acoust. Soc. Am.* ***81****, 1651 (May 1987).]*

Signal Processing with Fractals: A Wavelet Based Approach

Gregory W. Wornell

Prentice-Hall, Englewood Cliffs, NJ, 1996.
xi+177 pp. Price: $65.00.

Fractal geometry has attracted interest in the recent past for various reasons. One interest is the analysis of natural phenomena to see if there is an underlying fractal nature to it. Recently, Avnir *et al.*, searched *Physical Review A to E* and *Physical Review Letters* from 1990 to 1996 [D. Avnir *et al.*, ''Is the geometry of nature fractal,'' Science **279**, 39–40 (1998)] and found 96 papers which declared the fractal nature of several systems. Avnir *et al.*, expressed concern about the enthusiastic use of the term ''fractal.'' With that in mind, it seems appropriate to consider well-defined methods to deal with fractal signals. The author states in the introduction that he intends that this book present a development of a ''unified, wavelet-based framework for efficiently synthesizing, analyzing, and processing several broad classes of fractal signals.'' The broad classes of fractal interest include $1/f^{\gamma}$ signals where the power spectrum is assumed to decay as $1/f^{\gamma}$, where γ is assumed to be in the open interval from 0 to 2. The book also assumes ''a basic familiarity with continuous- and discrete-time signals and systems, with stochastic processes, detection and estimation theory, and with the geometry of linear vector spaces and linear algebra.'' The level of difficulty and rigor is comparable to Van Trees' notable volumes on detection and estimation theory. In my opinion this rigor is justified with a newer method of analysis of which most people, including the reviewer, have little intuitive understanding. An understanding of the material in this book should help a practitioner of signal processing to avoid mathematical pitfalls and traps when applying the methods presented.

This book is organized into seven chapters with four appendices of derivations and proofs. The first chapter contains a description of the synthesis and analysis problems of signal processing as well as a very brief introduction to the fractal nature of nature. The second chapter describes the continuous and discrete wavelet transform with sufficient detail to bring out all the relevant features of the wavelet transform. He presents some illustrative examples such as Haar-based multiresolution analysis. He gives ample references to original literature and also monographs on the subject.

The third chapter deals with a description of $1/f$ and nearly-$1/f$ processes from a theoretical standpoint, defining them as processes that are statistically self-similar. This means that random process $x(t)$ is probabilistically equivalent to $\alpha^{-\gamma}x(at)$. Interesting aspects of this definition are presented along with the interesting statement that the power law dependence of the spectrum generally ''extends over several decades of frequency,'' which is a point that Avnir *et al.*, appear to contend. He gives references to several physical phenomena that exhibit $1/f$ behavior, e.g., the Dow Jones Industrial Average. The wavelet spectrum of the 4096 points of over 78 years is presented and shows a spectrum with a surprisingly constant exponential decay in scale. Several precise definitions of a $1/f$ process, such as the modified convolution of a filter on white Gaussian noise, are presented. These presentations are useful in understanding the problems and intricacies of including frequencies near zero. Two methods for the synthesis of nearly $1/f$ processes are presented. One is based on an infinite-order, autoregressive moving-average model. This model has an infinite number of poles and zeros which are driven by white noise. The other approach is based on wavelets and is used extensively in the remainder of the book. The basic result is that a waveform, synthesized from a wavelet expansion where the coefficients are zero-mean, uncorrelated random variables with variances which decay exponentially with scale, is nearly $1/f$. In other words, the spectrum of the synthesized signal obeys a $1/f^{\gamma}$ spectrum. There are some technical difficulties with stationarity and ergodicity with this method, but they are discussed in the book.

The fourth chapter deals with detection and estimation with fractal processes using wavelet decomposition. He derives estimators for an unknown mixture of $1/f$ and white Gaussian noise. He also derives a detector for a known signal embedded in an unknown mixture of $1/f$ and white Gaussian noise. Chapter 5 defines deterministic signals which have energy or power spectra which decay as $1/f^{\gamma}$. These deterministic signals are then used as carrier signals in Chap. 6 where fractal modulation is introduced and described. Fractal modulation uses the wavelet transform to modulate the carrier signal so that higher frequency bands of the carrier are encoded at a higher data rate. Thus, if one low-frequency band was received, then a single low data-rate message would be obtained. But, if two frequency bands were received, then the message would be retrieved twice at two different data rates. This modulation scheme is said to be useful in ''the case in which both the bandwidth and duration parameters are either unknown or not available at the transmitter. This case . . . arises rather naturally in a range of both point-to-point and multi-user communication scenarios involving, for example, jammed and fading channels, multiple access channels, covert and low probability of intercept (LPI) communication, and broadcast communication to disparate receivers.'' I found this modulation scheme to be thought provoking.

The last chapter discusses linear, self-similar systems which are time-invariant as well as scale-invariant. This chapter is more speculative in nature and is, using the author's words, a ''preliminary investigation into system theoretic foundations of the concepts developed in this book.' How these systems are applied to the physical world is not intuitively obvious to me. The concepts presented are novel and may be of interest to researchers working with exotic systems. I was not surprised to find no applications in this chapter. The intent of the author in this chapter is not to present ideas that lead directly to application, but rather ''interesting and potentially rich open directions for higher research.''

In summary, the book appears to be an extension of Dr. Wornell's Ph.D. thesis at MIT in 1991, entitled ''Synthesis, Analysis and Processing of Fractal Signals.'' It provides a rather mathematically rigorous approach for using wavelets in signal processing. Thus, there are discussions of wide-sense stationarity vice stationarity, ergodicity, and convergence of integrals and sums. In addition to the theory, there are also well-defined equations that can be used to generate computer code to analyze signals. I noticed a few typographical errors, but none that were sufficiently egregious prevented me from understanding the text or equation. The inclusion of theory could be a curse if the reader is not equipped to handle it. However, an awareness of different aspects of theory can help a researcher when he has fallen into a pitfall. In my opinion, the book would be useful for researchers who are planning to research or to apply signal processing with signals which have fractional spectra, e.g., scattering from rough surfaces or approximately pink noise.

CHARLES F. GAUMOND
Office of Naval Research
Code 321US
800 North Quincy Street
Arlington, Virginia 22217-5660

REVIEWS OF ACOUSTICAL PATENTS

Daniel W. Martin
7349 Clough Pike, Cincinnati, Ohio 45244

The purpose of these acoustical patent reviews is to provide enough information for a Journal reader to decide whether to seek more information from the patent itself. Any opinions expressed here are those of reviewers as individuals and are not legal opinions. Printed copies of United States Patents may be ordered at $3.00 each from the Commissioner of Patents and Trademarks, Washington, DC 20231.

Reviewers for this issue:

GEORGE L. AUGSPURGER, *Perception Incorporated, Box 39536, Los Angeles, California 90039*
MAHLON D. BURKHARD, *31 Cloverdale Heights, Charles Town, West Virginia 25414*
RONALD B. COLEMAN, *BBN Acoustic Technologies, 70 Fawcett Street, Cambridge, Massachusetts 02138*
D. LLOYD RICE, *11222 Flatiron Drive, Lafayette, Colorado 80026*
CARL J. ROSENBERG, *Acentech Incorporated, 33 Moulton Street, Cambridge, Massachusetts 02138*
KEVIN P. SHEPHERD, M.S. 463, *NASA Langley Research Center, Hampton, Virginia 23681*
WILLIAM THOMPSON, JR., *The Pennsylvania State University, University Park, Pennsylvania 16802*
ROBERT C. WAAG, *University of Rochester Medical Center, 601 Elmwood Avenue, Rochester, New York 14642*

5,546,356

43.20.Rz WIDE BEAM ACOUSTIC PROJECTOR WITH SHARP CUTOFF AND LOW SIDE LOBES

W. J. Zehner, assignor to the United States of America
13 August 1996 (Class 367/88); filed 30 June 1993

An amplitude weighting procedure to be applied to a line array of periodically spaced transducers is discussed. The purpose is to produce a broad beamwidth directivity pattern with low side lobes. The weighting procedure actually zeros certain of the amplitudes, thereby reducing the required number of transducers.—WT

5,550,791

43.30.Yj COMPOSITE HYDROPHONE ARRAY ASSEMBLY AND SHADING

M. S. Peloquin, assignor to the United States of America
27 August 1996 (Class 367/153); filed 2 August 1995

A line hydrophone array is realized by bonding a series of arm bands of piezoelectric film onto a compliant, nonconducting hollow tube of plastic which also serves as the strength member to support towing forces. Relative amplitude weighting, or shading, of each individual hydrophone element can be accomplished in a variety of ways such as cyclically varying the wall thickness of the tube in the axial direction, varying the circumferential area that each band covers, varying the axial length of each band, having multiple wraps of the piezoelectric film, or a combination of these methods. Having overlapping portions of adjacent bands will tend to reduce grating lobes caused by the large wavelength spacing of the bands.—WT

5,546,361

43.30.Yj DIRECTIONAL ELECTRO-ACOUSTIC TRANSDUCERS COMPRISING A SEALED SHELL CONSISTING OF TWO PORTIONS

D. Boucher and C. Pohlenz, assignors to The French State
13 August 1996 (Class 367/158); filed in France 28 April 1988

The shell of a class IV flextensional transducer is fashioned in two parts **3a** and **3b**, one of which, **3a**, is terminated at either end along the major axis of the elliptical cross section by flange **4**. The parts **3a** and **3b** are separated at either end by air gap **10**. Only shell part **3a** is directly mechanically coupled to the piezoceramic motor section **1**. Stress bolt **7** and locking nuts **8** maintain static compression on the stack of piezoceramic elements

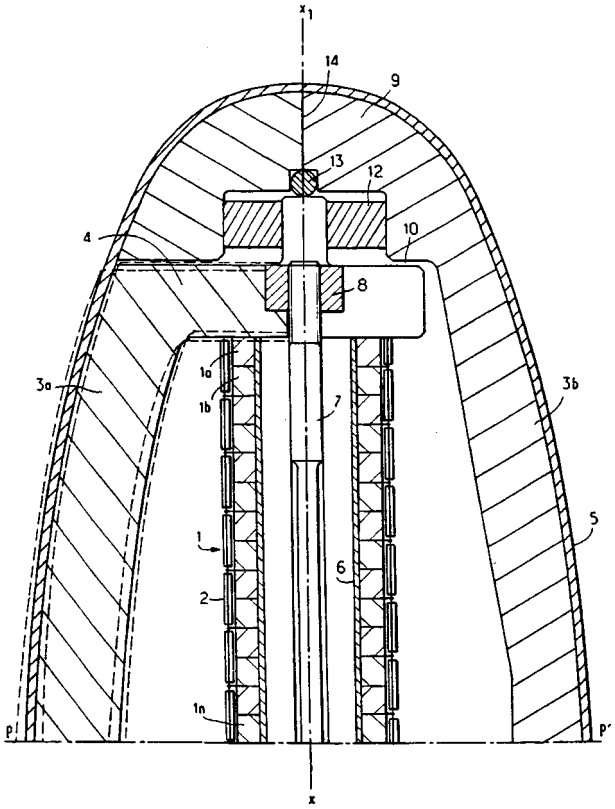

1a,**1b**,... . Elastic members **12** and **13** provide for correct axial and longitudinal alignment of the two shell parts **3a** and **3b** and also provide mechanical isolation between them. Therefore, only shell part **3a** vibrates. The only function of **3b** is to form, with **3a**, a complete and sealed outer envelope. Variations of the attachment of the piezoceramic motor section to the flanges **4** are discussed.—WT

5,550,792

43.30.Yj SLICED PHASED ARRAY DOPPLER SONAR SYSTEM

F. A. Crandall *et al.*, assignors to EDO Western Corporation
27 August 1996 (Class 367/155); filed 30 September 1994

A multi-element sonar transducer is formed by bonding a disk of piezoceramic onto a copper clad circuit board with conductive epoxy and

then, by use of a diamond cutting wheel, slicing the disk into a series of equi-thickness, equi-spaced, parallel rectangular plates. The depth of each cut is such as to pass through the piezoceramic, the conductive epoxy layer, and the copper layer, thereby achieving mechanical and electrical isolation between adjacent plates. Suitable electrical connections among the many plates are then made so as to produce a pair of beam patterns whose main beams are tilted away from the normal to the original disk in a plane orthogonally oriented to the directions of the cuts.—WT

5,517,739

43.35.Yb METHOD OF MAKING A POLARIZATION-SENSITIVE SHEAR WAVE TRANSDUCER

John A. Kosinski, assignor to the United States of America
21 May 1996 (Class 29/25.35); filed 7 October 1994

The objective is a mechanically fixed piezoelectric transducer that produces shear waves with an adjustable polarization in test object **51**. Four electrode segments are deposited on the surface of a piezoelectric substrate **50**, dilithium tetraborate, that is bonded to the test object. A polarization

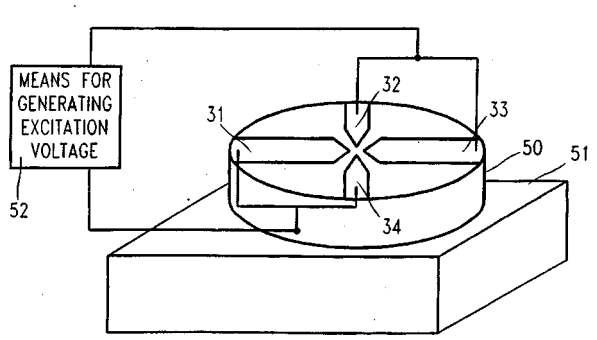

sensitive shear wave transducer is feasible, in materials like dilithium tetraborate, ''when an electrode capable of producing a lateral-field excitation of either 0° or 90° is disposed on a substrate with the appropriate orientation characteristics.''—MDB

5,523,643

43.35.Zc ULTRASONIC PIEZOELECTRIC TRANSDUCER AND ULTRASONIC ACTUATOR

Takanao Fujimura *et al.*, assignors to Olympus Optical Company Limited
4 June 1996 (Class 310/328); filed in Japan 18 August 1992

The actuator produces elliptical motions at its surface **45**. The motion can be applied, for example, to an element **46** to move it in a manufacturing or assembly process. Activating signal voltages for laminated piezoelectric

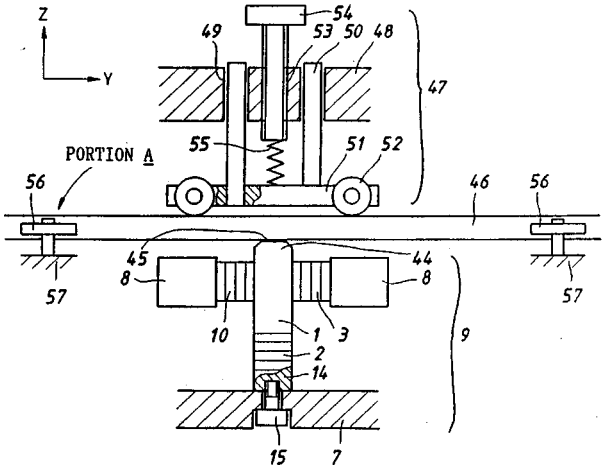

elements **3** and **10** are phased at +90° and −90° relative to the signal voltage applied to element **2**.—MDB

5,546,360

43.38.Ar ELECTRICALLY STEERED ACOUSTIC LENS

T. Deegan, Portsmouth, RI
13 August 1996 (Class 367/150); filed 14 November 1994

An acoustic lens, designed to blanket an array of transducers, is fashioned of an electrorheological material such as mineral oil with a suspension of semiconducting particles of aluminosilicate powder. The bulk modulus and consequently the speed of sound in this material can be changed by applying an electrical potential across it. Furthermore, by embedding a series of wires within the material so that a series of potential differences can be created, the gradient of the speed of sound can be controlled. Numerous applications of the various beam patterns that can then be formed are discussed.—WT

5,550,790

43.38.Ar ACOUSTIC TRANSDUCER FOR LEVEL MEASUREMENT IN CORROSIVE CHEMICAL ENVIRONMENTS

S. Velamoor and K. P. Mesterton, assignors to Kistler-Morse Corporation
27 August 1996 (Class 367/140); filed 10 February 1995

A simple tonpilz-type transducer, with a low rho-*c* layer bonded to the radiating head to provide a better impedance match to a gaseous medium, is enclosed in a housing made from a polymeric material such as PVC. To allow the transducer to withstand exposure to a broad range of industrial chemicals, the entire assembly is coated with Polyparaxylylene, a highly crystalline material that possesses superior barrier properties. This coating is deposited by free molecular dispersion in a vacuum resulting in a pinhole-free layer.—WT

5,511,296

43.38.Fx METHOD FOR MAKING INTEGRATED MATCHING LAYER FOR ULTRASONIC TRANSDUCERS

J. Fleming Dias *et al.*, assignors to Hewlett Packard Company
30 April 1996 (Class 29/24.35); filed 8 April 1994

A transducer is fabricated with an acoustic impedance matching layer on a piezoelectric substrate. The bulk of the matching layer is deposited and then patterning of the matching layer is performed with photolithographic techniques. The result is an array of ''posts'' of matching layer material.—MDB

5,514,927

43.38.Fx PIEZOELECTRIC AUDIO TRANSDUCER

Thomas H. Tichy, assignor to Motorola, Incorporated
7 May 1996 (Class 310/330); filed 28 February 1994

A circular disk piezoelectric bender **101** is suspended on posts **103**. Distance **104** between the housing **200** and the bender is predetermined. A rectangular cantilever-supported construction with distance between the

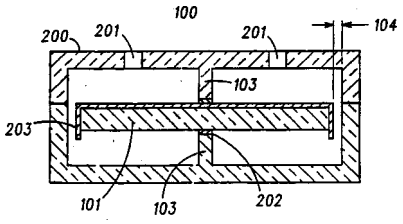

bender and the housing being predetermined is also described. ''This predetermined distance provides an acoustic impedance such that sound may resonate from the transducer.''—MDB

5,541,894

43.38.Fx LOW DISTORTION HYDROPHONE

L. W. Erath, assignor to Syntron, Incorporated
30 July 1996 (Class 367/157); filed 26 May 1995

Consider two, normally identical, flexural disc hydrophones subjected to the same incident acoustic pressure. However, one of the two is equipped with some mechanical means of amplifying this pressure, such as a cone-shaped baffle or horn. Hence that hydrophone produces more output voltage than the other, both in its fundamental and its second harmonic components. In addition, because of nonlinearities associated with the larger pressure amplitude acting on one of them, the ratio of second harmonic output to fundamental output is not the same for the two. The larger output of the second hydrophone is then adjusted, by means of a parallel capacitor, so that the second harmonic levels of both hydrophones are equal. Hence when the total outputs are subtracted, the second harmonic levels should exactly cancel while the difference of the nonequal fundamentals will not, resulting in a useful net output. Of course, because of the nonlinear responses, the value of the capacitor would have to be adjusted with changing level of incident pressure.—WT

5,506,908

43.38.Hz DIRECTIONAL MICROPHONE SYSTEM

John C. Baumhauer, Jr. *et al.*, assignors to AT&T Corporation
9 April 1996 (Class 381/92); filed 30 June 1994

Signals from each of several microphones are encoded into digital formats with Codecs. The digitally formated signals are processed with the aid of a digital signal processor (DSP). Processing includes delays of the signals that are prescribed according to the desired polar pattern and direction of sound pickup. Preferred relative positions of three omnidirectional microphones are disclosed.—MDB

5,511,130

43.38.Hz SINGLE DIAPHRAGM SECOND ORDER DIFFERENTIAL MICROPHONE ASSEMBLY

Charles S. Bartlett and Michael A. Zuniga, assignors to AT&T Corporation
23 April 1996 (Class 381/170); filed 4 May 1994

A first-order differential microphone (FOD) is mounted within a housing. A FOD has a single diaphragm exposed to sound impinging on either side. A pair of conduits, front conduits, conduct acoustic energy from first and second front ports to a front cavity on one side of the FOD. Similarly, a pair of rear conduits conduct acoustic energy from first and second rear ports to a rear cavity on the other side of the FOD. Cavity, conduit, and port dimensions are selected to allow no more than one resonant frequency less than 3500 Hz.—MDB

5,515,445

43.38.Hz LONG-TIME BALANCING OF OMNI MICROPHONES

John C. Baumhauser, Jr. *et al.*, assignors to AT&T Corporation
7 May 1996 (Class 381/92); filed 30 June 1994

With the aid of digital signal processing (DSP), two or more microphone channels are electronically and dynamically adapted to one another. In particular, ''the long term average broad band gain of the signal channels of individual microphone elements is dynamically adjusted, an energy estimate of each microphone signal channel is averaged over the long term and the difference in energy between the signal channels is used to readjust the long term average broad band gain of the microphone signal channels to minimize those differences.''—MDB

5,646,381

43.38.Ja ROOF MOUNTED SOUND HORNS FOR VEHICLES

James M. Boyte, Jr., assignor to Top Source Technologies
8 July 1997 (Class 181/141); filed 19 September 1995

A pair of loudspeakers is mounted in a central roof pod at the front or rear of an automobile. Sound is squirted through waveguides to emerge at the left and right edges of the windshield or rear window. ''The invention frees up vehicle packaging space for other features...and maximizes audio performance while utilizing relatively inexpensive but efficient speakers.''—GLA

5,734,132

43.38.Ja CONCENTRIC TUBE SUSPENSION SYSTEM FOR LOUDSPEAKERS

Lucio Proni, Miramar, FL
31 March 1998 (Class 181/171); filed 19 July 1996

Assuming that the magnetic assembly is small enough to make this

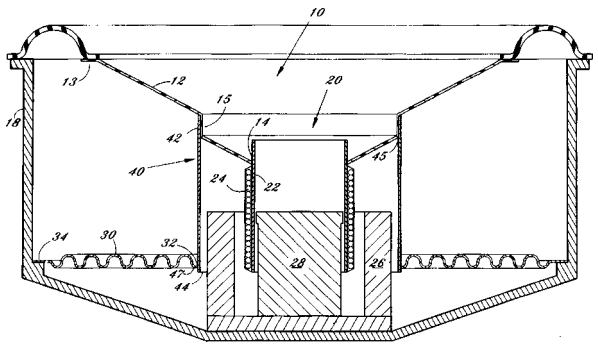

scheme practical, it certainly should suppress cone rocking modes.—GLA

5,734,728

43.38.Ja PORTABLE SOUND SPEAKER SYSTEM AND DRIVING CIRCUIT THEREFOR

Juergen P. Meissner, Randolph, NJ
31 March 1998 (Class 381/89); filed 30 November 1994

An upward-firing coaxial loudspeaker assembly is mounted in a vented box. The vent is formed by a peripheral slot around the bottom edge of the box. Sound from the loudspeaker assembly is conducted through a demountable vertical tube and emerges from its upper end. The tube can be of any suitable diameter and any desired length. Standing waves are suppressed by one or more internal ''diffuser screens.'' Vent output takes the form of a low-frequency ground wave which is said not to travel upward. ''As a result, the ground wave does not rise off the ground until it is much further

away from (the) speaker system, and thereby provides better impedance matching in the room in which (the) speaker system is situated, and also reduces the power necessary to drive the system.'' We live in an age where new acoustical principles are discovered every day.—GLA

5,737,435

43.38.Ja SOUND REPRODUCING APPARATUS COMPRISING AN ACOUSTIC HORN, AND ACOUSTIC HORN FOR USE IN THE APPARATUS

Gerrit F. M. De Poortere *et al.*, assignors to U.S. Philips Corporation
7 April 1998 (Class 381/156); filed in European Patent Office 23 December 1994

To save space in a TV set, side-firing stereo loudspeakers can be located near the rear with sound conducted to the front of the cabinet by short horns. Frequency response can be smoothed and extended by introducing a partial obstacle near the loudspeaker.—GLA

5,742,690

43.38.Ja PERSONAL MULTIMEDIA SPEAKER SYSTEM

Albert Durr Edgar, assignor to International Business Machines Corporation
21 April 1998 (Class 381/24); filed 28 June 1996

The text of the patent bubbles over with eagerness to tell about the marvelous features derived from two vertical loudspeaker arrays flanking a video screen. With suitable processing, the arrays are intended to perform three tasks: (1) reproduce audio program material, (2) operate as a sonar array to provide touch-screen capability, and (3) combine the first two functions to sense the user's location and generate virtual sound images accordingly. Because a line array is quite directional, sound is concentrated in a restricted listening area. Additional directionality and low-frequency enhancement are provided by an unusual rear waveguide. A front-to-back divider separates a variable impedance maze (upper left) from a slotted treble sheet (lower right). Apparently there is some kind of acoustic demon at the juncture of the two, guiding low frequencies into the maze while directing high frequencies to the treble slots. The low-frequency maze provides acoustic equalization by expanding its cross-sectional area at some points and restricting it at others. The rear-loading design will not function anything like the explanation given.—GLA

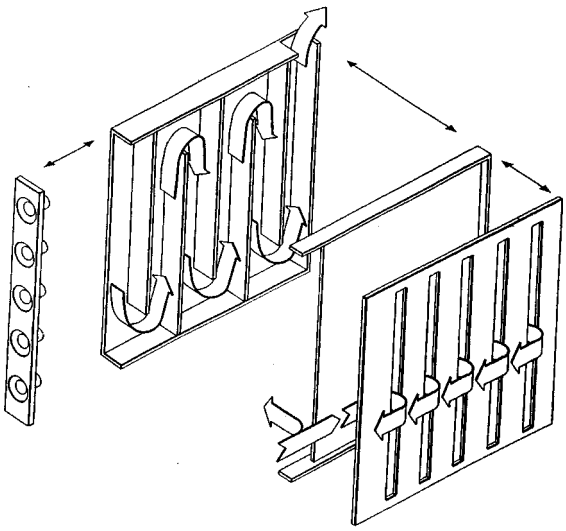

5,748,753

43.38.Ja HIGH POWER AUDIO SUBWOOFER

Robert W. Carver, Snohomish, WA
5 May 1998 (Class 381/96); filed 2 January 1996

An unusual loudspeaker is combined with a special power amplifier and a small enclosure to make a compact, high-power subwoofer system. An otherwise conventional cone suspension is designed for very long travel (more than 60 mm peak-to-peak). Voice coils **122** and **124** are alternately energized during positive and negative portions of the input waveform. In effect, this is a Class B loudspeaker. The coils are driven by separate positive and negative voltage tracking amplifiers that waste very little power regardless of signal level. The text of the patent is discursive and not always easy to follow, but there are more than 20 illustrations that clearly show various aspects of the design.—GLA

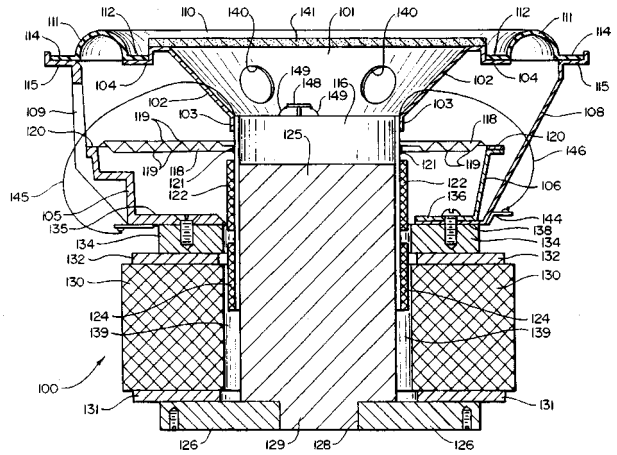

5,748,760

43.38.Ja DUAL COIL DRIVE WITH MULTIPURPOSE HOUSING

Douglas J. Button, assignor to Harman International Industries, Incorporated
5 May 1998 (Class 381/199); filed 12 February 1997

JBL's latest dual-coil woofer design is described in detail. The loudspeaker cone is driven by a dual voice coil structure which is combined with a small, neodymium magnet and a heat dissipating housing. The patent argues that this arrangement is able to produce more acoustic power per mass than a conventional transducer.—GLA

5,751,821

43.38.Ja SPEAKER SYSTEM WITH RECONFIGURABLE HIGH-FREQUENCY DISPERSION PATTERN

David L. Smith, assignor to McIntosh Laboratory, Incorporated
12 May 1998 (Class 381/90); filed 28 October 1993

Some professional monitor loudspeaker systems have mid- and high-frequency transducers mounted on a removable square panel. If the box must be rotated 90 degrees to fit available space, then the panel can also be rotated to maintain the desired high-frequency coverage pattern. That idea is clearly the basis for this patent, but what has actually been patented is not so clear.—GLA

5,745,586

43.38.Lc SOUND QUALITY CONTROL SYSTEM

Ryo Tagami and Mitsuhiko Serikawa, assignors to Matsushita Electric Industrial Company
28 April 1998 (Class 381/103); filed in Japan 25 April 1995

In the 1970's Richard Heyser published a series of papers suggesting methods of mapping measurable audio characteristics into alternative geometries. Why should audio controls be associated with frequency and level when we tend to evaluate music reproduction in subjective terms like ''dull'' or ''punchy?'' This patent discloses a fairly elaborate method for giving the user direct control over such characteristics—for example, three sliders labeled ''clarity,'' ''fullness,'' and ''beauty.''—GLA

5,747,753

43.50.Gf MUFFLER FOR AN INTERNAL COMBUSTION ENGINE, PARTICULARLY A SINGLE-ENGINE DIESEL ENGINE

Erich Eder, assignor to Motorenfabrik Hatz GmbH
5 May 1998 (Class 181/282); filed in Germany 15 July 1993

A silencer for a single-cylinder diesel engine is described in which exhaust gases exit through **2**. A baffle plate **5**, connected to a leaf spring **7**,

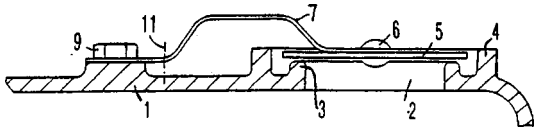

is designed to vibrate at the engine exhaust frequency. Means for turning the baffle plate are presented.—KPS

5,749,261

43.50.Gf NOISE INSULATION ARRANGEMENT FOR SHIFT LEVER

Youichi Numakami, assignor to Kinugawa Rubber Ind. Company
12 May 1998 (Class 74/18.1); filed in Japan 31 January 1995

An arrangement to reduce noise transmitted around an automobile gear

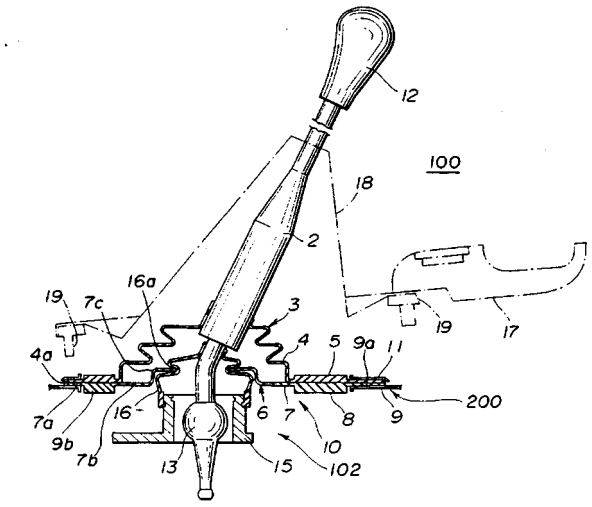

shift lever is described in which two resilient noise barriers are deployed.—KPS

5,758,497

43.50.Gf SILENCER

Svend Frederiksen and Lars Freeriksen, assignors to Silentor A/S
2 June 1998 (Class 60/229); filed in Denmark 19 May 1995

A combination muffler and catalytic converter for an internal combustion engine is described. Exhaust gas from the engine flows through duct **2**.

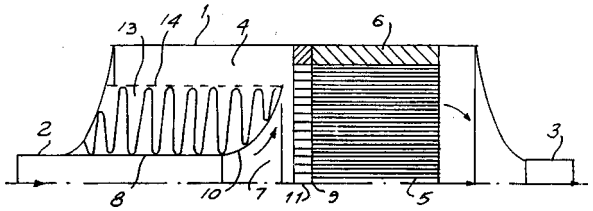

A diffuser section **7** distributes the gas across the catalyst **5**, and then exits through duct **3**. An acoustical compartment **4** contains mineral wool, held in place by a perforated pipe **14**.—KPS

5,758,614

43.50.Gf NOISE SUPPRESSION VANES IN THE INTAKE OF AN INTERNAL COMBUSTION ENGINE

Michael Choi, assignor to Ford Global Technologies, Incorporated
2 June 1998 (Class 123/184.53); filed 1 May 1997

This patent relates to noise generated from the air intake system of an internal combustion engine, specifically that caused by air flow around the butterfly valve in the throttle body. An air diffuser is placed downstream of the valve to diffuse and redirect the air flow to reduce the whooshing noise which occurs when the throttle is opened rapidly. Numerous variations of the diffuser geometry are described.—KPS

5,765,257

43.50.Gf MUFFLER

Christopher J. Steger *et al.*, assignors to Emerson Electric Company
16 June 1998 (Class 15/326); filed 1 August 1996

A muffler intended for use in wet/dry utility vacuum cleaners is described. Exhaust gases flow through pipe **15** into the muffler body for ab-

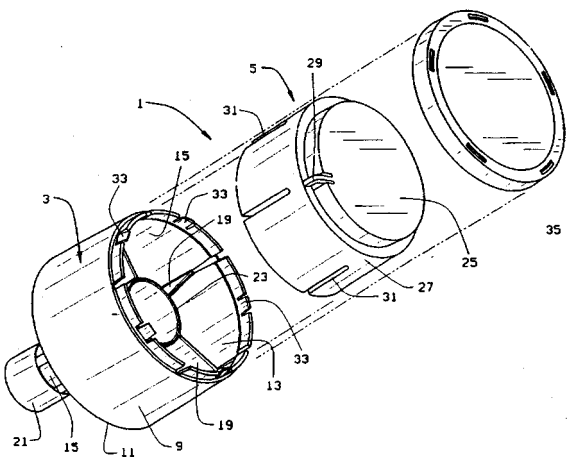

sorption by acoustical element **5**. The flow direction is reversed and exhaust gases exit through **11**.—KPS

5,768,778

43.50.Gf ONE-PIECE ENGINE INLET ACOUSTIC BARREL

Robert Elon Anderson and Charles A. Parente, assignors to Northrop Grumman Corporation
23 June 1998 (Class 29/888.01); filed 14 August 1996

An acoustical liner for the inlet of an aircraft turbofan engine is described. The liner is of a conventional type (perforated face sheet and honeycomb) but is constructed in a way which reduces the loss of absorption area due to splices between liner sections.—KPS

5,772,178

43.50.Gf ROTARY NOISE ATTENUATING VALVE

Roger Bey, assignor to Rotatrol AG
30 June 1998 (Class 251/127); filed 22 December 1995

An arrangement to reduce noise from rotary valves is described. Flow

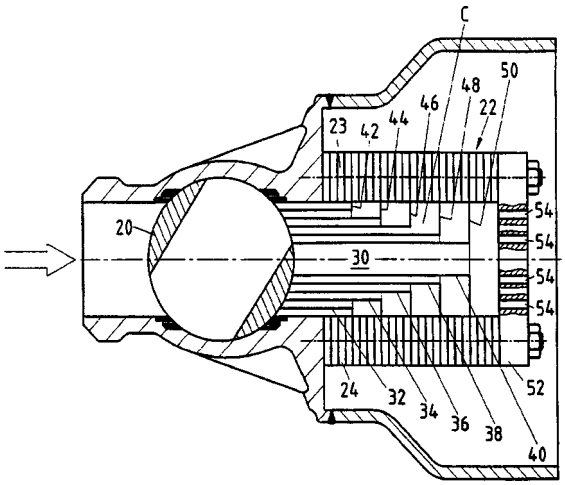

from a ball valve **20** passes through a multitude of passageways **24** such that more passageways are exposed as the valve is progressively opened.—KPS

5,765,800

43.50.Ki VIBRATION DAMPING APPARATUS

Katsuhide Watanabe *et al.*, assignors to Ebara Corporation
16 June 1998 (Class 248/550); filed in Japan 4 October 1995

An active vibration control system is described to suppress the effects of floor vibrations from reaching sensitive equipment located on an above-mount table. The static load of the table and equipment is supported by air springs, while horizontal positioning is achieved using relatively soft helical springs. Electromagnetic actuators in the vertical and horizontal directions are used to reduce relative motion across the air mounts and above mount motion.—RBC

5,765,817

43.50.Ki INTERFACE FOR VIBRATION REDUCTION IN STRUCTURAL-DYNAMIC SYSTEMS

Elmar Breitback, assignor to Deutsche Forschungsantalt Fur Luft-Und Raumfahrt
16 June 1998 (Class 267/136); filed in Germany 27 July 1995

An active interface device is described that may be useful in isolating, for example, a satellite from the vibrations caused by a starter rocket. The interfaces of concern are those in which large dynamic loads are transmitted in all directions between the structure and base unit. The axisymmetric device uses piezoelectric actuators together with a central tubular passive component to control forces transmitted along the symmetry axis and rotations about the transverse axes. The tubular component is relatively compliant in the length direction, yet stiff in the transverse directions to minimize shear forces acting on the actuators.—RBC

5,765,851

43.50.Ki VARIABLE TUNED HELMHOLTZ RESONATOR WITH LINEAR RESPONSE CONTROLLER

Ian McLean, assignor to Siemens Electric Limited
30 June 1998 (Class 123/184.57); filed 29 July 1997

A method is described for implementing a variably tuned Helmholtz resonator to reduce noise from the duct of an induction system for an internal combustion engine. A cylindrical component in contact with the fluid medium in the duct is rotated as a function of engine speed. Due to the geometric configuration of the inside of the cylindrical component, rotations modify the acoustic mass and stiffness of the resonator such that the resonance frequency is linearly related to the angle of rotation.—RBC

5,775,715

43.50.Ki PIEZOELECTRIC DAMPER FOR A BOARD SUCH AS A SNOW SKI OR SNOWBOARD

James Vandergrift, assignor to K-2 Corporation
7 July 1998 (Class 280/602); filed 1 August 1995

Piezoelectric actuators are used to reduce the resonant vibrations (flexural and torsional) of snow skis and snowboards. Used in a passive mode, the vibrational energy is converted to electrical energy via the piezoelectric transducer, and is dissipated through a resistance. Alternatively, the piezoelectric can be actuated in response to a signal from a vibration sensor also mounted on the ski or snowboard. In this mode, the system acts to suppress vibrations rather than adding damping.—RBC

5,778,081

43.50.Ki ACTIVE NOISE CONTROL USING PHASED-ARRAY ACTIVE RESONATORS

William Patrick, Glastonbury, CT
7 July 1998 (Class 381/71.5); filed 4 March 1996

Several ideas are presented to control sound propagation in ducts by mechanically or electrically phasing the actuation along the duct to account for propagation delay. Single and multiple actuator approaches are described with the intent of providing a phased array of actuation derived from a common actuation signal. The control scheme follows the traditional feedforward approach of incorporating reference and residual sensors to characterize the incident and controlled sound fields.—RBC

5,791,869

43.50.Ki NOISE KILLING SYSTEM OF FANS

Seungbae Lee, assignor to Samsung Electronics Company
11 August 1998 (Class 415/119); filed 6 February 1996

This patent describes the use of micro-electromechanical (MEMs) technology for controlling the unstable airflows along the body of a fan blade. The thin-film MEMs device is mounted to the fan blade, and includes a sensor, actuator, and integrated circuit. The approach is said to be useful in reducing sound radiation when operated to reduce unsteady airflows, or as a heat exchanger when operated to increase unsteady air flows.—RBC

5,791,875

43.50.Ki TIP VORTEX REDUCTION SYSTEM

Hieu Thien Ngo, assignor to McDonnell Douglas Helicopter Company
11 August 1998 (Class 416/90); filed 10 September 1996

An active control device is disclosed for modifying a tip vortex on a rotorcraft blade or aircraft foil to reduce blade-vortex interaction noise. The active control device includes a fluid source to provide a positive pressure of fluid, such as air, to the interior of the lifting body. In addition, a fluid router is used to direct a portion of the positive pressure of fluid out of the interior of the lifting body in a direction towards the surface on the body experiencing positive pressure. The purpose of introducing this controlled flow is to oppose or attenuate the natural flow of fluid from the positive to the negative pressure generating surfaces that result in tip vortices. Another aspect of the device is that it operates only when a positive pressure is detected on the positive-pressure-generating surface of the lifting body.—RBC

5,792,948

43.50.Ki ACTIVE VIBRATION CONTROL APPARATUS FOR VEHICLE

Kazushige Aoki *et al.*, assignors to Nissan Motor Company
11 August 1998 (Class 73/116); filed in Japan 10 April 1996

An active engine mount system is described to reduce passenger compartment vibration when the vehicle is moving, and to reduce vehicle body vibration when the vehicle is stopped. Details of an active/passive engine mount are presented. The device uses electromagnetic actuation in parallel with fluid-filled cavities. The porting between cavities provides for damping of high-amplitude, low-frequency motions, and active control of low-amplitude, high-frequency motions.—RBC

5,796,849

43.50.Ki ACTIVE NOISE AND VIBRATION CONTROL SYSTEM ACCOUNTING FOR TIME VARYING PLANT, USING RESIDUAL SIGNAL TO CREATE PROBE SIGNAL

Ronald Coleman, Bill Watters, and Roy Westerberg, assignors to Bolt Beranek and Newman, Incorporated
18 August 1998 (Class 381/71.8); filed 8 November 1994

A method is described for generating probe signals for the purpose of on-line (i.e., concurrent) system identification in active noise and vibration control systems that are subject to time-varying disturbances and/or plant transfer functions between actuators and sensors. The approach uses the spectral characteristics of the residual sensor response, together with shaping filters related to the plant transfer functions, to generate probe signals that are added to the actuator drive signal for the purpose of identifying changes in the plant over time. The contribution of the probe signal at the residual sensor is uniformly below the measured magnitude of the residual by a prescribed amount over the frequency range involved for system identification. As such, the probe signal strength is maximized over frequency in response to both temporal changes in the disturbance spectrum and plant transfer functions.—RBC

5,749,546

43.50.Nm METHOD AND APPARATUS FOR REDUCING AIRFRAME AEROSOUND

Anthony M. Blackner and Thomas A. Zierten, assignors to The Boeing Company
12 May 1998 (Class 244/215); filed 10 July 1995

Air flow over and around the trailing edge control surfaces of an aircraft wing generates noise. An arrangement is described in which a conventional, blunt flap side edge is replaced with a rounded edge which reduces noise in the middle and high-frequency ranges.—KPS

5,775,095

43.50.Nm METHOD OF NOISE SUPPRESSION FOR A TURBINE ENGINE

Steven H. Zysman *et al.*, assignors to United Technologies Corporation
7 July 1998 (Class 60/204); filed 20 December 1996

This patent relates to a method to reduce jet noise from low by-pass ratio engines. A multi-lobed mixer is described in which each major lobe contains a pair of minor lobes. These minor lobes are said to promote greater mixing between the core flow and fan by-pass flow.—KPS

5,768,836

43.55.Ti HEAT AND SOUND TRANSMISSION ATTENUATED FRAMING STRUCTURE, PARTICULARLY DOOR OR WINDOW FRAMING

Otto Bachmann, assignor to Sunshine Engineering AG
23 June 1998 (Class 52/204.51); filed in Switzerland 21 November 1995

This is a modified (simplified) variation of an earlier patent that incorporates only two profiled metal rails, joined by a chambered plastic strip. It is said that the system will improve the ability of the framing to reduce heat and sound transfer through the frame of a door or window, and to do so at less cost than before.—CJR

5,777,279

43.55.Ti SOUND ATTENUATING STRUCTURE

Marray M. Parker and Arthur J. Hustins, Jr., Nova Scotia, Canada
7 July 1998 (Class 181/287); filed 5 December 1995

This patent is for a sound attenuating structure such as an acoustical door or infill partition. The structure comprises metal panels on the outsides; these panels are stiffened with diagonal ribs that are placed in a mathematically calculated triangular arrangement, designed to eliminate panel resonances below 1500 Hz. There is a spring connection between the panels (maybe a silicone sealant), and insulation in the cavity, and maybe or maybe not a septum. The approach is designed to make the panel a nearly inert mass.—CJR

5,751,903

43.72.Ar LOW RATE MULTI-MODE CELP CODEC THAT ENCODES LINE SPECTRAL FREQUENCIES UTILIZING AN OFFSET

Kumar Swaminathan and Murthy Vemuganti, assignors to Hughes Electronics
12 May 1998 (Class 395/2.39); filed 19 December 1994

This code-excited linear prediction (CELP) vocoder converts LP spectral coefficients to line spectral frequency domain and then classifies each speech frame as voiced, unvoiced, or noise. The classification determines the methods used for scalar and vector quantization. For voiced segments, backward prediction is used to improve and simplify processing of the gain coefficient.—DLR

5,751,905

43.72.Ar STATISTICAL ACOUSTIC PROCESSING AND APPARATUS FOR SPEECH RECOGNITION USING A TONED PHONEME SYSTEM

Chengjun Julian Chen *et al.*, assignors to International Business Machines Corporation
12 May 1998 (Class 395/2.63); filed 15 March 1995

Intended for the strongly CV-structured and tonal Chinese language, this speech analyzer represents each syllable as a sequence of phonetic elements, called premes, and tone-bearing elements, called tonemes. A pitch analyzer extracts pitch values for each toneme, which are then classified into one of five Chinese tone patterns and used for syllable segmentation. The system is intended for use with a typical hidden Markov model decoder.—DLR

5,751,904

43.72.Bs SPEECH RECOGNITION SYSTEM USING NEURAL NETWORKS

Mitsuhiro Inazumi, assignor to Seiko Epson Corporation
12 May 1998 (Class 395/2.41); filed in Japan 18 June 1992

This speech recognizer is trained with the speech of many speakers by training a separate neural network with each individual voice pattern. During recognition, each network receives the acoustic feature vectors, producing its own recognized output along with an adaptation judgment. The network with the highest adaptation judgment is selected as having the best match to the speaker.—DLR

5,758,021

43.72.Bs SPEECH RECOGNITION COMBINING DYNAMIC PROGRAMMING AND NEURAL NETWORK TECHNIQUES

Heidi Hackbarth, assignor to Alcatel N.V.
26 May 1998 (Class 395/2.41); filed 12 June 1992

The use of a neural network for isolated word recognition provides advantages of good accuracy and robustness in noisy environments, but adding new vocabulary items often involves retraining the entire existing

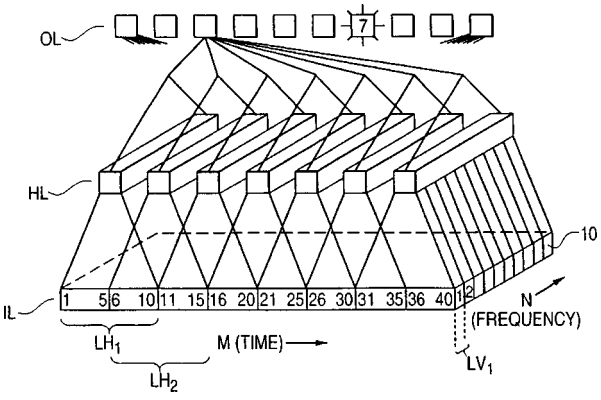

vocabulary. This patent overcomes that problem by using a common dynamic programming technique to provide immediate results with new items while simultaneously using the new items to start retraining a new neural network component.—DLR

5,758,022

43.72.Bs METHOD AND APPARATUS FOR IMPROVED SPEECH RECOGNITION FROM STRESS-INDUCED PRONUNCIATION VARIATIONS WITH A NEURAL NETWORK UTILIZING NON-LINEAR IMAGING CHARACTERISTICS

Michael Trompf and Heidi Hackbarth, assignors to Alcatel N.V.
26 May 1998 (Class 395/2.41); filed in Germany 6 July 1993

A method is described for expanding the range of patterns recognized by a speech recognizer to include variations such as phonetic changes induced by environmental stress (Lombard effects), dialectal variations, or

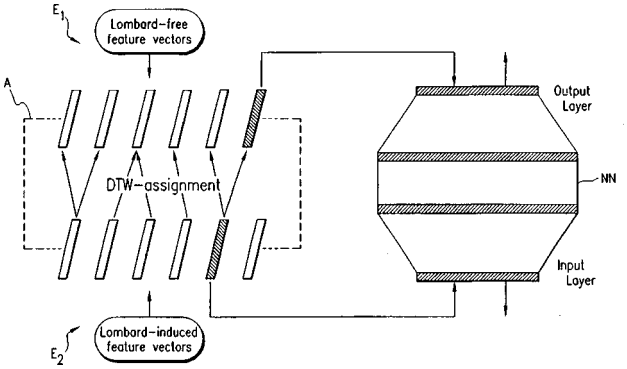

other such variations. A neural network is used to construct a mapping between features of the original primary pattern and features of the altered patterns. The mappings are referred to as nonlinear imaging methods.—DLR

5,752,226

43.72.Dv METHOD AND APPARATUS FOR REDUCING NOISE IN SPEECH SIGNAL

Joseph Chan and Masayuki Nishiguchi, assignors to Sony Corporation
12 May 1998 (Class 704/233); filed in Japan 17 February 1995

This noise reduction system uses energy changes, spectral analysis, and zero crossings to locate consonants in the speech signal. During consonant sounds, the adaptation to background noise characteristics is disabled, preventing the consonant sounds from altering the noise representation and saving some computation in the process.—DLR

5,765,134

43.72.Ew METHOD TO ELECTRONICALLY ALTER A SPEAKER'S EMOTIONAL STATE AND IMPROVE THE PERFORMANCE OF PUBLIC SPEAKING

Thomas David Kehoe, Monte Sereno, CA
9 June 1998 (Class 704/270); filed 15 February 1995

The patented device will alter a speech sound in many ways, including pitch change, delay, modulation, reverberation, chorus, flanging, rapid binaural alternation, and others. It is said that when a person hears his or her own voice in a headset with certain of such changes while speaking publicly, the result can be induced changes of perception by the speaker which can directly affect the speaker's attitude and, thereby, the performance.—DLR

5,754,974

43.72.Gy SPECTRAL MAGNITUDE REPRESENTATION FOR MULTI-BAND EXCITATION SPEECH CODERS

Daniel W. Griffin and John C. Hardwick, assignors to Digital Voice Systems, Incorporated
19 May 1998 (Class 704/206); filed 22 February 1995

In a multi-band excitation (MBE) vocoder, the speech signal is represented by sets of coefficients giving magnitude and voicing information for each of a number of harmonics of the pitch frequency. In this variation on the MBE design, harmonic magnitudes are still individually coded, but the voicing information is compressed by having each voicing indicator cover all of the harmonics which fall within one of several predetermined frequency bands.—DLR

5,761,633

43.72.Gy METHOD OF ENCODING AND DECODING SPEECH SIGNALS

Byung-goo Kong, assignor to Samsung Electronics Company
2 June 1998 (Class 704/219); filed in Republic of Korea 30 August 1994

This linear prediction vocoder uses two LP stages, but does not consider the second stage to be a pitch predictor in the usual sense. The residual from the first stage is low-pass filtered to 2 kHz and then processed by the

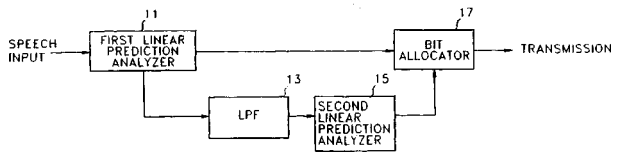

second LP stage. The intent is that additional tonal components in the low-frequency ranges important to voice quality would be captured by the second stage.—DLR

5,751,907

43.72.Ja SPEECH SYNTHESIZER HAVING AN ACOUSTIC ELEMENT DATABASE

Bernd Moebius *et al.*, assignors to Lucent Technologies, Incorporated
12 May 1998 (Class 395/2.76); filed 16 August 1995

In the most common method of speech synthesis today, phonetic patterns are reconstructed from stored segments of human speech, joined to build up the synthetic phonetic sequence. This patent describes a method of locating the cut points based on formant trajectories. The figure shows a

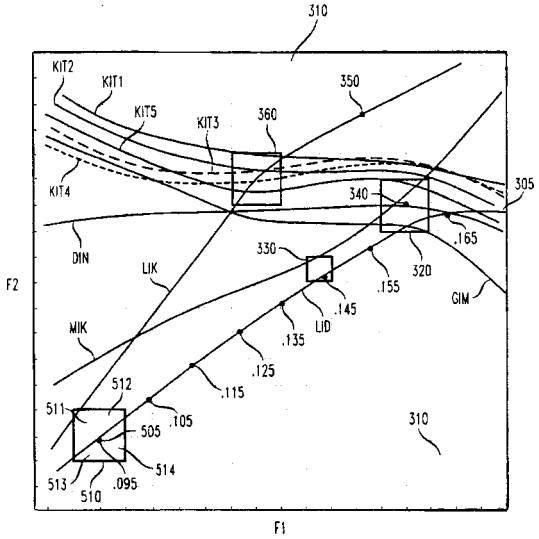

small part of the $F1-F2$ space including areas called tolerance regions, which are traversed by many trajectories. By cutting at these points, a large variety of cut segments may be smoothly recombined.—DLR

5,752,229

43.72.Kb INTELLIGENT NEAR-END SPEECH DETECTION

Donald Lars Duttweiler *et al.*, assignors to Lucent Technologies, Incorporated
12 May 1998 (Class 704/270); filed 28 June 1996

This telephone system near-end speech presence detector uses the line echo signal and accumulated information about the echo delay and spectral structure to aid in the accurate detection of near-end speech, specifically to be able to distinguish between near-end and far-end speech signals.—DLR

5,752,227

43.72.Ne METHOD AND ARRANGEMENT FOR SPEECH TO TEXT CONVERSION

Bertil Lyberg, assignor to Telia AB
12 May 1998 (Class 704/235); filed in Sweden 10 May 1994

The patent describes a speech recognition system based on linguistic theory rather than on statistical search techniques. The weak point is, without doubt, the assumption that a unique phonetic sequence can be extracted from the speech signal. Given the phonetic sequence, prosodic, syntactic, semantic, and other constraints are used to eliminate various alternate interpretations of the phonetic sequence until a single ''decoding'' remains.—DLR

5,754,972

43.72.Ne SPEECH RECOGNITION SYSTEM FOR LANGUAGES WITH COMPOUND WORDS

James K. Baker *et al.*, assignors to Dragon Systems, Incorporated
19 May 1998 (Class 704/200); filed 6 March 1992

The complexity of speech recognition in languages such as English and German, which have large numbers of compound words, may be significantly reduced if such words are handled as combinations of their root forms rather than as whole words. An example is given in which adding the item ''thermo'' to the recognizer vocabulary also adds words such as thermoregulatory, requiring only the addition of some logic to detect and recombine such forms after recognition.—DLR

5,754,978

43.72.Ne SPEECH RECOGNITION SYSTEM

Ivan Perez-Mendez *et al.*, assignors to Speech Systems of Colorado, Incorporated
19 May 1998 (Class 704/255); filed 27 October 1995

The patent describes a kind of voting procedure in which the text outputs of multiple speech recognizers are compared and identical portions accepted while differing portions are rejected. Similar systems have been described in which recognition scores are compared, however this requires that the scoring systems are of a comparable nature or can be converted so as to be comparable. This system avoids that requirement by looking directly at the decoded text outputs, allowing comparison of outputs from completely different types of recognition systems.—DLR

5,764,851

43.72.Ne FAST SPEECH RECOGNITION METHOD FOR MANDARIN WORDS

Chung-Mou Pengwu, assignor to Industrial Technology Research Institute
9 June 1998 (Class 395/2.51); filed 24 July 1996

This speech recognizer, designed especially for Mandarin Chinese, uses a two-stage hidden Markov model decoder. Each HMM stage deals primarily with a specific portion of the syllable. The primary advantage cited is a reduction in required computing power, but an added benefit pertains to a common tendency attributed to native speakers to elide or mispronounce syllable-initial consonants.—DLR

5,764,853

43.72.Ne VOICE RECOGNITION DEVICE AND METHOD USING A GUARANTEED GLOBAL MINIMUM (GGM) MAPPING

Masao Watari *et al.*, assignors to Sony Corporation
9 June 1998 (Class 395/2.52); filed in Japan 27 October 1994

It is known that hidden Markov models which use single Gaussian probability distributions do not provide a good fit to the acoustic feature vectors in many speech situations. The usual solutions are to use either

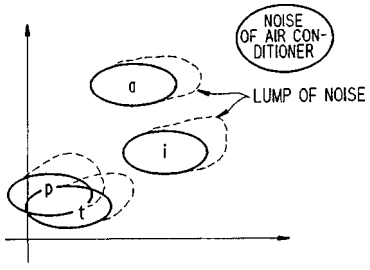

continuous distributions or mixtures of multiple Gaussians. Either form requires a considerable increase in memory and computation. This method instead performs a mapping of the multi-dimensional feature set, said to be better fit by a single Gaussian distribution.—DLR

5,548,564

43.80.Vj MULTI-LAYER COMPOSITE ULTRASONIC TRANSDUCER ARRAYS

S. W. Smith, assignor to Duke University
20 August 1996 (Class 367/140); filed 13 April 1994

A small, high-frequency, transducer array, particularly for biomedical ultrasonic imaging applications, is realized as a multilayer assembly where each layer comprises a two-dimensional gridlike array of thin, rectangular, piezoceramic elements. The piezoceramic layers are separated by electrode layers. The piezoceramic elements of the numerous layers are electrically connected in parallel by a number of vias that only allow connection to alternate electrode layers. The number of elements on each layer could be of the order of 1000. The impedance of these small elements is therefore maintained at a reasonable value because the piezoceramic layers are thin and the capacitances of the several layers are connected in parallel. The electrical and mechanical independence of the many elements allows for beam tilting in two orthogonal directions.—WT

5,779,641

43.80.Vj METHOD AND APPARATUS FOR THREE-DIMENSIONAL ULTRASOUND IMAGING BY PROJECTING FILTERED PIXEL DATA

William Thomas Hatfield and Harvey E. Cline, assignors to General Electric Company
14 July 1998 (Class 600/443); filed 7 May 1997

Ultrasonic *b*-scan or colorflow images of successive planes are stored. After smoothing to reduce speckle, pixel data in the volume of interest are projected onto a number of rotated image planes using a ray-casting technique. The data are further smoothed and then projected onto each successive image plane.—RCW

5,782,766

43.80.Vj METHOD AND APPARATUS FOR GENERATING AND DISPLAYING PANORAMIC ULTRASOUND IMAGES

Lee Weng *et al.*, assignors to Siemens Medical Systems, Incorporated
21 July 1998 (Class 600/443); filed 19 November 1996

Consecutive ultrasonic image frames are correlated to derive transducer motion information. Compound images are then formed using the motion information. A region of an image may be enlarged and color-coded velocity or power information may be superimposed on the image.—RCW

5,785,051

43.80.Vj SIGNAL GENERATING ENDOTRACHEAL TUBE APPARATUS

Randolph B. Lipscher and Jack G. Mottley, assignors to University of Rochester
28 July 1998 (Class 128/207.15); filed 21 June 1996

In a flexible tube that extends from the subject's oral or nasal cavity to within the trachea, an ultrasonic transducer is connected near the distal end and makes contact with the subject's trachea. A second transducer is placed on the skin of the subject's neck. By pulsing on one of the transducers and receiving on the other of the transducers, the position of the tube in the neck is determined.—RCW

5,785,654

43.80.Vj ULTRASOUND DIAGNOSTIC APPARATUS

Kazuhiro Iinuma *et al.*, assignors to Kabushiki Kaisha Toshiba
28 July 1998 (Class 600/441); filed in Japan 21 November 1995

The velocity of echos in each of a number of segments in an ultrasonic beam is determined. The position of at least one segment is tracked using this velocity instead of a change in brightness. In this way, the accuracy of tracking can be improved.—RCW

5,785,655

43.80.Vj TWO-DIMENSIONAL ULTRASOUND DISPLAY SYSTEM

Leonard James Goodsell, Jr. *et al.*, assignors to Acuson Corporation
28 July 1998 (Class 600/441); filed 24 March 1997

A line of study is defined by two or more icons placed on a two-dimensional motion image. At each point along the line of study, a velocity profile or estimated spectrum is displayed. The displayed motion parameters are computed using user-selected direction angles.—RCW

Acoustic scattering and the spectrum of atmospheric turbulence[a)]

D. Keith Wilson
U.S. Army Research Laboratory, ATTN: AMSRL-IS-EE, 2800 Powder Mill Road, Adelphi, Maryland 20783

James G. Brasseur
Department of Mechanical Engineering, Pennsylvania State University, University Park, Pennsylvania 16802

Kenneth E. Gilbert
Applied Research Laboratory and the Graduate Program in Acoustics, Pennsylvania State University, State College, Pennsylvania 16804

(Received 16 November 1997; revised 1 September 1998; accepted 4 September 1998)

Some issues regarding atmospheric turbulence modeling and its role in acoustic scattering calculations are discussed. Discrepancies between turbulence spectral models appearing in the acoustical and in the atmospheric sciences literature are noted, and it is argued that these discrepancies can be understood by recognizing that the acoustic wavelength and scattering geometry combine to act as an ''acoustic filter'' which selects a specific part of the turbulence spectrum. A particular model spectrum can yield satisfactory acoustic scattering predictions if it fits the actual spectrum well at the acoustically filtered turbulence scales, even if the model is a poor overall representation of the turbulence spectrum. Proper interpretation of length scales determined by fitting two-point correlation functions, and the importance of averaging times in estimating variances, are also discussed in relation to the action of the acoustic filter. © *1999 Acoustical Society of America.* [S0001-4966(98)03512-7]

PACS numbers: 43.10.Ln, 43.28.Fp [LCS]

INTRODUCTION

The important role played by turbulence in the propagation of sound waves through the atmosphere is now widely recognized. As a result there has been much discussion in recent years within the outdoor sound propagation research community regarding how to best represent the atmospheric turbulence, and thereby accurately predict its effects on the scattered acoustic field. The prominent issues concern both the appropriate spectral model for the turbulence (e.g., Gaussian, Kolmogorov, or von Kármán), as well as appropriate values for parameters such as the variances, length scales, and structure-function parameters (e.g., Refs. 1–13).

Resolution of these turbulence modeling issues would be straightforward if the inertial subrange alone had significant effects on the propagation: Kolmogorov[14] long ago developed universal statistical scalings for the inertial subrange, and these were subsequently applied to wave propagation by Tatarskii[15] and others. The difficulty is that sound waves propagating through the atmosphere, particularly at frequencies low in the audible range, are strongly affected by the large-scale motions of the energy-containing subrange. Statistical characterization of the large scales is not universal, depending on the details of the mean velocity and density profiles, as well as the boundary conditions. Generally, anisotropy and inhomogeneity of the turbulence structure must be considered.

[a)]''Selected research articles'' are ones chosen occasionally by the Editor-in-Cheif that are judged (a) to have a subject of wide acoustical interest, and (b) to be written for understanding by broad acoustical readership.

I. THE SPECTRUM OF ATOMOSPHERIC TURBULENCE

Much of the confusion concerning turbulence and scattering models can be resolved, in our view, by focusing on some well-known empirical facts about atmospheric turbulence structure, and by keeping clear the distinction between *actual* and *modeled* characteristics of the turbulence. Only characteristics of the turbulence that contribute significantly to a given scattering process need be modeled well.[16]

To elucidate these points, consider first Fig. 1, which shows some features of a turbulence spectrum in a high Reynolds-number flow such as the atmospheric boundary layer. Each of the three primary spectral subranges, the *energy-containing* (or *source*), the *inertial*, and the *dissipation*, can be characterized by its own length scale.

In the atmospheric boundary layer, the characteristic length scale of motions in the energy-containing subrange is the integral length scale, defined by

$$\mathscr{L}=\frac{1}{\sigma^2}\int_0^\infty R(r)dr, \tag{1}$$

where σ^2 and $R(r)$ are the variance and autocorrelation of a velocity component or temperature, and r is the spatial displacement. The integral length scale is essentially equivalent to the ''outer scale'' used in the wave propagation literature.[17] Kolmogorov's inertial-subrange scaling applies only to turbulence scales much smaller than $\mathscr{L}$.[14,17] However, there is no universal value for $\mathscr{L}$ in the atmosphere: the integral length scale varies tremendously with atmospheric conditions, the height from the ground, the terrain topology,

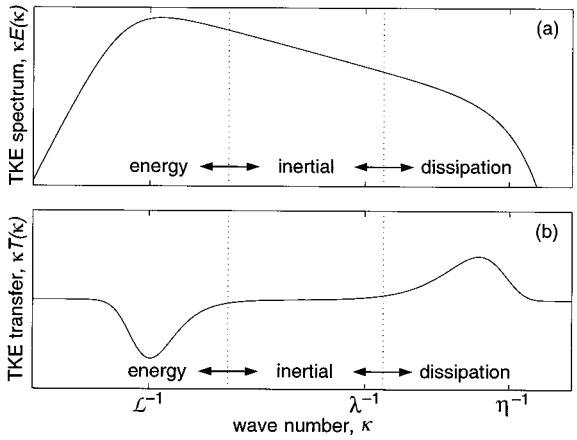

FIG. 1. Spectral view of the three subranges of high-Reynolds-number turbulence and the corresponding length scales. (a) Turbulent kinetic energy (TKE) spectrum (log abscissa scale, log ordinate scale). The quantity plotted is the weighted and normalized spectrum, $\kappa E(\kappa)/\sigma^2$, where $E(\kappa)$ is the TKE per unit mass. (b) TKE spectral transfer (log abscissa scale, linear ordinate scale). The quantity plotted is $\kappa T(\kappa)$, where $T(\kappa)$ is the net energy transfer from wave number κ to all other wave numbers. The behavior of $T(\kappa)$ implies that the energy input is in the energy subrange, and the loss is in the dissipation subrange.

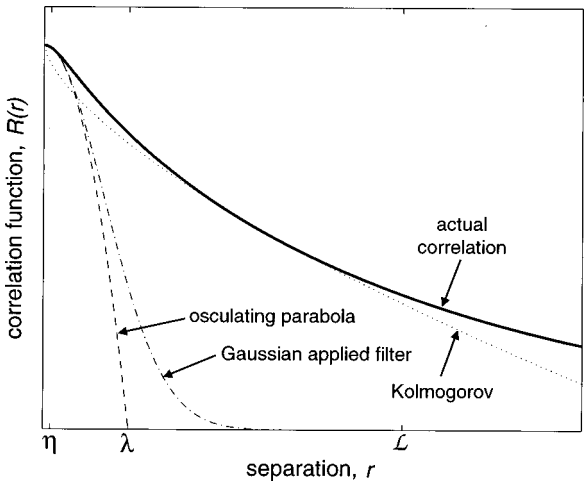

FIG. 2. Schematic of the autocorrelation $R(r)$ for velocity fluctuations in moderate Reynolds number turbulence (thick solid line), with the osculating parabola [Eq. (3)] that defines the Taylor microscale λ (dashed line). Also shown are the Gaussian applied filter using the Taylor microscale as the length scale (dashed), and Kolmogorov's inertial-subrange theory (dotted). (The abscissa and ordinate are both linear scales.)

the orientation of the displacement in the autocorrelation, and the particular variable of interest, e.g., turbulent fluctuations of temperature, horizontal velocity, or vertical velocity.

Table I in Wilson and Thomson[11] provides a summary of measurements of integral length scales and other similar quantities for atmospheric turbulence. Perhaps the most widely accepted and cited measurements are from the Kansas and Minnesota experiments, as first presented and analyzed by Kaimal *et al.*[18–20] Højstrup[21] developed a spectral model based on these data and empirically determined peak wavelengths for the spectra. These peak wavelengths are close in value to the integral length scales. Højstrup found that the peak wavelength for the near-ground horizontal velocity in the direction of the wind, λ_{mu}, varied in the range $0.02z_i < \lambda_{mu} < z_i$, where z_i is the height of the boundary-layer capping inversion (typically 500 to 2000 m during the daytime). According to this result, the integral length scale of horizontal velocity fluctuations can vary from meters to kilometers, depending on the height and atmospheric conditions. The shorter values occur when production of turbulence is dominated by wind shear (near neutral conditions), while the larger values occur when buoyant production is comparable to or larger than shear production (moderately to fully convective conditions).[20]

Whereas the integral length scale $\mathscr{L}$ is the characteristic length scale of the largest, most energetic, and least dissipative motions, the *Kolmogorov microscale* η is characteristic of the smallest, most dissipative, and least energetic motions. By definition, $\eta=(\nu^3/\epsilon)^{1/4}$, where ν is the kinematic viscosity of air and ϵ is the mean dissipation rate of turbulent kinetic energy. In atmospheric turbulence, η is of order 1 to 10 mm, many orders of magnitude smaller than $\mathscr{L}$.

The inertial subrange consists of turbulent motions having scales r between $\mathscr{L}$ and η ($\mathscr{L} \gg r \gg \eta$). The Taylor microscale λ falls within the inertial subrange and is given in isotropic turbulence by[17]

$$\lambda^2 = 15\nu\frac{\sigma_u^2}{\epsilon}, \tag{2}$$

where σ_u^2 is the variance of a turbulent velocity component. In high Reynolds number flows such as the atmospheric boundary layer, scaling arguments indicate that $\mathscr{L}/\eta \sim R_{\mathscr{L}}^{3/4}$ and $\lambda/\eta \sim R_{\mathscr{L}}^{1/2}$, where $R_{\mathscr{L}}=\sigma_u\mathscr{L}/\nu$ is the Reynolds number defined using the integral length scale of the velocity component. Hence $\mathscr{L} \gg \lambda \gg \eta$ in high Reynolds number turbulence. Another important interpretation of the Taylor microscale, which we shall refer to below, is given by expanding the autocorrelation as a Taylor series:[22]

$$R(r) \simeq \sigma_u^2(1-r^2/\lambda^2) + \ldots . \tag{3}$$

As illustrated in Fig. 2, the first term in Eq. (3) defines an osculating parabola with its vertex at the peak of the correlation curve; λ is the distance to the point where the parabola intersects the abscissa. Therefore the inertial subrange scale λ is a measure of the curvature of the autocorrelation at $r=0$. This local curvature increases with increasing Reynolds number, so that λ becomes smaller in comparison to $\mathscr{L}$ as $R_{\mathscr{L}}$ is increased.

II. ACOUSTIC SCATTERING AND DETERMINATION OF SPECTRAL PARAMETERS

It is apparent that atmospheric turbulence spans a very broad range of spatial scales, from millimeters to kilometers. No one model exists to accurately describe the entire turbulence spectrum in all flows. Only the spectrum in the inertial subrange can be regarded as universal and well defined. Given these difficulties in accurately modeling the entire spectrum, it is important to know which portion of the spectrum contributes significantly in a given acoustic propagation problem.

The dissipation subrange can generally be ignored for the prediction of acoustic propagation. For most frequencies within the audible range, the motions in the dissipation sub-

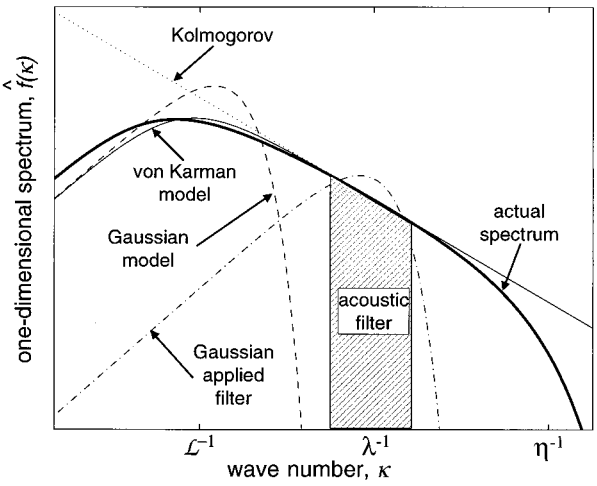

FIG. 3. Comparison of the von Kármán spectral model (thin solid line), the Gaussian spectral model (dashed), a Gaussian applied filter (dash-dot), and the Kolmogorov inertial-subrange spectrum (dotted), to an ''actual'' turbulence spectrum (thick solid). The values used for the integral length scale and the variance in the Gaussian applied filter are one-tenth and one-fifth, respectively, the values used in the von Kármán and Gaussian spectra. The cross-hatched region is meant to indicate the turbulence scales that are most important in a hypothetical scattering experiment, where the Gaussian applied filter may satisfactorily approximate the actual spectrum.

range are very small compared to the acoustic wavelength and hence unimportant. Therefore the energy-containing and inertial subranges of atmospheric turbulence play the primary role. Broadly speaking, the large-scale, energetic motions in the atmospheric boundary layer drive acoustic phase fluctuations, while smaller-scale motions with sizes on order of the acoustic wavelength drive the amplitude fluctuations.[11,23] However, the interplay between the propagation geometry, refraction, scattering, and acoustic wavelength often complicates this idealized picture.

The propagation geometry and acoustic frequency combine to create a filter that selects a specific part of the turbulence spectrum participating in the scattering. (The significant part of the spectrum can often be determined using simple Bragg scattering arguments.[24]) Only this filtered part of the spectrum needs to be modeled accurately to predict scattering. If the acoustically filtered part of the spectrum is very narrow, the choice of a spectral model is not so important, so long as the model agrees reasonably well with the actual turbulence spectrum *within the band of acoustically selected scales*. We call a spectral model that is employed in this manner an ''applied filter,'' as opposed to a rigorous model intended for a broad region of the spectrum. Any of the popular spectral model forms (e.g., Gaussian, Kolmogorov, or von Kármán) can be utilized as an applied filter, and can yield predictions of acoustic scattering levels in reasonable agreement with measurements, as long as the parameters of the applied filter yield good agreement with the actual spectrum at scales coincident with the acoustic filter. The parameters of the applied filter do not necessarily agree well with the actual spectrum. Previous applications of the Gaussian model for the energy spectrum to acoustic propagation (e.g., Refs. 2–4, 6, 9, 25, 26) have actually used it as an ''applied filter'' rather than a rigorous model for the spectrum. As we shall discuss, this observation helps to explain the discrepancies between the spectral models used in acoustics and those determined by boundary-layer meteorologists.

We illustrate this point graphically in Fig. 3, where one-dimensional von Kármán and Gaussian spectral models, a Gaussian applied filter, and the Kolmogorov inertial-subrange spectrum are compared to an idealized ''actual'' spectrum. The one-dimensional von Kármán model spectrum is given by

$$\hat{f}_V(\kappa)=\frac{\Gamma(5/6)}{\sqrt{\pi}\Gamma(1/3)}\frac{\sigma^2\ell_V}{(1+\kappa^2\ell_V^2)^{5/6}}, \tag{4}$$

where $\ell_V=\mathscr{L}\Gamma(1/3)/\sqrt{\pi}\Gamma(5/6)=1.34\mathscr{L}$ is the length scale parameter defining the energy-containing subrange. The Gaussian model spectrum is the Fourier transform of $R(r)=\sigma^2\exp(-r^2/\ell_G^2)$, which is

$$\hat{f}_G(\kappa)=\frac{\sigma^2\ell_G}{2\sqrt{\pi}}\exp\left(-\frac{\kappa^2\ell_G^2}{4}\right). \tag{5}$$

The Gaussian model was originally designed to approximate only the energy-containing subrange of turbulence, so that ℓ_G should be determined from the integral length scale; specifically, $\ell_G=2\mathscr{L}/\sqrt{\pi}=1.12\mathscr{L}$. The Gaussian model curve in Fig. 3 has the same variance and integral length scale as the von Kármán spectrum. This version of the Gaussian spectrum matches the von Kármán spectrum at the lowest wave numbers and approximates the actual spectrum tolerably well within the energy-containing subrange. The Gaussian model is not designed to capture the inertial subrange, however, and decays far too rapidly there.

It is common in the literature on outdoor sound propagation to find the value of 1 m or 1.2 m used as the Gaussian length scale for the effective index of refraction fluctuations near the ground.[2–4,9,25,26] This value was originally estimated by Daigle *et al.*[2,3] by approximating measured autocorrelations $R(r)$ at small r by a Gaussian function similar to the osculating parabola, as shown in Fig. 2. Johnson *et al.*[6] independently performed turbulence measurements and reported length scales similar to those estimated by Daigle *et al.* (One distinction is that Johnson *et al.* found the length scale to increase with height from the ground, varying from $\ell_G\simeq 1$ m at 1 m height, to about $\ell_G\simeq 10$ m at 33 m height.) Both groups determined length scales by fitting their data with Gaussian curves. Although the Gaussian approximation for $R(r)$ appears reasonable for small r, this procedure yields a length scale similar to the Taylor microscale [Eq. (3)],[27] not to the integral (or ''outer'') scale as the authors presumed. Their derived values of ℓ_G, are, consequently, much smaller than the actual value of $\mathscr{L}$ for their atmospheric conditions. As a result the peak in the Gaussian ''spectrum'' was unwittingly moved into the inertial subrange. Since its original appearance, the value $\ell_G\simeq 1$ m has been often used for modeling acoustical scattering (e.g., Refs. 9, 25, 26).

A secondary problem with the analysis of atmospheric data in some of the acoustical studies is the short averaging time.[16] In the early studies,[2,3] an averaging time only several minutes long was used. Because the outer large-eddy time

scale is of order 10 minutes, accurate calculation of second-order statistics from atmospheric data sets requires time series having two or more hours duration.[28] Shorter records provide insufficient sampling of low-frequency content in the signal, which normally causes the variance to be underestimated, and can also lead to smaller correlation length scales. Such unintentional filtering of low-frequency spectral energy is evident, for example, in the spectra shown in Fig. 4 of Ref. 2 and Fig. 8 of Ref. 4, where the ''spectral peak'' characteristic of the energy subrange is unresolved. This discrepancy helps explain why index-of-refraction variances appearing in the early studies[2,3] (and often used in subsequent propagation modeling[4,9,25,26]) are in the range $\sigma^2 = 10^{-6}$ to 2×10^{-6}, whereas values determined by field measurements described in the boundary-layer meteorology literature and by Johnson *et al.*[6] are typically an order of magnitude larger.[11,16]

But why, if (as we assert) the length scale used for many acoustical studies is too short, and the index-of-refraction variance too small, have researchers been able to obtain reasonable agreement between their scattering models and field observations? This can be understood by noting that the length scale ($\ell_G \simeq 1$) and variance ($\sigma^2 \simeq 10^{-6}$) in the early studies define an applied filter that approximates the actual turbulence spectrum within the range of scales defined by the acoustic filter. The curve labeled ''applied filter'' in Fig. 3 shows a Gaussian spectrum with the length scale one-tenth, and the variance one-fifth, the values used for the von Kármán spectrum. Over a narrow range of wave numbers, indicated by shading, the Gaussian spectrum approximates the actual spectrum[29] reasonably well. If this range happens to encompass the eddy sizes of significance in a given scattering problem, then the Gaussian model may be satisfactory when applied as a spectral filter. (Although one should not hope to predict the scattered signal successfully over a broad range of frequencies using the Gaussian model spectrum.)

In a later paper,[4] Daigle *et al.* note that their measurements conform well to the Kolmogorov spectrum, and recognize implicitly that they are using the Gaussian model spectrum as an applied filter (Fig. 8 and the accompanying discussion in Ref. 4). Stinson and Daigle[30] recently performed new turbulence measurements, and discussed the applied-filter relationship in more detail. Finally, it should be kept in mind that Daigle *et al.* performed their analysis for a specific site, scattering geometry, and range of acoustic frequencies. The same approach and parameters will not necessarily work well in other circumstances, as subsequent authors have often incorrectly assumed. In fact, Daigle *et al.*[4] recognized that the turbulence measurements at their site probably were not applicable to other sites having a more open fetch.

III. CONCLUDING REMARKS

Given these difficulties in quantifying the atmospheric turbulence spectrum, the reader may wonder what turbulence models should be used when the larger-scale turbulence of the energy subrange significantly affects the propagation. Here one is faced with a much more difficult task, since energy-subrange structure depends intimately on the dynamics and boundary conditions of a particular flow. Thus the energy subrange is normally estimated from measurement, and few satisfactory turbulence models that incorporate the energy-subrange component of the spectrum have been developed. The von Kármán and Gaussian models (with parameters correctly chosen) can be a reasonable approximation for the energy-containing subrange in some situations, because (unlike the Kolmogorov spectrum) they are mathematically well behaved at low wave number, and give roughly the correct qualitative behavior. But the limitations of these models must be kept in mind. For example, they are usually applied assuming homogeneous and isotropic turbulence when, in reality, the energy subrange is inherently inhomogeneous and anisotropic. In all likelihood it is an impossible goal to develop broadly applicable, quantitative equations for scattering by energy-subrange turbulence.[31] It might be possible to elucidate some of the energy subrange's salient features, however, by using numerical turbulence simulations,[32,33] or by adopting spectral models for some idealized cases. A couple such idealized cases in which progress has been made recently include turbulence in a constant shear layer[34] and the convective boundary layer over flat terrain.[35]

ACKNOWLEDGMENTS

We are very grateful to Dr. Gilles Daigle for his helpful comments on an earlier draft of this paper. J.G.B. received support for this work from NSF Grant No. INT-9512914 and ARO Grant No. DAAL03-92-G-0117 monitored by Dr. Walter Bach.

[1] C. I. Chessel, ''Observations of the effects of atmospheric turbulence on low-frequency sound propagation,'' J. Acoust. Soc. Am. **60**, 29–33 (1976).
[2] G. A. Daigle, J. E. Piercy, and T. F. W. Embleton, ''Effects of atmospheric turbulence on the interference of sound waves near a hard boundary,'' J. Acoust. Soc. Am. **64**, 622–630 (1978).
[3] G. A. Daigle, J. E. Piercy, and T. F. W. Embleton, ''Line-of-sight propagation through atmospheric turbulence near the ground,'' J. Acoust. Soc. Am. **74**, 1505–1513 (1983).
[4] G. A. Daigle, T. F. W. Embleton, and J. E. Piercy, ''Propagation of sound in the presence of gradients and turbulence near the ground,'' J. Acoust. Soc. Am. **79**, 613–627 (1986).
[5] W. Wilken, ''Experimental study of the influence of varying atmospheric conditions on sound propagation close to the ground'' Acustica **62**, 55–65 (1986).
[6] M. A. Johnson, R. Raspet, and M. T. Bobak, ''A turbulence model for sound propagation from an elevated source above ground level,'' J. Acoust. Soc. Am. **81**, 638–646 (1987).
[7] H. E. Bass, L. N. Bolen, R. Raspet, W. McBride, and J. Noble, ''Acoustic propagation through a turbulent atmosphere: Experimental characterization,'' J. Acoust. Soc. Am. **90**, 3307–3313 (1991).
[8] J. M. Noble, H. E. Bass, and R. Raspet, ''The effect of large-scale atmospheric inhomogeneities on acoustic propagation,'' J. Acoust. Soc. Am. **92**, 1040–1046 (1992).
[9] D. Juvé, P. Blanc-Benon, and P. Chevret, ''Sound propagation through a turbulent atmosphere: Influence of the turbulence model,'' in *Proceedings of the Sixth International Symposium on Long Range Sound Propagation*, edited by D. I. Havelock and M. R. Stinson (NRC Canada, Ottawa, Canada, 1994), pp. 270–282.
[10] V. E. Ostashev, ''Sound propagation and scattering in media with random inhomogeneities of sound speed, density and medium velocity,'' Waves Random Media **4**, 403–428 (1994).
[11] D. K. Wilson and D. W. Thomson, ''Acoustic propagation through anisotropic, surface-layer turbulence,'' J. Acoust. Soc. Am. **96**, 1080–1095 (1994).
[12] B. Brähler, ''Zur Schallstreuung in turbulenten Fluiden (On Sound Scat-

tering in Turbulent Fluids),'' Ph. D. thesis, Carl von Ossietzky Universität Oldenburg, 1996.
[13] V. E. Ostashev, G. Goedecke, B. Brähler, V. Mellert, and H. Auvermann, ''Coherence functions of plane and spherical sound waves in the turbulent atmosphere with von Karman spectra of temperature and wind velocity fluctuations,'' in *Proceedings of the Seventh International Symposium on Long Range Sound Propagation* (Ecole Centrale de Lyon, Lyon, France, 1996), pp. 349–357.
[14] A. N. Kolmogorov, ''The local structure of turbulence in incompressible viscous fluid for very large Reynolds numbers,'' C. R. Acad. Sci. URSS **30**, 301–305 (1941).
[15] V. I. Tatarskii, *The Effects of the Turbulent Atmosphere on Wave Propagation* (Keter, Jerusalem, 1971).
[16] Parts of this letter are based on the discussion in D. K. Wilson, ''A brief tutorial on atmospheric boundary-layer turbulence for acousticians,'' in *Seventh International Symposium on Long Range Sound Propagation* (Ecole Centrale de Lyon, Lyon, France, 1996), pp. 111–121.
[17] H. Tennekes and J. L. Lumley, *A First Course in Turbulence* (MIT, Cambridge, MA, 1972).
[18] J. C. Kaimal, J. C. Wyngaard, Y. Izumi, and O. R. Coté, ''Spectral characteristics of surface layer turbulence,'' Q. J. R. Meteorol. Soc. **98**, 563–589 (1972).
[19] J. C. Kaimal, J. C. Wyngaard, D. A. Haugen, O. R. Coté, and Y. Izumi, ''Turbulence structure in the convective boundary layer,'' J. Atmos. Sci. **33**, 2152–2169 (1976).
[20] J. C. Kaimal, ''Horizontal velocity spectra in an unstable surface layer,'' J. Atmos. Sci. **35**, 18–24 (1978).
[21] J. Højstrup, ''Velocity spectra in the unstable planetary boundary layer,'' J. Atmos. Sci. **39**, 2239–2248 (1982).
[22] J. O. Hinze, *Turbulence* (McGraw-Hill, New York, 1975).
[23] R. S. Lawrence and J. W. Strohbehn, ''A survey of clear-air propagation effects relevant to optical communications,'' Proc. IEEE **58**, 1523–1545 (1970).
[24] K. E. Gilbert, X. Di, and R. R. Korte, ''Distorted-wave Born approximation analysis of sound levels in a refractive shadow zone,'' in *Seventh International Symposium on Long Range Sound Propagation* (Ecole Centrale de Lyon, Lyon, France, 1996), pp. 373–389.
[25] K. E. Gilbert, R. Raspet, and X. Di, ''Calculation of turbulence effects in an upward refracting atmosphere,'' J. Acoust. Soc. Am. **87**, 2428–2437 (1990).
[26] P. Chevret, P. Blanc-Benon, and D. Juvé, ''A numerical model for sound propagation through a turbulent atmosphere near the ground,'' J. Acoust. Soc. Am. **100**, 3587–3599 (1996).
[27] It would be an oversimplification to assert that Daigle *et al.*'s measurements and procedure exactly reproduced the Taylor microscale. The actual situation is complicated by the slow response time of their instrumentation, which would cause the length scales they measured to be larger than the Taylor microscale.
[28] J. C. Wyngaard, ''Atmospheric turbulence,'' Annu. Rev. Fluid Mech. **24**, 205–233.
[29] The ''actual'' spectrum in Fig. 3 is modeled by a three-parameter equation involving the incomplete beta function. This equation allows for more realistic modeling of the energy subrange than the von Kármán spectrum, and is described in D. K. Wilson, ''A new model for turbulence spectra and correlations based in Meijer's *G*-functions,'' Technical Report No. ARL-TN-104, U.S. Army Research Laboratory, 2800 Powder Mill Road, Adelphi, MD 20783 (1998).
[30] M. Stinson and G. Daigle, ''Meteorological measurements for use in sound propagation calculations,'' in *Seventh International Symposium on Long Range Sound Propagation* (Ecole Centrale de Lyon, Lyon, France, 1996), pp. 137–147.
[31] V. A. Krasilnikov, ''Linear and nonlinear sound wave propagation in turbulent and inhomogeneous media,'' J. Acoust. Soc. Am. **101**, 3156 (1997).
[32] D. K. Wilson, ''Index-of-refraction and profile-curvature statistics derived from large-eddy simulations,'' in *Sixth International Symposium on Long Range Sound Propagation*, edited by D. I. Havelock and M. R. Stinson (NRC Canada, Ottawa, Canada, 1994).
[33] K. E. Gilbert, X. Di, M. J. Otte, S. Khanna, J. C. Wyngaard, and N. L. Seaman, ''A multi-scale approach for EM propagation assessment within the marine boundary layer,'' in *Proceedings of the 1997 Battlespace Atmospheric Conference* (SPAWAR Systems Center, San Diego, 1998), pp. 339–347.
[34] J. Mann, ''The spatial structure of neutral atmospheric surface layer turbulence,'' J. Fluid Mech. **273**, 141–168 (1994).
[35] D. K. Wilson, ''A three-dimensional correlation/spectral model for turbulent velocities in a convective boundary layer,'' Boundary-Layer Meteorol. **85**, 35–52 (1997).

Acoustics of the avian vocal tract[a)]

N. H. Fletcher[b)] and A. Tarnopolsky
School of Aerospace and Mechanical Engineering, Australian Defence Force Academy, Canberra 2600, Australia

(Received 3 January 1998; revised 8 July 1998; accepted 22 August 1998)

The general principles underlying the acoustic performance of the avian vocal tract are examined both theoretically and experimentally. The formant resonances produced both by the total vocal tract and by the bronchial tubes are evaluated quantitatively, and their dependence upon anatomical parameters is investigated. A simplified cylindrical model for the beak is examined theoretically, and experimental results are presented that confirm the predictions of the theory for this model. A similar theoretical and experimental investigation using a more realistic conical beak model is also reported, and behaves as predicted. Finally a theoretical study of the effect of mouth volume, as influenced by tongue position, is integrated with these other studies to produce a complete analysis. The implications of these studies for understanding the acoustical behavior of avian vocal tracts are discussed. [S0001-4966(98)00912-6]

PACS numbers: 43.10.Ln, 43.80.Ka, 43.64.Tk [FD]

INTRODUCTION

Despite the existence of a very large literature on behavioral, acoustic and physiological aspects of bird song [see, for example, the classic book by Greenewalt (1968) and many more recent papers] there has been very little attempt to analyze or synthesize the behavior of the avian syrinx and vocal tract in quantitative terms. This contrasts with the situation for the human larynx and vocal tract, for which there exists a multitude of aerodynamic and acoustic studies, both analytical and synthetic. There are, of course, obvious reasons for this difference, the prime one of which is that, as humans, we have a personal interest in the functioning, or malfunctioning, of our bodies, while studies of birds are motivated largely by simple interest.

A further difficulty in the case of birds is the great variety of their anatomical dimensions and the equally large variety in the form of their vocal utterances in comparison with those of humans. For these reasons the attention paid to any particular bird species is likely to be small, and it makes sense to seek out principles and approaches that can be applied fairly generally. It is the purpose of the present paper to examine the passive acoustics of the avian vocal tract, to exhibit the new techniques that must be applied, and to present some results that are of fairly general applicability. Because the treatment is properly quantitative and formalized, it can be applied to birds with quite different anatomical dimensions simply by inserting the appropriate numbers in the calculation. This is, however, only half the story, and the acoustics of the passive vocal tract must then be considered quantitatively in relation to the active sound generation mechanism of the syrinx in the manner discussed in an earlier paper (Fletcher, 1988).

Papers on sound production in birds often emphasize the difference between birds and humans, but it is important to recognize also the similarities. In both cases the air flow is modulated by some kind of vibrating valve—a pair of vocal folds in humans and a membrane valve in the syrinx of birds—and the acoustic output of this valve passes through the vocal tract where it is inevitably modified by the resonances of this tract, which can be controlled to some extent by changing the configuration of tongue, jaw and lips in the case of humans, and of tongue and beak in the case of birds. Some human languages use whistles interpolated among voiced sounds, and all use aerodynamic noise to produce consonants; birds similarly produce voiced harmonic sounds and also more or less pure-tone whistles. A recent survey of human voice production is given in papers in the volume edited by Davis and Fletcher (1996) while Brackenbury (1982) and Casey and Gaunt (1985) have discussed the situation for birds.

The anatomy of psittacine birds resembles that of humans in that there is one vocal valve located at the junction of the bronchi and trachea, though instead of consisting of two cartilaginous fleshy folds it comprises two membranes that are brought into opposition by inflating an external air sac. The actual motion of the vocal valve is complex in each case, and involves multiple degrees of freedom, leading to wavelike motion, or at least to a phase difference between different parts of the valve structure (Ishizaka and Flanagan, 1972; Sundberg, 1987). Nevertheless, it is possible to model the behavior to a reasonable approximation by assuming a much simpler single-mass-and-spring type of motion and considering the forces exerted upon it during air flow (Fletcher, 1988).

In song birds (Oscines), in contrast, the syrinx consists of two separate syringeal valves, one in each bronchus below its junction with the trachea. Each of these is a membrane valve and can be modeled as above. Some birds use only one of these valves for singing, but some use both simultaneously, producing either the same or a different frequency (Suthers, 1990, 1994). In either case a characteristic bronchial resonance can be observed in the song.

In both birds and humans the vocal valve is character-

[a)]''Selected research articles'' are ones chosen occasionally by the Editor-in-Chief that are judged (a) to have a subject of wide acoustical interest, and (b) to be written for understanding by broad acoustical readership.

[b)]Permanent address: Research School of Physical Sciences and Engineering, Australian National University, Canberra 0200, Australia.

ized as ''pressure-controlled'' in the same sense as the reed valve of a woodwind instrument or the lips of a trumpet player. There are, however, significant differences. The reed valves of woodwinds are ''blown closed'' by the activating pressure, while the lips of a trumpet player and the vocal valves of mammals and birds are ''blown open.'' There is a simple physiological safety reason for this design. A valve that is blown open by pressure can be set into autonomous oscillation at a frequency very close to that of its mechanical resonance provided the air supply driving it comes from an enclosed reservoir (Fletcher, 1993; Fletcher and Rossing, 1998). When the output of the valve is connected to some sort of resonator, such as a pipe, there are therefore two possible situations: in both the valve oscillates at its own resonance frequency, but in the first this is set well below the frequency of the first pipe resonance, while in the second the two frequencies match, giving a strong sound with emphasis on the fundamental.

In human speech the vocal fold frequency F_0 is well below that of the first vocal tract resonance F_1, and the same is true for much voiced bird song. The vibrations of the vocal valve produce a pulsating air stream with high harmonic content at frequencies $2F_0, 3F_0, 4F_0, \ldots$, because of nonlinearity in the flow equations. The strengths of these upper harmonics in the radiated sound are then modified by the vocal tract resonances, producing vowel formants in the case of humans, and similar formants that can be recognized in Sonagraph records for bird song (Patterson and Pepperberg, 1994). In high soprano song, however, the vocal fold frequency may be comparable with that of the first, or even the second, vocal tract resonance, and the singer must adjust these resonances to match the frequency of the vocal fold vibration to produce a strong sound. The same is probably true of some varieties of bird song (Brittan-Powell *et al.*, 1997). The precise origin of ''whistled'' song, however, still remains obscure (Fletcher, 1989).

It is important to recognize the distinction between this behavior and that of the ''blown closed'' valves of woodwind reed instruments, which can be maintained in oscillation at any frequency below their mechanical resonance by coupling to a suitable acoustic resonator (Fletcher, 1979; Fletcher and Rossing, 1998). Failure to recognize this difference has caused a good deal of confusion in the literature and a false emphasis on ''coupled'' and ''uncoupled'' vocal tract resonators. The vibration of the vocal valve will lock to the resonance of the vocal tract only when the frequencies of both are nearly equal. Evidence from experiments in which birds sang after breathing an atmosphere of helium and oxygen, which has a much higher sound velocity than air and therefore raises the vocal tract resonance frequencies proportionally, convincingly supports this general picture (Nowicki, 1987; Brittan-Powell *et al.*, 1997).

The purpose of the present paper is not to explore the whole mechanism of sound production in birds, but rather simply to investigate the resonances of the vocal tract. Whether the syringeal source vibrates at a frequency nearly identical to that of a vocal tract resonance, or at some lower frequency, the vocal tract still has a major influence on the song.

Discussions of the vocal tract in the literature have generally treated the vocal tract in a grossly simplified manner, characterizing it as a simple tube that is either acoustically open at both ends, open at one end only, or even closed at both ends (Brittan-Powell *et al.*, 1997), while even a cursory anatomical study shows that none of these models can be really appropriate. At its lower end, the trachea passes through the syringeal valve, which may be either open or closed at different parts of its oscillation cycle, and is terminated by a length of bronchial tube and the abdominal air sacs. These present an acoustic impedance that can, at least in principle and probably in practice, be evaluated (Fletcher, 1988). At its upper end, the trachea passes through the laryngeal constriction to enter the mouth, and this in turn is terminated by the complex geometry of the beak. At the very least, this combination presents an end-correction to the acoustic length of the trachea that is to some extent under the control of the bird. Detailed calculations show that the vocal tract resonances may approximate those of a singly closed tube for one part of the cycle and those of a doubly open tube for another part, giving a complex set of resonances that appear also in the song of the bird modeled (Fletcher, 1988). For these reasons, we simply calculate the acoustic input impedance of the upper vocal tract at the position of the syringeal valve, recognizing this as one important component of a more complex total system.

The first section of the paper deals explicitly with song birds, and with the consequences of their having syringeal valves that lie below the junction of the bronchi with the trachea. In particular, the bronchial resonance associated with this anatomy is calculated and displayed.

The discussion in the main part of the paper, however, is common to both song birds and those species with only a single syringeal valve at the foot of the trachea, for what is calculated is the input impedance of the trachea at this point. The trachea itself is a simple tube and holds little interest, while the larynx, mouth and tongue can be modeled as a constriction and as a short tube of variable cross section, respectively. Major interest is focused upon the beak, because its complex geometry makes it difficult to analyze in a simple way, while there is ample observational evidence that beak opening is strongly correlated with song frequency (Westneat *et al.*, 1993). To give some substance to the results of the calculations, they are compared with experimental results using a large-scale model.

I. THE BRONCHIAL FORMANT

The bronchial formant seems to have been first identified in work by Suthers (1994) in the song of the oil bird *Steatornis caripensis*. This bird is peculiar in that its vocal system lacks bilateral symmetry, so that the lengths of the two bronchi, measured from the syringeal valves to the junction with the trachea, are very different. The song shows two distinct formant bands, one at about 5 kHz and one at about 8 kHz, and Suthers was able to show, by blocking first one and then the other bronchus, that these are associated with resonances of the two bronchial segments, behaving essentially as quarter-wave pipe resonators. It is our aim here to place this observation on a quantitative footing by calculat-

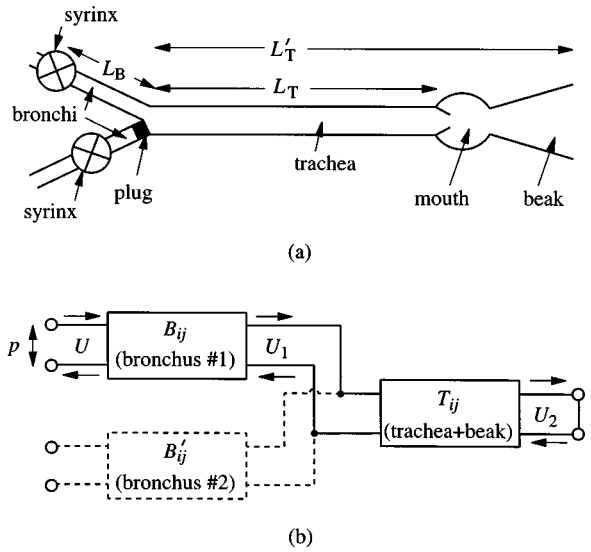

FIG. 1. (a) Model of the avian vocal tract with one blocked bronchus. The acoustic effect of the beak is taken into account by increasing the effective length of the trachea. (b) Analog network for calculation of the input impedance at the syringeal valve. When the other bronchus is unblocked, the part of the circuit indicated with broken lines becomes operative.

ing the vocal tract impedance presented to the syrinx valves. For the present we ignore the complexities of the mouth and beak, and assume the trachea to behave as a simple open tube with an appropriate end-correction to account for these.

The reason that the input impedance of the vocal tract at the syrinx valve is important is that the valve has a high impedance relative to the vocal tract, and so acts essentially as a flow source. The power that it supplies to the vocal tract is therefore proportional to the product of the vocal tract input impedance Z_V and the square of the acoustic volume flow U.

If we consider just one bronchus leading to the trachea, with the other being blocked as in the experiments of Suthers, then the vocal tract can be idealized as shown in Fig. 1(a). We simply have a bronchial tube of length L_B and cross sectional area S_B leading to a trachea of length L_T and area S_T. For simplicity in the model, we ignore for the moment the acoustic contribution of the beak and assume it to be taken into account by an adjustment of the tracheal length to a value L'_T appropriately greater than its geometric length L_T.

In Fig. 1(b) is shown the network analog from which the behavior of the system can be easily calculated, the case of one blocked bronchus involving only the circuit elements shown as full lines. Details of this approach are given by Fletcher (1992). Each tubelike element is described by a 2×2 matrix of impedance coefficients Z_{ij}, given explicitly for the case of a tube of length L and cross section S by

$$Z_{11}=Z_{22}=-j\frac{\rho c}{S}\tan kL,$$
$$Z_{12}=Z_{21}=-j\frac{\rho c}{S}\csc kL, \tag{1}$$

where ρ is the density of air, c is the speed of sound in air, $k=\omega/c+j\alpha$, $\omega=2\pi f$ is the angular frequency in which we are interested, and $\alpha\approx2\times10^{-5}(\omega/S)^{1/2}$ m^{-1} is the attenuation coefficient for sound propagation in the tube. As usual, $j=\sqrt{-1}$, and we assume SI units throughout. To avoid confusion, we shall replace Z_{ij} by B_{ij} when the coefficients refer to the bronchus, and by T_{ij} when they refer to the trachea. If we suppose p to be the acoustic pressure at the syrinx valve, U to be the flow through this valve, U_1 to be the flow from the bronchus to the trachea, and U_2 the flow out of the beak, then the network equations are

$$\begin{aligned}&B_{11}U-B_{12}U_1=p,\\&-B_{12}U+(B_{22}+T_{11})U_1-T_{12}U_2=0,\\&-T_{12}U_1+T_{22}U_2=0,\end{aligned} \tag{2}$$

which can be easily solved to give the input impedance Z_{in} as

$$Z_{\text{in}}=\frac{p}{U}=B_{11}-\frac{B_{12}^2T_{22}}{B_{22}T_{22}+T_{11}T_{22}-T_{12}^2}. \tag{3}$$

We have retained the distinction between B_{11} and B_{22} and between T_{11} and T_{22} in this analysis, so that the results apply also to the case in which the bronchus and trachea are tapering rather than uniformly cylindrical, provided we use appropriate generalizations of the impedance coefficients Z_{ij}.

It is reasonable to ask, at this stage, whether it is adequate to treat biological tubes, such as those of the vocal system, as though they have rigid walls, which is the implicit assumption underlying Eqs. (1) above. While the walls of the trachea are not particularly soft, they are certainly not ideally rigid. It is simple to include this lack of rigidity in the wave propagation equations for the tube using the formalism of Appendix B, in which the lack of rigidity of the walls simply adds a parallel element to the compressibility Y of the enclosed air. This, in turn, simply modifies the sound propagation velocity c. In practice there may be complications to the calculation because of the elastic resonance of the walls, but they are in general sufficiently thick that the correction to c, and thus to the wave number k, is much less than 10%. It is therefore reasonable to neglect this in our calculations, and in the model experiments to follow. There will also be an extra contribution to the damping coefficient α, but all this does is to slightly broaden any resonance peaks.

The expression in Eq. (3) can easily be evaluated numerically, as a function of frequency, when we insert specific values for the anatomic dimensions involved. For the case of the oil bird these dimensions are given in Table I for the two separate bronchi, and the calculated results are shown in Fig. 2. We see that each curve exhibits a number of resonances with a 1, 3, 5,..., frequency sequence, based upon a fundamental frequency of about 600 Hz. These are the resonances

TABLE I. Assumed anatomical dimensions.

	Case (a)	Case (b)
Length of trachea	100 mm	100 mm
Length of bronchus	10 mm	15 mm
Acoustic length of beak	20 mm	20 mm
Diameter of trachea	5 mm	5 mm
Diameter of bronchus	3 mm	3 mm

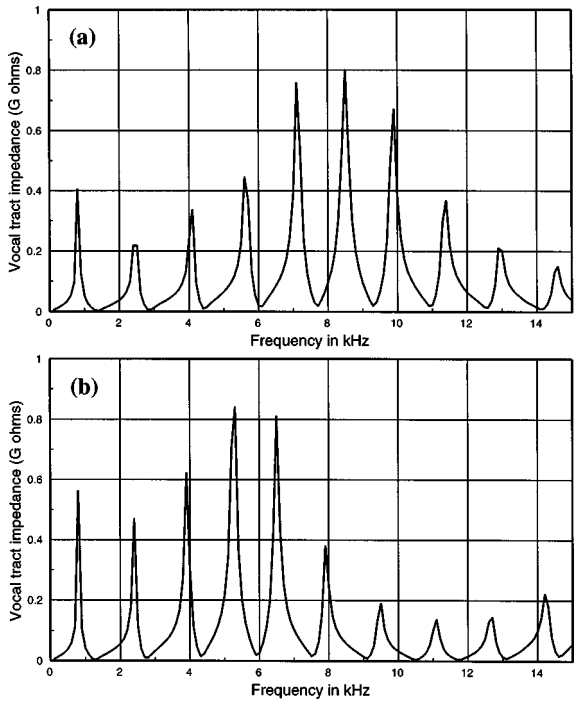

FIG. 2. Calculated vocal tract input impedance for the simple model of Fig. 1, using the anatomical dimensions given in Table I for cases (a) and (b).

of the complete vocal tract consisting of bronchus, trachea and beak. In human speech, the vocal-fold frequency F_0 is very much less than the frequency of the lowest of these resonances, and they would constitute the normal vocal formants. A bird, however, adopts a song strategy that is similar to that of a coloratura soprano singer, for whom F_0 is comparable with the frequency of the first vocal tract resonance. In this case, song is produced most efficiently if the vocal tract shape is adjusted so that one of its low resonances coincides with F_0, or perhaps its second harmonic $2F_0$.

Each curve in Fig. 2 also shows a peak in the envelope of the resonances, at about 8.5 kHz in the case of the shorter bronchus in (a) and at about 5.5 kHz for the longer bronchus in (b). This is the formant imposed by the bronchial resonance and noted by Suthers, and does indeed correspond fairly closely to a quarter-wave resonance condition of the bronchial segment between the syringeal valve and the junction with the trachea. Indeed it is interesting to note that, at this resonance, the bronchial tube constitutes a quarter-wave transformer which improves the acoustic matching between the syringeal generator and the trachea.

The fact that Eq. (3) gives a quantitative prediction of behavior allows us to examine the consequences of variations in anatomic quantities such as the lengths and diameters of the various sections of the vocal tract. Such numerical experimentation immediately establishes that a discontinuity in diameter at the junction between bronchus and trachea is essential for the production of this high formant, as we expect on acoustic grounds, since reflection is necessary to establish a resonance.

We can see the algebraic origin of these resonances quite clearly from (3). There will be peaks in the impedance Z_{in} when the denominator in the second term becomes very small so that

$$(B_{22}+T_{11})T_{22}-T_{12}^2\approx 0. \tag{4}$$

If we neglect damping by setting $\alpha=0$ in k, then B_{ij} and T_{ij} become pure imaginary and this expression can be made to vanish exactly, giving a good approximation to the resonance frequencies. If the bronchus is narrower than the trachea, so that $S_B<S_T$, then these frequencies lie a little above the values for which $\omega=(2n-1)c/4(L_T+L_B)$, that is the quarter-wave resonances of the total vocal tract length consisting of bronchus plus trachea plus beak. These are the primary vocal tract resonances.

If we are near in frequency to a quarter-wave resonance of the bronchus, then $B_{11}=B_{22}\to 0$ and $B_{12}\to Z_B$, and the second term in (3), which contains the resonance, approaches its maximum value. When the frequency is midway between these quarter-wave bronchial resonances, on the other hand, then all the $B_{ij}\to\infty$ and the two terms in (3) cancel so that the primary resonances are suppressed. This is the explanation for the shape of the envelope of the resonances in Fig. 2.

It is worthwhile to examine briefly the effect of going to the natural case in which both bronchi are open, as shown by removing the plug in Fig. 1(a). The analog network, shown in Fig. 1(b), then includes the branch shown with broken lines. This network can be solved in just the same way, and yields the result

$$Z_{\text{in}}=B_{11}-\frac{B_{12}^2(B'_{11}T_{22}+T_{11}T_{22}-T_{12}^2)}{B'_{11}(B_{22}T_{22}+T_{11}T_{22}-T_{12}^2)+B_{11}(T_{11}T_{22}-T_{12}^2)}, \tag{5}$$

where B refers to the bronchus in which we are interested (No. 1) and B' to the other bronchus (No. 2), the valve of which is assumed to be closed. (A similar expression could be deduced if we assume the other syrinx to be open.) We can see that, if the second bronchus is closed at its junction with the trachea, so that $B'_{11}=\infty$, this expression reduces to that in (3), as indeed it must.

Once again the envelope of the resonances reaches a maximum at the quarter-wave resonances of the active bronchus No. 1 and for the same reason as before. Thus although the detailed frequencies of the peaks of the impedance curve will be a little altered, it will still show a formant band at the same position as for the simple case. The same is true if the bird is using the syringeal valve in bronchus No. 2. Use of both syringeal valves simultaneously will thus produce both formants, which is what was observed by Suthers (1994).

Though the oil bird is a peculiar anatomical case, we expect similar behavior for all song birds. The distinction is perhaps that the syrinx membranes are usually located rather high in the bronchi, close to its junction with the trachea, so that the bronchial formant frequency is very high and perhaps outside the frequency range normally studied.

II. THE BEAK

As mentioned in the Introduction, acoustic analysis of the beak is made complex because of the fact that it opens along its sides for a considerable distance. This means that we must consider radiation loading on this opening, and also means that the acoustic behavior may vary in a rather com-

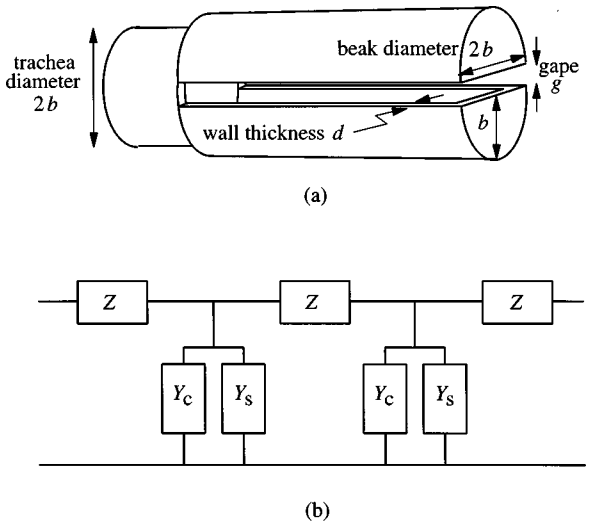

FIG. 3. (a) Simplified model of the bird beak. (b) Network analog used to calculate the behavior. The repeating sections indicate the series impedance Z and the two shunt admittances Y_c and Y_s (all per unit length) for the enclosed volume and the slit, respectively.

plex manner with beak gape. We attack this problem by a combination of theoretical analysis and direct experiment.

Clearly a rigorous model of the acoustic behavior of the beak must be three dimensional, to allow for the complex acoustic flows involved. While such an analysis could be carried out numerically, using some sort of finite element program, its results would probably not be very illuminating in a general sense, though reasonably accurate for the particular case studied. It is therefore more useful to approach the problem by constructing a model that is simple enough to solve analytically, but at the same time is sufficiently realistic to incorporate the key features of an actual beak. To this end we investigate first a very simple model and then one that is more complex and more realistic.

We should emphasize at the outset that our objective here is to obtain a reasonable understanding of the acoustic characteristics of the avian beak, rather than to carry out a precise study of the behavior of our simple models. For this reason we have been satisfied with quite modest theoretical rigor and experimental accuracy, and the results should not be judged on this basis.

A. Cylindrical beak model

Our first highly simplified model is shown in Fig. 3(a). The model is cylindrical, with uniform side openings. The major advantage of such a model is its easy geometrical description, which allows simple calculation of its acoustic behavior. We want to understand the general behavior of such a beak as a preliminary to investigating a more realistic model that is not so straightforward to analyze.

From an acoustical point of view, the beak may be regarded as a slotted transmission duct with a radiation admittance that is uniformly distributed along its length. The behavior of such a duct is characterized by its series impedance and shunt admittance, both per unit length of duct. Suppose that the series impedance per unit length of the beak at frequency ω is $Z(\omega)$. Then $Z(\omega)$ is essentially the masslike inertive load contributed by axial flow of the air in the duct, and has the value

$$Z(\omega)=R_w+j\frac{\rho\omega}{S}, \tag{6}$$

where S is the cross-sectional area of the beak, R_w is the small viscous resistance at the walls, and the other symbols have their usual meanings. Similarly, let $Y(\omega)$ be the shunt admittance per unit length of the beak. Then $Y(\omega)$ has two parts, one a compliance Y_c contributed by the compressibility of the air in the beak, and the other the admittance Y_s per unit length of the slits on each side of the beak, as shown in Fig. 3(b). We can thus write

$$Y(\omega)=Y_c+Y_s=j\frac{S\omega}{\rho c^2}+Y_s. \tag{7}$$

The beak cross-sectional area S is related to the slit width, or gape, g by

$$S=\pi b^2+2bg. \tag{8}$$

The acoustic impedance S_s of unit length of slit has two parts, Z_{flow} associated with flow between the slit walls and Z_{radn} associated with the flow transitions (radiation impedance) at the open ends of the slit. The first of these is easily evaluated (Olson, 1957, p. 89) and is approximately

$$Z_{\text{flow}}(\omega)\approx\frac{12\eta d}{g^3}+j\frac{6\rho d\omega}{5g}, \tag{9}$$

where η is the viscosity of air. The radiation impedance of unit length of a slit of width g is more difficult to calculate, but we can derive an approximate result as shown in Appendix A. If we neglect the small conductive part of the admittance, this result has the form

$$Y_{\text{radn}}\approx j\frac{\pi}{\rho\omega\ln(kg/4)}, \tag{10}$$

where $k=\omega/c$ as usual.

We can now add Z_{flow} and Z_{radn} to estimate the slit admittance Y_s per unit length along the beak. Remembering that there are two slits, and that $Z_{\text{radn}}=(Y_{\text{radn}})^{-1}$ when we deal with unit length of slit, we can write

$$Y_s\approx 2[Z_{\text{flow}}+(Y_{\text{radn}})^{-1}]^{-1}. \tag{11}$$

We can get an insight into the behavior of this beak model by neglecting the small resistive components of Z_{flow} and Z_{radn} and retaining only the imaginary parts of these expressions. We also assume that the gape g is within the range typical of bird beaks so that, as shown in Appendix A, it is a reasonable approximation to take the end correction at the slit to be $\delta\approx g$. We can then write

$$Y_s\approx -j\left(\frac{3\rho\omega d}{5g}+\frac{\rho\omega}{2}\right)^{-1}. \tag{12}$$

When we combine this with the compressive compliance Y_c of the enclosed air, as in (7), we have an expression of the form

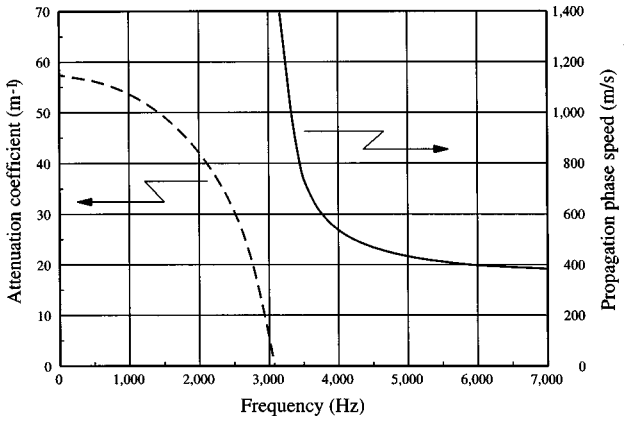

FIG. 4. Calculated behavior of the simplified beak model of Fig. 3, with beak diameter 10 mm, wall thickness 2 mm and gape 5 mm. Above the cutoff frequency $f^*=\omega^*/2\pi$, which is here about 3100 Hz, a sound wave is transmitted with phase velocity v that is greater than the normal sound velocity $c\approx 340\ \mathrm{m\,s^{-1}}$. Below f^* the wave is attenuated, and the attenuation coefficient behaves as shown.

$$Y(\omega)=j\left(A\omega-\frac{B}{\omega}\right), \tag{13}$$

where

$$A=\frac{\pi b^2+2bg}{\rho c^2}, \quad B=\left(\frac{3\rho d}{5g}+\frac{\rho}{2}\right)^{-1}. \tag{14}$$

It is clear from (13) that $Y(\omega)$ is negative imaginary for small values of ω, goes through zero, and then becomes positive imaginary, as ω increases. The frequency $\omega=\omega^*$ for which $Y(\omega)=0$ is a sort of transverse Helmholtz resonance frequency for the slotted duct, with only flow through the slit taken into account. We call ω^* the propagation cutoff frequency for the slotted beak, for a reason that will appear in a moment, and it can be calculated by setting $Y(\omega)=0$ in Eq. (13).

Returning to the transmission behavior of the slotted duct, it is easy to show from standard transmission-line theory (see Appendix B) that its characteristic impedance is

$$Z_0(\omega)=(Z/Y)^{1/2} \tag{15}$$

and that the phase speed v and wave number $k=\omega/v$ of waves in the duct are

$$v(\omega)=\omega/(ZY)^{1/2}, \quad k(\omega)=(ZY)^{1/2}. \tag{16}$$

We note that these expressions reduce to their normal forms $Z_0=\rho c/S$, $v=c$, and $k=\omega/c$ when the slit is closed, so that $g=0$, and the small contribution R_w to Z from wall losses is neglected.

From our discussion of the behavior of $Y(\omega)$ above, we see immediately that $k(\omega)$ is imaginary for $\omega<\omega^*$, so that the wave is exponentially damped as $\exp(-|k|x)$ below the cutoff frequency, rather than propagating through the slotted duct. For ω just greater than ω^*, Y is small and the phase speed v is very large, while for $\omega\gg\omega^*$ the slits have little effect and $v\approx c$. This behavior is illustrated in Fig. 4.

The behavior of the cutoff frequency with beak gape is clearly of interest. An approximate result can be derived from (13) by setting $Y=0$, and has the form

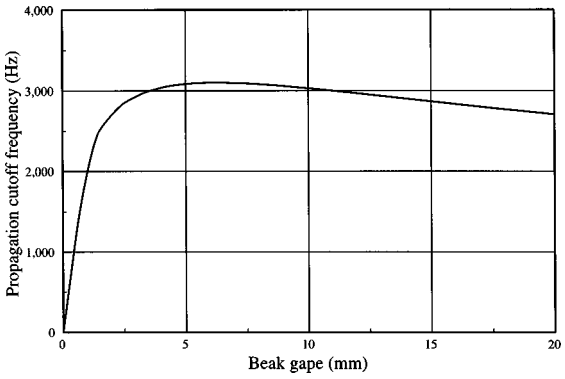

FIG. 5. Calculated propagation cutoff frequency, as a function of the gape, for a simple cylindrical beak of internal diameter 10 mm and wall thickness 2 mm.

$$\omega^*\approx\left[\frac{10gc^2}{S(6d+5g)}\right]^{1/2} \tag{17}$$

with $S=\pi b^2+2bg$ as in (8). The curve in Fig. 5 shows the general form of the behavior for a model approximating a real bird beak in dimensions. For a more accurate calculation, which is hardly justified, the logarithmic expression for the slit radiation impedance as given in Appendix A should be used, and the resulting equation solved numerically. As expected, the propagation cutoff frequency scales simply inversely with beak size, provided diameter, gape and wall thickness are all kept in proportion.

As a final theoretical exercise, it is straightforward to calculate the acoustic reactance presented by such a beak to the trachea, and from this the end correction can be evaluated. If we neglect resistive losses by radiation from the beak slits, then the impedance coefficients K_{ij} for the beak can be found from the expressions (2), simply by substituting (8) for the effective cross-sectional area and using the phase velocity v, given by (16), in place of the free propagation sound speed c. An expression for the impedance Z_K is similarly easy to derive. The input admittance of the beak is then

$$Z_{\mathrm{beak}}=K_{11}-\frac{K_{12}^2}{K_{22}+Z_K}. \tag{18}$$

When this expression is evaluated numerically, however, the behavior is dominated by longitudinal resonances of the beak cavity unless damping by radiation from the slit is included. The calculation is therefore not of much value for comparison with experiment.

B. Experimental verification

To verify these predictions, experiments were conducted using a large-scale beak model. The trachea was represented by a plastic pipe, about 1 m in length, 34 mm in internal diameter, and 4 mm in wall thickness, and the beak by an extension of this pipe formed by slitting a 100-mm-long section of it longitudinally and partly closing the remote end with two semicircular plugs. The gape opening of this model beak could be adjusted between zero and about 30 mm. The end correction, evaluated at the junction between the plain pipe and the model beak, was measured using a standing-wave tube as normally used for measuring acoustic imped-

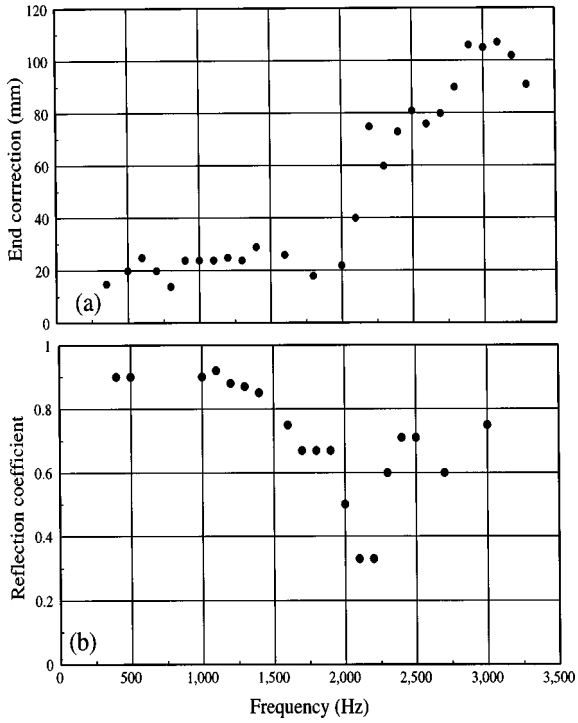

FIG. 6. (a) Measured end-correction, as a function of frequency, for the experimental cylindrical beak model with a gape of 10 mm. The calculated cutoff frequency $f^*=\omega^*/2\pi$ for sound transmission along the slotted duct is 1800 Hz in this case. Note that the end-correction is actually undefined to within a half-wavelength. (b) The measured reflection coefficient R. Note the minimum near the cutoff frequency.

ance (Beranek, 1988). The standing-wave ratio in the pipe was also measured, thus giving an indication of the losses at the beak end. Choice of the diameter of the model trachea to match that of the beak reduces complications and is easily generalized later.

The measured end-correction behaved just as expected. At low frequencies the beak presented very nearly an ''open-end'' termination to the trachea, with the actual value of the end-correction depending upon the gape but not significantly upon the frequency. This end-correction exhibited a sharp transition at about the frequency predicted by the theory, and for higher frequencies increased as would be expected for a wave propagating to the more-or-less closed remote end of the beak. This behavior is illustrated in Fig. 6(a). The value to be assigned to the end correction above the cutoff frequency is arbitrary to the extent of an added half-wavelength, and has been taken to have the smallest possible positive value for convenience.

Also of importance is the measured standing-wave ratio H, which is just the ratio of the maximum to the minimum amplitude in the trachea tube. From H we can determine the reflection coefficient R at the beak from the relation

$$R=\frac{H-1}{H+1}. \tag{19}$$

This quantity is shown in Fig. 6(b), from which it is clear that there is a minimum in the reflection coefficient, corresponding to a maximum radiation efficiency, just above the cutoff frequency. This is what we might expect, for the phase

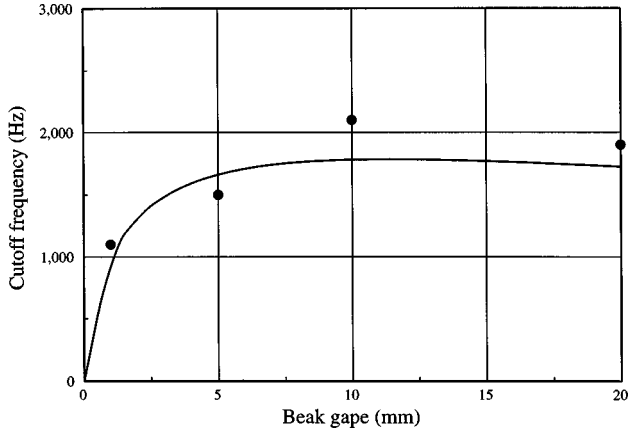

FIG. 7. Measured variation of the transmission cutoff frequency of the model beak as a function of beak gape (symbols), compared with the calculated variation of the cutoff frequency.

velocity in the beak is then high, and the two slots radiate as sources with uniform phase.

The measured variation of the cutoff frequency with beak gape is shown in Fig. 7, where it is compared with the calculated variation of $f^*=\omega^*/2\pi$ as evaluated from (17). It can be seen that the agreement is acceptably good for small gapes. For large gapes the radiation losses are so large that it is not possible to distinguish the cutoff behavior.

The next part of the experiment examined the variation of radiation directivity with frequency and beak gape. The directivity behavior measured in the horizontal plane (the plane of the slit) was simple: below the transmission cutoff frequency f^*, the radiation pattern is not far from being omnidirectional, with the 0° forward direction dominating the 180° rearward direction by only about 3 dB. Near f^* there is a transition to a more nearly figure eight pattern with a minimum in the 90° direction, and this pattern is maintained at higher frequencies. Example measurements are shown in Fig. 8. The reason for this behavior is clear. At low frequencies, the standing wave in the slotted pipe is exponentially attenuated with distance along the slot, giving two

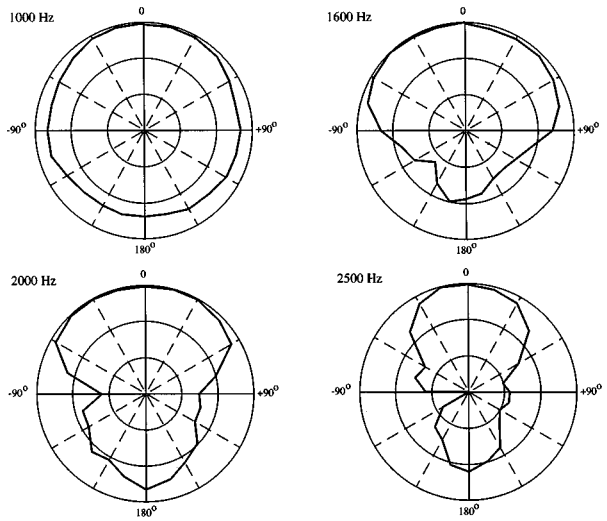

FIG. 8. Measured directivity patterns for the cylindrical model beak with a gape of 10 mm. The propagation cutoff frequency in this case is about 1600 Hz.

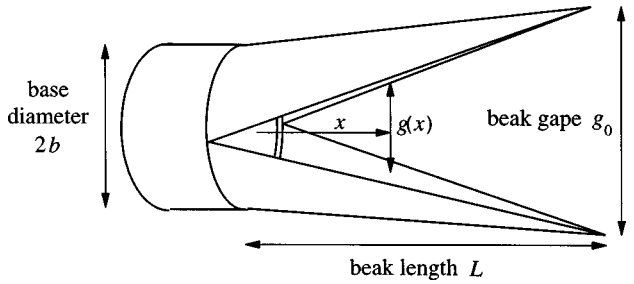

FIG. 9. A more realistic beak model, with important dimensions marked.

short slot sources separated by much less than a wavelength, so that they behave quite like a single point source. Just below the cutoff frequency, the standing wave extends along nearly the whole length of the slotted pipe, because the attenuation becomes very small, while just above cutoff the behavior is similar because the wave is transmitted and has a very high phase velocity. These two longer cophase sources are efficient radiators. At frequencies further above cutoff, however, the slotted pipe is long enough to encompass more than one half-wavelength of the standing wave, and the lateral separation between the two slit sources is also an appreciable fraction of a wavelength. This complex source has good axial radiation efficiency but low efficiency in the transverse 90° direction. When similar measurements were carried out in the vertical plane, the response on the axis was necessarily unchanged, while that at 90° increased so as to nearly eliminate the minimum, suggesting that it is the phase delay between the two slits that is primarily responsible for it.

To complete the study of this simplified model, we should examine the behavior of the transfer function between internal acoustic pressure and the total radiated sound pressure. This is essentially equivalent to evaluating the magnitude of the real part of the radiation impedance as a function of beak gape and frequency. Because the cylindrical beak model is very artificial, we shall not report this study here, but defer it for mention in relation to the conical beak model of the next section.

In relating these experimental results to the behavior of real bird beaks, it is important to correct the scaling. The model used in the experiments was larger than typical bird beaks by a fact ranging from about 3 to 10. Fortunately the scaling law is quite simple, at least to a first approximation. If we scale all geometrical dimensions similarly, say by a factor ξ, then the end correction also scales as ξ and the frequency response scales as ξ^{-1}. All the frequencies reported in our experiments should therefore be scaled upwards by a factor between about 3 and 10 for the smaller beaks of typical birds.

C. Conical beak model

While it is possible, using finite-element numerical methods, to calculate the acoustic behavior of a fairly realistic model beak, this tells us rather little about general principles. We therefore explore in a much less accurate manner the acoustics of a simplified but improved beak model. As shown in Fig. 9, this model consists of a cone, split lengthwise and opened along the split plane. For convenience the gape g_0 is defined to be measured at the tip of the beak, as shown.

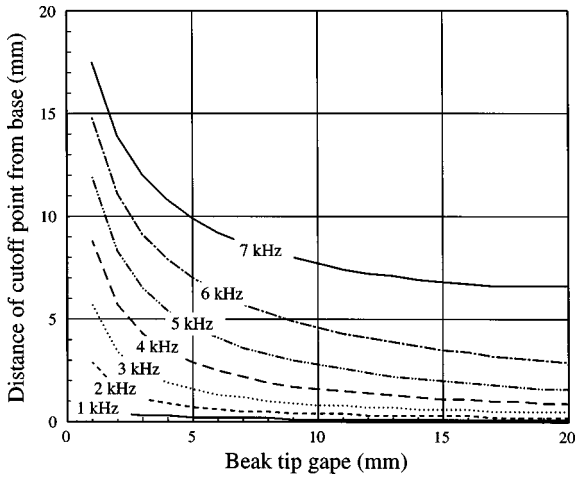

FIG. 10. Calculated distance of the cutoff position from the beak base, as a function of gape and frequency, for a beak 50 mm long, 10 mm in base diameter, and with a wall thickness 1 mm.

When we attempt to analyze the behavior of this beak model, we see immediately that a proper treatment would be quite difficult. It is, however, enough for our present purposes to proceed in a very first-order manner, using a one-dimensional slotted duct approach as before. The difference is that, in the present case, the duct has a progressively changing cross section, and the slits similarly vary in width with distance along the beak. The treatment we propose is reasonably well justified for the portion of the beak where the slit width is much less than the beak diameter, but ceases to be valid when this condition is no longer satisfied. Despite this, and in the absence of a better simple approach, it makes at least qualitative sense to extrapolate the formal results to cover the behavior of the complete beak from root to tip.

Suppose that the beak length is L, its base radius b, and its gape at the tip is g_0. Then we can approximate the local slit width $g(x)$ at a distance x from the base of the beak by

$$g(x) = g_0 x/L \tag{20}$$

and the duct cross section $S(x)$ at x by

$$S(x) = \frac{\pi b^2 (L-x)^2}{L^2} + \frac{2 g_0 b x (L-x)}{L^2}. \tag{21}$$

The local cutoff frequency for transmission along the duct is therefore given, in this approximation at least, by substituting these values in the treatment of the previous section.

The result of this calculation is shown in Fig. 10. The cutoff position moves towards the tip of the beak at higher frequencies, but towards the base of the beak as the gape is increased. This is just what we would expect from our discussion of the simple cylindrical beak. The numerical reliability of the calculation is, however, not high, because the assumptions upon which it is based are rather far from being satisfied—the slit is not uniform, and is not very long compared with its width, though both of these assumptions are closer to being satisfied when the gape is small. The unreal-

ity of some of the assumptions shows up at higher frequencies and larger gapes than those illustrated in the figure. At 8 kHz, for example, the solution diverges for gapes larger than about 10 mm, which suggests that the calculated x values at 7 kHz and large gapes are probably too large. Despite this, it is not unreasonable to suppose that the calculation describes the actual behavior at least qualitatively, and perhaps semiquantitatively.

We can go a little further and see what this means in terms of end-correction behavior at the beak. This is not simple, because the acoustic load past the cutoff position depends upon gape and frequency, but we can make some qualitative statements. Certainly we should expect from Fig. 10 that the end-correction will decrease as the gape is increased, and that it will decrease as the frequency is lowered. Both of these aspects of the acoustical behavior are similar to those deduced for the cylindrical beak model, but here the change with frequency is gradual, rather than having an abrupt discontinuity.

D. Conical beak measurements

A conical beak model was constructed by making a light sheet-metal cone, 200 mm in length, to fit on the end of the plastic trachea, so that its diameter at the base was about 40 mm. The cone was then slit lengthwise to make a fairly realistic beak, and hinged to the tracheal tube to make a model vocal tract. Once again, measurements of end correction and standing-wave ratio were made using a modified acoustic impedance tube. The gape g_0 was defined in this case to be the opening at the beak tip. This model is, of course, large compared with the beak of a typical bird, but the acoustic parameters we are investigating scale simply with size, provided that we also scale frequency inversely with size. For the beak of a typical large bird, the model dimensions should be reduced by about a factor of 5, and the frequency increased by the same factor.

Figure 11 shows the measured end correction to the tracheal tube, as a function of beak gape, for several frequencies in the range of interest. The important conclusion, which we were led to expect from our theoretical analysis, is that the effective end correction for a given gape is a good deal larger at high frequencies than at low frequencies. This is, as once again we expect, a general progressive behavior, rather than involving a sharp transition of the type found for our simplified cylindrical beak model. Only the results for a frequency of 2500 Hz appear anomalous. The reason for this is not clear, but the standing-wave ratio for larger gapes at this frequency is very low, making measurements rather difficult and inaccurate.

The general form of the behavior displayed in Fig. 11 is remarkably similar to that calculated from the simple theory and displayed in Fig. 10. To compare the two figures, we must remember that the calculated beak in Fig. 10 is smaller than the experimental beak by about a factor of 4 in all dimensions. We must therefore multiply all the distances in Fig. 10 by four and divide the frequencies by four for the comparison. Having done this, it is clear that there is remarkably good semiquantitative agreement between theory and experiment. It is gratifying that such a simple theory is able

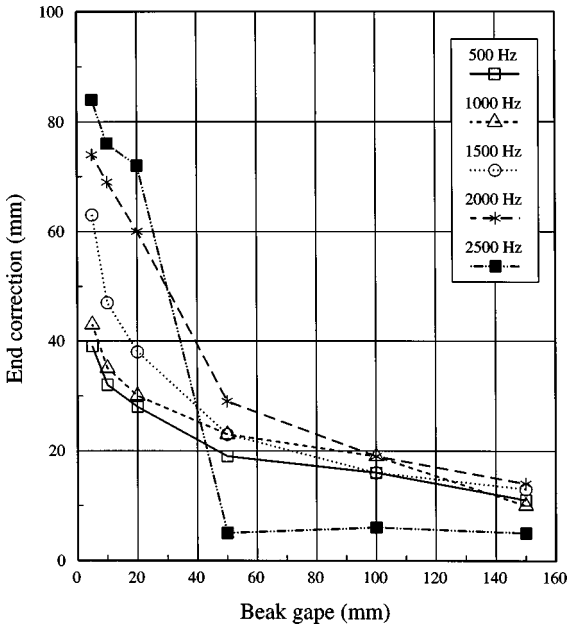

FIG. 11. Measured end correction to the trachea tube, when terminated by the tapered beak model, as a function of beak gape for a range of frequencies.

to provide such a good description of actual behavior. The fact that the experimental results become anomalous at about the same relative frequency as that at which the theory fails should not be taken to be significant.

It is useful to have an approximate expression for the end correction δ in the general case, as a function of gape and frequency. Clearly the measured end correction should scale, in both magnitude and frequency, with the size of the beak, if the geometric proportions remain similar. An empirical expression that describes the measured results and that has been appropriately scaled is

$$\delta(f,g) \approx 0.05L + 10^{-5} f L^2/g, \tag{22}$$

where L is the length of the beak and g is the tip gape, both in meters, and f is the frequency in hertz. The length to root diameter ratio of the beak is assumed to be about 6. This expression is a reasonable approximation for $g < L$, that is for a gape angle of less than about 60°, and for $f < 500/L$ numerically, but makes no claims to accuracy.

When the scaled version of this formula is compared with the theoretical results shown in Fig. 10 for the propagation distance of the wave into the beak, it is found that the end correction is about twice the propagation distance. Such a result is about what we might expect.

The next set of measurements to be made were of the radiation directivity patterns, which were made in the same way as for the cylindrical beak. In addition to their intrinsic interest, these measurements are important in relation to the radiation transfer function, as we see later. The results of these measurements, as shown in Fig. 12, are qualitatively quite similar to those for the cylindrical beak model, except that there is no pronounced ''figure-eight'' region, presumably because of the beak taper. Measurements taken in the vertical plane are very similar to those in the horizontal plane.

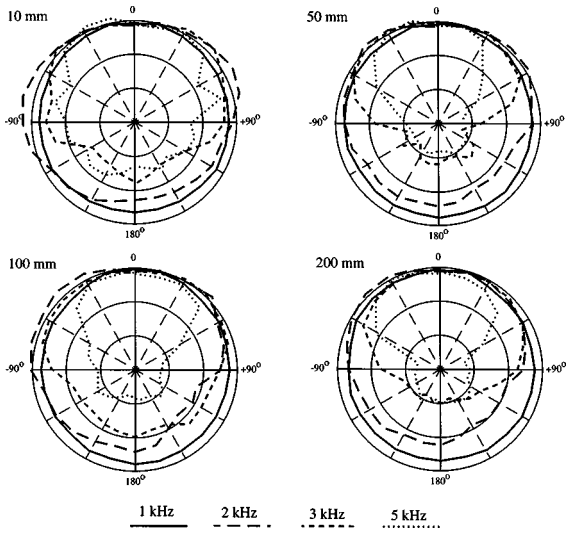

FIG. 12. Measured directivity patterns as a function of frequency and gape for the conical beak model.

Figure 13 summarizes the behavior in the form of a directional index $G(f,g)$, which we define to be the ratio, in decibels, between the measured radiated intensity on the axis and the intensity at the same distance that would be radiated by an isotropic simple source. Thus

$$G(f,g) = -10\log_{10}\left[\frac{1}{4\pi}\int_0^{\pi} 10^{0.1F(\theta)} 2\pi \sin\theta \, d\theta\right], \quad (23)$$

where $F(\theta)$ is the level at angle θ relative to the level on the axis, at the given gape and frequency. To an adequate accuracy for our present purposes, the experimental results may be approximated by

$$G(f,g) \approx 0.005 f(g+0.2) \ \text{dB}, \quad (24)$$

where g is in meters and f in hertz.

We are now in a position to evaluate the radiation transfer function for the beak. The external radiated power level is easy to define and measure. Suppose the measured root-mean-square sound pressure at a distance r on the beak axis is p_R, then the total radiated power is

$$P_R = 4\pi r^2 10^{-0.1G(f,g)} p_R^2/\rho c, \quad (25)$$

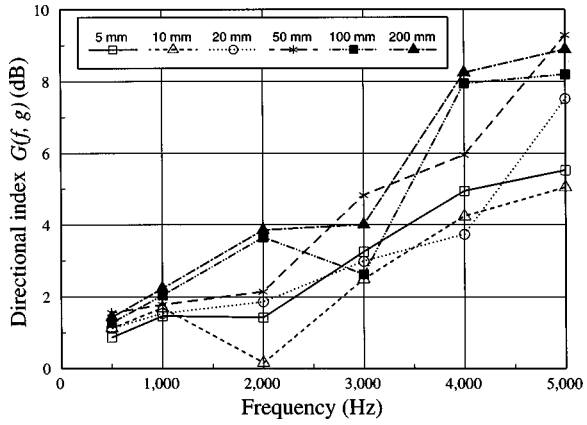

FIG. 13. Measured directional index $G(f,g)$ for the conical beak model at various gapes g, as a function of frequency f.

where the directional index $G(f,g)$, defined by (23), allows for the directivity pattern of the radiation. Internally we can most easily measure the sound pressure p_I at the pressure maxima in the standing wave pattern produced by the incident wave and the wave reflected from the beak. We can then define an internal power quantity P_I by

$$P_I = p_I^2/Z = p_I^2 S/\rho c, \quad (26)$$

where $Z = \rho c/S$ is the characteristic impedance of the trachea pipe, assumed to have area S. The justification for adopting this measure will be set out below.

Dividing these two power quantities and taking logarithms to convert the squared pressures to measured sound pressure levels L_R and L_I, respectively, relative to the same reference, we define the transfer function $T(f,g)$, in decibels, to be

$$T(f,g) = 10\log_{10}(P_R/P_I)$$
$$= L_R - L_I - G(f,g) + 10\log_{10}(4\pi r^2/S) \ \text{dB}. \quad (27)$$

The interpretation of this power transfer function is important. The radiated power P_R is clearly defined and needs no qualification. The internal power quantity P_I as defined by (26), however, can be rewritten in the form

$$P_I = U_I^2 \rho c/S, \quad (28)$$

where U_I is the volume flow amplitude at the flow antinodes in the tracheal pipe, one of which is at the beak. Since the radiated power is simply $R_R U_I^2$, where R_R is the real (resistive) part of the radiation impedance at the beak, this means that $T(f,g)$ measures, in decibels, the radiation resistance at the beak relative to the characteristic impedance $\rho c/S$ of the tracheal tube. The behavior of this radiation resistance is well known for a simple open tube, so that measurement of $T(f,g)$ allows us to evaluate the acoustic influence of the beak.

To perform the measurements, a small subtlety is required, for we do not generally know the exact location of the pressure nodes and antinodes in the model trachea, and we must evaluate the internal pressure level at a pressure maximum. To make the measurement, we therefore sealed the syrinx end of the model trachea, and inserted into it at this point a small sound source and a pressure microphone. The frequency was varied until this microphone indicated a local pressure maximum, at which point the trachea-beak system was at a resonance and the microphone was at a pressure maximum. In our experiments, actual measurement of the transfer function made use of a two-channel FFT analyzer, and the level difference $L_R - L_I$ was the envelope of the minima of the displayed transfer function.

To give a reference, we first measured the radiation transfer function for the pipe with the beak removed. This measurement should give the radiation impedance of an open tube, which is known to rise at 6 dB/oct for low frequencies and to saturate at the value $\rho c/S$, or 0 dB on our scale, for $2\pi f/ca > 2$, which corresponds here to about 6 kHz (Beranek, 1954). The measured function behaves approximately in this manner as expected, but not with great accuracy. It

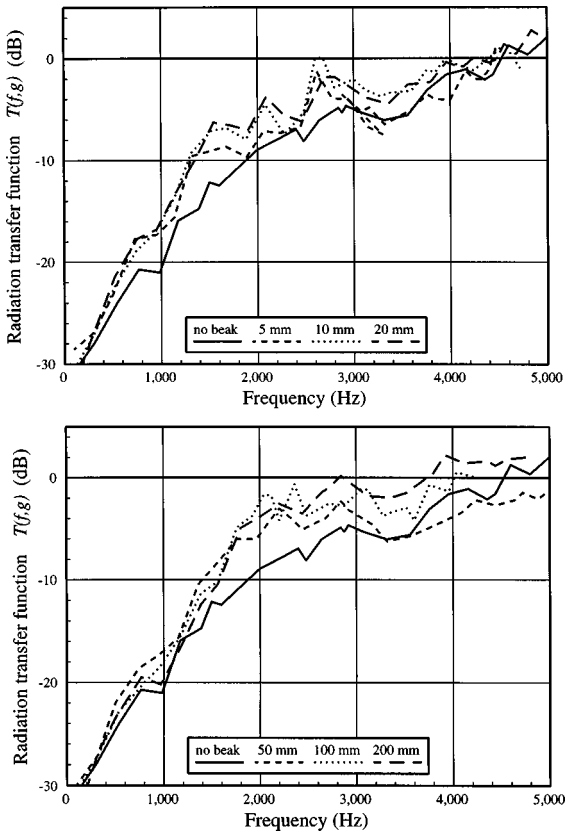

FIG. 14. Measured radiation transfer function for the conical beak model for a range of gapes. The measured transfer function for the unbaffled tracheal tube alone is shown for comparison.

can be used, however, as a reference with which the measured behavior of the beak can be compared, thus minimizing experimental errors.

Figure 14 shows the measured behavior of the radiation transfer function $T(f,g)$ for the conical beak model over a wide range of frequencies and gapes. In each part of the figure, the radiation function for the bare tube is shown for comparison. We conclude that the effect of the beak is to enhance the acoustic radiation by an amount up to about 6 dB over a limited and gape-dependent frequency range. For narrow gapes, between 5 and 20 mm, as shown in the upper part of the figure, the radiation enhancement increases with gape and occurs over the range from about 500 to 3000 Hz. For wide gapes between about 50 and 200 mm, as shown in the lower part of the figure, the enhancement once again increases with increasing gape and occurs over a range from about 1500 to 4500 Hz. When these frequencies are increased by a factor of 3 or so in order that they apply to a moderate-sized bird, it is clear that beak gape contributes a significant vocal formant to the upper parts of the song frequency range, and that this formant rises in frequency as the gape is increased. Casual listening and observation, of course, would have led one to expect this.

It is interesting to note, in passing, that the measured radiation function for the cylindrical beak model exhibits pronounced maxima, separated by about 900 Hz, above the transmission cutoff frequency, as shown in Fig. 15. These can be attributed to longitudinal half-wave resonances within the beak cavity.

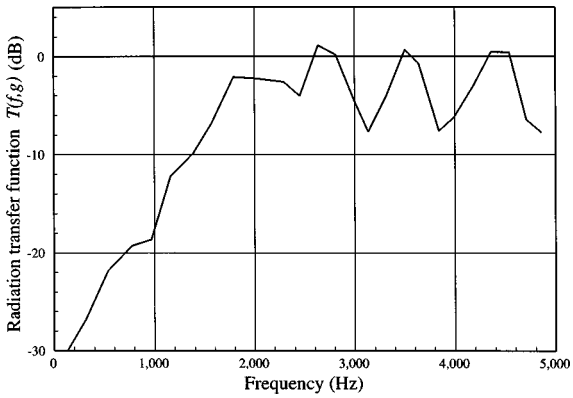

FIG. 15. Measured radiation transfer function for the cylindrical beak model for a gape of 10 mm. Note the oscillations above the transmission cutoff frequency, which is in this case about 2000 Hz.

E. Beak input impedance

Finally we need an expression for the input impedance of the beak, as seen from the mouth. A detailed solution of this problem is similar to that for a slotted, tapered waveguide or transmission line (Slater, 1942), and generally requires a numerical approach for each particular case, even given the simplifying assumptions used in our treatment. To undertake such a study would not be appropriate here, so we seek instead an approximate treatment.

The most appropriate model would seem to be to regard that part of the beak in which the sound can propagate as a short cylindrical pipe, of length equal to about half the end correction $\delta(f,g)$ given by (22), terminated by the balance of the end correction and the radiation resistance, although actually we can neglect the radiation resistance, in the interests of simplicity, because most of the acoustic damping of the system arises from losses to the walls of the narrow trachea. For the parameters of the short propagation length in the beak we could use an average of those along its length, but it is adequate to approximate these by those for the cross-section S_B and characteristic impedance $Z_B=\rho c/S_B$ at the beak root. Solving the simple network for this situation, as shown in Fig. 16(a) and detailed in Appendix C, we find for the input impedance $K(f,g)$ of the beak

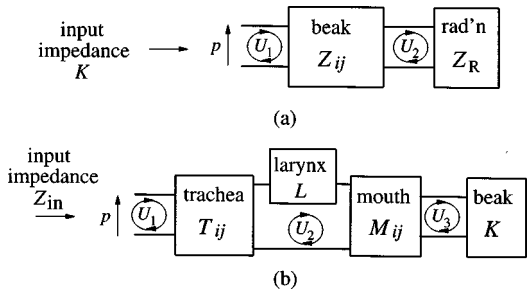

FIG. 16. (a) An approximate model for the input impedance K of the beak represents it as a tube of length $\delta/2$, described by the impedance coefficients Z_{ij}, terminated by a radiation impedance Z_R that accounts for the other half of the end correction δ. (b) The acoustic behavior of the mouth and beak can be included explicitly in the vocal-tract network of Fig. 1 by replacing the simple trachea plus mouth plus beak impedance T_{ij} by separate impedances describing trachea (T_{ij}), mouth (M_{ij}) and beak (K).

$$K(f,g)\approx jZ_B\left[-\cot\left(\frac{k\delta}{2}\right)+\frac{\csc^2(k\delta/2)}{\cot(k\delta/2)-k\delta/2}\right], \qquad (29)$$

where $k=2\pi f/c$ as usual.

From these measurements it can be concluded that the beak has a rather small overall effect on total vocal tract acoustics. Certainly it adds an end-correction, the magnitude of which varies with beak gape, but, as will be discussed below, this effect is not large. Probably more importantly, a wide beak gape increases the radiation efficiency for high frequencies by as much as 10 dB. In the model experiment this enhancement began at about 1 kHz and was greatest at about 2 kHz. Translating this a more typical bird beak of length 50 mm gives a radiation enhancement beginning at about 4 kHz and reaching a maximum of about 10 dB at about 8 kHz for a wide beak gape. This effect is certainly acoustically significant.

There are just a few reported studies in the literature that refer to the role of beak gape. One of the most thorough is that of Westneat *et al.* (1993) who examined the correlation between song frequency and beak gape for two species of sparrows, *Sonotrichia albicollis* and *Melospiza georgiana*. They found a strong and consistent correlation, with gape increasing from 10° to 50° as the song frequency increased from 3 to 7 kHz in *M. georgiana*, and a similar but smaller range in both frequency and gape in *S. albicollis*. We should expect the bird to gain several advantages from this strategy: it should be somewhat easier to align vocal tract resonances with the song frequency; the frequency shift in radiation transfer function with gape, as shown in Fig. 14 could be exploited; and the directional index, and hence audibility distance (Fig. 13), should be improved. In another study, Hausberger *et al.* (1991) examined the calls of the barnacle goose, and concluded that those with ''wide mouths'' had higher-pitched voices, a finding that is again in accord with the increased radiativity and directivity of beaks with large gape at high frequencies.

F. Vocal tract impedance

The trachea of the bird opens into the mouth at the back of the tongue through the variable constriction of the larynx. The cross-sectional area of the mouth cavity is a good deal larger than that of the trachea, but it can be modified to a considerable extent by movement of the tongue, despite its rather stiff form. The outer end of the mouth makes a transition to the beak, which we discussed in the previous section.

The acoustical behavior of the avian mouth is very similar to, though less flexible than, that of the human mouth. It functions essentially as a cavity resonator, driven from the rather high impedance of the trachea and vented by the rather low impedance of the beak. A detailed discussion cannot, however, rely upon such a simple approximation. Rather, the mouth must be considered as a short length of duct, with a diameter that can be varied by raising the tongue, inserted between the trachea and the beak. The simplified trachea plus beak impedance T_{ij} of Fig. 1 is thus replaced by the more complex combination shown in Fig. 16(b). The relevant impedances are given, once again, simply by inserting appropriate values for cross section and length in formulas (1).

TABLE II. Assumed anatomical dimensions.

Length of trachea	30 mm
Length of mouth	10 mm
Length of beak	15 mm
Diameter of trachea	3 mm
Diameter of mouth	3–15 mm
Diameter of beak root	10 mm
Beak tip gape	1–15 mm

Finally, we should include the effect of the larynx, which constricts the opening between the trachea and mouth to a variable extent. This can be represented by a simple series impedance $L=j\omega\rho l/S$, where l is the length and S the cross-sectional area of the larynx constriction, and ρ is the density of air.

The formal solution for the input impedance Z_{in} of this network at the base of the trachea is given in Appendix C, and leads to the result

$$Z_{\text{in}}=\frac{p}{U_1}=T_{11}-\frac{T_{12}^2(M_{22}+K)}{(T_{22}+M_{11}+L)(M_{22}+K)-M_{12}^2}. \qquad (30)$$

This expression can be evaluated numerically for particular combinations of effective mouth diameter, as determined by tongue position, and beak gape. We discuss some results of this calculation in the next section.

III. DISCUSSION

Now that we have set up all the formal apparatus for calculating, at least to a first approximation, the linear acoustic properties of the avian vocal tract, it is important to see where this leads us. In the present part of the discussion we omit the complicating influence of the bronchial resonances, which can be added in later for the case of song birds. We also omit the complication of a larynx constriction and assume it to be fully open.

By way of example, the calculation is made for a rather small bird with the anatomical dimensions shown in Table II. The effective diameter of the mouth has been assumed to be variable between 3 and 15 mm, the reduction in cross-sectional area, and thus in effective radius, being accomplished by raising the tongue, while the beak gape has been varied between 1 and 15 mm. To limit the number of curves to be displayed, it is further assumed that beak gape and effective mouth diameter are varied together, as seems reasonable. The results of three such calculations are displayed in Fig. 17, each curve being labeled with the effective mouth diameter and beak gape in millimeters.

The frequency range displayed is just sufficient to encompass the first three vocal tract resonances, and it is clear that the adjustments to the mouth and beak do have a significant effect. There are also effects on the resonances at higher frequencies, but their significance is not immediately apparent. The main conclusion is that the frequency of the first resonance, which would be termed F_1 for a human vocal system, is very little affected by the adjustments, though a

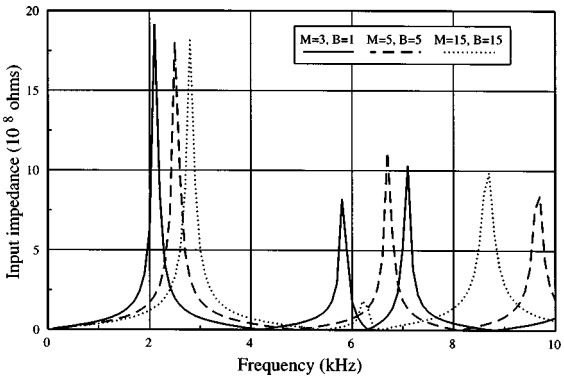

FIG. 17. Calculated vocal tract input impedance as effective mouth diameter *M* and beak gape *B*, given in millimeters for each curve, are varied. The other anatomical dimensions have the values given in Table II. The units for input impedance are 10^8 acoustic ohms, and frequencies are in kilohertz.

raised tongue and a closed beak do lower its frequency somewhat. The situation is quite different for the second and third resonances F_2 and F_3, both the frequency and height of which are considerably affected by the mouth and beak adjustments. Indeed these adjustments make it possible to position at least one resonance peak almost anywhere in the range between 5 and 10 kHz, though this resonance is sometimes F_2 and sometimes F_3. We conclude that the bird has reasonable opportunity to match a resonance to its syringeal frequency F_0 over this range, if that is the song strategy to be adopted. This does depend, however, upon the initial dimensions of the elements of the vocal tract and upon the range of variation in tongue position and beak gape that the bird can achieve.

We have not yet attempted to systematize the resonance effects illustrated in these diagrams or to check them experimentally. Such an experimental check on input impedances, using a model vocal system of the type we have employed here for the beak, is straightforward in principle, using techniques such as those developed by Benade (1960), Backus (1974), Pratt *et al.* (1977) or Wolfe *et al.* (1995) for musical wind instruments, but practical difficulties in making these measurements on live birds may be almost insuperable.

Finally, it is useful to summarize in an equation the implications of these curves and other elements that were discussed earlier. Ideally we should use a complete model in which the interaction of the vocal tract resonances on the vibrations of the syringeal valve are included (Fletcher, 1988), but for the moment it is adequate to neglect this and to consider the vibrating valve with its underlying air reservoir simply as a high-impedance acoustic source that delivers a nonsinusoidal, and therefore harmonically rich, flow to the vocal tract. If $U(f)$ is the component of this flow at frequency *f*, then the internal pressure generated at the input to the vocal tract is $p_I = Z_I(f)U(f)$ where $Z_I(f)$ is the input impedance of the vocal tract, including the bronchi as discussed in Sec. I for the case of a song bird. The total radiated acoustic power is then

$$P_I(f) = \left(\frac{\rho c}{S_B}\right) T(f,g)[Z_I(f)U(f)]^2. \tag{31}$$

This sound power is radiated with a beak formant described by $T(f,g)$ and a directionality described by the function $G(f,g)$. A similar equation applies for each harmonic component of the syringeal flow, and these can be combined to describe the radiated song, whether the syringeal frequency is closely matched to a vocal tract resonance or not.

IV. CONCLUSION

In this paper we have made a modest beginning to the quantitative exploration of the acoustics of the avian vocal system. In particular, we have confirmed the role of bronchial resonances in at least some birds, though they may not be important in all; we have elucidated the acoustic behavior of the beak in its dependence upon frequency and gape geometry; and we have shown how these elements can be combined into a model from which it is possible to make quantitative predictions about the acoustic behavior of the complete vocal tract. It is, indeed, the fact that the approach is properly quantitative to a reasonable accuracy that makes it significant—qualitative studies may be generally useful but do not provide a framework for proper testing.

Further studies—theoretical, experimental and observational—will be required in order to codify these changes in input impedance and to relate them to the acoustic strategies used by different bird species in their singing. It is not necessary for the song frequency F_0 to be rigidly tied to a vocal tract resonance frequency—indeed this is not done in human singing, except for high notes of the soprano range. Just as skilled trombone players (in whom the lips behave analogously to the syringeal valve) can play a one-octave glissando while keeping the instrument slide (and thus its resonances) fixed, or can move the slide over its full range while maintaining a steady pitch (Taylor, 1992), analogous feats should be within the capabilities of birds. There is, however, some acoustic advantage to be gained from aligning the song frequency with a vocal tract resonance, as in a musical instrument. Whatever the strategy used, however, shifts in the vocal tract resonances are bound to have a significant effect on the timbre of the resulting song.

On the basis of the results we have obtained, and the associated quantitative formulations, it should now be possible to attempt a more detailed analysis of the acoustics of bird song. The linear vocal tract resonances, of course, provide only one part of this understanding, and must be considered in combination with the nonlinear sound-production mechanism in the syrinx.

The specific graphical results presented in this paper are simply meant as examples, and do not refer to any particular species of bird. They are meant simply to indicate the typical magnitude of the effects discussed, and are certainly much more specific than mere qualitative assertions. To be really useful, however, they must be applied to the anatomy of a particular bird and compared with behavioral and acoustic data. With the aid of the formulas and equations presented in the text, such a specific application should be readily possible.

ACKNOWLEDGMENTS

This work is part of a program supported by a grant from the Australian Research Council. We are grateful to Andrew Dombek for technical support and to Martin Monteiro-Haig for assistance with some of the measurements.

APPENDIX A: RADIATION ADMITTANCE OF A SLIT

Determination of the radiation impedance at the open slots in the model beak is a complex problem. For our present purposes, however, a very roughly approximate solution is fortunately adequate, and this will now be outlined.

Provided the wavelength is long compared with the beak diameter, it is reasonable to model the right and left halves of the beak separately with each comprising a narrow slit in an infinite reflecting plane. This approximation is valid because the symmetry of the problem mandates that there is no acoustic flow across the vertical symmetry plane. We can then go further and model each slit as half of a narrow circular cylinder embedded in this plane, and the flow out of the slit as a corresponding radial dilation of the cylinder. We can then reassemble the whole into a long circular cylinder whose radius dilates at the signal frequency ω. If the length of the beak is very large compared with the width of the slit (diameter of the cylinder), then it is an adequate approximation to take this length to be infinite, and the problem then becomes one with cylindrical symmetry.

The outgoing pressure wave generated by a cylinder with radius varying at frequency ω is given by

$$p(r)=Ae^{j\omega t}[J_0(kr)-jN_0(kr)]$$
$$\approx Ae^{j\omega t}[1-(k^2r^2/4)+j(2/\pi)\ln(kr/2)], \quad \text{(A1)}$$

where J and N are, respectively, Bessel and Neumann functions, $k=\omega/c$, and A is a constant (Morse, 1954). The second form of writing is an appropriate approximation if $kr \ll 1$. This pressure wave can, in turn, be related to the displacement velocity $u(r)$ through the equation

$$\rho\frac{\partial u}{\partial t}=-\frac{\partial p}{\partial r} \quad \text{(A2)}$$

so that

$$u(r)\approx -\frac{A}{\rho c}\left(\frac{2}{\pi kr}+j\frac{kr}{2}\right)e^{j\omega t}. \quad \text{(A3)}$$

If the cylinder radius is a and the radial velocity of its surface is $u(a)$, then the acoustic admittance per unit length of slit, which is half the cylinder, is

$$Y_{\text{radn}}(\omega)=\frac{\pi a u(a)}{p(a)}\approx\left(\frac{\pi a}{\rho c}\right)\frac{1}{\ln(ka/2)}\left(-\frac{\pi ka}{4}+\frac{j}{ka}\right) \quad \text{(A4)}$$

and we can relate this to the beak gape g by substituting $g/2$ for a.

This result is inaccurate for several reasons. In the first place, the length of the beak is not infinite, so that we expect the result given above to be inaccurate once the gape exceeds about one-tenth of the beak length. A second inaccuracy resides in the neglect of beak surface curvature in the immediate vicinity of the slits, this should not be a serious problem, but may introduce a systematic inaccuracy. Third, we have assumed that the slit is uniformly illuminated by an acoustic signal, with no amplitude or phase difference along its length; neither of these conditions is fulfilled at all accurately in the real situation. Despite these inaccuracies, however, the results quoted above will be sufficient to guide us in a semiquantitative manner through our analysis.

This result can be related to the effective end-correction δ to the slit length provided by the radiation load through the normal relation

$$Y_{\text{radn}}=\frac{g}{j\rho\omega\delta}, \quad \text{(A5)}$$

which gives

$$\delta\approx-(g/\pi)\ln(kg/4). \quad \text{(A6)}$$

For bird beak geometries and song frequencies, kg is typically in the range 0.03–0.3, so that we expect $0.5g<\delta<2g$. In most cases it will be a reasonable approximation to take $\delta=g$.

We shall not concern ourselves with solving the case of a slit of finite length, but a qualitative remark is in order. The factor $1/\ln(kg/4)$ in the radiation admittance, and hence the reciprocal of this in the end-correction δ, derives essentially from the progressive change in propagation phase from different parts of the slit to the region of interest. If the slit length L is large compared with g but short compared with the sound wavelength, then $\ln(kg/4)$ should be replaced by a factor of order $\ln(g/L)$, which thus eliminates the apparent divergence of δ at low frequencies.

APPENDIX B: SLOTTED DUCT EQUATIONS

Here we derive briefly the two important results (15) and (16). In a network analog, electric potential takes the place of acoustic pressure, electric current takes the place of acoustic volume flow, and the duct becomes a transmission line. Suppose this transmission line has series impedance Z per unit length and shunt admittance Y per unit length. Then, for a current flow U, the change in voltage (pressure) over a very short length dx of line is

$$dp=-ZU\,dx. \quad \text{(B1)}$$

Similarly, if the pressure at the point considered is p, then the change in current over the length dx is

$$dU=-Yp\,dx. \quad \text{(B2)}$$

These two equations can be combined to give

$$\frac{\partial^2 p}{\partial x^2}=YZp \quad \text{(B3)}$$

which has the solution $p=ae^{\pm\gamma x}$ where $\gamma=(YZ)^{1/2}$. If both Y and Z are positive imaginary quantities, as they are, for example, in a simple lossless acoustic duct, then $\gamma=jk$ and the solution represents two waves traveling in opposite directions with phase velocity

$$v=\omega/k=\omega/(YZ)^{1/2}. \quad \text{(B4)}$$

We can find the characteristic impedance of an infinite line or duct by supposing that there is a small loss so that there is no reflected wave. Then $p = ae^{-\gamma x}$, and from the first equation above we find that $\gamma p = ZU$, so that the impedance of the infinite line, which is its characteristic impedance, is

$$Z_0 = p/U = Z/\gamma = (Z/Y)^{1/2}. \tag{B5}$$

APPENDIX C: UPPER VOCAL TRACT

Referring to the network of Fig. 16(a) and following the procedures given in Fletcher (1992), we can write the equations for the beak as

$$\begin{aligned} p &= Z_{11}U_1 - Z_{12}U_2, \\ 0 &= -Z_{21}U_1 + (Z_{22} + Z_R)U_2, \end{aligned} \tag{C1}$$

where the impedances Z_{ij} refer to a pipe of length $\delta/2$ and cross section S_B, and $Z_R = j\rho\delta/2S_B$ is the radiation reactance associated with the other half of the end-correction. From these equations, the beak input impedance K is

$$K = \frac{p}{U_1} = Z_{11} - \frac{Z_{12}^2}{Z_{22} + Z_R}. \tag{C2}$$

Inserting specific values for the impedances from (1), the results quoted in the text are obtained.

Similarly, using the network of Fig. 16(b) for the complete vocal tract, we can write the equations

$$\begin{aligned} p &= T_{11}U_1 - T_{12}U_2, \\ 0 &= -T_{12}U_1 + (T_{22} + M_{11} + L)U_2 - M_{12}U_3, \\ 0 &= -M_{12}U_2 + (M_{22} + K)U_3. \end{aligned} \tag{C3}$$

The solution is straightforward, and leads to the result

$$Z_{\text{in}} = \frac{p}{U_1} = T_{11} - \frac{T_{12}^2(M_{22} + K)}{(T_{22} + M_{11} + L)(M_{22} + K) - M_{12}^2} \tag{C4}$$

which can be evaluated numerically for particular values of the geometrical parameters.

Backus, J. (**1974**). ''Input impedance curves for the reed woodwind instruments,'' J. Acoust. Soc. Am. **56**, 1266–1279.

Benade, A. H. (**1960**). ''The physics of woodwinds,'' Sci. Am. **204**, 145–154.

Beranek, L. L. (**1954**). *Acoustics*, reprinted 1986 (Acoustical Society of America, Woodbury, New York), p. 122.

Beranek, L. L. (**1988**). *Acoustical Measurements* (Acoustical Society of America, Woodbury, New York), pp. 309–328.

Brackenbury, J. W. (**1982**). ''The structural basis of voice production and its relationship to sound characteristics,'' *Acoustic Communication in Birds*, edited by D. E. Kroodsma and E. H. Miller (Academic, New York), Vol. 1, pp. 53–73.

Brittan-Powell, E. F., Dooling, R. J., Larsen, O. N., and Heaton, J. T. (**1997**). ''Mechanisms of vocal production in budgerigars (Melopsittacus undulatus),'' J. Acoust. Soc. Am. **101**, 578–589.

Casey, R. M., and Gaunt, A. S. (**1985**). ''Theoretical models of the avian syrinx,'' J. Theor. Biol. **116**, 45–64.

Davis, P. J., and Fletcher, N. H. (editors) (**1996**). *Vocal Fold Physiology: Controlling Complexity and Chaos* (Singular, San Diego).

Fletcher, N. H. (**1979**). ''Excitation mechanisms in woodwind and brass instruments,'' Acustica **43**, 63–72; addendum, Acustica **50**, 155–159 (1982).

Fletcher, N. H. (**1988**). ''Bird song: A quantitative acoustic model,'' J. Theor. Biol. **135**, 455–481.

Fletcher, N. H. (**1989**). ''Acoustics of bird song—Some unresolved problems,'' Comments Theor. Biol. **1**, 237–251.

Fletcher, N. H. (**1992**). *Acoustic Systems in Biology* (Oxford U.P., New York), pp. 121, 178–203 and 309–311.

Fletcher, N. H. (**1993**). ''Autonomous vibration of simple pressure-controlled valves in gas flows,'' J. Acoust. Soc. Am. **93**, 2172–2180.

Fletcher, N. H., and Rossing, T. D. (**1998**). *The Physics of Musical Instruments*, 2nd ed. (Springer-Verlag, New York), Chap. 13.

Greenewalt, C. H. (**1968**) *Bird Song: Acoustics and Physiology* (Smithsonian Institution, Washington, DC).

Hausberger, M., Black, J. M., and Richard, J.-P. (**1991**). ''Bill opening and sound spectrum in barnacle goose loud calls: Individuals with 'wide mouths' have higher pitched voices,'' Anim. Behav. **42**, 319–322.

Ishizaka, K., and Flanagan, J. L. (**1972**). ''Synthesis of voiced sounds from a two-mass model of the vocal cords,'' Bell Syst. Tech. J. **51**, 1233–1268.

Morse (**1954**).

Nowicki, S. (**1987**). ''Vocal tract resonances in oscine bird sound production: Evidence from birdsongs in a helium atmosphere,'' Nature (London) **325**, 53–55.

Olson, H. F. (**1957**). *Acoustical Engineering* (Van Nostrand, New York).

Patterson, D. K., and Pepperberg, I. M. (**1994**). ''A comparative study of human and parrot phonation: Acoustic and articulatory correlates of vowels,'' J. Acoust. Soc. Am. **96**, 634–648.

Pratt, R. L., Elliott, S. J., and Bowsher, J. M. (**1977**). ''The measurement of the acoustic impedance of brass instruments,'' Acustica **38**, 236–245.

Slater, J. C. (**1942**). *Microwave Transmission* (McGraw-Hill, New York), pp. 69–78.

Sundberg, J. (**1987**). *The Science of the Singing Voice* (Northern Illinois U.P., DeKalb).

Suthers, R. A. (**1990**). ''Contributions to birdsong from the left and right sides of the intact syrinx,'' Nature (London) **347**, 473–477.

Suthers, R. A. (**1994**). ''Variable asymmetry and resonance in the avian vocal tract: A structural basis for individually distinct vocalizations,'' J. Comp. Physiol. A **175**, 457–466.

Taylor, C. (**1992**). *Exploring Music* (Institute of Physics Publishing, Bristol), p. 138.

Westneat, M. W., Long, J. H., Hoese, W., and Nowicki, S. (**1993**). ''Kinematics of birdsong: Functional correlation of cranial movements and acoustic features in sparrows,'' J. Exp. Biol. **182**, 147–171.

Wolfe, J., Smith, J., Brielbeck, G., and Stocker, F. (**1995**). ''A system for real time measurement of acoustic transfer functions,'' Acoustics Australia **23**, 19–20.

The effect of mean flow/source motion on sound-pressure fields with absorption

Jeffrey J. Kelly[a)]
Virginia Tech Vibration and Acoustics Laboratories, Virginia Consortium of Engineering & Science Universities, 303 Butler Farm Road, Suite 101, Hampton, Virginia 23666

(Received 24 August 1997; accepted 25 September 1998)

An analysis of sound-pressure fields relative to both uniformly translating and space-fixed reference frames is presented. By using Fourier transforms and separation of variables, a solution is determined in the source frame. Far-field approximations are transformed to emission coordinates which model the pressure field observed in a space-fixed reference frame. The influence of mean flow/forward flight on source-fixed directivity patterns is shown. A finite cylindrical source was considered and directivity patterns were constructed which show the effect of Mach number, frequency, and displacement pattern on the sound field. The influence of flow on absorption due to viscosity is also presented. © *1999 Acoustical Society of America.* [S0001-4966(99)03201-4]

PACS numbers: 43.20.Bi, 43.28.Py [DEC]

LIST OF SYMBOLS

a	radius of cylindrical radiator
c_0	ambient speed of sound
D	directivity function
H_n	$=J_n+iY_n$, Hankel function of the first kind
J_n	Bessel function (first kind)
k	axial wave number
L	length of active region of radiator
M	$=U/c_o$, source Mach number
p	complex acoustic pressure amplitude
p'	acoustic pressure
$\mathbf{r}$	position vector of observer at time t in frame K
$\mathbf{r}_1$	position vector of observer at time t in frame K_1
t	reception time
$\mathbf{U}$	source velocity vector
v	radial particle velocity
$\mathbf{v}$	fluid velocity
Y_n	Bessel function (second kind)
ζ	displacement of radiator
μ	viscosity
ρ_0	ambient density
τ	emission time
ω	frequency

INTRODUCTION

Concern about the impact of aircraft noise on current and future community noise standards has brought a new emphasis to the modeling and prediction of aircraft flyover noise. Most prediction schemes assume that the sound field propagates as from a point or compact source. Since many prediction methods are based on static noise measurements with forward flight corrections applied to the data for the overflight-radiated field, the importance of analyzing source motion effects is evident. Previous studies[1,2] addressed convective amplification due to point source motion. Another investigation[3] dealt with a pulsating compact body in motion and showed pressure amplification perpendicular to the source velocity. Convective amplification associated with the internal noise of a gas turbine engine has also been analyzed in a previous work.[4] The models used in the above studies predict a significant increase in the sound levels in the direction of the source velocity as the speed increases, which can be as much as 40 dB. The issue of these high predicted levels is addressed in another study,[5] in which a model of shock associated noise of supersonic jets is developed based on a finite, distributed noise source. This model does not predict the high levels associated with the previous models, which can be attributed to differences in the mathematical models used in the studies.

The sound field for a moving source can be described in either a source-fixed or space-fixed reference frame. Noise source modules for prediction codes are usually formulated in the source frame since this simplifies the boundary conditions associated with the acoustic field. Also, this allows consideration of a distributed source, which is important for Doppler effects. For community noise studies, noise metrics are computed in a groundbased coordinate system. In principle, the problem can be formulated and a solution sought in either frame of reference. Once the problem is solved in a particular reference frame, coordinate transformations allow the pressure field to be expressed in different reference frames.

In this study, the problem is formulated in a source-fixed frame. By using Fourier transforms and separation of variables, a solution is determined in the source frame. Directivity patterns are constructed for a cylindrical radiator, which show the influence of Mach number, frequency, and displacement pattern on the radiated sound field. The far-field acoustic relations are transformed to emission coordinates that depict what is observed from a space-fixed (ground) ref-

a)Electronic mail: jkelly@vces.larc.nasa.gov

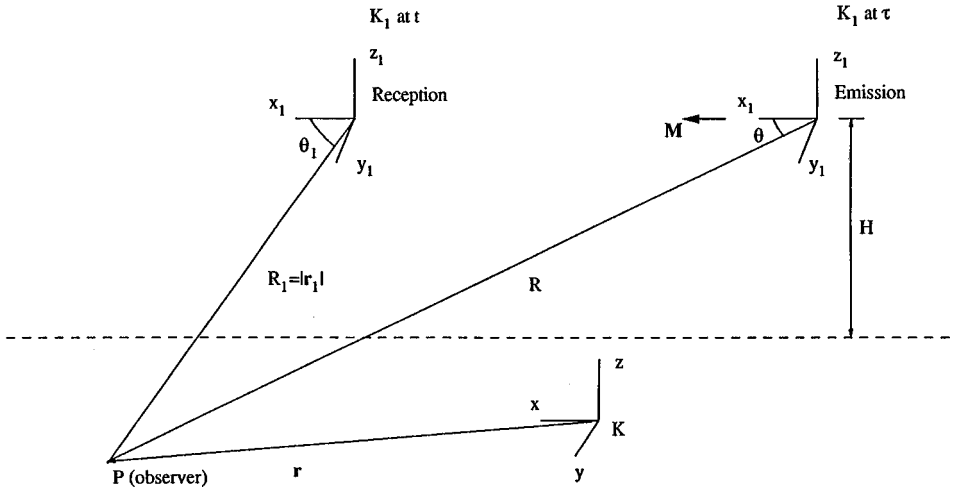

FIG. 1. Source-fixed and space-fixed reference frames.

erence frame. Effects of mean flow/forward flight on absorption due to viscosity are also presented.

I. PROBLEM FORMULATION AND SOLUTION

Figure 1 contains a geometrical description of a source-fixed reference frame, denoted by K_1, moving with uniform velocity **U**, with respect to a space-fixed reference frame denoted by K. Measurements and operations made with respect to K_1 are denoted by the subscript 1 and likewise, those made with respect to K are denoted without any subscript. For a quiescent, homogeneous medium, the acoustic pressure is governed by the following equation in terms of frame K,[6]

$$\left[\left(1+\gamma\frac{\partial}{\partial t}\right)\nabla^2-c_0^{-2}\frac{\partial^2}{\partial t^2}\right]p'(\mathbf{r},t)=0, \tag{1}$$

where $\gamma=4\mu/(3\rho_0 c_0^2)$ is the relaxation time. Note that the above equation contains viscosity. If the angular frequency ω is low enough and the relaxation time short enough, the absorption coefficient is equal to $\omega^2\gamma/(2c_0)$. Equation (1) can be transformed to the K_1 frame, which results in the convected wave equation given by

$$\left\{\left[1+\gamma\left(\frac{\partial}{\partial t}-U\frac{\partial}{\partial x_1}\right)\right]\nabla_1^2-c_0^{-2}\left(\frac{\partial}{\partial t}-U\frac{\partial}{\partial x_1}\right)^2\right\}p'(\mathbf{r}_1,t)=0. \tag{2}$$

This is the same equation that would result if K_1 were stationary and immersed in a fluid with mean flow **U** moving in the $-x_1$ direction. Since p' is a scalar, the following relation is valid at any instant of time:

$$p'(\mathbf{r}_1,t)=p'[\mathbf{r}_1(\mathbf{r},t),t]=p'(\mathbf{r},t). \tag{3}$$

A signal that is sinusoidal in K_1 is

$$p'(\mathbf{r}_1,t)=p(\mathbf{r}_1)e^{-i\omega t}, \tag{4}$$

which upon substitution into Eq. (2) results in a solution by means of a spatial Fourier transform and separation of variables[7] given by

$$p(r_1,\phi_1,x_1)=\frac{1}{2\pi}\left[\sum_{n=0}^{\infty}\cos n\phi_1\int_{-\infty}^{\infty}A_n(k)H_n(\kappa r_1)e^{ikx_1}\,dk+\sum_{n=1}^{\infty}\sin n\phi_1\int_{-\infty}^{\infty}B_n(k)H_n(\kappa r_1)e^{ikx_1}\,dk\right], \tag{5}$$

where

$$\kappa^2=\frac{\beta^2+i\gamma(\omega k^2+Uk^3)}{1-i\gamma(\omega+Uk)}, \tag{6}$$

$$\beta^2=(\omega/c_0)^2+2(\omega/c_0)Mk-k^2(1-M^2). \tag{7}$$

Equation (5) is explicitly stated in a cylindrical coordinate system described in Fig. 2 and satisfies the radiation condition of outward traveling waves only, since this study deals only with subsonic flow/motion ($M<1$). This expression yields the pressure field of a cylindrical source undergoing radial vibrations in which the active portion of the cylinder is bracketed between semi-infinite cylindrical baffles. It does not account for the pressure field contribution by axial vibrations of the cylinder's extremities. The coefficients A_n and B_n are determined from appropriate boundary conditions and characterize source modification due to motion. Due to its dependence on Mach number, H_n characterizes forward flight effects.

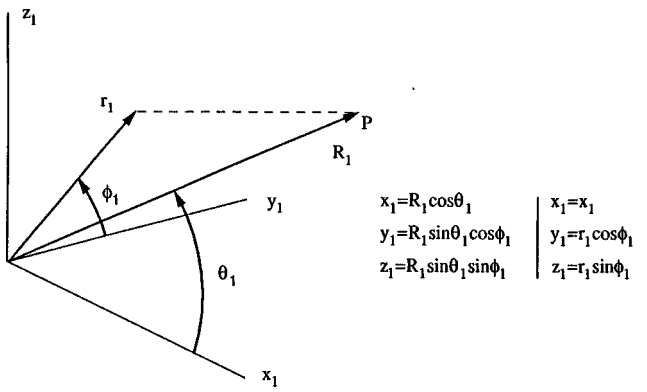

FIG. 2. Source-fixed coordinate systems.

Equation (5) is valid for both the near field and the far field. In order to develop an approximation to the far field, Eq. (5) is expressed in spherical coordinates (see Fig. 2) and for large argument, the asymptotic form for H_n is substituted. Evaluation of the far field can now be accomplished by the method of steepest descent,[8] which for small γ results in

$$p'(R_1,\phi_1,\theta_1,t)=\frac{e^{hR_1-i\omega t}}{\pi R_1\eta}\sum_{n=0}^{\infty}[A_n(k_0)\cos n\phi_1 + B_n(k_0)\sin n\phi_1]e^{-i(n+1)\pi/2}, \tag{8}$$

where

$$h=i\left(\frac{\omega}{c_0}\right)\frac{M\cos\theta_1+\eta}{1-M^2}-\frac{\gamma\omega^2}{2c_0\eta^2(\eta-M\cos\theta_1)^3}, \tag{9}$$

$$\eta=\sqrt{1-M^2\sin^2\theta_1}, \tag{10}$$

$$k_0=\frac{\omega}{c_0(1-M^2)}\left(M+\frac{\cos\theta_1}{\eta}\right). \tag{11}$$

It is assumed in this paper that $M<1$, thus η is always real. Setting $n=0$ results in an expression similar to that for a moving monopole source.[9] An effective wave number, $k_e(\theta_1)$, can be identified in Eq. (8) for a wave propagating in each θ_1 direction,

$$k_e(\theta_1)=\frac{\omega}{c_0}\left(\frac{M\cos\theta_1+\eta}{1-M^2}\right). \tag{12}$$

As will be shown later, the amplitude factor due to convection and k_e will appear as the Doppler amplitude and frequency shift in the space-fixed frame. Since absorption of sound increases with frequency and the observer spectrum in the space-fixed frame is shifted to higher frequencies in the forward arc, the effects of Doppler amplification will be reduced.[10]

Emission coordinates are referenced with respect to the source frame but specify the observer location in the space-fixed frame. Determination of emission coordinates is based on the transit time for a signal emitted at the origin of K_1 at time τ to arrive at the observer located in K at time t. Figure 1 describes the relation between emission and reception coordinates. To express Eq. (8) in emission coordinates, the following transformation must be substituted:

$$R_1=R\sqrt{1+M^2-2M\cos\theta}, \tag{13a}$$

$$\theta_1=\tan^{-1}\left(\frac{\sin\theta}{\cos\theta-M}\right), \tag{13b}$$

$$\phi_1=\phi. \tag{13c}$$

Thus p' in the space-fixed system is

$$p'(R,\phi,\theta,t)=\exp\left[i\frac{\omega}{c_0}(R-c_0t)-\frac{\gamma\omega^2}{2c_0(1-M\cos\theta)^2}R\right]\Big/ \pi R(1-M\cos\theta) \times\sum_{n=0}^{\infty}[A_n(k_f)\cos n\phi+B_n(k_f)\sin n\phi]e^{i(n+1)\pi/2}, \tag{14}$$

where

$$k_f=\frac{\omega\cos\theta}{c_0(1-M\cos\theta)}. \tag{15}$$

In Eq. (14), the phase angle can be written as

$$\psi=-\omega\left[t-\frac{R(\tau)}{c_0}\right]=-\omega\tau. \tag{16}$$

Here, the retarded time relation has been employed. Evaluating the instantaneous frequency, ω^*, will result in

$$\omega^*=-\frac{\partial\psi}{\partial t}=\frac{\omega}{1-M\cos\theta}, \tag{17}$$

which is the Doppler shifted frequency as seen by the observer in the K frame. Observe that ω^* is present in the absorption coefficient in Eq. (14). A few comments are in order about the singularity exhibited in Eq. (14) if $M\cos\theta=1$, which occurs in the transonic regime. This condition corresponds to the ''Mach wave'' directions along which weak ballistic shock waves travel. The analysis presented in this investigation is based on linear acoustic theory, which results in Eq. (14). For a transonic situation, it is well established that linear acoustic theory is not valid[11] and that a nonlinear analysis must be employed.[12]

In general, Eq. (17) relates the source and observer frequencies when there is relative motion. The following interpretation of an apparently negative frequency for $M>1$ is due to Rayleigh.[13] For a supersonic observer and a fixed source, acoustic disturbances generated after the motion begins would never reach the observer. Wave fronts that were propagating before the motion commenced are eventually overtaken and heard in the reverse of the natural order. If the observer is moving at $M=2$, the sound would be heard in perfect time and pitch but backwards.

II. RADIATOR CONFIGURATION AND DIRECTIVITY PATTERNS

Ignoring viscosity ($\mu=0$), the appropriate boundary condition is continuity of particle displacement,[14]

$$\frac{\partial F}{\partial t}+\mathbf{v}\cdot\nabla_1 F=0 \quad \text{on } F(\mathbf{r}_1,t)=0. \tag{18}$$

Here, F represents the radiating surface which can be either a solid or free surface. For cylindrical radiators, the boundary displacement and pressure field must be spatially periodic in ϕ_1. Therefore, both the boundary configuration and the sound field can be expressed as a Fourier series in ϕ_1. Equa-

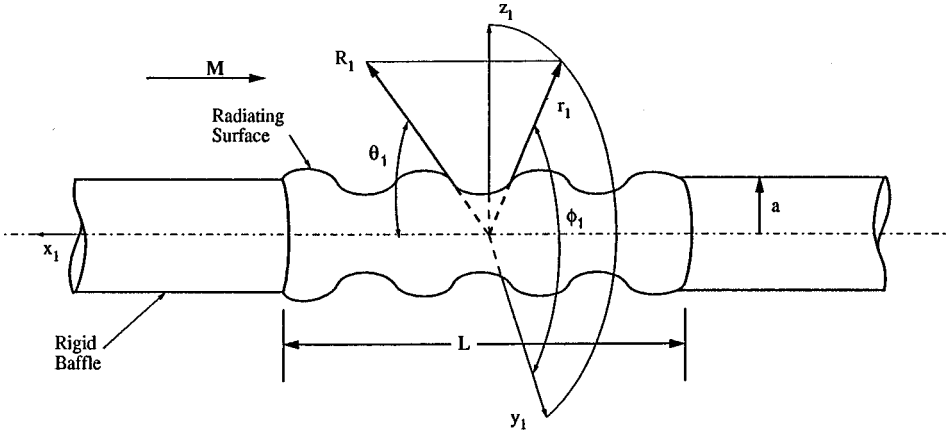

FIG. 3. Infinite cylindrical radiator with displacement distribution confined to finite length of cylinder.

tion (5), which describes the sound field, already expresses this fact. Figure 3 illustrates a cylindrical radiator configuration. In this case, F is

$$F(r_1,\phi_1,x_1,t)=r_1-a-\zeta(\phi_1,x_1)e^{-i\omega t}=0. \tag{19}$$

Here, ζ is the radial displacement of the cylinder about the cylinder radius a. Substituting this expression into Eq. (18) and linearizing the result produces

$$v=-i\omega\zeta-U\frac{\partial\zeta}{\partial x_1} \quad \text{at } r_1=a. \tag{20}$$

Applying the Fourier transform to Eq. (20) and using the radial momentum equation yields, for an axisymmetric sound field (no ϕ_1 dependence), the far-field pressure which is given by

$$p'(R_1,\theta_1,t)=\frac{-i\omega\rho_0c_0(M\cos\theta_1+\eta)^2\tilde{\zeta}(k_0)e^{i(\omega/c_0)\{[(M\cos\theta_1+\eta)/(1-M^2)]R_1-c_0t\}}}{\pi R_1\sin\theta_1 H_0'\left(\dfrac{\omega a\sin\theta_1}{c_0\eta}\right)(1-M^2)^2\eta^2}. \tag{21}$$

In the above expression, H_0' is the derivative with respect to the argument of the Hankel function of the first kind of the zero order. This result can be expressed in the K frame as

$$p'(R,\theta,t)=\frac{-i\omega\rho_0c_0\tilde{\zeta}(k_f)e^{i(\omega/c_0)(R-c_0t)}}{\pi R\sin\theta H_0'\left(\dfrac{\omega a}{c_0}\cdot\dfrac{\sin\theta}{1-M\cos\theta}\right)(1-M\cos\theta)^2}. \tag{22}$$

An important difference between Eqs. (21) and (22) is that for a fixed point in K_1, the former is independent of time and thus appears as a stationary signal in K_1, while the latter is time dependent and thus is nonstationary in K. These relations could be of significance for flight test data in determining forward flight effects and applying de-Dopplerization schemes,[15,16] since the above procedure gives some insight into relating the nonstationary pressure signal measured in K, Eq. (22), to the corresponding stationary pressure signal measured in K_1, Eq. (21).

As an example of a displacement mode, consider $\zeta(x_1)=\zeta_0\cos[(\pi/L)x_1]$ defined over the length $-L/2<x_1<L/2$. The transform is

$$\tilde{\zeta}(k_0)=\frac{2(\pi/L)\cos(k_0L/2)}{(\pi/L)^2-k_0^2}\zeta_0. \tag{23}$$

Since the signal is stationary in K_1, sound-pressure levels (SPL) can be computed without any ambiguity and plotted as a function of θ_1 using Eq. (21). From this relation and Eq. (23), it is evident that the sound field is dependent on a, L and ω in addition to M. This is in contrast to a point source where the radiated pressure is only a function of M. Figures 4–6 show directivity patterns for some representative cases based on SPL since this is the usual quantity measured in acoustic tests. The SPL has been normalized relative to a spherical radiator oscillating with the same values for ω and ζ_0 as the cylindrical radiator. Also, the radius of both the cylinder and sphere are set at 1 foot, requiring both to have the same surface area results in $L=2$ feet. Therefore, the values in the figures represent decibels above or below the field due to a spherical radiator. Each figure represents a particular frequency for three different Mach numbers, $M=0$, 0.3 and 0.9. Since the sound field is axisymmetic, the directivity patterns are computed for $0°\leqslant\theta_1\leqslant180°$ and then rotated about the cylinder axis to produce the figures.

Figure 4 depicts the sound fields for a 50-Hz signal. In Fig. 4(a), the quiescent situation ($M=0$) is shown. As is expected, the field is symmetric with respect to the fore and aft directions and the maximum level occurs along the radiator axis where the level is almost 4 dB less than that due to the spherical radiator. Figure 4(b) contains a pattern with flow, $M=0.3$, and it is seen that the pressure field is higher

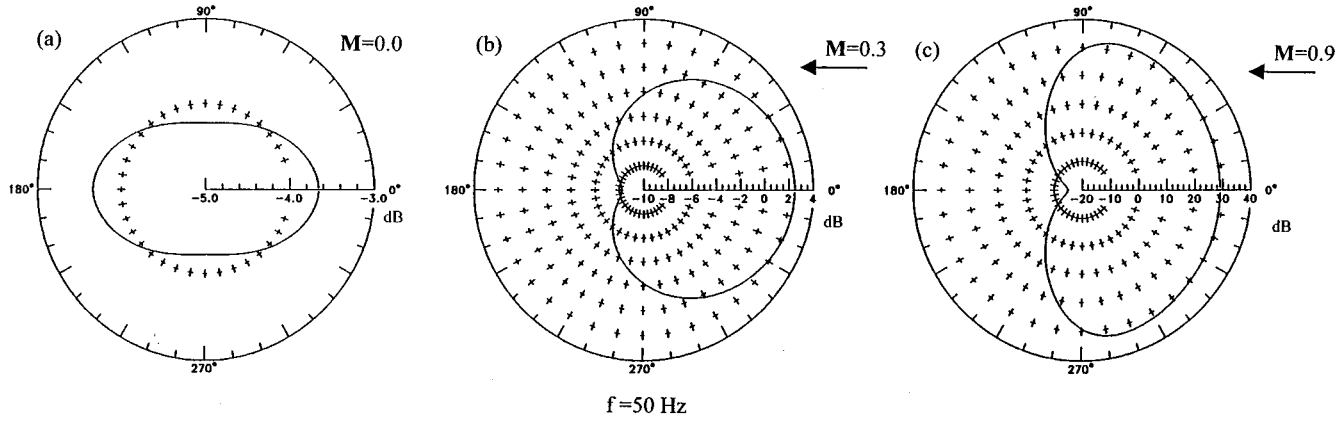

FIG. 4. Far-field pressure directivity pattern, frequency=50 Hz; (a) $M=0$; (b) $M=0.3$; (c) $M=0.9$.

in the forward direction. The maximum level occurs at $\theta_1=0°$ and is at least 6 dB greater than the maximum for the quiescent case, Fig. 4(a). Increasing the flow velocity to $M=0.9$ results in the pattern shown in Fig. 4(c). The maximum level of 36 dB above the quiescent case occurs at $\theta_1=73°$.

Shown in Fig. 5 are the SPL patterns for a 200-Hz oscillation. For $M=0$ and 0.3 the patterns are similar to those of the previous figure. Comparing Fig. 5(a) to Fig. 5(b) shows that the maximum level for the $M=0.3$ case is approximately 5 dB greater than the $M=0$ case. But, for $M=0.9$, Fig. 5(c), a pressure lobe appears downstream of the cylinder where the maximum level occurs at $\theta_1=103°$. The SPL is greater by 15 dB than the quiescent case.

Increasing the frequency to 500 Hz produces the directivity patterns displayed in Fig. 6. Note that for $M=0$ there are pressure lobes lateral to the cylinder axis in addition to the axial lobes and the maximum SPL occurs at $\theta_1=90°$. For $M=0.3$, shown in Fig. 6(b), the maximum level occurs at $\theta_1=89°$ and is slightly more than 1 dB above the high value for the no flow situation. In the $M=0.9$ case, the number of minor lobes increases. The peak level at $\theta_1=118°$ is about 8 dB higher than the peak level for the no flow case.

Observe in Figs. 4–6 that the directions for the maximum pressures, when flow is present, increase with increasing Mach number. Especially noticeable is the switching of the location of the maximum pressure between the upstream and downstream directions that occurs in Fig. 5 as the Mach number increases. This effect can be attributed to convection and coincidence.[7] Coincidence occurs when $k_0^2=(\pi/L)^2$ and $\tilde{\zeta}(k_0)$ takes an indeterminate form, as can be seen from Eq. (23). Therefore, the pressure at coincidence can be obtained by means of l'Hospital's rule. It is readily determined that the corresponding coincidence angle, θ_{1c}, is given by

$$\theta_{1c}=\cos^{-1}\left\{\frac{\left[(1-M^2)\dfrac{\lambda}{\lambda_w}-M\right]\sqrt{1-M^2}}{\sqrt{1-M^2\left[(1-M^2)\dfrac{\lambda}{\lambda_w}-M\right]^2}}\right\}, \qquad (24)$$

where $\lambda=2\pi c_0/\omega$ is the acoustic wavelength and $\lambda_w=2L$ (4 feet) is the flexural standing-wave wavelength. Equation (24) shows that the coincidence angle depends on the wavelength ratio (λ/λ_w) and Mach number. Also, the absolute value of the ratio in Eq. (24) must be less than or equal to unity for coincidence to occur. This requirement yields the following condition to be satisfied for coincidence to be present in the acoustic field:

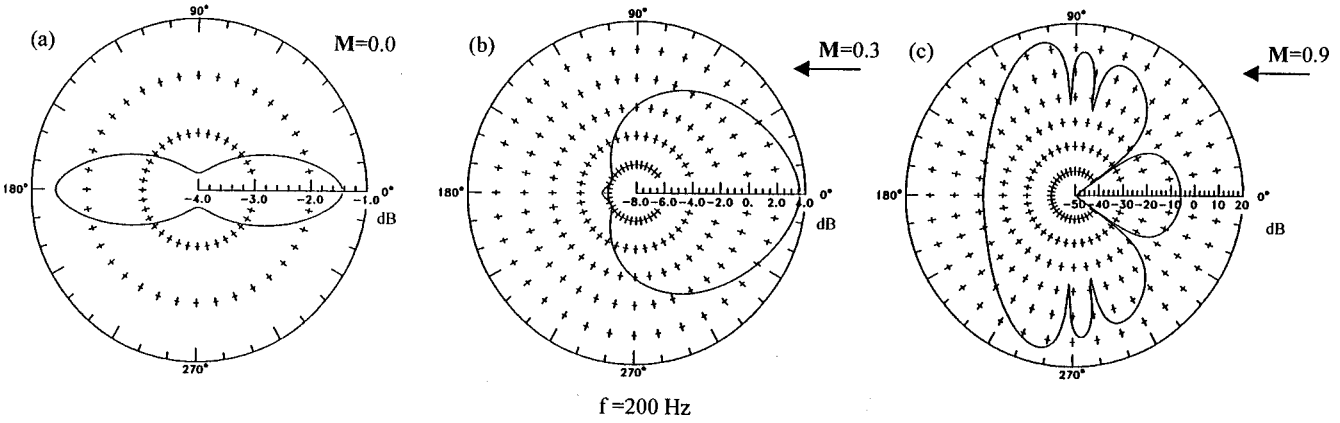

FIG. 5. Far-field pressure directivity pattern, frequency=200 Hz; (a) $M=0$; (b) $M=0.3$; (c) $M=0.9$.

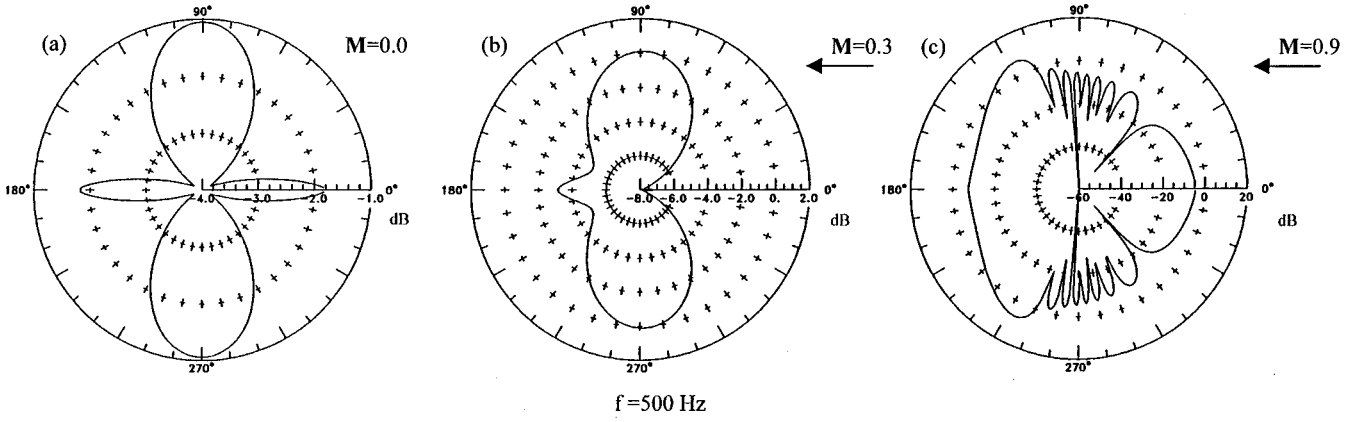

FIG. 6. Far-field pressure directivity pattern, frequency=500 Hz; (a) $M=0$; (b) $M=0.3$; (c) $M=0.9$.

$$\frac{\lambda}{\lambda_w} \leqslant \frac{1}{1-M}. \tag{25}$$

Because of the θ_1 dependence of H_0' in Eq. (21), the coincidence angle does not locate the pressure maximum precisely. For an axisymmetric sound field, in general, the coincidence angle is in the vicinity of the maximum pressure. In the cases presented, θ_{1c} increases with decreasing λ (increasing ω) and increasing M. If coincidence is absent, the pressure maximums are located at $\theta_1=0°$ in Figs. 4–6. Coincidence occurs in Figs. 4(c), 5(b), 5(c), 6(a), 6(b), and 6(c). In Fig. 5(b), coincidence is present in the upstream direction but occurs in the downstream region in Fig. 5(c).

III. INFLUENCE OF ABSORPTION ON THE SOUND FIELD

From Eq. (12), it is seen that the maximum value for k_e occurs at $\theta_1=0°$ and the minimum is at $\theta_1=180°$ which are, respectively, $\omega/[c_0(1-M)]$ and $\omega/[c_0(1+M)]$. Thus the wavelengths of rearward traveling waves are greater than those traveling forward. This is of relevance as an explanation for the alleviation of any signal amplification due to convection effects since attenuation increases for upstream propagation and decreases for downstream.[17,18]

Using Eq. (8), it can be shown that the power spectral density function (PSDF) in the far field is given by

$$G_{pp}(R_1,\phi_1,\theta_1,\omega)=\frac{e^{-\alpha\omega^2(R_1-R_{1s})}D(\phi_1,\theta_1)G_{ss}(\omega)}{(R_1/R_{1s})^2}. \tag{26}$$

In this relation, $\alpha=\gamma/[c_0\eta^2(\eta-M\cos\theta_1)^3]$ and G_{ss} is the PSDF associated with a reference sphere of radius R_{1s}. Equation (26) allows SPLs to be computed by way of

$$L(R_1,\phi_1,\theta_1,\Delta\omega)=L_s(\phi_1,\theta_1,\Delta\omega)-20\log(R_1/R_{1s}) + 10\log\left[\frac{\int_{\omega_1}^{\omega_2}e^{-\alpha\omega^2(R_1-R_{1s})}G_{ss}(\omega)d\omega}{\int_{\omega_1}^{\omega_2}G_{ss}(\omega)d\omega}\right], \tag{27}$$

where $\Delta\omega=\omega_2-\omega_1$, the bandwidth for the level. Also, L_s represents the source SPL ($R_1=R_{1s}$). The last term in Eq. (27) is the absorption loss due to viscosity only and it is plotted versus θ_1 in Figs. 7 and 8. In each figure, a particular frequency band is considered for three different Mach numbers, $M=0.3$, 0.6 and 0.9, for the propagation distance $\Delta R=R_1-R_{1s}$. For these results, the relaxation time is held constant with the value $\gamma=1.695\times10^{-10}$ s. For each Mach number, three absorption curves are plotted for the following source spectra:

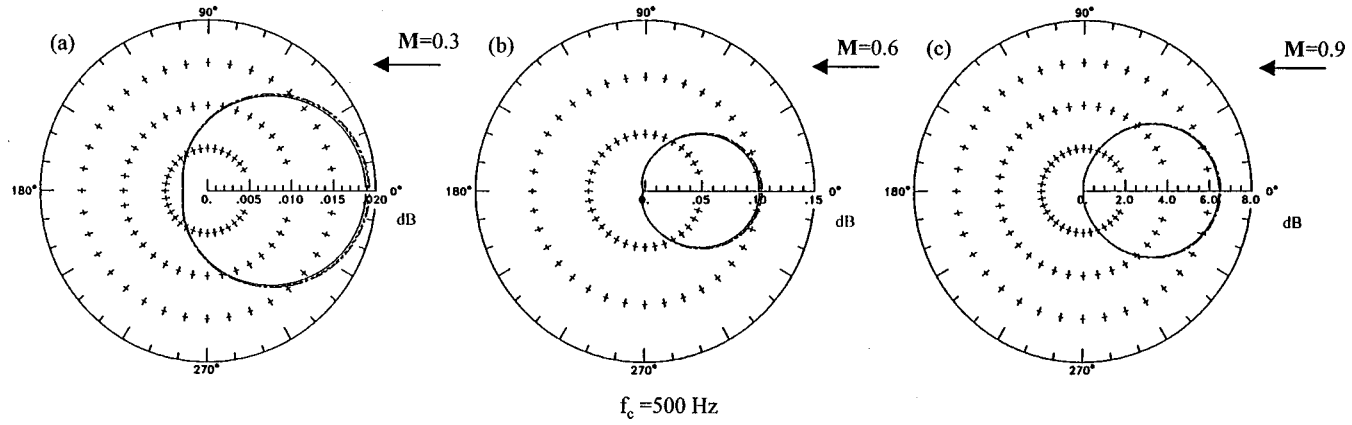

FIG. 7. Pressure field absorption loss, $f_c=500$ Hz; ———, tone; – – –, white noise; — – —, pink noise; (a) $M=0.3$; (b) $M=0.6$; (c) $M=0.9$.

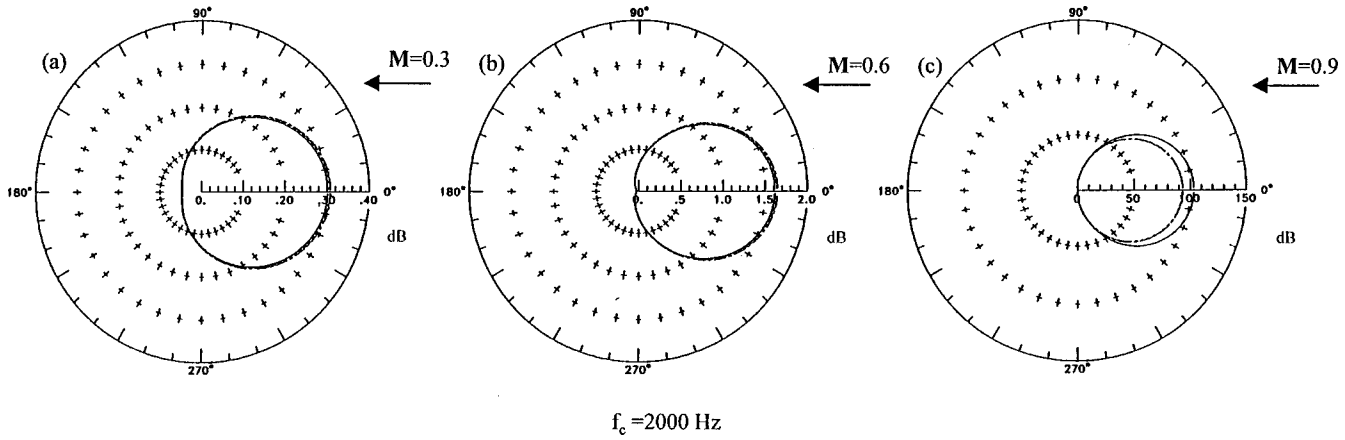

FIG. 8. Pressure field absorption loss, $f_c=2$ kHz; ———, tone; – – –, white noise; — – —, pink noise; (a) $M=0.3$; (b) $M=0.6$; (c) $M=0.9$.

$$G_{ss}(\omega)=\begin{cases} C\,\delta(\omega-\omega_c), & \text{tonal signal,} \\ C, & \text{white noise,} \\ C/\omega, & \text{pink noise,} \end{cases} \tag{28}$$

where C is a constant. Thus, Figs. 7 and 8 demonstrate the effects of flow (Mach number) and source frequency content (PSDF) on absorption. The 1/3-octave band centered at $f_c=500$ Hz ($f_1=450$, $f_2=560$ Hz) is shown in Fig. 7. For this value of ΔR (1000 ft.), absorption is insignificant for $M=0.3$ and 0.6. Note that all three curves are quite close to being coincident and therefore, for the 500-Hz band, the absorption loss is independent of the source spectral distribution. Actually, this was true up to the $f_c=1$ kHz band ($f_1=900$ Hz, $f_2=1.12$ kHz). Illustrated in Fig. 8 is the 1/3-octave band centered at $f_c=2$ ($f_1=1.8$, $f_2=2.24$ kHz). It is evident from Figs. 7 and 8 that absorption increases in the upstream direction with increasing Mach number. Also, observe the high attenuation for the $M=0.9$ case, Fig. 8(c), and that now source spectrum affects the absorption loss. The white and pink noise signals effectively coincide but attenuation of the tonal signal is 10 dB greater. Thus for 1/3-octave bands from $f_c=2$ kHz and above, absorption is dependent on whether the signal is broadband or tonal.

IV. SUMMARY AND CONCLUSIONS

An analysis of sound-pressure fields relative to both uniformly translating and space-fixed reference frames has been presented. A solution was determined, including viscosity, for a distributed source in the source frame of reference. Coordinate transformations then allowed the acoustic field to be expressed in terms of emission coordinates relative to the space-fixed (ground) reference frame. The influence of mean flow/forward flight on source-fixed directivity patterns is shown. A finite cylindrical source was considered which had a sinusoidal displacement pattern.

The following observations were obtained from the study:

(1) The directivity patterns were strongly influenced by Mach number.
(2) For the 50-Hz case the pressure field was higher in the upstream arc for $M=0.9$ in contrast to the higher frequencies.
(3) Peak levels shifted to greater angles with increasing frequency and Mach number.
(4) The greatest difference between peak values for $M=0$ and $M=0.9$ was for the 50-Hz case with a difference of 36 dB.
(5) These differences decreased with increasing frequency and were much less significant for 500 Hz (8 dB).
(6) Sound absorption was at a maximum directly upstream from the source and increased with increasing Mach number.
(7) For the propagation distance considered, $\Delta R=1000$ ft, source spectral characteristics influence absorption only for the 1/3-octave bands above $f_c=1$ kHz at the higher Mach numbers.

[1] M. V. Lowson, ''The sound field for singularities in motion,'' Proc. R. Soc. London, Ser. A **286**, 559–572 (1965).
[2] R. Mani, ''A moving source problem relevant to jet noise,'' J. Sound Vib. **25**, 337–347 (1972).
[3] A. Dowling, ''Convective amplification of real simple sources,'' J. Fluid Mech. **74**, 529–546 (1976).
[4] R. S. Larson, ''Convective amplification of gas turbine engine internal noise sources,'' J. Sound Vib. **74**, 123–137 (1981).
[5] C. K. W. Tam, ''Broadband shock associated noise of supersonic jets measured by a ground observer,'' AIAA Pap. **92-0502** (1992).
[6] L. E. Kinsler, A. R. Frey, A. B. Coppens, and J. V. Sanders, *Fundamentals of Acoustics*, 3rd ed. (Wiley, New York, 1982), p. 143.
[7] M. C. Junger and D. Feit, *Sound, Structures, and Their Interaction*, 2nd ed. (MIT, Cambridge, MA, 1986), pp. 173, 179.
[8] A. H. Nayfeh, *Introduction to Perturbation Techniques* (Wiley-Interscience, New York, 1981), pp. 79–101.
[9] A. P. Dowling and J. E. Ffowcs Williams, *Sound and Sources of Sound* (Ellis Horwood, Chichester, England, 1983), p. 192.
[10] J. J. Kelly and M. R. Wilson, ''Signal processing of noise data from high-speed flyovers,'' J. Aircraft **32**, 590 (1995).
[11] M. K. Myers and A. J. Callegari, ''On the singular behavior of linear acoustic theory in near-sonic duct flows,'' J. Sound Vib. **51**, 517–531 (1977).
[12] A. H. Nayfeh, J. J. Kelly, and L. T. Watson, ''Non-linear propagation in near sonic flows,'' J. Sound Vib. **75**, 359–370 (1981).
[13] J. W. Strutt (Baron Rayleigh), *The Theory of Sound*, 1894, 2nd ed. (reprinted by Dover, New York, 1945), Vol. 2, p. 154.

[14] K. Karamcheti, *Principles of Ideal Fluid Aerodynamics* (Wiley, New York, 1966), pp. 191–192.
[15] J. J. Kelly, ''Signal processing of aircraft flyover noise,'' J. Sound Vib. **160**, 485–501 (1993).
[16] J. J. Kelly and M. R. Wilson, ''De-Dopplerization of aircraft acoustic signals,'' J. Aircraft **32**, 1012–1017 (1995).
[17] A. H. Nayfeh, J. E. Kaiser, and D. P. Telionis, ''Acoustics of aircraft-engine duct systems,'' AIAA J. **13**, 130–153 (1975).
[18] S. H. Ko, ''Sound attenuation in lined rectangular ducts with flow and its application to the reduction of aircraft engine noise,'' J. Acoust. Soc. Am. **50**, 1418–1432 (1971).

The effect of evaporation-condensation on sound propagation in cylindrical tubes using the low reduced frequency approximation

Richard Raspet, Craig J. Hickey, and James M. Sabatier
National Center for Physical Acoustics, University of Mississippi, University, Mississippi 38677

(Received 30 March 1998; accepted for publication 25 September 1998)

In order to better understand the effects of water on sound attenuation in porous materials, Mao [J. Acoust. Soc. Am. **104**, 664–670 (1998)] has investigated sound propagation in a gas–water vapor mixture contained in a cylindrical tube. He used the Rayleigh eigenmode calculation to evaluate the high and low frequency limits of attenuation in an air-filled tube with wet walls. However, he was unable to obtain a general analytical expression and the interpretation of the limits is difficult because of their complexity. The formulation of the problem presented in this paper parallels the ''low reduced frequency method'' of Tijdeman [J. Sound Vib. **39**, 1–33 (1975)]. In contrast to the earlier results, an analytical solution for the propagation constant is obtained which allows for calculation of attenuation over a broad frequency range. The simple expressions obtained in the small and large shear wave number limits provide useful insight into the behavior of the gas–water vapor mixture. © *1999 Acoustical Society of America.* [S0001-4966(99)02901-X]

PACS numbers: 43.20.Bi, 43.20.Hq [DEC]

INTRODUCTION

Changes in velocity and attenuation of sound waves due to the presence of multiple fluids in poroelastic media, such as sandstones, have been investigated experimentally for quite some time.[1–8] For a water–air system, changes in phase velocity and attenuation of sound waves due to changes in saturation are observed to be greatest at very low saturation or near complete saturation. Knight and Dvorkin[9] studied the dependence of seismic and electrical properties of sandstones at very low saturations of water. They contend that the dependence at low saturation is distinctly different than at the higher saturation. In the very low saturation regime, rapid decreases in wave velocity and associated increases in attenuation are observed with the addition of small amounts of water.

Theoretical modeling of wave propagation for poroelastic media containing two fluids can be grossly subdivided into two categories based upon the approach used. One approach is to obtain a general description whereby the fluids are treated independently with the use of some type of homogenization scheme.[10,11] The governing system of equations in these formulations contains numerous parameters which are not well understood and experimental procedures for their measurements are usually not presented. The other approach is to utilize a theory for a fully saturated porous medium, such as Biot,[12] and account for the multiple fluid phases by replacing the original fluid parameters and some of the macroscopic parameters with ''effective'' parameters.[13,14] These effective parameters are obtained based upon specific assumptions about the interactions of the fluids at the pore scale.

Capillary tube models for porous media have been quite successful in predicting the acoustic wave in an air-filled rigid porous medium. Such models have also been used to modify the Biot theory[15,16] to model the ''slow'' compressional wave in air- and water-filled poroelastic media. Recent work[17] has used the Rayleigh eigenmode calculation to evaluate the high and low frequency limits of attenuation of sound in an air-filled tube with wet walls. The expressions for these approximations were quite complicated and difficult to interpret physically, and a general analytic expression could not be derived for the attenuation.

In this paper we report on the application of the ''low reduced frequency method,'' developed by Tijdeman[18] to calculate acoustic loss in gas-filled tubes, to the problem of attenuation in gas-filled tubes with mass transfer of vapor from the wet tube wall. By applying the low reduced frequency method, we are able to calculate the attenuation over a wide frequency range in an easily interpreted form which can be compared to standard porous media results. This calculation provides us with an estimate of the contribution of mass transfer to the attenuation of sound in porous media and develops simple and easily understood results for application to sound propagation in tubes containing gas–vapor mixtures.

In Sec. I we describe the basic equations governing sound propagation in an ideal gas–vapor mixture. These equations are then recast into cylindrical coordinates and subjected to conditions according to the ''low reduced frequency method.'' The boundary conditions at the tube wall are discussed and used to obtain a solution for the acoustic wave number. The small and large shear wave number limits for comparison with Mao's[17] earlier work conclude this section. In Sec. II calculations for an air–water vapor mixture are discussed, and Sec. III contains the conclusions.

I. THEORY OF SOUND PROPAGATION IN WET TUBES

A. Basic equations for a gas–vapor mixture

The model considered here is the same as Mao[17] and consists of a rigid cylindrical tube filled with air and satu-

rated water vapor. A thin layer of liquid coats the interior of the tube. Further, it is assumed that the heat capacity of the tube wall is high enough that the temperature of the tube wall and the layer of liquid do not fluctuate. The gas component cannot penetrate the tube wall or the liquid layer, and the gas–vapor mixture does not slip with respect to the liquid layer. The gas and vapor are treated as ideal gases. Properties of the mixture are computed according to the theory of gas mixtures.[19]

The equations governing sound propagation in an ideal gas–vapor mixture are the Navier–Stokes equation applied to the mixture, the continuity equation for each component and the mixture, the entropy equation for the mixture, the equation of state in the mixture, and the diffusion equation of the components.[20] In linearized form these are

$$\rho_0 \frac{\partial \mathbf{v}}{\partial t} = -\nabla p + \mu \nabla^2 \mathbf{v} + \left(\beta + \frac{1}{3}\mu\right) \nabla(\nabla \cdot \mathbf{v}), \tag{1}$$

$$\frac{\partial \rho_1}{\partial t} + \rho_1^0 (\nabla \cdot \mathbf{v}_1) = 0, \tag{2a}$$

$$\frac{\partial \rho_2}{\partial t} + \rho_2^0 (\nabla \cdot \mathbf{v}_2) = 0, \tag{2b}$$

$$\frac{\partial \rho}{\partial t} + \rho_0 (\nabla \cdot \mathbf{v}) = 0, \tag{2c}$$

$$-\frac{\partial p}{\partial t} + \frac{\gamma}{\gamma - 1} nk \frac{\partial T}{\partial t} - \kappa \nabla^2 T + k_T nkT \nabla \cdot (\mathbf{v}_1 - \mathbf{v}_2) = 0, \tag{3}$$

$$\frac{\partial p}{\partial t} = nk \frac{\partial T}{\partial t} + kT_0 \left(\frac{1}{m_1}\frac{\partial \rho_1}{\partial t} + \frac{1}{m_2}\frac{\partial \rho_2}{\partial t}\right), \tag{4}$$

and

$$\mathbf{v}_1 - \mathbf{v}_2 = D_{12}\left(\frac{1}{\rho_2^0}\nabla \rho_2 - \frac{1}{\rho_1^0}\nabla \rho_1 - \frac{n}{\rho_0 P_0}(m_2 - m_1)\nabla p - \frac{n^2}{n_1 n_2}\cdot \frac{k_T}{T_0}\nabla T\right). \tag{5}$$

In these equations variables ρ_1, ρ_2 are the density of the gas and of the vapor, $\rho = \rho_1 + \rho_2$ is the density of the mixture, $\mathbf{v}_1$, $\mathbf{v}_2$ are hydrodynamic velocity of the gas and of the vapor, $\mathbf{v} = (\rho_1 \mathbf{v}_1 + \rho_2 \mathbf{v}_2)/\rho$ is the hydrodynamic velocity of the mixture, p is the pressure of the mixture, and T is the temperature of the mixture. In the above equations constant μ is the viscosity of the mixture, β is the bulk viscosity of the mixture, m_1, m_2 are the molecular mass of gas and vapor, n_1, n_2 are the number density of the gas, of the vapor, $n = n_1 + n_2$ is the total number density, γ_1, γ_2 are the ratio of specific heats of the gas and of the vapor, $n\gamma/(\gamma - 1) = [n_1 \gamma_1/(\gamma_1 - 1)] + [n_2 \gamma_2/(\gamma_2 - 1)]$ is the ratio of nc_p/R for the mixture, c_p is the molar heat capacity at constant pressure, R is the universal gas constant, κ is the thermal conductivity of the mixture, D_{12} is the mass diffusion coefficient, k_T is the thermal diffusion ratio, as defined in Ref. 19, p. 541, and k is the Boltzmann constant.

The set of equations above differs from those of Tijdeman[18] by the presence of additional terms in the entropy equation and in the equation of state and by the presence of the diffusion equation [Eq. (5)]. The additional term in the entropy equation arises from the heat flux due to diffusion and the additional term in the equation of state express the change in density due to diffusion across the control surface.

Assuming the variables to have an $e^{-i\omega t}$ time dependence, we introduce normalized variables as follows:

$$p = \frac{\rho_0 c^2}{\gamma}(1.0 + p^* e^{-i\omega t}), \tag{6a}$$

$$\rho = \rho_0 (1.0 + \rho^* e^{-i\omega t}), \tag{6b}$$

$$T = T_0 (1.0 + T^* e^{-i\omega t}), \tag{6c}$$

$$\mathbf{v} = c\mathbf{v}^* e^{-i\omega t}, \tag{6d}$$

and

$$\mathbf{v}_1 - \mathbf{v}_2 = c\boldsymbol{\Delta} e^{-i\omega t}, \tag{6e}$$

where c is the sound speed in the mixture.

Next, we assume that the tubes are small enough that we may use cylindrical coordinates with no polar dependence. For convenience, we follow Tijdeman's notation and let

$$\mathbf{v}^* = u\hat{e}_x + v\hat{e}_r \tag{7a}$$

and, in addition, let

$$\boldsymbol{\Delta}^* = U\hat{e}_z + V\hat{e}_r. \tag{7b}$$

Finally, we define the nondimensional variable along the cylindrical axis as

$$\xi = \frac{\omega z}{c}, \tag{8a}$$

the nondimensional radial variable as

$$\eta = \frac{r}{R}, \tag{8b}$$

and the reduced frequency as

$$\Omega = \frac{\omega R}{c}, \tag{8c}$$

where R is the tube radius. The above equations can now be recast in terms of these normalized variables. The axial component of the Navier–Stokes equation transforms to

$$iu = \frac{1}{\gamma}\frac{\partial p^*}{\partial \xi} - \frac{\mu}{\rho_0 \omega}\frac{1}{R^2}\left\{\left[\frac{\partial^2 u}{\partial \eta^2} + \frac{1}{\eta}\frac{\partial u}{\partial \eta} + \Omega^2 \frac{\partial^2 u}{\partial \xi^2}\right] + \Omega\left(\frac{\beta}{\mu} + \frac{1}{3}\right)\frac{\partial}{\partial \xi}\left[\frac{1}{\eta}\frac{\partial \eta v}{\partial \eta} + \Omega \frac{\partial u}{\partial \xi}\right]\right\} \tag{9}$$

and the radial component becomes

$$i\Omega v = \frac{1}{\gamma}\frac{\partial p^*}{\partial \eta} - \frac{\Omega \mu}{\rho_0 \omega}\frac{1}{R^2}\left\{\left[\frac{\partial^2 v}{\partial \eta^2} + \frac{1}{\eta}\frac{\partial v}{\partial \eta} - \frac{v}{\eta^2} + \Omega^2 \frac{\partial^2 v}{\partial \xi^2}\right] + \Omega\left(\frac{\beta}{\mu} + \frac{1}{3}\right)\frac{\partial}{\partial \eta}\left[\frac{1}{\eta}\frac{\partial \eta v}{\partial \eta} + \Omega \frac{\partial u}{\partial \xi}\right]\right\}. \tag{10}$$

The continuity equation for the mixture gives

$$i\Omega\rho^* = \Omega\left(\frac{\partial u}{\partial \xi} + \frac{\partial v}{\partial \eta} + \frac{v}{\eta}\right), \tag{11}$$

the entropy equation for the mixture becomes

$$i\Omega T^* - i\Omega\left(\frac{\gamma-1}{\gamma}\right)p^* + \frac{\kappa}{nk}\left(\frac{\gamma-1}{\gamma}\right)\left(\frac{\Omega}{\omega R^2}\right)\left[\frac{\partial^2 T^*}{\partial \eta^2} + \frac{1}{\eta}\frac{\partial T^*}{\partial \eta} + \Omega^2\frac{\partial^2 T^*}{\partial \xi^2}\right] - k_T\left(\frac{\gamma-1}{\gamma}\right)\left[\frac{1}{\eta}\frac{\partial \eta V}{\partial \eta} + \Omega\frac{\partial U}{\partial \xi}\right] = 0, \tag{12}$$

and the equation of state becomes

$$\Omega(p^* - T^* - \rho^*) = \frac{in_1n_2}{n\rho_0}(m_1 - m_2)\left[\Omega\frac{\partial U}{\partial \xi} + \frac{1}{\eta}\frac{\partial V\eta}{\partial \eta}\right]. \tag{13}$$

Using the axial component of the diffusion equation gives

$$iU = \frac{-D_{12}}{\omega R^2}\Omega\frac{\partial}{\partial \xi}\left[\frac{1}{\eta}\frac{\partial \eta V}{\partial \eta} + \Omega\frac{\partial U}{\partial \xi}\right] - i\frac{D_{12}}{\omega R^2}\Omega^2 \times\left[\frac{n}{\rho_0}(m_2 - m_1)\frac{\partial p^*}{\partial \xi} + \frac{n^2}{n_1n_2}\kappa_T\frac{\partial T^*}{\partial \xi}\right], \tag{14}$$

and the radial component gives

$$i\Omega V = \frac{-D_{12}}{\omega R^2}\Omega\frac{\partial}{\partial \eta}\left[\frac{1}{\eta}\frac{\partial \eta V}{\partial \eta} + \Omega\frac{\partial U}{\partial \xi}\right] - i\frac{D_{12}}{\omega R^2}\Omega^2 \times\left[\frac{n}{\rho_0}(m_2 - m_1)\frac{\partial p^*}{\partial \eta} + \frac{n^2}{n_1n_2}\kappa_T\frac{\partial T^*}{\partial \eta}\right]. \tag{15}$$

The set of equations presented above could be solved exactly by the Rayleigh eigenmode analysis to find the attenuation and phase velocity of the acoustic mode. This result is quite complicated, and the high and low frequency approximations are only valid over a restricted range. A better technique that spans a large range of validity is the ''low reduced frequency'' analysis of Tijdeman.[18] We show that this technique can be applied to the mass transfer problem outlined above and produces easily interpreted analytical results consistent with the previous rigid porous media literature on attenuation due to viscosity and thermal conductivity alone.

The principal approximation is to require that the reduced frequency be small:

$$\Omega = \frac{\omega R}{c} = \frac{2\pi R}{\lambda} \ll 1. \tag{16}$$

This spans a wide range of frequencies for small tubes and, in fact, includes regions where the Kirchoff wide tube approximation holds, as well as the Rayleigh narrow tube/low frequency region. A second set of criteria are also used to retain some terms that would otherwise be neglected:

$$u \gg v \tag{17}$$

and

$$v \approx V. \tag{18}$$

We expect the first condition to be met since the radial velocity must be zero at the center and the displacement per cycle is at most on the order of one radius. The second condition arises since v and V are the same order of magnitude at the wall [see Eq. (31b)] and both are zero at the center.

Certain nondimensional groupings of parameters may be identified in Eqs. (9)–(15). These are

$$\lambda_\mu = R\sqrt{\rho\omega/\mu}, \tag{19}$$

the dimensionless shear wave number,

$$\lambda_T = R\sqrt{\frac{nk\gamma}{\gamma-1}\frac{\omega}{\kappa}} = R\sqrt{\frac{\rho\omega c_p}{\kappa}}, \tag{20}$$

the dimensionless thermal wave number, and

$$\lambda_D = R\sqrt{\omega/D_{12}}, \tag{21}$$

the dimensionless diffusion wave number.

We rewrite Eqs. (9)–(15), retaining the lowest-order terms in Ω. We treat terms in v and V as first-order terms in Ω, which is consistent with Eqs. (17) and (18). With the definitions above and the application of the low reduced frequency approximation, the governing set of equations becomes

$$iu = \frac{1}{\gamma}\frac{\partial p^*}{\partial \xi} - \frac{1}{\lambda_\mu^2}\left[\frac{\partial^2 u}{\partial \eta^2} + \frac{1}{\eta}\frac{\partial u}{\partial \eta}\right], \tag{22}$$

$$\frac{1}{\gamma}\frac{\partial p^*}{\partial \eta} = 0, \tag{23}$$

$$i\Omega\rho^* = \Omega\left(\frac{\partial u}{\partial \xi} + \frac{\partial v}{\partial \eta} + \frac{v}{\eta}\right), \tag{24}$$

$$T^* - \frac{\gamma-1}{\gamma}p^* - \frac{i}{\lambda_T^2}\left[\frac{\partial^2 T^*}{\partial \eta^2} + \frac{1}{\eta}\frac{\partial T^*}{\partial \eta}\right] + i\frac{k_T}{\Omega}\frac{\gamma-1}{\gamma}\left(\frac{1}{\eta}\frac{\partial \eta V}{\partial \eta} + \Omega\frac{\partial U}{\partial \xi}\right) = 0, \tag{25}$$

$$\Omega[p^* - \rho^* - T^*] = i\frac{n_1n_2}{n\rho_0}(m_1 - m_2) \times\left[\Omega\frac{\partial U}{\partial \xi} + \frac{1}{\eta}\frac{\partial \eta V}{\partial \eta}\right], \tag{26}$$

$$iU = 0, \tag{27}$$

and

$$iV = \frac{-1}{\lambda_D^2}\frac{\partial}{\partial \eta}\left[\frac{1}{\eta}\frac{\partial \eta V}{\partial \eta} + \Omega\frac{\partial U}{\partial \xi}\right]. \tag{28}$$

Equation (27) will be used to eliminate the $\partial U/\partial \xi$ term in Eqs. (25), (26), and (28).

Equations (22)–(24) are unchanged from Tijdeman.[18] Equation (23) demonstrates that the pressure is not a function of radial position and can be treated as $p^*(\xi)$ only. Equation (25) contains an additional term which vanishes when there is only one component because the thermal diffusion ratio, k_T, tends to zero as n_1 or n_2 goes to zero. Equation (26) contains an additional term on the right-hand side which van-

ishes when there is only one component, i.e., n_1 or $n_2=0$. It also vanishes if the two components have the same mass since the additional term describes density changes due to the species velocity differing from the hydrodynamic velocity. If the masses are equal, there is no density change due to differential velocities.

B. Boundary conditions

In order to solve the system above, we must develop the boundary conditions at the wall of the tube ($\eta=1$) and at the center ($\eta=0$) in terms of the variables used above. As stated earlier, we assume that a thin layer of liquid coats the interior of a cylindrical tube filled with gas and saturated vapor. Further, it is assumed that the heat capacity of the tube wall is high enough that the temperature of the tube wall and the layer of liquid do not fluctuate. The gas component cannot penetrate the tube wall or the liquid layer, and it is assumed that the gas–vapor mixture does not slip with respect to the liquid layer.

The boundary conditions at the tube wall ($\eta=1$) are

(a) temperature fluctuations are zero,

$$T^*=0; \tag{29}$$

(b) no slip for the mixture,

$$u=0; \tag{30}$$

(c) the gas cannot penetrate the wall,

$$v_1=0, \tag{31a}$$

which translates to a boundary condition on v and V as

$$v+\frac{\rho_2}{\rho}V=0; \tag{31b}$$

(d) the vapor pressure is constant at the wall since the vapor pressure is a function of T only and T is constant,

$$p_2=0, \tag{32a}$$

which is related to the set of variables p^*, T^*, u, U, v, V by use of the continuity equation for each component, the equation for Δ, and by the equation of state to give

$$i\Omega p^*=\frac{n_1}{n}\frac{1}{\eta}\frac{\partial \eta V}{\partial \eta}. \tag{32b}$$

The condition that $U=0$ is also used in deriving Eq. (32b).

The boundary conditions on the axis of the tube, $\eta=0$, are that T^*, u, U, ρ_1^*, and ρ_2^* must be finite. The latter two conditions on ρ_1^* and ρ_2^* can be related to v and V by the continuity equations, which are singular unless V and v are zero at $\eta=0$. Therefore,

$$\text{(e)}\quad V=0 \quad \text{at} \quad \eta=0 \tag{33}$$

and

$$\text{(f)}\quad v=0 \quad \text{at} \quad \eta=0 \tag{34}$$

complete the set of boundary conditions.

C. Solution

The use of the low reduced frequency approximation decouples the equations so that the wave number of the acoustic mode can be determined by directly integrating the equations. Equation (23) demonstrates that the pressure is not a function of radial position and can be treated as $p^*(\xi)$ only. Using this fact about the pressure, Eq. (22) can be integrated using the boundary condition $u=0$ at $\eta=1$ and u finite at $\eta=0$ to give

$$u=\frac{i}{\gamma}\frac{dp^*(\xi)}{d\xi}\left[1-\frac{J_0^*(\sqrt{i}\lambda_\mu\eta)}{J_0(\sqrt{i}\lambda_\mu)}\right], \tag{35}$$

where J_0 is the Bessel function of the first kind of order zero. Equation (28) is also directly integrable and gives

$$V(\xi,\eta)=f(\xi)J_1(\sqrt{i}\lambda_D\eta), \tag{36}$$

where J_1 is the Bessel function of the first kind of order one and $f(\xi)$ is the undetermined ξ dependence. Here $f(\xi)$ can be evaluated in terms of $p(\xi)$ using boundary condition (32). The resulting radial component of the relative velocity is

$$V(\xi,\eta)=i\Omega\,\frac{n}{n_1}\frac{J_1(\sqrt{i}\lambda_D\eta)}{\sqrt{i}\lambda_D J_0(\sqrt{i}\lambda_D)}\,p^*(\xi). \tag{37}$$

Next, Eq. (37) is used in the entropy equation [Eq. (25)] to develop a differential equation for T^* as a function of the coordinates and $p^*(\xi)$:

$$\frac{\gamma-1}{\gamma}\,p^*(\xi)\left[1+k_T\frac{n}{n_1}\frac{J_0(\sqrt{i}\lambda_D\eta)}{J_0(\sqrt{i}\lambda_D)}\right] = T^*-\frac{i}{\lambda_T^2}\left[\frac{\partial^2 T^*}{\partial\eta^2}+\frac{1}{\eta}\frac{\partial T^*}{\partial\eta}\right]. \tag{38}$$

This can be integrated using boundary conditions on T^* at $\eta=1$ and $\eta=0$ to obtain

$$T^*(\xi,\eta)=\frac{\gamma-1}{\gamma}\,p^*(\xi) \times\left[1-\frac{J_0(\sqrt{i}\lambda_T\eta)}{J_0(\sqrt{i}\lambda_T)}+\frac{\lambda_T^2}{\lambda_T^2-\lambda_D^2}\,k_T\frac{n}{n_1} \times\left(\frac{J_0(\sqrt{i}\lambda_D\eta)}{J_0(\sqrt{i}\lambda_D)}-\frac{J_0(\sqrt{i}\lambda_T\eta)}{J_0(\sqrt{i}\lambda_T)}\right)\right]. \tag{39}$$

It is convenient at this point to define

$$\mathcal{F}_j(\eta)=\left[1-\frac{J_0(\sqrt{i}\lambda_j\eta)}{J_0(\sqrt{i}\lambda_j)}\right], \tag{40}$$

with j representing μ,T,D for the viscosity, thermal, and diffusion terms. With this notation, ρ^* can be eliminated from Eqs. (24) and (26) and the solutions for T^* and u substituted:

$$\frac{1}{\eta}\frac{\partial \eta v}{\partial \eta}=i\Omega\left[\frac{\mathcal{F}_\mu(\eta)}{\gamma}\frac{d^2p^*(\xi)}{d\xi^2}+p^*(\xi)\right.$$
$$\times\left\{1+\frac{n_2(m_1-m_2)}{\rho_0}-\frac{\gamma-1}{\gamma}\right.$$
$$\times\left(1+\frac{\lambda_T^2}{\lambda_T^2-\lambda_D^2}\,k_T\,\frac{n}{n_1}\right)\mathcal{F}_T(\eta)-\left(\frac{n_2(m_1-m_2)}{\rho_0}\right.$$
$$\left.\left.\left.-\frac{\gamma-1}{\gamma}\,\frac{\lambda_T^2}{\lambda_T^2-\lambda_D^2}\,k_T\,\frac{n}{n_1}\right)\mathcal{F}_D(\eta)\right\}\right]. \tag{41}$$

Next, Eq. (41) is multiplied by $\eta d\eta$ and integrated from 0 to 1 and Eq. (31b) is applied to evaluate $v(1)$ in terms of $V(1)$. The integration of Eq. (40) defines

$$F(\lambda_j)=2\int_0^1 \mathcal{F}_j(\eta)\,\eta d\eta=1-\frac{2J_1(\sqrt{i}\lambda_j)}{\sqrt{i}\lambda_j J_0(\sqrt{i}\lambda_j)}. \tag{42}$$

The $F(\lambda_j)$ notation is used here because it can be easily adapted for other pore geometries.[21]

The resulting equation for $p^*(x)$ is

$$\frac{d^2p^*(x)}{dx^2}+\frac{\gamma}{F(\lambda_\mu)}\frac{\omega^2}{c^2}\left[1+\frac{n_2}{n_1}-\frac{\gamma-1}{\gamma}F(\lambda_T)-\frac{n_2}{n_1}F(\lambda_D)\right.$$
$$\left.-\left(\frac{\gamma-1}{\gamma}\,\frac{\lambda_T^2}{\lambda_T^2-\lambda_D^2}\,k_T\,\frac{n}{n_1}\right)(F(\lambda_T)-F(\lambda_D))\right]p^*(x)=0. \tag{43}$$

The complex wave number squared is easily identified from this equation as the coefficient of $p^*(x)$:

$$k^2=\frac{\gamma}{F(\lambda_\mu)}\frac{\omega^2}{c^2}\left[1+\frac{n_2}{n_1}-\frac{\gamma-1}{\gamma}F(\lambda_T)-\frac{n_2}{n_1}F(\lambda_D)\right.$$
$$\left.-\left(\frac{\gamma-1}{\gamma}\,\frac{\lambda_T^2}{\lambda_T^2-\lambda_D^2}\,k_T\,\frac{n}{n_1}\right)(F(\lambda_T)-F(\lambda_D))\right]. \tag{44}$$

This is the principle result of this paper and is a simple form easily compared to previous results without mass transfer. The usual form of the wave number squared for sound propagation with viscosity and thermal conductivity is recovered by setting $n_2=0$ and $k_T=0$.

The real and imaginary parts of the wave number are easily evaluated from Eq. (44). The imaginary part of k yields the attenuation and the real part is $\omega/v_{\rm ph}$ where $v_{\rm ph}$ is the phase velocity.

D. Small and large shear wave number limits

Several useful approximations can be developed for comparison with Mao's[17] earlier work and for comparison with predictions of sound propagation in tubes without mass transfer.

1. Low frequency/small λ_j

A useful approximation is developed following earlier porous media research where it is shown that for cylindrical pores

$$F(\lambda_j)=\left[\frac{4}{3}+\frac{i8}{\lambda_j^2}\right]^{-1} \tag{45}$$

for small to moderate λ_j. Equivalent forms have been derived for other pore shapes. Expanding Eq. (44) to $O(1/\lambda_j^2)$ yields

$$k^2=\gamma\frac{\omega^2}{c^2}\left[\left(1+\frac{n_2}{n_1}\right)\left(\frac{4}{3}+\frac{i8}{\lambda_\mu^2}\right)\right.$$
$$\left.-\frac{\gamma-1}{\gamma}N_P\left(1+k_T\frac{n}{n_1}\right)-\frac{n_2}{n_1}S_C\right], \tag{46}$$

where N_P is the Prandtl number, $N_P=(\lambda_T/\lambda_\mu)^2$, and S_C is the Schmidt number, $S_C=(\lambda_D/\lambda_\mu)^2$. The limit of very small λ_j corresponds to the Kirchoff narrow pore limit and results in

$$k^2=i\frac{\omega^2}{c^2}\frac{8\gamma}{\lambda_\mu^2}\left(1+\frac{n_2}{n_1}\right). \tag{47}$$

The formula for the wave number in a narrow tube is modified by the factor $1+n_2/n_1$. In addition, the properties γ,μ,ρ_0, and c^2 are now properties of the gas–vapor mixture.

2. High frequencies/large λ_j

In the high frequency/wide tube limit,

$$F(\lambda_j)\to 1.0-\frac{2\sqrt{i}}{\lambda_j}. \tag{48}$$

When this is substituted in Eq. (44), we find to $O(1/\lambda)$,

$$k^2=\frac{\omega^2}{c^2}\left[1+\frac{2\sqrt{i}}{\lambda_\mu}\left(1+\frac{\gamma-1}{\sqrt{N_P}}+\frac{n_2}{n_1}\frac{\gamma}{\sqrt{S_C}}-k_T(\gamma-1)\right.\right.$$
$$\left.\left.\times\frac{n}{n_1}\frac{1}{\sqrt{N_P}+\sqrt{S_C}}\frac{\sqrt{N_P}}{\sqrt{S_C}}\right)\right]. \tag{49}$$

The Rayleigh wide tube approximation is recovered when $n_2=0$ and $k_T=0$. In order to obtain a better convergence in the large λ limit, we expand to higher orders. Expanding to $O(1/\lambda^2)$,

$$F(\lambda_j)\to 1.0-\frac{2\sqrt{i}}{\lambda_j}+\frac{i}{\lambda_j^2} \tag{50}$$

and

$$F^{-1}(\lambda_j)\to 1.0+\frac{2\sqrt{i}}{\lambda_j}+\frac{3i}{\lambda_j^2}. \tag{51}$$

Substituting Eqs. (50) and (51) into Eq. (44), we find to $O(1/\lambda^2)$,

$$k^2=\frac{\omega^2}{c^2}\left[1+\frac{2\sqrt{i}}{\lambda_\mu}\left(1+\frac{\gamma-1}{\sqrt{N_P}}+\frac{n_2}{n_1}\frac{\gamma}{\sqrt{S_C}}-k_T(\gamma-1)\right.\right.$$
$$\times\frac{n}{n_1}\frac{1}{\sqrt{N_P}+\sqrt{S_C}}\frac{\sqrt{N_P}}{\sqrt{S_C}}\Bigg)+\frac{4i}{\lambda_\mu^2}\left(1+\frac{\gamma-1}{\sqrt{N_P}}+\frac{n_2}{n_1}\frac{\gamma}{\sqrt{S_C}}\right.$$
$$\left.-k_T(\gamma-1)\frac{n}{n_1}\frac{1}{\sqrt{N_P}+\sqrt{S_C}}\frac{\sqrt{N_P}}{\sqrt{S_C}}\right)-\frac{i}{\lambda_\mu^2}$$
$$\left.\times\left(1+\frac{\gamma-1}{N_P}+\frac{n_2}{n_1}\frac{\gamma}{S_C}-k_T(\gamma-1)\frac{n}{n_1}\frac{1}{S_C}\right)\right]. \quad (52)$$

When $n_2=0$ and $k_T=0$, Eq. (52) is in agreement with Weston's[22] expression for ''wide–narrow'' transition.

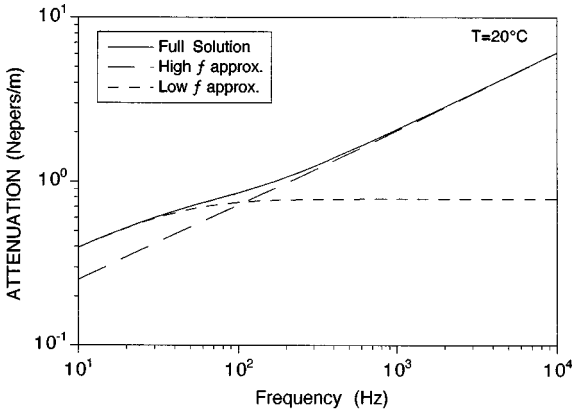

FIG. 1. Predictions of attenuation of sound in a tube filled with an air–water vapor mixture using the complete solution, small shear wave number limit, and large shear wave number limit.

II. AIR–WATER VAPOR MIXTURES

Consider a hypothetical experiment consisting of a rigid tube connected to a source of water vapor and to a source of gas. Starting with the tube under vacuum conditions, allow water vapor to enter the tube. After equilibrium is reached, disconnect from the water vapor source and slightly reduce the temperature of the tube so that some of the vapor condenses on the tube wall. This assures that the assumption of a wet tube wall is satisfied. The amount of water vapor and the water vapor pressure in the tube is a function of the tube temperature.[23] Various amounts of gas can be placed in the tube by connecting to a source of gas. The ideal gas law can be used to determine the number of moles of gas in the tube from measurements of the gas pressure and the tube temperature. The total pressure inside the tube is the sum of the vapor pressure and gas pressure.

Calculating the attenuation of sound from the above equations requires values for the properties of the components as well as values for the effective properties of the mixture. The ratio of specific heats and the specific heat at constant pressure for the components are independent of temperature and are calculated from basic kinetic theory, whereas the temperature dependence of the ambient sound speed of the components is taken into account.[24] The ratio of specific heats, the specific heat at constant pressure, and the temperature dependence of ambient sound speed of the mixture are derived based upon an average energy of the mixture. The temperature dependence of the viscosity,[25] thermal conductivity,[26] of the components and of the binary mixture are accounted for. The temperature and pressure dependence of mass diffusion[27] and the thermal diffusion ratio[28] of the binary mixture are also accounted for.

Calculations of the attenuation of sound in a tube filled with an air–water vapor mixture using the complete solution, Eq. (44), small shear wave number limit, Eq. (46), and large shear wave number limit Eq. (52), are shown in Fig. 1. The tube radius is 0.5 mm, the temperature is 20 °C, and the air pressure is set at 1.0 atm (1.01×10^5 Pa). There is only a small range of intermediate frequencies for which the limiting cases do not represent the complete solution accurately. For this air–water vapor mixture, the frequency range of 10 Hz to 10 kHz represents a range in shear wave number of about 1 to about 35. The limiting cases are good approximations for shear wave numbers less than 2 and greater than 10.

Varying the temperature changes the properties of the components and mixture as well as changing the mole fractions of the components. Figure 2 shows the variation in properties of air, water vapor, and the mixture as a function of temperature. Figure 2(a) shows that the mole fraction of water vapor is near zero at 0 °C, so there is mostly gas in the tube at this temperature. At 100 °C there are nearly equal mole fractions of gas and water vapor. If mole fractions of water vapor greater than 0.5 are wanted, the air pressure must be reduced to less than 1 atm. The speed of sound in both air and water vapor increase with increasing temperature as shown in Fig. 2(b). The sound speed in the mixture changes because of the changes in component properties and the change in mole fractions. Figure 2(c) shows that the viscosities of the components increase with increasing temperature. The viscosity of the mixture increases at a lesser rate, reaches a maximum value at about 70 °C, and then decreases as the temperature is further increased. The behavior of the viscosity of the mixture is due to the varying mole fractions of the components as well as other molecular interactions.[19] Figure 2(d) shows the variation in thermal conductivity as a function of temperature. What is interesting here is that the thermal conductivity of the mixture can be made to be less than the thermal conductivity of the individual components. The diffusion coefficient and thermal diffusion ratio, shown in Fig. 2(e), are properties of the binary mixture of gases. These coefficients account only for interaction between unlike molecules. Interactions between like molecules enter only in the second approximation.[19] For an air–water vapor mixture, the diffusion coefficient exhibits a maximum at about 50 °C. The thermal diffusion ratio increases with increasing temperature but is quite small in magnitude. The Prandtl numbers of air (0.7353) and water vapor (0.7616) are independent of temperature. There is no Schmidt number for the components because only mass diffusion within the mixture is considered. Figure 2(f) shows that the Prandtl number of the mixture increases with increasing temperature. The Schmidt number has a minimum at about 30 °C and a maximum at about 85 °C, but the overall range of the Schmidt

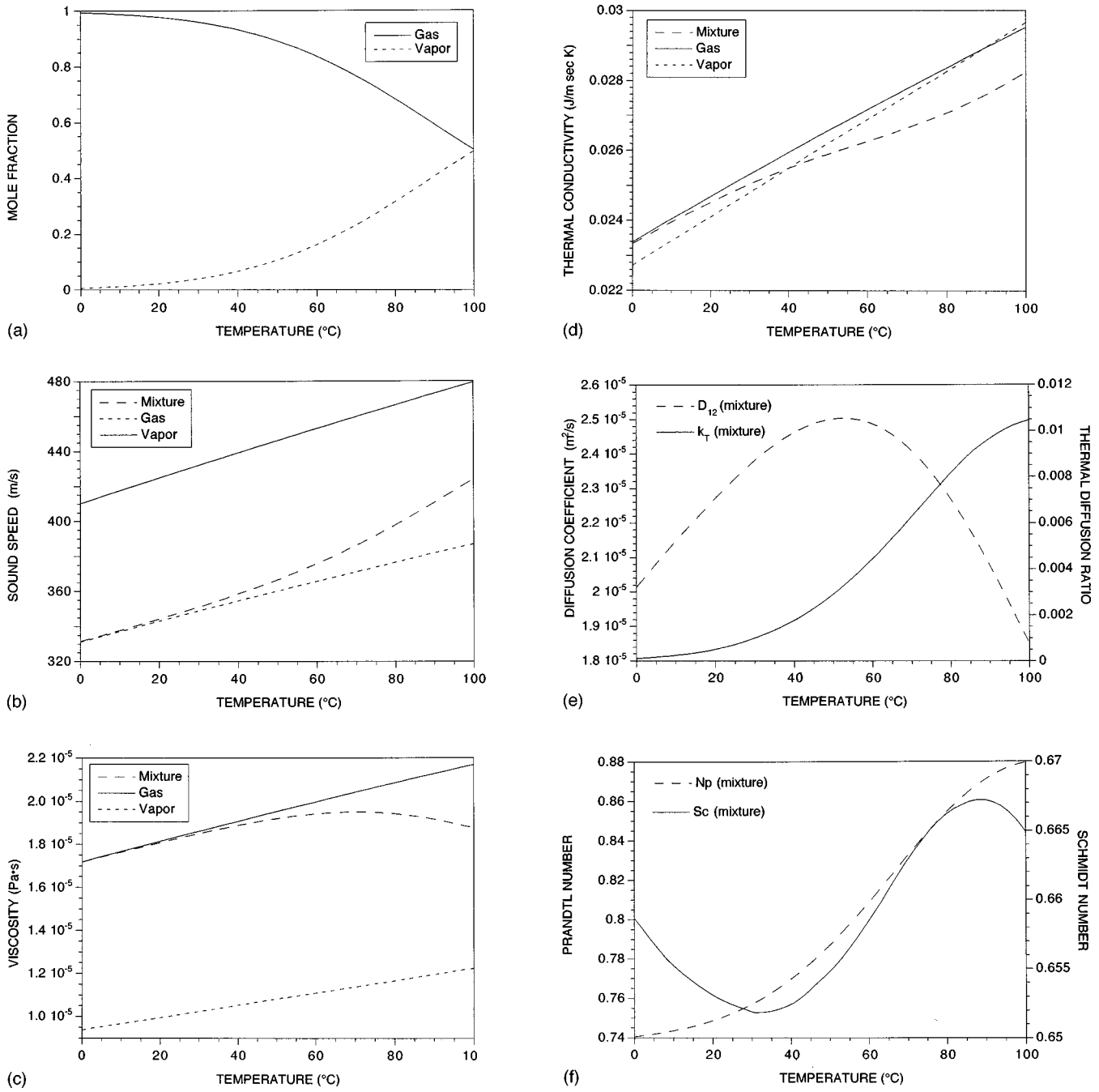

FIG. 2. The variation in properties of air, water vapor, and the air–water vapor mixture with temperature.

number is quite small. The heat capacity and ratio of specific heats of the components are temperature independent. The heat capacity and ratio of specific heat of the mixture vary with temperature solely because the mole fractions of the components change.

Predictions of attenuation of 10-kHz sound in a wet tube of radius 0.5 mm filled with an air–water vapor mixture is shown in Fig. 3. Calculations for the mixture-filled tube show an increase in attenuation if mass transfer is included but a decrease in attenuation if the mixture is treated as an effective fluid, i.e., without mass transfer. Such a prediction should be easy to qualitatively verify in experiment. The decrease in attenuation predicted by the effective fluid is due to the decrease in the kinematic viscosity of the mixture. The increase in attenuation due to mass transfer is associated with the phasing of the pressure perturbation of the acoustic wave and the evaporation-condensation of water vapor from the wall. The heat flux associated with the mass diffusion does not contribute to the attenuation. The thermal diffusion ratio, k_T, represents the coupling between diffusion and heat flux and is small for this case. At a temperature of 100 °C the attenuation in the mixture with mass transfer is about 35% larger than in the gas alone. If a lower gas (air) pressure is used, it will enable larger mole fractions of water vapor to occupy the tube. Using a gas pressure of 0.1 atm, it is possible for the attenuation with mass transfer to be a factor of 2 greater than the gas attenuation. If the mixture is modeled simply as an effective fluid, the attenuation is predicted to be

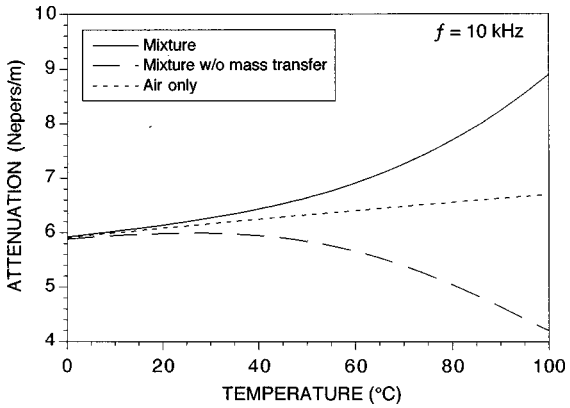

FIG. 3. Predicted attenuation of 10-kHz sound in a tube filled with an air–water vapor mixture with mass transfer, an air–water vapor mixture treated as an effective fluid, and only air as a function of temperature. The frequency is 10 kHz and the air pressure is 1 atm.

about four times smaller than in the gas alone.

Figure 4 shows the frequency dependence of the ratio of attenuation in the mixture to the attenuation in the gas only. At low frequency the difference in attenuation is solely due to the reduction in viscosity of the mixture. The water vapor does not contribute to the pressure fluctuations but is carried along with the gas by diffusion. As the frequency increases, the acoustic period is an insufficient time for the water vapor to condense into the wall and then totally evaporate back into the mixture in phase. Then evaporation-condensation removes energy from the acoustic wave and returns it to a lower pressure portion, causing enhanced attenuation of the high pressure portion.

III. CONCLUSIONS

The low reduced frequency method of Tijdeman[18] is used to produce easily interpreted predictions of the effect of wet walls on sound propagation in gas-filled tubes. These results contain additional terms compared to the standard forms used for predicting sound propagation in rigid porous media.

Our results confirm those of Mao,[17] who showed that mass diffusion is not a large enough contribution to explain the measurements of attenuation in sandstone. The results of this analysis can be used to measure the diffusion coefficient for gas–vapor mixtures by measuring the relative attenuation of a pure gas and of the gas–vapor mixture.

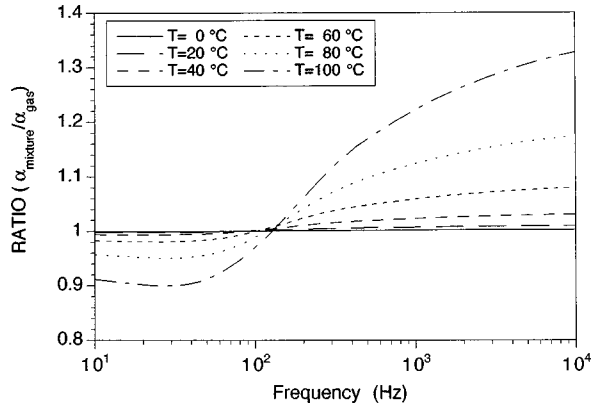

FIG. 4. Ratio of attenuation of an air–water vapor mixture to the attenuation of only air as a function of frequency for different temperatures. The air pressure is 1 atm.

ACKNOWLEDGMENTS

This work is supported jointly by the Office of Naval Research and the USDA-ARS National Sedimentation Laboratory. The authors thank H. E. Bass for sharing his insight on the behavior of gas mixtures. We thank the referees for their comprehensive reviews of this article.

[1] W. T. Born and J. E. Owen, ''Effect of moisture upon velocity of elastic waves in Amherst sandstone,'' American Association of Petroleum Geologist Bulletin **19**, 9–18 (1935).
[2] M. R. J. Wyllie, L. W. Gardner, and A. R. Gregory, ''Studies of elastic wave attenuation in porous media,'' Geophysics **27**, 569–589 (1962).
[3] B. I. Pandit and M. S. King, ''The variation of elastic wave velocities and quality factor *Q* of a sandstone with moisture content,'' Canadian Journal of Earth Sciences **16**, 2187–2195 (1979).
[4] V. A. Clark, B. R. Tittmann, and T. W. Spencer, ''Effect of volatiles on attenuation (*Q*-1) and velocity in sedimentary rocks,'' J. Geophys. Res. **85**, 5190–5198 (1980).
[5] B. R. Tittmann, V. A. Clark, J. M. Richardson, and T. W. Spencer, ''Possible mechanism for seismic attenuation in rocks containing small amounts of volatiles,'' J. Geophys. Res. **85**, 5199–5208 (1980).
[6] W. F. Murphy III, ''Effects of partial water saturation on attenuation in Massilon sandstone and vycor porous glass,'' J. Acoust. Soc. Am. **71**, 1458–1468 (1982).
[7] W. F. Murphy III, ''Acoustic measures of partial gas saturation in tight sandstones,'' J. Geophys. Res. **89**, 11549–11559 (1984).
[8] J.-C. Bacri and D. Salin, ''Sound velocity in sandstone saturated with oil and brine at different concentrations,'' Geophys. Res. Lett. **13**, 326–328 (1986).
[9] R. Knight and J. Dvorkin, ''Seismic and electrical properties of sandstones at low saturations,'' J. Geophys. Res. **97**, 17425–17432 (1992).
[10] L. Thigpen and J. G. Berryman, ''Mechanics of porous elastic materials containing multiphase fluids,'' Int. J. Eng. Sci. **23**, 1203–1214 (1985).
[11] J. A. Hawkins and A. Bedford, ''Variational theory of bubbly media with a distribution of bubble sizes II. Porous solid,'' Int. J. Eng. Sci. **30**, 1177–1186 (1992).
[12] M. A. Biot, ''Theory of propagation of elastic waves in a fluid-saturated porous solid. I. Low frequency range,'' J. Acoust. Soc. Am. **28**, 168–178 (1956).
[13] S. N. Domenico, ''Effect of water saturation on seismic reflectivity of sand reservoirs encased in shale,'' Geophysics **39**, 759–769 (1974).
[14] J. E. White, ''Computed seismic speeds and attenuation in rocks with partial gas saturation,'' Geophysics **40**, 224–232 (1975).
[15] M. A. Biot, ''Theory of propagation of elastic waves in a fluid-saturated porous solid. II. Higher frequency range,'' J. Acoust. Soc. Am. **28**, 179–191 (1956).
[16] K. Attenborough, ''On the acoustic slow wave in air-filled granular materials,'' J. Acoust. Soc. Am. **81**, 93–102 (1987).
[17] Y. Mao, ''Sound attenuation in a cylindrical tube due to evaporation-condensation,'' J. Acoust. Soc. Am. **104**, 664–670 (1998).
[18] H. Tijdeman, ''On the propagation of sound waves in cylindrical tubes,'' J. Sound Vib. **39**, 1–33 (1975).
[19] J. V. Hirschfelder, C. Curtiss, and R. B. Bird, *Molecular Theory of Gases and Liquids* (Wiley, New York, 1954).
[20] L. D. Landau and E. M. Liftshitz, *Fluid Mechanics* (Butterworth-Heinemann, Oxford, 1997), 2nd ed.
[21] W. P. Arnott, H. E. Bass, and R. Raspet, ''General formulation of thermoacoustics for stacks having arbitrarily shaped pore cross sections,'' J. Acoust. Soc. Am. **90**, 3228–3237 (1991).
[22] D. E. Weston, ''The theory of the propagation of plane waves in tubes,'' Proc. Phys. Soc. London, Sect. B **66**, 695–709 (1953).
[23] The vapor pressure as a function of temperature is calculated from the formula on p. 169 of *Physical Acoustics XVII*, edited by W. Mason and R.N. Thurston (Academic New York, 1984). The number of moles of vapor is calculated using the ideal gas law.
[24] The values and temperature dependence of the ambient sound speed of the components is calculated using Eq. 1-9.1 on p. 28, of A. D. Pierce, *Acous-*

tics: An Introduction to its Physical Principles and Applications (Acoustical Society of America, New York, 1991).

[25] The values and temperature dependence of the viscosity of the components are calculated using Eq. 8.2-18 on p. 528, the viscosity of the mixture is calculated using Eq. 8.2-22 on p. 530, and the polar nature of water vapor is also accounted for as given in section 8.6 pp. 597–604 of J. V. Hirschfelder, C. Curtiss, and R. B. Bird, *Molecular Theory of Gases and Liquids* (Wiley, New York, 1954).

[26] The values and temperature dependence of the thermal conductivity of the components are calculated using Eq. 8.2-31 on p. 534, and the thermal conductivity of the mixture is calculated using Eq. 8.2-36 on p. 535 of J. V. Hirschfelder, C. Curtiss, and R. B. Bird, *Molecular Theory of Gases and Liquids* (Wiley, New York, 1954). The polar nature of water vapor is accounted for.

[27] The values and temperature and pressure dependence of the mass diffusion coefficient of the mixture is calculated using Eq. 8.2-44 on p. 539 of J. V. Hirschfelder, C. Curtiss, and R. B. Bird, *Molecular Theory of Gases and Liquids* (Wiley, New York, 1954).

[28] The values and temperature and pressure dependence of the thermal diffusion ratio is calculated using Eq. 8.2-50 on p. 541 of J. V. Hirschfelder, C. Curtiss, and R. B. Bird, *Molecular Theory of Gases and Liquids* (Wiley, New York, 1954).

Rigorous solutions of acoustic wave diffraction by penetrable wedges

Bair V. Budaev[a] and David B. Bogy[b]
Department of Mechanical Engineering, University of California, Berkeley, California 94720

(Received 16 January 1998; revised 24 August 1998; accepted 9 September 1998)

A well-known problem of acoustic wave propagation in two fluid wedges with different densities and wave speeds is addressed by a recently developed approach to more general problems of wave propagation in bi-material solid wedges. The obtained solutions are valid for arbitrary frequencies and the approach is also extendable to wedge structures in which one or both wedges support propagation of shear waves. © *1999 Acoustical Society of America.* [S0001-4966(98)04112-5]

PACS numbers: 43.20.Fn [ANN]

INTRODUCTION

Problems of sound propagation in two adjacent wedge shaped media with different density and wave speeds is a challenging problem that has been considered for several decades. The most rigorous approaches to these problems are based on either the Kontorovich–Lebedev[1] transform or on the Maliuzhinetz technique,[2] but both approaches lead to similar functional equations that until recently have not been amenable to rigorous analysis. There are also numerous attempts to address the problem by direct finite-difference schemes,[3] by the method of parabolic equations,[4] by the method of multiple reflections which is often referred as a complex-ray method,[5] and by other methods.[6–10] It is, however, recognized that, although successful in some particular cases, none of these methods provides a uniform approach to the general problem of wave propagation in a system of two fluid wedges.

On the other hand, in recent years advances have been achieved[11–14] in the study of wave propagation problems in complicated wedge shaped configurations such as a general system of two adhering elastic wedges, which include as particular cases problems with two fluid wedges. Unlike in other approaches the general scheme[12–14] handles problems for all frequencies, with wave attenuation, and with one of the fluids replaced by the a solid medium supporting the propagation of shear waves. The goals of the present paper are to demonstrate the flexibility of the general scheme from Ref. 14, and by using it to develop a rigorous approach to acoustical problems for bi-fluid wedges that can handle fluid, solid, and even composite multi-wedge bottom models for a wide range of frequencies.

Here the general scheme from Ref. 14, which is valid for any bi-material wedge structure, is applied to a system of two fluid wedges. This method results in a representation of the studied wave fields in terms of a special function that is defined as the solution of a singular integral equation. Although our approach does not require any limitations on the wedge's angles, we focus on the case when the two fluid wedges together form a semispace where a thin ''water'' wedge lies over a fluid ''bottom.'' The immediate benefits from this assumption include the possibility of avoiding numerical inversion of integral equations that is certainly the most unattractive aspect of the general scheme. Most attention is given here to the fundamental plane problem with an arbitrary plane incident wave whose solution is then used for building solutions of more realistic problems with cylindrical and spherical incident waves by the superposition method.

Solutions of the problems are obtained as sums of the ''ray'' and scattered fields, where the ''ray'' fields are shown to coincide analytically with the approximate solutions delivered by the method of multiple reflections. The scattered fields are shown to be negligible in the water and in the area of the bottom located immediately behind the water wedge.

In Sec. I the problem is formulated in three different geometries: with a plane incident wave; with a cylindrical incident wave radiated by a line source parallel to the wedges edge; and with a spherical incident wave radiated by a point source.

In Sec. II the problem with a plane incident wave is considered. In Sec. II A the solution is represented by the Sommerfeld contour integrals and the problem is reduced to a system of functional equations with respect to amplitude functions of the Sommerfeld integrals. The singularities of these amplitude functions are associated with specific waves. In Sec. II B the functional equations are used for direct explicit computation of all poles associated with geometrically reflected-transmitted waves. The rest of Sec. II addresses only the computation of the scattered field formed by diffracted bulk waves and head waves originating from the vertex. In Sec. II C the functional equations are transformed to a one-dimensional singular integral equation that is shown to be effectively solvable by retaining the first few terms in the appropriate Neumann series, which means that for practical purposes the integral equation has an analytic solution. In Sec. II D we discuss how a solution of the integral equation can be converted into Sommerfeld's amplitude functions and then to wave fields.

The solution of the integral equation determines the amplitude functions in some vertical strips by explicit formulas involving contour integration. Then, the functional equations analytically continue the amplitude functions from those strips into any wider area and provide the precise analytic

[a]On leave from the Steklov Mathematical Institute, St. Petersburg, Russia.
[b]Electronic mail: dbogy@cml.me.berkeley.edu

description of all singularities. If the width of the area is finite the continuation requires only a finite number of recursive algebraic operations.

With information about the singularities of the amplitude functions the original Sommerfeld representation of the wave fields is modified to distinguish the physically different waves, such as the incident and geometrically reflected-transmitted waves, head waves, and diffracted bulk waves. The geometrical waves correspond to poles of the amplitude functions and are defined in a closed analytical form; the head waves are represented by integrals along cuts of a complex plane; the diffracted waves are defined by integration along the steepest-descent contour. Since the amplitude functions can be computed anywhere in the complex plane, computation of the head and diffracted waves can be performed either by direct numerical integration or by standard asymptotic approximations of the Sommerfeld integrals, but these questions are not discussed here.

In Sec. II E the recursive procedure of analytical continuation of the Sommerfeld amplitudes is analyzed from the numerical point of view, and it is shown that there is a cutoff number after which the contributions of the consecutive recursive steps rapidly vanish, thereby simplifying the practical computations.

In Sec. II F the solution provided by the developed rigorous approach is compared with the solution obtained by the method of multiple reflections. It is demonstrated that the intensity of the diffracted waves in the water is negligible and that, therefore, the acoustic field in the water can be considered to be formed only by geometrical waves, as assumed *a priori* in the method of multiple reflections. It is, however, predicted that the error of the multiple reflection method may reach an unacceptable level in some specified regions of the bottom, and this is confirmed by the numerical results presented.

In Sec. III problems with cylindrical and with spherical incident waves are considered. The solutions are constructed as the superposition of solutions of two-dimensional problems with plane incident waves with complex directions of propagation, as studied in Sec. II.

I. FORMULATION OF BASIC PROBLEMS WITH THE WEDGE GEOMETRY

Let (r,θ,z) be cylindrical coordinates. Let water occupy the wedge $\Gamma_1: 0<\theta<\alpha$, and let the bottom occupy the wedge Γ_2: $\alpha<\theta<\pi$. Let the pressure fields $p_{1,2}(r,\theta,z)$ in $\Gamma_{1,2}$ be represented as superpositions $p_1=p_1^{\rm inc}+\tilde{p}_1$, $p_2=\tilde{p}_2$, of pre-defined incident waves $p_1^{\rm inc}(r,\theta,z)$ and of unknown secondary fields $\tilde{p}_{1,2}(r,\theta,z)$. Then the problem is to find the solution of the Helmholtz equations

$$\nabla^2\tilde{p}_n+k_n^2\tilde{p}_n=0, \quad \text{in } \Gamma_n, \tag{1}$$

such that the fields $p_{1,2}$ satisfy the boundary conditions

$$p_1(r,0,z)=p_2(r,\pi,z)=0; \tag{2}$$

the interface conditions

$$p_1(r,\alpha,z)=p_2(r,\alpha,z), \tag{3}$$

$$\frac{1}{\varrho_1}\frac{\partial}{\partial\theta}p_1(r,\theta,z)\bigg|_{\theta=\alpha}=\frac{1}{\varrho_2}\frac{\partial}{\partial\theta}p_2(r,\theta,z)\bigg|_{\theta=\alpha}; \tag{4}$$

the conditions at the vertex $p_{1,2}(r,\theta,z)=O(1)$, $r\to 0$; and the radiation condition corresponding to the time dependence of the type $e^{i\Omega t}$. The wave numbers, $k_{1,2}$ are defined as $k_n=2\pi(\Omega/c_n)+2\pi i\epsilon_n$, $n=1,2$, where Ω is a frequency, $c_{1,2}$ are the wave speeds in the corresponding media, and $\epsilon_{1,2}$ are wave attenuation for the two wave numbers.

This problem will be considered with three kinds of the incident waves:

1. Plane waves

$$p_1^{\rm inc}(r,\theta,z;\theta_0)=e^{ik_1r\,\cos(\theta-\theta_0)}-e^{ik_1r\,\cos(\theta+\theta_0)}. \tag{5}$$

2. Cylindrical waves generated by line sources parallel to the coast line:

$$p_1^{\rm inc}(r,\theta,z;r_0,\theta_0)=H_0^{(2)}(k_1r_+)-H_0^{(2)}(k_1r_-),$$

$$r_\pm=\sqrt{r^2+r_0^2-2rr_0\,\cos(\theta\mp\theta_0)}. \tag{6}$$

3. Spherical waves generated by point sources:

$$p_1^{\rm inc}(r,\theta,z;r_0,\theta_0)=\frac{e^{-ik_1R_+}}{R_+}-\frac{e^{-ik_1R_-}}{R_-},$$

$$R_\pm=\sqrt{r_\pm^2+z^2}. \tag{7}$$

The third problem with spherical incident waves (7) presents the most realistic model of underwater sound propagation, but the principal part of the analysis of this problem as well as of the problem with cylindrical incident waves (6), is to solve the simplest two-dimensional problem with plane incident waves (5). This is explained by the existence of canonical decompositions of cylindrical and spherical waves into combinations of plane waves, which will be discussed later, after analysis of the two-dimensional problem with plane incident waves.

II. SCATTERING OF A PLANE INCIDENT WAVE

Two-dimensional problems of plane incident wave scattering in arbitrary bi-material wedges were addressed in Ref. 14 where they were reduced to some integral equations that had to be solved numerically. Typical bi-fluid wedge structures discussed above are certainly covered by the general scheme from Ref. 14, but these problems have some specific features that make it possible to solve the resulting integral equations without substantial effort and thus to get rigorous solutions of the scattering problems in a rational form.

A. Functional equations

Let us consider the problem of the scattering of plane incident waves (5). This is a two-dimensional problem whose study follows the general scheme from Ref. 14, based on the representation of the pressure fields $p_{1,2}(r,\theta)$ by Sommerfeld integrals

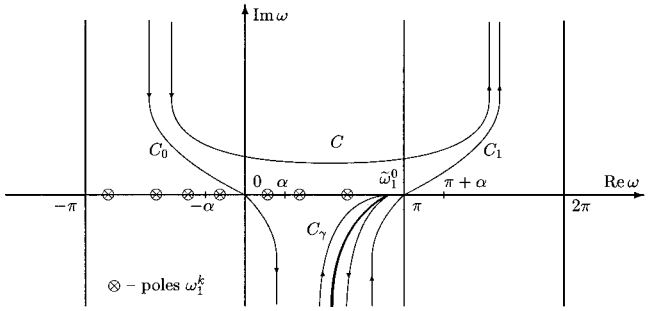

FIG. 1. Sommerfeld contours and singularities of $\Phi_1(\omega)$.

$$p_n(r,\theta) = \int_C [\Phi_n(\omega+\theta-\pi_n)-\Phi_n(\omega+\pi_n-\theta)]e^{ik_n r\cos\omega}\,d\omega, \tag{8}$$

$$\pi_1=0, \quad \pi_2=\pi,$$

taken over the standard $\cup$-like contour C running from $-\pi/2+i\infty$ to $3\pi/2+i\infty$ as shown in Fig. 1.

The Sommerfeld integrals (8) obey the vertex conditions if and only if the amplitudes $\Phi_n(\omega)$ are bounded at infinity. These integrals obey the radiation conditions if their amplitudes have the symmetry $\Phi_n(-\omega)=\Phi_n(\omega)$, if $\Phi_2(\omega)$ is regular in the strip $|\mathrm{Re}\,\omega|\leqslant\pi-\alpha$, and if $\Phi_1(\omega)$ has no singularities in the strip $|\mathrm{Re}\,\omega|\leqslant\pi-\alpha$, except single poles $\omega=\pm\theta_0$ with the residues $\pm 1/2\pi i$.

Boundary conditions (2) are satisfied by the integrals (8) automatically, and the interface condition (3) is equivalent to the functional equation

$$a(\omega)[\Phi_1(g(\omega)+\alpha_1)-\Phi_1(g(\omega)-\alpha_1)] + [\Phi_2(\omega+\alpha_2)-\Phi_2(\omega-\alpha_2)]=0, \tag{9}$$

where

$$a(\omega)=\frac{\sin\omega}{\sqrt{\gamma^2-\cos^2\omega}}, \quad g(\omega)=\arccos\left(\frac{1}{\gamma}\cos\omega\right),$$

$$\gamma=\frac{k_1}{k_2}>1, \quad \alpha_1=\alpha, \quad \alpha_2=\pi-\alpha.$$

The branch of the multivalued function $g(\omega)$ is fixed by cuts along the segments

$$(\gamma_*-\pi n,\gamma_*+\pi n),$$

$$\gamma_*=\arccos\gamma, \quad n=0,\pm1,\pm2,\ldots,$$

and the principal sheet of the complex plane ω is chosen from the condition $g(\pi/2)=\pi/2$, which provides an important identity

$$g(-\omega)=-g(\omega), \quad g(\omega+\pi n)=g(\omega)+\pi n,$$

valid on the principal sheet of ω.

The interface condition (4), is equivalent to the functional equation

$$\left(\frac{1}{\varrho_1}[\Phi_1(g(\omega)+\alpha_1)+\Phi_1(g(\omega)-\alpha_1)] - \frac{1}{\varrho_2}[\Phi_2(\omega+\alpha_2)+\Phi_2(\omega-\alpha_2)]\right)\sin\omega = C\sin\omega, \tag{10}$$

where the indefinite term $C\sin\omega$ in the right-hand side may always be set to zero, because the transitions $\Phi_n\to\Phi_n+C_n$, do not change the integrals (8), but result in the addition to (10) of $2(C_1/\varrho_1+C_2/\varrho_2)\sin\omega$. So, Eqs. (9), (10) may be replaced by:

$$\begin{aligned}&\mu[\Phi_1(g(\omega)+\alpha_1)+\Phi_1(g(\omega)-\alpha_1)]-[\Phi_2(\omega+\alpha_2)\\&\quad+\Phi_2(\omega-\alpha_2)]=0,\\&a(\omega)[\Phi_1(g(\omega)+\alpha_1)-\Phi_1(g(\omega)-\alpha_1)]\\&\quad+[\Phi_2(\omega+\alpha_2)-\Phi_2(\omega-\alpha_2)]=0,\end{aligned} \tag{11}$$

with the constant $\mu=\varrho_2/\varrho_1$.

Another important feature of these equations is that if $\Phi_{1,2}(\omega)$ satisfy (11), then the functions $\Phi'_{1,2}(\omega)\equiv\Phi_{1,2}(-\omega)$ are also solutions of (11). Indeed, let us substitute in (11) ''ω'' by ''$-\omega$'' and get the obvious relations

$$\Phi_1(g(-\omega)+\alpha_1)\pm\Phi_1(g(-\omega)-\alpha_1) \equiv\Phi'_1(g(\omega)-\alpha_1)\pm\Phi'_1(g(\omega)+\alpha_1), \tag{12}$$

$$\Phi_2(-\omega+\alpha_2)\pm\Phi_1(-\omega-\alpha_2) \equiv\Phi'_2(\omega-\alpha_2)\pm\Phi'_2(\omega+\alpha_2). \tag{13}$$

Then one can conclude that new functions $\Phi'_{1,2}(\omega)$ obey the equations

$$\begin{aligned}&\mu[\Phi'_1(g(\omega)+\alpha_1)+\Phi'_1(g(\omega)-\alpha_1)]-[\Phi'_2(\omega+\alpha_2)\\&\quad+\Phi'_2(\omega-\alpha_2)]=0,\\&-a(\omega)[\Phi'_1(g(\omega)+\alpha_1)-\Phi'_1(g(\omega)-\alpha_1)]\\&\quad-[\Phi'_2(\omega+\alpha_2)-\Phi'_2(\omega-\alpha_2)]=0,\end{aligned}$$

which are equivalent to (11). This property means that there is no need to be concerned about the symmetry of solutions, because for any solutions $\Phi'_{1,2}(\omega)$ that are found, the desired solution may be obtained by the formulas $\Phi_{1,2}(\omega)=\frac{1}{2}[\Phi'_{1,2}(\omega)+\Phi'_{1,2}(-\omega)]$.

B. Analytical continuation

Consider Eqs. (11) as linear algebraic equations with respect to $\Phi_1(g(\omega)+\alpha_1)$, $\Phi_2(\omega+\alpha_2)$, or similarly with respect to $\Phi_1(g(\omega)-\alpha_1)$, $\Phi_2(\omega-\alpha_2)$. Then we get new equations

$$\Phi_m(g_m(\omega)\pm\alpha_m)=\sum_{n=1}^{2}K_{mn}(\omega)\Phi_n(g_n(\omega)\mp\alpha_n), \tag{14}$$

with the auxiliary functions $g_1(\omega)\equiv g(\omega)$, $g_2(\omega)\equiv\omega$, and with the coefficients:

$$K_{11}(\omega)=\frac{a(\omega)-\mu}{a(\omega)+\mu},\quad K_{12}(\omega)=\frac{2}{a(\omega)+\mu},$$
$$K_{21}(\omega)=\frac{2\mu a(\omega)}{a(\omega)+\mu},\quad K_{22}(\omega)=\frac{\mu-a(\omega)}{a(\omega)+\mu}, \tag{15}$$

which are nothing but the reflection-transmission coefficients at the water bottom boundary.

Equations (14) may be used for analytical continuation of the functions $\Phi_1(\omega)$ and $\Phi_2(\omega)$ from co-axial vertical strips of widths $2\alpha_1$ and $2\alpha_2$ to the entire complex plane. From the properties of $K_{mn}(\omega)$, it is clear that if $\Phi_{1,2}(\omega)$ have the required regularity in the strips $|\mathrm{Re}\ \omega|\leqslant\alpha_{1,2}$, then all singularities of these functions may be located. In particular, one can see that in the strips $|\mathrm{Re}\ \omega|\leqslant(\pi/2)+\alpha_{1,2}$ these functions may not have singularities other than *a priori* known poles with pre-determined residues.

Indeed, since $\Phi_1(\omega)$ has the initial, let us say ''zero level,'' poles $\omega=\omega_1^{1,2}$, $\omega_1^1=-\theta_0$, $\omega_1^2=\theta_0$, with the residues $\pm 1/2\pi i$, then from (14), it follows that $\Phi_1(\omega)$ also has ''first-level'' poles $\omega=\pm\omega_1^{3,4}$, with the residues $\mathrm{Res}\ \Phi_1(\pm\omega_1^k)\equiv\pm Q_k^1$, where

$$\omega_1^3=2\alpha_1-\theta_0,\quad \omega_1^4=2\alpha_1+\theta_0,$$
$$Q_k^1\equiv\mathrm{Res}\ \Phi_1(\omega_1^{k-2})K_{11}(g_1^{-1}(\omega_k^1-\alpha_1)).$$

Similarly, $\Phi_2(\omega)$ has ''first-level'' poles $\omega=\pm\omega_2^{3,4}$ with the residues $\mathrm{Res}\ \Phi_2(\pm\omega_2^k)\equiv\pm Q_k^2$, where

$$\omega_2^k=\pm(g_1^{-1}(\omega_1^{k-1}+\alpha_1)+\alpha_2),$$
$$Q_k^2=\mathrm{Res}\ \Phi_1(\omega_2^{k-1})K_{21}(g_1^{-1}(\omega_k^2-\alpha_2))/g_1'(\omega_2^1-\alpha_2).$$

Physically, the ''zero-level'' poles correspond to the incident wave and to its reflection from the free surface. The ''first-level'' poles of $\Phi_1(\omega)$ correspond to waves once reflected from the water bottom interface, and the poles of $\Phi_2(\omega)$ correspond to waves once transmitted from the water to the bottom. Next, $\Phi_1(\omega)$ has ''second-level'' poles $\omega=\pm\omega_1^{5,6}$, $\omega_1^{5,6}=\omega_1^{3,4}+2\alpha_1$, corresponding to waves that were reflected first from the water bottom interface, then reflected by the free surface of the water, and, finally, reflected by the water bottom interface. So, all poles of $\Phi_{1,2}(\omega)$ corresponding to the multiply reflected incident waves are defined by the recursive process

$$\omega_1^{k+2}=\omega_1^k+2\alpha_1,\quad \omega_2^{k+2}=g_1^{-1}(\omega_1^k+\alpha_1)+\alpha_2, \tag{16}$$

and the amplitudes of these waves are defined by a similar recursion

$$Q_1^{k+2}\equiv\mathrm{Res}\ \Phi_1(\omega_1^{k+2})=Q_1^kK_{11}(g_1^{-1}(\omega_1^{k+2}-\alpha_1)),$$
$$Q_2^{k+2}\equiv\mathrm{Res}\ \Phi_2(\omega_2^{k+2})=Q_1^kK_{21}(g_1^{-1}(\omega_2^{k+2}-\alpha_2))/g_1'(\omega_2^{k+2}-\alpha_2). \tag{17}$$

Formulas (14) also make it clear that functions $\Phi_{1,2}(\omega)$ have some other singularities related with the structure of the coefficients $K_{mn}(\omega)$. For example, $\Phi_1(\omega)$ has branch points

$$\omega=\tilde{\omega}_1^k=\pi+\alpha_1-\gamma_*+2\alpha_1k,$$
$$\gamma_*=\arccos\left(\frac{1}{\gamma}\right),$$
$$k=0,1,2,\ldots, \tag{18}$$

corresponding to the head or lateral diffracted waves propagating in the water.

C. Singular integral equation

From the previous discussion it is clear that the unknown functions can be represented in the form

$$\Phi_n(\omega;\theta_0)=\Phi_n^0(\omega)+\tilde{\Phi}_n(\omega),$$
$$\Phi_n^0(\omega;\theta_0)=\frac{1}{2\pi i}\sum_k\frac{Q_n^k(\theta_0)}{\omega-\omega_n^k},\quad n=1,2, \tag{19}$$

where the functions $\tilde{\Phi}_{1,2}(\omega)$ are regular in the strips $|\mathrm{Re}\ \omega|\leqslant\pi/2+\alpha_{1,2}$, and the sums include poles from (16) located in these strips.

Now, substitute (19) into (11) and consider Eqs. (11) on the line $\mathrm{Re}\ \omega=\pi/2$, which is preferred because it is an invariant of the map $\omega\to g(\omega)$. Let

$$X_n(\omega)=\tilde{\Phi}_n(g_n(\omega)+\alpha_n)+\tilde{\Phi}_n(g_n(\omega)-\alpha_n),\quad n=1,2. \tag{20}$$

Then, following the scheme from Refs. 12–14, Eqs. (11) can be converted into the system of singular integral equations on the line $\mathrm{Re}\ \omega=\pi/2$:

$$\mu X_1(\omega)-X_2(\omega)=r_1(\omega),$$
$$a(\omega)\mathbf{H}_1X_1(\omega)+\mathbf{H}_2X_2(\omega)=r_2(\omega), \tag{21}$$

with the singular integral operators

$$\mathbf{H}_n\Phi(\omega)=\frac{1}{2\alpha_n}\int_{\pi/2-i\infty}^{\pi/2+i\infty}\frac{\Phi(\xi)g'(\xi)d\xi}{\sin(\pi(g_n(\xi)-g_n(\omega))/2\alpha_n)},$$

and with the right-hand sides

$$r_1(\omega)=-\mu[\Phi_1^0(\omega+\alpha_1)+\Phi_1^0(\omega-\alpha_1)],$$
$$r_2(\omega)=-a(\omega)[\Phi_1^0(\omega+\alpha_1)-\Phi_1^0(\omega-\alpha_1)]. \tag{22}$$

Equations (21) look similar to the ones from Refs. 12–14 that arise in the study of elastic wave propagation in a solid wedge, but the situation here is much simpler for at least two reasons. First, the index of (21)

$$\det\begin{pmatrix}\mu, & -1\\ a(\omega), & 1\end{pmatrix}=1+\mu+o(e^{-|\mathrm{Im}\ \omega|})$$

does not vanish at the infinite points $\pi/2\pm i\infty$ of the line of integration. Next, the condition $\alpha_1\ll\alpha_2$ guarantees explicit solvability of (21) in the Neumann series form. Indeed, obvious transformations convert (21) to the equation

$$X(\omega)+\mathbf{T}X(\omega)=R(\omega),$$
$$R(\omega)=\mu r_2(\omega)-a(\omega)\mathbf{H}_1r_1(\omega), \tag{23}$$

where

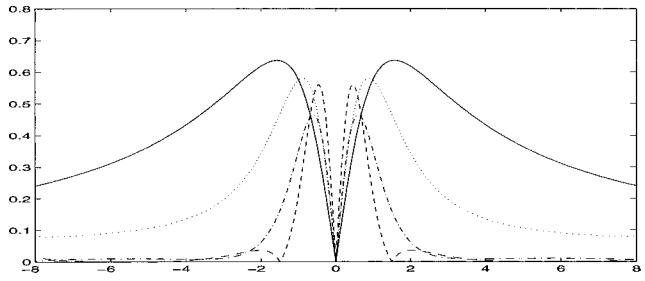

FIG. 2. Iterations of the right-hand side of the integral equation.

$$X(\omega)=\mu\mathbf{H}_2X_2(w),\quad \mathbf{T}X(\omega)=\frac{a(\omega)}{\mu}\,\mathbf{H}_1\mathbf{H}_2^{-1}X(\omega),$$

and

$$\mathbf{H}_n^{-1}F(\omega)=\frac{1}{2\alpha_n}\int_{\pi/2-i\infty}^{\pi/2+i\infty}F(\xi)\times\left(\cot\frac{\pi}{2\alpha_n}(g_n(\xi)-g_n(\omega))\right)g_n'(\xi)d\xi.$$

For given values of parameters when $\alpha_1\ll\alpha_2$ the Neumann series

$$X(\omega)=R(\omega)-\mathbf{T}R(\omega)+\mathbf{T}^2R(\omega)-\cdots, \tag{24}$$

rapidly converges, and retaining only the few first terms in (24) provides accuracy enough for most practical needs. This statement is confirmed by Fig. 2 where the graphs of the functions $|R(\omega)|$, $|\mathbf{T}R(\omega)|$, $|\mathbf{T}^2R(\omega)|$, and $|\mathbf{T}^3R(\omega)|$ on the line $\mathrm{Re}\,\omega=\pi/2$ are plotted together in assumption that $\alpha=2.86°$.

So, the assumptions that $\alpha\ll\pi-\alpha$, and $\mu\approx1$ result in approximate solutions of the integral equations in terms of explicit analytical expressions, providing any required accuracy. As for the general problem with wedges of arbitrary angles, the integral equations (21) or (23) are to be solved numerically.

D. Amplitude functions and acoustic fields

When Eq. (23) is solved then the values of $X_n(\omega)$ along the line $\mathrm{Re}\,\omega=\pi/2$ are determined by the integral $X_2(\omega)=(1/\mu)\mathbf{H}_2^{-1}X(\omega)$, and by the first line of (21). Then the integrals

$$\tilde{\Phi}_n(\omega)=\frac{1}{4i\alpha_n}\int_{\pi/2-i\infty}^{\pi/2+i\infty}\frac{X_n(\xi)g'(\xi)d\xi}{\cos(\pi(g_n(\xi)-g_n(\omega))/2\alpha_n)},\quad n=1,2, \tag{25}$$

together with (19) determine the Sommerfeld amplitudes $\Phi_{1,2}(\omega)$ in the corresponding vertical strips $|\mathrm{Re}\,\omega|\leqslant\alpha_{1,2}$, and (14) analytically continue $\Phi_{1,2}(\omega)$ into the entire complex plane.

Next, the Sommerfeld integrals (8) have to be computed. Let C_0 and C_1 be the steepest-descent contours of the phase function $i\cos\omega$ passing the saddle points $\omega=0$ and $\omega=\pi$ correspondingly. Transform the contour C in the integrals (8) into the sum of the contours C_0 and C_1 is shown in Fig. 1. Then, taking into account that the integrals over C_0 vanish due to the symmetry of C_0 and of the oddness of the integrands, we get the following representations of $p_{1,2}(r,\theta;\theta_0)$:

$$p_n(r,\theta;\theta_0)=p_n^{\mathrm{inc}}(r,\theta;\theta_0)+p_n^{\mathrm{geom}}(r,\theta;\theta_0)+p_n^{\mathrm{diff}}(r,\theta;\theta_0)+p_n^{\mathrm{hd}}(r,\theta;\theta_0),\quad n=1,2, \tag{26}$$

where the ''incident fields'' are given by (5) and the ''geometric fields'' are expressed as

$$p_n^{\mathrm{geom}}(r,\theta;\theta_0)=\sum_k\epsilon(\theta-\omega_n^k+\pi_n)Q_n^k(\theta_0)e^{ik_nr\cos(\theta-\omega_n^k+\pi_n)}-\sum_k\epsilon(\theta-\omega_n^k+\pi_n)Q_n^k(\theta_0)e^{ik_nr\cos(\theta+\omega_n^k-\pi_n)}, \tag{27}$$

$$\epsilon(\omega)=\begin{cases}1, & \text{if } \omega \text{ lies between } C_0 \text{ and } C_1,\\ 0, & \text{otherwise,}\end{cases} \tag{28}$$

and are, therefore, determined by the poles ω_n^k from (16), and where the ''diffracted fields'' and ''head fields''

$$p_n^{\mathrm{diff}}(r,\theta;\theta_0)=\int_{C_1}[\Phi_n(\omega+\theta-\pi_n;\theta_0)-\Phi_n(\omega-\theta+\pi_n;\theta_0)]e^{ik_nr\cos\omega}\,d\omega, \tag{29}$$

$$p_1^{\mathrm{hd}}(r,\theta;\theta_0)=\int_{C_\gamma}[\Phi_n(\omega+\theta-\pi_n;\theta_0)-\Phi_n(\omega-\theta+\pi_n;\theta_0)]e^{ik_nr\cos\omega}\,d\omega, \tag{30}$$

are determined by the integrals over the steepest-descent contour C_1 and over the contour C_γ, running along the cuts of the plane ω originated at the branch points (18) of $\Phi_1(\omega)$, respectively. As for the ''head field'' p_2^{hd} in the bottom, it is equal to zero.

The geometric field in the water is formed by plane waves reflected from the free surface $\theta=0$ and from the bottom. The geometric field in the bottom is formed by plane waves transmitted from the water through the bottom surface, and includes plane waves reflected from the free surface $\theta=\pi$. Diffracted fields $p_{1,2}^{\mathrm{diff}}(r,\theta)$ include cylindrical waves outgoing from the vertex $r=0$, and the head (lateral) field $p_1^{\mathrm{hd}}(r,\theta)$ includes specific waves radiated into the water by the bottom wave propagating along the water bottom interface with a higher speed. The poles $\omega_n^k\equiv\omega_n^k(\theta_0)$ and the residues $Q_n^k\equiv Q_n^k(\theta_0)$ are functions of the incident angle θ_0 and they are explicitly determined by the recursive algorithm (16), (17), which means that the geometric fields are also defined explicitly. As for the amplitudes $\Phi_{1,2}(\omega)\equiv\Phi_{1,2}(\omega;\theta_0)$, and therefore of the diffracted fields, they are defined in a more difficult way involving inversion of the integral equation.

E. Simplifications

Let us see that the presented solution is not so difficult for numerical evaluation as might be expected, and that the acoustic fields in the water, in particular, may be computed with good accuracy without dealing with any integral equations.

TABLE I. Poles ω_n^k and residues Q_n^k. (Angles are given in degrees.)

k	ω_1^k	$\lvert Q_1^k\rvert$	ω_2^k	$\lvert Q_2^k\rvert$
1	1.43	1.000		
2	4.24	1.000		
3	7.10	1.000	$177.2+28.9\cdot i$	4.398
4	9.96	1.000	$177.2+28.3\cdot i$	4.176
5	12.83	1.000	$177.2+27.3\cdot i$	3.884
6	15.70	1.000	$177.2+26.0\cdot i$	3.553
7	18.56	1.000	$177.2+24.2\cdot i$	3.205
8	21.43	1.000	$177.2+21.9\cdot i$	2.858
9	24.29	1.000	$177.2+18.9\cdot i$	2.518
10	27.15	1.000	$177.2+14.6\cdot i$	2.188
11	30.02	1.000	$177.2+7.3\cdot i$	1.865
12	32.89	0.666	188.2	1.261
13	35.75	0.546	195.0	0.895
14	38.62	0.322	200.2	0.387
15	41.42	0.241	204.8	0.284
16	44.29	0.133	209.0	0.145
17	47.15	0.095	213.0	0.148
18	50.02	0.050	216.7	0.095
19	52.88	0.034	220.4	0.074
20	55.75	0.018	224.0	0.042
21	58.61	0.012	227.5	0.030
22	61.48	0.006	231.0	0.016
23	64.34	0.004	234.4	0.011
24	67.20	0.002	237.7	0.005
25	70.07	0.001	241.2	0.004
26	72.88	0.000	244.4	0.002
27	75.75	0.000	247.7	0.001
28	78.60	0.000	251.0	0.000

Consider first sums (27) which, theoretically, must contain about $\pi/\alpha\approx 60$ (we assume that $\alpha=2.86°$ terms related with the poles $\omega=\omega_1^k$, located in the strip $\mathrm{Re}\,\omega<\pi+\alpha$.) In reality, however, there is no need to keep all these terms because starting from some number $k=k_0$ the coefficients $Q_{1,2}^k$ rapidly decay as is confirmed by Table I, which lists the values of these coefficients and of the corresponding poles for the case of the incident angle $\theta_0=\arctan(1/40)\approx 0.025$.

The decay of the coefficients $Q_{1,2}^k$ agrees with their physical interpretation as the amplitudes of multiply reflected plane waves bounced between the free surface and the bottom. Indeed, the reflection from the free surface is ideal, and the reflection coefficient from the bottom depends on the angle of incidence, but its modulus is always equal or smaller than unity.

The rapid decay of the coefficients $Q_{1,2}^k$ simplifies also the computation of the right-hand sides of integral equations (21), and even makes it possible to get a closed-form approximation of the amplitude $\Phi_1(\omega)$ corresponding to the acoustic fields in the water.

Indeed, it may be proven that the solution $X(t)$ of integral equation (21) is estimated as $\|X(t)\|=O(\alpha_1)$, and the computations displayed in Fig. 1 confirm that $\|X(t)\|\approx 5\times 10^{-3}$, from which it follows that $X_2(\omega)$ has a similar estimate and that the amplitude function $\tilde{\Phi}_2(\omega)$ defined by integral (25) does not exceed the level of of 5×10^{-3} in the strip $|\mathrm{Re}\,\omega-\pi/2|<\alpha_2$. Then, taking into account that the strips $|\mathrm{Re}\,\omega\pm\pi/2|<\alpha_2$ overlap ($\alpha_1\approx\pi$), we readily derive from (19) that in the strip $|\mathrm{Re}\,\omega|<\pi/2+\alpha_2\approx 1.5\pi$ the amplitude $\Phi_2(\omega)$ may be approximated by the sum

$$\Phi_2(\omega)=\Phi_2^0(\omega)=\sum_k Q_2^k(\theta_0)\sigma(\omega-\omega_2^k(\theta_0)),$$

$$|\mathrm{Re}\,\omega|<\pi/2+\alpha_2\approx 1.5\pi,$$

whose coefficients are explicitly known and rapidly decay as discussed above.

The diffracted field in the water is represented by the first integral from (29) depending on the values of the amplitude $\Phi_1(\omega)$ in the strips $|\mathrm{Re}\,\omega-\pi|<\alpha$. Let ω belong to this strip. Then, recursive application of the first line of (14) leads to the closed-form representation

$$\begin{aligned}\Phi_1(\omega)&=K_{12}(g^{-1}(\omega-\alpha_1))\sum_k P_1^k(\omega)\\&\quad\times\Phi_2^0(g^{-1}(\omega-(2k-1)\alpha_1)-\alpha_2),\\P_1^k(\omega)&=\prod_{\nu=1}^{k}K_{11}(g^{-1}(\omega-(2\nu-1))),\end{aligned}\tag{31}$$

which may be regarded as an approximate solution of functional equations (14) whose error in the area $\pi-\alpha<\mathrm{Re}\,\omega<\pi+\alpha$ is estimated as $P_N(\omega)\Phi_1(\omega-2N\alpha)$ and decays as $N\to\infty$ in a similar way as the coefficients $Q_{1,2}^k$ considered above.

F. Comparison with the method of multiple reflections

Let us consider different parts of (26) in detail and estimate their contributions to the total acoustical field. The terms p_n^{inc} and p_n^{geom} are defined explicitly, but they are not continuous and have discontinuities along the lines separating the ''light'' and ''shadow'' areas. So, the diffracted fields which compliment the incident and geometric fields to form the continuous solution of the problem may be expected to be weaker in the areas where the geometric field is smoother.

Consider, for example, the geometric field p_1^{geom} in the water. According to (27) this field consists of a number (about 120) of individual plane waves that completely illuminate the water wedge, and of four plane waves that illuminate this area only partially. The plane waves of the second kind correspond to the poles located in the strip $\pi-\alpha<\mathrm{Re}\,\omega_1^k<\pi+\alpha$. But the amplitudes $Q_1^k(\theta_0)$ of the plane waves from (27) rapidly decay when k grows, which results in the coefficients corresponding to these poles having an order below 10^{-7}. This means that the geometric field in the water is almost continuous and, therefore, it should be expected that the ray-theory field p_1^{ray} is close to the solution of the problem for the thin water wedge. Indeed, since the function $\Phi_1(\omega)$ is almost continuous near the segment $(\pi-\alpha,\pi+\alpha)$, it follows from (29) that the diffracted field in the water is estimated as $O(\alpha/\sqrt{k_1 r})$, which is in fact negligible. It should also be noted that the geometric field p_1^{geom} together with the incident field exactly satisfy the boundary condition at the free surface $\theta=0$.

Consider next the geometric field p_2^{geom} in the bottom. It is clear that all jumps in this field are due to the inclusion or exclusion of individual terms in the sums of (27). Let us see

that the terms of the second sum in (27) describe plane waves transmitted from the water to the bottom across the interface $\theta=\alpha$. Indeed, (16) implies that the exponents of the considered terms have the form

$$e^{ik_2 r\cos(\theta-\omega_*^k)}, \quad \omega_*^k=\pi-\omega_2^k\equiv\alpha-g^{-1}(\omega_1^{k-2}+\alpha), \tag{32}$$

where ω_1^{k-2} determine the directions of waves in the water and ω_*^k determine those of the transmitted waves in the bottom. From Table I one can readily see that the first few bottom waves ($k\leqslant 11$) have complex directions with the fixed real part $\mathrm{Re}\,\omega_*^k=-\alpha\approx-2.86°$. These waves completely illuminate the bottom but they are localized along the interface $\theta=\alpha$ and exponentially decay as an observer moves inside the bottom, which is explained by the complete reflection into the water of the waves meeting the interface at angles below the critical value. Next, waves of the type (32) with numbers $k>11$ have real-valued directions and penetrate inside the bottom, but these waves illuminate the bottom only partially, leaving the sectors $360°-\omega_2^k<\theta<180°$ in a shadow. So, the geometric field ϕ_2^{geom} has jumps along the rays $\theta=360°-\omega_2^k$. The amplitudes Q_2^k of these jumps decay as k grows, but they are considerable in the sector $\theta>150°$, as is evident from Table I.

It is a more delicate problem to interpret the terms of the first sum in (27), corresponding to the poles of $\Phi_2(\omega+\theta-\pi)$ captured when the contour C in (8) is deformed into the sum of C_0 and C_1. Comparing the location of the poles of $\Phi_2(\omega+\theta-\pi)$ with the inequality $0<\pi-\theta<\pi-\alpha$ held in the bottom, one can see that the discussed first sum in (27) is actually empty. So, the geometric field p_2^{geom} consists only of the first sum of (27) representing plane waves transmitted from the water, and this field together with the incident and geometric fields in the water obeys the interface condition at $\theta=\alpha$, but p_2^{geom} does not satisfy the boundary condition at the free surface $\theta=\pi$ and this field has discontinuities along several rays.

On the other hand, one can see that each term of the first sum in (27) can be interpreted as an ideal reflection by the free surface $\theta=\pi$ of the corresponding term of the second sum of (27) describing a plane wave transmitted to the bottom from the water. If the function $\epsilon(\omega)$ involved in (27) is defined as

$$\epsilon(\omega)=\begin{cases}1, & \text{if } 0<\mathrm{Re}\,\omega<\pi,\\ 0, & \text{otherwise,}\end{cases} \tag{33}$$

rather than as in (28), then every plane wave from the first sum in (27) has a counterpart in the second sum which illuminates the free face $\theta=\pi$, and the geometric field p_2^{geom} obeys the boundary condition on the face $\theta=\pi$, as well as the interface condition at $\theta=\alpha$.

The fields defined by (27), (33) are nothing but the approximate solution of the problem by the method of multiple reflections. This solution exactly satisfies all boundary and interface conditions, but it is not continuous.

So, whichever definition (27), (28), or (27), (33) of the geometric field is used, an approximate solution retaining only incident and geometric waves is expected to be accurate in the area $\theta<90°$ located directly under the water, but the error of this approximation is expected to eventually increase as the observer moves from the vertical line $\theta=90°$ toward the free surface $\theta=180°$.

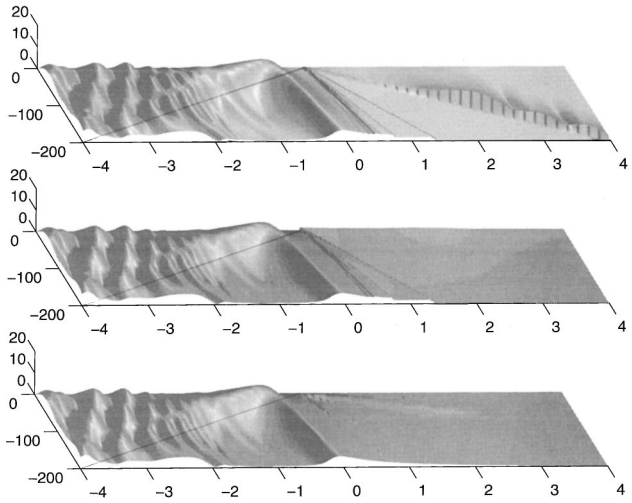

FIG. 3. Acoustics pressure fields.

In order to analyze the contributions of the different components of the rigorous solution of the problem under consideration and, therefore, to estimate areas of applicability of the simple geometric-optic approximations, we performed a series of numerical experiments. We computed the geometric solutions defined by (27), (28), and by (27), (33), and the total wave theory solution obtained by our approach. All computations are done for the two-dimensional problem with the plane incident wave. The results are displayed in Fig. 3.

The first plot of Fig. 3 displays the geometric field (27), (33), which presents the approximate solution of the problem by the method of multiple reflections. This field absolutely satisfies all boundary and interface conditions, but it is obviously discontinuous in the bottom. The second plot displays the geometric field (27), (28). This field is also not continuous in the bottom, although its jumps are not as large as in the previous field, but this field does not satisfy the boundary condition at the free surface $\theta=180°$. The last plot displays the full wave theory solution obtained by the suggested approach. This field is totally continuous and satisfies all boundary conditions with accuracy depending on the accuracy of the solution of integral equation (23) and of the accuracy of evaluation of the Sommerfeld integrals (29).

From the presented results it is clear that in the considered configuration with the small angle α and with moderate contrast between the characteristics of the wave supporting media, the method of multiple reflections gives a suitable approximation to the solution in the water wedge, which is supposed to be thin, and in the areas of the bottom immediately below the water. However, in the other areas of the bottom the multiple reflection method does not provide accurate results. On the other hand, the suggested rigorous approach makes it possible to compute the acoustic fields in any region both in the water and in the bottom, as well as to

solve the problem for any wedge angles and media's characteristics. But this method is, of course, much more computationally intensive than the method of multiple reflections.

III. SCATTERING OF CYLINDRICAL AND SPHERICAL INCIDENT WAVES

A. Scattering of a cylindrical wave from a line source

Due to the linearity of the problem it is clear that in order to solve it with the cylindrical incident waves (6) it is sufficient to represent these waves as superpositions of the plane waves (5).

Let us start from the well-known formula

$$H_0^{(2)}(r_\pm)=\sum_{n=-\infty}^{\infty} J_n(k_1 r_<)H_n^{(2)}(k_1 r_>)e^{in(\theta\mp\theta_0)},$$

where

$$r_\pm=\sqrt{r^2+r_0^2-2rr_0\cos(\theta\mp\theta_0)},$$

$$r_<=\min\{r,r_0\},\quad r_>=\max\{r,r_0\}.$$

Assume for definiteness that $r<r_0$, and replace the Hankel functions in this series by the integrals

$$H_\nu^{(2)}(k_1 r_0)=\frac{1}{\pi}\int_{C_1} e^{ik_1 r_0\cos\xi+i\nu(\xi-\pi/2)}\,d\xi, \tag{34}$$

taken over the contour C_1 running from $\pi/2-i\infty$ to $3\pi/2+i\infty$. Then, exchanging the order of integration and summation, and applying the identity $\Sigma_{n=-\infty}^{\infty}J_n(z)e^{in\theta}=e^{iz\sin\theta}$, we get the expressions

$$H_0^{(2)}(k_1 r_\pm)=\frac{1}{\pi}\int_{\mathscr{L}} e^{ik_1 r\cos(\theta\mp\theta_0+\omega)}\cdot e^{-ik_1 r_0\cos\omega}\,d\omega,$$

which permit the representation of the incident field (6) in the form

$$p_1^{\rm inc}(r,\theta;r_0,\theta_0)=\frac{1}{\pi}\int_{\mathscr{L}}[e^{ik_1 r\cos(\theta-\theta_0-\xi)}-e^{ik_1 r\cos(\theta+\theta_0+\xi)}]e^{-ik_1 r_0\cos\xi}\,d\xi. \tag{35}$$

This is a decomposition of the cylindrical waves (6) into plane waves of the type (5), where the contour of integration $\mathscr{L}$ runs from $-\pi/2-i\infty$ to $\pi/2+i\infty$.

It was discussed in Sec. II how to compute the acoustic fields $p_{1,2}(r,\theta;\theta_0)$ generated by plane incident waves (5). Since this procedure admits complex incident angles, it is possible to define the solution of the problem with cylindrical incident waves by the integrals

$$p_n(r,\theta;r_0,\theta_0)=\frac{1}{\pi}\int_{\mathscr{L}} p_n(r,\theta;\theta_0+\xi)\times e^{-ik_1 r_0\cos\xi}\,d\xi,\quad n=1,2, \tag{36}$$

which together with (26)–(29) generate the representation of the solution as superpositions

$$p_n(r,\theta;r_0,\theta_0)=p_n^{\rm inc}(r,\theta;r_0,\theta_0)+p_n^{\rm geom}(r,\theta;r_0,\theta_0)+p_n^{\rm diff}(r,\theta;r_0,\theta_0)+p_n^{\rm hd}(r,\theta;r_0,\theta_0), \tag{37}$$

of the incident, geometric, diffracted and head fields. The incident field is defined by (6). The geometric and diffracted fields are defined by integrals of type (36) where $p_n(r,\theta;\theta_0+\xi)$ are substituted in the corresponding expressions (27) or (29). The head field $p_2^{\rm hd}$ in the bottom is zero and the head field $p_1^{\rm hd}$ in the water is defined by the integrals of the type (36), where $p_n(r,\theta;\theta_0+\xi)$ should be substituted in the corresponding expressions (30).

The geometric fields are represented by explicitly defined sums:

$$p_n^{\rm geom}(r,\theta;r_0,\theta_0)=\sum_k [P_n^k(r,\theta-\pi_n;r_0,\theta_0)-P_n^k(r,\pi_n-\theta;r_0,\theta_0)],\quad n=1,2, \tag{38}$$

$$P_n^k(r,\theta;r_0,\theta_0)=\frac{1}{\pi}\int_{\mathscr{L}} Q_n^k(\theta_0+\xi)e^{ik_n r\cos[\omega_n^k(\theta_0+\xi)-\theta]-ik_1 r_0\cos\xi}\,d\xi,$$

where the amplitudes Q_n^k and poles ω_n^k are defined by the recursive process (16), (17), and the contour $\mathscr{L}$ is supposed to pass below all branch points of $Q_n^k(\theta_0+\xi)$ located in the area $0<\mathrm{Re}\,\xi<\pi$. Taking into account the rapid decay of the coefficients Q_1^k from (27), we find that the summation in (38) includes only about 20 significant terms.

The path of integration in (38) can be deformed to the sum of the steepest-descent contour $\mathscr{L}_0$ of the phase functions

$$f_n(\xi)=ik_n r\cos[\omega_n^k(\theta_0+\xi)-\theta]-ik_1 r_0\cos\xi,$$

and of a number of loops $\mathscr{L}_\nu$ around cuts of the complex plane originating from the branch points of the coefficients $Q_n^k(\theta_0+\xi)$. Then, depending on the parameters, the integrals over $\mathscr{L}_0$, $\mathscr{L}_\nu$ can be computed either numerically or by appropriate asymptotic approximations. The integral over the steepest-descent contour $\mathscr{L}_0$ is associated with the direct multiply reflected ''eigenray'' and the integrals over the cuts $\mathscr{L}_\nu$ are associated with head waves generated by the concentrated source near the semispace with higher sound speed.

The geometric fields are identified as superpositions of multiply reflected plane waves with complex directions of propagation. The sums $p_n^{\rm ray}=p_n^{\rm inc}+p_n^{\rm geom}$ of the incident and geometric fields form exactly the approximate solution of the considered two-dimensional problem delivered by the complex ray method employed in Ref. 5. As was already mentioned, these sums are very close to the correct acoustic fields in the water and in the bottom directly behind the water, but in the sector $\theta>150°$ they do not correctly approximate the solution of the problem.

Next, consider the diffracted and the head fields from (37). Since the value of $k_1 r_0$ involved in (36) is large ($\approx$400) even at as low frequency as of 25 Hz, the integrals from (36)

corresponding to the diffracted and head fields can be evaluated by the stationary phase method with errors less than 1%. From the above it follows that in the water these fields are negligible, but in the bottom, especially in the domain $\theta > 150°$, the diffracted field may contribute considerably to the total acoustic field.

It is important to emphasize the existence of two kinds of ''head waves'' propagating in the water wedge. First, there are ''head waves'' p_1^{hd} generated by the vertex and described by the last terms of (37). These waves should be classified as a part of the scattered field and they are practically negligible everywhere except in a small area immediately near the vertex. Next, there are ''head waves'' described by the integrals (38) taken over the cuts $\mathscr{L}_\nu$ of the complex plane. These waves should be classified as components of the geometric field and they considerably contribute to the total acoustic field.

B. Scattering of a spherical incident wave from a point source

It is easy to extend our analysis to a point source for the case of a fluid bottom. Our treatment of this bi-fluid problem is based on the well-known integral representation

$$\frac{e^{-ikR_\pm}}{R_\pm} = \frac{ik}{2}\int_l H_0^{(2)}(\zeta k r_\pm) e^{-ik|z|\sqrt{1-\zeta^2}} \frac{\zeta\, d\zeta}{\sqrt{1-\zeta^2}},$$

$$R_\pm = \sqrt{r_\pm^2 + z^2}, \tag{39}$$

where the branch of $H_0^{(2)}(\zeta k r_\pm)$ is fixed by the cut along $(-\infty,0)$, and the branch of $\sqrt{1-\zeta^2}$ is fixed by the cuts $(\infty, -1)$, $(1,\infty)$, and by the condition $\sqrt{1}=1$. As for the contour of integration l it is supposed to run below the ray $(-\infty,0)$, but above the cut $(1,\infty)$.

Note, that if $r_\pm = \sqrt{r^2 + r_0^2 - \cos(\theta \mp \theta_0)}$, then substitution of (34) into (39) leads to the plane wave decomposition

$$\frac{e^{-ikR_\pm}}{R_\pm} = \frac{ik}{2\pi}\int_l \frac{\zeta\, d\zeta}{\sqrt{1-\zeta^2}} \times \int_{\mathscr{L}} e^{ikr\,\cos(\theta \mp \theta_0 - \xi) - i\zeta k r_0\,\cos\xi - ik|z|\sqrt{1-\zeta^2}}\, d\xi,$$

of a spherical wave radiated by a point source at $(r_0, \theta_0, 0)$.

Corresponding to (39), let as consider wave fields described by the form

$$p_n(r,\theta,z) = \frac{ik}{2}\int_l \phi_n(r,\theta;\zeta) e^{-ik|z|\sqrt{1-\zeta^2}} \frac{\zeta\, d\zeta}{\sqrt{1-\zeta^2}}. \tag{40}$$

Then it may be verified that in order for (40) to be a solution of a three-dimensional problem from the Introduction with the spherical incident waves (7), functions $\phi_n(r,\theta;\zeta)$ should be solutions of similar two-dimensional problems with cylindrical incident waves (6) modified by replacing the wave numbers k_1 and k_2 by $k_1\sqrt{\zeta^2+\gamma^2-1}$ and $k_2\zeta$.

Since the procedure from the previous section is valid for any complex wave numbers, solutions of the abovementioned auxiliary two-dimensional problems may be obtained in the form (36), (26), which, after substitution into (40), generates the solution of the three-dimensional problem of scattering of spherical waves (7). On the plane $z=0$ this solution has the form

$$p_n = p_n^{\rm inc} + p_n^{\rm geom} + p_n^{\rm diff} + p_n^{\rm hd}, \quad n = 1,2,$$

where the incident waves $p_n^{\rm inc}$ are defined by (7), and the diffracted waves are defined by double integrals

$$p_n^{\rm diff} = \frac{ik}{2\pi}\int_l \frac{\zeta\, d\zeta}{\sqrt{1-\zeta^2}} \times \int_{\mathscr{L}} p_n(\zeta r, \theta; \theta_0 + \xi) e^{-i\zeta k_1 r_0\,\cos\xi}\, d\xi,$$

involving solutions $p_n(\zeta r, \theta; \theta_0 + \xi)$ of problems with plane incident waves, considered in Sec. I. As for the geometrical fields $p_n^{\rm geom}$, their values in the plane $z=0$ are defined explicitly as sums

$$p_n^{\rm geom} = \sum_k \left[S_n^k(r, \theta - \pi_n; r_0, \theta_0) - S_n^k(r, \pi_n - \theta; r_0, \theta_0)\right],$$

where the separate terms

$$S_n^k = \frac{ik}{2\pi}\int_l \frac{\zeta\, d\zeta}{\sqrt{1-\zeta^2}} \times \int_{\mathscr{L}} Q_n^k(\theta_0 + \xi) e^{i\zeta k_n r\,\cos[\omega_n^k(\theta_0+\xi) - \theta] - i\zeta k_1 r_0\,\cos\xi}\, d\xi,$$

correspond to multiply reflected incident waves. Indeed, the exponents $e^{i\zeta k_n r\,\cos[\omega_n^k(\theta_0+\xi)-\theta]}$, are nothing but plane waves with wave numbers ζk_n propagating along the direction $\theta = \omega_n^k(\theta_0+\xi)$, and $Q_n^k(\theta_0+\xi)$, defined by (17), and are the cumulative products of consequent reflection coefficients of plane waves arriving from infinity along the direction $\theta_0 + \xi$.

One can easily see that the sum $p_n^{\rm ray} = p_n^{\rm inc} + p_n^{\rm geom}$ of incident and geometrically reflected waves forms exactly the ''complex ray method solution'' suggested in Ref. 5. From the above it follows that the ''complex ray solution'' may not be sufficiently accurate in the region $\theta > 150°$ of the bottom where the diffracted field should be taken into consideration.

ACKNOWLEDGMENT

This work was supported by endowment income from the William S. Floyd, Jr., Distinguished Professorship in Engineering held by D. B. Bogy.

[1] L. B. Felsen and N. Marcuvitz, *Radiation and Scattering of Waves*, Prentice-Hall microwaves and fields series (Prentice-Hall, Englewood Cliffs, NJ, 1972).

[2] G. D. Maliuzhinets, ''Excitation, reflection and emission of surface waves from a wedge with given face impedances,'' Sov. Phys. Dokl. **3**, 572–755 (1958).

[3] R. A. Stephen, ''Modeling sea surface scattering by the time-domain finite-difference method,'' J. Acoust. Soc. Am. **100**, 2070–2078 (1996).

[4] D. Lee, ''The state-of-the-art parabolic equation approximation applied to underwater acoustic propagation,'' Rep. TD-7247, Naval Underwater Systems, New London, CT (1984).
[5] E. K. Westwood, ''Complex ray methods for acoustic interaction at a fluid–fluid interface,'' J. Acoust. Soc. Am. **85**, 1872–1884 (1989).
[6] G. Gillette, ''Coupled modes in waveguide with a range-dependent rigid basement,'' J. Acoust. Soc. Am. **93**, 2284(A) (1993).
[7] D. Chu, ''Impulse response of density contrast wedge using normal coordinates,'' J. Acoust. Soc. Am. **86**, 1883–1896 (1989).
[8] A. D. Rawlins, ''Diffraction by a dielectric wedge,'' J. Inst. Math. Appl. **19**, 231–279 (1977).
[9] M. A. Biot and I. Tolstoy, ''Formulation of of wave propagation in infinite media by normal coordinates with an application to diffraction,'' J. Acoust. Soc. Am. **29**, 381–391 (1957).
[10] A. M. J. Davis, ''Two dimensional acoustical diffraction by a penetrable wedge,'' J. Acoust. Soc. Am. **100**, 1316–1324 (1996).
[11] E. Marx, ''Computed fields near the edge of a dielectric wedge,'' IEEE Trans. Antennas Propag. **38**, 1438–1442 (1990).
[12] B. V. Budaev and D. B. Bogy, ''Rayleigh wave scattering by a wedge,'' Wave Motion **22**, 239–257 (1995).
[13] B. V. Budaev and D. B. Bogy, ''Rayleigh wave scattering by a wedge. II,'' Wave Motion **24**, 307–314 (1996).
[14] B. V. Budaev and D. B. Bogy, ''Rayleigh wave scattering by two adhering elastic wedges,'' Proc. R. Soc. London, Ser. A (to be published).

Resonant phenomena in bulk-wave scattering by in-plane periodic cracks

Eugene J. Danicki
Polish Academy of Science, 21 Świętokrzyska Str., 00-049 Warsaw, Poland

(Received 30 March 1998; accepted for publication 15 September 1998)

A resonant phenomenon is investigated for the generation of interfacial waves when bulk waves are scattered by in-plane periodic cracks embedded in an isotropic elastic body. A new method of analysis is developed and numerical results are presented. This analysis can have useful applications involving the generation of surface acoustic waves by comb transducers. © *1999 Acoustical Society of America.* [S0001-4966(98)05512-X]

PACS numbers: 43.20.Fn, 43.20.Gp [DEC]

INTRODUCTION

Scattering of waves from cracks in an elastic body has been studied in numerous papers (see Ref. 1 and the references given there). Here, we study this phenomenon from a very particular point of view. Namely, we expect that this is the fundamental phenomenon involved in the generation of surface acoustic waves in solids by comb transducers.[2,3]

In a certain approximation which is convenient for theoretical investigation, the interface between the comb transducer and the substrate to which it is attached looks like a periodic system of thin voids that can be modeled as cracks between two solids. (The small but finite thickness of these cracks allows us to neglect possible nonlinear phenomena.[1] In fact, the motivation for this research is the frequency selective property of so-called comb transducers which may be advantageous in nonlinear ultrasonic investigations of materials.[4]) These two solids remain in solid contact between the voids (cracks) when the comb is glued to the substrate, or in sliding contact when the comb is applied to the substrate using a thin layer of oil. In typical transducer applications, the angle of incidence of the wave is close to normal; therefore, in this paper we deal primarily with this case.

It will be shown that, under certain conditions, large interface vibrations occur that have a resonant character. They are similar to the interfacial waves discussed earlier.[5] However, here a less dense system of cracks is considered (roughly one crack per acoustic wave length, compared to the previous case of more than two cracks per wave length).

The problem is formulated in Secs. I–III, and solved using a similar method of analysis to that used previously,[5,6] which is briefly presented in Sec. IV. We conclude by presenting several instructive numerical examples in Secs. V–VII. These examples clearly show that the interface vibrations can indeed have resonant character, with amplitudes much larger than the amplitude of the incident wave that excite them. The dependence of the interface vibration amplitude on the crack wave number (corresponding to the frequency dependence for a given crack system and variable frequency of incident wave) closely resembles the typical resonant curve.

The passband of the resonance is relatively narrow for the case in which the cracks and the spacing between them are of equal width. This narrow passband means that the phenomenon discussed can be discerned only by a thorough analysis of bulk-wave scattering by cracks in a very narrow domain of the crack wave number, just above the cutoff wave number of bulk waves.

I. FORMULATION OF THE SCATTERING PROBLEM

We consider two isotropic elastic half-spaces bonded to each other at the interface plane $y=0$ (Fig. 1). The interface consists of domains of period Λ in which there is perfect bonding ($2w$ wide, called ''bonds''), separated by regions of perfect disbonding. The disbonded regions are called cracks, which they actually are in the case when both bonded half-spaces are of the same material. The cracks are infinitely long in the z direction; in this paper, the wave field under consideration is independent of z.

The polarization of the incident harmonic plane bulk wave is either longitudinal (denoted by the subscript l) or transverse with its polarization in the sagittal plane (x,y) (subscript t). The incident wave propagates in the half-space $y<0$ toward the system of cracks at the interface $y=0$. Here the wave is scattered and produces a variety of wave field harmonic components (Bloch waves). The generated waves are reflected into the half-space $y<0$ or transmitted into the half-space $y>0$, and contain evanescent components which vanish on both sides of the interface. This situation is the Bragg scattering of waves at a periodic system of cracks. Thus the wave numbers of Bloch waves at the interface $y=0$ differ from the wave number of the incident wave by an integral number n of the crack system wave number $K=2\pi/\Lambda$:

$$\exp(j\omega t - jp_n x), \quad p_n = r + nK. \tag{1}$$

Here, ω is the angular frequency of the incident wave, and $r+IK=p_I$ is the x projection of the incident wave vector (the projection onto the interface). The integer I is chosen such that $r\in(0,K)$.

The wave field in the interior of the half-space is a superposition of the corresponding Bloch longitudinal and transversal components, with the general form

$$\exp(j\omega t - jp_n x - jq_{l,t} y), \quad q_{l,t} = (k_{l,t}^2 - p_n^2)^{1/2}, \tag{2}$$

where k_l and k_t are the wave numbers of longitudinal and shear waves, respectively. The wave numbers k_l and k_t may

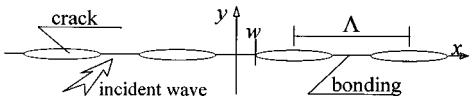

FIG. 1. The system of cracks in an elastic body or at the interface of two bonded elastic half-spaces. In numerical examples, the bond is considered either solid or sliding throughout the entire periodic system.

be different in the two half-spaces if the half-spaces are made of different materials. In this paper, we assume real values for r and thus for p_n.

The value of q_n may be complex, but q_I is always real for real $k_{l,t}$. This is because p_I never produces negative values under the square root in Eq. (2), since it is the projection of the incident wave vector $\mathbf{k}_l$ or $\mathbf{k}_t$. A discussion of how to choose the proper sign of q_n is provided in next section.

At the interface $y=0$, in the limit $y\to 0$ from both the upper and lower sides, the wave field can be expanded as follows (time dependence dropped):

$$
\begin{aligned}
&y=-0:\\
&\mathbf{u}^-(x)=\sum_{-\infty}^{\infty}\mathbf{u}_n^- e^{-j(r+nK)x}+\mathbf{u}^I e^{-jk_I x},\\
&\mathbf{T}^-(x)=\sum_{-\infty}^{\infty}\mathbf{T}_n^- e^{-j(r+nK)x}+\mathbf{T}^I e^{-jk_I x};\\
&y=+0:\\
&\mathbf{u}^+(x)=\sum_{-\infty}^{\infty}\mathbf{u}_n^+ e^{-j(r+nK)x},\\
&\mathbf{T}^+(x)=\sum_{-\infty}^{\infty}\mathbf{T}_n^+ e^{-j(r+nK)x}=\mathbf{T}(x),
\end{aligned}
\tag{3}
$$

where

$$
\mathbf{u}=\begin{bmatrix}u_1\\ u_2\end{bmatrix},\quad \mathbf{T}=\begin{bmatrix}T_{21}\\ T_{22}\end{bmatrix} \tag{4}
$$

(in tensor notation). To shorten the notation, $\mathbf{T}=[T_1\ \ T_2]^T$, where the superscript T means matrix transposition, and $\mathbf{T}_n^+=\mathbf{T}_n$.

The boundary conditions at the plane of cracks ($y=0$) are

$$
\begin{aligned}
&\mathbf{u}^+(x)=\mathbf{u}^-(x),\quad \mathbf{T}^+(x)=\mathbf{T}^-(x),\quad \text{at bonds},\\
&\mathbf{T}^+(x)=\mathbf{T}^-(x)=0,\quad \text{at cracks},\\
&|x-i\Lambda|\in(w,\Lambda/2).
\end{aligned}
\tag{5}
$$

These are the boundary conditions assuming perfect mechanical contact of the elastic half-spaces between periodic cracks. (In Sec. VII, sliding contact between the half-spaces, where $u_2^+=u_2^-$ in the bonded regions and $T_{21}=0$ everywhere, will be considered.)

To formulate the boundary value problem of the scattering of incident waves by cracks, we need the relationship between $\mathbf{T}(x)$ and $\mathbf{u}(x)$. In the case under consideration of a periodic system of cracks, the relationship $\mathbf{u}_n=\mathbf{G}(p_n)\mathbf{T}_n$ is adequate, where $\mathbf{G}$ is the planar harmonic Green's function discussed in the next section.

II. PLANAR HARMONIC GREEN'S FUNCTION

Applying a traction $\mathbf{T}=[T_{21}\ \ T_{22}]^T\exp(j\omega t-jpx)$ to the surface of the elastic half-space $y>0$, the resulting particle displacements $\mathbf{u}=[u_1\ \ u_2]^T\exp(j\omega t-jpx)$ at the interface $y=0$ are:[5]

$$
\begin{aligned}
&\mathbf{u}=G(p)\mathbf{T},\\
&\mathbf{G}=\frac{j}{\mu D}\begin{bmatrix}k_t^2 q_t & p(k_t^2-2p^2-2q_l q_t)\\ -p(k_t^2-2p^2-2q_l q_t) & k_t^2 q_l\end{bmatrix},\\
&D=(k_t^2-2p^2)^2+4p^2 q_l q_t,
\end{aligned}
\tag{6}
$$

$$
\begin{aligned}
&k_t^2=\rho\omega^2/\mu,\\
&k_l^2=\rho\omega^2/(\lambda+2\mu).
\end{aligned}
\tag{7}
$$

Here, ρ is the mass density and μ and λ are the Lamè constants of the half-space. The values of $q_{l,t}$ (for real $k_{l,t}$ and p) are chosen following the rule

$$
q_a=\sqrt{k_a^2-p^2}=-j\sqrt{p^2-k_a^2},\quad a=l,t, \tag{8}
$$

in order to satisfy the radiation conditions (2) by the wave field in the half-space $y>0$. In the following discussion, $q_{l,t}$ are assumed to have been chosen according to the above rule. Thus in the lower half-space, the wave field satisfying the radiation condition at $y\to-\infty$ is assumed to be of the form $\exp(-jpx+jq_{l,t}y)$. Generally, the rule of choice of the sign of q results from

$$
\Pi_2=-\frac{1}{2}\,\mathrm{Re}\{T_{2i}^*(j\omega u_i)\}=\frac{\omega}{2}\,\mathrm{Im}\{\mathbf{T}^*\mathbf{G}\mathbf{T}\}>0, \tag{9}
$$

which says that the energy is transported from the surface to infinity. Π_2 is the y-component of the Poynting vector[7] of the wave field in the half-space $y>0$.

Equations (6) can be applied for any $\mathbf{u}_n$, $\mathbf{T}_n$ involved in Eq. (3), $y>0$,

$$
\mathbf{u}_n=\mathbf{u}_n^+=\mathbf{G}(p_n)\mathbf{T}_n,\quad p_n=r+nK. \tag{10}
$$

Moreover, in spite of the fact that the incident wave exists only in the domain ($y<0$), it also satisfies the above equation with p_n replaced by p_I. This is because the incident wave satisfies the radiation conditions at $y\to\infty$.

It results from the above discussion and from Eqs. (7) that in order to satisfy the radiation conditions at $y\to-\infty$, the wave field in the lower elastic half-space is subject to the condition

$$
\mathbf{u}_n^-=-\mathbf{G}^T(p_n)\mathbf{T}_n^-. \tag{11}
$$

$\mathbf{G}$ is the matrix evaluated from Eqs. (7) using the material constants of the lower elastic half-space. This matrix will be later denoted by $\overline{\mathbf{G}}$.

III. REFORMULATION OF THE SCATTERING PROBLEM

Following our previous development,[5] we introduce the function $\Delta\mathbf{u}$ of the particle displacement discontinuity at the interface $y=0$:

$$\Delta\mathbf{u}(x)=\mathbf{u}^{+}(x)-\mathbf{u}^{-}(x). \tag{12}$$

Using the expansion in Eq. (3) and the boundary condition $\mathbf{T}^{+}(x)=\mathbf{T}^{-}(x)$, we obtain

$$\begin{aligned}\Delta\mathbf{u}(x)&=\sum_{-\infty}^{\infty}\,[\mathbf{u}_n^{+}-(\mathbf{u}_n^{-}+\mathbf{u}^I\delta_{nI})]e^{-jp_nx}\\&=\sum\,[\mathbf{G}(p_n)\mathbf{T}_n+\overline{\mathbf{G}}^T(p_n)(\mathbf{T}_n-\mathbf{T}^I\delta_{nI})\\&\quad+\overline{\mathbf{G}}(p_I)\mathbf{T}^I\delta_{nI}]e^{-j(r+nK)x}.\end{aligned} \tag{13}$$

Here, δ_{nI} is the Kronecker delta and $\mathbf{T}^I$ and $\mathbf{u}^I$ characterizes the incident wave.

Next, we introduce the function

$$\mathbf{V}(x)=\frac{\partial}{\partial x}\,\Delta\mathbf{u}(x)=\sum\,\mathbf{V}_ne^{-jp_nx}, \tag{14}$$

whose expansion coefficients are

$$\mathbf{V}_n=\mathbf{g}(p_n)\mathbf{T}_n-\dot{\mathbf{g}}(p_I)\mathbf{T}^I\delta_{nI},$$

with

$$\begin{aligned}\mathbf{g}(p_n)&=-jp_n[\mathbf{G}(p_n)+\overline{\mathbf{G}}^T(p_n)],\\\dot{\mathbf{g}}(p_I)&=-jp_I[\overline{\mathbf{G}}(p_I)+\overline{\mathbf{G}}^T(p_I)].\end{aligned} \tag{15}$$

Note that the function $\mathbf{V}(x)$ does not determine $\Delta\mathbf{u}(x)$ uniquely. Furthermore, $\Delta\mathbf{u}(x)=0$ is required in the bonds. This condition can be split into two parts: (a) $\mathbf{V}(x)=0$ at the bonds, and (b) $\Delta\mathbf{u}(x=0)=0$. Indeed, the first condition requires $\Delta\mathbf{u}(x)$ to differ from zero by a constant at most, and the second condition sets this constant to zero.

The boundary conditions in Eq. (5) can now be rewritten as

$$\begin{aligned}&\mathbf{T}(x)=0\ \text{ at cracks},\\&\mathbf{V}(x)=0\ \text{ at bonds},\\&\Delta\mathbf{u}(0)=0\ \text{ at the center between cracks}.\end{aligned} \tag{16}$$

Note that the condition $\mathbf{T}^{+}(x)=\mathbf{T}^{-}(x)$ was already exploited in Eq. (13).

IV. THE BIS EXPANSION

A solution to this problem can be obtained using the method[6] of analysis first developed by Blǿtekjær *et al.* This method assumes a finite series expansion for both $\mathbf{V}_n$ and $\mathbf{T}_n$ in the form

$$\begin{aligned}\mathbf{T}_n&=\sum_{M_1}^{M_2}\,\mathbf{t}_mP_{n-m}(\cos\,\Delta),\\\mathbf{V}_n&=\sum_{M_1}^{M_2}\,\mathbf{v}_mS_{n-m}P_{n-m}(\cos\,\Delta).\end{aligned} \tag{17}$$

This is the BIS expansion. Here, $S_\nu=1$ for $\nu\geqslant 0$ and -1 otherwise; P_ν is the Legendre polynomial, and $\Delta=\pi w/\Lambda$ depends on the bond width w. When used in the series form of $\mathbf{T}(x)$ and $\mathbf{V}(x)$, these expressions automatically satisfy the first two of the reformulated boundary conditions in Eq. (16).

The summation limits $M_{1,2}$ result indirectly from the following approximation to the function $\mathbf{g}(p_n)$, $p_n=r+nK$:

$$\mathbf{g}(p)=S_p\mathbf{g}_\infty,\ \text{ if }\ |p|>p_\infty, \tag{18}$$

where p_∞ is at least several times greater than k_t in magnitude. [In the computations described below, $p_\infty=5k_t$ was used because $\mathbf{g}(5k_t)\approx\mathbf{g}_\infty=\mathbf{g}(p\to+\infty)$ for typical isotropic elastic materials.]

Applying the expansions in Eq. (17) to Eqs. (15) for $n<N_1\leqslant 0$ and $n>N_2\geqslant 0$, $N_1\leqslant I\leqslant N_2$, with $N_{1,2}$ chosen to ensure $|r+nK|>p_\infty$ in these two domains, we find

$$\sum_m\,\mathbf{v}_mS_{n-m}P_{n-m}=S_n\sum_m\,\mathbf{g}_\infty\mathbf{t}_mP_{n-m},\qquad n<N_1\ \text{ or }\ n>N_2. \tag{19}$$

Here, $r\in(0,K)$ is assumed. Equation (19) must be satisfied for infinite numbers of n. Assuming that the summation limits over m are finite, this results in

$$\mathbf{v}_m=\mathbf{g}_\infty\mathbf{t}_m. \tag{20}$$

Further analysis shows that[6]

$$M_1=N_1,\quad M_2=N_2+1. \tag{21}$$

This means that there are (N_2-N_1+2) unknown $\mathbf{t}_m$ in the scattered wave field expansion series which we seek.

At our disposal are (N_2-N_1+1) forms of (15) taken for $N_1\leqslant n\leqslant N_2$, and the last boundary condition of Eqs. (16). This makes (N_2-N_1+2) equations altogether that allow us to evaluate all unknown $\mathbf{t}_m$ by $\mathbf{T}^I$.

Equations (15) can be rewritten in the form

$$[\mathbf{g}_\infty S_{n-m}-\mathbf{g}(r+nK)]\mathbf{t}_mP_{n-m}(\cos\,\Delta)=-\dot{\mathbf{g}}(p_I)\mathbf{T}^I\delta_{nI}. \tag{22}$$

(In this equation and the rest of the paper, summation over m has been dropped.) This equation is nontrivial for $N_1\leqslant n\leqslant N_2$ only. The last boundary condition (16) can be evaluated explicitly for $r\neq 0$ in the form $\overline{\mathbf{u}}=0$ where

$$\begin{aligned}\overline{\mathbf{u}}=\Delta\mathbf{u}(x=0)&=\int\,\mathbf{V}(x)dx=\mathbf{v}_m\sum_n\,\frac{S_{n-m}P_{n-m}(\cos\,\Delta)}{-j(r+nK)}\\&=\frac{j\pi(-1)^m}{K\,\sin\,\pi r/K}\,\mathbf{g}_\infty\mathbf{t}_mP_{-m-r/K}(-\cos\,\Delta).\end{aligned} \tag{23}$$

It has already been shown[5] how to evaluate the above sum for $r\to 0$. It is much more convenient, however, to carry out computations for sufficiently small r instead, using double precision accuracy.

Similarly, we can evaluate the complementary value of the total traction at the interface in the bonded regions near $x=0$ [$\mathbf{T}(x)=0$ at cracks]:

$$\overline{\mathbf{T}}=\int_{-\Lambda/2}^{\Lambda/2}\mathbf{T}(x)dx=\Lambda\mathbf{t}_mP_{-m-r/K}(\cos\,\Delta). \tag{24}$$

This relationship can be exploited in a certain generalization of the boundary conditions of Eqs. (16) by allowing $\Delta\mathbf{u}$ to be

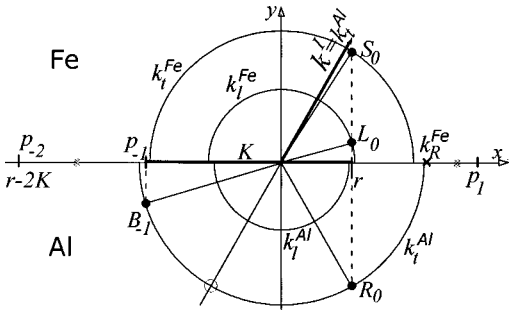

FIG. 2. Wave numbers of Bloch wave field components (p_n) and the corresponding wave vectors of bulk waves in isotropic elastic half-spaces, here in steel for $y>0$ and aluminium for $y<0$. (The semicircles correspond to slowness curves of these materials drawn to scale.) The vector k^I is the wave vector of the incident wave (in aluminum), whose x projection is r. The corresponding zeroth-order Bloch component of the interface wave field is coupled to the longitudinal (L_0) and transverse (S_0) transmitted waves in steel, and to the transverse reflected wave in aluminum (R_0). The Bragg scattering produces only one $-$first order wave B_{-1} in aluminum. Higher-order Bloch components are all evanescent modes because their wave numbers p_n lie outside the region of possible x projection of any bulk-wave vectors in the system. k_R is the wave number of Rayleigh wave in steel; it lies just above k_t of aluminum, the largest bulk-wave number in the system.

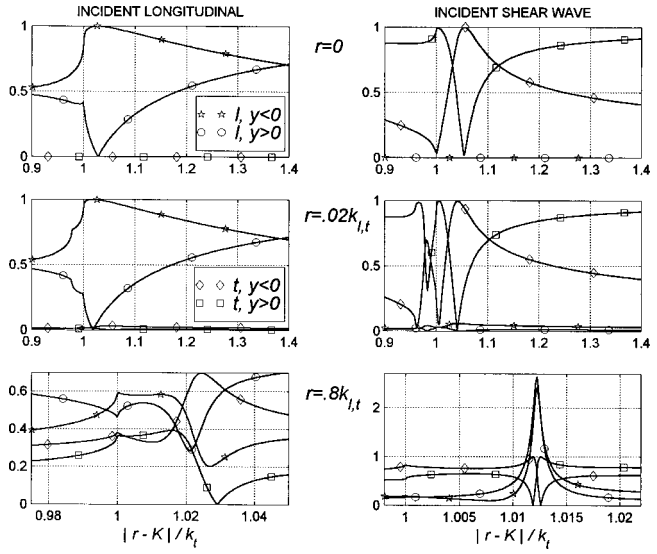

FIG. 3. Amplitudes [defined by Eq. (A5) in Appendix A] of waves scattered by cracks in a homogeneous body (steel). The left and right columns show the amplitudes for incident longitudinal and shear waves, respectively. The rows show the amplitudes for different angles of incidence described by the x projection wave number r. $r=0$ corresponds to normal incidence of the wave onto the interface; $r=0.02k_l$ and $0.8k_l$ (longitudinal incident waves) and $r=0.02k_t$ and $0.8k_t$ (shear waves) correspond to oblique incidence. The incident wave amplitude is unity. The graphs depict the dependence on the crack wave number K of the zeroth-order transmitted and reflected waves only (see Fig. 2, points S_0, L_0 and R_0; the curve marked by squares corresponds to S_0, and by circles, to L_0, for instance). The conversion of the incident longitudinal to shear wave (left column), and vice versa, shear to longitudinal (right column), is small for close to normal incidence. At large K we notice that the transmission coefficient across the cracked interface approaches unity. Legends to curves are common for all figures presented here, and similarly in other figures.

different from zero at the bonds. This is the case if the bonding contains a certain amount of elasticity, for instance in the real case of two surfaces bonded by a glue. Then $\overline{\mathbf{u}}$ differs from zero by an amount proportional to the average traction $\overline{\mathbf{T}}$. The coefficient of proportionality should be chosen such that the energy of the interface vibration is absorbed by the glue, for example, $\overline{\mathbf{u}}=-j\epsilon\overline{\mathbf{T}}$ with ϵ small and positive.

V. GENERAL DESCRIPTION OF THE SCATTERED FIELD

In the numerical examples presented below, we consider relatively dense cracks (more than one crack per acoustic wavelength) of width $\Lambda/2$. Therefore, $\cos\Delta=0$ and $K=2\pi/\Lambda>k_t$, so that $I=0$. The first-order Bloch wave field component is thus always an evanescent mode ($p_1>k_t$ resulting in $q_{l,t}$ imaginary). However, the $-$first-order Bloch component, which has the wave number $p_{-1}=r-K$, can consist of propagating modes in the bulk. These modes may be either longitudinal, transverse, or a combination of the two with wave vector x projections equal to $p_{-1}<-k_{l,t}$ and corresponding real $q_{l,t}$.

The zeroth-order Bloch wave, having the wave number $r=p_I$ in the case $I=0$ under consideration, always produces at least one propagating mode in one or both half-spaces, as is illustrated in Fig. 2. Figure 3 presents the dependence of the reflected and transmitted wave amplitudes on the crack wave number K for given r. Only the propagating modes of zeroth-order Bloch components are shown. Figure 3 shows the amplitude dependence for a given direction of incidence of either longitudinal or shear waves of unit amplitude. The definition of the wave amplitude is given in Appendix A. In this example, both half-spaces were the same material, steel. Table I contains the values of the parameters used. For convenience, the horizontal axis is plotted in units of $|r-K|/k_t$, that is, $|p_{-1}|/k_t$. We notice that:

(i) for denser cracks, as $K\to\infty$, the transmission through the cracked interface goes to 1 and the reflection coefficient goes to 0;

(ii) for $|r-K|<k_t$, the scattered zeroth-order Bloch waves have smaller amplitudes because part of the incident wave power is scattered to the $-$first-order waves; and

(iii) for $r\approx 0$ and at certain K above k_t, there is zero transmission and full reflection from the interface. This results from an interaction of the incident wave with cracks involving all evanescent Bragg components making $(\mathbf{T}_0)^+_{21}=0$ or $(\mathbf{T}_0)^+_{22}=0$ for shear or longitudinal incident waves, respectively. Checking the amplitudes of these components, we do not see anything peculiar; they all have rather small amplitudes and behave smoothly as functions of K in this region.

Figure 4 presents similar graphs for two different bonded half-spaces, steel ($y>0$) and aluminium ($y<0$).

The applied ''full-wave'' method of analysis has the attractive property that the numerically evaluated wave field always satisfies the energy conservation law. This is illustrated in Fig. 5, which presents the normal components of Poynting vectors (Π_2) in the upper and lower half-spaces for a given order of Bloch wave components. (The zero and $\pm$first orders only are shown.) The amplitude of Π_2 for the incident wave is assumed to be unity. We notice that the sum

TABLE I. Material constants used in computations, taken from Ref. 7. Also shown are the wave numbers of bulk and Rayleigh waves at $\omega = 10^6$/s for aluminum (Al) and steel (Fe).

	$c_{11}[10^9\ \mathrm{Nm}^{-2}]$	$c_{44}[10^9\ \mathrm{Nm}^{-2}]$	$\rho[10^3\ \mathrm{kgm}^{-3}]$	$k_l[10^3\ \mathrm{m}^{-1}]$	$k_t[10^3\ \mathrm{m}^{-1}]$	$k_R[10^3\ \mathrm{m}^{-1}]$
Al	111	25	2.695	0.1558	0.3283	0.3509
Fe	277	82	7.87	0.1686	0.3098	0.3346

of Poynting vector y components equals $\Pi_2 = 1$ of the incident wave, on both sides of the interface and for all Bloch component orders that are outgoing propagating modes.

VI. THE INTERFACE VIBRATION, $r = 0$

To evaluate the scattered wave field, we solve the system of inhomogeneous linear equations given in (22) and (23) whose matrix is **A**. For $r > k_t$ and $r - K < -k_t$, all the matrix coefficients A_{ij} of the system are purely imaginary; also, at certain real r dependent on K, the determinant of the matrix **A** can be zero. This r is the wave number of the crack interfacial waves previously discussed.[5]

In the scattering problem, however, we always have $r < k_t$ because it is the x projection of $\vec{k}_{l,t}$ and thus is smaller than k_t or $k_l < k_t$. In such cases, matrix **A** is complex, and we cannot expect that its determinant can be set to zero by varying only one variable, the real part of r (or K for given r). Indeed, we do not observe any singularities in the solutions presented in Figs. 3–5 that would appear if the system of Eqs. (22), (23) had a vanishing determinant at certain K.

We will show that this determinant can be close to zero for small r, the case not considered earlier.[5] We will also show that, in spite of generally complex **A**, its determinant can be zero at certain K and $r = 0$. This solution is called the interface vibration because it vanishes on both sides of the interfacelike interfacial waves,[5] but does not transport energy along the x-axis because $r = 0$ and the average $\Pi_1 = 0$.

In the case of cracks in a homogeneous body, both $\mathbf{g}_n$ and $\mathbf{g}_\infty$ are diagonal matrices. Then the system of Eqs. (22), (23) separates into two independent systems: one for the first vector component of $\mathbf{t}_m$ (its matrix is $\mathbf{A}_1$), and a second for the other vector component of $\mathbf{t}_m$ (matrix $\mathbf{A}_2$). Neglecting the index m, the unknown vector is therefore either $\mathbf{t} = [t_1\ 0]^T$ or $[0\ t_2]^T$. It can be easily checked numerically that $\det(\mathbf{A}_2) \neq 0$ for all K and r considered here, but $\det(\mathbf{A}_1)$ can indeed be close to zero for certain K if r is small, or even exactly equal to zero for $r = 0$.

This is shown in a pair of plots of the real and imaginary parts of $d = \det(\mathbf{A})$ as dependent on K for given real r, presented in Fig. 6. We notice that, in spite of the fact that matrix **A** is generally complex, both the real and imaginary parts of d cross zero at almost the same values of K, and exactly at the same K if $r = 0$. This means that, at $r = 0$, there is a nontrivial solution to systems (22), (23) even if its right hand side is equal to zero; that is, without an incident wave. (In this case only the shear wave that produces T_{21}^I different from zero at $r = 0$ is meaningful.) This is the free interface vibration at the angular frequency determined by $k_t = \omega / v_t$ (at given K), where v_t is the shear wave velocity. (For greater K, ω should be scaled proportionally.)

If $r \neq 0$ but is still small, it is possible that certain complex values of r could be found such that $d = 0$, or complex ω of a free interface vibration. (This is not analyzed directly here, since real valued r are assumed.) This expectation is reasonable and will be proved indirectly in numerical examples in the next section. For $r \neq 0$, the existing zero-order Bloch component is coupled to the bulk propagating modes. These bulk waves take part of the energy of interface vibration and transport it to infinity. Such vibrations must vanish either in time (resulting in a complex ω), or in space (complex eigenvalue r).

The case $r \to 0$ can be considered analytically in a certain simplification by using $N_1 = -1$ and $N_2 = 1$, the lowest values possible in the analysis presented below for cracks in homogeneous body. Neglecting the vector index by using the notation $t_m = (\mathbf{t}_m)_1$, $v_m = (\mathbf{v}_m)_1$, $T^I = (\mathbf{T}^I)_1 = T_{21}^I$,

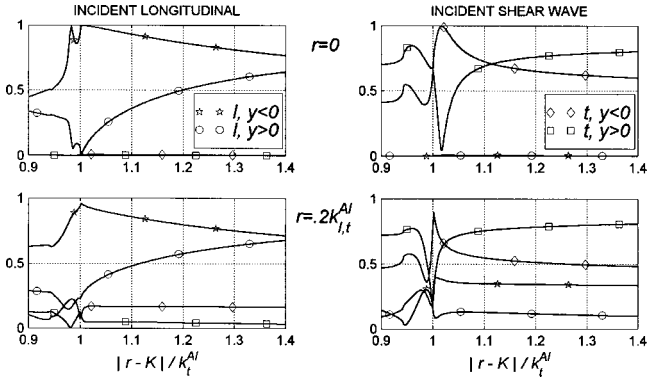

FIG. 4. Dependence of amplitudes of the zeroth-order transmitted and reflected waves for two different bonded solids, aluminum and steel (incidence from the aluminum side). In general, the dependence is similar to that in Fig. 3, but the transmission is never complete, even for $K \to \infty$, because of the difference in the acoustic impedances of aluminium and steel.

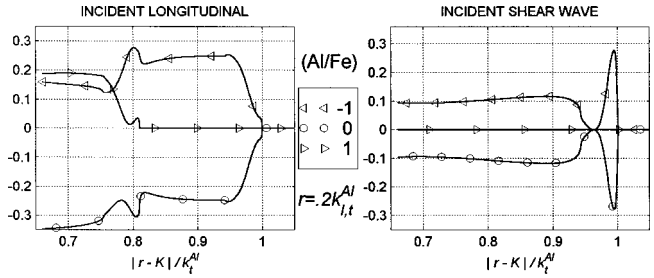

FIG. 5. The y component of Poynting vector differences, Eq. (B2), at the interface between aluminium and steel, for zeroth and $\pm$first orders of Bloch components. Note that the sum of all Π_2 is zero as required by the energy conservation law. In this example the incident wave propagates obliquely ($r = 0.2k_l$ or $0.2k_t$ in aluminum, for the incident longitudinal and shear wave, respectively). It is clearly seen that part of the power of the incident wave (that is, accounted for in the zeroth-order wave field), is transformed to the $\pm$first Bloch waves if $r \pm K$ falls in the region $(-k_t, k_t)$, the area of existence of bulk waves (Fig. 2).

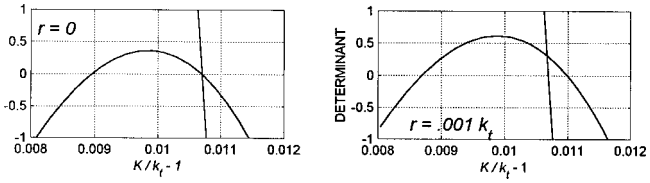

FIG. 6. Real and imaginary parts of the determinant of the system of equations governing the wave scattering as formulated in this paper for unknown $\mathbf{t}_m$. Note that for $r=0$, there is a certain value of K where both the real and imaginary parts of general complex determinant turn simultaneously to zero. For $r\neq 0$, real and imaginary parts have zeros at different K's. This means that the determinant is different from zero, but can be close to zero over a certain domain of K dependent on r. This will result in large (resonant) solutions for $\mathbf{t}_m$.

$G_n=(\mathbf{G}_n)_{11}=(\overline{\mathbf{G}}_n)_{11}$, $g_n=(\mathbf{g}_n)_{11}$, and $g_\infty=(\mathbf{g}_\infty)_{11}$, we first find the limit $r\to 0$ of last boundary conditions in Eqs. (16) and (23):

$$\begin{aligned}\Delta u|_{x=0}=0=v_m\sum_n \left.\frac{S_{n-m}P_{n-m}}{-j(r+nK)}\right|_{r\to 0}\\ \to \Delta u|_{n=0}+v_m\sum_{n\neq 0}\frac{S_{n-m}P_{n-m}}{-j(r+nK)}\\ =G_0T_0-[-\overline{G}_0(T_0-T^I\delta_{0I})+u^I\delta_{0I}]\\ +v_m\left(\sum_n \frac{S_{n-m}P_{n-m}}{-j(r+nK)}-\frac{S_{-m}P_{-m}}{-jr}\right)_{r\to 0},\end{aligned} \tag{25}$$

that results in

$$\left[2G_0P_{-m}+\frac{j}{K}(-1)^m\frac{d}{ds}P_{-m-s}g_\infty\right]t_m=2G_0T^I\delta_{0I}, \tag{26}$$

where $G_0=G(0)$ and $P_\nu=P_\nu(0)$ have been used to shorten the notation.

The system of equations (22) yields (note that $g_0=0$ and $P_{-1-l}=P_l$, $P_1=0$)

$$\begin{aligned}&n=-1:\quad (g_\infty-g_{-1})t_{-1}+(-g_\infty-g_{-1})t_0+(-g_\infty-g_{-1})t_2P_2=0,\\ &n=0:\quad g_\infty t_0-g_\infty t_1=0,\\ &n=1:\quad (g_\infty-g_1)t_{-1}P_2+(g_\infty-g_1)t_1+(-g_\infty-g_1)t_2=0.\end{aligned} \tag{27}$$

Taking into account that $P_2=1/4$, and $g_1=-g_{-1}=g$, these give

$$\begin{aligned}&t_0=t_1,\\ &(g_\infty+g)t_{-1}+(-g_\infty+g)t_0+(-g_\infty+g)t_2/4=0,\\ &(-g_{-\infty}+g)t_{-1}/4+(-g_\infty+g)t_1+(g_\infty+g)t_2=0.\end{aligned} \tag{28}$$

It results from (17) that in the approximation used,

$$T_0=t_mP_{0-m}=t_0+t_1. \tag{29}$$

Because $t_0=t_1$, $T_0\neq 0$ for any $t_0\neq 0$. However, any nonzero T_0 would generate a bulk wave in the half-spaces, and this does not allow the desired undamped solution for real ω and $r=0$. Therefore, we conclude that $T_0=0$, and thus

$$t_0=t_1=0, \tag{30}$$

if the desired interface wave is to exist. Boundary condition (26) yields

$$2G(0)T_0+\frac{j}{K}v_m(-1)^m\frac{d}{ds}P_{-m-s}|_{s=0}=2G(0)T^I\delta_{0I}, \tag{31}$$

where $v_m=g_\infty t_m$. For interface waves, $T^I=0$, and thus

$$\begin{aligned}&\frac{j}{K}(-t_{-1}p_1+t_0p_0-t_1p_{-1}+t_2p_{-2})=0,\\ &p_m=\frac{d}{ds}P_{-m-s}|_{s=0}.\end{aligned} \tag{32}$$

Taking into account (30) and $p_{-2}=-p_1$, we obtain

$$t_{-1}=-t_2. \tag{33}$$

Finally, the condition for a nonzero solution of Eqs. (28), (32) is $g_\infty+g=(-g_\infty+g)/4$, which yields

$$\sqrt{K^2-k_t^2}=\frac{5}{6}\frac{(k_t^2-2K^2)^2-4K^2\sqrt{K^2-k_l^2}\sqrt{K^2-k_t^2}}{K(k_t^2-k_l^2)}. \tag{34}$$

Equation (34) has a real solution for $K>k_t$.

It is important to note that, although all Bloch components of the wave field formally exist in the solution, the only component that falls in the area of bulk waves [$r\in(-k_t,k_t)$ in Fig. 2], namely the zeroth-order Bloch component, vanishes and produces $T_0=0$. This means that bulk waves are not generated during the interface vibrations of the above solution. These are free undamped interface vibrations.

When $T^I\neq 0$, $t_{-1}\neq -t_2$ and we obtain the regular solution for the scattering problem. This solution is orthogonal to the interface vibrations. This means that any incident wave (only the shear wave is meaningful, because the longitudinal wave does not produce T_{21}^I different from zero at $r=0$) cannot excite these free interface vibrations; they are perfectly decoupled from bulk waves because $T_0=0$. However, for small $r\neq 0$, we expect that the interface vibrations still exist and can be excited by the incident wave. These vibrations shed their energy into the bulk waves, contributing to the scattered wave field. The free vibrations would decay in time; otherwise, for real ω, the eigenvalue r will take a complex value. Such a wave is called a leaky wave.

VII. LEAKY INTERFACE WAVES

Figure 7 presents the zeroth-order wave amplitudes resulting from the scattering of transverse waves by cracks of a specific period embedded in a homogeneous body. The zeroth order is the only propagating mode in this case. The figure shows a graph similar to Fig. 2 but in greater detail for a certain domain of K. Note that there is sharp drop in the transmission coefficient (and a corresponding rise in the reflection coefficient to unity) over a very narrow domain of K

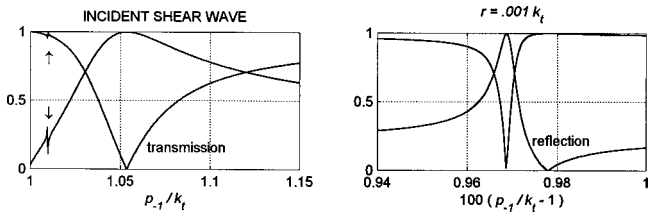

FIG. 7. For cracks in steel, the dependence of zeroth-order transmitted and reflected wave amplitudes is presented in greater detail for a certain domain of K (cf. Fig. 3). The right figure shows details of the region indicated by the arrows in the left figure. (Note how much the applied scale of K has been expanded.) For a certain value of K, we observe full reflection of the incident shear wave, as if the wave was reflected from the free half-space surface. But the interface is not free; there are periodic solid bonds instead. The narrow domain of K where the phenomenon takes place indicates that a resonant phenomenon is involved.

above k_t. Because K is expressed relative to k_t, the variation in K is equivalent to a variation of $1/\omega$ assuming constant Λ.

Figure 8 presents the amplitudes of the $\pm$first-order Bloch components, $\|\mathbf{T}_{\pm 1}\|/\|\mathbf{T}^I\|$. Note that these Bloch components are not coupled to any bulk propagating modes, because their wave numbers are $|r \pm K| > k_t$. These components are evanescent modes vanishing on both sides of the interface: the interface vibration. The figure shows the typical resonance curve of vibration in a lossy system. In this

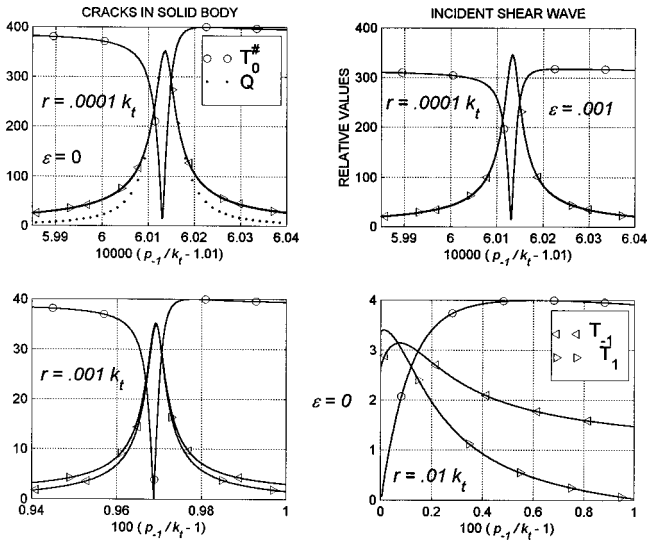

FIG. 8. Oblique incidence of shear wave (note the corresponding r in the subsequent figures) onto the cracks in steel. The relative amplitude $\mathbf{T}_0$ describes the transmission coefficient [see the dependence of the wave amplitudes on $\mathbf{T}$ given by Eq. (A3)]. In all figures, the coefficient $\|\mathbf{T}_{\pm 1}\|/\|\mathbf{T}^I\|$ (which has a maximum value of unity), is drawn expanded to full range of vertical axis ($\mathbf{T}^{\#}$). The upper right figure presents the influence of the bond viscosity (as modeled at the end of Sec. IV), and should be compared to the upper left figure. By relaxing the interface stress, the transmission coefficient of wave through the interface is reduced. However, the resonant values of $\mathbf{T}_{\pm 1}$ remain the same as for perfect solid bonding ($\epsilon = 0$, the left figure) because, at resonance, the interface stress $\mathbf{T}_0$ is already close to zero. [This zeroth-order stress is the main component of $\overline{\mathbf{T}}$ in Eq. (24) that is evaluated from the similar series as for $\overline{\mathbf{u}}$ above, where the coefficient $1/(r+nK)$ becomes very large if r is small and $n=0$.] The resonant values of $\mathbf{T}_{\pm 1}$ are smaller for larger r. This is due to stronger coupling of the interface vibrations to bulk waves, and the resulting larger radiation losses of the vibrations. For r above $0.01k_t$, the resonant curve $\|\mathbf{T}_{\pm 1}\|/\|\mathbf{T}^I\|$ can be barely recognized. This is in contrast to small r in the upper left figure, where the dotted line presents the typical resonance curve as evaluated from Eq. (35).

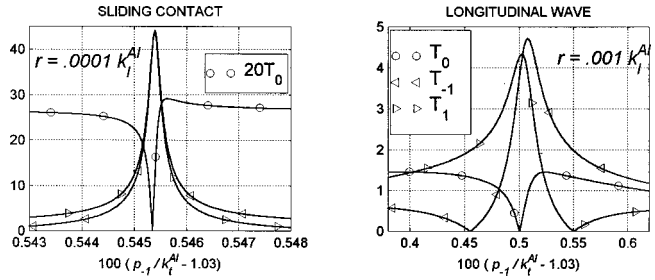

FIG. 9. Cracks at the interface between aluminum and steel with sliding bonding; the incident wave is a longitudinal wave in aluminium. The dependence is similar to that in Fig. 8, and a similar resonant phenomenon for generation of the interface vibrations ($\mathbf{T}_{\pm 1}$) is observed for small r.

case, the source is the incident wave, and the vibration is the crack interface vibration ($\pm$first-order Bloch components). The loss mechanism is the reradiation of bulk waves that, for $r \neq 0$, are coupled through the zeroth-order Bloch components. The resonance takes place at the synchronism of the exciting interface force (resulting from the incident wave) having wave number $p_{\pm 1}$ close to that of an interfacial waves having its wave numbers described by $\det(\mathbf{A}) = 0$.

For larger r, the resonance curve has smaller peaks (Fig. 8) because the reradiation losses are higher. (The coupling of the interface vibration to bulk waves is stronger at larger r.) Above certain r, the values of $\|\mathbf{T}_{\pm 1}\|/\|\mathbf{T}^I\|$ do not rise above unity. The physical interpretation of this is that the interface vibration no longer exists as a distinct mode.

The resonance character of the excited vibration $\|\mathbf{T}_{\pm 1}\|/\|\mathbf{T}^I\|$ is confirmed by its approximation, shown by the dotted line in Fig. 8, according to the typical resonance curve

$$Q = \left| \frac{a}{K - K_0 + jb} \right|, \tag{35}$$

where values for the parameters a and b have been chosen to fit the curves, and K_0 is the resonance value of K.

Similar phenomena can be observed in the case of cracks between two different elastic bodies, steel ($y > 0$) and aluminum ($y < 0$), in sliding contact at the interface:

$$\begin{aligned} &u_2^+(x) = u_2^-(x) \ \text{ and } \ T_{22}^+(x) = T_{22}^-(x) \ \text{ at bonds,} \\ &T_{22}^{\pm}(x) = 0 \ \text{ on cracks and } \ T_{21}^{\pm}(x) = 0 \ \text{ everywhere,} \end{aligned} \tag{36}$$

and for the longitudinal incident wave (producing T_{22}^I at the interface) with small wave number r.

For $r = 0$, both the real and imaginary values of the corresponding determinant $\mathbf{A}$ vanish at the same K above the largest value of k_t for both half-spaces. It happens that this value of K is close to k_R in steel. The resonance curve of $\|\mathbf{T}_{\pm 1}\|/\|\mathbf{T}^I\|$ for $r \neq 0$ is shown in Fig. 9. Its physical interpretation is similar to that presented above for two steel half-spaces. A sliding interface vibration is excited in which both the aluminum and steel move accordingly at the interface, in a direction normal to it, and arbitrarily in the tangential direction (in the assumed frictionless case).

The common phenomenon of a vanishing transmission coefficient of the incident wave at resonant values K_0 can be interpreted as follows. Due to the crack periodicity, the incident wave (wave number r) is coupled to the interface vibra-

tion (wave number $|r \pm K|$ just above k_t). For small r, this interface vibration is weakly coupled to bulk waves and thus is able to build up quite large amplitude. The reversal coupling of this energetic vibration produces the zeroth-order interface stress $\mathbf{T}_0$ that compensates the corresponding interface stress of the incident wave $\mathbf{T}^I$. Thus the incident wave ''feels'' a stress-free half-space surface at $y=0$, and is reflected accordingly.

VIII. SUMMARY AND CONCLUSIONS

In this paper, it has been shown how interface vibrations affect bulk-wave scattering by periodic cracks. The greatest effects are observed at close to normal incidence of the wave onto the plane of cracks, and for certain narrow domains of the crack period. Under perfect conditions, the reflection coefficient of the incident wave approaches unity, and the transmission coefficient falls to a negligible value.

To solve the problem, the BIS method of wave analysis for certain periodic systems was applied using discontinuous boundary conditions. The method has proven useful and, in spite of certain approximations, produced numerical results that satisfy the energy conservation law. (This is not always the case for numerical methods.)

The amplitude of the excited interface vibrations can be much higher than the amplitude of the incident wave. This can be exploited in the generation of Rayleigh waves by comb transducers.[2,4] For theoretical purposes, a comb transducer may be modeled as a finite system of cracks between the transducer and the substrate. Waves incident from the comb side generate large interfacial vibrations (with wave numbers close to k_R of the substrate in the optimal cases) that, at the end of comb, transform to a Rayleigh wave propagating on the free surface of the substrate outside the comb.

The next natural step toward the theory of comb transducers is the analysis of an infinite comb and finite, narrow incident wave beam propagating in it toward the interface. This can be modeled by applying the known $\overline{u}$ different from zero in certain domain of x (the domain of incidence), and subsequently evaluating the resulting $\overline{\mathbf{T}}$ from Eq. (24). In this analysis, the function $\mathbf{R}(r)=\overline{\mathbf{T}}/\overline{\mathbf{u}}$, $r \in (0,K)$, represents the ''periodic'' harmonic Green's function. It exhibits sharp peaks at the wave numbers of interface waves, and these peaks contribute to the far field of the generated interface wave field outside the x domain of incidence. Further problem of transformation of interface wave into Rayleigh wave at the edge the finite comb transducer must be solved separately.

ACKNOWLEDGMENTS

This paper is dedicated to the memory of the late Dr. Christopher M. Fortunko. Financial support was provided by the Polish-US Maria Sklodowska Curie Joint Fund II under Grant No. PAN/NIST-97-300. The author gratefully acknowledges many valuable discussions with Dr. Donna Hurley and Dr. Chris Fortunko of the National Institute of Standards and Technology, and the kind assistance of Dr. Hurley in the preparation of this manuscript. The shape of this work has been established with her kind participation when the author visited NIST in Boulder earlier this year.

APPENDIX A: BULK WAVE AMPLITUDES

It can be shown from the equation of motion for an isotropic body that at $y=0$,

$$\begin{bmatrix} u_1 \\ u_2 \end{bmatrix} = \frac{1}{\omega\sqrt{\rho\omega}} \begin{bmatrix} p & -q_t \\ q_l & p \end{bmatrix} \begin{bmatrix} F_l \\ F_t \end{bmatrix} \tag{A1}$$

for an arbitrary $F_{l,t}$ which describes the longitudinal and transverse parts of the wave field. Similarly, the stress components at $y=0$ are

$$\begin{bmatrix} T_{21} \\ T_{22} \end{bmatrix} = -j\,\frac{\mu/\omega}{\sqrt{\rho\omega}} \begin{bmatrix} 2pq_l & 2p^2-k_t^2 \\ k_t^2-2p^2 & 2pq_t \end{bmatrix} \begin{bmatrix} F_l \\ F_t \end{bmatrix}. \tag{A2}$$

This relation can be used to evaluate $\mathbf{T}^I$ for known $F_{l,t}$. The reciprocal relation is

$$\begin{bmatrix} F_l \\ F_t \end{bmatrix} = j\,\frac{\omega}{\mu}\,\frac{\sqrt{\rho\omega}}{D} \begin{bmatrix} 2pq_t & k_t^2-2p^2 \\ 2p^2-k_t^2 & 2pq_l \end{bmatrix} \begin{bmatrix} T_{21} \\ T_{22} \end{bmatrix}, \tag{A3}$$

where $F_{l,t}$ are related to the magnitude of the Poynting vector through

$$\Pi^{(i)} = |F_i|^2 k_i/2, \quad i=l,t. \tag{A4}$$

Using the definition of the wave amplitudes A_i as

$$\Pi^{(i)} = |A_i|^2/2, \tag{A5}$$

this equation shows that the relation between A_i and F_i is $A_i = F_i\sqrt{k^i}$, $i=l,t$.

The y component of the Poynting vector at $y=0$ is evaluated from Eq. (9) as

$$\Pi_2 = \mathrm{Re}\{q_l|F_l|^2 + q_t|F_t|^2\}/2. \tag{A6}$$

This is convenient in our analysis, because Π_2 vanishes as required if the corresponding $q_{l,t}$ is imaginary (that is, for evanescent modes). This, in fact, justifies the use of F_i in the above relations.

Having evaluated the Bloch components $\mathbf{T}_n$, the above relations allow the scattered wave amplitudes of corresponding Bloch orders to be evaluated. Note that to evaluate $\mathbf{F}$ and subsequently the amplitudes of reflected waves at n-th Bloch order, we must substitute $(\mathbf{T}_n - \mathbf{T}^I\delta_{nI})$ into right hand side of (A3). This results from boundary conditions (5). Indeed, because $\mathbf{T}^+(x)=\mathbf{T}^-(x)$ at the interface, the comparison of coefficients of Fourier expansion (3) for stress yields $\mathbf{T}_n^- = \mathbf{T}_n - \mathbf{T}^I\delta_{nI}$, and this $\mathbf{T}_n^-$, together with Eq. (10), describes the wave field in the half-space $y<0$.

APPENDIX B: THE ENERGY CONSERVATION LAW

The y components of the Poynting vectors on both sides of the interface for the nth Bloch order are:

$$\begin{aligned} \Pi_2^- &= \mathrm{Re}\{\mathbf{T}_n^*[j\omega(\mathbf{u}_n + \mathbf{u}^I\delta_{nI})]\}/2, \\ \Pi_2^+ &= \mathrm{Re}\{\mathbf{T}_n^*(j\omega\mathbf{u}_n)\}/2. \end{aligned} \tag{B1}$$

Therefore, the requirement of a balance of power at the interface for the nth Bloch order is

$$\Delta\Pi = \Pi_2^+ - \Pi_2^- = \frac{\omega}{2r}\,\mathrm{Re}\{\mathbf{T}_n^*(g_n\mathbf{T}_n - \dot{g}\mathbf{T}^I\delta_{nI})\}. \tag{B2}$$

See Eqs. (15) for denotations of $\mathbf{g}$ and $\dot{\mathbf{g}}$.

It is evident that the definition of Π_2 in Appendix A may also be used to check the energy balance at the interface. In this case, the balance is zero for $n=0$ only if the zeroth-order Bloch components include propagating modes in either of the half-spaces. However, the balance is not zero if other (higher-order) Bloch waves produce propagating waves. The total balance of acoustic power must include all appropriate Bloch field components.

[1] S. Hirose and J. D. Achenbach, ''Higher harmonics in the far field due to dynamics crack-face contacting,'' J. Acoust. Soc. Am. **93**, 142–147 (1993).

[2] I. A. Victorov, *Rayleigh and Lamb Waves: Physical Theory and Applications* (Plenum, New York, 1967), Chap. 1.

[3] J. L. Rose, S. P. Pelts, and M. J. Quarry, ''A comb transducer for mode control in guided wave NDE,'' 1996 IEEE Ultras. Symp. Proc. 857–860 (1996).

[4] D. C. Hurley, ''Measurements of surface-wave harmonic generation in nonpiezoelectric materials,'' J. Acoust. Soc. Am. **103**, 2926(A) (1998).

[5] E. Danicki, ''Interfacial waves in an elastic body fractured by periodic cracks,'' J. Acoust. Soc. Am. **100**, 2942–2948 (1996).

[6] E. Danicki, B. Langli, and K. Bløtekjær, ''Spectral theory of EM scattering by periodic strips,'' IEEE Trans. Antennas Propag. **AP-43**, 97–104 (1995).

[7] B. A. Auld, *Acoustic Waves and Fields in Solids* (Wiley, New York, 1973), Chap. 5.

A boundary integral equation method for two-dimensional acoustic scattering problems

S. A. Yang
Department of Naval Architecture and Marine Engineering, National Cheng Kung University, Tainan, Taiwan

(Received 24 August 1997; accepted for publication 5 October 1998)

This work formulates the singularity-free integral equations to study 2-D acoustic scattering problems. To avert the nonuniqueness difficulties, Burton's and Burton and Miller's methods are employed to solve the Dirichlet and Neumann problems, respectively. The surface Helmholtz integral equations and their normal derivative equations in bounded form are derived. The weakly singular integrals are desingularized by subtracting a term from the integrand and adding it back with an exact value. Depending on the relevant problem, the additional integral can finally be either expressed in an explicit form or transformed to form a surface source distribution of the related equipotential body. The hypersingular kernel is desingularized further using some properties of an interior Laplace problem. The new formulations are advantageous in that they can be computed by directly using standard quadrature formulas. Also discussed is the Γ-contour, a unique feature of 2-D problems. Instead of dividing the boundary surface into several small elements, a parametric representation of a 2-D boundary curve is further proposed to facilitate a global numerical implementation. Calculations consist of acoustic scattering by a hard and a soft circular cylinder, respectively. Comparing the numerical results with the exact solutions demonstrates the proposed method's effectiveness. © *1999 Acoustical Society of America.* [S0001-4966(99)04401-X]

PACS numbers: 43.20.Fn, 43.20.Tb [DEC]

INTRODUCTION

The surface Helmholtz integral equation is conventionally used for the acoustic scattering by obstacles. This approach is advantageous in that the problem's dimensionality is reduced by one and an infinite domain is transformed to finite boundaries in which the far-field radiation condition is automatically satisfied. Combining this approach with boundary element methods (i.e., local methods) has been a standard practice. It is known, however, that the standard Helmholtz integral equation fails to yield unique solutions at certain frequencies. For direct formulations (using the Helmholtz integral equation), both the Dirichlet and Neumann problems have the same characteristic frequencies at the eigenfrequencies of the interior Dirichlet problem. Nonuniqueness is a purely mathematical problem arising from the breakdown of boundary integral representation rather than from the nature of the physical problem. To avert this limitation, two conventional techniques have been applied for the acoustically hard body scattering. The first one is called CHIEF, the combined Helmholtz integral equation formulation, due to Schenck,[1] which is perhaps the most extensively used in engineering applications. A series of works has been reported after Schenck,[1] among which are included in Refs. 2–6. The second technique is derived by Burton and Miller[7] which linearly combined the Helmholtz integral equation with its normal derivative equation. Comparing these two methods reveals that they introduce their own particular complications.[8–11] Recently, Benthien and Schenck[12] reviewed various methods for handling the nonexistence and nonuniqueness problems associated with integral equation methods in acoustics.

The CHIEF method uses the surface Helmholtz integral equation, combined with the corresponding interior Helmholtz equation, to form an overdetermined system of equations which can then be solved using a least-squares procedure. This method may not function properly at the characteristic frequencies when some of the interior points coincide with a nodal surface of the related interior problems. More CHIEF points may be required to yield unique solutions at the characteristic frequencies. Therefore, in this method, the number and location of CHIEF points must be effectively selected, particularly in the high-frequency range.

Burton and Miller's formulation is severely limited in that the hypersingular integral must be evaluated. Previous investigations have derived the tangential derivative formulation to eliminate the highly singular kernels.[13,14] For a three-dimensional problem, this approach alleviates the highly singular behavior only, and leaves an additional $1/R$ type of singularity in the final formulation. Unique quadrature schemes are needed to locally assess the lower-order singular integrals. The highly singular integral equations can also be interpreted as the Hadamard finite-part sense.[15,16] However, this approach is not straightforward in numerical implementation and has not gained much acceptance in practice, at least in the acoustic field. Chien *et al.*[17] employed certain identities arising in the integral equation related to an interior Laplace problem. The order of hypersingularity is reduced and, then, a polar coordinate transformation and other unique techniques are locally applied to eliminate the lower-order singular integrals. Hwang[18] refined the process and attained integral equations with bounded kernels for easier numerical computation. In a related work, Yang[19] examined the acoustic scattering across a wide frequency range by combining Hwang's formulation[18] and Filon's method.[20]

Nonuniqueness also occurs in the acoustic scattering by soft bodies. Leis,[21] Panich,[22] and Brakhage and Werner[23] demonstrated that this difficulty can be averted by appropriately combining single- and double-layer potentials. The coupling factor must be chosen to be strictly complex when the wave frequency is real. Burton[24] later derived a similar formulation, indicating that the integral operator of his formulation is the transpose of that appearing in Brakhage and Werner's method.[23] The problem of acoustic scattering by soft bodies has been somewhat neglected, perhaps owing to that numerically implementing the weak singularity is much easier than that for the hypersingularity, and also that the soft scatterers may be less useful in engineering applications. Nevertheless, Yang[19] presented a desingularized formulation for the soft body scattering.

Burton and Miller's method[7] and Burton's method[24] possess a more rigorous mathematical background than the CHIEF method. Furthermore, Hwang's[18] and Yang's[19] formulations can efficiently implement such methods. In line with their desingularization procedures, this work derives some new formulations related to the Helmholtz integral equations and their normal derivative equations for 2-D acoustic scattering problems. These formulations are numerically preferable in that they can be computed by directly using standard quadrature formulas. The rest of this paper is organized as follows. In Sec. I we introduce the Helmholtz differential equation, interior Laplace equation, and related integral formulations. In Secs. II and III we derive the corresponding desingularized formulations. In Sec. IV we propose a parametric presentation of a 2-D boundary curve to facilitate numerical implementation. In Sec. V we examine the proposed method's effectiveness by comparing the numerical results with the exact solutions for the scattering by a circular cylinder of radius a which is subject to Dirichlet and Neumann boundary conditions, respectively. Three values of the characteristic wave number, $ka=3.83171$, 7.01559, 10.17347, are tested. Concluding remarks are finally made in Sec. VI.

I. A BRIEF SUMMARY OF THE INTEGRAL EQUATION FORMULATIONS

The integral formulations of 2-D acoustic scattering problems are extensively found in textbooks and literature. In this section, we summarize the relevant equations to ensure completeness and introduce notion. The governing equation for the propagation of acoustic waves through an unbounded homogeneous medium is described by the following wave equation:

$$\nabla^2\phi(r,t)=\frac{1}{c^2}\frac{\partial^2\phi(r,t)}{\partial t^2}, \tag{1}$$

where ∇^2 denotes the Laplacian operator in two dimensions, ϕ is the velocity potential at a point r at time t, and c is the speed of sound in the medium at the equilibrium state. The velocity potential ϕ is related to the velocity by

$$\mathbf{u}=\nabla\phi, \tag{2}$$

and can be expressed as

$$\phi=\phi^i+\phi^s, \tag{3}$$

where ϕ^i denotes the incident velocity potential and ϕ^s represents the scattered velocity potential. The excess acoustic pressure can be written as

$$p=-\rho_0\frac{\partial\phi}{\partial t}, \tag{4}$$

where ρ_0 denotes the density of the fluid at the equilibrium state. The acoustic pressure can also be written by summing up the two parts as follows:

$$p=p^i+p^s, \tag{5}$$

where p^i denotes the incident pressure and p^s represents the scattered pressure. For time-harmonic waves with a time factor $\exp(-i\omega t)$, the Helmholtz differential equation can be written as follows:

$$(\nabla^2+k^2)\phi=0, \tag{6}$$

where i is the imaginary unit, ω is the angular frequency, and $k=\omega/c$ is the wave number. Under this circumstance, Eq. (4) becomes

$$p=i\omega\rho_0\phi. \tag{7}$$

At the surface of a soft scatterer, the excess pressure is zero. Hence,

$$\phi=0. \tag{8}$$

At the surface of a hard scatterer, the normal component $\mathbf{u}\cdot\mathbf{n}$ of the particle velocity $\mathbf{u}$ is zero. Hence,

$$\frac{\partial\phi}{\partial n}=0, \tag{9}$$

where $\mathbf{n}$ denotes the unit vector normal to the surface of the body and into the surrounding space, and n represents the distance along the external normal vector $\mathbf{n}$. Conditions (8) and (9) are generally referred to as Dirichlet and Neumann boundary conditions, respectively. The scattered velocity potential must also satisfy the Sommerfeld radiation condition which is written in a 2-D form as follows:

$$\lim_{r\to\infty} r^{1/2}\left|\frac{\partial\phi^s}{\partial r}-ik\phi^s\right|=0. \tag{10}$$

The equivalent integral formulation of Eq. (6) takes the following form:

$$\phi^i(P)+\int_{\partial B}\left[\phi(Q)\frac{\partial G_k(P,Q)}{\partial n_Q}-G_k(P,Q)\frac{\partial\phi(Q)}{\partial n_Q}\right]dS_Q$$
$$=\begin{cases}\phi(P), & P\in B_e,\\ \dfrac{\phi(P)}{2}, & P\in\partial B,\\ 0, & P\in B_i,\end{cases} \tag{11}$$

where n_Q denotes the distance in the direction of the outward normal at the source point $Q(\xi,\eta)$, $P(x,y)$ is the field point, G_k is the free-space Green's function, ∂B is the closed surface, B_e is the infinite domain exterior to ∂B, and B_i is the interior domain enclosed by ∂B. In Eq. (11), the single- and

double-layer potentials over a Liapunov surface ∂B are assumed to satisfy a Hölder condition. A Liapunov surface, although having a continuously varying tangent plane at each point, does not necessarily possess a curvature everywhere. A Hölder condition, although generally stronger than continuity, is weaker than differentiability.[25] Notably, Eq. (11) already considers the radiation boundary condition (10). The free-space Green's function G_k for the Helmholtz equation in a 2-D form can be expressed as

$$G_k(P,Q)=\frac{i}{4}H_0^{(1)}(kR), \tag{12}$$

where $H_0^{(1)}(kR)$ denotes the Hankel function of the first kind and R represents the distance between the field point P and the moving point Q. The boundary formula of Eq. (11) fails to yield unique solutions at certain critical frequencies. The nonuniqueness is a purely mathematical problem, i.e., no physical meaning is connected to it. To avert this difficulty, a second integral equation can be written as follows by differentiating Eq. (11) in the normal direction at P:

$$\frac{\partial\phi^i(P)}{\partial n_P}+\frac{\partial}{\partial n_P}\int_{\partial B}\phi(Q)\,\frac{\partial G_k(P,Q)}{\partial n_Q}\,dS_Q - \int_{\partial B}\frac{\partial G_k(P,Q)}{\partial n_P}\,\frac{\partial\phi(Q)}{\partial n_Q}\,dS_Q=\frac{1}{2}\,\frac{\partial\phi(P)}{\partial n_P},\quad P\in\partial B, \tag{13}$$

Linearly combining boundary formula of (11) with (13) allows us to obtain unique solutions for all real frequencies when the coupling parameter is selected such that its imaginary part is nonzero.[7,24]

Since some properties of the interior Laplace problem are used during the desingularization procedures in Secs. II and III, the relevant equations are outlined as follows. The integral equation formulation of an interior Laplace equation, $\nabla^2\phi_0(r,t)=0$, can be written as

$$\int_{\partial B}\left[-\phi_0(Q)\,\frac{\partial G_0(P,Q)}{\partial n_Q}+G_0(P,Q)\,\frac{\partial\phi_0(Q)}{\partial n_Q}\right]dS_Q = \begin{cases} 0, & P\in B_e,\\ \dfrac{\phi_0(P)}{2}, & P\in\partial B,\\ \phi_0(P), & P\in B_i. \end{cases} \tag{14}$$

The assumptions in Eq. (14) closely resemble those in Eq. (11). Taking normal derivative of Eq. (14) at P yields

$$-\frac{\partial}{\partial n_P}\int_{\partial B}\phi_0(Q)\,\frac{\partial G_0(P,Q)}{\partial n_Q}\,dS_Q + \int_{\partial B}\frac{\partial G_0(P,Q)}{\partial n_P}\,\frac{\partial\phi_0(Q)}{\partial n_Q}\,dS_Q=\frac{1}{2}\,\frac{\partial\phi_0(P)}{\partial n_P},\quad P\in\partial B, \tag{15}$$

where G_0 denotes the free-space Green's function for the Laplace equation. A 2-D form of G_0 can be expressed as

$$G_0=-\frac{1}{2\pi}\ln(R). \tag{16}$$

II. DESINGULARIZATION OF SINGULAR KERNELS FOR THE SOFT BODY SCATTERING

For the soft body scattering, we have, from Eqs. (11) and (8),

$$0=\phi^i(P)-\int_{\partial B}G_k\,\frac{\partial\phi(Q)}{\partial n_Q}\,dS_Q,\quad P\in\partial B. \tag{17}$$

This equation contains a logarithmic type of singularity when the moving point $Q(\xi,\eta)$ coincides with the fixed point $P(x,y)$. A novel formulation is developed herein to eliminate the singular kernel. The technique, which is classic in the fields of potential theory and acoustics (e.g., Refs. 26 and 19), subtracts a function from the integrand so that the subsequent kernel becomes bounded. Then, an accurate integration of the function is added back to the equation. Thus, Eq. (17) is rearranged as follows:

$$0=\phi^i(P)-\int_{\partial B}(G_k-G_0)\,\frac{\partial\phi(Q)}{\partial n_Q}\,dS_Q - \int_{\partial B}G_0\left[\frac{\partial\phi(Q)}{\partial n_Q}-\frac{\partial\phi(P)}{\partial n_P}\right]dS_Q - \frac{\partial\phi(P)}{\partial n_P}\int_{\partial B}G_0\,dS_Q. \tag{18}$$

The kernel of the first integral in the preceding equation is bounded as R tends to zero, as demonstrated in the following. By definition, the first kernel can be written as

$$G_k-G_0=\frac{i}{4}H_0^{(1)}(kR)+\frac{\ln(R)}{2\pi}=\frac{\ln(R)}{2\pi}-\frac{Y_0(kR)}{4}+\frac{i}{4}J_0(kR), \tag{19}$$

where J_0 and Y_0 denote the Bessel functions of the first and second kind and zeroth order, respectively. The ascending series of $J_0(kR)$ and $Y_0(kR)$ can be expressed as[27]

$$J_0(kR)=1-\frac{1}{(1!)^2}\frac{1}{4}(kR)^2+\frac{1}{(2!)^2}\frac{1}{4^2}(kR)^4 - \frac{1}{(3!)^2}\frac{1}{4^3}(kR)^6+\cdots, \tag{20}$$

$$Y_0(kR)=\frac{2}{\pi}\left[\ln\left(\frac{kR}{2}\right)+\gamma\right]J_0(kR)+\frac{2}{\pi}\left[\frac{1}{(1!)^2}\frac{1}{4}(kR)^2 - \left(1+\frac{1}{2}\right)\frac{1}{(2!)^2}\frac{1}{4^2}(kR)^4 + \left(1+\frac{1}{2}+\frac{1}{3}\right)\frac{1}{(3!)^2}\frac{1}{4^3}(kR)^6-\cdots\right], \tag{21}$$

where $\gamma=0.577215...$, i.e., Euler's constant. Substituting Eqs. (20) and (21) into Eq. (19) yields

$$\lim_{R\to 0}(G_k - G_0) = -\frac{1}{2\pi}\left(\gamma + \ln\frac{k}{2}\right) + \frac{i}{4}. \tag{22}$$

Yang[19] confirmed that the integrand of the second integral in Eq. (18) is bounded and, furthermore, its value can be set equal to zero when Q coincides with P. The final integral in Eq. (18), although still singular in its current form, can be desingularized using potential theory, as demonstrated in the following. Applying the property of the equipotential body yields

$$\begin{aligned}\int_{\partial B} G_0\, dS_Q &= \int_{\partial B}\left[1 - \frac{\sigma(Q)}{\sigma(P)}\right] G_0\, dS_Q + \frac{1}{\sigma(P)} \\ &\quad \times \int_{\partial B} \sigma(Q) G_0\, dS_Q \\ &= \int_{\partial B}\left[1 - \frac{\sigma(Q)}{\sigma(P)}\right] G_0\, dS_Q - \frac{\Phi_e}{\sigma(P)},\end{aligned} \tag{23}$$

where σ denotes a source distribution on ∂B and makes the surface an equipotential of potential Φ_e which is defined by

$$\Phi_e = -\int_{\partial B} \sigma(Q) G_0\, dS_Q. \tag{24}$$

Notably, the integrand on the right-hand side of Eq. (23) can be set equal to zero when $R=0$. The fact that Φ_e remains constant in the interior of an equipotential surface accounts for why its value can be conveniently computed by locating point P inside the boundary surface. For instance, locating P at the origin leads to

$$\Phi_e = \frac{1}{2\pi}\int_{\partial B} \sigma(Q) \ln(\xi^2 + \eta^2)^{1/2}\, dS_Q. \tag{25}$$

Notably, Eq. (25) yields a unique solution for any given constant Φ_e with one exception, that the boundary ∂B is a Γ-contour.[28] For instance, if ∂B is the boundary of a unit circle, then σ has no finite value. The lack of a finite value is owing to that, for a circle of radius a, Eq. (25) gives

$$\Phi_e = 2\pi a \sigma\, \ln(a). \tag{26}$$

Petrovsky[29] first observed this feature of the unit circle. Jaswon and Symm[25] extended the above notion to more general body configurations. For instance, for an ellipse with surface coordinates (x,y), or $(a\,\cos\theta, b\,\sin\theta)$, Eq. (25) yields

$$\Phi_e = 2\pi(a^2\,\sin\,\theta + b^2\,\cos\,\theta)^{1/2}\sigma\,\ln\frac{a+b}{2}. \tag{27}$$

The Γ-contour, which appears at $(a+b)/2=1$, again causes σ to have no finite value. Nevertheless, the difficulty can always be averted by scaling. An alternative means of solving σ can be written as follows:

$$\sigma(P) = -2\int_{\partial B} \sigma(Q)\,\frac{\partial G_0}{\partial n_P}\, dS_Q. \tag{28}$$

The singular kernel in Eq. (28) can be removed by writing this equation in the following form:

$$\begin{aligned}\sigma(P) &= -2\int_{\partial B}\left[\sigma(Q)\,\frac{\partial G_0}{\partial n_P} - \sigma(P)\,\frac{\partial G_0}{\partial n_Q}\right] dS_Q \\ &\quad -2\sigma(P)\int_{\partial B}\frac{\partial G_0}{\partial n_Q}\, dS_Q.\end{aligned} \tag{29}$$

Applying the Gauss flux theorem,

$$\int_{\partial B}\frac{\partial G_0}{\partial n_Q}\, dS_Q = -\frac{1}{2}, \tag{30}$$

In Eq. (29) yields

$$0 = \int_{\partial B}\left[\sigma(Q)\,\frac{\partial G_0}{\partial n_P} - \sigma(P)\,\frac{\partial G_0}{\partial n_Q}\right] dS_Q. \tag{31}$$

The integrand in Eq. (31) can again be set equal to zero when $R=0$. The solution of Eq. (31) is not unique and needs specifying a given value of σ at some point on the surface in order to make the solution unique. Notably, it does not matter which solution of Eq. (31) is selected. In the sequel, the bounded form of the Helmholtz integral equation (17) can be written in the following:

$$\begin{aligned}0 &= \phi^i(P) - \int_{\partial B}(G_k - G_0)\,\frac{\partial\phi(Q)}{\partial n_Q}\, dS_Q \\ &\quad - \int_{\partial B} G_0\left[\frac{\partial\phi(Q)}{\partial n_Q} - \frac{\partial\phi(P)}{\partial n_P}\right] dS_Q \\ &\quad - \frac{\partial\phi(P)}{\partial n_P}\int_{\partial B}\left[1 - \frac{\sigma(Q)}{\sigma(P)}\right] G_0\, dS_Q + \frac{\partial\phi(P)}{\partial n_P}\,\frac{\Phi_e}{\sigma(P)},\end{aligned} \tag{32}$$

where the source intensity σ is given by Eq. (31) and the equipotential Φ_e is given by Eq. (25).

The normal derivative of the Helmholtz integral equation (13) for soft bodies takes the following form:

$$\frac{1}{2}\,\frac{\partial\phi(P)}{\partial n_P} = \frac{\partial\phi^i(P)}{\partial n_P} - \int_{\partial B}\frac{\partial G_k}{\partial n_P}\,\frac{\partial\phi(Q)}{\partial n_Q}\, dS_Q, \quad P\in\partial B. \tag{33}$$

Applying the technique resembling that in the previous case yields

$$\begin{aligned}\frac{1}{2}\,\frac{\partial\phi(P)}{\partial n_P} &= \frac{\partial\phi^i(P)}{\partial n_P} - \int_{\partial B}\left[\frac{\partial G_k}{\partial n_P}\,\frac{\partial\phi(Q)}{\partial n_Q} - \frac{\partial G_0}{\partial n_Q}\,\frac{\partial\phi(P)}{\partial n_P}\right] dS_Q \\ &\quad - \frac{\partial\phi(P)}{\partial n_P}\int_{\partial B}\frac{\partial G_0}{\partial n_Q}\, dS_Q.\end{aligned} \tag{34}$$

By using the Gauss flux theorem, Eq. (34) can be written in the following:

$$0 = \frac{\partial\phi^i(P)}{\partial n_P} - \int_{\partial B}\left[\frac{\partial G_k}{\partial n_P}\,\frac{\partial\phi(Q)}{\partial n_Q} - \frac{\partial G_0}{\partial n_Q}\,\frac{\partial\phi(P)}{\partial n_P}\right] dS_Q, \tag{35}$$

where the integrand is set equal to zero when Q coincides with P.

It can be shown that, although solutions of the standard integral equation (32) and its normal derivative equation (35) exist for all wave numbers, they are not unique. In the case

of Eq. (32), nonuniqueness occurs when the wave numbers equal the characteristic wave numbers of the interior Dirichlet problem; in the case of Eq. (35), nonuniqueness occurs when the wave numbers equal the characteristic wave numbers of the interior Neumann problem. Linearly combining Eq. (32) and Eq. (35) and assigning a coupling constant of a nonzero imaginary part yield a unique solution, even at a characteristic frequency.[24] The composite equation can be directly computed using standard quadrature formulas.

One may contend that the proposed formulations require extra computational time to obtain the equipotential Φ_e and the source function σ. Primary emphasis is clearly on σ, not on Φ_e, because Φ_e can be easily obtained from Eq. (25) if σ is given. Notably, σ is only a function of the shape of a given scatterer, i.e., σ is independent of the acoustic wave frequencies and the boundary conditions. Moreover, the function $\partial G_0/\partial n$ in integral equation (31), which is used to solve σ, is a part of the function $\partial G_k/\partial n$ in integral equation (35). This event can be easily observed by viewing the definitions of G_0 and G_k given in Eqs. (16) and (12), respectively, in which G_k contains the Hankel function $H_0^{(1)}$ and, in turn, $H_0^{(1)}$ is a sum of the Bessel functions, J_0 and Y_0. The Bessel function Y_0 explicitly contains the Green's function G_0. Therefore, G_0 and $\partial G_0/\partial n$ do not need to be recalculated during the computer programming. Restated, the matrix elements resulted from discretizing Eq. (31) are directly obtained from the matrix elements of Eq. (35). Notably, this procedure and the LU decomposition method solving for σ require only a small amount of computational time in the solution to the acoustic scattering across a frequency range. For small-scale problems, this requirement is confirmed by the fact that a substantial amount of computational time is normally expended on evaluating the matrix elements, not on evaluating the solution to the system of simultaneous linear algebraic equations itself. On the other hand, to minimize the computational time, a grid system solving for σ with an acceptable accuracy can be different from that solving for the acoustic scattering. This treatment is particularly useful for resolving higher-frequency problems, in which a higher-order quadrature formula must be adopted to attain convergent and accurate solutions. Thus, a denser grid system is used to solve the acoustic scattering. Under this circumstance, σ at the collocation points of the denser system can be estimated by applying an appropriate interpolation method in a looser grid system, which is initially used to evaluate σ.

The proposed desingularization method is also compared with other methods. The proposed approach is advantageous in that the subsequent formulations are free of singularity and, therefore, are conducive to computation by directly using standard quadrature formulas over the entire integration domain. Thus, the proposed approach can be referred to as a global method from a numerical perspective. Other alternative approaches, e.g., the polar coordinate transformation, can also be applied to solve the combined equation of Eqs. (17) and (33). Such approaches are generally referred to as a local method, or commonly referred to as a boundary element method. According to this method, the body surface is divided into a set of flat (or curved) subsurfaces and, then, the singular kernel in each subsurface is locally regularized by applying a transformation formula. The unknown function in each subsurface can be assumed to either remain constant or can be approximated by a higher-order equation. An analytic form of the integral may or may not be derived; thus, a quadrature formula is generally applied along each subsurface, resulting in a system of linear algebraic equations. This system is used to solve the unknown function. The proposed method outperforms the local method in that (a) the quadrature formula is globally applied and (b) the collocation points are exactly the positions at which the integration points are located. In contrast, the local method requires a quadrature formula in each subsurface, i.e., more computational time is necessary. Moreover, removing a singularity at a certain point inside the integration domain by the proposed method smooths out the integration function globally. In contrast, the integration function is only locally smoothed out using a local method. Restated, the local method leaves a significantly varying integration function over the elements which surround a singular element initially containing an infinity at a certain point. This observation implies that the integrals in the proposed formulations can be evaluated more efficiently than those in the local method. Therefore, the proposed method is definitely much easier and more economic than the conventional local method, especially for small-scale problems.

III. DESINGULARIZATION OF SINGULAR KERNELS FOR THE HARD BODY SCATTERING

For a hard body, we have, from Eqs. (11) and (9),

$$\frac{\phi(P)}{2} = \phi^i(P) + \int_{\partial B} \phi(Q)\,\frac{\partial G_k}{\partial n_Q}\,dS_Q, \quad P \in \partial B. \tag{36}$$

The integral in the preceding equation can be desingularized using the technique resembling that in the previous section. Thus, Eq. (36) becomes

$$\frac{\phi(P)}{2} = \phi^i(P) + \int_{\partial B}\left[\phi(Q)\,\frac{\partial G_k}{\partial n_Q} - \phi(P)\,\frac{\partial G_0}{\partial n_Q}\right]dS_Q + \phi(P)\int_{\partial B}\frac{\partial G_0}{\partial n_Q}\,dS_Q. \tag{37}$$

Applying the Gauss flux theorem in Eq. (37) yields

$$\phi(P) = \phi^i(P) + \int_{\partial B}\left[\phi(Q)\,\frac{\partial G_k}{\partial n_Q} - \phi(P)\,\frac{\partial G_0}{\partial n_Q}\right]dS_Q, \tag{38}$$

where the integral is bounded and the integrand can be set equal to zero when Q coincides with P.

By taking the normal derivative of Eq. (36) at point P, or from Eq. (13), we have the following integrodifferential equation:

$$\frac{\partial \phi^i(P)}{\partial n_P} = -\frac{\partial}{\partial n_P}\int_{\partial B}\phi(Q)\,\frac{\partial G_k}{\partial n_Q}\,dS_Q, \quad P \in \partial B, \tag{39}$$

which contains a hypersingular kernel as point Q coincides with point P. The derivative $\partial/\partial n_P$ cannot be taken inside the integral since a hypersingular kernel is nonintegrable.

The right-hand side of Eq. (39) can be written as

$$\frac{\partial}{\partial n_P}\int_{\partial B}\phi(Q)\,\frac{\partial G_k}{\partial n_Q}\,dS_Q$$
$$=\frac{\partial}{\partial n_P}\int_{\partial B}\left[\phi(Q)\,\frac{\partial G_k}{\partial n_Q}-\phi(P)\,\frac{\partial G_0}{\partial n_Q}\right]dS_Q$$
$$+\frac{\partial}{\partial n_P}\int_{\partial B}\phi(P)\,\frac{\partial G_0}{\partial n_Q}\,dS_Q. \tag{40}$$

The second term on the right-hand side of Eq. (40) contains the integration of $\partial G_0/\partial n_Q$, motivating us to use the Gauss flux theorem (30) for further treatment. Equation (30) can be rewritten as

$$\int_{\partial B}\phi(P)\,\frac{\partial G_0}{\partial n_Q}\,dS_Q=-\frac{1}{2}\,\phi(P). \tag{41}$$

Next, the normal derivative on the both sides is taken to obtain

$$\frac{\partial}{\partial n_P}\int_{\partial B}\phi(P)\,\frac{\partial G_0}{\partial n_Q}\,dS_Q=-\frac{1}{2}\,\frac{\partial\phi(P)}{\partial n_P}. \tag{42}$$

The first term on the right-hand side of Eq. (40) only contains a weak singularity and, therefore, the normal derivative $\partial/\partial n_P$ can be taken inside the integral. Using Eq. (42) in Eq. (40) yields

$$\frac{\partial}{\partial n_P}\int_{\partial B}\phi(Q)\,\frac{\partial G_k}{\partial n_Q}\,dS_Q$$
$$=\int_{\partial B}\left[\phi(Q)\,\frac{\partial^2 G_k}{\partial n_P\,\partial n_Q}-\frac{\phi(P)}{\partial n_P}\,\frac{\partial G_0}{\partial n_Q}\right.$$
$$\left.-\phi(P)\,\frac{\partial^2 G_0}{\partial n_P\,\partial n_Q}\right]dS_Q-\frac{1}{2}\,\frac{\partial\phi(P)}{\partial n_P}$$
$$=\int_{\partial B}\left[\phi(Q)\,\frac{\partial^2 G_k}{\partial n_P\,\partial n_Q}-\phi(P)\,\frac{\partial^2 G_0}{\partial n_P\,\partial n_Q}\right]dS_Q, \tag{43}$$

in which the Gauss flux theorem is applied. Equation (43) can further be written as

$$\frac{\partial}{\partial n_P}\int_{\partial B}\phi(Q)\,\frac{\partial G_k}{\partial n_Q}\,dS_Q$$
$$=\int_{\partial B}\phi(Q)\,\frac{\partial^2(G_k-G_0)}{\partial n_P\,\partial n_Q}\,dS_Q$$
$$+\int_{\partial B}[\phi(Q)-\phi(P)]\,\frac{\partial^2 G_0}{\partial n_P\,\partial n_Q}\,dS_Q$$
$$\equiv I_1+I_2. \tag{44}$$

The kernel of I_1 can be written as

$$\frac{\partial^2(G_k-G_0)}{\partial n_P\,\partial n_Q}$$
$$=\frac{k^2}{4\pi}\left(\frac{1}{2}-\ln\frac{k}{2}-\gamma\right)-\frac{k^2}{4\pi}\ln(R)+i\,\frac{k^2}{8}+O(R^2). \tag{45}$$

The detailed derivation of this identity is presented in the Appendix, in which the relationship,

$$\frac{\partial^2 R}{\partial n_P\partial n_Q}=-\frac{1}{R}+O(R), \tag{46}$$

is derived as well. Using Eq. (45) in I_1 yields

$$\int_{\partial B}\phi(Q)\,\frac{\partial^2(G_k-G_0)}{\partial n_P\,\partial n_Q}\,dS_Q$$
$$=\int_{\partial B}\left[\phi(Q)\,\frac{\partial^2(G_k-G_0)}{\partial n_P\,\partial n_Q}-\phi(P)\,\frac{k^2G_0}{2}\,\frac{\sigma(Q)}{\sigma(P)}\right]dS_Q$$
$$-\phi(P)\,\frac{k^2\Phi_e}{2\sigma(P)}, \tag{47}$$

where

$$\lim_{R\to 0}\left[\phi(Q)\,\frac{\partial^2(G_k-G_0)}{\partial n_P\,\partial n_Q}-\phi(P)\,\frac{k^2G_0}{2}\,\frac{\sigma(Q)}{\sigma(P)}\right]$$
$$=\frac{k^2}{4\pi}\left(\frac{1}{2}-\ln\frac{k}{2}-\gamma\right)+i\,\frac{k^2}{8}. \tag{48}$$

Treating I_2 in Eq. (44) is not as straightforward as that of the other cases. In addition, a novel technique is developed to transform the acoustic problem to a related interior Laplace problem. Günter[30] and Chien *et al.*[17] discussed the existence of I_2 (Liapunov condition), which involves a more stringent requirement on the unknown function than that of the Cauchy principal value integrals. Notably, the smoothness requirement has been assumed *a priori*. For the zero frequency (static) case, Eq. (43) is recast to the following form:

$$\frac{\partial}{\partial n_P}\int_{\partial B}\phi(Q)\,\frac{\partial G_0}{\partial n_Q}\,dS_Q$$
$$=\int_{\partial B}[\phi(Q)-\phi(P)]\,\frac{\partial^2 G_0}{\partial n_P\,\partial n_Q}\,dS_Q. \tag{49}$$

In Eq. (49), the velocity potential ϕ for an acoustic problem can be interpreted as a counterpart ϕ_0 of a potential problem, according to the physical meaning of the free-space Green's function G_0. By assigning ϕ to be equivalent to ϕ_0 on the boundary ∂B, Eq. (15) gives

$$\frac{\partial}{\partial n_P}\int_{\partial B}\phi_0(Q)\,\frac{\partial G_0}{\partial n_Q}\,dS_Q$$
$$=\int_{\partial B}\frac{\partial G_0}{\partial n_Q}\,\frac{\partial\phi_0(Q)}{\partial n_Q}\,dS_Q-\frac{1}{2}\,\frac{\partial\phi_0(P)}{\partial n_P}. \tag{50}$$

Combining Eqs. (49) with (50) yields

$$\int_{\partial B}[\phi(Q)-\phi(P)]\,\frac{\partial^2 G_0}{\partial n_P\,\partial n_Q}\,dS_Q$$
$$=\int_{\partial B}\frac{\partial G_0}{\partial n_P}\,\frac{\partial \phi_0(Q)}{\partial n_Q}\,dS_Q-\frac{1}{2}\,\frac{\phi_0(P)}{\partial n_P}$$
$$=\int_{\partial B}\left[\frac{\partial G_0}{\partial n_P}\,\frac{\partial \phi_0(Q)}{\partial n_Q}-\frac{\partial G_0}{\partial n_Q}\,\frac{\partial \phi_0(P)}{\partial n_P}\right]dS_Q$$
$$+\frac{\partial \phi_0(P)}{\partial n_P}\int_{\partial B}\frac{\partial G_0}{\partial n_Q}\,dS_Q-\frac{1}{2}\,\frac{\partial \phi_0(P)}{\partial n_P}$$
$$=\int_{\partial B}\left[\frac{\partial G_0}{\partial n_P}\,\frac{\partial \phi_0(Q)}{\partial n_Q}-\frac{\partial G_0}{\partial n_Q}\,\frac{\partial \phi_0(P)}{\partial n_P}\right]dS_Q-\frac{\partial \phi_0(P)}{\partial n_P},\tag{51}$$

where the Gauss flux theorem is applied and the final integrand can be set equal to zero when Q coincides with P. Notably, an additional unknown function $\partial\phi_0/\partial n$ appears in Eq. (51). The boundary formula of Eq. (14) gives

$$\int_{\partial B}\left[-\phi_0(Q)\,\frac{\partial G_0}{\partial n_Q}+G_0\,\frac{\partial \phi_0(Q)}{\partial n_Q}\right]dS_Q=\frac{\phi_0(P)}{2}.\tag{52}$$

The bounded form of Eq. (52) solving for $\partial\phi_0/\partial n$ can be written as follows:

$$\int_{\partial B}G_0\left[\frac{\partial \phi_0(Q)}{\partial n_Q}-\frac{\sigma(Q)}{\sigma(P)}\,\frac{\partial \phi_0(P)}{\partial n_P}\right]dS_Q-\frac{\Phi_e}{\sigma(P)}\,\frac{\partial \phi_0(P)}{\partial n_P}$$
$$=\int_{\partial B}[\phi_0(Q)-\phi_0(P)]\,\frac{\partial G_0}{\partial n_Q}\,dS_Q,\tag{53}$$

where all integrands are set equal to zero when Q coincides with P. By substituting Eqs. (44), (47), and (51) into Eq. (39), we end up with the bounded formulation of the normal derivative equation for the Neumann problem in the following:

$$\frac{\partial \phi^i(P)}{\partial n_P}$$
$$=-\int_{\partial B}\left[\phi(Q)\,\frac{\partial^2(G_k-G_0)}{\partial n_P\,\partial n_Q}-\phi(P)\,\frac{k^2 G_0}{2}\,\frac{\sigma(Q)}{\sigma(P)}\right]dS_Q$$
$$-\int_{\partial B}\left[\frac{\partial G_0}{\partial n_P}\,\frac{\partial \phi_0(Q)}{\partial n_Q}-\frac{\partial G_0}{\partial n_Q}\,\frac{\partial \phi_0(P)}{\partial n_P}\right]dS_Q+\frac{\partial \phi_0(P)}{\partial n_P}$$
$$+\phi(P)\,\frac{k^2\Phi_e}{2\sigma(P)}.\tag{54}$$

Resembling the problem of the soft body scattering, a unique solution is derived by combining the surface Helmholtz equation (38) with its normal derivative equation (54), in concert with Eq. (53) for the additional unknown function $\partial\phi_0/\partial n$, with a coupling factor which has a nonzero imaginary part of the real wave number k. Until now, we have completed the bounded formulations subject to Dirichlet and Neumann boundary conditions, respectively.

Also of notable interest is the proposed method's efficiency with respect to hard body scattering. One may contend that simultaneously solving the additional unknown function $\partial\phi_0/\partial n$ with the unknown function ϕ doubles the size of the matrix. Doubling a matrix implies eight times the amount of the computational time. Equation (53) also indicates that solving $\partial\phi_0/\partial n$ requires solving σ and Φ_e in advance. However, only a minimum amount of computational time is necessary to solve σ and Φ_e, as mentioned in the previous section. Therefore, solving the matrix for function $\partial\phi_0/\partial n$ itself is of primary concern. Closely examining Eq. (53) indicates that the integrands in Eq. (53) contain functions G_0 and $\partial G_0/\partial n$. Again, functions G_k and $\partial G_k/\partial n$ explicitly contain G_0 and $\partial G_0/\partial n$, respectively. Evaluating $\partial\phi_0/\partial n$ therefore requires only a minimum amount of computational time for small-scale problems. Notably, when the number of unknowns exceeds, say, 1000, the solution time will exceed the matrix formulation time. Under such a circumstance, one should pay attention to the solution's accuracy and the programming's efficiency of the proposed global method against that of other local methods. For instance, Krishnasamy *et al.*[15] presented a technique to locally reduce the hypersingular integral into a few regular surface integrals plus some line integrals. The regularization is then performed on each local singular element.

IV. A PARAMETRIC REPRESENTATION OF BOUNDARY CURVES

This section presents a parametric presentation of boundary curves to facilitate numerical implementation. Referring to a Cartesian coordinate system, the boundary ∂B can be written by a vector function as follows:

$$\mathbf{r}(S)=x(S)\mathbf{i}+y(S)\mathbf{j},\tag{55}$$

where S denotes the arc length of ∂B. Equation (55) can easily be converted to a parametric representation in the form:

$$\mathbf{r}(t)=x(t)\mathbf{i}+y(t)\mathbf{j},\tag{56}$$

where t denotes any parameter. Furthermore, the closed surface ∂B is divided into several small elements

$$\partial B=\sum_{k=1}^{K}\partial B(k),\tag{57}$$

such that $x(t)$ and $y(t)$ on each element $\partial B(k)$ are single-valued functions of t. In terms of the global sense, we require that the value of K be as small as possible. The ordinary line integral of single-valued function $f(x,y)$ along the element $\partial B(k)$ can be written by virtue of the parameter t as

$$\int_{\partial B(k)}f(x,y)dS$$
$$=\int_{t(k)}^{t(k+1)}f(x(t),y(t))\,\frac{dS}{dt}\,dt$$
$$=\int_{t(k)}^{t(k+1)}f(x(t),y(t))\left[\left(\frac{dx}{dt}\right)^2+\left(\frac{dy}{dt}\right)^2\right]^{1/2}dt.\tag{58}$$

In most cases, $y(t)$ is not known analytically and given by a set of data. For the latter case, $y(t)$ can be simulated by appropriate approximation methods. For example, a simple cubic spline would be one of them. Equation (58) is then the

basic representation for implementing the formulations presented in Secs. II and III. The terms, $\partial x/\partial n$ and $\partial y/\partial n$, involved implicitly in those formulations can be obtained by the normal vector

$$\mathbf{n}=\frac{\partial x(t)}{\partial n}\,\mathbf{i}+\frac{\partial y(t)}{\partial n}\,\mathbf{j}=\frac{\nabla g_k(t)}{|\nabla g_k(t)|}, \tag{59}$$

where

$$\nabla g_k(t)=-\frac{\partial h_k}{\partial t}\frac{\partial t}{\partial x}\,\mathbf{i}+\mathbf{j}, \tag{60}$$

and $g_k(x(t),y(t))=y(t)-h_k(x(t))=0$ is the equation of element $\partial B(k)$.

V. NUMERICAL CALCULATIONS

Consider the acoustic scattering of plane waves with unit amplitude at normal incidence on a circular cylinder with radius a. For comparison, the numerical results of the composite equations were obtained by a direct method without approximating the body shape and the method proposed in the previous section. Regarding the first method, the extended trapezoidal rule with equal segments was directly applied to evaluate the integrals. Atkinson[31] proved that the extended trapezoidal rule is often the best numerical integration rule for periodic functions. The system of linear algebraic equations was solved using the LU decomposition method. Since no surface approximation is made, the first method can be regarded as ''the most accurate numerical method.'' It is known, however, that this method is only available for bodies whose surface coordinates can be analytically defined.

Regarding the second method, the body surface is represented in a parametric form. Notably, the surface equation $x^2+y^2=a^2$ in the form of $y=h(x)$ is not analytic at $x=\pm a$. Directly using the approximation rules fails to accurately simulate the surface boundary. To avert this difficulty, a so-called double exponential formula[32]

$$x=-a\,\tanh(\alpha\,\sinh\,t) \tag{61}$$

was adopted, where α is a factor. This formula transforms the integral $\int_{-a}^{a}f(x)\,dx$ to $\int_{\infty}^{-\infty}f(x(t))\,dt$. Correspondingly, the value of K in Eq. (57) was set at 2, i.e., one for the upper surface and another for the lower surface. Using the transformation relationship (61), we have

$$\frac{dx(t)}{dt}=-\frac{a\alpha\,\cosh\,t}{\cosh^2(\alpha\,\sinh\,t)}. \tag{62}$$

The factor α was set at 0.5, although $\alpha=\pi/2$ is suggested in Ref. 32. The value of 0.5 was selected through a numerical test for the type of integral in this study. To facilitate numerical integration, the limits of integration on the transformed coordinate t were set at 3.5 and -3.5, which correspond to $x/a=-0.99\,999\,987$ and $0.99\,999\,987$. The main contribution of using Eqs. (61) and (62) is that dy/dt approaches zero, rather than infinity (i.e., unanalytic), at the limits of integration, $t=\pm 3.5$. To obtain values of $y(t)$ and dy/dt at the integration points, eighty equal intervals of a cubic spline along each transformed element (in the present case, we have two elements) were used for all test cases presented below. In doing so, the absolute errors of $y(t)$ and dy/dt have the values around 10^{-7} and 10^{-6}, respectively. The extended trapezoidal rule was adopted again for the numerical integration. This rule has been proved to be the most efficient method for evaluating integrals in the form, $I=\int_{-\infty}^{\infty}f(x)dx$, in which $f(x)$ is assumed to be analytical

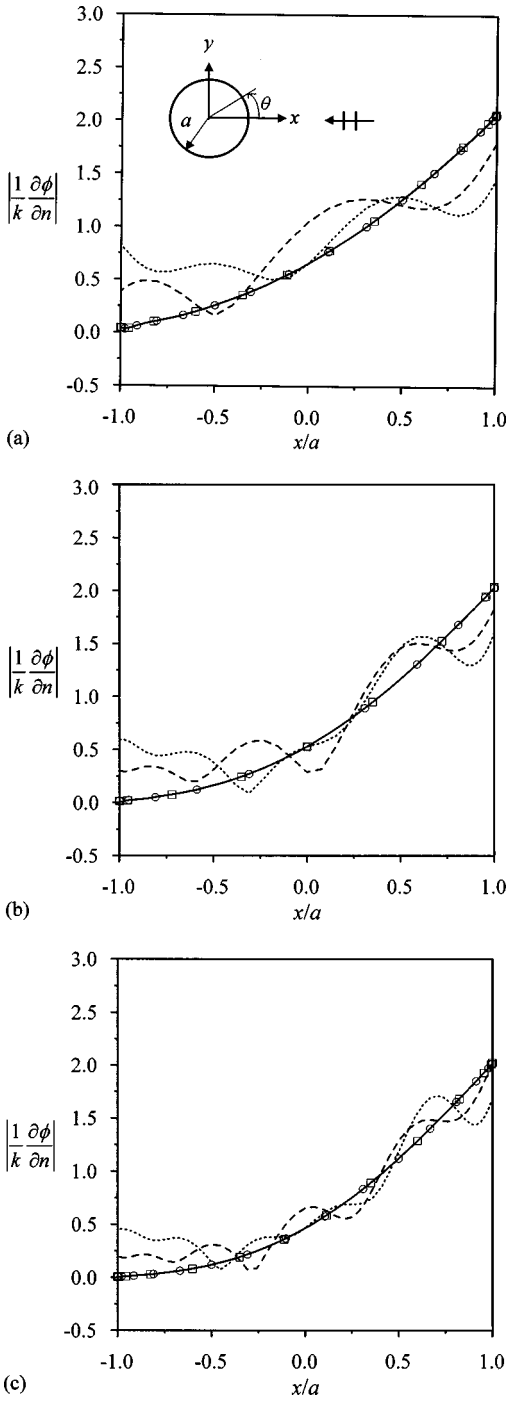

FIG. 1. Amplitude of surface field for a soft circular cylinder exposed to a plane wave with (a) $ka=3.83171$, (b) $ka=7.01559$, and (c) $ka=10.17347$ [solid line: exact solution; dotted line: Eq. (32) with method 1; dashed line: Eq. (35) with method 1; ○: composite equation, Eq. (32)$+i/ka\times$Eq. (35), with method 1; □: composite equation, Eq. (32)$+i/ka\times$Eq. (35), with method 2, where method 1 denotes a numerical method without approximating the body surface and method 2 denotes a numerical method using the proposed boundary simulation technique].

over $(\infty, -\infty)$.[32] The system of linear equations after the discretization was also solved by the LU decomposition method.

Calculations were performed for acoustic scattering by a soft and a hard circular cylinder with radius a, respectively. For convenience, the coupling factor of the composite integral equations was set at i/ka. Three values of the nondimensional characteristic wave number, i.e., $ka=3.83171$, 7.01559, 10.17347, were tested; three numbers of integration points, i.e., $N=31$, 41, 61 for $0\leqslant\theta\leqslant\pi$, were assigned as well. Notably, the selected ka values are zeros of both the Bessel function $J_0(ka)$ and its first derivative $-J_1(ka)$ which correspond to the eigenfrequencies of the related interior Dirichlet and Neumann problems, respectively. The eigenfrequencies for a circular cylindrical cavity can be easily obtained by applying the method of separation of variables (see, for example, Ref. 33). The purposely selected values simultaneously cause the surface Helmholtz integral equation and its normal derivative equation to have no unique solution, as discussed in Sec. II. Such a choice is then to demonstrate the breakdown of these two equations and the efficacy of the composite equation. Figure 1 displays the computed amplitudes of the surface field by two numerical methods described previously and the exact solution for the acoustically soft body scattering. On the surface of a soft circular cylinder, the exact solution can be expressed as[34]

$$\frac{1}{k}\frac{\partial\phi}{\partial n}=\frac{2}{\pi ka}\sum_{n=0}^{\infty}\varepsilon_n\frac{(-i)^n}{H_n^{(1)}(ka)}\cos n\theta, \tag{63}$$

where ε_n denotes the Neumann symbol, and $\varepsilon_0=1$; $\varepsilon_n=2$ for $n=1,2,3,\ldots$. Figure 1 indicates that only the composite equation can produce satisfactory results, as to be expected. This figure also indicates that both numerical methods (using the composite equation) can yield excellent results. More clearly, Fig. 2 displays the relative errors, defined by |(computed result-exact solution)/maximum of exact solution on the surface|, of the numerical results. Calculated results using the method with the proposed boundary simulation technique are comparable with that using the method without simulating the body shape, except in the proximity of $x/a=1$. In general, an accuracy of 10^{-3} was achieved for all cases.

Figure 3 illustrates the computed amplitudes of the surface field for the acoustically hard body scattering. Figure 4 depicts the corresponding relative errors. Again, three values of the characteristic wave number, i.e., $ka=3.83171$, 7.01559, 10.17347, were tested; three numbers of integration points, i.e., $N=31$, 51, 61 for $0\leqslant\theta\leqslant\pi$, were assigned as well. On the surface of a hard circular cylinder, the exact solution can be expressed as[34]

$$\phi=\frac{2}{\pi ka}\sum_{n=0}^{\infty}\varepsilon_n\frac{(-i)^{n-1}}{H_n^{(1)'}(ka)}\cos n\theta. \tag{64}$$

According to Figs. 3 and 4, the calculated results of the composite equation closely correspond to the exact solution. The accuracy of the second numerical method is about one order less than that of the first method. Thus, Figs. 1–4 confirm the effectiveness of the transformed formulations and the proposed numerical method.

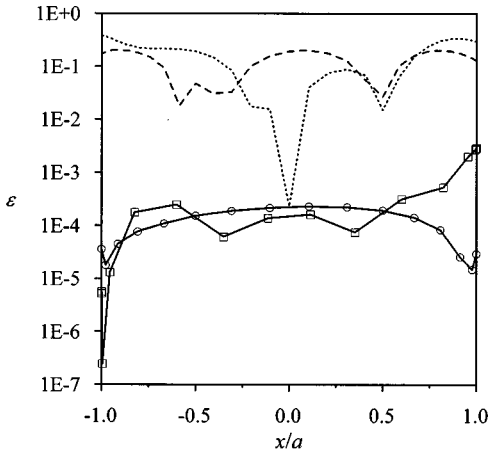

(a) $ka=3.83171$

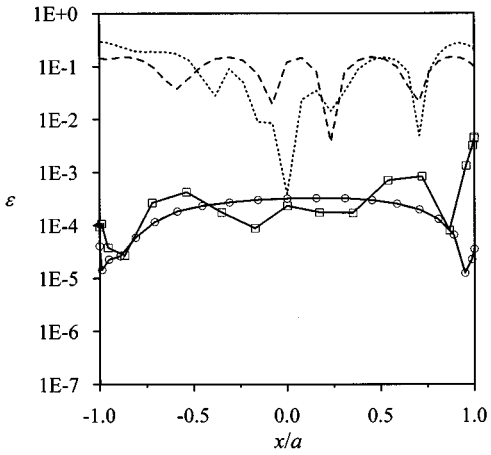

(b) $ka=7.01559$

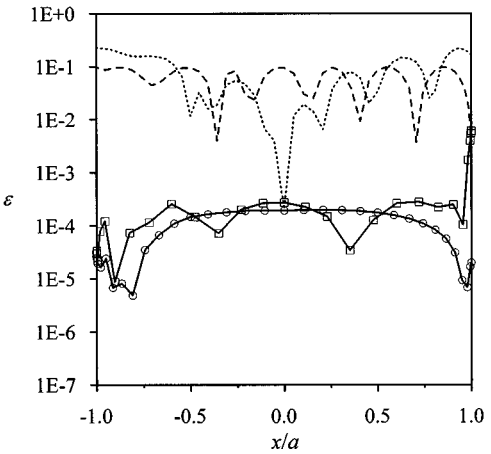

(c) $ka=10.17347$

FIG. 2. Relative error ε of computed amplitude of surface field in Fig. 1. Other definitions are given in Fig. 1.

VI. CONCLUSIONS

This work derives desingularized integral formulations related to the Helmholtz integral equations and their normal derivative equations to investigate the 2-D acoustic scattering subject to the Neumann and Dirichlet boundary condi-

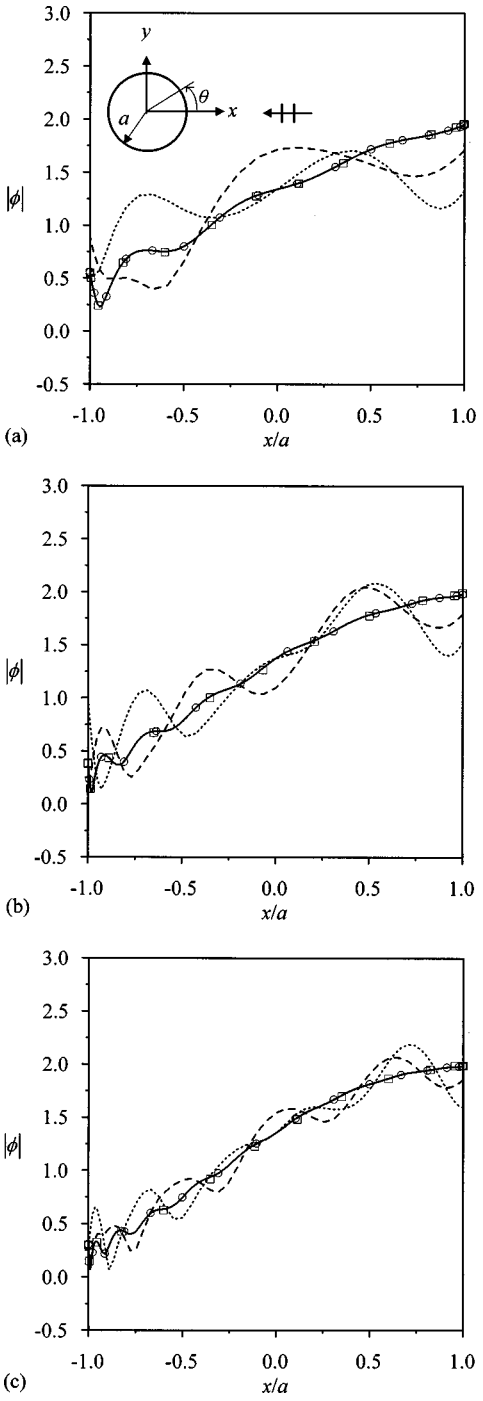

FIG. 3. Amplitude of surface field for a hard circular cylinder exposed to a plane wave with (a) $ka=3.83\,171$, (b) $ka=7.01\,559$, and (c) $ka=10.17\,347$ [solid line: exact solution; dotted line: Eq. (38) with method 1; dashed line: Eq. (54) with method 1; ○: composite equation, Eq. (38) $+i/ka\times$Eq. (54), with method 1; □: composite equation, Eq. (38)$+i/ka\times$Eq. (54), with method 2].

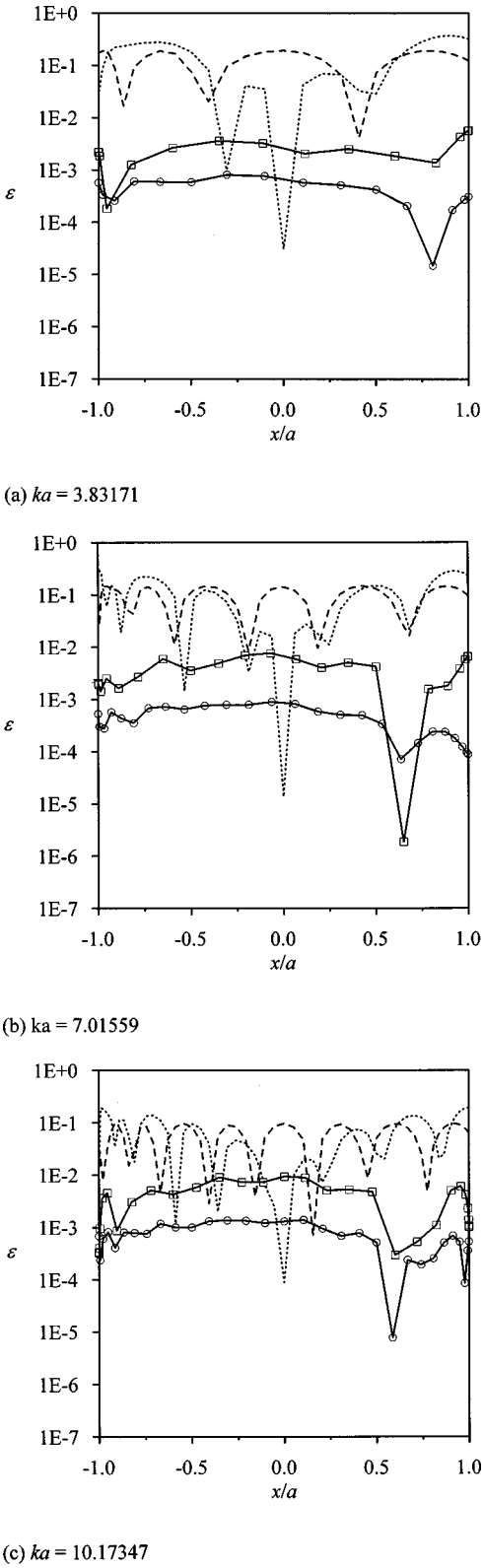

FIG. 4. Relative error ε of computed amplitude of surface field in Fig. 3. Other definitions are given in Fig. 3.

tions. The effectiveness of the transformed formulations is confirmed by comparing the calculated results with the exact solutions for the acoustic scattering from a soft and a hard circular cylinder, respectively. This work converts weakly singular and hypersingular kernels into bounded kernels by solving additional unknowns which are related to some properties of a Laplace problem. However, this approach is an acceptable tradeoff since the related computer programming for the procedure to solve the additional unknowns is rather easy.

A parametric representation of a 2-D boundary curve is further proposed to facilitate a global numerical implementation. The main feature of this approach is that the body

shapes can be accurately simulated before the main computations are executed. Thus, solution's accuracy is simply affected by the numerical quadrature methods. For small-scale problems, the proposed method is advantageous over the local methods since (a) the transformed formulations are already in a singularity-free form, i.e., one can immediately implement the formulations to study an acoustic scattering problem without considering other special treatments; (b) the proposed formulations are conducive to computation by directly using a quadrature formula over the entire integration domain, i.e., the proposed approach is a global method; (c) the collocation points are exactly the positions at which the integration points are located, i.e., no approximations made in boundary element (local) methods are required; and (d) the converted integration function is globally smoothened out, i.e., the integration can be efficiently evaluated.

A future study includes applying the proposed numerical method to high-frequency problems. Tobocman's[35] and Yang's[19] approaches can be adopted for such an extension. Extending the proposed numerical method to 3-D acoustical problems is conceptually straightforward.

ACKNOWLEDGMENTS

The author would like to thank the National Science Council, R.O.C., for partially supporting this research under Contract No. NSC 86-2611-E-006-004. C. H. Lee is also appreciated for his programming assistance.

APPENDIX: DERIVATIONS OF SOME IDENTITIES

1. Demonstrate that $\partial^2 R/\partial n_P\,\partial n_Q = -1/R + O(R)$

Let $f(x,y,z)=0$ be the equation of the body surface ∂B. The direction cosines of the point $P(x,y,z)$ of ∂B are given by

$$\frac{\partial x}{\partial n_P}=\frac{f_x}{D_P},\quad \frac{\partial y}{\partial n_P}=\frac{f_y}{D_P},\quad \frac{\partial z}{\partial n_P}=\frac{f_z}{D_P}, \tag{A1}$$

where f_x, f_y, and f_z denote partial derivatives of $f(x,y,z)$ with respect to x, y, and z, respectively, and

$$D_P=(f_x^2+f_y^2+f_z^2)^{1/2}. \tag{A2}$$

The distance R between the field point $P(x,y,z)$ and the source point $Q(\xi,\eta,\zeta)$ can be written as

$$R=[(x-\xi)^2+(y-\eta)^2+(z-\zeta)^2]^{1/2}. \tag{A3}$$

Thus, we have

$$\begin{aligned}\frac{\partial R}{\partial n_P}&=\frac{1}{R}\left[(x-\xi)\,\frac{\partial x}{\partial n_P}+(y-\eta)\,\frac{\partial y}{\partial n_P}+(z-\eta)\,\frac{\partial z}{\partial n_P}\right]\\&=\frac{1}{R}\,\frac{1}{D_P}\left[(x-\xi)\,\frac{\partial f}{\partial x}+(y-\eta)\,\frac{\partial f}{\partial y}+(z-\eta)\,\frac{\partial \phi}{\partial z}\right]\\&=\frac{1}{R}\,\frac{\mathbf{R}\cdot\boldsymbol{\nabla}_P f}{D_P},\end{aligned} \tag{A4}$$

where $\mathbf{R}=(x-\xi,y-\eta,z-\zeta)$. Similarly, we have

$$\frac{\partial R}{\partial n_Q}=-\frac{1}{R}\,\frac{\mathbf{R}\cdot\boldsymbol{\nabla}_Q f}{D_Q}. \tag{A5}$$

From Eqs. (A4) and (A5), we obtain

$$\frac{\partial^2 R}{\partial n_Q\partial n_P}=\frac{1}{R^3}\,\frac{\mathbf{R}\cdot\boldsymbol{\nabla}_Q f}{D_Q}\,\frac{\mathbf{R}\cdot\boldsymbol{\nabla}_P f}{D_P}-\frac{1}{R}\,\frac{\boldsymbol{\nabla}_Q f\cdot\boldsymbol{\nabla}_P f}{D_Q D_P}. \tag{A6}$$

When Q is near P, we can write the Taylor series

$$\frac{1}{D_Q}=\frac{1}{D_P}+\mathbf{R}\cdot\boldsymbol{\nabla}_P\left(\frac{1}{D_P}\right)+\cdots. \tag{A7}$$

Also, we have

$$\boldsymbol{\nabla}_Q f=\boldsymbol{\nabla}_P f+(\mathbf{R}\cdot\boldsymbol{\nabla}_P)\boldsymbol{\nabla}_P f+\cdots. \tag{A8}$$

Substituting Eqs. (A7) and (A8) into Eq. (A6) yields

$$\begin{aligned}\frac{\partial^2 R}{\partial n_Q\partial n_P}=\frac{1}{R^3}&\left[\frac{1}{D_P^2}\,(\mathbf{R}\cdot\boldsymbol{\nabla}_P f\,)^2+\text{higher-order terms}\right]\\&-\frac{1}{R}\left\{\frac{1}{D_P^2}\,\boldsymbol{\nabla}_P f\cdot\boldsymbol{\nabla}_P f+\frac{1}{D_P^2}\,[(\mathbf{R}\cdot\boldsymbol{\nabla}_P)\boldsymbol{\nabla}_P f]\cdot\boldsymbol{\nabla}_P f\right.\\&+\frac{1}{D_P}\left[\mathbf{R}\cdot\boldsymbol{\nabla}_P\left(\frac{1}{D_P}\right)\right]\boldsymbol{\nabla}_P f\cdot\boldsymbol{\nabla}_P f\\&\left.+\text{higher-order terms}\right\}.\end{aligned} \tag{A9}$$

Since $f(x,y,z)=f(\xi,\eta,\zeta)=0$, we obtain

$$\mathbf{R}\cdot\boldsymbol{\nabla}_P f\sim O(R^2). \tag{A10}$$

By making use of the following formulas,

$$\boldsymbol{\nabla}(\mathbf{a}\cdot\mathbf{a})=2(\mathbf{a}\cdot\boldsymbol{\nabla})\mathbf{a}+2\mathbf{a}\times(\boldsymbol{\nabla}\times\mathbf{a}), \tag{A11}$$

$$\boldsymbol{\nabla}\times\boldsymbol{\nabla}g=0, \tag{A12}$$

where $\mathbf{a}$ denotes any vector and g denotes any scalar, we have

$$\begin{aligned}\boldsymbol{\nabla}_P\left(\frac{1}{D_P}\right)&=-\frac{\boldsymbol{\nabla}_P(\boldsymbol{\nabla}_P f\cdot\boldsymbol{\nabla}_P f\,)}{2D_P^3}\\&=-\frac{(\boldsymbol{\nabla}_P f\cdot\boldsymbol{\nabla}_P)\boldsymbol{\nabla}_P f+\boldsymbol{\nabla}_P f\times(\boldsymbol{\nabla}_P\times\boldsymbol{\nabla}_P f\,)}{D_P^3}\\&=-\frac{(\boldsymbol{\nabla}_P f\cdot\boldsymbol{\nabla}_P)\boldsymbol{\nabla}_P f}{D_P^3}.\end{aligned} \tag{A13}$$

Substituting Eqs. (A10) and (A13) into Eq. (A9) yields

$$\begin{aligned}\frac{\partial^2 R}{\partial n_Q\,\partial n_P}=-\frac{1}{R}-\frac{1}{R}&\left\{\frac{[(\mathbf{R}\cdot\boldsymbol{\nabla}_P)\boldsymbol{\nabla}_P f]\cdot\boldsymbol{\nabla}_P f}{D_P^2}\right.\\&\left.-\frac{\mathbf{R}\cdot[(\boldsymbol{\nabla}_P f\cdot\boldsymbol{\nabla}_P)\boldsymbol{\nabla}_P f]}{D_P^2}\right\}+O(R).\end{aligned} \tag{A14}$$

Using the vector identity

$$[(\mathbf{R}\cdot\boldsymbol{\nabla}_P)\boldsymbol{\nabla}_P f]\cdot\boldsymbol{\nabla}_P f=\mathbf{R}\cdot[(\boldsymbol{\nabla}_P f\cdot\boldsymbol{\nabla}_P)\boldsymbol{\nabla}_P f], \tag{A15}$$

Eq. (A14) becomes

$$\frac{\partial^2 R}{\partial n_Q\,\partial n_P}=-\frac{1}{R}+O(R). \tag{A16}$$

2. Demonstrate that $\partial^2(G_k-G_0)/\partial n_P\,\partial n_Q = k^2/4\pi(1/2 - \ln k/2 - \gamma) - k^2/4\pi\,\ln(R) + i\,k^2/8 + O(R^2)$

By the definitions of G_k and G_0, we have

$$G_k - G_0 = \frac{i}{4} H_0^{(1)}(kR) + \frac{1}{2\pi}\ln(R) = -\frac{1}{4} Y_0(kR) + \frac{1}{2\pi}\ln(R) + \frac{i}{4} J_0(kR), \quad \text{(A17)}$$

where J_0 and Y_0 denote the Bessel functions of the first and second kind and zeroth order, respectively. The ascending series of $Y_0(kR)$ can be written as

$$Y_0(kR) = \frac{2}{\pi}\left[\ln\left(\frac{kR}{2}\right)+\gamma\right]J_0(kR) + \frac{2}{\pi}\left[\frac{1}{(1!)^2}\frac{1}{4}(kR)^2 - \left(1+\frac{1}{2}\right)\frac{1}{(2!)^2}\frac{1}{4^2}(kR)^4 + \left(1+\frac{1}{2}+\frac{1}{3}\right)\frac{1}{(3!)^2}\frac{1}{4^3}(kR)^6 - \cdots\right]. \quad \text{(A18)}$$

Substituting (A18) into (A17) yields

$$G_k - G_0 = \frac{1}{2\pi}(1-J_0(kR))\ln(R) - \frac{1}{2\pi}\left(\ln\frac{k}{2}+\gamma\right)J_0(kR) - \frac{1}{8\pi}(kR)^2 + \cdots + \frac{i}{4}J_0(kR), \quad \text{(A19)}$$

where γ is known as Euler's constant and $\gamma = 0.577215\ldots$. Taking differentiation of Eq. (A19) with respect to n_P yields

$$\frac{\partial(G_k-G_0)}{\partial n_P} = \frac{1}{2\pi}(1-J_0(kR))\frac{1}{R}\frac{\partial R}{\partial n_P} - \frac{k}{2\pi}\frac{\partial J_0(kR)}{\partial(kR)} \times \frac{\partial R}{\partial n_P}\ln(R) - \frac{k}{2\pi}\left(\ln\frac{k}{2}+\gamma\right)\frac{\partial J_0(kR)}{\partial(kR)}\frac{\partial R}{\partial n_P} - \frac{k^2}{4\pi}R\frac{\partial R}{\partial n_P} + \cdots + \frac{ik}{4}\frac{\partial J_0(kR)}{\partial(kR)}\frac{\partial R}{\partial n_P}. \quad \text{(A20)}$$

The ascending series of $J_0(kR)$ can be written as

$$J_0(kR) = 1 - \frac{1}{(1!)^2}\frac{1}{4}(kR)^2 + \frac{1}{(2!)^2}\frac{1}{4^2}(kR)^4 - \frac{1}{(3!)^2}\frac{1}{4^3}(kR)^6 + \cdots. \quad \text{(A21)}$$

Thus, we have

$$\frac{\partial J_0(kR)}{\partial(kR)} = -\frac{1}{(1!)^2}\frac{1}{2}(kR) + \frac{1}{(2!)^2}\frac{1}{4}(kR)^3 - \frac{1}{(3!)^2}\frac{3}{32}(kR)^5 + \cdots. \quad \text{(A22)}$$

From Eqs. (A20)–(A22), we have

$$\frac{\partial^2(G_k-G_0)}{\partial n_P\,\partial n_Q} = \frac{k^2}{4\pi}\left(\frac{-1}{2}+\gamma+\ln\frac{k}{2}+\ln(R)\right) \times R\frac{\partial^2 R}{\partial n_P\,\partial n_Q} - i\frac{k^2}{8}R\frac{\partial^2 R}{\partial n_P\,\partial n_Q} + O(R^2). \quad \text{(A23)}$$

By making use of Eq. (A16) in Eq. (A23), we have

$$\frac{\partial^2(G_k-G_k)}{\partial n_P\,\partial n_Q} = \frac{k^2}{4\pi}\left(\frac{1}{2}-\ln\frac{k}{2}-\gamma\right) - \frac{k^2}{4\pi}\ln(R) + i\frac{k^2}{8} + O(R^2). \quad \text{(A24)}$$

[1] H. A. Schenck, ''Improved integral formulation for acoustic radiation problems,'' J. Acoust. Soc. Am. **44**, 41–58 (1968).
[2] D. T. Wilton, ''Acoustic radiation and scattering from elastic structures,'' Int. J. Numer. Methods Eng. **13**, 128–138 (1978).
[3] A. F. Seybert, B. Soenarko, F. J. Rizzo, and D. J. Shippy, ''An advanced computational method for radiation and scattering for acoustic waves in three dimensions,'' J. Acoust. Soc. Am. **77**, 362–368 (1985).
[4] A. F. Seybert, B. Soenarko, F. J. Rizzo, and D. J. Shippy, ''A special integral equation formulation for acoustic radiation and scattering for axisymmetric bodies and boundary conditions,'' J. Acoust. Soc. Am. **80**, 1241–1247 (1986).
[5] A. F. Seybert and T. K. Rengarajan, ''The use of CHIEF to obtain unique solutions for acoustic radiation using boundary integral equations,'' J. Acoust. Soc. Am. **81**, 1299–1306 (1987).
[6] A. F. Seybert and T. W. Wu, *BEMAP User's Manual* (Spectronics, Inc., New York, 1989), Version 2.4.
[7] A. J. Burton and G. F. Miller, ''The application of integral equation methods to the numerical solution of some exterior boundary value problems,'' Proc. R. Soc. London, Ser. A **323**, 201–210 (1971).
[8] W. S. Hall and W. H. Robertson, ''Standard Helmholtz integral equation calculations near characteristic frequencies,'' J. Sound Vib. **126**, 367–368 (1988).
[9] A. F. Seybert, ''A note on methods for circumventing nonuniqueness when using integral equations,'' J. Sound Vib. **115**, 171–172 (1987).
[10] Z. Reut, ''On the boundary integral methods for the exterior acoustic problem,'' J. Sound Vib. **103**, 297–298 (1985).
[11] David T. I. Francis, ''A gradient formulation of the Helmholtz integral equation for acoustic radiation and scattering,'' J. Acoust. Soc. Am. **93**, 1700–1709 (1993).
[12] W. Benthien and A. Schenck, ''Nonexistence and nonuniqueness problems associated with integral equation methods in acoustics,'' Comput. Struct. **65**, 295–305 (1997).
[13] W. L. Meyer, W. A. Bell, B. T. Zinn, and M. P. Stallybrass, ''Boundary integral solutions of three dimensional acoustic radiation problems,'' J. Sound Vib. **59**, 245–262 (1978).
[14] I. C. Mathews, ''Numerical techniques for three-dimensional steady-state fluid–structure interaction,'' J. Acoust. Soc. Am. **79**, 1317–1325 (1986).
[15] G. Krishnasamy, L. W. Schmerr, T. J. Rudolphi, and F. J. Rizzo, ''Hypersingular boundary integral equations: Some applications into acoustic and elastic wave scattering,'' J. Appl. Mech. **57**, 404–414 (1990).
[16] Yijun Liu and F. J. Rizzo, ''A weakly singular form of the hypersingular boundary integral equation applied to 3-D acoustic wave problems,'' Comput. Methods Appl. Mech. Eng. **96**, 271–287 (1992).
[17] C. C. Chien, H. Rajiyah, and S. N. Atluri, ''An effective method for solving the hypersingular integral equations in 3-D acoustics,'' J. Acoust. Soc. Am. **88**, 918–937 (1990).
[18] W. S. Hwang, ''Hypersingular boundary integral equations for exterior acoustic problems,'' J. Acoust. Soc. Am. **101**, 3336–3342 (1997).
[19] S. A. Yang, ''Acoustic scattering by a hard or soft body across a wide frequency range by the Helmholtz integral equation method,'' J. Acoust. Soc. Am. **102**, 2511–2520 (1997).
[20] L. N. G. Filon, ''On a quadrature formula for trigonometric integrals,'' Proc. R. Soc. Edinburgh **49**, 38–47 (1928).
[21] R. Leis, ''Zur Dirichletschen Randwertaufgabe des Außenraumes der Schwingungsgleichung,'' Math. Z. **90**, 205–211 (1965).
[22] O. I. Panich, ''On the question of the solvability of the exterior boundary

problem for the wave equation and Maxwell's equation (in Russian),'' Usp. Mat. Nauk. **20**, 221–226 (1965).
[23] H. Brakhage and P. Werner, ''Über das Dirichletsche Aussenraumproblem für die Helmholtzsche Schwingungsgleichung,'' Arch. Math. **16**, 325–329 (1965).
[24] A. J. Burton, ''The solution of Helmholtz equation in exterior domains using integral equations,'' NPL Report NAC 30, National Physical Laboratory, January (1973).
[25] M. A. Jaswon and G. T. Symm, *Integral Equation Methods in Potential Theory and Elastostatics* (Academic, London, 1977).
[26] L. Landweber and M. Macagno, ''Irrotational Flow about Ship Forms,'' IIHR Report No. 123, Iowa Institute of Hydraulic Research, The University of Iowa, 1969.
[27] *Handbook of Mathematical Functions with Formulas, Graphs, and Mathematical Tables*, edited by M. Abramowitz and I. A. Stegun (Dover, New York, 1972), 9th printing, p. 360.
[28] M. A. Jaswon, ''Integral equation methods in potential theory. I,'' Proc. R. Soc. London, Ser. A **275**, 23–32 (1963).
[29] I. G. Petrovsky, *Lectures on Partial Differential Equations* (Interscience, New York, 1954).
[30] N. M. Günter, *Potential Theory and Its Application to Basic Problems of Mathematical Physics* (Ungar, New York, 1967).
[31] K. E. Atkinson, *An Introduction to Numerical Analysis* (Wiley, New York, 1989), Chap. 5.
[32] H. Takahashi and M. Mori, ''Double exponential formulas for numerical integration,'' Research Institute for Mathematical Sciences, Publications, Kyoto University, Kyoto **9**(3) (1974).
[33] C. J. Huang, C. Y. Chen, and S. A. Yang, ''Diffraction of acoustic waves by perfectly soft bodies,'' Proc. Natl. Sci. Counc., Repub. China, Part A: Phys. Sci. Eng. **22**(2), 199–213 (1998).
[34] *Electromagnetic and Acoustic Scattering by Simple Shapes*, edited by J. J. Bowman, T. B. A. Senior, and P. L. E. Uslenghi (Hemisphere, New York, 1987), Chap. 2.
[35] W. Tobocman, ''Extension of the Helmholtz integral equation method to shorter wavelengths,'' J. Acoust. Soc. Am. **80**, 1828–1837 (1986).

A modal-type analysis of the interactions for submerged elastic structures with the surrounding heavy acoustic medium

Pei-Tai Chen[a)]
Department of Naval Architecture, National Taiwan Ocean University, 2 Pei Ning Road, Keelung, Taiwan, Republic of China

(Received 14 January 1998; revised 9 September 1998; accepted 9 September 1998)

The work investigates submerged elastic structures interacting with the surrounding acoustic medium. The equation of motion under mono-frequency oscillations for the coupled structural/acoustic system is formulated where a symmetrical complex matrix represents the acoustic loading. A surface acoustic reciprocal principle verifies the matrix symmetry. Such symmetrical formulation allows the ratio of real part to imaginary part of the complex power exerted by external forces to become the division of two quadratic forms of the structural vibration velocity. Consideration of the stationarity of the ratio leads to a symmetric eigenvalue problem, in which the eigenvalue is related to the radiation efficiency of the coupled system. The corresponding eigenvector defines a mode, which is referred to as the coupled structural/acoustic radiation mode. Based on the set of coupled structural/acoustic radiation modes, the forced vibration of the submerged structure can be decomposed into a set of decoupled complex impedance equations. Each impedance equation describes the relationship between a modal external force and the responded velocity amplitude. Moreover, the radiated acoustic power due to each coupled radiation mode is one-half of the square of the external modal force multiplying an effective modal admittance. The effective admittance depends on the structural properties, acoustic loading characteristics, and the exciting frequency. Furthermore, the effective modal admittance is applied to analyze resonant phenomena of submerged elastic structures. Spherical and spheroidal shells are selected to demonstrate the physical meanings of the modal-type analysis proposed herein, and the various aspects of resonant phenomena of submerged structures.
[S0001-4966(98)04212-X]

PACS numbers: 43.20.Tb, 43.40.Rj [ANN]

INTRODUCTION

Natural modes for linear elastic structures play a crucial role in structural dynamics. The associated eigenvalue problem transforms a structure of infinite degrees of freedom into a set of finite modal modes, characterizing the structural dynamic properties. Although submerged elastic structures in a heavy acoustic medium have been thoroughly investigated, a modal-type formulation that decouples the coupled structural/acoustic system into a set of modal equations is still lacking. Chen[1] recently derived as well as presented a formulation for submerged elastic structures in terms of a set of radiation modes. That study categorized the displacements into two groups: the normal displacement of the wetted surface of the structures, and the remaining displacements other than the normal displacement. The equation of the structures is expressed as the variable of the wetted normal displacement by eliminating the displacements other than the normal direction. The equation is then transformed into a set of generalized coordinates provided by the radiation modes. Thus, the structural response is represented by radiation mode characteristics. This formulation is further used to demonstrate how radiation characteristics depend on structure's member alterations.

Of particular concern in relation to acoustic characteristics is the resonant phenomena of submerged structures in which large amounts of acoustic energy are radiated into far fields at some vibrating frequencies. A study involving a submerged elastical spherical shell in water subjected to a concentrated force[2] indicated that significant acoustic powers radiated into fluids at several discrete frequencies and that the phases between the point force and displacements exhibited 180° changes near the resonant frequencies. A related study[3] noted that a slender spheroidal shell under a uniform alternative surface force displayed no peaks for the frequency dependence of radiated power. However, in that same investigation, a significant peak for a vibrational modal amplitude was observed and a phase change arose between the uniform surface force and the responded vibrational modal amplitude, where the modal amplitude is the natural vibration mode.

In the course of structural dynamics for situations involving light damping vibrations, the dynamic characteristics of structures are described by natural frequencies and natural vibrational modes. The structure vibrates with large amplitudes at natural frequencies. In light of the eigenanalyses in structural dynamics, this study presents a novel modal-type analysis procedure for the structure coupled with the acoustic medium. In the modal formulation, the dynamic characteristics of the structure and radiation characteristics for the wetted surface of the acoustic loading are considered, allowing us to accurately describe the coupled system in terms of

a)Electronic mail: ptchen@mail.na.ntou.edu.tw

complex modal impedance for each mode. Each mode reacts independently. The mode is referred to herein as a coupled structural/acoustic radiation mode. Thus, the forced response of the submerged structure can be decoupled by the set of modes derived from the coupled system. Correspondingly, the modal-type analysis proposed herein attempts to account for the resonant phenomena of submerged structures.

An intimate relationship with the proposed analysis procedure is the subject of radiation mode. Radiation modes have been proposed by investigators such as Borgiotti,[4] Photiadis,[5] and Sarkissian.[6] Those investigations decoupled the surface normal velocity into modal representations where each mode has its own radiation efficiency to radiate acoustic power into far fields. Thus, the surface normal velocity can be quantified by the radiation mode theory for the efficiency radiating acoustic power. Essentially, the radiation modes are divided into strong radiators, which radiate powers into far fields, and weak radiators, subsequently producing evanescent fields near the surface.

Chen and Ginsberg later[7] developed another formulation for radiation mode theory. That investigation derived radiation modes starting from a reciprocity principle for surface acoustic responses, leading to two sets of eigenvalue problems for the surface normal velocity and pressure, respectively. Notably, the eigensolutions of the two sets of eigenvalue problems have identical eigenvalues and the corresponding eigenvectors define velocity radiation modes and pressure radiation modes. Those two sets of radiation modes are mutually orthogonal, enabling one to expand the surface pressure and normal velocity into modal representations. Owing to the mutual orthogonality, this type of modal representation is adopted to represent surface acoustics for the study. In addition, spherical and spheroidal shells are chosen to demonstrate not only the effectiveness of the proposed analysis procedure but also various aspects of dynamic and radiation characteristics for the shells.

I. ACOUSTIC LOADING AND RADIATION MODE

A submerged elastic structure vibrating at a mono-frequency ω leads to the equation of motion,

$$\begin{aligned}&[D_{nn}]\{X_n\}+[D_{ni}]\{X_i\}+[N]^T\{p\}=\{f_n\},\\&[D_{in}]\{X_n\}+[D_{ii}]\{X_i\}=\{f_i\},\end{aligned}\tag{1}$$

where n denotes the degree of freedom outward normal to the wetted surface of the structure, i represents the remaining degrees of freedom of the structure which include displacements tangent to the wetted surface and the degrees of freedom of the internal structural members, $\{X_n\}$ and $\{X_i\}$ are the displacements, respectively, $\{f_n\}$ and $\{f_i\}$ are the corresponding amplitudes of alternative applying forces, and $[D_{pq}]$ $(p,q=i,n)$ is defined by the mass matrices $[M_{pq}]$ and stiffness matrices $[K_{pq}]$

$$[D_{pq}]=[K_{pq}]-\omega^2[M_{pq}],\quad p,q=i,n.\tag{2}$$

In the above equation, the acoustic loading is represented by the discretized pressure variable $\{p\}$ and the shape factor matrix N arises from discretizing the surface acoustics and normal displacement, where T denotes the transposition of the matrix. The mono-frequency oscillation of the time factor is $e^{i\omega t}$, where i denotes $\sqrt{-1}$. The subscript i, such as that used in Eq. (1) and equations herein, denotes meanings based on contexts; it is not the imaginary value $\sqrt{-1}$. The shape factor matrix N is obtained by considering the virtual work due to the surface pressure on the normal velocity,

$$\begin{aligned}\delta W&=-\int_s\left[\left(\sum_i p_i\psi_i\right)\left(\sum_j v_j\phi_j\right)\Big/\, i\omega\right]dS,\\&=\sum_i\sum_j p_iv_j\int_s\psi_i\phi_j\,dS/i\omega=\sum_i\sum_j p_iv_jN_{ij}/i\omega,\end{aligned}\tag{3}$$

where p_i and v_j denote the discretized surface pressure and normal velocity, respectively, Ψ_i and ϕ_j represent the corresponding discretization functions, which can be defined locally or globally over the wetted surface, the ''s'' under the surface integral sign is the integrations over the wetted surface, and dS denotes the differential area on the surface. The surface pressure and normal velocity can be related to Helmholtz integral equations[8] or alternative formulations of the integral equations.[3,8,9] The discretized form of the equations has the following representation:

$$[H]\{p\}=[G]\left\{\frac{\partial p}{\partial n}\right\}=[G](-\rho_0 i\omega\{v_n\}),\tag{4}$$

in which the normal derivative of surface pressure $\{\partial p/\partial n\}$ is related to the normal velocity $\{v_n\}$ by the momentum equation of the acoustic particles, where $[H]$ and $[G]$ are complex square matrices, and ρ_0 is the density of the medium. By using Eq. (4), the pressure loading term in Eq. (1) becomes

$$\begin{aligned}[N]^T\{p\}&=[N]^T[H]^{-1}[G](-\rho_0 i\omega\{v_n\})\\&=(-\rho_0 i\omega[N]^T[H]^{-1}[G])\{v_n\},\\&=[h]\{v_n\},\end{aligned}\tag{5}$$

where the complex square matrix h is defined as

$$[h]=-\rho_0 i\omega[N]^T[H]^{-1}[G].\tag{6}$$

The above acoustic loading matrix is closely related to the surface complex acoustic power P due to Eq. (4) and the following derivation that

$$\begin{aligned}P&=\frac{1}{2}\int_S\left(\sum_i p_i\psi_i\right)\left(\sum_j v_j\phi_j\right)dS=\frac{1}{2}\sum_i\sum_j p_iv_jN_{ij},\\&=\tfrac{1}{2}\{v_n^*\}^T[h]\{v_n\}.\end{aligned}\tag{7}$$

Our earlier investigation[7] demonstrated that the complex matrix $[h]$ is symmetric by applying a reciprocal principle of surface acoustics. Diagonalizing the real and imaginary parts of the matrix $[h]$ simultaneously leads to a set of velocity radiation modes Φ_i where the eigenvalues denote the radiated acoustic powers of those modes. The magnitudes of the radiation modes are normalized to generate one-half the unit reactive powers. If the complex surface acoustic power P in Eq. (7) is expressed in terms of surface pressure $\{p\}$, another set of pressure radiation modes Ψ_i emerges as the complex power is diagonalized. The surface pressure and normal velocity can thus be expanded by the sets of velocity and pres-

sure radiation modes, respectively. Those expansions and mutual orthogonal conditions can be found in Refs. 1 and 7. Moreover, the complex power P has been shown to be

$$P=\frac{1}{2}\sum_i (\lambda_i+i)|\alpha_i|^2, \tag{8}$$

where α_i is the velocity modal expansion coefficient. Let $[h]$ be written as real and imaginary matrices

$$[h]=[h_R]+i[h_I], \tag{9}$$

and the modal matrix Φ formed from the set of velocity radiation modes

$$[\Phi]=[\Phi_1,\Phi_2,\ldots,\Phi_n], \tag{10}$$

where n denotes the order of the matrix $[h]$. Then, the orthogonality condition for the matrix $[\Phi]$ with respect to h_R and h_I is

$$[\Phi]^T(h_R+ih_I)[\Phi]=[\lambda]+iI, \tag{11}$$

where $[\lambda]$ is the diagonal matrix whose diagonal element is λ_j, and I is the unit square matrix.

II. COUPLED STRUCTURAL/ACOUSTIC RADIATION MODE

Equation (1) can now be written as the velocity variables $\{v_n\}$ and $\{v_i\}$,

$$\begin{aligned}&\frac{[D_{nn}]}{i\omega}\{v_n\}+\frac{[D_{ni}]}{i\omega}\{v_i\}+([h_R]+i[h_I])\{v_n\}=\{f_n\},\\ &\frac{[D_{in}]}{i\omega}\{v_n\}+\frac{[D_{ii}]}{i\omega}\{v_i\}=\{f_i\}.\end{aligned} \tag{12}$$

Above equation indicates that the symmetrical matrix $[h_R]$, which is responsible for the radiated acoustic power, causes the responded velocities v_n and v_i to have a phase shift with the external forces f_n and f_i under the mono-frequency forced vibration. The matrix $[h_I]$, which corresponds to the reactive power shown in Eq. (7), is the inertia effects toward the structural equation.

The radiated power due to the external forces f_n and f_i can be computed as

$$\begin{aligned}&\mathrm{Re}\{\tfrac{1}{2}(\{f_n\}^T\{v_n^*\}+\{f_i\}^T\{v_i^*\})\}\\ &=\mathrm{Re}\left\{\frac{1}{2}\left[\frac{[K_{nn}]}{i\omega}\{v_n\}+\frac{[K_{ni}]}{i\omega}\{v_i\}+([h_R]+i[h_I])\{v_n\}\right]^T\{v_n^*\}\right.\\ &\quad\left.+\frac{1}{2}\left[\frac{[K_{in}]}{i\omega}\{v_n\}+\frac{[K_{ii}]}{i\omega}\{v_i\}\right]^T\{v_i^*\}\right\},\\ &=\tfrac{1}{2}\{v_n^*\}^T[h_R]\{v_n\}.\end{aligned} \tag{13}$$

The reactive power due to the external forces is

$$\begin{aligned}&\mathrm{Im}\{\tfrac{1}{2}(\{f_n\}^T\{v_n^*\}+\{f_i\}^T\{v_i^*\})\}\\ &=\frac{1}{2}\{v_n^*\}^T\left(-\frac{[K_{nn}]}{\omega}\{v_n\}-\frac{[K_{ni}]}{\omega}\{v_i\}+[h_I]\{v_n\}\right)\\ &\quad+\frac{1}{2}\{v_i^*\}^T\left(-\frac{[K_{in}]}{\omega}\{v_n\}-\frac{[K_{ii}]}{\omega}\{v_i\}\right).\end{aligned} \tag{14}$$

In the above two equations, ''Re'' and ''Im'' denote the real and imaginary parts of complex variables, respectively. The power radiated into far field or, equivalently, consumed by the damping matrix $[h_R]$, is affected by the phase angle between the external forces f_n and f_i with the responded velocities v_n and v_i. A zero phase angle indicates the most efficient way of the external forces to deliver power into the system (the structure plus the acoustic medium), while a 90° phase angle represents a situation in which no net power is delivered to the system. Therefore, it is natural to consider the ratio η between the real and imaginary parts of the complex power due to the forces f_n and f_i. That is,

$$\eta=\frac{v_n^{*T}h_Rv_n}{v_n^{*T}(-(K_{nn}/\omega)v_n-(K_{ni}/\omega)v_i+h_Iv_n)+v_i^{*T}(-(K_{in}/\omega)v_n-(K_{ii}/\omega)v_i)}. \tag{15}$$

The ratio η becomes a large value when the external forces and responded velocities are more in-phase, while a small value of η indicates that the phase tends toward 90°. This ratio η depends on the velocities of v_n and v_i, implying that stationary values for η can be considered when the velocities v_n and v_i are varied. This variation yields a symmetric eigenvalue problem at stationarity, such that

$$\begin{bmatrix}[h_R] & 0\\ 0 & 0\end{bmatrix}\begin{Bmatrix}v_n\\ v_i\end{Bmatrix}=\eta\begin{bmatrix}-\frac{[K_{nn}]}{\omega}+[h_I] & -\frac{[K_{ni}]}{\omega}\\ -\frac{[K_{in}]}{\omega} & -\frac{[K_{ii}]}{\omega}\end{bmatrix}\begin{Bmatrix}v_n\\ v_i\end{Bmatrix}. \tag{16}$$

The eigenvalue η is the ratio in Eq. (15) when the velocity distribution of v_n and v_i is the eigenvector of Eq. (16). In terms of the solution of such symmetric eigenvalue problems, one of the matrices must be definite to use ordinary symmetric eigenvalue problem solvers. The matrix on the left hand side of Eq. (16) is semi-positive definite because the radiated power shown in the numerator of Eq. (15) cannot be a negative value. Therefore, to solve the eigenvalue problem, Eq. (16) can be recast into the following form. The velocity v_i is expressed in terms of v_n by using the second subequation of Eq. (16), leading to

$$\{v_i\}=-[K_{ii}]^{-1}[K_{in}]\{v_n\}. \tag{17}$$

Substituting the v_i into the first subequation of Eq. (16) yields

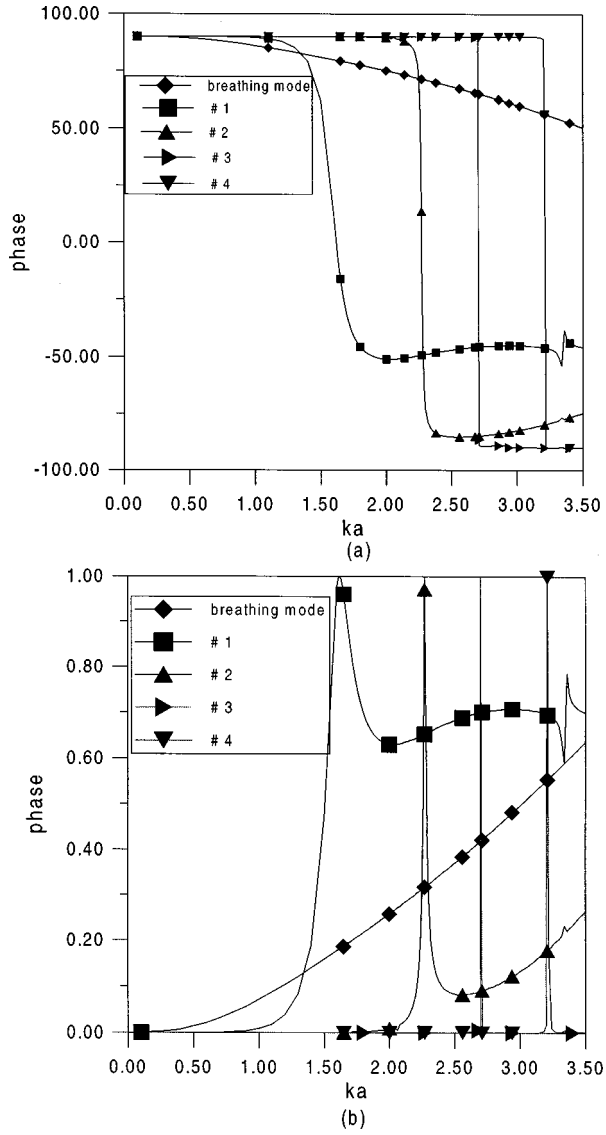

FIG. 1. (a) Modal phase angles θ_i versus nondimensional exciting frequency ka for the spherical shell. (b) Modal power factors $\cos\theta_i$ versus nondimensional exciting frequency ka for the spherical shell.

$$[h_R]\{v_n\}=\eta[H]\{v_n\}, \tag{18}$$

where the matrix H is defined as

$$[H]=-\frac{[K_{nn}]}{\omega}+\frac{[K_{ni}]}{\omega}[K_{ii}]^{-1}[K_{in}]+[h_I]. \tag{19}$$

Equation (18) resembles Eq. (16) of the stationary condition only in terms of the normal velocity v_n as a variable. Our previous study[7] indicated that the eigenvalues are nearly zero or zero for weak radiation modes, implying that the matrix $[h_R]$ in Eq. (18) is still nearly semi-positive definite. To avert this situation, the normal velocity v_n is transformed into the set of radiation modes, which is in a matrix notation as

$$\{v_n\}=[\Phi]\{V\}, \tag{20}$$

where the components of the vector $\{V\}$ are the amplitude coefficients of the radiation modes and $[\Phi]$ is defined in Eq. (10). Substituting Eq. (20) into Eq. (18) and premultiplying $[\Phi]^T$ on the both side of Eq. (18) yield

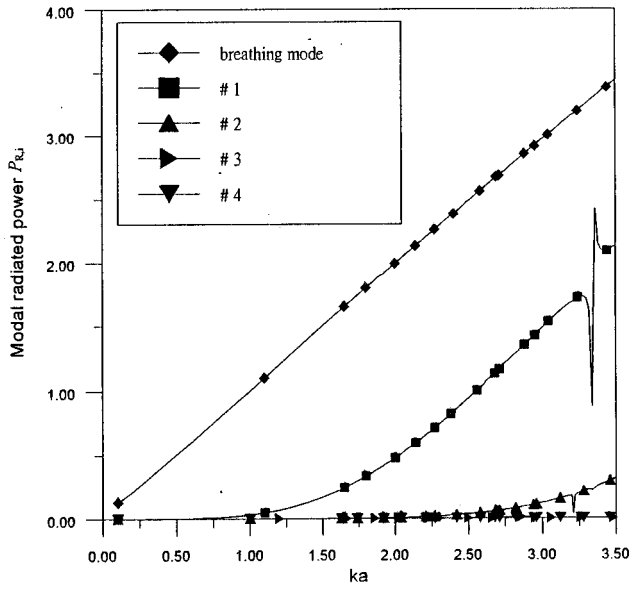

FIG. 2. Modal radiated powers $P_{R,i}$ versus nondimensional exciting frequency ka for the spherical shell.

$$[\lambda]\{V\}=\eta[\Phi]^T[H][\Phi]\{V\}=\eta[\bar{H}]\{V\}, \tag{21}$$

where the diagonal matrix $[\lambda]$ is derived from the identity $[\lambda]=[\Phi]^T[h_R][\Phi]$ in Eq. (11), and $[\bar{H}]$ is as follows:

$$[\bar{H}]=[\Phi]^T[H][\Phi]. \tag{22}$$

The magnitude of the eigenvector $\{V\}$ in Eq. (21) is quantified as the corresponding normal velocity profile having an one-half reactive power. The reactive power of the normal velocity profile associated with the eigenvector $\{V\}$ is identified by Eq. (20) for which the reactive power has the following derivation:

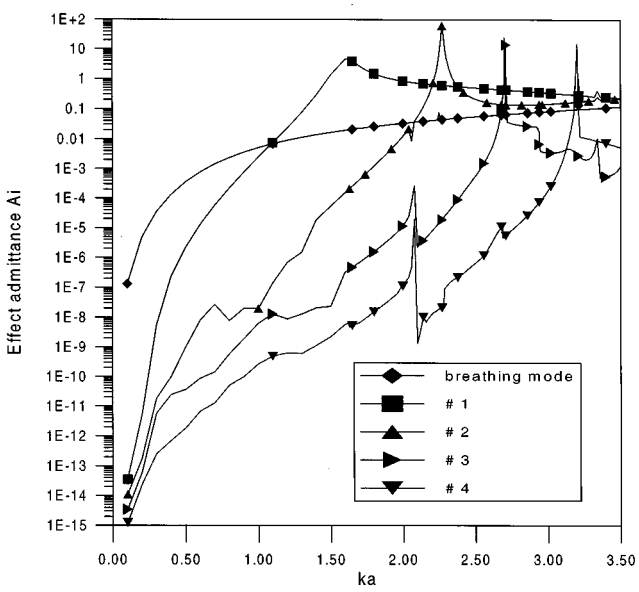

FIG. 3. Effective modal admittance A_i versus nondimensional exciting frequency ka for the spherical shell.

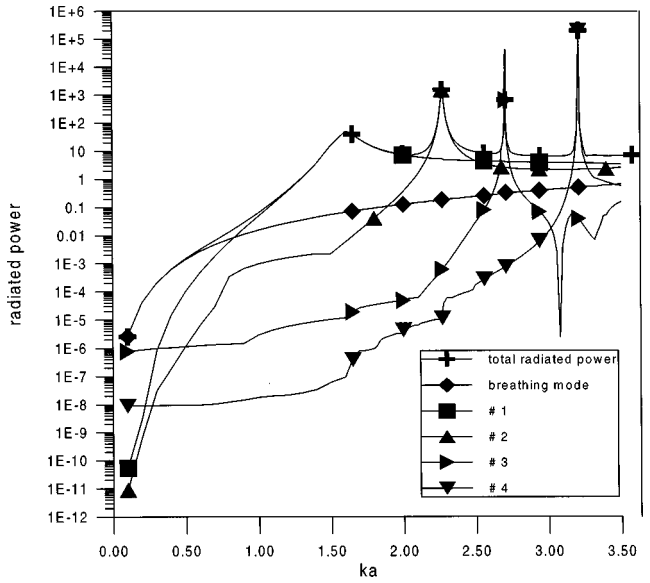

FIG. 4. The total radiated power and radiated powers due to individual coupled structural/acoustic radiation modes versus nondimensional exciting frequency *ka* for the spherical shell where the external force is a pair of concentrated normal forces applied at the apexes.

$$\tfrac{1}{2}([\Phi]\{V\})^T[h_I]([\Phi]\{V\}) = \tfrac{1}{2}\{V\}^T[\Phi]^T[h_I][\Phi]\{V\} = \tfrac{1}{2}\{V\}^T\cdot\{V\} = \tfrac{1}{2}, \tag{23}$$

which leads to the magnitude of the eigenvector in Eq. (21) to be

$$\{V\}^T\cdot\{V\} = 1. \tag{24}$$

As mentioned earlier, the eigenvalues in the diagonal matrix $[\lambda]$ can be divided into two categories: larger than zero and nearly zero. Let the numbers of the eigenvalues associated with the two groups denote n_1 and n_2, respectively, that n_1 plus n_2 equals n, the dimension of the matrix $[h]$. Partitioning the vector $\{V\}$ in Eq. (21) into strong and weak radiators $\{V_1\}$ and $\{V_2\}$ leads to

$$\{V\} = \begin{Bmatrix} V_1 \\ V_2 \end{Bmatrix}, \tag{25}$$

and the corresponding $[\overline{H}]$ and $[\lambda]$ can be partitioned into

$$\overline{H} = \begin{bmatrix} [\overline{H}_{11}], & [\overline{H}_{12}] \\ [\overline{H}_{21}], & [\overline{H}_{22}] \end{bmatrix}, \tag{26}$$

$$\lambda = \begin{bmatrix} [\hat{\lambda}] & 0 \\ 0 & 0 \end{bmatrix}, \tag{27}$$

where, in Eq. (27), the eigenvalues corresponding to weak radiators have been set to zero, and $[\hat{\lambda}]$ denotes the diagonal matrix with diagonal elements of the nonzero eigenvalues obtained from the strong radiation modes. Consequently, Eq. (21) becomes an eigenvalue problem by eliminating the component of weak radiator modes $\{V_2\}$, that is,

$$[\hat{\lambda}]\{V_1\} = \eta[\hat{H}]\{V_1\}, \tag{28}$$

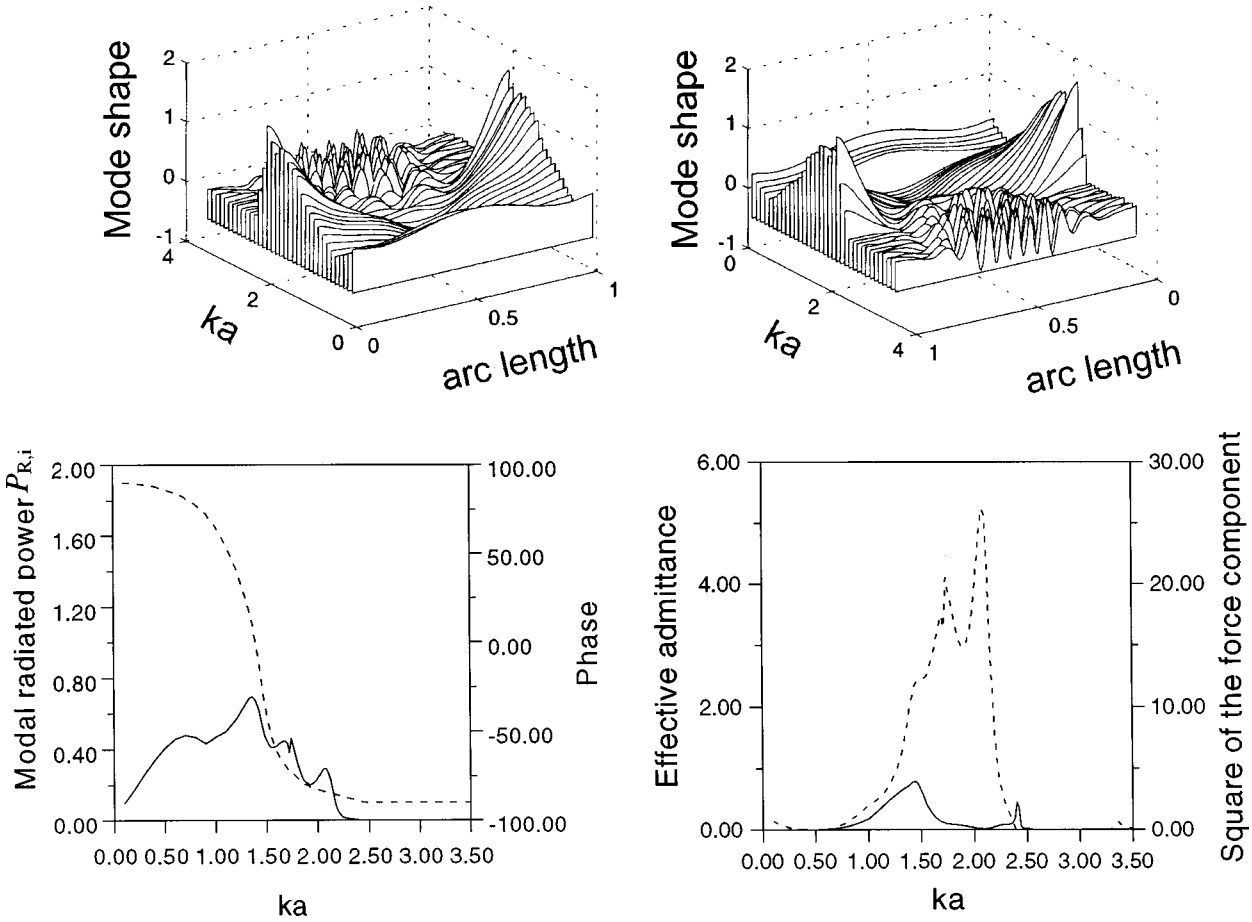

FIG. 5. Frequency dependence of modal properties for the first coupled structural/acoustic radiation mode for the spheroidal shell.

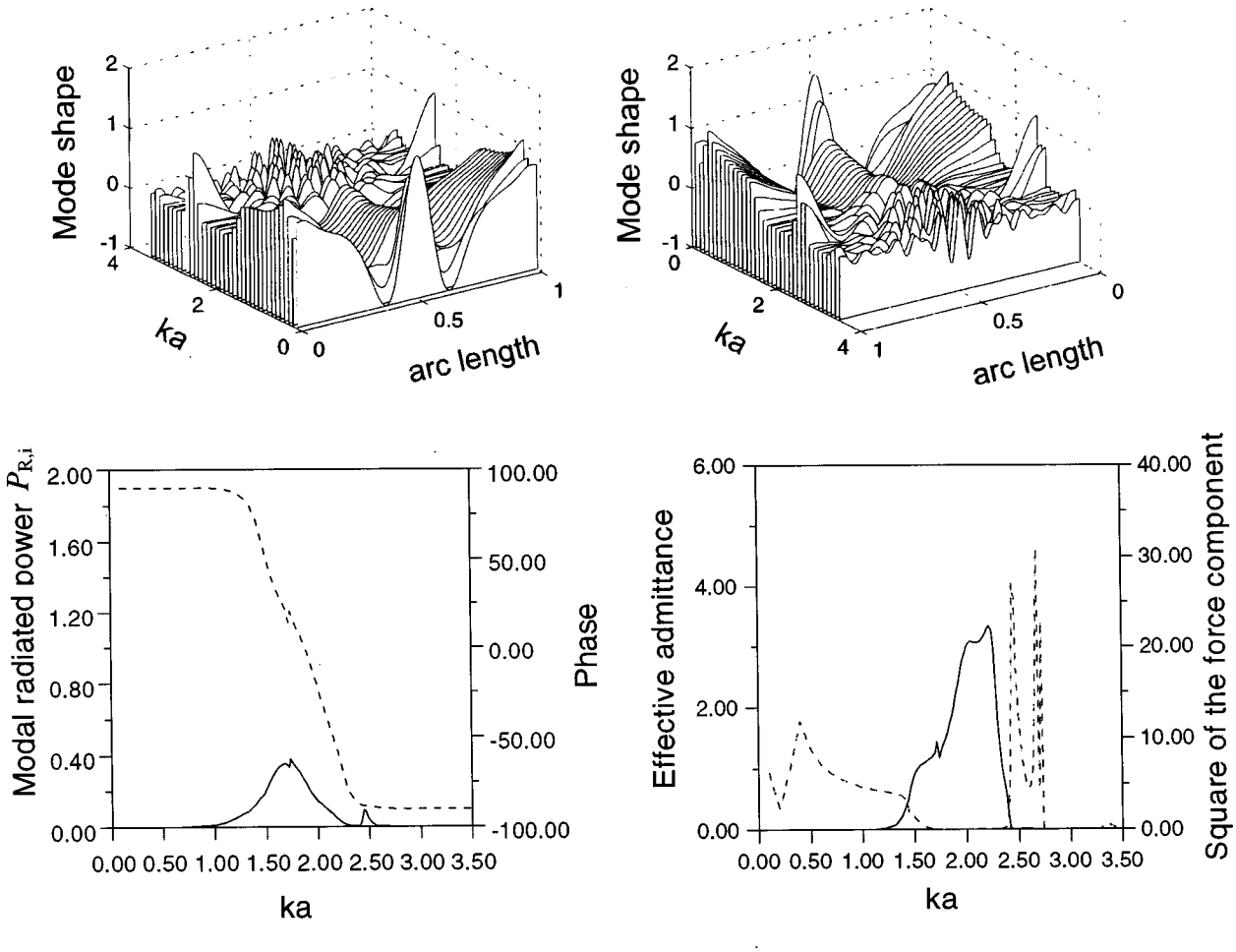

FIG. 6. Frequency dependence of modal properties for the second coupled structural/acoustic radiation mode.

where matrix $[\hat{H}]$ is identified as

$$[\hat{H}]=[\overline{H}_{11}]-[\overline{H}_{12}][\overline{H}_{22}]^{-1}[\overline{H}_{21}], \tag{29}$$

and the vector component $\{V_2\}$ in Eq. (25) is related to $\{V_1\}$ by

$$\{V_2\}=-[\overline{H}_{22}]^{-1}[\overline{H}_{21}]\{V_1\}. \tag{30}$$

Thus, Eq. (28) is a standard symmetric eigenvalue problem with the matrix $[\hat{\lambda}]$ positive definite, which can be solved by a standard eigensolver. The solved eigenvectors $\{V_1\}$ form a set of n_1 mutually orthogonal eigenvectors to the matrices $[\hat{\lambda}]$ and $[\hat{H}]$. The eigensolution of Eq. (21) is constructed by Eq. (30) with the magnitude of the eigenvector $\{V\}$ quantified by Eq. (24). The corresponding eigenvalue in Eq. (21) is identical to the one obtained from Eq. (28). Correspondingly, n_1 pairs of eigenvectors and eigenvalues are obtained from Eqs. (28) and (30) which satisfy the eigensolutions of Eq. (21). Closely examining Eq. (21) with the partitioned matrices shown in Eqs. (26) and (27) allows us to infer that the remaining n_2 eigensolutions have eigenvalues of zero. The corresponding eigenvectors are n_2 mutually orthogonal vectors of dimension n and also orthogonal to the n_1 eigenvectors whose eigenvalues are not zero. These n_2 vectors can be obtained using the Gram–Schmidt orthogonalization process. Such an operation allows n pairs of eigenvectors and eigenvalues to satisfy Eq. (21). As mentioned earlier in Eqs. (20) and (25), the components of $\{V_2\}$ are the amplitudes of weak velocity radiation modes, which radiate no powers to the far field. Closely examining Eq. (21) with its partition matrices in Eqs. (26) and (27) allows us to infer that the eigensolutions, whose eigenvalues are zero, have zero components of $\{V_1\}$. Consequently, the normal velocity profiles corresponding to the n_2 eigensolutions do not radiate acoustic powers into the far field. Moreover, the number of nonzero eigenvalues of Eq. (21) is the same as the number of the strong radiation modes.

The eigensolutions $\{V_i\}$ in Eq. (21) define the normal velocities by Eq. (20). Therefore, the normal velocity $[\Phi]\{V_i\}$ and the ratio η_i in Eq. (18) are termed as a coupled structural/acoustic radiation mode. The mode $[\Phi]\{V_i\}$ radiates acoustic power by each radiation mode Φ_j with modal amplitude coefficient V_{ij} where ''j'' refers to radiation mode Φ_j whose eigenvalue is λ_j. Correspondingly, the radiated power $P_{R,i}$ attributed to the ith coupled structural/acoustic radiation mode $[\Phi]\{V_i\}$ is computed by taking the real part of Eq. (8), which is

$$P_{R,i}=\frac{1}{2}\sum_{j=1}^{n_1}\lambda_j|V_{ij}|^2, \tag{31}$$

where ''R'' denotes the radiated power, and the summation

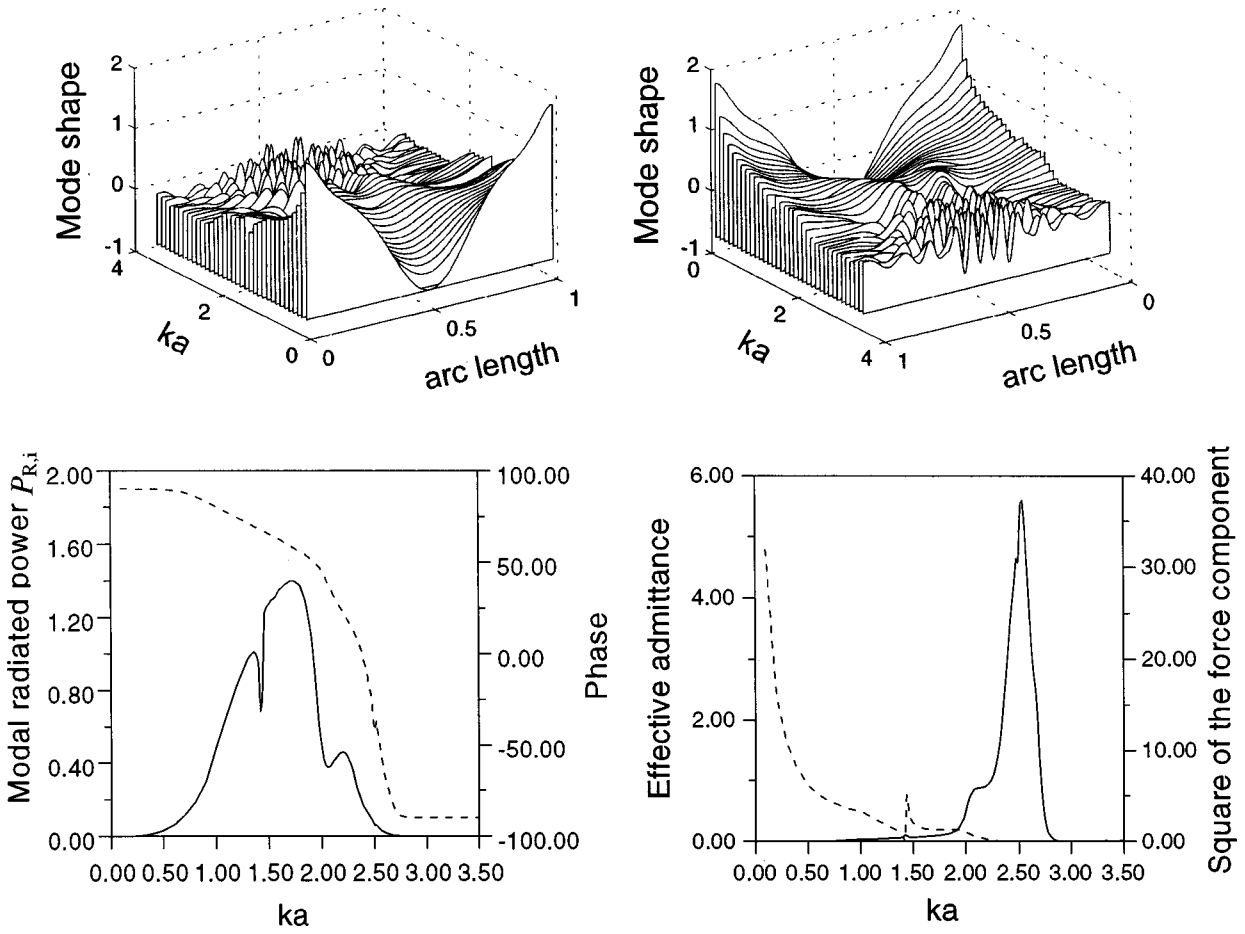

FIG. 7. Frequency dependence of modal properties for the third coupled structural/acoustic radiation mode.

upper limit is n_1 because weak radiator modes have eigenvalues to be nearly zero or zero. Moreover, for those coupled radiation modes in which the eigenvalues η_j are zero, the components of V_{ij} associated with strong radiators are zero, as stated earlier. Those coupled radiation modes, although vibrating with nonvanishing normal velocities, do not radiate acoustic powers into the far field. The orthogonality conditions associated with Eq. (21) for the coupled structural/acoustic radiation modes are

$$\{V_i\}^T\overline{H}\{V_j\}=\frac{1}{\eta_i}P_{R,i}\delta_{ij},$$
$$\{V_i\}^T[\lambda]\{V_j\}=P_{R,i}\delta_{ij}, \tag{32}$$

or equivalently,

$$([\Phi]\{V_i\})^T[H]([\Phi]\{V_i\})=\frac{1}{\eta_i}P_{R,i}\delta_{ij},$$
$$([\Phi]\{V_i\})^T[h_R]([\Phi]\{V_j\})=P_{R,i}\delta_{ij}. \tag{33}$$

According to Eqs. (33), the first equation denotes the reactive power due to the structural equation and acoustic inertia loading, and the second equation is the active or radiated power attributed to the acoustic radiation.

III. REPRESENTATION OF FORCED VIBRATIONS USING THE COUPLED STRUCTURAL/ ACOUSTIC RADIATION MODES

The forced vibration of the coupled structural/acoustic system described in Eq. (12) can be investigated by the coupled structural/acoustic radiation modes. Since the coupled radiation modes are defined on normal velocity of the wetted surface, the forced vibration of Eq. (12) is represented in terms of the velocity variable $\{v_n\}$. Using the second equation of Eq. (12) to eliminate the velocity variable $\{v_i\}$ from the first equation leads to

$$[h_R]\{v_n\}+i[H]\{v_n\}=\{\hat{f}_n\}, \tag{34}$$

where matrix $[H]$ is identified as the same expression as in Eq. (19) and the external force $\{\hat{f}_n\}$ is defined by

$$\{\hat{f}_n\}=\{f_n\}-[D_{ni}][D_{ii}]^{-1}\{f_i\}. \tag{35}$$

The velocity variable $\{v_i\}$ is related to the variable $\{v_n\}$ by

$$\{v_i\}=\left(\frac{[D_{ii}]}{i\omega}\right)^{-1}\left(\{f_i\}-\frac{[D_{in}]}{i\omega}\{v_n\}\right). \tag{36}$$

The normal velocity $\{v_n\}$ on the wetted surface of the structure can be expanded by linearly combining the coupled structural/acoustic radiation modes $[\Phi]\{V_i\}$ developed in the previous section. That is,

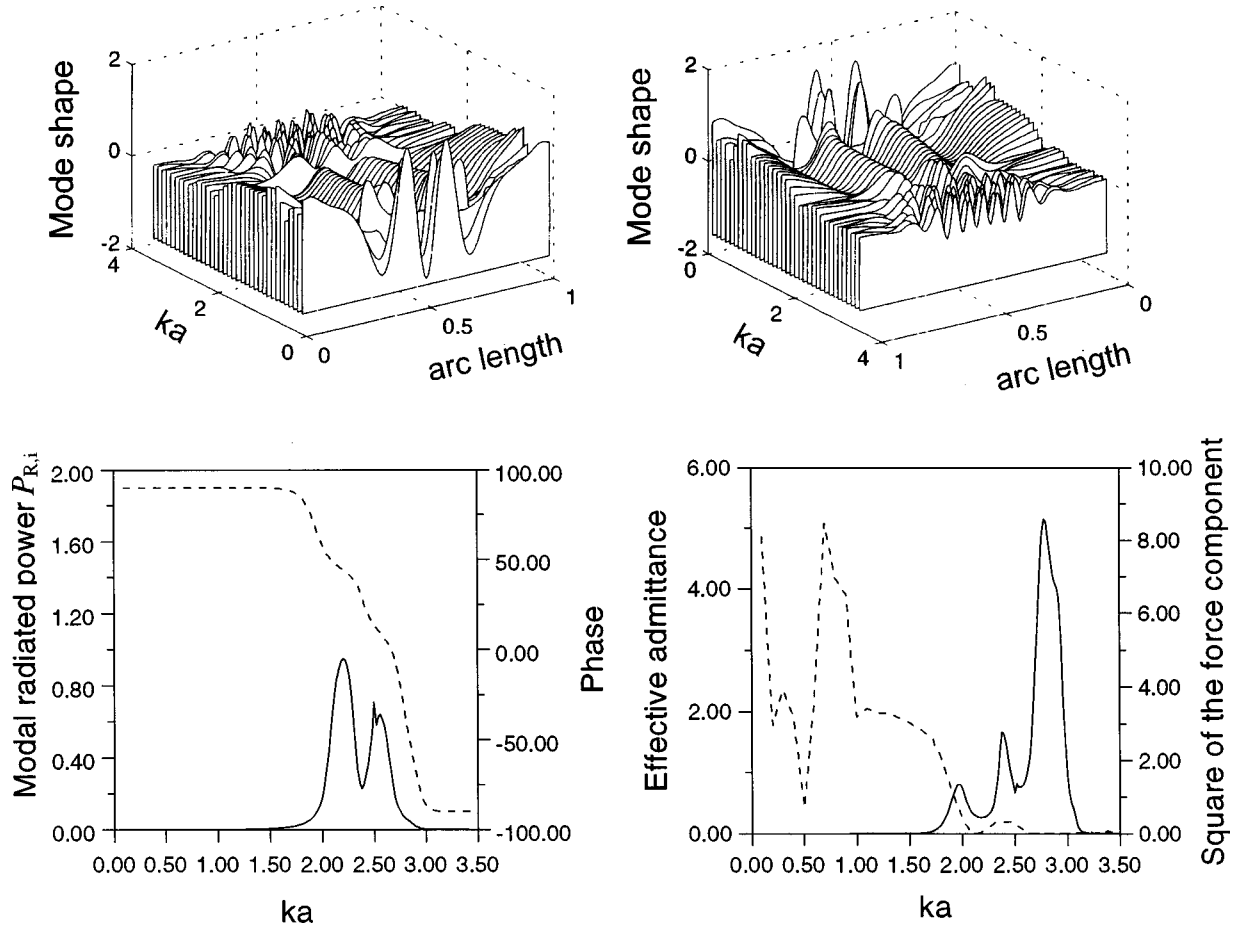

FIG. 8. Frequency dependence of modal properties for the fourth coupled structural/acoustic radiation mode.

$$\{v_n\}=\sum_i a_i[\Phi]\{V_i\}, \tag{37}$$

where a_i is the amplitude coefficient. Substituting Eq. (37) into Eq. (34) and premultiplying $([\Phi]\{V_i\})^T$ on the both sides yields the set of decoupled equations for amplitudes a_i,

$$[([\Phi]\{V_i\})^T[h_R][\Phi]\{V_i\}+i([\Phi]\{V_i\})^T[H][\Phi]\{V_i\}]a_i$$
$$=([\Phi]\{V_i\})^T\{\hat{f}_n\}, \quad i=1,2,\ldots . \tag{38}$$

Above equations have applied the orthogonality conditions provided in Eq. (33) and can be further written as

$$\left(P_{R,i}+i\,\frac{P_{R,i}}{\eta_i}\right)a_i=([\Phi]\{V_i\})^T\{\hat{f}_n\}. \tag{39}$$

Equation (39) provides the relationship of the coupled radiation modal amplitude a_i with the component of the external force $\{\hat{f}_n\}$ projected on the direction of the coupled radiation mode $[\Phi]\{V_i\}$. The ratio η_i, i.e., the eigenvalue of Eqs. (18) or (21), is an indicator of the efficiency of the coupled radiation mode $[\Phi]\{V_i\}$ to radiate acoustic power. A large value of η_i makes the external force $([\Phi]\{V_i\})^T\{\hat{f}_n\}$ more in-phase with the responded amplitude a_i, implying an efficient acoustic power radiation. A small value of η_i implies a poor acoustic radiation. The magnitude of η_i and $P_{R,i}$ determine the responded amplitude a_i. The coefficient a_i is obtained from Eq. (39):

$$a_i=\frac{([\Phi]\{V_i\})^T\{\hat{f}_n\}}{P_{R,i}+i(P_{R,i}/\eta_i)}. \tag{40}$$

The total radiated power is computed by taking the real part of Eq. (7) with the fact that $[h]$ is symmetrical. Thus, the total radiated power P_R is a quadratic form of the normal velocity $\{v_n\}$ with respect to the matrix $[h_R]$, i.e.,

$$P_R=\tfrac{1}{2}\{v_n^*\}^T[h_R]\{v_n\}. \tag{41}$$

Substituting Eq. (37) into the above equation and applying the second equation of the orthogonal conditions in Eq. (33) with the definition of $P_{R,i}$ in Eq. (31) transforms the above equation into

$$P_R=\frac{1}{2}\left(\sum_i a_i[\Phi]\{V_i\}\right)^{*T}[h_R]\left(\sum_j a_j[\Phi]\{V_j\}\right),$$
$$=\frac{1}{2}\sum_i\sum_j a_i^*a_j\{V_i\}^T[\Phi]^T[h_R][\Phi]\{V_j\},$$
$$=\frac{1}{2}\sum_i\sum_j a_i^*a_j\{V_i\}^T[\lambda]\{V_j\},$$
$$=\frac{1}{2}\sum_{i=1}^{n_1}|a_i|^2P_{R,i}, \tag{42}$$

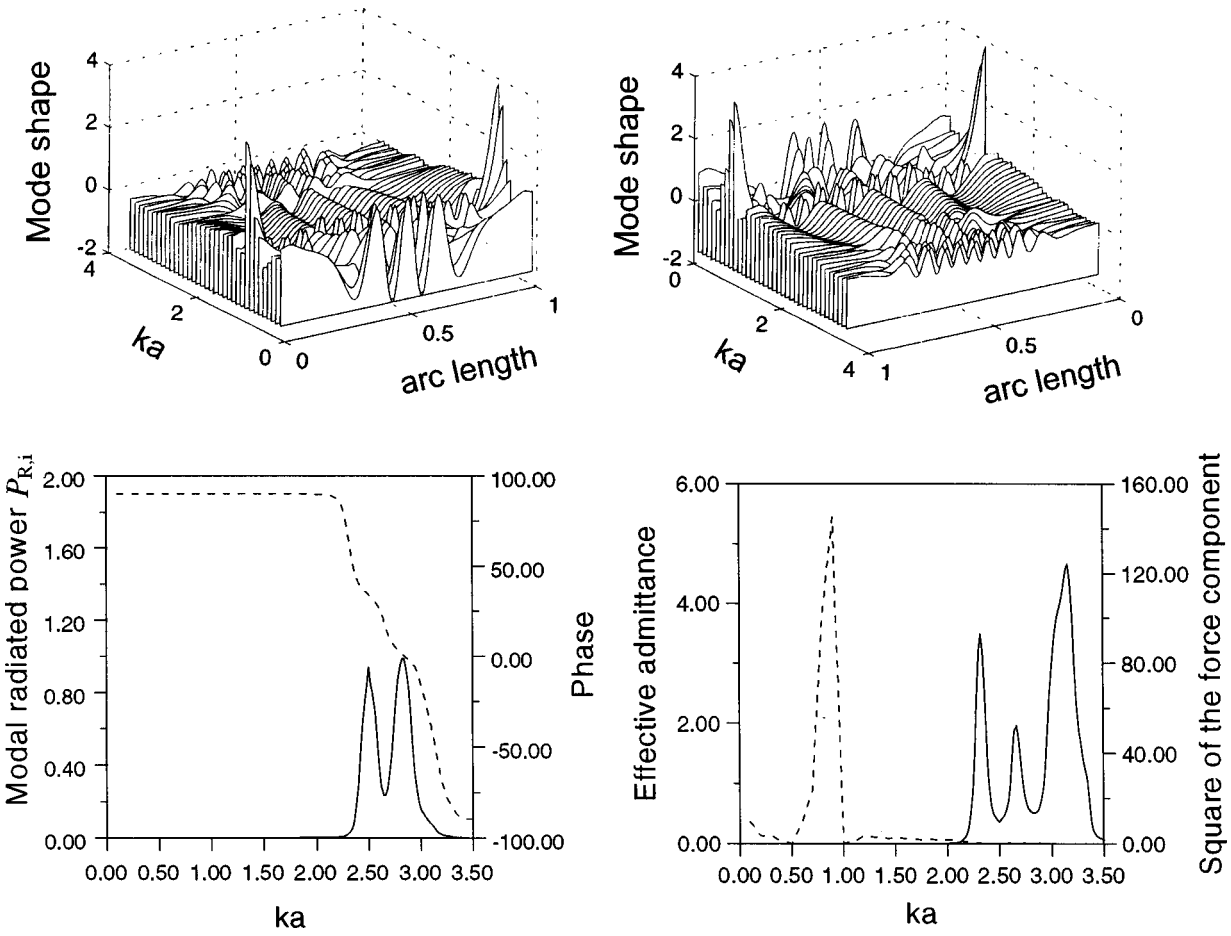

FIG. 9. Frequency dependence of modal properties for the fifth coupled structural/acoustic radiation mode.

where the last equation has its summation limit to n_1 because the coupled radiation modes having zero eigenvalues η_i radiate no net power to the far field. Equation (42) states that the radiated power from the vibrating structure is attributed to the contribution of every coupled structural/acoustic radiation modes, whose eigenvalues η_i are not zero. Importantly, Eqs. (39) and (42) state that the coupled structural/acoustic system can be decoupled into modal components so as to describe the dynamic responses; the total radiated power is algebraically summed up by each coupled radiation mode. Restated, the set of coupled radiation modes decouples the coupled structural/acoustical system. The radiated power attributed to the individual coupled mode can be derived by using Eq. (40), which is

$$\frac{1}{2}|a_i|^2 P_{R,i} = \frac{1}{2}\frac{\eta_i^2 |([\Phi]\{V_i\})^T\{\hat{f}_n\}|^2}{P_{R,i}(\eta_i^2+1)}, \tag{43}$$

in which the equation relates to the eigenvalue η_i, the external force component $([\Phi]\{V_i\})^T\{\hat{f}_n\}$, and the modal power $P_{R,i}$ radiated by $[\Phi]\{V_i\}$. Equation (43) is a representation of the radiated power in terms of the complex modal impedance $P_{R,i}+i(P_{R,i}/\eta_i)$ that the term $\eta_i^2/(\eta_i^2+1)$ is associated with the phase difference between the responded amplitude a_i and the external force $\hat{f}_n$, which will be interpreted in the next section.

IV. EFFECTIVE ADMITTANCE OF THE COUPLED RADIATION MODE

The term $\eta_i^2/(\eta_i^2+1)$ in Eq. (43) is examined by considering the complex power arisen from an applying force f to a system represented by a complex impedance for which the system oscillates at a mono-frequency. The responded velocity v has a phase difference θ with force f that the complex power is

$$\tfrac{1}{2} f \cdot v^* = \tfrac{1}{2}|f||v|(\cos\,\theta + i\,\sin\,\theta). \tag{44}$$

The ratio η of the real part to imaginary part of the complex power is cot θ, indicating

$$\eta = \cot\,\theta. \tag{45}$$

Therefore, the expression of $\eta^2/(\eta^2+1)$ is the square of the power factor cos θ due to the phase difference θ between the applying force f and responded velocity v. Consequently, in terms of each coupled radiation mode, Eq. (43) can be written as

$$\frac{1}{2}|a_i|^2 P_{R,i} = \frac{1}{2}\frac{|\cos\,\theta_i([\Phi]\{V_i\})^T\{\hat{f}_n\}|^2}{P_{R,i}}, \tag{46}$$

where the modal power factor cos θ_i is related to the eigenvalue η_i of Eq. (18) or (21) as

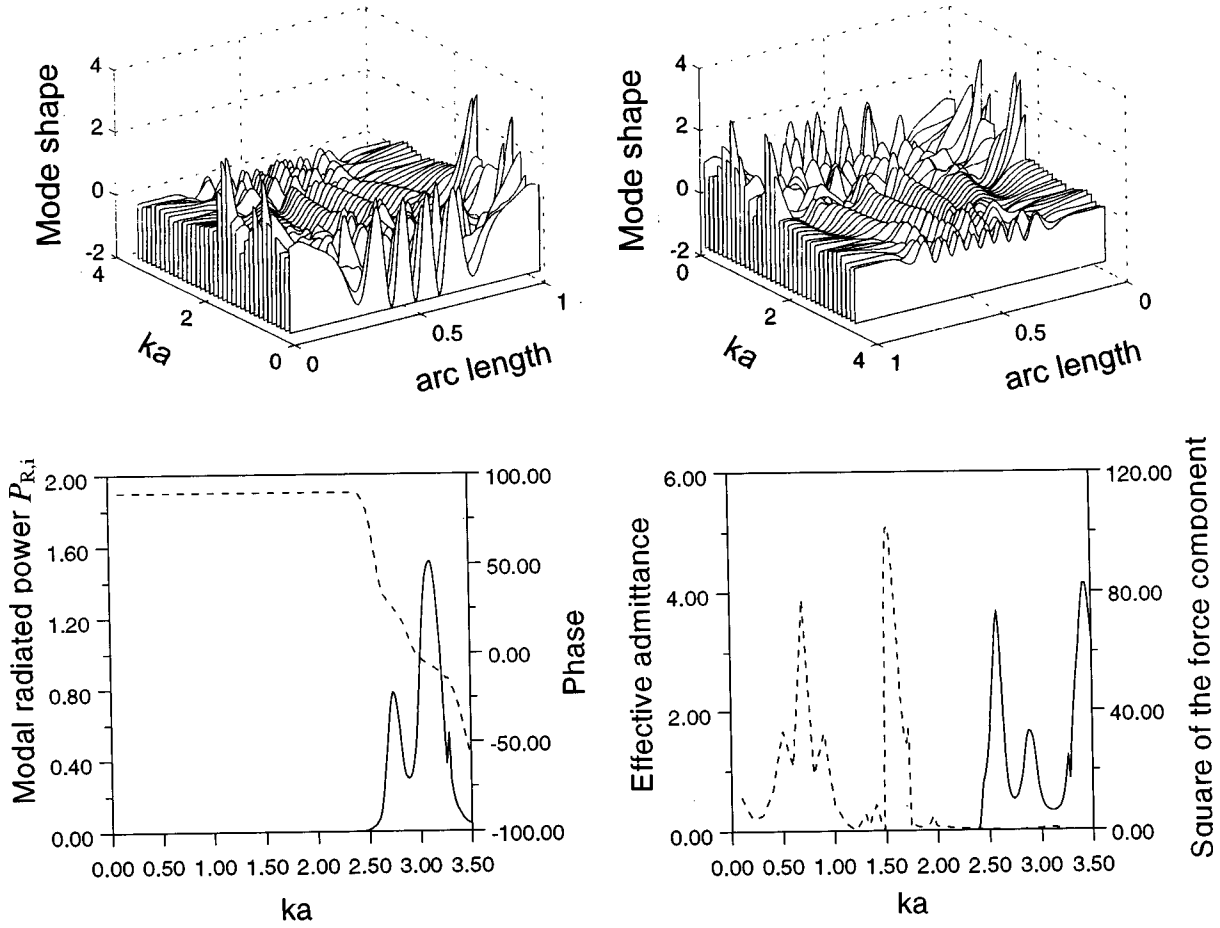

FIG. 10. Frequency dependence of modal properties for the sixth coupled structural/acoustic radiation mode.

$$\theta_i = \tan^{-1}\left(\frac{1}{\eta_i}\right). \tag{47}$$

The interpretation of Eq. (43) becomes evident when one examines Eq. (39) for the amplitude a_i that the quantity $P_{R,i}+i(P_{R,i}/\eta_i)$ is the complex impedance and that the quantity $([\Phi]\{V_i\})^T\hat{f}_n$ is the applied force. The real part $P_{R,i}$ is responsible for power radiating to the far field. Meanwhile, the imaginary part $i(P_{R,i}/\eta_i)$ is attributed to the structural inertia and stiffness effects plus the added mass effects by the acoustic loading. The radiated power for Eq. (39) is obtained by taking the real part of Eq. (44), which is

$$\begin{aligned}
&\mathrm{Rel}[\tfrac{1}{2}([\Phi]\{V_i\})^T\hat{f}_n a_i^*] \\
&= \mathrm{Rel}\left[\frac{1}{2}([\Phi]\{V_i\})^T\hat{f}_n \frac{([\Phi]\{V_i\})^T\{\hat{f}_n\}}{P_{R,i} - i\,\dfrac{P_{R,i}}{\eta_i}}\right], \\
&= \frac{1}{2}\frac{|([\Phi]\{V_i\})^T\hat{f}_n|^2}{P_{R,i}}\frac{\eta_i^2}{\eta_i^2+1} \\
&= \frac{1}{2}\frac{|([\Phi]\{V_i\})^T\hat{f}_n|^2\cos^2\theta_i}{P_{R,i}},
\end{aligned} \tag{48}$$

where the derivation has used Eq. (40) and the phase θ_i is related to the ratio η_i of Eq. (47). Thus, Eq. (39) exactly represents the impedance equation for the coupled structural/acoustic radiation mode $[\Phi]\{V_i\}$ with the radiated power given by Eq. (46) or (48). The quantity $\cos^2\theta_i/P_{R,i}$, which is independent of the external force $\hat{f}_n$, is referred to as an effective modal admittance A_i of the coupled radiation mode $[\Phi]\{V_i\}$,

$$A_i = \frac{\cos^2\theta_i}{P_{R,i}}, \tag{49}$$

which is the quantity of an admittance as if the external forces are in phase with the responded velocity. Thus, the radiated power is one-half of the square of the applied force multiplying the effective modal admittance A_i. In addition, the effective modal admittance is independent of the external applied force. However, it depends on the structural characteristics and surface acoustics described by the radiation modes. Therefore, the quantity defined by Eq. (49) is a coupled structural/acoustic radiation modal feature for describing the effectiveness of radiating acoustic power for the coupled structural/acoustic radiation modes.

V. NUMERICAL EXAMPLE OF A SUBMERGED SPHERICAL SHELL

The first numerical example is a case involving a submerged spherical shell whose analytical solution is available

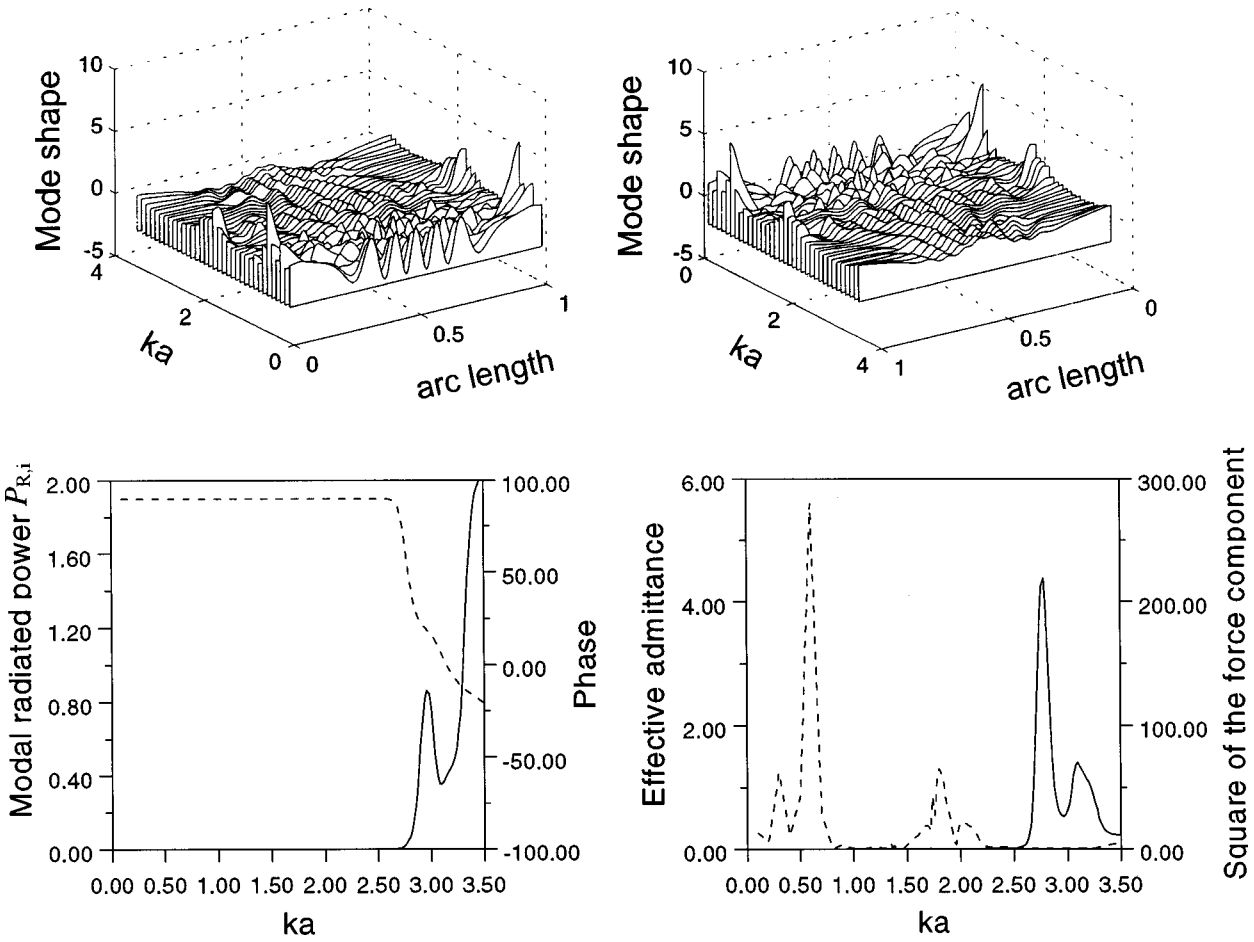

FIG. 11. Frequency dependence of modal properties for the seventh coupled structural/acoustic radiation mode.

from Ref. 2. The characteristic functions for both the acoustic wave equation under mono-frequency vibrations and the shell equations in the normal direction of the wetted surface are Legendre functions. Correspondingly, the coupled radiation modes solved from Eq. (18) are also Legendre functions. The numerical implementation in this study applies Hamilton's principles in conjunction with the displacements expanded by a Rayleigh–Ritz assumed mode expansions. In addition, the surface acoustic loading is implemented by a surface variational principle, which is a variational formulation applied to the normal derivative of a Helmholtz integral equation. Detailed derivations for the shell equation and the surface variational principle can be found in literature.[3] The coupled structural/acoustic radiation mode and the associated eigenvalue η_i are obtained by Eq. (18) or (28).

The material constants adopted herein are the same as those in our previous study:[3] the ratio of shell's thickness h to the radius of the shell a is 0.03, the ratio of dilatational wave speed $C_d(=(E/\rho_s)^{1/2})$ of the shell's material to the acoustic sound speed C_0 is 3.368, the density ratio of the shell's material ρ_s to the acoustic medium density ρ_0 is 7.69, and the possion ratio ν for the shell is 0.3. Two concentrated alternative point forces with magnitudes $\rho_0 c_0^2 \pi a^2$ are normally applied to the apexes with the same oscillating phase. The powers displayed in the following figures are nondimensionalized by $\rho_0 c_0^3 \pi a^2$. These two point forces cause the response of the shell and acoustics to be symmetrical about the equator of the shell of which only the modes symmetrical about the equator are excited. The two concentrated forces are selected simply to excite only the symmetrical modes and, in doing so, to achieve a better visualization, as presented in the following figures. Figure 1(a) depicts the modal phase angles of coupled radiation modes, which relate to the eigenvalues η_i by Eq. (47), versus the nondimensional vibrational exciting frequency ka, where $K=\omega/c$.

The modal numbers for the coupled radiation modes are ordered on the basis of the vibrating frequencies crossing over the zero phase angle. The first mode is the lowest frequency of zero phase crossing, the second mode is the second lowest frequency of zero phase crossing, and etc. Figure 1(b) illustrates the corresponding modal power factors cos θ_j versus vibrating frequency which display sharp peaks when the phase angles are zero. The breathing mode is associated with the zeroth order Legendre function, a constant along the meridian. The first four coupled radiation modes correspond to the second, fourth, sixth, and eighth orders of Legendre functions because of the modes symmetric about the equator. Figure 2 depicts the modal radiated powers $P_{R,i}$ due to the coupled radiation modes where the breathing mode displays the largest radiated power among other modes. According to this figure, the radiated modal powers increase with the exciting frequencies and decrease with the ascendent modal numbers. Figure 3 illustrates the effective modal admittance A_i defined in Eq. (49) for each coupled radiation mode, in-

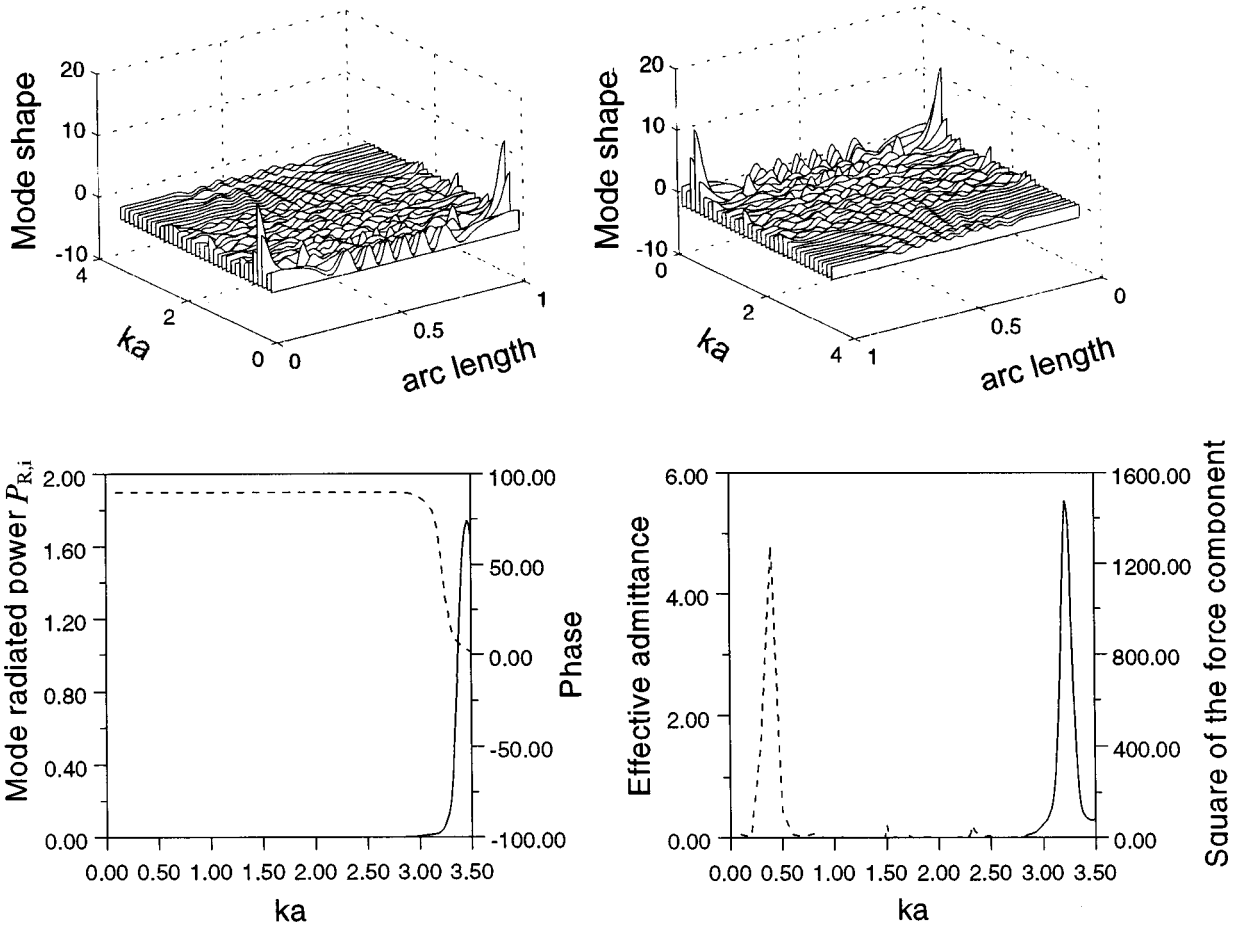

FIG. 12. Frequency dependence of modal properties for the eighth coupled structural/acoustic radiation mode.

dicating that each mode displays a significant peak value at a specific resonance frequency. Figure 4 summarizes the total radiated power as well as the powers radiated by the individual coupled radiation modes. There are sharp peaks at third and fourth modes at frequency $ka=2.08$ corresponding to a degenerated frequency due to the surface variational formulation which fails at interior Neumann cavity frequencies. As discussed earlier in Eq. (48), the powers radiated due to the coupled radiation modes are the modal effective admittances multiplying the square of the force components on the corresponding modes. Plots of the effective modal admittances in Fig. 3 obviously reveal that the forced vibration of the shell displays very significant peak values at the resonance frequencies.

As mentioned earlier, the characteristic functions for the acoustic loading and the spherical shell are Legendre functions. Therefore, the coupled structural/acoustic radiation modes are also the Legendre functions. Thus, the coupled radiation modes are independent of vibration frequencies. For an arbitrarily elastic shell, coupled structural/acoustic radiation modes depend on vibration frequencies, which are shown in the following by submerged spheroidal shells. The material constants and thickness ratio of the shell are identical to the spherical shell where the thickness ratio is referred to the minor axis a.

VI. NUMERICAL EXAMPLE OF SUBMERGED SPHEROIDAL SHELLS

A slender spheroidal shell is selected to present a geometrical configuration other than the spherical shell. The aspect ratio for the major axis to minor axis is four. The external forces are two concentrated forces $\rho_0 c_0^2 \pi a^2$ applied normally at two apexes. According to Eqs. (43), (47), and (48), the contribution to the total radiated power due to each coupled radiation mode is one-half of the product of the effective modal admittance with the square of the force component in that coupled radiation mode. Those two quantities depend on the mode shapes of coupled radiation modes. Figures 5–12 present the modal properties of the coupled radiation modes for the spheroidal shell. In each figure, the upper two plots show the progressive changes of mode shapes versus the nondimensional frequency ka. Because the responses are axisymmetric, the mode shapes are displayed by the normal velocity profiles along the meridian. A nondimensional arclength is defined as the arclength of a position to one apex dividing the total arclength between two apexes. The two plots presented herein are from two opposite perspective views to achieve a better visualization. The left bottom plot shows the modal radiated power $P_{R,i}$ with a coordinate in reference to the left axis depicted by a solid line and the phase θ_i vs ka which is in reference to the right axis presented by a dotted line. The right bottom displays the effec-

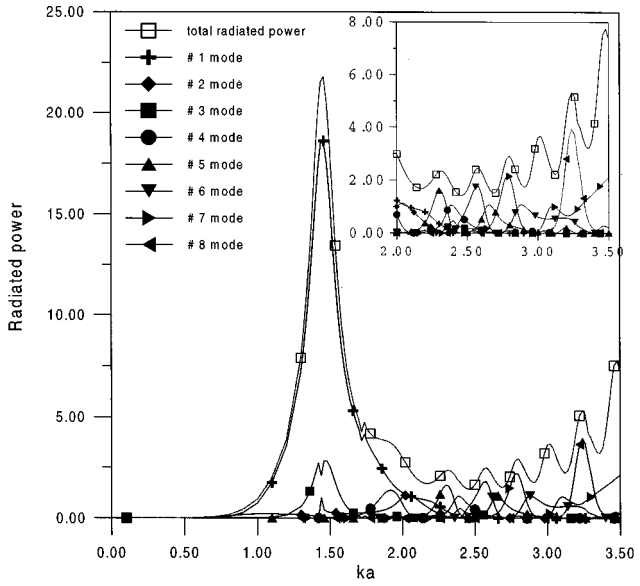

FIG. 13. The total radiated power and radiated powers due to individual coupled structural/acoustic radiation modes versus nondimensional exciting frequency *ka* for the spheroidal shell where the external force is a pair of concentrated normal forces applied at the apexes.

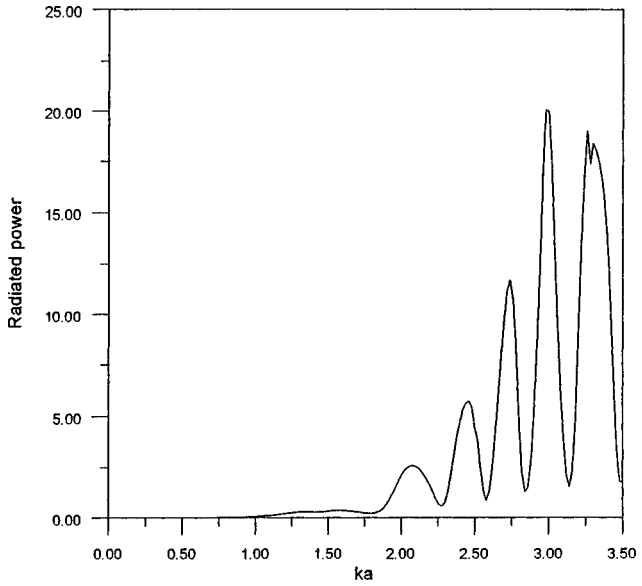

FIG. 14. The total radiated power versus nondimensional exciting frequency *ka* for the spheroidal shell where the external force is a pair of ring normal forces applied at the positions of meridians $s/s_0=0.3$ and 0.7, where s is the arclength measured from one apex and s_0 is the total arclength.

tive modal admittance with a solid line and the squared force component projected on the coupled radiation mode, $([\Phi]\times\{V_i\})^T\{\hat{f}_n\}$, as denoted by a dotted line.

Several observations regarding these modal characteristics are worth mentioning. The plots in the left bottoms for the $P_{R,i}$ and θ_i vs *ka* indicate that the modal radiated powers generally provide the largest values at the phases θ_i crossing over zero degrees. The effective admittances at the right bottoms generally have the largest values around the frequencies where the maximum $P_{R,i}$ values occur. According to Eq. (48), the effective admittances are inversely proportional to the $P_{R,i}$ and proportional to the square of the power factors. The features of the effective admittances versus *ka* shown in Figs. 5–12 reflect a situation in which the decaying of the square of power factors away from the zero-degree phase is markedly faster than the decaying of the $P_{R,i}$ away from the *ka* values, where the maximum values of $P_{R,i}$ occur. Thus, the maximum effective admittances occur in proximity of the regions that $P_{R,i}$ exhibits maximum values. In addition, the bandwidths for the modes radiating acoustic powers to far field are over finite vibrating frequency intervals. Except for the intervals, the normal velocity profiles vibrate, but do not radiate powers owing to the diminishing effect of the effective admittances. This point becomes more obvious if one examines the mode shapes on the upper two plots from Figs. 5–12. The mode shapes correspond to the frequency regions that the effective admittances are not zero, displaying the profiles of the mode shapes to be slowly varying. The mode shapes in frequency regions that have zero admittances present more variations, indicating that no power radiates to the far field.

According to Eq. (39), the force component projected on a coupled radiation mode excites the coupled radiation mode. The dotted lines on the right bottom plots from Fig. 5 to Fig. 12 denote the force components on the coupled radiation modes for the present case where the applied external force is a pair of two concentrated forces exerted normally at the apexes. Those plots reveal that only the first coupled radiation mode (Fig. 5), whose force component overlaps with its effective modal admittance, provides a substantial acoustic power radiating into the far field at frequencies around $ka=1.5$. The other modes, in which the force components do not overlap that much with their effective admittances, emit few powers from the structure, mainly producing evanescent fields near the surface.

The total radiated power is the algebraic sum contributed from each coupled radiation mode, as indicated in Eq. (42). Figure 13 presents the powers due to every coupled mode, as well as the total radiated power for the spheroidal shell. This situation is also confirmed by the mode shapes of the coupled radiation modes depicted in the upper two plots from Figs. 5–12. According to these figures, the force components on the coupled radiation modes do not have many components beyond the first mode because the normal velocities at the apexes have small values. If one applies two ring normal forces at the positions on nondimensional arclength at 0.3 and 0.7, respectively, there are some force components on the coupled radiation modes beyond the first mode. Consequently, the second to the fifth coupled radiation modes are excited, which provide significantly radiated powers for exciting frequencies *ka* ranging between 2 and 3.5. Figure 14 depicts the radiated power for the two ring forces which presents several peak values for *ka* beyond two. The numerical examples for the spherical and spheroidal shells demonstrate the significant difference of the radiation characteristics for these two shells.

To demonstrate the progressive changes of a spherical shell to a slender spheroidal shell, Figs. 15, 16, and 17 illustrate the admittances and force components on the coupled radiation modes for aspect ratios 1.5, 2.5, and 3.5, respectively, where the external forces are two normal concentrated forces applied at the apexes. For each curve in these figures,

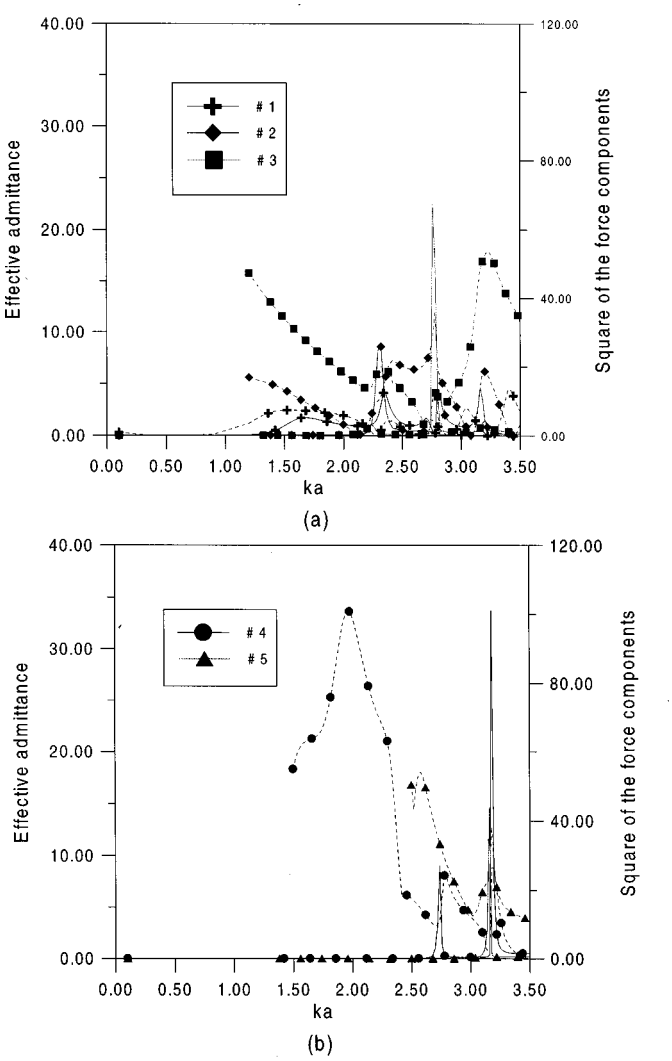

FIG. 15. Frequency dependence of effective modal admittances and force components projected on the coupled radiation modes for a spheroidal shell of aspect ratio 1.5 where the external force is a pair of concentrated normal forces applied at apexes; Solid lines referred to modal admittances and dotted lines referred to force components.

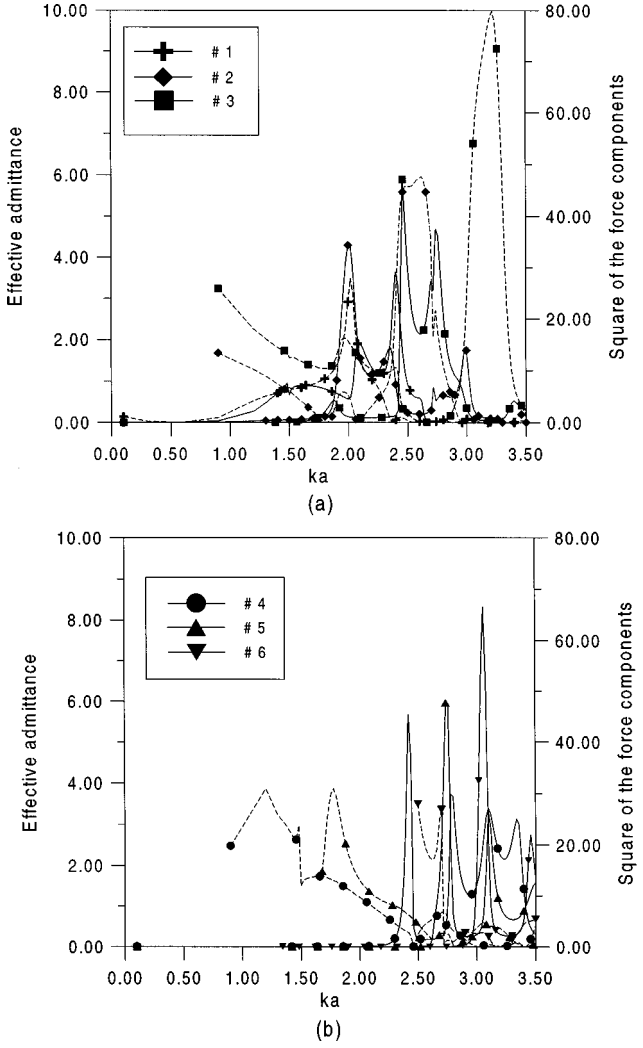

FIG. 16. Frequency dependence of effective modal admittances and force components projected on the coupled radiation modes for a spheroidal shell of aspect ratio 2.5 where the external force is a pair of concentrated normal forces applied at apexes; Solid lines referred to modal admittances and dotted lines referred to force components.

the solid line represents an admittance and the corresponding dotted line with the same symbol denotes the square of the force component. These figures display that the peak admittance values of the shell for aspect ratio 1.5 are very sharp and narrow, and the peak values tend to decrease when the aspect ratios increase. Notably, the scales for the effective admittances are different for the figures. As mentioned earlier, the radiated power attributed to a coupled radiation mode depends on the overlapping of the admittance and force component over the exciting frequencies. These figures also indicate that the force components and admittances beyond the first coupled radiation mode become nonoverlapped with an increase of the aspect ratios. Owing to such progressive changes, the radiated powers versus *ka* for the three aspect ratios are displayed in Fig. 18 that the resonant peaks become lower as the aspect ratios increase. In addition, the peak responses for higher aspect ratio's spheroidal shells are primarily attributed to the first coupled radiation mode under the pair of concentrated normal forces applied at the apexes.

VII. CONCLUSIONS

This work presents a novel modal-type analysis procedure to characterize the radiation characteristics of submerged elastic structures in a heavy acoustic medium. The equation of motion for an elastic structure is discretized into the normal direction of the wetted surface as well as the degrees of freedom other than the normal direction. The acoustic loading is represented by a symmetric complex acoustic matrix. Owing to the symmetrical nature of the structural equation and the acoustic loading matrix, the coupled equation for the coupled structural/acoustic system is symmetric. A symmetric eigenvalue problem arises when one adopts the stationary condition of the ratio of the complex power's real part to imaginary part. This eigenvalue problem can be recast into a smaller order eigenvalue problem in the variable of normal velocity. This reduced eigenvalue problem describes the radiation characteristics for the coupled structural/acoustic system. The arctangent of the reciprocal eigenvalues is the phase differences between the

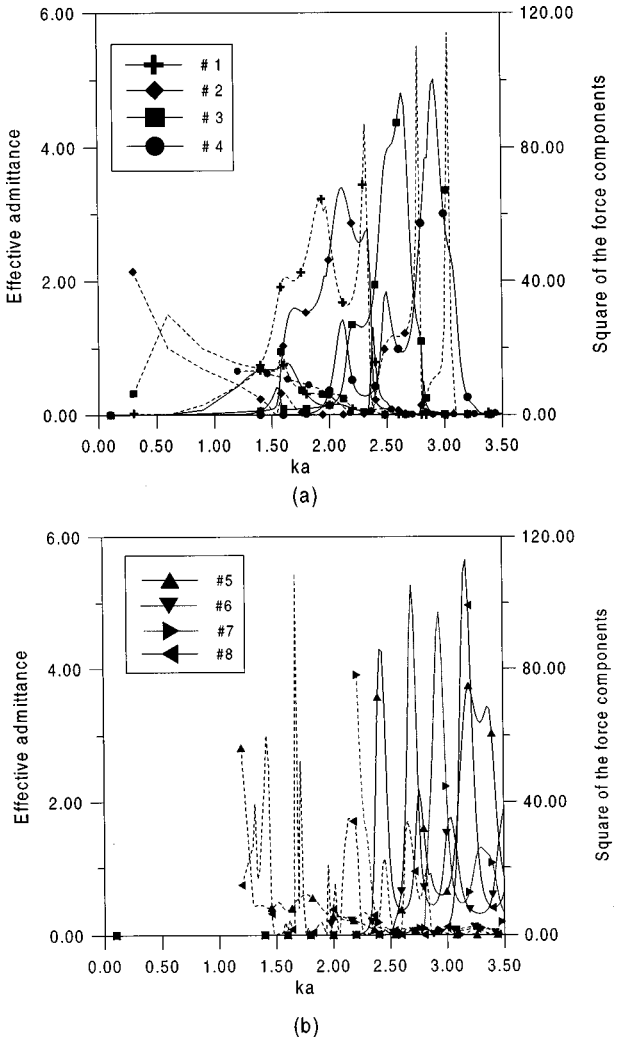

FIG. 17. Frequency dependence of effective modal admittances and force components projected on the coupled radiation modes for a spheroidal shell of aspect ratio 3.5 where the external force is a pair of concentrated normal forces applied at apexes; Solid lines referred to modal admittances and dotted lines referred to force components.

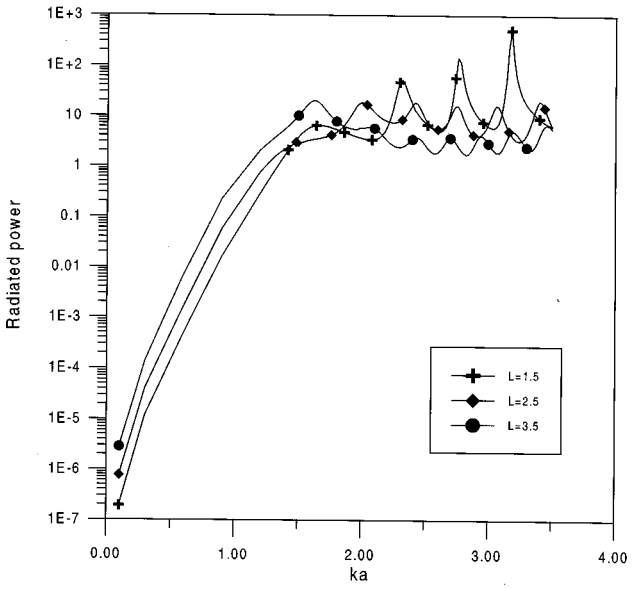

FIG. 18. The total radiated powers versus *ka* for the shells of aspect ratios 1.5, 2.5, and 3.5 for pairs of concentrated normal forces applied at the apexes.

corresponding normal modal velocity with the external forces. The eigensolutions are termed as the coupled structural/acoustic radiation modes.

The set of the coupled radiation modes is then applied to forced vibrations. The normal velocity of the wetted surface is expanded in terms of the coupled radiation modes that the coupled equation for the forced vibration is decomposed into a set of uncoupled complex impedance equations. The impedance of each equation consists of a complex value where the real part is the active damping responsible for acoustic power radiating into far field. In addition, the imaginary part is attributed to effects of structural vibration and acoustic inertia loading on the structure. Furthermore, the total radiated power is the algebraic sum of each individual mode radiated. The power radiated due to each mode is related to the real part of the complex impedance and the square of the power factor of the mode, as well as the square of the force component on the mode. The former two factors are independent of the external force and can be combined together to define an effective modal admittance. The effective modal admittance of each coupled radiation mode characterizes radiation characteristics.

Spherical and slender spheroidal shells are used to demonstrate the proposed analysis procedures. The effective modal admittances for the submerged spherical shell are extremely narrow and sharp which causes the resonant responses to radiate tremendous powers. In the case of the spheroidal shell, the coupled radiation modes depend on vibration frequencies and their effective modal admittances exhibit relative wide bands and less sharp peaks. The resonant phenomenon depends on the characteristics of the admittances and the force components of applied forces. Finally, the progressive changes of the radiation characteristics from the spherical shell to the slender spheroidal shell are also presented to interpret the various features of the resonant responses.

The analysis procedure proposed herein can be applied to any numerical implementations. In the case involving using of finite element method to discretize structure equations, the procedure involves matrix inversions which make banded matrices becomes fully populated matrices. However, this operation causes numerical difficulty for solving large degrees of freedom because the fully populated matrix requires tremendous memory storages and computation capacities. Another difficulty is eigenvalue search methods for matrices should have large dimensions and not definite. Efficient numerical algorithms are worth pursuing for handling large degrees of freedom.

ACKNOWLEDGMENTS

The authors would like to thank the National Science Council of the Republic of China for financially supporting this research under Contract No. NSC 85-2611-E-019-027.

[1] P. T. Chen, ''Vibrations of submerged structures in a heavy acoustic medium using radiation modes,'' J. Sound Vib. **208**, 55–71 (1997).
[2] S. Hayek, ''Vibration of a spherical shell in an acoustic medium,'' J. Acoust. Soc. Am. **40**, 342–348 (1966).
[3] P. T. Chen and J. H. Ginsberg, ''Variational formulation of acoustic radiation from submerged spheroidal shells,'' J. Acoust. Soc. Am. **94**, 221–233 (1993).
[4] G. V. Borgiotti, ''The power radiated by a vibrating body in an acoustic fluid and its determination from boundary measurements,'' J. Acoust. Soc. Am. **88**, 1884–1893 (1990).
[5] D. M. Photiadis, ''The relationship of Singular value decomposition to wave-vector filtering in sound radiation problem,'' J. Acoust. Soc. Am. **88**, 1152–1159 (1990).
[6] A. Sarkissian, ''Acoustic radiation from finite structures,'' J. Acoust. Soc. Am. **90**, 574–578 (1991).
[7] P. T. Chen and J. H. Ginsberg, ''Complex power, reciprocity, and radiation modes for submerged bodies,'' J. Acoust. Soc. Am. **98**, 3343–3351 (1995).
[8] G. C. Everstine and F. M. Henderson, ''Coupled finite element/boundary element approach for fluid structure interaction,'' J. Acoust. Soc. Am. **87**, 1938–1947 (1990).
[9] R. A. Jeans and I. C. Mathews, ''Solution of fluid-structure interaction problems using a coupled finite element and variational boundary element technique,'' J. Acoust. Soc. Am. **88**, 2459–2466 (1990).

A mode-based measure of field sensitivity to geoacoustic parameters in weakly range-dependent environments

Ronald T. Kessel
School of Earth and Ocean Sciences, E-Hut 132A, University of Victoria, P.O. Box 3055, Victoria, British Columbia V8W 3P6, Canada

(Received 24 November 1997; revised 28 May 1998; accepted 22 September 1998)

The most sensitive environmental parameters are often deemed most important because errors and uncertainties in their values are among the most likely sources of error in propagation modeling. The usual ''snapshot'' investigation of sensitivity (overlaying graphs of the modeled sound field before and after the environment is changed) falls short of *measuring* sensitivity because it fails to assign a physically meaningful quantity to each parameter, signifying its ability to influence the field. Here a new measure of sensitivity is formulated from the adiabatic-mode theory of sound propagation. The measure is practical because it applies as a statistical rule when the propagation scenario is uncertain. It is insightful because it can be explained physically as the combined effect of (1) a uniform change of the long-range phase common to all modes, (2) a nonuniform (jumbling) of the relative phase between modes, and (3) changes in energy loss. All three work together in a single analytic formulation, or they can be isolated to emphasize their particular roles. The measure is demonstrated for shallow-water environments.
[S0001-4966(99)02401-7]

PACS numbers: 43.30.Bp, 43.30.Pc [DLB]

INTRODUCTION

Environmental parameters influence the long-range sound field in varying degrees. To demonstrate that influence, researchers ordinarily proceed as follows: A propagation scenario is fully specified, and the sound field is computed using a sound propagation model. Then a parameter of the environment is changed, and the field recomputed for comparison against the original, usually by overlaying plots of each or arranging them side by side (see for example Refs. 1–4); the influence of the parameter being evident from the alteration in the field. Needless to say, such before-and-after ''snapshots'' are empirical—illustrating instances of sensitivity without explaining them, at best affirming principles derived by other means. They also fall short of *measuring* parameter sensitivity because they ultimately do not assign a physically meaningful quantity to the environmental parameter that signifies its expected ability to influence the sound field.

The object here is to formulate a new measure of sensitivity that is at once quantitative, physically meaningful, and theoretically tractable. Expressed in words, the measure is an estimate of the root mean squared (rms) relative change in the acoustic field produced by a small change in the environment, averaged over many trial source–receiver configurations. No trials are required, however, because the average is estimated directly from adiabatic-mode theory, by focusing on the horizontal phase of the modes, which is the most sensitive part of the field at long ranges. The new measure can therefore be explained as the combined effect of (1) a uniform change of the long-range phase common to all modes, (2) a nonuniform (jumbled) change of relative phase between one mode and another, and (3) the altered strength of the field due to changes in energy loss. All three work together in a single analytic formulation, or they can be isolated to focus on just one aspect of field sensitivity of particular interest.

A mode approach separates the analysis of sensitivity in two parts: (1) how changes to the environment change the local modes, and (2) how changes to the modes will, on average, change the field. The second can be treated apart from the first by taking before-and-after snapshots of the modes using a mode-search program, rather than of the field itself, and then formulating the mean change of the field analytically in terms of the change in the modes. That is the approach followed here. A complete understanding of sensitivity must also address how changes to the environment change the local modes, but that has been considered elsewhere.[5]

I. SENSITIVITY ''SNAPSHOTS''

Suppose that a sound propagation model has been used to compute the acoustic pressure field $p(\mathbf{x},\mathbf{x}_s)$ due to a source at position $\mathbf{x}_s$, evaluated at point $\mathbf{x}$. Now imagine changing the environment slightly, then recomputing the field $p'(\mathbf{x},\mathbf{x}_s)$ in the modified environment. The change is

$$\Delta p(\mathbf{x},\mathbf{x}_s)=p'(\mathbf{x},\mathbf{x}_s)-p(\mathbf{x},\mathbf{x}_s), \tag{1}$$

and a possible measure of the field sensitivity is the magnitude of the change relative to a suitable norm $\|p(\mathbf{x},\mathbf{x}_s)\|$,

$$S_1(\mathbf{x},\mathbf{x}_s)\equiv\frac{|\Delta p(\mathbf{x},\mathbf{x}_s)|}{\|p(\mathbf{x},\mathbf{x}_s)\|}. \tag{2}$$

Regardless of what norm is used, S_1 varies considerably with changes in the source–receiver configuration $\mathbf{x}$ or $\mathbf{x}_s$ (as demonstrated later by example), and with changes in the starting environment (owing to the sensitivity of the long-range phase, as shown later), both of which determine the interference pattern constituting p and p', and thereby Δp.

The sensitivity to a slight change in the environment is therefore masked by comparable or greater sensitivity to the source–receiver configuration and starting environment. This masking is unavoidable in a single before-and-after snapshot of sensitivity.

II. THE AVERAGE SENSITIVITY

To account for uncertain source and receiver positions, we can imagine averaging S_1 over many trial positions representative of those likely to be encountered in a particular application. In shallow water environments, a large number of trial sources and receivers might be placed at depths throughout the water column; in deep water, at depths where manmade sources and receivers are usually deployed. In any case, the horizontal position of sources and receivers, r_s and r, should not vary too widely or averaging will suppress the range dependence of the measure. As we will see, the mean sensitivity is a smooth function of r and r_s, so they could often be replaced by their mean values for source and receiver arrays.

If there are N trial source–receiver positions $\mathbf{x}_s^t = (r_s, z_s^t)$ and $\mathbf{x}^t = (r, z^t)$ for $t = 1 \cdots N$, at fixed ranges, r_s and r, then the rms value for all trials is itself a measure of sensitivity,

$$S_2(r, r_s) = \sqrt{\overline{S_1(r, r_s)^2}}, \tag{3}$$

where the overhead bar denotes the average,

$$\overline{S_1(r, r_s)^2} = \frac{1}{N} \sum_{t=1}^{N} S_1(\mathbf{x}^t, \mathbf{x}_s^t)^2. \tag{4}$$

Rather than actually modeling many trial source–receiver configurations for each environmental perturbation, however, let us derive an estimate using adiabatic modes.

A. Adiabatic mode model

Under the adiabatic mode approximation it is assumed that each normal mode of sound propagation is characterized by a local horizontal wave number $k_m(r)$ and vertical mode function $\Psi_m(\mathbf{x})$, both of which can be computed using a range-independent mode model, much as if the environment were locally range independent.[6] It is assumed, moreover, that the farfield acoustic pressure $p(\mathbf{x}, \mathbf{x}_s)$ with harmonic time dependence $e^{-i\omega t}$ can be written as the superposition of M dominant modes propagating independently,

$$p(\mathbf{x}, \mathbf{x}_s) = \sum_{m=1}^{M} p_m(\mathbf{x}, \mathbf{x}_s), \tag{5}$$

where p_m is the contribution of the mth mode,

$$p_m(\mathbf{x}, \mathbf{x}_s) \simeq A_m(\mathbf{x}_s) \Psi_m(\mathbf{x}) \frac{e^{i\zeta_m R}}{\sqrt{\zeta_m R}}; \tag{6}$$

$A_m(\mathbf{x}_s)$ being its source-dependent excitation, ζ_m its mean horizontal wave number between source and receiver,

$$\zeta_m = \zeta_m(r, r_s) = \frac{1}{r - r_s} \int_{r_s}^{r} k_m(r) dr, \tag{7}$$

and R the horizontal source–receiver separation,

$$R = |r - r_s|. \tag{8}$$

If the media absorbs energy, then ζ_m, like k_m, is complex,

$$\zeta_m = \gamma_m + i\alpha_m, \tag{9}$$

with $\alpha_m \geqslant 0$ for all modes, and $\alpha_m \approx 0$ for propagating modes.

B. Field sensitivity based on modal phase

Let us assume that the adiabatic mode model was used to compute the original $p(\mathbf{x}, \mathbf{x}_s)$. Now the environment is changed slightly, giving a new field $p'(\mathbf{x}, \mathbf{x}_s)$ owing to slightly different modes $k'_m(r)$, $\Psi'_m(\mathbf{x})$, and $A'_m(\mathbf{x}_s)$, and the change in pressure (1) is the sum of differences,

$$\Delta p(\mathbf{x}, \mathbf{x}_s) = \sum_{m=1}^{M} (p'_m(\mathbf{x}, \mathbf{x}_s) - p_m(\mathbf{x}, \mathbf{x}_s)). \tag{10}$$

The overall tendency of Δp, as opposed to its particular fluctuations with $\mathbf{x}$ and $\mathbf{x}_s$, is sufficient to judge the degree of influence an environmental perturbation exerts on the field. Hence, much as the overall tendency of the *transmission loss* $|p(\mathbf{x}, \mathbf{x}_s)|^2$ can be represented by the incoherent mode sum, called the *incoherent transmission loss*,[6]

$$|p(\mathbf{x}, \mathbf{x}_s)|^2_{\text{incoh}} = \sum_{m=1}^{M} |p_m|^2, \tag{11}$$

the overall tendency of the perturbation $|\Delta p(\mathbf{x}, \mathbf{x}_s)|^2$ can be represented by the incoherent mode sum,

$$\begin{aligned} |\Delta p(\mathbf{x}, \mathbf{x}_s)|^2_{\text{incoh}} &\equiv \sum_{m=1}^{M} |p'_m - p_m|^2, \\ &= \sum_{m=1}^{M} |p'_m|^2 + |p_m|^2 - 2\,\text{Re}(p'_m p_m^*), \end{aligned} \tag{12}$$

in which* denotes a complex conjugation. This *incoherent* form will be used in the estimate for the average sensitivity S_2 in (3).

For the moment, however, let us return to the contribution of a single mode (6), and note that the long-range horizontal phase $e^{i\zeta_m R}$ of the modes is the most sensitive part of the field to small changes in large regions of the environment, because small environmentally induced changes in the mean wave number ζ_m become amplified by large R. Hence, it is reasonable to assume that the long-range field in the slightly modified environment consists of much the same modes as in the original environment, $(A'_m, \Psi'_m) \approx (A_m, \Psi_m)$, but their phase has now been altered by an amount $e^{i\Delta\zeta_m R}$,

$$p'_m(\mathbf{x}, \mathbf{x}_s) \approx p_m(\mathbf{x}, \mathbf{x}_s) e^{i\Delta\zeta_m R}, \tag{13}$$

where $\Delta\zeta_m$ is the change in the mean wave number,

$$\Delta\zeta_m = \zeta'_m - \zeta_m = \Delta\gamma_m + i\Delta\alpha_m. \tag{14}$$

Substituting (13) into (12), then simplifying, we have

$$|\Delta p(\mathbf{x},\mathbf{x}_s)|^2_{\text{incoh}} = \sum_{m=1}^{M} |p_m|^2 \Omega_m(r,r_s), \tag{15}$$

in which

$$\Omega_m(r,r_s) = 1 + e^{-2\Delta\alpha_m R} - 2e^{-\Delta\alpha_m R} \cos \Delta\gamma_m R. \tag{16}$$

Now imagine taking the average of a large number of source–receiver positions at fixed ranges as before. The mean of (15) is

$$\begin{aligned}\overline{|\Delta p(r,r_s)|^2_{\text{incoh}}} &= \frac{1}{N}\sum_{t=1}^{N} |\Delta p(\mathbf{x}^t,\mathbf{x}_s^t)|^2_{\text{incoh}},\\ &= \frac{1}{N}\sum_{t=1}^{N}\sum_{m=1}^{M} |p_m|^2 \Omega_m(r,r_s)\\ &= \|p(r,r_s)\|^2 \overline{\Omega(r,r_s)},\end{aligned} \tag{17}$$

in which $\overline{\Omega(r,r_s)}$ is a weighted average over modes,

$$\overline{\Omega(r,r_s)} = \frac{1}{\|p(r,r_s)\|^2} \sum_{m=1}^{M} \overline{|p_m|^2} \Omega_m(r,r_s), \tag{18}$$

with weighting

$$\overline{|p_m|^2} = \frac{1}{N}\sum_{t=1}^{N} |p_m(\mathbf{x}^t,\mathbf{x}_s^t)|^2, \tag{19}$$

and total weight, by (11), equal to the *mean incoherent transmission loss* for the unperturbed field when averaged over all source–receiver trials,

$$\begin{aligned}\|p(r,r_s)\|^2 = \sum_{m=1}^{M} \overline{|p_m|^2} &= \frac{1}{N}\sum_{t=1}^{N}\sum_{m=1}^{M} |p_m(\mathbf{x}^t,\mathbf{x}_s^t)|^2,\\ &= \frac{1}{N}\sum_{t=1}^{N} |p(\mathbf{x}^t,\mathbf{x}_s^t)|^2_{\text{incoh}}.\end{aligned} \tag{20}$$

Substituting (17) into the measure of sensitivity (3), using (20) as the norm, gives a theoretical estimate of the mean relative change in the field,

$$S_2(\mathbf{x},\mathbf{x}_s) \approx S_3(r,r_s) = \sqrt{\overline{\Omega(r,r_s)}}. \tag{21}$$

A value $S_3 = 1.0$ indicates an average relative change of 100% in the field—high sensitivity; whereas $S_3 \approx 0.0$ indicates no relative change—low sensitivity.

To evaluate S_3 for a given environmental change we must (1) compute the before-and-after local wave numbers $k_m(r)$ and $k'_m(r)$ using a suitable (range-*in*dependent) normal mode program applied to both the original and modified environments; (2) compute the corresponding change in modal phase $\Delta\zeta_m R$ using (7) and (14); and (3) compute the weighted mean $\overline{\Omega(r,r_s)}$ using (18), whose square root is the sensitivity S_3 in (21). The first two steps can be performed very efficiently if the change $\Delta k_m(r)$ produced by a small change $\Delta\tau(r)$ in any geoacoustic parameter τ is approximated as

$$\Delta k_m = k'_m - k_m \approx (\partial k_m/\partial\tau)\Delta\tau, \tag{22}$$

where $\partial k_m/\partial\tau$ is the partial derivative of the modal wave number computed directly from the local vertical mode function $\Psi_m(\mathbf{x})$, as described in Ref. 5. Then one mode search for the starting environment suffices for an extensive sensitivity study involving any number of geoacoustic parameters.

III. PHYSICAL EXPLANATION OF SENSITIVITY

A. Weighted average over modes

Let the N source–receiver trials consist of all combinations of N_s source positions $\mathbf{x}_s^a = (r_s, z^a)$, $a = 1\cdots N_s$, and N_r receiver positions $\mathbf{x}^b = (r, z^b)$, $b = 1\cdots N_r$. Then $N = N_s N_r$, and the weighting for each mode (19) becomes

$$\begin{aligned}\overline{|p_m|^2} &= \frac{1}{N_s N_r}\sum_{a=1}^{N_s}\sum_{b=1}^{N_r} |A_m(\mathbf{x}_s^a)|^2 |\Psi_m(\mathbf{x}^b)|^2 \frac{e^{-2\alpha_m R}}{\zeta_m R},\\ &= \frac{e^{-2\alpha_m R}}{\zeta_m R} \overline{|A_m(r)|^2}\ \overline{|\psi_m(r)|^2}.\end{aligned} \tag{23}$$

Here $\overline{|A_m(r_s)|^2}$ is the mean square source excitation of a mode,

$$\overline{|A_m(r_s)|^2} = \frac{1}{N_s}\sum_{a=1}^{N_s} |A_m(\mathbf{x}_s^a)|^2, \tag{24}$$

$\overline{|\Psi_m(r)|^2}$ is the mean square value of the vertical mode function at the receiver,

$$\overline{|\Psi_m(r)|^2} = \frac{1}{N_r}\sum_{b=1}^{N_r} |\Psi_m(\mathbf{x}^b)|^2, \tag{25}$$

and $e^{-2\alpha_m R}/\zeta_m R$ is the combined relative energy loss of a mode due to absorption by the media, leakage of energy out of the sound channel, and cylindrical spreading. A mode therefore contributes to the operative mean $\overline{\Omega(r,r_s)}$ roughly in proportion to the degree that its energy is, on average, excited and detected in the source–receiver trials. Modes that do not contribute significantly to the field therefore do not contribute to the measure of sensitivity, as we should expect.

To simplify the measure, we might assume that all modes are, on average, equally excited by a source and detected by a receiver; that is,

$$\overline{|A_m(r_s)|^2} \approx \overline{|\Psi_m(r)|^2} \approx 1, \tag{26}$$

in which case the mode weighting (19) becomes

$$\overline{|p_m|^2} \approx e^{-2\alpha_m R}/\zeta_m R, \tag{27}$$

and so depends on the source–receiver separation R alone, not on their trial depths. This is often a reasonable assumption for the sake of a sensitivity study, especially in shallow water, provided that we take care to limit the mode series $m = 1\cdots M$ to just those modes that are likely to be significantly excited and received in the trials, because sensitivity cannot depend on modes that do not contribute to the field. The full weighting (19) [and here equivalently (23)] eliminates unimportant modes automatically.

TABLE I. Geoacoustic parameters for a simple two-layer environment. The sea floor is limestone.

Water depth	200 m
P-wave speed in water	1500 m/s
Density of water	1000 km/m^3
P-wave speed in sea floor	3000 m/s
S-wave speed in sea floor	1700 m/s
S-wave absorption in sea floor	0.5 dB/λ
Density of sea floor	2400 km/m^3

B. The role of horizontal phase

To isolate the role of the long-range horizontal phase, assume that changes to the absorption rate are unimportant for a given model application. Setting $\Delta\alpha_m R \approx 0$ in (16) simplifies (18) to

$$\overline{\Omega(r,r_s)} = 2(1-\overline{\cos\,\Delta\gamma R}), \tag{28}$$

where $\overline{\cos\Delta\gamma R}$ is a weighted average over modes with weighting (23). Assuming once again that all modes are, on average, equally excited and received (26), and therefore mode weighting (27); and further assuming that all modal wave numbers ζ_m lie in a narrow band along the real wave number axis such that $1/\zeta_m$ is roughly the same for all modes (often true for dominant propagating modes), making the weights (27) roughly equal for all modes; the weighted average $\overline{\cos\Delta\gamma R}$ then becomes a straightforward unweighted mean that is amenable to statistical analysis.

Suppose, for instance, that we bypass all of the before-and-after mode computations by simply assuming from the outset that the change to the environment, whatever it may be, perturbs the phase of each mode randomly such that the change in real phase $\phi = \Delta\gamma_m R/2\pi$ accumulated by a mode can be represented by a single random variable with normal probability distribution of mean μ and standard deviation σ,

$$P(\phi,r,r_s) = \frac{1}{\sqrt{2\pi}\sigma}\exp\left\{-\frac{(\phi-\mu)^2}{2\sigma^2}\right\}. \tag{29}$$

The units of ϕ, μ, and σ are revolutions of phase. The mean $\mu = \mu(r,r_s)$ is a change common to the phase of all modes giving a uniform advance or delay of the entire field $e^{i2\pi\mu}$. The standard deviation $\sigma = \sigma(r,r_s)$ is a measure of the change in relative phase between modes, or the chaotic ''jumbling'' of the modes with respect to each other. For a large number of modes M, the expected value $\overline{\cos\Delta\gamma R}$ is then

$$\begin{aligned}\overline{\cos\,\Delta\gamma R} &\approx \int_{-\infty}^{\infty}\cos(2\pi\phi)P(\phi,r,r_s)\,d\phi \\ &= e^{-2\pi^2\sigma}\cos 2\pi\mu,\end{aligned} \tag{30}$$

whereby

$$S_3(r,r_s) \approx S_4(\mu,\sigma) = \sqrt{2(1-e^{-2\pi^2\sigma^2}\cos 2\pi\mu)}. \tag{31}$$

Notice that $S_4(\mu,\sigma)$ is periodic in the mean phase change μ; being maximal at $\mu = \pm\{1/2,3/2,\ldots\}$, where the phase of the modified pressure field is shifted uniformly by π radians, giving roughly a sign reversal between the original and perturbed fields—a condition of maximal perturbation to the field; and being minimal at $\mu = \pm\{0,1,2,\ldots\}$, where the phase of the modified pressure field is aligned as much as possible with the original field—a condition of minimal perturbation. The measure S_4 also ''saturates'' beyond $\sigma > 0.5$ revolutions, where $S_4 \approx \sqrt{2}$ because $e^{-2\pi^2\sigma^2} \ll 1$, indicating that the relative phase jumbling between modes is so great that a distinct measure of sensitivity cannot be assigned. The long-range phase of the modified field bears no relation to the original, though the mode content is essentially the same.

If the wave number sensitivity is known, then the degree of uniform phase shift and phase jumbling, μ and σ, can be estimated from the perturbed modes using the weighted mean and standard deviation of the change in modal phase,

$$\begin{aligned}\mu(r,r_s) &\approx \frac{1}{\|p(r,r_s)\|^2}\sum_{m=1}^{M}\overline{|p_m|^2}\Delta\gamma_m R \\ &\approx \left[\sum_{m=1}^{M} e^{-2\alpha_m R}\Delta\gamma_m R\right] \Big/ \left[\sum_{m=1}^{M} e^{-2\alpha_m R}\right],\end{aligned} \tag{32}$$

and

TABLE II. Complex modal wave numbers ($1/m$) computed by the mode program ORCA for the model in Fig. 2, at frequency $f = 75.0$ Hz, before and after the P- and S-wave speeds have been perturbed by $+1.0\%$.

m	k_m unperturbed	k_m perturbed S-wave speed	k_m perturbed P-wave speed
1	0.313 758 63+i3.67E-7	0.313 757 20+i3.53E-7	0.313 758 34+i3.80E-7
2	0.312 555 96+i1.48E-6	0.312 550 16+i1.42E-6	0.312 554 83+i1.53E-6
3	0.310 549 99+i3.41E-6	0.310 536 61+i3.25E-6	0.310 547 50+i3.52E-6
4	0.307 739 86+i6.28E-6	0.307 715 02+i5.97E-6	0.307 735 54+i6.49E-6
5	0.304 126 39+i1.04E-5	0.304 084 92+i9.81E-6	0.304 119 85+i1.07E-5
6	0.299 716 66+i1.62E-5	0.299 650 97+i1.52E-5	0.299 707 67+i1.68E-5
7	0.294 531 70+i2.47E-5	0.294 430 22+i2.29E-5	0.294 520 40+i2.55E-5
8	0.288 617 05+i3.69E-5	0.288 462 38+i3.39E-5	0.288 604 57+i3.82E-5
9	0.282 057 20+i5.70E-5	0.281 818 15+i4.99E-5	0.282 046 63+i5.89E-5
10	0.275 005 50+i4.98E-4	0.274 722 14+i1.36E-4	0.275 000 23+i5.02E-4
11	0.266 258 66+i1.04E-3	0.266 172 97+i9.34E-4	0.266 257 66+i1.04E-3
12	0.256 225 00+i1.31E-3	0.256 157 77+i1.26E-3	0.256 226 55+i1.32E-3

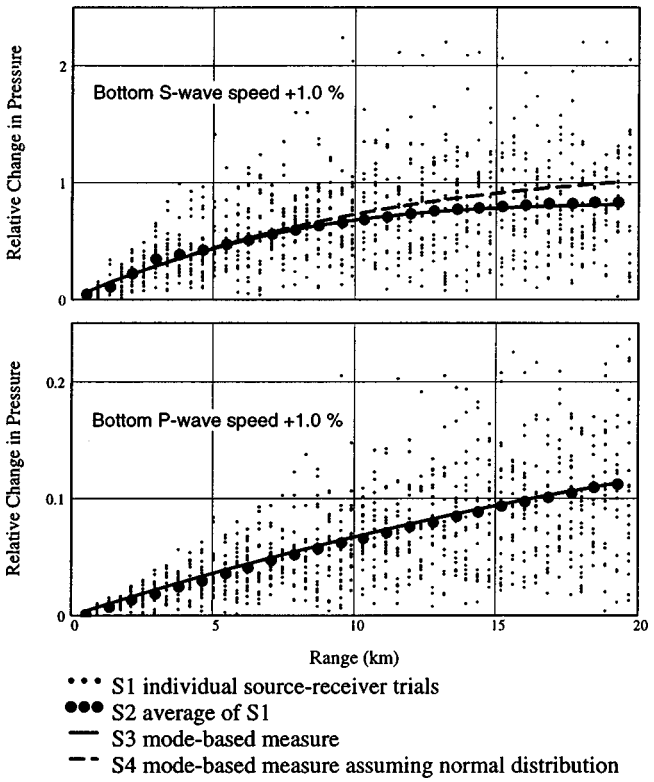

FIG. 1. The sound-field sensitivity computed four different ways for S- and P-wave speed perturbations to the bottom layer (limestone) of the two-layer environment in Table I. Only one in ten trials has been plotted in S_1 for clarity. Note that the vertical scales differ by an order of magnitude between the upper and lower graphs, and that S_2, S_3, and S_4 are visually coincident in the lower.

$$\sigma^2(r,r_s) \approx \frac{1}{\|p(r,r_s)\|^2} \sum_{m=1}^{M} \overline{|p_m|^2} (\Delta\gamma_m R - \mu)^2,$$

$$\approx \frac{[\Sigma_{m=1}^{M} e^{-2\alpha_m R} (\Delta\gamma_m R - \mu)^2]}{[\Sigma_{m=1}^{M} e^{-2\alpha_m R}]}. \quad (33)$$

A corresponding estimate of the phase-dependent sensitivity S_4 can be computed by substituting these into (31).

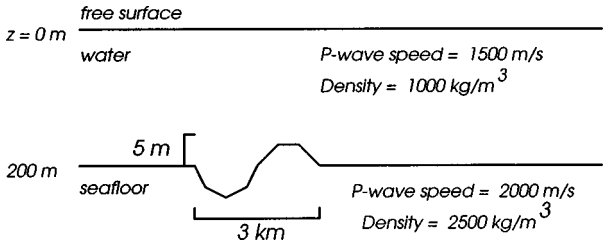

FIG. 2. Range-dependent perturbation to bathymetry in a simple two-layer environment.

The phase statistics μ and σ are specialized measures of field sensitivity in their own right. Quantities equivalent to $2\pi\mu/R$ and $2\pi\sigma/R$ were derived from heuristic arguments by Ozard *et al.*[7] as predictors of the sensitivity of the Bartlett processor to model a mismatch in Matched-Field Processing (MFP) for the source location in range-independent environments. They point out that a uniform phase shift μ is inconsequential for the Bartlett processor for vertical receiver arrays, making σ the main parameter of interest.

C. The role of absorption

Changing the energy absorption rate of the media causes the field to decay more or less quickly with the range. The effect can be dramatic over long ranges. To illustrate, assume that real horizontal phase is unchanged ($\Delta\gamma_m R \approx 0$), hence (16) for the mth mode becomes

$$\Omega_m(r,r_s) = 1 + e^{-2\Delta\alpha_m R} - 2e^{-\Delta\alpha_m R}. \quad (34)$$

If $\Delta\alpha_m$ is *positive* for all modes, then $e^{-\Delta\alpha_m R} \ll 1$ at sufficiently long ranges, in which case $\Omega_m(r,r_s) \approx \overline{\Omega(r,r_s)} \approx S_3 \approx 1$ indicating a 100% change to the field—total decay of the field due to increased absorption. On the other hand, if $\Delta\alpha_m$ is *negative*, then $e^{-\Delta\alpha_m R} \gg 1$, in which case the perturbed field is considerably larger than the original. Because it is the *relative* change in the field, the sensitivity S_3 now grows exponentially with range R, although the perturbed field nevertheless decays with range because α_m', like α_m, is always positive, as noted in Sec. III A.

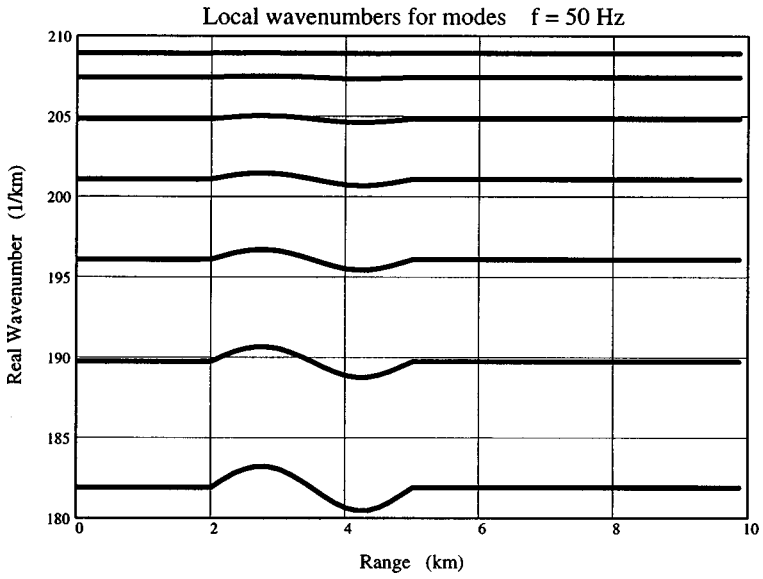

FIG. 3. The real part of the local wave numbers k of the modes for the environment computed at each point as if the environment were locally range independent, then plotted as a function of range.

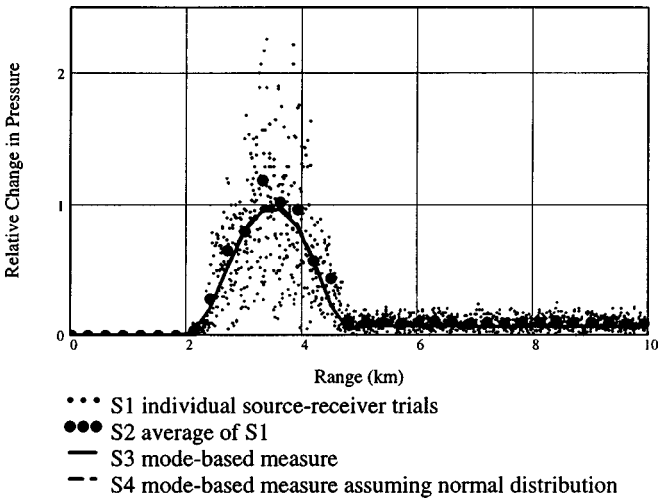

FIG. 4. The sound-field sensitivity computed four different ways for the bathymetric perturbations. Only one of every 30 trials has been plotted in S_1 for clarity. The two mode-based measures, S_3, and S_4, are visually coincident.

IV. EXAMPLES

A. Sensitivity to P- and S-wave speeds in limestone sea floor

Consider the sensitivity of the sound field to the P- and S-wave speeds in the sea floor (limestone) for a simple two-layer range-independent environment described in Table I. Table II lists the wave numbers for the dominant modes at frequency $f=75$ Hz, computed by the mode program ORCA[8] before and after the P- and S-wave speeds in the sea floor were increased by $+1\%$ of their original values. Figure 1 shows the sensitivity computed using the four methods considered above:

(a) $S_1(\mathbf{x},\mathbf{x}_s)$, the highly variably ''snapshot'' definition in (2), though impractical, is plotted as individual points, each point representing the sensitivity of the field for one of ten trial source depths z_s (evenly spaced through the water column, with the source always at $r_s=0$), computed on a regular grid of receiver points (20 points in depth spanning the water column, and 50 points in range from 0.1 to 20 km from the source).

(b) $S_2(r,r_s)$, the straightforward average (3) of S_1, taken over $10\times 20=200$ source–receiver trials at each range step, using a normalization $\|p(\mathbf{x},\mathbf{x}_s)\|$ equal to the rms pressure of all 20 receiver trial depths at each range.

(c) $S_3(r,r_s)$, the first mode-based measure of sensitivity (21), the main subject of this paper;

(d) $S_4(\mu,\sigma)$, the simplified horizontal phase measure of sensitivity (31) using μ in (32) and σ in (33).

The scattered points in Fig. 1 show how much the ''snapshot'' sensitivity S_1 varies with the source and receiver position, making it unreliable. The straightforward average of many trials S_2 verifies that new measures S_3 and S_4, computed much more efficiently from the modes, work rather well. Note that the sensitivity increases with range because the environmental change, made uniformly at all ranges, has more of an opportunity to influence the field as the source–receiver separation increases. Also note that the sensitivity of the S-wave speed in limestone, because it is closer to the P-wave speed in the water column, is roughly an order of magnitude greater than that of the P wave. All four measures of the sensitivity to S-wave speed ultimately saturate owing to ''phase-jumbling,'' as predicted in Sec. IV B.

B. Range-dependent bathymetry

Consider the sensitivity of the field to a gentle sinusoidal bump on the sea floor shown in Fig. 2. Figure 3 shows the real part of the local wave numbers for the first seven modes plotted as a function of range, computed at 50 Hz by ORCA, assuming that the media is locally range independent. The higher-order modes (smaller real wave number) respond more sensitively to the bathymetry because they interact more strongly with the bottom. Figure 4 shows the sensitivity computed four different ways as before, but this time a range-dependent parabolic equation model called RAM[9] was used to verify the mode-based measures, by computing the field for many source–receiver configurations with and without the bump, without the adiabatic-mode approximations assumed thus far. Here again, the straightforward averaging of many trials verifies the efficient mode-based measures of sensitivity. Notice that the crest of the sinusoidal bump tends to undo (though not completely) the perturbations caused by the leading symmetric trough, restoring the unperturbed field somewhat, reducing the sensitivity accordingly.

TABLE III. The geoacoustic properties for the Western Bank.

Sed. layer	Type	Upper depth (m)	P-wave speed cP (m/s)	S-wave speed cs (m/s)	P-wave absorp. (dB/λ)	S-wave absorp. (dB/λ)	Density rho (kg/m^3)
	Sea water	0	1505	0	0	0	1000
	Sea water	10	1500	0	0	0	1000
	Sea water	20	1480	0	0	0	1000
	Sea water	30	1470	0	0	0	1000
	Sea water	40	1467	0	0	0	1000
	Sea water	50	1460	0	0	0	1000
	Sea water	60	1455	0	0	0	1000
1	Sable is. Sand/grav.	100	1600	100	0	2.73	1900
2	Scotian shelf drift	140	1800	400	0	2.73	2100
3	Bedrock	240	5100	2500	0.21	2.13	2700

TABLE IV. The field sensitivity for seafloor properties in the Western Bank model given in Table III. The geoacoustic property names *cp*1, *cp*2, and *cp*3 denote the P-wave speed in the sediment layer 1, 2, and 3, respectively. Those beginning with *cs*, *h*, and *rho*, likewise denote the S-wave speed, layer thickness, and density, respectively. *hw* is the water depth (bathymetry).

Sea floor property	Value	Change	Units	Field sensitivity $S3$			
				30 Hz	60 Hz	120 Hz	240 Hz
*cp*1	1600	1.0	m/s	0.050 29	0.113 98	0.201 72	0.406 78
*cp*2	1800	1.0	m/s	0.028 17	0.038 48	0.105 09	0.159 08
*cp*3	5100	1.0	m/s	0.000 07	0.000 07	0.000 07	0.000 06
*cs*1	100	10.0	m/s	0.012 93	0.015 32	0.014 89	0.016 02
*cs*2	400	10.0	m/s	0.030 59	0.023 29	0.023 96	0.027 77
*cs*3	2500	10.0	m/s	0.006 92	0.008 72	0.009 38	0.008 62
hw	100	0.1	m	0.069 48	0.183 95	0.333 74	0.637 42
*h*1	40	0.1	m	0.018 62	0.044 08	0.097 80	0.204 30
*h*2	100	0.1	m	0.003 09	0.009 43	0.018 99	0.032 44
*rho*1	1900	10.0	kg/m^3	0.023 05	0.024 73	0.023 83	0.026 23
*rho*2	2100	10.0	kg/m^3	0.007 70	0.008 86	0.009 40	0.010 78
*rho*3	2700	10.0	kg/m^3	0.001 62	0.001 62	0.001 51	0.001 34

C. Western Bank

To illustrate the method for a more realistic environment, consider Table III, detailing a shallow-water scenario representing the Western Bank on the Scotian Shelf (43° 20.15′N, 61° 12.75′W). The 100-m water column is downward refracting, and the sea floor is a sand–gravel mix (40-m thick), overlying glacial till (100-m thick), and bedrock (assumed infinitely thick).[10] Table IV reports the mode-based measure of sensitivity S_3 for prescribed changes made to the main bottom parameters, for a source–receiver separation $R=5$ km, and computed at four different frequencies $f=30,60,120,240$ Hz. In this case, just one mode search was performed for each frequency, and the variations of the modal wave numbers with each geoacoustic parameter were computed using (22) together with partial derivatives computed as described in Ref. 5, implemented by a mode program called SAMPLE.[11]

Figure 5 scales the sensitivities in Table IV on an equal footing, showing the expected relative change in the field S_3 due now to the *same* relative change in each parameter. The first five parameters—bathymetry *hw*, the upper sediment compressional speeds, *cp*1 and *cp*2, and layer thicknesses, *h*1 and *h*2, which characterize the P-wave speed profile in the upper sea floor—clearly dominate at the higher frequencies; their individual sensitivities being roughly an order of magnitude greater than the combined influence of remaining sea floor properties. In other words, the values of these five most important parameters must as a rule be known with a relative accuracy more than ten times greater than that of the other parameters.

Figure 5 provides quantitative information about the effect of geoacoustic parameters for the Western Bank environment: showing the roughly equal sensitivity of the two most important parameters, bathymetry *hw* and the upper P-wave speed *cp*1; the roughly proportional increase of sensitivity with frequency for the five most important parameters, as opposed to the roughly constant sensitivity for the remaining parameters; the general decrease in sensitivity with depth in the sediment properties. The figure may change when the source–receiver separation is reduced; the relative sensitivity of deeper parameters increasing as the contributions of higher-order (deeper penetrating) modes increases.

D. Sensitivity as a function of depth

Environmental changes can also be made on vertical scales much thinner than the layer thickness to identify depths at which a parameter is most sensitive. Figure 6 shows the field sensitivity S_3 to P-wave speed as a function of depth, at 30 Hz, for the Western Bank profile given above. The P-wave speed was increased uniformly by 1.0 m/s in (1) each layer (including the water column), (2) each of a series of equal bands 20-m thick, and (3) bands 5-m thick. The figure shows how the sensitivity to P-wave speed decays where the sound intensity is very weak—near the sea surface, and within the second sediment layer (140–240 m). Smaller sensitivities occur for smaller band thicknesses be-

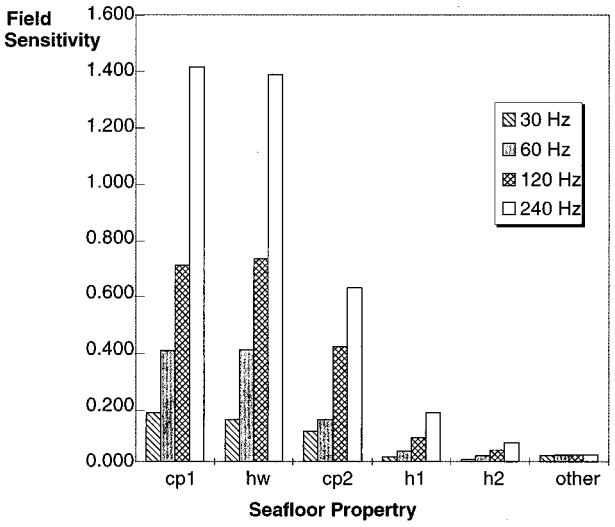

FIG. 5. The field sensitivities in Table V scaled to a common dimensionless basis (divide the tabulated sensitivity by the relative change given to each variable, *change/value*, in Table V, then scale all uniformly to make the largest sensitivity equal to saturation $S_3 \approx \sqrt{2}$). The five most sensitive parameters are shown by frequency. The sum of all remaining parameter sensitivities is denoted *other*.

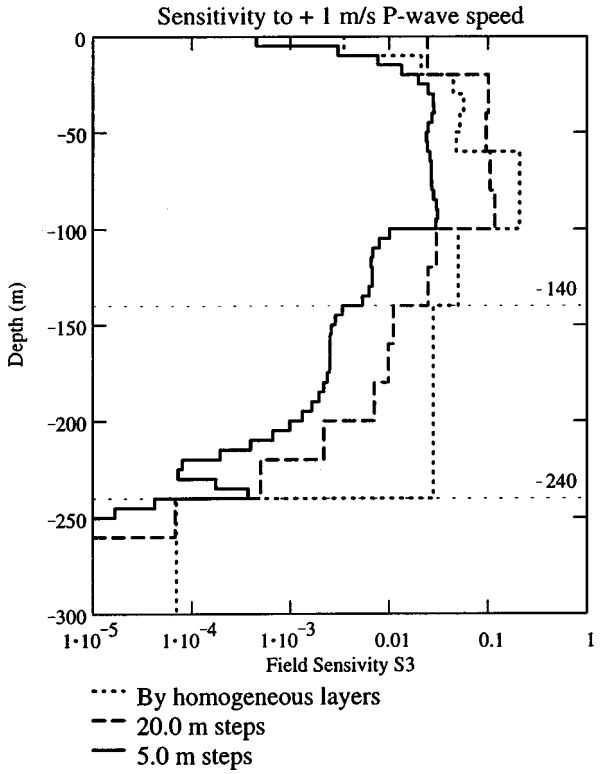

FIG. 6. A plot of field sensitivity to P-wave speed as a function of depth for the Western Bank profile given in Table III. Each ''staircase'' marks the relative change in the field expected for a change in the P-wave speed (an increase of 1 m/s) made uniformly between two depths set by three different schemes: (1) by the thickness of the layers in the model; (2) in equal 20-m steps; and (3) equal 5-m steps. The frequency is 30 Hz, and the source–receiver separation is 5 km.

cause the net volumetric change to the environment is proportional to the thickness. Sensitivity as a function of depth, on a vertical scale less than layer thickness has apparently not been considered in the literature. It is not feasible using snapshots of sensitivity S_1, and becomes computationally intensive using snapshot averages S_2 because each small step in the sensitivity-versus-depth plot requires its own large population of snapshots.

V. CONCLUSIONS

The new mode-based measure of sensitivity (21) gauges the combined effect of changes to the long-range phase and attenuation of the dominant modes of propagation. It was shown how the predominant roles of modal phase and attenuation can be isolated, giving another four specialized measures of field sensitivity, each concentrating one aspect that may be of particular interest: (1) the uniform change in phase μ (32); (2) the nonuniform change in phase σ (33) of importance for the Bartlett processor; (3) the combined effect of μ and σ (31); and (4) the change in absorption alone using (34) in (21).

A normal mode model designed for range-*in*dependent environments is adequate for evaluating the measure of sensitivity in weakly range-dependent environments because forward propagation of the field is not required. The mode-based measure is particularly efficient when used together with a linear perturbation approach to changes in the modes,[6] in which case a single mode search suffices for an extensive sensitivity study. The measure might also be applied somewhat beyond the limits of the adiabatic mode approximation, for strongly range-dependent environments, but then its physical interpretation as an estimate of the mean change in the acoustic field may no longer apply. It could also be applied for random perturbations, to gauge the influence of range-dependent random uncertainties.

ACKNOWLEDGMENTS

This work was supported in part by research grants from the Canadian Department of National Defence and the National Sciences and Engineering Research Council of Canada.

[1] Z. Y. Zhang and C. T. Tindle, ''Improved equivalent fluid approximations for a low shear speed ocean bottom,'' J. Acoust. Soc. Am. **98**, 3391–3396 (1995).
[2] K. P. Bongiovanni, M. Badiey, and W. L. Siegmann, ''Shallow water sediment layer structure and composition effects on range-dependent acoustic propagation in the Atlantic Generating Station (AGS) site,'' J. Acoust. Soc. Am. **98**, 2249–2261 (1995).
[3] A. K. Rogers and T. Yamamoto, ''Experimental investigation of sediment effect on acoustic wave propagation in the shallow ocean,'' J. Acoust. Soc. Am. **93**, 1747–1761 (1993).
[4] J. I. Arvelo and H. Uberall, ''Adiabatic normal mode theory of sound propagation including shear waves in a range-dependent ocean floor,'' J. Acoust. Soc. Am. **88**, 2316–2325 (1990).
[5] R. T. Kessel, ''The variation of modal wave numbers with geoacoustic parameters in layered media,'' J. Acoust. Soc. Am. **102**, 2690–2696 (1997).
[6] F. B. Jensen, W. A. Kuperman, M. B. Porter, and H. Schmidt, *Computational Ocean Acoustics* (American Institute of Physics, New York, 1994).
[7] J. M. Ozard and M. L. Yeremy, ''Effects of mismatch on matched-field processing for Arctic and Pacific shallow water, 22nd meeting, TTCP GTP9 Subgroup G (October 1993), pp. 18–22.
[8] E. K. Westwood, C. T. Tindle, and N. R. Chapman, ''A normal mode model for acoustoelastic ocean environments,'' J. Acoust. Soc. Am. **100**, 3631–3645 (1996).
[9] M. D. Collins, ''A split-step Padé solution for the parabolic equation method,'' J. Acoust. Soc. Am. **93**, 1736–1742 (1993).
[10] J. C. Osler, ''A geo-acoustic and oceanographic description of several sites on the Scotian Shelf,'' Defence Research Establishment Atlantic (Canada) Technical Memorandum DREA/TM/94/216, November 1994.
[11] T. W. Dawson and R. T. Kessel, ''SAMPLE: A seismo-acoustic mode program for layered environments, theoretical background,'' Defence Research Establishment Atlantic (Canada) Technical Memorandum DREA/TM/95/225, October 1995.

Scattering from rigid and soft targets near a planar boundary: Numerical results

Garner C. Bishop and Judy Smith
Naval Undersea Warfare Center Division Newport, Newport, Rhode Island 02840

(Received 5 January 1998; accepted for publication 5 October 1998)

A *T*-matrix formalism for plane-wave scattering from a fluid-loaded elastic spherical shell near a rough fluid–elastic boundary that includes target–boundary scattering effects [J. Acoust. Soc. Am. **101**, 767–788 (1997)] is specialized to scattering from a planar boundary and generalized to include scattering from rigid and soft spheres and finite cylinders with hemispherical endcaps and rigid, soft, fluid, viscoelastic, and fluid-saturated poroelastic sediments. Scattering from a variety of target and sediment combinations is considered, and numerical results are shown that indicate some of the effects of target–boundary scattering and the dependence of target–boundary scattering on target and sediment parameters. [S0001-4966(99)05001-8]

PACS numbers: 43.30.Hw, 43.30.Gv [DLB]

INTRODUCTION

This is the second paper in which scattering from a fluid-loaded target near a sediment boundary is investigated. In the first paper,[1] a null-field *T*-matrix formalism was developed for plane-wave scattering from a stationary fluid-loaded elastic spherical shell near a fluid–elastic boundary with an arbitrary roughness profile. Then two special cases of the general formalism were considered: First, scattering from an elastic spherical shell near a fluid–elastic boundary with periodic roughness was considered and an ''exact'' solution was obtained. Then, a perturbative solution was obtained for small amplitude arbitrary roughness. In both cases, it was shown that the scattered pressure field can be expressed in terms of the free-field *T*-matrices for the target and the sediment so that scattering from different targets and sediments can be calculated by using the appropriate free-field *T*-matrices. In this paper, this result is exploited, and in addition to the elastic sediment considered in the first paper, rigid, soft, fluid, and poroelastic sediments and rigid and soft spheres and finite cylinders with hemispherical endcaps are considered. However, since scattering from a planar boundary, i.e., zeroth-order perturbation theory, (1) is fundamental to establish the correctness of the rough surface formalism and computer codes, (2) provides a basis from which to determine the effects of surface roughness, and (3) since scattering from targets near planar penetrable sediment boundaries, particularly nonspherical targets, has not been considered extensively, scattering from targets near planar sediment boundaries is considered. Therefore, this paper is an extension of some of the earlier work[2–15] on target–boundary scattering.

I. SCATTERING FROM A TARGET NEAR A PLANAR INTERFACE: THEORY

In this section, the formalism developed in Ref. 1 specialized to scattering from a planar interface is briefly summarized and notation for discussion of the numerical results is introduced. It is assumed that a stationary source and target are immersed in a homogeneous, isotropic, inviscid, and semi-infinite fluid half-space that is bounded below by the surface of a semi-infinite sediment half-space located a distance $d^{(2)}$ below the center of the target. The volume exterior to the target and above the sediment is denoted $v^{(1)}$, and $v^{(2)}$ is the volume within the sediment. The surfaces $s^{(2)}$ and $s^{(3)}$ are, respectively, the surfaces of the sediment and the target.

The origin of a fixed set of space coordinates is located at the center of the target with the z axis directed upward and normal to the planar boundary. For nonspherical but rotationally symmetric targets, a second coordinate system fixed in the target is defined with the z axis along the symmetry axis. Initially the target and space coordinate systems are coincident. Then the orientation of the target is given by a sequence of Euler angle rotations, so that, in general, it is necessary to construct the representation of the target *T*-matrix in the fixed space coordinate system. The details of this process are described in Appendix A for a hemispherical endcapped cylinder.

It is assumed that the source field and all scattered fields are time harmonic with time dependence $e^{-i\omega t}$. However, in the following, the factor $e^{-i\omega t}$ and explicit dependence on time are omitted. In this paper, the incident field is a plane wave with wave number $k_p^{(1)}$, polar angle $\theta^{(i)}$, and azimuthal angle $\phi^{(i)}$.

When the perturbative solution developed in Ref. 1 is specialized to scattering from a planar boundary, the scattered pressure field is given by

$$
\begin{aligned}
p^{(1s)}(\mathbf{r}) = {} & R(k_z^{(i)})\chi(\mathbf{r};\mathbf{k}_p^{(1+)})e^{2ik_{pz}^{(1)}d^2} \\
& + \frac{1}{(2\pi)^2}\int_{-\infty}^{\infty} d\mathbf{K}_\perp\ \chi(\mathbf{r};\mathbf{K}_p^{(1+)}) \\
& \times\left[t^{(22)}(\mathbf{K}_\perp,\mathbf{k}_\perp) + \sum_{\boldsymbol{\lambda}} t_{\boldsymbol{\lambda}}^{(23)}(\mathbf{K}_\perp)a_{\boldsymbol{\lambda}}(\hat{k}^{(i)})\right] \\
& + \sum_{\boldsymbol{\lambda}} t_{\boldsymbol{\lambda}}^{(32)}(\mathbf{k}_\perp)\psi_{\boldsymbol{\lambda}2}(\mathbf{r};k_p^{(1)}) \\
& + \sum_{\boldsymbol{\lambda}}\sum_{\boldsymbol{\lambda}'} \psi_{\boldsymbol{\lambda}2}(\mathbf{r};k_p^{(1)})t_{\boldsymbol{\lambda};\boldsymbol{\lambda}'}^{(33)}a_{\boldsymbol{\lambda}'}(\hat{k}^{(i)}). \qquad (1)
\end{aligned}
$$

The quantity $R(k_z^{(i)})$ is the plane-wave amplitude reflection

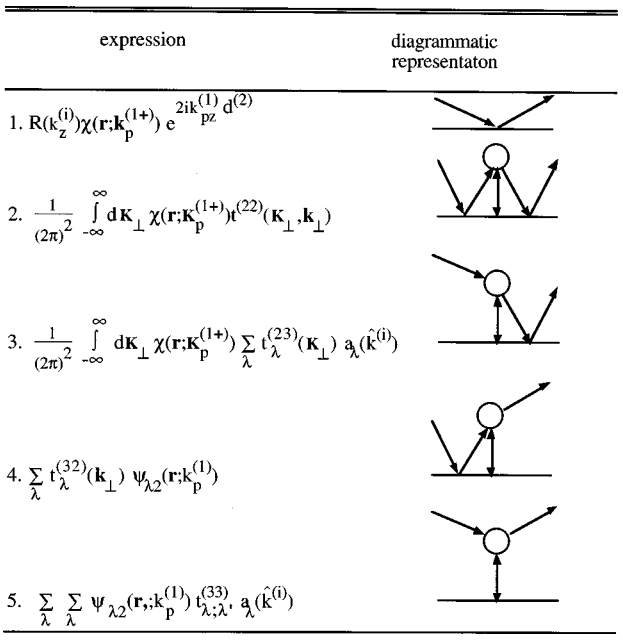

FIG. 1. Diagrammatic representation of scattering processes from a target near a planar interface.

coefficient for the sediment with $\mathbf{k}^{(i)}=k_p^{(1)}\sin\theta^{(i)}[\cos\phi^{(i)}\hat{x}+\sin\phi^{(i)}\hat{y}]k_p^{(i)}\cos\theta^{(i)}\hat{z}$. The quantity $\chi(\mathbf{r};\mathbf{k}_p^{(1+)})$ is an outgoing Weyl plane wave and $\psi_{\boldsymbol{\lambda}2}(\mathbf{r};k_p^{(1)})$ is an outgoing spherical wave. The spherical spectral amplitude of the incident field is $a_{\boldsymbol{\lambda}}(\hat{k}^{(i)})$ where $\boldsymbol{\lambda}=(\lambda,\mu,\nu)$ with $\lambda=1,2$, $0\leqslant\nu\leqslant\infty$, and $0\leqslant\mu\leqslant\nu$. Specific representations of these functions are given in Ref. 1. The quantities $t^{(22)}(\mathbf{K}_\perp,\mathbf{k}_\perp)$, $t_{\boldsymbol{\lambda}}^{(23)}(\mathbf{K}_\perp)$, $t_{\boldsymbol{\lambda}}^{(32)}(\mathbf{K}_\perp)$, and $t_{\boldsymbol{\lambda};\boldsymbol{\lambda}'}^{(33)}$ are T-matrices that describe four scattering processes that are shown diagrammatically in Fig. 1. $t^{(22)}(\mathbf{K}_\perp,\mathbf{k}_\perp)$ describes scattering from the boundary accompanied by target–boundary multiple scattering; $t_{\boldsymbol{\lambda}}^{(23)}\times(\mathbf{K}_\perp)$ describes scattering from the boundary of the field produced by target–boundary multiple scattering of the scatter from the target; $t_{\boldsymbol{\lambda}}^{(32)}(\mathbf{k}_\perp)$ is essentially the inverse of $t_{\boldsymbol{\lambda}}^{(23)}(\mathbf{K}_\perp)$ and describes scattering from the target of the field produced by target–boundary multiple scattering of the scatter from the boundary; and $t_{\boldsymbol{\lambda};\boldsymbol{\lambda}'}^{(33)}$ describes target scattering accompanied by target–boundary multiple scattering. In the absence of the interface, this term describes free-field scattering from the target. The free-field T-matrix for plane-wave scattering from a planar interface is $t^{(2)}(\mathbf{K}_\perp,\mathbf{K}'_\perp)=(2\pi)^2\delta(\mathbf{K}_\perp-\mathbf{K}'_\perp)R(K_{pz}^{(1)})$, and when it is used to evaluate the expressions for the zeroth-order T-matrices that include target-interface multiple scattering given in Ref. 1, these T-matrices are given by

$$t^{(22)}(\mathbf{K}_\perp,\mathbf{K}'_\perp)=R(K_{pz}^{(1)})t^{(32)}(\mathbf{K}_\perp,\mathbf{K}'_\perp)e^{2iK_{pz}^{(1)}d^{(2)}}, \quad (2a)$$

$$t_{\boldsymbol{\lambda}}^{(23)}(\mathbf{K}_\perp)=R(K_{pz}^{(1)})t_{\boldsymbol{\lambda}}^{(33)}(\mathbf{K}_\perp)e^{2iK_{pz}^{(1)}d^2}, \quad (2b)$$

$$t_{\boldsymbol{\lambda}}^{(32)}(\mathbf{K}_\perp)=\sum_{\boldsymbol{\lambda}'} t_{\boldsymbol{\lambda};\boldsymbol{\lambda}'}^{(33)}t_{\boldsymbol{\lambda}'}^{(2)}(\mathbf{K}_\perp;d^{(2)}), \quad (2c)$$

and

$$t_{\boldsymbol{\lambda};\boldsymbol{\lambda}'}^{(33)}=[\mathbf{T}^{(\mathbf{3})^{-1}}-\Sigma]_{\boldsymbol{\lambda};\boldsymbol{\lambda}'}^{-1}, \quad (2d)$$

with

$$\Sigma_{\boldsymbol{\lambda};\boldsymbol{\lambda}'}=\int_{-\infty}^{\infty} d\mathbf{K}'_\perp R(K_{pz}^{\prime(1)})a_{\boldsymbol{\lambda}}(\hat{K}_p^{\prime(1+)}) \times b_{\boldsymbol{\lambda}'}(\hat{K}_p^{\prime(1-)})e^{2iK'_{pz}d^{(2)}}, \quad (2e)$$

and their projections

$$t_{\boldsymbol{\lambda}}^{(2)}(\mathbf{K}'_\perp;d^{(2)})=a_{\boldsymbol{\lambda}}(\hat{K}_p^{\prime(1+)})R(K_{pz}^{\prime(1)})e^{2iK_{pz}^{\prime(1)}d^{(2)}}, \quad (2f)$$

$$t^{(32)}(\mathbf{K}_\perp,\mathbf{K}'_\perp)=(2\pi)^2\sum_{\boldsymbol{\lambda}} b_{\boldsymbol{\lambda}}(\hat{K}_p^{(1-)})t_{\boldsymbol{\lambda}}^{(32)}(\mathbf{K}'_\perp), \quad (2g)$$

$$t_{\boldsymbol{\lambda}}^{(33)}(\mathbf{K}_\perp)=(2\pi)^2\sum_{\boldsymbol{\lambda}'} b_{\boldsymbol{\lambda}'}(\hat{K}_p^{(1-)})t_{\boldsymbol{\lambda};\boldsymbol{\lambda}'}^{(33)}, \quad (2h)$$

$$T_{\boldsymbol{\lambda}}^{(3)}(\mathbf{K}_\perp)=\sum_{\boldsymbol{\lambda}'} b_{\boldsymbol{\lambda}'}(\hat{K}_p^{(1-)})T_{\boldsymbol{\lambda}';\boldsymbol{\lambda}}^{(3)}, \quad (2i)$$

with $K_{pz}^{(1)}=\sqrt{k_p^{(1)^2}-K_x^2-K_y^2}$. The quantity $T_{\boldsymbol{\lambda}';\boldsymbol{\lambda}}^{(3)}$ is the free-field T-matrix for the target constructed on a spherical basis. The quantities $a_{\boldsymbol{\lambda}}(\hat{K})$ and $b_{\boldsymbol{\lambda}}(\hat{K})$ are, respectively, the spectral amplitudes in a spherical wave representation of a plane wave and a plane-wave representation of an outgoing spherical wave, i.e., a $\psi_{\boldsymbol{\lambda}2}(\mathbf{r};k)$. Explicit expressions for these quantities are given in Ref. 1.

The T-matrix $t_{\boldsymbol{\lambda};\boldsymbol{\lambda}'}^{(33)}$ may be formally expanded in an infinites series so that

$$t_{\boldsymbol{\lambda};\boldsymbol{\lambda}'}^{(33)}=T_{\boldsymbol{\lambda};\boldsymbol{\lambda}'}^{(3)}+\sum_{\boldsymbol{\lambda}_1}\sum_{\boldsymbol{\lambda}_2} T_{\boldsymbol{\lambda};\boldsymbol{\lambda}_1}^{(3)}\Sigma_{\boldsymbol{\lambda}_1;\boldsymbol{\lambda}_2}T_{\boldsymbol{\lambda}_2;\boldsymbol{\lambda}'}^{(3)} + \sum_{\boldsymbol{\lambda}_1}\sum_{\boldsymbol{\lambda}_2}\sum_{\boldsymbol{\lambda}_3}\sum_{\boldsymbol{\lambda}_4} T_{\boldsymbol{\lambda};\boldsymbol{\lambda}_1}^{(3)}\Sigma_{\boldsymbol{\lambda}_1;\boldsymbol{\lambda}_2}T_{\boldsymbol{\lambda}_2;\boldsymbol{\lambda}_3}^{(3)} \times\Sigma_{\boldsymbol{\lambda}_3;\boldsymbol{\lambda}_4}T_{\boldsymbol{\lambda}_4;\boldsymbol{\lambda}'}^{(3)}+\cdots. \quad (3)$$

This is the Dyson equation for target–boundary scattering, and since it describes the multiple scattering process between the boundary and the target, Σ is called the target-boundary multiple scattering vertex. The multiple scattering vertex describes a process in which an outgoing spherical wave from the target is projected onto a plane wave, the plane wave is reflected from the boundary, and then the reflected plane wave is projected onto another spherical wave that is incident on the target. Although the free-field T-matrix $T_{\boldsymbol{\lambda};\boldsymbol{\lambda}'}^{(3)}$ for a spherical target is diagonal, the Σ matrix is not and, consequently, neither is $t_{\boldsymbol{\lambda};\boldsymbol{\lambda}'}^{(33)}$: The dynamics introduced by the target–boundary multiple scattering vertex are not spherically symmetric and the spherical symmetry is broken. However, when the target is a hemispherical endcapped cylinder, dynamical symmetry breaking occurs only when the symmetry axis of the cylinder is rotated with respect to the normal to the planar boundary.

II. NUMERICAL CONSIDERATIONS

A. Target scattering

In the following, some of the numerical techniques and considerations used in the evaluation of Eq. (1) are de-

scribed. Evaluation of the T-matrices for the rigid and soft hemispherical endcapped cylinders is complicated by the fact that they are constructed on a spherical basis so that the order of the matrix necessary to obtain a numerically convergent solution rapidly increases with aspect ratio $[a/(L+a)]$ (L and a are, respectively, the half-length and radius of the cylinder) and frequency, and the Q-matrix, from which the T-matrices are calculated, rapidly becomes ill-conditioned. The ill-conditioning is caused by loss of precision due to large values of some of the matrix elements produced by the spherical Hankel functions. To mitigate ill-conditioning problems, the preconditioning algorithm developed by Waterman,[16] in which Gaussian elimination is used to reset to zero the large terms, was used to precondition the cylinder Q-matrix elements. It is important to note that this algorithm provides a T-matrix that is explicitly symmetric and unitary so that these symmetries cannot be used to verify the correctness of the T-matrix elements. However, since it was not used to evaluate the T-matrices for spherical targets, unitarity and symmetry were used to verify the correctness of the elements of these T-matrices.

To perform the integration over the polar angle θ that occurs in the matrix elements, the integral was partitioned into angular integrals over the endcap and the cylinder. Then a 32-point Gauss–Legendre algorithm with adaptive subsectioning was used to evaluate each integral. In each case, subsectioning was continued until the real and imaginary parts of the integral converged numerically to within an infinitesimal $\varepsilon=0.01$ or a maximum of 100 subpartitions was reached.

To validate the computer code, the length of the cylinder was set to zero and scattering from rigid and soft spheres was calculated, and the results were compared with those from the sphere T-matrix codes. Essentially identical results were obtained so that these calculations verified the overall numerical integration scheme, the procedure to obtain the T-matrix, and the diagonal Q-matrix elements. Then scattering from a rigid hemispherical endcapped cylinder was evaluated and the results were compared with those obtained by Sarkissian *et al.*[17] Essentially identical results were obtained so that these calculations verified the off-diagonal Q-matrix elements that include the polar angle integration over the cylinder. These calculations verified the correctness of all matrix elements and procedures necessary to calculate scattering from a rigid finite cylinder with hemispherical endcaps.

Numerical evaluation of scattering from a hemispherical endcapped cylinder is significantly more intensive than scattering from a sphere in at least three respects: (1) The Q-matrix elements require numerical integration. (2) It is necessary to evaluate the rotation matrix. (3) Since a large number of spherical wave modes is required to obtain numerical convergence, it is necessary to allocate memory for several high-order arrays. Since the number of spherical wave modes $(\nu+1)^2$ increases with kL, memory limitations restricted calculations to those for which all convergence criteria were satisfied with $\nu\leqslant 24$ which occurred for $k(L+a)\leqslant 10$.

B. Target–boundary multiple scattering vertex

To calculate the target–boundary multiple scattering vertex and projections of quantities constructed on a spherical basis onto a Weyl plane-wave basis and vice versa, it is necessary to calculate the spectral amplitudes $a_{\boldsymbol{\lambda}}(\hat{K})$ and $b_{\boldsymbol{\lambda}}(\hat{K})$. Evaluation of these quantities requires evaluation of a Legendre function with both pure real and imaginary arguments. As noted in Ref. 1, the proper analytic continuation of the associated Legendre function onto the physical Reimann sheet for an imaginary argument $i|z|$ with $|z|>1$ is $P_\nu^\mu(i|z|)$. These functions were evaluated and the results verified by comparison with tabular values.[18]

Evaluation of the elements of the target–boundary multiple scattering vertex requires evaluation of the wave number integral in Eq. (2e). Since evaluation of this integral requires considerable computational effort, it is important to note that the number of elements that need to be evaluated can be reduced by using the symmetry $\Sigma_{\boldsymbol{\lambda};\boldsymbol{\lambda}'}=\Sigma_{\boldsymbol{\lambda}';\boldsymbol{\lambda}}$. To begin, a change of variables was made from rectangular to polar coordinates and then, since the plane-wave reflection coefficient is independent of azimuthal angle ϕ_K, the ϕ_K-integration was performed. The resulting expression for $\Sigma_{\boldsymbol{\lambda}\boldsymbol{\lambda}'}$ is given by

$$\Sigma_{\boldsymbol{\lambda};\boldsymbol{\lambda}'}=\delta_{\lambda,\lambda'}\delta_{\mu,\mu'}N_{\boldsymbol{\lambda}\boldsymbol{\lambda}'}\times\frac{1}{k_p^{(1)}}\int_0^\infty dK\,\frac{K}{K_{pz}^{(1)}}\,R(K_{pz}^{(1)})P_\nu^\mu(K_{pz}^{(1)}/k_p^{(1)})\times P_{\nu'}^{\mu'}(K_{pz}^{(1)}/k_p^{(1)})e^{2iK_{pz}^{(1)}d^{(2)}},\tag{4a}$$

with

$$N_{\boldsymbol{\lambda};\boldsymbol{\lambda}'}=2\pi i^{(\nu-\nu')}(-1)^{(\nu+\mu')}\left(\varepsilon_\mu\,\frac{2\nu+1}{4\pi}\,\frac{(\nu-\mu)!}{(\nu+\mu)!}\right)^{1/2}\times\left(\varepsilon_{\mu'}\,\frac{2\nu'+1}{4\pi}\,\frac{(\nu'-\mu')!}{(\nu'+\mu')!}\right)^{1/2}\tag{4b}$$

and $K_{pz}=\sqrt{{k_p^{(1)}}^2-K^2}$. Evaluation of the K-integral is complicated by the singularity at the branch point $K=k_p^{(1)}$. To evaluate the singular K-integral, the contour was deformed into the fourth quadrant of the complex K-plane by making the substitution $K=K'-i\varepsilon_K$, with $\varepsilon_K=3K_{\max}^2/2\pi k_p^{(1)}N_s$, and the integration was truncated at $K=K_{\max}$, for which the integrand was less than 10^{-4}.[19,20] The value of ε_K given here differs from that given in Ref. 19 by the factors $K_{\max}/k_p^{(1)}$ and $1/\log e$. Initially, these factors were introduced as a result of a programming error. However, it was discovered that this value of ε_K provided a more accurate result than the form given in Ref. 19. It is important to note that the integration was performed on the physical Riemann sheet of the complex K-plane, and on this sheet there are no poles of the reflection coefficient in the fourth quadrant, so that contributions from contour deformations around poles of the reflection coefficient do not arise. To evaluate the resulting integral, a Gauss–Legendre algorithm with adaptive subpartitioning and 100 sample points per subpartition was used. The length of each subpartition was $\Delta K=k_p^{(1)}/N_K$, where N_K is an integer, so that the deflected branch point is always

on the endpoint of a subpartition. It was found that this method for calculating ΔK seemed to improve the accuracy of the calculation. The integral was evaluated first with $N_K=1$ and $N_s=K_{\max}/k_p^{(1)}+1$ subpartitions. Then N_K was incremented by one, the integral evaluated with the new subpartitioning, and the new result compared with the previous result. The process was repeated until the real and imaginary parts of the integral converged numerically to within $\varepsilon=0.01$.

The number of spherical wave modes used to calculate the scattered pressure field $p^{(1s)}(\mathbf{r})$ was determined in the following manner: First, free-field target scattering was calculated and the number of spherical wave modes iterated until the scattered pressure field and form function converged numerically on two successive iterations. It was found that two successive convergences were required to avoid premature convergence due to oscillations of the Bessel functions that occur in the T-matrices. Then the target–boundary scattering calculation was begun at $\nu=\nu_0-4$, where ν_0 is the value of ν for which convergent free-field target scattering occurred, and then ν was iterated until the real and imaginary parts of $p^{(1s)}(\mathbf{r})$ converged numerically to within $\varepsilon=0.01$.

Since the computational effort required to populate the $t^{(33)}_{\boldsymbol{\lambda};\boldsymbol{\lambda}'}$ array, evaluate the target–boundary multiple scattering vertex Σ, and iterate the number of wave modes to obtain a numerically convergent pressure field is considerable, a CRAY T3D was used to obtain the numerical results shown in this paper.

III. NUMERICAL RESULTS

In this paper, the effects of target–boundary scattering as given by the last term in Eq. (1) are considered. The quantity of interest is target strength given by

$$\mathrm{TS}=10\log\frac{1}{4\pi k_p^{(1)^2}}\left|\sum_{\boldsymbol{\lambda}}(-i)^{\nu}p^{(1s)}_{\boldsymbol{\lambda}}Y_{\boldsymbol{\lambda}}(\theta^{(f)},\phi^{(f)})\right|^2, \tag{5a}$$

with

$$p^{(1s)}_{\boldsymbol{\lambda}}=\begin{cases}\displaystyle\sum_{\boldsymbol{\lambda}'}T^{(3)}_{\boldsymbol{\lambda};\boldsymbol{\lambda}'}a_{\boldsymbol{\lambda}'}(\hat{k}^{(i)}) & \text{(free-field target scattering)}\\ \displaystyle\sum_{\boldsymbol{\lambda}'}t^{(33)}_{\boldsymbol{\lambda};\boldsymbol{\lambda}'}a_{\boldsymbol{\lambda}'}(\hat{k}^{(i)}) & \text{(target–interface scattering)}\end{cases}, \tag{5b}$$

where $\theta^{(f)}$ and $\phi^{(f)}$ are, respectively, the polar and azimuthal angles of the field point. The free-field T-matrix $T^{(3)}_{\boldsymbol{\lambda};\boldsymbol{\lambda}'}$, and the T-matrix that includes target–boundary scattering $t^{(33)}_{\boldsymbol{\lambda};\boldsymbol{\lambda}'}$, are used to calculate the spectral amplitude of the scattered field so that the extent to which target strength that includes target-boundary multiple scattering differs from the free-field target strength can be assessed.

To validate the formalism and computer code, calculations identical to those performed by Gaunaurd and Huang[9,10] were performed: The backscattered form functions

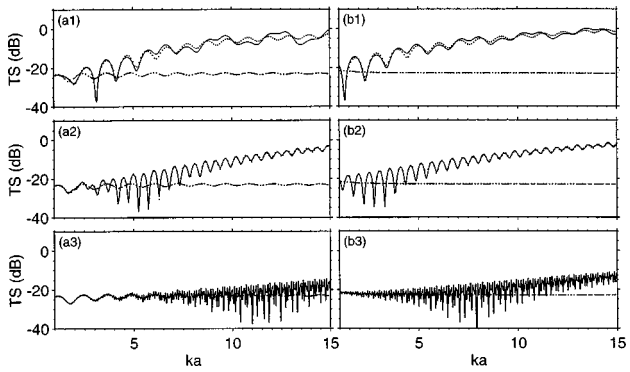

FIG. 2. Backscattered target strength versus ka for rigid $[(a1)$-$(a3)]$ and soft $[(b1)$-$(b3)]$ spheres in an infinite fluid medium $(-\cdot)$ and near a rigid boundary with $d^{(2)}=1.0$ m $[(a1)$ and $(b1)]$, $d^{(2)}=2.5$ m $[(a2)$ and $(b2)]$, and $d^{(2)}=12.5$ m $[(a3)$ and $(b3)]$, with $\theta^{(i)}=0°$ including all orders of target-boundary multiple scattering $(-)$ and a single order of target-boundary scattering $(\cdots)$.

for rigid and soft spheres near rigid and soft boundaries with and without the target–boundary multiple scattering were calculated as a function of $ka=k_p^{(1)}a$ from $ka=1$ to 15 with $\theta^{(i)}=\theta^{(f)}=45°$, $a=0.5$ m, $d^{(2)}=1.0$, 2.5 and 12.5 m. The results of these calculations were found to be essentially identical to those of Gaunaurd and Huang.

The parameters used to obtain the numerical results that follow are $\theta^{(i)}=\theta^{(f)}=0°$, $\phi^{(i)}=0°$, $\phi^{(f)}=180°$, $a=L=0.5$ m, $c_p^{(1)}=1480$ m/s, and $\rho_f^{(1)}=1000$ kg/m^3, and those for a fluid-saturated sandy sediment given by Chotiros.[21] The parameters for fluid and elastic sediments are, respectively, the same as those for the ''classical'' pressure and shear waves of the poroelastic sediment with the porosity set to zero, so that some of the effects of changing the acoustic model of the sediment, i.e., the dynamical degrees of freedom, can be assessed. These parameters remain fixed unless specifically noted otherwise. The plane-wave reflection coefficients for fluid and elastic sediments are well known[22] and the reflection coefficient for a fluid-saturated poroelastic sediment suitable for use in the present problem is given in Appendix B.

A. Scattering from rigid and soft spheres

To provide an estimate of the relative importance of high-order multiple scattering in the target–boundary scattering process, the Dyson equation for $t^{(33)}_{\boldsymbol{\lambda};\boldsymbol{\lambda}'}$ was truncated at first order in Σ so that only a single target–boundary scattering was included. Then both the exact and approximate expressions of the multiple scattering vertex were used to perform calculations; some of the results of these calculations are shown in Figs. 2 and 3.

Figure 2 shows backscattered target strength as a function of ka for a plane-wave normally incident on rigid $[(a1)-(a3)]$ and soft $[(b1)-(b3)]$ spheres in an infinite fluid medium and near a rigid boundary for $d^{(2)}=1$ m $[(a1)$ and $(b1)]$, $d^{(2)}=2.5$ m $[(a2)$ and $(b2)]$, and $d^{(2)}=12.5$ m $[(a3)$ and $(b3)]$, and Fig. 3 shows similar results for a soft boundary. The exact calculations are similar to the ''benchmark'' calculations performed by Gaunaurd and Huang[9,10] and are shown here to contrast with the approximate calcu-

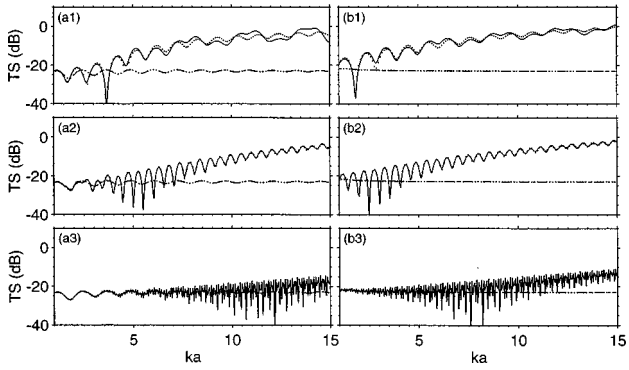

FIG. 3. Same calculations as shown in Fig. 2 for a soft boundary.

lations to assess the relative importance of high-order multiple scattering and to contrast with similar results for penetrable sediments and hemispherical endcapped cylinders to assess the importance of target geometry and sediment properties on target-boundary scattering. These figures show that when a plane wave is normally incident on a rigid or soft sphere near a rigid or soft boundary, target–boundary scattering may be the dominant contribution to target strength and significantly change the target strength of both types of spheres from their free-field values, and that the effect of target–boundary multiple scattering depends on the type of sphere, target–boundary separation, type of boundary, and ka. For example, when $ka=15$ and a hard (soft) sphere is $d^{(2)}=1.0$ m away from a hard boundary, target strength that includes target–boundary scattering is 22.6 dB (20.2 dB) higher than the free-field target strength, but decreases to 1.4 dB (10.2 dB) when $d^{(2)}=12.5$ m. When the boundary is soft, target strength that includes target–boundary scattering is 15 dB (24.1 dB) higher than the free-field target strength when $d^{(2)}=1.0$ m, but decreases to 8.6 dB (9.9 dB) when $d^{(2)}=12.5$ m.

These figures also show that the maxima and minima that occur when target–boundary scattering occurs between a hard sphere and either type of boundary may differ in shape, amplitude, location, and frequency from the free-field maxima and minima, and that for a soft sphere, target–boundary scattering introduces maxima and minima and produces a fundamental change in the frequency dependence of the target strength. This result may be understood by consideration of the Dyson equation. The Dyson equation suggests that target–boundary scattering may be regarded as the superposition of free-field target scattering and target–boundary scattering or as the superposition of the free-field scatter of a plane wave and the free-field scatter of field with spectral amplitude $A_{\boldsymbol{\lambda}'}(\hat{k}^{(i)})$ given by

$$A_{\boldsymbol{\lambda}'}(\hat{k}^{(i)})=\sum_{\boldsymbol{\lambda}_1}\sum_{\boldsymbol{\lambda}_2}\Sigma_{\boldsymbol{\lambda}';\boldsymbol{\lambda}_1}T^{(3)}_{\boldsymbol{\lambda}_1;\boldsymbol{\lambda}_2}a_{\boldsymbol{\lambda}_z}(\hat{k}^{(i)})+\sum_{\boldsymbol{\lambda}_1}\sum_{\boldsymbol{\lambda}_2}\sum_{\boldsymbol{\lambda}_3}\sum_{\boldsymbol{\lambda}_4}\Sigma_{\boldsymbol{\lambda}';\boldsymbol{\lambda}_1}T^{(3)}_{\boldsymbol{\lambda}_1;\boldsymbol{\lambda}_2}\Sigma_{\boldsymbol{\lambda}_2;\boldsymbol{\lambda}_3}\times T^{(3)}_{\boldsymbol{\lambda}_3;\boldsymbol{\lambda}_4}a_{\boldsymbol{\lambda}_4}(\hat{k}^{(i)})+\cdots, \tag{6}$$

so that the pressure field scattered from the target is

$$p^{(33)}(\mathbf{r})=\sum_{\boldsymbol{\lambda}}\sum_{\boldsymbol{\lambda}'}\psi_{\boldsymbol{\lambda}2}(\mathbf{r};k_p^{(1)})t^{(33)}_{\boldsymbol{\lambda};\boldsymbol{\lambda}'}a_{\boldsymbol{\lambda}'}(\hat{k}^{(i)})=\sum_{\boldsymbol{\lambda}}\sum_{\boldsymbol{\lambda}'}\psi_{\boldsymbol{\lambda}2}(\mathbf{r};k_p^{(1)})T^{(3)}_{\boldsymbol{\lambda};\boldsymbol{\lambda}'}A_{\boldsymbol{\lambda}'}(\hat{k}^{(i)}). \tag{7}$$

Since free-field scattering from rigid and soft spheres is well understood in terms of interference between the reflected and circumnavigating creeping waves, the result given by Eq. (7) suggests that target–boundary scattering may be understood, at least qualitatively, in terms of the interference between creeping waves excited by free-field plane-wave scattering, creeping waves excited by scattering of a field with spectral amplitude $A_{\boldsymbol{\lambda}'}(\hat{k}^{(i)})$, and the reflected fields.

Creeping waves excited by target–boundary scattering differ from those excited by the incident plane wave in that they depend on the boundary properties, incidence angle, and target–boundary separation. Target–boundary scattering may produce secondary maxima (minima) when the creeping waves excited by target–boundary scattering interfere constructively (destructively) with the plane-wave-excited circumnavigating creeping waves and the reflected waves.

Figures 2 and 3 show that for a fixed target–boundary separation and for the range of frequencies shown in these figures, target–boundary scattering tends to increase backscattered target strength as ka increases, that the amplitudes of the interference maxima and minima introduced by target–boundary scattering tend to decrease as ka and $d^{(2)}$ increase, that the frequency of the amplitude oscillations increases with $kd^{(2)}$, and that the phase difference between the amplitude oscillations for the hard and soft boundaries tends to 180° as $d^{(2)}$ increases.

The linearized form of $t^{(33)}_{\boldsymbol{\lambda};\boldsymbol{\lambda}'}$ shows that the fields produced by a single target–boundary scattering between a soft sphere and a hard boundary and between a soft sphere and soft boundary differ in phase by 180° and that the only dependence on the target–boundary separation $d^{(2)}$ is in the phase term $\exp[2iK'_{pz}d^{(2)}]$. Deviations from this phase difference suggest that the single target-boundary scattering approximation is not sufficient and that higher-order multiple scattering occurs. Comparison of the results for a single target–boundary scattering with those for the full high-order multiple scattering series shows that the single target–boundary scattering approximation is not accurate when $d^{(2)}=1$ m, particularly for the soft sphere, and that it is still not always accurate even when the target–boundary separation is increased to $d^{(2)}=2.5$ m. However, although it is somewhat difficult to see in these figures, when $d^{(2)}=12.5$ m, the single target–boundary scattering approximation does seem to be reasonably accurate. Further numerical results, not shown here, suggest that for target–boundary separations larger than $d^{(2)}=12.5$ m, target-boundary scattering becomes negligible.

The fact that target–boundary scattering tends to increase backscattered target strength as ka increases is a consequence of the forward diffracted field: At normal incidence, the forward diffracted field is directed toward the interface below the sphere. As frequency increases, it be-

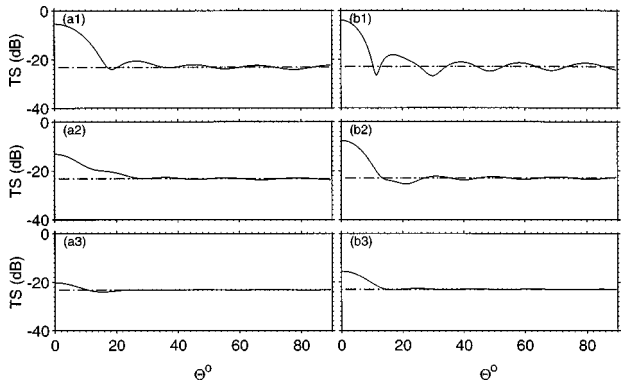

FIG. 4. Backscattered target strength versus $\theta=\theta^{(i)}=\theta^{(f)}$ for rigid $[(a1)$-$(a3)]$ and soft $[(b1)$-$(b3)]$ spheres in an infinite fluid medium $(-\cdot)$ and near a rigid boundary $(-)$ with $d^{(2)}=1.0$ m $[(a1)$ and $(b1)]$, $d^{(2)}=2.5$ m $[(a2)$ and $(b2)]$, and $d^{(2)}=12.5$ m $[(a3)$ and $(b3)]$ and $ka=10$.

comes increasingly ''focused'' in the forward direction and increases the field produced by target–boundary scattering and, when the sphere is near the boundary, results in a high-order multiple scattering process. In contrast, when a plane wave is not normally incident, the forward diffracted field is not directed toward the boundary below the sphere, and as frequency increases, it increases at the expense of that portion of the diffracted field that participates in the target–boundary scattering process and the field produced by the target–boundary scattering decreases. In general, when scattering from complex structures, the dependence of the field produced by target–boundary scattering on incidence angle may be complicated by fields diffracted from structural elements: Strong target–boundary scattering may occur at incidence angles for which scattering from a structural element produces a strong diffracted field in the direction of the boundary below the structure.

To determine some of the effects of sediment type on target–boundary scattering, scattering from rigid and soft spheres near the boundary of a sandy sediment modeled as a viscous fluid, viscoelastic solid, and fluid-saturated poroelastic solid were calculated, in addition to scattering from rigid and soft sediment boundaries. Since the poroelastic sediment is weakly dispersive and the viscous fluid and viscoelastic solid are not dispersive, and to indicate the extent to which target–boundary scattering depends on the polar angle of incidence angle, scattering as a function of the polar angle of

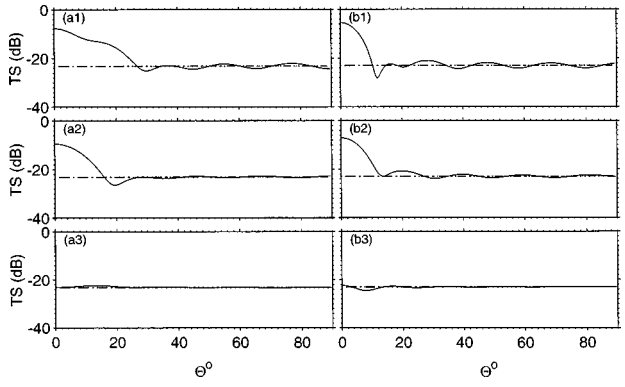

FIG. 5. Same calculations as Fig. 4 for a soft boundary.

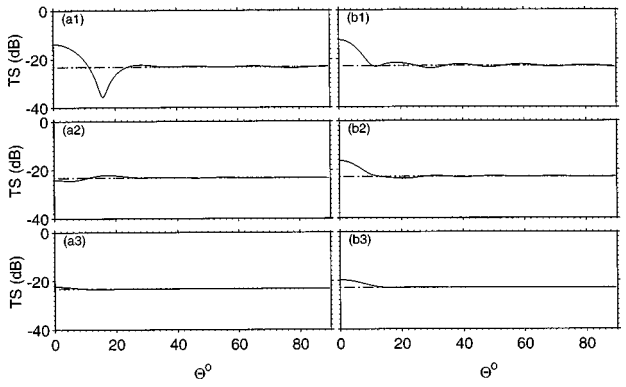

FIG. 6. Same calculations as Fig. 4 for a viscous fluid sediment.

incidence was calculated for $ka=10$. Some of the results of these calculations are shown in Figs. 4–8.

Figures 4–8 show that the effects of target–boundary scattering tend to decrease as $\theta^{(i)}$ and target–boundary separation increase for all the sediment types considered here. It is interesting to note that when the incident plane wave propagates parallel to the boundary, i.e., $\theta^{(i)}=90°$, target-boundary scattering effects become essentially negligible for large target–boundary separations, but when the target is near the boundary, target–boundary scattering effects are still observed. These effects occur as a result of the interaction of the field diffracted from the target in the direction of the boundary. Although it is not shown here, it may be conjectured that scattering from a spherical target and a planar boundary become essentially independent scattering processes even when $\theta^{(i)}=90°$ and the target is near the boundary at frequencies for which the diffracted field is essentially in the forward direction and the diffracted field in the direction of the boundary is negligible.

When the results for scattering from rigid and soft targets near rigid and soft boundaries are compared with those for scattering near penetrable boundaries, it is shown that penetrable sediments reduce the effects of target–boundary scattering. This result suggests that energy is lost from the target–boundary scattering process due to the excitation and propagation of fields in the sediment. Since the results for a viscous fluid and viscoelastic solid are essentially identical, this suggests that energy is lost from the target–boundary scattering process, almost exclusively, due to the excitation and propagation of *p* waves in the sediment. As a result,

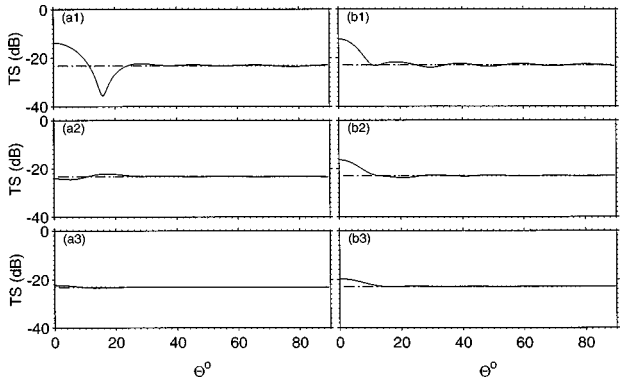

FIG. 7. Same calculations as Fig. 4 for a viscoelastic sediment.

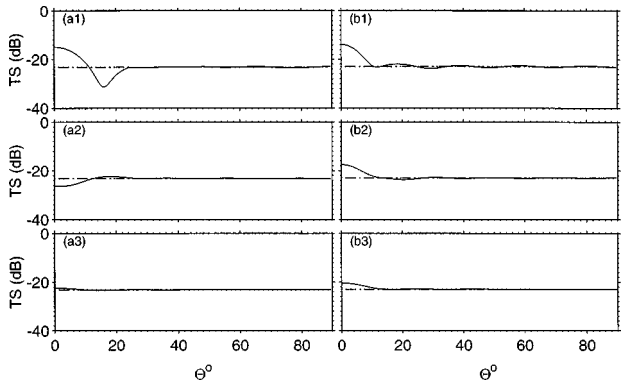

FIG. 8. Same calculations as Fig. 4 for a fluid-saturated poroelastic sediment.

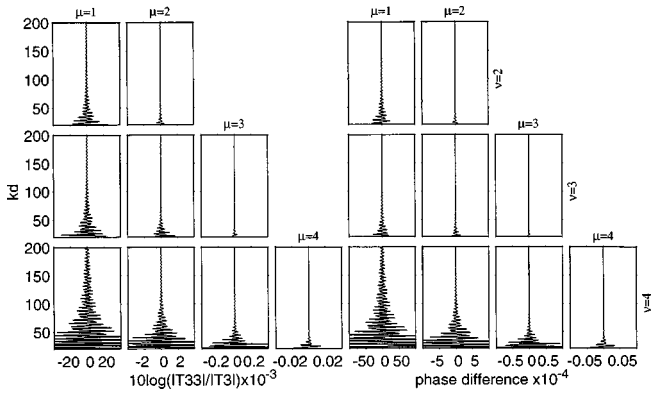

FIG. 10. Same calculations as Fig. 9 for a soft sphere.

when a spherical wave mode is scattered from the target and is represented in terms of a spectrum of Weyl plane waves, the target–boundary scattering process is dominated by that portion of the plane-wave spectrum for which the incident angle is above the critical angle for shear wave excitation. In addition, since the target strength for a sphere near a poroelastic sediment is somewhat lower than that for any of the other sediments, this suggests additional energy is lost due to the excitation and propation of the Biot slow wave.

In the presence of a planar boundary, the spherical symmetry is partially broken and the scattered field is no longer independent of the azimuthal angle or the azimuthal index μ, although the parity symmetry remains as a consequence of the residual cylindrical symmetry. Some of the effects of dynamical symmetry breaking have been observed in the polar angle dependence of target strength shown in Figs. 4–8. However, it is of interest to calculate the effects of symmetry breaking on the T-matrix elements themselves. Figures 9–12 show the magnitude and phase of the T-matrix elements $t^{(33)}_{\nu\mu 1;\nu\mu 1}$ relative to $T^{(3)}_{\nu\mu 1;\nu\mu 1}$ for $\nu=2:4$ and $\mu=1:\nu$ for rigid and soft spheres near rigid and poroelastic sediments as a function of the target–boundary separation for normal incidence with $ka=10$. To obtain the results shown in these figures, the T-matrix elements $t^{(33)}_{\nu\mu 1;\nu\mu 1}$ and $T^{(3,)}_{\nu\mu 1;\nu\mu 1}$ were expressed in polar form so that $t^{(33)}_{\nu\mu 1;\nu\mu 1}=|t^{(33)}_{\nu\mu 1;\nu\mu 1}|\exp[i\phi^{(33)}_{\nu\mu 1;\nu\mu 1}]$ and $T^{(3)}_{\nu\mu 1;\nu\mu 1}=|T^{(3)}_{\nu\mu 1;\nu\mu 1}|\exp[i\phi^{(3)}_{\nu\mu 1;\nu\mu 1}]$. Then the deviation in the magnitude and phase of $t^{(33)}_{\nu\mu 1;\nu\mu 1}$ from $T^{(3,)}_{\nu\mu 1;\nu\mu 1}$ was obtained by calculating $10\log|t^{(33)}_{\nu\mu 1;\nu\mu 1}|/|T^{(3)}_{\nu\mu 1;\nu\mu 1}|$ and $\phi^{(33)}_{\nu\mu 1;\nu\mu 1}-\phi^{(3)}_{\nu\mu 1;\nu\mu 1}$. Symmetry breaking occurs when $10\log|t^{(33)}_{\nu\mu 1;\nu\mu 1}|/|T^{(3)}_{\nu\mu 1;\nu\mu 1}|\neq 0$ and $\phi^{(33)}_{\nu\mu 1;\nu\mu 1}-\phi^{(3)}_{\nu\mu 1;\nu\mu 1}\neq 0$ and differences arise between T-matrix elements that differ only in the index μ.

Symmetry breaking of the T-matrix elements is observed by comparing results in Figs. 9–12 for values of $\mu=1:\nu$ for a fixed ν, i.e., comparing subplots along rows in Figs. 9–12. It is important to note that the horizontal scales in the subplots in these figures decrease by an order of magnitude for each increment in the index μ. These figures show that dynamical symmetry breaking as manifest in the relative magnitude and phase of the T-matrix elements is a somewhat subtle effect, even when the target is near the boundary where the strongest symmetry breaking effects occur. However, these figures also show that symmetry breaking effects depend strongly on target-boundary separation: The symmetry breaking amplitude and phase exhibit interference maxima and minima as $kd^{(2)}$ increases when the target is near the boundary, but the maximum amplitude of these interference maxima and minima decrease as $kd^{(2)}$ increases. For large values of $kd^{(2)}$, interference phenomena are not observed in any of the T-matrix elements, the processes of target and boundary scattering become essentially uncoupled, and spherical symmetry in the target scatter is restored.

In addition, these figures show that the effect of target-

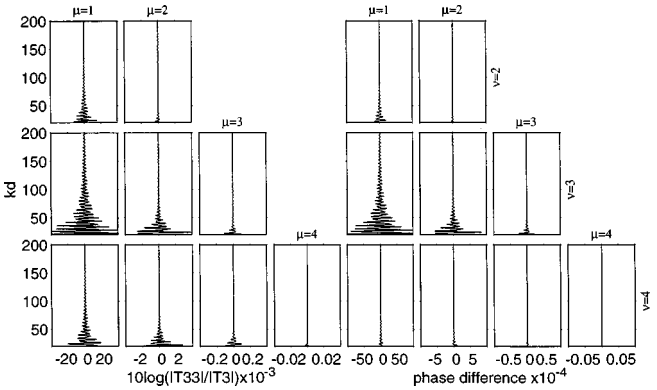

FIG. 9. $10\log|t^{(33)}_{1\nu\mu;1\nu\mu}|/|T^{(3)}_{1\nu\mu;1\nu\mu}$ land phase difference $\phi^{(33)}_{1\nu\mu;1\nu\mu}-\phi^{(3)}_{1\nu\mu;1\nu\mu}$ for $\nu=2:4$ and $\mu=1:\nu$ for a rigid sphere near a rigid boundary with $ka=10$ and $\theta=\theta^{(f)}=\theta^{(i)}=0°$.

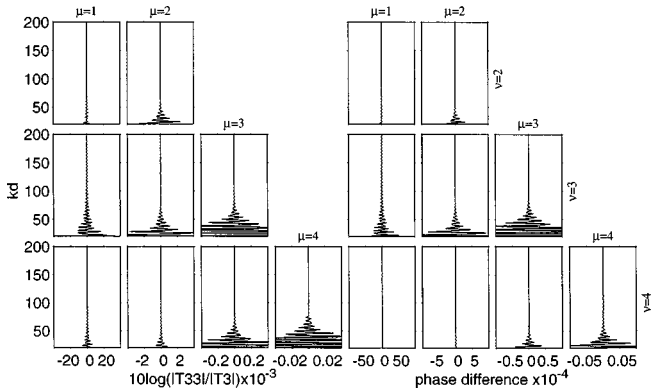

FIG. 11. Same calculations as Fig. 9 for a fluid-saturated poroelastic sediment.

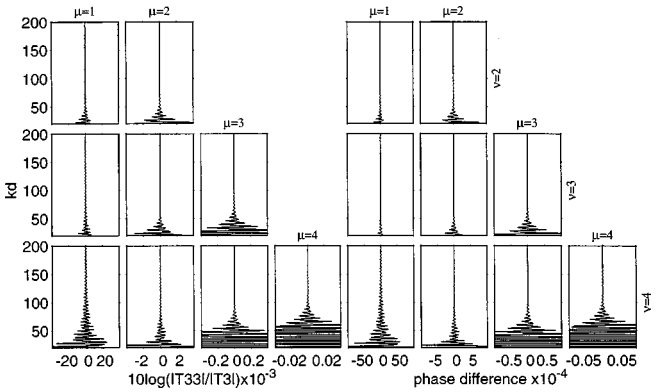

FIG. 12. Same calculations as Fig. 9 for a soft sphere and a fluid-saturated poroelastic sediment.

boundary scattering decreases as μ increases, that target-boundary scattering effects persist longest, i.e., the largest $kd^{(2)}$, for the $\mu=1$ mode, and that the mode most effected by target–boundary scattering depends on the target and the boundary: These results are qualitatively consistent with those obtained by Sammelmann and Hackman,[14] who studied scattering from an elastic sphere in a homogeneous waveguide. They noted that the strength of target–boundary scattering depends on the strength of the lobe in the vertical direction and that the vertical lobes of the associated Legendre polynomials $P_\nu^\mu(\cos\theta)$ tend to decrease as μ increases. For a rigid sphere, the mode most effected by target–boundary scattering is the $\nu=3$ mode, but for a soft sphere, it is the $\nu=4$ mode. This result appears to be true for both types of boundaries considered.

Comparison of the results for a rigid boundary with those for a poroelastic sediment boundary shows that the poroelastic sediment weakens target–boundary coupling for low μ modes but strengthens it for high μ modes. The penetrable sediment weakens the acoustic coupling between the target and the sediment not only by coupling energy into the excitation of *p*-waves in the sediment, but also by coupling to weaker higher-order spherical modes of the *T*-matrix. This result suggests that when scattering from an elastic target near a penetrable boundary, the fine structure in the free-field resonant spectrum introduced by the symmetry breaking is characteristic of the sediment boundary.

B. Scattering from rigid and soft hemispherical endcapped cylinders

In this section, scattering from rigid and soft hemispherical endcapped cylinders near a planar boundary is considered. Since target–boundary scattering depends, among other things, on the field diffracted in the direction of the normal to the boundary, target–boundary scattering from hemispherical endcapped cylinders depends on the orientation of the cylinder with respect to the boundary and the plane of incidence. In the following, the cylinder is rotated so that its symmetry axis is parallel to the planar boundary. In this orientation, the geometric cylindrical symmetry is broken and the dynamics of the target–boundary scattering process may produce dynamical symmetry breaking in the *T*-matrix and target scatter.

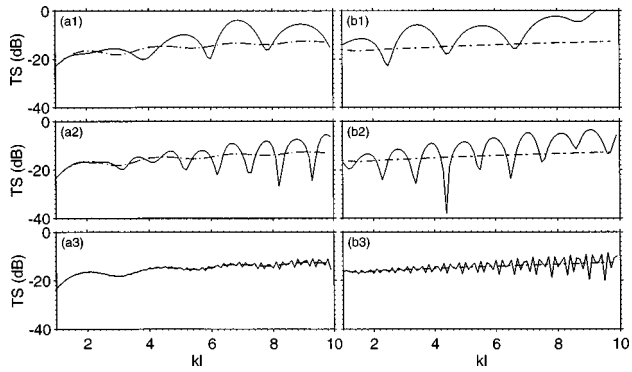

FIG. 13. Backscattered target strength versus $kl=k(L+a)$ for rigid $[(a1)$-$(a3)]$ and soft $[(b1)$-$(b3)]$ horizontally oriented hemispherical endcapped cylinders in an infinite fluid medium $(-\cdot)$ and near a rigid boundary $(-)$ with $d^{(2)}=1.0$ m $[(a1)$ and $(b1)]$, $d^{(2)}=2.5$ m $[(a2)$ and $(b2)]$, and $d^{(2)}=12.5$ m $[(a3)$ and $(b3)]$ for a plane-wave incident at $\theta^{(i)}=0°$.

Calculations of backscattered target strength as a function of $kl=k(L+a)$ and $\theta^{(i)}$ similar to those for rigid and soft spheres were performed for rigid and soft hemispherical endcapped cylinders. Figure 13 shows backscattered target strength as a function of *kl* for a normally incident plane wave, i.e., $\theta^{(i)}=0°$, on horizontally oriented rigid $[(a1)-(a3)]$ and soft $[(b1)-(b3)]$ hemispherical endcapped cylinders in an infinite fluid medium and near a rigid boundary for $d^{(2)}=1$ m $[(a1)$ and $(b1)]$, $d^{(2)}=2.5$ m $[(a2)$ and $(b2)]$, and $d^{(2)}=12.5$ m $[(a3)$ and $(b3)]$, and Fig. 14 shows similar results for a soft boundary. These figures show that the target strength of rigid and soft hemispherical endcapped cylinders that includes target-boundary scattering differs from the free-field target strength and, similar to the target strength of rigid and soft spheres that includes target–boundary scattering shown in Figs. 2 and 3, tends to be dominated by the target–boundary contribution and depends on the type of cylinder, target–boundary separation, type of boundary, and *kl*. However, comparison of the results shown in these figures with similar results for scattering from spheres, shows that the effects of target–boundary scattering for horizontally oriented rigid and soft cylinders are not as dramatic as they are for rigid and soft spheres, and they tend to decrease more rapidly than target-boundary scattering effects for spheres as target–boundary separation increases. However, this result is not generally true and depends on the polar angle of incidence, but in this case is due, in part, to the

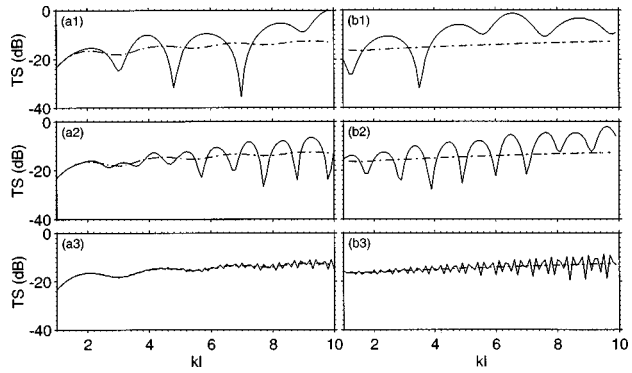

FIG. 14. Same calculations as Fig. 13 for a soft boundary.

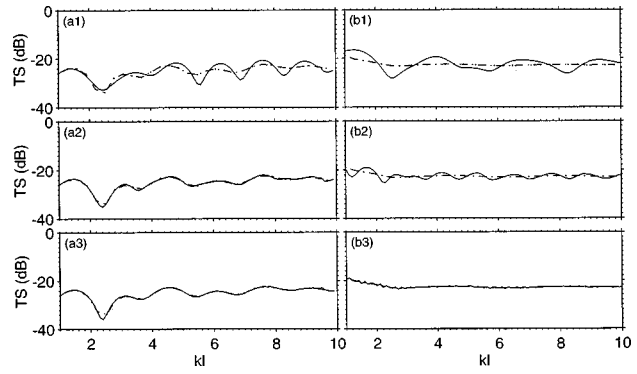

FIG. 15. Same calculations as Fig. 13 for a plane-wave incident at $\theta^{(i)}=45°$ above the axis.

fact cylinders are not as efficient as spheres in ''focusing'' the forward diffracted field.[23]

To illustrate the dependence of target–boundary scattering on the orientation of the cylinder relative to the plane of incidence, scattering was calculated from horizontally oriented rigid and soft hemispherical endcapped cylinders near a rigid boundary for plane waves axially incident with $\phi^{(i)}=0°$ and $\theta^{(i)}=45°$ and radially incident with $\phi^{(i)}=270°$ and $\theta^{(i)}=45°$. The results of these calculations are shown in Figs. 15 and 16. These figures show that target–boundary scattering effects depend strongly on the orientation of the cylinder relative to the plane of incidence. For example, when a plane wave is axially incident on a rigid hemispherical endcapped cylinder located $d^{(2)}=1$ m from a rigid boundary, the maximum positive and negative differences between the free-field target strength and target strength that includes target–boundary scattering are, respectively, 3.2 dB at $kl=2.4$ and -4.6 dB at $kl=5.6$, and for a soft cylinder they are, respectively, 3.9 dB at $kl=1.4$ and -5.0 dB at $kl=2.5$. However, when the plane wave is radially incident, the maximum positive and negative differences between the free-field target strength and target strength that includes target–boundary scattering are, respectively, 2.9 dB at $kl=6.3$ and -4.2 dB at $kl=5.5$, and for a soft cylinder they are, respectively, 4.3 dB at $kl=3.6$ and -16.3 dB at $kl=2.7$. Although numerical results for scattering a plane-wave incident at $\theta^{(i)}=45°$ from rigid and soft spheres near a rigid boundary are not shown here, it was observed that the difference between the target strength that includes target–boundary scattering and the free-field target strength for cylindrical targets tends to be greater than that for spherical targets, particularly for radial incidence. This difference, in part, is due to the fact that a cylinder is not as efficient as a sphere in focusing the forward diffracted field, so when a plane wave is not normally incident, the field diffracted by a cylinder in the direction of the boundary is greater than that for a sphere and, consequently, so are the effects of target–boundary scattering.

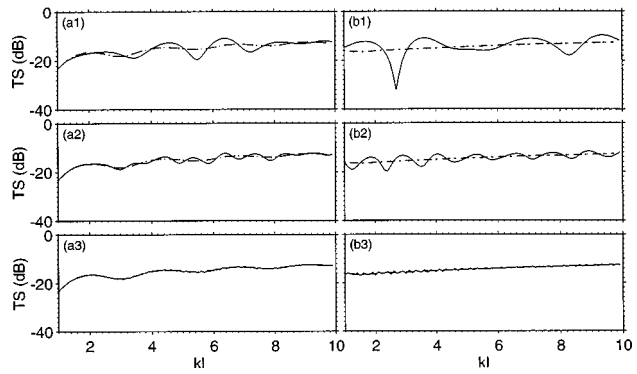

FIG. 16. Same calculations as Fig. 13 for a plane-wave incident at $\theta^{(i)}=45°$ along a radius.

In addition, these figures show that when the cylinders are near the boundary, target–boundary scattering changes the amplitude and location of interference minima and maxima in the target strength frequency dependence for rigid cylinders, and introduces interference maxima and minima in the target strength frequency dependence for soft cylinders. For both cylinder types, the amplitude of the interference maxima and minima produced by target boundary scattering tends to decrease as kl decreases and $kd^{(2)}$ increases. For a fixed frequency, however, the effects of target-boundary scattering depend on cylinder type, target–boundary separation $d^{(2)}$, cylinder orientation, and boundary type. When a rigid cylinder is near either boundary type, target–boundary scattering is essentially negligible when the target–boundary separation $d^{(2)}\geqslant 2.5$ m and $\phi^{(i)}=0°$; however, when $\phi^{(i)}=270°$, target–boundary scattering effects are clearly present when $d^{(2)}=2.5$ but are negligible when $d^{(2)}=12.5$ m. For a soft cylinder, however, target–boundary scattering effects are present when the target–boundary separation $d^{(2)}=2.5$ m for both boundary types and cylinder orientations, but become negligible for both boundary types and orientations when $d^{(2)}=12.5$ m.

To assess some of the effects of different types of sediments on the multiple scattering process between rigid and soft hemispherical endcapped cylinders and a planar sediment boundary, to investigate the extent to which target–boundary scattering produces dynamical symmetry breaking, and to assess the angular dependence of target–boundary multiple scattering for hemispherical endcapped cylinders, backscattered target strength was calculated as a function of the polar angle of incidence in a vertical plane through the center of the cylinder normal to the cylinder axis with $kl=10$ for rigid, soft, and poroelastic sediments. The results of these calculations are shown in Figs. 17–19. Results for viscous fluid and viscoelastic solid sediments are not shown since they were similar to the results for a poroelastic sediment, except for $\theta^{(i)}\lesssim 35°$, where the target strengths were slightly greater than those for the poroelastic sediment in much the same way they were when similar calculations for the spherical targets were considered. This result suggests that the target-boundary scattering process for cylindrical targets is similar to that for spherical targets, and is dominated by the portion of the plane-wave spectrum for which shear waves are not excited in the sediment, and that penetrable sediments tend to decouple target–boundary scattering when energy is lost from the target–boundary scattering process to excite pressure fields in the sediment. These figures show several additional qualitative features that were observed in the corresponding results for spherical targets: The effects of target–boundary scattering tend to be greatest near normal

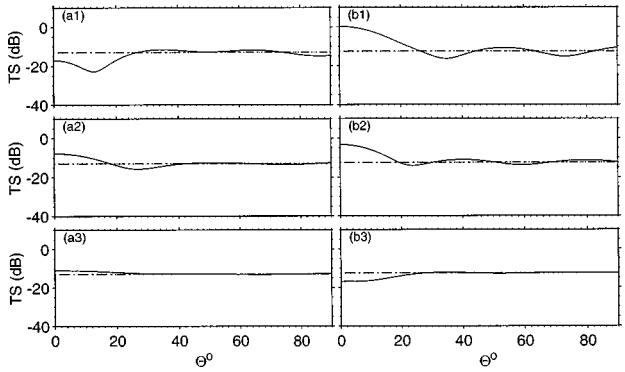

FIG. 17. Backscattered target strength versus $\theta=\theta^{(i)}=\theta^{(f)}$ for horizontally oriented rigid $[(a1)$-$(a3)]$ and soft $[(b1)-(b3)]$ hemispherical endcapped cylinders in an infinite fluid medium $(-\cdot)$ and near a rigid boundary $(-)$ with $d^{(2)}=1.0$ m $[(a1)$ and $(b1)]$, $d^{(2)}=2.5$ m $[(a2)$ and $(b2)]$, and $d^{(2)}=12.5$ m $[(a3)$ and $(b3)]$ and $k(L+a)=10$.

incidence, to decrease as kl, $kd^{(2)}$, and $\theta^{(i)}$ increase for all the sediment types considered, and to persist even when the incident plane wave propagates parallel to the boundary when the target–boundary separation $d^{(2)}=1$ m. For cylindrical targets, however, these effects tend to be enhanced when the plane wave is radially incident and the cylinder is near rigid and soft boundaries.

The free-field target strength of the horizontal cylinder is, of course, independent of the incident polar angle. However, when the cylinder is near a planar boundary, target–boundary scattering may produce dynamical symmetry breaking so that the resulting target strength depends on the polar angle. These figures show that dynamical symmetry breaking occurs and is greatest near normal incidence when the cylinders are near the boundary. For both types of cylinders, dynamical symmetry breaking is observed for all angles when the target–boundary separation $d^{(2)}\lesssim 2.5$ m but when $d^{(2)}=12.5$ m, it is essentially negligible for all angles $\theta^{(i)}\gtrsim 35°$. Figure 19 shows that a penetrable boundary reduces symmetry breaking effects so that it is essentially negligible for all angles $\theta^{(i)}\gtrsim 30°$, even when the target–boundary separation $d^{(2)}=1.0$ m.

IV. CONCLUSIONS

It may be concluded that target–boundary scattering is a multiple scattering process that may significantly change the target strength of a rigid or soft target and that the extent to

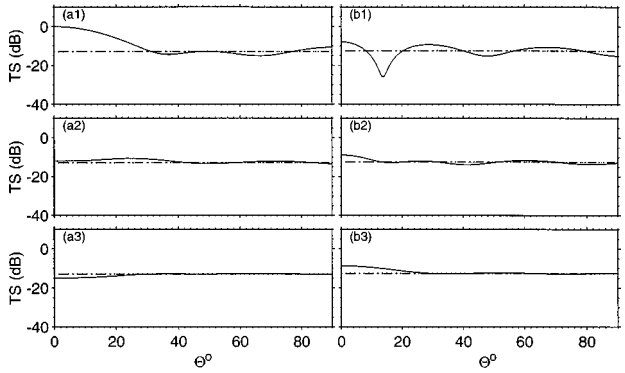

FIG. 18. Same calculations as Fig. 17 for a soft boundary.

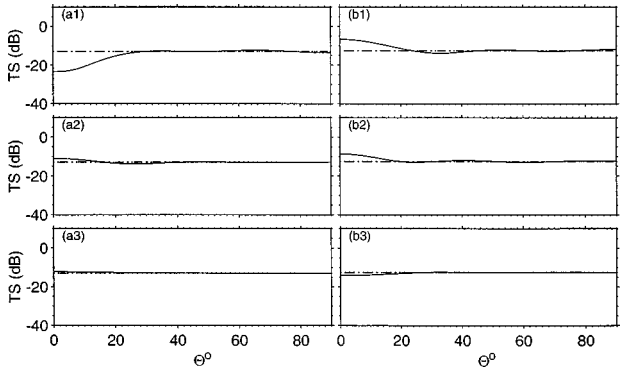

FIG. 19. Same calculations as Fig. 17 for a fluid-saturated poroelastic sediment.

which the target strength is changed depends on the geometry and type of target, target–boundary separation, frequency, incidence angles, and sediment type, and for cylindrical targets, it also depends on cylinder orientation. Target geometry and, when scattering from nonspherical scatterers, target orientation, are important in the target–boundary scattering process since, in part, they determine the field diffracted by the target in the direction of the boundary. Target type, i.e., rigid or soft, is important since it determines the nature of the creeping waves: Free-field creeping waves for soft targets are weaker than those for rigid targets, so that interference maxima and minima produced by target–boundary scattering are more pronounced in scattering from soft targets than from rigid targets.

Target–boundary separation effects the relative phase of the boundary scatter incident on the target so that target strength that includes target–boundary scattering exhibits interference maxima and minima as the target–boundary separation is incremented. However, for sufficiently large target–boundary separations, target–boundary scattering becomes negligible. The minimum target–boundary separation for which target–boundary scattering becomes negligible depends strongly on frequency and incidence angles, moderately on target type, and weakly on sediment type: It tends to be smaller for soft targets than for rigid targets, smaller for penetrable sediments than for rigid or soft sediments, and tends to decrease as frequency and the polar incidence angle increase.

Frequency plays a critical role in the target–boundary scattering process since it strongly influences the field diffracted by the target in the direction of the normal to the boundary below the target and the relative phase of the scatter from the boundary that is rescattered by the target.

Target–boundary scattering depends strongly on whether or not the boundary is penetrable. Penetrable sediment boundaries tend to weaken target–boundary scattering since energy is lost from the target–boundary scattering process due to the excitation of fields within the sediment. However, target–boundary scattering does not seem to excite strong shear waves in the sediment, so that target–boundary scattering from viscous fluid and viscoelastic sediments are essentially identical and somewhat stronger than scattering from a fluid-saturated poroelastic sediment in which Biot slow waves may be excited.

Whether the target–boundary scattering process is approximated by a single target–boundary interaction or is modeled as a high-order multiple scattering process, the total scattered field may be viewed as the superposition of fields produced by free-field scattering of the incident plane wave and the incident field produced by target-boundary scattering, and may be understood, at least qualitatively, in terms of the interference between the creeping waves excited by each of the incident fields and the reflected fields.

ACKNOWLEDGMENTS

We would like to acknowledge Mr. George Petit of the Advanced Scientific and Engineering Center at the Naval Undersea Warfare Center Division Newport, who transformed several computer codes that were developed to run on a CRAY YMP to codes that could run on multiple processors on a CRAY T3D.

APPENDIX A: *T*-MATRIX FOR SCATTERING FROM RIGID AND SOFT FINITE CYLINDERS WITH HEMISPHERICAL ENDCAPS

In this Appendix, the *T*-matrices for scattering from rigid and soft finite cylinders with hemispherical endcaps immersed in an inviscid homogeneous fluid medium are derived. The derivation is similar to that given previously for an elastic cylinder with hemispherical endcaps.[24–26] To simplify the discussion, the superscripts used to denote the various volumes and surfaces in the target–interface problems are temporarily suppressed.

In general, the cylinder orientation is given by a set of three Euler angles α, β, and γ.[27] However, in this paper only rotations for which $\alpha=\gamma=0$ were considered, so that basis functions in the target coordinate system $\psi^{(t)}_{\mathbf{\lambda}\sigma}(\mathbf{r}';k)$ are expressed in terms of basis functions in the space coordinate system $\psi_{\mathbf{\lambda}\sigma}(\mathbf{r};k)$ in the following manner:

$$\psi^{(t)}_{\mathbf{\lambda}\sigma}(\mathbf{r};k)=\sum_{\mu'=-\nu}^{\nu}\mathscr{D}_{\mathbf{\lambda}'\sigma';\mathbf{\lambda}\sigma}(\beta)\psi_{\mathbf{\lambda}'\sigma'}(\mathbf{r}';k) \tag{A1a}$$

with

$$\begin{aligned}\mathscr{D}_{\mathbf{\lambda}'\sigma';\mathbf{\lambda}\sigma}(\beta)=\delta_{\sigma,\sigma'}\delta_{\nu,\nu'}i^{\lambda-\lambda'}\frac{\sqrt{e_\mu e_{\mu'}}}{4}\\ \times[d^{\nu}_{\mu'\mu}(\beta)+(-1)^{\lambda'+\mu'}d^{\nu}_{-\mu'\mu}(\beta)\\ +(-1)^{\lambda+\mu}d^{\nu}_{\mu'-\mu}(\beta)\\ +(-1)^{\lambda'+\lambda+\mu+\mu'}d^{\nu}_{-\mu',-\mu}(\beta)].\end{aligned} \tag{A1b}$$

An explicit representation of $d^{\nu}_{\mu'\mu}(\mathrm{B})$ is given in Ref. 27. It is important to note that since the basis functions used here are real, whereas the basis functions in Ref. 27 are complex, the form of the rotation operator $\mathscr{D}_{\mathbf{\lambda}'\sigma';\mathbf{\lambda}\sigma}(\beta)$ given in Eq. (A1b) differs from that given in Ref. 27.

The surface of the cylinder is given by

$$r'(\theta')=\begin{cases}L\cos\theta'+\sqrt{a^2-L^2\sin^2\theta'}, & 0<\theta'<\theta_0,\\ a/\sin\theta', & \theta_0<\theta'<\pi-\theta_0,\\ -L\cos\theta'+\sqrt{a^2-L^2\sin^2\theta'}, & \pi-\theta_0<\theta'<\pi,\end{cases} \tag{A2}$$

where a and L are, respectively, the radius and half-length of the cylinder and $\theta_0=\tan^{-1}a/L$ is the polar angle of the endcap–cylinder junction.

To evaluate the Helmholtz–Kirchhoff integral, it is necessary to construct the outwardly directed unit normal vector $\hat{n}(\mathbf{r}')=n_r(\theta')\hat{r}'+n_\theta(\theta')\hat{\theta}'$ and the surface area element $ds'=d\Theta' d\phi'$. The quantities $n_r(\theta')$, $n_\theta(\theta')$, and $d\Theta'$ are given by

$$n_r(\theta')=\begin{cases}\sqrt{L-\left(\frac{L}{a}\right)^2\sin^2\theta'}, & 0\leqslant\theta'\leqslant\theta_0;\pi-\theta_0\leqslant\theta'\leqslant\pi,\\ \sin\theta', & \theta_0\leqslant\theta'\leqslant\pi-\theta_0,\end{cases} \tag{A3a}$$

$$n_\theta(\theta')=\begin{cases}\frac{L}{a}\sin\theta', & 0\leqslant\theta'\leqslant\theta_0,\\ \cos\theta', & \theta_0\leqslant\theta'\leqslant\pi-\theta_0,\\ -\frac{L}{a}\sin\theta', & \pi-\theta_0\leqslant\theta'\leqslant\pi,\end{cases} \tag{A3b}$$

and

$$d\Theta'=\begin{cases}\frac{ar'^2(\theta')\sin\theta'}{\sqrt{a^2-L^2\sin^2\theta'}}d\theta', & 0\leqslant\theta'\leqslant\theta_0;\pi-\theta_0\leqslant\theta'\leqslant\pi,\\ r'^2(\theta')d\theta', & \theta_0\leqslant\theta'\leqslant\pi-\theta_0.\end{cases} \tag{A4}$$

It is important to note that the symmetries of $n_r(\theta')$, $n_\theta(\theta')$, and $r'(\theta')$ can be exploited to reduce the range of integration over the surface of the cylinder to $0\leqslant\theta'\leqslant\pi/2$.

The Helmholtz–Kirchhoff integral equation representation of the scattered field, the representations of the incident and scattered fields, and the scalar Green function in terms of spherical space basis functions are given in Ref. 26. Specific representations of the spherical basis functions $\psi_{\mathbf{\lambda}1}(\mathbf{r};k)$ and $\psi_{\mathbf{\lambda}2}(\mathbf{r};k)$ are given in Refs. 26 and 1. The surface fields are represented in terms of target basis functions and are given by

$$\begin{aligned}p_+(\mathbf{r}')=\lambda k\sum_{\mathbf{\lambda}'}p_{\mathbf{\lambda}'}\psi^{(t)}_{\mathbf{\lambda}'1}\\ \times(\mathbf{r}';k)\Big|_{r'\in s'}\quad(\text{rigid boundary})\end{aligned} \tag{A5a}$$

and

$$\hat{n}(\mathbf{r}')\cdot\nabla' p_+(\mathbf{r}')=\lambda k\sum_{\boldsymbol{\lambda}'} p_{\boldsymbol{\lambda}'}\hat{n}(\mathbf{r}')\cdot\nabla'\psi^{(t)}_{\boldsymbol{\lambda}'1}\times(\mathbf{r}';k)\Big|_{r'\in s'}$$

(soft boundary) (A5b)

where s' is the surface of the cylinder.

The representations of the various fields are used in the Helmholtz–Kirchhoff and null-field equations and Eq. (A1) is used to express the surface fields in terms of space basis functions. Then the inner product of these equations and the spherical basis functions defined in the space coordinates system is evaluated. The resulting null-field equation is solved for the surface field spectral amplitude, the result is used in the equation for the scattered field spectral amplitude, and the T-matrix is constructed.

$$T_{\boldsymbol{\lambda};\boldsymbol{\lambda}'}(\hat{\Theta})=\sum_{\boldsymbol{\lambda}''}\sum_{\boldsymbol{\lambda}'''} D_{\boldsymbol{\lambda}\boldsymbol{\lambda}''}(\hat{\Theta})T_{\boldsymbol{\lambda}'';\boldsymbol{\lambda}'''}[D_{\boldsymbol{\lambda}''';\boldsymbol{\lambda}'}(\hat{\Theta})]^{-1}, \tag{A6a}$$

and

$$T_{\boldsymbol{\lambda}'';\boldsymbol{\lambda}'''}=Q_{\boldsymbol{\lambda}''1;\boldsymbol{\lambda}'''1}[Q_{\boldsymbol{\lambda}''2;\boldsymbol{\lambda}'''1}]^{-1}, \tag{A6b}$$

where

$$Q_{\boldsymbol{\lambda}\sigma;\boldsymbol{\lambda}'\sigma'}=ik^2\delta_{\lambda,\lambda'}\delta_{\mu,\mu'}\Delta^{(+)}_{\nu\nu'}M_{\mu,\lambda}N_{\mu,\nu}N_{\mu,\nu'}\int_0^{\pi/2}d\Theta'\times\left\{\frac{\partial}{\partial\chi}z^{(\sigma)}_\nu(\chi)j_{\nu'}(\chi)P^\mu_\nu(\cos\theta')P^\mu_{\nu'}(\cos\theta')n_r+\frac{z^{(\sigma)}_\nu(\chi)}{\chi}j_{\nu'}(\chi)\frac{\partial}{\partial\theta'}P^\mu_\nu(\cos\theta')P^\mu_{\nu'}(\cos\theta')n_\theta\right\}$$

(rigid boundary) (A6c)

and

$$Q_{\boldsymbol{\lambda}\sigma;\boldsymbol{\lambda}'\sigma'}=-ik^2\delta_{\lambda,\lambda'}\delta_{\mu,\mu'}\Delta^{(+)}_{\nu\nu'}M_{\mu,\lambda}N_{\mu,\nu}N_{\mu,\nu'}\int_0^{\pi/2}d\Theta'\times\left\{z^{(\sigma)}_\nu(\chi)\frac{\partial}{\partial\chi}j_{\nu'}(\chi)P^\mu_\nu(\cos\theta')P^\mu_{\nu'}(\cos\theta')n_r+\frac{z^{(\sigma)}_\nu(\chi)}{\chi}j_{\nu'}(\chi)\frac{\partial}{\partial\theta'}P^\mu_\nu(\cos\theta')P^\mu_{\nu'}(\cos\theta')n_\theta\right\}$$

(soft boundary) (A6d)

with

$$\Delta^{(\pm)}_{\nu\nu'}=[1\pm(-1)^{\nu+\nu'}], \tag{A6e}$$

$$N_{\mu,\nu}=\sqrt{\varepsilon_\mu\frac{2\nu+1}{4\pi}\frac{(\nu-\mu)!}{(\nu+\mu)!}}, \tag{A6f}$$

$$M_{\mu,\lambda}=\pi[1+\delta_{\mu,0}(2\delta_{\lambda,2}-1)], \tag{A6g}$$

$\chi=kr'(\theta')$, and ε_μ is the Neumann factor. In writing the elements of the Q-matrix, the ϕ'-integration has been performed and the rotational and mirror symmetries of the cylinder have been exploited to restrict the θ' integration to $0\leqslant\theta'\pi/2\leqslant\theta'$.

APPENDIX B: REFLECTION COEFFICIENT FOR A FLUID-SATURATED POROELASTIC SEDIMENT

In this Appendix, the plane-wave reflection coefficient for a fluid-saturated poroelastic sediment is calculated. The notation closely follows that of Stoll and Kan[28] and Stern *et al.*[29] In the following, the superscript (2) used to designate sediment quantities in this paper is temporarily suppressed.

The equations of motion given by Chotiros[21] for the displacement of the skeletal frame $\mathbf{u}$ and the displacement $\mathbf{w}=\beta\mathbf{W}$, where $\mathbf{W}$ is the displacement of the fluid relative to the solid and β is the sediment porosity, may be separated into a system of two coupled equations for time harmonic transverse fields $\mathbf{u}_t$ and $\mathbf{w}_t$,

$$\nabla\times\nabla\times\mathbf{u}_t=k_s^2\mathbf{u}_t \tag{B1a}$$

and

$$\mathbf{w}_t=\gamma\mathbf{u}_t, \tag{B1b}$$

and a system of two coupled equations for time harmonic longitudinal fields $\mathbf{u}_1$ and $\mathbf{w}_1$,

$$(\nabla^2+\kappa_s^2)\mathbf{u}_1=\zeta_s^2\mathbf{w}_1 \tag{B2a}$$

and

$$(\nabla^2+\chi_f^2)\mathbf{w}_1=\lambda_f^2\mathbf{u}_1. \tag{B2b}$$

Explicit expressions for k_s^2, κ_s^2, ζ_s^2, χ_f^2, and λ_f^2 are given in Ref. 29.

The displacement fields must also satisfy the following boundary conditions:

(i) The fluid movement in and out of the skeletal frame normal to the interface is continuous:

$$\hat{n}(\mathbf{r}')\cdot[\mathbf{u}_-(\mathbf{r}')-\mathbf{w}_-(\mathbf{r}')]=\hat{n}\cdot\mathbf{u}_+(\mathbf{r}'). \tag{B3a}$$

(ii) The traction normal to the surface is continuous:

$$\begin{aligned}\hat{n}(\mathbf{r}')\cdot[\hat{n}(\mathbf{r}')\cdot\vec{\vec{\tau}}_-(\mathbf{r}')]&=\hat{n}(\mathbf{r}')\cdot\{\vec{\vec{I}}[\mu_r\nabla'\cdot\mathbf{u}_-(\mathbf{r}')-C\nabla'\cdot\mathbf{w}_-(\mathbf{r}')]\\&\quad+\mu_r\{[\nabla'\mathbf{u}_-(\mathbf{r}')+\mathbf{u}_-(\mathbf{r}')\nabla']\}\\&=-p_+(\mathbf{r}')\hat{n}(\mathbf{r}').\end{aligned} \tag{B3b}$$

(iii) The pore pressure is continuous:

$$M\nabla'\cdot\mathbf{w}_-(\mathbf{r}')-C\nabla'\cdot\mathbf{u}_-(\mathbf{r}')=p_+(\mathbf{r}'). \tag{B3c}$$

(iv) The tangential traction is continuous:

$$\hat{n}(\mathbf{r}')\times[\hat{n}(\mathbf{r}')\cdot\vec{\vec{\tau}}_-(\mathbf{r}')]=0. \tag{B3d}$$

The subscripts + and − are used, respectively, to indicate that a surface field is evaluated in the limit in which $\mathbf{r}'$ approaches the surface from above and below the surface.

The equations for the fields $\mathbf{u}_t(\mathbf{r})$ and $\mathbf{w}_t(\mathbf{r})$ indicate that these fields are not coupled and that a solution for both fields

is obtained from a solution to the homogeneous vector Helmholtz equation for $\mathbf{u}_t(\mathbf{r})$. However, to obtain a solution for the longitudinal fields, it is necessary to solve the system of coupled scalar equations given by Eq. (B2).

Representations of the transverse and longitudinal fields that satisfy the field equations are given by

$$\mathbf{u}_t(\mathbf{r}) = u_{s1}\hat{X}_1(\mathbf{r};\mathbf{k}_s^{(-)}) + u_{s2}\hat{X}_2(\mathbf{r};\mathbf{k}_s^{(-)}), \tag{B4a}$$

$$\mathbf{w}_t(\mathbf{r}) = \gamma u_{s1}\hat{X}_1(\mathbf{r};\mathbf{k}_s^{(-)}) + \gamma u_{s2}\hat{X}_2(\mathbf{r};\mathbf{k}_s^{(-)}), \tag{B4b}$$

$$\mathbf{u}_1(\mathbf{r}) = u_{p1}\hat{B}_3(\mathbf{r};\mathbf{k}_{p1}^{(-)}) + u_{p2}\hat{B}_3(\mathbf{r};\mathbf{k}_{p2}^{(-)}), \tag{B4c}$$

and

$$\mathbf{w}_1(\mathbf{r}) = \delta_1 u_{p1}\hat{B}_3(\mathbf{r};\mathbf{k}_{p1}^{(-)}) + \delta_2 u_{p2}\hat{B}_3(\mathbf{r};\mathbf{k}_{p2}^{(-)}), \tag{B4d}$$

with

$$\delta_1 = (\nu_s^2 - k_{p1}^2)/\zeta_s^2, \quad \delta_2 = (\nu_s^2 - k_{p2}^2)/\zeta_s^2, \tag{B4e}$$

$$k_{p1}^2 = \tfrac{1}{2}(\kappa_s^2 + \chi_f^2) - \tfrac{1}{2}[(\kappa_s^2 - \chi_f^2)^2 + 4\zeta_s^2\lambda_f^2]^{1/2}, \tag{B4f}$$

and

$$k_{p2}^2 = \tfrac{1}{2}(\kappa_s^2 + \chi_f^2) + \tfrac{1}{2}[(\kappa_s^2 - \chi_f^2)^2 + 4\zeta_s^2\lambda_f^2]^{1/2}. \tag{B4g}$$

The quantities u_{s1}, u_{s2}, u_{p1}, u_{p2}, w_{p1}, and w_{p2} are the unknown amplitudes of the scattered fields and the quantities $\hat{X}_i(\mathbf{r};\mathbf{k}_i^{(-)})$ $(i=1-3)$ are vector basis functions for the transverse and longitudinal components of the displacement fields. These functions are defined and some of their properties are given in Ref. 1. Expressions for the parameters γ, κ_s, χ_f, ζ_s, and λ_f are given in Ref. 29. The two wave numbers k_{p1} and k_{p2} are obtained as a solution to the secular equation for the system of longitudinal fields and correspond, respectively, to the ''classical'' *p*-wave for a homogeneous elastic solid and the slow Biot *p*-wave.

For a plane-wave incident from the fluid half-space, the incident and scattered pressure fields are, respectively, $p^{(i)}(\mathbf{r}) = p_0\chi(\mathbf{r};\mathbf{k}_p^{(i-)})$ and $p^{(1s)}(\mathbf{r}) = p_0 R\chi(\mathbf{r};\mathbf{k}_p^{(+)})$. The reflection coefficient and the displacement field amplitudes are determined by the boundary conditions. The boundary conditions require that $k_{p1x} = k_{p2x} = k_{sx} = k_{px}^{(i)}$ and $k_{p1y} = k_{p2y} = k_{sy} = k_{py}^{(i)}$, so that Snell's law is obeyed that $u_{s1} = 0$ and that

$$\begin{pmatrix} -\dfrac{p_0 k_{pz}}{\rho_0\omega^2} & -\dfrac{k_{p1z}}{k_{p1}}\Delta_1 & -\dfrac{k_{p2z}}{k_{p2}}\Delta_2 & -i\dfrac{(k_x^2+k_y^2)^{1/2}}{k_s}\Gamma \\ p_0 & \mu_r\Omega_1 & \mu_r\Omega_2 & -i\mu_r\Theta_s \\ -p_0 & \Xi_1 & \Xi_2 & 0 \\ 0 & \Theta_1 & \Theta_2 & -i\Pi_s \end{pmatrix} \times \begin{pmatrix} R \\ u_{p1} \\ u_{p2} \\ u_{s2} \end{pmatrix} = \begin{pmatrix} -\dfrac{p_0 k_{pz}^{(i)}}{\rho_0\omega^2} \\ -p_0 \\ p_0 \\ 0 \end{pmatrix}, \tag{B5}$$

with

$$\Delta_i = 1 - \delta_i, \quad \Gamma = 1 - \gamma, \tag{B6a}$$

$$\Xi_i = k_i(B - M\delta_i), \tag{B6b}$$

$$\Omega_i = k_i\frac{\delta_i C - H}{\mu_r} + 2\frac{k_x^2 + k_y^2}{k_i}, \tag{B6c}$$

$$\Theta_i = 2k_{iz}\frac{(k_x^2 + k_y^2)^{1/2}}{k_i}, \tag{B6d}$$

and

$$\Pi_i = \frac{k_{iz}^2 - k_x^2 - k_y^2}{k_i}, \tag{B6e}$$

where the subscripts $i=1$ and 2 denote, respectively, quantities for the fast and slow *p*-waves. The reflection coefficient is obtained in the solution of Eq. (B5).

[1] G. C. Bishop and J. Smith, ''Scattering from an elastic shell and a rough fluid-elastic interface: Theory,'' J. Acoust. Soc. Am. **101**, 767–788 (1997).

[2] A. A. Kleshchev, ''Sound scattering by spheroidal bodies near an interface,'' Sov. Phys. Acoust. **23**, 225–228 (1977).

[3] G. Kristensson and S. Strom, ''Scattering from buried inhomogeneities—a general three-dimensional formalism,'' J. Acoust. Soc. Am. **64**, 917–936 (1978).

[4] C. L. Bennet and H. Mieras, ''Space-time integral equation solution for rigid and soft targets in the presence of a rigid or soft half-space,'' Wave Motion **5**, 399–411 (1988).

[5] I. Tolstoi, ''Superresonant systems of scatterers I,'' J. Acoust. Soc. Am. **80**, 282–294 (1986).

[6] G. C. Gaunaurd and M. McCarthy, ''Resonances of elastic bodies in a fluid half spaces,'' IEEE J. Ocean Eng. **OE-12**, 395–404 (1987).

[7] M. F. Werby and G. C. Gaunaurd, ''Resonances in the back scattered echoes from elastic shells near an interface,'' in *Elastic Wave Propagation*, edited by M. F. McCarthy and M. A. Hayes (Elsevier Science, New York, 1989), pp. 393–398.

[8] G. C. Gaunaurd, ''Distortions in the backscattering cross-sections of a submerged elastic target produced by its proximity to the sea surface or bottom,'' in *Computational Acoustics-Scattering, Gaussian Beams, and Aeronautics*, edited by D. Lee, A. Cakmak, and R. Vichnevetsky (North-Holland, Amsterdam, 1990), Proceedings of the 2nd IMACS Symposium on Computational Acoustics, Princeton, NJ, 15–17 March 1989, pp. 25–37.

[9] G. C. Gaunaurd and H. Huang, ''Sound scattering by a spherical object near a rigid flat bottom,'' IEEE Trans. Ultrason. Ferroelectr. Freq. Control **43**, 690–700 (1996).

[10] G. C. Gaunaurd and H. Huang, ''Acoustic scattering by a spherical body near a plane boundary,'' J. Acoust. Soc. Am. **96**, 2526–2536 (1994).

[11] A. Sarkissian, ''Method of superposition applied to scattering from a target in shallow water,'' J. Acoust. Soc. Am. **95**, 2340–2345 (1994).

[12] A. Sarkissian, ''Multiple scattering effects when scattering from a target in a bounded medium,'' J. Acoust. Soc. Am. **96**, 3137–3144 (1994).

[13] R. H. Hackman and G. S. Sammelmann, ''Acoustic scattering in an inhomogeneous waveguide: Theory,'' J. Acoust. Soc. Am. **80**, 1447–1458 (1986).

[14] G. S. Sammelmann and R. Hackman, ''Acoustic scattering in a homogeneous waveguide,'' J. Acoust. Soc. Am. **82**, 324–336 (1987).

[15] R. H. Hackman and G. S. Sammelmann, ''Multiple-scattering analysis for a target in an oceanic waveguide,'' J. Acoust. Soc. Am. **84**, 1813–1825 (1988).

[16] P. C. Waterman, ''Numerical solution of electromagnetic scattering problems,'' in Computer Techniques for Electromagnetics, edited by R. Mittra (Hemisphere, New York, 1987), pp. 97–157.

[17] A. Sarkissian, C. F. Gaumond, and L. R. Dragonette, ''T-matrix implementation of forward scattering from rigid structures,'' J. Acoust. Soc. Am. **94**, 3448–3453 (1993).

[18] A. N. Lowan, *Tables of Associated Legendre Functions* (Cambridge U.P., New York, 1945).

[19] F. B. Jensen, W. A. Kuperman, M. B. Porter, and H. Schmidt, *Computational Ocean Acoustics* (AIP, New York, 1994), pp. 234–240.

[20] R. Lim, ''Scattering by an obstacle in a plane-stratified poroelastic medium: Application to an obstacle in ocean sediments,'' J. Acoust. Soc. Am. **95**, 1223–1244 (1994).

[21] N. P. Chotiros, ''Biot model of sound propagation in water-saturated sand,'' J. Acoust. Soc. Am. **97**, 199–214 (1995).
[22] L. M. Brekhovskikh, *Waves in Layered Media* (Academic, New York, 1980), 2nd ed., pp. 5–11 and pp. 41–50.
[23] M. F. Werby, G. J. Tango, and L. H. Green, ''Eigenvalue and matrix transform methods in the solution of acoustical scattering problems for submerged objects,'' in *Computational Acoustics: Algorithms and Applications*, edited by D. Lee, R. L. Sternberg, M. H. Schultz (Elsevier Science–North-Holland, Amsterdam, 1988), Vol. 2, pp. 257–278.
[24] S. K. Numrich, V. V. Varadan, and V. K. Varadan, ''Scattering of acoustic waves by a finite elastic cylinder immersed in water,'' J. Acoust. Soc. Am. **70**, 1407–1411 (1981).
[25] J. Su, V. V. Varadan, and V. K. Varadan, ''Acoustic wave scattering by a finite elastic cylinder in water,'' J. Acoust. Soc. Am. **68**, 686–691 (1980).
[26] V. K. Varadan, V. V. Varadan, J. H. Su, and T. A. K. Pillai, ''Comparison of sound scattering by rigid and elastic obstacles in water,'' J. Acoust. Soc. Am. **71**, 1377–1383 (1982).
[27] M. E. Rose, *Elementary Theory of Angular Momentum* (Wiley, New York, 1957), pp. 48–57.
[28] R. D. Stoll and T. K. Kan, ''Reflection of acoustic waves at a water-sediment interface,'' J. Acoust. Soc. Am. **70**, 149–156 (1981).
[29] M. Stern, A. Bedford, and H. R. Millwater, ''Wave reflection from a sediment layer with depth dependent properties,'' J. Acoust. Soc. Am. **77**, 1781–1788 (1985).

A new rough surface parabolic equation program for computing low-frequency acoustic forward scattering from the ocean surface

Allan P. Rosenberg[a)]
Johns Hopkins University, Applied Physics Laboratory, Johns Hopkins Road, Laurel, Maryland 20723

(Received 6 January 1998; accepted for publication 22 September 1998)

The parabolic equation acoustic propagation program RAM has been extended to handle a rough air–water interface treated as a series of stair steps. Because much finer vertical spacing may be needed to resolve the interface than to propagate a low-frequency acoustic wave accurately in the rest of the domain, an option to use one vertical spacing near the surface and a coarser one in the rest of the ocean has been implemented. The necessary Galerkin approximations of derivatives on an unequally spaced grid have been worked out using computer algebra. The new program, Rrsfc, is efficient enough to compute the frequency spectrum of the field scattered off a moving surface by treating the surface as a sequence of frozen surfaces. A comparison of one such spectrum with actual ocean data is provided. In order to make a more detailed assessment of the program, both the depth-dependent pressure for individual surfaces and the frequency spectrum for sequences of surfaces are compared with the results of numerically exact integral equation calculations for a few constant sound speed test cases.
[S0001-4966(99)02501-1]

PACS numbers: 43.30.Hw, 43.20.Fn [DLB]

INTRODUCTION

The scattering of underwater sound from the ocean surface is an interesting though complicated problem. In addition to the difficulty of solving the wave equation with a moving boundary, there is the possibility that the motion of the surface has produced bubble clouds that modify near-surface acoustic propagation. There has also been a suggestion of additional effects due to the subsurface currents that accompany the surface waves.[1] For acoustic frequencies below a kilohertz there is, to the best of my knowledge, no evidence in the sparse experimental data of either of these effects playing an important role. Both effects are neglected here and attention is focused on the direct complications caused by the changing shape of the boundary. Because the acoustic frequency is much larger than any significant surface wave frequency, it is a reasonable approximation to neglect the motion of the interface when considering its interaction with the acoustic wave. The vertical position of the interface will change with time, but at each moment it can be considered as instantaneously fixed. A careful discussion of this point may be found in Holford.[2] The appropriate boundary condition is just that the pressure vanish at the instantaneous position of the interface. The ability to handle an arbitrary stationary interface therefore implies the ability to handle a moving one. Although this is a considerable simplification, predicting the amount of scattering in an arbitrary direction still leaves the formidable computational problem of solving the wave equation for nonconstant sound speed with a rough air–water interface. For an environment that is cylindrically symmetric except for the rough surface, neglecting scattering out of the plane of propagation of the acoustic wave and backscattering within that plane lightens the computational load considerably. These conditions are within the scope of the two-dimensional parabolic approximation to the wave equation[3–6] and the problem can be handled by existing flat surface implementations except for effects due to the rough boundary.

There have been a few earlier programs that added a rough surface to a parabolic equation program. Dozier[7] used conformal mapping to transform a section of the rough surface to a flat surface parallel to the waveguide. The method was implemented for the split-step Fourier program of Hardin and Tappert.[5] Later Norton, Novarini, and Keiffer[8] implemented Dozier's idea in the finite-element-based program FEPE.[9] A different approach to flattening the surface has recently been taken by Evans.[10] Tappert and Nghiem-Phu[11] generalized the standard image source method of enforcing vanishing pressure at a flat surface by having an ''image ocean'' with a modified index of refraction above the rough surface. Propagation in the enlarged domain was handled using the split-step Fourier algorithm. An independent implementation and study of the image ocean method was performed by Thorsos, Ballard, and Ewing.[12] The method is employed in the widely available University of Miami parabolic equation model UMPE,[13] whose manual provides a discussion of its theoretical basis.

I have modified the parabolic propagation program RAM[14–16] to produce a new program, Rrsfc,[17,18] which directly enforces the boundary condition on a one-dimensional rough surface treated as a series of stair steps. (An advantage of this method is that it is just as easy to implement for a two-dimensional surface as for a one-dimensional one. That extension should ultimately help in judging the physical validity of the current restriction to scattering within the plane of propagation.) The geometry of the situation is shown in

a)Electronic mail: allan.rosenberg@jhuapl.edu

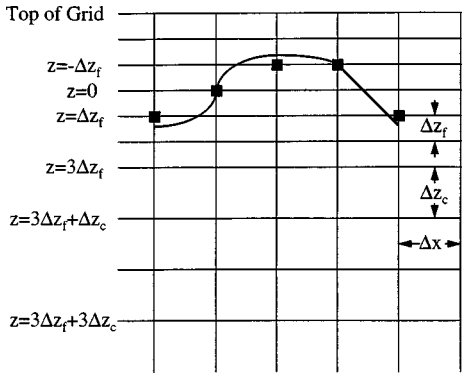

FIG. 1. Sample stair-stepped surface and dual grid. At each range the surface is placed at the vertical grid point nearest to the actual height. The surface points for five successive ranges are shown as black rectangles. The depth labeled $z=0$ is mean sea level. The fine grid spacing is Δz_f and the coarse grid spacing Δz_c. In this example, the transition from the fine to the coarse grid occurs at $z=3\Delta z_f$.

Fig. 1. At each range the surface is placed at the vertical grid point nearest to the actual height. The pressure is zero at the surface point. The surface points for five successive ranges are shown as black rectangles in Fig. 1. The depth labeled $z=0$ is mean sea level. For low acoustic frequencies and moderate winds, the vertical grid spacing needed to accurately track the interface is often much finer than the vertical resolution needed to model propagation with a flat interface. A numerical example may make this clearer. Suppose the acoustic frequency is 150 Hz. With a nominal sound speed of 1500 m/s, this gives an acoustic wavelength of 10 m. For ordinary flat surface calculations one would expect that a vertical grid spacing of a tenth of a wavelength, 1 m in this case, would be adequate. Suppose the wind speed is 15 knots (7.7 m/s) measured at 10 m above sea-level. Using the Pierson–Moskowitz spectrum to estimate the surface properties gives a rms wave height of 0.37 m. Quantizing the surface elevation in 1-m steps leaves the surface very inaccurately described. In this case a uniform vertical grid that is fine enough to accurately track the interface will lead to a large number of vertical grids points and hence to long running times. To alleviate this problem, Rrsfc can be run so that a fine resolution is used near the surface and a coarser resolution elsewhere. The dual grid structure is also shown in Fig. 1. Multiple resolution grids are fairly widespread in other fields but rare in ocean acoustics. In cases of interest to us, speedup by a factor of 7 is typical. At the boundary between the two resolution regions, it is necessary to numerically approximate complicated derivative operators on an unequally spaced grid. The computer mathematics program Mathematica®[19] was used to make the very messy algebra involved relatively painless.

It is important to realize that a rough surface puts additional stress on both the acoustic propagation part of the program and on the knowledge of the environment required as input to the program. Consider a ray going upward from the source at a very steep angle in an environment with a flat bottom. With a flat surface the ray will reflect downward at the same steep angle, enter the sediment still at a steep angle, and not propagate to long ranges from the source. With a rough surface, there is a potential for the steep upward-going ray to scatter into a shallower angle and propagate. Near a distant receiver the reverse effect can occur. In the flat surface case rays near the receiver will be shallow because the bottom will have stripped off the steep rays. With a rough surface some of these shallow rays can be transformed into steep rays at ranges near enough to the receiver to propagate to it. In both cases it is necessary for the program to handle steep rays more accurately than is usually necessary in the flat surface case. The quantitative description of these effects requires knowledge of the wave number spectrum of the ocean surface waves. The above discussion may lead one to suspect, correctly as it turns out, that for shallow water the frequency spectrum of the acoustic pressure will also be sensitive to details of the sediment.

The remainder of the paper is organized as follows. The next section gives a concise overview of the numerical implementation at a fairly high level while attempting to provide some essential details—the method of advancing in range when the surface height changes and the approximations used at the interface between the fine and coarse parts of the grid. That section also contains a few remarks on computational efficiency. The section following that provides comparison with exact integral equation[20,21] results for a constant sound speed environment. Both the depth-dependent pressure for single surfaces and the frequency spectrum of the scattered field for sequences of surfaces are compared to the integral equation results. Section III contains a comparison of the modeled and actual frequency spectrum for a low-frequency shallow water case (Gulf of Mexico, bottom depth 188 m, source frequency 240 Hz, significant wave height 2.7 m, range 9.35 km). The final section provides a summary along with a brief discussion of open issues and work in progress.

I. NUMERICAL IMPLEMENTATION

In this section we discuss the distinctive details of our rough surface extension of the parabolic equation. The treatment is intended for readers with some prior familiarity with the parabolic approximation in the flat surface case. While the first part of this section does provide an overview of the parabolic equation in the flat surface case, the discussion is terse and is intended as a refresher and to establish notation.

In a cylindrically symmetric range-independent environment, the Helmholtz equation in a source-free region can be factored into two one way equations—one describing waves propagating in toward the vertical axis and one describing propagation outward from the vertical axis. Assuming the range dependence is sufficiently gradual that backscattering is negligible, the parabolic equation works only with the equation propagating outward from the vertical axis. Range dependence is treated by approximating the environment as a succession of range-independent regions. This procedure reduces an elliptic boundary-value problem to an initial value problem in range with a large reduction in memory requirements and a large gain in efficiency. Let P be the complex pressure. RAM and Rrsfc are implemented using the variable $\tilde{p}$ defined by

$$P(r,z)=r^{-1/2}\alpha_p\tilde{p}(r,z). \tag{1}$$

In this expression, r is the horizontal distance from the origin, z is the depth below the ocean surface, and $\alpha_p=(\rho c)^{1/2}$, where ρ is the density and c is the depth-dependent sound speed. The factor $r^{-1/2}$ accounts for cylindrical spreading. Removing the factor α_p leads to more accurate solutions across the vertical interface between range-independent regions.[22–24] The equation satisfied by $\tilde{p}$ is

$$\frac{\partial\tilde{p}}{\partial r}=ik_0(1+X)^{1/2}\tilde{p}, \tag{2}$$

where $k_0=\omega/c_0$ with c_0 a representative phase speed and ω the circular frequency of the transmitted sound. Here X is defined as

$$X=k_0^{-2}\left(\frac{\rho}{\alpha_p}\frac{\partial}{\partial z}\frac{1}{\rho}\frac{\partial}{\partial z}\,\alpha_p+k^2-k_0^2\right), \tag{3}$$

where $k=(1+i\eta\beta)\omega/c$ is the wave number, β is the attenuation in dB/λ, and $\eta=(40\pi\,\log_{10}e)^{-1}$. The formal solution of Eq. (2) is

$$\tilde{p}(r+\Delta r,z)=\exp(ik_0\Delta r(1+X)^{1/2})\tilde{p}(r,z), \tag{4}$$

with Δr the range step. In RAM 1.0 and Rrsfc the exponential is approximated as the product of $\exp(ik_0\,\Delta r)$ and an n-term rational function,[14,25,26] giving

$$\tilde{p}(r+\Delta r,z)=\exp(ik_0\Delta r)\prod_{j=1}^{n}\frac{1+\alpha_{j,n}X}{1+\beta_{j,n}X}\,\tilde{p}(r,z). \tag{5}$$

The variable n is the Padé order. The complex coefficients $\alpha_{j,n}$ and $\beta_{j,n}$ are defined by placing accuracy and stability constraints on the rational function. When doing this, the operator structure of X is neglected and it is just treated as a number. In particular $\alpha_{j,n}$ and $\beta_{j,n}$ are independent of the depth dependence of k and ρ. In Eq. (5) the factor $\exp(ik_0\,\Delta r)$ can be inserted at the end since it is independent of z, so the code actually works with p defined as $\tilde{p}(r,z)=\exp(ik_0\,r)p(r,z)$. Equation (5) is solved by defining $p_0(z)\equiv p(r,z)$ and

$$p_j(z)=\frac{1+\alpha_{j,n}X}{1+\beta_{j,n}X}\,p_{j-1}(z),\quad j=1,...,n, \tag{6}$$

and then finding in succession p_1, p_2 and so on up to $p_n\equiv p(r+\Delta r,z)$ from Eq. (6). The programs actually use Eq. (6) in the form

$$(1+\beta_{j,n}X)p_j(z)=(1+\alpha_{j,n}X)p_{j-1}(z),\quad j=1,...,n. \tag{7}$$

Since p_{j-1} is known from the previous stage, the expression on the right-hand side is directly computable.

In the Galerkin discretization scheme employed by RAM and Rrsfc (see Sec. I B below), the operator $R_{j,n}\equiv(1+\beta_{j,n}X)$ on the left-hand side of Eq. (7) becomes a tridiagonal matrix as does the operator $S_{j,n}\equiv(1+\alpha_{j,n}X)$ on the right-hand side. The tridiagonal nature of $R_{j,n}$ and $S_{j,n}$ is independent of whether or not the vertical grid points are equally spaced. Tridiagonal equations such as Eq. (7) can be solved very efficiently. RAM and Rrsfc differ in the way this is done. In RAM, since changing surface height is not a concern, the calculation is laid out to minimize the amount of new computation needed when the bottom depth changes. It would be inefficient if the surface height were to change. In Rrsfc, since the surface height is generally changing much more rapidly than the bottom depth, the calculation is laid out the other way round.

All the dependence of $R_{j,n}$ on the environment is contained in X. In computing X, a rough surface code faces an issue of whether or not at a given depth below mean sea level to correct the sound speed to reflect actual distance below the rough surface rather than just the depth below mean sea-level. Rrsfc does not make this correction and, consistent with that approximation, assigns to water positions shallower than mean sea-level the sound speed value at mean sea-level. (In accordance with these approximations ''depth,'' unqualified, will henceforth be taken to mean distance below mean sea-level.) A consequence is that, for a given ocean depth and set of profiles for sound speed, density, and attenuation, X and $R_{j,n}$ can be computed over the maximal possible vertical grid independent of the actual depth of the rough surface. When solving Eq. (7) attention must be restricted to the submatrix of $R_{j,n}$ appropriate to the current depth of the rough surface. Similar considerations apply to $S_{j,n}$.

The subtlety that arises in the rough surface case is that in Eq. (5) and therefore in at least one stage of Eq. (7) the range of z values will not always be the same on the right- and left-hand sides.

A. Solution when the surface height changes

If the two sides of Eq. (5) have the surface at different depths, say index j_{rs} on the right and i_{rs} on the left, the basic question is what indices do we use for p_j, $j=1,...,n-1$ in solving Eq. (7). Clearly p_0 must have the surface at j_{rs} and p_n must have the surface at i_{rs}. Rrsfc sets the surface for all of p_1 to $p_{n/2}$ at j_{rs} and for all of $p_{(n/2)+1}$ to p_n at i_{rs}. It is possible to imagine other algorithms, for example, shifting height at p_1 or at p_n or some more elaborate scheme like having the index for p_j set to $j_{rs}+(j/n)(i_{rs}-j_{rs})$. Tests do not, so far, show any advantage for these alternate schemes. Here are the details.

In Rrsfc, $R_{j,n}$ is decomposed as

$$R_{j,n}=U_{j,n}L_{j,n},\quad j=1,...,n, \tag{8}$$

with $U_{j,n}$ upper triangular, $L_{j,n}$ lower triangular, and $L_{j,n}$ has ones along the diagonal. This decomposition can be made over the maximal possible vertical grid independent of the actual position of the rough surface as long as in solving Eq. (7) attention is restricted to the appropriate submatrices. Consider first the case when the rough surface is at the same depth, say depth index k_{rs}, on both sides of Eq. (7) and let m be the index of the bottom of the computational depth grid. The not automatically zero elements of p_j and p_{j-1} are those with indices $k_{rs}+1$ to $m-1$. Likewise the appropriate submatrices of $R_{j,n}$ and $S_{j,n}$ are those with row and column indices in that range. Let $R_{j,n,k_{rs}}$, $S_{j,n,k_{rs}}$, $U_{j,n,k_{rs}}$, and $L_{j,n,k_{rs}}$ indicate these submatrices. Equation (7) is solved by first solving

$$U_{j,n,k_{rs}}p_j'(z)=S_{j,n,k_{rs}}p_{j-1}(z) \tag{9}$$

from the bottom up for p_j', and then solving

$$L_{j,n,k_{rs}} p_j(z) = p_j'(z) \tag{10}$$

from the top down for p_j.

Suppose now that the rough surface for p_{j-1} is at depth index j_{rs} and the rough surface for p_j is at depth index k_{rs}. In this case elements 1 to k_{rs} of the resultant vector on the right side of Eq. (7) are explicitly set to zero and the equation is solved only for elements of p_j from $k_{rs}+1$ on down. Thus if $j_{rs}<k_{rs}$, the right-hand side of Eq. (7) will be zero at some indices where p_{j-1} itself is not equal zero, while if $j_{rs}>k_{rs}$ the right-hand side may be nonzero even at indices for which p_{j-1} itself is zero.

B. Galerkin approximation of derivatives on an unequally spaced grid

Let Q be some expression involving derivatives with respect to z, let $a(z)$ be an arbitrary function of z, let Δz be the grid spacing, and let $f_i(z)$ be the basis functions defined to be zero for $|z-z_i|>\Delta z$, linearly increasing from 0 to 1 over $z_{i-1}<z<z_i$, and linearly decreasing from 1 to 0 over $z_i<z<z_{i+1}$. Galerkin's method then approximates the result of applying Q to $a(z)$ at the point z_i as

$$Qa|_{z=z_i} \simeq \frac{\int f_i Qa \, dz}{\int f_i \, dz}. \tag{11}$$

For RAM and Rrsfc the main expressions to which Galerkin's method needs to be applied are

$$ab|_{z=z_i} \tag{12}$$

and

$$a\frac{\partial}{\partial z} b \frac{\partial}{\partial z} cu\bigg|_{z=z_i} = -\left(\frac{\partial a}{\partial z}\right) b\left(\frac{\partial (cu)}{\partial z}\right)\bigg|_{z=z_i} + \frac{\partial}{\partial z}\left(ab\,\frac{\partial (cu)}{\partial z}\right)\bigg|_{z=z_i}, \tag{13}$$

where a, b, c, and u are arbitrary functions. For RAM these were originally evaluated for a uniformly spaced grid.[23,27] Using a subscript i to mean evaluation at $z=z_i$, the result for Eq. (12) is

$$(ab)_i = \tfrac{1}{12}\left((a_{i-1}+a_i)b_{i-1} + (a_{i-1}+6a_i+a_{i+1})b_i + (a_{i+1}+a_i)b_{i+1}\right). \tag{14}$$

In evaluating Eq. (13) for the evenly spaced case, it was assumed that $a_{i-1}=a_i=a_{i+1}$ and $(cu)_i=c_iu_i$. Equation (13) then evaluates to

$$\left(a\frac{\partial}{\partial z} b \frac{\partial}{\partial z} cu\right)_i \simeq \left(\frac{a_i}{2(\Delta z)^2}\right)\left((b_{i-1}+b_i)c_{i-1}u_{i-1} - (b_{i-1}+2b_i+b_{i+1})c_iu_i + (b_{i+1}+b_i)c_{i+1}u_{i+1}\right). \tag{15}$$

I have used Mathematica®[19] to evaluate the unequally spaced case. To display the results in a fashion that can be compared with the earlier results, it is convenient to define

$$z_{i+1}-z_{i-1} = 2\Delta_0, \tag{16}$$

$$z_{i+1}-z_i = \gamma_p\Delta_0, \tag{17}$$

$$z_i-z_{i-1} = \gamma_m\Delta_0. \tag{18}$$

Note that $\gamma_m+\gamma_p=2$ and that in the equally spaced limit, $\Delta_0\to\Delta z$, $\gamma_p\to 1$, and $\gamma_m\to 1$. The results for the unequally spaced case are

$$(ab)_i = \tfrac{1}{12}\left(\gamma_m(a_{i-1}+a_i)b_{i-1} + (\gamma_m a_{i-1}+6a_i+\gamma_p a_{i+1})b_i + \gamma_p(a_{i+1}+a_i)b_{i+1}\right), \tag{19}$$

and, making the same approximations as above,

$$\left(a\frac{\partial}{\partial z} b \frac{\partial}{\partial z} cu\right)_i \simeq \left(\frac{a_i}{2\gamma_m\gamma_p(\Delta_0)^2}\right)\left(\gamma_p(b_{i-1}+b_i)c_{i-1}u_{i-1} - (\gamma_p b_{i-1}+2b_i+\gamma_m b_{i+1})c_iu_i + \gamma_m(b_{i+1}+b_i)c_{i+1}u_{i+1}\right). \tag{20}$$

These clearly reduce to Eqs. (14) and (15) in the equal spacing limit. It is possible to evaluate the left-hand side of Eq. (13) without making simplifying approximations, but the result is very messy and will not be displayed here.

C. Stepped surface

If the actual surface height at a range point is between two vertical grid points, Rrsfc puts the surface at the grid point which is closest to the actual height. See Fig. 1. The surface elevation is thus quantized. This quantization introduces a form of numerical noise over and above that caused by the finite precision of computer arithmetic. If one has a temporal sequence of surfaces, the elevation spectrum for the quantized surface heights will show a noise floor compared to the spectrum for the unquantized spectrum. The coarser the quatization step, the higher the noise floor. Because of the large dynamic ranges involved, it is particularly important to use a fine surface quantization when computing a frequency spectrum of the acoustic pressure.

D. Efficiency considerations

Perhaps the simplest question one can ask is how the run time for Rrsfc with a single rough surface compares with that for RAM for the same environment but a flat surface and running on the same computer? Even this question is not as straightforward as it seems. If the bottom is flat, the Padé order the same, the range steps the same, and the vertical spacing in RAM the same as the coarse vertical spacing in Rrsfc, the answer just depends on the ratio of the coarse to fine vertical spacing in Rrsfc and the fraction of the total domain covered by the fine grid. Let r be the coarse grid spacing divided by the fine grid spacing, $\Delta z_c/\Delta z_f$ in the notation of Fig. 1, and let F be the fraction of the domain which is covered by the fine grid. F is proportional to the wave height and inversely proportional to the ocean depth. A crude but useful rule of thumb is that, in this case, the Rrsfc run time divided by the RAM run time will be $1.1(1-F+rF)$. I have found $r=8$ to give good results in the cases I

have run. It is the value most used in the test cases in the next section. Typically F is small, giving run-time ratios near 1.1.

As the bottom starts to slope, Rrsfc becomes less efficient relative to RAM because, each time the bottom depth is stepped, Rrsfc must recompute the whole of the tridiagonal matrices $R_{j,n}$ and $S_{j,n}$ [defined just after Eq. (7)] while RAM needs only to modify a few rows near the bottom. Clearly this effect is worse the steeper the slope.

So far this discussion has assumed that RAM and Rsfc are taking the same range steps. In practice RAM is often able to be run with larger range steps. A range step that was reasonable in the flat surface case might, for example, in the rough surface case reach from crest to trough and back to the next crest. The effect would be to underestimate the variation of the surface elevation. Also, as discussed in the Introduction, a rough surface program will usually deal with steeper propagation and the concomitant need for smaller range steps and/or higher Padé order to attain a given accuracy. In any event, for both codes the run time is inversely proportional to the range step size.

II. CONSTANT SOUND SPEED TEST CASES

The test cases discussed in this section have an isovelocity ocean and a cw acoustic field. The accuracy of Rrsfc is studied by comparing its predictions with ''exact'' results found by numerically solving an integral equation that is obtained as a limit of the Helmholtz integral formula. The particular version of the method used here is due to Eric Thorsos to whom these test case calculations are also due. The method is described in detail in Ref. 20 and will only be sketched here.

In the isovelocity case with the pressure release (=Dirichlet) boundary condition at the surface, the scattered field can be straightforwardly computed from the normal derivative of the total pressure $\partial p/\partial n$ on the surface. For each surface the quantity $\partial p/\partial n$ on the surface is found by solving an integral equation of the first kind. This equation is obtained by using the Helmholtz integral formula and letting the point for which the formula gives the pressure approach the surface. The incident field is then added to the scattered field to give the total field.

The form of the starting field at zero range used by Rrsfc for these test cases is

$$p(z)=\exp\left(\frac{-(z-z_s)^2}{g_w^2}\right)\exp\,(ik_z z), \tag{21}$$

with

$$k_z=-k\,\sin\,(\theta_i), \tag{22}$$

where k is the acoustic wave number, $\pi/5$ m^{-1} for the sound speed of 1500 m/s and acoustic frequency of 150 Hz used in all the cases of this section, θ_i is the grazing angle for this tapered plane wave, and the parameters z_s and g_w control the tapering. This tapered field is not strictly zero at the surface, but for the sets of parameters used here ($g_w=200$, $z_s=700$, $\theta_i=25$ degrees; $g_w=200$, $z_s=800$, $\theta_i=45$ degrees; $g_w=200$, $z_s=800$, $\theta_i=60$ degrees) it is very close. Propagating this field strictly to the right, Green's theorem can be used to find the incident field on the surface, needed as input for the integral equation method, from the field on the vertical slice at zero range.[28] The integral equation method handles the strict two-dimensional case, while Rrsfc deals with a cylindrically symmetric three-dimensional problem. To compare the two cases it is only necessary not to insert in the Rrsfc results the factor of $r^{-1/2}$ that is normally put in at the end to account for cylindrical spreading. The homogeneous half-space problem that the integral equation solves is approximated for Rrsfc as a deep water column overlaying an absorbing sediment having the same density and sound speed as the water. The deep domain can lead to equations that are numerically not as well conditioned. In order to alleviate this problem, all the Rrsfc calculations in this section were done in double precision. A Padé order of 8 was used for all the Rrsfc results.

The rough surface realizations were constructed using a spectral method[20] to be consistent with a one-dimensional Pierson–Moskowitz spatial wave number spectrum[21] for a wind speed of 15 m/s. The one-dimensional Pierson–Moskowitz spectrum falls rapidly at wave numbers below the peak of the spectrum and rolls off as k_w^{-3} well above the peak, where k_w is the spatial wave number. In some cases an upper cutoff at 4.25 times the spectral peak was used. In all cases the surface waves are propagating down the track.

The following comparisons look first at a flat surface and uniform grid to get some feel for the accuracy ideally attainable. This is followed by results for individual rough surfaces with the incident beams at grazing angles of 45, 25, and 60 degrees. Finally frequency spectra are examined for incident grazing angles of 25, 45, and 60 degrees. The steeper angles were included because, as discussed in the Introduction, the ability of a rough surface to convert steep rays to shallower ones makes them potentially important.

We start by examining the case of a flat surface and a uniform grid for a beam incident at 45 degrees from horizontal. Figure 2(a) plots the absolute value of the acoustic pressure versus depth for the first 50 m below the surface at a range of 1000 m. In this case there are no rough surface or dual grid effects to consider, and Rrsfc gives the same answers as RAM. Along with exact integral equation results, Rrsfc results are given for two vertical grid spacings—0.25 and 0.5 m. Throughout this section, the range step is 1 m. In this case with a steep incident field, the finer grid is clearly better. With an incidence angle of 25 degrees, the curves on a similar plot would be indistinguishable. Figure 2(a) uses a linear scale for the pressure, as do all the results in this section plotting pressure as a function of depth. Figure 2(b) plots the difference between the integral equation and Rrsfc results for the phase of the pressure as a function of depth. The smaller grid spacing again gives better results—the offset at the surface is smaller and it remains more constant as a function of depth.

Figure 3 has the same 45 degree incidence angle and the results are examined at the same range, but now there is a rough surface. Results are presented for the integral equation, for Rrsfc with a dual grid, and for Rrsfc with a uniform grid. In the dual grid case the coarse grid vertical spacing, Δz_c in

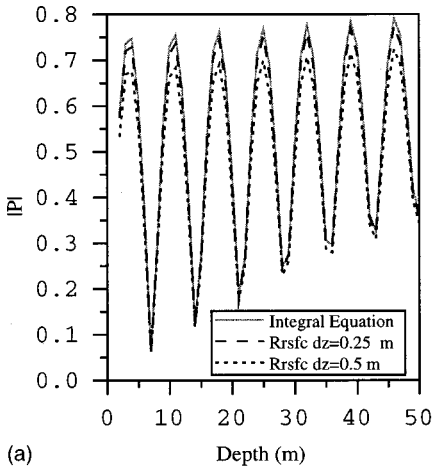

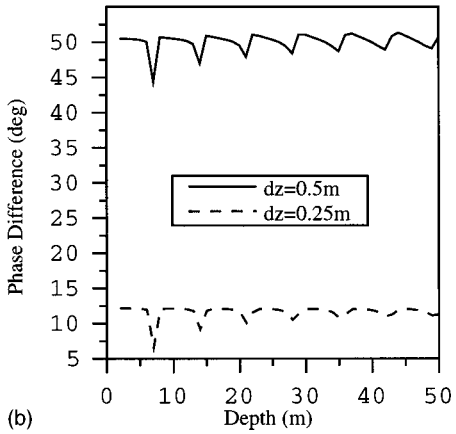

FIG. 2. (a) Effect of vertical grid spacing for a flat surface and a uniform grid. The absolute value of the pressure is plotted as a function of depth (0–50 m) at a range of 1000 m with the incident beam at 45 degrees from horizontal. (b) Effect of vertical grid spacing for a flat surface and a uniform grid. The difference in the phase of the pressure between the integral equation and Rrsfc results is plotted as a function of depth (0–50 m) at a range of 1000 m with the incident beam at 45 degrees from horizontal.

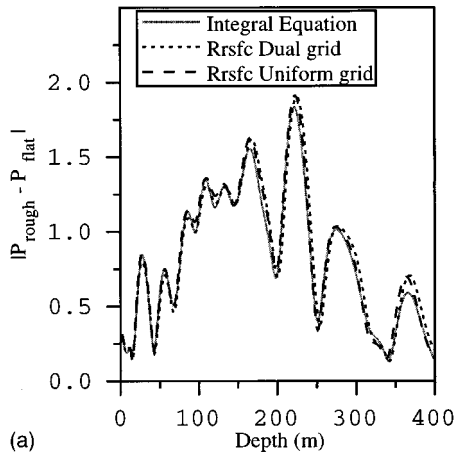

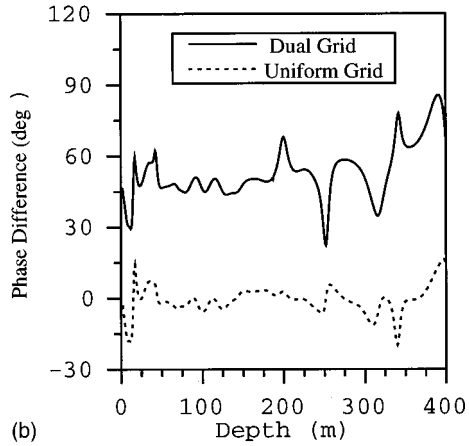

FIG. 3. (a) Effect of the dual grid on the scattered field in a rough surface case. The absolute value of the pressure difference in the rough and flat surface cases is plotted as a function of depth (0–400 m) at a range of 1000 m with the incident beam at 45 degrees from horizontal. In the dual grid case $\Delta z_c = 0.5$ m and $\Delta z_f = 0.0625$ m while in the uniform case $\Delta z = 0.0625$ m. (b) Effect of the dual grid on the scattered field in a rough surface case. The phase of the pressure difference in the rough and flat surface cases is computed for both the integral equation and Rrsfc with a dual grid and a uniform grid. The difference in integral equation and Rrsfc phases is plotted as a function of depth (0–400 m) at a range of 1000 m with the incident beam at 45 degrees from horizontal. In the dual grid case $\Delta z_c = 0.5$ m and $\Delta z_f = 0.0625$ m while in the uniform case $\Delta z = 0.0625$ m.

the terminology of Fig. 1, is 0.5 m and the fine grid spacing Δz_f is $0.5/8 = 0.0625$ m. All of the dual grid calculations in this section were made with these values. The Rrsfc uniform grid results were made with a vertical spacing of $0.5/8 = 0.0625$ m—the same as the fine grid spacing in the dual grid case. In order to highlight the effect of the rough surface, the variable considered is rough surface pressure minus the flat surface pressure. Figure 3(a) plots its absolute value as a function of depth from 0 to 400 m, while Fig. 3(b) plots the difference in its phase between the integral equation and Rrsfc results. At the deepest depth the nominal scattering angle from horizontal at the surface is 63.4 degrees. The uniform grid results are clearly better, but the dual grid results are not bad at all. From here on out, only dual grid results are given for Rrsfc.

Figure 4 again plots the absolute value of the difference in the rough and flat surface pressures. The beam was incident at 25 degrees from horizontal and the results shown are at a range of 1500 m. In generating the surface for Fig. 4, the surface wave spectrum was cut off for wave numbers above $0.13\ \mathrm{m}^{-1}$, which was 4.25 times the wave number of the spectral peak.

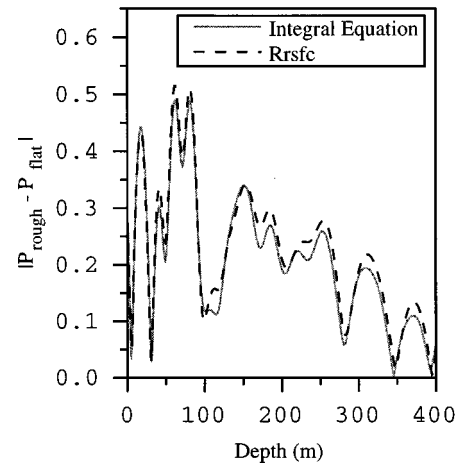

FIG. 4. Absolute value of the difference of the rough surface and flat surface pressures as a function of depth (0–400 m) at a range of 1500 m for an incident beam at 25° from horizontal; Pierson–Moskowitz surface wave spectrum for a wind speed of 15 m/s with the higher wave numbers cut off.

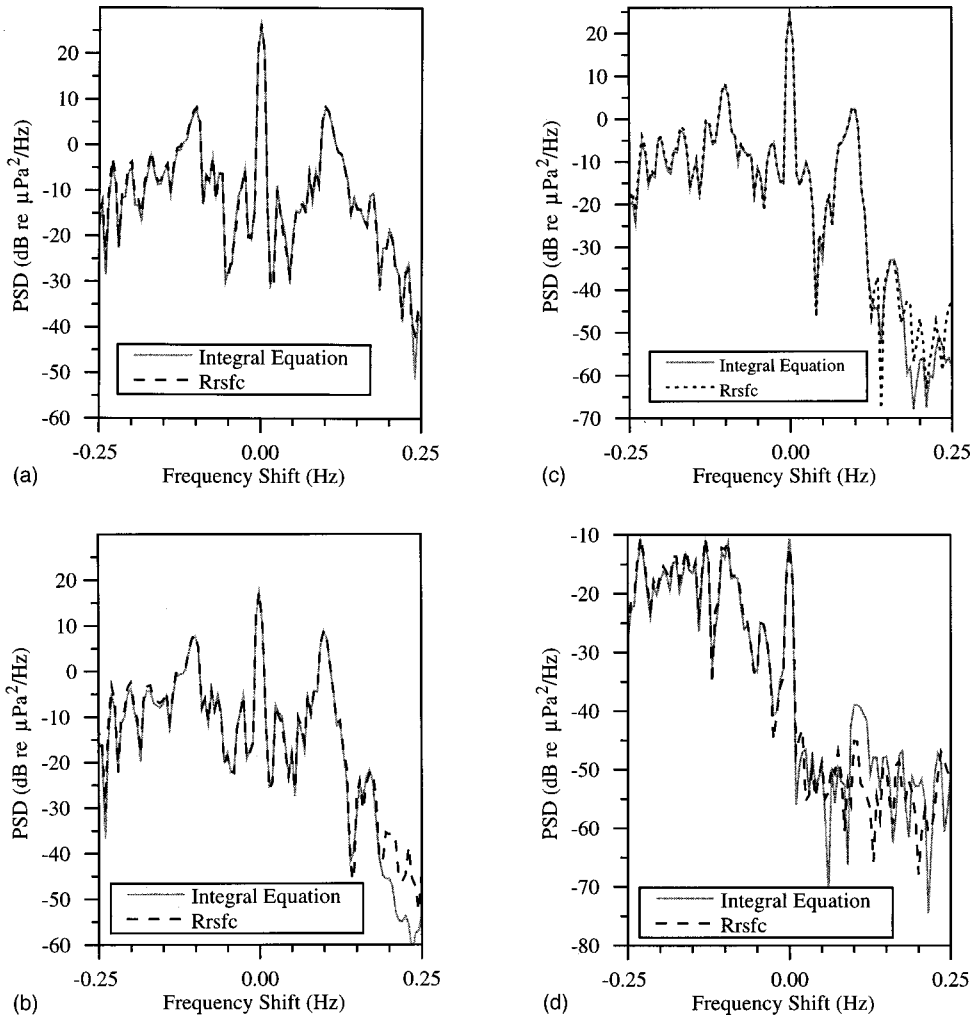

FIG. 5. (a) Frequency spectrum of the pressure at a range of 1500 m and a depth of 5 m with the incident beam at 25 degrees from horizontal; Pierson–Moskowitz surface wave spectrum for a wind speed of 15 m/s with the higher wave numbers cut off. (b) Frequency spectrum of the pressure at a range of 1500 m and a depth of 25 m with the incident beam at 25 degrees from horizontal; Pierson–Moskowitz surface wave spectrum for a wind speed of 15 m/s with the higher wave numbers cut off. (c) Frequency spectrum of the pressure at a range of 1500 m and a depth of 100 m with the incident beam at 25 degrees from horizontal; Pierson–Moskowitz surface wave spectrum for a wind speed of 15 m/s with the higher wave numbers cut off. (d) Frequency spectrum of the pressure at a range of 1500 m and a depth of 400 m with the incident beam at 25 degrees from horizontal; Pierson–Moskowitz surface wave spectrum for a wind speed of 15 m/s with the higher wave numbers cut off.

Figures 5–7 are all comparisons of the frequency spectrum of the acoustic pressure at various depths for a variety of incidence angles. In all cases 200 successive surfaces 1 s apart were generated, and the pressure field calculated for each of them. The time series of the pressure at the depth and range of interest was then Fourier transformed using Hanning weighting and a spectrum calculated. Normally, to smooth the spectrum, one would take partially overlapping Fourier transforms of length less than 200 and average the resulting spectra. In order to provide for a more detailed comparison here, all 200 points were used in the Fourier transform and no averaging was performed. In the plots, the

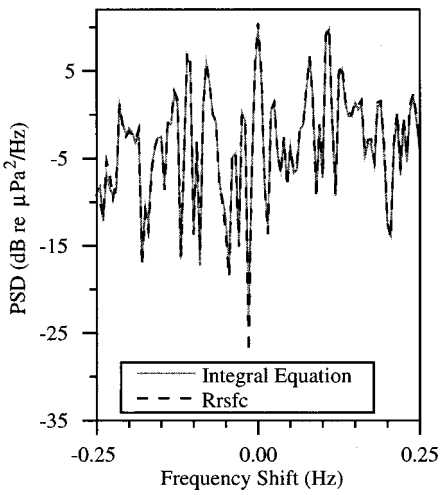

FIG. 6. Frequency spectrum of the pressure at a range of 1000 m and a depth of 100 m with the incident beam at 45 degrees from horizontal; Pierson–Moskowitz surface wave spectrum for a wind speed of 15 m/s.

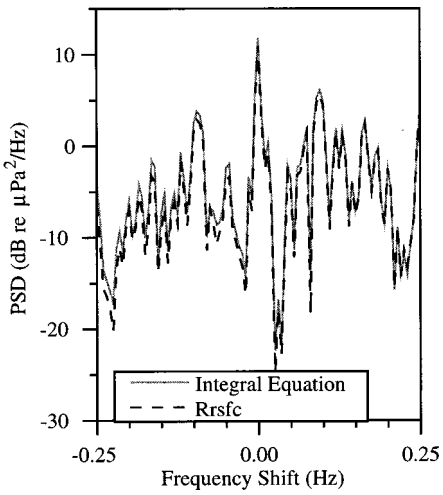

FIG. 7. Frequency spectrum of the pressure at a range of 600 m and a depth of 100 m with the incident beam at 60 degrees from horizontal; Pierson–Moskowitz surface wave spectrum for a wind speed of 15 m/s.

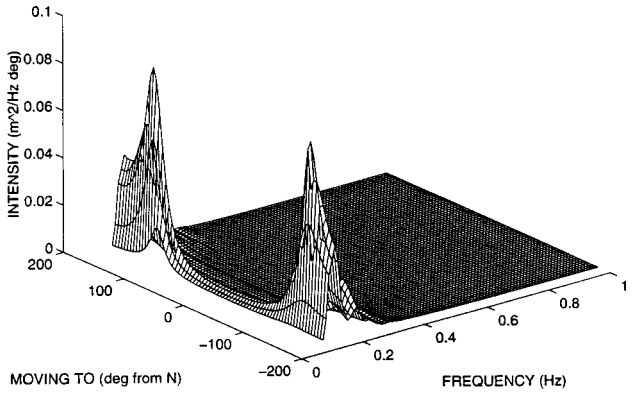

FIG. 8. Surface wave frequency-angle spectrum used in making the prediction in Fig. 9. The significant wave height is 2.7 m.

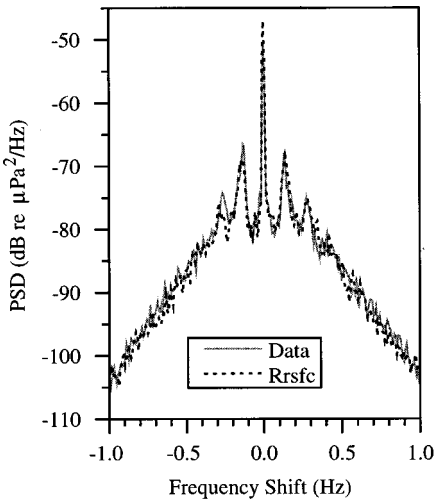

FIG. 9. Comparison of the predicted and measured frequency spectrum of the acoustic pressure at a hydrophone on the bottom (188 m) at a range of 9.35 km and for a 240-Hz source at a depth of 187 m. The significant wave height was 2.7 m.

frequency axis is the shift away from the carrier frequency.

In Fig. 5, the beam was incident at 25 degrees from the horizontal. In generating the set of surfaces for this case, the surface wave spectrum was cut off for wave numbers above $0.13\ \mathrm{m}^{-1}$, which was 4.25 times the wave number of the spectral peak. An estimate of the restrictions that this cutoff imposes on the scattering can be obtained from perturbation theory. The simple Bragg condition that follows from first-order perturbation theory (see, for example, Ref. 29) relates the grazing angle for a scattered plane wave to the grazing angle of the incident plane wave and to the wave number of the surface wave component doing the scattering

$$k\ \cos\ \theta_s = k\ \cos\ \theta_i + k_w, \tag{23}$$

where θ_i and θ_s are, respectively, the grazing angle of the incident and scattered wave, k is the acoustic wave number, and k_w is the wave number of the scattering surface wave component. In the case at hand, 0 degrees $< \theta_s <$ 46 degrees. At the lower limit the scattered wave is just on the border of becoming evanescent. In Eq. (23), the scattered wave becomes evanescent for $k_w = 0.0589$. In this simple approximation, the frequency of the scattering surface wave component corresponds to the frequency shift seen in the spectrum. Using the dispersion relation

$$f = \frac{1}{2\pi}\,(g k_w)^{1/2}, \tag{24}$$

where $g = 9.8\ \mathrm{m/s}^2$ is the acceleration of gravity, gives a frequency $f = 0.12$ Hz as the point where the scattered wave first becomes evanescent.

The depths for which spectra are shown in Fig. 5 are 5 m in Fig. 5(a), 25 m in Fig. 5(b), 100 m in Fig. 5(c), and 400 m in Fig. 5(d). Comparing Fig. 5(a) and (b) near an upshift of 0.12 Hz shows the steepening of the spectral fall with frequency at the greater depth where the contribution of the evanescent wave will have weakened. Figure 5(d) shows Rrsfc finally becoming less accurate at a depth of 400 m with its generally steeper scattering angles. This is particularly true at the larger frequency shifts.

Figures 6 and 7 are at a depth of 100 m, the same as Fig. 5(c), with incident beams at 45 and 60 degrees from horizontal, respectively. The ranges are 1000 m for Fig. 6 and 600 m for Fig. 7. In neither case was the surface wave number spectrum cut off.

III. COMPARISON WITH AN EXPERIMENTAL FREQUENCY SPECTRUM

The results shown in the previous section are quite good, but the ocean is a significantly more complicated environment with the possibility for a ray to interact repeatedly with the surface and bottom. Figure 8 shows the surface wave spectrum, and Fig. 9 compares the measured and Rrsfc predicted frequency spectrum of the acoustic pressure at a hydrophone on the ocean floor, water depth 188 m, in the Gulf of Mexico. The receiver was 9.35 km to the northwest of the 240 Hz cw source which was 1m off the ocean floor. The bathymetry along the source receiver track was almost perfectly flat. Although there was a 2-D wave buoy near the source, its output was not being recorded at the time of the measurements. The 2-D wave spectrum used as input to the surface generation program was reconstructed by J. L. Hanson and L. H. White[30] from measurements with other instruments. They extracted a directional spread function from a National Buoy Data Center wave buoy located about 50 nautical miles east of the source in shallower water, then applied it to a 1-D wave spectrum measured by the Institute of Ocean Sciences Water Acoustic Structure Profiler located approximately 10 kms from the receiver and at the same depth. It is their reconstructed spectrum that is plotted in Fig. 8. The highest peak in the spectrum is at 0.13 Hz and the significant wave height is 2.7 m. The uptrack direction is along 148 degrees, which is near one of the peaks in the spectrum. The other peak lies in a direction roughly perpendicular to the track.

Fifteen minutes of data were used to compute the experimental spectrum in Fig. 9. Notice that there are clear peaks in the spectrum at frequency shifts of once and twice the frequency of the peak in the surface wave spectrum. The

Rrsfc prediction was generated using 2048 successive surfaces spaced a half-second apart. This spacing puts the Nyquist frequency well beyond any interesting features in the experimental acoustic spectrum. In computing the spectrum, 128 second-long Fourier transforms were used giving a frequency spacing of 7.8 mHz. Successive segments were overlapped 50%. The 31 individual spectra from the 128 second-long time series were then averaged to produce the Rrsfc prediction in Fig. 9. When performing the Fourier transforms a Hanning window was used for both the experimental and model data. The agreement is excellent, especially when one realizes that, even if the spectral reconstruction were perfect, the model and the data see two different realizations of the underlying surface wave spectrum. For example, the $\sim$2.5-dB difference that is seen at the first downshifted peak is the same order of magnitude as the variation sometimes visible in the same place in successive 15-min data segments. Notice that not only is there good agreement at frequency shifts equal to plus or minus the frequency of the peak in the surface wave spectrum, but there is also pretty good agreement for the peaks centered at shifts of twice the frequency of the surface wave peak.

IV. CONCLUSION

I have extended the parabolic equation acoustic propagation program RAM to handle a one-dimensional rough air–water interface treated as a series of stair steps. By using a fine vertical spacing near the surface and a coarser one in the rest of the ocean, the efficiency of the resulting program has been significantly improved for moderate winds and acoustic frequencies up to around 1 kHz. Comparison with exact results for the pressure and frequency spectrum in a homogeneous half-space show that the new program, Rrsfc, is very accurate, even for steep incident rays. Comparison with an experimental frequency spectrum from a shallow water ocean environment featuring a moderately rough surface, 2.7-m significant wave height, and repeated surface and bottom interaction shows that the model is also accurate in that particular case.

It is, perhaps, worth mentioning that the method of treating the surface extends without difficulty from the one-dimensional rough surfaces treated so far to two-dimensional surfaces. Although computational load issues are likely to keep one from doing many computations with two-dimensional surfaces, such an extension would allow one to address the interesting physical issue of out of plane scattering.

ACKNOWLEDGMENTS

The integral equation results were calculated by E. Thorsos who also generated the surfaces and did most of the design of these test cases. Over the course of this research I have benefited from helpful discussions with M. Collins, R. Evans, J. Hanna, J. Hanson, Y. Lee, S. Magruder, K. McCann, L. Rogers, D. Rubenstein, C. Spofford, P. Stokes, E. Thorsos, and L. White. The research on which this paper was based was supported by the Office of the Chief of Naval Operations. Preparation for publication was aided by a Janney fellowship from the Johns Hopkins University Applied Physics Laboratory.

[1] O. A. Godin, ''Sound scattering at surface waves in the ocean, revisited,'' J. Acoust. Soc. Am. **98**, 2897(A) (1995).
[2] R. L. Holford, ''Scattering of sound waves at the ocean surface: A diffraction theory,'' J. Acoust. Soc. Am. **70**, 1103–1115 (1981).
[3] M. A. Leontovich and V. A. Fock, ''Solutions of the problem of propagation of electromagnetic waves along the earth's surface by the method of the parabolic equation,'' J. Exp. Theor. Phys. **16**, 557–573 (1946).
[4] V. A. Fock, *Electromagnetic Diffraction and Propagation Problems* (Pergamon, New York, 1965), pp. 213–234.
[5] R. H. Hardin and F. D. Tappert, ''Applications of the split-step Fourier method to the numerical solution of nonlinear and variable coefficient wave equations,'' SIAM (Soc. Ind. Appl. Math.) Rev. **15**, 423 (1973).
[6] F. D. Tappert, ''The parabolic approximation method,'' in *Wave Propagation and Underwater Acoustics*, edited by J. B. Keller and J. S. Papadakis, Lecture Notes in Physics, Volume 70 (Springer-Verlag, New York, 1977).
[7] L. B. Dozier, ''PERUSE: A numerical treatment of rough surface scattering for the parabolic wave equation,'' J. Acoust. Soc. Am. **75**, 1415–1432 (1984).
[8] G. V. Norton, J. C. Novarini, and R. S. Keiffer, ''Coupling scattering from the sea surface to a one-way marching propagation model via conformal mapping: Validation,'' J. Acoust. Soc. Am. **97**, 2173–2180 (1995).
[9] M. D. Collins, ''Applications and time-domain solution of higher-order parabolic equations in underwater acoustics,'' J. Acoust. Soc. Am. **86**, 1097–1102 (1989).
[10] R. B. Evans, ''The flattened parabolic equation,'' J. Acoust. Soc. Am. **104**, 2167–2173 (1998).
[11] F. D. Tappert and L. Nghiem-Phu, ''A new split-step Fourier algorithm for solving the parabolic wave equation with rough surface scattering,'' J. Acoust. Soc. Am. Suppl. 1 **77**, S101 (1985).
[12] E. I. Thorsos, J. W. Ballard, and T. E. Ewart, ''Rough surface scattering with the parabolic wave equation using the split-step method,'' J. Acoust. Soc. Am. Suppl. 1 **84**, S220–S221 (1988).
[13] K. B. Smith and F. D. Tappert, ''UMPE: The University of Miami Parabolic Equation Model, Version 1.1,'' MPL Technical Memorandum **432** (May 1993 revised September 1994).
[14] M. D. Collins, ''A split-step Padé solution for the parabolic equation method,'' J. Acoust. Soc. Am. **93**, 1736–1742 (1993).
[15] R. J. Cederberg and M. D. Collins, ''Application of an Improved Self-Starter to Geo-Acoustic Inversion,'' IEEE J. Ocean Eng. **22**, 102–109 (1997).
[16] M. D. Collins, ''User's Guide for RAM Versions 1.0 and 1.0p,'' Naval Research Laboratory, Washington, DC.
[17] An earlier implementation of this approach [A. P. Rosenberg and S. F. Magruder, ''An Accurate, Efficient Parabolic Equation Program That Permits a Rough Ocean Surface,'' STD-N-1004 (September 1994), The Johns Hopkins University, Applied Physics Laboratory, Laurel, MD] was based on FEPE. I have switched over to RAM for two reasons. It is a cleaner implementation and therefore easier to work on. As discussed later in the text, a rough surface leads to a more stringent requirement for accurate propagation of steep rays and RAM is better at this than FEPE.
[18] The unmelliflous acronym is short for RAM Rough Surface Fine Coarse.
[19] There are several other computer algebra programs which could equally well have been used.
[20] E. I. Thorsos, ''The validity of the Kirchoff approximation for rough surface scattering using a Gaussian roughness spectrum,'' J. Acoust. Soc. Am. **83**, 78–92 (1988).
[21] E. I. Thorsos, ''Acoustic scattering from a ''Pierson–Moskowitz'' sea surface,'' J. Acoust. Soc. Am. **88**, 335–349 (1990).
[22] M. B. Porter, F. B. Jensen, and C. M. Ferla, ''The problem of energy conservation in one-way models,'' J. Acoust. Soc. Am. **89**, 1058–1067 (1991).
[23] M. D. Collins and E. K. Westwood, ''A higher-order energy-conserving parabolic equation for range-dependent ocean depth, sound speed, and density,'' J. Acoust. Soc. Am. **89**, 1068–1075 (1991).
[24] M. D. Collins, ''An energy-conserving parabolic equation for elastic media,'' J. Acoust. Soc. Am. **94**, 975–982 (1993).
[25] RAM 1.0 is the version on which our code is based. There is also a

version 1.0p, designed for parallel processing, which expands the rational function in partial fractions.
[26] M. D. Collins, ''Generalization of the split-step Padé solution,'' J. Acoust. Soc. Am. **96**, 382–385 (1994).
[27] M. D. Collins, ''A higher-order parabolic equation for wave propagation in an ocean overlying an elastic bottom,'' J. Acoust. Soc. Am. **86**, 1459–1464 (1989).
[28] E. I. Thorsos, private communication.
[29] L. M. Brekhovskikh and Yu. P. Lysanov, *Fundamentals of Ocean Acoustics* (Springer-Verlag, New York, 1990), 2nd ed.
[30] L. H. White and J. L. Hanson, ''Synthesis of Directional Wave Spectra from Disparate Observations in the Gulf of Mexico,'' in *Proceedings of the Ocean Community Conference '98* (Marine Technology Society, Washington, DC, 1998), Vol. 2, pp. 696–702.

Piezoelectric thin shell theoretical model and eigenfunction analysis of radially polarized ceramic cylinders

D. D. Ebenezer and Pushpa Abraham
Transducer Group, Naval Physical and Oceanographic Laboratory, Naval Base, Kochi 682 004, India

(Received 21 November 1997; accepted for publication 29 August 1998)

A piezoelectric thin shell theoretical model of radially polarized ceramic cylinders is first developed. An eigenfunction approach is then used to determine the displacement, stress, electric field, and input electrical admittance of the cylinder. In the model, the effect of bending strain is included and it is assumed that the electric field varies linearly between the electrodes. It is then shown that the displacement and electric field are uncoupled, i.e., it is possible to first determine the displacement and then determine the electric field. It is also noted that, irrespective of the dimensions of the cylinder and the boundary conditions, the electric field can be much greater than the ratio of the applied voltage to the distance between electrodes. Next, the equations of motion and the boundary conditions are derived by using Hamilton's variational principle. They are solved by using the eigenfunction approach. The eigenfunctions are determined here by using a general method and, therefore, cylinders with arbitrary boundary conditions can be analyzed. The same method can be used even if other thin shell theories are used. It is shown that experimental resonance frequencies and input electrical admittance of free–free cylinders are in good agreement with those computed using the present model. It is also shown that the electric field is in good agreement with the work of other investigators. © *1999 Acoustical Society of America.* [S0001-4966(98)02512-0]

PACS numbers: 43.38.Ar, 43.38.Fx, 43.40.Ey, 43.20.Ks [SLE]

INTRODUCTION

A very large number of investigators have modeled elastic circular cylindrical shells of finite length by using exact theory as well as approximate theories such as membrane theory, and several thin and thick shell theories. For example, Greenspon[1] has compared the resonance frequencies of ''freely supported'' cylinders of various thickness to radius ratios and length to radius ratios obtained using exact elastic theory with those obtained using approximate theories.

In contrast to this, only a few investigators have considered piezoelectric shells of finite length and most of them have used membrane theory. The input electrical admittances of radially polarized piezoelectric cylinders with free and fixed ends were determined by Haskins and Walsh.[2] Radially polarized cylinders with arbitrary boundary conditions were analyzed using three port parameters by Ebenezer[3] and an eigenfunction approach by Ebenezer and Abraham.[4] In all of these studies, it was assumed that the electric field is constant in the shell. Membrane theory was also used by Wang[5] who analyzed tangentially and radially polarized cylinders, and by Martin[6] who analyzed axially polarized cylinders.

A few investigators, however, have used thin shell theories to model piezoelectric shells. Ko and Pond[7] determined the acoustic sensitivity of a spherical shell after including the effect of shell bending. The equations of motion used in their analysis contain only elastic coefficients because it was assumed that the charge density is zero everywhere. Drumheller and Kalnins[8] and later Rogacheva[9] developed thin shell theories for piezoelectric shells. They used equilibrium equations and did not explicitly derive equations of motion. A numerical method was used in Ref. 8 to solve the equations, while an approximate method was used in Ref. 9.

In this article, a model of radially polarized piezoelectric ceramic cylinders excited by an applied voltage is first developed by using a thin shell theory. It is assumed that the bending strain and the electric field vary linearly between the electrodes. The first approximation is consistent with Kirchoff's hypothesis[10] and the second is significantly better then assuming that the electric field is constant in the shell. These approximations are of higher order than those used in membrane theory. The electric field–displacement relationship is then determined by using the electrostatic equation for charge density. Next, Hamilton's variational principle[10–12] is used to derive the equations of motions and the boundary conditions. The equations of motion depend on the elastic, dielectric, and piezoelectric coefficients. Next, the equations are solved by using an eigenfunction approach.[4] In this approach the displacement is expressed as the sum of the static solution and a weighted sum of eigenfunctions. The weights are the modal velocities and the eigenfunctions satisfy the equations of motion and the boundary conditions of the short-circuited cylinder. The displacement is determined by using the orthogonal property of the eigenfunctions and then used to determine the electric field. Since the displacement can be very large at resonance even in a lossy cylinder, it follows that the electric field can be much greater than the ratio of the applied voltage to the distance between the electrodes. An expression for the input electrical admittance in terms of the displacements is also derived. Next, general methods to determine the static solution and the eigenfunctions are presented. They are applicable even when other thin shell theories are used to obtain the equations of motion. Next, the special case of a free–free cylinder is presented to illustrate the approach. It is of interest since experimental results can be very easily obtained. In this case, the eigen-

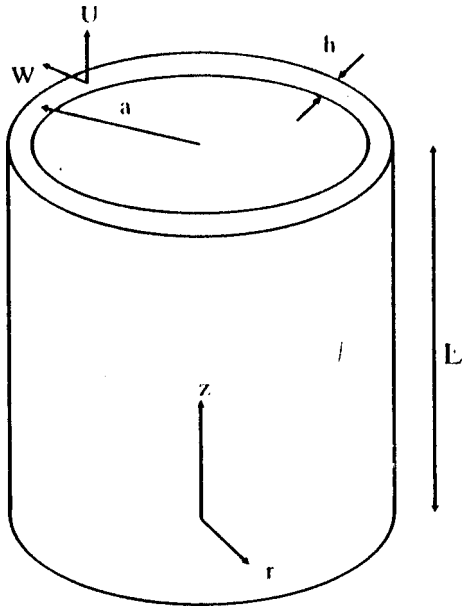

FIG. 1. A radially polarized piezoelectric ceramic cylinder with electrodes on the inner and outer curved surfaces.

functions cannot be obtained by inspection and they are obtained by using the general method. The analysis is therefore more involved than, for example, that of a simply or freely supported cylinder whose eigenfunctions can be obtained by inspection. Numerical results are also presented. The theoretical resonance frequencies and input electrical admittance obtained using this model are compared with measured values and the electric field is compared with the results obtained by using numerical methods[8] to solve the governing equations.

I. THEORETICAL ANALYSIS

Consider a thin radially polarized piezoelectric cylindrical shell of length L, mean radius a, and thickness h, where h is much less than the radius and length as shown in Fig. 1. The displacement, stress, and electric field in the shell and the input electrical admittance (IEA) when a voltage is applied across the electrodes which completely cover the inner and outer curved surfaces are of interest.

A. Equations of motion and boundary conditions

It is assumed that Kirchhoff's hypothesis[10] is valid. Therefore, the strain–displacement relations of a thin piezoelectric cylindrical shell can be expressed in cylindrical coordinates as

$$s_\theta(r,z,t)=w(a,z,t)/(a+x)\cong w(a,z,t)/a \tag{1a}$$

and

$$s_z(r,z,t)=\partial u(a,z,t)/\partial z-x\partial^2 w(a,z,t)/\partial z^2, \tag{1b}$$

where u and w are the radial and axial displacements, respectively, at $r=a$, $x=r-a$, s_θ and s_z are the strains in the θ and z directions, respectively, and t denotes time. The term containing x in Eq. (1b) is used to account for bending strain. It is neglected when using the membrane approximation.

Since the shell is thin, and it has been assumed that Kirchhoff's hypothesis is valid, the stress in the radial direction can be neglected. Therefore, the piezoelectric equations of state can be expressed[2] as

$$s_\theta(r,z,t)=s_{11}^E\tau_\theta(r,z,t)+s_{12}^E\tau_z(r,z,t)+d_{31}e_r(r,z,t), \tag{2a}$$

$$s_z(r,z,t)=s_{12}^E\tau_\theta(r,z,t)+s_{11}^E\tau_z(r,z,t)+d_{31}e_r(r,z,t), \tag{2b}$$

$$d_r(r,z,t)=d_{31}\tau_\theta(r,z,t)+d_{31}\tau_z(r,z,t)+\epsilon_{33}^T e_r(r,z,t), \tag{2c}$$

where τ_θ and τ_z are the normal stresses in the θ and z directions, respectively, and d_r and e_r are the charge density and electric field, respectively. The electroelastic coefficients s_{11}^E, s_{12}^E, d_{31}, and ϵ_{33}^T have their usual definitions. Equations (2a) and (2b) can be rearranged to obtain

$$\tau_z(r,z,t)=[Y/(1-\sigma^2)](s_z(r,z,t)+\sigma s_\theta(r,z,t) - d_{31}(1+\sigma)e_r(r,z,t)) \tag{3a}$$

and

$$\tau_\theta(r,z,t)=[Y/(1-\sigma^2)](s_\theta(r,z,t)+\sigma s_z(r,z,t) - d_{31}(1+\sigma)e_r(r,z,t)), \tag{3b}$$

where

$$Y=1/s_{11}^E \tag{3c}$$

and

$$\sigma=-s_{12}^E/s_{11}^E. \tag{3d}$$

The charge density, $d_r(r,z,t)$, must satisfy the electrostatic condition

$$\frac{1}{r}\frac{\partial}{\partial r}(rd_r(r,z,t))=0. \tag{4a}$$

The exact solution to Eq. (4a) has the form

$$d_r(r,z,t)=d_0(a,z,t)/(a+x), \tag{4b}$$

and an approximate solution has the form

$$d_r(r,z,t)\cong d_0(a,z,t)/a, \tag{4c}$$

where $d_0(a,z,t)$ is not a *constant* but merely independent of r.

Next, it is assumed that the electric field can be expressed as

$$e_r(r,z,t)=\frac{v(t)}{h}+\frac{x}{h}e(a,z,t), \tag{5a}$$

where v is the applied voltage and e is a function which has the dimensions of electric field and is to be determined. It is noted that the assumption is consistent with

$$\int_{-h/2}^{h/2} e_r(r,z,t)dx=v(t). \tag{5b}$$

The model used here is called a piezoelectric thin shell model because it is assumed that the axial strain and the electric field vary linearly between the electrodes.

It can now be seen by substituting Eqs. (1), (3), and (5a) into Eq. (2c) that

$$d_r(r,z,t)=\left[\frac{d_{31}Y}{1-\sigma}\left(\frac{\partial}{\partial z}\,u(a,z,t)+\frac{1}{a}\,w(a,z,t)\right)+\frac{\epsilon_{33}^{T}(1-\sigma-2k_{31}^{2})}{1-\sigma}\,\frac{v(t)}{h}\right]\frac{a-x}{a}, \tag{6a}$$

when

$$e(a,z,t)=-\frac{v(t)}{a}+\frac{hk_{31}^{2}}{d_{31}(1-\sigma-2k_{31}^{2})}\left(\frac{\partial^{2}}{\partial z^{2}}\,w(a,z,t)-\frac{1}{a}\frac{\partial}{\partial z}\,u(a,z,t)-\frac{1}{a^{2}}\,w(a,z,t)\right), \tag{6b}$$

where

$$k_{31}^{2}=d_{31}^{2}/(s_{11}^{E}\epsilon_{33}^{T}). \tag{6c}$$

Then, on comparing Eq. (4b) with (6a) it can be seen that the latter is approximately equal to the exact solution of Eq. (4a). The difference is of the order of $(x/a)^2$. Similarly, it can be seen that

$$d_r(r,z,t)=\frac{d_{31}Y}{1-\sigma}\left(\frac{\partial}{\partial z}\,u(a,z,t)+\frac{1}{a}\,w(a,z,t)\right)+\frac{\epsilon_{33}^{T}(1-\sigma-2k_{31}^{2})}{1-\sigma}\,\frac{v(t)}{h} \tag{7a}$$

when

$$e(a,z,t)=\frac{hk_{31}^{2}}{d_{31}(1-\sigma-2k_{31}^{2})}\,\frac{\partial^{2}}{\partial z^{2}}\,w(a,z,t), \tag{7b}$$

and that Eq. (7a) is an approximate solution to Eq. (4a) and has the form of Eq. (4c).

Since the approximation $1/(a+x)\cong 1/a$ has already been used in Eq. (1a) and the coefficients of the highest order derivative, $(\partial^2/\partial z^2)w(a,z,t)$, in Eqs. (6b) and (7b) are the same, Eqs. (7a) and (7b) and not Eqs. (6a) and (6b) are used in the rest of this article. If Eqs. (6a) and (6b) are used, some additional terms will appear in the equations of motion which can however be solved by using the approach used here.

The equations of motion can now be derived by using Hamilton's variational principle.[10–12] It states that

$$\delta\int_{t_1}^{t_2}(\mathbb{T}(t)-\mathbb{V}(t)+\mathbb{E}(t))\,dt=0, \tag{8a}$$

where δ denotes variation, t_1 and t_2 are an initial time and a final time, respectively, at which the displacements are fixed,

$$\mathbb{T}(t)=\varrho\,\pi a\int_0^L\int_{-h/2}^{h/2}\left(\frac{\partial}{\partial t}\,u(a,z,t)\right)^{2}+\left(\frac{\partial}{\partial t}\,w(a,z,t)\right)^{2}dx\;dz \tag{8b}$$

is the total kinetic energy of the shell,

$$\mathbb{V}(t)=\pi a\int_0^L\int_{-h/2}^{h/2}[\,\tau_z(r,z,t)s_z(r,z,t)+\tau_\theta(r,z,t)s_\theta(r,z,t)]dx\;dz \tag{8c}$$

is the total work energy, and

$$\mathbb{E}(t)=\pi a\int_0^L\int_{-h/2}^{h/2}d_r(r,z,t)e_r(r,z,t)dx\;dz \tag{8d}$$

is the total electric energy. The approximation $\pi(a+x)\cong\pi a$ has been used in Eqs. (8b)–(8d).

It can be shown after substituting Eqs. (1), (3), and (7) into Eqs. (8b)–(8d) that

$$\delta\mathbb{T}(t)=2\varrho\,\pi ah\int_0^L\left(\frac{\partial u}{\partial t}\,\frac{\partial}{\partial t}\,\delta u+\frac{\partial w}{\partial t}\,\frac{\partial}{\partial t}\,\delta w\right)dz, \tag{9a}$$

$$\delta\mathbb{V}(t)=\frac{2\pi ahY}{1-\sigma^{2}}\times\int_0^L\left\{\left(\frac{\partial u}{\partial z}\,\frac{\partial}{\partial z}+\frac{\sigma}{a}\,w\,\frac{\partial}{\partial z}-\frac{d_{31}(1+\sigma)v}{2h}\,\frac{\partial}{\partial z}\right)\times\delta u+\left(\frac{\sigma}{a}\,\frac{\partial u}{\partial z}+\frac{w}{a^{2}}+\frac{h^{2}}{12}\,(1+\varphi)\,\frac{\partial^{2}w}{\partial z^{2}}\,\frac{\partial^{2}}{\partial z^{2}}-\frac{d_{31}(1+\sigma)v}{2ah}\right)\delta w\right\}dz, \tag{9b}$$

and

$$\delta\mathbb{E}(t)=\frac{\pi aYd_{31}}{(1-\sigma)}\,v\int_0^L\left\{\left(\frac{\partial}{\partial z}\right)\delta u+\frac{1}{a}\,\delta w\right\}dz, \tag{9c}$$

where

$$\varphi=\frac{(1+\sigma)k_{31}^{2}}{1-\sigma-2k_{31}^{2}}. \tag{9d}$$

Equations (9a)–(9c) can now be integrated by parts and substituted into Hamilton's Eq. (8a). The resulting equation can be expressed in the form

$$\int_{t_1}^{t_2}\int_0^L[(\;)\,\delta u+(\;)\,\delta w]dz\;dt+\int_{t_1}^{t_2}(\;)\,\delta u\Big|_0^L+(\;)\,\delta w\Big|_0^L+(\;)\,\frac{\partial}{\partial z}\,\delta w\Big|_0^L dt=0. \tag{10}$$

It must be satisfied for arbitrary δu, δw, and $(\partial/\partial z)\delta w$ and the coefficients of these quantities must therefore be zero.

After equating the coefficients in the double integrals of Eq. (10) to zero, the following equations are obtained:

$$[\Gamma]\begin{Bmatrix}u(a,z,t)\\ w(a,z,t)\end{Bmatrix}+\varrho h\begin{Bmatrix}\frac{\partial^{2}}{\partial t^{2}}\,u(a,z,t)\\ \frac{\partial^{2}}{\partial t^{2}}\,w(a,z,t)\end{Bmatrix}=\begin{Bmatrix}0\\ Cv(t)\end{Bmatrix}, \tag{11a}$$

where

$$[\Gamma]=\frac{Yh}{a^2(1-\sigma^2)}\begin{bmatrix} -a^2\dfrac{\partial^2}{\partial z^2} & -\sigma a\dfrac{\partial}{\partial z} \\ \sigma a\dfrac{\partial}{\partial z} & 1+\beta^2(1+\varphi)a^4\dfrac{\partial^4}{\partial z^4}\end{bmatrix}, \tag{11b}$$

$$\beta^2=h^2/(12a^2), \tag{11c}$$

and

$$C=d_{31}Y/([a(1-\sigma)]. \tag{11d}$$

It is noted that Eq. (11) is the same as the equations of motion[10] of a thin elastic cylindrical shell of length L, radius a, and thickness $h(1+\varphi)^{1/2}$.

Similarly, after equating to zero the coefficients in the single integrals of Eq. (10) the following boundary conditions are obtained:

$$[B]\begin{Bmatrix} u(a,z,t) \\ w(a,z,t) \\ v(t)\end{Bmatrix}=\begin{Bmatrix}0\\0\\0\end{Bmatrix}, \quad z=0,L, \tag{12a}$$

where

$$[B]=\begin{bmatrix} \partial/\partial z & \sigma/a & -d_{31}(1+\sigma)/h \\ 0 & \partial^2/\partial z^2 & 0 \\ 0 & \partial^3/\partial z^3 & 0\end{bmatrix}. \tag{12b}$$

It is noted that the boundary conditions in Eqs. (12) are for a free–free piezoelectric cylindrical shell. Specifically, it can be seen by using Eqs. (1) and (3a) that Eqs. (12) indicate that the axial stress at $r=a$ is zero at the ends of the cylinder. Equations (12) also indicate that the shear force and bending moment are zero. The boundary conditions for a free–free cylinder are indicated by Eqs. (12) because boundary forces and moments have been assumed to be zero[12] in the expression, Eq. (8c), for the total work energy. In the general case, the impedances at the ends are nonzero but the boundary conditions can be expressed in the form of Eq. (12a).

After defining a Fourier transform pair

$$f(t)=\frac{1}{2\pi}\int_{-\infty}^{\infty}F(\omega)\exp(+j\omega t)d\omega; \tag{13a}$$

$$F(\omega)=\int_{-\infty}^{\infty}f(t)\exp(-j\omega t)dt, \tag{13b}$$

where lowercase and uppercase letters are used to denote time and frequency dependent variables, respectively, Eqs. (11a) and (12a) can be expressed as

$$[\Gamma]\begin{Bmatrix}U(a,z,\omega)\\W(a,z,\omega)\end{Bmatrix}-\omega^2\varrho h\begin{Bmatrix}U(a,z,\omega)\\W(a,z,\omega)\end{Bmatrix}=\begin{Bmatrix}0\\CV(\omega)\end{Bmatrix}; \tag{14}$$

and

$$[B]\begin{Bmatrix}U(a,z,\omega)\\W(a,z,\omega)\\V(\omega)\end{Bmatrix}=\begin{Bmatrix}0\\0\\0\end{Bmatrix}, \quad z=0,L, \tag{15}$$

respectively.

It is assumed that $V(\omega)$ is equal to a constant V_0 in the rest of this article.

B. Solution

The solution to the inhomogeneous equations of motion (14) which satisfies the boundary conditions in Eq. (15) can be expressed in the form[4]

$$\begin{Bmatrix}U(a,z,\omega)\\W(a,z,\omega)\end{Bmatrix}=V_0\begin{Bmatrix}U_{\rm dc}(a,z)\\W_{\rm dc}(a,z)\end{Bmatrix}+V_0\begin{Bmatrix}U_{\rm sc}(a,z,\omega)\\W_{\rm sc}(a,z,\omega)\end{Bmatrix}. \tag{16}$$

The first term on the right-hand side of Eq. (16) is the dc solution. It satisfies the static equations

$$[\Gamma]\begin{Bmatrix}U_{\rm dc}(a,z)\\W_{\rm dc}(a,z)\end{Bmatrix}=\begin{Bmatrix}0\\C\end{Bmatrix}, \tag{17a}$$

obtained by setting $\omega=0$ in Eq. (14), and also satisfies six boundary conditions which can be expressed in the form

$$[B]\begin{Bmatrix}U_{\rm dc}(a,z)\\W_{\rm dc}(a,z)\\1\end{Bmatrix}=0, \quad z=0,L. \tag{17b}$$

The second term on the right-hand side of Eq. (16) can be expressed as[4]

$$\begin{Bmatrix}U_{\rm sc}(a,z,\omega)\\W_{\rm sc}(a,z,\omega)\end{Bmatrix}=\sum_{m=M}^{M}\sum_{i=1}^{I_m}V_{mi}(\omega)\{\Phi_{mi}(z)\}, \tag{18a}$$

where

$$\{\Phi_{mi}(z)\}=\begin{Bmatrix}\psi_{mi}(z)\\\phi_{mi}(z)\end{Bmatrix} \tag{18b}$$

are the eigenfunctions of the short-circuited cylinder, $M=0$ or 1, $M=\infty$ and $I_m=1$ or 2. Each eigenfunction satisfies the homogeneous equations of motion

$$[\Gamma]\begin{Bmatrix}U_{\rm sc}(a,z,\omega)\\W_{\rm sc}(a,z,\omega)\end{Bmatrix}-\omega^2\varrho h\begin{Bmatrix}U_{\rm sc}(a,z,\omega)\\W_{\rm sc}(a,z,\omega)\end{Bmatrix}=\begin{Bmatrix}0\\0\end{Bmatrix}, \tag{19}$$

at an angular resonance frequency ω_{mi}, and the boundary conditions of the short-circuited cylinder

$$[B]\begin{Bmatrix}U_{\rm sc}(a,z,\omega)\\W_{\rm sc}(a,z,\omega)\\0\end{Bmatrix}=0, \quad z=0,L \tag{20}$$

at all frequencies where Eqs. (19) and (20) are obtained by setting $V_0=0$ in Eqs. (14) and (15), respectively. The angular resonance frequencies ω_{m1} and ω_{m2} are referred to as being in the lower and upper branches, respectively.

It is noted that the eigenfunctions form a complete set of functions. However, in most cases, they are complete only in the ordinary Fourier or normwise sense. Sets of functions which are complete in the ordinary Fourier or normwise sense and are not all zero at the same point are said to be pointwise complete.[13] It was shown in Ref. 4 that the series expression for the displacement may converge to an incorrect value if the dc term is not used in Eq. (16).

The displacement coefficients per unit voltage, $V_{mi}(\omega)$, can be determined by using the equations of motion of the piezoelectric cylinder and the orthogonal property of the eigenfunctions. It can be shown that[4]

$$V_{mi}(\omega)=\frac{F_{mi}(\omega)}{K_{mi}-\omega^2 M_{mi}}, \tag{21a}$$

where

$$F_{mi}(\omega)=\omega^2 2\pi a\varrho h\int_0^L\{\Phi_{mi}(z)\}^T\begin{Bmatrix}U_{\rm dc}(z)\\ W_{\rm dc}(z)\end{Bmatrix}dz, \tag{21b}$$

$$K_{mi}=\omega_{mi}^2\varrho h N_{mi}, \tag{21c}$$

$$M_{mi}=\varrho h N_{mi}, \tag{21d}$$

$$2\pi a\int_0^L\{\Phi_{nk}(z)\}^T\{\Phi_{mi}(z)\}dz=N_{mi}\delta_{mn}\delta_{ik} \tag{21e}$$

and δ_{mn} is the Kronecker delta function. It is noted that $F_{mi}(\omega)$, K_{mi}, and M_{mi} are the modal force, stiffness, and mass, respectively. It is also noted that F_{mi} is zero at zero frequency as indeed should be the case.

The stresses in the cylinder can now be easily determined by using Eqs. (3), (1), and (16).

Next, the electric field can be easily obtained by using Eqs. (5a), (7b), and (16). It can be shown that

$$E_r(r,z,\omega)=V_0\left[\frac{1}{h}+\frac{xk_{31}^2}{d_{31}(1-\sigma-2k_{31}^2)}\frac{\partial^2}{\partial z^2}\times\left(W_{\rm dc}+\sum_{m=M}^{M}\sum_{i=1}^{I_m}\frac{F_{mi}(\omega)}{K_{mi}-\omega^2 M_{mi}}\phi_{mi}\right)\right]. \tag{22}$$

Equation (22) indicates that at resonance, irrespective of the boundary conditions and dimensions of the cylinder, the electric field becomes infinity in a lossless cylinder and can be much greater than V_0/h in a lossy cylinder.

The input electrical admittance can now be obtained. After substituting Eqs. (3) and (22) into the equation of state (2c) and integrating over the mean surface, the total charge on the mean surface, $Q(\omega)$, can be obtained. Finally, after using the expression for $Q(\omega)$ and Eqs. (1) and (16) the input electrical admittance, $Y(\omega)$, can be expressed as

$$Y(\omega)=j\omega Q(\omega)/V_0 \tag{23a}$$

$$=j\omega C_0\left\{1-2k_{31}^2/(1-\sigma)+(d_{31}h/[\epsilon_{33}^T s_{11}^E(1-\sigma)L])\times\left[U_{\rm dc}(L,\omega)-U_{\rm dc}(0,\omega)+\frac{1}{a}\int_0^L W_{\rm dc}(z,\omega)dz+\sum_{m=M}^{M}\sum_{i=1}^{I_m}V_{mi}(\omega)\times\left(\psi_{mi}(L)-\psi_{mi}(0)+\frac{1}{a}\int_0^L\phi_{mi}(z)dz\right)\right]\right\}, \tag{23b}$$

where

$$C_0=2\pi aL\epsilon_{33}^T/h. \tag{23c}$$

C. General methods to find the static solution and the eigenfunctions

It can be easily seen from the static Eq. (17a) that

$$\frac{\partial}{\partial z}U_{\rm dc}=\frac{1}{\sigma a}\left(d_{31}(1+\sigma)a/h-1+\beta^2(1+\varphi)a^4\frac{\partial^4}{\partial z^4}\right)W_{\rm dc} \tag{24a}$$

and

$$\frac{\partial^5}{\partial z^5}W_{\rm dc}+\eta^4\frac{\partial}{\partial z}W_{\rm dc}=0, \tag{24b}$$

where

$$\eta^4=\frac{1-\sigma^2}{\beta^2(1+\varphi)a^4}. \tag{24c}$$

It therefore follows that the solution[14] to Eq. (17a) can be expressed as

$$\begin{Bmatrix}U_{\rm dc}\\ W_{\rm dc}\end{Bmatrix}=\begin{Bmatrix}\frac{1}{\sigma a}\left[d_{31}(1+\sigma)az/h-\sum_{n=1}^{4}A_n\exp(\mu_n z)(1/\mu_n-\beta^2(1+\varphi)a^4\mu_n^3)-A_5 z\right]+A_6\\ \sum_{n=1}^{4}A_n\exp(\mu_n z)+A_5\end{Bmatrix}, \tag{25a}$$

where

$$[\mu_1,\mu_2,\mu_3,\mu_4]=\left[\frac{\eta(1+j)}{2^{1/2}},\frac{\eta(1-j)}{2^{1/2}},-\frac{\eta(1+j)}{2^{1/2}},\frac{\eta(1-j)}{2^{1/2}}\right], \tag{25b}$$

and the six coefficients A_n, $n=1,2,...,6$ are to be determined by using the static boundary conditions. Since the displacements are real and μ_n, $n=1,2,3,4$ are complex, it follows that $A_1=A_2^*$ and $A_3=A_4^*$, where * denotes complex conjugate. In general, the eigenfunctions cannot be obtained by inspection. However, they can be determined by using a gen-

eral approach which can be used for all boundary conditions.

It can be shown that the eigenfunctions can be expressed in the form[15]

$$\{\Phi_{mi}(z)\}=\begin{Bmatrix}\psi_{mi}(z)\\ \phi_{mi}(z)\end{Bmatrix}=\sum_{s=1}^{6} G_{mis}\{\zeta_s(\omega_{mi},z)\}, \tag{26a}$$

where

$$\{\zeta_s(\omega,z)\}=\begin{Bmatrix}\alpha_s(\omega)\exp[\lambda_s(\omega)z]\\ \exp[\lambda_s(\omega)z]\end{Bmatrix} \tag{26b}$$

are solutions to the equations of motion (19) of the short-circuited cylinder at the angular frequency ω. It can be easily seen by substituting Eq. (27b) into Eq. (19) that the functions $\alpha_s(\omega)$ and $\lambda_s(\omega)$ can be obtained from

$$\begin{bmatrix}-a^2\lambda_s^2(\omega)-\Omega^2 & -\sigma a\lambda_s(\omega)\\ \sigma a\lambda_s(\omega) & 1+\beta^2(1+\varphi)a^4\lambda_s^4(\omega)-\Omega^2\end{bmatrix}\begin{Bmatrix}\alpha_s(\omega)\\ 1\end{Bmatrix}=\begin{Bmatrix}0\\ 0\end{Bmatrix}, \tag{26c}$$

where

$$\Omega^2=\omega^2a^2/c_p^2 \tag{26d}$$

and

$$c_p^2=Y/[\varrho(1-\sigma^2)], \tag{26e}$$

i.e., $\lambda_s(\omega)$ are the solutions to

$$\begin{vmatrix}-a^2\lambda_s^2(\omega)-\Omega^2 & -\sigma a\lambda_s(\omega)\\ \sigma a\lambda_s(\omega) & 1+\beta^2(1+\varphi)a^4\lambda_s^4(\omega)-\Omega^2\end{vmatrix}=0 \tag{26f}$$

and

$$\begin{aligned}\alpha_s(\omega)&=\sigma a\lambda_s(\omega)/(-a^2\lambda_s^2(\omega)-\Omega^2)\\ &=-(1+\beta^2(1+\varphi)a^4\lambda_s^4(\omega)-\Omega^2)/[\sigma a\lambda_s(\omega)].\end{aligned} \tag{26g}$$

The six values of λ_s which satisfy the cubic Eq. (26f) in λ_s^2 can be obtained by using standard formulas.[16] It can be easily shown that if the pth solution to Eq. (26f) is λ_p, then the qth solution will be equal to $-\lambda_p$. Further, if λ_p is a complex number, then the rth solution will be equal to λ_p^* and it can be shown by using Eq. (26g) that α_r will be equal to α_p^*. However, ψ_{mi} and ϕ_{mi} are real valued functions and it therefore follows that G_{mir} will be equal to G_{mip}^*. Since G_{mis} may be complex it is convenient to rewrite Eq. (26a) in the form

$$\begin{aligned}\{\Phi_{mi}(z)\}=\sum_{s=1}^{S}&(\mathrm{Re}[2G_{mis}]\mathrm{Re}\{\zeta_s(\omega_{mi},z)\}\\ &-\mathrm{Im}[2G_{mis}]\mathrm{Im}\{\zeta_s(\omega_{mi},z)\})\\ &+\sum_{s=2S+1}^{6} G_{mis}\{\zeta_s(\omega_{mi},z)\},\end{aligned} \tag{27}$$

where G_{mis}, $s=1,...,S$ are the complex conjugates of G_{mis}, $s=S+1,...,2S$, respectively, and G_{mis}, $s=2S+1,...,6$ are real.

The eigenfunctions must satisfy not only the equations of motion but also the boundary conditions of the short-circuited cylinder. The values of G_{mis} in Eq. (27) and the angular resonance frequencies, ω_{mi}, can be determined by using three boundary conditions at each end of the cylinder. After substituting Eq. (27) into the boundary conditions in Eq. (20), the resulting equation can be expressed in the form

$$[Y(\omega)]\begin{Bmatrix}\mathrm{Re}[2G_{mi1}]\\ -\mathrm{Im}[2G_{mi1}]\\ \mathrm{Re}[2G_{mi2}]\\ -\mathrm{Im}[2G_{mi2}]\\ G_{mi5}\\ G_{mi6}\end{Bmatrix}=\begin{Bmatrix}0\\0\\0\\0\\0\\0\end{Bmatrix}, \tag{28}$$

where S has been assumed to be two for the purpose of illustration and the elements of $[Y]$ are functions of α_s and λ_s. A solution to Eq. (28) exists only when

$$|Y(\omega)|=0. \tag{29}$$

The angular frequencies, ω_{mi}, at which Eq. (29) is satisfied can be determined by using numerical search methods. The values of G_{mis} can then be determined by solving Eq. (28) after assigning an arbitrary value to one of them. Finally, the eigenfunctions can be obtained by using Eq. (27).

II. SPECIAL CASE

As a special case, consider a thin cylindrical shell with zero axial stress, shear stress, and bending moment at both the ends. This case is of special interest since experimental results can be easily obtained. The boundary conditions for the cylinder can be obtained from Eqs. (12b) and (15).

The static solution for this special case can be determined either by inspection or by using Eqs. (17b) and (25). In the latter case, any five of the six boundary conditions can be used to determine A_n, $n=1,2,...,5$. A_6 can be determined by using symmetry considerations since it does not occur in the equations for the boundary conditions. It can be shown that

$$\begin{Bmatrix}U_{\mathrm{dc}}(a,z)\\ W_{\mathrm{dc}}(a,z)\end{Bmatrix}=\begin{Bmatrix}d_{31}(z-L/2)/h\\ d_{31}a/h\end{Bmatrix}. \tag{30}$$

It is noted that Eq. (30) is also the static solution for a cylinder with zero axial stress at the ends when membrane theory[4] is used.

It can be easily shown by using Eqs. (18a), (26a), and (26b) in the boundary conditions for the short-circuited cylinder that the $[Y]$ matrix for this special case can be expressed as

$$
[Y] = \begin{bmatrix}
\mathrm{Re}\left(\alpha_1\lambda_1+\frac{\sigma}{a}\right) & \mathrm{Im}\left(\alpha_1\lambda_1+\frac{\sigma}{a}\right) & \mathrm{Re}\left(\alpha_2\lambda_2+\frac{\sigma}{a}\right) & \mathrm{Im}\left(\alpha_2\lambda_2+\frac{\sigma}{a}\right) & \alpha_5\lambda_5+\frac{\sigma}{a} & \alpha_6\lambda_6+\frac{\sigma}{a} \\
\mathrm{Re}\left[\left(\alpha_1\lambda_1+\frac{\sigma}{a}\right)\exp(\lambda_1 L)\right] & \mathrm{Im}\left[\left(\alpha_1\lambda_1+\frac{\sigma}{a}\right)\exp(\lambda_1 L)\right] & \mathrm{Re}\left[\left(\alpha_2\lambda_2+\frac{\sigma}{a}\right)\exp(\lambda_2 L)\right] & \mathrm{Im}\left[\left(\alpha_2\lambda_2+\frac{\sigma}{a}\right)\exp(\lambda_2 L)\right] & \left(\alpha_5\lambda_5+\frac{\sigma}{a}\right)\exp(\lambda_3 L) & \left(\alpha_6\lambda_6+\frac{\sigma}{a}\right)\exp(\lambda_6 L) \\
\mathrm{Re}(\lambda_1^2) & \mathrm{Im}(\lambda_1^2) & \mathrm{Re}(\lambda_2^2) & \mathrm{Im}(\lambda_2^2) & \lambda_5^2 & \lambda_6^2 \\
\mathrm{Re}[\lambda_1^2\exp(\lambda_1 L)] & \mathrm{Im}[\lambda_1^2\exp(\lambda_1 L)] & \mathrm{Re}[\lambda_2^2\exp(\lambda_2 L)] & \mathrm{Im}[\lambda_2^2\exp(\lambda_2 L)] & \lambda_5^2\exp(\lambda_5 L) & \lambda_6^2\exp(\lambda_6 L) \\
\mathrm{Re}(\lambda_1^3) & \mathrm{Im}(\lambda_1^3) & \mathrm{Re}(\lambda_2^3) & \mathrm{Im}(\lambda_2^3) & \lambda_5^3 & \lambda_6^3 \\
\mathrm{Re}[\lambda_1^3\exp(\lambda_1 L)] & \mathrm{Im}[\lambda_1^3\exp(\lambda_1 L)] & \mathrm{Re}[\lambda_2^3\exp(\lambda_2 L)] & \mathrm{Im}[\lambda_2^3\exp(\lambda_2 L)] & \lambda_5^3\exp(\lambda_5 L) & \lambda_6^3\exp(\lambda_6 L)
\end{bmatrix}, \tag{31}
$$

TABLE I. The resonance frequencies in the lower ($i=1$) and upper ($i=2$) branches computed using the piezoelectric thin shell theory presented here, membrane theory, and measured values.

m,i	Resonance frequency (kHz)		
	Piezoelectric thin shell theory	Membrane theory	Experiment
1,1	31.43	31.35	31.35
2,1	31.78	31.74	
3,1	40.50	31.80	38.5
4,1	76.44	31.83	
5,1	140.06	31.84	108.5
6,1	227.76	31.84	
7,1	338.38	31.84	321
1,2	84.58	84.56	84.56
2,2	167.09	167.04	
3,2	250.13	250.05	245
4,2	333.31	333.17	
5,2	416.60	416.33	390

where it has again be assumed that $S=2$ for the purpose of illustration. The eigenfunctions and resonance frequencies can now be obtained by solving Eq. (29) after substituting Eq. (31) in it. Finally, the displacement, stress and electric field distributions and the input electric admittance can be determined by using the equations in Sec. I B.

III. NUMERICAL AND EXPERIMENTAL RESULTS AND DISCUSSION

Numerical results are presented to illustrate the approach and to compare the results obtained using this model with those obtained using membrane theory as well as with experimental results.

The approximate values of the dimensions, density, and coefficients of a cylinder used to illustrate some results are $L=20$ mm, $a=15$ mm, $h=2.5$ mm, $\varrho=7150$ kg/m^3, and $\epsilon_{33}^T/\epsilon_0=2000$ $s_{11}^E=15\times10^{-12}$ m^2/N, $s_{12}^E=-6\times10^{-12}$ m^2/N, and $g_{31}=-10\times10^{-3}$ Vm/N, respectively.

The resonance frequencies, displacement, stress, electric field, etc. of a cylinder with zero axial stress, shear force, and bending moment obtained using piezoelectric thin shell theory can be compared with those obtained using membrane theory. When membrane theory is used, only one boundary condition can be specified at each end. The appropriate boundary condition for the purpose of comparison is zero axial stress at the ends.

The resonance frequencies of the cylinder obtained by using the piezoelectric thin shell theory used in this article and the membrane theory used in Ref. 4 are compared with experimental values in Table I. $i=1$ and 2 refer to the lower and upper branches, respectively. The values of the electroelastic coefficients used in the computation were determined[17] by using experimental data and membrane theory. Therefore, the lowest resonance frequencies in the lower and upper branches obtained using membrane theory are in exact agreement with experimental results. All the resonance frequencies in the lower branch obtained using membrane theory are less than the hoop mode resonance

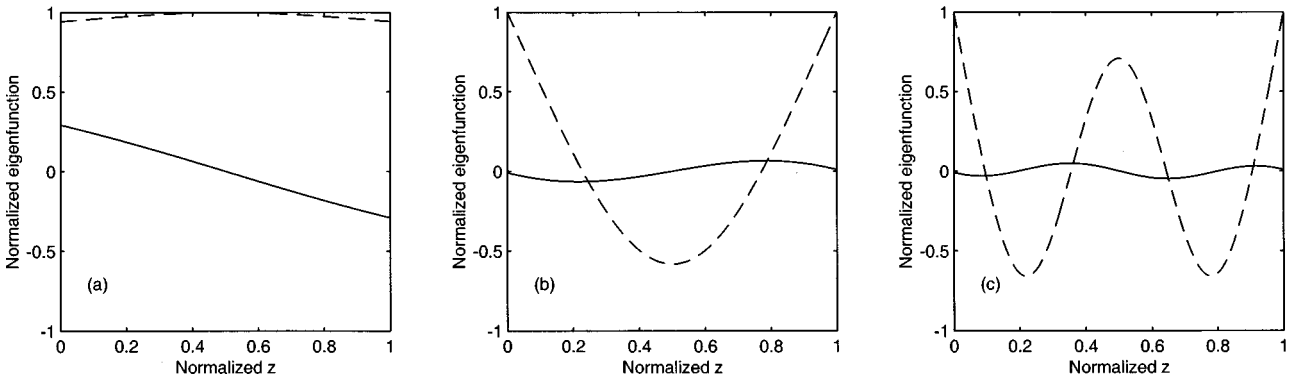

FIG. 2. The eigenfunctions Φ_{m1}, $m=1,3,5$ which are in the lower branch. ——— ψ_{m1} (axial component). – – – – ϕ_{m1} (radial component). The corresponding resonance frequencies are (a) 31.43 kHz, (b) 40.50 kHz, and (c) 141.06 kHz, respectively, as shown in Table I.

frequency, $1/[2\pi a(\varrho s_{11}^{E})^{1/2}]$ which is equal to 31.85 kHz. Therefore, the resonance frequencies in the lower branch obtained using membrane theory, except the lowest resonance frequency, are in poor agreement with experimental values. The resonance frequencies obtained using the piezoelectric thin shell theory is in much better agreement with experiment. The resonance frequencies in the upper branch obtained by using the two models are nearly the same and approximately equal to the experimental values. The experimental values were obtained by measuring the input electrical admittance. Since the electrodes fully cover the curved surfaces, only the eigenfunctions whose radial components, $\phi_{mi}(z)$, are symmetric with respect to the center of the cylinder are excited. Therefore, only the corresponding resonance frequencies could be measured.

The eigenfunctions Φ_{m1}, $m=1,3,5$ obtained using piezoelectric theory are shown in Fig. 2. They are in the lower branch. The eigenfunctions Φ_{m2}, $m=1,3,5$ which are in the upper branch are shown in Fig. 3. All the eigenfunctions in Figs. 2 and 3 can be electrically excited. They have been normalized to make the maximum value of the components one. The radial and axial components are shown by solid and dashed lines, respectively. It can be seen from the figures that in this case the maximum value of the radial component, $\phi_{mi}(z)$, is greater than the maximum value of the axial component, $\psi_{mi}(z)$, for eigenfunctions in the lower branch and vice versa for those in the upper branch. When membrane theory is used to analyze a cylinder with zero axial stress at the ends, the radial components of all the eigenfunctions are zero at the ends of the cylinder.[4] It can be seen from Figs. 2 and 3 that this is not so when piezoelectric thin shell theory is used, i.e., the eigenfunctions form a pointwise complete set of functions.

At frequencies much less than the lowest resonance frequency, there is no significant difference between the displacements, stresses, and input electrical admittances of free cylinders obtained using membrane and piezoelectric thin shell theories because they depend primarily on the static displacements. However, at higher frequencies there may be a significant difference for two reasons. First, as already shown, the resonance frequencies, $f_{mi}=\omega_{mi}/2\pi$, obtained by using the two theories may differ considerably. Second, bending stresses are not included in membrane theory. To illustrate this the axial stresses at 30 kHz and 31 kHz when 1 V is applied across the electrodes are shown in Fig. 4(a) and (b), respectively. The stresses computed using piezoelectric thin shell and membrane theories are shown by solid and dashed lines, respectively, over half the length of the cylinder. The resonance frequencies, f_{11}, obtained using the thin shell and membrane theories are 31.43 kHz and 31.35 kHz, respectively. It can be seen from the figures that as the excitation frequency approaches 31.35 kHz the difference be-

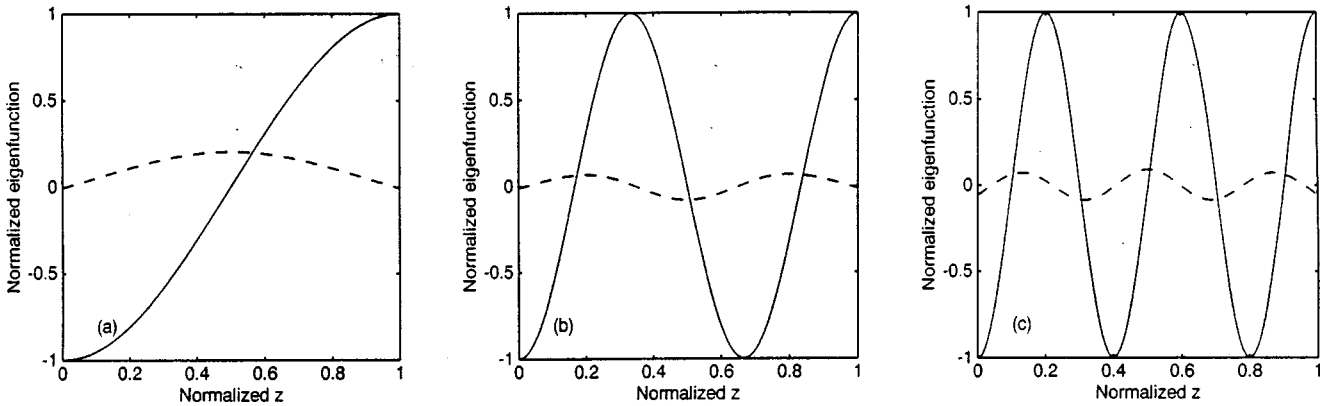

FIG. 3. The eigenfunctions Φ_{m2}, $m=1,3,5$ which are in the upper branch. ——— ψ_{m2} (axial component). – – – – ϕ_{m2} (radial component). The corresponding resonance frequencies are (a) 84.58 kHz, (b) 250.13 kHz, and (c) 416.60 kHz, respectively, as shown in Table I.

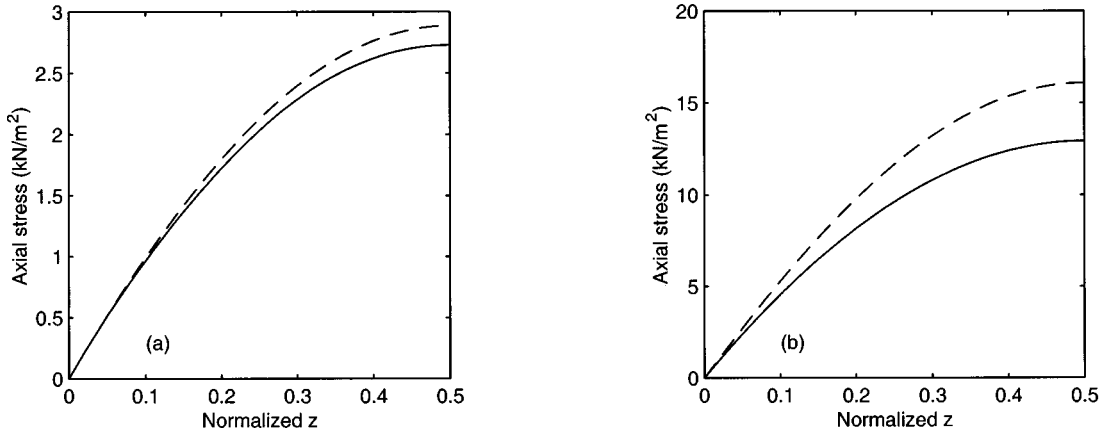

FIG. 4. The axial stress at $r=a$ when 1 V is applied at (a) 30 kHz, and (b) 31 kHz. ——— Piezoelectric thin shell theory. – – – – Membrane theory.

tween the stresses computed using the two theories increases even though the resonance frequencies are nearly the same and bending stress is not very significant when m is 1. The difference between the stresses can be much greater at higher frequencies and specially when the excitation frequency is approximately equal to 1), f_{m1}, $m>1$, where f_{m1} is determined by using either theory because the resonance frequencies differ considerably or 2) f_{mi}, $m\gg 1$ because bending stress will be significant.[14]

The measured input electrical susceptance (IES) of the shell is shown by a dashed line in Fig. 5 and the IES computed using piezoelectric thin shell theory is shown by a solid line. Among the resonance frequencies in the lower branch shown in Table I, only the one at 31 kHz can be seen in the measured curve. The others cannot be seen in the measured curve because of the scale used and are seen as sharp lines in the theoretical curve.

The potential fields at $z=L/2$ obtained by using piezoelectric thin shell and membrane theories are now compared. The potential field is the integral of the electric field with respect to x. It is arbitrarily set as zero at the inner curved surface, i.e., at $x=-h/2$. The approximate dimensions of the cylinder used in the comparison are $L=33$ mm, $a=11$ mm, and $t=3.2$ mm, and the applied voltage is 130 V. The exact values of the dimensions and properties of the cylinder used in the computation are the same as those used by Drumheller and Kalnins.[8] When membrane theory is used, the electric field is assumed to be a constant and equal to the ratio of the applied voltage to the distance between the electrodes, i.e., V_0/h. The potential field in this case varies linearly between the electrodes and is shown in Fig. 6 by solid line. In the figure $2x/h=-1$ and $+1$ correspond to the inner and outer curved surfaces, respectively. The potential fields at $\omega=3\times10^5$ rad/s (47.75 kHz) and 3.021×10^5 rad/s (48.08 kHz), computed using the approach presented here, are also shown in Fig. 6 by dashed and solid-asterisk lines, respectively. The frequencies differ only by 0.7% but there is considerable difference in the potential fields because there is a resonance at approximately 48.17 kHz and the electric field becomes infinity at resonance. The potential field at $\omega=3.021\times10^5$ rad/s computed by using only the eigenfunction which resonates at 48.17 kHz is also shown in Fig. 6 by a solid-x line. It is very close to the solid-asterisk line which was computed using six eigenfunctions whose radial compo-

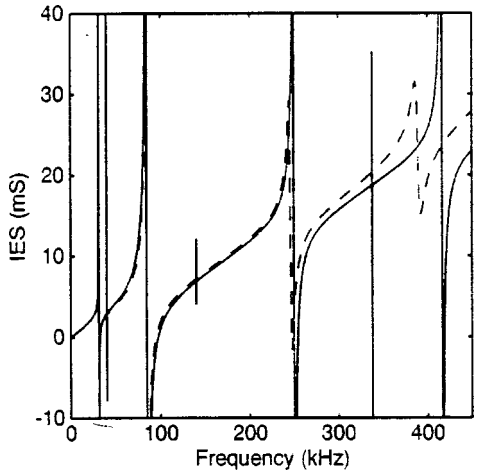

FIG. 5. The input electrical susceptance. ——— Piezoelectric thin shell theory. – – – – Experiment.

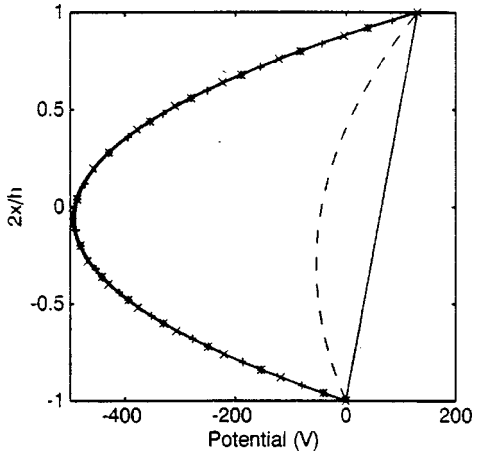

FIG. 6. The potential field between electrodes at $z=L/2$. ——— Membrane theory. —+— From Drumheller and Kalnins (Ref. 8), $\omega=3\times10^5$ rad/n. – – – – Present theory, $\omega=3\times10^5$ rad/s. —*— Present theory, $\omega=3.021\times10^5$ rad/s, 6 eigenfunctions. —×— Present theory, $\omega=3.021\times10^5$ rad/s, 1 eigenfunction.

nents are symmetric with respect to the center of the cylinder and resonate at 41.97, 48.17, 58.89, 79.13, 157.5, and 164.5 kHz, respectively. The potential field in the shell at $\omega=3\times10^5$ rad/s when 130 V is applied between the electrodes, as computed by Drumheller and Kalnins and shown in Fig. 8 of their article, is shown in Fig. 6 by a solid-plus line. It is stated in Ref. 8 that the electric field for this case can be expressed as $130/h$ V/m$+\times4.4\times10^8$ V/m^2. The potential field was computed by using this expression for the electric field. The potential field computed at 3.021×10^5 rad/s using the present approach is approximately equal to the field computed at 3×10^5 rad/s in Ref. 8. The approximations used to derive the governing equations in Ref. 8 are not the same as those used here. Therefore, there may be small differences between the resonance frequencies obtained using the two approaches which can be significant when making comparisons at a frequency close to a resonance frequency. However, there is fairly good agreement between the electric fields.

IV. CONCLUSIONS

An improved model of thin radially polarized piezoelectric cylindrical shells has been presented. The model is an extension of the Kirchoff–Love theory for elastic shells to piezoelectric shells. It was first assumed that the bending strain and electric field vary linearly between the electrodes. Then the electric field was expressed in terms of the applied voltage and the displacement by using the electrostatic condition for charge density. Next, the equations of motion were derived by using Hamilton's variational principle and solved by using an eigenfunction approach. A general method was used to determine the eigenfunctions and the resonance frequencies. This method can be used to analyze cylinders with arbitrary and conditions. It can also be used when models are developed using other approximations, such as those used in Ref. 8. The special case of a free–free cylinder was presented to illustrate the method.

The resonance frequencies and input electrical susceptance determined by using the model were compared with experimental data. It was shown that experimental values of the resonance frequencies in the lower branch are in much better agreement with those obtained using the model presented here than with those obtained using membrane theory.

The axial stresses computed using membrane and thin shell theories were also compared. It was observed that the difference will be small only at frequencies much lesser than the lowest resonance frequency.

In Ref. 8 a system of equations was derived and the unknowns which include the axial and radial displacements and the electric field were solved simultaneously. Therefore, it was referred to as coupled analysis. It was shown in this article that it is possible to first determine the displacement and then use it to determine the electric field. It was also shown that at frequencies close to resonance frequencies, irrespective of the boundary conditions and dimensions of the cylinder, the electrical field can be much greater than the ratio of the applied voltage to the distance between the electrodes. Further, the electric field obtained by using the model was shown to be in good agreement with that obtained by Drumheller and Kalnins.[8] The electric field and stress affect the power handling capacity of electroacoustic transducers.[18]

ACKNOWLEDGMENT

Permission from Director, NPOL, to publish this paper is gratefully acknowledged.

[1] J. E. Greenspon, ''Vibrations of a thick-walled cylindrical shell—Comparison of the exact theory with approximate theories,'' J. Acoust. Soc. Am. **32**, 571–578 (1960).
[2] J. K. Haskins and J. L. Walsh, ''Vibrations of ferroelectric cylindrical shells with transverse isotropy. I. Radially polarized case,'' J. Acoust. Soc. Am. **29**, 729–734 (1957).
[3] D. D. Ebenezer, ''Three port parameters and equivalent circuit of radially polarized piezoelectric ceramic cylinders of finite length,'' J. Acoust. Soc. Am. **99**, 2908–2912 (1996).
[4] D. D. Ebenezer and P. Abraham, ''Eigenfunction analysis of radially polarized piezoelectric cylindrical shells of finite length,'' J. Acoust. Soc. Am. **102**, 1549–1558 (1997).
[5] H. Wang, ''On the tangentially and radially polarized piezoceramic thin cylindrical tube transducers,'' J. Acoust. Soc. Am. **79**, 164–176 (1986).
[6] G. E. Martin, ''Vibrations of longitudinally polarized ferroelectric cylindrical tubes,'' J. Acoust. Soc. Am. **35**, 510–520 (1963).
[7] S. H. Ko and H. I. Pond, ''Improved design of spherical multimode hydrophone,'' J. Acoust. Soc. Am. **64**, 1270–1277 (1978).
[8] D. S. Drumheller and A. Kalnins, ''Dynamic shell theory for ferroelectric ceramics,'' J. Acoust. Soc. Am. **47**, 1343–1353 (1970).
[9] N. N. Rogacheva, *The Theory of Piezoelectric Shells and Plates* (CRC, London, 1993).
[10] M. C. Junger and D. Feit, *Sound, Structures, and Their Interaction* (MIT, Cambridge), Chap. 9.
[11] H. F. Tiersten, ''Hamilton's principle for linear piezoelectric media,'' Proc. IEEE **55**, 1523–1524 (1967).
[12] W. Soedel, *Vibration of Shells and Plates* (Marcel Dekker, New York, 1993).
[13] R. Holland and E. P. EerNisse, *Design of Resonant Piezoelectric Devices*, MIT Research Monograph No. 56 (MIT, Cambridge, 1969), pp. 99, 146, 153.
[14] W. Flugge, *Stresses in Shells* (Springer-Verlag, New York, 1973), Chap. 5.
[15] K. Forsberg, ''Influence of boundary conditions on the modal characteristics of thin cylindrical shells,'' AIAA J. **2**, 2150–2157 (1964).
[16] M. Abramowitz and I. A. Stegun, *Handbook of Mathematical Functions* (Dover, New York, 1965), Sec. 3.8.2.
[17] D. D. Ebenezer and A. J. Sujatha, ''New methods to characterize radially polarized piezoelectric ceramic cylindrical shells of finite length,'' J. Acoust. Soc. Am. **102**, 1540–1548 (1997).
[18] D. A. Berlincourt, D. R. Curran, and H. Jaffe, ''Piezoelectric and piezomagnetic materials and their function in transducers,'' in *Physical Acoustics*, edited by W. P. Mason (Academic, New York, 1964), Vol. 1A.

Free vibration of a kinked cantilever with attached masses

B. S. Reddy, K. R. Y. Simha, and A. Ghosal
Department of Mechanical Engineering, Indian Institute of Science, Bangalore—560 012, India

(Received 25 August 1997; revised 2 July 1998; accepted 22 September 1998)

In this paper free vibration characteristics of a centrally kinked cantilever beam of unit mass carrying masses at the kink (m_k) and at the tip (m_t) are analyzed. Frequency factors are presented for the first two modes for different combinations of m_k, m_t and the kink angle δ. A relationship of the form $f(m_k, m_t, \delta) = m_k + m_t(4 + \frac{10}{3}\cos\delta + \frac{2}{3}\cos^2\delta) = \text{const}$ appears to give the same fundamental frequency for a given δ and different combinations of $[m_k, m_t]$. Mode shapes as well as bending moments at the support and at the kink are also discussed. The utility of a discrete beam model in understanding the free vibration characteristics is also highlighted. © *1999 Acoustical Society of America.* [S0001-4966(99)02201-8]

PACS numbers: 43.40.Cw [CBB]

LIST OF SYMBOLS

m_k	nondimensional kink mass
m_t	nondimensional tip mass
m_{ek}	effective kink mass
m_{et}	effective tip mass
M_k	bending moment at kink
M_s	bending moment at support
δ	kink angle
w	bending displacement
w_t	tip displacement
w_k	kink displacement
EI	flexural rigidity
E	Young's modulus
I	moment of inertia
ρ	mass density of beam
A	area of beam cross section
L	beam length
K	$[\omega_j^2 \rho A/EI]^{1/4}$
y_j	$(KL)_j$ eigenvalue of jth mode of vibration
C_j	mode shape constants
ω_j	frequency
p_j	frequency factor
$\hat{M}_{\text{stat}}$	static moment at support per unit tip deflection
$\hat{M}_{\text{dyn}}$	dynamic moment at support per unit tip deflection
D_s	$\hat{M}_{\text{dyn}}/\hat{M}_{\text{stat}}$ at support
D_k	M_k/M_s
F	flexibility matrix
K_s	stiffness matrix
M	mass matrix
α	mass ratio (m_{ek}/m_{et})

INTRODUCTION

Free vibration of cantilevers carrying discrete masses along their length constitutes a fundamental problem in acoustics, seismology, flexible manipulators and a variety of other engineering applications. This classical problem has been approached at different levels of approximation ranging from the simplest discrete model of a massless beam with flexural rigidity to Timoshenko models which take into account shear deformation as well as rotary inertia.[1] Extensive work has been done using the massless beam formulation for analyzing the seismic response of multistoried buildings.[2,3] Similarly, a large amount of results are also available for straight beams with only a tip mass[4,5] or a system of masses.[6] Continuous beam formulation for a kinked cantilever carrying a tip mass and central mass using the Euler–Bernoulli theory appears not to have been studied analytically. One of the reasons for this lacuna might be the explosive growth of numerical methods for vibration and modal analysis in the past few decades. Notwithstanding this situation, it is important to extend analytical methods to gain better insight for engineering design.

A kinked cantilever beam, as shown in Fig. 1, is a viable model of a two link flexible manipulator with m_k representing a motor and m_t the payload. In flexible manipulators with rotary joints, the joints permit free rotation of link during the motion of the payload, however, the rotations at the joints are stopped by control (actuator) torques once the payload reaches a desired destination. This maneuver typically induces vibrations in the flexible manipulator and suppression of unwanted vibration is an important problem in flexible manipulators.[7] The two link manipulator can be modeled as a single cantilever with a kink of some angle δ with the torques M_k and M_s representing the bending moments at the kink and support, respectively. Another example of a kinked cantilever situation arises in plastic bending under impact at the kink.[8] The resulting response after the kink formation is the free vibration of a kinked elastic beam. In addition, attaching masses to reduce noise and vibration levels have been widely used for beams, plates and shells.[9] Although the emphasis in vibration engineering is on reducing acoustic radiation, it is important to understand the dynamic stress levels during free or forced vibration. Hence, understanding free vibration characteristics of a kinked cantilever carrying masses can help in evolving better active or passive control schemes in the case of flexible manipulators, better design

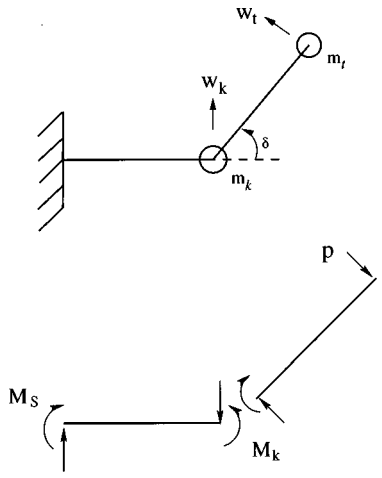

FIG. 1. A kinked cantilever.

procedures in impact engineering or reducing acoustic radiation.

In this paper we deal with the effect of varying tip mass and the central mass on free vibration characteristics of a kinked cantilever beam. Nondimensional design factors for the natural frequencies, mode shapes and bending moments are provided in the form of tables, charts and graphs for ready reference to the designer. Analytical results derived in this paper are verified using a commercial FEM software package. This paper is arranged as follows: in Sec. I we present the mathematical formulation of expressions for the frequencies, mode shapes and the bending moments of a kinked beam. In Sec. II we describe, in brief, the FE model used to validate the analytical results. In Sec. III we present and discuss the numerical results obtained from analytical and FE models. The results of the analytical model appear to be in general agreement with the FEM results but they deviate for large kink angles. A relationship in the form $f(m_k,m_t,\delta)=m_k+m_t(4+\frac{10}{3}\cos\delta+\frac{2}{3}\cos^2\delta)=\text{const}$ appears to give the same fundamental frequency for a given δ and different combinations of m_k and m_t. In Sec. IV we present the conclusions of this paper.

I. MATHEMATICAL FORMULATION

The free vibration of a cantilever beam is governed by the well-known partial differential equation

$$EI\frac{\partial^4 w}{\partial x^4}+\rho A\frac{\partial^2 w}{\partial t^2}=0, \tag{1}$$

where w is the transverse deflection, EI is flexural rigidity, ρ is mass density and A is the cross sectional area.

The above partial differential equation can be solved by the well-known technique of the separation of variables. For a kinked cantilever of total length L, we consider a solution of the form $w_i(x,t)=X_i(x)T(t)$ where $i=1,2$, denotes the two halves of the beam. The mode shapes X_1 and X_2 for the two halves of the beam are of the form

$$X_1=C_1\cos(Kx)+C_2\sin(Kx)+C_3\cosh(Kx)+C_4\sinh(Kx),$$

$$X_2=C_5\cos(Kx)+C_6\sin(Kx)+C_7\cosh(Kx)+C_8\sinh(Kx), \tag{2}$$

where $K^4=(\omega_j^2\rho A)/(EI)$.

The boundary conditions to determine the constants C_j are as follows.

At the fixed support,

$$w_1=w_1'=0. \tag{3}$$

The bending displacement continuity at the kink stipulates

$$w_1\cos\delta=w_2. \tag{4}$$

The shear force balance at the kink, taking an effective mass of $m_k+(m_t+1/2)\sin\delta$, gives

$$EI(w_1'''-w_2'''\cos\delta)=[m_k+(m_t+1/2)\sin\delta]\ddot{w}_1. \tag{5}$$

At the kink, the continuity of the slope and bending moment requires

$$w_1'=w_2', \qquad w_1''=w_2''. \tag{6}$$

Finally, at the free end,

$$w_2''=0, \qquad EIw_2'''=m_t\ddot{w}_2. \tag{7}$$

In the above equations $(\,)'$ and $(\ddot{})$ denote derivatives with respect to x and t, respectively. Thus, there are two boundary conditions at both the free end and the fixed end, and four conditions at the kink giving a total of 8 equations for 8 unknown coefficients C_j. Substitution of assumed solutions (2) in the boundary conditions lead to the eigen equation

$$F(KL)[C_1\cdots C_8]^T=0, \tag{8}$$

where $F(KL)$ is an 8×8 matrix whose elements are given in the Appendix. For nontrivial solutions, $\det(F)=0$ gives the equation for the natural frequencies as a function of m_k,m_t and δ. The roots of this equation give positive values of KL which are used to obtain the frequencies and the coefficients C_j. The eigenvalue $y_j=KL$ is related to the frequency ω_j by

$$\omega_j=\left(\frac{y_j}{L}\right)^2\sqrt{\frac{EI}{\rho A}}. \tag{9}$$

Equations (8) and (9) were solved numerically for various sets of values of m_k, m_t and δ and these results are presented and discussed in detail in Sec. III. A frequency factor, p_j, is helpful in presenting the results and is defined as the ratio of the frequency of a kinked beam for a given (m_k,m_t,δ) to the frequency of a straight beam with no attached masses. For mode 1 $(j=1)$ and mode 2 $(j=2)$, p_j is given by

$$p_j=\frac{\omega_j(m_k,m_t,\delta)}{\omega_j(0,0,0)}. \tag{10}$$

A. Bending moments

The bending moments of the kinked cantilever beam can be obtained from the Euler–Bernoulli beam theory. At the mid-point of the kinked beam, $x=L/2$, the moment at the kink in terms of $y=KL$ is given by

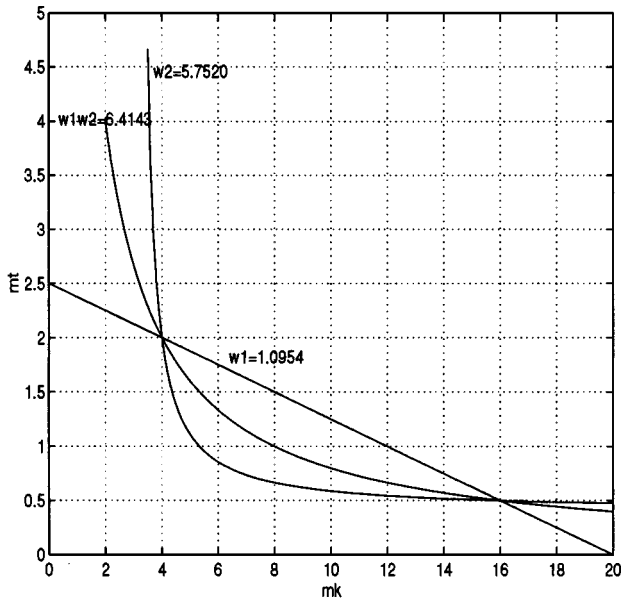

FIG. 2. Variations of ω_1, ω_2 and $\omega_1\omega_2$ with m_k and m_t.

$$M_k = \frac{EIy^2}{L^2}\left[-C_1 \cos\frac{y}{2} - C_2 \sin\frac{y}{2} + C_3 \cosh\frac{y}{2} + C_4 \sinh\frac{y}{2}\right]. \tag{11}$$

At the support, $x=0$, the moment is given by $M_s = -2EIC_1y^2/L^2$. The ratio of the moments at the kink and support, denoted by D_k, is given by

$$D_k = \frac{M_k}{M_s} = \frac{1}{2}\left[\cos\frac{y}{2} + \frac{C_2}{C_1}\sin\frac{y}{2} - \frac{C_3}{C_1}\cosh\frac{y}{2} - \frac{C_4}{C_1}\sinh\frac{y}{2}\right]. \tag{12}$$

The dynamic bending moment normalized with respect to a unit tip deflection is

$$\hat{M}_{\text{dyn}} = \frac{EIX''(0)}{X_2(L)}. \tag{13}$$

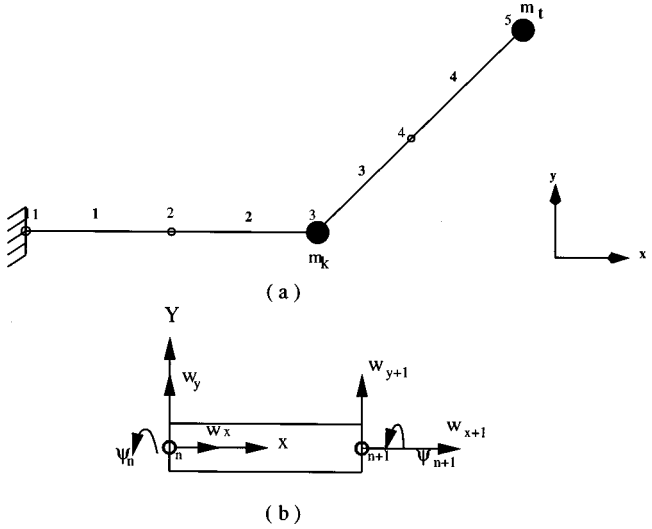

FIG. 3. (a) The FEM model of the kinked beam. (b) A typical element of the model.

In order to compare the dynamic bending moment with the static situation, a static load P at the tip is considered (see Fig. 1). In the static case the bending moment at the support is given as

$$M_{\text{stat}} = \frac{PL}{2}(1+\cos\delta). \tag{14}$$

The corresponding tip deflection is given by

$$\frac{PL^3}{24EI}[4+3\cos\delta+\cos^2\delta]. \tag{15}$$

Hence, the bending moment per unit tip deflection is given by

$$\hat{M}_{\text{stat}} = \frac{3EI}{L^2}\,\frac{4(1+\cos\delta)}{4+3\cos\delta+\cos^2\delta}. \tag{16}$$

For the straight beam with $\delta = 0$, $\hat{M}_{\text{stat}} = 3EI/L^2$. It is useful to define the ratio of $\hat{M}_{\text{dyn}}$ to $\hat{M}_{\text{stat}}$ for a straight beam as D_s, given by

$$D_s = \frac{\hat{M}_{\text{dyn}}}{3(EI/L^2)}. \tag{17}$$

It may be noted that $\hat{M}_{\text{stat}}$ is zero for $\delta = \pi$ [see Eq. (16)].

The quantity D_k is the ratio of bending moment at the kink to that at the support under a dynamic condition. Thus, the dynamic bending moment factors D_s and D_k provide the amplification in bending moments due to free vibrations. In Sec. III, numerical values of bending moments and the ratios discussed above are presented for various values of m_k, m_t and δ.

B. Discrete analysis of the kinked beam

A discrete model of a continuous system often helps in understanding the dynamic characteristics with regard to frequencies, displacements and moments. In this section, a discrete model, with the beam assumed to be massless, is derived. The discrete model gives inaccurate results for small values of m_k and m_t, however, it is shown that the discrete element model predicts many important features of the continuous kinked beam system.

Assuming that E, I and L are unity, the flexibility matrix of a discrete kinked beam is given by

$$F = \frac{1}{48}\begin{bmatrix} 2 & 3+2\cos\delta \\ 3+2\cos\delta & 8+6\cos\delta+2\cos^2\delta \end{bmatrix},$$

The stiffness and mass matrices are given as

$$K_s = F^{-1}, \qquad M = \begin{bmatrix} m_{ek} & 0 \\ 0 & m_{et} \end{bmatrix}, \tag{18}$$

where $m_{ek} = m_k + m_t \sin\delta$; $m_{et} = m_t$. Expanding $|K_s - M\omega^2| = 0$ gives the frequency equation

TABLE I. Frequency factors for kinked beam.

m_k	m_t	δ	Mode 1 Analytical	Mode 1 FEM	Mode 2 Analytical	Mode 2 FEM
0	0	0°	1.0000	1.0000	1.0000	1.0000
0	1	⋯	0.4430	0.4449	0.7375	0.7539
1	1	⋯	0.4256	0.4276	0.4297	0.4437
8	1	⋯	0.3380	0.3397	0.2235	0.2317
80	10	⋯	0.1128	0.1134	0.0727	0.0755
0	0	30°	1	1.0299	0.8149	0.8674
0	1	⋯	0.4432	0.4577	0.4592	0.511
1	1	⋯	0.4318	0.4348	0.3485	0.3790
8	1	⋯	0.3409	0.3433	0.2142	0.2206
80	10	⋯	0.1134	0.1144	0.0708	0.0728
0	0	60°	1.1136	1.1271	0.6897	0.6977
0	1	⋯	0.5000	0.5012	0.3557	0.3658
1	1	⋯	0.4773	0.4772	0.2922	0.2998
8	1	⋯	0.3636	0.3627	0.1978	0.2018
80	10	⋯	0.1136	0.1144	0.0653	0.0660
0	0	90°	1.3295	1.3159	0.5789	0.5808
0	1	⋯	0.5909	0.5859	0.2922	0.2942
1	1	⋯	0.5455	0.5504	0.2450	0.2489
8	1	⋯	0.3864	0.3891	0.1815	0.1854
80	10	⋯	0.1250	0.1259	0.0599	0.0603
0	0	150°	2.0114	2.2520	0.4537	0.4733
0	1	⋯	0.8636	0.8788	0.2577	0.3187
1	1	⋯	0.7955	0.8010	0.1960	0.2169
8	1	⋯	0.4545	0.4577	0.1615	0.1659
80	10	⋯	0.1477	0.1488	0.0544	0.0547
0	0	175°	2.5909	2.6777	0.4483	0.4620
0	1	⋯	0.9205	0.9303	0.3721	0.4469
1	1	⋯	0.8750	0.8811	0.2105	0.2244
8	1	⋯	0.4773	0.4806	0.1597	0.1659
80	10	⋯	0.1477	0.1488	0.0544	0.0547

$$\omega^4-\left(\frac{96}{7}\right)\left(\frac{1}{m_{et}}+\frac{4+3\cos\delta+\cos^2\delta}{m_{ek}}\right)\omega^2+\frac{48^2}{7}\frac{1}{m_{ek}m_{et}}=0.$$

From the above equation, we conclude that the product of $\omega_1^2\omega_2^2$ is invariant with respect to the product $m_{ek}m_{et}$. Defining a mass ratio $\alpha=m_{ek}/m_{et}$ the individual values of ω_1^2,ω_2^2 are

$$\omega_{1,2}^2=\frac{48}{7m_{ek}}[(\alpha+4+3\cos\delta+\cos^2\delta)\pm\sqrt{(\alpha+4+3\cos\delta+\cos^2\delta)^2-7\alpha}]. \tag{19}$$

The fundamental frequency is given by

$$\omega_1^2=\frac{48}{7m_{ek}}(\alpha+4+3\cos\delta+\cos^2\delta)\times\left[1-\sqrt{1-\frac{7\alpha}{(\alpha+4+3\cos\delta+\cos^2\delta)^2}}\right]. \tag{20}$$

Assuming $7\alpha/(\alpha+4+3\cos\delta+\cos^2\delta)^2\ll 1$, we get

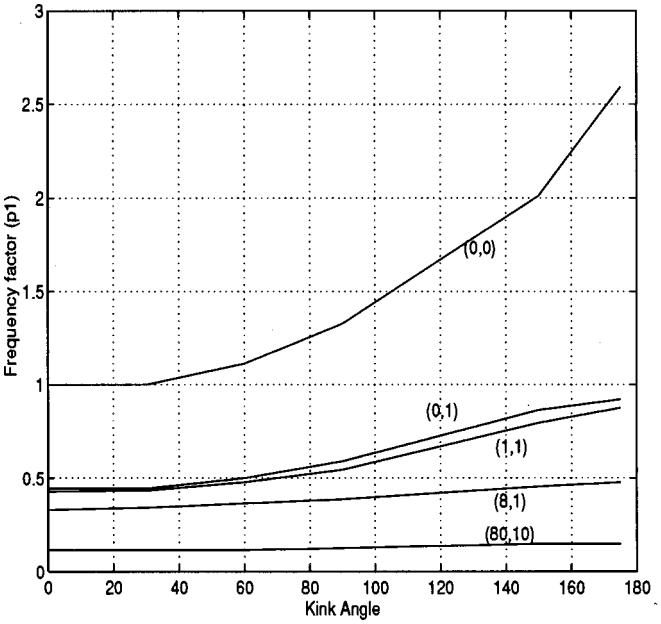

FIG. 4. The mode 1 frequency factor versus the kink angle (δ) for different (m_k,m_t).

$$\omega_1^2=\frac{24}{m_{ek}+m_{et}(4+3\cos\delta+\cos^2\delta)}. \tag{21}$$

The above result implies that the fundamental frequency will not change if $m_{ek}+m_{et}(4+3\cos\delta+\cos^2\delta)$ is held constant. Recalling that $m_{ek}=m_k+m_t\sin\delta$ and $m_{et}=m_t$, the condition yields $m_k+m_t(4+3\cos\delta+\sin\delta+\cos^2\delta)=C$, a constant, for the constant fundamental frequency. As an example, when $\delta=0$, the iso-frequency locus of ω_1 in the m_k-m_t plane is a straight line $m_k+8m_t=C$. Figure 2 shows the ω_1 locus for $C=20$. In the same figure ω_2 and $\omega_1\omega_2$ loci are also shown with all the loci passing through (2,4) and (16,0.5) in the m_k-m_t plane. These observations are useful

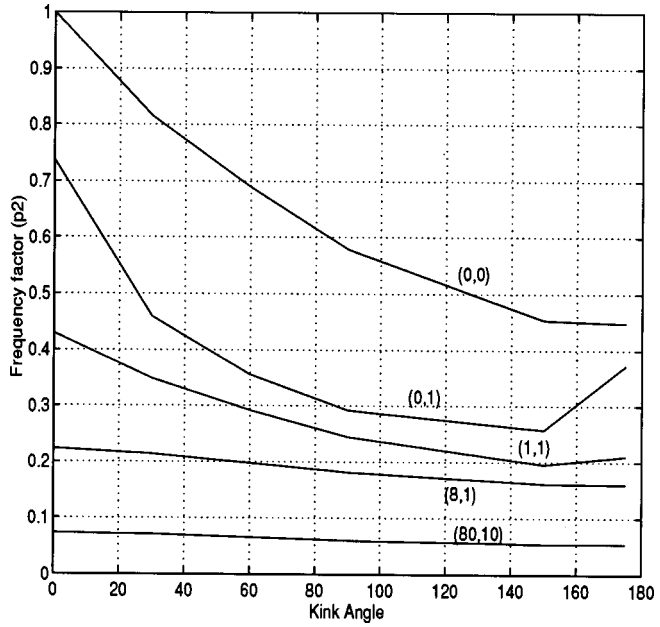

FIG. 5. The mode 2 frequency factor versus the kink angle (δ) for different (m_k,m_t).

TABLE II. Mode shape coefficients for mode 1.

δ	m_k	m_t	C_1	C_2	C_3	C_4	C_5	C_6	C_7	C_8
	0	0	1	−0.7341	−1	0.7341	1	−0.7341	−1	0.7341
	0	1	1	−0.8650	−1	0.8650	0.9999	−0.8649	−0.9999	0.8648
0°	1	1	1	−0.9678	−1	0.9678	0.8945	−0.8173	−0.8805	0.7485
	8	1	1	−1.4340	−1	1.4340	0.5032	−0.6146	−0.4515	0.3298
	80	10	1	−2.5144	−1	2.5144	0.4307	−0.7665	−0.4116	0.5842
	0	0	1	−0.7617	−1	0.7617	0.9609	−0.6772	−0.8445	0.5929
	0	1	1	−0.8791	−1	0.8791	0.9913	−0.8305	−0.9442	0.8111
30°	1	1	1	−0.9830	−1	0.9830	0.8842	−0.7841	−0.8256	0.6956
	8	1	1	−1.4479	−1	1.4479	0.4947	−0.5896	−0.4108	0.2909
	80	10	1	−2.5329	−1	2.5329	0.4181	−0.7373	−0.3884	0.5487
	0	0	1	−0.7195	−1	0.7195	1.0578	−0.5336	−0.6513	0.4204
	0	1	1	−0.7671	−1	0.7671	1.1352	−0.7934	−0.9624	0.8299
60°	1	1	1	−0.8981	−1	0.8981	0.9867	−0.7408	−0.8059	0.6778
	8	1	1	−1.4294	−1	1.4294	0.5081	−0.5399	−0.3318	0.2157
	80	10	1	−2.5074	−1	2.5074	0.4084	−0.6854	−0.3484	0.4842
	0	0	1	−0.6594	−1	0.6594	1.1884	−0.2516	−0.2295	0.0324
	0	1	1	−0.5390	−1	0.5390	1.4601	−0.7247	−1.0606	0.9251
90°	1	1	1	−0.7452	−1	0.7452	1.1896	−0.6598	−0.7915	0.6644
	8	1	1	−1.4116	−1	1.4116	0.5163	−0.4579	−0.1951	0.0848
	80	10	1	−2.4846	−1	2.4846	0.3843	−0.5985	−0.2776	0.3739
	0	0	1	−0.7208	−1	0.7208	0.8453	0.4882	2.0752	−2.1691
	0	1	1	1.4715	−1	−1.4715	4.9379	−0.5271	−3.8153	3.5671
150°	1	1	1	−0.1647	−1	0.1647	2.1385	−0.3559	−1.0582	0.9145
	8	1	1	−1.4459	−1	1.4459	0.4539	−0.2598	0.1737	−0.2713
	80	10	1	−2.5328	−1	2.5328	0.2798	−0.3742	−0.0771	0.0800
	0	0	1	−0.7596	−1	0.7596	0.4897	0.7074	3.6960	−2.1691
	0	1	1	26.8455	−1	−26.8455	49.8275	−2.3398	−48.4828	46.5149
175°	1	1	1	1.0607	−1	−1.0607	4.2824	−0.3376	−2.9800	2.7592
	8	1	1	−1.4391	−1	1.4391	0.4453	−0.2240	0.2485	−0.3438
	80	10	1	−2.5250	−1	2.5250	0.2622	−0.3368	−0.0402	0.0277

in discussing the frequency results for the continuous kinked beam presented in Sec. III.

The ratio of tip displacement to kink displacement in the fundamental mode is only a function of α,

$$\frac{\delta_t}{\delta_k} = \frac{256+25\alpha}{80+10\alpha}.$$

The bending moment at the support per unit tip deflection in the fundamental mode also depends only on α:

$$\frac{M_s}{\delta_t} = 24\left(\frac{\alpha+8}{7}\right)\left(\frac{5}{16-(\alpha+8)(1-\sqrt{1-7\alpha/(\alpha+8)^2})}+\frac{2}{\alpha}\right) \times\left(1-\sqrt{1-\frac{7\alpha}{(\alpha+8)^2}}\right). \quad (22)$$

II. FINITE ELEMENT ANALYSIS

In order to assess the validity of the results obtained using the Euler–Bernoulli beam model, a FE analysis was undertaken. The beam is modeled using four 2-D beam elements as shown in Fig. 3 which also shows a typical beam element. Each element has two nodes and each node has 3 degrees of freedom so that it can translate in X and Y directions and rotate in the XY plane. For the node at the fixed end all the degrees of freedom are arrested. A mass element is attached at the tip and at the kink. A commercial FEM package NISA is used to solve the eigenvalue problem using a conventional, subspace iteration method for fixed values of E, I, A, L and for different combinations of m_k, m_t and δ.

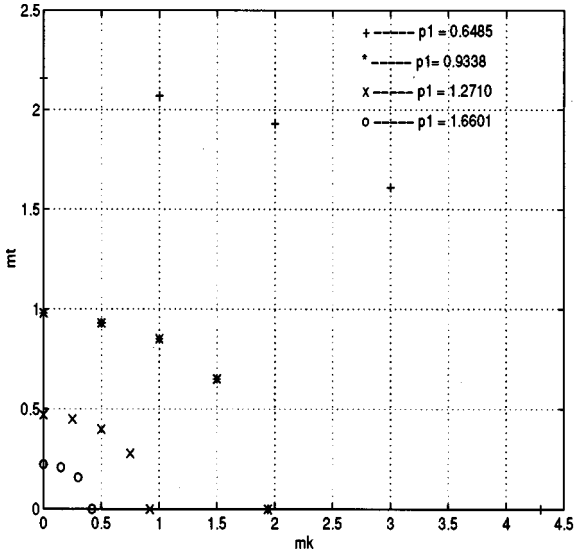

FIG. 6. The iso-frequency chart for a 175° kink.

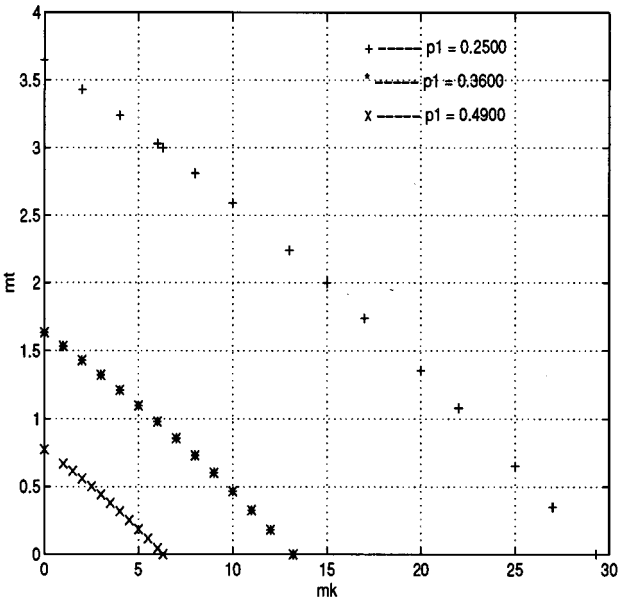

FIG. 7. The iso-frequency chart for a 0° kink.

Results for the frequencies, and mode shapes, and a comparison of the FEM results with the analytical results are discussed in Sec. III.

III. RESULTS AND DISCUSSION

In this section, results related to the natural frequencies, mode shapes and bending moments in a kinked cantilever with masses attached at the kink and free end are presented and discussed. Only the effect of m_k, m_t and δ on the free vibration characteristics are considered although E, I, L also affect the free vibration characteristics.

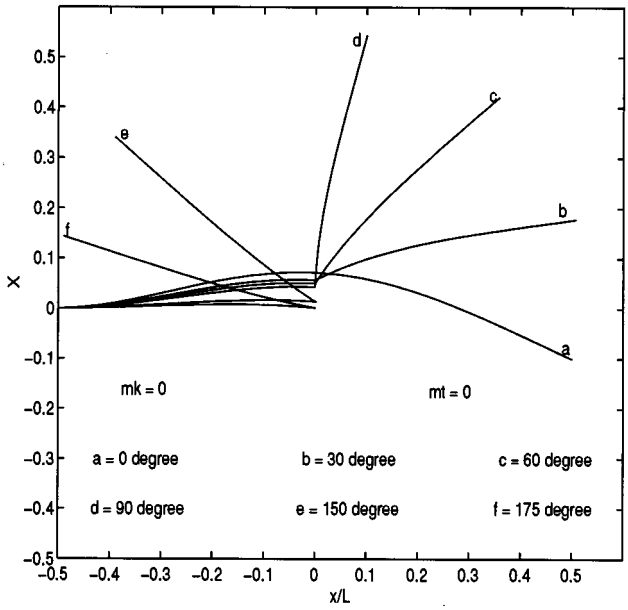

FIG. 9. Mode 2 for $m_k = m_t = 0$.

A. Frequency analysis

To obtain frequency factors, Eq. (8) was solved numerically using the software package MATLAB[10] and KL was obtained for various values of m_k, m_t and δ. Once KL is known, the frequency ω_j and the frequency factor p_j is obtained from Eqs. (9) and (10), respectively. The FEM results, as mentioned before, were obtained from NISA.

Frequency factors and the FEM results are tabulated in Table I for the first two modes for different combinations of m_k, m_t and δ. As the values of attached masses increase, the frequency factors drop as seen in Table I. It can be also seen from Figs. 4 and 5 that as the kink angle increases the frequency factors increase in mode 1 and the decrease in mode

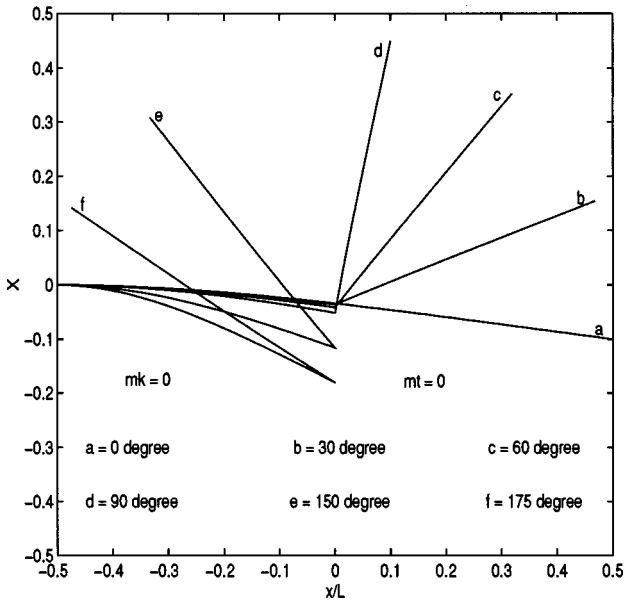

FIG. 8. Mode 1 for $m_k = m_t = 0$.

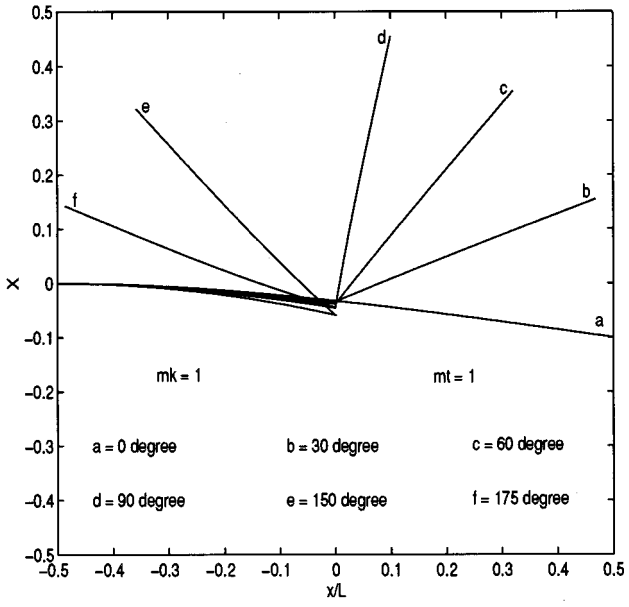

FIG. 10. Mode 1 for $m_k = m_t = 1$.

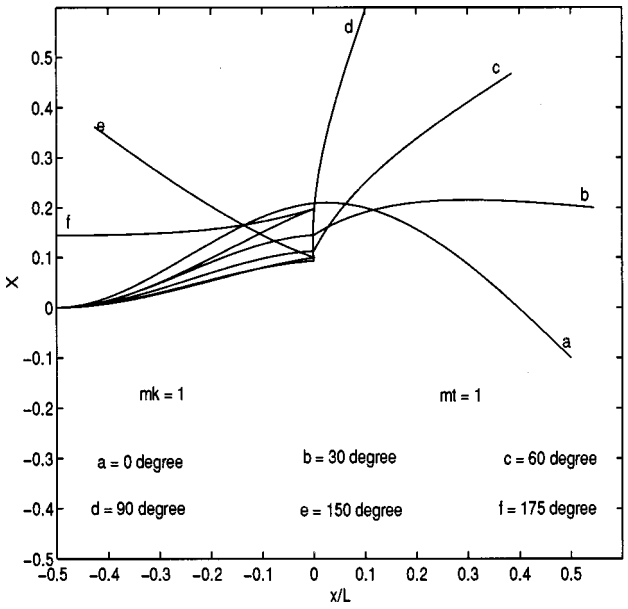

FIG. 11. Mode 2 for $m_k = m_t = 1$.

2 for a given combination of m_k and m_t. It may be noted that the fundamental frequency increases roughly 3 times as the kink angle increases from 0 to π. For a 90° kink, the increase in fundamental frequency is about 30% from its value for a straight beam. Thus, the kink effect becomes more pronounced after 90°.

It may be noted that the FEM and analytical results in Table I are in good agreement except at large kink angles for some combinations of m_k and m_t. A possible reason for this discrepancy could be that in the FEM model the nodes were allowed to translate in the axial direction and hence axial vibration is not arrested. Regarding the mode 2 frequency factors displayed in Fig. 5, there is an unexplained deviation in the trend for $m_k = 0$, $m_t = 1$ around $\delta = 150°$. This combination of m_k, m_t and δ also results in large unexplained values for mode shape coefficients in Table II.

For a given kink angle it is possible to find an infinite number of m_k and m_t combinations that give the same fundamental frequency. These combinations appear to fit the equation $m_k + m_t(4 + \frac{10}{3}\cos\delta + \frac{2}{3}\cos^2\delta) = \text{const}$. This result was obtained after trial and error and was motivated by the discrete beam analysis presented in Sec. I, which shows that $m_k + [4 + 3\cos\delta + \cos^2\delta + \sin\delta]m_t = \text{const}$. It may be noted that the expression inside the bracket, $(4 + \frac{10}{3}\cos\delta + \frac{2}{3}\cos^2\delta)$, is equal to 8 when $\delta = 0$ as required by the discrete model. It should, however, be noted that the above fit is not accurate for low values of m_k and m_t, or for high kink angles. For a hairpin like kinked beam, e.g., $\delta = 175°$, the loci of iso-frequency points are curved as shown in Fig. 6. For

TABLE III. Mode shape coefficients for mode 2.

δ	m_k	m_t	C_1	C_2	C_3	C_4	C_5	C_6	C_7	C_8
	0	0	1	−1.0185	−1	1.0185	1	−1.0185	−0.9997	1.0181
	0	1	1	−1.0060	−1	1.0060	0.9999	−1.0061	−0.9998	1.0058
0°	1	1	1	−1.2857	−1	1.2857	−0.2806	−1.2444	1.8464	−1.8358
	8	1	1	−1.9881	−1	1.9881	−1.6194	−0.6874	2.9547	−2.9305
	80	10	1	−3.4869	−1	3.4869	−2.1743	0.8403	2.6279	−2.9910
	0	0	1	−1.0985	−1	1.0985	0.3995	−1.3732	2.0224	−1.9933
	0	1	1	−1.2262	−1	1.2262	−0.1308	−1.1886	1.8176	−1.8088
30°	1	1	1	−1.4239	−1	1.4239	−0.6603	−1.0697	2.2806	−2.2694
	8	1	1	−2.0519	−1	2.0519	−1.6951	−0.6050	3.0424	−3.0173
	80	10	1	−3.5849	−1	3.5849	−2.2148	0.9225	2.6697	−3.0573
	0	0	1	−1.1627	−1	1.1627	−0.1461	−1.3411	3.8169	−3.7784
	0	1	1	−1.3512	−1	1.3512	−0.5302	−0.9013	2.4185	−2.4120
60°	1	1	1	−1.5309	−1	1.5309	−0.8641	−0.7959	2.5424	−2.5339
	8	1	1	−2.1543	−1	2.1543	−1.7940	−0.4477	3.1800	−3.1544
	80	10	1	−3.7572	−1	3.7572	−2.2704	1.0711	2.7337	−3.1672
	0	0	1	−1.2378	−1	1.2378	−0.6265	−1.1328	4.9242	−4.8734
	0	1	1	−1.4221	−1	1.4221	−0.6437	−0.5666	2.6044	−2.6046
90°	1	1	1	−1.6177	−1	1.6177	−0.9351	−0.5013	2.6453	−2.6425
	8	1	1	−2.3014	−1	2.3014	−1.9401	−0.2666	3.3715	−3.3437
	80	10	1	−4.0067	−1	4.0067	−2.3806	1.2752	2.8560	−3.3549
	0	0	1	−1.5685	−1	1.5685	−1.6262	−1.1656	6.1934	−6.0757
	0	1	1	−1.2433	−1	1.2433	−0.1887	−0.0395	2.5244	−2.5477
150°	1	1	1	−1.6044	−1	1.6044	−0.6750	−0.0994	2.4487	−2.4648
	8	1	1	−2.6869	−1	2.6869	−2.4504	−0.0289	3.9407	−3.8969
	80	10	1	−4.6274	−1	4.6274	−2.8291	1.7450	3.3223	−3.9719
	0	0	1	−1.8783	−1	1.8783	−2.4117	−1.8136	7.0139	−6.8313
	0	1	1	−0.9772	−1	0.9772	0.0574	0.2764	3.6476	−3.6691
175°	1	1	1	−1.3826	−1	1.3826	−0.2979	−0.0179	2.2831	−2.3104
	8	1	1	−2.7589	−1	2.7589	−2.5616	−0.0060	4.0570	−4.0093
	80	10	1	−4.7415	−1	4.7415	−2.9298	1.8284	3.4246	−4.1005

TABLE IV. Vibration amplitude ratio.

m_k	m_t	δ	Mode 1 Analytical	Mode 1 FEM	Mode 2 Analytical	Mode 2 FEM
0	0	0°	2.9453	2.9497	−1.4012	−1.3777
0	1	⋯	3.1494	3.1488	−0.2093	−0.2070
1	1	⋯	3.0878	3.0885	−0.4799	−0.4769
8	1	⋯	2.8419	2.8425	−2.6178	−2.6085
80	10	⋯	2.8299	2.8300	−2.8034	−2.8000
0	0	30°	2.7819	2.8184	−1.7700	−1.4938
0	1	⋯	3.0008	3.0301	−0.3940	−0.3264
1	1	⋯	2.9387	2.9624	−0.6910	−0.5976
8	1	⋯	2.6938	2.7036	−2.9717	−2.8485
80	10	⋯	2.6834	2.6906	−3.1472	−3.0568
0	0	60°	2.4288	2.4599	−1.9910	−1.8095
0	1	⋯	2.6890	2.7142	−0.5403	−0.5204
1	1	⋯	2.6061	2.6275	−0.8870	−0.8508
8	1	⋯	2.3121	2.3208	−3.6031	−3.5403
80	10	⋯	2.3002	2.3068	−3.8265	−3.7940
0	0	90°	1.9483	1.9717	−2.3143	−2.2273
0	1	⋯	2.3206	2.3366	−0.6319	−0.6575
1	1	⋯	2.1798	2.4078	−1.0734	−1.0854
8	1	⋯	1.7799	1.7869	−4.7490	−4.7148
80	10	⋯	1.7668	1.7722	−5.0571	−5.0519
0	0	150°	0.8629	1.1705	−7.1548	−2.6714
0	1	⋯	2.5030	2.8752	−0.3017	−0.1662
1	1	⋯	1.7019	1.9521	−1.0045	−0.8056
8	1	⋯	0.7895	0.8015	−10.6223	−9.8592
80	10	⋯	0.7873	0.7949	−10.7502	−10.2860
0	0	175°	0.5540	1.3360	−74.3250	−1.5727
0	1	⋯	3.7362	3.8643	−0.03610	−0.0231
1	1	⋯	2.2342	2.3500	−0.5075	−0.4419
8	1	⋯	0.6362	0.6512	−12.7434	−12.3061
80	10	⋯	0.6362	0.6381	−12.6762	−12.5252

smaller kink angles the loci are nearly straight as shown in Fig. 7.

B. Mode shapes

The solution of Eq. (8) also yields C_j, $j=1,\ldots,8$, which determine the mode shapes for the kinked cantilever. The mode shapes for $m_k=m_t=0$ for different kink angles are presented in Figs. 8 and 9. The mode shapes for $m_k=m_t=1$ for different kink angles are shown in Figs. 10 and 11.

Mode shape coefficients for various sets of m_k and m_t for the first two modes are given in Tables II and III. It is possible to use this information to construct the mode shapes for all the combinations of m_k, m_t and δ by means of interpolation. Table II applies for the first mode of vibration in which both segments of the kinked beam bend in the same direction. Table III applies for the second mode of vibration where the two segments bend in opposite directions. This is indicated by a negative sign for the amplitude ratios presented in Table IV.

The ratio of bending displacements at the tip (w_t) and at the kink (w_k) presented in Table IV decreases with an increasing kink angle, and for kink angles larger than 90°, deviations from this trend are noted. There is a good agreement between analytical results and results obtained from FEM, and it can be observed that for large values of m_k or m_t, the kinked cantilever beam can be reasonably approximated by a discrete model, as described in Sec. I.

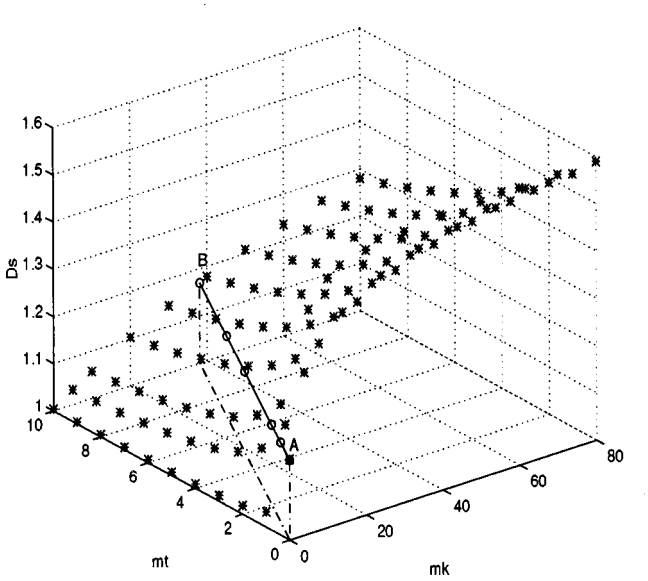

FIG. 12. The dynamic moment for a straight beam in mode 1.

The ratio of w_k to w_t is important in controlling the vibrations of flexible robots. As an example, consider a 2-link flexible manipulator that delivers a payload to its destination at a velocity of v_t with a kink angle of 60°. Assuming $m_k=8$ and $m_t=1$, the frequencies are $\omega_1=1.278$ rad/s and $\omega_2=4.35$ rad/s for a beam of unit length. Let A_{1t} and A_{2t} be the amplitudes of resulting free vibrations at the tip in mode 1 and mode 2, respectively. Assuming the velocity at the kink be v_k, it is possible to use Table IV to adjust the velocities v_t and v_k such that the amplitude of free vibration at the tip is minimum. Theoretically it is possible to achieve a zero amplitude of free vibration at the tip. Of course, in this example only the first two modes of vibrations are assumed to be excited. In the general problem the above assumption may not hold, and higher order modes may also be required to predict a correct response of the kinked beam.

C. Bending moments

The static bending moment at the support can be calculated using Eq. (16). The dynamic moment per unit tip deflection is given by $3(EI/L^2)D_s$. Hence the ratio of the dynamic to static bending moment can be calculated for any particular configuration. It may be noted that this ratio becomes infinite for $\delta=\pi$, even though the dynamic moment remains finite, equal to $3(EI/L^2)D_s$. Multiplying the dynamic moment at the support by D_k gives the dynamic moment at the kink. The dynamic moment at the support for a straight beam in mode 1 is shown in Fig. 12. The kink mass, m_k is varied between 0 and 80. The tip mass, m_t is varied between 0 and 10. The three-dimensional (3-D) surface has a maximum dynamic bending moment factor, D_s, of 1.6 for $m_k=80$ and $m_t=0$, i.e., for negligible tip mass. When the kink mass becomes negligible, the dynamic factor becomes

TABLE V. Bending moments.

m_k	m_t	δ	Mode 1 $\hat{M}_{\text{dyn}}$	Mode 1 D_s	Mode 1 D_k	Mode 2 $\hat{M}_{\text{dyn}}$	Mode 2 D_s	Mode 2 D_k
0	0	0°	−3.5160	−1.1720	0.3395	22.0334	7.3445	−0.7137
0	1	⋯	−3.0965	−1.0322	0.4659	107.1191	35.7064	−0.6137
1	1	⋯	−3.2262	−1.0754	0.4132	47.3841	15.7947	−0.8364
8	1	⋯	−3.8057	−1.2686	0.2215	11.4306	3.8102	−1.1712
80	10	⋯	−3.8402	−1.2801	0.2087	10.7814	3.5938	−1.2031
0	0	30°	−3.7648	−1.2549	−0.3134	17.2794	5.7598	−0.8713
0	1	⋯	−3.2659	−1.0886	−0.4534	56.0590	18.6863	−0.7881
1	1	⋯	−3.4085	−1.1362	−0.4002	33.1692	11.0564	−0.8816
8	1	⋯	−4.0335	−1.3445	−0.2113	10.3283	3.4428	−1.1939
80	10	⋯	−4.0661	−1.3554	−0.1999	9.8329	3.2776	−1.2219
0	0	60°	−4.3044	−1.4348	−0.3227	14.7938	4.9313	−0.9339
0	1	⋯	−3.5771	−1.1924	−0.5007	39.2978	13.0993	−0.7930
1	1	⋯	−3.8013	−1.2671	−0.4277	25.1528	8.3843	−0.8740
8	1	⋯	−4.7241	−1.5747	−0.2000	8.7789	2.9263	−1.2208
80	10	⋯	−4.7690	−1.5897	−0.1881	8.3690	2.7897	−1.2483
0	0	90°	−5.3640	−1.7880	−0.3353	12.2433	4.0811	−0.9726
0	1	⋯	−5.1032	−1.7011	−0.3463	31.2866	10.4289	−0.7331
1	1	⋯	−4.4333	−1.4778	−0.4905	19.7541	6.5847	−0.8340
8	1	⋯	−6.2030	−2.0677	−0.1770	7.1373	2.3791	−1.2751
80	10	⋯	−6.2742	−2.0914	−0.1654	6.8291	2.2764	−1.3032
0	0	150°	−13.4840	−4.4947	−0.1460	6.0608	2.0203	−1.3482
0	1	⋯	−2.2366	−0.7455	−2.3108	51.8472	17.2824	−0.4202
1	1	⋯	−4.9191	−1.6397	−0.8821	17.8500	5.9500	−0.6364
8	1	⋯	−14.5509	−4.8503	−0.0933	4.8344	1.6115	−1.5205
80	10	⋯	−14.5771	−4.8590	−0.0916	4.7550	1.5850	−1.5292
0	0	175°	−22.9307	−7.6436	−0.0205	4.0924	1.3641	−1.8459
0	1	⋯	−0.2359	−0.0786	−25.3771	408.9152	136.3051	−1.8459
1	1	⋯	−2.7272	−0.9091	−1.9628	31.1179	10.3726	−0.4496
8	1	⋯	−18.1914	−6.0638	−0.0784	4.5742	1.5247	−1.5767
80	10	⋯	−18.1526	−6.0509	−0.0786	4.5192	1.5064	−1.5797

unity for $m_t=10$ and $m_k=0$ along the axis of $m_k=0$. The dynamic factor increases from its unit value for large m_t to a maximum value of 1.17 for $m_k=m_t=0$ corresponding to a straight beam without attached masses. This particular value of $D_s=1.17$ is obtained for a fixed ratio of $m_k/m_t=3.8$. For this particular mass ratio, therefore, the dynamic moment at the support is invariant as shown by the line AB.

The above observation can be partially explained using the discrete model outlined in Sec. I. According to Eq. (22), the dynamic moment per unit tip deflection is an explicit function of the mass ratio (m_k/m_t), and, for $m_k/m_t=3.8$, there is no change in M_s. For mass ratios greater than 3.8, the dynamic moment factor increases towards the maximum value of 1.6 depending on the value of m_k. For mass ratios less than 3.8, the dynamic factor decreases towards the minimum value of 1 as shown.

Table V gives the bending moments at the kink and at the support. This information is useful to design the cross sectional dimensions of the links of a flexible manipulator once the tip displacement is specified. In general, the bending moment at the support is more than that at the kink in mode 1. However, as the kink angle becomes more than $\pi/2$, there is a reversal in the trend for small values of m_k and m_t. Eventually at $\delta=\pi$, the bending moment at the kink becomes many times larger than the value at the support.

IV. CONCLUSION

In this paper we deal with the free vibration characteristics of a kinked cantilever beam carrying discrete masses. Euler beam theory is used to obtain natural frequencies, mode shapes and static and dynamic bending moments. The presence of masses at the tip and kink significantly alters the natural frequencies, mode shapes and bending moments in a kinked beam. The results obtained in this paper are useful for analysis and design of control schemes for flexible manipulators, or for predicting the seismic response of two-storied structures. In particular, the dynamic moment factors provide useful guidelines in design for practical problems. A similar analysis can be extended to composite beams or multi-link configurations. Finally, in this paper we highlight the utility of a simple discrete model of a kinked cantilever model which leads to a better understanding of the results obtained from numerical and analytical models.

ACKNOWLEDGMENT

Support for this work from the Department of Space, and Department of Science and Technology of the Government of India is gratefully acknowledged.

APPENDIX: ELEMENTS OF THE 8×8 MATRIX $F(KL)$ IN EQ. (8)

$a(1,1)=1;\quad a(1,2)=0;\quad a(1,3)=1;\quad a(1,4)=0;\quad a(1,5)=a(1,6)=0;\quad a(1,7)=a(1,8)=0;$

$a(2,1)=0;\quad a(2,2)=1;\quad a(2,3)=0;\quad a(2,4)=1;\quad a(2,5)=0;\quad a(2,6)=0;$

$a(2,7)=0;\quad a(2,8)=0;\quad a(3,1)=\cos(0.5*y_j)*\cos(\delta);\quad a(3,2)=\sin(0.5*y_j)*\cos(\delta);$

$a(3,3)=\cosh(0.5*y_j)*\cos(\delta);\quad a(3,4)=\sinh(0.5*y_j)*\cos(\delta);\quad a(3,5)=-\cos(0.5*y_j);$

$a(3,6)=-\sin(0.5*y_j);\quad a(3,7)=-\cosh(0.5*y_j);\quad a(3,8)=-\sinh(0.5*y_j);$

$a(4,1)=-\sin(0.5*y_j);\quad a(4,2)=\cos(0.5*y_j);\quad a(4,3)=\sinh(0.5*y_j);\quad a(4,4)=\cosh(0.5*y_j);$

$a(4,5)=\sin(0.5*y_j);\quad a(4,6)=-\cos(0.5*y_j);\quad a(4,7)=-\sinh(0.5*y_j);$

$a(4,8)=-\cosh(0.5*y_j);\quad a(5,1)=-\cos(0.5*y_j);\quad a(5,2)=-\sin(0.5*y_j);$

$a(5,3)=\cosh(0.5*y_j);\quad a(5,4)=\sinh(0.5*y_j);\quad a(5,5)=\cos(0.5*y_j);\quad a(5,6)=\sin(0.5*y_j);$

$a(5,7)=-\cosh(0.5*y_j);\quad a(5,8)=-\sinh(0.5*y_j);\quad a(6,1)=\sin(0.5*y_j)+m^*_{ek}y^*_j\cos(0.5*y_j);$

$a(6,2)=-\cos(0.5*y_j)+m^*_{ek}y^*_j\sin(0.5*y_j);\quad a(6,3)=\sinh(0.5*y_j)+m^*_{ek}y^*_j\cosh(0.5*y_j);$

$a(6,4)=\cosh(0.5*Y)+m^*_{ek}y^*_j\sinh(0.5*y_j);\quad a(6,5)=-\sin(0.5*y_j)*\cos(\delta);$

$a(6,6)=\cos(0.5*y_j)*\cos(\delta);\quad a(6,7)=-\sinh(0.5*y_j)*\cos(\delta);\quad a(6,8)=-\cosh(0.5*y_j)*\cos(\delta);$

$a(7,1)=0;\quad a(7,2)=0;\quad a(7,3)=0;\quad a(7,4)=0;\quad a(7,5)=\cos(y_j);\quad a(7,6)=\sin(y_j);$

$a(7,7)=-\cosh(y_j);\quad a(7,8)=-\sinh(y_j);\quad a(8,1)=0;\quad a(8,2)=0;\quad a(8,3)=0;$

$a(8,4)=0;\quad a(8,5)=\sin(y_j)+m^*_{et}y^*_j\cos(y_j);\quad a(8,6)=-\cos(y_j)+m^*_{et}y^*_j\sin(y_j);$

$a(8,7)=\sinh(y_j)+m^*_{et}y^*_j\cosh(y_j);\qquad a(8,8)=\cosh(y_j)+m^*_{et}y^*_j\sinh(y_j).$

[1] K. F. Graff, *Wave Motion in Elastic Solids* (Clarendon, New York, 1975).
[2] R. W. Clough and J. Penzien, *Dynamics of Structures* (McGraw-Hill, New York, 1993).
[3] A. K. Chopra, *Dynamics of Structures, Theory and Applications to Earthquake Engineering* (PHI Pvt. Ltd., New Delhi, 1996).
[4] P. A. A. Laura, J. L. Pombo, and E. A. Susemihl, ''A note on the vibrations of a clamped–free beam with a mass at the free end,'' J. Sound Vib. **37**, 161–168 (1974).
[5] H. Abramovich and O. Hamburger, ''A vibration of a cantilever Timoshenko beam with a tip mass,'' J. Sound Vib. **148**, 162–170 (1991).
[6] H. H. Pan, ''Transverse vibration of an Euler beam carrying a system of heavy bodies,'' J. Appl. Mech. **32**, 434–437 (1965).
[7] Z. H. Luo, ''Direct strain feedback control of flexible robot arms: New theoretical and experimental results,'' IEEE Trans. Autom. Control. **38**, 1610–1622 (1993).
[8] W. Johnson, *Impact Strength of Materials* (Edward Arnold Ltd., London, 1972).
[9] C. M. Harris, *Handbook of Acoustical Measurements and Noise Control*, 3rd ed. (McGraw-Hill, New York, 1991), Chap. 27.
[10] *Matlab Users Manual* (The MathWorks, Inc., Natick).

Natural frequencies of a fluid-filled anisotropic spherical shell

W. Q. Chen[a] and H. J. Ding
Department of Civil Engineering, Zhejiang University, Hangzhou, 310027, People's Republic of China

(Received 16 April 1998; revised 21 July 1998; accepted 29 September 1998)

In this paper, the general nonaxisymmetric free vibration of a spherically isotropic elastic spherical shell filled with a compressible fluid medium is investigated. To this end, the three-dimensional elasticity solution method recently developed by the authors [H. J. Ding and W. Q. Chen, Int. J. Solids Struct. **33**, 2575–2590 (1996)] is employed. The effect of fluid is considered by introducing a relation between the normal displacement and the normal stress of the shell at the inner spherical surface. It is shown that the coupled vibration can be divided into two independent classes as in the case of empty spherical shell. The exact three-dimensional frequency equations are then derived. As the exact elasticity solution can serve as a benchmark to check various approximate theories, frequency equations of three typical shell theories are also presented. Numerical examples are given and comparisons between four theories are made.
[S0001-4966(99)03801-1]

PACS numbers: 43.40.Ey, 43.20.Ks [CBB]

INTRODUCTION

One basic problem of elastodynamics that has attracted continuous attention from engineering is the free vibration of spherical shells.[1–5] Practically speaking, most spherical shell systems operate in complex environments, coupled with acoustic media in many areas, such as oil storage tanks, nuclear reactors, rocket motors, and chemical vessels. It is obvious that their dynamic behavior will be different from those of the uncoupled ones. For many years, the concept of safety design has required that the dynamic behavior of the coupled system be investigated. Rayleigh[6] first solved the problem of axisymmetric vibrations of a fluid in a rigid spherical shell. The solution for vibrations of a fluid-filled spherical membrane appears in Morse and Feshbach.[7] Junger[8] calculated both the reflection from an air-filled shell submerged in a fluid and the transmission through the shell interior of an incidental plane wave. Goodman and Stern,[9] using elasticity theory and numerical integration of a system of ordinary differential equations, investigated the steady state response of a fluid-filled spherical shell submerged in another fluid. Rand and DiMaggio[10] obtained analytic form frequency equations and mode shapes for the axisymmetric, extensional, nontorsional vibrations of fluid-filled elastic spherical shells and rigid prolate spheroidal shells. Motivated by the fact that the human head can be represented as a shell filled with fluid, Engin and Liu[11] considered the free vibrations of a thin, homogeneous spherical shell containing an inviscid irrotational fluid. To develop a hybrid numerical technique for the free vibration analysis of the sound-structure interaction problem, Bai and Wu[12] presented their results by investigating a fluid-filled spherical shell. There are also many recent works concerned with (fluid-filled) spherical shells submerged in fluid in the discipline of acoustics.[13–15]

Today's advanced technologies have resulted in the need for new types of structures providing performance unattainable by the classical structures built up of isotropic materials. Consequently, anisotropic (composite) materials, with high strength-to-weight and stiffness-to-weight ratios, have been used widely in coupled structures and systems. Among them, spherically isotropic material is of particular interest because of its application in aerospace and nuclear technology.[16] The latest geophysical result reveals the Earth, in fact, should be modeled as a spherically isotropic inhomogeneous sphere containing a liquid central nucleus.[17] As regards spherically isotropic elasticity, Hu[18] introduced two displacement potentials to represent displacement components and then simplified the basic equations of equilibrium; he showed that the general solutions may be found through the use of spherical harmonics. Cohen and Shah[19] investigated the free vibration of a spherically isotropic spherical shell by employing two auxiliary variables; they found that, as in the isotropic case, the vibration can be divided into two classes. But it was difficult to derive the expressions of displacements and stresses by their method. Recently, the authors[20] used three displacement functions to simplify the basic equations of a spherically isotropic media and considered the coupled vibration of an embedded spherical shell; two classes of vibrations were observed.

To the authors' knowledge, the free vibration problem of a spherically isotropic spherical shell filled with a fluid medium has not been investigated within the framework of the three-dimensional theory of elasticity. This problem is the main subject of our study. Another purpose of the paper is to use the exact solution to check the suitability of three typical shell theories for the analysis of coupled dynamic behaviors of anisotropic shells. In Sec. I, the basic equations and the simplification procedure developed in Ref. 20 are briefly reviewed and the solutions to the resulted ordinary differential equations are given. The effect of internal compressible fluid is then considered and the frequency equations are presented in Sec. II. Ramakrishnan and Shah[21] used the Hamilton's

[a]Current address: Department of Aeronautics and Astronautics, Faculty of Engineering, The University of Tokyo, Japan; electronic mail: tt79326@hongo.ecc.u-tokyo.ac.jp

principle to develop a six-mode theory to analyze the free vibration of an empty spherically isotropic spherical shell. In Sec. III, their method is employed and generalized to derive the corresponding frequency equations of a fluid-filled spherical shell. Frequency equations of two other lower-order shell theories are also given there. Numerical calculations are presented in Sec. IV and some conclusions are finally obtained.

I. BASIC FORMULATIONS AND THE ELASTICITY METHOD

For a spherically isotropic elastic medium, the linear constitutive relations can be expressed in the spherical coordinates (r,θ,ϕ) as follows:

$$\begin{aligned}
&\sigma_{\theta\theta}=c_{11}s_{\theta\theta}+c_{12}s_{\phi\phi}+c_{13}s_{rr}, \quad \sigma_{r\theta}=2c_{44}s_{r\theta},\\
&\sigma_{\phi\phi}=c_{12}s_{\theta\theta}+c_{11}s_{\phi\phi}+c_{13}s_{rr}, \quad \sigma_{r\phi}=2c_{44}s_{r\phi},\\
&\sigma_{rr}=c_{13}s_{\theta\theta}+c_{13}s_{\phi\phi}+c_{33}s_{rr}, \quad \sigma_{\theta\phi}=(c_{11}-c_{12})s_{\theta\phi},
\end{aligned} \tag{1}$$

where σ_{ij} and s_{ij} are the stress and strain tensors, respectively; c_{ij} are the elastic stiffness constants. The equations of motion and the geometric relationships can be found in any textbook. To simplify the basic equations, Ding and Chen[20] employed three displacement functions to rewrite the displacement components as follows:

$$\begin{aligned}
&u_\theta=-\frac{1}{\sin\theta}\frac{\partial\psi}{\partial\phi}-\frac{\partial G}{\partial\theta}, \quad u_\phi=\frac{\partial\psi}{\partial\theta}-\frac{1}{\sin\theta}\frac{\partial G}{\partial\phi},\\
&u_r=w.
\end{aligned} \tag{2}$$

It is obvious that the present use of three displacement functions is much superior to the Helmholtz formulas, wherein an additional equation for the vector potential function is required.[22] It is also simpler than that of two potential functions employed by other authors.[18,19] It has been shown in Ding and Chen[20] that the substitution of Eq. (2) into the basic equations leads to an uncoupled partial differential equation and a coupled system of two partial differential equations. Moreover, on assuming

$$\begin{aligned}
&\psi=R\sum_{n=1}^{\infty}U_n(\xi)S_n^m(\theta,\phi)e^{i\omega t},\\
&w=R\sum_{n=0}^{\infty}W_n(\xi)S_n^m(\theta,\phi)e^{i\omega t},\\
&G=R\sum_{n=1}^{\infty}V_n(\xi)S_n^m(\theta,\phi)e^{i\omega t},
\end{aligned} \tag{3}$$

where $\xi=r/R$ is the nondimensional radial variable and R is the mean radius of the spherical shell; $S_n^m(\theta,\phi)$ are spherical harmonics; n and m are integers; ω is the circular frequency, one can further transfer the partial differential equations to the following ordinary ones:

$$\begin{aligned}
&\xi^2U_n''+2\xi U_n'\\
&\quad+\{\Omega^2\xi^2-[2+(n-1)(n+2)(f_1-f_2)/2]\}U_n=0,
\end{aligned} \tag{4}$$

$$\xi^2W_n''+2\xi W_n'+(\Omega^2\xi^2/f_4+p_1)W_n-p_2\xi V_n'-p_3V_n=0, \tag{5}$$

$$\xi^2V_n''+2\xi V_n'+(\Omega^2\xi^2+p_4)V_n-p_5\xi W_n'-p_6W_n=0, \tag{6}$$

where a prime stands for differentiation with respect to ξ, $\Omega^2=\rho_s\omega^2R^2/c_{44}$ is the nondimensional frequency, here ρ_s is the mass density of the shell, and

$$\begin{aligned}
&p_1=[2(f_3-f_1-f_2)-n(n+1)]/f_4,\\
&p_2=-n(n+1)(f_3+1)/f_4,\\
&p_3=n(n+1)(f_1+f_2+1-f_3)/f_4,\\
&p_4=f_1-f_2-n(n+1)f_1-2,\\
&p_5=f_3+1, \quad p_6=f_1+f_2+2,\\
&f_1=c_{11}/c_{44}, \quad f_2=c_{12}/c_{44},\\
&f_3=c_{13}/c_{44}, \quad f_4=c_{33}/c_{44}.
\end{aligned} \tag{7}$$

Equation (4) is a special case of the confluent hypergeometric differential equation; its solution is

$$U_n(\xi)=\xi^{-1/2}[B_{n1}J_\eta(\Omega\xi)+B_{n2}Y_\eta(\Omega\xi)] \quad (n\geqslant 1), \tag{8}$$

where J_η and Y_η are the first and second kinds of Bessel functions, respectively; B_{n1} and B_{n2} are arbitrary constants, and $\eta^2=\frac{1}{4}[9+2(n^2+n-2)(f_1-f_2)]>0$. Generally speaking, Eqs. (5) and (6) are coupled except for $n=0$, for which the coupled system degenerates to the following ordinary differential equation:

$$\xi^2W_0''+2\xi W_0'+(1/f_4)(\Omega^2\xi^2+2f_3-2f_1-2f_2)W_0=0, \tag{9}$$

with its solution as

$$W_0(\xi)=\xi^{-1/2}[C_{01}J_\nu(\Omega\xi/f_4^{1/2})+C_{02}Y_\nu(\Omega\xi/f_4^{1/2})], \tag{10}$$

where C_{01} and C_{02} are arbitrary constants and $\nu^2=\frac{1}{4}+2(f_1+f_2-f_3)/f_4>0$. Ding *et al.*[23] have developed a matrix Frobenius power series method to obtain the solution to the coupled system when $n>0$. Details are omitted here for simplicity. The general solution to Eqs. (5) and (6) finally can be expressed as the linear combination of four independent solutions as follows:

$$W_n(\xi)=\sum_{j=1}^{4}C_{nj}W_{nj}(\xi), \quad V_n(\xi)=\sum_{j=1}^{4}C_{nj}V_{nj}(\xi), \tag{11}$$

where C_{nj} are arbitrary constants and W_{nj} and V_{nj} are convergent, infinite series in the variable ξ.

II. EFFECT OF FLUID AND THE FREQUENCY EQUATIONS

It is well known that the velocity potential of an inviscid, compressible fluid satisfies the wave equation, whose solution can be obtained by the method of separation. Allowing for the finite value condition at the origin of the internal fluid, the velocity potential, Φ, can be finally written as

$$\Phi=\sum_{n=0}^{\infty}D_nj_n(kr)S_n^m(\theta,\phi)e^{i\omega t}, \tag{12}$$

where j_n are spherical Bessel functions of the first kind; D_n are arbitrary constants; and $k=\omega/c_f$ is the wave number, here c_f is the sound velocity in the fluid. From Eq. (12), one can derive the relation between the dynamic pressure, P_f, and the velocity, ν_f, of the fluid as follows:

$$\frac{P_f(r,\theta,\phi)}{\nu_f(r,\theta,\phi)}=-i\omega\rho_f\frac{j_n(kr)}{d[j_n(kr)]/dr} \quad (n=0,1,2,...), \tag{13}$$

where ρ_f is the density of the fluid medium.

Now let's consider the free vibration of a spherical shell filled with an internal fluid medium. Suppose its inner and outer radii to be a and b, respectively, then we have the following boundary conditions at the two spherical surfaces

$$\sigma_r=0, \quad (r=b), \quad \tau_{r\theta}=\tau_{r\phi}=0 \quad (r=a,b), \tag{14a}$$

$$\sigma_r=-P_f, \quad \frac{\partial w}{\partial t}=\nu_f \quad (r=a). \tag{14b}$$

Substitution of Eq. (13) into Eq. (14b) gives

$$\sigma_r=-\rho_f\omega c_f g_n(kr)w \quad (r=a,n=0,1,2,...), \tag{15}$$

where $g_n(x)=xj_n(x)/[nj_n(x)-xj_{n+1}(x)]$.

Using the solutions presented in Sec. I to obtain expressions of stresses, and allowing for the boundary conditions (14a) and (15), one can derive two sets of linear homogeneous algebraic equations of undetermined constants B_{ni} and C_{ni}, respectively. For nontrivial solutions to exist, the coefficient determinants of the two systems should vanish so that the corresponding frequency equations are obtained. The procedure is very similar to that of an embedded spherical shell.[20] It is found that the coupled vibration is again separated into two classes: The first class is identical to that of an empty spherical shell,[19,20] while the second changes due to the coupling effect of the internal fluid. In what follows, we will thus focus only on the second class of vibration of a fluid-filled, spherically isotropic spherical shell, of which the following frequency equations can be obtained: When $n=0$

$$|E^0_{ij}|=0 \quad (i,j=1,2), \tag{16}$$

where

$$\begin{aligned}
E^0_{11}&=[2+(\nu-\tfrac{1}{2})(f_4/f_3)]J_\nu(\alpha\xi_1)\\
&\quad-(f_4/f_3)\alpha\xi_1 J_{\nu+1}(\alpha\xi_1)+F_0(\xi_1)\xi_1 J_\nu(\alpha\xi_1)/f_3,\\
E^0_{12}&=[2+(\nu-\tfrac{1}{2})(f_4/f_3)]Y_\nu(\alpha\xi_1)\\
&\quad-(f_4/f_3)\alpha\xi_1 Y_{\nu+1}(\alpha\xi_1)+F_0(\xi_1)\xi_1 Y_\nu(\alpha\xi_1)/f_3,\\
E^0_{21}&=[2+(\nu-\tfrac{1}{2})(f_4/f_3)]J_\nu(\alpha\xi_2)\\
&\quad-(f_4/f_3)\alpha\xi_2 J_{\nu+1}(\alpha\xi_2),\\
E^0_{22}&=[2+(\nu-\tfrac{1}{2})(f_4/f_3)]Y_\nu(\alpha\xi_2)\\
&\quad-(f_4/f_3)\alpha\xi_2 Y_{\nu+1}(\alpha\xi_2),
\end{aligned} \tag{17}$$

and $\alpha=\Omega f_4^{-1/2}$, $\xi_1=a/R=1-e/2$, $\xi_2=b/R=1+e/2$, here $e=(b-a)/R$ is the thickness-to-mean radius ratio of the shell. And,

$$F_n(x)=\rho_0 c_0\Omega g_n(\Omega x/c_0), \tag{18}$$

where $\rho_0=\rho_f/\rho_s$ and $c_0=c_f/\nu_s=c_f/\sqrt{c_{44}/\rho_s}$ are ratios of density and velocity between fluid and shell, respectively. Frequency equation (16) corresponds to the purely radial vibration, i.e., the so-called ''breathing mode.'' When $n>0$,

$$|E^n_{ij}|=0 \quad (i,j=1,2,...,4), \tag{19}$$

where

$$\begin{aligned}
E^n_{1i}&=2W_{ni}(\xi_1)/\xi_1+n(n+1)V_{ni}(\xi_1)/\xi_1\\
&\quad+(f_4/f_3)W'_{ni}(\xi_1)+F_n(\xi_1)W_{ni}(\xi_1)/f_3,\\
E^n_{2i}&=W_{ni}(\xi_1)/\xi_1+V_{ni}(\xi_1)/\xi_1-V'_{ni}(\xi_1),\\
E^n_{3i}&=W_{ni}(\xi_2)/\xi_2+V_{ni}(\xi_2)/\xi_2-V'_{ni}(\xi_2),\\
E^n_{4i}&=2W_{ni}(\xi_2)/\xi_2+n(n+1)V_{ni}(\xi_2)/\xi_2\\
&\quad+(f_4/f_3)W'_{ni}(\xi_2) \quad (i=1,2,...,4).
\end{aligned} \tag{20}$$

III. SHELL THEORIES

To investigate the dynamics of an empty spherically isotropic spherical shell, Ramakrishnan and Shah[21] employed the Hamilton's principle to derive the controlling equations corresponding to the so-called six-mode shell theory, in which, not only the effects of shear deformation and rotary inertia, but also that of transverse normal strain, are included. We here follow their method to derive the frequency equations for a fluid-filled spherically isotropic spherical shell. For the internal coupled vibration, the Hamilton's principle can be expressed as

$$\delta\int_{t_0}^{t_1}(T-U+W)dt=0, \tag{21}$$

where δ is the variation, and T and U are the total kinetic energy and strain energy of the shell, respectively. W represents the work done by the internal fluid dynamic force

$$W=\int_0^{2\pi}\int_0^{\pi}P_f(a,\theta,\phi)w(a,\theta,\phi)a^2\sin\theta\,d\theta\,d\phi. \tag{22}$$

The followed procedure is similar to that presented in Ref. 21 so that details are not given for the sake of simplicity. It can be shown that the vibration is also divided into two classes: The first class is identical to that of an empty spherical shell,[21] while the second changes. Like three-dimensional elasticity analysis, we give in the following only the frequency equations of the second class. To check the applicability of different shell theories, frequency equations of two lower order ones, i.e., the five-mode theory and the classical bending theory, are also presented. It is noted here that the classical bending theory presented in the following is of the Federhofer type, which can be obtained by setting $k_s=k_2=k_r=C_r=0$ and $k_1=1$, along with neglecting the secondary effects, in the relevant equations for the six-mode theory.[21]

A. Six-mode theory

$$\gamma_1\gamma_4-\gamma_2\gamma_3=0 \quad (n=0), \tag{23}$$

$$\begin{aligned}
&n^4(n+1)^4-a_1n^3(n+1)^3+a_2n^2(n+1)^2\\
&\quad-a_3n(n+1)+a_4=0 \quad (n>0),
\end{aligned} \tag{24}$$

where

$$\gamma_1=-2(f_1+f_2)+k_1\Omega^2+(\xi_1^2/e)F_0(\xi_1),$$

$$\gamma_2=-2f_3+k_2\Omega^2+(\xi_1^2/2)F_0(\xi_1),$$

$$\gamma_3=-2f_3k_3+C_r\Omega^2+6(\xi_1/e)^2F_0(\xi_1), \tag{25}$$

$$\gamma_4=-(2f_1+2f_2+4f_3+f_4)-f_4k_3+k_r\Omega^2+3(\xi_1^2/e)F_0(\xi_1),$$

$$a_1=\alpha_1+\alpha_6+\alpha_{11}+\alpha_{16}-\alpha_7-\alpha_8\alpha_{14}-\alpha_3\alpha_9-\alpha_4\alpha_{13},$$

$$\begin{aligned}a_2=&\alpha_{11}\alpha_{16}-\alpha_{12}\alpha_{15}+(\alpha_1+\alpha_6)(\alpha_{11}+\alpha_{16})\\&+\alpha_1(\alpha_6-\alpha_7-\alpha_8\alpha_{14})+\alpha_7(\alpha_{12}\alpha_{14}-\alpha_{16})\\&+\alpha_2(\alpha_7\alpha_9-\alpha_5+\alpha_8\alpha_{13})+\alpha_8(\alpha_{15}-\alpha_{11}\alpha_{14})\\&+\alpha_3(\alpha_5-\alpha_6\alpha_9+\alpha_{12}\alpha_{13}-\alpha_9\alpha_{16})\\&+(\alpha_3\alpha_8-\alpha_4\alpha_7)(\alpha_9\alpha_{14}-\alpha_{13})\\&+\alpha_4(\alpha_5\alpha_{14}-\alpha_6\alpha_{13}-\alpha_{11}\alpha_{13}+\alpha_9\alpha_{15}),\end{aligned} \tag{26}$$

$$\begin{aligned}a_3=&(\alpha_1+\alpha_6)(\alpha_{11}\alpha_{16}-\alpha_{12}\alpha_{15})+(\alpha_1\alpha_6-\alpha_2\alpha_5)\\&\times(\alpha_{11}+\alpha_{16})+(\alpha_1\alpha_7-\alpha_3\alpha_5)(\alpha_{12}\alpha_{14}-\alpha_{16})\\&+(\alpha_1\alpha_8-\alpha_4\alpha_5)(\alpha_{15}-\alpha_{11}\alpha_{14})+(\alpha_3\alpha_6-\alpha_2\alpha_7)\\&\times(\alpha_{12}\alpha_{13}-\alpha_9\alpha_{16})+(\alpha_2\alpha_8-\alpha_4\alpha_6)\\&\times(\alpha_{11}\alpha_{13}-\alpha_9\alpha_{15}),\end{aligned}$$

$$a_4=(\alpha_1\alpha_6-\alpha_2\alpha_5)(\alpha_{11}\alpha_{16}-\alpha_{12}\alpha_{15}),$$

$$\alpha_1=(f_1-f_2-1/k_s+k_1\Omega^2)/f_1,$$

$$\alpha_2=(1/k_s+k_2\Omega^2)/f_1,$$

$$\alpha_3=(f_1+f_2+1/k_s)/f_1,\quad \alpha_4=f_3/f_1,$$

$$\alpha_5=(k_3/k_s+C_r\Omega^2)/f_1,$$

$$\alpha_6=(-k_3/k_s+f_1-f_2+k_r\Omega^2)/f_1,\quad \alpha_7=-k_3/(k_sf_1),$$

$$\alpha_8=(f_1+f_2+f_3)/f_1,\quad \alpha_9=-1-(f_1+f_2)k_s,$$

$$\alpha_{10}=1.0, \tag{27}$$

$$\alpha_{11}=[-2(f_1+f_2)+k_1\Omega^2+(\xi_1^2/e)F_n(\xi_1)]k_s,$$

$$\alpha_{12}=[-2f_3+k_2\Omega^2+(\xi_1^2/2)F_n(\xi_1)]k_s,$$

$$\alpha_{13}=-f_3k_3k_s,$$

$$\alpha_{14}=-(f_1+f_2+f_3)k_s,$$

$$\alpha_{15}=[-2f_3k_3+C_r\Omega^2+6(\xi_1/e)^2F_n(\xi_1)]k_s,$$

$$\alpha_{16}=[-(2f_1+2f_2+4f_3+f_4)-f_4k_3+k_r\Omega^2+3(\xi_1^2/e)F_n(\xi_1)]k_s,$$

with $k_1=1+e^2/12$, $k_2=e^2/6$, $k_3=12/e^2$, $k_r=1+3e^2/20$, $C_r=2$, and k_s is the shear correction factor.[21]

B. Five-mode theory

$$\gamma_1=0\quad (n=0), \tag{28}$$

$$n^3(n+1)^3-b_1n^2(n+1)^2+b_2n(n+1)-b_3=0\quad (n>0), \tag{29}$$

where

$$\begin{aligned}b_1=&\alpha_1+\alpha_6+\alpha_{11}-\alpha_7-\alpha_3\alpha_9,\\b_2=&(\alpha_1+\alpha_6)\alpha_{11}+\alpha_1(\alpha_6-\alpha_7)\\&+\alpha_2(\alpha_9\alpha_7-\alpha_5)+\alpha_3(\alpha_5-\alpha_6\alpha_9),\\b_3=&\alpha_{11}(\alpha_1\alpha_6-\alpha_2\alpha_5).\end{aligned} \tag{30}$$

C. Classical bending theory

$$\Omega^2+F_0(1)/e-2(f_1+f_2)=0\quad (n=0), \tag{31}$$

$$c_1n(n+1)-c_2=0\quad (n>0), \tag{32}$$

where

$$\begin{aligned}c_1=&f_1\Omega^2+f_1F_n(1)/e-f_1^2+f_2^2,\\c_2=&\Omega^4-[f_1+3f_2-F_n(1)/e]\Omega^2\\&-2(f_1^2-f_2^2)+(f_1-f_2)F_n(1)/e.\end{aligned} \tag{33}$$

It seems paradoxical at first glance that the integer m, included in the spherical harmonics, and which represents the non-axisymmetric motion ($m\neq 0$) of the sphere does not appear in the frequency equations of three shell theories as well as in the exact ones. The reason has in fact been given by Silbiger[24] to explain the same phenomenon of an empty, thin isotropic spherical shell. It is obvious that his explanation can be applied here for a spherically isotropic sphere filled with a compressible fluid medium.

The corresponding frequency equations for the isotropic spherical shell can be obtained simply upon the following substitution:

$$c_{11}=c_{33}=\lambda+2\mu,\quad c_{12}=c_{13}=\lambda,\quad c_{44}=\mu, \tag{34}$$

where λ and μ are the Lame constants.

It is also noted here that, if the fluid is incompressible, all frequency equations are unchanged, except that the following formula should be used instead of Eq. (18):

$$F_n(x)=\rho_0\Omega^2x/n. \tag{35}$$

IV. NUMERICAL RESULTS AND COMPARISON

Two types of material are checked throughout the numerical calculation. Material I ($f_1=3.64$, $f_2=1.60$, $f_3=1.32$, and $f_4=3.76$) is nearly isotropic like magnesium, while material II ($f_1=20$, $f_2=12$, and $f_3=f_4=2$) is a hypothetical one, exhibiting substantial anisotropy. The elastic constants of these two materials are available in Ref. 21 and have been nondimensionalized here.

As we can see, each frequency equation has more than one root. However, only the smallest positive root, which is of physical significance, will be presented in the following.

TABLE I. Natural frequencies of anisotropic spherical shells (breathing mode).[a,b]

Theory	Case[c]	e 0.01	0.05	0.1	0.3	0.5	0.8	1.0
Exact	I, filled	0.829 97	2.156 51	2.783 34	2.954 80	2.848 05	3.040 05	3.123 78
	I, empty	2.935 01	2.935 54	2.937 20	2.954 29	2.984 97	3.035 80	3.046 77
	II, filled	0.890 30	4.799 39	5.592 59	6.984 71	7.092 13	7.477 48	7.015 76
			(6.062 39)		(7.573 54)	(7.768 25)		
	II, empty	7.483 53	7.488 75	7.504 84	7.654 49	7.811 51	7.478 43	7.015 44
Six mode	I, filled	0.830 76	2.160 89	2.791 89	2.940 84	2.852 72	2.942 05	2.930 68
	I, empty	2.935 02	2.935 73	2.937 96	2.960 36	2.998 32	3.055 81	3.071 21
	II, filled	0.890 79	6.071 40	5.599 54	7.628 27	7.827 89	7.648 95	7.250 17
	II, empty	7.483 57	7.489 74	7.508 65	7.677 90	7.860 77	7.668 47	7.242 98
Five mode	I, filled	0.841 56	2.180 31	2.871 97	3.162 44	2.890 10	3.153 30	3.144 28
	I, empty	3.236 59	3.236 27	3.235 26	3.224 54	3.203 41	3.153 60	3.109 63
	II, filled	0.892 11	6.080 62	5.600 90	7.999 60	7.857 66	7.760 19	7.684 37
	II, empty	7.999 97	7.999 17	7.996 67	7.970 17	7.917 95	7.794 84	7.686 15
Classical	I, filled	0.841 06	2.177 79	2.865 63	3.155 62	2.879 97	3.229 66	3.278 65
	I, empty				3.236 60			
	II, filled	0.892 00	6.078 92	5.599 52	6.999 90	7.099 83	7.799 25	7.961 48
	II, empty				8.000 00			

[a]The nondimensional fluid parameters are selected as: $\rho_0 = c_0 = 0.2$.
[b]Data in parentheses are the second lowest frequencies of the exact analysis.
[c]I, filled—material I, filled with compressible fluid, and so on.

A. Breathing mode ($n=0$)

Apparently, it is impossible for the spherical shell to vibrate at any frequency in the breathing mode if the filled fluid is incompressible. Therefore, in Table I, only results of the empty spherical shell and the compressible fluid filled one are tabulated for the sake of comparison. Moreover, seven values of thickness-to-mean radius ratio (e) are considered to cover a wide thickness range of the spherical shell from very thin (0.01) to very thick (1.0).

It can be seen from Table I that the six-mode theory is generally superior to the other two lower order ones, and seems better to describe the breathing mode even for the thicker shell, except for some values of e (0.05, 0.3 and 0.5 in Table I), when the spherical shell is filled with compressible fluid. In these cases, the smallest frequencies predicted by the exact three-dimensional theory are quite different from those by shell theories. Further calculations show that the second smallest frequencies of the exact analysis (data in parentheses) are very close to those corresponding to the smallest ones of shell theories. Moreover, any shell theory behaves better for material I than for material II, when compared to the exact analysis. These facts may have a strong impact on the traditional engineering design based on any two-dimensional approximated shell theory, especially for coupled dynamics of composite elements and structures. It is also noted here that, for the empty problem, the nondimensional frequency predicted by the classical theory does not vary with the thickness-to-mean radius ratio, as we can see from Eq. (31).

To show the effects of the two nondimensional fluid parameters, ρ_0 and c_0, on the breathing mode vibration, Table II gives the smallest frequencies of a material II spherical shell for several different cases calculated by the exact three-dimensional theory.

It can be seen that the nondimensional parameter c_0 has a significant effect on the natural frequency of the purely radial vibration. This shows that the effect of the compressibility of the fluid should be included, if the fluid is compressible. Also we can see that for a very thick shell (e

TABLE II. Effects of fluid parameters on breathing mode frequencies of a fluid-filled spherical shell.

ρ_0, c_0	e 0.1	0.3	0.5	1.0
0.2, 0.2	5.592 59	6.984 71	7.092 13	7.015 76
0.2, 0.4	5.862 42	5.099 02	5.780 97	7.015 59
0.2, 0.6	4.759 79	5.371 97	6.092 49	7.015 58
0.4, 0.2	5.572 36	6.958 11	7.074 25	7.016 03
0.6, 0.2	5.553 43	6.934 48	7.057 35	7.016 28

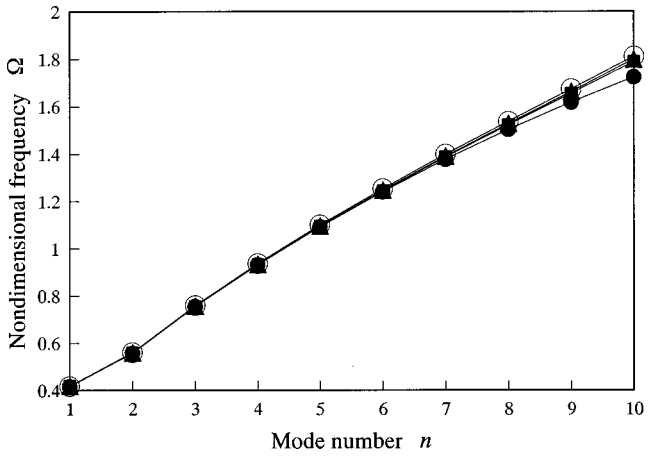

FIG. 1. Nonbreathing mode frequencies of a spherical shell (material II) filled with compressible fluid for $e=0.01$: ● Classical bending; ■ exact; ▲ six mode; ○ five mode.

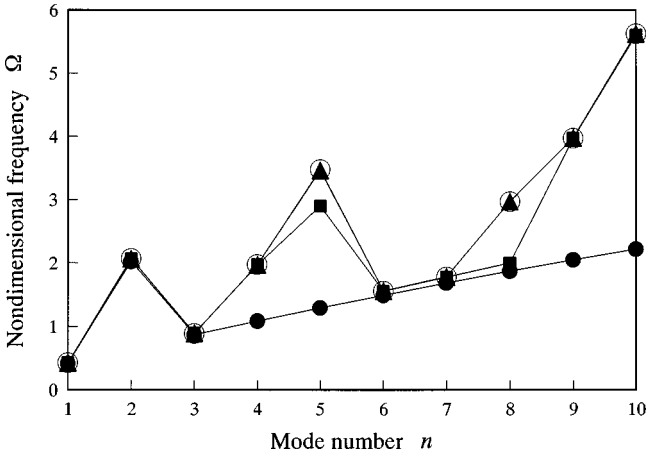

FIG. 2. As Fig. 1 but for $e=0.05$.

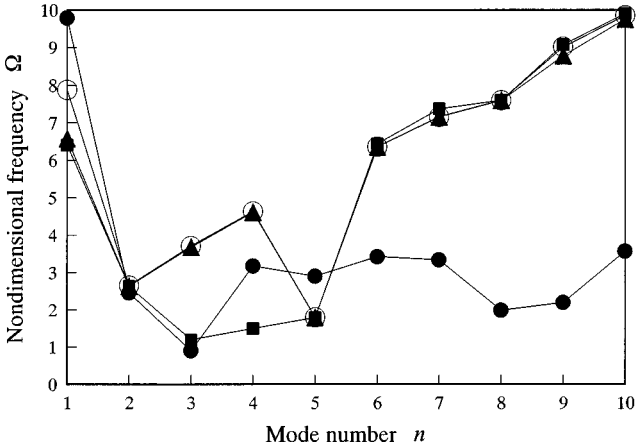

FIG. 5. As Fig. 1 but for $e=0.5$.

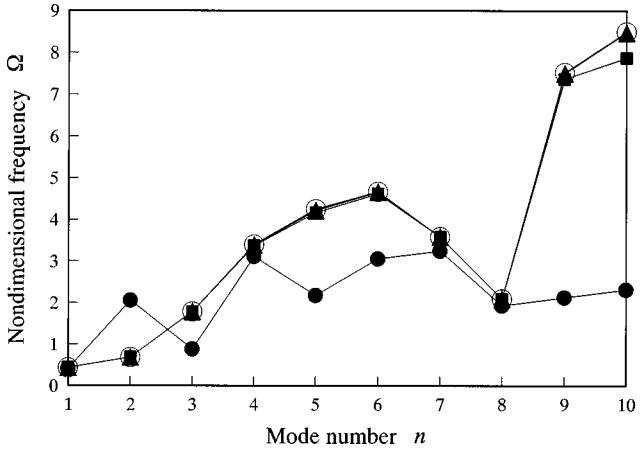

FIG. 3. As Fig. 1 but for $e=0.1$.

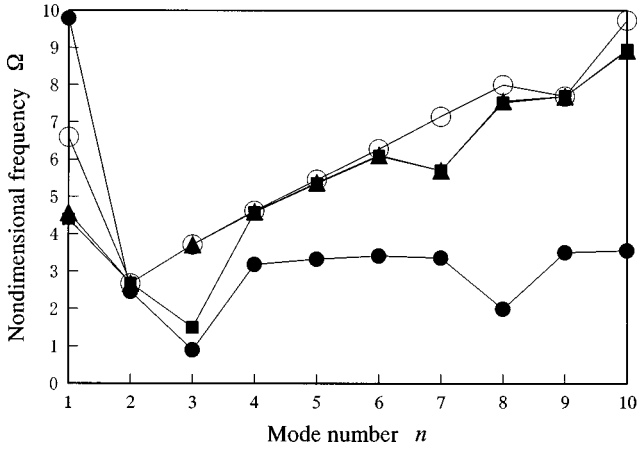

FIG. 6. As Fig. 1 but for $e=0.8$.

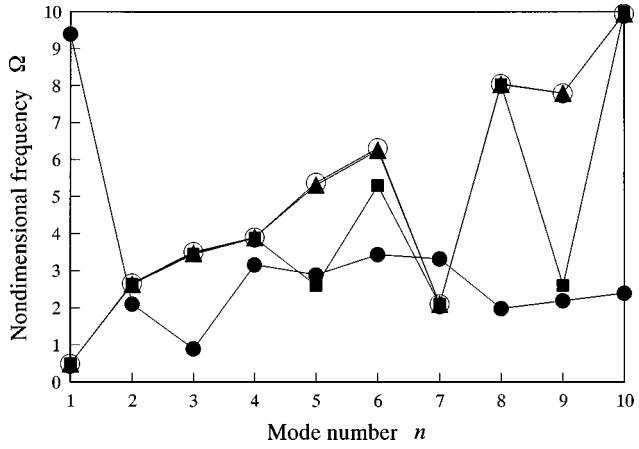

FIG. 4. As Fig. 1 but for $e=0.3$.

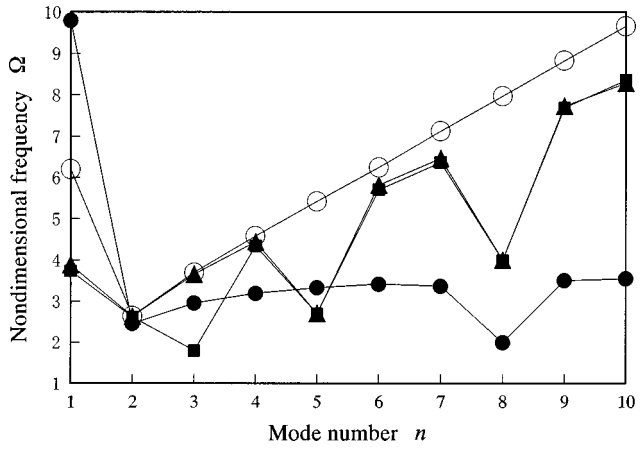

FIG. 7. As Fig. 1 but for $e=1.0$.

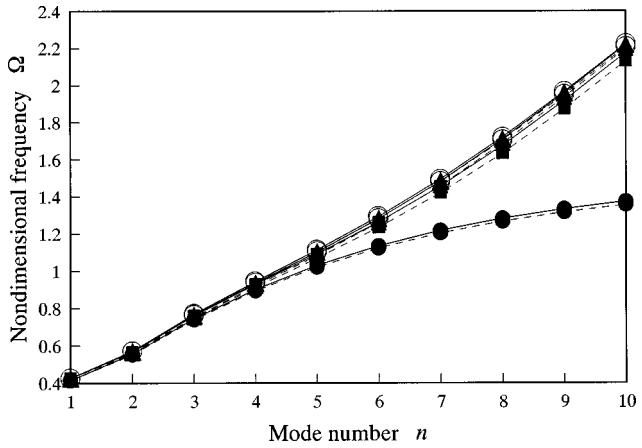

FIG. 8. Nonbreathing mode frequencies of a spherical shell filled with compressible fluid for $e=0.05$. (Solid line: Material I, dotted line: isotropic material with Poisson's ratio $\nu_0=0.3$): ● Classical bending; ■ exact; ▲ six mode: ○ five mode.

$=1.0$, for example), the effects of both fluid parameters become negligible. This is true, as one can imagine, directly from a physical point of view that for a very thick shell, the natural frequency will greatly depend on its own physical properties.

B. Nonbreathing modes ($n>0$)

Figures 1–7 present curves of the smallest nondimensional frequency Ω versus mode number n for seven values of thickness-to-mean radius ratio e, respectively, of a material II spherical shell filled with compressible fluid. The fluid parameters are chosen as $\rho_0=c_0=0.2$. It is mentioned that only those points corresponding to integral values of the mode number are of physical significance in the following figures. Figure 1 shows that for a very thin spherical shell, four theories agree with each other very well; that is to say, all shell theories are sufficient to describe the coupled dynamic behaviors of a very thin spherical shell. As we can see from Fig. 1, the larger the mode number is, the higher the frequency becomes. However, it is not the case for other six values of e. In fact, curves for these cases become irregular and for some mode numbers, the differences between exact analysis and shell theories are very significant. In particular,

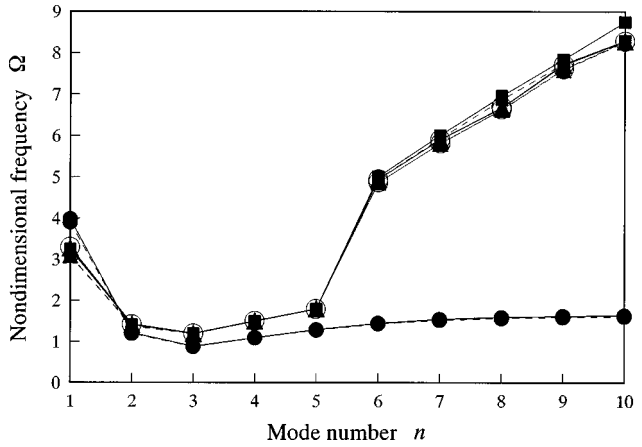

FIG. 9. As Fig. 8 but for $e=0.5$.

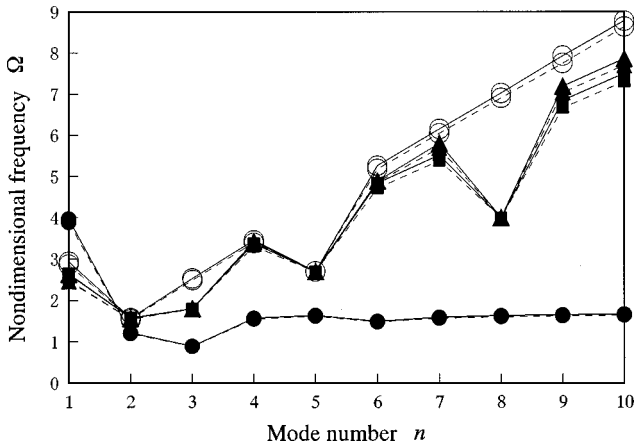

FIG. 10. As Fig. 8 but for $e=1.0$.

the classical bending theory is even closer to the exact three-dimensional analysis than the six and five mode theories, for example, at modes $n=9$ in Fig. 4 and $n=3$ in Figs. 5 and 6. In fact, at these modes, the second smallest frequencies of the three-dimensional theory are much closer to the corresponding ones of six and five mode theories, as we have also observed in the breathing mode. Generally speaking, the six mode theory is the most suitable one in predicting the coupled natural frequencies amongst these three shell theories, especially for very thick shell ($e=1.0$, Fig. 7). However, only three-dimensional exact theory can give accurate predictions in all cases. The results illustrate that before the use of shell theories in coupled problems, their suitability should be checked by comparing with the exact analysis.

For the sake of comparison, the frequency spectra of a material I spherical shell filled with compressible fluid are given in Figs. 8–10 (solid lines) for three values of e, as examples. The corresponding curves for isotropic material (Poisson's ratio is selected to be 0.3) are simultaneously displayed in Figs. 8–10 (dotted lines). The fluid parameters are the same as those employed in the preceding example, i.e., $\rho_0=c_0=0.2$.

Since material I is nearly isotropic, the difference between the results of material I and the isotropic material is

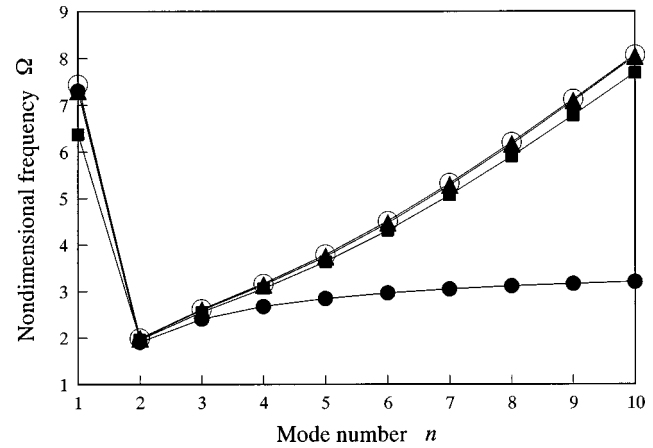

FIG. 11. Nonbreathing mode frequencies of a spherical shell (material II) filled with incompressible fluid for $e=0.1$: ● Classical bending; ■ exact; ▲ six-mode; ○ five mode.

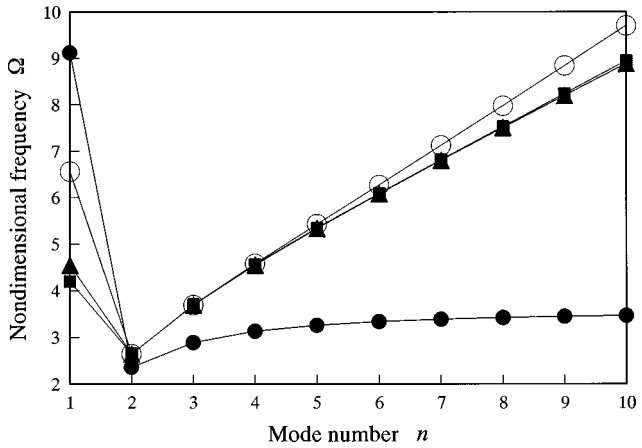

FIG. 12. As Fig. 11 but for $e=0.8$.

not significant. However, by comparing Figs. 8–10 with the corresponding ones for material II, it can be seen that the anisotropy of the material has a great effect on the nondimensional frequency. Similar to what has been shown in the breathing mode, shell theories are more suitable for isotropic materials than for anisotropic materials. However, for some values of e, frequencies obtained by shell theories also will be quite different from the exact ones at certain mode numbers, even for isotropic, moderately thin spherical shell, if filled with compressible fluid.

The irregularity of the frequency spectra of a spherical shell filled with compressible fluid is solely induced by the compressibility of the fluid. This has been demonstrated in Figs. 11 and 12 for a spherical shell filled with incompressible fluid, and, in Fig. 13 for an empty spherical shell, respectively. It is shown that for the latter two problems, except for $n=1$, the nondimensional frequency Ω increases monotonously when the mode number n becomes larger. Obviously, the six mode theory always has a good ability in predicting the natural frequencies of a spherical shell. This is somehow quite different from the compressible fluid case. In fact, it is very similar to that of an embedded spherical shell.[25]

Figure 14 gives several spectra of the smallest frequency

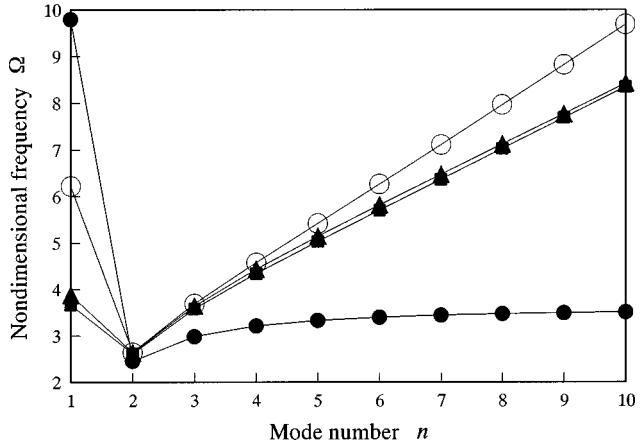

FIG. 13. Nonbreathing mode frequencies of an empty spherical shell (material II) for $e=1.0$: ● Classical bending; ■ exact; ▲ six mode; ○ five mode.

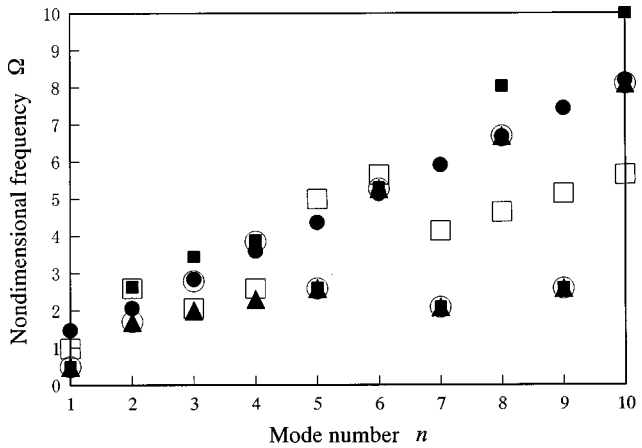

FIG. 14. Effects of fluid parameters on nonbreathing modes of a fluid-filled spherical shell (material II): ρ_0, c_0=■ 0.2, 0.2; □ 0.2, 0.4; ● 0.2, 0.6; ○ 0.4, 0.2; ▲ 0.6, 0.2.

Ω versus the mode number n of a material II spherical shell for five values of the nondimensional fluid parameters, ρ_0 and c_0, to show their effects on the nonbreathing mode vibration. The thickness-to-mean radius ratio is selected as $e=0.3$. Only exact frequencies are presented therein. It can be seen that no regulation exists for the nondimensional frequency varying with the fluid parameters.

V. CONCLUSIONS

The following is a summary of the main results of this paper:

(1) Exact three-dimensional frequency equations of a spherically isotropic spherical shell filled with compressible fluid were derived; the ones corresponding to three typical shell theories were also presented.

(2) Numerical comparisons between the exact analysis and shell theories for several different cases were made and some interesting phenomena were observed. In particular, for problems of empty spherical shell and spherical shell filled with incompressible fluid, the frequency spectra are very regular and the six mode shell theory always has a good ability to describe the dynamic behaviors of the shell. For moderately thick and thin spherical shell, respectively, the five mode theory and classical bending theory also behave well and are able to give frequencies that are very close to the exact ones. However, for problems of spherical shell filled with compressible fluid, this is no longer true. In fact, the frequency spectra become irregular and, except for very thin shell, the exact frequencies become quite different from the ones predicted by shell theories at certain mode numbers. All three shell theories are no longer exact enough to describe the dynamic behaviors of the spherical shell in these cases. This fact shows that before the use of any shell theory in analyzing the coupled dynamics of shell structures, its suitability should be strictly checked by comparison with exact analysis or other approximated methods based on three-dimensional elasticity.

(3) By comparing results for material I with those for mate-

rial II, one can conclude that all the three shell theories are more suitable to be used to analyze isotropic shells than to analyze strong anisotropic shells.

(4) The compressibility of fluid has a significant effect on the natural frequencies of a fluid-filled spherical shell. In fact, as numerical results show, because of the inclusion of the compressible effect, the traditional engineering design based on any two-dimensional approximated theory should be reexamined.

ACKNOWLEDGMENTS

This work has been supported by the National Natural Science Foundation of China and the Zhejiang Provincial Natural Science Foundation. One of the authors (C.W.O.) would like to acknowledge financial support by the Japanese Ministry of Culture, Sports, Education and Science. He is also indebted to Professor Tadashi Shioya for his kindness and help.

[1] C. F. Long, ''Frequency analysis of complete spherical shells,'' J. Eng. Mech. **95**, 505–518 (1969).
[2] V. P. Singh and S. Mirza, ''Asymmetric modes and associated eigenvalues for spherical shells,'' J. Pres. Vess. Tech. **107**, 77–82 (1985).
[3] B. P. Gautham and N. Ganesan, ''Free vibration analysis of thick spherical shells,'' Comput. Struct. **45**, 307–313 (1992).
[4] M. Sathyamoorthy, ''Vibrations of moderately thick shallow spherical shells at large amplitudes,'' J. Sound Vib. **172**, 63–70 (1994).
[5] R. B. Evans, ''Modal impedances for nonaxisymmetric vibrations of a thin spherical shell,'' J. Acoust. Soc. Am. **100**, 1242–1245 (1996).
[6] L. Rayleigh, ''On the vibrations of a gas contained within a rigid spherical envelope,'' Proc. London Math. Soc. **4**, 93–103 (1872).
[7] P. M. Morse and H. Feshbach, *Methods of Theoretical Physics, Part II* (McGraw-Hill, New York), 1953, pp. 1469–1472.
[8] M. C. Junger, ''Sound scattering by thin elastic shells,'' J. Acoust. Soc. Am. **24**, 366–373 (1952).
[9] R. R. Goodman and R. Stern, ''Reflection and transmission of sound by elastic spherical shells,'' J. Acoust. Soc. Am. **34**, 338–344 (1962).
[10] R. Rand and F. DiMaggio, ''Vibrations of fluid-filled spherical and spheroidal shells,'' J. Acoust. Soc. Am. **42**, 1278–1286 (1967).
[11] A. E. Engin and Y. K. Liu, ''Axisymmetric response of a fluid-filled spherical shell in free vibrations,'' J. Biomech. **3**, 11–22 (1970).
[12] M. R. Bai and K. R. Wu, ''Free vibration of a thin spherical shell containing a compressible fluid,'' J. Acoust. Soc. Am. **95**, 3300–3310 (1994).
[13] G. Kaduchatk and P. L. Marston, ''Backscattering of chirped bursts by a thin spherical shell near the coincidence frequency,'' J. Acoust. Soc. Am. **93**, 2700–2706 (1993).
[14] J. M. Ho and L. B. Felsen, ''Fully three-dimensional exact and ray asymptotic formulation of the characteristic wave fields on a spherical shell surface,'' J. Acoust. Soc. Am. **95**, 265–285 (1994).
[15] A. G. Pathak and P. R. Stepanishen, ''Acoustic harmonic radiation from fluid-loaded spherical shells using elasticity theory,'' J. Acoust. Soc. Am. **96**, 2564–2575 (1994).
[16] M. Maiti, ''Stress in anisotropic nonhomogeneous sphere,'' J. Eng. Mech. **101**, 101–108 (1975).
[17] J. P. Montagner and D. L. Anderson, ''Constrained reference mantle model,'' Phys. Earth Planet. Inter. **54**, 205–227 (1989).
[18] H. C. Hu, ''On the general theory of elasticity for a spherically isotropic medium,'' Acta Scientia Sinica **3**, 247–260 (1954).
[19] H. Cohen and A. H. Shah, ''Free vibrations of a spherically isotropic hollow sphere,'' Acustica **26**, 329–333 (1972).
[20] H. J. Ding and W. Q. Chen, ''Nonaxisymmetric free vibrations of a spherically isotropic spherical shell embedded in an elastic medium,'' Int. J. Solids Struct. **33**, 2575–2590 (1996).
[21] C. V. Ramakrishnan and A. H. Shah, ''Vibration of an aeolotropic spherical shell,'' J. Acoust. Soc. Am. **47**, 1366–1374 (1970).
[22] P. J. Schafbuch, F. J. Rizzo, and R. B. Thompson, ''Eigenfrequencies of an elastic sphere with fixed boundary conditions,'' J. Appl. Mech. **59**, 458–459 (1992).
[23] H. J. Ding, W. Q. Chen, and Z. Liu, ''Solutions to equations of vibrations of spherical and cylindrical shells,'' Appl. Math. Mech. **16**, 1–15 (1995).
[24] A. Silbiger, ''Non-axisymmetric modes of vibrations of thin spherical shell,'' J. Acoust. Soc. Am. **34**, 862 (1962).
[25] W. Q. Chen and H. J. Ding, ''On free vibrations of an embedded anisotropic spherical shell,'' J. Pres. Vess. Tech. **119**, 481–487 (1997).

Experimental analysis of acoustic scattering from lengthwise soldered cylindrical shells

J. Chiumia, N. Touraine, D. Décultot, and G. Maze
Laboratoire d'Acoustique Ultrasonore et d'Electronique, LAUE, URA CNRS 1373, Université du Havre, Place Robert Schuman, 76610 Le Havre, France

A. Klauson and J. Metsaveer
Tallinn Technical University, Department of Mechanics, Ehitajate tee 5, 19086 Tallinn, Estonia

(Received 4 November 1997; accepted for publication 26 September 1998)

Through an experimental approach, this paper explores the acoustic wave scattering processes involved in the acoustic backscattering from air-filled submerged cylindrical shells having axial discontinuity. The discontinuity is caused by lengthwise soldering along the tubes in the course of manufacture from flat sheets, and is represented as an internal axial mass layer. The tubes are excited by a plane wave at normal incidence. In the time domain, different echoes on short pulse responses (echo wave forms), are identified by the arrival times and related wave type. This enables the localization of additional wave generating sites and scattering centers due to the solder. A number of detected echo series are thus identified. In the frequency domain analysis, the influence of supplementary echoes and that of inter-echo interferences on both backscattering and resonance spectra is presented. The influence of the angular position of the solder, relative to the direction of the incident sound wave, on the amplitudes of spectra, is analyzed. The key phenomena in this study are wave generation at the solder when it is directly insonified (prevalent over classical wave generations of considered waves) and the wave type conversions observed when propagating waves encounter obstacles in the shell, geometric or material discontinuities (in this case the solder). The wave types studied are the A wave (Scholte–Stoneley) and the S_0 compressional wave, in the midfrequency region, $ka=25-90$, where $k=\omega/C_1$ is the wave number in water, C_1 is the sound velocity in water and a the external radius of the tube. This analysis of the influence of discontinuities in the propagation medium on the acoustic scattering is carried out with a view to the investigation of scattering of assembled objects such as cylindrical shells with hemispherical endcaps. [S0001-4966(99)02101-3]

PACS numbers: 43.40.Ey, 43.20.Fn, 43.30.Gv [CBB]

INTRODUCTION

Acoustic scattering from objects of relatively simple geometry (spherical and cylindrical), is widely investigated in numerous studies, both theoretically and experimentally.[1–9] In particular, the isolation and identification of resonances allow the explanation of different acoustic phenomena and the characterization of acoustic properties of objects through, among other methods, the application of the condition of phase matching. Far-field time domain short-pulse responses from relatively thin shells, primarily consist of distinct echoes associated with specular reflection and with circumnavigations of dominant surface waves. Frequency domain studies allow the determination of acoustic signatures of the objects in terms of backscattering and resonance spectra.

A number of acoustic scattering studies on plates have shown that localized changes in the geometry, plate thickness, for example, cause wave type conversions in these regions. Briers *et al.*[10] discuss the conversion of the Scholte–Stoneley wave into a generalized Rayleigh wave at the extremity of a thick plate immersed in water. The reverse process, acoustic volume wave converted into the Scholte–Stoneley wave, is illustrated by the same authors.[11] Further, phase changes of the Scholte–Stoneley wave propagating through an inclusion in the structure, is also examined.[12] Experimental verifications of observations from these theoretical works are provided by Tinel.[13] In another study Ech-Cherif El-Kettani *et al.*[14,15] consider the conversion of Lamb waves as well as reflection and retro-reflection phenomena at the edge of an immersed plate. Ditri[16] studies the scattering of horizontal shear (SH) waves from structures having material and geometric waveguide step discontinuities, and suggests that similar considerations could be applied in the case of Lamb waves. In studies presented by Tinel *et al.*[17] the interaction of the A wave with a tenon or a mortise results in its conversion into A_0, S_0 and A_1 Lamb waves, each being detectable at a different critical angle of observation, in the receiving end. This last type of conversion is closest to some of the significant observations in the present study.

The effect of discontinuities and mass loads on the acoustic properties of thin, air-filled, finite, elastic cylindrical shells is investigated by Bondaryk and Schmidt.[18] In progressive modeling, from an empty thin shell to one with idealized internal structures, their work attempts to analyze fundamental acoustic components of real structures such as submarines. I-Tai Lu,[19] applies a hybrid ray-mode (wave front-resonance) method, in analyzing acoustic radiation and scattering from fluid loaded objects with different internal structures. The case of oblique incidence on finite cylindrical shells in water is examined by, among other authors,

Rumerman[20] and Morse *et al.*[21] The two studies, in the frequency-angle space, illustrate backscattering enhancement due to the presence of a discontinuity, represented by the shell edge. Other recent studies concern work by Klauson *et al.*,[22,23] where the modeling of internally single side axially attached plate, is analyzed theoretically and experimental verification provided in the $ka=15-35$ frequency region. The authors observe wave type conversions taking place along the plate–tube junction. They show how ribs and stringers act as additional wave generating centers, and therefore contributing, in a significant way, to the complexity of the echo wave signal in the time domain analysis, and to the modification of mode numbers and resonance frequency positions, in the spectral analysis. A comparison of resonance amplitudes between the stiffened and nonstiffened shells, shows how the position of the structural discontinuities, relative to the nodes and antinodes of cylindrical shell vibration, influences both backscattering and resonance spectra.

In light of results from these and a number of other studies, the present work examines the case of a geometrically simple object, cylindrical shell, with an equally simple discontinuity, a solder (internal axial mass layer) in the absence of internal structures. The explanation of experimental results obtained from acoustic components introduced by the solder, in both time and frequency domains, is provided. These results are sought in the perspective of the studies on the influence of the solder on more complex objects where soldering is used to assemble together geometrically simple objects, for example, cylindrical shells to which hemispherical endcaps are attached.[24,25]

In Sec. I we outline geometric characteristics of a studied object and provide experimental conditions. In Sec. II the arrival time formulas for predicted echoes due to the two wave types, A and S_0, are developed. In the calculations of echo arrival times, the type of wave propagating, the distance traveled and corresponding group velocities are considered. In addition, eventual wave generation and wave type conversions, occurring at the solder, accompanied by transmission or reflection, are taken into account. The dependence of the amplitude and arrival times of certain echoes, on the incidence angle of the incident wave front, relative to the solder, is illustrated. The evolution of the echo arrival times as a function of the incidence angle, allows the identification of various echo series. The influence of the solder on the resonance and backscattering spectra is treated in Sec. III. This influence is principally through wave generation and wave type conversions at the solder, as well as on the position of the solder relative to the direction of the incident wave. The influence on the spectra, of the interference between the echo from direct reflection at the solder and the specular echo, is also illustrated.

I. THE OBJECTS AND CONDITIONS OF EXPERIMENTS

The soldered tubes are made from flat sheets rolled and soldered lengthwise. The external surface is smoothed out such that the mass layer due to the solder is only visible internally. The shells are made of stainless steel of density $\rho=7900$ kg/m^3 with the velocities of shear and compressional waves, respectively, $C_T=3100$ m/s and $C_L=5790$ m/s. Dimensional characteristics of the tubes are external radius $a=15.30$ mm, radii ratio $b/a=0.97$, where b is the internal radius, total length $L=200$ mm, and the mass layer having an average thickness of the order of magnitude of the thickness of the shell, $h=0.46$ mm and its width is twice this value. The air-filled tube, closed on both ends by a stainless steel disk of the same thickness as the tube, is vertically suspended in water and insonified normally to its axis. The vertical position of the tube is a factor of particular importance so as to avoid the generation of guided waves from oblique incidence. A water tank of diameter 3 meters and depth 2 meters is equipped with a computer controlled mechanism to command the displacements of the transducer around the objects. Figure 1 shows the sketch of the experimental setup. The transducer used is broad band Panametrics, model V392-SU, with central frequency equal to 1 MHz ($ka=65.4$). The time and frequency domain characteristics of the transducer are presented in Fig. 2. The diameter of its radiating surface is 40 mm. The frequency range of the study extends over 400–1400 kHz ($ka=25-90$), the wavelength λ, of the incident wave is of the order of magnitude of the mass layer width. An electric signal pulse of Dirac type from a pulse generator excites the transducer. The distance between the transducer and the object is about 1 m. In this two dimensional backscattering configuration and considering the ratio a^2/λ, conditions of the far field are satisfied and the incident wave can be considered to be plane.[3] Also, in the frequency range studied and given the physical characteristics of the shells (material and the ratio b/a), only the A wave (Scholte–Stoneley) and the S_0 wave are experimentally observed. This study, therefore, is confined to these two types of waves only. The broad pass-band of the transducers ensures sufficient separation of frequency zones, in which the A wave and the S_0 wave are generated. This separation facilitates the scattering analysis both in the time and frequency domains. The backscattering investigations are made at different angular positions around the tube, in the azimuthal plane.

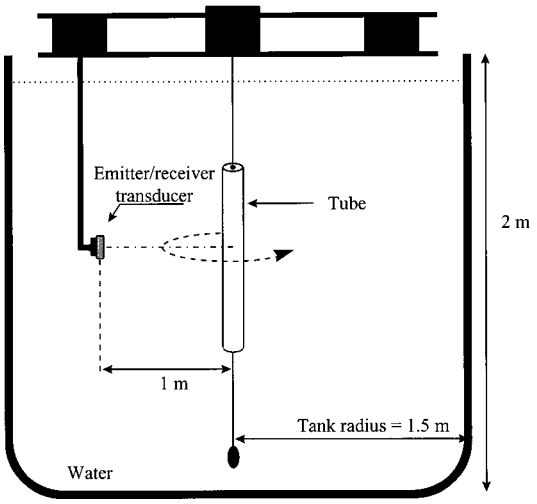

FIG. 1. Experimental setup.

The short pulse monostatic setup[26,27] is used to obtain

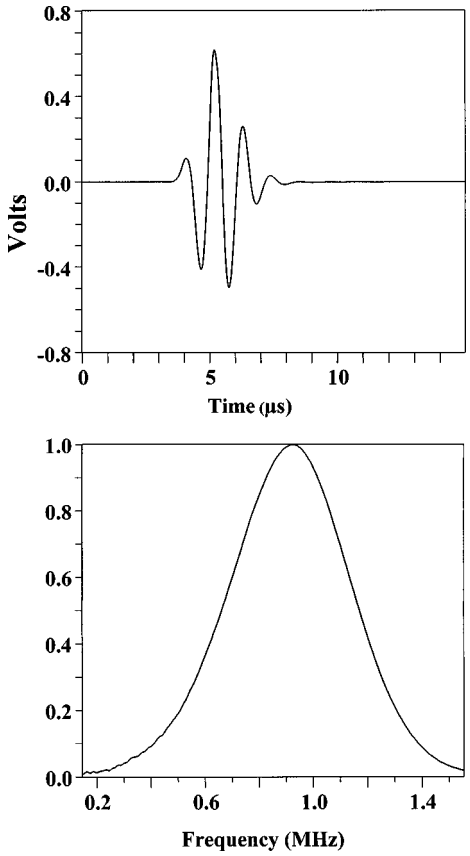

FIG. 2. Time and frequency characteristics of the transducer.

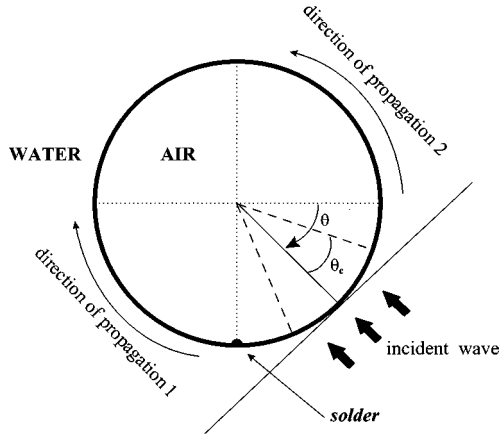

FIG. 3. Cross section of the tube in the experimental setup.

experimental results presented in the time domain analysis. A short pulse is sent to the object from the transducer and the backscattered signal is received by the same transducer. The received signal, the echo wave form, is visualized on the oscilloscope and recorded for further signal processing and analysis. In the frequency domain analysis, the monostatic quasi-harmonic setup[28,29] is used and consists in sending a train of sinusoidal signal covering the frequency range of the band pass of the transducer, with a duration sufficiently long (500 μs) such that a steady state is established on the object. The form of the backscattered signal depends on the central frequency of the incident burst. Close to (and at) the resonance frequencies of the insonified object the backscattered signal shows a characteristic tail at the end of the forced excitation. Recordings are made either in the forced excitation zone (backscattering spectra) or in the free reemission zone (resonance spectra).

II. TIME DOMAIN ANALYSIS

The prediction of echo arrival times is carried out as follows: wave types and respective generation points on the shell are identified, possible wave travel paths on the objects are determined, considering eventual wave type conversions, at the solder. Taking into account respective wave group velocities, echo arrival times are calculated and allow the localization of individual echoes on the echo wave form. Studies on the evolution of the arrival time of various echoes as a function of the incidence angle θ allow the identification and explanation of different echo series, this facilitates the localization of echo origins.

Figure 3 presents the cross section of the experimental setup. The angular position θ, in the azimuthal plane, of the transducer (incident wave), is noted for each recording. This incident angle can be measured from any arbitrarily fixed point on the tube, in the present study the solder is at $\theta=90°$ ($\pi/2$ radians) from the chosen starting point. The S_0 wave is generated at critical angle θ_c ($\theta_c=\sin^{-1} C_1/C_{S_0}^{\mathrm{ph}}$ where $C_1=1470$ m/s is the sound velocity in water and $C_{S_0}^{\mathrm{ph}}$ is the phase velocity of the S_0 wave for which $\theta_c=16°$).[30] The A wave is generated in the neighborhood of the tangent to the tube. For both wave types two directions of propagation from the generation points are defined and labeled 1 and 2 (clockwise and anti-clockwise, respectively).

Echo wave form recordings made around the soldered tube, at 1° angular intervals and placed next to each other, are shown on the grayscale presentation of Fig. 4(a), in the angle-time space, for angles $\theta=90°$ to 270°, the other angular section being the mirror image of this part. On this global representation of the evolution of echo arrival times, echoes from wave types generated in the higher frequency region (S_0 wave) are identified by finer rippled bands, whereas those in the lower frequency region (A wave) have wider ripples. The first echoes of some of the identified echo series are indicated on the figure. Figure 4(b) shows the evolution of these echoes as a function of the incidence angle obtained from calculations using arrival times formulas which are developed in the following paragraphs. The evolution of the calculated arrival times [Fig. 4(a)] matches with that obtained experimentally [Fig. 4(b)].

A. Echoes independent of the solder

Echo *Sp* is the specular reflection, from the sparkling point on the tube and, its arrival time serves as a reference to calculations of all other arrival times. The S_0^1 echo is the first of the echo series labeled S_0^m due to the S_0 wave generated and re-emitted at critical angle θ_c. The integer m is the circumnavigation index indicating the order of arrival of the echoes on the waveform and equals the number of turns the corresponding wave makes around the tube. The first echo of

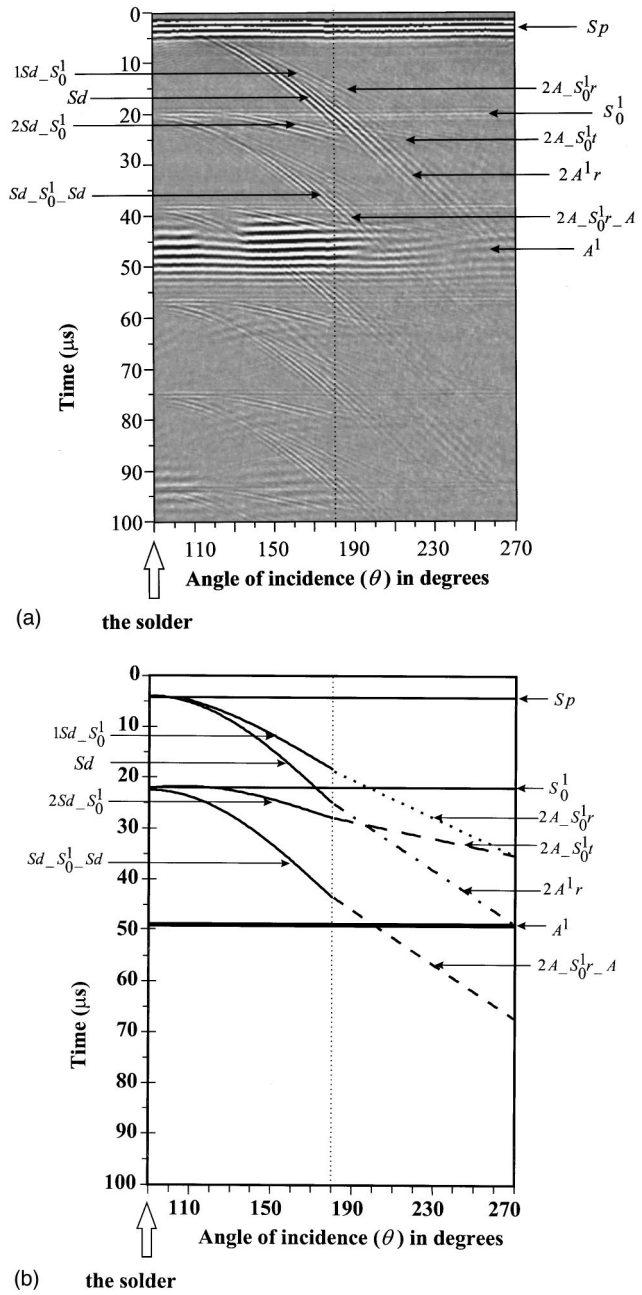

FIG. 4. (a) Evolution of experimental echo arrival times as a function of the incidence angle θ. (b) Evolution of calculated echo arrival times as a function of the incidence angle θ.

each series, $m=1$, does not make a complete turn around the shell, except for echoes generated and re-emitted at the solder. In a number of relations in this paper particular symbols have been used in order to shorten and simplify their write-up. These symbols are grouped in Table I for easy referencing. The travel time of sound in water between the sparkling point and the S_0 wave generation point is noted $\delta=a(1-\cos\theta_c)/C_1$. The time taken by an S_0 wave to travel round the tube is equal to $\gamma_{S_0}=2\pi a/C_{S_0}$, where C_{S_0} is the group velocity of the S_0 wave on the tube. The arrival time of echoes of the series S_0^m is therefore given by

$$t_{S_0^m}=2\delta+2a(\pi-\theta_c)/C_{S_0}+(m-1)\gamma_{S_0}, \quad m=1,2, \ldots . \tag{1}$$

Likewise, echo A^1 is the first echo of the series A^m due to the A wave generated and re-radiated tangentially at the surface of the shell. The travel time of sound in water between the sparkling point and the point where the A wave is generated is equal to $\eta=a/C_1$ and the time the A wave takes to travel one turn around the tube is $\gamma_A=2\pi a/C_A$, where C_A is its group velocity. Thus the arrival time of echoes of this series is obtained from

$$t_{A^m}=2\eta+\pi a/C_A+(m-1)\gamma_A, \quad m=1,2, \ldots . \tag{2}$$

Echo series S_0^m and A^m are independent of the solder position and appear in Fig. 4(a) as horizontal bands. These are the echoes normally observed on the unsoldered tubes.

The time interval between two successive echoes (peak-to-peak), representing single turn travel time for respective wave types is experimentally measured [Fig. 4(a)] and found to be equal to 18.5 μs for the S_0 wave and 48.1 μs for the A wave. From the circumference of the tube, $2\pi a$, the average group velocities of each wave type are deduced, the numerical values obtained are $C_{S_0}=5200$ m/s and $C_A=2000$ m/s. These values are used in the evaluation of arrival times throughout this paper. It is accurate enough to use these average values since the present work is limited to the frequency region where the dispersion of group velocities for both wave types is relatively small.

B. Influence of the solder

1. Reflection of the S_0 wave at the solder

The S_0 wave generated at critical angle θ_c, in both directions of propagation (1 and 2), is partially reflected at the solder and re-emitted at the same critical angle, this results in the echo series noted $1S_0^m r$ and $2S_0^m r$, r indicates reflection and numbers 1 and 2 indicate initial propagation directions. When the incidence is in the neighborhood of the solder, at θ_c on either side of it, abrupt changes in wave propagation path take place. The changes result in either one more or one less circumnavigation tour of the wave before re-emission. The two angular limits shall be defined as $\alpha'=\pi/2-\theta_c$ and $\alpha''=\pi/2+\theta_c$ and the arrival time formulas involving the influence of the solder on the S_0 wave shall be written as a function of angular zones delimited by these points. The echo arrival times of the series $1S_0^m r$ are obtained by the relation

$$t_{1S_0^m r}=2\delta+2a(\varphi+\alpha'-\theta)/C_{S_0}+(m-1)\gamma_{S_0}, \quad m=1,2, \ldots , \tag{3a}$$

such that $\varphi=0$ for $0\leqslant\theta\leqslant\alpha'$ and $\varphi=2\pi$ for $\alpha'<\theta<2\pi$. In the propagation direction 2, the arrival time is determined by

$$t_{2S_0^m r}=2\delta+2a(\varphi+\theta-\alpha'')/C_{S_0}+(m-1)\gamma_{S_0}, \quad m=1,2, \ldots , \tag{3b}$$

where $\varphi=2\pi$ for $0\leqslant\theta\leqslant\alpha''$ and $\varphi=0$ for $\alpha''<\theta<2\pi$. These series of echoes are hardly observable in the frequency range of the present study, but they are clearly identified in the higher frequency study of Ref. 31 (with a transducer of central frequency 2.25 MHz), in which the presence of the S_0 wave, generated at a critical angle, is more significant.

TABLE I. Symbols of some constants and variables used in the arrival time formulas.

Symbol	Expression represented	Travel time represented
δ	$a(1-\cos\theta_c)/C_1$	Between the sparkling point and S_0 generation point (in water)
$\beta(\theta)$	$a(1-\cos(\pi/2-\theta))/C_1$	Between the sparkling point and the solder (in water)
γ_{S_0}	$2\pi a/C_{S_0}$	A single circumnavigation of the S_0 wave around the tube
γ_A	$2\pi a/C_A$	A single circumnavigation of the A wave around the tube
η	a/C_1	Between the sparkling point and A wave generation point (in water)
		Limit of angle θ in case of
α'	$\frac{\pi}{2}-\theta_C$	Re-emission of the S_0 wave propagating in direction 2
α''	$\frac{\pi}{2}+\theta_C$	Re-emission of the S_0 wave propagating in direction 1

2. Wave generation and re-emission at the solder

Two geometrically distinct zones are defined on the tube, the zone where the solder is directly insonified by the incident wave, the *clear* zone, $\theta=0°$ to 180° [90° to 180° in Fig. 4(a) and (b)] and the other is designated the *shadow* zone (180° to 270° in the figures). Figure 5 is an echo wave form from the *clear* zone, at $\theta=146°$. The amplitude of the specular echo, *Sp*, is deliberately saturated in order to enhance the amplitudes of subsequent echoes. The echo labeled *Sd* is from direct reflection of the incident wave at the solder. The time interval between this echo and the specular depends on the term $\beta(\theta)=a(1-\cos(\pi/2-\theta))/C_1$. The arrival time of this echo is thus determined by

$$t_{Sd}=2\beta(\theta), \quad \text{over } 0\leqslant\theta\leqslant\pi. \tag{4a}$$

At $\theta=90°$ the relation (4a) vanishes, the transducer is in front of the solder and therefore coincides with the sparkling point as can be seen in Fig. 4(a) and (b).

Echo series $Sd\_S_0^m\_Sd$ corresponds to the direct generation, at the solder, of the S_0 wave and re-emission at the same point after each turn. Either way the distance traveled is the same, thus the direction of propagation is of no importance here. The arrival time of echoes of this series is given by the relation (4a) plus circumnavigation periodicity of the S_0 wave, over $0\leqslant\theta\leqslant\pi$;

$$t_{Sd\_S_0^m\_Sd}=2\beta(\theta)+m\gamma_{S_0}, \quad m=1,2,\ \ldots\ . \tag{4b}$$

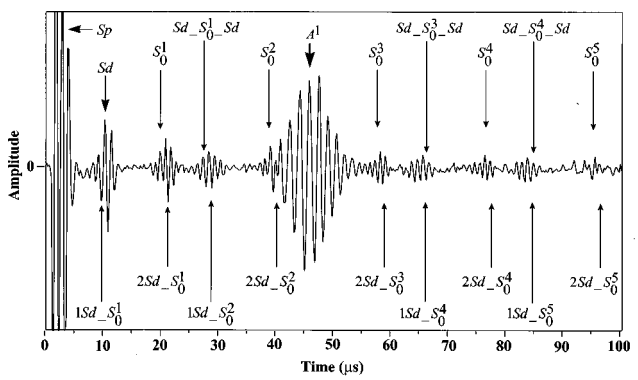

FIG. 5. Echo wave form from the soldered tube at $\theta=146°$.

Echoes corresponding to $m=1$, 3 and 4 are visible in Fig. 5; the second echo ($m=2$) arrives within the time interval covered by the echo A^1.

When the solder generated S_0 wave is instead re-emitted at critical angle θ_c, it becomes propagation direction dependent and gives rise to the echo series $1Sd\_S_0^m$ and $2Sd\_S_0^m$. The corresponding arrival times are given by

$$t_{1Sd\_S_0^m}=\beta(\theta)+a(\varphi+\theta-\alpha'')/C_{S_0}+\delta+(m-1)\gamma_{S_0}, \quad m=1,2,\ \ldots\ , \tag{4c}$$

with $\varphi=2\pi$ over $0\leqslant\theta\leqslant\alpha''$ and $\varphi=0$ over $\alpha''<\theta<\pi$ for the former, and for the latter series

$$t_{2Sd\_S_0^m}=\beta(\theta)+a(\varphi+\alpha'-\theta)/C_{S_0}+\delta+(m-1)\gamma_{S_0}, \quad m=1,2,\ \ldots\ , \tag{4d}$$

with $\varphi=0$ over $0\leqslant\theta\leqslant\alpha'$ and $\varphi=2\pi$ over $\alpha'<\theta<\pi$.

In the *clear* zone the significant phenomenon is the wave generation and re-emission at the solder. The wavelength of the incident wave, within the frequency band of the study, is of the order of magnitude of the width of the solder mass layer; it therefore interacts with it to generate the S_0 wave. The evolution of arrival of this category of echoes is closely linked to the cosine term in the relation $\beta(\theta)$ in the form of arcs, particularly pronounced close to the solder ($\theta=90°$) as shown in Fig. 4(a) and (b). In Fig. 5 ($\theta=146°$) a number of these echoes have arrival times very close to each other and are therefore difficult to separate. This is the case for echoes *Sd* and $1Sd\_S_0^1$, the series S_0^m and $2Sd\_S_0^m$ and the series $1Sd\_S_0^m$ and $Sd\_S_0^m\_Sd$. However, in Fig. 4(a) it is possible to see how strongly this phenomenon depends on incidence angle θ, such that echoes from different series having close arrival times at one angle can be completely separable at another angle.

3. Reflection of the A wave at the solder

In the *shadow* zone, echoes related to the *A* wave and to its conversion are dominant. Figure 6 shows a response from this zone at $\theta=193°$. When the *A* wave generated tangentially on the shell is reflected at the solder, propagates back

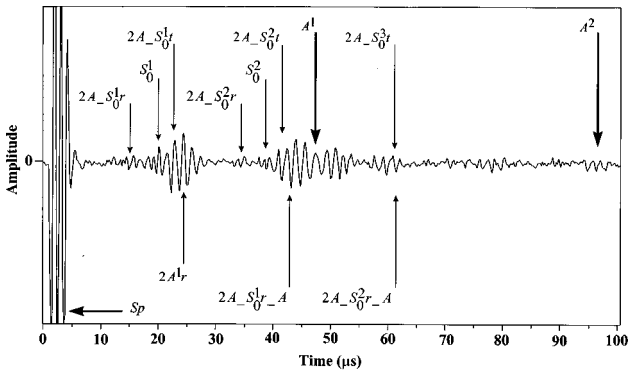

FIG. 6. Echo wave form from the soldered tube at θ=193°.

and is reemitted tangentially again, the result is the echo series $1A^m r$ in initial propagation direction 1, with arrival time, over $0 \leqslant \theta < 2\pi$ obtained from

$$t_{1A^m r} = 2a(2\pi - \theta)/C_A + 2\eta + (m-1)\gamma_A, \quad m = 1,2, \ldots . \tag{5a}$$

In this direction the A wave path decreases steadily over the whole angular zone. Whereas in initial direction 2 there is a sudden change in the propagation path at $\theta = \pi$ as the incidence direction passes through the solder, the arrival time formula of the series $2A^m r$ becomes

$$t_{2A^m r} = 2a(\varphi + \theta)/C_A + 2\eta + (m-1)\gamma_A, \quad m = 1,2, \ldots , \tag{5b}$$

with $\varphi = \pi$ for $0 \leqslant \theta \leqslant \pi$ and $\varphi = -\pi$ for $\pi < \theta < 2\pi$. Only the first echo of this series is clearly visible in Fig. 6. In initial propagation direction 1 the path taken by the A wave is longer than that in direction 2 [relations (5a) and (5b)] thus is not possible to observe echoes of the series $1A^m r$ in the time window represented in the figure.

4. Conversion of wave types at the solder

The A wave propagating on the tube may undergo conversion on encountering the solder. Thus part of the energy of the A wave generated as above (3), can be converted at the solder into S_0 wave, which is then re-emitted at critical angle. This conversion accompanied by transmission results in series labeled $1A\_S_0^m t$ and $2A\_S_0^m t$ with echo arrival time determined by

$$t_{1A\_S_0^m t} = \eta + a(2\pi - \theta)/C_A + a(\varphi + \theta - \alpha'')/C_{S_0} + \delta + (m-1)\gamma_{S_0}, \quad m = 1,2, \ldots , \tag{6a}$$

with $\varphi = 2\pi$ over $0 \leqslant \theta \leqslant \alpha''$ and $\varphi = 0$ over $\alpha'' < \theta < 2\pi$, in the propagation direction 1. In direction 2 the arrival time relation becomes

$$t_{2A\_S_0^m t} = \eta + a(\pi + \theta)/C_A + a(\varphi + \alpha' - \theta)/C_{S_0} + \delta + (m-1)\gamma_{S_0}, \quad m = 1,2, \ldots , \tag{6b}$$

with $\varphi = 0$ for $0 \leqslant \theta \leqslant \alpha'$ and $\varphi = 2\pi$ for $\alpha' < \theta \leqslant \pi$. Then over the range $\pi < \theta < 2\pi$ (with the $\varphi = 2\pi$) the relation becomes

$$t_{2A\_S_0^m t} = \eta + a(\theta - \pi)/C_A + a(\varphi + \alpha' - \theta)/C_{S_0} + \delta + (m-1)\gamma_{S_0}, \quad m = 1,2, \ldots . \tag{6c}$$

In the case of conversion accompanied by reflection the series related to propagation direction 1 is labeled $1A\_S_0^m r$ with an arrival time given by

$$t_{1A\_S_0^m r} = \eta + a(2\pi - \theta)/C_A + a(\varphi + \alpha' - \theta)/C_{S_0} + \delta + (m-1)\gamma_{S_0}, \quad m = 1,2, \ldots , \tag{7a}$$

with $\varphi = 0$ for $0 \leqslant \theta \leqslant \alpha'$ and $\varphi = 2\pi$ over $\alpha' < \theta < 2\pi$. In direction 2 the series is labeled $2A\_S_0^m r$ and the arrival time determined by

$$t_{2A\_S_0^m r} = \eta + a(\pi + \theta)/C_A + a(\varphi + \theta - \alpha'')/C_{S_0} + \delta + (m-1)\gamma_{S_0}, \quad m = 1,2, \ldots . \tag{7b}$$

with $\varphi = 2\pi$ over $0 \leqslant \theta \leqslant \alpha''$ and $\varphi = 0$ over $\alpha'' < \theta \leqslant \pi$. In the angular zone $\pi < \theta < 2\pi$ (with the $\varphi = 0$) the relation becomes

$$t_{2A\_S_0^m r} = \eta + a(\theta - \pi)/C_A + a(\varphi + \theta - \alpha'')/C_{S_0} + \delta + (m-1)\gamma_{S_0}, \quad m = 1,2, \ldots . \tag{7c}$$

Note that in formulas (6a) through (7c) the propagation directions 1 and 2 are those of the generated A wave, whereas the circumnavigating wave is the S_0 wave; hence the index m is on this wave type. In Fig. 6 only the series in propagation direction 2, for both reflection and transmission cases, are clearly observable. In propagation direction 1 the A wave travels a longer path before conversion; consequently the converted wave has a weaker amplitude.

When the converted S_0 wave is reconverted back into the A wave type on the following encounter with the solder, after reflection or transmission, and the consequent A wave travels on and is re-emitted tangentially. The resulting echo series in the case of reflection are labeled $1A\_S_0^m r\_A$ and $2A\_S_0^m r\_A$ and the corresponding arrival times are given by

$$t_{1A\_S_0^m r\_A} = 2a(2\pi - \theta)/C_A + 2\eta + m\gamma_{S_0}, \quad m = 1,2, \ldots , \tag{8a}$$

over $0 \leqslant \theta \leqslant 2\pi$, and

$$t_{2A\_S_0^m r\_A} = 2a(\varphi + \theta)/C_A + 2\eta + m\gamma_{S_0}, \quad m = 1,2, \ldots , \tag{8b}$$

with $\varphi = \pi$ over $0 \leqslant \theta \leqslant \pi$ and $\varphi = -\pi$ over $\pi < \theta < 2\pi$.

In the case of transmission the resulting series labeled $A\_S_0^m t\_A$ is not dependent on the direction of propagation; its arrival time is calculated from

$$t_{A\_S_0^m t\_A} = 2\eta + a(3\pi + \varphi)/C_A + m\gamma_{S_0}, \quad m = 1,2, \ldots , \tag{8c}$$

with $\varphi = 0$ over $0 \leqslant \theta \leqslant \pi$ and $\varphi = -2\pi$ over $\pi < \theta < 2\pi$.

The important phenomena in the *shadow* zone are wave type conversion and wave reflection at the solder, as illustrated in Fig. 6, where echo series $2A\_S_0^m r$, $2A\_S_0^m t$, $2A\_S_0^m r\_A$ and $2A^m r$ are dominant. The effect of close arrival times is more pronounced in this case for, the above series together with the series S_0^m and A^m, form packets of a

continuum of echoes in which precise isolation becomes difficult, particularly when the different echoes have, in addition, close central frequencies. For instance echoes $2A\_S_0^2t$, $2A\_S_0^1r\_A$, S_0^2 and A^1 form one such extensive echo. Thus what sometimes appears to be a single wide or narrow echo, may, in fact, be composed of two or more echoes from different series. In some cases there is a reduction in amplitude of the resultant echo, as in Fig. 6, due to destructive interference between echoes, while in others, constructive interference brings about echo amplitude enhancement.

The generation of the *A* wave on thin shells within a patch close to the tangent line on the surface has been shown to depend on the ratio *b/a* and to be limited in a defined frequency window.[32–35] This is true where the ratio $b/a > 0.6$. With an appropriate correction of the shell material density, this frequency window, in shells considered here, is deduced from Ref. 32, and is found to cover the range $30 < ka < 45$. According to other studies in Refs. 36–37 the condition required in order to be in the midfrequency enhancement zone is $kh \approx 1$ (h is shell thickness), assuming that $ka \gg 1$. In the case of the considered tube the midfrequency zone is situated around $ka \approx a/h = 33$, which is well within the *A* wave generation frequency zone. This explains the relatively strong amplitude of the first echo of the *A* wave, A^1 in Fig. 5 compared to those of the S_0 wave, S_0^1 and S_0^2, for example, even though the generation frequency window of the *A* wave is in the lower end of the band pass of the transducer. In general, it is shown in Fig. 4(a) that echo A^1 is stronger over the $90° < \theta < 180°$ angular window than over $180° < \theta < 270°$. This is due to the fact that in the first case, the propagating *A* wave does not encounter the solder on its path, before re-emission to give echo A^1. Whence it conserves most of its energy. In the second case, however, there is loss of energy due to conversion and reflection at the solder. This phenomenon applies to echo A^2 as well.

It is also important to note that echoes resulting from wave types which have undergone conversion, tend to maintain the frequency characteristics of the first generated wave whilst assuming the speed of the wave type into which they are converted. More echo series are presented in Ref. 31, where the use of a transducer having a central frequency of 2.25 MHz enables the generation of the S_0 wave with a stronger signal level.

There is a remarkable continuity of the presence of echoes over what may be considered as the solder illumination boundary between the *clear* and the *shadow* zones situated at $\theta = 180°$. However, no visible distinction of echoes series in Fig. 4(a) and (b) or an abrupt change in arrival times is observable even though echoes change their source and therefore their designation, across this angle. The echo *Sd* becomes $2A^1r$, echo series $1Sd\_S_0^m$ continues into series $2A\_S_0^m r$ and series $Sd\_S_0^m\_Sd$ changes to $2A\_S_0^m r\_A$ in a smooth transition. A general higher amplitude of echoes in the *clear* zone, than in the *shadow* zone, is manifest and is explained by the contribution of additional energy from wave generation at the solder.

In addition to this smooth transition of echo types, a further analysis of the signals has revealed a continuous evolution of the central frequency of the echo designated *Sd*, to one designated $2A^1r$. The central frequency varies from one close to the central frequency of the transducer (for the echo *Sd*), to the frequency of the *A* wave, in the frequency window where it is observed (for the echo $2A^1r$) as the angle θ and the travel distance increase, Fig. 7. This feature is observed in a number of other echo series transitions which are dependent on the solder. These acoustic phenomena on this object seem to undergo smooth transitions (echo series and echo central frequency) despite the otherwise abrupt geometric change between the two zones.

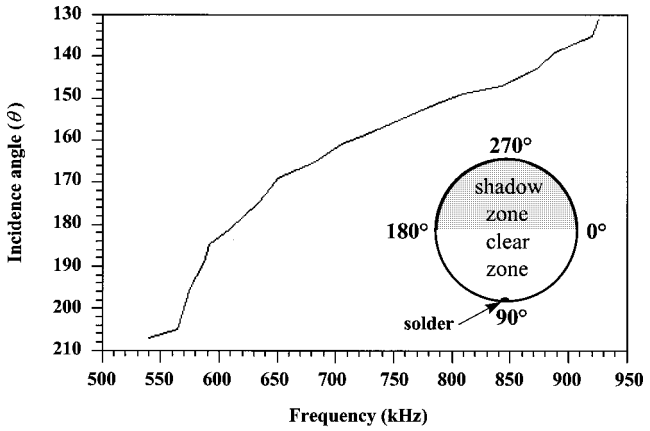

FIG. 7. Evolution of the central frequency of the echo labeled *Sd* (over $0 \leqslant \theta \leqslant 180°$) and labeled $2A^1r$ (over $180 < \theta \leqslant 360$).

III. SPECTRAL ANALYSIS

The monostatic quasiharmonic setup of the method described in Sec. I, is used to obtain spectral responses. As in the case of the time domain study, recordings are made at 1° intervals around the shell. Systematic spectral analysis highlights angular zones in which the influence of the solder on backscattering is most significant. It also allows the observation of the amplitude variations of certain resonance transitions at various angular positions θ of the solder relative to the incident plane wave.

A. Resonance spectra

Resonance spectrum recordings are made sufficiently far in the free re-emission region to avoid the influence of the direct reflection (nonresonant) from the solder. Results obtained are presented in Fig. 8, for the angular window $90° \leqslant \theta < 240°$. Two zones of interest stand out clearly, the lower frequency range, in which the influence of the *A* wave resonances is more significant, and the higher frequency region where the presence of the S_0 resonances is more consequential. Resonances due to the S_0 wave type appear in Fig. 8 as regularly spaced vertical lines situated at the same frequencies (and with the same mode numbers) as for the unsoldered tube.[38] The frequency span between successive resonance ''lines'' is relatively constant, $\Delta f = 54.1$ kHz ($\Delta ka = 3.53$), which indicates that in the frequency domain of the study, the group velocity variations are very small. Another significant feature in this figure is the enhancement of resonance amplitudes covering the angular zone $120° \leqslant \theta \leqslant 200°$. The distance traveled by the *A* wave before

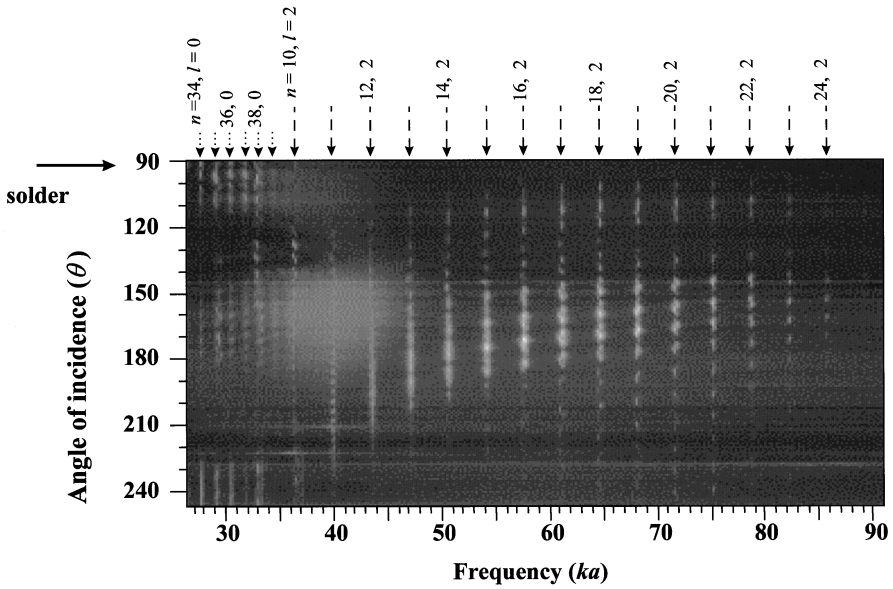

FIG. 8. Evolution of resonance spectra from the soldered tube as a function of the incidence angle θ.

conversion is shorter within this zone and therefore on arrival at the solder its high frequency component is still sufficiently strong. The converted S_0 wave is thus manifest well into the high frequencies. Outside this zone, the high frequency component of the *A* wave, whose energy is dissipated into the surrounding water faster than that of the lower one, has a limited influence; thus conversion is more significant in the lower frequencies. The condition of phase matching is equally satisfied for the S_0 wave generated at the solder, directly or by conversion; this results in the enhancement of amplitude of its resonances. This is true in the *clear* zone where the generation and re-emission of the S_0 at the solder is predominant as well as in the *shadow* zone where the contribution of the conversion phenomenon is significant.

It can also be seen from the same figure that vertical lines representing resonances due to the S_0 wave type are not continuous throughout the angular window of observation, but they appear as dashed lines. This is the result of periodic variations in the amplitude of resonance peaks as a function of the incidence angle θ, at each resonance frequency. This modulative effect is present throughout the $\theta=120°–200°$ zone in Fig. 8. Below incident angle $\theta=120°$ and above $\theta=200°$ resonances are not so easily observable, under the experimental conditions of the present study. Considering the effect of the internal plate in association to its position in either the nodes or the antinodes of the vibrating shell, studied in Ref. 22, similar phenomenon can be extended to the present study to explain these variations. However, in the case of the soldered shell, the radial dimensions of the solder do not allow it to generate waves at its proper vibration modes in such a way as to add to the spectral response. Thus, in our present study there is neither resonance frequency shift nor additional resonance peaks on the spectra. Vertical lines representing resonances due to the $A(l=0)$ wave are present over the whole angular window ($\theta=90°–270°$) for frequencies below $ka=35$. This region corresponds to the predicted generation frequency window of this wave mentioned earlier on. The frequency interval between successive resonances, smaller than that of S_0 resonances, is equal to $\Delta f=17.8$ kHz ($\Delta ka=1.19$).

In some cases this variation in amplitude is such that certain resonances considered absent at one incident angle appear with a strong amplitude a few degrees later (or earlier). The angular dependent amplitude modulation effect is illustrated in Fig. 9 for two resonance spectra at close incidence angles, 158° and 155°. Note the differences in amplitudes of the S_0 resonances ($l=2$), in the two spectra. The presence of the S_0 resonances in the lower frequency zone relative to those in the unsoldered tube is due to the generation of this wave type by direct insonation at the solder. The

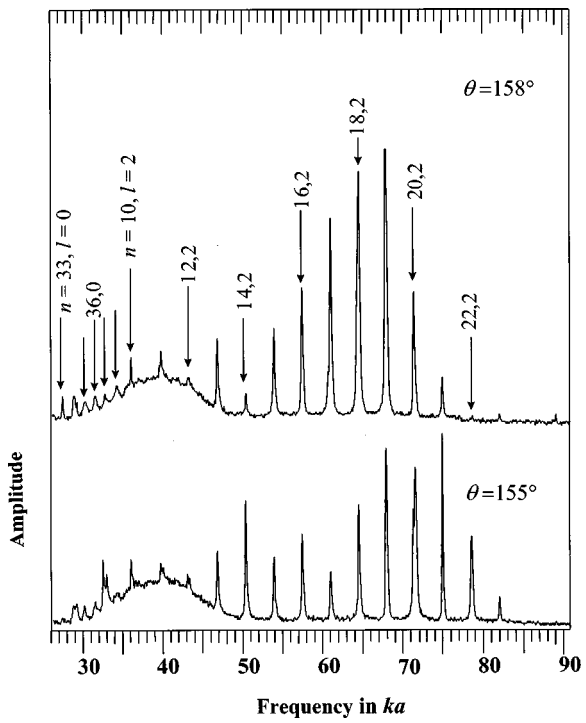

FIG. 9. A comparison of resonance spectra from the soldered tube at incidence angles $\theta=155°$ and $\theta=158°$.

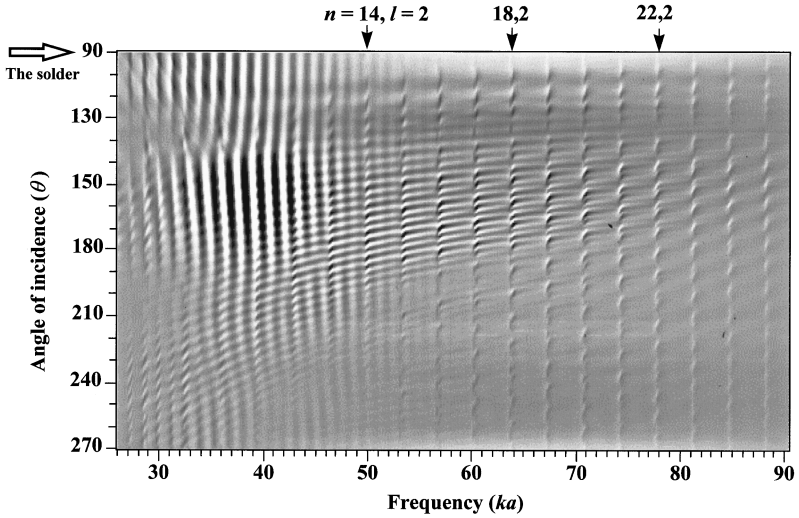

FIG. 10. Evolution of backscattering spectra from a soldered tube as a function of the incident angle θ.

amplitude variations are obviously not uniform for all resonance peaks for a given change of incidence angle. This is simply due to the fact that the position of the solder (relative to a node or anti-node) depends on the vibration mode number n of each resonance frequency. The relative low amplitude of the A wave resonances is due to the fact that the generation of the S_0 wave at the solder and by conversion from the A wave predominates that of the A wave alone. Nevertheless, in Fig. 9 the amplitude enhancement centered around $ka=40$ (610 kHz) is in relation with the central frequency of echo A^1 of the A wave which has not encountered the solder, at these angles (155° and 158°).

B. Backscattering spectra

Backscattering spectra at 1° intervals around the tube are presented in Fig. 10 for the incidence range θ=90°–270°. Resonances due to S_0 wave are clearly observable from $ka=45$ to $ka=90$, influenced by angular modulation, as vertical rippled lines, similar to the modulation phenomenon discussed in the resonance spectrum. For frequencies below $ka=45$ the influence of the A wave is dominant over those of the S_0 wave, particularly in the angular window $90°<\theta<180°$ (*clear* zone), which corresponds to one where the A^1 echo is predominant.

The backscattering spectrum of the unsoldered tube is compared to a spectrum of a soldered tube recorded at θ=170°, Fig. 11. The region below $ka=45$ is marked by a strong influence of the A wave identical in both spectra. On the unsoldered tube the amplitudes of S_0 resonances are weaker, in general, over the whole frequency window and, in particular, in the frequency zone $ka=45$ to 60 where they are too narrow to be experimentally observable. On the contrary, they are significantly enhanced in the same zone on the soldered tube. However, respective resonance frequency positions and vibration mode numbers remain unchanged. Both the generation of the S_0 wave directly at the solder and by partial conversion of the A wave contribute to the constitution of S_0 wave resonances with relatively high energy.

In addition, transitions due to S_0 resonances in the soldered tube appear to be superimposed on a regular modulation in a sort of a new modulation phenomenon explained by the interaction between echoes *Sp* and *Sd* (Fig. 4). The frequency of the modulating signal is associated with the time interval separating the two echoes, given as $2\beta(\theta)$, by relation (4a). As the incidence angle θ changes, so does the time interval between the two echoes, which leads to the change in the modulation frequency and the way the backscattering spectrum is modified, in particular, between $ka=45$ and $ka=60$. At incidence angle θ=170° the two echoes are separated by $t=14.6$ μs, the inverse of which gives the modulating frequency of 68.5 kHz ($ka=4.48$), equal to that observed on the spectrum.

Figure 12 shows the evolution of the effect brought about by the interference between the two echoes for the incidence angle θ varying from 178° to 182°. Relatively small changes in θ causes significant modifications on the maxima or minima of transitions attributed to the S_0 wave,

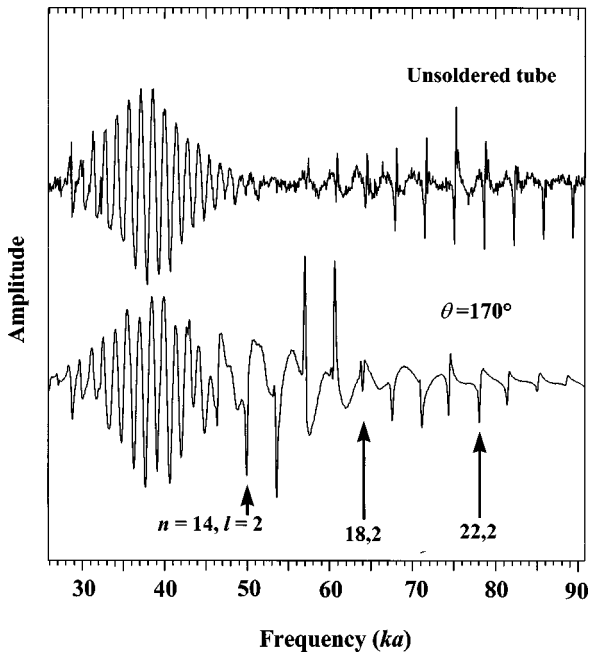

FIG. 11. A comparison of backscattering spectrum from the unsoldered tube and of backscattering spectrum from the soldered tube at incidence angle θ=170°.

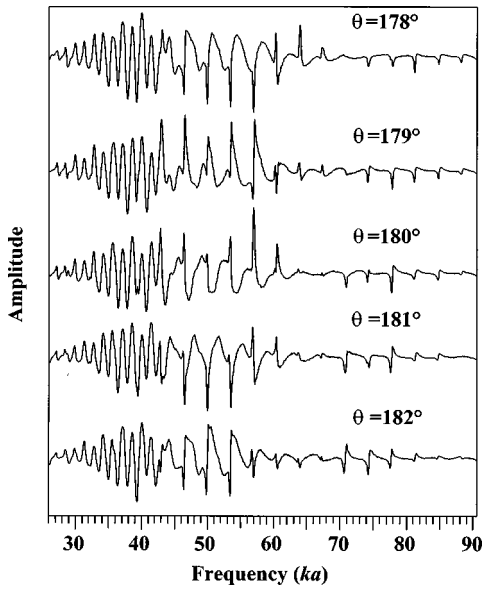

FIG. 12. Backscattering spectra at various angles of incidence relative to the solder.

on the spectra. The interval between successive S_0 transitions remains unchanged. Note also that this interference becomes that between the *Sp* and the A^1r (into which the *Sd* echo evolves), beyond 180° into the *shadow* zone.

IV. CONCLUSION

In the three cases examined, time domain response, backscattering and resonance spectra, the influence of the solder is evident and is manifest in various ways in the experimental results obtained in this study. In the time domain analysis, the complex impulse responses from the soldered tubes are explained by considering the solder as an additional wave excitation site, additional wave scattering site and wave conversion site. A number of echo series are determined by considering different combinations of these three phenomena (in addition to classical wave generation and reemission), together with wave transmission and reflection at the solder, in the calculation of echo arrival times. The influence of the solder on the amplitude and echo composition of these responses is found to be strongly dependent on whether or not the solder is directly illuminated by the incoming sound wave. However, acoustic properties of the objects undergo a smooth transition (echo series and echo central frequencies) across this distinct geometric frontier (*clear/shadow* zone). This continuity is quite striking.

In the frequency domain analysis, the presence of the solder follows an angular pattern of influence similar to that in the time domain. On the resonance spectra the presence of the solder variably enhances the amplitude of resonances, depending on the incident wave direction *vis-à-vis* the solder. In particular, it has been possible to observe S_0 wave resonances in the frequency zone $45<k_1a<60$ where they are not observable on the unsoldered tube of the same characteristics. At different angular positions, the S_0 resonances appear with variable amplitudes. On the backscattering spectra similar observations are made from the results obtained. In addition, the influence on the spectra of the variation in magnitude of the first echo of *A* wave, depends on whether or not this wave has encountered the solder. Further, the interference of the specular echo with the echo from direct reflection at the solder (or with the first echo of the reflected *A* wave) results in the modulation of the backscattering spectra. This modulation modifies the appearance of resonances on the backscattering spectra. The study highlights some of the important considerations that are to be made in the study of acoustic scattering of objects having complex assembled geometric structures comprising of inhomogeneities such as solders.

ACKNOWLEDGMENTS

The support from the French Ministère des Affaires Etrangères and from the NATO Grant No. HTECH.LG 93 1633 is hereby gratefully acknowledged.

[1] D. C. Gazis, ''Three-dimensional investigation of the propagation of waves in hollow circular cylinders. I. Analytical Foundation,'' J. Acoust. Soc. Am. **31**, 568–573 (1959).
[2] H. Überall, L. R. Dragonette, and L. Flax, ''Relation between creeping waves and normal modes of vibration of curved body,'' J. Acoust. Soc. Am. **61**, 711–715 (1977).
[3] G. Maze, J. Ripoche, A. Derem, and J. L. Rousselot, ''Diffusion d'une onde ultrasonore par des tubes remplis d'air immergés dans l'eau,'' Acustica **55**, 69–85 (1984).
[4] L. Flax, L. R. Dragonette, and H. Überall, ''Theory of elastic resonance excitation by sound scattering,'' J. Acoust. Soc. Am. **63**, 723–731 (1978).
[5] M. de Billy, ''Determination of the resonance spectrum of elastic bodies via the use of short pulses and Fourier transform theory,'' J. Acoust. Soc. Am. **79**, 219–221 (1986).
[6] M. Talmant, J-M. Conoir, and J-L. Rousselot, ''High frequency scattering by shells,'' Acta Acust. **3**, 509–515 (1995).
[7] J. H. Heimann and H. Kolsky, ''The propagation of elastic waves in thin cylindrical shells,'' J. Mech. Phys. Solids **14**, 121–130 (1966).
[8] J. L. Rousselot, ''Comportement acoustique d'un tube cylindrique mince en basse fréquence,'' Acustica **58**, 291–297 (1985).
[9] B. K. Sinha, T. J. Plona, S. Kostek, and S-K. Chang, ''Axisymmetric wave propagation in fluid-loaded cylindrical shells. I: Theory,'' J. Acoust. Soc. Am. **92**, 1132–1273 (1992).
[10] R. Briers, O. Leroy, and G. N. Shkerdin, ''Conversion of a Stoneley wave at the extremity of a fluid loaded plate,'' J. Acoust. Soc. Am. **101**, 1347–1357 (1997).
[11] R. Briers, O. Leroy, and G. N. Shkerdin, ''The generation of a Stoneley wave at the end of a fluid loaded plate by an incident bounded beam,'' J. Acoust. Soc. Am. **101**, 1366–1372 (1997).
[12] R. Briers, O. Leroy, and G. N. Shkerdin, ''Influence of an inclusion on the phase of a Stoneley wave,'' J. Acoust. Soc. Am. **101**, 1358–1365 (1997).
[13] A. Tinel, ''Diffraction de l'onde de Scholte par un dièdre et par un réseau de stries,'' Ph.D. thesis, Université Le Havre, France, 1991.
[14] M. Ech-Cherif El-Kettani, P. Pareige, F. Luppé, and J. Ripoche, ''Experimental study of the conversion of Lamb waves at the end of an immersed plate,'' Acust. Acta Acust. **82**, 251–259 (1996).
[15] M. Ech-Cherif El-Kettani, P. Pareige, and F. Luppé, ''Conversion de modes de Lamb à l'extrémité d'une plaque immergée,'' *3ème Congrès Français d'Acoustique*, J. de Phy. IV, Colloque No. 5, Suppl. JP III, No. 5, 1994, pp. 873–876.
[16] J. J. Ditri, ''Some results on the scattering of guided elastic SH waves from material and geometric waveguide discontinuities,'' J. Acoust. Soc. Am. **100**, 3078–3087 (1996).
[17] A. Tinel, H. Duflo, and J. Duclos, ''Onde de type Scholte sur une plaque fine. Interaction avec un défaut de surface,'' *4ème Congrès Français d'Acoustique*, Marseille, France, Congress Proceedings, 1997, pp. 889–892.
[18] J. E. Bondaryk and H. Schmidt, ''Array processing for the analysis of stiffened, fluid loaded, cylindrical shells,'' J. Acoust. Soc. Am. **97**, 1067–1077 (1995).
[19] I-Tai Lu, ''A hybrid ray-mode (wavefront-resonance) approach for ana-

lyzing acoustic radiation and scattering by submerged structures,'' J. Acoust. Soc. Am. **99**, 114–132 (1996).
[20] M. L. Rumerman, ''Contribution of membrane wave reradiation to scattering from finite cylindrical steel shells in water,'' J. Acoust. Soc. Am. **93**, 55–65 (1993).
[21] S. F. Morse, P. L. Marston, and G. Kaduchak, ''High-frequency backscattering enhancements by thick finite cylindrical shells in water at oblique incidence: Experiments, interpretation, and calculations,'' J. Acoust. Soc. Am. **103**, 785–794 (1998).
[22] A. Klauson, J. Metsaveer, D. Décultot, G. Maze, and J. Ripoche, ''Identification of the resonances of the cylindrical shell stiffened by an internal lengthwise rib,'' J. Acoust. Soc. Am. **100**, 3135–3143 (1996).
[23] A. Klauson, J. Metsaveer, D. Décultot, G. Maze, and J. Ripoche, ''Sound scattering by a fluid-loaded cylindrical shell with an internal axial stiffener,'' *Acoustic Interactions With Submerged Elastic Structures*, edited by A Guran, J. Ripoche, and F. Ziegler (World Scientific, Singapore, 1996), Pt. I, pp. 242–274.
[24] B. Dubus, A. Lavie, D. Décultot, and G. Maze, ''Elastic scattering by a thin cylindrical shell bounded by hemispherical endcaps at various incidence,'' J. Acoust. Soc. Am. **92**, 2473 (1992).
[25] J. Chiumia, E. H. Aassif, N. Touraine, D. Décultot, and G. Maze, ''Acoustic scattering from a cylindrical shell bounded by two hemispherical endcaps: Case of axial incidence,'' *4ème Congrès Français d'Acoustique*, Marseille, France, Conference Proceedings, 1997, pp. 14–18.
[26] P. Pareige, P. Rembert, J. L. Izbicki, G. Maze, and J. Ripoche, ''Méthode impulsionnelle numérisée (MIN) pour l'Isolement et l'Identification des Résonances de tubes immergés,'' Phys. Lett. A **135**, 143–146 (1989).
[27] C. W. Horton, Sr. and M. V. Mechler, ''Circumferential Waves in a Thin-Walled Air-Filled Cylinder in a Water Medium,'' J. Acoust. Soc. Am. **51**, 295–303 (1972).
[28] G. Maze and J. Ripoche, ''Méthode d'Isolement et d'Identification des Résonances (M.I.I.R.) de cylindres et de tubes soumis à une onde acoustique plane dans l'eau,'' Rev. Phys. Appl. **18**, 319–326 (1983).
[29] G. Maze, ''Acoustic scattering from submerged cylinders. MIIR Im/Re: Experimental and theoretical study,'' J. Acoust. Soc. Am. **89**, 2559–2566 (1991).
[30] H. Überall, ''Surface waves in acoustics,'' in *Physical Acoustics*, edited by W. P. Mason and R. N. Thurston (Academic, New York, 1973), Vol. 10, pp. 1–60.
[31] J. Chiumia, D. Décultot, G. Maze, A. Klauson, and J. Metsaveer, ''Analysis of echoes on the time domain backscattered signal from cylindrical shells with axial inhomogeneity,'' *4th International Congress on Sound and Vibration*, St. Petersburg, Russia, Conference Proceedings, 1996, pp. 139–146.
[32] M. Talmant, J.-L. Izbicki, G. Maze, G. Quentin, and J. Ripoche, ''External wave resonances on thin cylindrical shells,'' J. Acoust. **4**, 509–523 (1991).
[33] G. Maze, F. Léon, J. Ripoche, A. Klauson, and J. Metsaveer, ''Nature de l'onde d'interface de Scholte sur une coque cylindrique,'' Acustica **81**, 201–213 (1995).
[34] B. Clotteau, J-M. Conoir, J. L. Rousselot, and A. Derem, ''Ondes de Franz et onde de Stoneley généralisées pour un cylindre élastique immergé,'' J. Acoust. **3**, 213–242 (1990).
[35] J. L. Izbicki, J. L. Rousselot, A. Gérard, G. Maze, and J. Ripoche, ''Analysis of resonances related to Scholte-Stoneley waves around circular cylindrical shells,'' J. Acoust. Soc. Am. **90**, 2602–2608 (1991).
[36] P. L. Marston and N. H. Sun, ''Backscattering near the coincidence frequency of a thin cylindrical shell: Surface wave properties from elasticity theory and an approximate ray synthesis,'' J. Acoust. Soc. Am. **97**, 777–783 (1995).
[37] L. G. Zhang, N. H. Sun, and P. L. Marston, ''Midfrequency enhancement of the backscattering of tone bursts by thin spherical shells,'' J. Acoust. Soc. Am. **91**, 1862–1874 (1992).
[38] P. Pareige, G. Maze, J. L. Izbicki, J. Ripoche, and J. L. Rousselot, ''Internal acoustic excitation of shells: Scholte and whispering gallery-type waves,'' J. Appl. Phys. **65**, 2636–2644 (1989).

Stick–slip oscillations: Dynamics of friction and surface roughness

M. T. Bengisu
General Motors Corporation, GM Technical Center, Warren, Michigan 48090

Adnan Akay
Mechanical Engineering Department, Carnegie Mellon University, Pittsburgh, Pennsylvania 15213

(Received 11 May 1997; accepted for publication 2 October 1998)

While its classical model is relatively simple, friction actually depends on both the interface properties of interacting surfaces and on the dynamics of the system containing them. At a microscopic level, the true contact area changes as the surfaces move relative to each other. Thus at a macroscopic level, total friction and normal forces are time-dependent phenomena. This paper introduces a more detailed friction model, one that explicitly considers deformation of and adhesion between surface asperities. Using probabilistic surface models for two nominally flat surfaces, the stick–slip model sums adhesive and deformative forces over all asperities. Two features distinguish this approach from more traditional analyses: (i) Roughness distributions of the two interacting surfaces are considered to be independent, (ii) Intersurface contacts occur at both asperity peaks, as in previous models, and on their slopes. Slope contacts, in particular, are important because these oblique interactions produce motion normal to the plane of sliding. Building the model begins by analyzing local friction forces as composites of resistance to elastic deformation and shear resistance arising from adhesion between asperity surfaces. By extending the expressions obtained for normal and tangential friction forces over the macroscopic surfaces, the model then describes the stick–slip behavior frequently observed in dynamic systems and permits simulating a rigid body on a moving platform. Numerical results for several surface and system parameters illustrate both time-dependent and time-averaged frictional forces. These analyses also show that, although total averaged friction remains constant with respect to sliding velocity for the cases considered, the relatively small deformation component exhibits resonancelike behavior at certain speeds. Stick–slip occurs only within a narrow range around these critical speeds of a system. External damping can prevent stick–slip motion, and both deformative and adhesive frictional forces must be present for it to occur at all. [S0001-4966(99)03701-7]

PACS numbers: 43.40.Ga, 43.40.Dx [CBB]

INTRODUCTION

In modeling friction-induced vibration and noise problems, friction force is often treated phenomenologically, as a function of relative velocity between surfaces. These functional relationships mostly originate from measured values of coefficient of friction on test devices. Friction values obtained from such measurements are normally averaged over time and surface areas on which they are measured.

Traditionally, functional relationships between friction force and velocity are confined only to the direction of sliding, neglecting any contribution of normal components of contact forces during sliding. In reality, sliding between, even nominally flat, surfaces also develops a time-dependent normal force component and, therefore, a response in a direction normal to sliding. The forces developed in the normal direction, combined with the continuous change of true contact area during sliding, make friction force to depend also on system dynamics. Such interaction between friction and the response of the system within which it exists can not be modeled through the traditional use of coefficient of friction.

Friction and normal forces develop at the true contact areas between surfaces. Between two nominally flat surfaces, true contact takes place among the asperities. Each asperity adheres and deforms as it slides over another. The direction and magnitude of the deformation and adhesion forces at each contact change during sliding. Thus the topography of the surfaces and the dynamic response of the system together determine the distribution of the contact positions and direction of the forces at each contact. Modeling of friction within a dynamic system thus involves solving coupled equations that describe the system dynamic response and the distribution of contact forces during sliding. Such a combination relates microscopic-scale contact processes to the macroscopic-scale system response.

Many physical and chemical processes contribute to friction. They take place primarily at or near the true contact areas on the sliding surfaces. The vector sum of resistive forces at the contact areas constitutes the friction force. Although a detailed description of all the processes that contribute to friction is beyond the scope of this paper and the current state of the art, it is possible to describe some components of friction and relate them to dynamic behavior of the system in which they exist. We present a model that includes two such dynamic processes that contribute to friction: elastic deformation of asperities and adhesion between them.

Many of the previous models of contact between nomi-

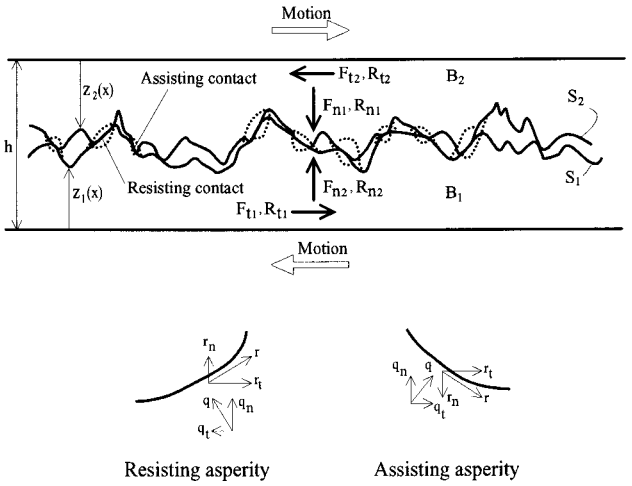

FIG. 1. Cross section of two rough surfaces in contact. F and R represent sums of the local deformation and adhesion forces, respectively. Subscripts n,t denote normal and tangential components. Local contact forces f and r are decomposed with respect to local coordinates.

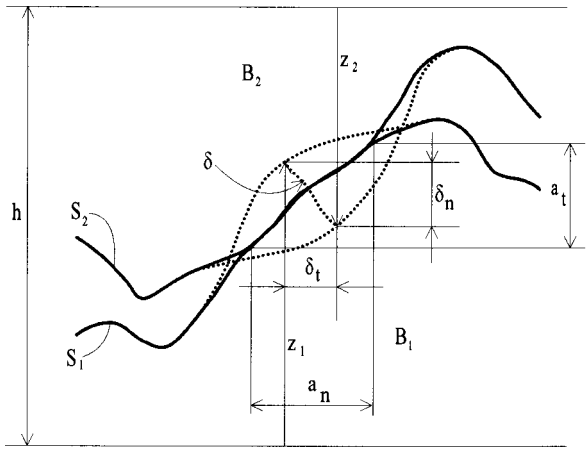

FIG. 2. Cross section of a typical asperity contact with projections of deformation and contact areas. Solid lines represent deformed surfaces and dotted lines represent undeformed surfaces.

nally flat surfaces utilize the assumption that contact between two rough surfaces can be described by contact between a rough surface and a smooth one.[1–6] This assumption dictates that contacts may occur only at surface peaks with contact areas parallel to the mean plane of the surface. In reality, however, contacts between rough surfaces also occur obliquely. In particular, for surfaces with uncorrelated surface asperity distributions, the probability for contacts to occur at asperity peaks is very small.

Oblique contacts couple sliding motion to normal motion. The slope at an oblique contact partitions the contact forces to their components in the direction of sliding and normal to it. As the contact position between two asperities moves, its slope also changes, altering the direction of the contact forces and their projections onto friction and normal forces. Thus as a result of oblique contacts between asperities, sliding motion between two surfaces can also generate oscillations in the normal direction.

The kinematic relationship between friction, $\mathscr{F}_t$, and normal, $\mathscr{F}_n$, forces and the contact area projections resulting from oblique contacts was previously developed by the authors for generalized contact forces in two dimensions,[7]

$$\mathscr{F}_t(t)=F_t+R_t=\frac{A_t}{A_n}\mathscr{F}_n+\left(1+\frac{A_t^2}{A_n^2}\right)R_t, \tag{1}$$

$$\mathscr{F}_n(t)=F_n+R_n. \tag{2}$$

Sums of the tangential components of all local deformation forces, F_t, and adhesion forces, R_t, over the interface constitute the total friction force. Similarly, the corresponding normal components, F_n and R_n, make up the normal contact force at the interface. The sign convention regarding their directions is shown in Fig. 1.

The model in this paper, based on Eq. (1), relates the time-dependent contact area projections, $A_n(t)$, $A_t(t)$, to the motion of the dynamic system through a set of differential equations (Sec. I). The model also expresses contact forces in Eq. (1), F due to deformation and R due to adhesion, in terms of contact area projections (Sec. II). Simultaneous solution of differential equations for the contact areas and for the motion of the bodies then yield both friction $\mathscr{F}_t$ and normal $\mathscr{F}_n$ forces as well as the response of the system to friction (Sec. III).

I. DYNAMICS OF CONTACT AREAS

True contact areas change as a result of both relative motion of surfaces and deformation of asperities during this motion. For example, time-rate of deformation, $\dot{\delta}$, of material point and area, a, at each contact depend on the relative motion of two surfaces through a kinematic relationship,[7]

$$\begin{aligned} &-\dot{h}a_n^i+\dot{s}a_t^i=\dot{\delta}_t^i a_t^i+\dot{\delta}_n^i a_n^i, \quad i=1,...,k,\\ &-\dot{h}a_n^j-\dot{s}a_t^j=\dot{\delta}_t^j a_t^j+\dot{\delta}_n^j a_n^j, \quad j=1,...,l, \end{aligned} \tag{3}$$

where indices i and j indicate resisting and assisting contacts, respectively, and subscripts t and n refer to components in tangential and normal directions to the mean plane. (The forces that result from elastic deformation of asperities either assist or resist the relative tangential motion, depending on the slope of the contact area relative to the direction of motion. *Resisting contacts* have a tangential component that opposes relative motion. *Assisting contacts* possess tangential components in the same direction as the relative motion.[7]) The relative velocity of the surfaces has components $\dot{h}$ in normal direction and $\dot{s}$ in tangential direction, as indicated in Fig. 2. *Normal contact* and *tangential contact areas*, a_n and a_t, refer to local contact area projections that are parallel and perpendicular to the mean planes of the surfaces, respectively, as illustrated in Fig. 1.

The total numbers of resisting and assisting contacts, k and l, in Eqs. (3), can be approximated using the results of the Greenwood and Williamson (1967) model for random surfaces,

$$k=\gamma A_n^r, \quad l=\gamma A_n^a, \tag{4}$$

where γ is a constant and superscripts (r,a) denote resisting and assisting asperities.

Deformation velocities $\dot{\delta}_n$ and $\dot{\delta}_t$ in Eq. (3) can also be expressed in terms of contact areas through contact deforma-

tion models. In elastic contact problems involving rough surfaces, Hertz contact theory is used commonly with the assumption that asperities are spherical and contact is elastic;[9] the contact area, a, between two spherical objects of radius ρ_1 and ρ_2, is expressed as

$$a=\pi\rho\delta, \tag{5}$$

where $1/\rho=1/\rho_1+1/\rho_2$ and δ is the maximum value of deformation.

Differentiating Eq. (5) with respect to time and substituting its normal and tangential components into Eqs. (3) yields a direct relationship between local contact areas and relative velocities. Summing the resulting equations over the total numbers (k and l) of resisting and assisting local contact areas, respectively, leads to expressions describing the dynamic relationship between the total contact areas and the normal and sliding velocities,

$$\begin{aligned} -\dot{h}A_n^r+\dot{s}A_t^r &\cong \frac{1}{k\pi\rho}\,(A_t^r\dot{A}_t^r+A_n^r\dot{A}_n^r),\\ -\dot{h}A_n^a-\dot{s}A_t^a &\cong \frac{1}{l\pi\rho}\,(A_t^a\dot{A}_t^a+A_n^a\dot{A}_n^a), \end{aligned} \tag{6}$$

where A is the total contact area summed over all asperities on one of the surfaces S_1. (The combined radius ρ now represents the combination of the average asperity radii on surface S_1: $\rho_1=[1/(k+l)]\Sigma_{i=1}^{k+l}\rho_1^i$.)

Further simplification of Eq. (6) may be made by expressing A_t in terms of A_n through space-averaged (but time-dependent) slope of contact areas. Such a relationship between the sums of the normal and tangential projections of contact areas may be obtained by approximating deformation velocity $\dot{\delta}$ at each contact by a uniform velocity distribution. This approximation, also used in the development of Eq. (3), implies that the local contact areas are plane surfaces and the contact slope $Z'_\iota=\partial Z/\partial\chi_1^\iota$ $(\iota=i,j)$ is constant throughout a given (local) contact surface. With these assumptions the tangential components of the contact areas can be expressed in terms of the normal components,

$$a_t^i=Z'_i a_n^i, \quad a_t^j=-Z'_j a_n^j, \tag{7}$$

where the slopes of contact areas are with respect to the direction of motion.

Summing expressions in Eq. (7) over the interface gives the following relationships between summations of tangential and normal contact areas:

$$\begin{aligned} A_t^r=\sum_{i=1}^{k} a_t^i &\cong \left(\frac{1}{k}\sum_{i=1}^{k} Z'_{1i}\right)\left(\sum_{i=1}^{k} a_n^i\right)=\langle Z'_+\rangle A_n^r,\\ A_t^a=\sum_{j=1}^{l} a_t^j &\cong -\left(\frac{1}{l}\sum_{j=1}^{l} Z'_{1j}\right)\left(\sum_{j=1}^{l} a_n^j\right)=-\langle Z'_-\rangle A_n^a. \end{aligned} \tag{8}$$

The average resisting and assisting contact slopes, $\langle Z'_+\rangle$ and $\langle Z'_-\rangle$, in Eqs. (8) are the expected values of the positive and negative contact slopes and they can be calculated for given probability densities of the asperity slopes.

Finally, substituting the approximate relationships given by Eqs. (4) into Eqs. (6) yields two ordinary differential equations for the total resisting and assisting normal contact areas in terms of relative velocities between the surfaces,

$$\begin{aligned} \alpha(\langle Z'\rangle^2+1)\dot{A}_n^r &= -(\alpha\langle Z'\rangle\langle\dot{Z}'\rangle+\dot{h}-\langle Z'\rangle\dot{s})A_n^r,\\ \alpha(\langle Z'\rangle^2+1)\dot{A}_n^a &= -(\alpha\langle Z'\rangle\langle\dot{Z}'\rangle+\dot{h}+\langle Z'\rangle\dot{s})A_n^a, \end{aligned} \tag{9}$$

where $\alpha=1/\gamma\pi\rho$ and $\langle Z'\rangle=\langle Z'_+\rangle=-\langle Z'_-\rangle$ for a random distribution of surface roughness.

The solutions of Eq. (9) for resisting and assisting contacts are combined to give the projections of total contact area required for the friction force in Eq. (1),[7]

$$A_n=A_n^r+A_n^a=\sum_{i=1}^{k} a_n^i+\sum_{j=1}^{l} a_n^j. \tag{10}$$

The tangential component of the total contact area, A_t, on the other hand, is defined as the difference between resisting and assisting contacts. (Considering only the resisting contacts overestimates the friction force because the presence of assisting contacts offsets some of the resistance.)

$$A_t^r-A_t^a=\sum_{i=1}^{k} a_t^i-\sum_{j=1}^{l} a_t^j. \tag{11}$$

Equations (8) and (11) lead to an expression that relates the tangential component A_t to the normal component obtained from Eqs. (9),

$$A_t=\langle Z'\rangle(A_n^r-A_n^a). \tag{12}$$

Although the expression in this section are derived for surface S_1, similar ones can be written for S_2.

In addition to A_t from Eq. (12) and A_n from the solution of Eqs. (9), calculation of friction force in Eq. (1) requires expressions for the contact force components F_n, R_n, and R_t. In the next section expressions are developed for deformation and adhesion forces at each contact and related to the sum of true contact areas A.

II. CONTACT AND FRICTION FORCES

Because of the cause-and-effect relationship between elastic deformation forces and contact areas, deformation force at each asperity contact can be expressed in terms of the resulting contact area. Similarly, because adhesion forces depend independently on both the normal pressure, or the deformation force, and the contact area, they also can be expressed in terms of contact areas.

A. Deformation forces

In cases such as metals, where the local tangential adhesive force r is typically smaller than the normal force f by an order of magnitude or more,[8] its contribution to elastic deformation of an asperity may be neglected to simplify the calculations. Thus only the local normal contact forces, f, cause elastic deformation and they are obtained using Hertz contact theory with the assumption that asperity tips are spherical.[1,3,9]

The physics of the contact problem treated here also requires consideration of energy dissipation from the contact area during deformation. Because use of complex elasticity modulus in nonlinear transient problems leads to physically

unrealizable results,[10] energy dissipation during elastic deformation is modeled here as proportional to the deformation rate of an asperity. Such a consideration is equivalent to the loss of deformation energy by means of propagation of elastic waves into the bulk of the contacting bodies, i.e., radiation loss away from contact areas. Hence, the sum of the Hertz contact force and a dissipation force that depends on the rate of deformation constitutes the elastic deformation force

$$\mathrm{f}=\mathscr{K}a^{3/2}+\eta\dot{\epsilon}. \tag{13}$$

The constant $\mathscr{K}$ is defined as

$$\mathscr{K}=\frac{4E}{3\rho\pi^{3/2}},$$

where η is the loss factor of the material and ρ is composite asperity radius as defined before. E is the composite modulus of elasticity related to the moduli of the two materials and their Poisson's ratios ν_1 and ν_2,

$$\frac{1}{E}=\frac{1-\nu_1^2}{E_1}+\frac{1-\nu_2^2}{E_2}. \tag{14}$$

Recalling that the contact surfaces are assumed to be planar, such that $a^2=a_t^2+a_n^2$ and $a_t/a_n=Z'$, the rate of deformation of a material at a contact surface can be expressed as

$$\dot{\epsilon}=\frac{1}{2\pi\rho}\frac{d}{dt}\,(a_t^2+a_n^2)=\frac{1}{\pi\rho}\,\dot{a}a_n(1+Z'^2)^{1/2} \tag{15}$$

and

$$a^{3/2}=a a_n^{1/2}(1+Z'^2)^{1/4}. \tag{16}$$

After substituting Eqs. (15) and (16) into Eq. (13), the sum of the normal components of the deformation contact forces at the interface can be expressed as

$$F_n=\frac{\mathscr{K}}{\gamma^{1/2}}\,A_n\left(1+\frac{1}{4}\,\langle Z'^2\rangle+\cdots\right)+\frac{\eta}{\pi\rho}\,\dot{A}_n\left(1+\frac{1}{2}\,\langle Z'^2\rangle+\cdots\right), \tag{17}$$

where

$$\langle Z'^2\rangle=\frac{1}{k}\sum_i^k Z_i'^2=\frac{1}{l}\sum_j^l Z_j'^2$$

is the mean-square value of either the positive or the negative contact slopes. For asperity profiles such that $a_t/a_n<1(Z'^2\ll 1)$, the series of even moments in Eq. (17) can be truncated after the first term.

B. Adhesive contact forces

The local adhesive forces are considered here to be similar to the rheological shear resistance of the third phase that forms between the contact surfaces of two materials. Following Kragelsky *et al.*,[8] the local adhesive contact force, r, is expressed with a binomial expression, as a combination of two shear terms

$$\mathrm{r}=\tau a+\beta\mathrm{f}, \tag{18}$$

where the constants τ and β are determined empirically. (The signs of τ and β depend on the relative velocity at the interface and are negative for positive relative velocity.) The adhesion force r in Eq. (18) is in the tangential direction to the local contact surface. Its first part is independent of normal contact force, whereas the second part is proportional to the contact pressure and contact area: $\mathrm{f}=\int q\,da$.

By separating Eq. (18) into its normal and tangential components with respect to the mean planes and summing over all resisting and assisting contact areas, the normal and tangential components of the total adhesive contact force can be expressed in terms of sums of contact area projections,

$$R_n=-\tau A_t-\beta F_t, \quad R_t=\tau A_n+\beta F_n. \tag{19}$$

R_n and R_t are uncoupled because of the orthogonality of the local elastic deformation and adhesion forces. In cases where, for example, the influence of adhesive forces on elastic deformation is not negligible, R_n and R_t will be coupled. The negative signs in the first of Eqs. (19) are a consequence of the convention of directions shown in Fig. 1.

C. Friction and normal force

Friction force, defined here as the force that resists sliding motion, is obtained by summing the tangential forces at the interface. Similarly, the normal force is the sum of all the forces in a direction normal to the interface. Expressions for friction force and normal force are obtained by substituting Eqs. (19) into Eqs. (1) and (2). The results explicitly show the relationships of the friction and normal forces to deformation and adhesive forces and to the normal and tangential projections of the contact areas,

$$\begin{aligned}\mathscr{F}_t(t)&=\left(\frac{A_t}{A_n}+\beta\right)F_n+\tau A_n,\\ \mathscr{F}_n(t)&=\left(1-\beta\,\frac{A_t}{A_n}\right)F_n-\tau A_t,\end{aligned} \tag{20}$$

where, F_n, sum of the normal components of deformation forces, is given by Eq. (17). Thus Eqs. (20), together with Eq. (17), define the friction force, and the resulting normal force, in terms of contact areas and even-movements of the contact slope distribution.

F_n, A_n, and A_t are based on statistical distributions of the slopes of asperities as described, earlier; τ and β are experimentally determined constants. Both $\mathscr{F}_t(t)$ and $\mathscr{F}_n(t)$ are time dependent because of the changes in F_n, A_n, and A_t due to relative motion. Thus true friction force is obtained in conjunction with the dynamic response of the system within which it exists, as shown in the next section.

III. FRICTION FORCE AND SYSTEM RESPONSE

An example of the interaction of friction force with system dynamics is demonstrated with a simple, idealized dynamic system: a rigid block (with deformable surface asperities) connected to a linear spring and a viscous damping element, is subject to frictional force at its interface with a flat platform that moves at a constant speed, as depicted in Fig. 3. The rigid block is free to move both in normal and

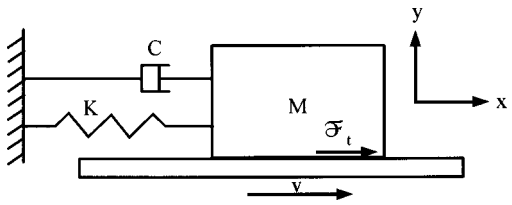

FIG. 3. Block on a moving platform. Block is free to move in x and y directions.

tangential directions with respect to the platform but without rotation. Both the block and the platform are assumed to have nominally flat surfaces, each with a random asperity height distribution statistically independent of the other.

The equations of motion of the dynamic system are written in terms of the coordinates x and y which also describe its displacements in tangential and normal directions with respect to the moving platform,

$$M\ddot{x}+C\dot{x}+Kx=-\mathcal{F}_t,$$
$$M\ddot{y}=-Mg+\mathcal{F}_n. \tag{21}$$

Parameters M, C, and K describe the mass, viscous damping, and the stiffness, respectively. The differential Eqs. (9) for the contact areas are rewritten by substituting for $\dot{h}=\dot{y}$ and $\dot{s}=\dot{x}-v$, where, v is the speed of the platform,

$$\alpha(\langle Z'\rangle^2+1)\dot{A}_n^r=-\{\alpha\langle Z'\rangle\langle\dot{Z}'\rangle+\dot{y}-\langle Z'\rangle(\dot{x}-v)\}A_n^r,$$
$$\alpha(\langle Z'\rangle^2+1)\dot{A}_n^a=-\{\alpha\langle Z'\rangle\langle\dot{Z}'\rangle+\dot{y}+\langle Z'\rangle(\dot{x}-v)\}A_n^a. \tag{22}$$

Numerical solutions of Eqs. (21) and (22) are obtained using expressions for friction and normal forces in Eq. (20) and for the contact areas in Eqs. (10) and (12). The mean value of the contact slopes, $\langle Z'\rangle$, and its relation to separation, h, between the surfaces are obtained from the description of surface roughnesses for the rigid body and the platform as shown in the next section.

A. Surface model

Calculating contact areas in Eq. (22), and normal contact force F_n in Eq. (17), requires mean value of contact slopes and their even moments for each surface. Randomly varying, uncorrelated continuous functions Z_1' and Z_2', each with a Gaussian distribution, represent the slopes of asperities on each surface as a function of their separation, h. Because the subset of slopes at the contact areas is also Gaussian, the mean value of the positive contact slopes can be found using Z_1' and Z_2'. Then, for slopes ranging between zero and some maximum contact slope, $Z'_{\max}$,

$$\langle Z'\rangle=\frac{1}{\sigma\sqrt{2\pi}}\int_0^{Z'_{\max}}Z'e^{-Z'^2/2\sigma^2}\,dZ', \tag{23}$$

where σ is the standard deviation. The even moments of the slopes are

$$\langle Z'^m\rangle=\frac{1}{\sigma\sqrt{2\pi}}\int_0^{Z'_{\max}}Z'^m e^{-Z'^2/2\sigma^2}\,dZ' \quad m=2,4,..., \tag{24}$$

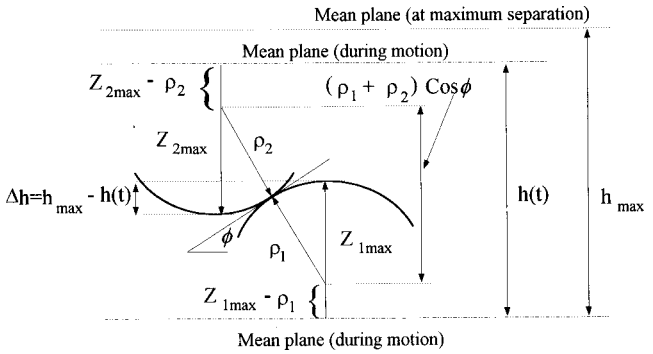

FIG. 4. Schematic representation of the highest asperities in contact and the relationship of the maximum contact slope to separation.

where the value of the upper limit $Z'_{\max}$ changes with interference between the surfaces. These expressions are the same for both surfaces, but with different values of $Z'_{\max}$ for each. The integral in Eq. (23) can be evaluated in closed form to give

$$\langle Z'\rangle=\frac{\sigma}{\sqrt{2\pi}}(1-e^{-Z'^2_{\max}/2\sigma^2}). \tag{25}$$

The second and higher moments about origin have negligible effects on the normal force.

The mean value of contact slopes, $\langle Z'\rangle$, relates to separation h through the maximum contact slope $Z'_{\max}$ in expression (25) which varies with separation during sliding. When separation is large, contacts occur closer to asperity tips. At the maximum value of separation, contact area is parallel to the mean plane. For smaller values of separation, contacts are oblique and contact slopes are larger. Accordingly, the mean value of the contact slopes is also a function of separation between the surfaces.

In cases where the relationship between the maximum contact slope and separation can be expressed explicitly, e.g., for spherically shaped asperities, it is possible to evaluate $\langle Z'\rangle$ in Eq. (25). For spherical asperities, the maximum contact slope occurs on the tallest asperities of the surfaces. The asperities located farthest from the mean planes on each surface define the maximum value of the separation, $h_{\max}$ (or the minimum value of geometric approach) between the two surfaces. With these considerations, a relationship can be defined for separation h in terms of average asperity size on each surface. Using the geometric relationship for such a contact condition as illustrated in Fig. 4, separation between surfaces is expressed as

$$h=Z_{1\,\max}-\rho_1+(\rho_1+\rho_2)\cos\,\phi+Z_{2\,\max}-\rho_2, \tag{26}$$

where ρ_1 and ρ_2 represent the average asperity radii for surfaces S_1 and S_2, respectively, $Z_{1\,\max}$ and $Z_{2\,\max}$ are the maximum values of the functions describing the surface profiles, and ϕ is the contact slope as defined in Fig. 4. At the maximum value of h, by definition, the corresponding maximum contact slope is zero, $\phi=0$.

Substituting $\cos\phi\cong1-\phi^2/2$ in Eq. (26) yields $\phi^2=\Delta h/\varrho$, where the value of $\varrho=(\rho_1+\rho_2)/2$ is the average of the mean asperity radius for each surface. The difference between the maximum and instantaneous values of separation is

TABLE I. Numerical values of the parameters used in calculations. The tangential damping value of $C=2$ kg/s is used during dynamic simulations, whereas $C=200$ kg/s is used for averages. The friction pair chosen for all cases is a steel–copper pair having a composite elasticity modulus of 77 800 MPa.

Case	σ (rad)	$(1/2\pi)\sqrt{K/M}$ (Hz)	τ (MPa)	β
1	0.3	10	0	0
2	0.2	10	0	0
3	0.1	10	0	0
4	0.1	31.6	0	0
5	0.1	100	0	0
6	0.1	10	9.8	0.075
7	0.1	31.9	9.8	0.075
8	0.1	100	9.8	0.075

M (kg)	C (kg/s)	R (mm)	η (kg/m^2 s)
10	2–200	0.06	200

$$\Delta h(t)=Z_{1\,\max}+Z_{2\,\max}-h=h_{\max}-h(t).$$

For small values of ϕ, $\phi\cong\tan\phi=Z'_{\max}$. Thus the maximum contact slope can be expressed in terms of separation,

$$Z'_{\max}\cong\sqrt{\frac{\Delta h}{\varrho}}. \tag{27}$$

By replacing $Z'_{\max}$ in Eq. (25) with Eq. (27), the expected value $\langle Z'\rangle$ of contact slopes can be expressed in terms of separation of the surfaces.

The model is now complete and can be solved numerically to investigate the interaction of friction and the dynamic response of the system that contains it.

B. Computations

Dynamic response of the system and the friction force that excites it mutually depend on each other through contact area changes as shown in Eqs. (21) and (22). In the following sections, equations describing the system response and the corresponding friction and normal forces are solved for the cases listed in Table I. The values given in Table I are for steel–copper pairs for which empirical values of the parameters τ and β are available.[8] Surface properties used in the examples reported below come from published surface data;[1] asperity tip radii have a Gaussian distribution with a mean radius of 60 μm and the maximum asperity heights reach 3–4 μm, typical for ground mild steel.[1] Maximum value of average slope is determined by setting $Z'_{\max}$ in Eq. (27) to 3σ.

By numerically integrating the expressions in (21) and (22), first, the time-averaged friction force is examined as a function of platform speed. Then, the time-dependent friction force is analyzed along with the corresponding response of the dynamic system. In both cases, friction force is normalized with respect to normal contact force.

Because of the asymptotic nature of $\langle Z'\rangle$ in Eq. (25), to circumvent computational difficulties, in all the computations reported here contact slope is taken to be zero when relative approach reduces to less than 0.001 μm.

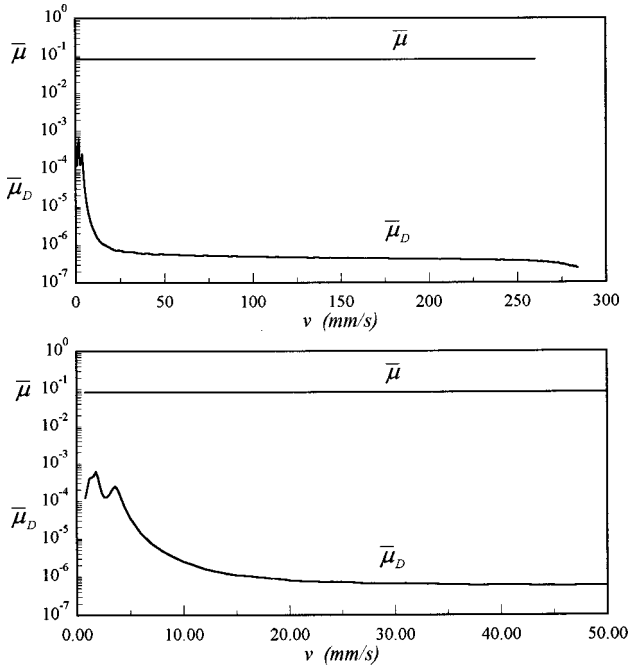

FIG. 5. Change of $\bar{\mu}$ and $\bar{\mu}_D$ with platform velocity.

C. Averaged normalized friction force

Time averaging the ratio of the instantaneous values of friction and normal forces gives $\bar{\mu}$, the time-averaged normalized friction force,

$$\bar{\mu}=\lim_{T\to\infty}\frac{1}{T}\int_0^T\frac{\mathscr{F}_t}{\mathscr{F}_n}\,dt.$$

Because adhesion depends on the deformation force, $\bar{\mu}$ is a complex combination of the similarly time-averaged normalized deformation ($\bar{\mu}_D$) and adhesion ($\bar{\mu}_A$) components. $\bar{\mu}$ reduces to $\bar{\mu}_D$ when constants τ and β are zero. (Use of the term coefficient of friction is avoided because of its diverse connotations and different definitions in the literature.)

An examination of the averaged normalized friction force, $\bar{\mu}$, in Fig. 5 shows that, for cases 3 and 6 in Table I, a negligibly small part of $\bar{\mu}$ results from elastic deformation, leaving adhesion as the dominant source of friction. This is not an unexpected result since the effects of resisting and assisting contacts largely offset each other.

Numerical results show that $\bar{\mu}$ with respect to platform speed is nearly constant, whereas $\bar{\mu}_D$ shows significant variation as a function of platform speed. In particular, at some platform speeds, the deformation component $\bar{\mu}_D$ shows resonancelike peaks. The platform speeds, at which resonancelike peaks occur, increase with tangential natural frequency, f_0, of the dynamic system. This dependence is illustrated in Fig. 6 with plots of $\bar{\mu}_D$ corresponding to $f_0=10$, 3.16, and 100 Hz of the system (cases 3, 4, and 5 in Table I); the speeds corresponding to the peak values of $\bar{\mu}_D$ are tabulated in Table II.

Asperity slope distributions also influence the velocities at which the peak values of $\bar{\mu}_D$ occur. For example, for smoother surfaces which have higher standard deviations, as indicated by Eq. (25), peak values of $\bar{\mu}_D$ occur at higher

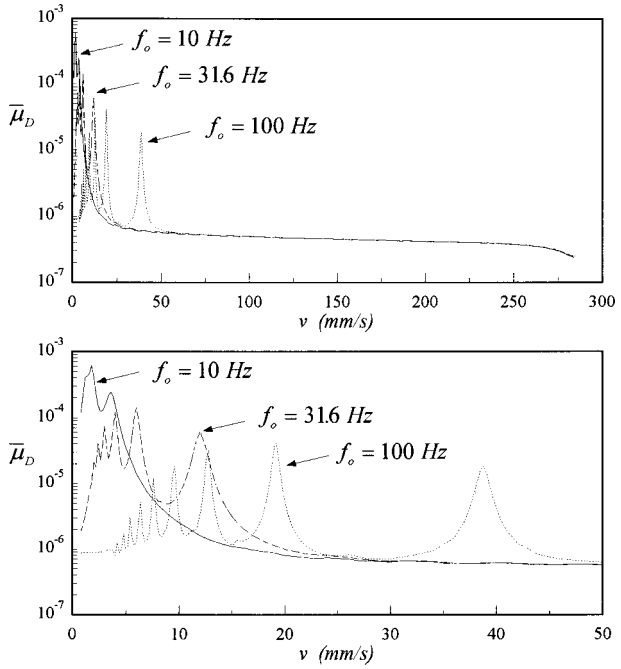

FIG. 6. Variation of $\overline{\mu}_D$ with platform velocity for various tangential natural frequencies of the dynamical system.

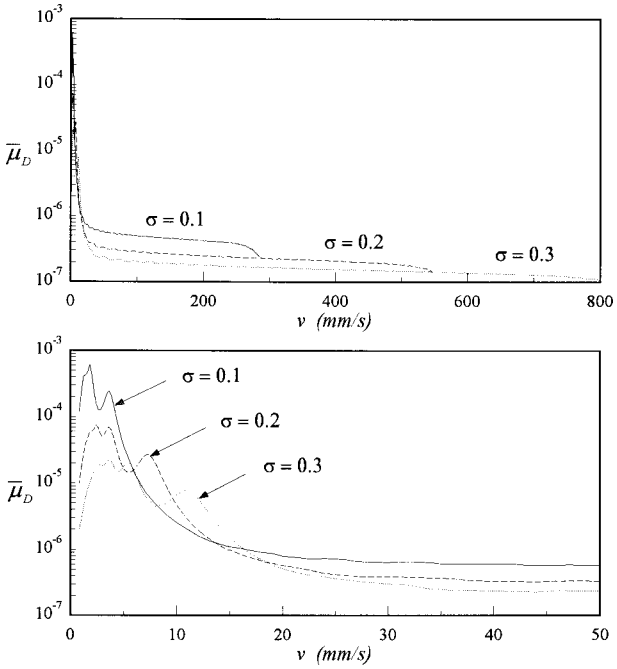

FIG. 7. Variation of $\overline{\mu}_D$ with platform velocity for different standard deviation of surface roughness.

platform velocities; Fig. 7. The parameters used in Fig. 7 and the results tabulated in Table III correspond to cases 1–3 in Table I.

The composite modulus of elasticity of the materials does not have a detectable influence on the variation of $\overline{\mu}_D$ or on the resonancelike peaks at lower platform speeds. However, it has some influence at higher platform speeds.

D. Instantaneous friction and stick–slip oscillations

Stick–slip oscillations of the system occur at platform speeds within a narrow band of the peak values of $\overline{\mu}_D$ shown in Fig. 6. Oscillations at platform speeds corresponding to different peaks have significantly different spectra. Oscillations at platform speeds outside of these bands are sustained, but without stick–slip.

Phase planes and spectra of the motion of the block and the corresponding instantaneous friction force, given in Figs. 8–14, help explain stick–slip oscillations and their relationship with the resonancelike peaks of $\overline{\mu}_D$. The instantaneous normalized friction force, plotted in Figs. 8–14, is defined as $\mu(t)=\mathcal{F}_t(t)/\mathcal{F}_n(t)$.

Figure 8 demonstrates an example (case 6; $\sigma=0.1$) for which the platform speed (2.7 mm/s) is away from the speed bands that lead to peaks. By comparison with the corresponding case given in Fig. 9, Fig. 8 shows a smaller amplitude of oscillations that are not repetitive (transient parts of the solutions are excluded in all the results). Also, the tangential velocity in its phase plane never reaches the velocity of the platform and, thus, does not achieve ''stick'' condition; the relative velocity is always larger than zero. In the same figure, friction force varies through many cycles of oscillations of the dynamic system and exhibits multiple values for a given relative tangential velocity. The spectrum corresponding to the response velocity of the block exhibits several harmonics and side bands, indicative of nonlinearities.

At platform speeds, 3.6, 1.8, and 1.2 mm/s, corresponding to the peak values of $\overline{\mu}_D$ shown in Fig. 6, response of the same system as in Fig. 8 (case 6; $\sigma=0.1$) exhibits higher amplitudes that are periodic. At these speeds both the friction force and response of the mass show that the oscillator reaches the platform speed, achieving the condition of ''stick;'' Figs. 9–11. In terms of phase-plane diagrams, system response shows a doubling and tripling of its period as the platform speed is decreased from 3.6 mm/s to the lower speeds 1.8 and 1.2 mm/s, respectively. The corresponding changes also manifest themselves in the spectrum for each case as additional harmonics and one-half subharmonic. In all cases, friction-relative velocity trajectory follows a differ-

TABLE II. Some platform speeds where averaged normalized deformation friction forces reach their peak values for the surface with $\sigma=0.1$.

f_0 (Hz)	v_1 (mm/s)	v_2 (mm/s)	v_3 (mm/s)	v_4 (mm/s)	v_5 (mm/s)	v_6 (mm/s)
10	3.6	1.8	1.2	⋯	⋯	⋯
31.6	12.0	6.0	4.0	3.0	2.4	2.0
100	38.75	19.15	12.8	9.6	7.6	6.4

TABLE III. Platform speeds where averaged normalized deformation forces reach their peak values for the dynamic system with 10 Hz tangential natural frequency.

σ	v_1 (mm/s)	v_2 (mm/s)	v_3 (mm/s)	v_4 (mm/s)
0.1	3.6	1.8	1.2	⋯
0.2	7.3	3.65	2.43	1.83
0.3	11.0	5.5	3.66	2.75

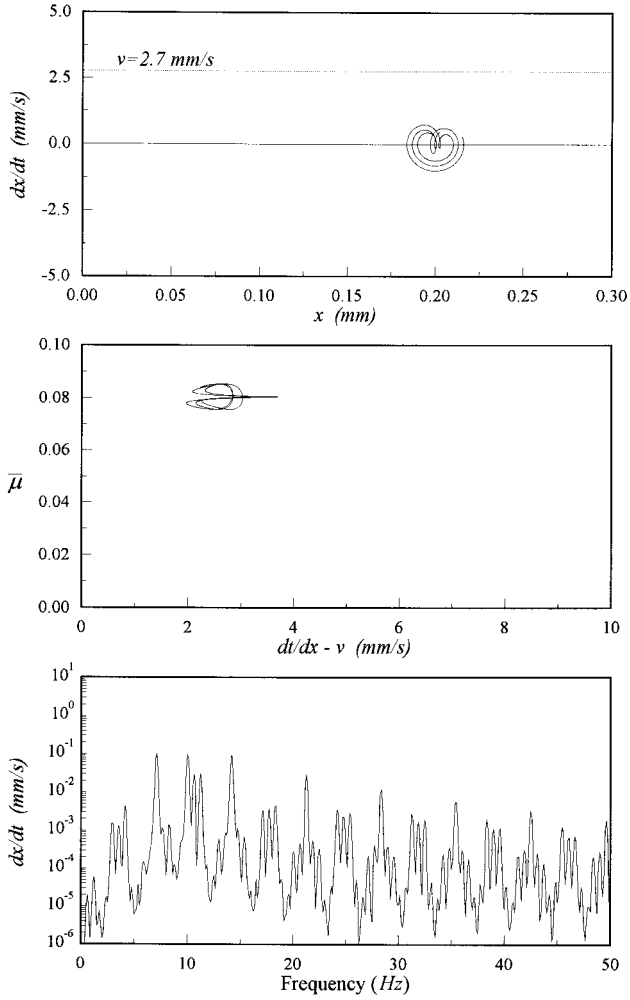

FIG. 8. Response of the dynamic system with a tangential natural frequency of $f_0 = 10$ Hz displays sustained oscillations at a platform speed of 2.7 mm/s.

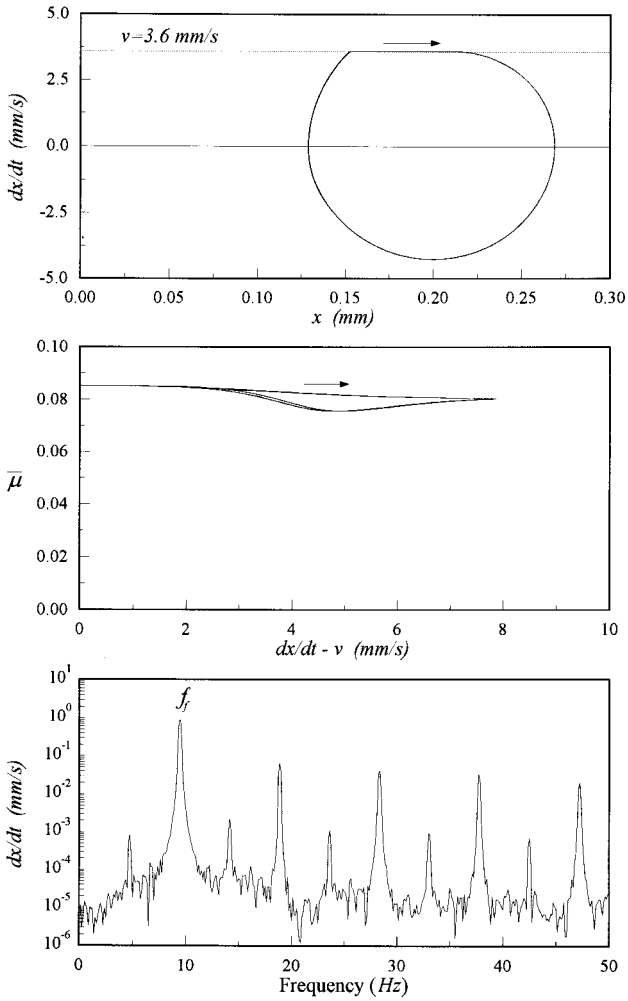

FIG. 9. Response of the dynamic system with a tangential natural frequency of $f_0 = 10$ Hz displays stick–slip oscillations at a platform speed of 3.6 mm/s.

ent path when it moves in the direction of the platform than against it.

A similar, but not easily observed, result relates to the total period of oscillation of the block as shown in the phase-plane plots (and the corresponding frequency spectra). For example, in Fig. 9 (top) the phase plane appears to have a single path where, in reality, it consists of two paths that are very close to each other. Evidence of this is seen in the middle figure where friction force follows two separate paths. This slight variation every other cycle is seen in the tangential velocity spectrum of the mass as a half-frequency subharmonic of the fundamental frequency corresponding to the single loop observed in the phase plot in Fig. 9.

The apparent self-intersection of the trajectories in the phase planes in Figs. 9 through 14 results from the projection of the multidimensional phase-space trajectory onto the tangential velocity-displacement plane of the block; the actual six-dimensional phase-space trajectory of the system does not self-intersect.

The stick–slip behavior of the dynamic system presented here is very much reminiscent of the response of a friction-excited system even when the friction force-velocity relationship is predefined.[11,12]

IV. STICK–SLIP OSCILLATIONS: DISCUSSION

A. Periodicity and nonlinearity

The assumption that the spatial distribution of contact slopes at a given time is a stationary random function implies that the average contact slope, $\langle Z' \rangle$, is independent of the tangential position of the mass with respect to the platform. On the other hand, the average contact slope, $\langle Z' \rangle$, depends on the the separation between the mean planes, as described in Eqs. (25) and (27). As a result, the average contact slope, $\langle Z' \rangle$, remains independent with respect to tangential position of the mass but changes periodically with its normal motion. Thus the influence of asperities on the motion of the system is nearly periodic, albeit nonlinear.

The periodic nature of the average contact slope $\langle Z' \rangle$ leads to nearly periodic solutions of the differential Eq. (9) for A_n^r and A_n^a. Hence, in accordance with Eqs. (10), (12), and (20), the resulting net normal and tangential forces are also nearly periodic, causing nearly periodic motion of the block both in normal and tangential directions. Both the normal and tangential components of the contact force exhibit the same fundamental frequency even though they may have different overall spectra.

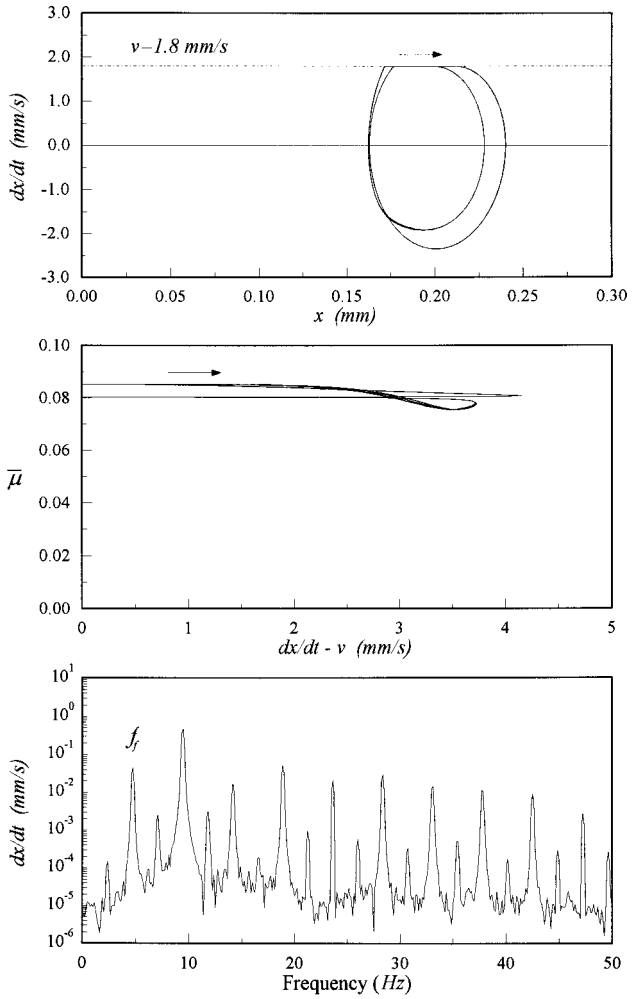

FIG. 10. Response of the dynamic system with a tangential natural frequency of $f_0=10$ Hz displays stick–slip oscillations at a platform speed of 1.8 mm/s.

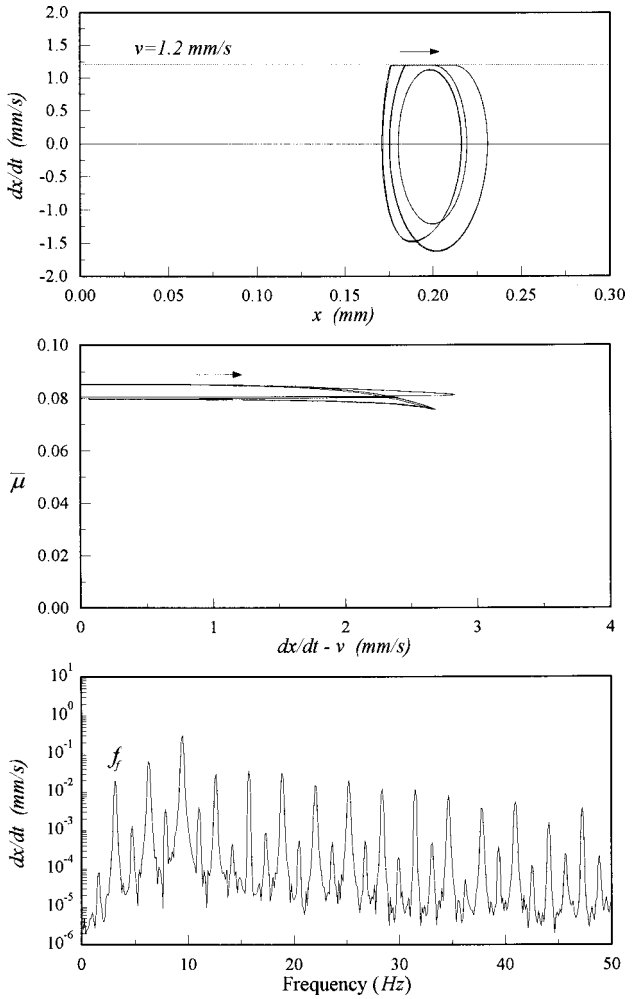

FIG. 11. Response of the dynamic system with a tangential natural frequency of $f_0=10$ Hz displays stick–slip oscillations at a platform speed of 1.2 mm/s.

In cases of nonstationary contact slope distributions, however, average contact slope changes from one cycle to the next as the block and the platform slide against each other.

B. Critical speeds and fundamental frequency

Stick–slip oscillations, and the corresponding peak values of $\overline{\mu_D}$, occur when the tangential natural frequency, f_0, of the system coincides with the fundamental frequency, f_f, of the friction force or one of its harmonics. The fundamental frequency of the friction force approximately relates to the platform speed as

$$f_f \cong (v/\lambda), \tag{28}$$

where λ is the wavelength corresponding to the relative tangential displacement of the block during a cycle of its combined normal and tangential oscillation. The platform speeds at which integer multiples of f_f equal f_0, i.e., $nf_f=f_0$, are referred to as the critical speeds, $v=v_{c_n}$.

The *fundamental critical speed*, v_{c_1}, is the highest platform speed at which stick–slip occurs and the fundamental frequency of the friction force equals the natural frequency $f_f=f_0$. At a lower critical speed, roughly described as v_{c_1}/n, the harmonic multiple of f_f becomes equal to the natural frequency; $nf_f=f_0$; Figs. 9–14.

The wavelength λ represents the average distance between resisting and assisting contacts. Its value can be obtained using the average slope of contacts, $\langle Z' \rangle$, and the normal displacement, or approach Δh, during the oscillations,

$$\lambda = 2\int_0^{\Delta h_{\max}} \frac{dh}{\langle Z' \rangle}, \tag{29}$$

where $\langle Z' \rangle$ is given by Eqs. (25) and (27) and $\Delta h_{\max}$ is the maximum relative approach during the motion of the block. Both $\Delta h_{\max}$ and $\langle Z' \rangle$ depend on surface roughness as well as system response through the solutions to differential equations Eqs. (21) and (22).

Values of λ, plotted in Fig. 15 as a function of maximum relative approach, can be used to predict v_{c_n}. For example, for $\sigma=0.1$, a relative approach of 0.3 μm (the maximum relative approach considered in this paper), indicates a wavelength of $\lambda/2=0.175$ mm. For a system with a natural tan-

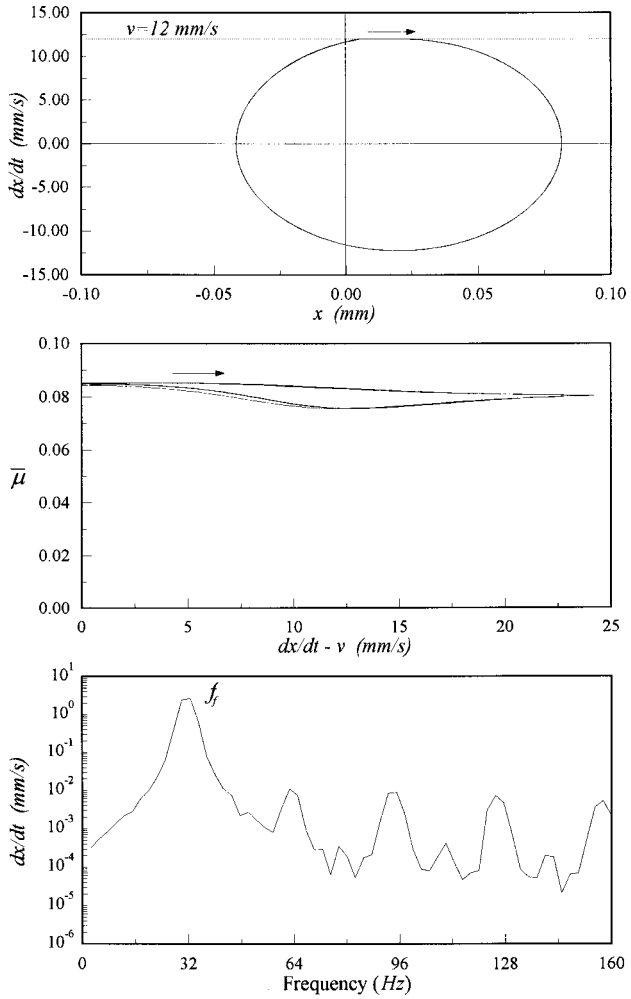

FIG. 12. Response of the dynamic system with a tangential natural frequency of $f_0 = 31.6$ Hz displays stick–slip oscillations at a platform speed of 12 mm/s.

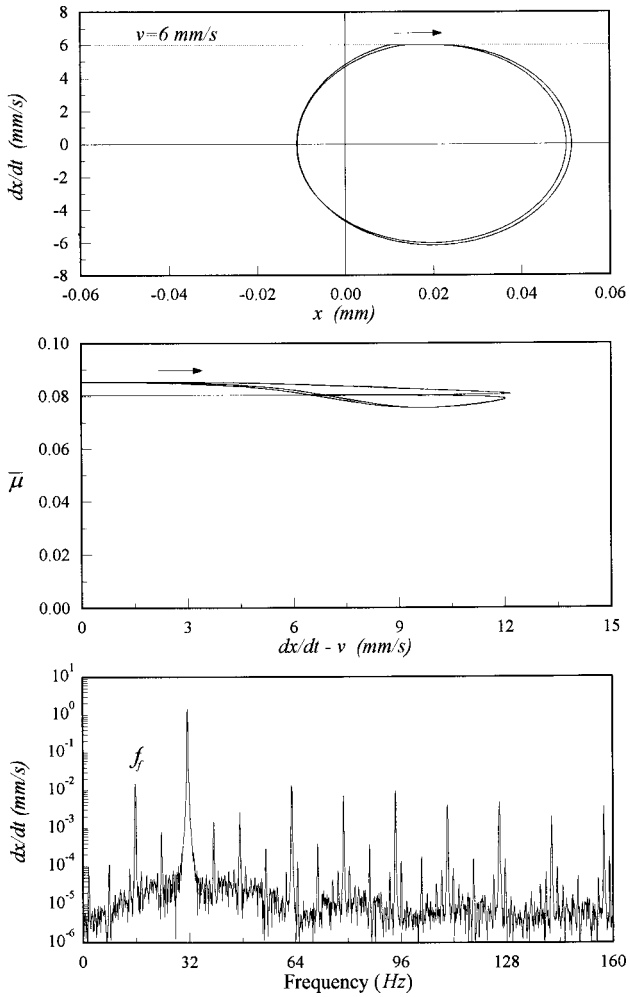

FIG. 13. Response of the dynamic system with a tangential natural frequency of $f_0 = 31.6$ Hz displays stick–slip oscillations at a platform speed of 6 mm/s.

gential frequency of 10 Hz, Eq. (28) indicates the fundamental critical speed to be 3.5 mm/s. The corresponding result from numerical simulations is 3.6 mm/s.

At $v = v_{c_1}$, oscillations exhibit a single loop. At the lower values of v_{c_n}, integer multiples of the fundamental period of oscillations appear, as described by the increased number of loops in the phase planes and corresponding subharmonics in the spectra. For example, the period is doubled at v_{c_2}, tripled at v_{c_3}, and so on. Although only a limited number of such platform speeds are revealed in these results (Tables II and III), there may be an infinite number of them for each combination of surface roughness and tangential natural frequency.

In accordance with Eq. (28), critical speeds at which stick–slip occurs (and $\overline{\mu}_D$ reaches its peak values) shift to higher values with increasing tangential natural frequency of the dynamic system. However, their values decrease with an increase in surface roughness, i.e., increased expected value of slopes. Further, values of the critical speeds are not affected by the changes in the tangential damping of the dynamic system or by the adhesive forces at the interface.

External damping inhibits stick–slip response of the system. Suppression of stick–slip by a small amount of damping is more acute for systems with higher tangential natural frequency or lower mean values of contact slopes.

Development of stick–slip also requires presence of both the deformation and adhesion forces. Without adhesion, direction of the deformation component of time-dependent friction force fluctuates, crossing zero-velocity state without reaching the condition of stick. Adhesion assures existence of the sticking condition when the relative velocity reaches zero, for at that moment the adhesive force changes direction and maintains, even for a short moment, zero relative velocity. In the absence of adhesion, deformation force can switch direction without sticking. On the other hand, adhesion, without the deformation forces, causes only static displacement of the block, without oscillations.

C. Stick–Slip bands

Numerical results indicate that around each critical speed there is a band of platform speeds within which stick–slip motion occurs, provided the external damping is sufficiently small. Outside of these *stick–slip bands*, stick–slip motion may not develop, regardless of the amount of damping. The widths of the bands differ at each critical speed: they appear to be the narrowest at the highest critical speeds

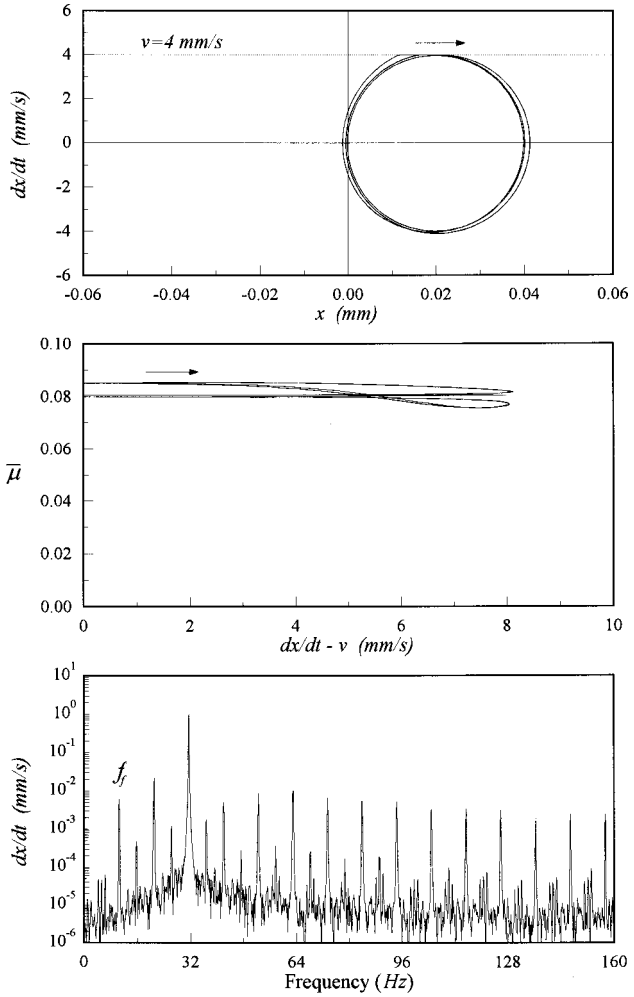

FIG. 14. Response of the dynamic system with a tangential natural frequency of $f_0 = 31.6$ Hz displays stick–slip oscillations at a platform speed of 4 mm/s.

and become wider at lower speeds. At very low speeds, however, the bandwidths increase again. The apparent dependence of stick–slip bandwidth on the critical speed could not be generalized with the limited number of results obtained here.

In some cases, stick–slip band is so narrow that external damping must be nearly zero for stick–slip motion to exist. In such cases, stick–slip response may not be sustained, but develops intermittently. Such stick–slip conditions are considered here to be ''unstable,'' unlike the ''stable'' conditions that lead to sustained stick–slip motion.

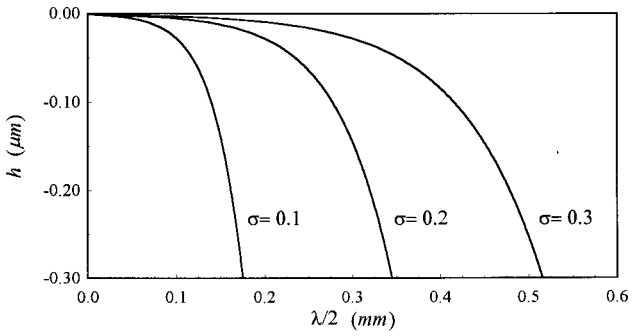

FIG. 15. Variation of λ/2 as a function of relative approach for different values of standard deviation σ of contact slope distribution.

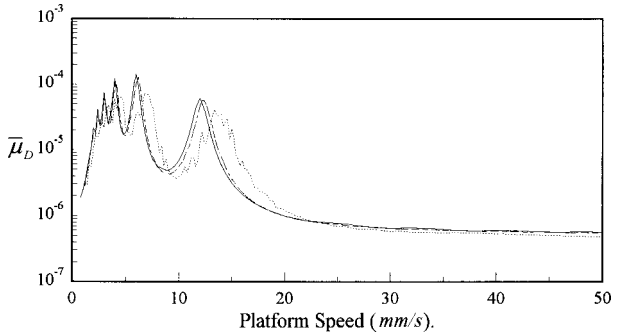

FIG. 16. Variation of $\overline{\mu}_D$ with platform speed for an unstable system characterized by a continuously changing variance. The dynamic system has a tangential natural frequency of $f_0 = 31.6$ Hz. Solid line indicates results for contact slope distribution with a constant variation. The dashed and dotted lines show unstable stick–slip resulting from changes of variance within 5% and 25% of the nominal.

When stick–slip oscillations are stable, system response settles to one stable limit cycle following an initial transient state. In cases of unstable stick–slip conditions, system response moves between two concentric, unstable limit cycles. Stick–slip takes place when the phase-plane trajectory follows the outer limit cycle. Following several stick–slip periods on or near the outer limit cycle, system response slowly diminishes and the phase-plane trajectory moves to the inner limit cycle. The inner limit cycle is also unstable; system response starts to grow until it reaches the outer limit cycle and stick–slip begins again. Figure 12 illustrates an unstable stick–slip response where the poor resolution of the velocity spectra results from the very short duration of stick and slip at the outer limit cycle.

D. Effects of surface roughness

Numerical results show that some critical speeds do not coincide with exact integer divisors of the fundamental critical speed. This is an indication of the existence of a modest nonperiodicity in the motion. Such behavior becomes more obvious when the distribution of contact slopes is nonstationary.

In cases of nonstationary contact slope distribution, the average contact slope, $\langle Z' \rangle$, becomes nonperiodic. The effect of nonstationarity of contact slopes on friction and system response is investigated numerically by randomly changing the variance of contact slope during oscillations. Results for which variance of slope distribution changes within 5% and 25% of its nominal value are plotted in Fig. 16. When compared with the corresponding stationary case, 5% variance in $\langle Z' \rangle$ has only minor effects on the value of critical speeds, while more significant changes develop with a 25% variance; Fig. 16. Further, the stick-slip oscillations could still be observed when the change in random variance is confined to within 5%, while it was not possible to obtain any stick–slip with variance changes within 25% as the surface roughness becomes less stationary.

In the numerical cases treated in this paper, resonance-like peaks of $\overline{\mu}_D$ occur at and below the fundamental critical

velocity v_{c_1}. As illustrated in Fig. 6, beyond v_{c_1}, $\overline{\mu}_D$ does not depend on the tangential natural frequency of the system, and smoothly wanes with increasing platform speed. At such high speeds compared with v_{c_1}, separation between surfaces remains large and approaches its maximum value, for there is not sufficient time for the surfaces to completely approach each other and fully undergo the effects of surface roughness. Near the speeds where $\overline{\mu}_D$ vanishes, computations become unstable and the current model is no longer applicable. For example, in the case of $\sigma = 0.1$ in Fig. 7, the $\overline{\mu}_D$ vanishes around a platform speed of 285 mm/s, whereas, for $\sigma = 0.2$ and $\sigma = 0.3$, it vanishes at platform speeds 550 and 800 mm/s, respectively. The numerical instability beyond the limiting platform speeds is ascribed to contact loss at the interface.

V. SUMMARY AND CONCLUDING REMARKS

The model developed in this paper demonstrates that friction depends on both the interface properties of the surfaces and on the dynamic response of the system that embodies them. The model relates macro-scale friction force to micro-scale forces developed at the true contact areas between surfaces. Expressing the contact forces in terms of contact areas and summing them statistically establishes this relationship. This study also considers contacts at the slopes of asperities, producing normal forces resulting from tangential relative motion of surfaces that sets this model apart from the previous ones.

A simplified mathematical model of a dynamic system is used to demonstrate the frequently observed stick–slip behavior in dynamic systems. An important result found in the cases considered above points to the significance of the deformation component of the friction force even if it is dominated by the adhesive component. Although the average friction force is essentially constant with respect to the mean sliding velocity of a friction platform, the deformation component of friction force shows a resonancelike behavior, reaching peak values at certain critical speeds. Numerical results show that stick–slip occurs only at and within a narrow band of each critical speed of the platform, defined here as *the stick–slip bands* of the critical speeds. The widths of the stick–slip bands are observed to depend on the critical speed. It is notable that at the *fundamental critical speed* of the platform, the system response is periodic, and at the progressively lower values of critical speeds, system response exhibits multiplicity of periods, such as doubling at the next lower speed, tripling at the following, and so on.

Stick–slip vibrations occur only in the presence of both deformation and adhesion components of frictional forces. An increase in surface roughness increases the strength of stick–slip motion, making it possible to develop even in the presence of large damping. On the other hand, changes in the magnitude of adhesive forces do not affect development of stick–slip as long as adhesive force magnitudes are above a certain threshold. This threshold roughly corresponds to the magnitude of the deformation forces.

The existence of stick–slip is also related to the stationarity of the contact slope distribution. For a stationary contact slope distribution, the average contact slope is a periodic function of separation, and stick–slip can be generated at certain sliding velocities. On the other hand, nonstationary contact slope distributions lead to nonperiodic average contact slopes, which do not produce stick–slip vibrations unless the nonstationarity of the distribution, or the deviation from the nominal, is small. The implication here is that surfaces that have a stationary distribution of asperity slopes (roughness), as may be the case for machined surfaces, have a higher propensity to exhibit stick–slip than surfaces that have nonstationary roughnesses.

The friction force expression developed in this paper may be expanded to include other processes that contribute to friction to the extent that they can also be expressed in terms of contact areas.

ACKNOWLEDGMENTS

One of the authors (A.A.) would like to thank the AlliedSignal Foundation and the Chrysler Challenge Fund for their support for this project.

[1] J. A. Greenwood and J. B. P. Williamson, ''Contact of nominally flat surfaces,'' Proc. R. Soc. London, Ser. A **295**, 300–319 (1966).
[2] J. A. Ogilvy, ''Numerical simulation of friction between contacting rough surfaces,'' J. Phys. D **24**, 2098–2109 (1991).
[3] A. Majumdar and B. Bhushan, ''Fractal model of elastic-plastic contact between surfaces,'' ASME J. Tribol. **113**, 1–11 (1991).
[4] W. R. Chang and I. Etson, ''An elastic-plastic model for the contact of rough surfaces,'' ASME J. Tribol. **109**, 257–263 (1987).
[5] A. Soom and C. Kim, ''Interactions between dynamic normal and frictional forces during unlubricated sliding,'' J. Lubr. Technol. **105**, 221–229 (1983).
[6] E. Rabinowicz, *Friction and Wear of Materials* (Wiley, New York, 1965).
[7] M. T. Bengisu and A. Akay, ''Relation of dry-friction to surface roughness,'' ASME J. Tribol. **119**, 18–25 (1997).
[8] L. V. Kragelsky, M. N. Dobychin, and V. S. Kombalov, *Friction and Wear Calculation Methods* (Pergamon, New York, 1982).
[9] J. A. Greenwood and J. H. Tripp, ''The contact of two nominally flat rough surfaces,'' Proc. Inst. Mech. Eng. **185**, 625–633 (1970).
[10] L. Cremer and M. Heckl, *Structure-Borne Sound* (Springer-Verlag, New York, 1987).
[11] M. T. Bengisu and A. Akay, ''Stability of friction-induced vibrations in multi-degree-of-freedom systems,'' J. Sound Vib. **171**, 557–570 (1994).
[12] J. A. C. Martins, J. T. Oden, and F. M. F. Simoes, ''A study of static and kinetic friction,'' Int. J. Eng. Sci. **28**, 29–92 (1990).

An improved state-space method for coupled fluid–structure interaction analysis

Kenneth A. Cunefare
G. W. Woodruff School of Mechanical Engineering, Georgia Institute of Technology, Atlanta, Georgia 30332-0405

Sergio De Rosa
Dipartimento di Progettazione Aeronautica, University of Naples ''Frederico II,'' Via Claudio 21, 80125 Naples, Italy

(Received 3 October 1997; accepted for publication 25 August 1998)

This paper presents an improved state-space method for incorporating fluid–structure interaction into structural acoustic analyses. Giordano and Koopmann [J. A. Giordano and G. H. Koopmann, ''State-space boundary element-finite element coupling for fluid–structure interaction analysis,'' J. Acoust. Soc. Am. **98**, 363–372 (1995)] introduced a state-space approach for the coupled analysis of fluid-loaded structures. Giordano's method employed a third-order interpolation of the fluid impedance, coupled with state-space formalism, permitting the direct eigenvalue analysis of the coupled system, and thereby yielding the fluid-loaded modes and natural frequencies. This is in contrast to the common technique of sweeping through a range of frequencies so as to identify the natural frequencies and mode shapes. The original state-space approach yielded system matrices of order $4N$, where N is the number of degrees of freedom in the underlying model. Where Giordano's method employed an interpolation based on surface velocity, the work presented in this paper uses an interpolation based on surface displacement. This simple modification to the method yields a system order of $3N$, with concomitant reduction in the required computational effort, storage, etc. We further present a method to assess the validity of the resonances obtained through this approximation technique. The method is demonstrated here for an infinite 1-D panel in a baffle, using the surface variational principle and the method of assumed modes to develop the coupled fluid–structure problem. This structure and the analysis methods are not fundamental to the state-space development, and are used solely as vehicles to demonstrate the new formulation. [S0001-4966(98)01512-4]

PACS numbers: 43.40.Rj [CBB]

INTRODUCTION

The problem of determining the fluid-loaded resonances and response shapes for coupled fluid–structure systems has long been of interest. As has been clearly known, the addition of fluid loading to a system, if the fluid is ''heavy'' in some sense, shifts the resonance frequencies to lower values, and alters the response shapes at those resonances, as compared to *in vacuo*. Typically, we may analyze the dynamic response of a fluid-loaded system through expansion techniques based on *in vacuo* structural modes,[1] or through techniques that seek a set of ''wet modes'' at a fixed frequency.[2,3] Note that we have cited examples only, and do not pretend to have cited the full wealth of literature in this subject area. We do not provide such a review, as all such literature, with one known exception, has a common feature: These modeling approaches provide no ready means to identify the resonance frequencies of the underlying systems, nor the response shapes at those resonances.

The exception to the above is that Giordano and Koopmann[4] introduced a technique whereby the use of a least-square sense interpolated approximation to the fluid-impedance matrix permitted a recasting of the dynamical equations of motion in state-space form. This state-space form could then be analyzed using common eigenvalue techniques to directly determine the fluid-loaded resonances and response shapes.

In the work at hand, we demonstrate a simple modification to the method introduced by Giordano and Koopmann that leads to significant savings in computational effort, storage requirements, etc. Where the method of Giordano and Koopman yielded systems of equations of order $4N$, where N is the number of structural degrees of freedom, our development yields a system of order $3N$, while still using the same order of interpolation. This reduction in the order of the system of equations yields the savings mentioned above, and should also improve the numerical performance (accuracy) of the overall method.

In the following, we use the example of a baffled one-dimensional infinite beam as the basis for our coupled system of equations. The particular structure, and the method and technique of obtaining the system of equations, is not fundamental to the development. Rather, it is what we do once we have such a system that is the focus of this work. Our technique is applicable to any coupled fluid-loaded system, not just baffled panels.

I. COUPLED STRUCTURAL ACOUSTIC MODEL

Rather than replicate developments that may be found in great detail elsewhere,[5] we present here only a brief state-

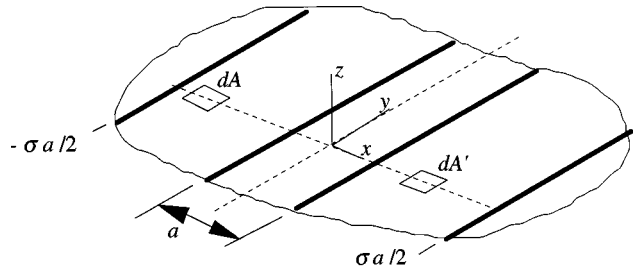

FIG. 1. Semi-infinite fluid-loaded elastic plate in rigid baffle.

ment of the system equations for our example structure. We consider a semi-infinite plate that is simply supported in a rigid baffle with one wetted surface, as shown in Fig. 1. We use the surface variational principle[6] (SVP) and the method of assumed modes to represent the fluid and structural responses, respectively. Note that this structure, the use of the SVP and the method of assumed modes are only the means to the end of obtaining a coupled fluid–structure system: The ultimate focus of this work is not dependent on such considerations.

We express the surface pressure distribution over a region of the baffle, $-\sigma/2 \leqslant \xi \leqslant \sigma/2$, as a Ritz expansion with M linearly independent basis functions,

$$p(\xi) = \boldsymbol{\psi}^T(\xi)\mathbf{p}, \tag{1}$$

where $\boldsymbol{\psi}$ and $\mathbf{p}$ are $M \times 1$ vectors of basis functions and assumed pressure mode amplitudes, with $\psi_i(\xi) = 0$ for $\xi = \pm\sigma/2$. We assume the pressure vanishes beyond the distance $r = \sigma a/2$.[5,7] Therefore, it is only necessary that the basis functions in $\boldsymbol{\psi}$ be both continuous and piecewise differentiable. Similarly, the surface displacement is expressed over the plate surface, $-1/2 \leqslant \xi \leqslant -1/2$, as

$$w(\xi,t) = a\boldsymbol{\phi}^T(\phi)\mathbf{q}(t), \tag{2}$$

where $\boldsymbol{\phi}$ and $\mathbf{q}$ are $N \times 1$ vectors of basis functions and modal coordinate amplitudes, with $\phi_i(\xi) = 0$ for $\xi = \pm 1/2$. The basis functions $\phi(\xi)$ are continuous and piecewise differentiable. We must select M larger than N by a factor of σ (i.e., $M = \sigma N$). We assume a harmonic time dependence for the generalized modal coordinate,

$$q_j(t) = \mathrm{Re}(W_j e^{-i\omega t}). \tag{3}$$

Therefore, the nondimensional normal surface velocity is

$$v_n(\xi,t) = -ika\boldsymbol{\phi}^T(\xi)\mathbf{q}(t), \tag{4}$$

where ω is the frequency of excitation and $ka = a\omega/c$ is the nondimensional wave number.

By applying the surface variational principle, we obtain a system of equations relating the unknown modal pressure amplitudes, P_i, and unknown displacement amplitudes, W_j. The coupled equations for the structural vibration are found by applying Lagrange's equation to the potential and kinetic energy expressions for the plate. The resulting $M+N$ by $M+N$ system of fully coupled equations is

$$\begin{bmatrix} \mathbf{A} & -2\pi(ka)^2\mathbf{R}^T \\ \mathbf{R} & \mathbf{D} \end{bmatrix} \begin{Bmatrix} \mathbf{p} \\ \mathbf{w} \end{Bmatrix} = \begin{Bmatrix} 0 \\ 0 \end{Bmatrix}. \tag{5}$$

Equation (5) represents the homogeneous form of the coupled equations of motion, absent external forcing. This form is suitable to our purposes here, the determination of the fluid-loaded resonances. Details on the form of the fluid matrix **A**, the fluid–structure coupling matrix **R**, the dynamical matrix **D**, and the incorporation of external forcing into Eq. (5) is addressed in Ref. 5.

Note that we may consider Eq. (5) to be representative for *any* fluid-loaded system, baffled or otherwise. Ultimately, it is the form of Eq. (5) and its sequel in which we are interested.

II. IMPEDANCE FORM FOR FLUID–STRUCTURE COUPLING

We follow here the method used by Shepard[8] for reducing the coupled equation of motion in terms of the pressure amplitudes and displacement amplitudes, Eq. (5), to an equivalent system in terms of displacements alone. We solve the first line in Eq. (5) for **p** and substitute the result into the second line. This yields an impedance formulation for the displacements as

$$\mathbf{Z}_{\mathrm{sys}}\mathbf{w} = 0, \tag{6}$$

where the combined system impedance matrix $\mathbf{Z}_{\mathrm{sys}}$ is of size $N \times N$. We may write the system impedance matrix as being composed of impedance contributions from the fluid loading and from the structure as

$$\mathbf{Z}_{\mathrm{sys}} = \mathbf{Z}_{\mathrm{fl}} + \mathbf{Z}_{\mathrm{st}}, \tag{7}$$

where the fluid-loading impedance component is

$$\mathbf{Z}_{\mathrm{fl}} = 2\pi(ka)^2\mathbf{R}\mathbf{A}^{-1}\mathbf{R}^T, \tag{8}$$

and the structural impedance matrix is simply

$$\mathbf{Z}_{\mathrm{st}} = \mathbf{D}. \tag{9}$$

Note that in the absence of fluid loading, we may use Eq. (6) and an assumed harmonic response to obtain *in vacuo* natural frequencies and mode shapes. In the presence of fluid loading, incorporating Eq. (7) into Eq. (6) and expressing the fluid matrix as a function of wave number, we obtain

$$[\mathbf{Z}_{\mathrm{fl}}(ka) + \mathbf{Z}_{\mathrm{st}}]_{\mathrm{sys}}\mathbf{w} = \mathbf{0}. \tag{10}$$

Here, it is evident that the typical method of determining system natural frequencies and mode shapes is rendered inapplicable since the elements of the system impedance matrix are explicitly functions of frequency. For this very reason, a direct eigensolution based on Eq. (10) is not possible. In the following, we demonstrate how the use of a state-space representation leads to a formulation that does permit direct eigensolution for the fluid-loaded resonances and corresponding response shapes.

III. STATE-SPACE REPRESENTATION

A formally elegant and basically simple approximate solution to the difficulty encountered at the end of the previous section may be found in the work of Giordano and Koopmann.[4] Giordano demonstrated that a frequency-based interpolation for the elements of the fluid matrix in Eq. (8) leads to a state-space representation for the coupled problem

that is amenable to analysis by standard eigenvalue techniques. The penalty for this technique is an increase in the order of the system of equations under consideration, from N to $4N$. In the following, we develop an alternative formulation that only increase the system order to $3N$. While this may be viewed by some as a trivial modification, the associated reduction in computational effort and storage requirements is significant. For example, in a full-storage mode, the memory required to store the new representation is 9/16 of that required for the Giordano representation. Note that the actual size of the system will depend on the order of the interpolation method described below; however, our approach will always yield a system size N less than that of Giordano and Koopmann, for the same order interpolation.

As with Giordano,[4] we use a polynomial fit in ka to approximate the individual elements of the fluid impedance matrix,

$$\mathbf{Z}_{\mathrm{fl}}(ka)_{ij}=\sum_{l=0}^{L} C_{lij}(ka)^{l}. \tag{11}$$

It is evident from Eq. (11) that there will be $L+1$ $\mathbf{C}$ matrices containing the coefficients of the interpolation for each term of the fluid matrix, where L is the order of the polynomial expansion. As with Giordano and Koopmann, we use a third-order least-square polynomial fit, such that

$$\mathbf{Z}_{\mathrm{fl}}=\mathbf{C}_0+\mathbf{C}_1(ka)+\mathbf{C}_2(ka)^2+\mathbf{C}_3(ka)^3. \tag{12}$$

The fitted coefficient matrices $\mathbf{C}$ will depend on the range of ka over which the fit is performed as well as the number of discrete frequencies within the range for which $\mathbf{Z}_{\mathrm{fl}}$ is available. The coefficient matrices are complex, and may be generated by any suitable curve fitting algorithm. To perform the fit, then, we must first compute the full fluid impedance matrix at a number of discrete frequencies. The selection of these frequency points are at our discretion, subject only to the necessity of obtaining a valid fit.

Up to this point in the development, there is no difference between the above and that developed by Giordano to the equivalent point. The critical distinction is in the sequel; Where Giordano used an impedance representation based on velocity,

$$\mathbf{Z}^{*}_{\mathrm{fl}}(ka)\mathbf{v}=\mathbf{p}, \tag{13}$$

our impedance definition is in terms of displacement,

$$\mathbf{Z}_{\mathrm{fl}}(ka)\mathbf{w}=\mathbf{p}. \tag{14}$$

Note that we designate the impedance matrix used by Giordano as $\mathbf{Z}^{*}$, in order to clearly discriminate it from ours. If the same methods are employed to obtain $\mathbf{Z}^{*}$ and $\mathbf{Z}$, then they differ only by a factor of $i\omega$. From Eq. (12), we may recast the left-hand side of the above as

$$\mathbf{Z}_{\mathrm{fl}}(ka)\mathbf{w}=\mathbf{C}_0\mathbf{w}+\mathbf{C}_1(ka)\mathbf{w}+\mathbf{C}_2(ka)^2\mathbf{w}+\mathbf{C}_3(ka)^3\mathbf{w}. \tag{15}$$

Now, given that

$$\dot{\mathbf{w}}=-i\mathbf{w}(ka),\quad \ddot{\mathbf{w}}=-\mathbf{w}(ka)^2,\quad \dddot{\mathbf{w}}=i\mathbf{w}(ka)^3, \tag{16}$$

we rewrite Eq. (15) using the displacement vector and its derivative (the highest-order derivative is obviously determined by selecting the limit L of the expansion),

$$\mathbf{Z}_{\mathrm{fl}}(ka)\mathbf{w}=\mathbf{C}_0\mathbf{w}+i\mathbf{C}_1\dot{\mathbf{w}}-\mathbf{C}_2\ddot{\mathbf{w}}-i\mathbf{C}_3\dddot{\mathbf{w}}. \tag{17}$$

Separating the structural operator into mass and stiffness components, we recast the fluid–structure eigenproblem in state-space form as

$$\begin{bmatrix} -i\mathbf{C}_3 & \mathbf{0} & \mathbf{0} \\ \mathbf{0} & \mathbf{I} & \mathbf{0} \\ \mathbf{0} & \mathbf{0} & \mathbf{I} \end{bmatrix} \begin{Bmatrix} \dddot{\mathbf{w}} \\ \ddot{\mathbf{w}} \\ \dot{\mathbf{w}} \end{Bmatrix} + \begin{bmatrix} -\mathbf{C}_2+\mathbf{M} & i\mathbf{C}_1 & \mathbf{C}_0+\mathbf{K} \\ -\mathbf{I} & \mathbf{0} & \mathbf{0} \\ \mathbf{0} & -\mathbf{I} & \mathbf{0} \end{bmatrix} \times \begin{Bmatrix} \ddot{\mathbf{w}} \\ \dot{\mathbf{w}} \\ \mathbf{w} \end{Bmatrix} = \begin{Bmatrix} \mathbf{0} \\ \mathbf{0} \\ \mathbf{0} \end{Bmatrix}, \tag{18}$$

where $\mathbf{I}$ is the identity matrix. Where the method of Giordano yielded a $4N$ system, Eq. (18) is only of order $3N$, even though both methods used a third-order polynomial fit, and both terminal equations were in terms of displacement. The key difference leading to this alternative representation is the use of displacement in Eq. (14), rather than velocity. The above representation is a more compact, efficient implementation than that originally proposed by Giordano. All the benefits of reduced system size for computational efficiency and accuracy therefore devolve to this improved implementation.

In general, the standard eigenvalue analysis applied to the system represented by Eq. (18) will yield $3N$ eigenvalues and eigenvectors. Clearly, there can be only N physical eigenvalues, as that corresponds to the number of dynamical degrees of freedom in the underlying structural model. In the absence of fluid loading, the $3N$ eigenvalues become N imaginary conjugate pairs corresponding to the *in vacuo* resonances, and N nonphysical eigenvalues. The conjugate pairs are redundant, thereby yielding only N true resonances. With fluid loading, the eigenvalue problem no longer yields conjugate pairs, yet of the $3N$ eigenvalues and eigenvectors, only N can correspond to fluid-loaded resonances. As noted following Eq. (12), the $\mathbf{C}$ matrices are complex. Therefore, a complex-valued eigenvalue routine is required. The eigenvalues will be complex, with the real part proportional to the damping ratio, and the imaginary part corresponding to the frequency.

At present, we are unaware of any eigenvalue theory applicable to a system constructed in the manner and form of Eq. (18) that would permit us to analytically characterize the resulting eigenvalues. Therefore, to discriminate the physical resonances from the nonphysical, we apply the following physical rules:

(1) Negative damping ratio (real part of the eigenvalue);
(2) Damping ratio less than the critical ratio (less than unity);

TABLE I. *In-vacuo* and fluid-loaded resonances of the plate.

Mode #	*In vacuo*	Fluid-loaded
1	0.46	0.22
2	1.83	1.37
3	4.12	3.43

TABLE II. Eigenvalues, mean and maximum value of fit correlation coefficients obtained using least-square fit for $0<ka<5$.

Case	*ka* min	*ka* max	*ka* step	$\omega 1$	$\omega 2$	$\omega 3$	$\omega 4$	Mean $1-r_{ij}^2$	Max $1-r_{ij}^2$
1	0.05	5.0	0.05	0.135	1.36	3.42	6.38	0.015	0.093
2	0.25	5.0	0.25	0.132	1.37	3.42	6.38	0.014	0.085
3	1.0	5.0	1.0	0.176	1.35	3.42	6.36	0.001	0.009

(3) Negative frequency component (imaginary part of the eigenvalue).

These are effectively the same rules used by Giordano, and ensure that the eigenvalues we obtain using these rules correspond to oscillatory solutions.

On a practical application note, it is probably not efficient to use a general all-value eigenvalue solver applied to Eq. (18), for the following reasons. First, as noted above, of the $3N$ eigenvalues, only N will be significant. Second, since the coefficient matrices in Eq. (18) are generated over a limited bandwidth, only some of the remaining N eigenvalues will fall within this bandwidth (issues related to this point are addressed in the following section). Therefore, any numerical implementation of this technique should take advantage of those eigenvalue solver routines that extract eigenvalues near a specific value (e.g., inverse iteration[9]), with starting trial values selected based on the curve fit bandwidth.

IV. RESULTS

To demonstrate the efficacy of this improved formulation, we apply it to our example problem described above. We use 20 structural basis functions and 100 fluid basis functions [Eqs. (1) and (2) of this paper, and Ref. 5 for more detail]. Upon reduction to the impedance formulation, Eq. (6), we are left with a system of equations of size 20×20. The state-space representation leads us to a system of size 60×60. In Table I, we list the *in vacuo* and fluid-loaded resonances of the plate. The *in vacuo* resonances were obtained analytically, while the fluid-loaded resonances were obtained by a frequency sweep with *ka* increments of 0.01.

We first evaluate the ''goodness of fit'' to the individual elements of the fluid impedance matrix. For the real and imaginary components of each element within the impedance matrix, we calculate a correlation coefficient as

$$1-r_{ij}^2=1-\frac{\Sigma_{n=1}^{NS}(\Sigma_{l=0}^{L}C_{lij}(ka)_n^l-\overline{\mathbf{Z}}_{\mathrm{fl},ij})^2}{\Sigma_{n=1}^{NS}(\mathbf{Z}(ka)_{\mathrm{fl},nij}-\overline{\mathbf{Z}}_{\mathrm{fl},ij})^2}, \tag{19}$$

where NS is the number of discrete sample frequencies included in the least-square approximation for $\mathbf{Z}_{\mathrm{fl}}$ and $\overline{\mathbf{Z}}_{\mathrm{fl},ij}$ is the mean value of element ij over the NS samples. The goodness of fit is best assessed by consideration of the quantity $1-r_{ij}^2$, where values close to zero indicate a good fit.[10]

Table II presents the eigenvalues obtained using the method developed above as applied to the example problem. The table includes the *ka* range and *ka* step size over which the least-square fit was performed. The table also includes measures of the goodness of fit based on the mean of all correlation coefficients for a given fit, and the maximum value of the correlation coefficients for the fit. The *ka* range used to obtain the fits in Table II span the range of the first three eigenvalues in Table I, while the fourth eigenvalue is outside the range of the fit. We include this to show the ability of the technique to capture eigenvalues outside the span of the fit. However, we note that none of the three fits presented in Table I accurately generate the lowest eigenvalue. This implies that the correlation coefficients for the fit do not provide sufficient information to assess whether the eigenvalues found with a given fit are accurate.

To explore the inability of the method to capture the first eigenvalue, and to develop alternative means of assessing the validity of individual eigenvalues, we narrow the span of the fit, with the results presented in Table III. Note that case 4 did not yield a valid eigenvalue consistent with the third eigenvalue. However, given the range of the fit for case 4, only the first eigenvalue falls within that range, and all higher eigenvalues fall outside the range. This demonstrates that while the technique is capable of predicting eigenvalues outside the range of the underlying fit, there is no guarantee of accurately predicting such eigenvalues.

Note that while case 5 captured the first and second eigenvalue quite well, its correlation coefficient measure is no better than that of case 3 in Table II, a case that failed to localize the first eigenvalue. Hence, we conclude that a low value of these correlation coefficient is a necessary condition for accurate eigenvalues, but it is not sufficient to guarantee accurate eigenvalues.

In light of the above, we therefore propose the following methodology to assess the validity of the predicted eigenvalues:

(1) Obtain the least-square fit for the fluid impedance matrix as described above;

TABLE III. Eigenvalues, mean and maximum value of fit correlation coefficients obtained using least-square fit for and narrowed *ka* span of fits.

Case	*ka* min	*ka* max	*ka* step	$\omega 1$	$\omega 2$	$\omega 3$	$\omega 4$	Mean $1-r_{ij}^2$	Max $1-r_{ij}^2$
4	0.05	1.0	0.05	0.191	1.35	⋯	6.06	0.011	0.086
5	0.05	0.50	0.05	0.221	1.36	3.23	6.22	0.002	0.007

TABLE IV. Eigenvalues and associated mean and maximum value of correlation coefficients based on the immediate vicinity of the eigenvalue.

Case	$\omega 1$	Mean $1-r_{ij}^2$	Max $1-r_{ij}^2$	$\omega 2$	Mean $1-r_{ij}^2$	Max $1-r_{ij}^2$	$\omega 3$	Mean $1-r_{ij}^2$	Max $1-r_{ij}^2$	$\omega 4$	Mean $1-r_{ij}^2$	Max $1-r_{ij}^2$
1	0.135	$-1.3e12$	$5.9e12$	1.36	-136	552	3.42	-618	$6.2e4$	6.38	$-1.3e4$	$1.6e6$
3	0.176	$-3.3e12$	$1.6e13$	1.35	-497	$2.2e3$	3.42	-660	$3.8e4$	6.36	$-9.3e3$	$2.1e6$
5	0.221	-1.9	6.9	1.36	$-1.6e4$	$8.6e4$	3.23	$-6.1e7$	$2.2e9$	6.22	$-5.0e8$	$7.0e10$

(2) Determine the eigenvalues;
(3) Calculate global correlation coefficients from the entire sample used in the fit;
(4) For each eigenvalue, calculate correlation coefficients based on the fit obtained in step 1, but using sample points only in the immediate vicinity of each predicted eigenvalue.

Step 4 provides us a means to assess how good the fit to the fluid impedance matrix is in the immediate vicinity of the predicted eigenvalues. If this fit is poor, then there is no basis to believe that the predicted eigenvalue is correct. Note that the correlation coefficient based on only a limited number of the total sample of points will probably not be as good as that for the total sample. We apply this ''local'' correlation analysis to cases 1, 3, and 5, and present the results in Table IV. We observe that the 'local' analysis, when the magnitude of the measures is less than 10^5, is a good indicator of eigenvalue validity.

V. CONCLUSIONS

The state-space approximation technique presented here and by Giordano and Koopmann permits the ready determination of fluid-loaded resonances through classical analyses means (e.g., eigenvalue decomposition). The method we have presented has a clear computational advantage over the original state-space formulation of Giordano and Koopmann, in terms of reduced memory requirements and computational effort.

For both our approach and that of Giordano and Koopmann, the quality of the results depends on the quality of the underlying fit to the fluid impedance. Our results demonstrate that the method is capable of producing both correct and incorrect eigenvalues, and that global correlation measures are insufficient to ensure the accuracy of the results. However, we have demonstrated that a valuable test to determine validity is a local test of the correlation between the obtained fit and directly calculated values for the fluid impedance in the immediate vicinity of an eigenvalue. We view this local test as an essential step in assessing the results produced by the technique. Any implementation of the technique should incorporate means to assess both the global and local quality of fit.

Additionally, while the technique can predict eigenvalues that fall outside the range of the underlying curve fit, we observe that there is no guarantee that the technique will, in fact, produce all such out-of-range eigenvalues, and may predict spurious eigenvalues outside the range. The greatest reliability placed on the results must therefore be on those eigenvalues that fall within the range of the underlying curve fit.

ACKNOWLEDGMENTS

The work presented in this paper was performed during Mr. De Rosa's three-month visiting research period at the Georgia Institute of Technology, from September 20th to December 19th, 1996. The visit was made possible by a Fulbright Grant. The authors would like to acknowledge the Council For The International Exchange Of Students and the Commissione Per Gli Scambi Culturali Fra L'Italia E Gli Stati Uniti for having selected and approved the research plan. These organizations gave the authors the opportunity to increase their knowledge and experience by working together. The authors further would like to acknowledge the assistance of Dr. Jeffrey Giordano, who extended every courtesy in helping the authors understand the subtleties of his original state-space approach.

[1] R. Clough and J. Penzien, *Dynamics of Structures* (McGraw-Hill, New York, 1975).
[2] M. M. Ettouney, R. P. Daddazio, and F. L. DiMaggio, ''Wet modes of submerged structures—Part 1: Theory,'' ASME J. Vib. Acoust. **114**, 433–439 (1992).
[3] R. P. Daddazio, M. M. Ettouney, and N. Abboud, ''Wet modes of submerged structures—Part 2: Applications,'' ASME J. Vib. Acoust. **114**, 440–448 (1992).
[4] J. A. Giordano and G. H. Koopmann, ''State space boundary element-finite element coupling for fluid-structure interaction analysis,'' J. Acoust. Soc. Am. **98**, 363–372 (1995).
[5] J. H. Ginsberg, K. A. Cunefare, and H. Pham, ''A spectral description of inertial effects in fluid-loaded plates,'' ASME J. Vib. Acoust. **117**, 206–212 (1995).
[6] X.-F. Wu, A. D. Pierce, and J. H. Ginsberg, ''Variational method for computing acoustic pressure on vibrating bodies, applied to transversely oscillating disks,'' IEEE J. Ocean Eng. **12**, 412–418 (1987).
[7] J. H. Ginsberg and J. G. McDaniel, ''An acoustic variational principle and component mode synthesis applied to the analysis of acoustic radiation from a concentrically stiffened plate,'' ASME J. Vib. Acoust. **113**, 401–408 (1991).
[8] W. S. J. Shepard, ''The impact of attached feature scales and spatial distributions on the response of structural-acoustic systems,'' Ph.D. dissertation, The Georgia Institute of Technology, 1996.
[9] William H. Press, Brian P. Flannery, Saul A. Teukolsky *et al.*, *Numerical Recipes in Fortran: The Art of Scientific Computing* (Cambridge U.P., Cambridge, MA, 1992), 2nd ed.
[10] T. G. Beckwith, R. D. Marangoni, and J. H. Lienhard, *Mechanical Measurements* (Addison-Wesley, Reading, MA, 1993).

Modal filtering for flexible beams using optical fibers

Hiromasa Semba
Mechanics and Electronics Division, Industrial Research Center of Ehime Prefecture, 487-2 Kumekubota-machi, Matsuyama-shi, Ehime, Japan

Nobuo Tanaka
Department of Production, Information and Systems Engineering, Tokyo Metropolitan Institute of Technology, 6-6 Asahigaoka, Hino-shi, Tokyo, Japan

(Received 8 May 1997; accepted for publication 30 September 1998)

This paper describes a vibration-mode filtering method for one-dimensional structures such as a cantilevered beam using a two-mode optical fiber as a distributed-effect sensor. One of the most important problems regarding the optical measurement is how to alter the sensor sensitivity spatially along the longitudinal direction of the beam when the sensor is mounted on the beam surface. In this study, spatial variation of the sensor orientation with respect to the longitudinal direction is included in the sensor model. The sensor sensitivity can be experimentally measured and used for design, incorporating the orthogonality of the mode shapes of the structure. Moreover, in light of practical considerations, a design procedure of optimal fiber placement utilizing bipolar weighting functions is presented. Finally, theoretical predictions are confirmed by experimental results and efficient vibration-mode filtering is demonstrated. © *1999 Acoustical Society of America.*
[S0001-4966(99)03901-6]

PACS numbers: 43.40.Vn, 43.35.Ar [PJR]

INTRODUCTION

Recently, distributed-effect sensors such as polyvinylidene fluoride (PVDF) film and optical fibers have attracted some interest as a new class of sensors. Optical fiber sensors have been especially used and are particularly attractive for smart structures because they have low mass, are flexible, and are easily embedded in a variety of materials. Moreover, they are not easily influenced by electromagnetic waves.

In fact, after the fundamental studies on the optical fiber,[1,2] vibration control using such optical fibers[3] has been studied, two-mode optical fiber sensor implementation methods[4] have been developed, and surface-mounted optical fibers[5] have been discussed. The use of distributed-effect sensors in vibration control helps to extract structural vibration modes needed in modal control.[6] Furthermore, distributed filters, in contrast to point sensors, have the ability to act as spatial filters. Practical modal filtering using PVDF film has been expanded to two-dimensional structures.[7]

Shortcomings of PVDF film are that it is difficult to apply to a complicated structure because it is a face type sensor, and that it needs relatively complicated wiring as well as precautionary treatment against electrical noise. So the development of modal filters using flexible optical fibers is significant.

One may note that recent studies on modal filtering using optical fibers have been reported,[8,9] but they did not obtain successful results. The reasons why successful results have not been achieved are that for distributed-effect sensors possessing a linear shape such as optical fibers, it is difficult to implement a weighting function spatially along the sensor length. Modal filtering design based on utilizing mode orthogonality requires the engineer to vary sensor sensitivity spatially corresponding to the desired weighting function. The well-known and easily employed method of cutting PVDF film in a pattern that corresponds to a desired spatial weighting function, contrasts the difficult task of varying the sensor sensitivity of an optical fiber spatially, due to its thin core and clad diameter. This paper offers a simple method for carrying out such a task, corresponding to the desired weighting function. The optical fiber sensor's orientation with respect to the longitudinal direction of a structure is included in the sensor model. A one-dimensional structure is selected to be filtered in order to confirm the design procedure using optical fibers. The ability to act as a modal filter is discussed from both theoretical and experimental points of view. The optical intensity emitted from the endface of an optical fiber placed on a one-dimensional structure is modeled so that the fiber orientation with respect to the longitudinal direction of the beam should function as a sensor sensitivity. It is then shown that this method allows the optical fiber to act as a modal filter, using the orthogonality of the mode functions to extract a desired vibration mode. A method is derived for measuring the sensor sensitivity with respect to various orientations. This sensitivity is needed for the filter design, and is derived both theoretically and experimentally. Moreover, in light of practical considerations, a design procedure for optimal fiber placement utilizing bipolar weighting functions is proposed. Finally, theoretical predictions are confirmed by experimental results using a type of bow-tie optical fiber and efficient vibration-mode filtering is demonstrated.

I. THE PRINCIPLE OF MODAL FILTERING

A. Output signal through a two-mode optical fiber

This section considers a two-mode optical fiber, the case for which only two modes propagate down the fiber. A relationship between the strain over the fiber and the output of

the optical signal should be considered. Consider the jth mode propagating in a step-index optical fiber of length l with core and cladding indices n_{co} and n_{cl}, respectively. When the strain is induced in the fiber, the phase of the jth mode is given by

$$\phi_j(t)=\int_0^{\ell}\beta_j(\varepsilon(s,0))ds+\psi_j+\int_0^{\ell}\beta_j(\varepsilon(s,t))\varepsilon(s,t)ds, \tag{1}$$

where β_j, which is a function of the strain distribution, is the s component of the propagation constant for the waveguide mode, ψ_j is the phase upon entering the fiber, $\varepsilon(s,0)$ is the initial longitudinal strain distribution over the fiber at $t=0$, and $\varepsilon(s,t)$ is change in strain from the initial distribution.

In this equation, summation of the first term and the second term on the right-hand side denotes static phase, while the third term denotes dynamic phase. The transverse components of the electric and magnetic fields in the fiber core for the two modes considered can be expressed as

$$\mathbf{E}_j(\rho,\varphi,t)=\mathbf{E}_j(\rho,\varphi)\exp\left[i\left\{\int_0^{\ell}\beta_j(\varepsilon(s,0))ds+\psi_j+\int_0^{\ell}\beta_j(\varepsilon(s,t))\varepsilon(s,t)ds-\omega t\right\}\right], \tag{2}$$

$$\mathbf{H}_j(\rho,\varphi,t)=\mathbf{H}_j(\rho,\varphi)\exp\left[i\left\{\int_0^{\ell}\beta_j(\varepsilon(s,0))ds+\psi_j+\int_0^{\ell}\beta_j(\varepsilon(s,t))\varepsilon(s,t)ds-\omega t\right\}\right], \tag{3}$$

where ω is the optical angular frequency.

The intensity resulting from the combination of the two modes at the fiber output endface is then the complex Poynting vector. The resulting expression is

$$\begin{aligned}I(\rho,\varphi,t)=&I_1(\rho,\varphi)+I_2(\rho,\varphi)+1/2\{\mathbf{E}_1(\rho,\varphi)\times\mathbf{H}_2^*(\rho,\varphi)\\&+\mathbf{E}_2(\rho,\varphi)\times\mathbf{H}_1^*(\rho,\varphi)\}\Bigg[\\&\times\cos\left\{\int_0^{\ell}\Delta\beta(\varepsilon(s,0))ds+\Delta\psi\right\}\\&\times\cos\left\{\int_0^{\ell}\Delta\beta(\varepsilon(s,t))\varepsilon(s,t)ds\right\}\\&+\sin\left\{\int_0^{\ell}\Delta\beta(\varepsilon(s,0))ds+\Delta\psi\right\}\\&\times\sin\left\{\int_0^{\ell}\Delta\beta(\varepsilon(s,t))\varepsilon(s,t)ds\right\}\Bigg],\end{aligned} \tag{4}$$

where

$$I_1(\rho,\varphi)=\tfrac{1}{2}(\mathbf{E}_1\times\mathbf{H}_1^*),\quad I_2(\rho,\varphi)=\tfrac{1}{2}(\mathbf{E}_2\times\mathbf{H}_2^*),$$

$$\Delta\psi=\psi_1-\psi_2,\quad \Delta\beta=\beta_1-\beta_2.$$

For a small distance $\int_0^{\ell}\Delta\beta(\varepsilon(s,t))\varepsilon(s,t)ds\ll 1$, the expression reduces considerably to

$$\begin{aligned}I(\rho,\varphi,t)\cong&I_1(\rho,\varphi)+I_2(\rho,\varphi)+\tfrac{1}{2}\{\mathbf{E}_1(\rho,\varphi)\times\mathbf{H}_2^*(\rho,\varphi)\\&+\mathbf{E}_2(\rho,\varphi)\times\mathbf{H}_1^*(\rho,\varphi)\}\\&\cdot\left\{\cos\left(\int_0^{\ell}\Delta\beta(\varepsilon(s,0)(ds+\Delta\psi\right)\right.\\&-\sin\left(\int_0^{\ell}\Delta\beta(\varepsilon(s,0))ds+\Delta\psi\right)\\&\left.\times\int_0^{\ell}\Delta\beta(\varepsilon(s,t))\varepsilon(s,t)ds\right\}.\end{aligned} \tag{5}$$

Then the two constants I_1^0 and I_2^0, neither of which depends on the strain, are defined as

$$I_1^0=I_1(\rho,\varphi)+I_2(\rho,\varphi), \tag{6}$$

$$I_2^0=1/2\{\mathbf{E}_1(\rho,\varphi)\times\mathbf{H}_2^*(\rho,\varphi)+\mathbf{E}_2(\rho,\varphi)\times\mathbf{H}_1^*(\rho,\varphi)\}. \tag{7}$$

Now Eq. (5) is rewritten as

$$\begin{aligned}I(\rho,\varphi,t)=&I_1^0+I_2^0\left\{\cos\left(\int_0^{\ell}\Delta\beta(\varepsilon(s,0))ds+\Delta\psi\right)\right.\\&-\sin\left(\int_0^{\ell}\Delta\beta(\varepsilon(s,0))ds+\Delta\psi\right)\\&\left.\times\int_0^{\ell}\Delta\beta(\varepsilon(s,t))\varepsilon(s,t)ds\right\}.\end{aligned} \tag{8}$$

The total intensity at the fiber output endface is given by integration over the whole sectional area. When I_1 and I_2 are defined as the integration of I_1^0 and I_2^0, respectively, the total intensity I is given by

$$\begin{aligned}I(t)=&I_1+I_2\left\{\cos\left(\int_0^{\ell}\Delta\beta(\varepsilon(s,0))ds+\Delta\psi\right)\right.\\&-\sin\left(\int_0^{\ell}\Delta\beta(\varepsilon(s,0))ds+\Delta\psi\right)\\&\left.\times\int_0^{\ell}\Delta\beta(\varepsilon(s,t))\varepsilon(s,t)ds\right\}.\end{aligned} \tag{9}$$

Equation (9) denotes the intensity based on the strain distribution over the two-mode fiber.

B. Sensor model for modal filtering

In order to develop the theory for vibration-mode filtering, Eq. (9) has to be modified so as to include the sensor sensitivity. Therefore the sensor orientation with respect to the longitudinal direction of the one-dimensional structure is used to alter the sensor sensitivity, then the output signal from the fiber endface is clarified as based on it.

Now, consider the upper model of Fig. 1 in which an optical fiber is placed on a beam. The z axis is the longitudinal axis and the s axis run along the optical fiber. The optical fiber is inclined at an angle θ_z with respect to the longitudinal direction of the beam at the position z.

Let $\varepsilon(z,t)$ denote the beam strain at position z and time t. A small change dz in the length of the beam induces a change

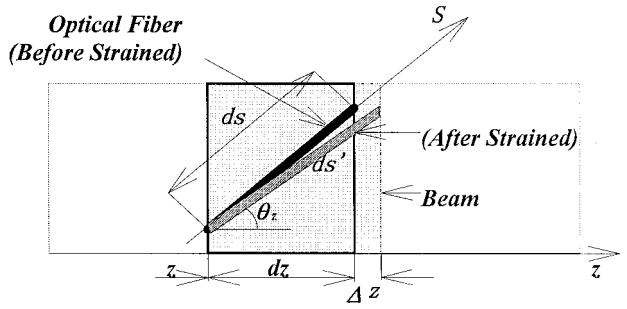

FIG. 1. Optical fiber placed on a beam.

$\varepsilon(s,t)ds$ of the length of fiber. The relationship between the change in length of the beam and that of the fiber is assumed as follows using a function $f(\theta_z)$ only of attachment angle, not of the beam's strain:

$$\varepsilon(s,t)ds = f(\theta_z)\varepsilon(z,t)dz. \tag{10}$$

Then Eq. (9) becomes

$$\begin{aligned} I(t) = I_1 + I_2 \Bigg\{ & \cos\left(\int_0^{\ell} \Delta\beta(\varepsilon(s,0))ds + \Delta\psi \right) \\ & - \sin\left(\int_0^{\ell} \Delta\beta(\varepsilon(s,0))ds + \Delta\psi \right) \\ & \times \int_\Omega \Delta\beta(f(\theta_z)\varepsilon(z,t)) \cdot f(\theta_z)\varepsilon(z,t)dz \Bigg\}, \end{aligned} \tag{11}$$

where Ω is the structural domain of the beam in which the fiber is attached.

In the case that $\Delta\beta$ is constant, the smallness of the fiber strain allows simplification of Eq. (11),

$$\begin{aligned} I(t) = I_1 + I_2 \Bigg\{ & \cos(\Delta\beta\ell + \Delta\psi) - \sin(\Delta\beta\ell + \Delta\psi)\Delta\beta \\ & \times \int_\Omega f(\theta_z)\varepsilon(z,t)dz \Bigg\}. \end{aligned} \tag{12}$$

Equation (12) gives the optical power based on the beam strain.

Moreover, upon decomposing into AC and DC components, Eq. (12) becomes

$$I(t) = \tilde{I}_1 - \tilde{I}_2 \Delta\beta \int_\Omega f(\theta_z)\varepsilon(z,t)dz, \tag{13}$$

where

$$\tilde{I}_1 = I_1 + I_2 \cos\left(\int_0^{\ell} \Delta\beta(\varepsilon(s,0))ds + \Delta\psi \right), \tag{14}$$

$$\tilde{I}_2 = I_2 \sin\left(\int_0^{\ell} \Delta\beta(\varepsilon(s,0))ds + \Delta\psi \right), \tag{15}$$

are both constant, determined by fiber length and initial fiber strain distribution.

C. The principle of modal filtering

The previous modeling will define the method of modal filtering. Consider a beam subject to a distributed force. For small deflections, the strain at the surface of the beam is proportional to the second derivative of the deflection, so that

$$\varepsilon(z,t) = -\frac{h}{2}\frac{\partial^2 w(z,t)}{\partial z^2}, \tag{16}$$

where h denotes the thickness of the beam. Writing the deflection in terms of its modal decomposition, the strain is approximated by

$$\varepsilon(z,t) = -\frac{h}{2}\sum_{n=1}^{\infty} \Phi_n''(z)\,\eta_n(t), \tag{17}$$

where $\Phi_n''(z)$ denotes the second derivative of the nth modal function with respect to the position, and $\Phi_n(z)$ denotes the nth modal amplitude. Consider only the AC component of Eq. (13).

Substituting this approximation into Eq. (13), the sensor output becomes

$$\begin{aligned} I_{\mathrm{AC}}(t) &= \tilde{I}_2 \Delta\beta \int_\Omega f(\theta_z)\varepsilon(z,t)dz \\ &= \frac{h}{2}\tilde{I}_2 \Delta\beta \int_\Omega f(\theta_z) \sum_{n=1}^{\infty} \Phi_n''(z)\,\eta(t)dz \\ &= \frac{h}{2}\tilde{I}_2 \Delta\beta \sum_{n=1}^{\infty} \left[\int_\Omega f(\theta_z)\Phi_n''(z)dz \right] \eta(t). \end{aligned} \tag{18}$$

Utilizing the orthogonality of the mode shapes, if the weighting function $f(\theta_z)$ for the fiber sensor is chosen such that

$$f(\theta_z) = k\Phi_M''(z), \tag{19}$$

the sensor output becomes

$$I_{\mathrm{AC}}(t) = \frac{h}{2}\tilde{I}_2 \Delta\beta \left\{ \int_\Omega f(\theta_z)\Phi_M''(z)dz \right\} \eta(t). \tag{20}$$

Modes other than the Mth mode are suppressed and do not appear in the sensor output, $l_{\mathrm{ac}}(t)$. For example, Fig. 2 shows some plots of the second derivatives from the first to the fifth mode for a cantilevered beam. When $f(\theta_z)$ is proportional to the Mth mode, only the Mth vibration mode signal appears in the sensor output. It is apparent from the figure that if filtering of the second mode or higher is desired, then the sensor sensitivity $f(\theta_z)$ must take values less than zero at the position where the value of the second derivative of the desired mode is negative.

The sensor sensitivity function $f(\theta_z)$ usually takes positive values. This can be seen from Eq. (10). Therefore, the following measures should be taken. When a tensile strain $\varepsilon(z,t)$ occurs on the upper surface of the beam at the position z, the same amount of compressive strain $-\varepsilon(z,t)$ should occur on the lower surface of the beam at the same position.

In addition, $f(\theta_z)\varepsilon(z,t)dz$ of Eq. (13) is equal to $(-f(\theta_z))(-\varepsilon(z,t)dz)$. Thus the sensor sensitivity $f(\theta_z)$ can

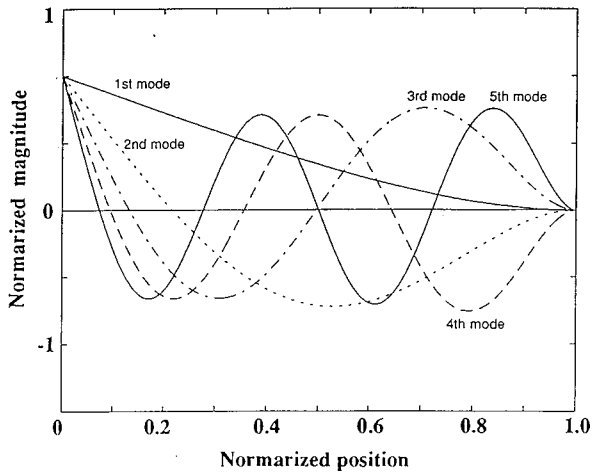

FIG. 2. Second derivatives with respect to position of the mode shapes for a cantilevered beam.

take a negative value by using the lower surface.
When both surfaces of the beam are not available for sensor placement, employment of a bipolar weighting method will overcome the problem as described later. With this method, two optical fibers attached on either surface of the beam may achieve the modal filtering.

II. THE METHOD FOR MEASURING SENSOR SENSITIVITY

A. The principle for measuring sensor sensitivity

In the preceding section, when the fiber is attached to the beam with an appropriate angle with respect to the longitudinal direction, the desired mode is achieved. In order to decide the fiber placement for modal filtering, the relationship between the attachment angle θ_z and its sensitivity, $f(\theta_z)$ needs to be clarified. Therefore, a simple method for measuring the sensor sensitivities with respect to various fiber attachment angles is proposed in this section.

Now, consider the case where an optical fiber is attached to a beam at the same constant orientation with respect to the longitudinal direction of the beam, and the beam oscillates at its first natural frequency ω_1 at a constant amplitude A.

When the beam oscillates solely in its first vibration mode, the beam strain can be denoted as

$$\varepsilon(z,t)=-\frac{h}{2}\frac{\partial^2 w(z,t)}{\partial z^2}=-\frac{h}{2}\Phi_1''(z)\eta_1(t)$$

$$=-\frac{h}{2}\Phi_1''(z)\{A\sin\omega_1 t\}. \tag{21}$$

By substituting Eq. (21) for Eq. (12), the equation becomes

$$I(t)=I_1+I_2\{\cos(\Delta\beta\ell+\Delta\psi)+\Delta\phi\sin(\Delta\beta\ell+\Delta\psi)\sin\omega_1 t\}, \tag{22}$$

where

$$\Delta\phi=\Delta\beta f(\theta)\frac{Ah}{2}\int_\Omega\Phi_1''(z)dz=\Delta\beta f(\theta)\Delta L_A \tag{23}$$

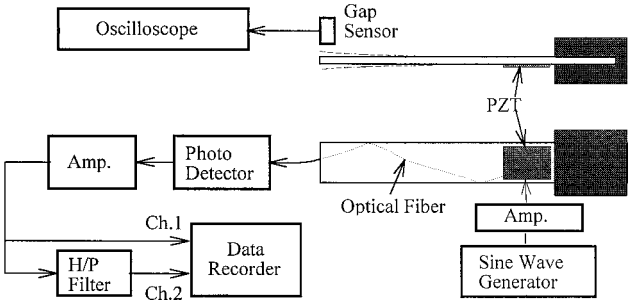

FIG. 3. Experimental setup for measuring sensor sensitivity.

$$\Delta L_A=\frac{Ah}{2}\int_\Omega\Phi_1''(z)dz, \tag{24}$$

where $\Delta\phi$ is much smaller than 1. The symbol ΔL_A of Eq. (23) denotes an oscillation amplitude of the length of surface of the beam in the case that the beam oscillates at its first natural frequency at a constant amplitude A. Moreover when α, X, and Y are set to be $\alpha=\Delta\beta l+\psi$, $X=I_1+I_2\cos\alpha$, and $Y=I_2\Delta\phi$, respectively, and α is eliminated, the relationship between X and Y is described by the equation of an ellipse

$$\left(\frac{X-I_1}{I_2}\right)^2+\left(\frac{Y}{I_2\Delta\phi}\right)^2=1, \tag{25}$$

where X and Y, respectively, denote the DC and AC components of the intensity emitted from the endface of the fiber.

$$\Delta\phi=2Y_{\max}/\{X_{\max}(0)-X_{\min}(0)\}. \tag{26}$$

Consider $\Delta\phi$ with respect to fiber orientation when the fiber is attached at a different constant orientation. It may be noted from Eq. (23), that when the beam oscillates at the same amplitude and natural frequency of the first mode, the ratio of the attachment angle θ to $\Delta\phi$ is equal to the ratio of θ to $f(\theta)$. This is because both $\Delta\beta$ and ΔL_A are constant.

B. The results of sensor sensitivity

Based on the previous principle, the experimental setup of Fig. 3 illustrates the measurement of the sensor sensitivity with respect to various sensor orientations.

Consider an aluminum cantilevered beam whose length, width, and thickness are 400, 40, and 3.5 mm, respectively. A Pb(Zr-Ti)O_3(PZT) patch, whose length and width are 40 and 60 mm, respectively, acting as an exciter, is attached to the opposite surface of the fiber attachment's surface by using epoxy adhesive.

The optical fiber is attached angles of 0, 2, 5, 10, 15, 20, 25, 30 deg, respectively, with respect to the longitudinal direction of the beam by using both face's adhesive tape. The part of the fiber jutting out of the beam is formed into a circle and turned down. That is, the fiber is attached on the beam in a zigzag shape with constant attachment angle due to the restriction of the beam's width. While the piezoelectric transducer (PZT) is supplied by an alternating current of 14 Hz, the beam oscillates at the first natural frequency. The amplitude of the beam is controlled by the supplied voltage and is measured as a deflection of the end of the beam using a gap sensor.

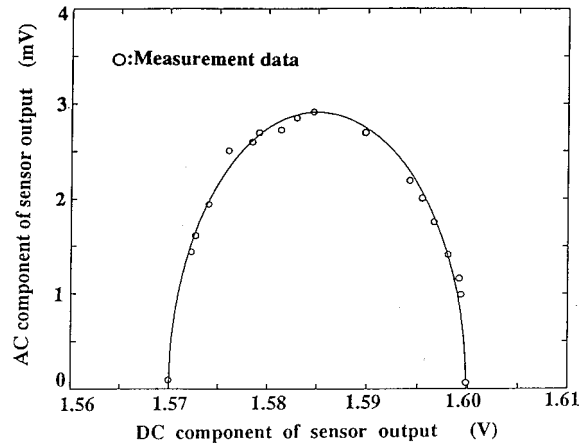

FIG. 4. Relationship between DC and AC component of sensor output.

The intensity emitting from the endface of the optical fiber passes through the photodetector and amplifier and is then changed into a voltage signal. This voltage signal is separated into two parts as shown in Fig. 3. One is recorded as a nonprocessed signal and the other is recorded after passing through a 2-Hz high pass filter. Data are analyzed using the above method for various orientations, then the values for $\Delta\phi$ corresponding to the various orientations are estimated. Figure 4 illustrates the calculations when the optical fiber is attached at constant zero angle. The DC and AC components of the optical output are plotted on the *x*-axis and *y*-axis, respectively. The solid line of the figure denotes the elliptical equation calculated using the two values for *X* nearest the *x*-axis and the maximum value for *Y*. The difference between the two *x* values corresponds to the length of the minor axis of the ellipse. The maximum *y* value corresponds to the half length of the major axis. The effectiveness of the method is indicated by the close agreement of the experimental values and the theoretical results.

Figure 5 shows the relationship between the oscillation amplitude of the surface of the beam estimated from the beam amplitude using a gap sensor located at the end of the beam.

The oscillation amplitude ΔL is calculated using

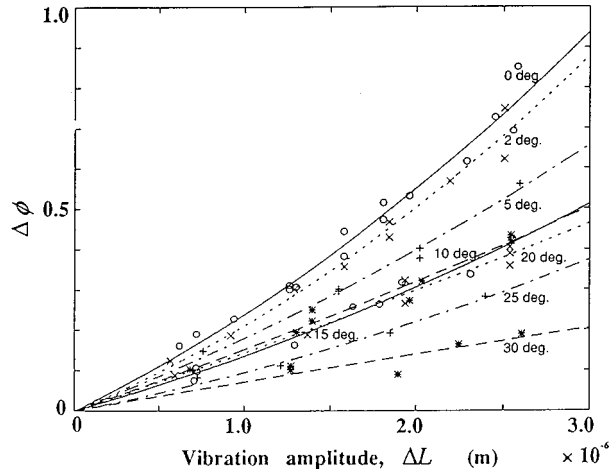

FIG. 5. Relationship between ΔL and $\Delta\phi$ for different values of the sensor orientation parameter.

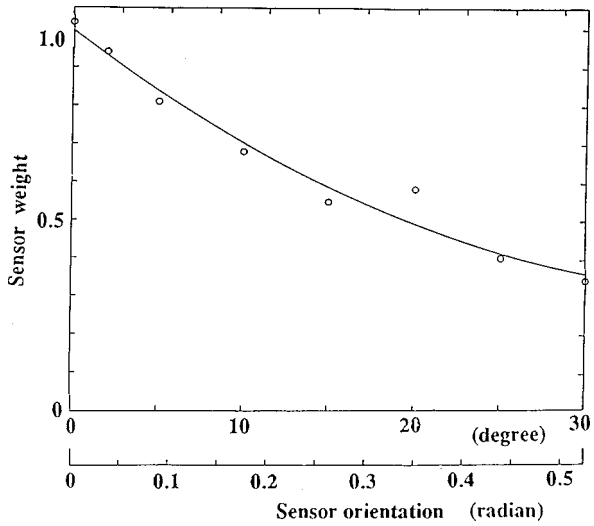

FIG. 6. Effect of sensor orientation on sensitivity.

$$\Delta L = \frac{h(k_1/L)\sin k_1 \sinh k_1}{2(\cos k_1 \sinh k_1 - \sin k_1 \cosh k_1)} w_0, \tag{27}$$

where h is the thickness of the beam (m); L is the length of the beam (m); w_0 is the deflection amplitude of the end of the beam (m); and k_1 is the first solution of $\cos k_1 \cosh k_1 = -1$. Figure 5 reveals that the larger the attachment angle with respect to the longitudinal direction of the beam gets, the smaller $\Delta\phi$ becomes. That is, the smaller the sensor sensitivity $f(\theta)$ becomes. Since the sensor sensitivity with regard to the attachment angle is given as the gradient, $\Delta\phi/\Delta L$; if it is regarded as independent of the strain of the fiber, the relationship between $\Delta\phi$ and ΔL must be linear. The figure, however, suggests that $\Delta\beta$ is a function of the fiber strain because the experimental results agree well with the curve calculating using the second-order least-squares method. Nevertheless, as the fiber strain is assumed small, and the field $\Delta\beta$ constant, the sensor sensitivity may be regarded as the slope of the curve in the figure.

As a result, Fig. 6 illustrates the normalized relationship between sensor orientation and sensor weight after the first maximum of the sensor sensitivity of the zero-degree orientation. An empirical equation for the sensor weight function obtained by using a second-order least-squares method is

$$f(\theta) = 1.3579\theta^2 - 1.9185\theta + 1.0000$$

$$\text{under the condition that } 0 \leqslant \theta \leqslant 0.52 \quad (\theta\text{: radians}). \tag{28}$$

If the relationship between sensor orientation and sensor sensitivity becomes clear before the sensor sensitivity takes a zero value, modal filtering is theoretically possible using the above method. In order to achieve $f(\theta)=0$, however, the fiber orientation must be at a right angle to the longitudinal direction of the beam. It is assumed, therefore, that right-angle attachment to the beam is needed in order to give $f(\theta)$ a zero weight. Consequently, it becomes difficult to attach the fiber to the beam because of the long length necessary to achieve modal filtering.

Moreover, the vibration mode of the beam is subject to change. The reason is as follows:

(i) Fiber attachment angle needs to be altered spacially along the beam for modal filtering;
(ii) The part of the fiber jutting out of the beam must be turned down due to the restriction of the beamwidth;
(iii) The number of turning down times increases as the attachment angle becomes larger;
(iv) As a result, the fiber is massed in the place where the attachment angle is large, and the beam's stiffness with respect to the longitudinal direction must be changed.

Therefore, in order to solve this problem, a bipolar weighting function method is proposed by which an arbitrary orientation range for fiber attachment is allowed in a design procedure for modal filtering.

C. The method using a bipolar weighting function

Now assume that the sensor sensitivity function $f(\theta_z)$ is restricted to a range of values

$$a \leqslant f(\theta_z) \leqslant b \quad (0 \leqslant a < b). \tag{29}$$

Let $g(z)$ denote a desired distributed-effect function, which can be expressed as

$$g(z) = g_+(z) - g_-(z), \tag{30}$$

where

$$g_+(z) = \begin{cases} g(z), & 0 \leqslant g(z), \\ 0, & g(z) \leqslant 0, \end{cases} \tag{31}$$

$$g_-(z) = \begin{cases} 0, & 0 \leqslant g(z), \\ -g(z), & g(z) \leqslant 0. \end{cases} \tag{32}$$

The desired weighting function $g(z)$ can be realized by defining two modal optical fiber sensitivity profiles

$$f_+(\theta_z) = (b-a)g_+(z) + a, \tag{33}$$

$$f_-(\theta_z) = (b-a)g_-(z) + a. \tag{34}$$

Equations (33) and (34) satisfy the constraints given in Eq. (29). The desired weighting function $g(z)$ is also expressed as

$$g(z) = \frac{1}{b-a}\{f_+(\theta_z) - f_-(\theta_z)\}. \tag{35}$$

Consequently, by using a bipolar weighting function, the AC component of the optical fiber output is given as

$$I(t) = (b-a)\tilde{I}_2 \Delta\beta \int_\Omega g(z)\varepsilon(z,t)dz$$

$$= \tilde{I}_2 \Delta\beta \left[\int_\Omega f_+(\theta_z)\varepsilon(z,t)dz - \int_\Omega f_-(\theta_z)\varepsilon(z,t)dz \right], \tag{36}$$

and it is shown that modal filtering is possible.

Although Eq. (36) indicates the necessity of taking a differential signal between two optical fibers attached to one surface of the beam, this signal is also extractable by utilizing both faces of the beam. By utilizing both faces of the beam, the differential signal of the second term in Eq. (36) becomes an additional signal because the $\varepsilon(z,t)$ signal changes to an $-\varepsilon(z,t)$ signal. This means that modal filtering is possible using only one optical fiber. When two optical fibers are placed on one surface of the beam, subtracting the fiber sensor outputs with the sensitivity distribution of $f+(\theta z)$ and $f-(\theta z)$ corresponding to each optical fiber sensor, respectively, performs the modal filtering, thereby yielding Eq. (36).

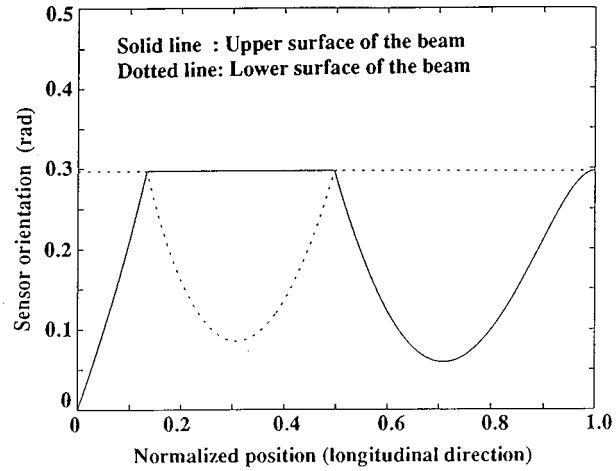

FIG. 7. Sensor orientation on the cantilevered beam for third vibration-mode filtering.

III. EXPERIMENT

In order to justify this theory, an experiment for modal filtering is carried out using an aluminum cantilevered beam of dimensions of $400 \times 40 \times 3$ mm. The fiber sensor orientation and its placement for the third mode filtering, employing the above technique, are shown in Figs. 7 and 8.

The design procedure for modal filtering starts with a choice for the values of a and b in Eq. (29). When performance using a shorter optical fiber is desired, a and b should be chosen so that a is close in value to b, after b is set to 1.

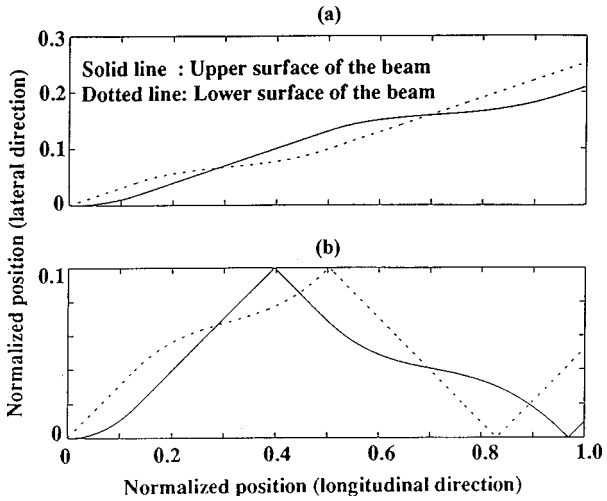

FIG. 8. Sensor placement for the 3rd vibration-mode filtering [(a) in theory (b) in practice].

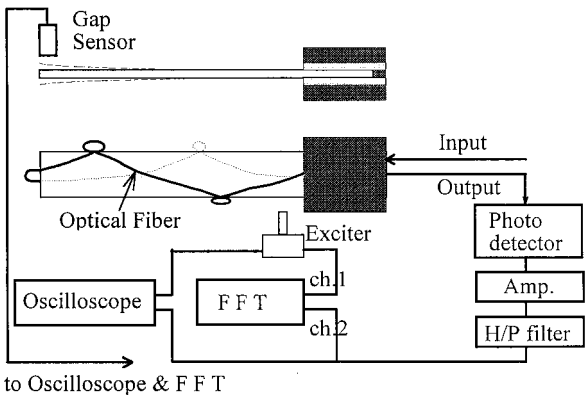

FIG. 9. Experiment setup for modal filtering.

This means that the fiber should be attached to the beam at an angle close to zero.

A rather inconvenient feature of this attachment measure is the requirement that the fiber should be attached very precisely to the beam. This is due to the fact that the weighting values need to be controlled by using the small range of attachment angles. In this example, a and b are set to 0.55 and 1, respectively.

Figure 7 shows the fiber sensor orientation in this case. In this figure, the solid line and dotted line denote the fiber orientation with respect to the beam position on the upper and lower surfaces of the beam, respectively. The reason for the existence of a range for constant angle attachment is that $f_+(z)$ and $f_-(z)$ take constant value of ''a'' in the range. This is due to the fact that $g_+(z)$ and $g_-(z)$ in Eqs. (31) and (32) are zero in the range.

Figure 8 shows the calculated fiber placement based on the above results. Although the fiber placement of the upper figure is more proper, the lower type placement is employed because of the restriction on the beamwidth. In the lower figure, the fiber is turned down at the end of the beamwidth because of the importance of fiber attachment angle as opposed to fiber placement.

Figure 9 shows the experimental setup for modal filtering. The sensor is a bow-tie optical fiber, employed as a two-mode optical fiber, attached to the beam with double-sided sticky tape. A He–Ne laser serves as a light source. When the beam is impacted by an impulse hammer at a point 15 mm away from the fixed end of the beam, the fiber experiences some strains. The optical signal generated then goes into a fast Fourier transform (FFT) analyzer through the photodetector, amplifier, and high pass filter. The impacted force signal also goes into the FFT analyzer at the same time. At the same time, the deflection at the end of the beam can be measured by a gap sensor.

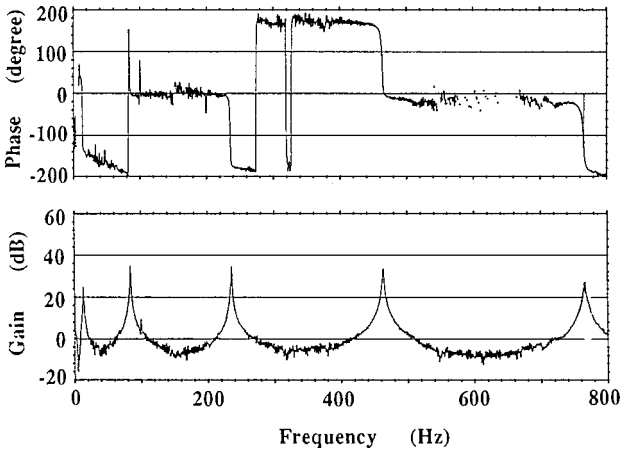

FIG. 11. Amplitude characteristics of the optical fiber sensor output for the case of attachment to the beam in a straight line parallel to the beam's longitudinal direction.

Figure 10 shows the frequency transfer function when the input signal is an impact force and the output signal is the deflection of the end of the beam. Figure 11 shows the frequency transfer function when the input signal is an impact force and the output signal is from an optical fiber sensor attached in a straight line parallel to the beam's longitudinal direction. Finally, Fig. 12 shows the frequency transfer function when the optical fiber sensor is placed on the beam so as to filter the third mode, as shown in Fig. 8. The frequency range is 0 to 800 Hz, there being five vibration modes of the beam in this range.

The number of peaks in the gain curve of Fig. 10 reveals that all of the first five modes are excited. Figure 11 suggests that attachment in a straight line does not allow modal filter-

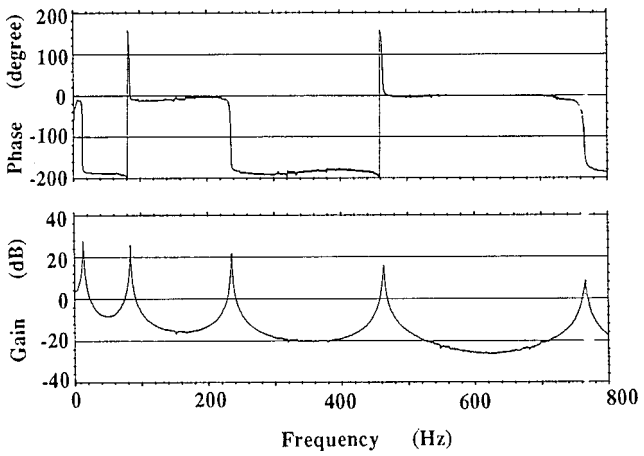

FIG. 10. Amplitude characteristics of the gap sensor output at the end of the cantilevered beam.

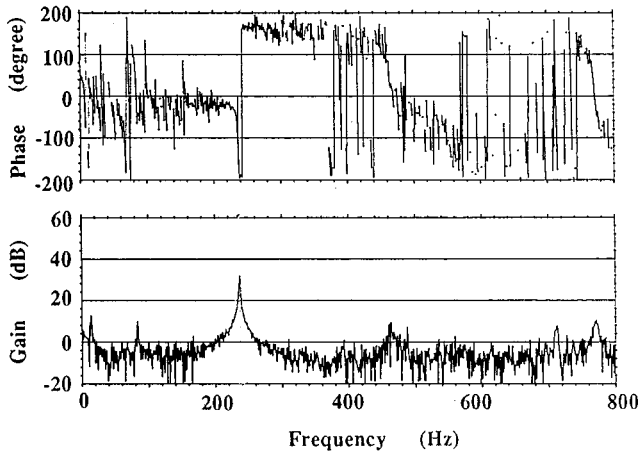

FIG. 12. Amplitude characteristics of the optical fiber sensor output for the case of attachment to the beam for third vibration-mode filtering.

ing. Finally, Fig. 12 shows that signals from modes other than the third mode are detected, but the difference between these signals and the third-mode signal is over 20 dB, with a phase shift of 180 deg. This indicates that the signal is sufficient for using as a controlled signal.

Although the aforementioned method is for one-dimensional structures, it can be easily extended to two-dimensional structures. For this purpose, two steps need to be taken. First, an angle between the orientation of an optical fiber placement and the longitudinal direction of a planar structure must be narrow, and hence the crosstalk due to the lateral direction of the planar structure becomes negligible. Second, a design procedure of a one-dimensional modal filter using PVDF film sensors[7] should be introduced. This methodology utilizes nodal lines of the structure for sensor placement, with the result that only the desired modal signals are obtained while unwanted modes are suppressed.

IV. CONCLUSIONS

A design procedure for vibration modal filtering of one-dimensional structures using an optical fiber has been proposed, which takes advantage of the fact that sensor sensitivity, namely the sensor weight, depends on optical orientation with respect to the longitudinal direction of the beam. Theoretical predictions match the experimental results well. The characteristics of a two-mode optical fiber output signal are clarified, and a mathematical model for modal filtering is constructed for the case where the sensor orientation is used for altering sensor sensitivity. It is shown that it is possible to filter a desired vibration mode by altering sensor sensitivity spatially, utilizing the orthogonality of the mode shapes. In the process, a method is devised for measuring sensor sensitivity with respect to the sensor orientation. In addition to this, a design procedure for optimal fiber placement utilizing bipolar function is proposed.

Consequently, it becomes possible to design a filter using a range of arbitrary attachment angles. Finally, experimental results confirm theoretical predictions and efficient vibration filtering is demonstrated.

[1] D. Gloge, ''Weakly guiding fibers,'' Appl. Opt. **10**, 2252–2258 (1971).
[2] M. R. Layton and R. O. Bucaro, ''Optical fiber acoustic sensor utilizing mode-mode interference,'' Appl. Opt. **18**, 666–670 (1979).
[3] D. Cox, D. Thomas, K. Reichard, D. K. Lindner, and R. O. Claus, ''Vibration control of a flexible beam using a distributed fiber optic sensor,'' in *Proceedings of the 28th IEEE Conference on Decision and Control, Tampa, FL* (IEEE, New York, 1989), pp. 2685–2686.
[4] K. Murphy, M. S. Miller, A. M. Vengsarker, and R. O. Claus, ''Elliptical-core, two-mode, optical fiber sensor implementation methods,'' J. Lightwave Technol. **8**, 1688–1696 (1990).
[5] J. S. Sirkis and H. W. Haslach, Jr., ''Interferometric strain measurement by arbitrary configured, surface-mounted, optical fibers,'' J. Lightwave Technol. **8**, 1497–1503 (1990).
[6] L. A. Gould and M. A. Murray-Lasso, IEEE Trans. Autom. Control. **11**, 729 (1966).
[7] N. Tanaka, Y. Kikushima, M. Kuroda, and H. Senba, ''Distributed parameter modal sensors,'' Trans. Jpn. Soc. Mech. Eng., Ser. C **62–596**, 1418–1425 (1996).
[8] A. M. Vengsakar, B. R. Fogg, W. V. Miller, K. A. Murphy, and R. O. Claus, ''Elliptical-core, two-mode optical fibers,'' Electron. Lett. **27**, 931–932 (1991).
[9] K. M. Reichard, ''Distributed-effect modal optical fiber sensors for flexible structure control,'' Ph.D. thesis, Virginia Polytechnic Institute and State University 1991.

Multivariable feedback active structural acoustic control using adaptive piezoelectric sensoriactuators

Jeffrey S. Vipperman[a)]
Department of Mechanical Engineering, 5711 Boardman Hall, University of Maine, Orono, Maine 04401-5711

Robert L. Clark
Department of Mechanical Engineering and Materials Science, Box 90300, Duke University, Durham, North Carolina 27708-0300

(Received 9 May 1997; accepted for publication 25 August 1998)

An experimental implementation of a multivariable feedback active structural acoustic control system is demonstrated on a piezostructure plate with pinned boundary conditions. Four adaptive piezoelectric sensoriactuators provide an array of truly colocated actuator/sensor pairs to be used as control transducers. Radiation filters are developed based on the self- and mutual-radiation efficiencies of the structure and are included into the performance cost of an $\mathscr{H}_2$ control law which minimizes total radiated sound power. In the cost function, control effort is balanced with reductions in radiated sound power. A similarity transform which produces generalized velocity states that are required as inputs to the radiation filters is presented. Up to 15 dB of attenuation in radiated sound power was observed at the resonant frequencies of the piezostructure. © *1999 Acoustical Society of America.* [S0001-4966(98)04812-7]

PACS numbers: 43.40.Vn [PJR]

INTRODUCTION

Control of structures and their associated sound radiation has been a topic of interest for both civil and military applications. Active control techniques have been found to be complimentary to passive control methods, which are best suited for high frequency (>1 kHz) noise and vibration. Applications for control include reduction of interior and exterior noise in aircraft, submarines, appliances, automobiles, and machinery. In active noise control (ANC), acoustic sensors are used to make measurements at points in the acoustic field and the information is then used to form a control signal. Loudspeakers are typically used to create the secondary field which is intended to cancel the primary or disturbance field. The same concept applies for active vibration control (AVC), except that structural based sensors and actuators are used. For ANC, it is not always feasible to measure the acoustic field, particularly for underwater or aviation applications. For these cases, the radiated acoustic power can often be related to structural-based measurements which then form the basis of the acoustic control objective.[1,2] This concept of controlling the radiated sound power through the realization of adaptive structures was proposed by Clark and Fuller[3,4] and is frequently denoted as active structural acoustic control, or ASAC. ASAC can also be applied to increase the transmission loss across panels.

Early implementations of ASAC used feedforward control topologies. The objective function minimized by the adaptive feedforward algorithm was typically composed of measurements of the far-field acoustic pressure[3] or from near field sensors[5] which naturally emphasized control of the modes which are efficient at radiating sound. Maillard and Fuller[1] developed real-time estimation filters for feedforward control of sound radiation that were based on an array of structural measurements which were considered to be discrete monopole radiators. Feedback ASAC has been largely confined to analytical studies.[6–8] The cost functionals typically provided an ad hoc method of more heavily weighting the modes of the structure that are known to be efficient acoustic radiators and similarly provided diminished weighting of the inefficiently radiating modes. Baumann *et al.*[2] used frequency-shaping concepts[9] to develop radiation filters which augment the structural states of the plant to proportionally weight each mode proportional to it's radiation efficiency. An analytical study[2] showed that radiation filters allow more control energy to be focused into the modes most responsible for the sound radiation.

In this work, a new transducer technology known as adaptive piezoelectric sensoriactuators (APSAs)[10,11] will be used to experimentally demonstrate a multi-input multi-output (MIMO) feedback active structural acoustic control (ASAC) system. The testbed is a simply supported plate with four adaptive piezoelectric sensoriactuators as control transducers. These self-sensing actuators provide truly collocated sensor/actuator pairs from each piezoceramic patch which greatly enhances stability robustness of the feedback controller. The chronological steps taken to implement the experimental ASAC control system were:

(1) Implement a 4×4 array of APSAs on a simply supported plate testbed;
(2) Experimentally measure all 16 frequency response functions (FRFs) between each possible APSA pairs;
(3) Fit a 20-state, four-input, four-output ($4i4o$) state-space model to the 16 measured FRFs;

[a)]Work performed as a Graduate Research Assistant at Duke University.

(4) Perform a similarity transform on the state space model such that the generalized velocities appear as internal states;
(5) Append analytical radiation filters to the transformed state space model of the piezostructure;
(6) Formulate an $\mathscr{H}_2$ cost functional based on acoustic radiation output of the model and design the control system that will minimize this cost;
(7) Experimentally implement the control system and measure open- and closed-loop acoustic power to evaluate the control system performance.

In Sec. I, the basic $\mathscr{H}_2$ control design philosophy is presented. Following in Sec. II is a description of the experimental setup used to demonstrate ASAC using adaptive piezoelectric sensoriactuators. Section III contains information pertaining to modeling the structural acoustic system, including the system identification of the plate piezostructure, appending analytical radiation filters to the plate model, and performing a similarity transform that produces generalized velocity states that are required as inputs to the radiation filters. Finally the results of the experiments are presented in Sec. IV and a summary of the findings is presented in Sec. V.

I. CONTROLS

$\mathscr{H}_2$ control design techniques in conjunction with linear quadratic Gaussian (LQG) weightings were used for the feedback active structural acoustic control design. Static feedback ASAC designs have been previously studied.[12] The cost functionals include frequency-shaping[9] that is proportional to the modal radiation efficiencies, as demonstrated analytically by Baumann[2] and later incorporated by others.[11–13] In this method, time-domain radiation filters are used to augment the states of the state-space piezostructure model such that the root-mean-square error variable is proportional to radiated sound power. In this way, the control system is able to focus more effort into modes which are efficient at radiating sound and less effort into those modes which are inefficient radiators.

The generalized plant model is of the form:

$$\dot{x} = \mathbf{A}\mathbf{x} + \mathbf{B}u + \mathbf{w_d}, \tag{1}$$

$$y = \mathbf{C}\mathbf{x} + \mathbf{w_n}, \tag{2}$$

where x is the state vector, $\dot{x}$ is the derivative of the state vector, and u is the 4×1 vector of control voltages to the piezoelectric sensoriactuators. The system matrix, **A**, and input and output influence matrices, **B** and **C**, respectively will be determined by experimental system identification of the piezostructure control paths. The process noise, $\mathbf{w}_d$, and sensor noise vectors, $\mathbf{w}_n$, are Gaussian processes that satisfy: $\mathbf{E}[\mathbf{w_d}(t)\mathbf{w_d}(\tau)^T] = \mathbf{W}\delta(t-\tau)$, $\mathbf{E}[\mathbf{w_n}(t)\mathbf{w_n}(\tau)^T] = \mathbf{V}\delta(t-\tau)$, $\mathbf{E}[\mathbf{w_n}(t)\mathbf{w_d}(\tau)^T] = 0$. Each state of the plate model was excited by the process noise, $\mathbf{w}_d$, and sensor noise, $\mathbf{w}_n$, was used to corrupt the four sensoriactuator outputs. Experimental characterization of the process and sensor noises was not conducted, but rather the magnitudes of these noise processes served as design parameters that were determined heuristically. The LQG cost is of the form:

$$J = \mathbf{E}\left[\lim_{T\to\infty}\frac{1}{T}\int_0^T \mathbf{z}(t)^T\mathbf{z}(t)dt\right], \tag{3}$$

$$J = \mathbf{E}\left[\lim_{T\to\infty}\frac{1}{T}\int_0^T (\mathbf{x}_v(t)^T\mathbf{Q}(\omega)\mathbf{x}_v(t) + \mathbf{u}(t)^T\mathbf{R}\mathbf{u}(t))dt\right], \tag{4}$$

where $\mathbf{Q}(\omega)$ is a positive semi-definite, frequency-dependent weighting matrix which determines the error or performance penalty that is proportional to radiated sound power, and **R** is a positive definite control penalty weighting matrix. Note that this cost functional is based upon the generalized velocity states, $\mathbf{x_v(t)}$, of the piezostructure such that the analytical radiation filters can be appended to each mode. This result will require a similarity transform be performed on the state-space model obtained from system identification of the piezostructure testbed.

Note from Fig. 1 that the $\mathscr{H}_2$ control problem has been cast in the standard two-port form with LQG-style weightings. There are optimization methods readily available to determine the optimal compensator for this configuration.[14]

II. EXPERIMENTAL SETUP

A. Simply-supported plate testbed

A classic simply supported plate test bed was designed and assembled. The x-y dimensions of the 2 mm thick steel plate are given in Fig. 2. Details of the construction can be found in the dissertation by Vipperman.[11] The locations of the four arbitrarily placed PZTs used for the control transducers are shown in Fig. 2. Also shown in Fig. 2 is the input location of a Ling Dynamics Systems V203 shaker, which was attached to the back of the plate frame and used for the disturbance excitation source.

B. Electronic hardware

Real-time signal processing was performed with a Spectrum Signal Processing, Inc. 50-MHz TMS320C40-based DSP system in conjunction with the Spectrum PC16IO8 16-input and 8-output analog I/O Card. Custom DSP software conveniently allowed the user to alternate between off-line training of the APSAs[10] or implementing the fixed feedback control as desired. Although you can theoretically train the APSAs simultaneously with control, this was found unnecessary since the APSAs remained stationary within the time scale of the system identification and control experiments. A sampling rate of 4 kHz was used for both the training of the APSAs and the active control experiments.

Many other peripheral items were needed to perform tasks such as filtering, adding or removing gain, and generating, measuring and analyzing signals, etc. A custom-designed sound intensity probe[15] was used to obtain sound intensity readings near the surface (70 mm) of the plate, allowing the sound power generated by the plate to be calculated by performing a discrete integration of the intensity across the measurement grid. Two high-quality Realistic electret tie-clip microphones spaced a distance of 43 mm in a handheld aluminum support comprised the sound intensity probe. Positioning errors between measurements were elimi-

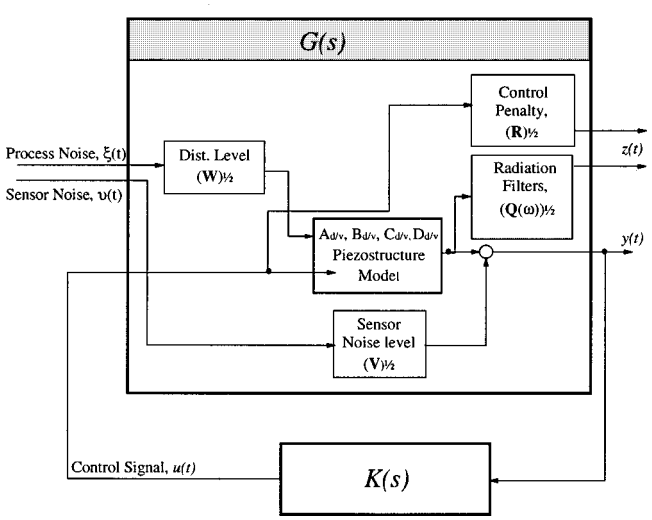

FIG. 1. Generalized plant used in two-port control design.

nated by performing the open-loop and three closed-loop measurements sequentially while the probe was positioned at each point. The high quality Brüel and Kjær 4190 microphone was used to calibrate the magnitude of each transducer. Transfer functions between the two electret microphones permitted phase correction factors for the intensity probe to be computed across the bandwidth in which measurements would be made.[15,16] Statistical tests for accuracy and repeatability were performed to verify the operation of the intensity probe. Far-field pressure measurements were taken using a Brüel and Kjær type 4190 microphone with type 5935 power supply. Although the pressure measurements are not presented, they were used to corroborate the sound power calculations. Additional hardware items include Ithaco 4302 Low pass Filters, Krohn-Hite 7600 Wideband Amplifiers, AVC Series 790 Wide band Amplifiers, DSPT, Inc. SigLab 2022 spectrum analyzers, and Ithaco 453 Gain Preamplifiers. A schematic of the experimental setup is depicted in Fig. 3.

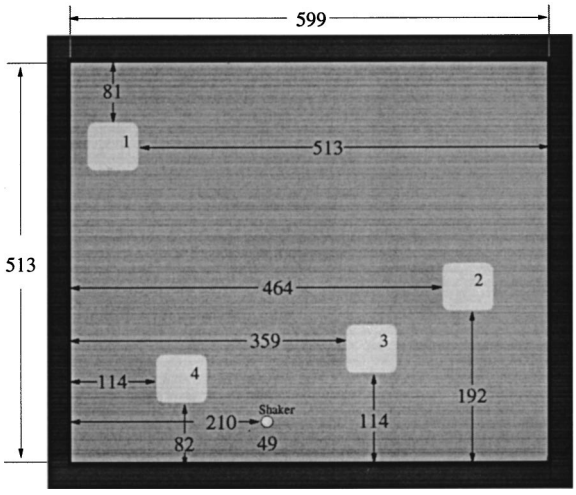

FIG. 2. Schematic diagram of experimental simply supported plate showing arbitrary locations of four PZT bending actuators (dimensions in mm).

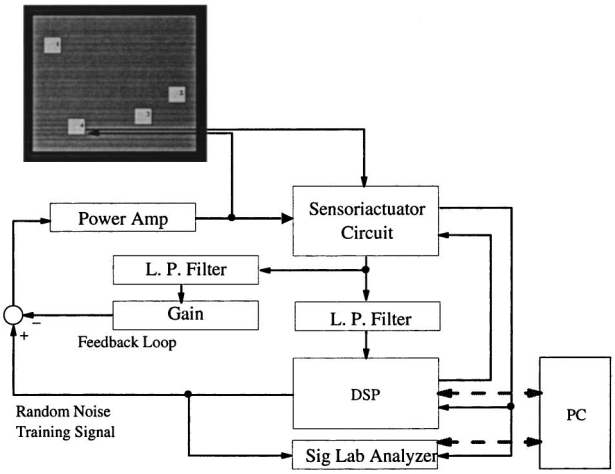

FIG. 3. Schematic diagram of hardware setup used for a single channel APSA with the plate test bed.

C. Adaptive piezoelectric sensoriactuators

Adaptive piezoelectric sensoriactuator (APSA) technology is mature and has been demonstrated for complex structural control problems.[11] The analog hardware was designed by the Adaptive Systems and Structures Laboratory at Duke University and constructed by NASA-Langley Research Center. The current capability of the hardware is to simultaneously adapt four channels of the piezoelectric sensoriactuator concurrently[10] using four separate, uncorrelated, white noise training signals generated by the DSP hardware. The adaptive piezoelectric sensoriactuators were typically trained once and then fixed for the duration of the system identification or control phases of the experiments.

D. Test facilities

Acoustic experiments were performed in the Duke University anechoic chamber test facility. The chamber has a volume of approximately 27 m^3 and a cutoff frequency of approximately 250 Hz. A baffle which spanned the width and height of the chamber was constructed from 13 mm thick plywood and 50×100 mm framing studs. A picture of the simply supported plate installed flush with the baffle wall is shown in Fig. 4. Figure 4 also includes a view of the sound

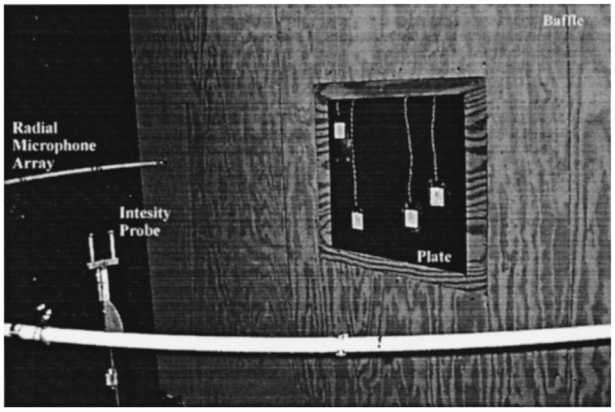

FIG. 4. Picture of simply supported plate test bed mounted in baffle wall inside anechoic chamber.

TABLE I. Modal properties of experimental plate test bed.

Mode	Modal indices	Strong acoustic radiator?	Theory natural freq. (Hz)	Measured resonant freq. (Hz)	Measured damping ratio
1	(1,1)	*	33.6	32.0	2.56%
2	(2,1)		76.2	70.8	1.56%
3	(1,2)		91.6	85.9	1.06%
4	(2,2)		135	125	0.64%
5	(3,1)	*	148	136	0.41%
6	(1,3)	*	189	173	0.92%
7	(3,2)		205	191	0.25%
8	(2,3)		231	212	0.42%
9	(4,1)		247	227	0.39%
10	(3,3)	*	302	279	0.20%

intensity probe which was used to measure intensity near the surface of the plate. The chamber is fitted with a radial microphone array seen in the figure which was not used in this experimental setup.

III. SYSTEM MODEL

A. System identification

Once the four APSAs were trained, all sixteen possible frequency response functions (FRFs) between the four APSAs were experimentally computed between 0 and 500 Hz. FRFs were measured in groups of four whereby one piezoceramic patch was driven with a random noise signal and the responses of all four patches were measured simultaneously by the Siglab spectrum analyzer. A four-input, four-output $(4i4o)$ state-space model having 40 states was then fit to the 16 FRFs using the SmartID[17] software package. The state-space model corresponds to the matrices $\mathbf{A}\in\Re^{40\times 40}$, $\mathbf{B}\in\Re^{40\times 4}$, $\mathbf{C}\in\Re^{4\times 40}$ which are presented in Eqs. (1) and (2). A typical comparison of measured and modeled FRFs is shown in Fig. 5 which corresponds to the PZT located at normalized plate coordinates {0.23, 0.20}. Similar results were achieved for all control paths of the multivariable system resulting in an accurate plant model which is essential for good control system performance.

The curve-fit of the FRFs allowed the resonant, modal properties of the structure to be extracted. The analytical and experimental modal properties of the plate are presented in Table I, where the modes are numbered consecutively in order of their resonant frequencies as well as listed by the corresponding (x,y) modal indices. In addition, Table I indicates whether a particular mode is an efficient sound radiator or not. Analytical resonant frequencies are slightly overestimated due to the weak torsional-spring boundary conditions of the experimental test rig which were not modeled analytically.

B. Appending radiation filters to experimentally determined models

Next, the analytical radiation filters for the plate were designed[2,11–13] and appended to the state-space model of the plate in order to create the acoustic cost functional for the control system. The inputs to the analytical radiation filters are the plate generalized velocity states (modal velocities for

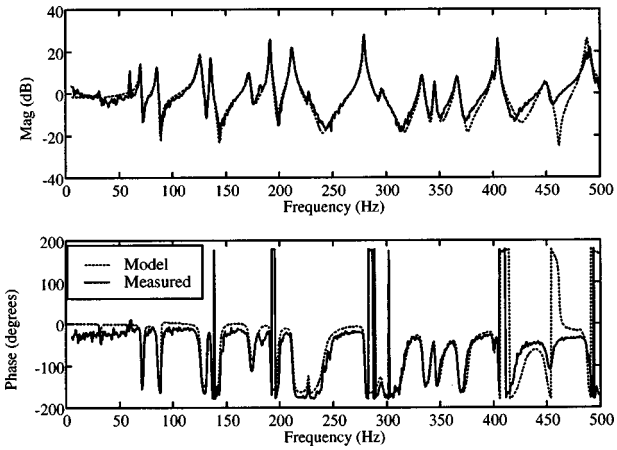

FIG. 5. Analytical and experimental frequency response functions across the adaptive piezoelectric sensoriactuator centered at normalized coordinates {0.23, 0.20}.

an ideal plate with no included mass or stiffness).[2] The internal states resulting from the system identification process unfortunately do not correspond to generalized plate velocities, but rather correspond to one of the infinitude of other valid state-space realizations for the system model. Two different state space realizations of the same system model, $\{\mathbf{A},\mathbf{B},\mathbf{C}\}$ and $\{\overline{\mathbf{A}},\overline{\mathbf{B}},\overline{\mathbf{C}}\}$, each having state vectors, $\mathbf{x}(t)$ and $\overline{\mathbf{x}}(t)$, respectively are related through the similarity transform, $\mathbf{T}_{\text{sim}}$, as[18]

$$\overline{\mathbf{x}}(t)=\mathbf{T}_{\text{sim}}\mathbf{x}(t), \tag{5}$$

$$\overline{\mathbf{A}}=\mathbf{T}_{\text{sim}}^{-1}\mathbf{A}\mathbf{T}_{\text{sim}}, \tag{6}$$

$$\overline{\mathbf{B}}=\mathbf{T}_{\text{sim}}^{-1}\mathbf{B}, \tag{7}$$

$$\overline{\mathbf{C}}=\mathbf{C}\mathbf{T}_{\text{sim}}, \tag{8}$$

provided that $\mathbf{T}_{\text{sim}}$ exists.

Analytical piezostructures models based on Galerkin's method whereby analytical mass, stiffness, and damping matrices are determined results in a state-space model having physical states that correspond to generalized plate velocities, $\dot{\boldsymbol{\eta}}(t)$, and displacements, $\boldsymbol{\eta}(t)$,[13] as:

$$\mathbf{x}(t)=\begin{Bmatrix}\boldsymbol{\eta}(t)\\ \dot{\boldsymbol{\eta}}(t)\end{Bmatrix}, \tag{9}$$

and the following corresponding system matrix, designated $\mathbf{A}_{d/v}$:

$$\mathbf{A}_{d/v}=\begin{bmatrix}0 & \mathbf{I}\\ (\mathbf{M}_{\text{tot}})^{-1}(\mathbf{K}_{\text{tot}}) & (\mathbf{M}_{\text{tot}})^{-1}\mathbf{C}_s\end{bmatrix}, \tag{10}$$

where $\mathbf{M}_{\text{tot}}$ is the sum of the mass contributions from the structure and the piezoceramic patches, $\mathbf{K}_{\text{tot}}$ is the sum of the structural and piezoceramic stiffness contributions, $\mathbf{C}_s$ is the assumed viscous structural damping used to bound the model, and $\mathbf{I}$ is the identity matrix. Since the modal properties that comprise the system matrix, $\mathbf{A}$, for any realization can be easily extracted from an eigenvalue decomposition, the desired matrix, $\mathbf{A}_{d/v}$, can be found from two successive similarity transforms of the arbitrary system matrix, $\mathbf{A}$, that is obtained from the system identification process.

First, the system identification model is transformed into a Modal canonical form, where the system matrix, $\mathbf{A}_J$, becomes a tri-diagonal matrix consisting of 2×2 submatrices composed of the eigenvalues for each second-order mode of the piezostructure. The transform matrix required to realize this form is simply the eigenvector matrix, $\mathbf{\Phi}(\cdot)$, of the current, arbitrary system matrix, or $\mathbf{T}_{\text{sim}}=\mathbf{\Phi}(\mathbf{A})$. The transform exists and is nonsingular, since there will be N linearly independent eigenvectors resulting from an accurate system identification of the piezostructure. Once in the Modal form, we can then find the inverse transform, $\acute{\mathbf{T}}_{\text{sim}}^{-1}$, that yields the displacement/velocity realization of the plant model. First, the resonant frequencies, ω_n, and damping ratios, ζ_n, are extracted from the eigenvalues of the system. These values can then be manually sorted and formed into a displacement/velocity form of the system matrix, Eq. (10), since $[\omega_n^2]=(\mathbf{M}_{\text{tot}})^{-1}(\mathbf{K}_{\text{tot}})$ and $[2\zeta_n\omega_n]=(\mathbf{M}_{\text{tot}})^{-1}\mathbf{C}_s$. The eigenvectors of this matrix then define the inverse of the similarity transform between Modal form and displacement/velocity form, $\acute{\mathbf{T}}_{\text{sim}}^{-1}=\mathbf{\Phi}(\mathbf{A}_J)$. To summarize, the steps to find $\mathbf{A}_{d/v}$ are:

(1) Find $\{\mathbf{A}_J,\mathbf{B}_J,\mathbf{C}_J\}$ using the transform $\mathbf{T}_{\text{sim}}=\mathbf{\Phi}(\mathbf{A})$;
(2) Extract and sort the natural frequencies, ω_n and damping ratios, ζ_n from $\mathbf{A}_J$ and manually form matrix $\mathbf{A}_{d/v}$.
(3) Find $\acute{\mathbf{T}}_{\text{sim}}=\mathbf{\Phi}(\mathbf{A}_{d/v})^{-1}$ and use it to transform $\{\mathbf{A}_J,\mathbf{B}_J,\mathbf{C}_J\}$ into $\{\mathbf{A}_{d/v},\mathbf{B}_{d/v},\mathbf{C}_{d/v}\}$.
(4) Once in displacement/velocity form, the following output matrix, $\mathbf{C}_{\text{gv}}$, can be appended to $\mathbf{C}_{d/v}$ such that the generalized velocities can be observed

$$\mathbf{C}_{\text{gv}}=[0|\mathbf{I}]\in\Re^{20\times 40}; \tag{11}$$

(5) The analytical mass matrix, $\mathbf{M}_s$, could be used to form a generalized modal input influence matrix to be appended to $\mathbf{B}_{d/v}$ which is computed from

$$\mathbf{B}_{\text{gv}}=\left[\frac{0}{\mathbf{M}_s^{-1}\mathbf{I}}\right]\in\Re^{40\times 20}. \tag{12}$$

Typical analytical and experimentally obtained generalized velocity outputs for individual generalized force inputs for the plate are shown in Fig. 6. The analytical and experimental curves of Fig. 6 compare well. Some small discrepancies in magnitude exist due to the difference in modal damping ratios between the analytical model (0.45% for all modes) the experimental model (see Table I for values). Note that if these were modal velocity outputs for a structure with no mass or stiffness discontinuities, each peak in in Fig. 6 would have uniform magnitude since the response would correspond to the true eigenfunctions.

IV. EXPERIMENTAL RESULTS

Control system performance is evaluated by experimentally measuring radiated sound power from the structure in the anechoic chamber for the open- and closed-loop cases. For the purpose of this study, three different ASAC systems were experimentally investigated. Each case differs by the number of modes which have radiation filters appended (either 4, 6, or 8). Increasing the number of radiation filters in the control system increases the number of plate modes that experience radiation control. However, the order of the controller will increase nearly quadratically with respect to the increase in radiation filters. Two results are presented: the spectrum of the highest order ASAC controller (filters appended to eight plate modes) and a bar chart summarizing the amount of control achieved by each ASAC controller at each plate resonance.

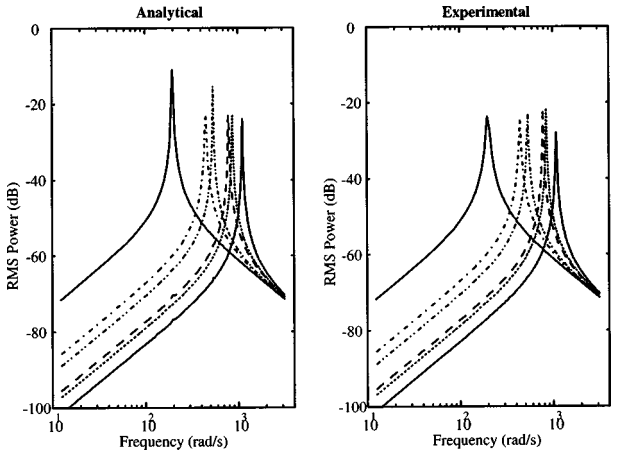

FIG. 6. Response between the generalized force inputs and generalized velocities for the first six plate modes for the analytical and experimental models.

Figure 7 presents the closed-loop performance of the most complex ASAC system used in this study (radiation filters appended to the first eight structural modes). The solid line represents the measured closed-loop acoustic power and the measured open-loop power is given by the dotted line. Also depicted in the figure are modal indices corresponding with each structural plate resonance as well as the cutoff frequencies corresponding to the system model truncation and the inclusion of the radiation filters. From inspection of Fig. 7, good reductions in acoustic power ($\geqslant$15 dB) are observed at the (3,1) and (1,3) modes at 136 and 173 Hz, respectively, which are excellent acoustic radiators. Note that despite the radiation efficiency of the (3,1) mode, the measured open-loop power is relatively low because it is only marginally excited by the disturbance shaker which was arbitrarily located near a nodal line of that mode. Excellent reduction is also observed in the (2,3) mode at 212 Hz which does not radiate as efficiently as the (odd,odd) modes, but for the particular arbitrary actuator placement, experiences significant coupling to the (1,3) and (3,1) radiation modes. Control of the (1,1) mode (34 Hz) is very limited since PZTs do not couple well to modes having a trace structural wavelength much longer than the dimension of the piezoceramic transducer.[19] The least amount of control is observed in the weakly radiating (2,2) mode at 125 Hz, as expected. Note that some control is observed beyond the bandwidth of the radiation filters and the structural plate model which is likely due to some coupling between the experimentally determined generalized velocities which is caused by the piezoceramic actuators.

Finally, a summary of the power reductions at each plate resonance for the open-loop and three closed-loop ASAC

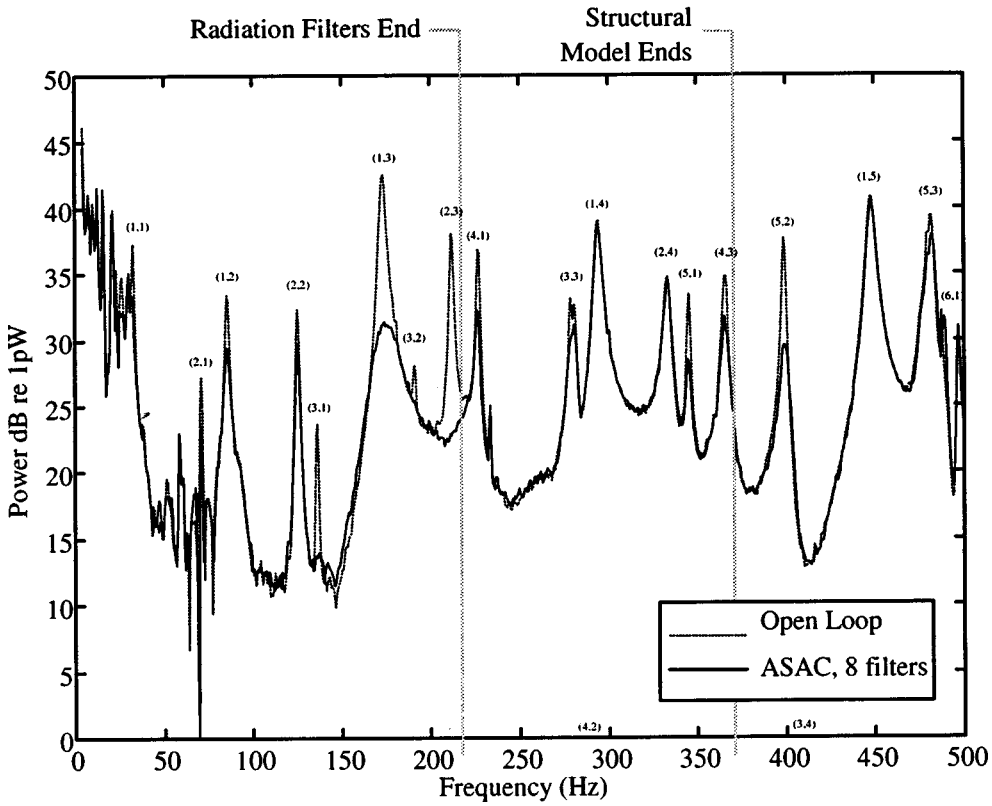

FIG. 7. Acoustic power measurements for multivariable $\mathscr{H}_2$ active structural acoustic control with eight radiation filters.

cases is presented in Fig. 8. Note that increasing the number of plate modes (4, 6, or 8) that have radiation filters appended increases the frequency range over which radiation control is observed, at the expense of increased controller complexity. For example, note that the acoustic response at the resonance frequency of the fifth or (3,1) mode is not controlled by the ''ASAC, 4 Filters'' closed-loop case, but is well-controlled by the 6- and 8-filter ASAC cases. For the latter two cases, the (3,1) mode is included into the structural-acoustic controller cost function and hence sound radiation at the resonance frequency of that mode is reduced by approximately 12 dB.

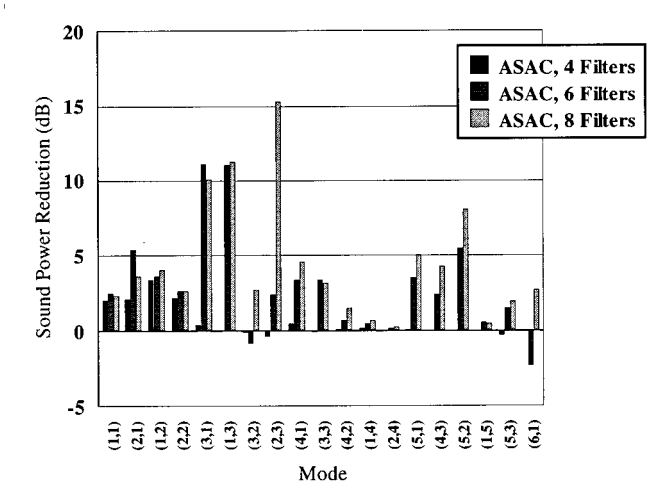

FIG. 8. Comparison of reductions achieved in acoustic power at each modal resonance for all control systems.

V. CONCLUSIONS

Multivariable feedback active structural acoustic control (ASAC) has been experimentally demonstrated using adaptive piezoelectric sensoriactuators as collocated control transducers. A performance cost which minimizes acoustic radiation from the baffled, simply supported plate test structure is accomplished by augmenting the experimentally obtained structural model with radiation filters that are designed using the self- and mutual-radiation efficiencies of the plate modes. A similarity transform to achieve an experimental state-space model having generalized velocity states is presented since the radiation filters require these velocity states as inputs. Acoustic control can thus be achieved without the need for sensors in the acoustic field which is consistent with ASAC. Reductions in acoustic power at the structural resonances from 1 to 15 dB were achieved within the frequency range of the appended radiation filters. The effects of increasing the number of modes (4, 6, or 8) that are appended with radiation filters was investigated. Since including more radiation filters effectively increases the frequency range of the control system, better overall performance was achieved (more modes are controlled and less spillover is observed).

ACKNOWLEDGMENTS

The authors gratefully acknowledge the Structural Acoustics Branch at NASA Langley Research Center for funding this research under Grant No. NAG-1-1570. The authors also acknowledge Dave Cox of the Guidance and Controls Branch at NASA Langley Research Center for help with the control system design as well as Ran Cabell of the Structural Acoustics Branch at NASA Langley Research Center for the TMS320C40 port of the sensoriactuator/control code.

[1] J. P. Maillard and C. R. Fuller, ''Advanced time domain sensing for structural acoustic systems I. Theory and design,'' J. Acoust. Soc. Am. **95**, 3252–3261 (1994).
[2] W. T. Baumann, W. R. Saunders, and H. H. Robertshaw, ''Suppression of acoustic radiation from impulsively excited structures,'' J. Acoust. Soc. Am. **90**, 3202–3208 (1991).
[3] R. L. Clark and C. R. Fuller, ''Control of sound radiation with adaptive structures,'' J. Intell. Mater. Syst. Struct. **2**, 431–452 (1991).
[4] R. L. Clark and C. R. Fuller, ''Experiments on active control of structurally radiated sound using multiple piezoceramic actuators,'' J. Acoust. Soc. Am. **91**, 3313–3320 (1991).
[5] R. L. Clark, ''Advanced sensing techniques for active structural acoustic control,'' Ph.D. thesis, VPI&SU, Blacksburg, VA 24061, 1992.
[6] L. Meirovitch and S. Thangjitham, ''Active control of sound radiation pressure,'' Journal of Vibration and Acoustics **112**, 237–244 (1990).
[7] O. Fluder and R. Kashani, ''Robust control of structure-borne noise using $\langle_\infty$ methods,'' in Proceedings of the ASME Winter Annual Meeting, Vol. DSC-38, pp. 191–204, November 1992.
[8] H. T. Banks, R. J. Silcox, and R. C. Smith, ''Approximation methods for control of structural acoustics models with piezoceramic actuators,'' J. Intell. Mater. Syst. Struct. **4**, 98–116 (1993).
[9] N. K. Gupta, ''Frequency-shaped cost functionals: Extension of linear-quadratic-Gaussian design methods,'' J. Guid. Control Dyn. **3**, 529–535 (1980).
[10] J. S. Vipperman and R. L. Clark, ''Implementation of an adaptive piezoelectric sensoriactuator,'' AIAA J. **34**, 2102–2109 (1996).
[11] J. S. Vipperman, ''Adaptive piezoelectric sensoriactuators for active structural acoustic control,'' Ph.D. thesis, Duke University, Durham, NC 27708, 1997.
[12] R. L. Clark and D. E. Cox, ''Multi-variable structural acoustic control with static compensation,'' J. Acoust. Soc. Am. **102**, 2747–2756 (1997).
[13] R. L. Clark, G. P. Gibbs, and W. R. Saunders, *Adaptive Structures, Dynamics and Control* (Wiley, New York, 1998).
[14] J. C. Doyle, K. Glover, P. P. Khargonekar, and B. A. Francis, ''State-space solutions to standard $\mathscr{H}_2$ / $\mathscr{H}_\infty$ control problems,'' IEEE Trans. Autom. Control. **34**, 831–847 (1989).
[15] N. M. An, ''Acoustic intensity probe,'' Technical Report M.E. 198 Graduation With Departmental Distinction, Duke University, Durham, NC, 1995.
[16] J. Y. Chung, ''Cross-spectral method of measuring acoustic intensity without error caused by instrument phase mismatch,'' J. Acoust. Soc. Am. **64**, 1613–1616 (1978).
[17] Active Control eXperts, Inc., 215 First Street, Cambridge, MA 12142. Smart ID System Identification Software.
[18] T. Kailath, *Linear Systems* (Prentice-Hall, Englewood Cliffs, NJ, 1980).
[19] J. S. Vipperman and R. L. Clark, ''Implications of using colocated strain-based transducers for output active structural acoustic control,'' J. Acoust. Soc. Am. (submitted).

Measurement and prediction of typical speech and background-noise levels in university classrooms during lectures

Murray Hodgson, Rod Rempel, and Susan Kennedy
Occupational Hygiene Programme, University of British Columbia, 3rd Floor, 2206 East Mall, Vancouver, British Columbia V6T 1Z3, Canada

(Received 3 November 1997; revised 12 August 1998; accepted 16 September 1998)

A method has been developed for determining typical long-term speech and background-noise levels during lectures. Lectures are recorded and the recordings digitized and processed to obtain sound-pressure-level frequency distributions to which three normal-distribution curves are fit. The maximum values of these curves are associated with long-term sound-pressure levels associated with speech, ventilation noise, and student-activity noise. Recordings made during 18 university lectures in 11 classrooms have been analyzed. Average (standard deviation) A-weighted levels for the various sound components were determined as follows: ventilation noise, 40.9 (3.9) dB; student-activity noise, 41.9 (4.0) dB; total background noise, 44.4 (3.5) dB; and received speech-signal, 50.8 (3.9) dB. The average (standard deviation) A-weighted speech-signal to background-noise ratio was 7.9 (3.1) dB. That of the instructor sound-power level was 64.5 (4.2) dB. Empirical models have been developed to predict the room-average A-weighted results using multivariable regression analysis. Further analysis in the 63- to 8000-Hz octave bands confirmed the spectra of ventilation noise and of speech, and determined the spectrum of student-activity noise and of the speech-signal to background-noise ratio.
[S0001-4966(98)05712-9]

PACS numbers: 43.55.Hy, 43.55.Gx, 43.50.Cb, 43.70.Gr [JDQ]

INTRODUCTION

As part of a study on classroom acoustics,[1] an experimental procedure has been developed for determining typical long-term speech and background-noise levels at student positions in university classrooms during lectures. A secondary objective was to determine typical levels of student-activity noise, as separate from equipment noise—previous work had suggested that it could be surprisingly high.[1] The procedure developed involved recording lectures, digitizing and filtering the recordings, determining long-term sound-pressure-level frequency distributions (in the statistical sense of frequency of occurrence, not in the acoustical sense of cycles per second), and fitting these with normal-distribution curves. The procedure has been applied to lectures in classrooms at the University of British Columbia.

Numerous measurements of typical classroom speech and background-noise levels, and of corresponding signal-to-noise ratios, have been reported in the literature; however, most pertain to preuniversity classrooms. For example, Markides[2] measured speech and background-noise levels in 12 school classrooms during classes. Houtgast[3] studied ten high school classes exposed to traffic noise. Pekkarinen and Viljanen[4] studied 31 school classrooms when unoccupied and occupied. Pearsons, Bennett, and Fidell[5] measured long-term speech levels at about 2 m in front of instructors in two high schools. They also measured speech levels at 1 m in front of the speaker in an anechoic environment, for male and female speakers and various vocal efforts. Representative A-weighted results from these studies are presented in Table I. Speech levels in the range of 40–80 dB were reported. Student-activity noise levels varied from 40–70 dB. Ventilation-noise levels were in the range 23–55 dB. Signal-to-noise ratios in the range −5–35 dB were reported. Cornelisse, Gagné, and Seewald[6] and Byrne *et al.*[7] determined long-term speech spectra; these typically peaked at 500 Hz and were about 20 and 15 dB down at 63 Hz and 8 kHz, respectively. Byrne *et al.* found long-term total levels for a large number of speakers to be approximately normally distributed. In most cases reported in the literature, the exact experimental/analysis method used to determine levels and, therefore, the exact significance of the measured levels, is not clear. With the possible exception of Markides,[2] no reliable determinations of student-activity noise level have been reported.

The method developed in the present work was based on the following reasoning. In the simplest case, a university lecture consists of an instructor speaking—and generating a relatively high sound-pressure level—in the presence of a relatively low background-noise level. The background noise consists of noise from the ventilation system and that generated by the students attending the lecture. Speech is quasi-continuous, with short breaks between sentences, and longer breaks when, for example, the instructor stops to write on the blackboard. The background noise would be expected to be more continuous. If the instructor stops speaking for significant lengths of time, student activity and the resulting noise may increase. Thus, the most reliable way to determine the level of background noise which occurs during, and interferes with, instructor speech is to measure it during the short breaks between sentences. If the speech and background noise were both perfectly continuous sounds, the time history of a lecture would be as in Fig. 1(a), the associated sound-pressure-level frequency distribution would consist of two spikes, as in Fig. 1(b). Of course, some temporal variation of

TABLE I. Representative range, average (s.d.) of A-weighted speech, student-activity and ventilation-noise levels, and signal-to-noise ratios, in dB, reported in the published literature.

Reference	Speech	Student	Ventilation	Signal-to-noise
Markides[2]	40–70 57.5 (8.4)	50–70 61.0 (5.5)	40–55 46.1 (5)	−4.5 average (speech) +11.5 average (ventilation)
Houtgast[3]	48–63 56.9 (5.1)	45–50 47.4 (3.1)		3–15 9.5 (4.6)
Pekkarinen and Viljanen[4]	58–79 67 (5)	40–58 49 (6)	23–49 33 (5)	0–35
Pearsons, Bennett, and Fidell[5]	59.5–63.5 −(5)			

the levels of the speech and noise would be expected, with a more realistic time history being as shown in Fig. 2(a); the associated level frequency distribution would consist of two peaks with nonzero widths, as shown in Fig. 2(b). As long as the speech-signal to background-noise ratio is sufficiently high for the two peaks to be distinct, the associated ''average'' long-term levels could be determined from the maximum values [X and Y in Figs. 1(b) and 2(b)] of the two peaks, since these indicate the level which occurred for the greatest proportion of the measurement period.

I. CLASSROOM RECORDINGS

A total of 18 lectures was recorded at three or four positions in 11 classrooms. These were the classes given by all consenting instructors teaching in the chosen 30 classrooms during the academic term during which the work was carried out. In the case of three of the classrooms, recordings were also made in the unoccupied room on the same day as the occupied tests; more tests were not possible due to heavy classroom usage. The classrooms were seminar and lecture rooms which contained from 10–291 seats and 6–254 students, with unoccupied midfrequency reverberation times that varied from 0.5–1.8 s. Both male and female instructors, teaching a wide variety of subjects at various academic levels, were involved. In most cases the classes consisted of lectures, with the instructor being the main source of speech. However, four classes were more in the form of discussions, with students contributing a considerable proportion of the speech. Generally, no significant noise from outside the classroom occurred; the ventilation system was the only equipment in operation.

Recordings were made using calibrated Bruel & Kjaer 4145 microphones and a TASCAM DA30 Mk II digital tape recorder. Data were collected for 10–15 min, in three blocks at the beginning, middle, and end of the class, at each position. As a crosscheck, ventilation-noise levels were measured at each test position in each classroom on a separate occasion using a sound-level meter. Unfortunately, these occasions were often days or weeks apart; ideally, they would have been done on the same day as the associated lecture, but heavy classroom usage made this difficult.

II. ANALYSIS PROCEDURE

The analysis procedure was finalized after extensive pilot work. Prior to analysis, sections of the recordings con-

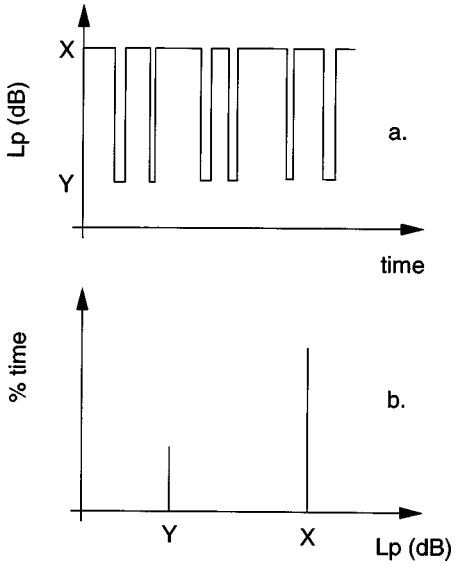

FIG. 1. (a) Time history and (b) frequency distribution of the sound-pressure level in a classroom during an idealized lecture.

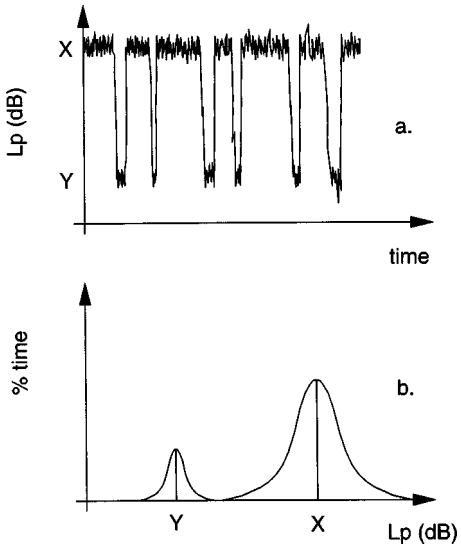

FIG. 2. (a) Time history and (b) frequency distribution of the sound-pressure level in a classroom during a realistic lecture.

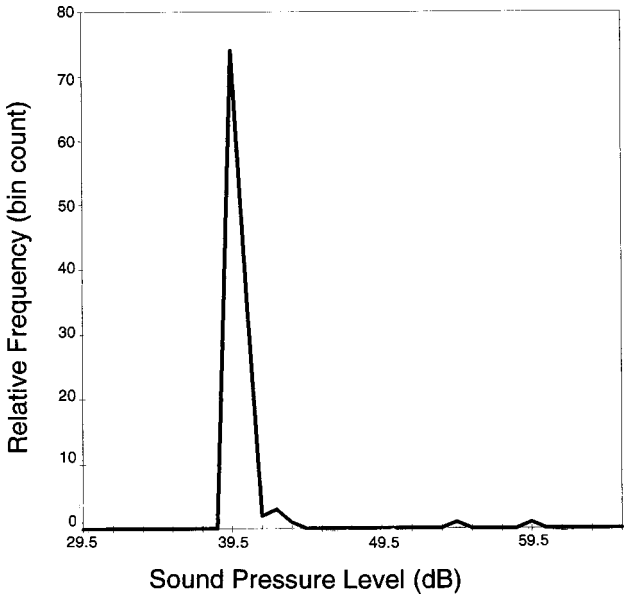

FIG. 3. Measured A-weighted sound-pressure-level frequency-distribution curve in an unoccupied classroom.

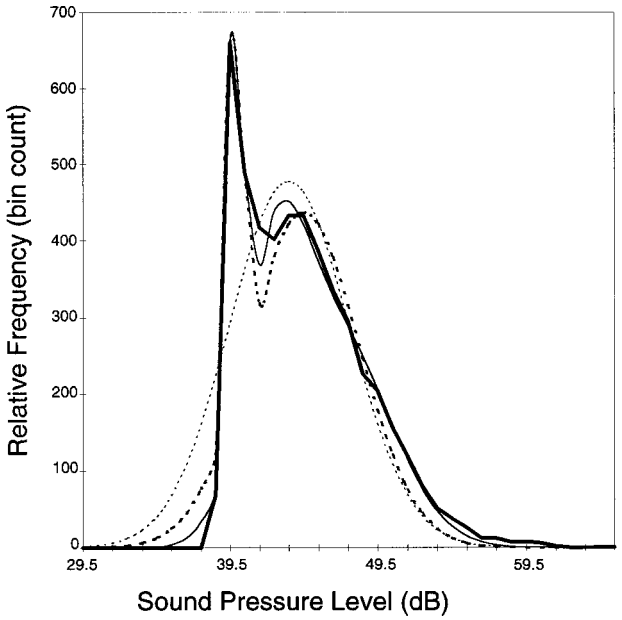

FIG. 4. A-weighted sound-pressure-level frequency-distribution curves for an occupied classroom, as (—) measured, and as fit by (···) one, (-–––) two, and (———) three normal-distribution curves.

taining significant noise from outside the classroom, such as passing equipment, or atypical classroom noise, such as bells, were removed. Typical classroom noises, such as coughing and chair movement, were not removed. The processed recordings at each position in each class were digitized and filtered using a digital A-weighting filter. Software processed the resulting pressure time-histories as follows:

(i) the signals were squared;
(ii) short-term, mean-square pressures were calculated. The time interval of 200 ms corresponded to ten cycles at the lowest frequency of interest, 50 Hz. This was chosen to be 1.5 times the minimum time interval required for convergence;
(iii) interval sound-pressure levels were calculated;
(iv) sound-pressure-level frequency distributions (again, in the statistical sense indicating the proportion of time for which the level took given values, not the acoustical sense) were determined and plotted;
(v) the resulting distributions were best fit by one, two, three, or more normal-distribution curves in an attempt to identify individual sound components. The maximum level, standard deviation (i.e., width), and area of each curve were recorded. The maximum level was taken to indicate the typical long-term sound-pressure level. Tests were done using other, nonsymmetrical—in particular, Poisson—distribution curves. Fitting Poisson-distribution curves gave better results than (symmetrical) normal-distribution curves when only one curve was fit, but slightly worse results when two or more curves were fit. This is as expected; the overall measured multicomponent distribution curves were generally highly nonsymmetrical (see Fig. 4), but the distributions of the individual components of the classroom sound were generally much more symmetrical (see Fig. 3). A normal distribution of the sound-pressure level in decibels—i.e., log(pressure^2)—of noise is consistent with the expected log-normal distribution of the zero-bounded squared pressure from which it is derived.

To obtain octave-band results, recordings were also filtered using digital 63–8000-Hz octave-band filters. In this case, the length of the intervals into which the time histories were divided always corresponded to ten cycles at the lowest band frequency—i.e., it decreased over the test frequency range from about 200 ms to about 1 ms. Only a few recordings were analyzed in octave bands because of the massive analysis time involved; furthermore, it was expected that only limited useful information would be obtained from the octave-band analysis, given the detailed A-weighted analysis already done. Clearly, octave-band speech or background-noise levels can be obtained from A-weighted total levels if the associated spectrum shape is known. The spectra of speech and ventilation-system noise, and the factors that affect them, are well understood.[5–7] However, it was of fundamental interest to determine the spectrum of the student-activity noise, and of the speech-signal to total background-noise ratio.

III. A-WEIGHTED RESULTS

A. Unoccupied classrooms

Figure 3 shows a typical measured level-distribution curve at one position in one unoccupied classroom, in which the only significant source of noise was the ventilation system. There is a single, symmetrical peak, with levels in the range 39–42 dB, which is quite narrow (s.d. of about 0.4 dB). This is indicative of a continuous source, such as a ventilation system. Generally, the measured curve was well fit by a single normal-distribution curve (the adjusted R^2 was typically 0.99). However, in one of the three rooms, the

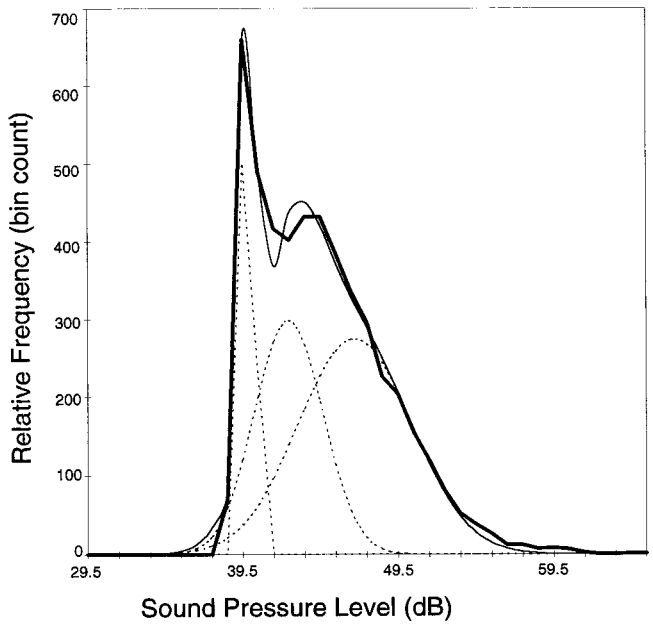

FIG. 5. A-weighted sound-pressure-level frequency-distribution curves for an occupied classroom, as (———) measured, and (———) as fit by three normal-distribution curves, (···) shown individually.

level-distribution curves were broader and contained spikes, indicating significantly time-varying sound-pressure levels and multiple sound components, possibly suggesting a system in need of servicing.

B. Occupied classrooms (lectures)

Figure 4 shows the measured level-distribution curve at the same position in the same classroom during a lecture. The result is fairly typical. There are now two prominent peaks—a lower-level, narrow one at around 40 dB and a higher-level, broader one at around 45 dB. The lower-level peak resembles, and has maximum levels and s.d. very similar to, that measured in the unoccupied classroom, suggesting that it corresponds to the ventilation-system noise.

As illustrated in Fig. 4, attempts to fit one normal-distribution curve to the results generally gave a poor result (typical adjusted R^2 of 0.8). Fitting two normal-distribution curves gave a significantly better result (typical adjusted R^2 of 0.95). Fitting three curves usually gave an even better fit (typical adjusted R^2 of 0.99). Fitting more than three curves did not significantly improve the fit; in fact it tended to simply identify spurious small, local peaks in the measured curves. As illustrated in Fig. 5, two of the normal-distribution curves, with maximum levels at about 41 and 47.5 dB, fit the two peaks of the level-distribution curve which are apparent; the third—in between the other two with a maximum level at about 43 dB according to the best-fit results—was often not apparent.

The three normal-distribution curves were identified with the three components of classroom sound at receiver positions—speech signal, ventilation noise, and student-activity noise. By correlating it with the single peak measured in the unoccupied classrooms, the lowest-level curve could be reliably associated with the ventilation noise. However, ventilation-noise levels so identified often agreed poorly with those measured on other occasions. It was concluded that ventilation-noise levels can vary significantly (up to 5 dB) from day to day. This was confirmed by further monitoring and in discussions with HVAC-noise experts.

Regarding the other two sound components, it was not obvious which of the two higher-level curves' best-fit levels corresponded to which component. To cast some light on this, levels were compared to typical long-term speech levels published in the literature.[2–5] The highest of the three maximum levels generally corresponded fairly well to expected speech levels and was, therefore, associated with instructor speech levels; the middle level tended to be low. Furthermore, the maximum level of the highest peak generally decreased with instructor/receiver distance, as would be expected for the speech signal, but not for the student-activity noise level. The middle level was associated with student-activity noise.

It is of interest to consider the normal-distribution-curve standard deviation and area results, and their significance, in more detail. The s.d. indicates the temporal variability of the rms noise level. The s.d. of the speech peaks was typically 4–10 dB, ten times higher than that of the ventilation peak, indicating considerable variability of the speech level, as might be expected. The s.d. of the student-activity peak was typically 2–6 dB, between those of the ventilation and speech peaks. The area under the level-distribution curves indicates the relative energy (i.e., combination of power and time) associated with each sound component during a lecture. In terms of the percentage of the total area under the measured level-distribution curves, the averages (standard deviations) of the areas of the ventilation, student-activity, and speech peaks were, respectively, 15 (8), 25 (19), and 64 (19) dB.

Exceptions to the typical results illustrated and discussed above occurred in a number of cases. For example, in two cases the frequency distribution appeared to have only a single peak, indicating low signal-to-noise ratio, and making identification of component levels impossible. A further complication is related to the classes consisting mainly of discussion. In these cases, the meaning of the results is less clear. In one case, the instructor seldom spoke; therefore, the highest level, which was several decibels lower than average, must correspond to student speech. In another case, both the students and the instructor spoke a significant proportion of the time. Is the highest level instructor and/or student speech; is the middle level student noise or speech? In discussion classes the middle level was, on average, about 1 dB lower than in lectures; the highest level was about 2 dB lower than in lectures.

In cases when the procedure identified three distinct levels, maximum levels for the three sound components were determined for each position in each lecture in each classroom, and the results analyzed. Note that the level of the middle peak, associated with student-activity noise, was not considered itself to be equal to the student-activity noise level. It corresponds to the energetic sum of the ventilation and student-activity levels—that is, to the total background-noise level—since these occurred concurrently. Student-

TABLE II. Minimum, maximum, and average values and standard deviations in decibels of the long-term, A-weighted sound-pressure levels associated with ventilation noise (VN), student-activity noise (SA), total background noise (BN), and instructor speech (SL), as well as signal-to-noise ratio (SN) and instructor speech-power level (LW).

Quantity	Minimum value	Maximum value	Average value	Standard deviation
VN	32.6	47.0	40.9	3.9
SA	30.0	50.2	41.9	4.0
BN	34.5	50.9	44.4	3.5
SL	43.0	59.0	50.8	3.7
SN	2.1	14.8	7.9	3.1
LW	53.6	73.4	64.5	4.2

TABLE III. Ranges of values of the parameters used in the empirical prediction models for the 18 classrooms.

Parameter name	Symbol	Units	Range of data
Room width	W	m	4.9–20.0
Room volume	V	m^3	110–957
Number of students	n	···	6–254
Instructor sex	I_{sex}	···	0–1
Instructor/student distance	r	m	1.9–13.6
Received speech level	SL	dB	43.0–59.0
Student-activity noise level	SA	dB	30.0–50.2
Total occupied-room absorption	A_0	m^2	30–305

activity levels were obtained by energetic subtraction of the lowest and middle levels. Similarly, the speech level was obtained by energetic subtraction of the highest and middle levels. Also calculated was the signal-to-noise ratio, by arithmetic subtraction of the speech level and the total background-noise level. Results were also calculated separately for male and female instructors, and for positions at the front and back of the classrooms.

Table II shows the ranges, averages, and standard deviations of the three levels for all reliable measurements. Following is a summary of the results.

1. Background noise

Ventilation-noise levels varied from 32.6–47.0 dB, with an average (s.d.) of 40.9 (3.9) dB. Student-activity noise levels varied from 30.0–50.2 dB, with an average (s.d.) of 41.9 (4.0) dB. These latter levels are considerably lower than those reported by Markides[2]—presumably because of the higher academic levels and ages of the students involved. Total background-noise levels varied from 34.5–50.9 dB, with an average (s.d.) of 44.4 (3.5) dB. These values agree well with those reported in the literature.

2. Speech level

Speech levels varied from 43.0–59.0 dB with an average (s.d.) of 50.8 (3.7) dB. Such levels are in the ranges reported in the literature (see Table I). On average, however, they were about 6 dB lower than teacher speech levels reported in the literature—again likely due to the higher student ages and academic levels, and the discussion classes. Differences between male and female speakers altered levels by ±1.3 dB from the average level. This is consistent with Pearsons *et al.*[5] Differences between front and back seat positions altered levels by typically ±1.5 dB from the average level. It was noted that speech levels did not vary strongly with room acoustical conditions. It can be hypothesized that instructors adjust their voice levels to compensate for the prevailing acoustical conditions, and maintain a constant speech level at student positions. To test this hypothesis, measured speech levels, the known classroom dimensions and average surface absorption coefficients, and diffuse-field theory were used to estimate long-term instructor sound-power levels. These varied from 53.6–73.4 dB with an average (s.d.) of 64.5 (4.2) dB. Once again, male/female differences varied the average value by ±1.3 dB, respectively. There was an apparent correlation with room size—average speech-power levels of about 62 dB (<30 seats), 65 dB (30–80 seats), 66 dB (>80 seats)—supporting the hypothesis. The variation of speech level with source/receiver distance, and of sound-power level with classroom size, will be discussed in more detail below.

3. Signal-to-noise ratio

Signal-to-noise ratios at individual positions varied from 2.1–14.8 dB, with an average (s.d.) of 7.9 (3.1) dB. These values are consistent with those reported in the literature. The signal-to-noise ratio never exceeded the value of 15 dB considered necessary for excellent speech intelligibility for normal-hearing adults.[8]

C. Empirical prediction models

It is clearly of interest to be able to predict typical levels of the three classroom sound components for a particular classroom. With this objective, empirical prediction models were developed from the A-weighted results using multivariable linear regression analysis using the statistical softwares SAS and SPSS. Candidate predictor parameters were chosen as those describing factors expected to be related to the variable being predicted, and combinations of them. Logarithms of parameters were usually used, since the quantities to be predicted were levels in decibels. Models were optimized by finding the minimum of physically justifiable, statistically significant ($p \leqslant 0.05$) parameters which explained the greatest amount of the variance. Subsequently, predictions were plotted against residuals for each predictor parameter to ascertain whether nonlinear forms of the parameters would improve the model. As for any empirical models, predictions by these models may be less accurate in the case of classrooms with values of the prediction parameters which are outside the range associated with the data from which the models were derived. These ranges are shown in Table III, and do not include very large classrooms.

1. Ventilation noise

The level of ventilation noise in a classroom would be expected to depend on the following factors:

(i) type of equipment—no information was available about this;

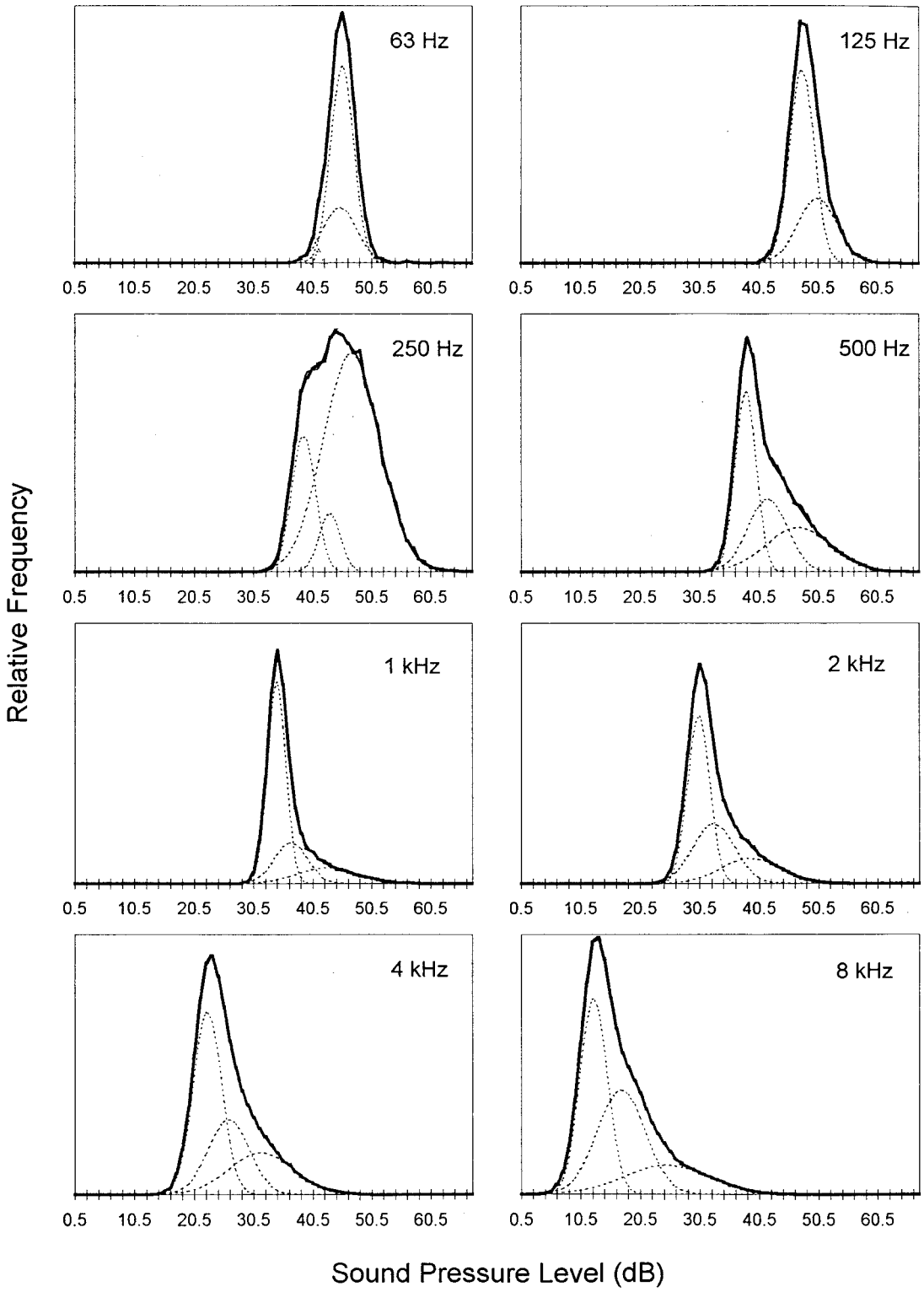

FIG. 6. Octave-band sound-pressure-level frequency-distribution curves for an occupied classroom, as (———) measured, and (———) as fit by three normal-distribution curves, (···) shown individually.

(ii) mechanical/acoustical power—this would be expected to be higher in larger rooms with more students. Parameters describing room size, and the number of seats and of students present, were tested;

(iii) source/receiver distance—this was quantified by the average distance from the receiver position to the ventilation outlets;

(iv) the classroom's acoustical characteristics—according to diffuse-field theory describing the reverberant field, this is related to log(1/total room absorption in m^2).

The following statistical model predicted room-average, A-weighted ventilation-noise level VN, accounting for 41% of the variance:

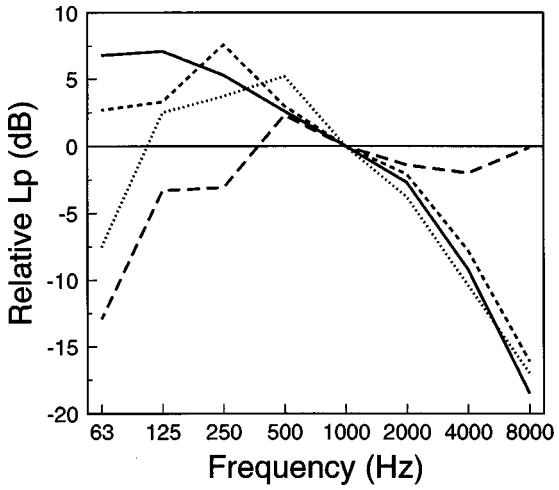

FIG. 7. Relative octave-band spectra of the room-average (———) ventilation noise, (- - - -) student-activity noise, (···) speech signal, and (— — —) signal-to-noise ratio in classrooms during lectures.

$$\mathrm{VN} = 57.6 + 10.3 \log n + 0.68W - 21.3 \log A_0 \quad \mathrm{dB}, \quad (1)$$

in which n is the number of students, W is the room width in m, and A_0 is the total occupied-room absorption in m^2.

2. Student-activity noise

The level of student-activity noise in a classroom would be expected to depend on the following factors:

(i) the number of students;
(ii) received speech level due to the instructor, SL;
(iii) the acoustical characteristics of the room.

The following statistical model predicted room-average, A-weighted student-activity noise level SA, accounting for 57% of the variance:

$$\mathrm{SA} = 9.22 + 6.4 \log n + 0.71\mathrm{SL} + 1.53I_{\mathrm{sex}} - 8.0 \log A_0 \quad \mathrm{dB}, \quad (2)$$

in which I_{sex} is 0 for a male instructor and 1 for a female instructor.

3. Instructor speech signal

The received level of the instructor speech signal in a classroom would be expected to depend on the following factors:

(i) instructor sex;
(ii) the student-activity noise level;
(iii) source/receiver distance;
(iv) the acoustical characteristics of the room.

The following statistical model predicted room-average, A-weighted instructor speech level SL, accounting for 66% of the variance:

$$\mathrm{SL} = 48.5 - 2.6I_{\mathrm{sex}} + 0.58\mathrm{SA} - 4.0 \log r + 0.013V - 11.7 \log A_0 \quad \mathrm{dB}, \quad (3)$$

in which r is the instructor/student distance in m, and V is the room volume in m^3.

According to Eq. (3), on average a female instructor generates speech levels which are 2.6 dB lower than a male instructor. This agrees with the results of Pearsons, Bennett, and Fidell.[5] Furthermore, on average the speech level decreases at 1.2 dB per distance doubling. Assume that students sitting at the front of small, medium, and large classrooms are 1, 2, and 4 m away from the instructor, respectively. Assume that students sitting at the back of small, medium, and large classrooms are 4, 8, and 16 m away from the instructor, respectively. Then speech levels will, on average, be 2.4 dB lower at the rear of classrooms than at the front, irrespective of classroom size. Similarly, levels at the front and back will be ± 1.2 dB with respect to levels at the center (i.e., average levels), consistent with the result previously reported in Sec. III B 2.

4. Instructor sound power

The instructor output sound power would be expected to depend on the same factors as the received speech level, except that it should not depend on source/receiver distance. The following statistical model predicted room-average, A-weighted instructor speech-power level LW, accounting for 69% of the variance:

$$\mathrm{LW} = 54.8 - 2.6I_{\mathrm{sex}} + 0.5\mathrm{SA} + 0.016V - 9.6 \log A_0 \quad \mathrm{dB}. \quad (4)$$

5. Alternative student-activity-noise model

The model for SA depends on SL, and vice versa. This is a problem if the objective is, for example, to use the models to predict speech intelligibility in classrooms. To achieve this, the speech-signal to total background (comprising ventilation and student-activity) noise ratio, and thus both SA and SL must be predicted. This is impossible if the quantities

TABLE IV. Average (standard deviation) octave-band relative spectral weightings (octave-band level minus that at 1000 Hz) in decibels of the ventilation noise (VN), student-activity noise (SA), speech level (SL), and signal-to-noise ratio (SN) in four occupied classrooms—see also Fig. 7.

	Octave band (Hz)							
Qty	63	125	250	500	1000	2000	4000	8000
VN	+6.8 (3.8)	+7.1 (3.2)	+5.3 (1.5)	+2.6 (2.2)	0.0 (0.0)	−2.7 (1.8)	−9.2 (2.1)	−18.5 (0.9)
SA	+2.7 (4.7)	+3.3 (3.7)	+7.6 (3.9)	+3.0 (2.1)	0.0 (0.0)	−2.2 (1.8)	−7.8 (1.1)	−16.1 (0.4)
SL	−7.5 (8.3)	+2.5 (2.9)	+3.7 (1.3)	+5.2 (1.8)	0.0 (0.0)	−3.8 (1.5)	−10.4 (1.7)	−17.0 (3.4)
SN	−12.9 (4.2)	−3.3 (1.9)	−3.1 (2.3)	+2.3 (3.0)	0.0 (0.0)	−1.4 (1.8)	−2.0 (2.3)	−0.1 (3.9)

can only be predicted from one another. In this case, an alternative model for one of the quantities, which does not depend on the other, is required. Following is such a model for SA, accounting for 69% of the variance:

$$\mathrm{SA} = 83.0 + 10.0 \log n - 34.4 \log A_0 + 0.081 A_0 \quad \mathrm{dB}. \tag{5}$$

IV. OCTAVE-BAND RESULTS

Figure 6(a)–(h) shows the 63–8000-Hz octave-band level frequency-distribution curves at a position in an occupied classroom. The shapes of the curves vary with frequency in a way which, of course, depends on the relative contributions of the three sound components. At low frequency, there was generally a single narrow, symmetrical peak. At higher frequencies, there was often evidence of two peaks.

Once again, three normal-distribution curves were found to fit the measured curves optimally in most cases. Adjusted R^2 values were similar to those reported for the A-weighted results. The lowest and highest curves could reliably be associated with ventilation noise and speech signals; thus, the middle peak was associated with student activity. Comparisons were made between the A-weighted energetic sum of the resulting octave-band levels for each sound component, and the values obtained from the A-weighting analysis discussed in the previous section. Agreement was usually good—within 1 or 2 dB—adding confidence in the results.

Levels corresponding to the three sound components were determined for each position in each room at each frequency. Then, octave-band spectral weightings relative to the levels at 1000 Hz were determined. The results were averaged over the positions in each room. Finally, the room-average results were averaged over all rooms. Figure 7 shows the average values of the resulting spectra; Table IV gives their averages and standard deviations. As expected, the ventilation-noise spectrum peaks at low frequency—being flat at 63 and 125 Hz—and decreases sharply with frequency at higher frequency. The student-activity noise is also greatest at low frequency, peaking at 250 Hz and decreasing sharply with frequency at higher frequency. Instructor speech spectra are highest in the range 125–500 Hz, peak at 500 Hz, and drop off outside this range. This generally agrees with speech spectra published elsewhere.[6,7] The spectrum of typical classroom signal-to-noise ratio is highest at middle and high frequencies, decreasing with decreasing frequency below 500 Hz. There was considerable room-to-room variation in the spectra, particularly at lower frequencies and with instructor speech level.

V. CONCLUSION

A method has been developed for determining long-term speech and background-noise levels in classrooms. The method appears to be practicable and valid. The results suggest that the background noise comprises two components: ventilation noise and student-activity noise. It has been applied to 18 lectures in 11 classrooms. Representative A-weighted speech and background-noise levels have been determined. This is believed to be the first time that classroom student-activity noise has been measured reliably. Instructor sound-power levels were calculated from the speech levels and the acoustical characteristics of the classrooms. Using multivariable regression analysis, empirical models for predicting the A-weighted speech levels and powers, and the background-noise levels, in a classroom, were developed. Typical octave-band spectra of the various classroom sound components were also determined. Clearly, there is a need to further validate the technique and to apply it to more classrooms. However, the results presented here should be representative of all but the largest classrooms intended for lectures.

ACKNOWLEDGMENTS

The authors would like to express their gratitude to all of the professors at the University of British Columbia who allowed their lectures to be recorded. Thanks also to Eric Wood and Mike Wrinch, who made the recordings and performed the initial tests on the analysis method, and to Edward Park, for his contribution to the analysis.

[1] M. R. Hodgson, ''Experimental investigation of the acoustical characteristics of university classrooms,'' J. Acoust. Soc. Am. (submitted for publication).
[2] A. Markides, ''Speech levels and speech-to-noise ratios,'' British Journal of Audiology **20**, 115–120 (1986).
[3] T. Houtgast, ''The effect of ambient noise on speech intelligibility in classrooms,'' Appl. Acoust. **14**, 15–25 (1981).
[4] E. Pekkarinen and V. Viljanen, ''Acoustic conditions for speech communication in classrooms,'' Scand. Audiol. **20**, 257–263 (1991).
[5] K. S. Pearsons, R. L. Bennett, and S. Fidell, ''Speech levels in various noise environments,'' Bolt, Beranek and Newman report to the USEPA, Canoga Park, CA (May 1977).
[6] L. E. Cornelisse, J.-P. Gagné, and R. C. Seewald, ''Ear-level recordings of the long-term average spectrum of speech,'' Ear and Hearing **12**(1), 47–54 (1991).
[7] D. Byrne, H. Dillon, K. Tran, S. Arlinger, K. Wilbraham, R. Cox, B. Hagerman, R. Hétu, J. Kei, C. Lui, J. Kiessling, M. Nasser Kotby, N. H. A. Nasser, W. A. H. El Kholy, Y. Nakanishi, H. Oyer, R. Powell, D. Stephens, R. Meredith, T. Sirimanna, G. Tavartkiladze, G. Folenkov, S. Westerman, and C. Ludvigsen, ''An international comparison of long-term average speech spectra,'' J. Acoust. Soc. Am. **96**, 2108–2120 (1994).
[8] J. S. Bradley, ''Uniform derivation of optimum conditions for speech in rooms,'' Report BRN 239 (National Research Council, Ottawa, Canada, 1985).

Fiber movements and sound attenuation in glass wool

Viggo Tarnow
Department of Applied Engineering Design and Production, Technical University of Denmark, Bygning 358, DK 2800 Lyngby, Denmark

(Received 24 December 1997; revised 24 August 1998; accepted 25 September 1998)

Propagation of a plane harmonic sound wave in fiber materials such as glass wool is studied theoretically and experimentally. Wave equations are set up that take into account the movement of the fiber skeleton. The attenuation of the sound wave in slabs of glass wool was calculated and measured. The main new result is that the experimental attenuation of a low-frequency propagating wave is lower when the fibers move. For a wave with frequency 100 Hz in glass wool of density 30 kg/m^3, the attenuation of a layer of thickness 0.20 m is 4 dB if the fibers move, and 12 dB if they do not move. The attenuation was computed from the fiber diameters and their density, which was found from the mass density. Measured attenuation is lower than the values calculated. Nevertheless, if the density is adjusted, a complete fit is obtained between experimental and theoretical values for frequencies 50–5000 Hz. © *1999 Acoustical Society of America.* [S0001-4966(99)02601-6]

PACS numbers: 43.58.Vb, 43.20.Jr, 43.55.Ev, 43.35.Mr [SLE]

INTRODUCTION

In theories that aim at computing the sound attenuation of fiber materials, one often assumes that the fibers do not move. However, several people have measured the effect of the movements of fibers.

Dahl *et al.*[1] measured the absorption coefficient of Kevlar samples with a thickness of 10 cm placed on a hard wall. They found a resonance in the absorption attributed to a mechanical resonance due to movement of fibers. The absorption was measured for densities 5–67 kg/m^3, and it was found that resonances were sharpest for the highest-density material, where the resonance frequency was about 600 Hz.

Allard *et al.*[2] measured the surface impedance of samples of glass wool with density 130 kg/m^3 attached to an impervious floor. They measured a resonance frequency of 470 Hz for a layer of thickness 10 cm, and 860 Hz for thickness 5.4 cm. These resonances were attributed to mechanical resonance of the samples due to the movements of fibers.

Lambert[3] reported measurements on Kevlar samples of thickness 10 cm placed on a hard wall. A resonance about 1000 Hz was found in the attenuation, the phase speed, the characteristic admittance of the material, the effective resistivity, and the effective dynamic density. These resonances were caused by moving fibers. In a second paper[4] Lambert gave further data for resonances in the effective resistivity and the effective dynamic density.

In the present work, measurements of the sound attenuation of glass wool are reported, which show that at frequencies below 200 Hz the fiber movement strongly influences the attenuation. The measurements were done on glass wool slabs with density 14 and 30 kg/m^3. The glass wool slabs had dimensions 100×600×900 mm and were placed in a stack of six units, and placed in a box made of chipboards open only at one side.

Several theories have been published that take into account the movements of the skeleton of porous materials. Biot published two papers[5,6] in which a porous solid filled with a fluid is studied.

The papers by Dahl *et al.*[1] and Lambert[3,4] explain the measured acoustic properties by resonances in single fibers. However, it is difficult to see how single fiber could resonate, because all fibers are strongly coupled, and the wavelength of a sound wave are much longer than the distance between the fibers. The theoretical model in the present paper does not use resonating single fibers.

In the paper by Allard,[2] the observed resonances were explained by the methods of the two Biot papers.[5,6] A similar approach was used in the paper by Johansen, Allard, and Brouard,[7] who used finite element methods to analyze acoustical measurements on fiber material samples placed in a tube with diameter 10 cm. Two thicknesses, 2 and 5 cm, were used. They found resonances due to fiber movements could be explained by assuming the skeleton moved as a continuous medium.

In the present paper the sound attenuation is computed, allowing for the fiber movements by regarding the skeleton as a continuous medium in the same way as Biot did. The dynamic resistivity and compressibility used here are computed more nearly accurately than the ones used by Biot.

The earlier reports by Allard *et al.*[2] and Johansen *et al.*[7] of observations of fiber movement used mechanical resonance in the samples to detect the movements of fibers. This is not so in this paper where the attenuation of propagating waves in glass wool is measured. The paper by Johansen, Allard, and Brouard[7] referred to measurements on samples with cylindrical shape and a diameter of 10 cm. They had to take into consideration the lateral movement of the fiber skeleton. This is not necessary for the measurements reported in this paper, because the samples used here are much wider. The dimensions are 10 cm×60 cm×90 cm.

I. THEORY OF SOUND PROPAGATION WITH FIBER MOVEMENTS

In fiber materials, such as glass wool, a coupling between movements of air and fibers exist; this coupling is mainly due to friction between air and fibers. Wavelengths of

audible sounds in air and fibers are much longer than the distance between fibers in ordinary glass wools. Therefore, the propagation of sound waves can be calculated by assuming the medium is continuous, and the waves cannot ''see'' the single fibers.

A. Elastic forces

We study plane waves in glass wool that propagate in the x direction of a rectangular coordinate system. The displacement of the fiber skeleton in the x direction is called u, and the mean displacement of air in the x direction is called ν. It is defined as the volume flow of air through a large cross section divided by the area of that cross section. [Biot[5] used another definition of mean air displacement: Volume flow of fluid (air) divided by area of fluid in that cross section. He assumed ''that the solid–fluid system is statistically isotropic.'' Glass wool is anisotropic, and for some boundary conditions, one needs the air volume flow through a cross section. This is, with our definition, simply equal to mean air displacement times the area of the cross section. However, this is not so with Biot's definition.]

The elastic forces on fibers and air can be found from the potential energy per unit volume. The potential energy density E is, in a linear theory, a quadratic form in the partial derivatives of the displacement of the fibers u_x and air ν_x. Thus

$$E=\tfrac{1}{2}c_{11}u_x^2+Au_x\nu_x+\tfrac{1}{2}K\nu_x^2, \tag{1}$$

where c_{11} is an elastic modulus of the fiber skeleton, when the air is not displaced ($\nu_x=0$); K is the bulk modulus of air, when the fibers do not move ($u_x=0$); A is a constant that couples movements of air and fibers.

The static value of c_{11} was measured by applying a known force to a sample of the glass wool and measuring the depression. c_{11} equals the force per area divided by the relative depression. The result was $c_{11}=2000$ and 16 000 Pa for the two glass wool types. We regard the glass fiber skeleton as a space lattice of glass fibers. They may vibrate, but the fibers are coupled. This system is similar to atoms in a crystal, the atoms are placed in a space lattice, they vibrate, but their vibrations are coupled. The dynamics of the space lattice show that the elastic moduli does not depend on frequency when the wavelength is longer than the distance between the fibers. Therefore, we assume the elastic modulus c_{11} does not depend on frequency. Measurements of the elastic moduli for glass wool as a function of frequency have not been published.

The bulk modulus of air equals

$$K=\frac{1}{\phi C}, \tag{2}$$

where ϕ is the porosity, and C is the dynamic compressibility of air itself, which will be computed by the self-consistent method of Tarnow.[8] Self-consistent methods were first used in atomic physics, Schiff.[9] A model with parallel, randomly placed cylinders (fibers) with equal diameters will be used. The procedure is described in Appendix A.

The value of A can be found by computing the pressure p from Eq. (1). This gives

$$-p=\frac{\partial E}{\partial \nu_x}=Au_x+K\nu_x. \tag{3}$$

If $p=0$ and the fibers move out of a volume, some air must flow into that volume to keep the air pressure zero. The volume of fibers going out of a unit volume of space is du_x, where d is the volume density of fibers, $d=1-\phi$. They are practically incompressible compared to air; therefore, the volume of air that streams out of a unit volume must be

$$\nu_x=-du_x. \tag{4}$$

From Eq. (3) ($p=0$) and Eq. (4), one gets

$$A=dK. \tag{5}$$

From Eqs. (1) and (5), the elastic energy density becomes

$$E=\tfrac{1}{2}c_{11}u_x^2+dK\ u_x\nu_x+\tfrac{1}{2}K\nu_x^2. \tag{6}$$

The stress σ in the fiber lattice can also be found from the elastic energy density, Eq. (6):

$$\sigma=\frac{\partial E}{\partial u_x}=c_{11}u_x+dK\nu_x. \tag{7}$$

From this equation one sees that the elastic modulus c_{11} should be measured by constant air volume ($\nu_x=0$). However, it was measured by constant pressure. The relation between the two moduli can be found by setting Eq. (4) into Eq. (7). Thus

$$\sigma=c_{11}u_x-d^2Ku_x. \tag{8}$$

From the last equation, one finds the relation between the elastic modulus for constant air pressure and volume c_{p11} and $c_{\nu 11}$. The result is

$$c_{p11}=c_{\nu 11}-d^2K. \tag{9}$$

However, the difference between the two elastic moduli is small, 2% and 1% for $d=0.0056$ and 0.016, which corresponds to mass density 14 and 30 kg/m^3.

B. Viscous and inertial forces

We assume a harmonic time variation, described by a complex time factor $e^{-i\omega t}$, where ω is the cyclic frequency and t is the time. In an earlier paper[10] by the author, the forces on the fibers from the air stream are computed when the fibers do not move. The movement of the fibers can be taken care of by changing the boundary condition on the fibers, and repeating the calculation in the paper.[10] When this is done, one finds the forces f_f on the fibers in a unit volume of glass wool,

$$f_f=-d\rho\omega^2u+R'_\perp i\omega(u-\nu), \tag{10}$$

where ρ is the mass density of air. $R'_\perp$ is the dynamic resistivity of the fibers, which will be computed by the self-consistent method of the paper in Ref. 10, summarized in Appendix B.

Equation (10) can be controlled in the high-frequency limit. It follows from the article in Ref. 10 that the high-frequency limit of the resistivity is

$$R'_\perp\to-2d\rho i\omega. \tag{11}$$

When this is set into Eq. (10), one obtains

$$f_f = d\rho\omega^2 u - 2d\rho\omega^2 \nu. \tag{12}$$

This is reasonable because the inertia of a cylinder oscillating perpendicular to its axis in a fluid is increased by the mass of fluid displaced by the cylinder, Lamb.[11] Equation (12) is also according to Eq. (11.9) in Sec. 12 of Landau and Lifschitz.[12] They assumed potential flow, which is valid for high frequencies, where the viscous boundary layer is very thin.

The viscous forces on the air follow from Newton's law of action and reaction. Therefore, the force on the air in a unit volume is

$$f_a = -R'_\perp i\omega(u-\nu). \tag{13}$$

This can be checked in the high-frequency limit. From Eqs. (11) and (13) one gets, in this limit,

$$f_a = 2d\rho\omega^2\nu - 2d\rho\omega^2 u. \tag{14}$$

By considering only inertial forces, and using Newton's second law $f_a = -\rho\omega^2\nu$. This is set into Eq. (14), and one gets

$$-(1+2d)\rho\omega^2\nu = -2d\rho\omega^2 u. \tag{15}$$

Rayleigh[13] computed the effective mass ρ_{eff} for potential flow perpendicular to fixed cylinders. He found

$$\rho_{\text{eff}} = \frac{1+d}{1-d}\,\rho. \tag{16}$$

To first order in d, this is $\rho_{\text{eff}} = (1+2d)\rho$, which agrees with the left side of Eq. (15).

C. Wave equations

The equations for a plane wave propagating in the x direction of a rectangular coordinate system can be found by applying Newton's second law to fibers and air in a unit volume. By computing the forces on a unit volume from the density of elastic energy, Eq. (6), and the viscous forces, Eqs. (10) and (13), one gets

$$-\omega^2\begin{bmatrix}\mu-d\rho & 0\\ 0 & \rho\end{bmatrix}\begin{bmatrix}u\\ \nu\end{bmatrix} = \begin{bmatrix}c_{11} & dK\\ dK & K\end{bmatrix}\begin{bmatrix}u_{xx}\\ \nu_{xx}\end{bmatrix} + i\omega R'_\perp\begin{bmatrix}1 & -1\\ -1 & 1\end{bmatrix}\begin{bmatrix}u\\ \nu\end{bmatrix}, \tag{17}$$

where μ is the ordinary mass density of glass wool, and u_{xx} and ν_{xx} are the second partial derivatives of the displacement of the fiber and air.

D. Solution of wave equations

We assume plane wave solutions to Eq. (17) of the form

$$\begin{bmatrix}u\\ \nu\end{bmatrix} = \begin{bmatrix}u_0\\ \nu_0\end{bmatrix}e^{ikx}, \tag{18}$$

where u_0 and ν_0 are constants, and k is a wave number. This equation is substituted in Eq. (17). A nontrivial solution exists if the following determinant is zero:

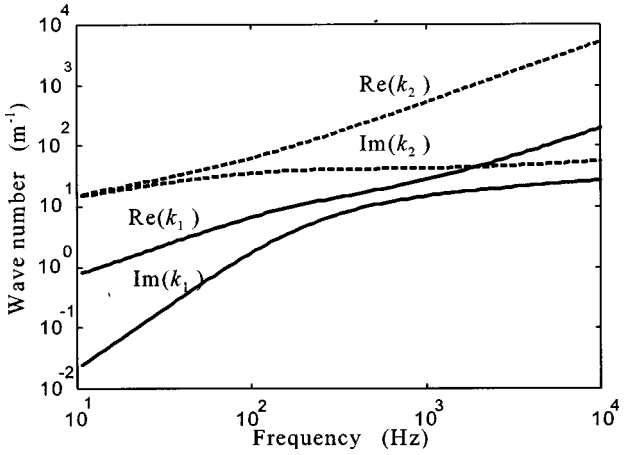

FIG. 1. Wave numbers computed for glass wool of density 14 kg/m^3, volume density 0.0056, diameter of fibers 6.8 μm, and elastic modulus 2000 Pa. The waves associated with k_1 carry most of the sound pressure, the ones associated with k_2 carry most of the mechanical stress of the fiber skeleton. The real part of the wave number gives the phase shift per meter, and the imaginary part the relative attenuation per meter.

$$\begin{vmatrix}-\omega^2(\mu-d\rho)+k^2c_{11} & k^2dK - i\omega R'_\perp\\ k^2dK - i\omega R'_\perp & -\omega^2\rho + k^2K\end{vmatrix} = 0. \tag{19}$$

This equation has two solutions k_1 and k_2, which are shown in Fig. 1 as a function of frequency. The curves were computed with a fiber diameter 6.8 μm, the distance between fibers 80 μm, volume density $d=0.0056$, and elastic modulus 2000 Pa; which parameters are valid for light glass wool of density 14 kg/m^3. Figure 2 shows the result for glass wool with the same fiber diameter, distance between fibers 58 μm, fiber density $d=0.016$, elastic modulus 16 000 Pa, and mass density 30 kg/m^3.

The constants u_0 and ν_0 of Eq. (18) are related by

$$\begin{bmatrix}-\omega^2(\mu-d\rho)+k^2c_{11} & k^2\,dK - i\omega R'_\perp\\ k^2\,dK - i\omega R'_\perp & -\omega^2\rho + k^2K\end{bmatrix}\begin{bmatrix}u_0\\ \nu_0\end{bmatrix} = \begin{bmatrix}0\\ 0\end{bmatrix}. \tag{20}$$

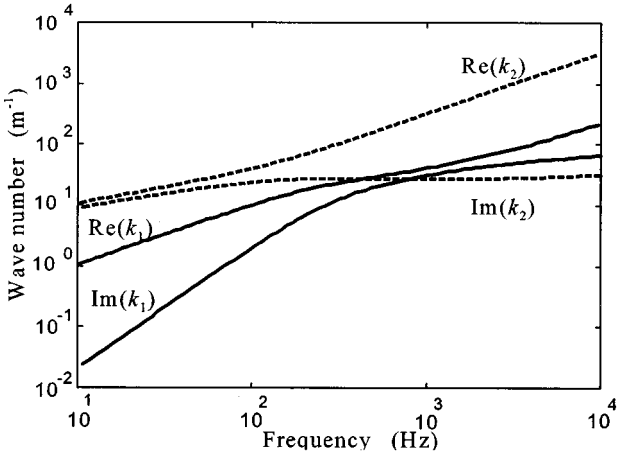

FIG. 2. Wave numbers computed for glass wool of density 30 kg/m^3, volume density 0.016, diameter of fibers 6.8 μm, and elastic modulus 16 000 Pa.

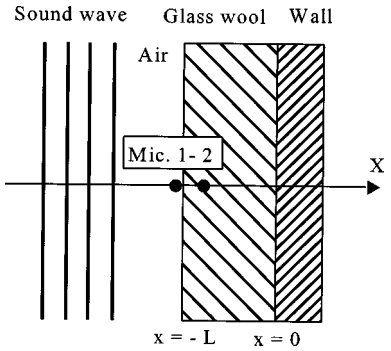

FIG. 3. Plane waves are coming in from the left. They propagate in the glass wool and are reflected by the hard wall. The pressure is measured at the surface of the glass wool and inside it.

In Eq. (20) $k=k_1$ or k_2, the two solutions of Eq. (19). Formulas for k_1 and k_2 are in Appendix C.

II. REFLECTIONS FROM THE REAR

In the measurements, a sound wave from a loudspeaker reaches a slab of glass wool, the rear side of which is placed on a wall. The wave front is parallel to the slab, as shown in Fig. 3. The sound pressure is measured inside the glass wool. Therefore, we compute the sound pressure of a plane wave inside an infinite slab, which is attached to a hard airtight wall and free on the other side.

The displacement of air particles and the fiber skeleton is zero at the wall. A coordinate system is chosen with an x axis perpendicular to the wall and the origin at the wall. The sound particle displacement ν can be written as

$$\nu=\nu_1 \sin(k_1x)+\nu_2 \sin(k_2x). \tag{21}$$

The constants ν_1 and ν_2 will be determined by the boundary condition on the free surface of the slab. The displacement of the fiber skeleton u can be written in a similar way,

$$u=u_1 \sin(k_1x)+u_2 \sin(k_2x); \tag{22}$$

here are u_1 and u_2 constants to be determined by the boundary condition on the free surface of the slab.

The slab is placed between $x=-L$ and $x=0$. At the free surface the stress on the fibers is zero. The boundary condition for the derivative of u and ν can be found from Eq. (7), but because the volume density of fibers is small, one gets

$$\left[\frac{du}{dx}\right]_{x=-L}=0. \tag{23}$$

On the free surface the sound pressure p_0 is given, from Eqs. (2) and (3) one gets because d is small,

$$\left[\frac{d\nu}{dx}\right]_{x=-L}=-\phi C p_0. \tag{24}$$

Equations (20), (23), and (24) determine the constants u_1, u_2, ν_1, ν_2. The constants u_1 and ν_1 are connected by Eq. (20), where they shall be substituted for u_0 and ν_0. The other two constants u_2 and ν_2 are treated in the same way. The air pressure inside the glass wool can be found from

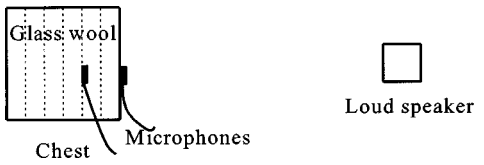

FIG. 4. The measuring setup is placed in an anechoic room. The chest is made of 22-mm thick chipboard with inside dimensions 0.60 m×0.60 m ×0.90 m. Six slabs 0.10-m thick of glass wool were placed in it. The chest is open toward the loudspeaker. The two condenser microphones are $\frac{1}{2}$ in. in diameter, and their axes are perpendicular to the direction to the loudspeaker. The distance from the chest to the loudspeaker is 1.70 m.

$$p=-\frac{1}{\phi C}\frac{d\nu}{dx}. \tag{25}$$

A formula for the pressure is given in Appendix C.

III. MEASUREMENT SETUP AND RESULTS

The attenuation of plane harmonic sound waves propagating in glass wool was measured. Figure 4 shows the setup, which was placed in an anechoic room. A rectangular chest made of 22 mm thick chipboard was used. It had one open side, which faced a loudspeaker 1.7 m away. In the chest, six slabs of glass wool each measuring 0.6 m ×0.9 m×0.1 m were laid, with fibers parallel to the open side. Two half-inch condenser microphones were used. One was set at the free surface of the glass wool and another was placed inside the glass wool. The axes of the microphones were parallel to the free surface.

The loudspeaker was connected to a sinusoidal voltage supply, the frequency of which could be swept through a range. Attenuation of sound waves was calculated by dividing the pressure at the surface by the pressure inside the glass wool. Measurements were done with the inside microphone 0.2 m from the free surface and placed in the middle.

Pressure sensitivities of the microphones are equal. At high frequencies, diffraction of waves about the microphone cause changes in the sensitivity. But because frequencies were always below 10 kHz, and the direction of propagation perpendicular to the axis of the microphone, this effect is smaller than 0.5 dB in free air. At 10 kHz the wavelength in the free air is almost equal to the one inside the glass wool. Therefore, the diffraction is small and equal for the two microphones; and has no influence on the measured attenuation.

The inside microphone is set between two glass wool slabs with thickness 100 mm; and the microphone cable is placed between the two slabs that touch each other. The glass wool is soft so there is some deformation of it in a small volume about the microphone. The diameter of this deformation is about 25 mm. Considering the thickness of the glass wool slabs and the lateral dimensions of the slabs, it can be assumed that the pressure measured by the microphone is close to the undisturbed pressure in the glass wool.

The volume density of fibers d equals the mass density of glass wool divided by the mass density of glass, which is 2550 kg/m^3. For glass wools of mass density 14 and 30 kg/m^3, one finds $d=0.0056$ and 0.016.

To compute the compressibility and resistivity of air as a function of frequency, one must know the radius of fibers a

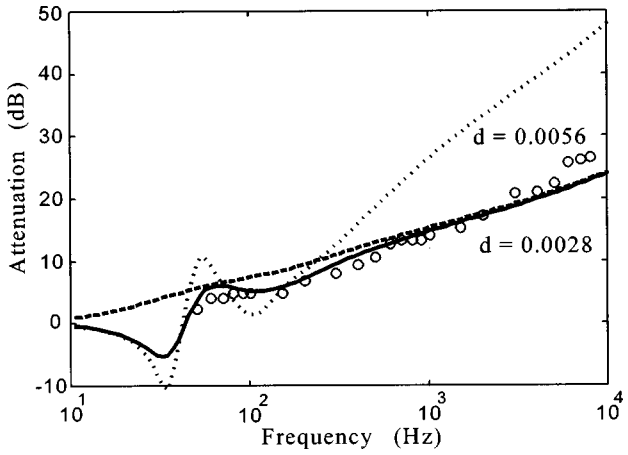

FIG. 5. Measured and computed attenuation of plane sound waves in glass wool of density 14 kg/m^3 and elastic modulus 2000 Pa. The fibers are parallel to the wave front. The attenuation was found 0.20 m inside the glass wool sample of thickness 0.60 m. The dotted line is computed for a volume density of fibers of 0.0056 and fiber diameter 6.8 μm. The circles are measurements. The full line is computed for a density of 0.0028. The dashed line is calculated with the same density but assuming the fibers do not move.

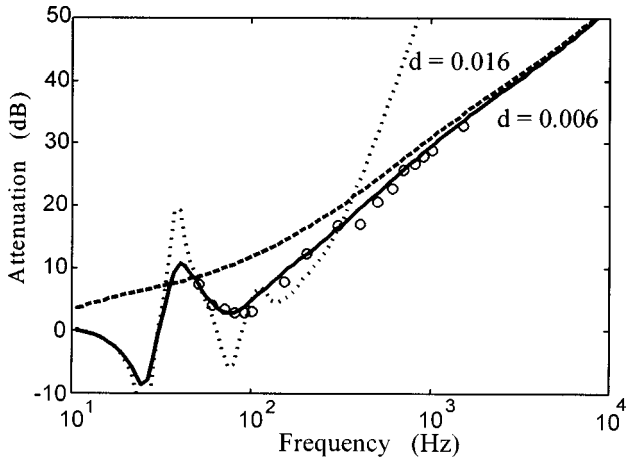

FIG. 6. Measured and computed attenuation of plane sound waves in glass wool of density 30 kg/m^3 and elastic modulus 16 000 Pa. The fibers are parallel to the wave front. The attenuation was found 0.20 m inside the glass wool sample of thickness 0.60 m. The dotted line is computed for a volume density of fibers of 0.016 and fiber diameter 6.8 μm. The circles are measurements. The full line is computed for a density of 0.006. The dashed line is calculated with the same density but assuming the fibers do not move.

and the distance b between fibers. The diameter of the fibers was measured by a microscope to 6.8 μm with a standard variation of 2.7 μm. The mean distance b is the square root of the area per fiber. It can be calculated from the volume density of fibers d, $b = a\sqrt{\pi/d}$, because we assume parallel fibers. One finds $b = 80$ and 58 μm for low- and high-density glass wool.

A theoretical calculation of attenuation with moving fibers requires the knowledge of the elastic moduli of the glass wool skeleton. It was measured by turning the chest so that the open side was up. A 22-mm thick chipboard plate with a clearance of 10 mm along the edge was put on the glass wool and loaded with weights. Depression of the plate was measured as a function of the weight placed on the chipboard plate. The elastic modulus equals the gravity force per area of the plate divided by the corresponding depression. For glass wool of density 14 and 30 kg/m^3, the elastic moduli were measured to be 2000 and 16 000 Pa.

The attenuation of sound waves by 0.20 m glass wool of density 14 kg/m^3 in a slab with a thickness of 0.60 m is shown in Fig. 5. The dotted line shows the computed pressure for a fiber volume density of 0.0056, fiber diameter 6.8 μm, and elastic modulus 2000 Pa. The measured attenuation is shown as circles. The full line is computed in the same way as the dotted one, but the density of fibers 0.0028 was chosen to make the curve fit the measuring points. The dashed line was computed from the same density, but it was assumed that the fibers did not move.

Figure 6 shows the attenuation for the same depth, thickness of slab, and fiber diameter, but the mass density is 30 kg/m^3. For the dotted line the volume density is 0.016, fiber diameter 6.8 μm, and elastic modulus 16 000 Pa. The circles are the measured attenuation. It is greater than in Fig. 5, because the mass density is higher. The full line is the calculated attenuation, where the density 0.006 was chosen to fit the curve to the measured points. The dashed line is the calculated attenuation for fixed fibers with the same density.

IV. DISCUSSION

The calculations of attenuation were based on a geometrical model consisting of parallel cylinders placed randomly. However, the measurements show that this model cannot be used to predict the actual attenuation when the volume density of fibers is computed from the diameters of fibers and the mass density of glass and glass wool. The measured attenuation at all frequencies can be computed if one fits the density of fibers. For the glass wool of density 14 kg/m^3, the volume density based on mass densities was 0.0056 and the density used to fit the data was 0.0028. For density 30 kg/m^3 the volume density was 0.016 and 0.006, respectively. Apparently real glass wool is more open than the model. A more complicated model is needed to compute all acoustic properties from the geometry of glass wool. One important property of the glass wool is the direct flow resistivity that cannot be correctly computed from the model with randomly placed, parallel cylinders.

The full line of Fig. 5 can be computed for frequencies above 100 Hz if one neglects the reflection of waves from the rear because the sound wave reflected from the rear side of the glass wool stack is much attenuated. A curve for attenuation without reflections is not shown in Fig. 5. The low-frequency resonance would be absent if the fibers did not move because the attenuation would be greater. The attenuation is smaller when the fibers move, because the relative velocity between air and fibers is smaller, and the energy dissipation is smaller. In Fig. 6 for the heavy glass wool, the reflections from the rear can be neglected for frequencies above 100 Hz.

Measurements and calculations show that the attenuation is smaller when the glass wool fibers can move. In Fig. 6 one can see that a propagating sound wave in glass wool of density 30 kg/m^3 and frequency 100 Hz is attenuated 4 dB by a layer of thickness 0.20 m if the fibers move and 12 dB if they do not move. That means that one could increase the

attenuation of glass wool by mechanical restriction of the movement of the glass wool.

The author's previous paper[14] reported measurements of the attenuation of glass wool samples, placed in a tube of diameter 102 mm, where they fitted tightly. These measurements could be explained by assuming the fibers did not move. For glass wool of density 40 kg/m^3 an attenuation of 14 dB for a layer of 0.20 m was measured at the frequency 100 Hz. Apparently the tube prevented the movements of the fibers.

APPENDIX A: CALCULATION OF THE DYNAMICAL COMPRESSIBILITY

The dynamic compressibility was computed from the temperature increase caused by the sound pressure by the methods of the paper by Tarnow.[8] The effective heat capacity of fibers per volume is called K_h. First set $K_h=0$, then compute the wave number of the heat wave in the air k_h from

$$k_h=\sqrt{\frac{i\omega(\rho c_p+K_h)}{\kappa}}, \tag{A1}$$

where $\rho=1.20$ kg/m at standard atmospheric pressure 101 kPa and temperature 20 °C, $c_p=1.00$ kJ K^{-1} kg^{-1} is the specific heat capacity of air at constant pressure, and $\kappa=2.57\times10^{-2}$ W m^{-1} K^{-1} is the coefficient of thermal conduction of air, both at 20 °C. K_h is then computed from

$$K_h=-\frac{2\pi a\kappa k_h H_1^1(k_h a)}{i\omega b^2 H_0^1(k_h a)}; \tag{A2}$$

here a is the radius of the fibers, b^2 the mean area per fiber, and $H_0^1(z)$ and $H_1^1(z)$ are Hankel functions. It is assumed that the heat capacity of the fibers is infinitely great. If it is finite, Eq. (A2) must be changed in the manner shown in an earlier paper by the author.[8] To obtain self-consistency, the value of K_h computed by Eq. (A2) is set into Eq. (A1) and a new value of k_h is computed. This is set into Eq. (A2), etc. until the process converges to a value of K_h. This requires normally four iterations.

The dynamic compressibility of the air is computed by setting K_h into the following equation:

$$C=\frac{1}{P}\left[1-\frac{(\gamma-1)\rho c_p}{\gamma(\rho c_p+K_h)}\right]; \tag{A3}$$

here $\gamma=1.40$ and P is the atmospheric pressure, 101 kPa normally.

APPENDIX B: CALCULATION OF DYNAMIC RESISTIVITY

The dynamic resistivity was also computed by a self-consistent procedure, which is in the paper by Tarnow.[10] One first chooses a value of the wave number k_ν of the viscous wave in the boundary layer, for example, $k_\nu=i/b$, then one computes the resistivity from

$$R_\perp'=\frac{2\pi\eta k_\nu a}{b^2}\left(-k_\nu a+\frac{2H_1^1(k_\nu a)}{H_0^1(k_\nu a)}\right); \tag{B1}$$

here $\eta=1.86\times10^{-5}$ Pa s, the viscosity of air at 20 °C.

Then one computes a new value of the wave number k_ν from

$$k_\nu=\sqrt{\frac{i\omega\rho-R_\perp'}{\eta}}. \tag{B2}$$

A new value of $R_\perp'$ is computed from Eq. (B1). After that, a new value of k_ν is found from Eq. (B2). This procedure is repeated until a stable value of the resistivity is obtained. This takes about four iterations.

APPENDIX C: FORMULAS FOR WAVE NUMBER AND ATTENUATION

The solution of Eq. (19) gives the wave numbers. The concentration d of fibers is small, therefore the terms proportional to d can be neglected, when this is done, one gets the wave number k_1 for the airborne wave,

$$k_1=\sqrt{-\frac{A}{2}-\sqrt{\frac{A^2}{4}-B}}, \tag{C1}$$

where

$$A=\rho\phi C\omega^2+\frac{\mu\omega^2}{c_{11}}+\frac{i\omega R_\perp'}{c_{11}}+i\omega R_\perp'+i\omega R_\perp'\phi C, \tag{C2}$$

and

$$B=(\rho\mu\omega^4+\rho i\omega^3 R_\perp'+\mu i\omega^3 R_\perp')\,\frac{\phi C}{c_{11}}. \tag{C3}$$

The wave number k_2 for the mechanical mode is

$$k_2=\sqrt{-\frac{A}{2}+\sqrt{\frac{A^2}{4}-B}}. \tag{C4}$$

The attenuation is computed from the coefficients u_1, u_2, ν_1, ν_2 of Eqs. (21) and (22). Set $v_1=1$, and use Eqs. (20) and (23) to find the rest. The pressure can be found by setting Eq. (21) into (24). In this way

$$p(x)=-\frac{k_1}{\phi C}\left[\cos k_1 x+D\cos k_2 x\right], \tag{C5}$$

where

$$D=\frac{(\omega R_\perp')^2\cos k_1 L}{(-\rho\omega^2+k_2^2/(\phi C)-i\omega R_\perp')(-\mu\omega^2+c_{11}k_1^2-i\omega R_\perp')\cos k_2 L}, \tag{C6}$$

when the thickness of the sample is L.

The attenuation is the absolute value of the sound pressure at the free surface divided by the pressure inside the sample,

$$\left|\frac{p(-L)}{p(x)}\right|, \tag{C7}$$

where $-L<x<0$.

[1] M. D. Dahl, E. J. Rice, and D. E. Groesbeck, ''Effects of fiber motion on the acoustic behavior of an anisotropic, flexible fibrous material,'' J. Acoust. Soc. Am. **87**, 54–66 (1990).
[2] J. F. Allard, C. Depollier, P. Guignouard, and P. Rebillard, ''Effect of a

resonance of the frame on the surface impedance of glass wool of high density and stiffness,'' J. Acoust. Soc. Am. **89**, 999–1001 (1991).
[3] R. F. Lambert, ''Acoustic resonance in highly porous, flexible, layered fine fiber materials,'' J. Acoust. Soc. Am. **93**, 1227–1234 (1993).
[4] R. F. Lambert, ''Low-frequency acoustic behavior in highly porous, flexible, layered fine fiber materials,'' J. Acoust. Soc. Am. **97**, 818–821 (1995).
[5] M. A. Biot, ''Theory of propagation of elastic waves in a fluid-saturated porous solid. I. low frequency range,'' J. Acoust. Soc. Am. **28**, 168–178 (1956).
[6] M. A. Biot, ''Theory of propagation of elastic waves in a fluid-saturated porous solid. II. Higher frequency range,'' J. Acoust. Soc. Am. **28**, 179–191 (1956).
[7] T. F. Johansen, J.-F. Allard, and B. Brouard, ''Finite element method for predicting the acoustical properties of porous samples,'' Acta Acoust. **3**, 487–491 (1995).
[8] V. Tarnow, ''Compressibility of air in fibrous materials,'' J. Acoust. Soc. Am. **99**, 3010–3017 (1996).
[9] L. I. Schiff, *Quantum Mechanics* (McGraw-Hill, New York, 1955), Sec. 38, p. 283.
[10] V. Tarnow, ''Calculation of the dynamic air flow resistivity of fiber materials,'' J. Acoust. Soc. Am. **102**, 1680–1688 (1997).
[11] H. Lamb, *Hydrodynamic* (Cambridge U.P., New York, 1993), Chap. IV, Sec. 68.
[12] L. D. Landau and E. M. Lifshitz, *Fluid Mechanics* (Pergamon, Oxford, 1959).
[13] J. W. S. Rayleigh, ''On the influence of obstacles arranged in a rectangular order upon the properties of a medium,'' Philos. Mag. **34**, 481–502 (1892).
[14] V. Tarnow, ''Measurement of sound propagation in glass wool,'' J. Acoust. Soc. Am. **97**, 2272–2281 (1995).

Development and analysis of a two-stage beamformer for multiple correlated interferers using rectangular array

T.-T. Lin and T.-S. Lee[a)]
Department of Communication Engineering, National Chiao Tung University, Hsinchu, Taiwan, Republic of China

(Received 8 July 1995; revised 24 July 1998; accepted 7 October 1998)

A two-stage two-dimensional (2-D) beamformer is proposed for signal enhancement in an environment of multiple correlated interferers using a rectangular array. In the first stage, subarray beamformers are constructed which exhibit reliable interference cancellation using difference-preprocessed and spatially smoothed data. A secondary combining of all possible subarray beamformers is then performed to fully exploit the array aperture. It is shown that, compared to the conventional one-stage optimum beamformer, the two-stage beamformer performs equally well and requires a much lower complexity of implementation when a suitable subarray size is chosen. [S0001-4966(99)04701-3]

PACS numbers: 43.60.Dh, 43.60.Gk [JCB]

INTRODUCTION

An adaptive beamformer performs spatial filtering by forming a beam in such a fashion that the desired signal can be received with a large gain, while unwanted interference and noise can be suppressed.[1] It has a wide range of acoustical applications, including sound-signal enhancement and underwater communications.[2–4] Conventional adaptive beamformers are effective in suppressing strong interference so long as the pointing error is small and the interferers are uncorrelated with the desired source. However, in the presence of beam-pointing errors and/or highly correlated interferers, these beamformers exhibit severe degradation in the output signal-to-interference-plus-noise ratio (SINR) as a result of signal cancellation.[5,6] To avoid such problems, the difference preprocessor[5] was proposed as a tool for removing the desired signal before beamforming. By difference preprocessing, the beamformer will not cancel the desired signal even in the presence of pointing errors and coherent interference.

In spite of the success of dealing with a single correlated interferer, the difference-preprocessed beamformer cannot handle multiple correlated interferers.[7] This is because the relationship that causes the mutual cancellation between the multiple interfering signals in the master beamformer is destroyed as the optimum weights are copied to the slave beamformer. To avoid such performance breakdown, the spatial-smoothing technique[8] was incorporated as a means of decorrelating the interfering signals. This ensures that the beamformer will suppress each of the interfering signals, instead of performing a mutual cancellation. Unfortunately, working with spatial smoothing results in a reduction of the array aperture, which in turn reduces the signal-to-noise ratio (SNR) gain, nulling capacity and resolution capability of the beamformer. A post combiner can be employed to recover the full aperture of the array.[7,9] This means that the weight vector associated with the (spatially smoothed) subarray beamformer is copied to each of the possible subarrays of the same size, and the overall beamformer is obtained via a secondary combining of all subarray beamformers.

We exploit here the post-combining concept to develop a two-stage 2-D beamformer for rectangular arrays. The beamformer first incorporates a 2-D difference preprocessor to alleviate desired signal cancellation due to pointing errors. The 2-D spatial smoothing[10] is then employed to decorrelate the interference left in the preprocessor output, leading to a rectangular subarray. The spatially smoothed correlation matrix is noise whitened and used to compute the 2-D weights which produce a null in each of the interfering directions. This set of weights can be applied back to each of the identical subarrays, leading to a set of ''interference cancellation'' beamformers. Finally, a full-aperture beamformer is obtained via a secondary combining of the interference-free subarray beamformers in accordance with the maximum-output SNR criterion. The two-stage procedure is algebraically organized in that each type of 2-D operation involved is represented by a matrix transformation, which facilitates the derivation of the correlation structure and weight vector. The proposed 2-D beamformer is suitable for acoustical signal acquisition in the presence of multipath reflections and strong interference. For example, the beamformer can be implemented on a microphone array[2] for remote sound-source analysis in an indoor environment contaminated with narrow-band manmade noise. It can also be used for acoustical communications in shallow water, where multipaths cause a major problem.[4] On the other hand, the algorithm for computing the 2-D weights can be executed in an adaptive fashion by using high-speed digital signal processors.[3,4] In this regard, the two-stage procedure is much more efficient than the conventional one-stage procedure in that the computational complexity is significantly reduced by breaking the original large 2-D array into two smaller ones.

a)Electronic mail: tslee@cc.nctu.edu.tw

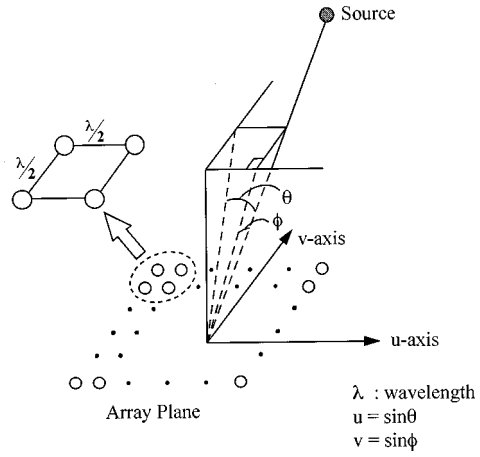

FIG. 1. Array geometry and coordinate system.

I. PROBLEM FORMULATION

A. Notations

Some of the key notations are defined as follows:

$\cdot^T(\cdot^H)$:	transpose (complex conjugate transpose)
$\mathbf{I}_n$:	$n\times n$ identity matrix
$\mathbf{J}_n$:	$n\times n$ reverse permutation matrix with ones on the antidiagonal and zeros elsewhere
$\mathbf{O}_{m\times n}$:	$m\times n$ zero matrix
$\mathbf{M}(i,k)$:	(i,k)th entry of matrix $\mathbf{M}$
$\mathbf{M}(i{:}k,l{:}m)$:	submatrix of entries from ith to kth rows and lth to mth columns of $\mathbf{M}$
Vec$\{\mathbf{M}\}$:	concatenation of columns of $m\times n$ matrix $\mathbf{M}$ into $mn\times 1$ column vector
Vec$^{-1}\{\mathbf{v}\}$:	inverse of $\mathbf{v}=$Vec$\{\mathbf{M}\}$
$\mathbf{L}\odot\mathbf{M}$:	Inner product of matrices $\mathbf{L}$ and $\mathbf{M}$ defined by $\mathbf{L}\odot\mathbf{M}=\sum_i\sum_k \mathbf{L}^*(i,k)\mathbf{M}(i,k)=\text{Vec}^H\{\mathbf{L}\}\text{Vec}\{\mathbf{M}\}$.
Diag$\{\mathbf{v}\}$:	diagonal matrix whose main diagonal entries are given by vector $\mathbf{v}$
$E\{\cdot\}$:	expectation
Corr$\{\mathbf{v}\}$:	correlation matrix of random vector $\mathbf{v}$ defined by Corr$\{\mathbf{v}\}=E\{\mathbf{v}\mathbf{v}^H\}$.

B. Array-data model

Consider the scenario involving a desired source and K possibly correlated interferers impinging on an $M\times N$ narrow-band rectangular array of identical elements equally spaced by a half-wavelength. These sources are assumed to be in the far field of the array such that the plane-wave model holds. The array data received at a certain sampling instant can be expressed as an $M\times N$ matrix:

$$\mathbf{X}=\sum_{i=1}^{K+1}\xi_i\mathbf{A}(u_i,v_i)+\mathbf{N}, \tag{1}$$

where $u_i=\sin(\theta_i)$ and $v_i=\sin(\phi_i)$ represent the sine-space angles of the ith source with respect to the u- and v-axis, respectively, as shown in Fig. 1. Note that the coordinate system inherently imposes the constraint $|\theta|+|\phi|\leqslant 90$ deg. The random scalar ξ_i denotes the complex envelop of the ith source received at the (1,1)th element of the array, and $\sigma_i^2=E\{|\xi_i|^2\}$ is the corresponding source power. The $M\times N$ matrix $\mathbf{A}(u,v)$ is the array-response matrix given by

$$\mathbf{A}(u,v)=\mathbf{a}_M(u)\mathbf{a}_N^T(v), \tag{2}$$

where

$$\begin{aligned}\mathbf{a}_m(u)&=[1,e^{j\pi u},\ldots,e^{j(m-1)\pi u}]^T\\ \mathbf{a}_n(v)&=[1,e^{j\pi v},\ldots,e^{j(n-1)\pi v}]^T\end{aligned} \tag{3}$$

[with $m=M$ and $n=N$ in (2)] are the 1-D response vectors along the u- and v-axis, respectively. Finally, $\mathbf{N}$ consists of the noise present at the elements. In the following development, we will assume that source 1 is the desired one and treat the others as interference. Also, the noise components in $\mathbf{N}$ are assumed spatially white with power σ_n^2.

One way of viewing the data matrix in $MN\times 1$ vector form is by concatenating the columns (u axis) of $\mathbf{X}$ into

$$\mathbf{x}=\text{Vec}\{\mathbf{X}\}=\sum_{i=1}^{K+1}\xi_i\mathbf{a}(u_i,v_i)+n=\mathbf{D}\mathbf{s}+\mathbf{n}, \tag{4}$$

where

$$\mathbf{a}(u,v)=\text{Vec}\{\mathbf{A}(u,v)\} \tag{5}$$

$$\mathbf{D}=[\mathbf{a}(u_1,v_1),\mathbf{a}(u_2,v_2),\ldots,\mathbf{a}(u_{K+1},v_{K+1})] \tag{6}$$

$$\mathbf{s}=[\xi_1,\xi_2,\ldots,\xi_{K+1}]^T \tag{7}$$

$$\mathbf{n}=\text{Vec}\{\mathbf{N}\}. \tag{8}$$

We refer to $\mathbf{x}$, $\mathbf{a}(u,v)$, and $\mathbf{n}$ as the vector representations of $\mathbf{X}$, $\mathbf{A}(u,v)$, and $\mathbf{N}$, respectively.

C. Beamforming issues

A beamformer transforms the array-data matrix into a scalar output y via an $M\times N$ weight matrix $\mathbf{W}$ according to

$$y=\mathbf{W}\odot\mathbf{X}=\mathbf{w}^H\mathbf{x}, \tag{9}$$

where $\mathbf{w}=\text{Vec}\{\mathbf{W}\}$ is the vector representation of $\mathbf{W}$ corresponding to $\mathbf{x}$.

The beamformer we will work with is the linearly constrained minimum variance (LCMV) beamformer,[11] which minimizes the output power subject to a fixed-response constraint in the look direction $(u_o,v_o)=[\sin(\theta_o),\sin(\phi_o)]$:

$$\min_{\mathbf{w}} E\{|y|^2\}\equiv\mathbf{w}^H\mathbf{R}_x\mathbf{w}$$
$$\text{subject to: } \mathbf{W}\odot\mathbf{A}(u_o,v_o)\equiv\mathbf{w}^H\mathbf{a}(u_o,v_o)=c, \tag{10}$$

where $\mathbf{R}_x$ is the $MN\times MN$ data-correlation matrix, and c is a nonzero constant. Invoking the spatial whiteness of $\mathbf{N}$ and using (4), we have

$$\mathbf{R}_x=\text{Corr}\{\mathbf{x}\}=\mathbf{D}\mathbf{P}\mathbf{D}^H+\sigma_n^2\mathbf{I}_{MN}, \tag{11}$$

where $\mathbf{P}=\text{Corr}\{\mathbf{s}\}$ and $\sigma_n^2\mathbf{I}_{MN}$ are the source and noise correlation matrices, respectively. The solution to (10) is

$$\mathbf{w}=\frac{\sigma_n^2}{\sqrt{MN}}\mathbf{R}_x^{-1}\mathbf{a}(u_o,v_o), \tag{12}$$

where we choose the scaling factor for the convenience of the subsequent analysis.

II. DIFFERENCE PREPROCESSING

The difference preprocessing technique[5] was proposed as a means of avoiding desired signal cancellation due to pointing errors or coherent interference. Although the technique was developed originally for uniform linear array, it can be equally incorporated into the 2-D array considered herein. Note first that an $M\times N$ rectangular array can be viewed as consisting of four identical rectangular subarrays of size $(M-1)\times(N-1)$. By linearly combining these subarrays with a judiciously chosen weight vector $\mathbf{h}=[h_{11},h_{21},h_{12},h_{22}]^T$, a difference preprocessed (DP) virtual subarray results. The DP subarray is an $(M-1)\times(N-1)$ rectangular array whose elements share the same response pattern:

$$h(u,v)=\mathbf{h}^H\mathbf{a}_q(u,v), \tag{13}$$

where

$$\mathbf{a}_q(u,v)=[1,e^{j\pi u},e^{j\pi v},e^{j\pi(u+v)}]^T \tag{14}$$

accounts for the relative phases among the four subarrays. By difference preprocessing, the desired signal is removed by choosing $\mathbf{h}$ such that $h(u_o,v_o)=0$.

Denote as

$$\tilde{\mathbf{A}}(u,v)=\mathbf{a}_{M-1}(u)\mathbf{a}_{N-1}^T(v) \tag{15}$$

$$\tilde{\mathbf{a}}(u,v)=\mathrm{Vec}\{\tilde{\mathbf{A}}(u,v)\} \tag{16}$$

$$\tilde{\mathbf{D}}=[\tilde{\mathbf{a}}(u_1,v_1),\tilde{\mathbf{a}}(u_2,v_2),\ldots,\tilde{\mathbf{a}}(u_{K+1},v_{K+1})] \tag{17}$$

the counterparts of $\mathbf{A}(u,v)$, $\mathbf{a}(u,v)$, and $\mathbf{D}$, respectively, for the DP subarray. The operation of the preprocessor yields the DP data matrix as given by

$$\tilde{\mathbf{X}}=\sum_{i=1}^{2}\sum_{k=1}^{2}h_{ik}^*\mathbf{X}(i:M+i-2,k:N+k-2). \tag{18}$$

Since the effect of difference preprocessing is to scale the ith signal with the complex gain $h(u_i,v_i)$, we can show that the vector representation of $\tilde{\mathbf{X}}$ is

$$\tilde{\mathbf{x}}=\mathrm{Vec}\{\tilde{\mathbf{X}}\}=\mathbf{H}^H\mathbf{x}=\tilde{\mathbf{D}}\mathbf{G}\mathbf{s}+\mathbf{H}^H\mathbf{n}, \tag{19}$$

where

$$\mathbf{G}=\mathrm{Diag}\{[h(u_1,v_1),h(u_2,v_2),\ldots,h(u_{K+1},v_{K+1})]^T\} \tag{20}$$

accounts for the preprocessor gain for the $K+1$ sources, and

$$\mathbf{H}=\begin{bmatrix}\mathbf{H}_1 & & & 0\\ \mathbf{H}_2 & \mathbf{H}_1 & & \\ & \mathbf{H}_2 & \ddots & \\ 0 & & \ddots & \mathbf{H}_1\\ & & & \mathbf{H}_2\end{bmatrix}_{MN\times(M-1)(N-1)} \tag{21}$$

with

$$\mathbf{H}_i=\begin{bmatrix}h_{1i} & & & 0\\ h_{2i} & h_{1i} & & \\ & h_{2i} & \ddots & \\ 0 & & \ddots & h_{1i}\\ & & & h_{2i}\end{bmatrix}_{M\times(M-1)} \qquad i=1,2 \tag{22}$$

is the matrix representation of the preprocessor operation in (18). Note that the Toeplitz–block–Toeplitz structure of $\mathbf{H}$, as a result of the rectangular-array geometry, leads to $\mathbf{H}^H\mathbf{D}=\tilde{\mathbf{D}}\mathbf{G}$. The expression in (19) makes it easy to derive the DP data-correlation matrix:

$$\tilde{\mathbf{R}}_x=\mathrm{Corr}\{\tilde{\mathbf{x}}\}=\tilde{\mathbf{D}}\mathbf{G}\mathbf{P}\mathbf{G}^*\tilde{\mathbf{D}}^H+\sigma_n^2\mathbf{H}^H\mathbf{H}, \tag{23}$$

which indicates that on the DP subarray, one observes the source-correlation matrix $\mathbf{GPG}^*$ and noise-correlation matrix $\sigma_n^2\mathbf{H}^H\mathbf{H}$.

A. Separable preprocessor

The separable preprocessor is a direct extension of the 1-D preprocessor obtained by choosing $\mathbf{h}=[1,-e^{j\pi u_o},-e^{j\pi v_o},e^{j\pi(u_o+v_o)}]^T$. It is called separable since the response pattern $h(u,v)=[1-e^{j\pi(u-u_o)}][1-e^{j\pi(v-v_o)}]$ is separable with respect to the two axes. Figure 2(a) shows that the preprocessor produces a cross-null pattern centered at $(\theta_o,\phi_o)=(0\text{ deg},0\text{ deg})$. This causes the problem that the preprocessor will eliminate interferes from either (u,v_o) or (u_o,v), where u and v can be arbitrary. If this is the case, then the beamformer attached to the preprocessor cannot ''see'' these interferes and will fail to cancel them.

B. Nonseparable preprocessor

To avoid interference cancellation by the preprocessor, the response pattern $h(u,v)$ should exhibit nulling only within a limited region around (u_o,v_o). A possible approach is as follows. First, the constraint $h(u_o,v_o)=0$ is guaranteed by forcing $\mathbf{h}=\mathbf{V}_q\mathbf{f}$, where $\mathbf{V}_q$ is the 4×3 matrix representation of the nullspace of $\mathbf{a}_q^H(u_o,v_o)$ and $\mathbf{f}$ is a 3×1 vector. Second, in order to enhance the robustness of the preprocessor against pointing errors, the response $h(u,v)$ should be minimized over an angular region R around (u_o,v_o). Third, to retain the interference scenario as much as possible, $h(u,v)$ should be as close to 1 as possible outside R. These requirements lead to the following constrained problem:

$$\begin{aligned}\min_{\mathbf{f}}&\int\int_R|h(u,v)|^2du\,dv+\epsilon\int\int_{\bar{R}}|h(u,v)-1|^2du\,dv\\ &\equiv\mathbf{f}^H\mathbf{V}_q^H\mathbf{T}\mathbf{V}_q\mathbf{f}+\epsilon\left[\mathbf{f}^H\mathbf{V}_q^H\bar{\mathbf{T}}\mathbf{V}_q\mathbf{f}-\mathbf{f}^H\mathbf{V}_q^H\bar{\mathbf{t}}_1-\bar{\mathbf{t}}_1^H\mathbf{V}_q\mathbf{f}\right.\\ &\quad\left.+\int\int_R du\,dv\right]\quad\text{subject to:}\quad\mathbf{f}^H\mathbf{i}_1=1\end{aligned} \tag{24}$$

where

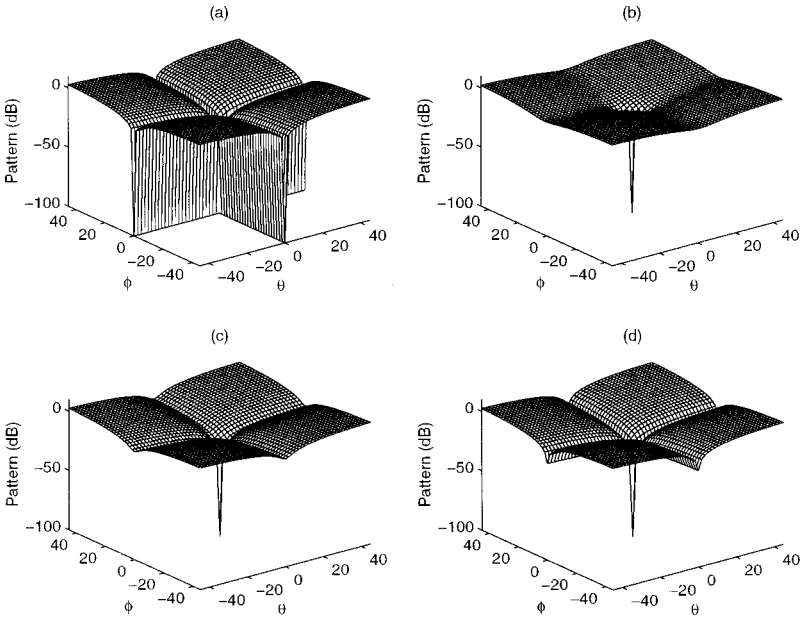

FIG. 2. Patterns of difference preprocessors. (a) separable preprocessor. (b) nonseparable preprocessor with $\epsilon=10^{-2}$. (c) nonseparable preprocessor with $\epsilon=10^{-4}$. (d) nonseparable preprocessor with $\epsilon=10^{-6}$.

$$\mathbf{T}=\int\int_R \mathbf{a}_q(u,v)\mathbf{a}_q^H(u,v)\,du\,dv \tag{25}$$

$$\overline{\mathbf{T}}=\int\int_{\overline{R}} \mathbf{a}_q(u,v)\mathbf{a}_q^H(u,v)\,du\,dv. \tag{26}$$

$\overline{\mathbf{t}}_1$ is the first column of $\overline{\mathbf{T}}$, $\mathbf{i}_1=[1,0,0]^T$, and ϵ is a parameter controlling the relative emphasis of the two cost terms. The constraint is included simply to avoid a trivial solution. Using the Lagrange multiplier technique, along with some algebraic manipulation, we get

$$\mathbf{h}=\mathbf{V}_q[\mathbf{V}_q^H(\mathbf{T}+\epsilon\overline{\mathbf{T}})\mathbf{V}_q]^{-1}[\epsilon\mathbf{V}_q^H\mathbf{t}_1+\eta\mathbf{i}_1], \tag{27}$$

where

$$\eta=\frac{1-\epsilon\overline{\mathbf{t}}_1^H\mathbf{V}_q[\mathbf{V}_q^H(\mathbf{T}+\epsilon\overline{\mathbf{T}})\mathbf{V}_q]^{-1}\mathbf{i}_1}{\mathbf{i}_1^H[\mathbf{V}_q^H(\mathbf{T}+\epsilon\overline{\mathbf{T}})\mathbf{V}_q]^{-1}\mathbf{i}_1}. \tag{28}$$

An example of the nonseparable preprocessor is given in Fig. 2(b)–(d), with $R=\{-5\ \text{deg}\leqslant\theta\leqslant 5\ \text{deg}, -5\ \text{deg}\leqslant\phi\leqslant 5\ \text{deg}\}$, $\overline{R}$ being the complement of R, and $\epsilon=10^{-2}$, 10^{-4}, and 10^{-6}, respectively. As expected, the modified preprocessor does not produce the cross-null pattern as in Fig. 2(a). Furthermore, a comparison of these patterns gives an indication as to how a tradeoff between desired signal removal in R and flatness of response in $\overline{R}$ can be achieved with a suitably chosen ϵ.

III. 2-D SPATIAL SMOOTHING

In the presence of multiple correlated interferers, as usually incurred with multipath propagation, the beamformer operating on the DP data cannot cancel these interferes individually. A remedy suitable for the rectangular array is to perform 2-D spatial smoothing[10] on the DP subarray before beamforming. Performing spatial smoothing in this fashion requires that the DP subarray be decomposed into $L=(M-M_1)(N-N_1)$ contiguous overlapping subarrays of size $M_1\times N_1$, as shown in Fig. 3, and that a spatially smoothed (SS) correlation matrix $\overline{\mathbf{R}}_x$ be formed as an average of the correlation matrices associated with these subarrays. With this operation, $\overline{\mathbf{R}}_x$ can be regarded as the correlation matrix associated with an $M_1\times N_1$ virtual subarray on which the desired signal has been removed and the interferes have been decorrelated. We refer to this subarray as the SS subarray, and denote as

$$\overline{\mathbf{A}}(u,v)=\mathbf{a}_{M_1}(u)\mathbf{a}_{N_1}^T(v) \tag{29}$$

$$\overline{\mathbf{a}}(u,v)=\text{Vec}\{\overline{\mathbf{A}}(u,v)\} \tag{30}$$

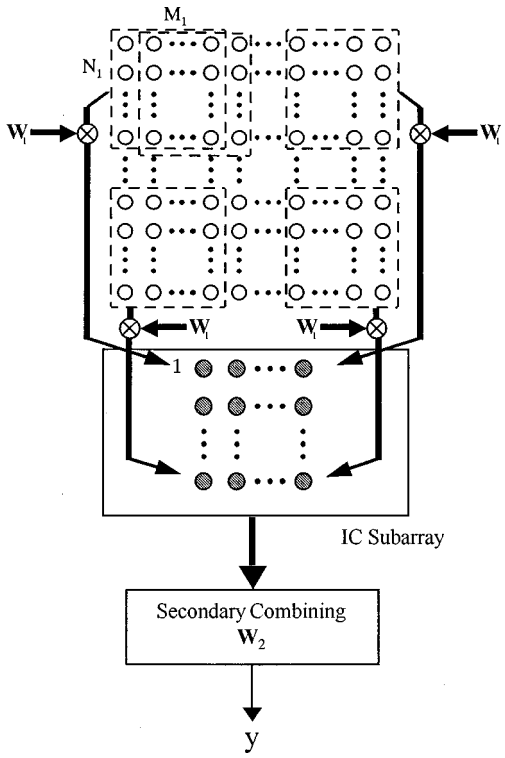

FIG. 3. Subarray configuration and schematic description of two-stage beamforming.

$$\overline{\mathbf{D}}=[\overline{\mathbf{a}}(u_1,v_1),\overline{\mathbf{a}}(u_2,v_2),\ldots,\overline{\mathbf{a}}(u_{K+1},v_{K+1})] \tag{31}$$

the counterparts of $\mathbf{A}(u,v)$, $\mathbf{a}(u,v)$, and $\mathbf{D}$, respectively, associated with it.

The symmetry of rectangular-array geometry allows for the incorporation of the forward–backward (FB) technique[12] to enhance the decorrelation effect of spatial smoothing. That is, we use the fact that

$$\mathbf{J}_{M_1N_1}\overline{\mathbf{a}}^*(u,v)=e^{-j\pi((M_1-1)u+(N_1-1)v)}\overline{\mathbf{a}}(u,v) \tag{32}$$

to double the effective number of subarrays. The FB–SS data-correlation matrix is thus formed by

$$\begin{aligned}\overline{\mathbf{R}}_x=&\frac{1}{2L}\sum_{i=1}^{M-M_1}\sum_{k=1}^{N-N_1}(\mathrm{Corr}\{\mathrm{Vec}\{\tilde{\mathbf{X}}(i:i+M_1-1,\\&k:k+N_1-1)\}\}\\&+\mathrm{Corr}\{\mathbf{J}_{M_1N_1}\mathrm{Vec}\{\tilde{\mathbf{X}}^*(i:i+M_1-1,k:k+N_1-1)\}\})\\=&\frac{1}{2L}\sum_{i=1}^{M-M_1}\sum_{k=1}^{N-N_1}(\mathbf{E}_{ik}\tilde{\mathbf{R}}_x\mathbf{E}_{ik}^T+\mathbf{J}_{M_1N_1}\mathbf{E}_{ik}\tilde{\mathbf{R}}_x^*\mathbf{E}_{ik}^T\mathbf{J}_{M_1N_1})\\=&\overline{\mathbf{R}}_s+\sigma_n^2\overline{\mathbf{R}}_n,\end{aligned} \tag{33}$$

where

$$\mathbf{E}_{ik}=\left[\begin{array}{c|ccc|c}\mathbf{O}_{M_1N_1\times(M-1)(k-1)} & \mathbf{F}_i & & 0 & \mathbf{O}_{M_1N_1\times(M-1)(N-N_1-k)}\\ & & \mathbf{F}_i & & \\ & 0 & & \ddots & \\ & & & \mathbf{F}_i & \end{array}\right] \tag{34}$$

with

$$\mathbf{F}_i=[\mathbf{O}_{M_1\times(i-1)}|\mathbf{I}_{M_1}|\mathbf{O}_{M_1\times(M-M_1-i)}] \tag{35}$$

is the selection matrix picking up the correlation matrix associated with the (i,k)th block $\tilde{\mathbf{X}}(i:i+M_1-1,k:k+N_1-1)$ from $\tilde{\mathbf{R}}_x$. The effective SS signal-only and noise-correlation matrices are given accordingly by

$$\begin{aligned}\overline{\mathbf{R}}_s=&\frac{1}{2L}\sum_{i=1}^{M-M_1}\sum_{k=1}^{N-N_1}(\mathbf{E}_{ik}\tilde{\mathbf{D}}\mathbf{G}\mathbf{P}\mathbf{G}^*\tilde{\mathbf{D}}^H\mathbf{E}_{ik}^T\\&+\mathbf{J}_{M_1N_1}\mathbf{E}_{ik}\tilde{\mathbf{D}}^*\mathbf{G}^*\mathbf{P}^*\mathbf{G}\tilde{\mathbf{D}}^T\mathbf{E}_{ik}^T\mathbf{J}_{M_1N_1})\\=&\overline{\mathbf{D}}\left[\frac{1}{2L}\sum_{i=1}^{M-M_1}\sum_{k=1}^{N-N_1}(\mathbf{\Phi}_{ik}\mathbf{G}\mathbf{P}\mathbf{G}^*\mathbf{\Phi}_{ik}^*\right.\\&\left.+\mathbf{\Psi}\mathbf{\Phi}_{ik}^*\mathbf{G}^*\mathbf{P}^*\mathbf{G}\mathbf{\Phi}_{ik}\mathbf{\Psi}^*)\right]\overline{\mathbf{D}}^H\end{aligned} \tag{36}$$

$$\begin{aligned}\overline{\mathbf{R}}_n=&\frac{1}{2L}\sum_{i=1}^{M-M_1}\sum_{k=1}^{N-N_1}(\mathbf{E}_{ik}\mathbf{H}^H\mathbf{H}\mathbf{E}_{ik}^T\\&+\mathbf{J}_{M_1N_1}\mathbf{E}_{ik}\mathbf{H}^T\mathbf{H}^*\mathbf{E}_{ik}^T\mathbf{J}_{M_1N_1}),\end{aligned} \tag{37}$$

where

$$\mathbf{\Phi}_{ik}=\mathrm{Diag}\left\{\begin{bmatrix}e^{j\pi((i-1)u_1+(k-1)v_1)}\\e^{j\pi((i-1)u_2+(k-1)v_2)}\\\vdots\\e^{j\pi((i-1)u_{K+1}+(k-1)v_{K+1})}\end{bmatrix}\right\}$$

$$i=1,\ldots,M-M_1,\quad k=1,\ldots,N-N_1 \tag{38}$$

accounts for the relative phase shifts among the data blocks $\tilde{X}(i:i+M_1-1,k:k+N_1-1)$, and

$$\mathbf{\Psi}=\mathrm{Diag}\left\{\begin{bmatrix}e^{-j\pi((M_1-1)u_1+(N_1-1)v_1)}\\e^{-j\pi((M_1-1)u_2+(N_1-1)v_2)}\\\vdots\\e^{-j\pi((M_1-1)u_{K+1}+(N_1-1)v_{K+1})}\end{bmatrix}\right\} \tag{39}$$

accounts for the relationship $\mathbf{J}_{M_1N_1}\overline{\mathbf{D}}^*=\overline{\mathbf{D}}\mathbf{\Psi}$ according to (32). We observe from (36) that the effective source-correlation matrix on the SS subarray is given by

$$\overline{\mathbf{P}}=\frac{1}{2L}\sum_{i=1}^{M-M_1}\sum_{k=1}^{N-N_1}(\mathbf{\Phi}_{ik}\mathbf{G}\mathbf{P}\mathbf{G}^*\mathbf{\Phi}_{ik}^*+\mathbf{\Psi}\mathbf{\Phi}_{ik}^*\mathbf{G}^*\mathbf{P}^*\mathbf{G}\mathbf{\Phi}_{ik}\mathbf{\Psi}^*). \tag{40}$$

Discussions on the performance of 2-D spatial smoothing can be found in the literature.[10]

IV. SUBARRAY BEAMFORMER AND APERTURE RECOVERY

With the signal condition largely improved, the beamformer constructed on the SS subarray (master beamformer) should exhibit good SINR performance when applied back to an $M_1\times N_1$ regular subarray (slave beamformer). This section discusses the issues about the subarray beamformer and shows how a secondary combining recovers the full aperture of the original array.

A. Subarray beamformer

Denote as $\mathbf{W}_1$ the weight matrix acting on the SS subarray, and $\mathbf{w}_1=\mathrm{Vec}\{\mathbf{W}_1\}$ the corresponding vector representation. With the SS subarray-correlation matrix given by (33), the subarray beamformer can be obtained via the LCMV criterion similar to that described in Sec. I C, except that the following substitutions are made:

$$\mathbf{a}(u_o,v_o)\rightarrow\overline{\mathbf{a}}(u_o,v_o)$$

$$\mathbf{R}_x\rightarrow\overline{\mathbf{R}}_x^w=\overline{\mathbf{R}}_x-\overline{\sigma}_n^2\overline{\mathbf{R}}_n+\overline{\sigma}_n^2\mathbf{I}_{M_1N_1}, \tag{41}$$

which account for the change of array size and data-correlation structure. The second substitution involves a ''whitening'' process which replaces the noise part in $\overline{\mathbf{R}}_x$ by $\overline{\sigma}_n^2\mathbf{I}_{M_1N_1}$, where $\overline{\sigma}_n^2$ is an estimate of the noise power.[13] This is necessary since the subarray beamformer is to be applied on a regular subarray and should optimize itself with respect to the corresponding noise-correlation structure, which is $\sigma_n^2\mathbf{I}_{M_1N_1}$. With the substitutions of (41) in (12), we obtain the LCMV subarray weight vector:

$$\mathbf{w}_1=\frac{\sigma_n^2}{\sqrt{M_1N_1}}(\overline{\mathbf{R}}_x^w)^{-1}\overline{\mathbf{a}}(u_o,v_o), \tag{42}$$

and the corresponding weight matrix $\mathbf{W}_1=\mathrm{Vec}^{-1}\{\mathbf{w}_1\}$.

B. Aperture recovery via secondary combining

The subarray weight matrix $\mathbf{W}_1$ can be applied on any of the M_2N_2 subarrays of size $M_1\times N_1$, where $M_2=(M-M_1+1)$ and $N_2=(N-N_1+1)$. As long as a sufficient degree of freedom is maintained, the resulting subarray beamformer will produce a null in each of the K interfering directions. Unfortunately, working with a single subarray beamformer results in an aperture loss. A remedy would be to construct a beamformer for each subarray using the same weight matrix $\mathbf{W}_1$, and then linearly combine these beamformers using an $M_2\times N_2$ weight matrix $\mathbf{W}_2$. With this operation, $\mathbf{W}_2$ is regarded as the weight matrix acting on an $M_2\times N_2$ virtual subarray, on which each element (subarray beamformer) eliminates all the interferers in the same way due to the response pattern $w_1(u,v)=\mathbf{w}_1^H\overline{\mathbf{a}}(u,v)$. We refer to this virtual subarray as the ''interference cancellation'' (IC) subarray. The set of linearly combined subarray beamformers, as a whole, is effectively a full-aperture beamformer. This is illustrated in Fig. 3.

Denote as

$$\hat{\mathbf{A}}(u,v)=\mathbf{a}_{M_2}(u)\mathbf{a}_{N_2}^T(v) \tag{43}$$

$$\hat{\mathbf{a}}(u,v)=\mathrm{Vec}\{\hat{\mathbf{A}}(u,v)\} \tag{44}$$

the counterparts of $\mathbf{A}(u,v)$ and $\mathbf{a}(u,v)$, respectively associated with the IC subarray. Similar to (18)–(22), we can show that the IC subarray-data matrix is given by

$$\hat{\mathbf{X}}=\sum_{i=1}^{M_1}\sum_{k=1}^{N_1}\mathbf{W}_1^*(i,k)\mathbf{X}(i:i+M_2-1,k:k+N_2-1), \tag{45}$$

and the corresponding vector representation, which is more useful, can be obtained as

$$\begin{aligned}\hat{\mathbf{x}}&=\mathrm{Vec}\{\hat{\mathbf{X}}\}\\&=\mathbf{U}^H\mathbf{x}\approx\xi_1\mathbf{U}^H\mathbf{a}(u_1,v_1)+\mathbf{U}^H\mathbf{n}\\&=w_1(u_1,v_1)\xi_1\hat{\mathbf{a}}(u_1,v_1)+\mathbf{U}^H\mathbf{n},\end{aligned} \tag{46}$$

where

$$\mathbf{U}=\begin{bmatrix}\mathbf{U}_1 & & 0\\ \vdots & \mathbf{U}_1 & \\ \mathbf{U}_{N_1} & \vdots & \ddots\\ & \mathbf{U}_{N_1} & & \mathbf{U}_1\\ & & \ddots & \vdots\\ 0 & & & \mathbf{U}_{N_1}\end{bmatrix}_{MN\times M_2N_2} \tag{47}$$

with

$$\mathbf{U}_i=\begin{bmatrix}\mathbf{W}_1(1,i) & & & 0\\ \vdots & \mathbf{W}_1(1,i) & & \\ \mathbf{W}_1(M_1,i) & \vdots & \ddots & \\ & \mathbf{W}_1(M_1,i) & & \mathbf{W}_1(1,i)\\ & & \ddots & \vdots\\ 0 & & & \mathbf{W}_1(M_1,i)\end{bmatrix}_{M\times M_2}$$

$$i=1,\ldots,N_1 \tag{48}$$

is a Toeplitz–block–Toeplitz matrix representation of $\mathbf{W}_1$. Note that the approximation in (46) holds since the interference has been removed in the first-stage beamformer, and the last equality results due to $\mathbf{U}^H\mathbf{a}(u,v)=w_1(u_1,v_1)\hat{\mathbf{a}}(u,v)$.

Let $\mathbf{w}_2=\mathrm{Vec}\{\mathbf{W}_2\}$ be the vector representation of $\mathbf{W}_2$. The expression in (46) suggests that the combiner acting on the IC subarray should be chosen so as to maximize the output SNR in the look direction (u_o,v_o). That is,

$$\begin{aligned}&\max_{\mathbf{w}_2}\frac{E\{|w_1(u_1,v_1)\xi_1\mathbf{w}_2^H\hat{\mathbf{a}}(u_o,v_o)|^2\}}{E\{|\mathbf{w}_2^H\mathbf{U}^H\mathbf{n}|^2\}}\\&\quad\equiv\frac{|w_1(u_1,v_1)|^2\sigma_1^2}{\sigma_n^2}\frac{|\mathbf{w}_2^H\hat{\mathbf{a}}(u_o,v_o)|^2}{\mathbf{w}_2^H\mathbf{U}^H\mathbf{U}\mathbf{w}_2},\end{aligned} \tag{49}$$

which is equivalent to

$$\min_{\mathbf{w}_2}\mathbf{w}_2^H\mathbf{U}^H\mathbf{U}\mathbf{w}_2\quad\text{subject to:}\quad\mathbf{w}_2^H\hat{\mathbf{a}}(u_o,v_o)=c. \tag{50}$$

This is again an LCMV-type problem whose solution is given by

$$\mathbf{w}_2=\frac{\sigma_n^2}{\sqrt{M_2N_2}}(\mathbf{U}^H\mathbf{U})^{-1}\hat{\mathbf{a}}(u_o,v_o). \tag{51}$$

Finally, the weight matrix is recovered via $\mathbf{W}_2=\mathrm{Vec}^{-1}\{\mathbf{w}_2\}$.

C. Structure and behavior of the full-aperture beamformer

The full-aperture weight matrix is obtained by the 2-D convolution of the two-stage subarray weight matrices $\mathbf{W}_1$ and $\mathbf{W}_2$:

$$\mathbf{W}(i,k)=\sum_{l=1}^{M_1}\sum_{m=1}^{N_1}\mathbf{W}_1(l,m)\mathbf{W}_2(i-l+1,k-m+1) \tag{52}$$

for $i=1,...,M$, $k=1,...,N$. The vector representation of $\mathbf{W}$ can be derived from (52), or by comparing (9) with $y=\mathbf{w}_2^H\hat{\mathbf{x}}=\mathbf{w}_2^H\mathbf{U}^H\mathbf{x}$ as observed in (46):

$$\mathbf{w}=\mathbf{U}\mathbf{w}_2=\mathbf{U}(\mathbf{U}^H\mathbf{U})^{-1}\hat{\mathbf{a}}(u_o,v_o)\propto\mathbf{U}(\mathbf{U}^H\mathbf{U})^{-1}\mathbf{U}^H\mathbf{a}(u_o,v_o). \tag{53}$$

It is interesting to note that the last expression in (53) can be interpreted algebraically as the orthogonal projection of $\mathbf{a}(u_o,v_o)$ onto the range space of $\mathbf{U}$. This makes sense, since $\mathbf{a}(u_o,v_o)$ is the optimum weight vector which maximizes the beamformer output SNR under the quiescent (spatially white-noise-only) condition. On the other hand, the range space of $\mathbf{U}$ represents the ''subspace of interference cancellation.'' Projecting $\mathbf{a}(u_o,v_o)$ onto the range space of $\mathbf{U}$ is equivalent to finding a vector lying in the subspace of interference cancellation which is closest to the optimum quiescent weight vector.

By applying the full-aperture weight vector $\mathbf{w}$ to the original array, a beamformer results which suppresses the interferers individually and nearly achieves the maximum SNR gain of the quiescent beamformer. Nevertheless, it should be pointed out that although the secondary combining can enhance the performance of the beamformer against uncorrelated noise, it cannot restore the interference cancellation capability of the original array. This is because interference cancellation is done entirely on the first-stage beamformer, and thus limited in performance by the subarray size. For example, interferers that are close to each other, or close to the look direction, will not be canceled successfully by the full-aperture beamformer due to the reduced resolution of the subarray. Some prior information about the interference scenario can help to determine a suitable subarray size to avoid this reduced aperture effect.

V. PERFORMANCE ANALYSIS OF THE TWO-STAGE BEAMFORMER

The following sections derive the output SINR of the two-stage beamformer for some cases of interest. The derivations are all based on the true ensemble data-correlation matrix. For a manageable analysis, we consider the case of two interferers ($K=2$) and make the following assumptions:

A1. No interfering signals are eliminated by the difference preprocessor.
A2. The interfering signals are nearly uncorrelated on the SS subarray.
A3. The desired signal is negligible compared to the interfering signals and noise on the SS subarray.
A4. The interference directions are well away from the look direction.

For brevity, some shorthand notations are defined as follows:

$$\overline{\mathbf{a}}_i=\overline{\mathbf{a}}(u_i,v_i)\quad i=o,1,2,3$$

$$\hat{\mathbf{a}}_i=\hat{\mathbf{a}}(u_i,v_i)\quad i=o,1,2,3$$

$$\kappa_i=|h(u_i,v_i)|^2\quad i=2,3$$

$$\gamma_i=\frac{\sigma_i^2}{\sigma_n^2}\quad i=1,2,3,$$

where we note that γ_1 denotes the input SNR, and γ_2 and γ_3 denote the input INR.

A. Output SINR of the first-stage beamformer

Under A1–A3, we can express the whitened SS subarray-correlation matrix in the following form:

$$\overline{\mathbf{R}}_x^w\approx\kappa_2\sigma_2^2\overline{\mathbf{a}}_2\overline{\mathbf{a}}_2^H+\kappa_3\sigma_3^2\overline{\mathbf{a}}_3\overline{\mathbf{a}}_3^H+\sigma_n^2\mathbf{I}_{M_1N_1}. \tag{54}$$

Using the matrix inversion lemma, we get

$$(\overline{\mathbf{R}}_x^w)^{-1}=\sigma_n^{-2}\left\{\mathbf{I}_{M_1N_1}-[\kappa_2\gamma_2\overline{\mathbf{a}}_2\quad\kappa_3\gamma_3\overline{\mathbf{a}}_3]\mathbf{\Gamma}^{-1}\begin{bmatrix}\overline{\mathbf{a}}_2^H\\ \overline{\mathbf{a}}_3^H\end{bmatrix}\right\}, \tag{55}$$

where

$$\mathbf{\Gamma}=\begin{bmatrix}1+M_1N_1\kappa_2\gamma_2 & M_1N_1\kappa_3\gamma_3\overline{\rho}_{23}\\ M_1N_1\kappa_2\gamma_2\overline{\rho}_{32} & 1+M_1N_1\kappa_3\gamma_3\end{bmatrix} \tag{56}$$

with

$$\overline{\rho}_{ik}=\frac{\overline{\mathbf{a}}_i^H\overline{\mathbf{a}}_k}{M_1N_1}=\frac{\sin\left(\frac{\pi}{2}M_1(u_k-u_i)\right)\sin\left(\frac{\pi}{2}N_1(v_k-v_i)\right)}{\sin\left(\frac{\pi}{2}(u_k-u_i)\right)\sin\left(\frac{\pi}{2}(v_k-v_i)\right)}\times e^{j(\pi/2)((M_1-1)(u_k-u_i)+(N_1-1)(v_k-v_i))}$$

$$i,k=o,1,2,3 \tag{57}$$

being the cosine angles between $\overline{\mathbf{a}}_i$ and $\overline{\mathbf{a}}_k$. Substituting (55) into (42) yields the first-stage weight vector:

$$\mathbf{w}_1=\frac{1}{\sqrt{M_1N_1}}\left\{\overline{\mathbf{a}}_o-[\kappa_2\gamma_2\overline{\mathbf{a}}_2\quad\kappa_3\gamma_3\overline{\mathbf{a}}_3]\mathbf{\Gamma}^{-1}\begin{bmatrix}M_1N_1\overline{\rho}_{2o}\\ M_1N_1\overline{\rho}_{3o}\end{bmatrix}\right\}$$

$$=\frac{1}{\sqrt{M_1N_1}}(\overline{\mathbf{a}}_o-\alpha\overline{\mathbf{a}}_2-\beta\overline{\mathbf{a}}_3), \tag{58}$$

where

$$\alpha=\frac{M_1N_1\kappa_2\gamma_2[\overline{\rho}_{2o}+M_1N_1\kappa_3\gamma_3(\overline{\rho}_{2o}-\overline{\rho}_{23}\overline{\rho}_{3o})]}{1+M_1N_1(\kappa_2\gamma_2+\kappa_3\gamma_3)+M_1^2N_1^2\kappa_2\kappa_3\gamma_2\gamma_3(1-|\overline{\rho}_{32}|^2)}, \tag{59}$$

$$\beta=\frac{M_1N_1\kappa_3\gamma_3[\overline{\rho}_{3o}+M_1N_1\kappa_2\gamma_2(\overline{\rho}_{3o}-\overline{\rho}_{32}\overline{\rho}_{2o})]}{1+M_1N_1(\kappa_2\gamma_2+\kappa_3\gamma_3)+M_1^2N_1^2\kappa_2\gamma_2\kappa_3\gamma_3(1-|\overline{\rho}_{32}|^2)}. \tag{60}$$

Denote as P_s, P_I, and P_n the desired signal, interference, and noise beamformer output powers, respectively. By A1–A4, $\mathbf{w}_1$ suppresses each of the interferers such that P_I is negligible compared to P_s and P_n. As a result, the output SINR of the first-stage beamformer is given approximately by

$$\mathrm{SINR}_1=\frac{P_s}{P_I+P_n}\approx\frac{P_s}{P_n}=\frac{|\mathbf{w}_1^H\overline{\mathbf{a}}_1|^2}{\mathbf{w}_1^H\mathbf{w}_1}\,\gamma_1. \tag{61}$$

Substitution of (58) into the above gives

$$\mathrm{SINR}_1 \approx \frac{|(\overline{\mathbf{a}}_o-\alpha\overline{\mathbf{a}}_2-\beta\overline{\mathbf{a}}_3)^H\overline{\mathbf{a}}_1|^2}{(\overline{\mathbf{a}}_o-\alpha\overline{\mathbf{a}}_2-\beta\overline{\mathbf{a}}_3)^H(\overline{\mathbf{a}}_o-\alpha\overline{\mathbf{a}}_2-\beta\overline{\mathbf{a}}_3)}$$
$$= \frac{M_1N_1|\overline{\rho}_{o1}-\alpha^*\overline{\rho}_{21}-\beta^*\overline{\rho}_{31}|^2\gamma_1}{1+|\alpha|^2+|\beta|^2-2\,\mathrm{Re}\{\alpha^*\overline{\rho}_{2o}+\beta^*\overline{\rho}_{3o}-\alpha\beta^*\overline{\rho}_{32}\}} \times\gamma_1. \quad (62)$$

Some cases of interest are considered below.

1. Case 1: High-input INR

With the assumption of high-input INR ($\gamma_i \gg 1$, $i=2,3$) and that κ_2 and κ_3 are not too small, we have

$$\alpha \approx \frac{\overline{\rho}_{2o}-\overline{\rho}_{23}\overline{\rho}_{3o}}{1-|\overline{\rho}_{32}|^2}, \quad (63)$$

$$\beta \approx \frac{\overline{\rho}_{3o}-\overline{\rho}_{32}\overline{\rho}_{2o}}{1-|\overline{\rho}_{32}|^2}. \quad (64)$$

Substituting these into (62), along with some algebraic manipulations, we get

$$\mathrm{SINR}_1 \approx \frac{M_1N_1|\overline{\rho}_{o1}(1-|\overline{\rho}_{32}|^2)-\overline{\rho}_{21}\overline{\rho}_{o2}-\overline{\rho}_{31}\overline{\rho}_{o3}+\overline{\rho}_{o3}\overline{\rho}_{32}\overline{\rho}_{21}+\overline{\rho}_{o2}\overline{\rho}_{23}\overline{\rho}_{31}|^2}{(1-|\overline{\rho}_{32}|^2)(1+2\overline{\rho}_{32}\overline{\rho}_{2o}\overline{\rho}_{o3}-|\overline{\rho}_{2o}|^2-|\overline{\rho}_{3o}|^2-|\overline{\rho}_{32}|^2)}\,\gamma_1. \quad (65)$$

In particular, with a small pointing error ($u_o \approx u_1$, $v_o \approx v_1$), we have $\overline{\rho}_{1o} \approx 1$ and $\overline{\rho}_{oi} \approx \overline{\rho}_{1i}$, $i=2,3$, such that (65) reduces to

$$\mathrm{SINR}_1 \approx M_1N_1\left(1-\frac{|\overline{\rho}_{21}|^2+|\overline{\rho}_{31}|^2-2\overline{\rho}_{21}\overline{\rho}_{13}\overline{\rho}_{32}}{1-|\overline{\rho}_{32}|^2}\right)\gamma_1. \quad (66)$$

2. Case 2: Low-input INR or orthogonal interference directions

With a low-input INR ($\gamma_i \approx 0$, $i=2,3$) and/or orthogonal interference directions ($\overline{\rho}_{io} \approx 0$, $i=2,3$), we have $\alpha \approx 0$ and $\beta \approx 0$ such that

$$\mathbf{w}_1 \approx \frac{1}{\sqrt{M_1N_1}}\,\overline{\mathbf{a}}_o, \quad (67)$$

and (62) reduces to

$$\mathrm{SINR}_1 \approx M_1N_1|\overline{\rho}_{o1}|^2\gamma_1, \quad (68)$$

which is the result obtained under the quiescent condition. Finally, with a small pointing error, we get

$$\mathrm{SINR}_1 \approx M_1N_1\gamma_1, \quad (69)$$

which is simply the maximum-output SNR of the optimum quiescent beamformer.[6]

B. Output SINR of the overall beamformer

Using (46) and (51), the output SINR of the overall two-stage beamformer (as observed at the second-stage beamformer output) is given by

$$\mathrm{SINR}_o \approx \frac{|\mathbf{w}_2^H\hat{\mathbf{a}}_1|^2}{\mathbf{w}_2^H\mathbf{U}^H\mathbf{U}\mathbf{w}_2}\,|w_1(u_1,v_1)|^2\gamma_1$$
$$= \hat{\mathbf{a}}_1^H(\mathbf{U}^H\mathbf{U})^{-1}\hat{\mathbf{a}}_1|\hat{\rho}_{1o}|^2|w_1(u_1,v_1)|^2\gamma_1, \quad (70)$$

where

$$\hat{\rho}_{1o} = \frac{\hat{\mathbf{a}}_1^H(\mathbf{U}^H\mathbf{U})^{-1}\hat{\mathbf{a}}_o}{[\hat{\mathbf{a}}_o^H(\mathbf{U}^H\mathbf{U})^{-1}\hat{\mathbf{a}}_o\hat{\mathbf{a}}_1^H(\mathbf{U}^H\mathbf{U})^{-1}\hat{\mathbf{a}}_1]^{1/2}}. \quad (71)$$

Again, two cases are considered below.

1. Case 1: High-input INR

With a high-input INR, we have from (58), (63), and (64)

$$w_1(u_1,v_1) \approx \sqrt{M_1N_1}\left(\overline{\rho}_{o1} - \frac{\overline{\rho}_{21}\overline{\rho}_{o2}+\overline{\rho}_{31}\overline{\rho}_{o3}-\overline{\rho}_{o3}\overline{\rho}_{32}\overline{\rho}_{21}-\overline{\rho}_{o2}\overline{\rho}_{23}\overline{\rho}_{31}}{1-|\overline{\rho}_{32}|^2}\right). \quad (72)$$

Substituting this into (70) yields

$$\mathrm{SINR}_o \approx \hat{\mathbf{a}}_1^H(\mathbf{U}^H\mathbf{U})^{-1}\hat{\mathbf{a}}_1|\hat{\rho}_{1o}|^2M_1N_1\left|\overline{\rho}_{o1} - \frac{\overline{\rho}_{21}\overline{\rho}_{2o}+\overline{\rho}_{31}\overline{\rho}_{3o}-\overline{\rho}_{21}\overline{\rho}_{o3}\overline{\rho}_{32}-\overline{\rho}_{31}\overline{\rho}_{o2}\overline{\rho}_{23}}{1-|\overline{\rho}_{32}|^2}\right|^2\gamma_1. \quad (73)$$

With a small pointing error, we have $\hat{\rho}_{1o} \approx 1$ such that

$$\mathrm{SINR}_o \approx \hat{\mathbf{a}}_1^H(\mathbf{U}^H\mathbf{U})^{-1}\hat{\mathbf{a}}_1M_1N_1 \times\left(1-\frac{|\overline{\rho}_{21}|^2+|\overline{\rho}_{31}|^2-2\overline{\rho}_{21}\overline{\rho}_{13}\overline{\rho}_{32}}{1-|\overline{\rho}_{32}|^2}\right)^2\gamma_1$$
$$= \hat{\mathbf{a}}_1^H(\mathbf{U}^H\mathbf{U})^{-1}\hat{\mathbf{a}}_1\left(1-\frac{|\overline{\rho}_{21}|^2+|\overline{\rho}_{31}|^2-2\overline{\rho}_{21}\overline{\rho}_{13}\overline{\rho}_{32}}{1-|\overline{\rho}_{32}|^2}\right) \times\mathrm{SINR}_1, \quad (74)$$

where we have used (66).

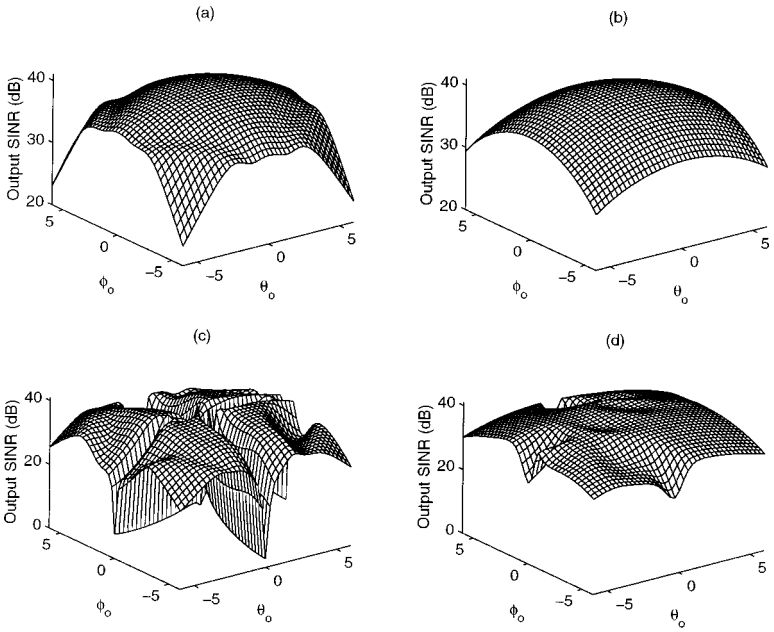

FIG. 4. Output SINR versus pointing error. $M_1=5$, $N_1=6$. $(\theta_1,\phi_1)=(0\ \text{deg},0\ \text{deg})$. $\mu=1$. (a) separable preprocessor. $(\theta_2,\phi_2)=(20\ \text{deg},20\ \text{deg})$, $(\theta_3,\phi_3)=(40\ \text{deg},40\ \text{deg})$. (b) nonseparable preprocessor. $(\theta_2,\phi_2)=(20\ \text{deg},20\ \text{deg})$, $(\theta_3,\phi_3)=(40\ \text{deg},40\ \text{deg})$. (c) separable preprocessor. $(\theta_2,\phi_2)=(0\ \text{deg},20\ \text{deg})$, $(\theta_3,\phi_3)=(40\ \text{deg},0\ \text{deg})$. (d) nonseparable preprocessor. $(\theta_2,\phi_2)=(0\ \text{deg},20\ \text{deg})$, $(\theta_3,\phi_3)=(40\ \text{deg},0\ \text{deg})$.

2. Case 2: Low-input INR or orthogonal interference directions

With a low-input INR and/or orthogonal interference directions, we have from the previous results that $w_1(u_1,v_1)=\sqrt{M_1N_1}\overline{\rho}_{o1}$ such that

$$\begin{aligned}\text{SINR}_o &\approx \hat{\mathbf{a}}_1(\mathbf{U}^H\mathbf{U})^{-1}\hat{\mathbf{a}}_1|\hat{\rho}_{1o}|^2M_1N_1|\overline{\rho}_{o1}|^2\gamma_1\\ &=\hat{\mathbf{a}}_1(\mathbf{U}^H\mathbf{U})^{-1}\hat{\mathbf{a}}_1|\hat{\rho}_{1o}|^2\text{SINR}_1,\end{aligned}\tag{75}$$

which means that the second-stage beamformer exhibits an SNR gain of $\hat{\mathbf{a}}_1^H(\mathbf{U}^H\mathbf{U})^{-1}\hat{\mathbf{a}}_1|\hat{\rho}_{1o}|^2$. Finally, the optimum quiescent beamformer output SINR is achieved with a small pointing error:

$$\text{SINR}_o\approx\hat{\mathbf{a}}_1^H(\mathbf{U}^H\mathbf{U})^{-1}\hat{\mathbf{a}}_1M_1N_1\gamma_1.\tag{76}$$

Although no closed-form expression of (76) is given, we have found by simulation that the maximum two-stage output SINR is fairly close to $MN\gamma_1$, which is the optimum one-stage output SINR achieved by the quiescent beamformer.

VI. SIMULATION RESULTS

Computer simulations on narrow-band signal extraction were conducted to ascertain the performance of the two-stage beamformer. The array was 10×12 with identical sensors equally spaced by a half-wavelength of the sources. The desired signal arrived from $(\theta_1,\phi_1)=(0\ \text{deg},0\ \text{deg})$, with an SNR of 20 dB. Except for one case, we put two interferers at $(\theta_2,\phi_2)=(20\ \text{deg},20\ \text{deg})$ and $(\theta_3,\phi_3)=(40\ \text{deg},40\ \text{deg})$, respectively, with the same INR of 30 dB. The source-correlation matrix, as defined in Sec. I C, was set to be

$$\mathbf{P}=\begin{bmatrix}\sigma_1^2 & \mu^*\sigma_1\sigma_2 & \mu^*\sigma_1\sigma_3\\ \mu\sigma_2\sigma_1 & \sigma_2^2 & \mu^*\sigma_2\sigma_3\\ \mu\sigma_3\sigma_1 & \mu\sigma_3\sigma_2 & \sigma_3^2\end{bmatrix},$$

which says that the three sources are mutually correlated with the same correlation coefficient μ. To measure the interference suppression performance of the two-stage beamformer, we defined the simulated output SINR as

$$\text{SINR}_o=\frac{\sigma_1^2\mathbf{w}^H\mathbf{a}_1\mathbf{a}_1^H\mathbf{w}}{\sigma_n^2\mathbf{w}^H\mathbf{w}+\Sigma_{i=2}^3\Sigma_{k=2}^3\mathbf{P}(i,k)\mathbf{w}^H\mathbf{a}_i\mathbf{a}_k^H\mathbf{w}}.$$

In all cases, we assumed that the three sources and noise were stationary over the processing period of the beamformer, and a sufficient amount of data were available such that the ensemble-correlation matrix and weight vectors could be obtained.

The first set of simulations examines the SINR performance of the two-stage beamformer against pointing errors. The look direction (θ_o,ϕ_o) was varied over the angular region $\{-6\ \text{deg}\leqslant\theta_o\leqslant6\ \text{deg},\ -6\ \text{deg}\leqslant\phi_o\leqslant6\ \text{deg}\}$. A coherent scenario was assumed by setting $\mu=1$. The subarray size was chosen as $M_1=5$, $N_1=6$. The resulting output SINR plots obtained with the separable and nonseparable (with $\epsilon=10^{-4}$) difference preprocessors are shown in Fig. 4(a) and (b), respectively. As expected, the output SINR drops as the pointing error increases. This is more significant for the separable preprocessor with a large pointing error. To see the result when the interferers are inside the cross-null region of $h(u,v)$, we changed the interference directions to $(\theta_2,\phi_2)=(0\ \text{deg},20\ \text{deg})$ and $(\theta_3,\phi_3)=(40\ \text{deg},0\ \text{deg})$, and repeated the above simulations. The results shown in Fig. 4(c) and (d) indicate that the separable preprocessor breaks down when θ_o or ϕ_o is zero. This is the case where at least one of the interferers is eliminated by $h(u,v)$. On the other hand, the nonseparable preprocessor performed reliably for a small pointing error, though certain degradation occurred near the four edges. In the remaining examples, only the nonseparable preprocessor (with $\epsilon=10^{-4}$) will be used.

The second set of simulations investigates the effect of subarray size. In this case, M_1 was varied from 2 to 9, and N_1 from 2 to 11. Fig. 5(a) and (b) show the output SINR plots obtained with $(\theta_o,\phi_o)=(0\ \text{deg},0\ \text{deg})$ and $(\theta_o,\phi_o)=(3\ \text{deg},3\ \text{deg})$, respectively, for $\mu=1$. Figure 5(c) and (d) show the corresponding results for $\mu=j$. We observe that

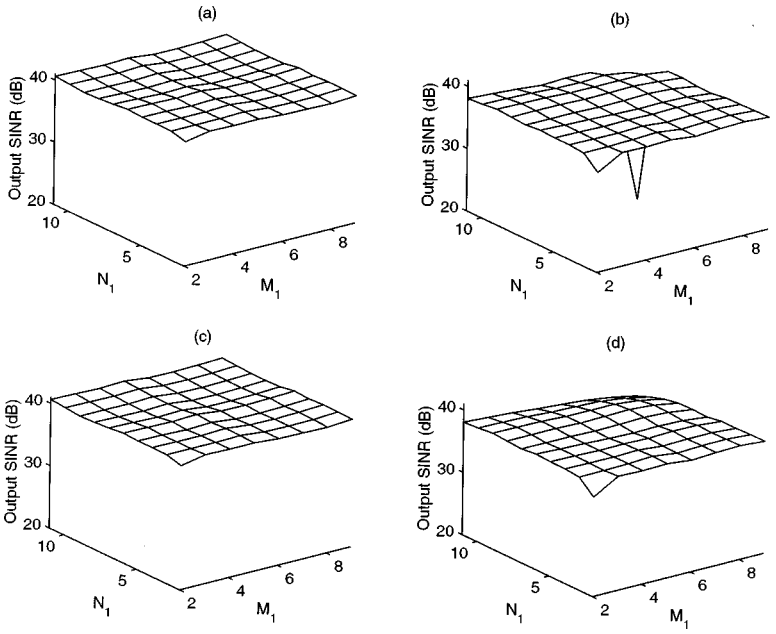

FIG. 5. Output SINR versus subarray size. $(\theta_1,\phi_1)=(0\ \text{deg},0\ \text{deg})$, $(\theta_2,\phi_2)=(20\ \text{deg},20\ \text{deg})$, $(\theta_3,\phi_3)=(40\ \text{deg},40\ \text{deg})$. (a) $(\theta_0,\phi_0)=(0\ \text{deg},0\ \text{deg})$. $\mu=1$. (b) $(\theta_0,\phi_0)=(3\ \text{deg},3\ \text{deg})$. $\mu=1$. (c) $(\theta_0,\phi_0)=(0\ \text{deg},0\ \text{deg})$. $\mu=j$. (d) $(\theta_0,\phi_0)=(3\ \text{deg},3\ \text{deg})$. $\mu=j$.

the output SINR is insensitive to the subarray size so long as a sufficient degree of freedom is given for interference cancellation. This also demonstrates that aperture recovery can be done successfully for any suitably chosen subarray size. In particular, the SINR achieved without pointing error is close to the optimum value $(10\log_{10}120+20=40.8)$ for all possible subarray sizes, except for the extreme cases of $M_1=N_1=2$, and $M_1=9$, $N_1=11$. Note that the performance breakdown with $M_1=9$, $N_1=11$ and $\mu=1$ in the presence of pointing errors was due to the mutual cancellation between the desired signal and interference as a result of poor decorrelation. This did not happen with $\mu=j$, for which effective decorrelation was achieved with FB averaging.

In the third set of simulations, we evaluate the effect of the correlation coefficient. The amplitude $(|\mu|)$ and phase $[\text{angle}(\mu)]$ of μ were varied from 0 to 1 and 0 to π, respectively. Figure 6(a) and (b) show the output SINR obtained with $(\theta_o,\phi_o)=(0\ \text{deg},0\ \text{deg})$ and $(\theta_o,\phi_o)=(3\ \text{deg},3\ \text{deg})$, respectively, for $M_1=5$, $N_1=6$. The results show that the proposed beamformer is robust to the change of μ. The simulation was then repeated with $M_1=9$, $N_1=11$ (no smoothing) and the results were plotted in Fig. 6(c) and (d). Surprisingly, the output SINR without pointing error did not exhibit any degradation. This is because the mutual cancellation between the two interferers was not significantly affected by the difference preprocessor. On the other hand, the beamformer suffered performance breakdown with pointing errors for $\mu\approx\pm1$, which is the case where FB averaging has almost no effect. This again ascertains that the proposed beamformer performs reliably with a properly chosen subarray size.

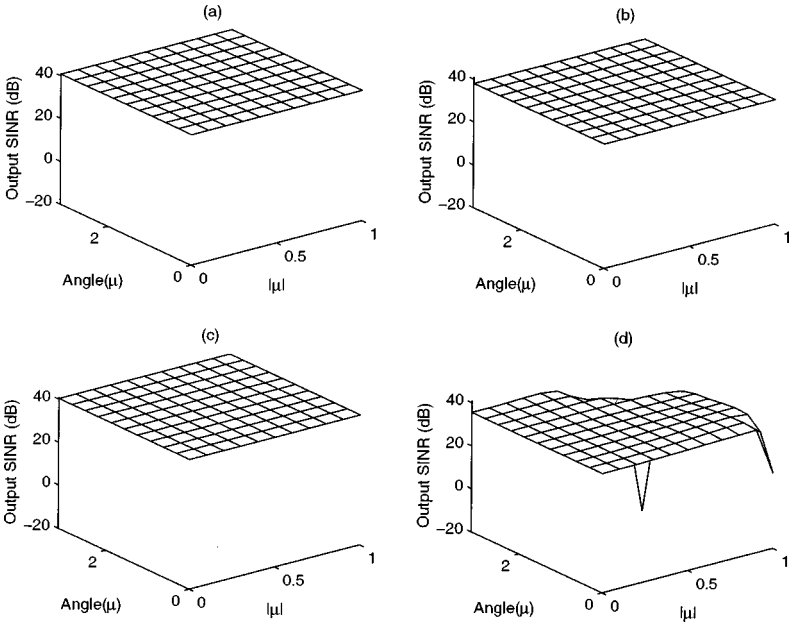

FIG. 6. Output SINR versus correlation coefficient. $(\theta_1,\phi_1)=(0\ \text{deg},0\ \text{deg})$, $(\theta_2,\phi_2)=(20\ \text{deg},20\ \text{deg})$. $(\theta_3,\phi_3)=(40\ \text{deg},40\ \text{deg})$. (a) $(\theta_0,\phi_0)=(0\ \text{deg},0\ \text{deg})$. $M_1=5$, $N_1=6$. (b) $(\theta_0,\phi_0)=(3\ \text{deg},3\ \text{deg})$. $M_1=5$, $N_1=6$. (c) $(\theta_0,\phi_0)=(0\ \text{deg},0\ \text{deg})$. $M_1=9$, $N_1=11$. (d) $(\theta_0,\phi_0)=(3\ \text{deg},3\ \text{deg})$. $M_1=9$, $N_1=11$.

VII. CONCLUSION

We have presented a two-stage 2-D adaptive beamforming scheme for combating multiple correlated interferers using a rectangular array. By difference preprocessing and spatial smoothing, a virtual subarray was obtained on which the desired-signal strength and correlation among interferers were reduced to a negligible order. An LCMV-type beamformer constructed on this smoothed subarray is ideal for desired-signal acquisition, but inefficient in terms of aperture utilization. A post-beamformer based on the maximum SNR criterion was thus employed in the second stage to recover the full array aperture. The derivation of the weight vector was eased by exploiting the distinctive Toeplitz–block–Toeplitz structure due to 2-D convolution. For a theoretical performance evaluation, an analysis on the output SINR of the proposed beamformer was presented for some cases of interest. Finally, the behavior of the proposed beamformer was examined and discussed via several sets of computer simulations. In particular, it was shown that the performance of the two-stage beamformer is fairly reliable approaching that of the optimum one-stage beamformer, provided that a suitable subarray size is chosen for successfully decorrelating the interference. The proposed beamformer is suitable for acoustical applications such as remote sound-source enhancement in a large room or subsea acoustical communications operated in shallow water, for which correlated multipaths cause a major problem.

ACKNOWLEDGMENT

This work was supported by the National Science Council of R.O.C. under Grant NSC 84-2213-E-009-119.

[1] R. A. Monzingo and T. W. Miller, *Introduction to Adaptive Arrays* (Wiley, New York, 1980).

[2] J. L. Flanagan, J. D. Johnston, R. Zahn, and G. W. Elko, ''Computer-steered microphone arrays for sound transduction in large rooms,'' J. Acoust. Soc. Am. **78**, 1508–1518 (1985).

[3] I. Claesson, S. E. Nordholm, B. A. Bengtsson, and P. Eriksson, ''A multi-DSP Implementation of a broad-band adaptive beamformer for use in a hands-free mobile radio telephone,'' IEEE Trans. Veh. Technol. **VT-40**, 194–202 (1991).

[4] G. S. Howe, P. S. D. Tarbit, O. R. Hinton, B. S. Sharif, and A. E. Adams, ''Subsea remote communications utilising an adaptive receiving beamformer for multipath suppression,'' Proc. IEEE Oceans Conf. **1**, 313–316 (1994).

[5] B. Widrow, K. M. Duvall, R. P. Gooch, and W. C. Newman, ''Signal cancellation phenomena in adaptive antennas: causes and cures,'' IEEE Trans. Antennas Propag. **AP-30**, 469–478 (1982).

[6] L. C. Godara, ''Error analysis of the optimal antenna processors,'' IEEE Trans. Aerosp. Electron. Syst. **AES-22**, 395–400 (1986).

[7] A. K. Luthra, ''A solution to adaptive nulling problem with a look-direction constraint in the presence of coherent jammers,'' IEEE Trans. Antennas Propag. **AP-34**, 702–710 (1986).

[8] T. J. Shan and T. Kailath, ''Adaptive beamforming for coherent signals and interference,'' IEEE Trans. Acoust., Speech, Signal Process. **ASSP-33**, 527–536 (1985).

[9] T. S. Lee and T. K. Tseng, ''Subarray-synthesized low-side-lobe sum and difference patterns with partial common weights,'' IEEE Trans. Antennas Propag. **AP-41**, 791–800 (1993).

[10] Y. M. Chen, ''On spatial smoothing for two-dimensional direction-of-arrival estimation of coherent signals,'' IEEE Trans. Signal Process. **SP-45**, 1689–1696 (1997).

[11] B. D. Van Veen and K. M. Buckley, ''Beamforming: A versatile approach to spatial filtering,'' IEEE ASSP Mag. **5**, 4–24 (1988).

[12] S. U. Pillai and B. H. Kwon, ''Forward/backward spatial smoothing techniques for coherent signal identification,'' IEEE Trans. Acoust., Speech, Signal Process. **ASSP-37**, 8–15 (1989).

[13] P. Stoica, T. Söderström and V. Šimonytė, ''On estimating the noise power in array processing,'' Signal Process. **26**, 205–220 (1992).

An L_∞-norm estimator for environmentally robust, shallow-water source localization

Brian F. Harrison[a)]
Naval Undersea Warfare Center, Submarine Sonar Department, Code 2121, Building 1320, Newport, Rhode Island 02841

(Received 18 February 1998; revised 30 July 1998; accepted 25 September 1998)

In this paper, the L_∞-norm estimator for robust matched-field source localization in the presence of environmental uncertainties is proposed. This estimator is derived from the maximum *a posteriori* (MAP) estimator by interpreting MAP as an exponentially weighted average over environmental realizations. In the presence of infinite averaging, MAP provides an optimal approach to robust matched-field source localization. However, in practice only a finite number of environmental realizations can be included in this average, resulting in a suboptimal processor. With finite environmental sampling, the L_∞-norm estimator provides superior performance over that of MAP. Also introduced is the concept of wave number gradients which provide physical insight for the performance of the L_∞-norm estimator. Simulation results from two shallow-water environments are presented, which show that at moderate signal-to-noise ratios, the proposed estimator provides nearly 90%-correct localization performance compared to less than 70% for MAP. Results using experimental data from the Mediterranean Sea are also presented. [S0001-4966(99)01801-9]

PACS numbers: 43.60.Gk, 43.30.Wi [JCB]

INTRODUCTION

Matched-field processing (MFP) methods utilize complex multipath propagation models for source localization. These models incorporate the parameters of the ocean environment. MFP has been seen as a promising approach to source localization in shallow water. However, it is well known that MFP methods can be extremely sensitive to small errors in the assumed values of the environmental parameters.[1,2] These errors may arise from imprecise *in situ* measurements or from perturbations of these parameters due to temperature fluctuations and wave motion. The environmental parameters may also vary between the source and the receiver. Therefore, MFP localization methods which are robust to uncertainties in the assumed values of the environmental parameters are required for real-world applications.

A statistically optimal approach to MFP source localization in the presence of environmental uncertainties is the maximum *a posteriori* probability (MAP) estimator. Using the MAP estimator, source range and depth are treated as the parameters of interest while the uncertain environmental parameters are treated as nuisance parameters. Prior probability density functions (PDF) are assumed for the uncertain environmental parameters from their uncertainty intervals based on *in situ* measurements and historical data. Location estimates are obtained by maximization over source location after integration over the uncertain environmental parameter space using the prior PDF. In practice, Monte Carlo integration techniques are used to approximate the integral. A MAP estimator derived in the context of robust MFP was given in Refs. 3 and 4 and called the optimum uncertain field processor (OUFP). However, a major issue in using the MAP estimator is the computation required to perform the integrations. As the number of nuisance parameters grows or their uncertainty intervals become large, the MAP estimator rapidly becomes computationally intensive. A computationally efficient approximate MAP estimator, which allows the integrations to be computed off-line, prior to the processing of data, was derived in Ref. 5. Also at issue with the MAP estimator is the number of Monte Carlo integration steps necessary for an accurate approximation.

Using a maximum-likelihood (ML) approach to source localization in an uncertain environment requires the joint estimation of source location and uncertain environmental parameters. Typically, this requires a multidimensional search over a large parameter space, making an exhaustive search computationally prohibitive. Also, due to the oscillatory nature of the likelihood surface which contains many local maxima, gradient-based techniques cannot be applied without good initial parameter estimates. Simulated annealing and genetic algorithms have been proposed as techniques for searching the multidimensional parameter space.[6,7] A robust technique for initializing the ML search was presented in Ref. 8. A survey of environmentally robust MFP techniques can be found in Ref. 9.

In this paper, we propose applying an L_p-norm estimator to the uncertain environment, source localization problem. It is derived from the interpretation of the MAP estimator as a weighted-averaging processor. In the limit as $p \to \infty$, the L_∞-norm estimator has the flavor of an ML estimator. However, in contrast to the ML estimator, the search is only conducted over the location parameter space using M sets of the environmental parameters randomly sampled from their prior PDF. The value of M is typically on the order of 100–200. This estimation technique is also much more computationally efficient than the global optimization performed by

a)Electronic mail: harrison_bf@ieee.org

simulated annealing and genetic algorithms. Using a small number of environmental realizations implies that localization can be accurately performed using combinations of the environmental parameters other than the true. We will show, using the modal horizontal wave numbers, why accurate source-location estimates can be obtained using environmental realizations besides the true.

I. PROBLEM DEVELOPMENT

A. Signal model

Using a normal mode model,[10] the signals received on a vertical array of N sensors from a point source can be expressed in vector form as

$$\mathbf{y}(\omega)=s(\omega)\mathbf{a}(\omega,\boldsymbol{\Theta},\boldsymbol{\Psi})+\mathbf{n}(\omega), \tag{1}$$

where the elements of $\mathbf{y}(\omega)$ are the components of the signal wave front observed on the sensors located at depths $\mathbf{z}=[z_1^r\cdots z_N^r]^T$ at radian frequency ω. The scalar $s(\omega)$ is the complex signal amplitude at ω. The vector $\mathbf{a}(\omega,\boldsymbol{\Theta},\boldsymbol{\Psi})$, which is called a replica vector, is the acoustic transfer function between a source at location $\boldsymbol{\Theta}=[r,z]$ and the array which is parametrized by the vector of environmental parameters $\boldsymbol{\Psi}$, i.e., sound-speed profile and bottom characteristics. The vector $\mathbf{n}(\omega)$ contains samples of complex Gaussian noise. Each replica vector is composed of a linear combination of the sampled mode functions for a given environment,

$$\mathbf{a}(\omega,\boldsymbol{\Theta},\boldsymbol{\Psi})=\boldsymbol{\Omega}(\omega,\mathbf{z},\boldsymbol{\Psi})\boldsymbol{\alpha}(\omega,\boldsymbol{\Theta},\boldsymbol{\Psi}), \tag{2}$$

where the columns of the modal amplitude matrix $\boldsymbol{\Omega}(\omega,\mathbf{z},\boldsymbol{\Psi})$ are the Q modes ϕ_m sampled at the receiver depths

$$\boldsymbol{\Omega}(\omega,\mathbf{z},\boldsymbol{\Psi})=\begin{bmatrix}\phi_1(z_1^r) & \cdots & \phi_Q(z_1^r)\\ \vdots & & \vdots\\ \phi_1(z_N^r) & \cdots & \phi_Q(z_N^r)\end{bmatrix}. \tag{3}$$

The vector of complex weights $\boldsymbol{\alpha}(\omega,\boldsymbol{\Theta},\boldsymbol{\Psi})$ is given by

$$\boldsymbol{\alpha}(\omega,\boldsymbol{\Theta},\boldsymbol{\Psi})=\begin{bmatrix}\left(\dfrac{2\pi}{k_1 r}\right)^{1/2}\phi_1(z)\exp\{jk_1 r-\gamma_1 r\}\\ \vdots\\ \left(\dfrac{2\pi}{k_Q r}\right)^{1/2}\phi_Q(z)\exp\{jk_Q r-\gamma_Q r\}\end{bmatrix}, \tag{4}$$

where the real-valued, positive parameters of the ocean channel k_m and γ_m are the modal horizontal wave numbers and mode attenuation coefficients, respectively.

B. The maximum *a posteriori* probability estimator

The MAP estimator derived in Ref. 3 assumes uniform PDF $p(\boldsymbol{\Psi})$ for the uncertain environmental parameters. If we further assume the noise is white and the replica vectors are normalized to have unit norm, the MAP estimator can be written as

$$\hat{\boldsymbol{\Theta}}=\arg\max_{\boldsymbol{\Theta}}\int_{\Psi}\exp\left\{\frac{\sigma_a^2|\mathbf{a}^H(\boldsymbol{\Theta},\boldsymbol{\Psi})\mathbf{y}|^2}{2(\sigma_a^2+1)}\right\}p(\boldsymbol{\Psi})d\boldsymbol{\Psi}, \tag{5}$$

where σ_a^2 is the signal amplitude variance. Dependence on ω has been dropped for convenience, since we will be assuming a monochromatic signal. The white-noise assumption was made for clarity in the subsequent development. It is a straightforward modification to (5) if non-white noise is assumed.

For numerical implementation of the MAP estimator, the integral is approximated by a sum over M realizations of the environment, i.e., M integration steps,

$$\hat{\boldsymbol{\Theta}}=\arg\max_{\boldsymbol{\Theta}}\sum_{i=1}^{M}\exp\left\{\frac{\sigma_a^2|\mathbf{a}^H(\boldsymbol{\Theta},\boldsymbol{\Psi}_i)\mathbf{y}|^2}{2(\sigma_a^2+1)}\right\}. \tag{6}$$

The M environmental realizations are taken from samples of the probability distributions of the environmental parameters. In Ref. 4, a Monte Carlo approach to computing (6) was proposed. Notice that the argument of the exponential in (6) is simply the conventional Bartlett processor scaled by $\sigma_a^2/2(\sigma_a^2+1)$. Therefore, (6) can be interpreted as an exponentially weighted average of Bartlett surfaces over M combinations of the environmental parameters. If we assume $\mathbf{y}$ is also normalized to unit norm, then $|\mathbf{a}^H(\boldsymbol{\Theta},\boldsymbol{\Psi}_i)\mathbf{y}|^2$ would equal 1 if $\boldsymbol{\Theta}$ and $\boldsymbol{\Psi}_i$ were perfectly matched to the data. Any other values of $\boldsymbol{\Theta}$ and $\boldsymbol{\Psi}_i$ would produce a value between zero and 1. Thus, those values of $|\mathbf{a}^H(\boldsymbol{\Theta},\boldsymbol{\Psi}_i)\mathbf{y}|^2$ nearer to 1, which correspond to *better* replica-data matches, are given more relative weight in the averaging process of (6).

We observe that the exact implementation of the MAP estimator in (5) assumes infinitesimally spaced samples of the environmental parameters. Thus, the true environment and combinations of the environmental parameters very close to the true are all included in the averaging process. This results in a clustering of reinforcing peaks near the true value of $\boldsymbol{\Theta}$. Therefore, the MAP estimator as implemented in (6) with finite sampling of the environmental parameters can be suboptimal. The minimum sampling density of the environmental parameter space using (6), to obtain an accurate approximation to (5), would be dependent on the sensitivity of the model to each of the environmental parameters. Also, since model sensitivity increases with frequency, sampling density would also need to be increased with frequency. However, finer sampling of the environmental parameter space rapidly leads to a computationally intensive processor which can become computationally prohibitive. In Ref. 4, for example, 51^7 integration steps were required at each $\boldsymbol{\Theta}$ for the OUFP to compute a localization estimate if all combinations of the environmental parameter samples were utilized. Even using a Monte Carlo approach can require thousands of integration steps[11] which can result in a computationally prohibitive estimator. A more computationally efficient approach is required for real-world systems application. In the next section, we present a technique which can provide excellent localization performance using a relatively small number of environmental realizations.

II. THE L_∞-NORM ESTIMATOR

As discussed previously, the MAP estimator computes robust localization estimates by forming an exponentially weighted average over environmental realizations. The MAP estimator also inherently assumes a continuum of environmental parameter samples. Therefore, with a finite sampling

of the environmental parameter space as would be required for practical applications (e.g., $M \leqslant 100$), a smaller number of better replica-data matches are possible. Thus, there is a smaller occurrence of the clustering of peaks in the vicinity of the true value of $\mathbf{\Theta}$. This increases the possibility of the true peak being averaged out and obscured by sidelobes reinforced over the averaging process. We can compensate for this by giving $|\mathbf{a}^H(\mathbf{\Theta},\mathbf{\Psi}_i)\mathbf{y}|^2$ values, corresponding to better replica-data matches, more significance and greater relative weight in the averaging process. This is accomplished by replacing the exponential weighting in (6) by a p-power weighting,

$$\hat{\mathbf{\Theta}} = \arg\max_{\mathbf{\Theta}} \sum_{i=1}^{M} (|\mathbf{a}^H(\mathbf{\Theta},\mathbf{\Psi}_i)\mathbf{y}|^2)^p, \tag{7}$$

where p would assume a large value, e.g., $p \geqslant 10$. This is essentially an L_p-norm over environmental realizations. These types of norms accentuate large values and attenuate small values. In this way, peaks resulting from better replica-data matches are less likely to be averaged out.

In the limit as $p \to \infty$, (7) becomes

$$\hat{\mathbf{\Theta}} = \arg\max_{\mathbf{\Theta},\mathbf{\Psi}_i} |\mathbf{a}^H(\mathbf{\Theta},\mathbf{\Psi}_i)\mathbf{y}|^2, \quad i = 1,2,...,M. \tag{8}$$

The averaging is eliminated. The estimator of (8) simply finds the best match over source location $\mathbf{\Theta}$ using the M realizations of the environmental parameters. Equation (8) is the L_∞-norm estimator. It resembles the ML estimator; however, it differs in that only the location parameter space is explicitly searched over. A range–depth ambiguity surface is computed at each of the M realizations and the overall peak of all of the surfaces is the source location estimate. Since it is unlikely that the precise true combination of the environmental parameters are included in the M realizations, the L_∞-norm estimator inherently assumes that other combinations of the environmental parameters can also produce accurate localization estimates. We will show the validity of this assumption next.

III. ENVIRONMENTAL SIMILARITY AS RELATED TO LOCALIZATION

In this section we will show why, in the context of localization, other environmental realizations can appear similar to the true and can produce accurate localization estimates. We begin by decomposing the replica vectors using Eqs. (3) and (4). We can express $\boldsymbol{\alpha}(\mathbf{\Theta},\mathbf{\Psi})$ as

$$\boldsymbol{\alpha}(\mathbf{\Theta},\mathbf{\Psi}) = \exp\left\{ j\,\frac{\pi}{4} \right\} \mathbf{G}(\mathbf{\Theta},\mathbf{\Psi})\boldsymbol{\mu}(\mathbf{\Theta},\mathbf{\Psi}), \tag{9}$$

where the diagonal matrix $\mathbf{G}(\mathbf{\Theta},\mathbf{\Psi}) = \mathrm{diag}[\exp\{-\gamma_1 r\}, ...,\exp\{-\gamma_Q r\}]$ contains the modal attenuation coefficients and

$$\boldsymbol{\mu}(\mathbf{\Theta},\mathbf{\Psi}) = \begin{bmatrix} \left(\dfrac{2\pi}{k_1 r}\right)^{1/2} \phi_1(z)\exp\{jk_1 r\} \\ \vdots \\ \left(\dfrac{2\pi}{k_Q r}\right)^{1/2} \phi_Q(z)\exp\{jk_Q r\} \end{bmatrix}. \tag{10}$$

Substituting (9) into (2) results in

$$\mathbf{a}(\mathbf{\Theta},\mathbf{\Psi}) = \exp\left\{ j\,\frac{\pi}{4} \right\} \mathbf{\Omega}(\mathbf{z},\mathbf{\Psi})\mathbf{G}(\mathbf{\Theta},\mathbf{\Psi})\boldsymbol{\mu}(\mathbf{\Theta},\mathbf{\Psi}). \tag{11}$$

Since the modal phases are composed of the products of the wave numbers and source range r, the effects of environmental mismatch are most significant in the modal phases. The modal attenuation terms given by the $\exp\{-\gamma_i r\}$ in $\mathbf{G}(\mathbf{\Theta},\mathbf{\Psi})$ also contain a multiplication by r. However, errors in the modal attenuation are much less significant in comparison, since the γ_i are typically orders of magnitude smaller than the k_i and appear as amplitude damping factors.

To investigate how the modal phases impact localization, we substitute (11) into (8) and expand out the magnitude-squared inner product, which gives

$$\mathbf{y}^H \mathbf{\Omega}(\mathbf{z},\mathbf{\Psi})\mathbf{G}(\mathbf{\Theta},\mathbf{\Psi})\boldsymbol{\mu}(\mathbf{\Theta},\mathbf{\Psi}) \times \boldsymbol{\mu}^H(\mathbf{\Theta},\mathbf{\Psi})\mathbf{G}(\mathbf{\Theta},\mathbf{\Psi})\mathbf{\Omega}^T(\mathbf{z},\mathbf{\Psi})\mathbf{y}. \tag{12}$$

The outer product $\boldsymbol{\mu}(\mathbf{\Theta},\mathbf{\Psi})\boldsymbol{\mu}^H(\mathbf{\Theta},\mathbf{\Psi})$ is the only term in (12) which contains the modal phases. This outer product produces a Hermitian matrix of the form

$$\frac{2\pi}{r}\begin{bmatrix} \dfrac{\phi_1^2(z)}{k_1} & \cdots & \dfrac{\phi_1(z)\phi_Q(z)}{(k_1 k_Q)^{1/2}}\exp\{j\Delta K_{1,Q} r\} \\ \vdots & \ddots & \vdots \\ \dfrac{\phi_1(z)\phi_Q(z)}{(k_1 k_Q)^{1/2}}\exp\{-j\Delta K_{1,Q} r\} & \cdots & \dfrac{\phi_Q^2(z)}{k_Q} \end{bmatrix}, \tag{13}$$

with element i,l equal to $[\phi_i(z)\phi_l(z)/(k_i k_l)^{1/2}]\exp\{j\Delta K_{i,l} r\}$, where $\Delta K_{i,l} = k_i - k_l$. From this, we observe that the modal phase of the L_∞-norm estimator is not dependent on the precise values of the wave numbers, but only on the relative differences between the wave numbers, i.e., the set of values $\Delta K_{i,l} = k_i - k_l$, $i = 1,...,Q$; $l = 1,...,Q$. Hence, the wave num-

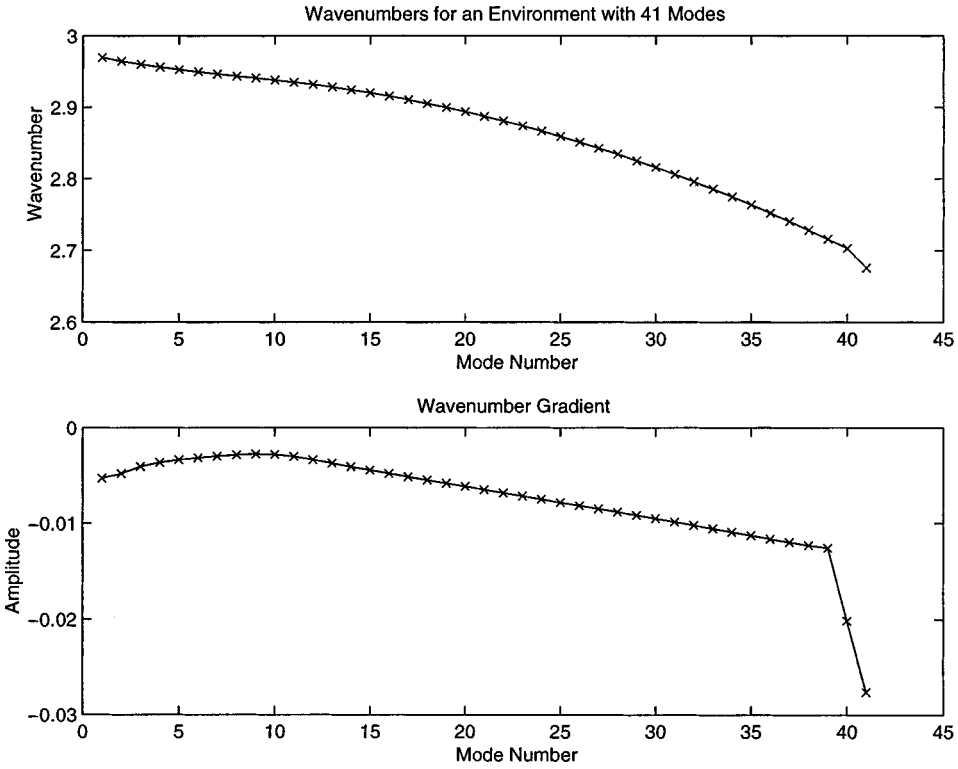

FIG. 1. Wave number curve for a shallow-water environment with 41 propagating modes and its associated wave number gradient.

bers computed using other combinations of the environmental parameters whose relative wave number differences $\Delta K_{i,l}$ are close to those at the true environment can produce similar ambiguity surfaces.

A method for quantifying the wave number differences of the environmental realizations is to use the wave number gradient. The wave number gradient (WG) is the gradient of the curve obtained by connecting the wave numbers k_i, for a particular environmental realization, by line segments, i.e., ''connecting the dots.'' As an illustration, Fig. 1 shows the wave number curve for a shallow-water environment with 41 propagating modes, along with its WG. Environmental realizations which have WGs similar to that at the true will have similar relative wave number differences and, as such, produce similar ambiguity surfaces. As a simple example, consider a set of environmental realizations whose wave numbers lie on different straight lines with varying slopes. It is easy to see that realizations which have identical slopes, or gradients, will have identical relative wave number differences. Therefore, a measure of similarity between environmental realizations is the error between the WG at the true environment and the WG at other realizations. The WG error is given by

$$e_{\mathrm{wg}}=\frac{1}{J}\sum_{i=Q_{\min}}^{Q_{\max}}|g_t(i)-g(i)|^2, \tag{14}$$

where $g_t(i)$ and $g(i)$ are the samples of the numerically computed WG at the true environment and an alternate environmental realization, respectively, and $J=Q_{\max}-Q_{\min}+1$. Notice that e_{wg} is only computed over the *effective* modes, $Q_{\min}$ to $Q_{\max}$, those modes with significant amplitude as sampled by the receiving array. We can compute (14) in simulation studies to substantiate our assertion that environmental realizations, other than the true, yielding small WG errors, produce similar ambiguity surfaces and accurate localization estimates. The general concept that many combinations of mismatched environmental parameters can pro-

TABLE I. Ranges of environmental uncertainty for Naval Postgraduate School environment.

Parameter	Range
surface sound-speed	1530±5 m/s
bottom sound-speed	1490±5 m/s
bottom depth	100±10 m
sub-bottom sound-speed	1604±75 m/s
bottom attenuation	0.192±0.19 dB/λ

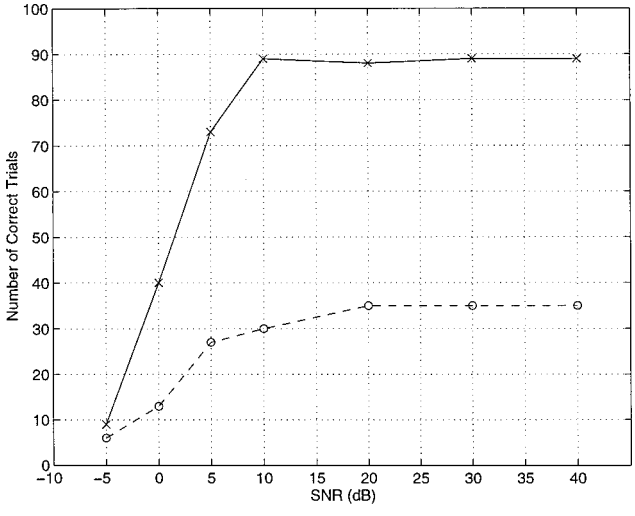

FIG. 2. Performance of estimators using Naval Postgraduate School environment; L_∞-norm—×, MAP—○.

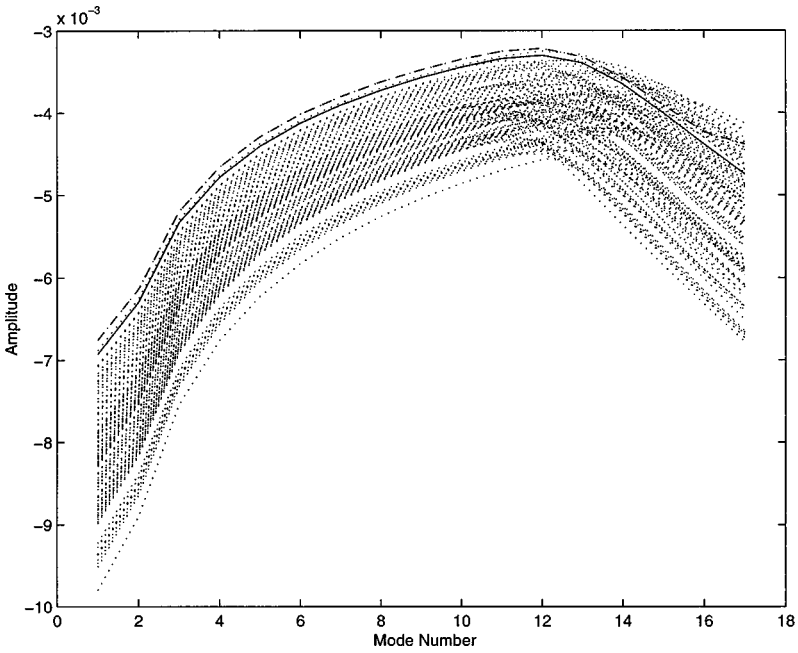

FIG. 3. WGs of the $M=100$ environmental realizations used by L_∞-norm estimator in the Naval Postgraduate School environment (dotted). WG of true environment from one trial (solid) and WG of environment, from the set of 100, which produced the peak localization estimate in that trial (dashed).

vide good localization estimates was also suggested in Ref. 6.

IV. SIMULATION RESULTS IN SHALLOW WATER

In this section, we will compare the performance of the MAP estimator with that of the L_∞-norm estimator for two different simulated environments. For both environments, localization performance was determined based on 100 Monte Carlo trials for each signal-to-noise ratio (SNR) from -5 to 40 dB. The Monte Carlo trials consisted of 100 synthesized data observations, each generated using a unique randomly selected source location and environmental realization from the uncertainty intervals of the environmental parameters. The appropriate level of noise was then added to the data for each SNR. The MAP and L_∞-norm estimators processed the 100 data observations using an independent set of $M=100$ randomly selected environmental realizations. A correct localization was defined as an estimate within a region of ± 300 m in range and ± 4 m in depth of the true source position. The additive noise in each trial was independent, zero-mean Gaussian. A single observation of the array output was used in each trial. A MATLAB version of the KRAKEN normal-mode propagation model was used to compute the data and replica vectors.[12]

The first environment was a two-layer, range-independent shallow-water waveguide with a linear sound–velocity profile. This environment was developed at the Naval Postgraduate School for localization algorithm testing at the Naval Undersea Warfare Center. It contained five uncertain environmental parameters whose ranges of uncertainty

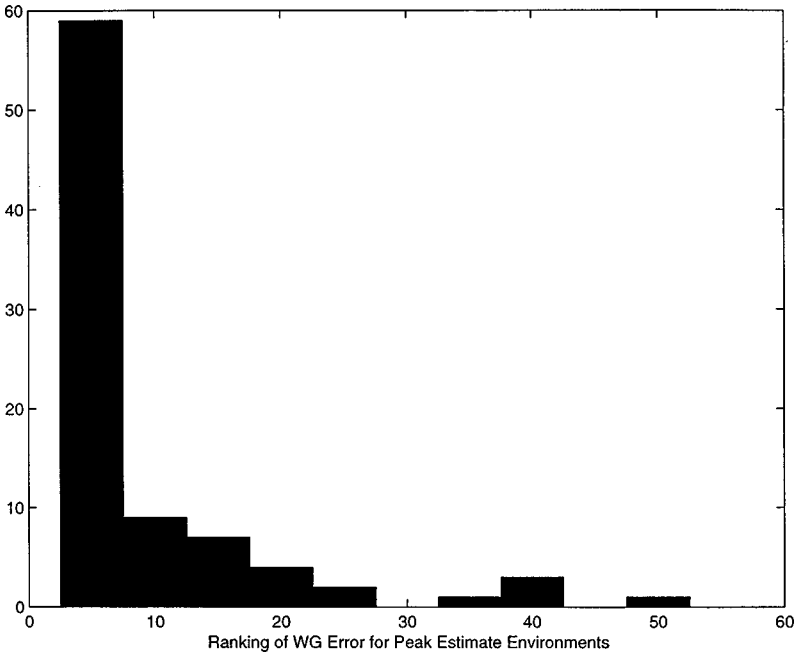

FIG. 4. Histogram of rank of WG errors in correct trials.

TABLE II. Ranges of environmental uncertainty for NRL Benchmark environment.

Parameter	Range
surface sound-speed	1500±2.5 m/s
bottom sound-speed	1480±2.5 m/s
bottom depth	102.5±2.5 m
sub-bottom sound-speed	1600±50 m/s
lower halfspace sound-speed	1750±100 m/s
bottom attenuation	0.35±0.25 dB/λ
bottom density	1.75±0.25

are given in Table I. The receiving array consisted of 20 equally spaced elements producing an aperture of 85 m, with the shallowest element at a depth of 5 m. The range–depth search region was 900 to 5000 m in range and 10 to 90 m in depth. A narrowband source at 700 Hz was used. Figure 2 presents the simulation results for this environment. The performance of the L_∞-norm estimator is significantly better than that of the MAP estimator. This is due to the fact that with only 100 environmental realizations, the MAP estimator does not benefit from the clustering of reinforcing peaks near the true source location, as discussed in Section I. However, the L_∞-norm estimator needs only a single environment producing a small WG error to achieve an accurate localization estimate. Clearly, in this case, 100 environmental realizations was a sufficient amount in which to obtain the small WG error needed.

To further illustrate the concept of wave number gradients, Fig. 3 displays the WGs of the 100 environmental realizations, corresponding to the effective modes, used by the L_∞-norm estimator to process the data. Also shown are the WG of the true environment from one of the Monte Carlo trials, together with the WG of the environmental realization, out of the set of 100, which produced the peak localization estimate in that trial. The WG of this environmental realization also produced the smallest WG error in that trial.

We can also use this simulation example to illustrate the relationship between WG error and correct localization estimates. For each of the 89 correct trials at a SNR of 40 dB, we computed the WG errors between the true environment in that trial and each of the 100 environmental realizations used by the L_∞-norm estimator to process the data. We then ranked the 100 environmental realizations according to their WG error from smallest to largest. This allows us to histogram the ranking of the environmental realizations which produced the localization estimate in each of the correct trials, i.e., the peak ambiguity surface from the $M=100$ realizations. Figure 4 shows the resulting histogram. Over all, in more than 70% of the correct trials the WG error of the environmental realization which produced the localization estimate was within the ten smallest. Thus, small WG errors correspond to accurate localization estimates.

The second environment used was the NRL Benchmark Environment.[13] This is a three-layer shallow-water environment with a linear sound–velocity profile. We will consider the general mismatch case, which contains seven uncertain environmental parameters. This scenario was the most complex benchmark case used in the May 1993 NRL Workshop

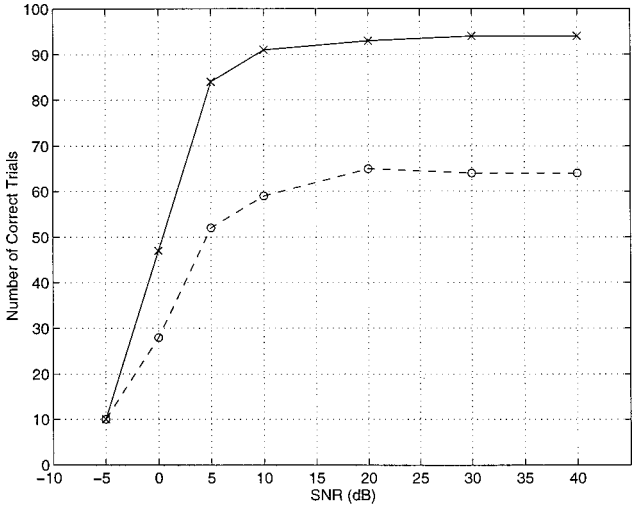

FIG. 5. Performance of estimators using NRL Benchmark environment; L_∞-norm—×, MAP—○.

on Acoustic Models in Signal Processing. Table II contains the uncertainty ranges for these parameters. The receiving array consisted of 20 elements spaced at 5 m with the shallowest element at a depth of 5 m. The range–depth search region was 5 to 10 km in range and 10 to 100 m in depth. For this environment a 250-Hz narrowband source signal was used. The results of the simulation trials are presented in Fig. 5. Again, because of the small number of environmental realizations, the performance of the L_∞-norm estimator was superior to that of the MAP estimator.

V. RESULTS WITH EXPERIMENTAL DATA

The L_∞-norm and MAP estimators were also tested using experimental data collected in the Mediterranean Sea by the NATO SACLANT Center. The details of this experiment can be found in Ref. 7. The environment consisted of three layers: water over sediment over a sub-bottom. Due to the setup of the experiment, the exact location of the stationary source was uncertain to a small degree. However, at all times it was known to be within the region of 5400±200 m in range from the receiving array and 77.5±7.5 m in depth. The source used was a narrowband signal centered at 169.9 Hz. A 48-element vertical receiving array spanning 94 m was used to collect the data. There were nine uncertain environmental parameters whose intervals of uncertainty are given in Table III. The sound–velocity profile in the water column was

TABLE III. Ranges of environmental uncertainty for Mediterranean Sea experiment.

Parameter	Range
channel depth	127.5±2.5 m
sediment upper-sound speed	1500±50 m/s
sediment lower-sound speed	1550±50 m/s
sediment density	1.7±0.5 g/cm^3
sediment attenuation	0.2±0.2 dB/λ
sediment thickness	3.0±3.0 m
bottom sound speed	1600±50 m/s
bottom density	1.7±0.5 g/cm^3
bottom attenuation	0.2±0.2 dB/λ

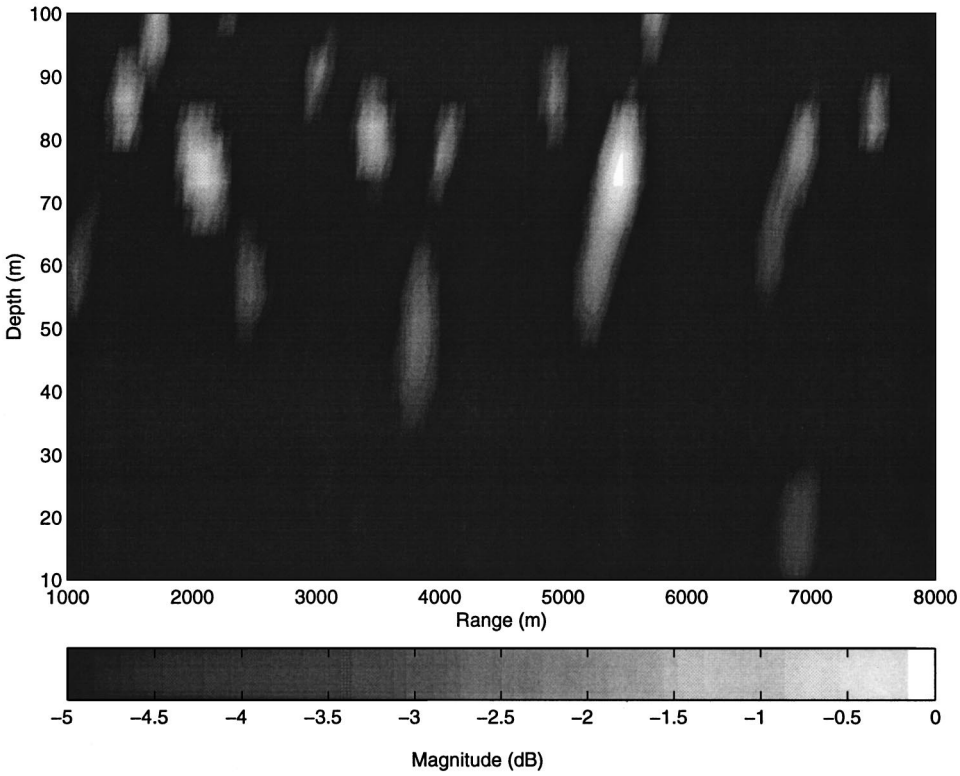

FIG. 6. Peak ambiguity surface of L_∞-norm estimator for Mediterranean Sea experiment; peak at [5480,77.5].

measured near the array and was assumed to be known.

As in the simulations, 100 environmental realizations were randomly selected from the uncertainty intervals of the parameters given in Table III to process the data. The resulting ambiguity surfaces for the L_∞-norm and MAP estimators are shown in Figs. 6 and 7. Figure 6 shows the peak ambiguity surface of the L_∞-norm estimator, which produced a location estimate of 5480 m in range and 77.5 m in depth. This estimate falls within the assumed true-source location region of 5400 ± 200 m in range and 77.5 ± 7.5 m in depth. In contrast, Fig. 7 shows the ambiguity surface for the MAP estimator, which produced an incorrect location estimate of 1420 m in range and 82 m in depth. Once again, the finite number of environments used to process the data was insuf-

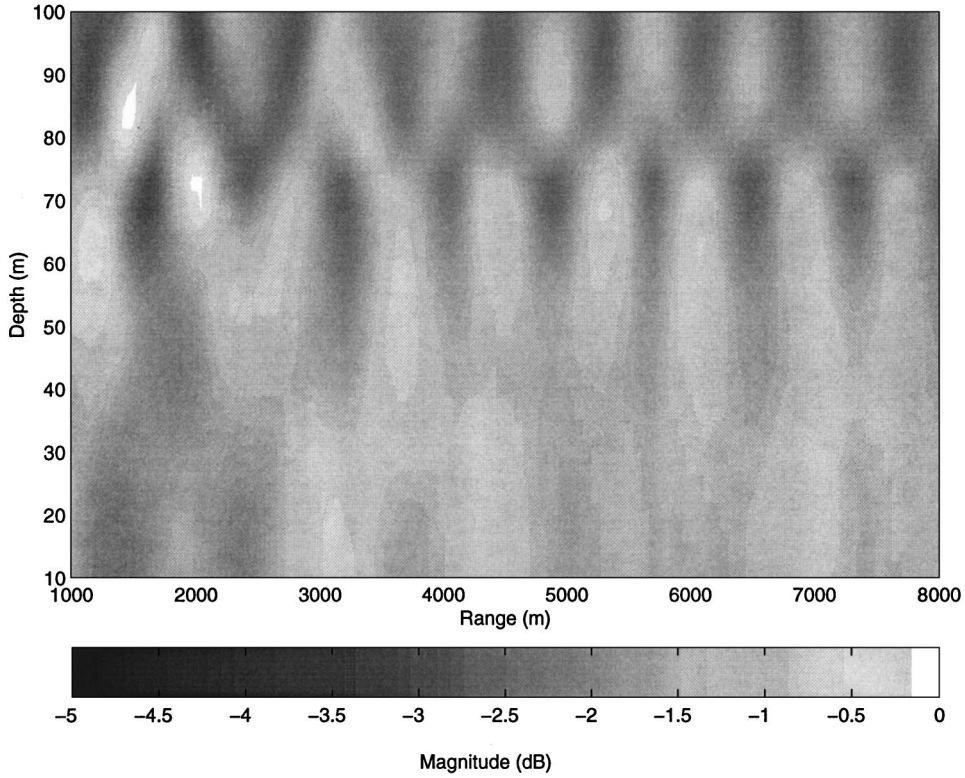

FIG. 7. Ambiguity surface of MAP estimator for Mediterranean Sea experiment; peak at [1420,82].

ficient for the MAP estimator to benefit from the effects of clustering.

VI. CONCLUSIONS

In this paper, it was shown that the MAP estimator applied to matched-field source localization can be suboptimal when a finite sampling of the environmental parameters is used. Using an L_∞-norm estimator in the presence of finite environmental sampling can provide significant localization performance improvement over the MAP estimator. It was also shown that for the localization problem, environmental realizations besides the true can provide accurate localization estimates. Simulation results from two shallow-water environments and experimental data results were presented to support these findings.

[1] D. F. Gingras, ''Methods for predicting the sensitivity of matched-field processors to mismatch,'' J. Acoust. Soc. Am. **86**, 1940–1949 (1989).

[2] A. Tolstoy, ''Sensitivity of matched-field processing to sound-speed profile mismatch for vertical arrays in a deep-water Pacific environment,'' J. Acoust. Soc. Am. **85**, 2394–2404 (1989).

[3] A. M. Richardson and L. W. Nolte, ''*A posteriori* probability source localization in an uncertain sound speed, deep ocean environment,'' J. Acoust. Soc. Am. **89**, 2280–2284 (1991).

[4] J. A. Shorey, L. W. Nolte, and J. L. Krolik, ''Computationally efficient Monte Carlo estimation algorithms for matched field processing in uncertain ocean environments,'' J. Comput. Acoust. **2**, 285–314 (1994).

[5] B. F. Harrison, D. W. Tufts, and R. J. Vaccaro, ''Fast, approximate maximum *a posteriori* probability parameter estimation,'' IEEE Signal Process. Lett. **4**, 96–99 (1997).

[6] M. D. Collins and W. A. Kuperman, ''Focalization: environmental focusing and source localization,'' J. Acoust. Soc. Am. **90**, 1410–1422 (1991).

[7] D. F. Gingras and P. Gerstoft, ''Inversion for geometric and geoacoustic parameters in shallow water: experimental results,'' J. Acoust. Soc. Am. **97**, 3589–3598 (1995).

[8] B. F. Harrison, R. J. Vaccaro, and D. W. Tufts, ''Robust source localization in an acoustic waveguide,'' J. Acoust. Soc. Am. **100**, 384–391 (1996).

[9] J. P. Ianniello, ''Recent developments in sonar signal processing,'' IEEE Signal Process. Mag. **15, no. 4**, 27–40 (1998).

[10] F. B. Jensen, W. A. Kuperman, M. B. Porter, and H. Schmidt, *Computational Ocean Acoustics* (AIP, New York 1994).

[11] J. A. Shorey and L. W. Nolte, ''Wideband optimal *a posteriori* probability source localization in an uncertain shallow ocean environment,'' J. Acoust. Soc. Am. **103**, 355–361 (1998).

[12] J. Ianniello, ''A MATLAB version of the KRAKEN normal mode code,'' Tech. Report TM 94-1096, Naval Undersea Warfare Center, October 1994.

[13] M. B. Porter and A. Tolstoy, ''The matched field processing benchmark problems,'' J. Comput. Acoust. **2**, 161–185 (1994).

Source levels for shallow underwater sound charges

D. E. Hannay
JASCO Research Ltd., Brentwood Bay, British Columbia V8M 1P7, Canada

N. R. Chapman[a)]
School of Earth and Ocean Sciences, University of Victoria, Victoria, British Columbia V8W 3P6, Canada

(Received 27 January 1998; accepted for publication 22 September 1998)

This paper presents a simple method for removing the surface-reflected component from the explosion waveform of signal underwater sound (SUS) charges detonated at shallow depths, in order to obtain accurate estimates of the source levels. The method is based on the repeated subtraction of time-shifted segments of portions of the source waveform that are uncontaminated by the surface reflection. The technique provides a method for an accurate estimation of the source levels for charges detonated at depths shallower than 90 m. The method is evaluated by comparing the source levels from the processed waveforms with results obtained by scaling source levels for deeper charges to depths of 58 and 18.3 m. © *1999 Acoustical Society of America.*
[S0001-4966(99)02301-2]

PACS numbers: 43.60.Pt, 43.30.Xm, 43.30.Lz [DLB]

INTRODUCTION

Small explosive charges have been used extensively in underwater acoustics for measuring quantities such as propagation loss, reverberation, and bottom reflection loss. The interpretation of the data obtained in experiments depends on having accurate values of the source levels of the charges. Over the years a number of groups have published source levels for Signal Underwater Sound (SUS) charges, probably the most widely used type of explosive. These have included the Gaspin and Shuler levels,[1] and more recently, those of Chapman,[2] which were based on the data from an experiment designed specifically to measure SUS source levels.

The published measurements for SUS charges detonated deeper than 90 m have provided source levels to an accuracy of ± 1 dB.[2] However, there remains a fundamental problem in determining source levels from experimental data for charges at shallower depths, due to the effects of multipath propagation. For very shallow charges, the signal from the surface-reflected (SR) path interrupts the bubble pulse waveform of the direct path signal. This contribution must be removed in order to obtain an uncontaminated bubble pulse waveform, which can be used for estimating the source levels. Previous work has ignored the distortion of the waveform introduced by the surface reflection, using only a simple linear interpolation through the negative phase portion of the data to eliminate the SR signal.[2] This approach undoubtedly introduces inaccuracies, particularly at low frequencies. Gaspin *et al.*[3] presented a method for deconvolving the SR signal, but restricted their application to larger charges at deeper depths.

In this paper we present a simple and effective method for removing the SR component from measured explosion waveforms in order to obtain accurate source levels for very shallow charges. The technique is based on subtracting a shifted and properly scaled copy of the uncontaminated direct path signal that immediately preceeds the surface reflection. The process is repeated, using the previously corrected portion to process succeeding sections of the waveform until a desired number of bubble pulses have been recovered. We demonstrate the method using data from a 0.82-kg SUS that was modified for a depth of approximately 60 m. The accuracy of the method is determined by comparing the processed source levels with source levels obtained by scaling the spectrum of a deeper charge, using an algorithm described by Hughes.[4] We then apply the method to obtain source levels for a SUS at the nominal depth of 18.3 m, and test the accuracy of the values by comparing with source levels scaled from the processed 60-m SUS spectrum.

I. METHOD

The multipath propagation for a shallow explosive charge at relatively short range is shown in Fig. 1. In sufficiently deep water there are two dominant propagation paths, the direct and the SR path. The surface reflection can be viewed as a delayed inverted copy of the direct signal, with the delay caused by the propagation along a slightly longer path. As the explosion depth becomes shallower, the travel time delay between the two paths decreases. The reason for the difficulty in determining source levels for very shallow charges is that the surface reflection arrives before the completion of the entire bubble pulse sequence for the direct path component. An example of a SUS waveform showing the interference from the SR signal is provided in Fig. 2(a). The surface reflection is delayed by a time dt, and at greater times the waveform is a superposition of the two signals.

The method for removing the SR component uses the uncontaminated portion of the waveform immediately preceding the surface reflection to adjust the adjacent segment of the waveform. A copy of the direct path signal out to the time dt [Fig. 2(b)] is first scaled in amplitude for the range of the SR path, time shifted by the delay dt, and then subtracted from the original waveform. The subtraction process removes the effect of the SR signal out to a time $2\,dt$, as

a)Electronic mail: chapman@uvic.ca

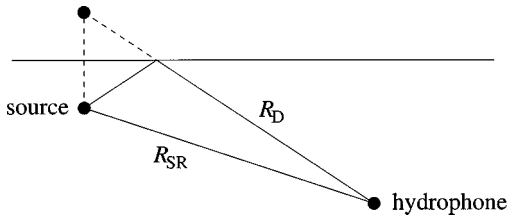

FIG. 1. Multipath propagation diagram for the direct path (D) and surface reflected (SR) signals.

shown in Fig. 2(c), and the corrected portion from dt to 2 dt is used to process the next segment of the waveform. This procedure is repeated until a desired number of bubble pulses have been recovered.

II. APPLICATION TO MEASURED SUS WAVEFORMS

We have applied the method to data that were obtained in an experiment designed to provide high quality measurements of the waveforms for shallow SUS charges in order to determine the depth dependence of the source level. The details of the experiment have been described previously[2] and will not be repeated here. The waveform measured for a 58.1-m, 0.82-kg SUS is shown in Fig. 3(a), displaying the surface-reflected shock wave arrival about 10 ms after the first bubble pulse of the direct path signal. This figure demonstrates an additional problem encountered with very shallow SUS data. The shock pulse for 0.82-kg SUS is strong enough to cause cavitation at the surface so that the reflected signal is noisy and not a simple mirror image of the direct path component. The waveform after processing to recover four bubble pulses is shown in Fig. 3(b). The SR pulses and the distortion due to the negative phases of the SR signal have been eliminated; the cavitation noise has been removed by smoothing the processed waveform, where necessary.

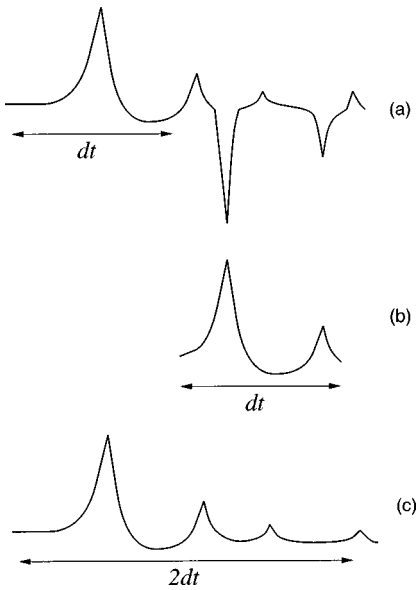

FIG. 2. Graphical description of the method. (a) Shot waveform truncated at three bubble pulses for the direct path, with the surface-reflected shock pulse and first bubble pulse. (b) Uncontaminated portion of the direct path waveform. (c) Processed waveform after subtraction of the direct path signal shown in (b).

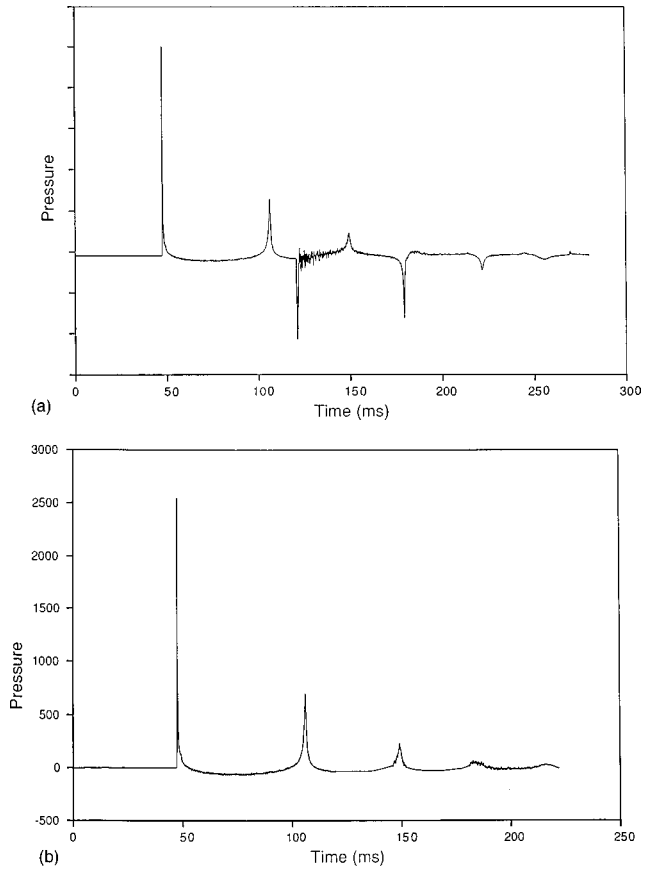

FIG. 3. (a) Measured waveform for the 58.1-m charge (b) Processed waveform, including four bubble pulses. (Pressure is in arbitrary units.)

The spectrum of the processed waveform; obtained using a 64K-FFT, is shown in Fig. 4. To determine the spectrum, the truncated waveform was smoothed exponentially to the baseline and zero padded after the end point. Although the spectrum is dominated by the modulations due to the first bubble pulse, the peak spectral energy is at about 20 Hz, slightly higher than the first bubble pulse frequency of 17.7 Hz. The frequency shift is due to the interference of the contributions from the higher bubble pulse components. The effect of the second and third bubble pulses can also be seen

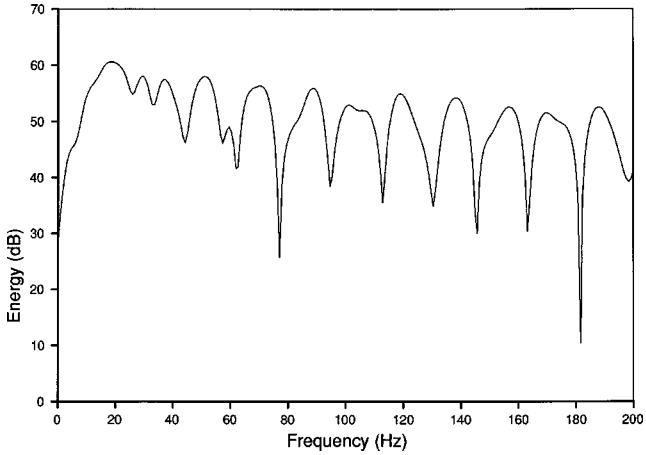

FIG. 4. Energy density spectrum in dB *re*: 1 erg/cm^2/Hz of the processed waveform for the 58.1-m charge.

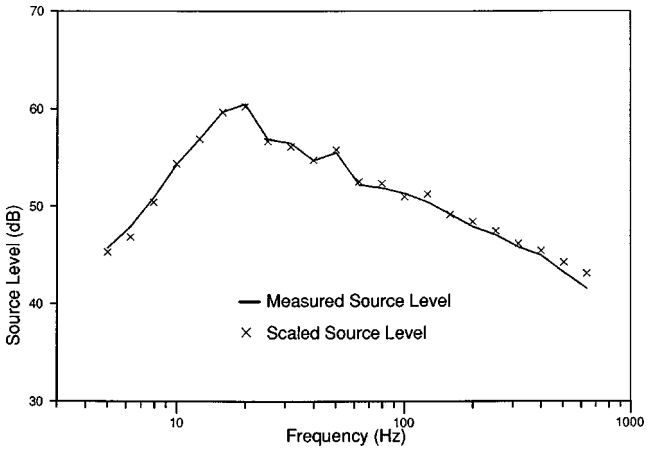

FIG. 5. Scaled and measured 1/3-octave band source levels in dB *re*: 1 erg/cm^2/Hz for the 58.1-m charge.

in the shoulders at about 12 and 6 Hz on the portion below the spectral peak, and in the splitting of the first bubble pulse modulations at higher frequencies. Source levels in 1/3 octave bands from 5 to 630 Hz were determined from the spectrum, and are shown in Fig. 5 and in Table I.

The accuracy of these values was determined by comparing with source levels that were measured from the depth scaled spectrum of a deeper SUS at 99.6 m. At this depth there is no interference from the SR path, and the direct path signal can be processed in a straightforward manner. The algorithm for depth scaling was developed by Hughes[4] and proceeds by scaling the spectral amplitudes by $(z/z_0)^{-0.55}$, and the frequency by $(z/z_0)^{-0.806}$, where z_0 is the hydrostatic depth of the calibration spectrum. The method has been shown to provide accurate results over the frequency band of interest for the relatively small depth change used here (less than a factor of 2). As seen in Fig. 5 the scaled values are in excellent agreement with the processed values.

TABLE I. Source levels in dB *re*: 1 erg/cm^2/Hz for 18.3-, 25.4-, and 58.1-m shots in 1/3 octave bands between 5 and 630 Hz.

Freq. (Hz)	18.3 m (dB)	25.4 m (dB)	58.1 m (dB)
5.00	54.9	53.35	45.32
6.30	58.6	56.12	46.86
7.93	61.3	58.55	50.44
9.99	62.0	61.99	54.39
12.58	58.6	61.02	56.94
15.85	57.2	58.70	59.67
19.96	55.8	57.42	60.26
25.15	56.6	55.17	56.69
31.67	55.2	55.89	56.14
39.89	53.7	54.92	54.76
50.25	52.3	53.18	55.82
63.29	51.9	52.75	52.56
79.71	51.1	51.42	52.36
100.41	50.1	51.05	50.99
126.47	49.3	49.88	51.27
159.30	47.8	48.37	49.16
200.64	47.0	47.62	48.43
252.72	45.7	46.56	47.47
318.31	44.8	45.33	46.17
400.93	44.0	44.64	45.42
504.99	43.0	43.76	44.24
636.06	41.7	42.62	43.09

TABLE II. Source levels in dB *re*: 1 erg/cm^2/Hz for an increasing number of bubble pulses for the 58.1-m shot.

Freq. (Hz)	Bubble pulses used				
	$n=1$	$n=2$	$n=3$	$n=4$	$n=5$
5.00	45.61	47.74	46.08	45.32	44.49
6.30	50.07	50.52	47.85	46.86	48.01
7.93	53.40	52.05	49.96	50.44	50.91
9.99	56.39	53.16	53.79	54.39	53.72
12.58	58.90	56.07	57.48	56.94	57.31
15.85	59.95	60.25	59.29	59.67	59.38
19.96	58.06	60.69	60.63	60.26	60.50
25.15	49.31	53.79	56.24	56.69	56.23
31.67	55.67	55.80	55.85	56.14	56.52
39.89	53.83	54.28	54.75	54.76	54.79
50.25	54.60	55.69	55.77	55.82	55.79
63.29	52.18	52.45	52.64	52.56	52.57
79.72	52.34	52.23	52.27	52.36	52.39
100.41	50.64	51.07	50.97	50.99	50.98
126.47	50.78	51.27	51.27	51.27	51.28
159.30	49.14	49.16	49.14	49.16	49.16
200.64	48.22	48.41	48.44	48.43	48.44
252.72	47.29	47.47	47.47	47.47	47.47
318.31	46.08	46.17	46.16	46.17	46.17
400.93	45.38	45.42	45.42	45.42	45.42
504.99	44.21	44.23	44.23	44.24	44.24
636.06	43.08	43.08	43.09	43.09	43.09

There is some question of how many bubble pulses should be used in determining the source levels. This was investigated by comparing the source levels for truncated versions of the processed waveform, starting with only one bubble pulse and then increasing by one bubble pulse component to a total of five. The results are shown in Table II. For frequencies greater than 63 Hz, the source levels are adequately represented using only the first bubble pulse, but at lower frequencies more bubble pulse components are required. This is expected because, although the spectral contributions from the higher bubble pulses decay faster with frequency there is significant modulation due to higher bubble pulses out to nearly 200 Hz (Fig. 4). However, the effect on the source levels is greatly diminished at frequencies greater than about two or three times the first bubble pulse frequency due to averaging in the 1/3 octave bands. From Table II it is evident that the source levels are adequately determined using four bubble pulses. These values are consistent within 0.5 dB of the values obtained using five bubble pulses, except at 5 and 6.3 Hz, where the difference is around 1 dB.

The method has also been applied to a standard 0.82-kg SUS at the nominal depth of 18.3 m. The actual explosion depth was 25.4 m, somewhat deeper than the nominal depth. This effect has been observed consistently for the northern waters, where the experiment was carried out, and has been attributed to the effect of the colder waters on the SUS detonation mechanism.[5] For this very shallow depth, the SR signal arrives before the first bubble pulse of the direct path signal, but this sequence did not present any fundamental problem in processing the data. The 1/3 octave band source levels are shown in Fig. 6 and listed in Table I. The accuracy

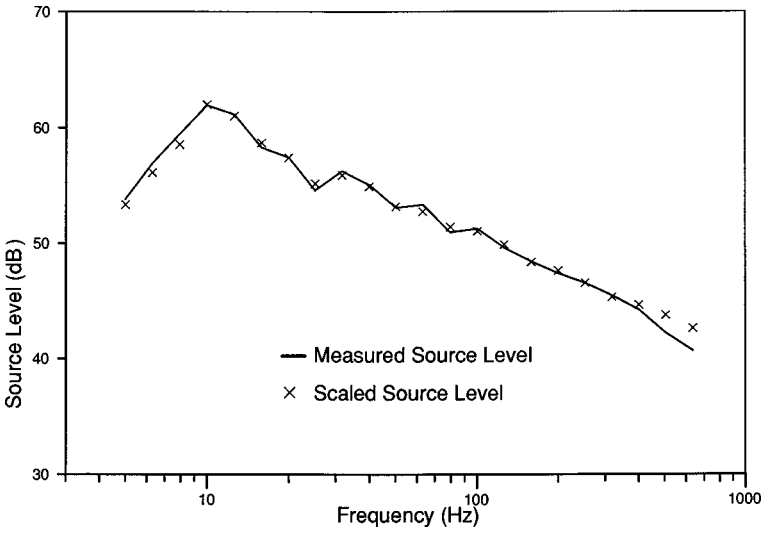

FIG. 6. Scaled and measured 1/3-octave band source levels in dB *re*: 1 erg/cm^2/Hz for a 25.4-m charge.

of the source levels was checked for this case by comparing with values scaled from the 58.1-m SUS, using the spectrum derived from the processed waveform.[6] There is again excellent agreement. The values at very low frequencies ($<$25 Hz) differ significantly from the previous estimates[2] for shallow SUS that were obtained by a simple linear interpolation to remove the SR pulses. The new method is expected to provide better results at very low frequencies because the distortion due to the negative phases of the SR signal has been removed.

As a concluding result, source levels for the nominal SUS depth of 18.3 m are presented in Table I. These values were obtained using the scaling method of Hughes to scale the processed spectrum for the 25.4-m depth. The scaling algorithm is expected to provide accurate results over such relatively small depth changes. These values are significantly improved over previous estimates, particularly for low frequencies below 25 Hz.

III. SUMMARY

An algorithm has been presented to remove the SR component from waveforms of SUS charges detonated at shallow depths. By removing a properly shifted and scaled copy of the early portion of the direct path signal, taken over the time dt before the SR signal begins to interfere, the effects of multipath propagation can be nullified up to the time $2\,dt$. The procedure may be successively repeated, using the newly corrected portion to correct the next segment of the waveform. Application of the method to 58.4- and 18.3-m SUS has facilitated the calculation of source levels for these depths. A comparison with data obtained by the scaling algorithm of Hughes[4] reveals excellent agreement, demonstrating that the algorithm has provided new estimates for source levels for these depths that are significantly improved over previous values, particularly at low frequencies.

ACKNOWLEDGMENTS

Much of the work in this paper was done while one of the authors (NRC) was employed at the Defence Research Establishment Pacific. Support from the Department of National Defence and the Natural Sciences Research and Engineering Council of Canada are greatly appreciated.

[1] J. B. Gaspin and V. K. Shuler, ''Source levels of shallow underwater explosions,'' Naval Ordinance Laboratory, NOLTR 71-160, 13 October 1971.
[2] N. R. Chapman, ''Source levels of shallow explosive charges,'' J. Acoust. Soc. Am. **84**, 697–702 (1988).
[3] J. B. Gaspin, J. A. Goertner, and I. M. Blatstein, ''The determination of acoustic source levels for shallow underwater explosions,'' J. Acoust. Soc. Am. **66**, 1453–1462 (1979).
[4] R. Hughes, ''Underwater explosives: scaling of source spectra,'' in *Underwater Acoustics and Signal Processing*, edited by L. Bjorno (Reidel, New York, 1981), pp. 87–91.
[5] R. J. Hecht and L. A. Mole, ''An analysis of the distribution of measured bubble pulse periods of explosive sources,'' in *Ocean 78 Proceedings*, Marine Technology Society, July 1978, p. 339.
[6] D. E. Hannay, ''Estimation of geoacoustic parameters of the ocean bottom by inversion of reflectionless data,'' Masters thesis, University of Victoria (1995).

Spectrographic measurement of instantaneous frequency and the time-dependent weighted average instantaneous frequency

Patrick J. Loughlin[a)]
348 Benedum Engineering Hall, Department of Electrical Engineering, University of Pittsburgh, Pittsburgh, Pennsylvania 15261

(Received 4 April 1997; accepted for publication 20 June 1998)

Instantaneous frequency (IF) is an important signal characteristic arising in many fields. It is a concept intimately linked to time–frequency analysis, where it can be obtained from a time–frequency distribution (TFD) as the first conditional moment in frequency, suggesting that the IF is the average frequency at each time. However, this interpretation is questionable, since it is well known that the IF often ranges beyond the spectral support of the signal. In addition, to obtain the IF from a spectrogram (which is one possible TFD), a very wideband—and thus severely spectrally distorted—spectrogram must be used. More reasonable bandwidths are investigated, and, in particular, give the conditions by which the first conditional moment of a spectrogram can indeed be interpreted as the average frequency at each time. Under these conditions, namely when the spectrogram bandwidth is less than the frequency separation of the signal components in the time–frequency plane, the spectrogram yields not the usual IF, but a time-dependent weighted average instantaneous frequency (WAIF) of the signal. Also, while the IF and WAIF are generally different, sometimes they are the same (in particular, when there is symmetry in the time–frequency spectrum of the signal); in that case, the first conditional spectral moments of both wideband and narrow band spectrograms are the same and interpretable as the average frequency at each time. [S0001-4966(99)02701-0]

PACS numbers: 43.60.Qv, 43.60.Gk, 43.58.Hp [JCB]

INTRODUCTION

The analysis of signals with changing spectral characteristics has important applications in acoustics, speech, communications, geophysics, biomedicine, and many other areas of science and engineering.[1–3] One of the tools available for the study of time-varying or nonstationary signals is the spectrographic analyzer, developed about 50 years ago to study the changing spectral structure of speech and other sounds.[4] The precursor to modern time–frequency analysis,[1] the spectrographic analyzer is widely used today (more commonly known as the ''spectrogram'') and is arguably the ''workhorse'' of time–frequency analysis methods.[1,5–8]

Often implemented on digital computers today via the fast Fourier transform,[9] early analog spectrographic analyzers were essentially implemented via a bank of bandpass filters, the outputs of which were magnitude squared to obtain an estimate of the time-varying energy density in different frequency bands. Mathematically, the spectrogram can be expressed as the squared magnitude of the short-time Fourier transform (STFT),[6,7]

$$P(t,\omega)=\left|x(t)*h(t)e^{j\omega t}\right|^2 = \left|\int x(\tau)h(t-\tau)e^{-j\omega\tau}\,d\tau\right|^2, \quad (1)$$

where $x(t)$ is the signal and, in the filter-bank interpretation of the spectrogram, $h(t)$ is the impulse response of a low-pass filter modulated by $e^{j\omega t}$ to different frequency bands. In the STFT interpretation of the spectrogram, $h(t)$ is a ''window,'' which isolates local sections of the signal for Fourier analysis.

One useful concept for describing the changing spectral structure of a time-varying signal is its average frequency at each time, which arises in time–frequency distribution (TFD) theory and is the first conditional moment in frequency (or conditional mean frequency, CMF) $\langle\omega\rangle_t$ of the distribution.[1] The spectrogram is one possible distribution, and the measurement of the CMF from the spectrogram, and the interpretation of that measurement, is the subject of this paper.

Clearly, the spectrographic CMF depends on the filter (or window) $h(t)$. For example, Cohen and Lee showed analytically that, for the signal $x(t)=A(t)e^{j\varphi(t)}$, the spectrographic CMF approaches the instantaneous frequency, $\varphi'(t)$, of the signal as the filter $h(t)$ becomes increasingly broadband.[10] At the other extreme, namely as the filter becomes increasingly narrow band, the CMF of the spectrogram approaches the average frequency, $\langle\omega\rangle$, of the signal. The relationship between the CMF of a TFD of the signal and the instantaneous frequency (IF) of the signal, and the definition and interpretation of the IF, has been extensively investigated and debated.[1,10–22]

In this paper, we compare the CMF measured from (very) wideband spectrograms to that measured from *narrow band* spectrograms. While the former closely approximates the IF of the signal, as predicted by Cohen and Lee, the latter frequency is, not surprisingly, often quite different; sometimes, however, it is the same, and we explore when that is

a)Electronic mail: pat@ee.pitt.edu

the case. An expression for this time-varying frequency is given in terms of the signal parameters, specifically it is shown to be a (time-dependent) weighted average instantaneous frequency (WAIF) of the signal. We give conditions on the bandwidth of a spectrogram such that its CMF equals the WAIF. Unlike the IF, the WAIF can always be interpreted as the time-varying average frequency of the signal. We also show that when the IF and WAIF are the same (which occurs when there is symmetry in the instantaneous spectrum),[23,24] the CMF of a wideband or narrow band spectrogram is the same.

Before proceeding, we remark that others have studied different weighted averages of instantaneous frequency, in particular with regard to auditory perception of two-tone complexes. Specifically, we note the ''envelope weighted average of instantaneous frequency (EWAIF)'' and the ''intensity weighted average of instantaneous frequency (IWAIF).'' [25–27] Unlike the WAIF considered here, however, the EWAIF and IWAIF are constants, independent of time. (Indeed, the IWAIF is the average frequency of the signal.) The weighted average instantaneous frequency (WAIF) considered here is a *time-dependent* frequency, and is hence a different concept and frequency than the EWAIF or IWAIF. However, the WAIF may share a similar role in the perception of two-*chirp* complexes (i.e., frequency-varying sinusoids) as do the IWAIF and EWAIF in the perception of two-tone complexes (i.e., constant frequency sinusoids), which is being explored by the author and colleagues.

I. INSTANTANEOUS FREQUENCY AND CONDITIONAL MEAN FREQUENCY OF A GENERAL SIGNAL

Consider a general two-component signal,

$$a_1(t)e^{j\varphi_1(t)}+a_2(t)e^{j\varphi_2(t)}=A(t)e^{j\varphi(t)}, \tag{2}$$

where a signal is ''multicomponent'' according to Cohen if the instantaneous bandwidths of the individual components are small compared to the separation between their instantaneous frequencies,[1,28]

$$\left|\frac{a_i'(t)}{a_i(t)}\right| \ll \left|\varphi_i'(t)-\varphi_k'(t)\right|, \quad i\neq k. \tag{3}$$

The instantaneous frequency $\varphi'(t)\equiv(d/dt)\varphi(t)$ of this signal is[10]

$$\varphi'(t)=\frac{a_1^2(t)\varphi_1'(t)+a_2^2(t)\varphi_2'(t)+a_1(t)a_2(t)(\varphi_1'(t)+\varphi_2'(t))\cos(\varphi_1(t)-\varphi_2(t))}{A^2(t)} + \frac{(a_1'(t)a_2(t)-a_2'(t)a_1(t))\sin(\varphi_1(t)-\varphi_2(t))}{A^2(t)}, \tag{4}$$

where

$$A^2(t)=a_1^2(t)+a_2^2(t)+2a_1(t)a_2(t)\cos(\varphi_1(t)-\varphi_2(t)). \tag{5}$$

Note that the instantaneous frequency and amplitude of the signal generally vary with time, as can the individual instantaneous frequencies and amplitudes of each component of the signal.

Our objective is to explore, in detail, the CMF of a spectrogram of this signal, and its relation to the instantaneous frequency of the signal. (The more general N-component case is given in the Appendix. It is a straightforward but lengthy extension of the two-component signal. Considering the two-component case first simplifies and streamlines the presentation of the main ideas.)

The CMF of a spectrogram of the signal $A(t)e^{j\varphi(t)}$ is given by[1,10,29]

$$\langle\omega\rangle_t=\frac{\int\omega P(t,\omega)d\omega}{\int P(t,\omega)d\omega}=\frac{\int A^2(\tau)\varphi'(\tau)h^2(t-\tau)d\tau}{\int A^2(\tau)h^2(t-\tau)d\tau}. \tag{6}$$

Note that $h^2(t)$ functions as a linear time-invariant (LTI) filter in the numerator and denominator of the CMF [Eq. (6)] (although the total expression is not LTI). It follows that as the filter becomes increasingly broadband, the CMF of the spectrogram approaches the IF of the signal,

$$\text{as } h^2(t)\to\delta(t), \quad \langle\omega\rangle_t\to\varphi'(t). \tag{7}$$

On the other hand, as the filter becomes increasingly narrow band, the CMF approaches the average frequency of the signal,

$$\text{as } h^2(t)\to 1, \quad \langle\omega\rangle_t\to\langle\omega\rangle. \tag{8}$$

[For $h^2(t)=1$, Eq. (6) is $\int A^2(\tau)\varphi'(\tau)d\tau/\int A^2(\tau)d\tau$, which is what Anantharaman *et al.*[25] define as the ''intensity weighted average of instantaneous frequency (IWAIF),'' and which equals the average frequency $\langle\omega\rangle$ of the signal $A(t)e^{j\varphi(t)}$.[1]]

What is not obvious is the result one obtains when neither of these extreme conditions is met (e.g., as with a practical narrow band spectrogram). We derive conditions on $h(t)$ such that the CMF is a weighted average of the individual instantaneous frequencies of the signal. We then give several examples of CMF measurements of the WAIF from spectrograms meeting the conditions on $h(t)$ as well as CMF measurements of the IF from very wideband spectrograms.

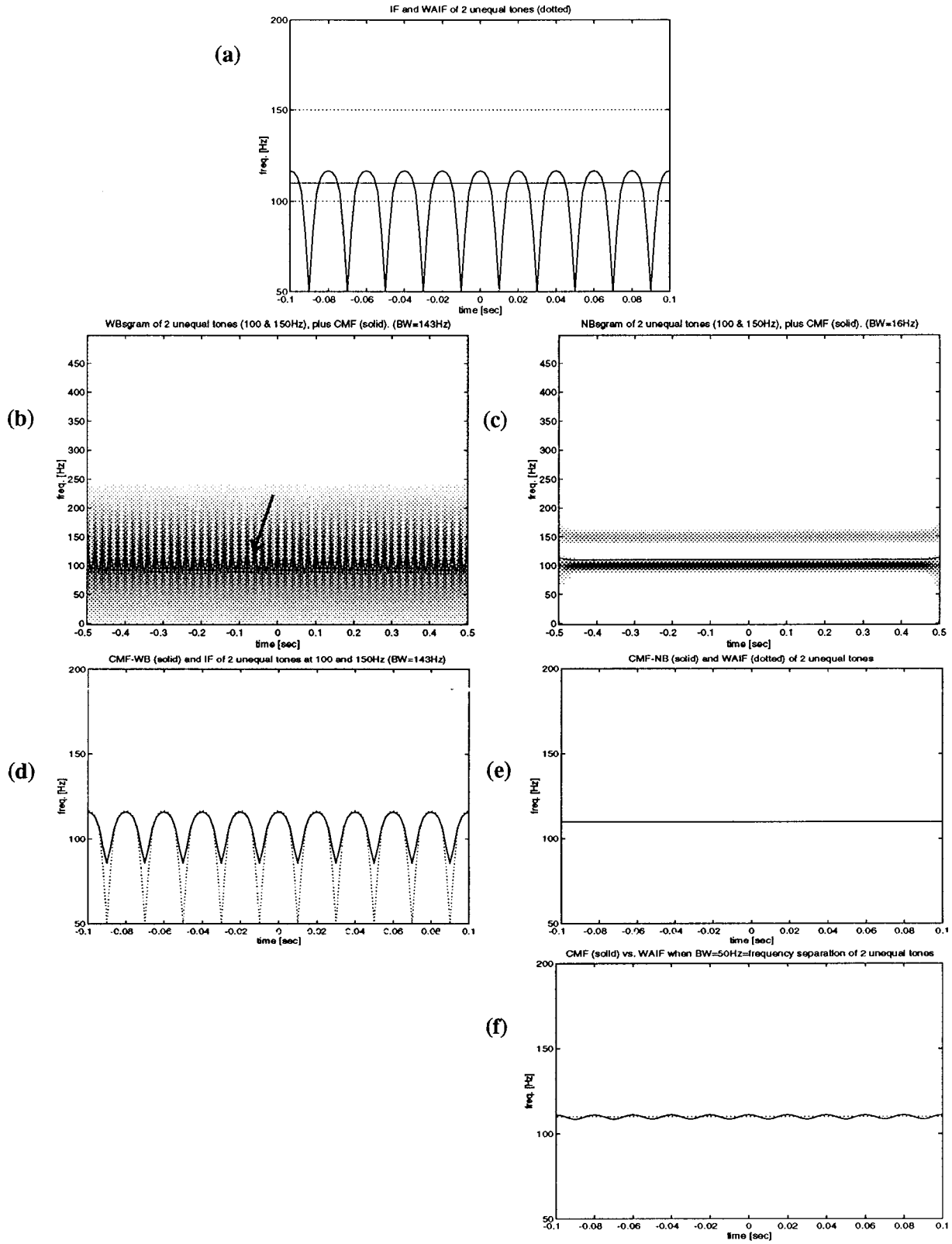

FIG. 1. (a) The WAIF (solid, constant) and IF (solid, varying) of an unequal amplitude two-tone signal. (Tone frequencies are shown as a dotted line. Amplitudes were 1.0 for a 100-Hz tone and 0.5 for a 150-Hz tone.) (b) A 143-Hz bandwidth spectrogram (gray scale) with its conditional mean frequency overlaid (CMF-WB, solid line under the arrow). (c) A 16-Hz bandwidth spectrogram (gray scale) and its conditional mean frequency (CMF-NB, solid line). (d) CMF-WB (solid) versus IF (dotted). (e) CMF-NB (solid) versus WAIF (dotted). (f) CMF (solid) when spectrogram filter cutoff equals the frequency separation of tones, compared to WAIF (dotted). Note the error in this CMF estimate of WAIF compared to CMF-NB, where the cutoff was below the 50-Hz separation of the tones.

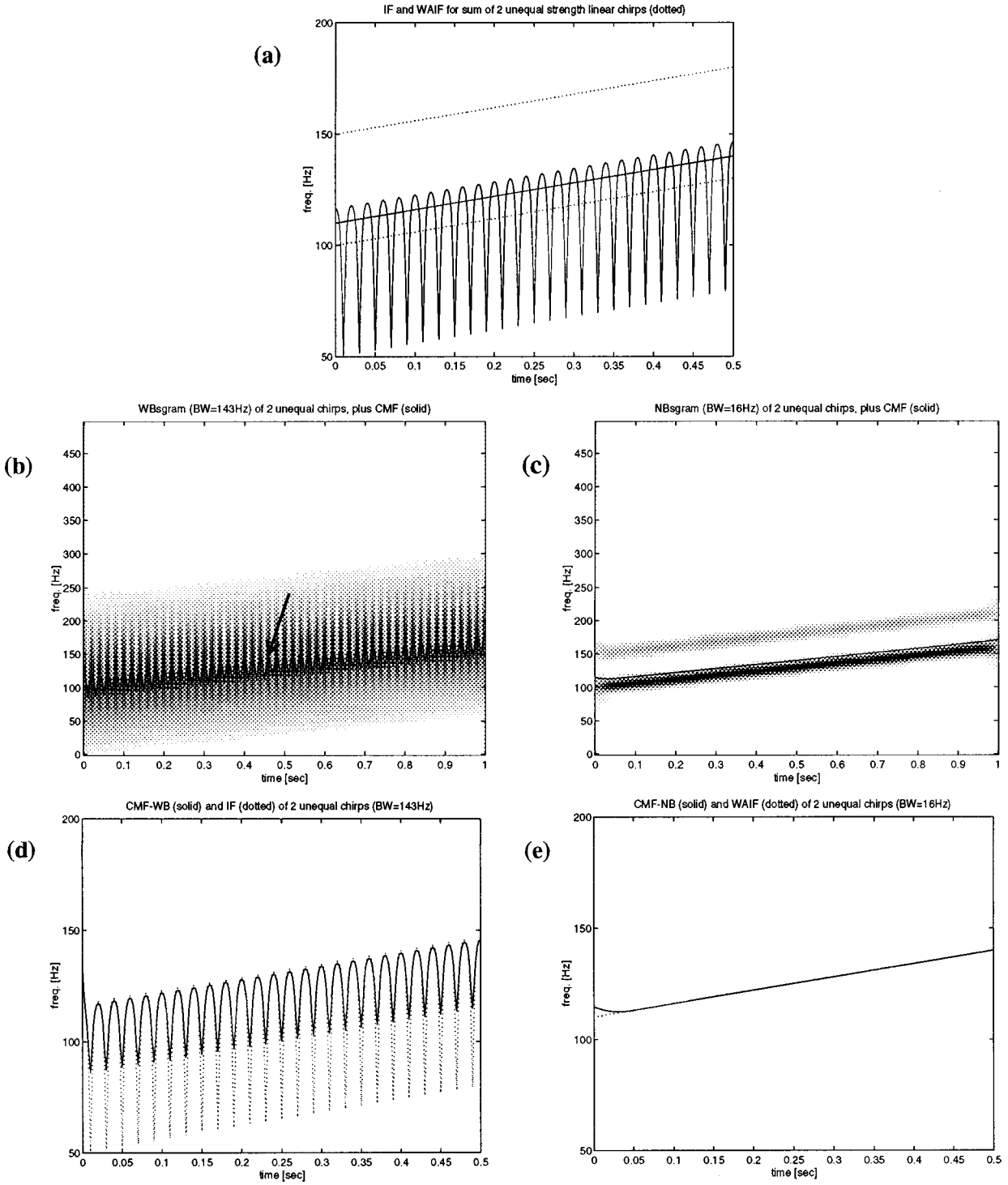

FIG. 2. (a) The WAIF (solid, linearly increasing) and IF (solid, varying and increasing) of the same unequal amplitude two-tone signal in Fig. 1, modulated by a linear FM chirp (modulated frequencies are shown as a dotted line). (b) A 143-Hz bandwidth spectrogram (gray scale) and its conditional mean frequency (CMF-WB, solid line under the arrow). (c) A 16-Hz bandwidth spectrogram (gray scale) and its conditional mean frequency (CMF-NB, solid). (d) CMF-WB (solid) versus IF (dotted). (e) CMF-NB (solid) versus WAIF (dotted).

II. THE WEIGHTED AVERAGE INSTANTANEOUS FREQUENCY (WAIF) AND ITS MEASUREMENT

For multicomponent signals $x(t)=\Sigma_{i=1}^{N} a_i(t)e^{j\varphi_i(t)}$, it has been suggested that the ''instantaneous frequency'' be defined as a weighted average of the individual instantaneous frequencies (WAIF),[14,30]

$$\varpi(t)=\frac{\Sigma_{i=1}^{N} a_i^2(t)\varphi_i'(t)}{\Sigma_{i=1}^{N} a_i^2(t)}. \tag{9}$$

Clearly, this time-varying frequency is different than the IF [given by Eq. (4) for $N=2$], although they are equal when the components are disjoint in time, i.e., when

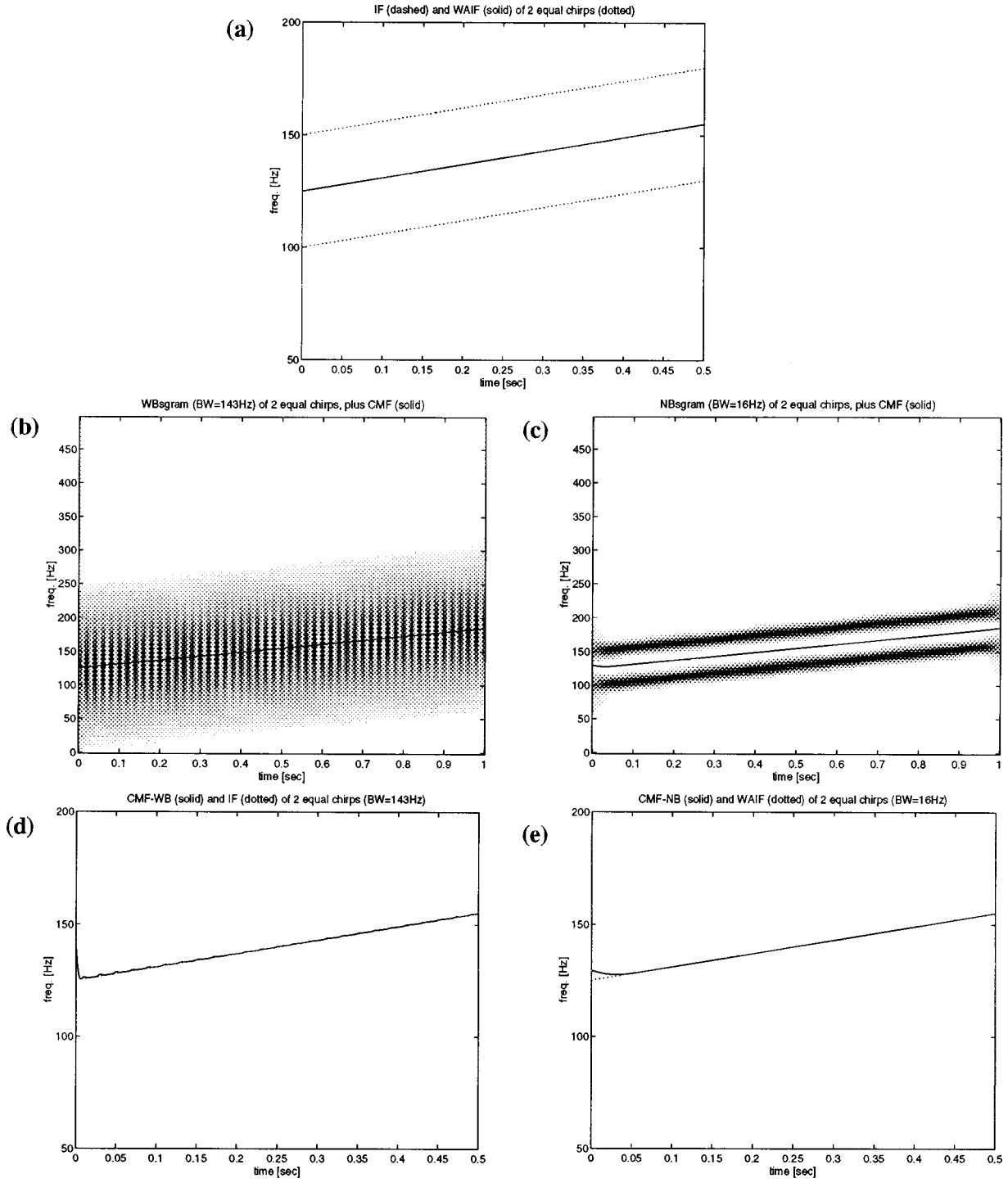

FIG. 3. The same as Fig. 2, only here the amplitudes of the two modulated tones are equal. Hence, the IF and WAIF are equal. (a) The WAIF (solid) and IF (dashed—coincides with WAIF) of the equal amplitude frequency modulated two-tone signal (modulated frequencies are shown as a dotted line). (b) A 143-Hz bandwidth spectrogram (gray scale) and its conditional mean frequency (CMF-WB, solid). (c) A 16-Hz bandwidth spectrogram (gray scale) and its conditional mean frequency (CMF-NB, solid). (d) CMF-WB (solid) versus IF (dotted). (e) CMF-NB (solid) versus WAIF (dotted).

$a_i(t)a_k(t) = 0$, $i \neq k$, and also for the two-component case when the amplitudes are of equal strength, i.e., when $|a_1(t)| = |a_2(t)|$.[16,17]

In addition to the equivalence between the IF and WAIF for limited situations (see the Appendix), our primary motivation for considering the WAIF is because of its clear physical interpretation, and because the CMF of an appropriate bandwidth spectrogram can equal this result *exactly*, as derived below and demonstrated via several examples. In addition, the common interpretation of instantaneous frequency in the time–frequency literature is that it is the average frequency at each time; however, that interpretation very often does not hold,[15–17] prompting the question: what *is* the average frequency at each time of a signal? We maintain that it is indeed the WAIF.

For the general two-component signal, the CMF of a spectrogram of this signal is obtained by substituting Eqs. (4) and (5) into Eq. (6), which yields

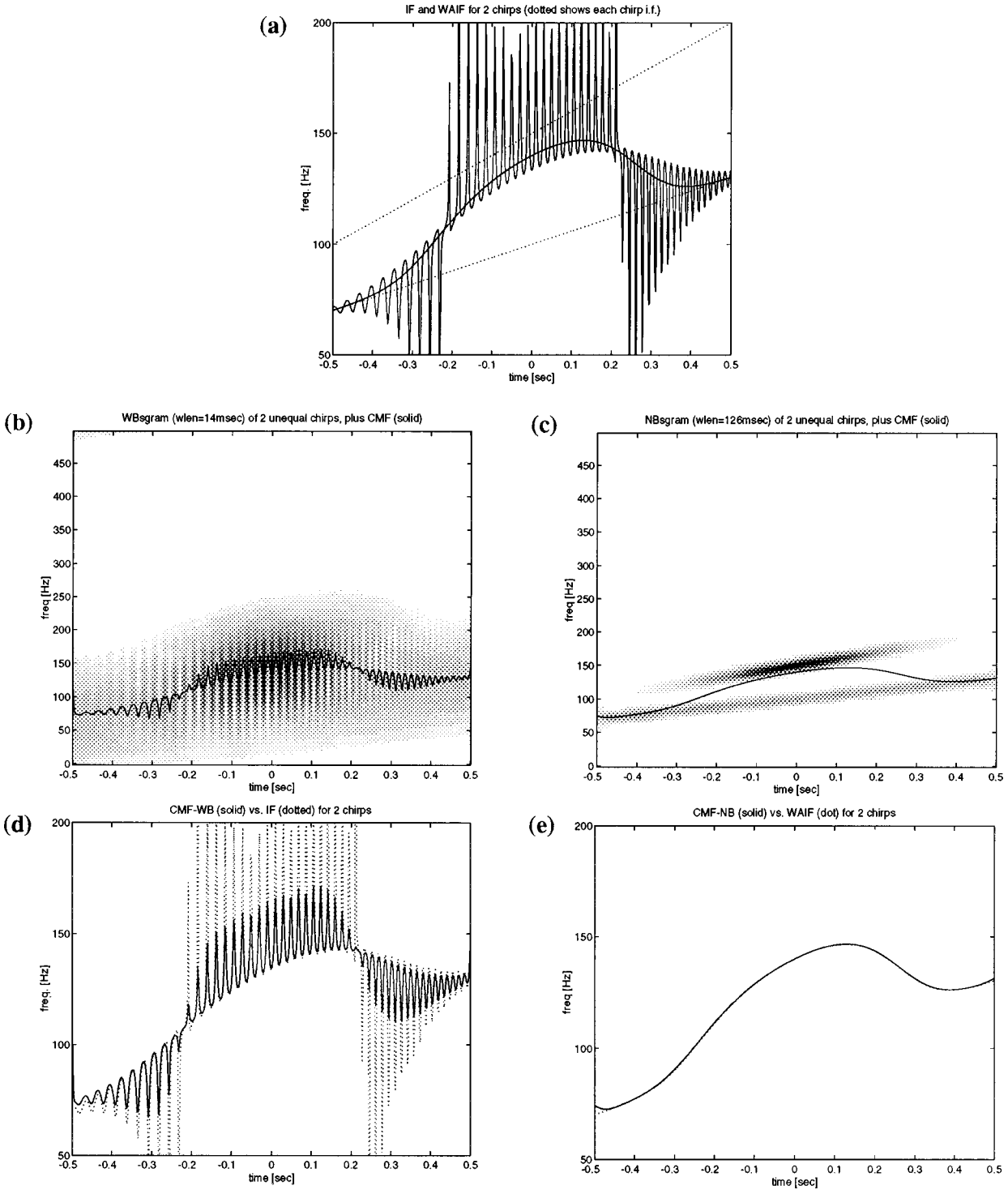

FIG. 4. (a) The WAIF (solid, smooth), the IF (solid, erratic), and the individual instantaneous frequencies (dotted) of a 2-chirp signal. (b) A 143-Hz bandwidth spectrogram (gray scale) and its conditional mean frequency (CMF-WB, solid). (c) A 16-Hz bandwidth spectrogram (gray scale) and its conditional mean frequency (CMF-NB, solid). (d) CMF-WB (solid) versus IF (dotted). (e) CMF-NB (solid) versus WAIF (dotted).

$$\langle \omega \rangle_t = \frac{\int h^2(t-\tau)\left(a_1^2(\tau)\varphi_1'(\tau) + a_2^2(\tau)\varphi_2'(\tau) + C(\tau) + S(\tau)\right)d\tau}{\int h^2(t-\tau)\left(a_1^2(\tau) + a_2^2(\tau) + 2a_1(\tau)a_2(\tau)\cos(\varphi_1(\tau) - \varphi_2(\tau))\right)d\tau}, \tag{10}$$

where

$$C(\tau) = a_1(\tau)a_2(\tau)\left(\varphi_1'(\tau) + \varphi_2'(\tau)\right)\cos(\varphi_1(\tau) - \varphi_2(\tau)), \tag{11}$$

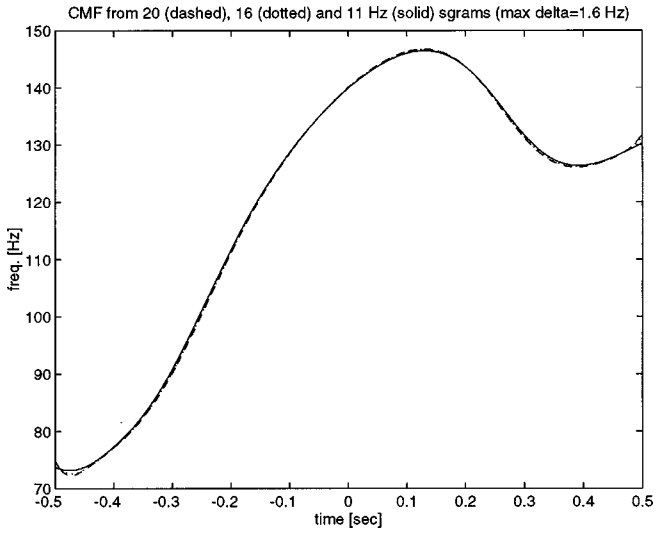

FIG. 5. CMF computed from three different spectrograms for the same signal as in Fig. 4. Spectrogram bandwidths were 20 Hz (dashed), 16 Hz (dotted), and 11 Hz (solid). The maximum difference between the three estimates is 1.6 Hz.

$$S(\tau)=(a_1'(\tau)a_2(\tau)-a_2'(\tau)a_1(\tau))\sin(\varphi_1(\tau)-\varphi_2(\tau)). \tag{12}$$

It is clear that if the cosine- and sine-modulated terms have higher spectral content distinct from that of the ''baseband'' terms $a_i^2(\tau)\varphi_i'(\tau)$ and $a_i^2(\tau)$ (as is often the case), then choosing $h^2(t)$ to be a low-pass filter with cutoff frequency below the modulated terms but above the baseband terms will keep only the baseband terms. In that case, the numerator and denominator of Eq. (10) are given by

$$N(t)=a_1^2(t)\varphi_1'(t)+a_2^2(t)\varphi_2'(t), \tag{13}$$

$$D(t)=a_1^2(t)+a_2^2(t), \tag{14}$$

respectively, from which it follows that the CMF equals the WAIF:

$$\langle\omega\rangle_t=\frac{N(t)}{D(t)}=\frac{a_1^2(t)\varphi_1'(t)+a_2^2(t)\varphi_2'(t)}{a_1^2(t)+a_2^2(t)}=\varpi(t). \tag{15}$$

A ''rule of thumb'' for choosing the cutoff frequency of the low-pass spectrographic filter $h^2(t)$ is that it be below the minimum separation of the instantaneous frequencies of the individual components,

$$\omega_{\text{cutoff}}<\min_{t\in T}|\varphi_1'(t)-\varphi_2'(t)|, \tag{16}$$

in the two-component case, where T designates the time support of the signal. (Note the obvious benefit of allowing time-varying filters, particularly if the individual instantaneous frequencies are very close at some times but have large separation elsewhere.) Several examples are presented next to illustrate results of the spectrographic measurement of the IF and WAIF of signals.

III. EXAMPLES

All spectrograms and computations were implemented on a digital computer for discrete-time signals with a sampling frequency of 500 Hz. Unit-energy normalized Hanning windows were used for $h(t)$ in computing spectrograms. The bandwidth of the spectrogram was defined to be the location of the first spectral zero of the window ($2/T$ Hz for a T second duraton Hanning window).

A. Two tones

Consider the sum of two tones,

$$A_1e^{j\omega_1 t}+A_2e^{j\omega_2 t}=A(t)e^{j\varphi(t)}. \tag{17}$$

The instantaneous frequency $\varphi'(t)$ and amplitude $A(t)$ are given by Eqs. (4) and (5), where $\varphi_i(t)=\omega_i t$ and $a_i(t)=A_i$. Note that when $|A_1|=|A_2|$, the IF is constant and equals the WAIF ($\frac{1}{2}(\omega_1+\omega_2)$), which equals the CMF of a narrow band or wideband spectrogram. When $|A_1|\neq|A_2|$, the IF and WAIF differ. In particular, the IF varies with time for unequal strength tones, while the WAIF is constant and equals the average frequency of the tones, $(A_1^2\omega_1+A_2^2\omega_2)/(A_1^2+A_2^2)$.[14,15,17] (Note then that for the special case of two-tone complexes, the WAIF and IWAIF[25] are the same.) In order for the spectrogram to accurately estimate the IF in this case, $h^2(t)$ must have a very broad frequency response (i.e., the spectrogram must be very wideband), while in order to accurately estimate the WAIF, $h^2(t)$ must be low pass and narrow band (specifically, it must have a cutoff frequency below $|\omega_1-\omega_2|$)—see Fig. 1 (note, in particular, the error in the CMF measure of the WAIF when the cutoff is near $|\omega_1-\omega_2|$).

B. Two linearly frequency modulated tones

Modulating the two tones by a linear FM chirp yields the signal

$$A_1e^{j(\omega_1 t+\beta t^2)}+A_2e^{j(\omega_2 t+\beta t^2)}=A(t)e^{j\varphi(t)} \tag{18}$$

[where, despite the same notation, the instantaneous amplitude $A(t)$ and phase $\varphi(t)$ are not the same as those in (17)]. As above, the minimum separation between the individual instantaneous frequencies is $|\omega_1-\omega_2|$, and hence a spectrogram computed with a low-pass filter $h^2(t)$ with cutoff below that frequency accurately estimates the WAIF, while a (very) wideband spectrogram yields a reasonably accurate estimate of the IF. See Fig. 2. Also, as with two tones, for equal strength components, the IF and WAIF are identical (although time varying here), and hence the CMF of either a wideband or a narrow band spectrogram is the same. See Fig. 3.

C. Two unequal chirps

Next we consider the measurements obtained for two chirps of unequal chirp rate and unequal, time-varying amplitude,

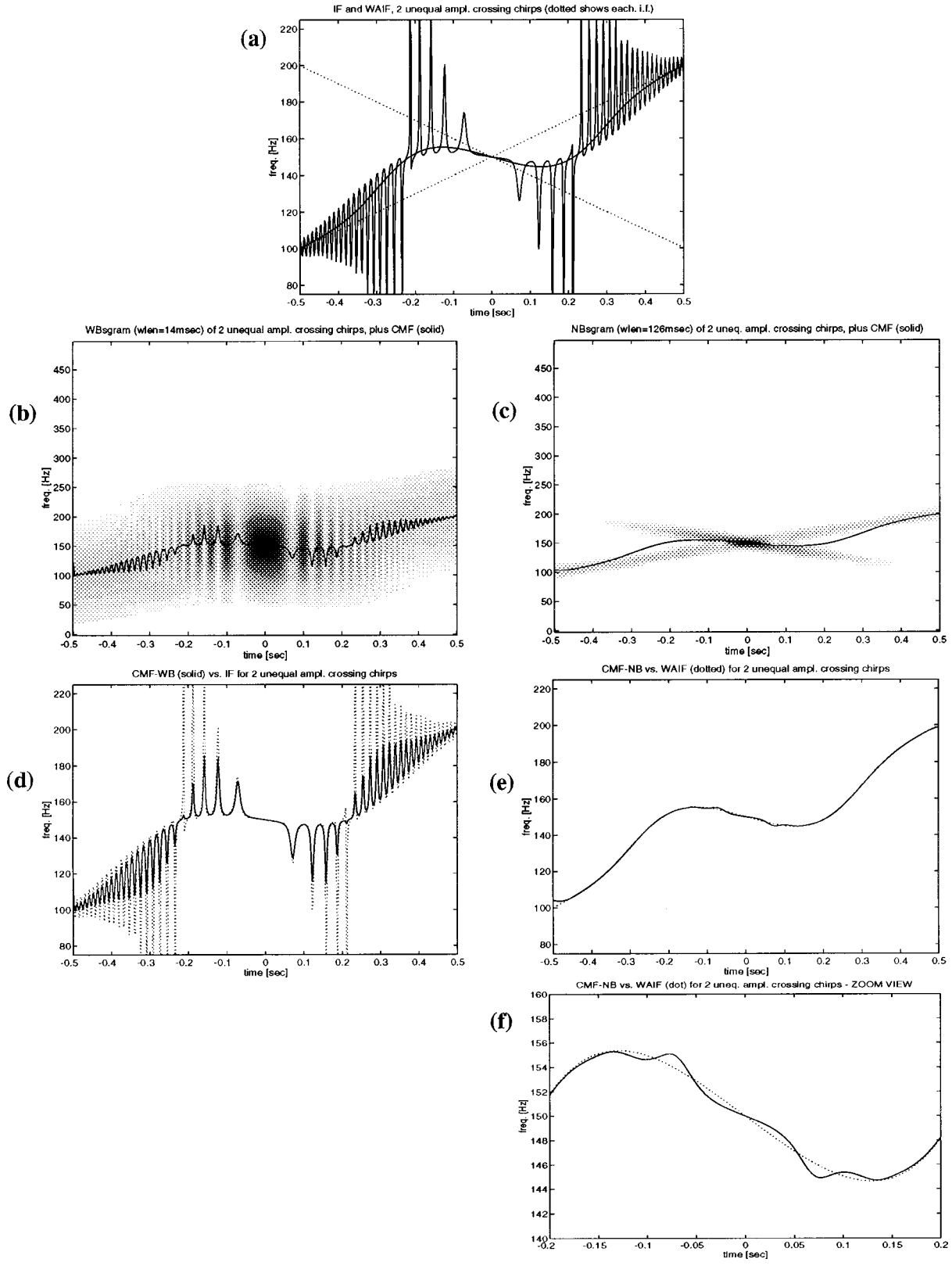

FIG. 6. (a) The WAIF (solid, smooth), the IF (solid, erratic), and the individual instantaneous frequencies (dotted) of a signal comprised of two crossing chirps of different amplitudes. (b) A 143-Hz bandwidth spectrogram (gray scale) and its conditional mean frequency (CMF-WB, solid). (c) A 16-Hz bandwidth spectrogram (gray scale) and its conditional mean frequency (CMF-NB, solid). (d) CMF-WB (solid) versus IF (dotted). (e) CMF-NB (solid) versus WAIF (dotted), with a zoom view (f) of the error, which occurs when the chirps cross, specifically when the difference in instantaneous frequencies is less than the bandwidth of the spectrogram (16 Hz).

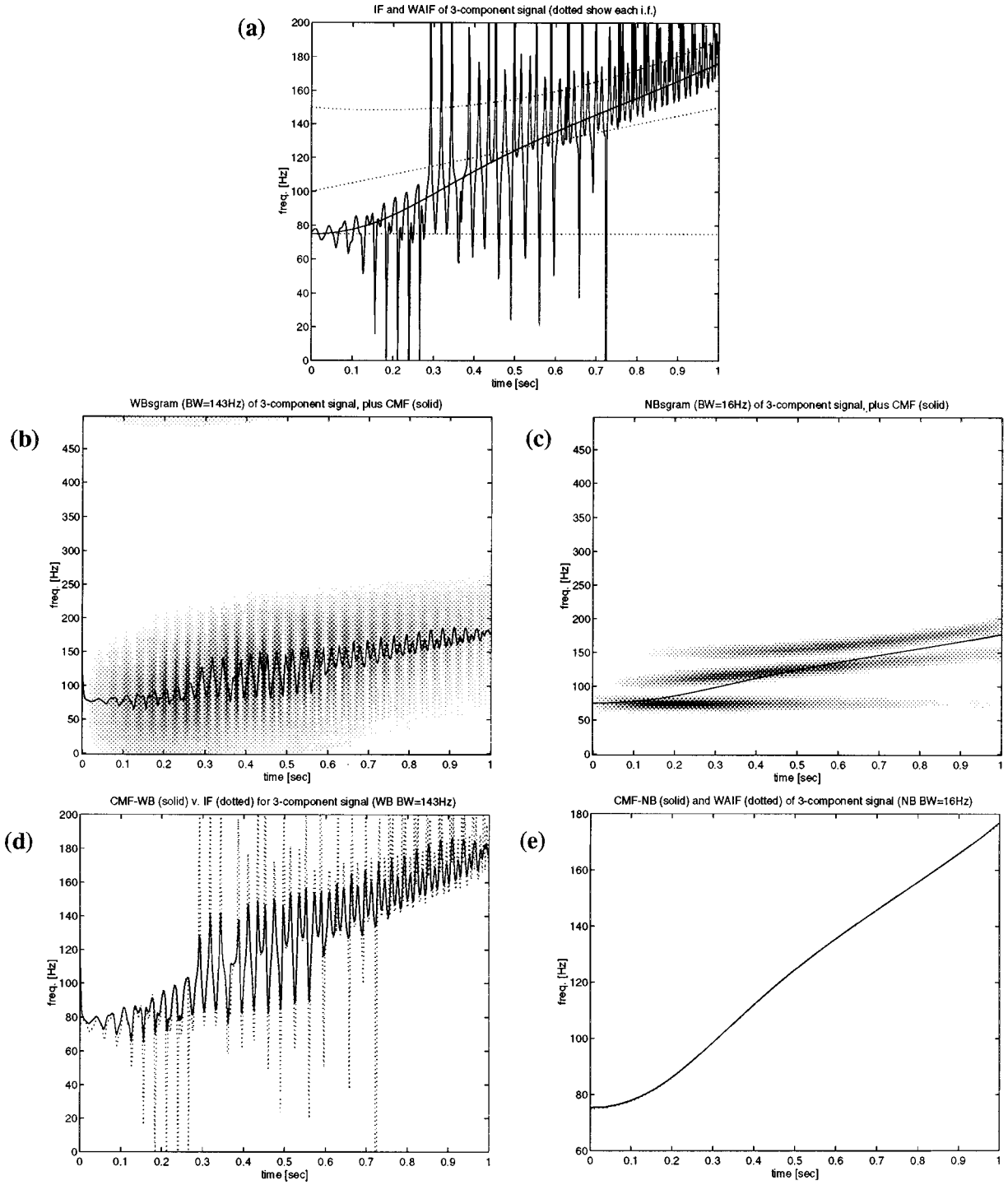

FIG. 7. (a) The WAIF (solid, smooth), the IF (solid, erratic), and the individual instantaneous frequencies (dotted) of a three-component signal. (b) A 143-Hz bandwidth spectrogram (gray scale) and its conditional mean frequency (CMF-WB, solid). (c) A 16-Hz bandwidth spectrogram (gray scale) and its conditional mean frequency (CMF-NB, solid). (d) CMF-WB (solid) versus IF (dotted). (e) CMF-NB (solid) versus WAIF (dotted).

$$0.5e^{j2\pi(100t+30t^2)}+e^{-15t^2}e^{j2\pi(150t+50t^2)}=A(t)e^{j\varphi(t)}. \qquad (19)$$

Results are shown in Fig. 4. The minimum separation of instantaneous frequencies over the time range considered ($-0.5\leqslant t\leqslant 0.5$) is 30 Hz at $t=-0.5$ s. Also, the Gaussian amplitude on the second component corresponds to $a_2^2(t)=e^{-30t^2}$ with Fourier transform $\sqrt{\pi/30}e^{-\omega^2/120}$. The spectral bandwidth (σ) of this component, obtained from the squared magnitude of the Fourier transform, is thus $\sqrt{30}$ rad/s$\approx$0.9 Hz. Accordingly, to accurately estimate the WAIF, the spectrogram filter should have a cutoff frequency at least less than 29 Hz. To get a ''ballpark'' idea of the lowest allowable value for the cutoff frequency, observe that the bandwidth of the baseband components for this signal [$a_1^2(\tau)\varphi_1'(\tau)$, $a_2^2(\tau)\varphi_2'(\tau)$, and $a_1^2(\tau)$, $a_2^2(\tau)$ per Eq. (10)] is again dominated by the Gaussian amplitude, i.e., the largest contribution to the bandwidth of the baseband terms is determined by $a_2^2(\tau)\varphi_2'(\tau)=e^{-30t^2}(150+100t)$ here. The Fourier transform of this function is $\sqrt{\pi/30}(150e^{-\omega^2/120}$

$+j\frac{100}{60}\omega e^{-\omega^2/120}$), the squared magnitude of which gives the spectral density. From the spectral density, we note that $(150e^{-\omega^2/120})^2$ is over 8000 times the intensity of $(\frac{100}{60}\omega e^{-\omega^2/120})^2$, and hence the contributions of this last term to the bandwidth are small. Accordingly, it follows that the bandwidth of the baseband terms is approximately $\sqrt{30}$ rad/s. If we take three standard deviations (3σ) as the effective width of the baseband and modulated terms, then the cutoff frequency should be in the range $3<\omega_{\text{cutoff}}<27$ Hz. Note that for this signal, the baseband and modulated terms are spectrally well separated.

As shown in the figure, the CMF from a 16-Hz bandwidth spectrogram yields an accurate measure of the WAIF, while the CMF from the wideband (143-Hz bandwidth) spectrogram yields a reasonable estimate of the IF of this signal. In addition, because the baseband and modulated terms are well separated in this signal, the CMF estimate of the WAIF is fairly insensitive to the spectrogram bandwidth, provided it is in the range specified above—see Fig. 5. For signals where the baseband and modulated terms are not well separated, there can be an error in the CMF estimate of the WAIF, as demonstrated next.

D. Two crossing chirps

For this example, we estimate the IF and WAIF from wideband and narrow band spectrograms, respectively, of the signal,

$$0.5e^{j2\pi(150t+50t^2)}+e^{-15t^2}e^{j2\pi(150t-50t^2)}=A(t)e^{j\varphi(t)}. \tag{20}$$

Note that the instantaneous frequencies of each component are equal at $t=0$. Hence, by our rough rule of thumb [Eq. (16)], we have that the cutoff frequency of the low-pass filter $h^2(t)$ needed to accurately estimate the WAIF from the CMF of a spectrogram is zero! But as we have seen, for $h^2(t)\rightarrow 1$ (which gives a zero bandwidth filter), the CMF equals the average frequency of the signal, not the time-varying average frequency, or WAIF. Hence, to obtain a time-varying average, the bandwidth of $h^2(t)$ is chosen greater than zero, and consequently some error in the CMF estimate of the WAIF is to be expected in this case. However, the error is only significant over the time period when the difference between the instantaneous frequencies is less than the filter bandwidth, which was 16 Hz here—see Fig. 6.

E. Three-component signal

Although the derivations of the spectrogram bandwidth conditions for accurately measuring the WAIF were derived for a two-component signal (for mathematical tractability), the ideas extend to general multicomponent signals (see the Appendix), as the following example demonstrates.

For the signal

$$10te^{-5t}(e^{j2\pi 75t}+3te^{j2\pi(100t+25t^2)}+5t^2e^{j2\pi(150t-10t^2+20t^3)}) =A(t)e^{j\varphi(t)}, \tag{21}$$

the minimum separation of instantaneous frequencies over the time interval considered $0\leqslant t\leqslant 1$ is 29.6 Hz at $t=0.58$ s. As shown in Fig. 7, the CMF of a 16-Hz bandwidth spectrogram provides an accurate measure of the WAIF of this signal. Also shown are results for a wideband spectrogram.

IV. CONCLUSION

The conditional mean frequency (CMF) of a spectrogram gives different measures of time-varying frequencies of a signal, depending on the bandwidth of the spectrogram [Eq. (6)]. At the two extremes, namely infinite bandwidth and infinitesimal bandwidth, the CMF equals the instantaneous frequency (IF) and the average frequency, respectively, of the signal. In this paper, we considered measurements obtained from ''intermediate'' bandwidth spectrograms. It was shown that, when the bandwidth of the spectrogram is less than the frequency separation of signal components in the time–frequency plane, the CMF of a spectrogram equals a weighted average of the individual instantaneous frequencies [WAIF, Eq. (9)] of the signal components. This time-varying frequency can be interpreted as the time-varying average frequency of the signal. Also, for some signals the WAIF and IF are identical,[16,23] and in those cases the CMFs of narrow band and wideband spectrograms are equal.

ACKNOWLEDGMENTS

Funding for this work was provided by the National Science Foundation (Grant No. MIP-9624089) and the Office of Naval Research (Grant No. N00014-96-1-0886), which the author gratefully acknowledges.

APPENDIX: IF AND WAIF FOR AN *N*-COMPONENT SIGNAL

The amplitude and phase for an arbitrary multicomponent signal,

$$\sum_{i=1}^{N} a_i(t)e^{j\varphi_i(t)}=A(t)e^{j\varphi(t)}, \tag{A1}$$

are readily calculated as

$$A^2(t)=\left(\sum_{i=1}^{N} a_i(t)\cos\,\varphi_i(t)\right)^2+\left(\sum_{k=1}^{N} a_k(t)\sin\,\varphi_k(t)\right)^2 =\sum_{i=1}^{N} a_i^2(t)+\sum_{i\neq k} a_i(t)a_k(t)\cos(\varphi_i(t)-\varphi_k(t)) \tag{A2}$$

and

$$\varphi(t)=\arctan\left(\sum_{k=1}^{N} a_k(t)\sin\,\varphi_k(t)\Big/\sum_{i=1}^{N} a_i(t)\cos\,\sigma_i(t)\right). \tag{A3}$$

Differentiating this last expression with respect to time yields the instantaneous frequency,

$$
\begin{aligned}
\varphi'(t) &= \frac{(d/dt)\ (\Sigma_{k=1}^{N} a_k(t)\sin\ \varphi_k(t)/\Sigma_{i=1}^{N} a_i(t)\cos\ \varphi_i(t))}{1+(\Sigma_{k=1}^{N} a_k(t)\sin\ \varphi_k(t))^2/(\Sigma_{i=1}^{N} a_i(t)\cos\ \varphi_i(t))^2} \\
&= \frac{\Sigma_{i=1}^{N} a_i(t)\cos\ \varphi_i(t)\ (d/dt)\ \Sigma_{k=1}^{N} a_k(t)\sin\ \varphi_k(t) - \Sigma_{k=1}^{N} a_k(t)\sin\ \varphi_k(t)\ (d/dt)\ \Sigma_{i=1}^{N} a_i(t)\cos\ \varphi_i(t)}{(\Sigma_{i=1}^{N} a_i(t)\cos\ \varphi_i(t))^2+(\Sigma_{k=1}^{N} a_k(t)\sin\ \varphi_k(t))^2} \\
&= \frac{\Sigma_{i=1}^{N} a_i(t)\cos\ \varphi_i(t)\Sigma_{k=1}^{N}(a_k'(t)\sin\ \varphi_k(t)+\varphi_k'(t)a_k(t)\cos\ \varphi_k(t))}{A^2(t)} \\
&\quad - \frac{\Sigma_{k=1}^{N} a_k(t)\sin\ \varphi_k(t)\Sigma_{i=1}^{N}(a_i'(t)\cos\ \varphi_i(t)-\varphi_i'(t)a_i(t)\sin\ \varphi_i(t))}{A^2(t)} \\
&= \frac{\Sigma_{i=1}^{N} a_i^2(t)\varphi_i'(t)+\frac{1}{2}\Sigma_{i\neq k} a_i(t)a_k(t)(\varphi_i'(t)+\varphi_k'(t))\cos(\varphi_k(t)-\varphi_i(t))}{A^2(t)} \\
&\quad + \frac{\frac{1}{2}\Sigma_{i\neq k}(a_i(t)a_k'(t)-a_i'(t)a_k(t))\sin(\varphi_k(t)-\varphi_i(t))}{A^2(t)}. \qquad \text{(A4)}
\end{aligned}
$$

As in the two-component case, there are baseband terms and modulated terms in the numerator and denominator of this expression. Substituting this expression into Eq. (6) yields the CMF of a spectrogram of this signal. Like the two-component case, if the baseband and modulated terms are spectrally distinct, then one can select the cutoff frequency of the low-pass filter $h^2(t)$ to eliminate the modulated terms, which yields the WAIF for the CMF of the spectrogram.

Also, we note that it has been recently shown that Eq. (A4) reduces to Eq. (9) (i.e., the IF identically equals the WAIF) when there is symmetry in the instantaneous spectrum, i.e., when the amplitudes $a_i(t), a_k(t)$ are of pairwise equal strength and their corresponding instantaneous phases $\varphi_i(t), \varphi_k(t)$ are centered about the median instantaneous phase of the signal components.[23,24]

[1] L. Cohen, *Time–Frequency Analysis* (Prentice–Hall, Englewood Cliffs, 1996).
[2] L. Cohen, ''Time–frequency distributions—A review,'' Proc. IEEE **77**, 941–981 (1989).
[3] P. Loughlin, Ed., special issue on ''Time–frequency analysis,'' Proc. IEEE **84**, 1195–1343 (1996).
[4] R. Koenig, H. Dunn, and L. Lacey, ''The sound spectrograph,'' J. Acoust. Soc. Am. **18**, 19–49 (1946).
[5] R. Fano, ''Short-time autocorrelation functions and power spectra,'' J. Acoust. Soc. Am. **22**, 546–550 (1950).
[6] J. Flanagan, *Speech Analysis, Synthesis and Perception*, 2nd ed. (Springer-Verlag, New York, 1972), Chap. V.
[7] S. H. Nawab and T. Quatieri, ''Short-time Fourier transform,'' in *Advanced Topics in Signal Processing*, edited by J. Lim and A. Oppenheim (Prentice-Hall, Englewood Cliffs, 1988), pp. 289–337.
[8] M. Schroeder and B. Atal, ''Generalized short-time power spectra and autocorrelation functions,'' J. Acoust. Soc. Am. **34**, 1679–1683 (1962).
[9] A. Oppenheim, ''Speech spectrograms using the fast Fourier transform,'' IEEE Spectr. **7**, 57–62 (1970).
[10] L. Cohen and C. Lee, ''Instantaneous frequency, its standard deviation, and multicomponent signals,'' Proc. SPIE Advanced Algs. Archs. Sig. Process. III **975**, 186–208 (1988).
[11] D. Gabor, ''Theory of communication,'' IEE J. Comm. Eng. **93**, 429–441 (1946).
[12] L. Fink, ''Relations between the spectrum and instantaneous frequency of a signal,'' translated in Probl. Inf. Transm. **2**, 11–21 (1966).
[13] M. Gupta, ''Definition of instantaneous frequency and frequency measurability,'' Am. J. Phys. **43**, 1087–1088 (1975).
[14] P. Loughlin, *Time–Frequency Energy Densities: Theory and Synthesis* (University Microfilms International, Ann Arbor, MI, 1992).
[15] P. Loughlin and B. Tacer, ''On the amplitude- and frequency-modulation decomposition of signals,'' J. Acoust. Soc. Am. **100**, 1594–1601 (1996).
[16] P. Loughlin and B. Tacer, ''Comments on the interpretation of instantaneous frequency,'' IEEE Signal Process. Lett. **4**, 123–125 (1997).
[17] P. Loughlin and B. Tacer, ''Instantaneous frequency and the conditional mean frequency of a signal,'' Signal Process. **60**, 153–162 (1997).
[18] B. Lovell, R. Williamson, and B. Boashash, ''The relationship between instantaneous frequency and time–frequency representations,'' IEEE Trans. Signal Process. **4**, 1458–1461 (1993).
[19] L. Mandel, ''Interpretation of instantaneous frequency,'' Am. J. Phys. **42**, 840–846 (1974).
[20] J. Shekel, '''Instantaneous' frequency,'' Proc. IRE **41**, 548 (1953).
[21] B. Tacer and P. Loughlin, ''Instantaneous frequency and time–frequency distributions,'' *IEEE Proceedings of the ICASSP'95*, 1995, pp. 1013–1016.
[22] J. Ville, ''Theorie et applications de la notion de signal analytique,'' *Cables e Transmissions* **2A**, 61–74 (1948) (translation by I. Selin, RAND Corp. Tech. Rep. T-92, Santa Monica, CA, 1958).
[23] W. Nho and P. Loughlin, ''When is instantaneous frequency the average frequency at each time?,'' submitted to IEEE Signal Process. Lett. . Also see P. Loughlin, ''Time-varying frequencies of a signal,'' Proc. SPIE **3162**, 109–122 (1997).
[24] P. Oliveira and V. Barroso, ''On the concept of instantaneous frequency,'' *Proceedings of the IEEE ICASSP'98*, 1998.
[25] J. Anantharaman, A. Krishnamurthy, and L. Feth, ''Intensity-weighted average of instantaneous frequency as a model for frequency discrimination,'' J. Acoust. Soc. Am. **94**, 723–729 (1993).
[26] H. Dai, ''On the pitch of two-tone complexes,'' J. Acoust. Soc. Am. **94**, 730–734 (1993).
[27] L. Feth, H. O'Malley, and J. Ramsey, Jr., ''Pitch of unresolved, two-component complex tones,'' J. Acoust. Soc. Am. **72**, 1403–1412 (1982).
[28] L. Cohen, ''What is a multi-component signal?,'' *IEEE Proceedings of ICASSP92*, 1992, Vol. 5, pp. 113–116.
[29] L. Cohen and C. Lee, ''Local bandwidth and optimal windows for the short-time Fourier transform,'' Proc. SPIE Adv. Alg. Arch. Signal Process. IV **1152**, 401–425 (1989).
[30] G. Jones and B. Boashash, ''Instantaneous frequency, instantaneous bandwidth, and the analysis of multicomponent signals,'' *Proceedings of the IEEE ICASSP'90*, 1990, pp. 2467–2470.

Experimental confirmation of the two-source interference model for the fine structure of distortion product otoacoustic emissions

Carrick L. Talmadge
National Center for Physical Acoustics, University of Mississippi, University, Mississippi 38677

Glenis R. Long
Department of Audiology and Speech Sciences, Purdue University, West Lafayette, Indiana 47907

Arnold Tubis
Department of Physics, Purdue University, West Lafayette, Indiana 47907

Sumit Dhar
Department of Audiology and Speech Sciences, Purdue University, West Lafayette, Indiana 47907

(Received 26 June 1998; accepted for publication 21 September 1998)

High-resolution measurements of distortion product otoacoustic emissions (DPOAEs) from three different experimental paradigms are shown to be in agreement with the implications of a realistic ''two-source'' cochlear model of DPOAE fine structure. The measurements of DPOAE amplitude and phase imply an interference phenomenon involving one source in the region of strong nonlinear interaction of the primary waves (the strong ''overlap'' or generation region), and the other source region around the DPOAE tonotopic place. The component from the DPOAE place can be larger than the one from the generator region. These findings are supported by the analysis of the onset and offset of the DPOAE when the higher-frequency primary is pulsed on and off. The two-source hypothesis was further tested by adding a third tone closer in frequency to the DPOAE which modifies the amplitude of the component from the DPOAE place and leaves the one from the generator region unchanged. The results agree well with the model prediction that the variation with frequency, and implied latency, of the phase of the DPOAE tonotopic-place component are greater than the corresponding quantities for the component from the generation region. [S0001-4966(99)01101-7]

PACS numbers: 43.64.Bt, 43.64.Ha, 43.64.Jb [BLM]

INTRODUCTION

Distortion product otoacoustic emissions (DPOAEs) (Kemp, 1979) are signals measured in the ear canal which are generated in the cochlea through the nonlinear interaction of two external primary tones of frequencies f_1 and f_2 with $f_2 > f_1$. The distortion product (DP) energy originates in the region of maximum overlap of the cochlear excitations produced by the two primaries, which is near the tonotopic location of the f_2 primary (e.g., Kummer *et al.*, 1995). Because DPOAEs are vulnerable to ipsilateral and/or contralateral stimulation, ototoxic drugs, and physiological insults to the cochlea, it has been proposed (see, e.g., reviews in Robinette and Glattke, 1997) that DPOAEs may provide a clinically important tool for the measurement of the health status of the cochlea. However, the experimental evaluation of this proposal has revealed limitations in the effectiveness of DPOAEs as a clinical tool (reviewed in Gorga *et al.*, 1994). It has been argued that these limitations are associated with the quasiperiodic variations of DPOAE amplitude and phase with variations of DP frequency known as DPOAE fine structure (cf. Heitmann *et al.*, 1996).

This disparity between expectation and practice may be, in part, a result of the commonly held conception that the DPOAE levels are determined only by the health of the cochlea in the overlap region of the primaries (cf. Mills, 1997). This contrasts with recent claims that one DPOAE component originates from the place of generation in the overlap region, and the other comes from the DP wave component that travels apically from the overlap region, is reflected near the DP tonotopic site, and then travels basally to the ear canal (e.g., Kummer *et al.*, 1995; Brown *et al.*, 1996; Gaskill and Brown, 1996; Talmadge *et al.*, 1996, 1997, 1998). In this two-source model of DPOAEs, the DPOAE fine structure is the result of the interference between these two cochlear sources. The general concept of such a disparate-place two-source model of DPOAEs was first proposed by Kemp and Brown (1983), although they did not specify the origin of the second DPOAE source.

Several pictures of the multiple sources of DPOAEs have been proposed. Input–output functions of DPOAEs in many species have a distinct and significant notch around primary levels of 55–70 dB SPL (reviewed in Mills, 1997). DPOAEs were proposed to be dominated by one source when the primary levels were below 55 to 60 dB SPL and a second source at higher primary levels. The notch in the input–output functions was interpreted as the result of phase cancellation between the two components. The idea of two level-dependent sources was supported by the differential vulnerability of DPOAEs that are produced by low-level and high-level primaries. DPOAEs generated with low-level pri-

maries have been universally found to be more vulnerable to insults such as administration of loop diuretics, aminoglycosides, induction of asphyxia, and even death, than those generated by higher-level primaries (reviewed in Mills, 1997). In these models, both components were hypothesized to come from the overlap region of the primaries. Any change in position of origin on the basilar membrane was assumed to stem from the changing shape of the traveling wave with level.

Recent modeling advances (Talmadge *et al.*, 1997, 1998) suggest that the disparate-place two-source picture is a general feature of any transmission line model of DPOAEs that has realistic basilar-membrane activity patterns and a low level of distributed inhomogeneities along the cochlear partition. In addition, it was concluded in these studies that for experiments in which the frequency ratio f_2/f_1 is held fixed while the DP frequency is varied, the DPOAE source component arising from the overlap region (termed hereafter the ''overlap-region'' component) would have a short latency and slow phase variation with DPOAE frequency. In contrast, the DPOAE component arising from cochlear reflection (termed hereafter the ''reflection-site'' component) would be expected to have a long latency and a rapid phase variation with DPOAE frequency. It is this difference in the phase variation of the two components that gives rise to DPOAE fine structure. A less straightforward further implication of the model relates to the relative amplitudes of the two components. The overlap-region component will not necessarily have a larger magnitude than the reflection-site component, even if $|R_a(\omega_{\mathrm{dp}})|$, the magnitude of the coefficient for reflectance around the DP tonotopic site (e.g., Talmadge *et al.*, 1998 and Sec. I A of this paper), is less than 1. These modeling results suggest that, in fact, DPOAEs constitute a much more complex cochlear phenomena than was originally contemplated, and this complexity may explain the lack of agreement in many cases between DPOAE and audiometric evaluations of cochlear status. Some of the essential features of these cochlear models will be reviewed in Sec. I below.

The question of a possible two-source model is explored in this paper using a number of experimental paradigms. In the two-source model of Talmadge *et al.* (1998), the rapidly varying phase of the reflection-site component makes it the main determinant of the frequency spacing of DPOAE fine structure. Consequently, in experimental measurements of multiple orders of DPOAEs, in which the frequency of the f_2 primary is held fixed, it is expected (Piskorski, 1997; Talmadge *et al.*, 1997, 1998) and observed that amplitude fine-structure maxima and minima of the varying orders of DPOAEs will approximately line up when DPOAE level is plotted versus DP frequency. Similarly, when the DPOAE frequency is held fixed and DPOAE level is plotted versus f_2 frequency, no significant fine structure is either expected or observed (Piskorski, 1997). These data provide strong, although somewhat indirect, tests of the two-source DPOAE model.

Other indirect evidence for two cochlear sources comes from the methodology of Brown *et al.* (1996), which is based on the assumption that two cochlear sources give DPOAE contributions with very different phase dependencies on the DPOAE frequency. Their study does not directly probe the basilar-membrane location of the component with the rapid phase variation, nor indicate whether or not this more rapidly varying component arises from a cochlear source region which is different from that of the slowly varying component. However, Brown *et al.* (1996) note that the different group delays suggest different places of origin. A further analysis technique proposed by Stover *et al.* (1996) offers the possibility of extracting the group delays of the fast- and slow-phase terms by inverse Fourier-transforming DPOAE amplitude and phase data that is obtained using the fixed f_2 paradigm. While suggestive of the possibility of two sources, the evidence of two sources provided by the data is indirect and somewhat difficult to interpret theoretically.

More direct evidence of the presence of two components is obtained by introducing a third tone as a suppressor close in frequency to the DPOAE, as was done by Kemp and Brown (1983), Kummer *et al.* (1995), Gaskill and Brown (1996) and Heitmann *et al.* (1997, 1998). The DPOAE fine structure was either decreased or entirely removed when a suppressor tone was introduced near in frequency to the DPOAE (Heitmann *et al.*, 1997, 1998). If the DPOAE were entirely rooted in the overlap region, this effect on DPOAE fine structure would not be expected from the introduction of such a suppressor tone.

In this paper, further evidence is presented in support of a two-source model of the type described in Talmadge *et al.* (1998). After the model is briefly summarized, it is applied to the case of fixed frequency-ratio DPOAE measurements. Here, the overlap-region component will have a phase which slowly varies with DP frequency, whereas the reflection-site component will have a more rapid phase variation. The resulting variations of DPOAE amplitude and phase with frequency are shown to provide a unique signature that can only be explained in terms of the interference of two components. Furthermore, the variation of the DPOAE phase with frequency for the case in which the overlap-region component is dominant is expected to be categorically different from the case in which the reflection-site component is dominant. For the case of a suppressor tone of varying level and close in frequency to the DPOAE, it is predicted that the relative contribution of the two components can be manipulated so as to allow for the transition from the case in which the reflection-site component is dominant to the one in which the overlap-region component is dominant.

A further test of this two-source model is provided by observing the temporal behavior of a DPOAE when one of its primaries is pulsed and the other is kept on continuously. This test is a variation of the one originally introduced by Whitehead *et al.* (1996). The predictions of this two-source model again indicate that the behaviors of the DPOAE amplitude and phase, in which one or the other source component is dominant, will be categorically different. As in the case of the fixed frequency-ratio, continuous-tone paradigm, when a suppressor tone is added, it is predicted that a transition in the observed temporal amplitude and phase behavior can be achieved. This type of experimental result would be extremely difficult to obtain in a single-source model of

DPOAE fine structure (e.g., Sun *et al.*, 1994a, b). Furthermore, since the two source contributions are expected to have very different latencies, one should also be able to unambiguously observe the short-latency component associated with the overlap region, either by itself or in combination with the long-latency component associated with the reflection site.

The model of Talmadge *et al.* (1998) is briefly described in Sec. I. The predictions of the model which are relevant to the experiments discussed in this paper are repeated in a less mathematical form in the description of the experiments (Secs. III–V).

I. MODEL

A. Overview

The underlying cochlear model is assumed to have a time-delayed stiffness feedback of the form suggested by Zweig (1991) in order to give realistic ''tall and broad'' activity patterns, together with the low-level distributed basilar-membrane roughness of the form suggested by Zweig and Shera (Shera and Zweig, 1993; Zweig and Shera, 1995), which gives rise to the apical reflectance responsible for the fine structure of otoacoustic emissions and threshold microstructure (Zweig and Shera, 1995; Talmadge *et al.*, 1996, 1997, 1998). The basilar membrane is also assumed to have a nonlinearity in damping, which is associated with the finite power level of the transduction mechanisms of the outer-hair cells responsible for cochlear amplification.

As was discussed in the Introduction, the disparate-place two-source model features the interference between two ear-canal components of the DPOAE which originate from different regions in the cochlea. In this model, the nonlinear interactions of the excitations created by the two primary tones of (angular) frequencies ω_1 and ω_2 $(\omega_2>\omega_1)$ generate DP waves in the cochlea of frequencies $\omega_{\rm dp}=(n+1)\omega_1-n\omega_2$ $(n=1,2,3,...)$. For the case of continuous-primary-tone and an apical DPOAE (i.e., one whose frequency corresponds to a tonotopic site apical to the overlap region, so that $\omega_{\rm dp}<\omega_1<\omega_2$), the two-source model prediction for the (complex) DPOAE wave amplitude can be written in the analytic form (Talmadge *et al.*, 1998):

$$P_e(\omega_2,\omega_2/\omega_1,\omega_{\rm dp}) = \frac{P_l(\omega_2,\omega_2/\omega_1,\omega_{\rm dp})+R_a(\omega_{\rm dp})P_r(\omega_2,\omega_2/\omega_1,\omega_{\rm dp})}{1-R_a(\omega_{\rm dp})R_b(\omega_{\rm dp})}. \tag{1}$$

Here, $P_l(\omega_2,\omega_2/\omega_1,\omega_{\rm dp})$ is the (complex) amplitude of the overlap-region contribution to the ear-canal pressure, the product $R_a(\omega_{\rm dp})P_r(\omega_2,\omega_2/\omega_1,\omega_{\rm dp})$ is the amplitude of the reflection-site contribution to the ear-canal pressure, and $R_a(\omega_{\rm dp})$ and $R_b(\omega_{\rm dp})$ are, respectively, the cochlear apical and basal reflectances. The quantity $P_r(\omega_2,\omega_2/\omega_1,\omega_{\rm dp})$ gives the ear-canal contribution from the reflection-site component in the limit that $R_a(\omega_{\rm dp})\to 1$ and $R_b(\omega_{\rm dp})\to 0$. If the auditory periphery were completely scale invariant, then the dependence of the complex amplitudes P_l and P_r on frequency would reduce to $P_l(\omega_2/\omega_1,\omega_{\rm dp})$ and $P_r(\omega_2/\omega_1,\omega_{\rm dp})$.

The precise meanings of $R_a(\omega)$ and $R_b(\omega)$ are given in relation to the trans-partition pressure wave near the cochlear base for the case of the complex time harmonic behavior $e^{i\omega t}$ (Talmadge *et al.*, 1998). In the case of external driving at frequency ω, the spatial part of this pressure is proportional to

$$\psi_r(x,\omega)+R_a(\omega)\psi_l(x,\omega), \tag{2}$$

where x is the distance from the cochlear base. In the case of no external driving (as is appropriate, e.g., for DPOAEs), it is proportional to

$$R_b(\omega)\psi_r(x,\omega)+\psi_l(x,\omega). \tag{3}$$

The right- and left-moving basis functions, $\psi_r(x,\omega)$ and $\psi_l(x,\omega)$, are normalized to 1 at $x=0$, and are given to a good approximation by the Wentzel–Kramers–Brillouin (WKB) approximations (e.g., Mathews and Walker, 1964; Zweig *et al.*, 1976):

$$\psi_r(x,\omega)=\sqrt{\frac{k(0,\omega)}{k(x,\omega)}}\exp\left\{-i\int_0^x k(x',\omega)dx'\right\}, \tag{4}$$

$$\psi_l(x,\omega)=\sqrt{\frac{k(0,\omega)}{k(x,\omega)}}\exp\left\{+i\int_0^x k(x',\omega)dx'\right\}, \tag{5}$$

where $k(x,\omega)$ is the local cochlear wave number. It should be noted that $R_b(x,\omega)$ is mainly determined by the dynamics of the middle ear and the ear canal, and $R_a(\omega)$ is determined by the apical reflections of the cochlear wave, which are concentrated around the tonotopic site for frequency ω.

The reflection-site DPOAE component was parameterized in Eq. (1) so as to emphasize that the ear-canal contribution from this component vanishes in the absence of apical reflections (e.g., $|R_a|\to 0$). Furthermore, the denominator term, $1-R_a(\omega_{\rm dp})R_b(\omega_{\rm dp})$, was left as a separate term, instead of being absorbed into the definitions of P_l and P_r, in order to directly parameterize the effects of the cochlear resonance arising from multiple internal reflections from the tonotopic region and the base of the cochlea (Talmadge *et al.*, 1998). Consequently, the P_l and P_r terms include just the effects of forward transmission through the outer/middle ear of the primary waves, with the level of nonlinear interaction giving rise to apically and basally moving DP traveling waves of differing amplitudes originating in the overlap region, and reverse transmission through the outer/middle ear at the DP frequency.

The main features of the dependence of $R_a(\omega_{\rm dp})$ and $R_b(\omega_{\rm dp})$ on $\omega_{\rm dp}$ can be determined using the results from Zweig and Shera (Shera and Zweig, 1993; Zweig and Shera, 1995) and Talmadge *et al.* (1998). Zweig and Shera were the first to point out the phenomena of ''dynamic symmetry creation,'' which results in a phase dependence of R_a given by

$$\arg[R_a(\omega_{\rm dp})]\cong\varphi_a+\hat{k}(\omega_{\rm dp})\hat{x}(\omega_{\rm dp}) \cong\varphi_a-\frac{\hat{k}(\omega_{\rm dp})}{k_\omega}\log\left(\frac{\omega_{\rm dp}}{\omega_0}\right), \tag{6}$$

where ω_0 is the tonotopic frequency of the basilar membrane at the base of the cochlea, $\hat{k}(\omega_{dp})$ is the wave number of the ω_{dp} traveling wave at the amplitude maximum of the activity pattern, and k_ω is a parameter in the cochlear frequency-place map,

$$\hat{x}(\omega_{dp}) \cong -(1/k_\omega)\log(\omega_{dp}/\omega_0). \tag{7}$$

As a consequence of the fact that apical reflectance arises from spatial filtering of distributed roughness, the expected value of $|R_a|$ will depend on the average roughness in the vicinity of the activity-pattern maximum. Because the amount of roughness may vary with position, this will result in a dependence of $|R_a|$ on frequency. In direct analogy to bandpass filtering of white noise in the time domain, the amplitude of $|R_a|$ will fluctuate with ω_{dp} [or equivalently $\hat{x}(\omega_{dp})$], with a correlation length in the fluctuations given by the bandwidth of the spatial filter, which in turn can be related to the width of the activity-pattern peak region.

B. Application of the model to fixed frequency-ratio measurements

The fixed frequency-ratio continuous-tone paradigm has a simplified theoretical interpretation relative to other DPOAE measurement paradigms. This is a result of the approximate scale invariance of the auditory periphery. The consequence of this approximate symmetry is that, for a given value of $r=\omega_2/\omega_1$, $P_l(r,\omega_{dp})$ and $P_r(r,\omega_{dp})$ will have slow phase variations with ω_{dp}.

A rough argument for this slow phase variation may be easily given. If the sound transducer voltage for two periodic signals ω_1 and ω_2 is

$$V(t)=A\cos\omega_1 t + B\cos\omega_2 t, \tag{8}$$

then the pressure variation of the cochlear wave at the $f_2=\omega_2/2\pi$ tonotopic place $\hat{x}(\omega_2)$, in the absence of nonlinearities, will be

$$P(t)\propto \tilde{A}\cos(\omega_1 t+\varphi(\omega_1,\hat{x}(\omega_2))+\varphi_1) + \tilde{B}\cos(\omega_2 t+\varphi(\omega_2,\hat{x}(\omega_2))+\varphi_2), \tag{9}$$

with

$$\varphi(\omega,\hat{x}(\omega_2)) \cong -\int_0^{\hat{x}(\omega_2)} dx\,\frac{2\pi}{\lambda(\omega,x)}, \tag{10}$$

where $2\pi/\lambda(\omega,x)$ is the real part of the cochlear traveling wave number $k(x,\omega)$. The assumption of scale invariance may be conveniently expressed by

$$\lambda(\omega,x)=\lambda\left(\frac{\omega}{\hat{\omega}(x)}\right), \tag{11}$$

where $\hat{\omega}(x)$ is the tonotopic (angular) frequency at location x along the basilar membrane,

$$\hat{\omega}(x)=\omega_0 e^{-k_\omega x}. \tag{12}$$

For a cochlear nonlinearity of order $2n+1$ in the neighborhood of $x=\hat{x}(\omega_2)[\equiv(1/k_\omega)\log(\omega/\omega_0)]$, the phase of the ω_{dp} DPOAE measured in the ear canal φ_e will be given approximately by

$$\varphi_e(\omega_{dp}) = -(n+1)\int_0^{\hat{x}(\omega_2)} dx\,\frac{2\pi}{\lambda(\omega_1/\hat{\omega}(x))} + n\int_0^{\hat{x}(\omega_2)} dx\,\frac{2\pi}{\lambda(\omega_2/\hat{\omega}(x))} - \int_0^{\hat{x}(\omega_2)} dx\,\frac{2\pi}{\lambda(\omega_{dp}/\hat{\omega}(x))}, \tag{13}$$

where the upper limit of integration has been set at the tonotopic location of the higher primary $\hat{x}(\omega_2)$—the approximate center of the overlap region. If the long-wave assumptions,

$$\frac{2\pi}{\lambda(\omega_1/\hat{\omega}(x))} \cong \text{const.}\ \frac{\omega_1}{\hat{\omega}(x)}, \tag{14}$$

$$\frac{2\pi}{\lambda(\omega_{dp}/\hat{\omega}(x))} \cong \text{const.}\ \frac{\omega_{dp}}{\hat{\omega}(x)}, \tag{15}$$

are made in Eq. (13), and it is noted that from scale invariance the second integral in Eq. (13) is very nearly independent of ω_2, it follows that $\varphi_e(\omega_{dp})$ is approximately only a function of the ratio ω_2/ω_1, and is thus very slowly varying with ω_{dp} for constant frequency ratios.

Based on these arguments, one is led to the prediction that the overlap-region component P_l in Eq. (1) will vary weakly with ω_{dp}, whereas the reflection-site component $R_a P_r$ will have a rapidly varying phase and a slowly varying magnitude, with the dominant phase variation in the second term arising from the phase variation of R_a. From Eq. (1), the amplitudes and phases of the total DPOAE signal and its two components (including the effects of the reflections at the cochlear base and DP tonotopic site) are given by the following notation:

$$a_e(\omega_{dp})=|P_e|, \quad a_{nl}(\omega_{dp})=\left|\frac{P_l}{1-R_a R_b}\right|, \quad a_{refl}(\omega_{dp})=\left|\frac{R_a P_r}{1-R_a R_b}\right|, \tag{16}$$

$$\varphi_e(\omega_{nl})=\arg(P_e), \quad \varphi_{nl}(\omega_{dp})=\arg\left(\frac{P_l}{1-R_a R_b}\right), \quad \varphi_{refl}(\omega_{dp})=\arg\left(\frac{R_a P_r}{1-R_a R_b}\right). \tag{17}$$

The subscript nl refers to the nonlinear-overlap-region component and the subscript refl refers to the reflection-site component. Figure 1 illustrates the underlying conceptual two-source model that is predicted by the theoretical formalism. It is also interesting to consider the group delay of the resulting DPOAE

$$\tau_e(\omega_{dp}) \equiv -\frac{d\varphi_e}{d\omega_{dp}}, \tag{18}$$

The expected behavior of a_e, φ_e, and τ_e for fixed-ratio experiment can be illustrated by assuming that $\varphi_{nl} \approx$ constant, so that the entire phase variation with ω_{dp} arises through the change of φ_{refl} with ω_{dp}. Under this assumption, the variation of φ_{refl} can be related to the variation of $\arg(R_a)$ with ω_{dp} so that

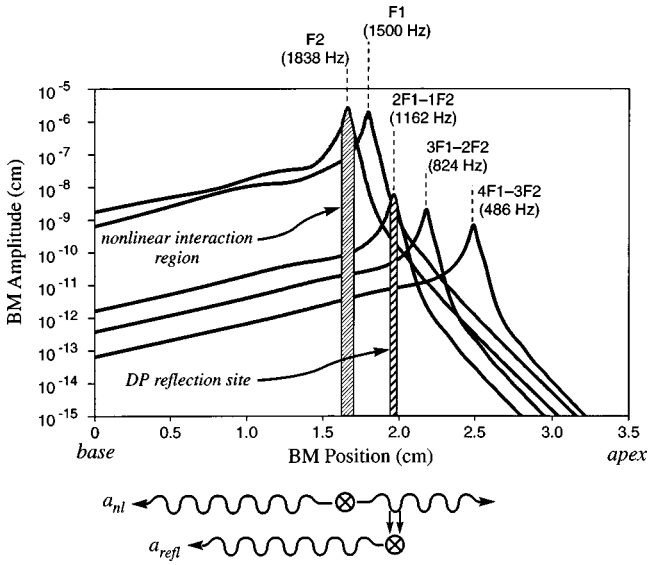

FIG. 1. Schematic diagram of the two-source model of DPOAE generation. Shown are the basilar membrane activity patterns of two primaries together with the resulting activity patterns of three apical DPOAEs generated by these primaries from a simulation using the model of Talmadge *et al.* (1998). The primaries interact in a region near the tonotopic place of the f_2 primary, so as to generate DP waves that travel both apically and basally. A fraction of the basally traveling DP wave is transmitted to the ear canal. The apically traveling DP wave propagates to the DP tonotopic place, where it is partially reflected basally, and is transmitted to the ear canal, where it interferes with the wave from the generation region. Not shown are multiple internal reflections of the two DP components, which in general will also be present.

$$\varphi_{\rm refl}(\omega_{\rm dp}) \cong \varphi_{\rm refl}(\omega_0) - \frac{\hat{k}(\omega_{\rm dp})}{k_\omega} \log\left(\frac{\omega_{\rm dp}}{\omega_0}\right). \tag{19}$$

Furthermore, the group delay τ_e can be related to the variation of $\varphi_{\rm refl}$ via:

$$\tau_e(\omega_{\rm dp}) \cong -\frac{d\varphi_e(\omega_{\rm dp})}{d\varphi_{\rm refl}(\omega_{\rm dp})} \frac{d\varphi_{\rm refl}(\omega_{\rm dp})}{d\omega_{\rm dp}}$$

$$= +\frac{\hat{k}}{2\pi\omega_{\rm dp}k_\omega} \frac{d\varphi_e(\omega_{\rm dp})}{d\varphi_{\rm refl}}. \tag{20}$$

In analyzing the predictions of the model under the assumption of $\varphi_{\rm nl} \approx$ constant, it is important to note that two cases are of importance, namely those for $a_{\rm nl} > a_{\rm refl}$ and $a_{\rm nl} < a_{\rm refl}$.

The resulting phasor diagrams of the interference between the two components are shown in Fig. 2(a), when $a_{\rm nl} > a_{\rm refl}$ (i.e., the overlap-region component is dominant). As is evident from this diagram, $-\pi < \varphi_e < +\pi$ as $\varphi_{\rm refl}$ is varied under these circumstances, with the most rapid phase variation of a_e and φ_e occurring when $\varphi_{\rm refl} \cong (2n+1/2)\pi$ $(n+0,\pm1,\pm2,...)$, as shown in Fig. 2(b). Also shown is the group delay τ_e, which has minima and maxima which positively correlate with the minima and maxima of a_e.

The phasor diagram of the two-component interference is shown in Fig. 2(c), for the case of $a_{\rm nl} < a_{\rm refl}$ (i.e., the reflection-site component is dominant). Under these circumstances, φ_e is unbounded, with the maximum variation of a_e and φ_e again occurring when $\varphi_{\rm refl} \cong (2n+1/2)\pi$, as shown in Fig. 2(d). Furthermore, τ_e now has minima and maxima which negatively correlate with the minima and maxima of a_e. Finally, it should be noted that the positive derivative of φ_e with respect to $\varphi_{\rm refl}$ will result in a negative slope of φ_e when plotted against $\omega_{\rm dp}$, as is evident from Eq. (19).

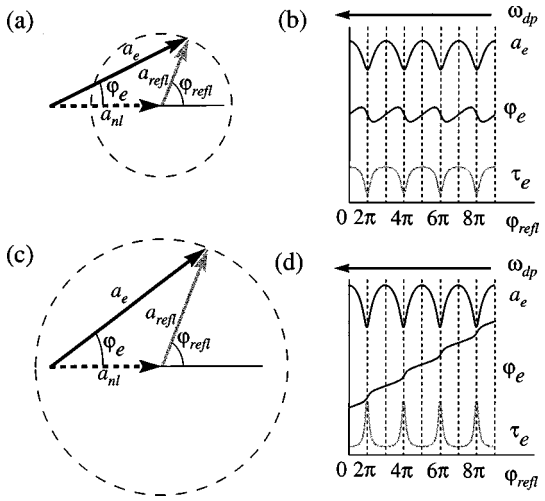

FIG. 2. Phasor diagrams and patterns of DPOAE amplitude (a_e), phase (ϕ_e) and group delay (τ_e) for the interference of two DP sources. Shown in (a) and (b) are the phasor diagram and resulting amplitude, phase, and group-delay behavior for the case $a_{\rm nl} > a_{\rm refl}$, where $a_{\rm nl}$ and $a_{\rm refl}$ are the DPOAE amplitudes corresponding, respectively, to the nonlinear generation region and to the reflection site. Similarly the phasor diagram and resulting amplitude, phase, and group-delay behavior are shown in (c) and (d), respectively, for the case $a_{\rm nl} < a_{\rm refl}$. Because an increasing $\varphi_{\rm refl}$ corresponds to a decreasing $\omega_{\rm dp}$ (as indicated by the arrows), a positive slope of φ_e when plotted against $\varphi_{\rm refl}$ corresponds to a negative slope when plotted against $\omega_{\rm dp}$.

Figure 2(b) and (d) show distinctive patterns of behavior for the DPOAE amplitude, phase, and group delay which are categorically different for the cases $a_{\rm nl} > a_{\rm refl}$ and $a_{\rm nl} < a_{\rm refl}$. Moreover, since the reflection-site component can be suppressed by an external tone near in frequency to the DPOAE (e.g., Kummer *et al.*, 1995; Gaskill and Brown, 1996; Heitmann *et al.*, 1997), this model implies that when the DPOAE amplitude, phase, and group delay follow that shown in Fig. 2(d), suppression by an external tone should shift the behavior to that shown in Fig. 2(b).

C. Application of model to pulsed-tone measurements

When one primary tone is pulsed and the other is on continuously, the DPOAEs generated by these tones will also be pulsed. Since the reflection-site component has a longer latency than the overlap-region component, this also means that during each DPOAE pulse, there will be a time interval (starting shortly after the turn-on of the primary tone) during which only the shorter-latency overlap-region component will be present, and an interval in which the longer-latency reflection-site component will dominate (starting shortly after the turn-off of the primary tone). Those situations are illustrated in Fig. 3, which shows the two components for the case (a) when $a_{\rm refl} > a_{\rm nl}$ (i.e., the reflection-site component is dominant), and case (b) when $a_{\rm refl} < a_{\rm nl}$ (i.e., the overlap site is dominant). In obtaining these plots, it was assumed that

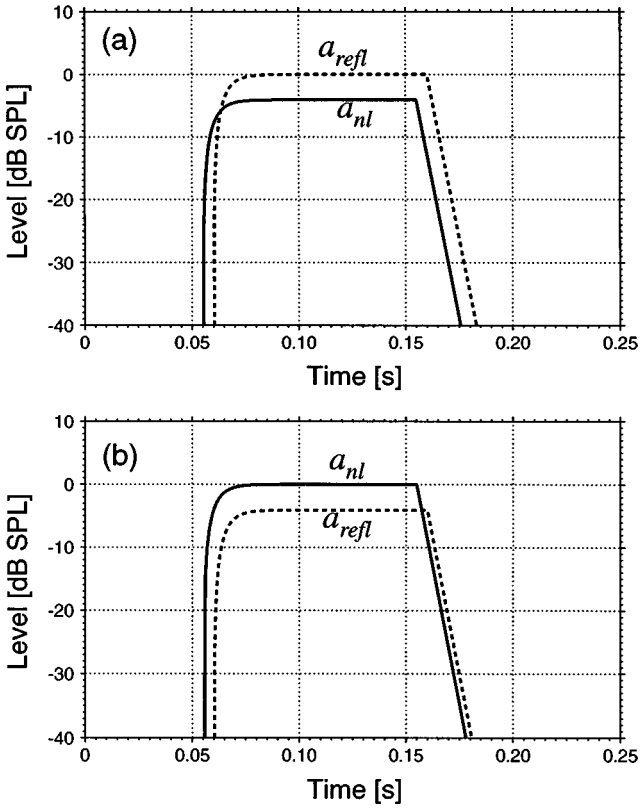

FIG. 3. The expected levels of the overlap-region component (solid line) and the reflection-site component (dashed line) for (a) the case $a_{\rm refl} > a_{\rm nl}$ and (b) the case when $a_{\rm refl} < a_{\rm nl}$. In both cases, the f_2 primary was assumed to be pulsed in the interval $0.05\ {\rm s} < t < 0.15\ {\rm s}$. The two DPOAE components were assumed to have exponential growth/decay behaviors, as described in the text [Eqs. (21) and (22)]. Note that the two lines intersect shortly after the turn-on of the external tone in (a) and shortly after the turn-off of the tone in (b).

each of the two components had exponential growth/decay behaviors, with the overlap-region component having a shorter latency than the reflection-site component. In more detail, the model used was

$$a_{\rm nl}(t) = \begin{cases} 0, & t < T_{\rm on} + \tilde{\tau}_{\rm n1} \\ a_{\rm nl}(1 - e^{-\gamma(t - T_{\rm on} - \tilde{\tau}_{\rm nl})}), & T_{\rm on} + \tilde{\tau}_{\rm n1} \leqslant t < T_{\rm off} + \tilde{\tau}_{\rm nl} \\ a_{\rm nl}\, e^{-\gamma(t - > T_{\rm off} - \tilde{\tau}_{\rm n1})}, & t \geqslant T_{\rm off} + \tilde{\tau}_{\rm nl}, \end{cases} \tag{21}$$

for the overlap-region component, and

$$a_{\rm refl}(t) = \begin{cases} 0, & t < T_{\rm on} + \tilde{\tau}_{\rm dp} \\ a_{\rm refl}(1 - e^{-\gamma(t - T_{\rm on} - \tilde{\tau}_{\rm dp})}), & T_{\rm on} + \tilde{\tau}_{\rm dp} \leqslant t < T_{\rm off} + \tilde{\tau}_{\rm dp} \\ a_{\rm refl} e^{-\gamma(t - T_{\rm off} - \tilde{\tau}_{\rm dp})}, & t \geqslant T_{\rm off} + \tilde{\tau}_{\rm dp}, \end{cases} \tag{22}$$

for the reflection-site component, where $\tilde{\tau}_{\rm dp} > \tilde{\tau}_{\rm nl}$. Here, $T_{\rm on}$ is the turn-on time of the f_2 external tone, and $T_{\rm off}$ is the turn-off time of the tone.

The parameters $\tilde{\tau}_{\rm nl}$ and $\tilde{\tau}_{\rm dp}$ can be shown to have simple forms in terms of the underlying travel times of the transpartition pressure waves for frequencies ω_2 and $\omega_{\rm dp}$. In terms of $\tau(x,\omega)$, the travel time of a pressure wave of frequency ω from the base to a location x on the basilar membrane, $\tilde{\tau}_{\rm nl}$ and $\tilde{\tau}_{\rm dp}$ may be expressed as

$$\tilde{\tau}_{\rm nl} = \hat{\tau}_2 + \tau(\hat{x}_2, \omega_{\rm dp}), \tag{23}$$

$$\tilde{\tau}_{\rm dp} = \hat{\tau}_2 + 2\hat{\tau}_{\rm dp} - \tau(\hat{x}_2, \omega_{\rm dp}), \tag{24}$$

where $\hat{\tau}_2 \equiv \tau(\hat{x}_2, \omega_2)$ and $\hat{\tau}_{\rm dp} = \tau(\hat{x}_{\rm dp}, \omega_{\rm dp})$. It should be noted that $\tau(\hat{x}_2, \omega_{\rm dp})$ is very small compared to either $\hat{\tau}_2$ or $\hat{\tau}_{\rm dp}$, for large ratios of ω_2/ω_1 (i.e., $\omega_2/\omega_1 \gtrsim 1.1$). This is a consequence of the fact that the reverse traveling wave from the tonotopic place $x = \hat{x}_2$ to the cochlear base ($x = 0$) occurs entirely in the long-wave region of the DP traveling wave.

In addition to the two components shown in Fig. 3, there will be DP components arising from multiple internal reflection of these two components. These can be obtained by expanding Eq. (1) with respect to $R_a R_b$. If

$$R_a(\omega_{\rm dp}) \cong |R_a(\omega_{\rm dp})| e^{i\phi_a - 2i\omega_{\rm dp}\tau_{\rm dp}}, \tag{25}$$

$$R_b(\omega_{\rm dp}) \cong |R_b(\omega_{\rm dp})| e^{i\phi_b - i\omega_{\rm dp}\tau_b}, \tag{26}$$

then

$$\begin{aligned} P_e(\omega_{\rm dp}, t) &= a_e(t)\cos[\omega_{\rm dp} t + \varphi_e(t)] \\ &= a_{\rm nl}(t)\cos(\omega_{\rm dp} t + \phi_{\rm nl}) + a_{\rm refl}(t)\cos(\omega_{\rm dp} + \phi_{\rm dp}) \\ &\quad + |R_a(\omega_{\rm dp}) R_b(\omega_{\rm dp})| a_{\rm nl}(t - 2\hat{\tau}_{\rm dp} - \hat{\tau}_b) \\ &\quad \times \cos[\omega_{\rm dp}(t - 2\hat{\tau}_{\rm dp} - \hat{\tau}_b) + \varphi_{\rm nl} + \phi_a + \phi_b] \\ &\quad + |R_a(\omega_{\rm dp}) R_b(\omega_{\rm dp})| a_{\rm refl}(t - 2\hat{\tau}_{\rm dp} - \hat{\tau}_b) \\ &\quad \times \cos[\omega_{\rm dp}(t - 2\hat{\tau}_{\rm dp} - \hat{\tau}_b) + \varphi_{\rm refl} + \phi_a + \phi_b] \\ &\quad + \cdots . \end{aligned} \tag{27}$$

Equation (25) was obtained by noting that $d\varphi_a/d\omega_{\rm dp} \cong -2\hat{\tau}_{\rm dp}$ (e.g., Talmadge *et al.*, 1998). A detailed derivation of a generalization of Eq. (27), for several types of simplifying assumptions about Eq. (1), will be presented in a future publication.

The predicted DPOAE amplitude and phase behavior from this model are shown in Fig. 4. From this figure, the experimental DPOAE phenomenology is expected to be fairly complex for the two-source model, in part because of the presence of two time-delayed (with different delay amounts) components, plus multiple internal reflections of these components. In Fig. 4, only the case where the overlap-region and reflection-site components destructively interfere is considered. In addition, the phase shifts of each of the multiple internal reflections were also chosen to give destructive interference. Models which do not have significant internal reflection would not give rise to multiple-delay DPOAE components, and are expected to have a much simpler phenomenology as a result.

The presence of the nulls in Fig. 4 can be understood by noting the location of the intersection of the curves for the two components in Fig. 3(a) and (b), which in the case of destructive interference would correspond to the location of minima (''nulls'') in the DPOAE amplitude. The case for $a_{\rm refl} > a_{\rm nl}$ is represented in Fig. 3(a). The two curves intersect shortly after the f_2 primary is turned on. This behavior indi-

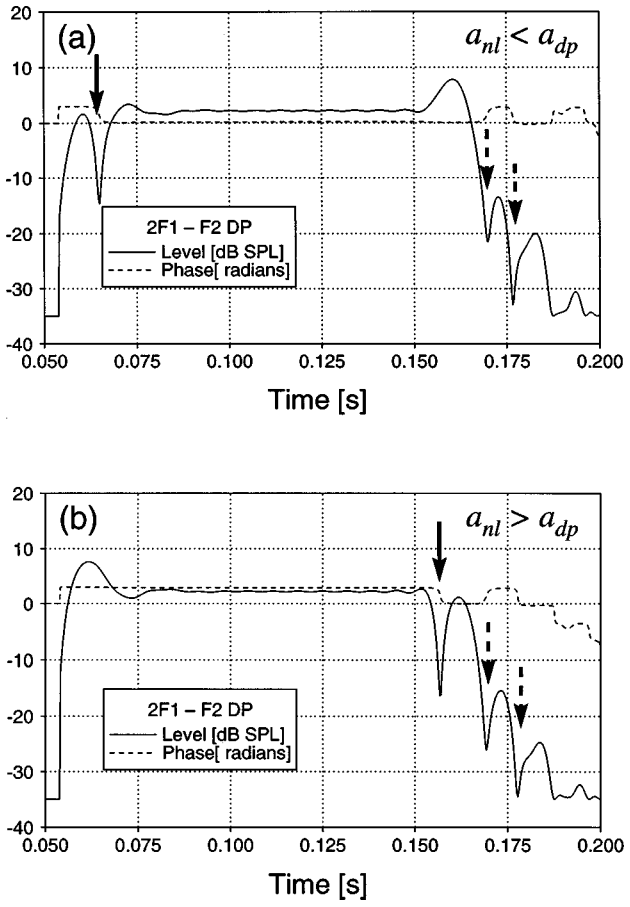

FIG. 4. Predicted DPOAE amplitude and phase, when the phases of the overlap-region and reflection-site components are 180 deg out of phase for the cases (a) when the component from the reflection site is 6 dB larger than that from the overlap site, and (b) when the reflection-site component is 6 dB smaller than the component from the overlap site. The f_2 primary was assumed to be pulsed in the interval $0.05\ \text{s} < t < 0.15\ \text{s}$. The DPOAE signal was filtered by a 300-Hz-wide bandpass filter and a -35 dB SPL additive noise floor was included in order to simulate realistic experimental conditions. For both cases, the phase difference between the overlap and the reflection-site components and the phase shift from multiple internal was -3.0 rad. Notice the presence of a null [see the solid arrow in (a)] in DPOAE amplitude and a corresponding step in DPOAE phase shortly after the turn-on of the f_2 tone for case (a), which is shifted [see the solid arrow in (b)] to a position which is shortly after the turn-off of the f_2 tone for case (b). The interference notches after turn-off of the external tones that are present in both cases are due to destructive interference between successive multiply reflected components, and is a result of the -3.0 rad choice of phase shift per multiple reflection.

cates the presence of an interference null shortly after signal turn-on. For the case $a_{\text{refl}} < a_{\text{nl}}$ illustrated in Fig. 3(b), the curve for the reflection-site component is shifted downward relative to the curve for the overlap-region component, which in turn shifts the intersection of the two curves (and the associated null in DPOAE amplitude) shortly after the f_2 primary is turned off.

II. GENERAL METHODS

A. Subjects

The four subjects used in this study were volunteers from the Purdue University community and varied in age from 20 to 54 years. The subjects were selected after intensive screening procedures, which included multifrequency tympanometry, audiometric thresholds, audiologic history, and the evaluation of spontaneous, transient-evoked and distortion product otoacoustic emissions. The subjects were selected from a larger group on the basis of the pattern of DPOAEs seen in their ears.

B. Data collection

Data were collected with the subject seated in a recliner chair inside a double-walled IAC sound-treated booth. In order to reduce the variability in the measurements, no recordings were obtained until approximately 15 min after the subject was seated in the booth. An Etymotic ER10 low-noise microphone assembly was coupled to the ear by the appropriately sized GSI tip. The signal was amplified by the preamplifier supplied by Etymotic, and then filtered (300–10000 Hz, roll off=6 dB/octave, gain=200) by a battery-run Stanford SR-560 low-noise amplifier under control of a NeXT computer. The signal from the SR-560 amplifier was connected to a Singular Solutions 64x A/D converter via balanced microphone cables. The A/D 64x generated 16-bit samples at a sampling rate of 44.1 kHz. The signal was 64 times over-sampled and converted using a bit-stream A/D converter. A customized program was used to control the presentation of the stimuli and recording of responses. The data were reduced by averaging successive segments (usually 44 100 samples—1 s) before being saved to disk to be analyzed off-line.

Acoustic signals were digitally generated using the floating point coprocessor of the NeXTstation computer with software written in our laboratory. It was then converted to analog signals via the NeXTstation's on-board 16-bit D/A converters at 44 100 Hz. The system clock on the NeXTstation is not identical with the clock on the A/D 64x. The clock on the computer was continually monitored by recording a stimulus from the NeXT computer and determining the frequency using the A/D 64x. The output frequencies were modified to compensate for the differences in the clocks. The acoustic signals were then passed through TDT attenuators, whose levels were controlled through a serial line by the NeXTstation, before being passed through TDT microphone buffers to two Etymotic ER-2 tube-phone assemblies coupled to the ER10 microphones. Most of the studies were done with just the two primaries, which were generated in separate channels and controlled by separate attenuators. A third tone was needed in DPOAE fine-structure suppression experiments (e.g., Kemp and Brown, 1983; Heitmann *et al.*, 1998). In these experiments, the two furthest-separated tones (the suppressor tone and f_2) were generated in one channel, and presented through the same ER2.

The stimulus-delivery setup was calibrated using a Zwislocki coupler. Since the ER-2 transducer is designed to produce a flat response in a Zwislocki coupler (DB-100) when properly coupled to an ER-10 probe, the frequency response of the ER-2 transducer when used with the ER-10 probe would be nearly flat at the eardrum in the average human ear. For these reasons we used the iso-voltage stimulus-presentation strategy, in which the voltage presented to transducers is held constant over frequency. The iso-voltage strategy is not subject to the large, idiosyncratic

increases of eardrum stimulus SPL between 3.5 and 7 kHz that are produced by the alternate in-the-ear adjustment strategy (Siegel and Hirohata, 1994; Whitehead *et al.*, 1995). Variations in geometry of individual ear canals and eardrum impedances can, however, produce differences between the SPL produced in an ear by the ER-2 and that in a Zwislocki coupler, which was not designed to accurately simulate real ears above 4 kHz. These departures are not relevant for the frequencies used here and are smaller than the discrepancies produced by calibrating at the position of the probe.

Custom-built programs were used to generate and control the stimuli, record the data, and control the durations, levels, and frequencies of the stimuli, which were presented in random order. The progress of the experiment was monitored using the computer display, which indicated which stimuli were being presented and the peak levels of the data throughout the experiment. Additional monitoring was done by fast Fourier-transform (FFT) analysis of completed data files on additional NeXT computers in the laboratory, which were networked with the data-collection computer.

C. Data Analysis

All data analysis was done off-line. Since the frequencies of the distortion products have a known relationship to those of the primaries, the data can be fit to a model of the expected frequencies of the known signal components. A least-squares fit (LSF) analysis (see Long and Talmadge, 1997) is then performed on the averaged data to determine the levels and phases of these components. The LSF analysis uses a series of basic sinusoidal functions of known frequencies in order to fit a particular signal. It has the advantage that any known frequency component can be distinguished and measured, even if it does not fall within one bin of the FFT. Such resolution would be otherwise impossible to achieve with a standard FFT algorithm. It also allows for the separation of a small signal from the spectral splatter of a neighboring larger one, which would inherently add the energy (aliasing effect) in the common frequency bin of the usual FFT and elevate the measured level. Another advantage of the LSF technique is the overall reduction in required CPU time. While the FFT algorithm performs $N \log N$ operations to evaluate N frequency components per window of length N, the LSF filter performs only $k \cdot N$ operations, for k discrete frequency components inside a spectral window of width N (Long and Talmadge, 1997). This technique removes correlations between adjacent frequency components. It therefore provides a significant improvement in frequency resolution over the conventional FFT by permitting the elimination of spectral splatter at the cost of a poorer signal-to-noise ratio when the DPOAE is close to a stimulus component. FFT analysis was done on a subset of the data in order to establish that the LSF paradigm gives equivalent data.

III. STUDY 1: CONTINUOUS PRIMARIES

The root source of distortion in the model is the nonlinear interaction of the traveling waves of the two primaries on the basilar membrane. Maximal interaction occurs in the overlap region around the f_2 place. The generated waves with acoustic energy at the DPOAE frequency propagates in both directions—basally towards the oval window and apically towards the DP tonotopic place (see Fig. 1). The DP wave transmitted apically from the generator region is partially reflected when it gets to the DP place, due to very small irregularities on the cochlear partition in conjunction with a tall/broad activity pattern (for details, see Talmadge *et al.*, 1998). The ''place-fixed'' nature of the reflection mechanism will result in a rapid variation of the phase of the reflectance with DP frequency. On the other hand, the phase of the DPOAE component from the overlap region, for the fixed f_2/f_1 paradigm, will be only weakly dependent on the DP frequency from the approximate scale invariance of the cochlea. DPOAEs are the result of the summation of these two waves (plus any subsequent cochlear waves basally incident on the oval window stemming from multiple basal/apical reflections of the DP waves in the cochlea). The different rates of phase change of the two components produce the interference pattern known as DPOAE fine structure. This interference pattern is not completely regular because the amplitude and phase of the reflection-site component depends on the nature of the cochlear irregularities and cochlear filtering (see Talmadge *et al.*, 1998).

A comparison of the amplitude and phase behavior of DPOAE from fixed-ratio experiments permits evaluation of the relative amplitudes of the components from two sources. If a small component a_{refl} with rapidly changing phase is added to a larger one a_{nl} which is slowly changing in phase ($a_{\mathrm{nl}} > a_{\mathrm{refl}}$), the resulting phase will fluctuate around the slowly varying one of the generation-region component and have a rounded, sawtoothed appearance [see Fig. 2(b)]. In contrast, if a large component with rapidly changing phase is added to a small component with slowly changing phase ($a_{\mathrm{refl}} > a_{\mathrm{nl}}$), the resulting phase will change more rapidly in a ramp-like fashion near the DPOAE minima [see Fig. 2(d)]. Since group delay is the derivative of phase, DPOAE group delay will be positively correlated with amplitude fine structure when $a_{\mathrm{nl}} > a_{\mathrm{refl}}$, and negatively correlated with the amplitude fine structure when $a_{\mathrm{refl}} > a_{\mathrm{nl}}$ (see Fig. 2).

A. Methods

The ratio of continuous primaries was kept constant as the frequencies of the primaries were varied so as to sweep the frequency of the DPOAE through a range of values. The recording of the ear-canal signal was triggered to start at signal onset when the two primaries had zero phase. Four s of data were reduced to 1 s by averaging, and then stored to disk to be analyzed later using a least-squares fit analysis (see below) to obtain the amplitudes, phases, and noise floors of the two primaries and a number of their cubic distortion products ($f_{\mathrm{dp}}^{n} = nf_1 + n(f_2 - f_1)$; $n = -3, -2, -1, 0, 1, 2, 3, 4$). The frequency ratio of the primaries for these measurements was $f_2/f_1 = 1.225$ and the levels were $L_1 = 65$ dB and $L_2 = 50$, 55, 60, or 65 dB SPL). These measurement conditions are optimal for generating the $2f_1 - f_2$ distortion product, which is the only one considered in this paper.

An algorithm based on summation and subtraction of overlapping data segments (whose lengths were an integral

number of periods associated with the frequencies of the stimuli and of the DPOAEs) was used to estimate the level of the DPOAE and the level of the noise floor for each DPOAE. This algorithm reduces the noise floor through the performance of additional averages, and provides an estimate of the noise floor at the frequency of each DPOAE (cf. Stover *et al.*, 1996). The subtraction cancels out the DPOAE components of the signal but leaves noise components which are not correlated with the signal. Depending on the sample length used for the least-squares-fit estimate (7350 or 11 020 samples), several estimates of the level of the DPOAE were obtained from each pair of primaries. The medians of these estimates were calculated and used as the estimate of the DPOAE level.

The group delay was obtained by performing a least-squares fit to a straight line in consecutive 10-point intervals of the DPOAE phase. The group delay for this algorithm was just $-m_\varphi/2\pi$, where m_φ is the slope of the straight line. This algorithm produced estimates for the group delay which were far less noisy than those obtained with other alternatives, such as numerical differentiation of the DPOAE phase.

1. Experimental protocol

A prospective subject was first screened using the fixed-ratio paradigm with a relatively coarse frequency step-size. The step-size varied with DPOAE frequency and was chosen to correspond to separations in DPOAE tonotopic position along the basilar membrane of 0.05 mm, based on the Greenwood place–frequency map (Greenwood, 1990). For frequencies in the range 1500–2000 Hz, this tonotopic spacing corresponded to frequency spacings of 18–24 Hz. Since the tonotopic separation between adjacent DPOAE amplitude maxima corresponds to approximately 0.4 mm (e.g., Talmadge *et al.*, 1993), the granularity of the DPOAE measurements resulted in approximately eight DPOAE values per fine-structure period.

Subjects were selected for further testing using the criteria that the $2f_1-f_2$ DPOAEs were high enough in level to give at least a 40-dB signal-to-noise ratio at the fine-structure maxima, and that the amplitude variations of the fine structure were at least 10 dB. In some cases, a selection was also made on the basis that the amplitude and group delay fine structures were anticorrelated (e.g., Talmadge *et al.*, 1998). These criteria assured that the main predictions of the two-source model could easily be tested in follow-up measurements.

Detailed fine-structure measurements on selected subjects were made using the fixed-ratio paradigm. For each subject, one or more fine-structure regions extending between two adjacent maxima was chosen for further investigation. Fine structures were selected so as to provide examples of the situations in which the generation-region DPOAE was dominant [see Fig. 2(a), (b); rounded saw-tooth phase behavior] or the DP-place component was dominant [see Fig. 2(c), (d); ramp-like phase behavior]. For each fine structure investigated, the DPOAE frequencies were selected so that they covered a frequency region containing two adjacent DPOAE amplitude maxima, and the frequencies of the primaries were selected to provide DPOAE estimates every 6 Hz, except near deep-amplitude minima, where the frequency spacing was reduced to 2 Hz.

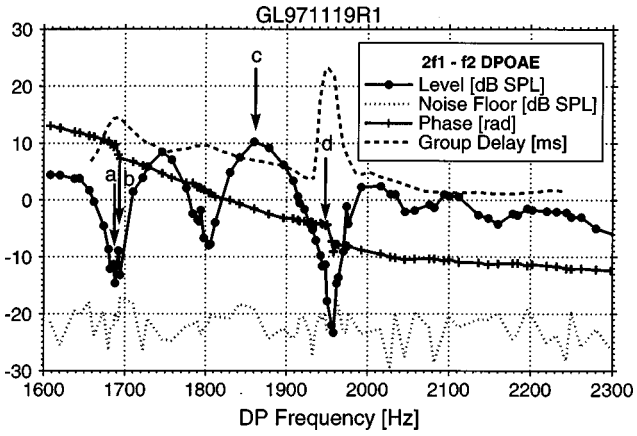

FIG. 5. $2f_1-f_2$ DPOAE level, phase, and group delay as a function of the DPOAE frequency for subject GL, where $f_2/f_1=1.225$, $L_1=65$ dB SPL, and $L_2=55$ dB SPL. The arrows indicate the frequencies for which pulsed-tone measurements are plotted in Fig. 8.

B. Results

The amplitude, phase, and group delay of DPOAEs are presented for three of the six subjects in Figs. 5, 6, and 7. Close examination of Figs. 5, 6, and 7 reveals that whenever there was a minimum in the DPOAE fine structure, there was also a change in the overall trend of a slowly decreasing phase with increasing frequency. The rate of departure from this background phase depended on the depth of the amplitude minimum (note the different frequency scales for the different subjects). The phase transition was either a steep, localized slope in phase giving a ramp-like appearance (see Fig. 5) or a temporary increase in phase providing a saw-toothed appearance (see Figs. 6 and 7). The change in the phase was maximal at the amplitude minimum. The extracted group delay was negatively correlated with DPOAE level for subject GL [compare with Fig. 2(d)] and positively correlated for subjects NZ and AB [compare with Fig. 2(b)].

When the two components were nearly equal in level (deep fine structure), the phase changed rapidly and very fine resolution was needed to distinguish between the two phase behaviors. The problem was exacerbated by the (expected) poor signal-to-noise ratio near these minima. Frequency sweeps with improved frequency resolution serve to better define the phase transition. Note the increased proximity of the points near fine structure minima in Figs. 5, 6, and 7). This reflects the additional data from the fine-resolution sweeps. Examples of the fine-resolution sweeps on a more expanded scale can be seen in Figs. 11 and 12. When the two components were nearly equal in level (deep fine structure), the pattern could vary on different days or with different recording conditions. An example of this may be seen by comparing the the sharp minimum near 1950 Hz, which is shown in Figs. 5 and 11. Similarly, compare the minimum near 1200 Hz in Figs. 7 and 13. For this reason, a complete set of measurements were obtained in a single session (preferably without removing the probe from the ear) whenever possible.

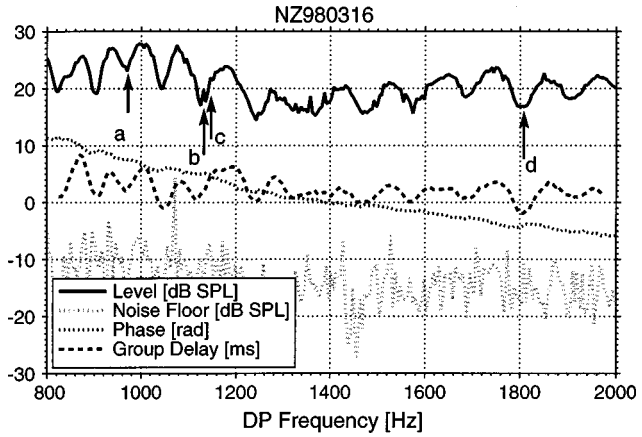

FIG. 6. $2f_1-f_2$ DPOAE level, phase, and group delay as a function of the DPOAE frequency for subject NZ, where $f_2/f_1=1.225$, $L_1=65$ dB SPL, and $L_2=50$ dB SPL. The arrows indicate the frequencies for which pulsed-tone measurements are plotted in Fig. 9. Too many data points were collected to permit the use of symbols to differentiate the different sets of data. Line styles are used instead.

C. Discussion

The two patterns seen in the mathematical model (see Fig. 2) can also be seen in the data (see Figs. 5, 6, and 7). In Fig. 5, the DPOAE amplitude minima around 1690, 1800, and 1950 Hz, and the associated phase and group delays correspond to the case of $a_{\text{refl}}>a_{\text{nl}}$ in Fig. 2(c) and (d). In Figs. 6 and 7, the amplitude minima correlate with the group delay minima, as expected for the case $a_{\text{refl}}<a_{\text{nl}}$ in Fig. 2(a) and (b). Although the data presented in this paper show a consistent pattern in a given subject, this is not always the case. It is possible for two adjacent minima to differ in the sense that for one, $a_{\text{nl}}>a_{\text{refl}}$, while for the other, $a_{\text{refl}}>a_{\text{nl}}$. When the two components are very nearly equal in level, so that there is a deep DPOAE minimum due to nearly complete cancellation, small changes in the components from session to session could cause a large change in the DPOAE level. Changes in cochlear function, in the properties of the middle ear, or in the impedance or location of the probe assembly in the ear canal could produce these small changes in the source amplitudes.

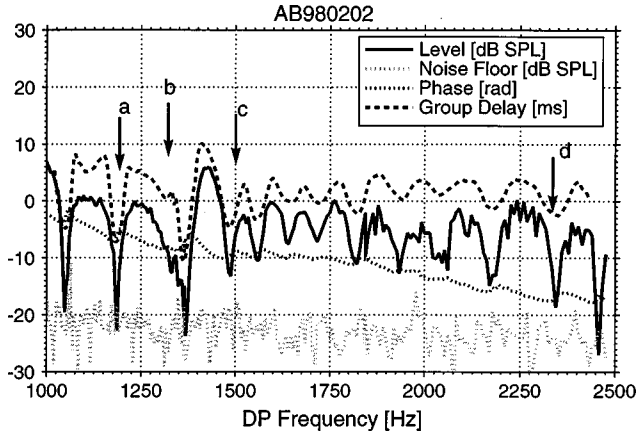

FIG. 7. $2f_1-f_2$ DPOAE level, phase, and group delay as a function of the DPOAE frequency for subject AB, where $f_2/f_1=1.225$, $L_1=65$ dB SPL, and $L_2=50$ dB SPL. The arrows indicate the frequencies for which pulsed-tone measurements are plotted in Fig. 10.

IV. STUDY 2: PULSED PRIMARY

The DPOAE components are expected to have different latencies. The latency of a_{nl} will be only slightly longer than the time for propagation of the f_2 wave from the cochlear base to the f_2 tonotopic place [see Eq. (23)]. This travel time is the main determinant of the latency of the generator-site component of the DPOAE. This is because the travel time for propagation of a DP wave from the f_2 tonotopic site to the cochlear base will be very short, since the travel occurs in the long-wave region of the DP traveling wave. The associated phase will vary weakly with DP frequency, and consequently the phase derivative (related to group delay) will also be small. The latency of a_{refl} is approximately the latency of a_{nl} plus twice the travel time for a DP wave to propagate from the f_2 tonotopic site to the DP place [see Eq. (24)]. Consequently, a second way of separating these components is to examine the level and phase at DPOAE turn-on and turn-off.

Whitehead *et al.* (1996) provided some support for two sources of DPOAEs by showing that the phase of the DPOAE could change soon after its onset. This was confirmed for the $2f_1-f_2$ DPOAE by Martin *et al.* (1998). A modification of the procedure used by Whitehead *et al.* permits the study of the growth and decay of the DPOAE when the level of the higher-frequency primary was modulated in level. Our models make it clear that, although other characteristics of pulsed DPOAE provide information about the relative levels of the components, there is one feature that clearly identifies which of the two components is greater in magnitude.

If a pulsed DPOAE paradigm measurement is performed at a DP frequency near a fine-structure minimum (where the two components are approximately out of phase), there will always be a clear notch either shortly after f_2 signal turn-on for $a_{\text{refl}}>a_{\text{nl}}$, or shortly after f_2 signal turn-off for $a_{\text{refl}}<a_{\text{nl}}$ (see Fig. 4). The notch is the result of destructive interference between the two components and occurs when the two components are very nearly equal in level. The location of the notch is represented in Fig. 3 by the intersection point of the a_{nl} and a_{refl} curves. As can be seen from this figure, there is exactly one intersection point of the two curves, which occurs either shortly after f_2 signal turn-on ($a_{\text{refl}}>a_{\text{nl}}$), or shortly after f_2 signal turn-off ($a_{\text{refl}}<a_{\text{nl}}$).

If all of the DP waves basally incident on the oval window were transmitted through the middle ear to the ear canal, one would have a summation of just the two components previously described. Since there is not, in general, a perfect impedance match, the incident DP waves at the oval window will be partially reflected back into the cochlea, and consequently re-reflected from the DPOAE site for the same reasons that the original apically traveling wave was reflected. This component will not be seen unless there is some reflection from the DP place. The re-reflected component will also sum with the original two sources, and some portion of these re-reflected waves will be reflected from the oval window to travel back to the DP place and be again reflected back towards the base of the cochlea, and so on. Consequently, even though there are only two cochlear sources, the additional reflections can produce a relatively complex temporal wave

form, as is seen in Fig. 4, if successive reflections are out of phase. The additional components occurring after stimulus turn-off are indicated by the dashed arrows. These additional reflections may also produce ripples after stimulus turn-on. If the successive multiple internally reflected components are in phase, a long tail in the decay of the DPOAE pulse will be observed instead.

A. Methods

For the pulsed primary tone (''pulsed-tone'') measurements, the f_2 primary was pulsed for 100 ms every 250 ms. The stimuli were presented for 16 s. The phases of the primaries were both 0 deg at the beginning of each signal, with the beginning of the first f_2 pulse occurring 50 ms into the signal. The turn-on and turn-off of the f_2 pulse was achieved using a rise/fall function with a 1-ms rise/fall time. In order to obtain partial cancellation of the primaries after averaging, the phase of the f_1 primary was rotated by 90 deg and the f_2 primary by 180 deg every 250 ms (e.g., Whitehead *et al.*, 1996). This choice of phase rotations left the $2f_1-1f_2$ DPOAE phase invariant under each rotation. The recording program was triggered to start recording the ear-canal signal at the start of the signal, and data was streamed to disk. When all of the four consecutive 250-ms segments of this signal are averaged together, the primary signals should cancel. Normally, about 55 dB of cancellation was achieved. The primaries did not cancel exactly due to clock-rate mismatches between the clocks for the D/A and the A/D, and because the frequencies of the clocks drifted slightly over the duration of a measurement (the total variation in the clock rates was about 0.02 Hz per h).

The phase rotation was achieved for most measurements by requiring that the frequencies of f_1 and f_2 be multiples of 4 Hz (to prevent an undesirable shift in the phases of the primaries between each 250-ms interval), and then rotating the phase of each primary using the signal-generation software. The disadvantage of this method was that an audible click was sometimes generated by the necessary change in the phase of the f_1 stimulus. Any transient evoked otoacoustic emission evoked by this click would have been minimal at the time of the onset of the f_2 pulse, which occurred 50 ms later. An alternative technique, which was used in some experiments, was to require that frequency f_1 be an odd number and f_2 be an even number not divisible by 4. In this way, no phase variation was required by the signal-generation software, since the phase offset of the f_1 primary was different by 90 deg and that of the f_2 primary by 180 deg every 250 ms. No clicks were detected with this method. There was no significant difference in the DPOAE responses obtained with the two methods.

The recorded data were averaged in 1-s nonoverlapping intervals (containing 4 250-ms pulses). Noisy data segments were identified and rejected by first histogramming the peak values in each 1-s interval. This histogram had a Gaussian-like distribution of peak values, and in some cases a small number of peak values which were much greater in value than the maximum of the Gaussian-like distribution. The 1-s average of the recorded data was made with the exclusion of the noisy data segments identified in this way.

Each 1-s average was then further averaged using 250-ms nonoverlapping intervals. Because of the phase rotation of the primaries between consecutive 250-ms intervals, this resulted in a signal dominated by the DPOAE of interest ($2f_1-f_2$ in this experiment) together with the remaining noise. Because of the nonexact cancellation of the primaries described above, a small residual signal at the f_1 and f_2 frequencies was usually also present.

A least-squares-fit filter with a window size of 150 points (giving a filter width of 300 Hz) was constructed and used to analyze the frequency components, $4f_1-3f_2$, $3f_1-2f_2,\ldots,4f_2-3f_1$. This filter was applied to the 250-ms averaged data using a 50-point offset between consecutive applications of the filter.

1. Experimental protocol

As discussed in the Introduction and Sec. I, the two-source DPOAE model of Talmadge *et al.* (1997, 1998) makes definitive, testable predictions for the relationship between the DPOAE amplitude and phase for both fixed-ratio and pulsed-tone measurements. In order to test the self-consistency of these predictions, it was necessary that both sets of measurements be performed as close together in time as possible. Part of the reason for this is that removal and reinsertion of the microphone assembly in the ear canal could produce potentially confounding effects. Additionally, it was noted during the measurements that some shifts in the levels and phases of the DPOAEs occurred from day to day. Consequently, care was taken to perform pulsed and continuous primary measurements in the same experimental session whenever possible. Selected DPOAE frequencies from the detailed sweeps in experiment 1 were chosen for the pulsed-tone measurements. Experiments under a given set of conditions were typically repeated 16–32 times to improve the signal-to-noise ratio.

B. Results

The changes in the levels and phases of DPOAEs at the turn-on and turn-off of f_2 pulses were evaluated for the conditions indicated by the lettered arrows in Figs. 5, 6, and 7. When the DPOAE frequency was near that of a fine-structure amplitude maximum (so that the signals from the two sources were in phase), it was not easy to separate the two components [e.g., Fig. 8(c)]. When the DPOAE frequency was near that for a deep fine-structure minimum (corresponding to an approximately 180 deg phase difference or destructive interference), the DPOAE level was largest at the turn-on and turn-off of the DPOAE pulse (when only one component was present). The signal-to-noise ratio is poor for the remainder of the pulse when the two components are present [see Fig. 8(d)]. The measured phase in the two bursts regions was consistent with that giving destructive interference.

The most interesting patterns are those obtained on the steep slopes surrounding a fine-structure amplitude minimum when the components were partially canceled (see Figs. 8, 9, and 10). The signal-to-noise was much better for this choice

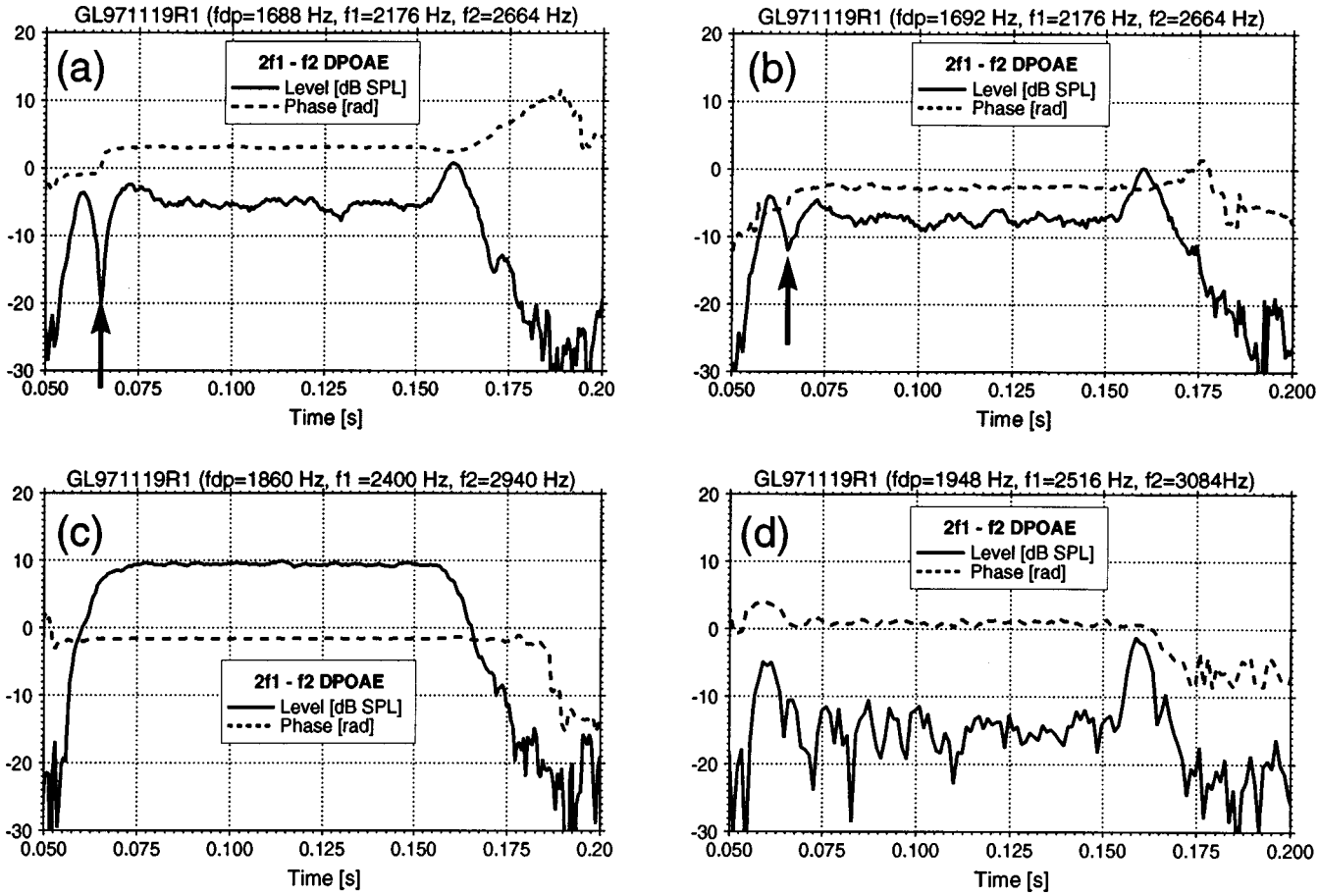

FIG. 8. 2 f_1-f_2 DPOAE level and phase as a function of time for subject GL for various choices of f_{dp} when f_2 is pulsed on from 50 ms to 150 ms. The frequency ratio and levels of the primaries are the same as in Fig. 5. The arrows in this figure point to the interference notch discussed in Sec. IV C and indicated in Fig. 4.

(typically>10 dB) and it produced the clearest representations of the (destructive) interference of the two DPOAE components. The responses to the pulsed f_2 tone from GL [Fig. 8(a) and (b)] had a downward notch after stimulus onset, and the data from the other two subjects NZ and AB (Figs. 9 and 10) had a similar notch after stimulus turn-off. The notches are indicated by arrows. Whenever there was a notch in the amplitude function, there was a rapid change in the phase of the DPOAE. Note that not only the notches near stimulus turn-on and turn-off (indicated by the arrows) can be detected, but additional lobes with predictable amplitude and phase transitions can clearly be seen after stimulus turn-off. There are also regular ripples in the DPOAE amplitude after the notch at DPOAE onset [e.g., Fig. 9(b), (c)].

C. Discussion

When the continuous-tone phase behavior was ramp-like and thus indicated that $a_{refl}>a_{nl}$, the pulsed DPOAE data [see Figs. 8(a), (b)] was very similar to the model data for these conditions in Fig. 4(a). When the phase behavior for the continuous tones indicated that $a_{nl}>a_{refl}$, the pulsed DPOAE data [see Figs. 9, 10, and 15(b)] were similar to the model data for the same conditions [see Fig. 4(b)]. A step-like change in phase at the position of the notch can be used to aid in identification of the notch in noisy data such as Fig. 8(c). In addition to the notches after stimulus turn-on or turn-off, one can also see the expected pattern of additional lobes due to multiple reflections from the oval window and the DP site seen in Fig. 4.

Since the initial response is always from the generation region, and the response after stimulus turn-off is primarily from the reflection component, it might be thought that the initial and final DPOAE bursts could be used as an indicator of relative amplitudes of the two DPOAE components. Although the relative amplitudes of these two bursts were always consistent with the position of the notch, these indicators may not be reliable. The initial burst may not have time to reach its final amplitude before the onset of the component from the DP site starts to reduce the DPOAE level, reflections from the oval window may modify the level of the response after signal turn-off and efferent stimulation (cf. Liberman *et al.*, 1996), or fatigue may also modify the DPOAE level from the beginning to the end of the pulse.

The DPOAE amplitude fine structure of a given subject was observed to vary from session to session, and even over the course of a single session. This variability is suggestive of that for the variation of spontaneous otoacoustic emissions previously reported by Whitehead (1991). As was the case with Whitehead's observations, the most significant variation within a session usually came during the first 30 min after the subject was placed in the recording booth. (As was discussed in the Methods section, no measurements were taken

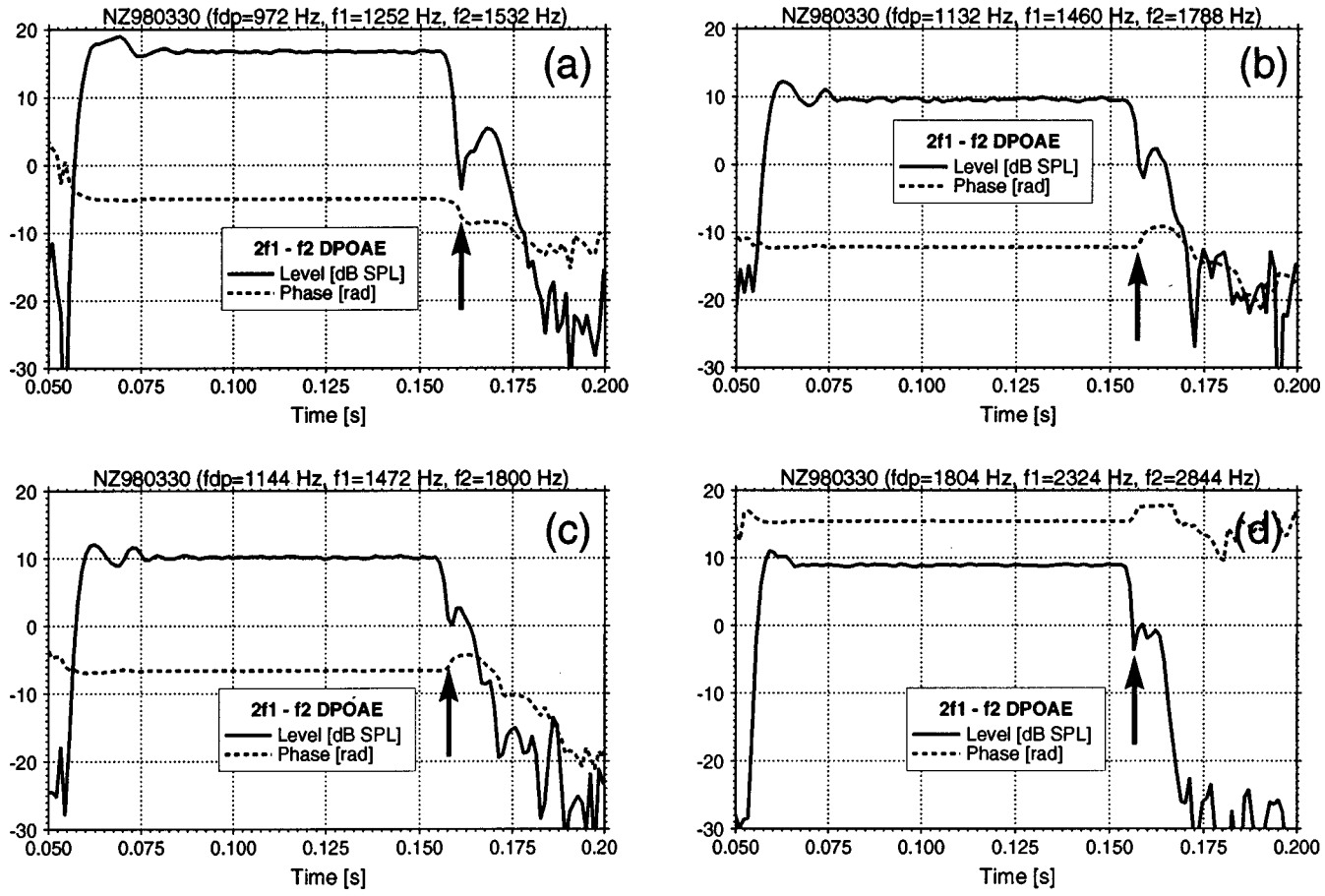

FIG. 9. 2 f_1-f_2 DPOAE level and phase as a function of time for subject NZ for various choices of f_{dp}. The frequency ratio and levels of the primaries are the same as in Fig. 6. The arrows point to the interference notch discussed in Sec. IV C.

during the first 15 min after the subject was placed in the booth in order to reduce this variability.) The variability of the DPOAE amplitude fine structure observed in these experiments (e.g., compare Figs. 6 and 9, and Figs. 7 and 10) is exaggerated by the fact that many of the measurements were obtained near deep DPOAE amplitude fine-structure minima. Because the levels of the two DPOAE components are nearly equal for deep minima, any small variation in either component will cause a small frequency shift in the location of the minimum in these cases. This small shift in the minimum location results in large DPOAE amplitude changes when the frequencies used in the measurements are held fixed.

In addition to providing evidence for the two-source model, the pulsed DPOAE paradigm provides a basis for evaluation of the latency, phase, and amplitude of each of the components. There is a frequency-specific shift in the onset of the response (the onset latencies increase with decreasing f_2). Rough estimates of latency can be obtained by observing the time-to-peak amplitude for the initial and final bursts. Accurate estimates of the latencies of the two components depend on fitting the pulsed DPOAE data to a model of the components from the two sources and their reflections [e.g., Eq. (27)]. A similar model can be applied to the continuous-tone data to extract the levels and phases of the two components. The results of these analyses will be presented in a later paper.

Group delay has been used to estimate travel times for DPOAEs (cf. Bowman *et al.*, 1997). The frequency of one of the primaries is swept over a narrow range and the group delay extracted from the slope of the phase is taken as an estimate of the travel time to and from the place of DPOAE generation. The estimate of latencies obtained in this manner is used as the basis for speculations concerning the mechanisms underlying DPOAEs. This procedure may be very misleading. The steady-state DPOAE phase may be dominated by the component from the reflection site and, in general, the interpretation of the group delay is complicated by the presence of two cochlear sources of DPOAEs, which results in the group-delay fine structure reported upon in this study.

V. STUDY 3: THE USE OF SUPPRESSION TO MANIPULATE THE RELATIVE LEVELS OF THE TWO SOURCES

A suppressor tone with a frequency close to that of the DPOAE should have a larger effect on the amplitude of the reflection-site DPOAE component than on that of the nonlinear-overlap-region component (Kummer *et al.*, 1995; Gaskill and Brown, 1996; Heitmann *et al.*, 1998). It should thus be possible to manipulate the relative levels of the two components by the addition of such a suppressor tone. As the

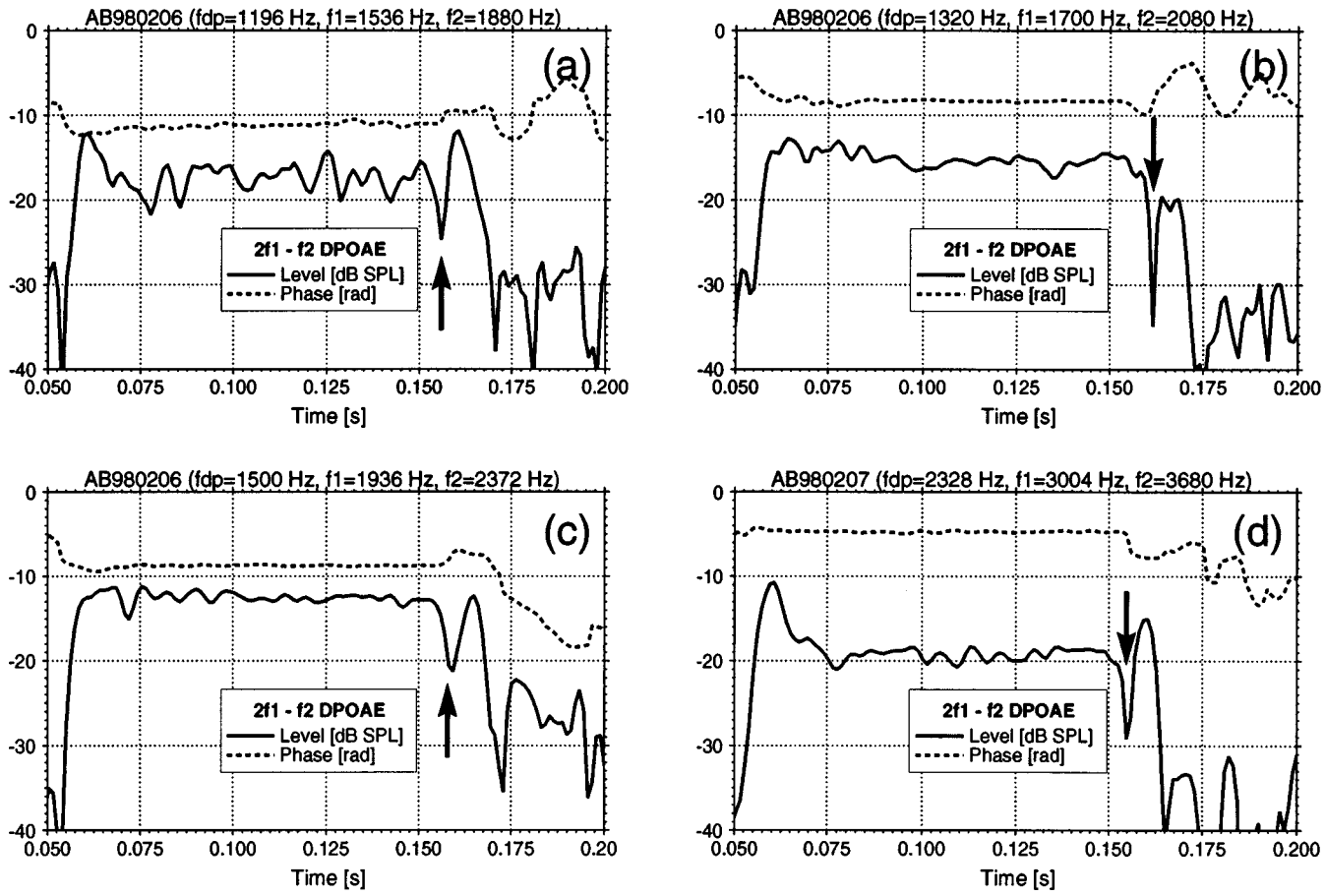

FIG. 10. 2 f_1-f_2 DPOAE level and phase as a function of time for subject AB for various choices of f_{dp}. The frequency ratio and levels of the primaries are the same as in Fig. 7. The arrows point to the interference notch discussed in Sec. IV C.

suppressor tone increases in level, it will initially have no noticeable effect, but will then reduce a_{refl} without significantly changing a_{nl}. Further increases in the level of the third tone will eventually suppress a_{nl} and the overall level of the DPOAE. The position of the notch in the pulsed-tone paradigm should shift from the beginning to the end of the pulsed response (e.g., Fig. 3) when there is a transition from a ramp-like to a rounded saw-tooth phase function (e.g., Fig. 2) in the fixed-ratio sweeps with increasing suppressor level.

The model predicts that multiple interference notches will occur after f_2 signal turn-off if the internal reflection is large enough for the observation of multiple internally reflected components, and if each successive component arrives at the stapes out of phase with the previous component. If the model prediction is correct, then complete suppression of the reflection-site DPOAE component will not only remove the DPOAE fine structure, but will obliterate the trailing interference notches associated with multiple internal reflection.

A. Methods

1. Continuous primaries

Detailed fixed-ratio measurements were made in some of the fine-structure regions with the inclusion of a suppressor tone. For most of the measurements, the frequency of the suppressor tone was located 24 Hz above that of the 2 f_1-f_2 DPOAE, and measurements over the entire frequency range were made for suppressor levels typically ranging from 10 to 80 dB SPL (see Heitmann *et al.*, 1998). The range in levels of the suppressor tone was chosen so that the effect on fine structure ranged from no significant effect (lowest levels) to obliteration of the fine structure (highest levels).

2. Pulsed primary

In order to use the pulsed-tone paradigm with suppression and still permit the clear resolution of the pulsed DPOAE and the suppressor tone, the suppressor tone was shifted to approximately 300 Hz below that of the DPOAE. The primary frequencies were once again chosen to cover a range of DPOAE levels which include two maxima and a single minimum. After the continuous-tone data had been obtained, a DPOAE frequency which corresponds to a DPOAE level greater than 10 dB above the amplitude minimum was chosen for the pulsed primary paradigm to produce the clearest representations of the (destructive) interference of the two DPOAE components. Two suppressor levels were used for the pulsed-tone paradigm: One was 10 dB lower in level and one was 10 dB higher in level than that needed to produce the transition. A smaller number of replications of the pulsed tone paradigm was obtained in order to allow all of the data from the various paradigms to be collected over a period of 1 1/2 h.

A specific test of the hypothesis that the trailing pulses expected from the model (e.g., Fig. 4), observed in some of

the experimental measurements originated from multiple internal reflection of the DP wave, was performed for subject ER for $2f_1-f_2=1908$ Hz, $f_2/f_1=1.225$, $L_1=65$ dB SPL, $L_2=55$ dB SPL for a suppressor 318 Hz below the frequency of the DPOAE with suppressor levels ranging from 10 to 75 dB SPL. This frequency region was selected because large DPOAE pulses were observed in the pulsed-primary-tone measurements.

B. Results

1. Continuous primaries

Two effects of the third tone on the level and phase of the fine structure were seen. If the phase behavior was a rounded saw-tooth in the absence of suppression (Fig. 11), then increasing the level of the suppressor tone reduced the phase and amplitude fine structure. At the highest suppression levels, the level and phase of the DPOAE both changed slowly with frequency. On the other hand, when the phase had a localized steep slope (ramp-like) around the amplitude minimum (Figs. 12 and 13) the initial effect of increasing suppressor-tone level was to deepen the amplitude fine structure and increase the phase slope at the amplitude minimum. Further increases of the suppressor tone reduced the amplitude fine structure and changed the phase behavior to a rounded sawtooth fluctuation.

2. Pulsed primary

The effects of increasing the level of a suppressor tone 316 Hz below the DP frequency are shown in Fig. 14. The DPOAE frequency was swept from 1760–1850 Hz for suppressor levels from 20 to 60 dB SPL in 10-dB steps. A more intense suppressor level (60 dB SPL) was needed to produce a transition in the phase behavior than was needed when the suppressor-tone frequency was only 24 Hz above that of the DPOAE (40 dB SPL). The change in phase behavior was associated with the deepest amplitude minimum. Once the suppressor levels necessary to produce this change in phase behavior were established, two primary frequencies were chosen so as to produce a DPOAE near the fine-structure minimum ($f_1=2323$ Hz, $f_2=2846$ Hz, $2f_1-f_2=1800$ Hz), and the pulsed f_2 paradigm was conducted with suppressor tones (1482 Hz) of 40 and 60 dB SPL.

When the 40-dB SPL suppressor was used, the notch in the pulsed DPOAE amplitude occurred near the turn-on of the pulsed f_2 tone [Fig. 15(a)], and the phase behavior was ramp-like [Fig. 14(b)]. On the other hand, when the 60-dB SPL suppressor was used, the notch in the pulsed DPOAE amplitude was shifted to shortly after the turn-off of the pulsed f_2 tone [Fig. 15(b)] and the phase behavior was rounded saw-toothed [Fig. 14(b)]. The 60-dB suppressor tone also eliminated the three additional secondary pulses after f_2 turn-off which were present in the case of the 40-dB SPL suppressor.

Suppression of the secondary pulses was also noted in other pulsed-tone suppression experiments. Representative data from these measurements are shown in Fig. 16 for $L_s=20$ dB SPL and $L_s=70$ dB SPL. These data are much noisier than most of the earlier data because they were obtained with just 32 s of data per presentation conditions. However, two secondary pulses are readily observable in Fig. 16(a), but are suppressed below the noise floor in Fig. 16(b).

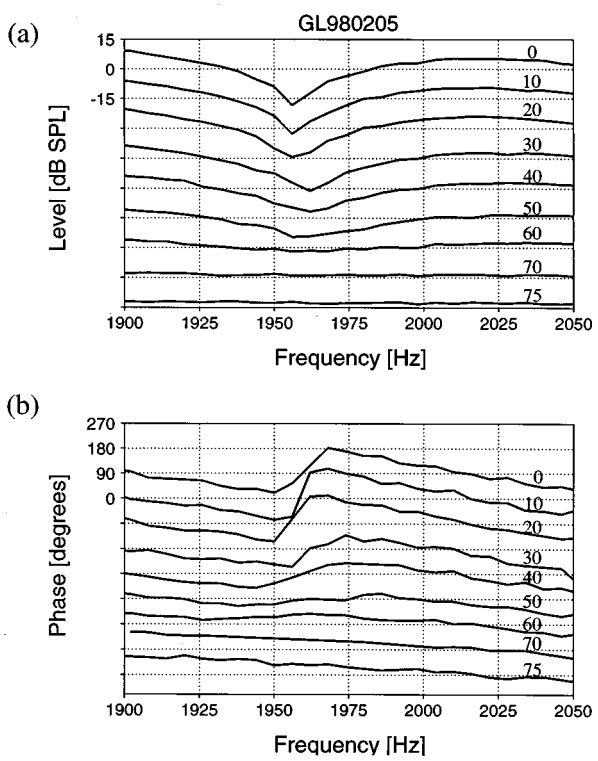

FIG. 11. Amplitude (a) and phase (b) of the $f_{dp}=2f_1-f_2$ DPOAE for $f_2/f_1=1.225$, and suppressor frequency $f_s=f_{dp}=24$ Hz for subject GL. The curves for successive levels of suppression (indicated on the right-hand end of each curve) are shifted downwards by 15 dB for (a) and by 90 deg for (b). Note that both the level minimum and the ''step'' in phase are eliminated for high suppressor levels.

C. Discussion

1. Continuous primaries

Figure 11 shows an example of the suppression of the DPOAE fine structure of a subject for which $a_{\text{refl}}<a_{\text{nl}}$ for the unsuppressed case [compare with Fig. 2(b)]. For this case, increasing the suppressor level removes the amplitude fine structure, and flattens the phase function (which in all cases would exhibit a rounded saw-tooth behavior).

Figures 12 and 13 provide examples where $a_{\text{refl}}>a_{\text{nl}}$ for the unsuppressed case [compare with Fig. 2(d)]. Here, increasing the suppressor level (10–30 dB SPL for Figs. 12 and 10, 20 dB SPL for Fig. 13) initially makes a_{refl} become approximately equal to a_{nl} and consequently deepens the amplitude fine structure. The phase behavior remains ramp-like, with an increasing slope with increasing suppressor level. Once the suppressor is high enough in level (40–70 dB SPL for Fig. 12 and 30–60 dB SPL for Fig. 13), a_{refl} becomes less than a_{nl}, the amplitude fine structure begins to decrease, and eventually disappears. A categorical shift in phase behavior from ramp-like to rounded saw-tooth-like behavior is also seen. Further increases in the suppressor level causes the phase function to flatten as in the first case described above. For high-enough suppressor levels (>70 dB SPL in Fig. 12),

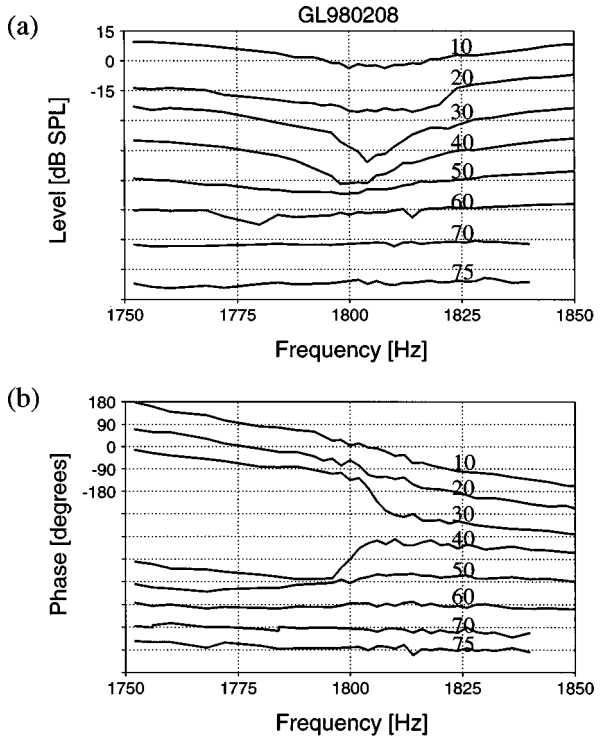

FIG. 12. Amplitude (a) and phase (b) of the $f_{dp}=2f_1-f_2$ DPOAE for $f_2/f_1=1.225$, and suppressor frequency $f_s=f_{dp}+24$ Hz for subject GL. The curves for successive levels of suppression (indicated on the right-hand end of each curve) are shifted downwards by 15 dB for (a) and by 90 deg for (b). Note that the level minimum initially deepens before becoming more shallow as the suppressor level is increased. Additionally, the phase behavior transitions from a ramp-like function to a step-like function as the suppressor level is increased.

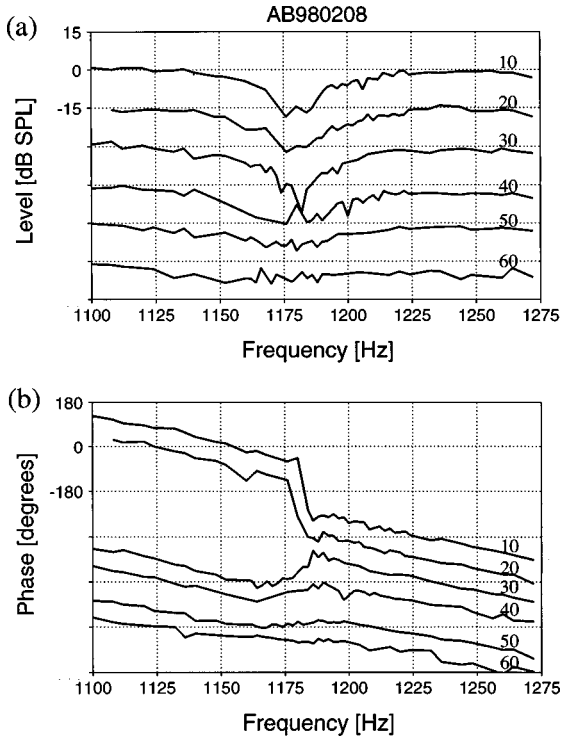

FIG. 13. Amplitude (a) and phase (b) of the $f_{dp}=2f_1-f_2$ DPOAE for $f_2/f_1=1.225$, and suppressor frequency $f_s=f_{dp}+24$ Hz for subject AB. The curves for successive levels of suppression (indicated on the right-hand end of each curve) are shifted downwards by 15 dB for (a) and by 90 deg for (b).

both the reflection-site and the overlap-region components are suppressed, and the overall level of the DPOAE decreases. The ability to predictably change the correlation between group delay and amplitude fine structure by suppressing the component from the DP site provides additional evidence for our two-source theory.

2. Pulsed primary

Figure 15 provides an example in which a direct manipulation (the inclusion of a suppressor tone) is able to shift the behavior of the phase from ramp-like (associated with $a_{refl}>a_{nl}$) to rounded saw-tooth-like, and is able to shift (in a predictable fashion) the location of the interference notch between the two source components from shortly after the f_2 signal turn-on until shortly after f_2 turn-off. The ability to predict the position of the notch in the pulsed DPOAE data from the phase characteristics of the continuous data (with and without suppression) provides a rigorous test of the two-source model.

As predicted, the suppressor tone not only changed the position of the notch for subject GL, but also eliminated the sequences of bursts after stimulus turn-off [see Fig. 15(b)]. There can be reflections even if $a_{nl}>a_{refl}$ and the notch is at the end of a pulse [see Fig. 16(a)]. The addition of a suppressor tone reduces a_{refl} to the noise floor and removes the bursts of predictable amplitude and phase following stimulus turn-off [see Fig. 16(a)].

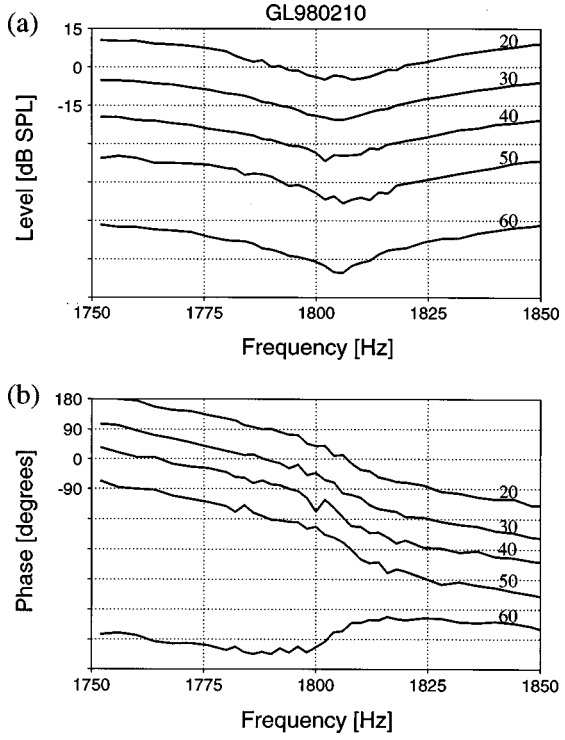

FIG. 14. Amplitude (a) and phase (b) of the $f_{dp}=2f_1-f_2$ DPOAE for $f_2/f_1=1.225$, and suppressor frequency $f_s=f_{dp}-300$ Hz for subject GL. The curves for successive levels of suppression (indicated on the right-hand end of each curve) are shifted downwards by 15 dB for (a) and by 90 deg for (b).

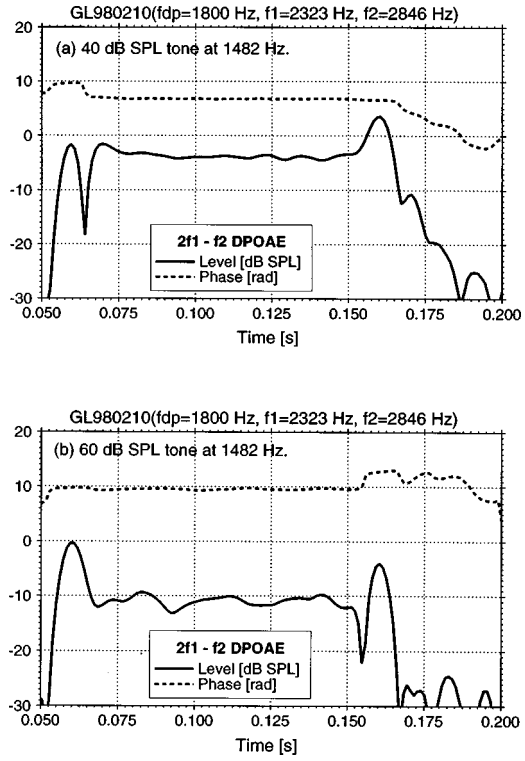

FIG. 15. $2f_1-f_2$ DPOAE level and phase as a function of time for $f_{dp}=1800$ Hz, $f_2/f_1=1.225$, $L_1=65$ dB SPL, and $L_2=55$ dB SPL for subject GL on the same day and conditions as Fig. 14. A suppressor tone at 1482 Hz was 40 dB SPL in (a) and 60 dB SPL in (b). Note the movement of the notch from the onset (a) to the offset (b) of the DPOAE at levels of the suppressor which produce a change in the phase behavior at the amplitude minimum in Fig. 14.

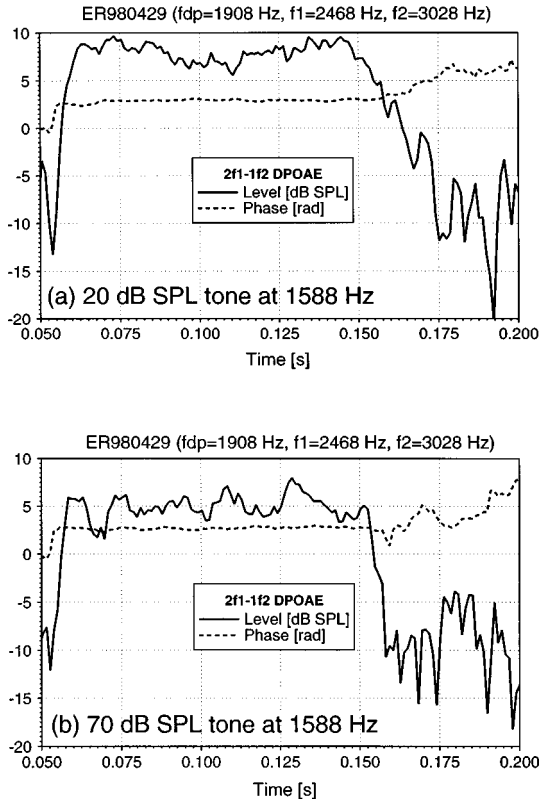

FIG. 16. $2f_1-f_2$ DPOAE level and phase as a function of time for $f_{dp}=1908$ Hz, $f_2/f_1=1.225$, $L_1=65$ dB SPL, and $L_2=55$ dB SPL for subject ER. A suppressor tone at 1588 Hz was 20 dB SPL in (a) and 70 dB SPL in (b). Note the disappearance of the train of secondary pulses in (b).

VI. CONCLUSIONS

A model of DPOAEs as the sum of two sources permits the prediction of the outcome of three different experimental paradigms and the evaluation of the relative amplitudes and latencies of the two source components. The pattern of the fixed-ratio sweeps (within each experimental session) permitted the prediction of the pattern of results for the other two experimental paradigms.

When the spacing between adjacent DPOAE frequencies with a fixed frequency-ratio paradigm was made fine enough to unambiguously determine the total phase of the DPOAE, the patterns of DPOAE amplitude fine structure, phase variation, and group-delay fine structure agreed with those expected from the model of Talmadge *et al.* (1998). In some cases, the patterns of amplitude fine structure, phase variation, and group-delay fine structure are consistent with amplitude dominance of the overlap-region component, and in other cases, with the dominance of the component from the DP tonotopic place.

Measurements of the time courses of the amplitude and phase of DPOAEs were extracted from a paradigm in which the DPOAE is pulsed by pulsing the f_2 primary tone on and off, while keeping the f_1 primary tone continuous in level. Under circumstances in which the overlap-region component is expected to be dominant from fixed-ratio measurements, an interference notch is observed in the DPOAE amplitude shortly after turn-off of the f_2 primary, as expected from the theory. Similarly, when the DP tonotopic-place component is expected to be dominant from fixed-ratio measurements, an interference notch is observed in the DPOAE amplitude shortly after turn-on of the f_2 primary.

By introducing a suppressor tone near in frequency to the DPOAE, a transition was brought about in the patterns of amplitude, phase, and group delay from those in which the reflection-site component is dominant to patterns in which the overlap-region component is dominant. Furthermore, it was possible to shift the location of the interference null until after turn-off of the f_2 primary, consistent with the theory.

It is important to note that the degree of specificity of predictions given in this paper can only be given by a *detailed* two-source model. Simply positing that two sources exist, without a detailed mathematical description of their origins and amplitude and phase behavior with ω_1, ω_2, and ω_{dp}, is not sufficient to give rise to unique predictions for either continuous-tone or pulse-tone DPOAE measurements. For example, papers such as Kemp and Brown (1983), Gaskill and Brown (1996), and Heitmann *et al.* (1998), which suggested the possibility of a two-source origin for DPOAEs, did not give rise to well-defined predictions for the fixed frequency-ratio experiments, the pulsed-DP experiments, and especially did not predict the relationship between the two experimental paradigms reported in this study. In order for a two-source model to reproduce the phenomenology reported in this study, it is necessary that the model give a complete description of how the second (reflection-

site) source varies in phase with the DPOAE frequency, and this was not done in these earlier studies.

ACKNOWLEDGMENTS

We would like to thank Christopher Tong for reading this manuscript. This research was supported in part by the NIH/NIDCD grant No. R29 DC03094.

Bowman, D. M., Brown, D. K., Eggermont, J. J., and Kimberley, B. P. (**1997**). ''The effect of sound intensity on $f1$-sweep and $f2$-sweep distortion product otoacoustic emissions phase delay estimates in human adults,'' J. Acoust. Soc. Am. **101**, 1550–1559.

Brown, A. M., Harris, F. P., and Beveridge, H. A. (**1996**). ''Two sources of acoustic distortion products from the human cochlea,'' J. Acoust. Soc. Am. **100**, 3260–3267.

Gaskill, S. A., and Brown, A. M. (**1996**). ''Suppression of human acoustic distortion product: dual origin of $2f_1-f_2$,'' J. Acoust. Soc. Am. **100**, 3268–3274.

Gorga, M. P., Neely, S. T., BM, B. M. B., Beauchaine, K. L., Kaminski, J. R., and Liu, Z. (**1994**). ''Towards understanding the limits of distortion product otoacoustic emission measurements,'' J. Acoust. Soc. Am. **96**, 1494–1500.

Greenwood, D. D. (**1990**). ''A cochlear frequency position function for several species—29 years later,'' J. Acoust. Soc. Am. **87**, 2592–2605.

Heitmann, H. J., Waldmann, B., Schnitzler, H. U., Plinkert, P. K., and Zenner, H.-P. (**1997**). ''Suppression growth functions of DPOAE with a suppressor near $2f1-f2$ depends on DP fine structure: Evidence for two generation sites for DPOAE,'' in *Abstracts of the Twentieth Midwinter Research Meeting of the Association for Research in Otolaryngology*, edited by G. R. Popelka (Association for Research in Otolaryngology, Des Moines, IA), p. 190.

Heitmann, J., Waldmann, B., and Plinkert, P. K. (**1996**). ''Limitations in the use of distortion product otoacoustic emissions in objective audiometry as the result of fine structure,'' European Archives of Otolaryngology **253**, 167–171.

Heitmann, J., Waldmann, B., Schnitzler, H. U., Plinkert, P. K., and Zenner, H. P. (**1998**). ''Suppression of distortion product otoacoustic emissions (dpoae) near $2f(1)=f(2)$ removes *dp*-gram fine structure—evidence for a secondary generator,'' J. Acoust. Soc. Am. **103**, 1527–1531.

Kemp, D. T. (**1979**). ''The evoked cochlear mechanical response and auditory microstructure—evidence for a new element in cochlear mechanics,'' Scand. Audiol. Suppl. **9**, 35–47.

Kemp, D. T., and Brown, A. M. (**1983**). ''An integrated view of the cochlear mechanical nonlinearities observable in the ear canal,'' in *Mechanics of Hearing*, edited by E. de Boer and M. A. Viergever (Martinus Nijhoff, The Hague, The Netherlands), pp. 75–82.

Kummer, P., Janssen, T., and Arnold, W. (**1995**). ''Suppression tuning characteristics of the $2f_1-f_2$ distortion product otoacoustic emission in humans,'' J. Acoust. Soc. Am. **98**, 197–210.

Liberman, M., Puria, S., and Guinan, J. J. (**1996**). ''The ipsilaterally evoked olivocochlear reflex causes rapid adaptation of the $2f1-f2$ distortion product otoacoustic emission,'' J. Acoust. Soc. Am. **949**, 3572–3584.

Long, G. R., and Talmadge, C. L. (**1997**). ''The frequency of spontaneous otoacoustic emissions is modulated by heartbeat,'' J. Acoust. Soc. Am. **102**, 2831–2848.

Martin, G. K., Jassir, D., Stagner, B. B., Whitehead, M. L., and Lonsbury-Martin, B. (**1998**). ''Locus of generation for the $2f12\,f2$ vs $2f22\,f1$ distortion-product otoacoustic emissions in normal-hearing humans revealed by suppression tuning, onset latencies, and amplitude correlations,'' J. Acoust. Soc. Am. **103**, 1957–1971.

Mathews, J., and Walker, R. (**1964**). *Mathematical Methods of Physics* (Benjamin, New York).

Mills, D. M. (**1997**). ''Interpretation of distortion product otoacoustic emission measurements: I. Two stimulus tones,'' J. Acoust. Soc. Am. **102**, 413–429.

Piskorski, P. (**1997**). ''The origin of the distortion product otoacoustic emission fine structure,'' Ph.D. thesis, Purdue University, West Lafayette, IN.

Robinette, M. S. and Glattke, T. J., editors (**1997**). *Otoacoustic Emissions: Clinical Applications* (Thieme, New York).

Shera, C. A., and Zweig, G. (**1993**). ''Order from chaos: Resolving the paradox of periodicity in evoked otoacoustic emission,'' in *Biophysics of Hair Cell Sensory Systems*, edited by H. Duifhuis, J. W. Horst, P. van Dijk, and S. M. van Netten (World Scientific, Singapore), pp. 54–63.

Siegel, J., and Hirohata, E. (**1994**). ''Sound calibration and distortion product otoacoustic emissions at high frequencies,'' Hearing Res. **80**, 146–152.

Stover, L. J., Neely, S. T., and Gorga, M. P. (**1996**). ''Latency and multiple sources of distortion product emissions,'' J. Acoust. Soc. Am. **99**, 1016–1024.

Sun, X. M., Schmiedt, R. A., He, N.-J., and Lam, C. F. (**1994a**). ''Modeling the fine structure of the $2f(1)-f(2)$ acoustic distortion product. I. Model development,'' J. Acoust. Soc. Am. **96**, 2166–2174.

Sun, X. M., Schmiedt, R. A., He, N.-J., and Lam, C. F. (**1994b**). ''Modeling of the fine structure of the $2f(1)-f(2)$ acoustic distortion product. II. Model evaluation,'' J. Acoust. Soc. Am. **96**, 2175–2183.

Talmadge, C., Long, G. R., and Tubis, A. (**1993**). ''New off-line method for detecting spontaneous otoacoustic emissions in human subjects,'' Hearing Res. **71**, 170–182.

Talmadge, C., Tubis, A., Long, G. R., and Piskorski, P. (**1998**). ''Modeling otoacoustic emission and hearing threshold fine structures in humans,'' J. Acoust. Soc. Am. **104**, 1517–1543.

Talmadge, C., Tubis, A., Piskorski, P., and Long, G. R. (**1997**). ''Modeling otoacoustic emission fine structure,'' in *Diversity in Auditory Mechanics*, edited by E. Lewis, G. Long, R. Lyon, P. Narins, and C. Steele (World Scientific, Singapore), pp. 462–471.

Talmadge, C. L., Tubis, A., Long G. R., and Piskorski, P. (**1996**). ''Evidence for multiple spatial origins of the fine structure of distortion product otoacoustic emissions in humans, and its implications: Experimental and modeling results,'' in Abstracts of the Nineteenth Midwinter Research Meeting of the Association for Research in Otolaryngology, edited by D. J. Lim (unpublished), p. 94. Abstract.

Whitehead, M. L. (**1991**). ''Slow variations of the amplitude and frequency of spontaneous otoacoustic emissions,'' Hearing Res. **53**, 269–280.

Whitehead, M., Stagner, B., Martin, G., and Lonsbury-Martin, B. (**1995**). ''Effects of ear-canal standing waves on measurements of distortion-product otoacoustic emissions,'' J. Acoust. Soc. Am. **98**, 3200–3214.

Whitehead, M., Stagner, B., Martin, G., and Lonsbury-Martin, B. (**1996**). ''Visualization of the onset of distortion-product otoacoustic emissions, and measurement of their latency,'' J. Acoust. Soc. Am. **100**, 1663–1679.

Zweig, G. (**1991**). ''Finding the impedance of the organ of Corti,'' J. Acoust. Soc. Am. **89**, 1229–1254.

Zweig, G., Lipes, R., and Pierce, J. R. (**1976**). ''The cochlear compromise,'' J. Acoust. Soc. Am. **59**, 975–982.

Zweig, G., and Shera, C. A. (**1995**). ''The origins of periodicity in the spectrum of evoked otoacoustic emissions,'' J. Acoust. Soc. Am. **98**, 2018–2047.

Contralateral suppression of transiently evoked otoacoustic emissions by harmonic complex tones in humans

Christophe Micheyl
Université Claude Bernard LYON 1, Laboratoire ''Neurosciences & Systèmes Sensoriels'' UPRESA CNRS 5020, Hôpital E. Herriot-Pavillon U, 69003 Lyon, France and MRC Applied Psychology Unit, 15 Chaucer Road, Cambridge CB2 2EF, England

Stéphane Maison
Université Claude Bernard LYON 1, Laboratoire ''Neurosciences & Systèmes Sensoriels'' UPRESA CNRS 5020, Hôpital E. Herriot-Pavillon U, 69003 Lyon, France

Robert P. Carlyon
MRC Applied Psychology Unit, 15 Chaucer Road, Cambridge CB2 2EF, England

Guillaume Andéol and Lionel Collet
Université Claude Bernard LYON 1, Laboratoire ''Neurosciences & Systèmes Sensoriels'' UPRESA CNRS 5020, Hôpital E. Herriot-Pavillon U, 69003 Lyon, France

(Received 15 January 1998; accepted for publication 18 September 1998)

Variations in the amplitude of transiently evoked otoacoustic emissions (TEOAEs) produced by a contralateral complex tone were measured in 26 normal-hearing human subjects. TEOAEs were evoked using a 1-kHz tone pip at 60 dB SPL. The contralateral complex consisted of harmonic components with frequencies between 400 and 2000 Hz; it was presented at levels ranging from 40 to 50 dB SL and its fundamental frequency ($F0$) was varied. In experiment 1, the dependence of TEOAE amplitude variations on the $F0$ of the contralateral complex was measured by varying the $F0$ from 50 to 400 Hz in octave steps. The results revealed a nonmonotonic dependence of TEOAE amplitude variations on contralateral $F0$, with significantly larger TEOAE suppression for $F0$'s of 100 and 200 Hz than for $F0$'s of 50 and 400 Hz. Experiment 2, in which the harmonics were summed in alternating sine–cosine phase instead of constant sine phase, showed a shift of the function relating TEOAE attenuation to $F0$ towards lower $F0$'s, indicating that the waveform repetition rate, rather than harmonic spacing, was the actual factor of the dependence of contralateral TEOAE attenuation on $F0$. Furthermore, significantly smaller suppression was observed with the alternating-phase complexes than with the sine-phase complexes, suggesting an influence of the waveform crest factor. Experiment 3 showed no difference between the contralateral TEOAE attenuation effects produced by positive and negative Schroeder-phase complexes. Overall, these results bring further arguments for the notion that contralaterally induced medial olivocochlear bundle (MOCB) activity, as measured through the contralateral suppression of TEOAEs in humans, is sensitive to the rate of temporal envelope fluctuations of the contralateral stimulus, with preferential rates around 100–200 Hz.
[S0001-4966(99)01201-1]

PACS numbers: 43.64.Jb, 43.64.Kc, 43.64.Ri [BLM]

INTRODUCTION

It was discovered more than 50 years ago that the auditory system comprises neural efferent pathways originating in the vicinity of the superior olivary complex and projecting onto the cochlea (Rasmussen, 1946). More recently, it was demonstrated that this olivocochlear bundle (OCB) is in fact composed of two subsystems: the lateral OCB, synapsing with the type-I primary afferent fibers of the auditory nerve that innervate the base of the inner-hair cells, and the medial OCB (MOCB), contacting directly the outer-hair cells (OHCs) of the cochlea (Warr and Guinan, 1979). Today, the functioning of the OCB and its function in hearing still remain poorly understood and highly controversial. With only a few exceptions (Capps and Ades, 1968; Dewson, 1968), early studies in which behavioral measures were performed after surgical section of the OCB in animals failed to evidence a significant role of this system in a wide range of perceptual tasks, including absolute detection, intensity discrimination, and frequency discrimination both in quiet and in noise (Igarashi, 1972, 1979a, 1979b; Trahiotis and Elliott, 1970). Psychoacoustical measures performed in human subjects with the OCB cut following vestibular neurotomy have also been taken as evidence for a lack of significant role of the OCB in auditory perception—with the only exception of frequency selectivity under attentional control (Scharf *et al.*, 1994, 1997). On the other hand, however, several physiological studies have revealed strong effects of OCB stimulation on peripheral auditory responses. In particular, reductions in the amplitude of auditory-nerve compound or unit responses to signals in quiet (Wiederhold and Kiang, 1970; Buño, 1978; Warren and Liberman, 1989), and increases in the amplitude of responses to signals in noises have been

evidenced (Dolan and Nuttall, 1988; Nieder and Nieder, 1970; Winslow and Sachs, 1987; Kawase and Liberman, 1993; Kawase *et al.*, 1993; Kawase and Takasaka, 1995). In the light of these results, it has become increasingly clear that the OCB could play a role either in protecting the inner ear from acoustic overstimulation (Rajan, 1988a, 1988b) or in enhancing the encoding of signals in noise (Liberman, 1988; Winslow and Sachs, 1987, 1988; Kawase and Liberman, 1993; Kawase *et al.*, 1993). The latter hypothesis has recently been supported by the demonstration of a detrimental effect of OCB section on intensity and formant discrimination in noise in cats (May and McQuone, 1995; Hienz *et al.*, 1998). At the same time, lines of evidence for psychophysical correlates of OCB activation, such as improved detection and intensity discrimination of tones in noise, have also begun to appear in the literature (Micheyl *et al.*, 1995, 1997; Micheyl and Collet, 1996).

Besides differences in methods and subjects, a reason for the discrepancy between the results of these various studies may be that, for the role of OCB in hearing to be revealed, it is first necessary that this system be sufficiently activated (Liberman, 1988; Littman *et al.*, 1992), and it may be that this activation requires specific stimulation conditions which were met in certain studies but not in others. This question of the stimulus specificity of OCB activation was ''by-passed'' in studies in which OCB neurons were driven at high rates by direct electrical stimulation of the OCB (Galambos, 1956; Wiederhold and Kiang, 1970; Gifford and Guinan, 1987). Studies involving contralateral acoustic stimulation of the OCB have suggested that the degree of activation of this system depends to a large extent on the characteristics of the stimulus: while high OCB neuron-discharge rates can be obtained using noises, especially when these are presented to both ears, much weaker discharge rates have been observed with tone pips; so low, in fact, that the question of whether they might have any influence on the auditory periphery was raised (Liberman, 1988). In this context, the characterization of the spectral and temporal properties that lead to activation of the OCB in natural acoustic stimulation conditions appears as an important prerequisite for the understanding of the role played by this system in hearing.

The activity of the MOCB can be studied in humans through the contralateral suppression of evoked otoacoustic emissions (EOAEs) (Collet *et al.*, 1990). This effect corresponds to the fact that EOAE amplitude is reduced by the presentation of an acoustic stimulus in the opposite ear. In agreement with the notion that the MOCB can be excited by contralateral acoustic stimulation (Buño, 1978) and that the fast motility of the cochlear outer-hair cells to which it projects is the origin of otoacoustic emissions (Manley and Gallo, 1997), this effect has been proposed to reflect the influence of MOCB activity on outer-hair-cell motility (Collet *et al.*, 1990). This view is today supported by the results of numerous studies (Berlin *et al.*, 1993; Collet *et al.*, 1990, 1992; Giraud *et al.*, 1995; Norman and Thorton, 1991; Ryan *et al.*, 1991; Veuillet *et al.*, 1991). It is worth noting that contralateral EOAE suppression effects, although statistically significant, remain relatively weak—generally less than 1 dB—and thus appear unlikely to play a significant functional role in hearing in their own respect. However, OCB activation by contralateral acoustic stimuli has been shown in several physiological studies to elicit substantial alterations in peripheral auditory-system functioning, such as shifts in auditory-nerve fiber responses (Liberman, 1988; Warren and Liberman, 1989; Kawase and Liberman, 1993; Kawase *et al.*, 1993) and basilar-membrane motion (Russell and Murugasu, 1997). The fact that contralateral EOAE attenuation effects remain of limited size as compared to other effects of OCB stimulation on the auditory periphery may be due to various reasons. Among these is the fact that these effects consist of variations in the amplitude of signals—the EOAEs—that are of limited amplitude and reflect only some aspects of the cochlear functioning, which may not be the most sensitive to OCB influence. Also, contralateral EOAE suppression effects reflect predominantly uncrossed MOCB fibers, which are known based on data in the literature to be about two times less numerous than crossed fibers. In addition, the ipsilateral stimulus used to evoke OAEs may already activate the ipsilaterally responsive fibers, thereby reducing the effect of contralateral stimulation. In spite of all these limitations, there has been increasing interest in contralateral OAE suppression effects over the past years because such effects provide a unique means of obtaining information on MOCB functioning noninvasively in humans.

Until very recently, studies of the contralateral TEOAE amplitude-attenuation effect had almost exclusively involved, as contralateral stimuli, stationary broadband noises which, in contrast to steady tone pips, had been shown to elicit significant TEOAE suppression at low to moderate levels—i.e., from about 30 dB SL (Collet *et al.*, 1990; Veuillet *et al.*, 1992). Consistent with such EOAE findings, electrophysiological data had earlier led to the notion that the OCB would mainly be involved in listening situations involving background noise. Recently, however, it was demonstrated that significant TEOAE suppression could also be obtained at similarly low levels of stimulation with contralateral amplitude-modulated (AM) tones at the frequency of the OAE-evoking stimulus (Maison *et al.*, 1997). This finding was extended in a subsequent study which showed that AM white noise produced larger suppression than stationary broadband noises of the same energy (Maison *et al.*, 1998b). Even more recently, these findings were complemented by the demonstration of significant contralateral TEOAE suppression by frequency-modulated (FM) tones (Maison *et al.*, 1998a). Altogether, these results contribute to the view, initially proposed by Gummer *et al.* (1998), that MOCB activity is particularly sensitive to temporal fluctuations in the stimuli. Temporal amplitude and frequency fluctuations are an important characteristic of ecological stimuli and communication signals; in particular, vocalizations. Indications that MOCB activation is specifically sensitive to these characteristics suggest that this system is effectively activated by such signals and therefore likely to exert its influence in their context. However, the implications of the experimental results obtained so far for the understanding of MOCB activation in natural listening conditions is partly limited by the fact that vocalic or musical sounds have little in common with a pure

tone whose amplitude or frequency is sinusoidally modulated over time. Instead, these sounds are generally composed of several frequency components which are harmonically related, and the temporal fluctuations that their envelopes show are associated to the repetition rate of the waveform, which is generally equal to their fundamental frequency.

In the present study, in order to characterize further the dependence of MOCB activation on the temporal and spectral characteristics of auditory stimulation in humans, MOCB activation, as estimated through the contralateral suppression of EOAEs, was studied using harmonic complex tones using different $F0$'s and phase conditions. Besides the fact that they are more prototypical of sounds encountered in everyday-listening conditions, the advantage of complex tones over modulated pure tones is that, by a careful choice of the phase of their harmonics, some of their temporal and spectral characteristics can be varied independently and the respective contributions of these characteristics assessed. This is the case, in particular, of the number of peaks in the temporal envelope and of the crest factor before and after cochlear filtering, which can be varied independently of the magnitude spectrum of the signals, and whose role in MOCB activation was investigated here.

I. MATERIAL AND METHODS

A. Subjects

The study involved 26 subjects (18 male and 8 female; mean age=23.85 years, s.d.=5.62) with normal hearing, i.e., absolute auditory thresholds within 10 dB HL between 250 and 8000 Hz at octave intervals on pure-tone audiograms. As assessed using an Amplaid 702 impedancemeter, all the subjects demonstrated middle-ear acoustic reflexes in response to contralateral white-noise stimuli.

B. TEOAE recordings and analysis

EOAEs were recorded and analyzed following the method and apparatus devised by Bray and Kemp (1987) and by Kemp *et al.* (1990). Stimulus presentation, data recording and averaging were carried out using the Otodynamics ILO88 software and hardware. The probe comprised a Knowles 1843 microphone and a BP 1712 earphone transducer, both embedded in a plastic earplug. The stimulus was a 1-kHz tone pip with a duration of 4 ms (2-ms plateau, 1-ms cosine ramps). The intensity of the stimulus was adjusted so that the level measured in the ear canal of each subject was 60 ± 3 dB SPL peak. The stimulus presentation rate was 50 Hz. EOAEs were acquired over the 20 ms separating successive stimulus onsets. To remove stimulus artifacts, only the last 14 ms of the responses were taken into account in the analysis, the first 6 ms being canceled. The averaging process stopped when 512 responses were obtained. TEOAE recordings were performed in the right ear of subjects reclining in a soundproof room.

The TEOAE recordings with different contralateral complex tones were performed in random order in each subject, so as to rule out eventual sequence effects. To obtain a reliable baseline, the amplitude of EOAEs in the absence of contralateral stimulation was measured eight times in each subject; these eight measurements were interspersed among the ones performed with a contralateral stimulus present. A one-way repeated-measure analysis of variance (RMANOVA) indicated the absence of significant differences across these eight measurements. Consequently, they were averaged so as to obtain a robust estimate of the baseline TEOAE amplitude; all amplitude variations caused by contralateral stimulation were calculated relative to this baseline.

II. EXPERIMENT 1. DEPENDENCE OF TEOAE ATTENUATION BY CONTRALATERAL HARMONIC COMPLEXES ON *F*0

A. Rationale

The general aim of this experiment was to test for the TEOAE attenuation effects produced by contralateral harmonic complexes, and, in particular, to establish the dependence of these effects on the $F0$ and level of the contralateral sound. Results from an earlier study have suggested that variations in the rate of temporal envelope fluctuations of the contralateral stimulus have an important effect on the size of TEOAE amplitude variations; namely, this size varies nonmonotonically with the rate of sinusoidal amplitude modulation of the contralateral stimulus, reaching a maximum for modulation rates around 100 Hz and decreasing slowly below and above that value (Maison *et al.*, 1997). Because, when the AM rate and the $F0$ are equal, the envelopes of an AM tone and of a constant-phase harmonic complex exhibit fluctuations at the same rate, it was predicted that the dependency of contralateral TEOAE attenuation effects on contralateral $F0$ would be similar to that on the AM rate. To test this prediction, contralateral TEOAE attenuation was measured as a function of $F0$, with the $F0$ varying over a range identical to that over which the AM rate varied in previous studies (Maison *et al.*, 1997, 1998b).

B. Stimuli

The contralateral stimuli consisted of harmonic complex tones generated digitally in the temporal domain by summing the waveforms of all harmonics of a given $F0$ whose frequencies were comprised between 400 and 2000 Hz. This frequency range was chosen for three main reasons. First, because on an octave scale, it spanned approximately identical frequency extents below and above 1 kHz, which was the carrier frequency of the TEOAE-evoking stimulus. Second, because at all $F0$ values used, there were harmonics with frequencies matching these two values so that the frequency range spanned by the complex remained unchanged. Finally, because this range was similar to that used in previous studies involving Schroeder-phase harmonic complexes (Smith *et al.*, 1986; Kohlrausch and Sander, 1995; Carlyon and Datta, 1997a, 1997b) so that comparisons between the psychophysical findings of these studies and the physiological results of experiment 3, also involving such Schroeder-phase harmonic complexes, were possible.

The $F0$ of the complexes was varied in octave steps over a range extending from 50 to 400 Hz. The main motivation for this choice of range was to allow for comparisons

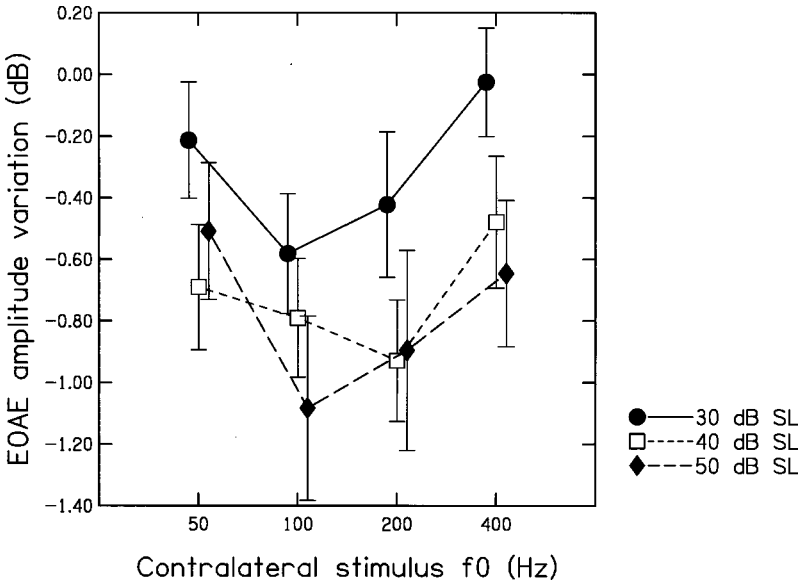

FIG. 1. TEOAE amplitude variation as a function of contralateral stimulus $F0$ for contralateral stimuli consisting of constant-phase harmonic complexes. The different symbols and lines represent results obtained for complexes with different levels per component as indicated by the legend. Changes in TEOAE amplitude are expressed relatively to the TEOAE amplitude measured in absence of contralateral stimulation. Negative values on the ordinate indicate a decrease in TEOAE amplitude upon contralateral stimulation; positive values indicate an increase. The data points represent the average across subjects. The error bars indicate the variability across subjects expressed as the standard error of the mean.

with the results of our earlier studies on the attenuation of EOAEs by AM stimuli in which corresponding AM rates were tested (Maison *et al.*, 1997, 1998b). The complexes were presented at three different levels corresponding to 30, 40, and 50 dB above the absolute threshold—measured beforehand in each listener—of the 100-Hz $F0$ complex; for brevity, these levels are referred to as 30, 40, and 50 dB SL in the following. The contralateral stimulus was continuous.

C. Results

Figure 1 shows the variations in TEOAE amplitude produced by the contralateral harmonic complexes as a function of the $F0$ of the complex for the different stimulation levels. As can be seen in this figure, the dependence of TEOAE amplitude variations on contralateral stimulus $F0$ is nonmonotonic; the reduction in TEOAE amplitude is largest at $F0$'s around 100–200 Hz and decreases at lower and higher $F0$'s. This initial observation was confirmed using two approaches. First, the statistical significance of the TEOAE amplitude variations corresponding to each $F0$ was tested using Student's pairwise comparisons between the baseline amplitude of EOAEs—in the absence of contralateral stimulation—and the amplitude of EOAEs in presence of the contralateral stimulus considered. The results of these comparisons indicated that while, at the lowest stimulation level (30 dB SL), the reduction in TEOAE amplitude elicited by the contralateral complex was statistically significant only when the $F0$ was 100 Hz ($t=2.99$, $p<0.01$, $df=24$), at the highest stimulation level (50 dB SL), significant TEOAE amplitude attenuation was obtained at all $F0$s except the lowest (100 Hz: $t=3.62$, $p=0.001$; 200 Hz: $t=2.76$, $p<0.0125$; 400 Hz: $t=2.72$, $p<0.0125$; $df=23$ in all cases).[1] At the intermediate level (40 dB SL), significant effects were observed at all $F0$s except the highest (50 Hz: $t=3.39$, $p<0.005$; 100 Hz: $t=4.09$, $p<0.001$; 200 Hz: $t=4.70$, $p<0.001$; $df=25$ in all cases).

A second view of the influence of $F0$ in the contralateral attenuation effects was provided by the results of a two-way RMANOVA involving the TEOAE amplitude variation caused by the contralateral stimulus as a dependent variable and the level and $F0$ of this stimulus as factors. These results indicated no significant effect of the level but a highly significant effect of the $F0$ [$F(3,66)=7.93$, $p<0.001$]. *Post hoc* pairwise comparisons using Student's paired *t*-test allowed for further characterization of the influence of $F0$; they revealed that the 100-Hz $F0$ complex produced a significantly larger contralateral attenuation effect than the 400-Hz $F0$ complex at all levels tested (30 dB SL: $t=4.32$, $p<0.001$, $df=24$; 40 dB SL: $t=2.30$, $p<0.05$, $df=25$; 50 dB SL: $t=2.59$, $p<0.05$, $df=23$)and the 50-Hz complex at two of the levels tested (30 dB SL: $t=3.01$, $p<0.01$, $df=24$ and 50 dB SL: $t=2.82$, $p=0.01$, $df=23$). Furthermore, the 200-Hz $F0$ complex proved to have a larger effect than the 400-Hz $F0$ complex at two of the levels tested (30 dB SL: $t=2.85$, $p<0.01$, $df=24$ and 40 dB SL: $t=4.32$, $p<0.001$, $df=25$) and the 50-Hz $F0$ complex at 50 dB SL ($t=2.29$, $p<0.032$). No significant difference was observed between the effects of complexes having $F0$'s of 50 and 400 Hz, nor between those of complexes having $F0$'s of 100 and 200 Hz.

D. Discussion

The results reveal, first, that significant contralateral TEOAE suppression effects can be obtained with complex tones at levels as low as 30 dB SL. From that point of view, harmonic complexes appear to be more efficient contralateral suppressors than tone pips, which start eliciting significant contralateral suppression only at levels as high as about 60 dB SL (Berlin *et al.*, 1993), and at least as efficient as broadband noises or AM tones which also elicit significant contralateral suppression at about 30 dB SL (Collet *et al.*, 1990; Veuillet *et al.*, 1992; Maison *et al.*, 1997). Though no significant effect of level was found, possibly due to large variability in this effect across subjects, significant TEOAE suppression was obtained at only one $F0$ at the lowest level and at all $F0$'s at the highest level. This suggests, in agreement with previous results using other kinds of contralateral

stimuli, that the level of contralateral stimulation influences the amount of contralateral suppression (Collet *et al.*, 1990; Maison *et al.*, 1997).

A second important outcome of the results is that TEOAE suppression effects are strongly dependent on the $F0$ of the contralateral stimulus. This dependence on $F0$ is similar to the dependence on contralateral AM rate reported in previous studies (Maison *et al.*, 1997, 1998b). In these earlier studies, contralateral TEOAE attenuation effects elicited by contralateral AM tones having an AM rate between 50 and 800 Hz proved to be the largest for AM rates around 100 Hz. In the present study, contralateral TEOAE attenuation effects elicited by complex tones with an $F0$ varying between 50 and 400 Hz proved to be significantly larger for $F0$'s of 100 and, to a lesser extent, 200 Hz.

The observed dependence of TEOAE attenuation on contralateral stimulus $F0$ cannot be imputed entirely to the variations in the overall level of the contralateral stimulus occurring with variations in number of components. First, this dependence is nonmonotonic, whereas variations in overall level varied monotonically with $F0$. Second, if the overall level of the contralateral stimulus determined entirely the contralateral TEOAE attenuation, the level of the 400-Hz stimulus being only 5.31 dB lower than that of the 100 Hz complex, then raising the testing level from 30 to 40 dB should have led the former to produce significant TEOAE suppression, which it did not. Therefore, it appears likely that variations in the overall level of the contralateral stimulus with $F0$ did not play a major role in this study.

One interpretation for the striking correspondence between the results of these two studies is based on the fact that, like that of AM tones, the waveform of harmonic complexes summed in constant phase shows marked temporal envelope fluctuations and that, when the $F0$ and AM rates are equal, both waveforms repeat themselves at the same rate. Therefore, to the extent that the temporal envelope fluctuation rate of the contralateral stimulus is a factor of the contralaterally induced TEOAE suppression, comparable effects should be obtained with harmonic complexes and AM tones. From that point of view, the results of the previous and the present studies together support the notion that the neurophysiological mechanism underlying the contralateral suppression of EOAEs is sensitive to temporal fluctuations in the contralateral stimulus and exhibits a selectivity to the rate of these fluctuations. Though the chain of neurophysiological events underlying the contralateral TEOAE attenuation is still not fully understood at present, it appears very likely that this chain involves contralateral activation of the MOCB (Collet *et al.*, 1990, 1992; Giraud *et al.*, 1995; Ryan *et al.*, 1991; Veuillet *et al.*, 1992). In this context, the observation that AM is selectively enhanced in the responses of MOCB neurons measured electrophysiologically in guinea pigs (Gummer *et al.*, 1988) may be related to the finding of a selectivity of TEOAE suppression to the envelope fluctuations in the contralateral stimulus in humans. Such a relationship is the more likely as the preferred rate found in all these studies is the same; namely, 100 Hz.

Further insights into the mechanisms possibly underlying the observed dependence of MOCB activation on contralateral stimulus $F0$ can be obtained by considering, rather than the physical characteristics of the contralateral stimulus, the output of the inner ear in response to this stimulus. Figure 2 shows the temporal waveforms of the stimuli used in experiment 1 and the outputs of a ''gammachirp'' filter[2] (Irino and Patterson, 1997) in response to these stimuli. It can be seen that at an $F0$ of 100 Hz, due to the fact that several harmonics fall in the filter bandpass, the output shows pronounced temporal envelope fluctuations and repeats over time at the $F0$ rate. For the 400-Hz $F0$ signal, fewer harmonics interact within the passband of the auditory filter and the output of this filter thus shows fewer marked envelope fluctuations. If the mechanism underlying contralateral EOAE suppression is sensitive to the depth of envelope fluctuations at the output of auditory filters, this might explain the fact that less suppression was observed with the 400-Hz than with the 100-Hz $F0$ signal. This line of reasoning does, however, not allow to explain the decrease in contralateral EOAE attenuation observed at the lowest $F0$ (i.e., 50 Hz): at this $F0$, several components fall in the auditory-filter passband and the output fluctuates markedly over time. This falloff in suppression at low $F0$'s appears likely to originate at a higher level than the cochlea, and to reflect some form of selectivity of the neural mechanisms underlying the contralateral TEOAE suppression to the rate of temporal envelope fluctuations in the contralateral stimulus.

III. EXPERIMENT 2: DEPENDENCE OF CONTRALATERAL TEOAE ATTENUATION BY HARMONIC COMPLEXES ON WAVEFORM REPETITION RATE

A. Rationale

The results of the previous experiment indicate a strong dependency of the contralateral TEOAE amplitude-attenuation effect on the $F0$ of the harmonic complexes used as contralateral stimuli. As discussed above, one interpretation for this finding is that the mechanism underlying contralateral TEOAE attenuation is sensitive to the rate of temporal envelope fluctuations in the contralateral stimulus; when this stimulus is a complex tone, the rate is determined by the $F0$. However, since the frequency spacing of components is also determined by the $F0$, the results of the previous experiment do not show whether the actual factor of the observed dependency of contralateral TEOAE attenuation on contralateral $F0$ consists of the envelope fluctuation repetition or of the harmonic spacing. The latter could be the case if, for example, MOCB activation were sensitive to the spectral density of the contralateral stimulus. To dissociate these two factors, we applied a phase relationship to the harmonics which doubled the envelope fluctuation rate of the waveform. Under the hypothesis that TEOAE attenuation depended on the rate of temporal fluctuations in the contralateral stimulus rather than on the—spectral—$F0$, the prediction was that the function relating TEOAE attenuation to $F0$ measured in this second experiment should be shifted leftward—i.e., toward lower $F0$'s—relative to that measured in experiment 1.

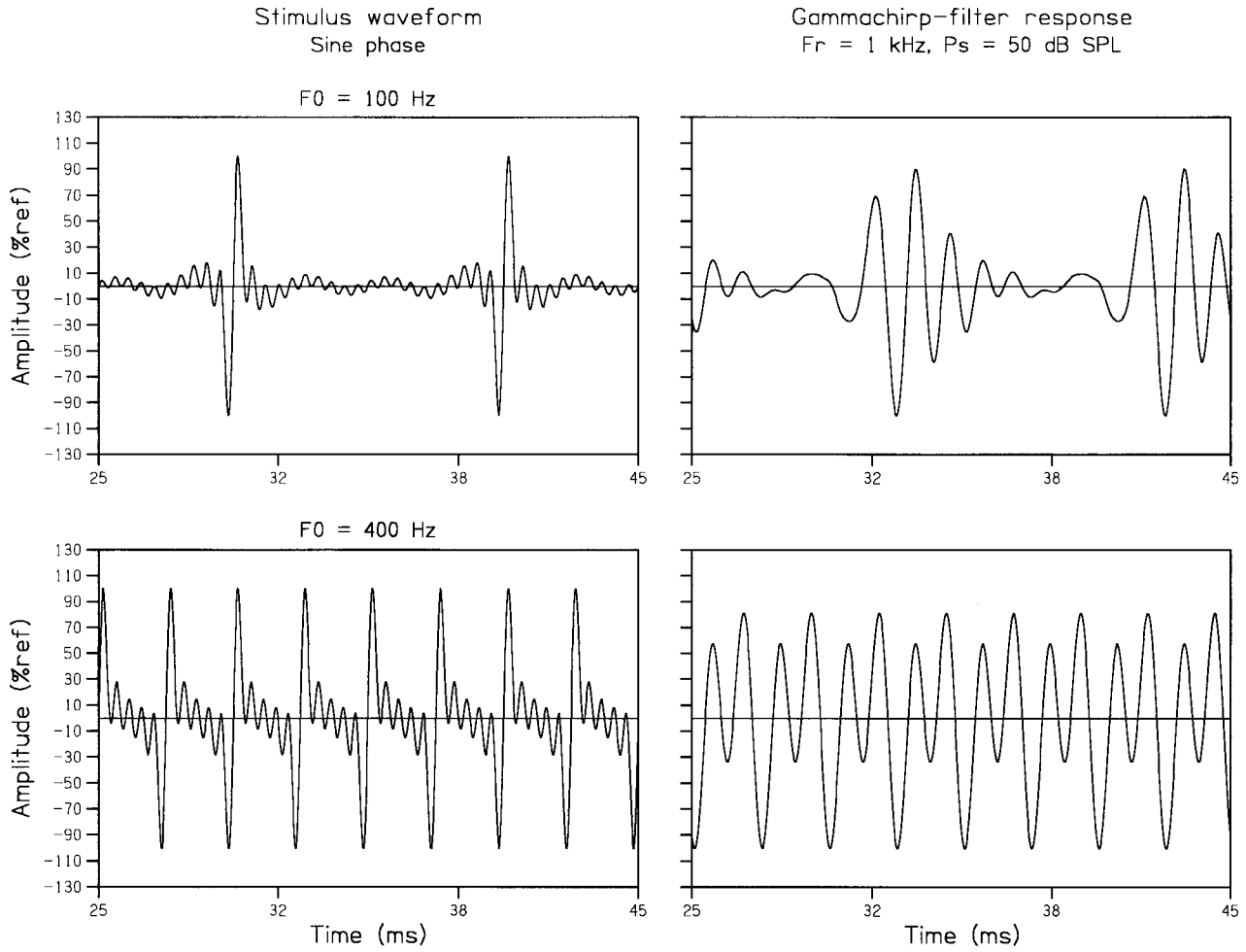

FIG. 2. Examples of waveforms (left) and simulated auditory-filter outputs (right) corresponding to sine-phase harmonic complexes used in experiment 1. Top: $F0$ of the harmonic complex stimulus set to 100 Hz. Bottom: $F0$ of the harmonic complex stimulus set to 400 Hz. The amplitude is expressed in percent of a reference consisting of the maximum instantaneous amplitude of the sine-phase complex at the same $F0$ in the graphs showing stimulus waveforms, and of the maximum instantaneous amplitude of the simulated auditory-filter response to the same phase complex in the graphs showing filter outputs. Over the time slice shown, the simulated filter output was in steady state. Details on the simulation parameters are provided in footnote 2.

B. Stimuli

Harmonic complex tones with the same parameters as those in experiment 1 were used, but the phase of the components was altered. Whereas in experiment 1, all components had a constant starting phase of 0 degree in this experiment, the odd-numbered harmonics had a starting phase of 0 degree but the even-numbered harmonics had a starting phase of 90 degree. The effect of summing the components using such an alternating-phase scheme are made clear by comparing the left panels of Figs. 2 and 3; it can be seen that the repetition rate of the waveform is doubled in the alternating-phase condition relative to the constant sine-phase condition.

C. Results

Figure 4 shows that in the alternating-phase condition, the contralateral suppression of TEOAE amplitude decreased monotonically with increasing $F0$. A two-way RMANOVA similar to that used in the processing of the results of the first experiment indicated a significant effect of $F0$ [$F(3,66) = 5.42$, $p < 0.005$]. Comparison of the results of the present and previous experiments was performed by means of a three-way RMANOVA involving the harmonic phase relationship—i.e., sine or alternating the level, and the $F0$ of the contralateral stimulus as factors and the TEOAE suppression as a dependent variable. The results revealed a significant interaction between the phase and $F0$ factors [$F(3,66) = 5.25$, $p < 0.005$], indicating a difference between the influence of the $F0$ on the contralateral TEOAE suppression between the present and the previous experiments. *Post hoc* comparisons using pairwise *t*-tests indicated that at 50 dB SL, the TEOAE amplitude attenuation elicited by the 100-Hz $F0$ contralateral complex was significantly larger in the sine- than in the alternating-phase condition ($t = 2.77$, $p < 0.05$, $df = 23$); at the same stimulus level, the attenuation produced by the 100-Hz $F0$ complex in sine phase was also significantly larger than that produced by the 50-Hz $F0$ complex in alternating phase ($t = 2.17$, $p < 0.05$, $df = 23$). At 40 dB SL, the only difference observed between the attenuation effects obtained in the two phase conditions was for complexes having an $F0$ of 200 Hz, with the sine-phase condition lending to larger TEOAE attenuation than the alternating-phase condition at this $F0$ ($t = 2.60$, $p < 0.05$,

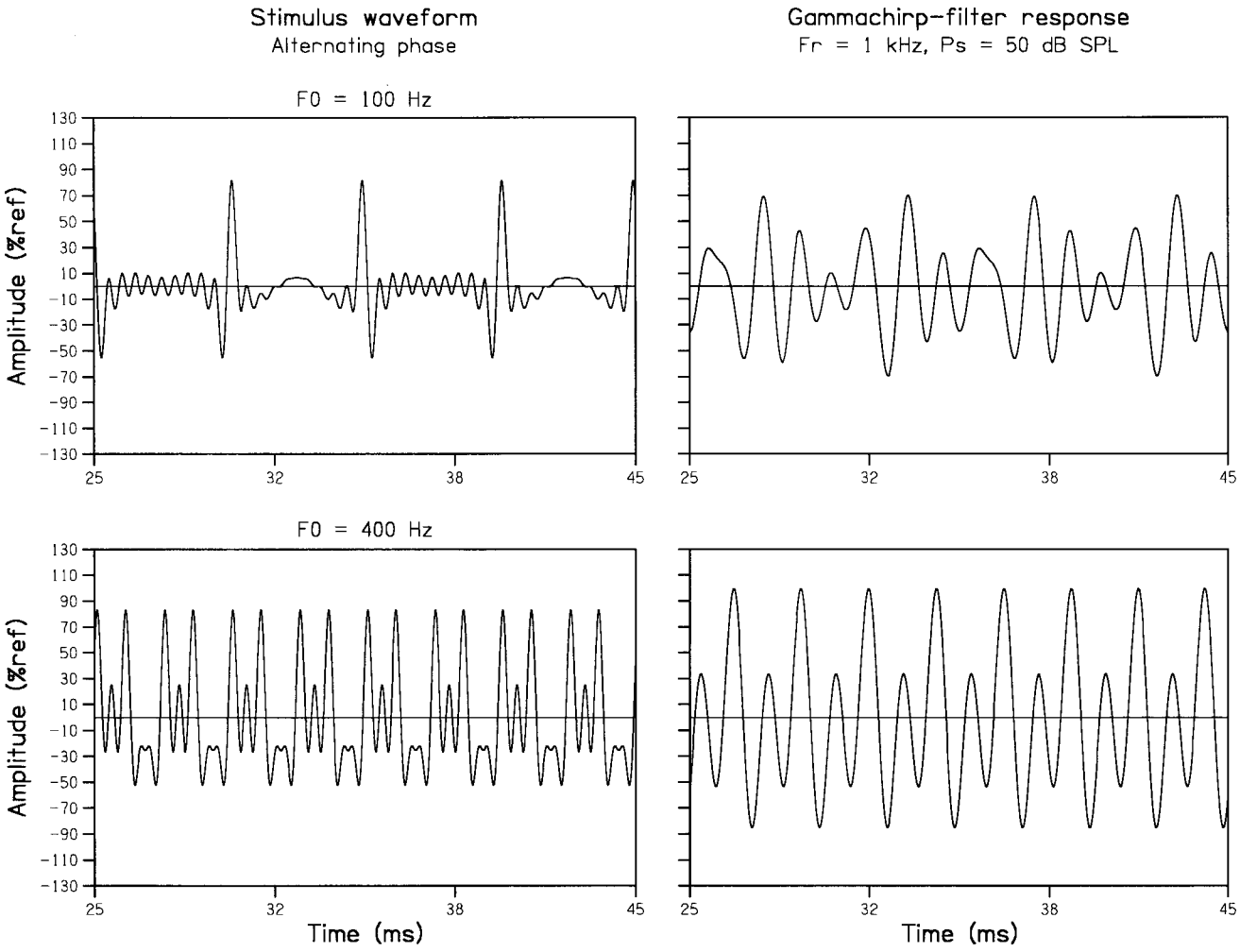

FIG. 3. Examples of waveforms (left) and simulated auditory-filter outputs (right) corresponding to alternating-phase harmonic complexes used in experiment 2. Top: *F*0 of the harmonic complex stimulus set to 100 Hz. Bottom: *F*0 of the harmonic complex stimulus set to 400 Hz. The amplitude is expressed in percent of a reference consisting of the maximum instantaneous amplitude of the sine-phase complex at the same *F*0 in the graphs showing stimulus waveforms, and of the maximum instantaneous amplitude of the simulated auditory-filter response to the same phase complex in the graphs showing filter outputs. Over the time slice shown, the simulated filter output was in steady state. Details regarding the auditory-filter simulations are provided in footnote 2.

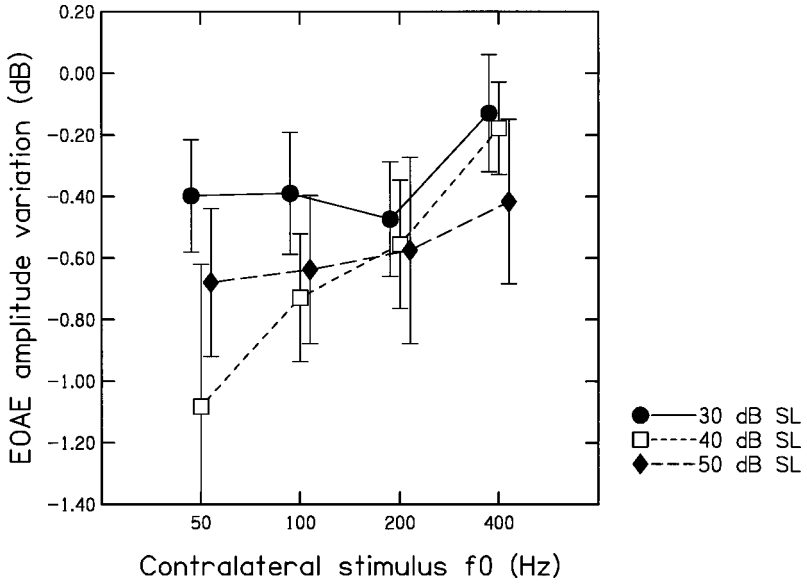

FIG. 4. TEOAE amplitude variation as a function of contralateral stimulus *F*0 for contralateral stimuli consisting of alternating-phase harmonic complexes. The different symbols and lines represent results obtained for complexes with different levels per component. Changes in TEOAE amplitude are expressed relative to the TEOAE amplitude measured in absence of contralateral stimulation. Negative values on the ordinate indicate a decrease in TEOAE amplitude upon contralateral stimulation; positive values indicate an increase. The data points represent the average across subjects. The error bars indicate the variability across subjects expressed as the standard error of the mean.

$df = 25$). At the lowest stimulus level considered (30 dB SL), no significant difference was observed whatsoever between the attenuation effects obtained in the two harmonic-phase conditions.

D. Discussion

In both this and the previous experiment, a substantial dependence of the variations in TEOAE amplitude induced by a contralateral harmonic tone on the $F0$ of this tone were observed. However, as confirmed by the significant interaction of the phase and $F0$ factors in the previous analysis, this dependence was not the same in the two experiments. The only difference between the stimuli used in these two experiments is that, while in the first the harmonics were summed in sine phase, in the second they were summed in alternating phase. Because the magnitude spectrum of the contralateral stimulus was left unaffected by this phase manipulation, the finding of a difference in the results of the two experiments brings support to the notion that a factor other than the frequency spacing between components underlies the observed dependency of the TEOAE suppression on the contralateral stimulus $F0$. Consequently, changes in the temporal fluctuation rate of the contralateral stimulus envelope that occurred with variations in $F0$ appear as the most likely factor of the observed dependency. The difference in the shape of the function relating TEOAE attenuation to $F0$ between the sine- and alternating-phase conditions further argues for this hypothesis: the shift of this function towards lower $F0$'s from the first to the second experiment is consistent with the fact that summing the components in the alternating phase increased the temporal fluctuation rate of the stimulus temporal envelope relative to the sine condition. Due to the fact that this fluctuation rate was doubled by summing the harmonics in the alternating rather than the sine phase, it could have been expected that the TEOAE attenuation effect elicited by a contralateral stimulus having an $F0$ of 50 Hz in the second experiment would be comparable to the TEOAE attenuation effect produced by a stimulus having an $F0$ of 100 Hz in the first experiment. Using the same line of reasoning, the attenuation effect obtained with an $F0$ of 100 Hz in the first experiment should be comparable to that obtained using an $F0$ of 200 Hz in the second experiment. In spite of the overall consistency of the experimental results with those predictions, it is worth noting that some of the outcomes of the detailed statistical comparison between the results of the two experiments did not entirely fit into the picture. In particular, the effect obtained using an $F0$ of 50 Hz in the second experiment proved to be significantly smaller than that obtained using an $F0$ of 100 Hz in the first experiment.

The first possible reason for such a discrepancy can be easily understood by considering the output of auditory filters in response to harmonic complexes in alternating phase at different $F0$'s, which are shown in Fig. 3. It can be seen that at an $F0$ of 100 Hz, the envelope of the filter output follows that of the stimulus and repeats itself at the same rate, while at an $F0$ of 400 Hz, the filter output envelope contains half as many peaks as that of the stimulus waveform. Consequently, at this high $F0$, the rate of temporal fluctuations in the filter output is unaffected by the phase

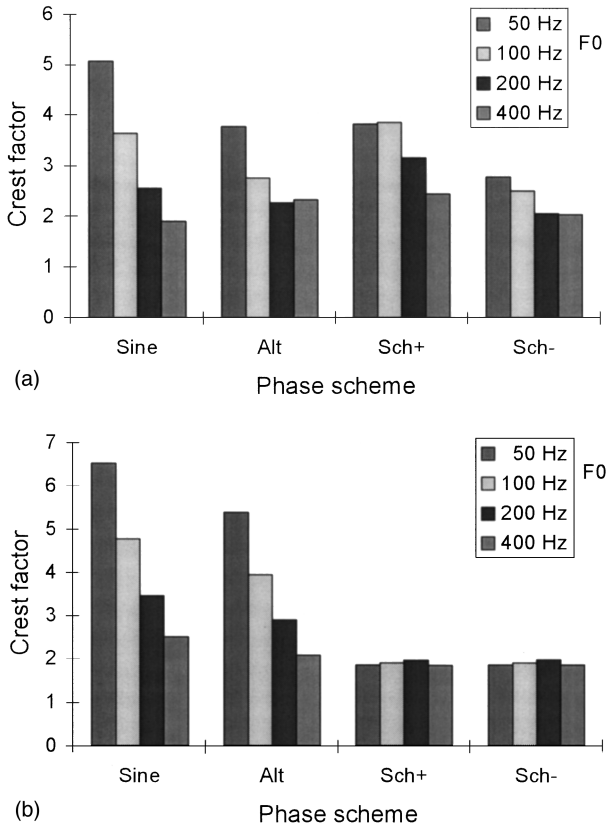

FIG. 5. Crest factors of harmonic complexes for different $F0$'s and harmonic-phase relationships. (a) Crest factors of the stimulus waveforms. (b) Crest factors at the output of a gammachirp auditory filter centered on 1000 Hz, at an input level of 50 dB SPL.

relationship of the harmonics—as confirmed by comparison with the response to a sine-phase complex at the same $F0$ shown in Fig. 2. This phenomenon comes from the fact, already mentioned in the discussion of the first experiment, that at the highest $F0$, the filter output is dominated by only two components. This phenomenon may explain why no difference was observed between the experimental results obtained in the sine- and alternating-phase conditions for complexes having an $F0$ as high as 400 Hz.

The second possible reason for which the TEOAE attenuation effects elicited by sine-phase and alternating-phase stimuli were significantly different, even when $F0$'s leading to equal envelope fluctuation rates in the two phase conditions were considered, relates to differences in the amount of envelope fluctuations produced by the two phase conditions. Previous results (Maison *et al.*, 1997, 1998b) indicating an influence of the modulation depth of contralateral tones on TEOAE suppression suggest that the size of the fluctuations in the envelope of the contralateral stimulus is a factor of the effect. The crest factors of the sine- and alternating-phase complexes used in the present study are shown in Fig. 5(a). The former are, on average, about 17% larger than the latter. Differences between alternating- and sine-phase complexes can also be seen in the responses of the simulated auditory filters shown in Fig. 5(b); the crest factor of the filter output in response to the 50- and 100-Hz complexes is about 25% larger in the sine- than in the alternating-phase condition.

This suggests that not only the rate, but also the size of the envelope fluctuations in the peripheral auditory response to a stimulus is a factor of the contralateral EOAE suppression effect elicited by that stimulus. The third experiment, which is presented below, aimed to test this interpretation further.

IV. EXPERIMENT 3: COMPARISON OF CONTRALATERAL TEOAE ATTENUATION ELICITED BY POSITIVE AND NEGATIVE SCHROEDER-PHASE HARMONIC COMPLEXES

A. Rationale

Previous results suggest that, at equal SLs stimuli whose temporal envelope shows fluctuations in amplitude over time constitute more efficient contralateral suppressors of TEOAE amplitude than stimuli with a steady envelope; in particular, AM tones or noises have been shown to elicit significantly larger contralateral TEOAE attenuation than their unmodulated versions (Maison *et al.*, 1997, 1998b). The hypothesis that the size of the fluctuations in the envelope of the contralateral stimulus is a factor in the contralateral TEOAE attenuation effect was further suggested by the observation, in the same study, that TEOAE suppression increased with contralateral stimulus modulation depth (Maison *et al.*, 1997). This hypothesis is consistent with the results of the second experiment of the present study, which reveal smaller effects of alternating- rather than sine-phase stimuli. However, rather than fluctuations in the stimulus itself, fluctuations in the excitation that this stimulus produces in the auditory system are likely to constitute an actual factor in the contralateral TEOAE attenuation effect. This might explain why broadband noises and FM tones, though their temporal envelope is flat, produce large contralateral TEOAE amplitude attenuation (Maison *et al.*, 1998a); after processing in the cochlea, wideband noises are transformed into bandpass noises exhibiting envelope fluctuations which increase with decreases in the bandwidths of the auditory filters through which they pass, and FM tones, by sweeping through the passband of different auditory filters, induce AM at the output of these filters. Experiment 3 further tested the influence of temporal envelope fluctuations by exploiting the possibility of adjusting the phase relationship of the harmonics in complex tones so as to emphasize the differences in their ''physiological'' crest factors—i.e., the magnitude of the temporal envelope fluctuations in auditory system activity that they elicit—while leaving their physical crest factor unchanged. The prediction was that stimuli with equal ''physical'' crest factors but different physiological crest factors would produce different amounts of contralateral TEOAE attenuation.

B. Stimuli

Stimuli consisted of harmonic complexes with the same upper and lower frequency bounds used in the previous experiments—i.e., 400 and 2000 Hz—but with components summed in Schroeder phase, as defined by the following formula (Schroeder, 1970); $\theta_n = \pm \pi n(n+1)/N$, where θ_n is the phase of the nth harmonic in radians and N is the number of harmonics in the complex. The sign in front of the right term is chosen depending on whether one wants to produce a positive or negative Schroeder-phase complex.

The interesting properties of positive and negative Schroeder-phase complexes with respect to the functioning of the peripheral auditory system are illustrated in Fig. 6. As can be seen by comparing the top-left and bottom-left panels of this figure, the waveforms of positive and negative Schroeder-phase complexes are simply time-reversed and inverted versions of each other. However, as shown in the right panels of the same figure, when passed through simulated auditory filters, the positive Schroeder-phase complex produces an output with a many-peaked envelope, whereas the negative Schroeder-phase complex produces an output with a very smooth envelope. The interpretation for this property is that the phase gradient of the stimulus adds to that of the auditory filter so that it is increased when of the same sign, or decreased, and eventually cancelled, when of a different sign (Smith *et al.*, 1986). This interpretation has received experimental support in several studies (Kohlrausch and Sander, 1995; Carlyon and Datta, 1997a,b).

In this third experiment, Schroeder-phase complexes were used as a means of testing the sensitivity of contralateral TEOAE attenuation to the magnitude of temporal envelope fluctuations in the responses of the peripheral system to the contralateral stimulus. $F0$'s of 100 and 200 Hz, at which differences between positive and negative Schroeder-phase complexes were evidenced in previous studies (Smith *et al.*, 1986; Kohlrausch and Sander, 1995; Carlyon and Datta, 1997a,b) were used and contralateral stimulation levels of 40 and 50 dB SL were tested.

C. Results

No substantial difference was observed between the effects of positive and negative Schroeder-phase complexes (Fig. 7). A three-way RMANOVA involving as factors the contralateral stimulus phase sign, level, and $F0$ indicated no significant main effects of these factors or significant interactions between them. Furthermore, when comparing the TEOAE attenuation measured using Schroeder-phase complexes to that obtained using sine- or alternating-phase complexes, no significant difference was obtained. Pairwise comparisons further revealed that Schroeder-phase complexes significantly reduced the contralateral amplitude of EOAEs in only two conditions: in positive Schroeder phase at 40 dB SL ($t=3.10$, $p=0.005$, $df=24$) and in negative Schroeder phase at 50 dB SL ($t=3$, $p<0.01$, $df=23$),[3] with an $F0$ of 200 Hz in both cases.

D. Discussion

The results of this experiment failed to demonstrate a difference between positive and negative Schroeder-phase harmonic complexes regarding contralateral TEOAE attenuation effects. A possible interpretation of this negative outcome is that the contralateral stimulus levels used were too low for the EOAE suppression effects of positive and negative Schroeder-phase complexes to differ significantly. Most experiments published in the literature that indicate percep-

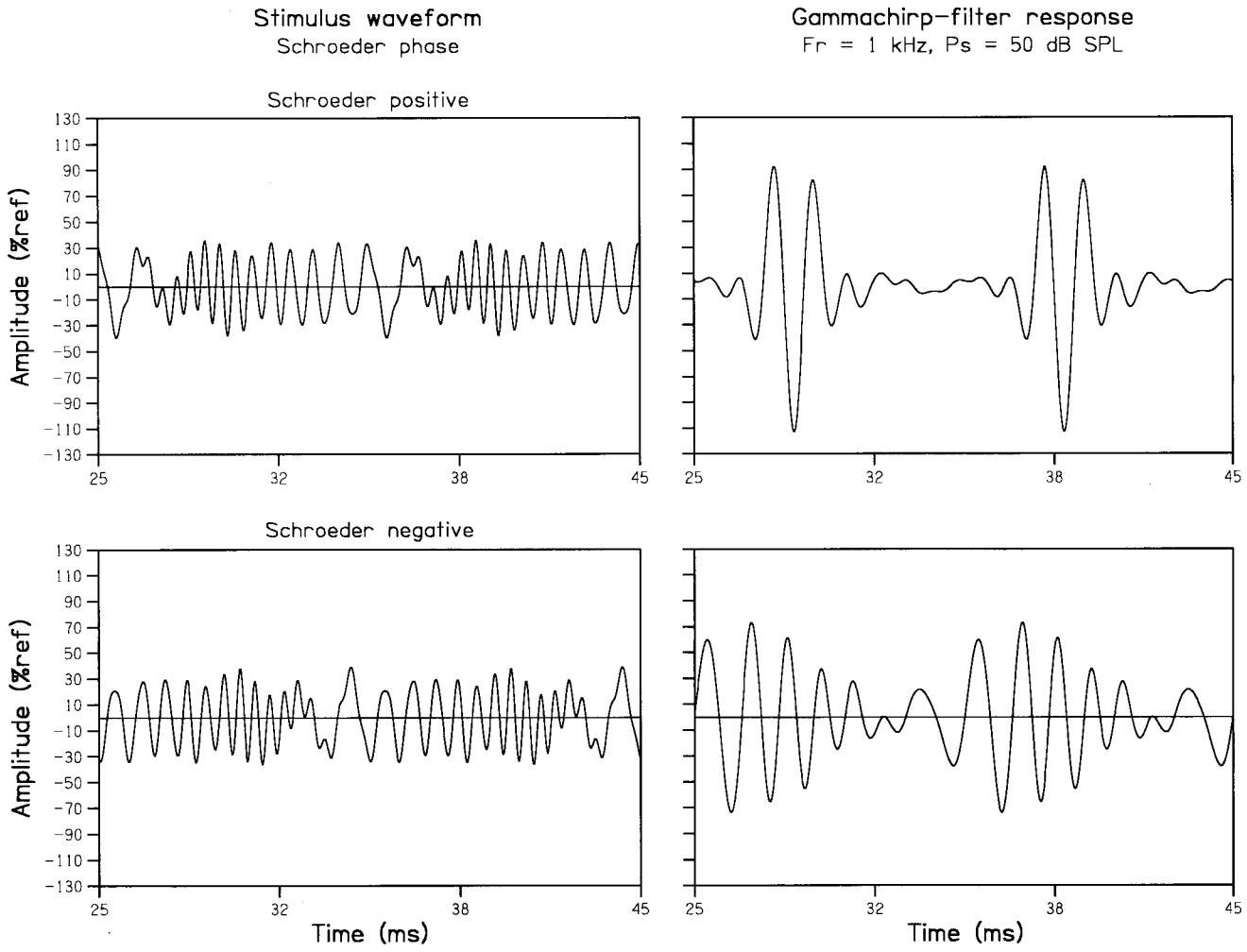

FIG. 6. Examples of waveforms (left) and simulated auditory-filter outputs (right) corresponding to Schroeder-phase harmonic complexes used in experiment 3. Top: positive Schroeder-phase condition. Bottom: negative Schroeder-phase condition. The *F*0 was 100 Hz in both cases. The amplitude is expressed in percent of a reference consisting of the maximum instantaneous amplitude of the 100-Hz sine-phase complex in the graphs showing stimulus waveforms and of the maximum instantaneous amplitude of the simulated auditory-filter response to that 100-Hz sine-phase complex in the graphs showing filter outputs. Over the time slice shown, the simulated filter output was in steady state. Details regarding the auditory-filter simulation are provided in footnote 2.

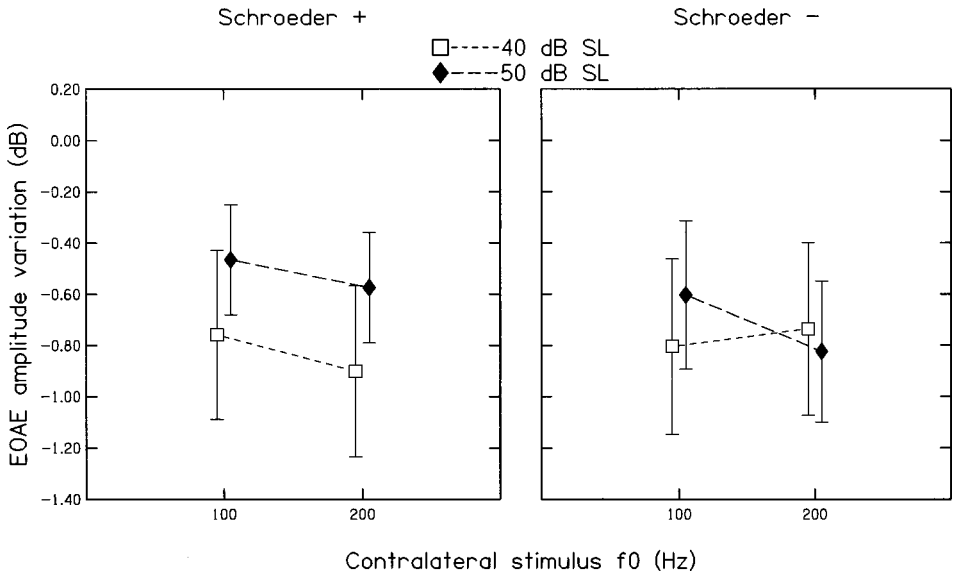

FIG. 7. TEOAE amplitude variation as a function of contralateral stimulus *F*0 for contralateral stimuli consisting of alternating-phase harmonic complexes. The different symbols and lines represent results obtained for complexes with different levels per component. Changes in TEOAE amplitude are expressed relative to the TEOAE amplitude measured in absence of contralateral stimulation. Negative values on the ordinate indicate a decrease in TEOAE amplitude upon contralateral stimulation; positive values indicate an increase. The data points represent the average across subjects. The error bars indicate the variability across subjects expressed as the standard error of the mean.

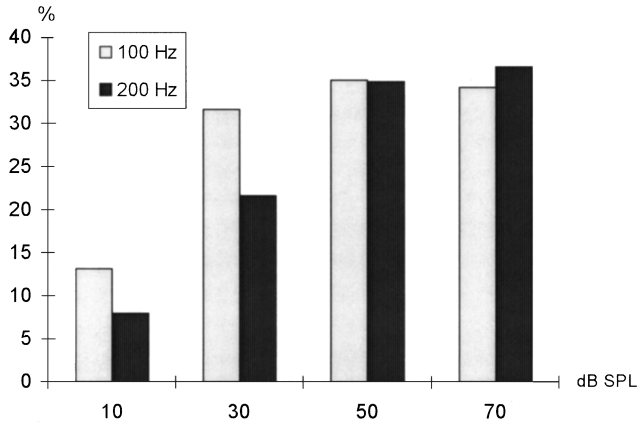

FIG. 8. Percent differences in the crest factors of gammachirp auditory-filter responses to positive and negative Schroeder-phase complexes as a function of level, at $F0$'s of 100 and 200 Hz.

tual differences between positive and negative Schroeder-phase complexes involved stimulus levels between about 55 and 69 dB SPL per component (Smith *et al.*, 1986; Kohlrausch *et al.*, 1995; Carlyon and Datta, 1997a,b). In normal-hearing subjects, the SLs of 30, 40, and 50 dB used here can be estimated to correspond to SPLs per component of about 29, 39, and 49 dB.[4] Higher stimulus levels were avoided because of the likely occurrence of transcranial transfer and middle-ear effects at levels of about 60 dB SL (Veuillet *et al.*, 1991). Although data by Carlyon and Datta (1997a) suggest that differences in forward-masking effects between positive and negative Schroeder-phase complexes start to arise progressively at levels above about 40 dB SPL per component, these data also show that the effects decrease drastically with level. This effect can be explained by the fact that as the stimulus level is reduced, first, cochlear compression is reduced and, second, the auditory-filter bandwidth becomes too small for a sufficient number of harmonics to interact within the filter passband. The latter phenomenon can be explained in part on the basis of differences in the crest factors of the simulated gammachirp auditory-filter responses to positive and negative Schroeder-phase complexes, which are represented in Fig. 8; as can be seen, these differences are larger at higher, rather than lower, levels. It may be the case that at the stimulus levels used in this study, the differences in peripheral auditory-filter outputs between positive and negative Schroeder-phase complexes may have been too small to lead to differences in contralateral EOAE attenuation.

Once the fact that experiment 3 results cannot be accounted for in terms of the crest factors after peripheral auditory filtering is acknowledged, it is worth considering the crest factors before auditory filtering. As can be seen in Fig. 5(a), the crest factors of the positive and negative Schroeder-phase complexes are smaller than those of the sine-phase signals (by about 60% at an $F0$ of 100 Hz and 43% at an $F0$ of 200 Hz). This observation fits very well into the view suggested earlier in the comparison of experiments 1 and 2, according to which the amount of contralateral EOAE attenuation elicited by a stimulus is positively related to the crest factor of this stimulus. It is consistent with the fact that Schroeder-phase complexes did not systematically elicit significant TEOAE suppression at the two $F0$'s tested, whereas the sine-phase complexes did.

V. SUMMARY AND CONCLUSION

The findings of this study can be summarized as follows: Significant attenuation of TEOAE amplitude can be obtained using harmonic complex tones as contralateral stimuli at levels as low as 30 dB SL. For sine-phase complexes, there exists a strong dependence of the amount of TEOAE attenuation on the $F0$ of the contralateral complex; the largest and most significant effects are obtained for $F0$'s of 100 and, to a lesser extent, 200 Hz. From that point of view, the dependence of contralateral TEOAE attenuation on $F0$ shown in this study is comparable to the dependence on AM rate shown in previous studies (Maison *et al.*, 1997, 1998b). As suggested by the fact that the largest effects are obtained for lower $F0$'s when the harmonics are summed in alternating- instead of constant-sine phase, the observed dependence of TEOAE attenuation on $F0$ is determined by the repetition rate of the waveform, rather than by the frequency spacing between components. This finding agrees with the notion, suggested by previous results, that the rate of temporal fluctuations in the contralateral stimulus envelope are an important factor of contralateral TEOAE attenuation effects. However, the hypothesis that the amount of fluctuations at the output of the peripheral auditory filters in response to the contralateral stimulus determines the amount of TEOAE attenuation failed to be supported by the comparison of contralateral TEOAE attenuation effects elicited by positive and negative Schroeder-phase complexes. Overall, the results are in agreement with the notion that the amount of contralateral suppression depends on both the number and relative size of peaks in the stimulus waveform.

ACKNOWLEDGMENTS

The work presented in this study was performed in the framework of an international joint research project between the Centre National de la Recherche Scientifique and the Medical Research Council. Toshio Irino and Roy Patterson are acknowledged for providing the MATLAB code of the ''gammachirp'' auditory filter, which was used in the simulations presented in this paper. Johannes Lyzenga is acknowledged for helpful comments.

[1]Using Bonferroni's correction, the critical probability corresponding to the significance level (0.05) was divided by four to account for the fact that four pairwise comparisons were made on the same set of data at each contralateral stimulus level considered. The resulting critical probability was thus 0.0125.

[2]All the auditory-filter simulations presented in this article were performed using the ''gammachirp'' filter defined by Irino and Patterson (1997). The impulse response of this filter is: $g_c(t)=at^{n-1}\times\exp(-2\pi b\mathrm{ERB}(f_r)t)\cos(2\pi f_r t+c\ln(t)+\phi)$, where a, b, n, c, and f_r are parameters. In all simulations, a was set to 1 and the amplitude of both the input stimulus and the filter response were normalized so that their maximum absolute instantaneous amplitude was 1. The level dependence of the filter was taken into account by making the parameter c a function of the input level of the filter P_s; following the results of Irino and Patterson (1997), c was set to $-0.109P_s$, with $P_s=50$ dB SPL. Parameters n and b were assigned their suggested default values: 4 and 1.51, respectively. f_r

defines the resonance frequency of the filter, in Hz. ERB(f_r) is the equivalent rectangular bandwidth of the filter of characteristic frequency f_r according to the formula given in Glasberg and Moore (1990); ERB(f_r) $= 24.7 + 0.108 f_r$. The resonance frequency (f_r) of the simulated auditory filter was set to the frequency of the ipsilateral tone pip used to evoke EOAEs: 1000 Hz. This choice of resonant frequency was motivated by the assumption that the influence of a contralateral stimulus in one ear on the amplitude of tone-pip EOAEs recorded in the opposite ear mainly depend on those components of the contralateral stimulus that fall around the frequency at which EOAEs are evoked. This assumption, which was made in this and other studies for simplification, is based on the known tonotopic correspondence of afferent and efferent pathways from and to the cochlea.

[3]These statements were true after application of Bonferroni's correction to account for four comparisons—two Schroeder-phase-gradient signs × two $F0$'s—which brought the critical probability down to 0.0125. It is worth mentioning that the significance level (p's) obtained in all the considered pairwise comparisons were below 0.05. Therefore, it cannot be excluded that some of these pairwise comparisons could have indicated significant differences if a correction less conservative than Bonferroni's had been applied.

[4]The threshold of complex tones with about the same number of components as the 100-Hz complex used in this study ($N = 17$)has been shown to be about 6 dB lower than that of a tonal component in isolation (Green *et al.*, 1959). The absolute threshold for a tone at 1000 Hz is, on average, 7 dB SPL (ANSI standard 1969, TDH39 earphones). Consequently, it can be estimated that the SPL per component at the highest SL tested in this study was approximately 49 dB.

ANSI (**1969**). ANSI S3. 6-1969, ''Specifications for audiometers'' (American National Standards Institute, New York).

Berlin, C. I., Hood, L. J., Cecola, R. P., Jackson, D. F., and Szabo, P. (**1993**). ''Contralateral suppression of non-linear click-evoked otoacoustic emissions,'' Hearing Res. **71**, 1–11.

Bray, P., and Kemp, D. T. (**1987**). ''An advanced cochlear echo technique suitable for infant screening,'' Br. J. Audiol. **21**, 191–204.

Buño, W. (**1978**). ''Auditory nerve activity influenced by contralateral ear sound stimulation,'' Exp. Neurol. **59**, 62–74.

Capps, M. J., and Ades, H. W. (**1968**). ''Auditory frequency discrimination after transection of the olivo-cochlear bundle in squirrel monkeys,'' Exp. Neurol. **21**, 147–158.

Carlyon, R. P., and Datta, A. J. (**1997a**). ''Excitation produced by Schroeder-phase complexes: Evidence for fast-acting compression in the auditory system,'' J. Acoust. Soc. Am. **101**, 3636–3647.

Carlyon, R. P., and Datta, A. J. (**1997b**). ''Masking period patterns of Schroeder-phase complexes: Effects of level, number of components, and phase of flanking components,'' J. Acoust. Soc. Am. **101**, 3648–3657.

Collet, L., Kemp, D. T., Veuillet, E., Duclaux, R., Moulin, A., and Morgon, A. (**1990**). ''Effect of contralateral auditory stimuli on active cochlear micromechanical properties in human subjects,'' Hearing Res. **43**, 251–262.

Collet, L., Veuillet, E., Bene, J., and Morgon, A. (**1992**). ''Effects of contralateral white noise on click-evoked emissions in normal and sensorineural ears: Towards and exploration of the medial olivo-cochlear system,'' Audiology **31**, 1–7.

Dewson, J. H. (**1968**). ''Efferent olivocochlear bundle: some relationships to stimulus discrimination in noise,'' J. Neurophysiol. **31**, 122–130.

Dolan, D. F., and Nuttall, A. L. (**1988**). ''Masked cochlear whole-nerve response intensity functions altered by electrical stimulation of the crossed olivocochlear bundle,'' J. Acoust. Soc. Am. **83**, 1081–1086.

Galambos, R. (**1956**). ''Suppression of auditory-nerve fiber activity by stimulation of efferent fibers to the cochlea,'' J. Neurophysiol. **19**, 424–437.

Gifford, M. L., and Guinan, J. J. (**1987**). ''Effects of electrical stimulation of medial olivocochlear neurons on ipsilateral and contralateral cochlear responses,'' Hearing Res. **29**, 179–194.

Giraud, A. L., Collet, L., Chery-Croze, S., Magnan, J., and Chays, A. (**1995**). ''Evidence of medial olivocochlear involvement in contralateral suppression of otoacoustic emissions in humans,'' Brain Res. **705**, 15–23.

Glasberg, B. R., and Moore, B. C. J. (**1990**). ''Derivation of auditory filter shapes from notched-noise data,'' Hearing Res. **47**, 103–138.

Green, D. M., McKey, M. J., and Licklider, J. C. R. (**1959**). ''Detection of a pulsed sinusoid as a function of frequency,'' J. Acoust. Soc. Am. **31**, 1446–1452.

Gummer, M., Yates, G. K., and Johnstone, B. M. (**1988**). ''Modulation transfer function of efferent neurones in the guinea pig cochlea,'' Hearing Res. **36**, 41–52.

Hienz, R. D., Stiles, P., and May, B. J. (**1998**). ''Effects of bilateral olivocochlear lesions on vowel formant discrimination in cats,'' Hearing Res. **116**, 10–20.

Igarashi, M., Alford, B. R., Nakai, Y., and Gordon, W. P. (**1972**). ''Behavioral auditory function after transection of crossed olivo-cochlear bundle in the cat. I. Pure-tone threshold and perceptual signal-to-noise ratio,'' Acta Oto-Laryngol. **73**, 455–466.

Igarashi, M., Cranford, J. L., Allen, E. A., and Alford, B. R. (**1979a**). ''Behavioral auditory function after transection of crossed olivo-cochlear bundle in the cat. I. Pure-tone intensity discrimination,'' Acta Oto-Laryngol. **87**, 429–433.

Igarashi, M., Cranford, J. L., Nakai, Y., and Alford, B. R. (**1979b**). ''Behavioral auditory function after transection of crossed olivo-cochlear bundle in the cat. IV. Study on pure tone frequency discrimination,'' Acta Oto-Laryngol. **87**, 79–83.

Irino, T., and Patterson, R. D. (**1997**). ''A time domain, level-dependent auditory filter. The gammachirp,'' J. Acoust. Soc. Am. **101**, 412–419.

Kawase, T., and Takasaka, T. (**1995**). ''The effects of contralateral noise on masked compound action potential in humans,'' Hearing Res. **91**, 1–6.

Kawase, T., Delgutte, B., and Liberman, M. C. (**1993**). ''Antimasking effects of the olivocochlear reflex. II. Enhancement of auditory-nerve response to masked tones,'' J. Neurophysiol. **70**, 2533–2549.

Kawase, T., and Liberman, M. C. (**1993**). ''Antimasking effects of the olivocochlear reflex. I. Enhancement of compound action potentials to masked tones,'' J. Neurophysiol. **70**, 2519–2532.

Kemp, D. T., Ryan, S., and Bray, P. (**1990**). ''A guide to the effective use of otoacoustic emissions,'' Ear. Hear. **11**, 93–105.

Kohlrausch, A., and Sander, A. (**1995**). ''Phase effects in masking related to dispersion in the inner ear. II. Masking period patterns of short targets,'' J. Acoust. Soc. Am. **97**, 1817–1829.

Liberman, M. C. (**1988**). ''Response properties of cochlear efferent neurons: monaural vs binaural stimulation and the effects of noise,'' J. Neurophysiol. **60**, 1779–1798.

Littman, T. A., Cullen, Jr., J. K., and Bobbin, R. P. (**1992**). ''The effect of olivocochlear bundle transection on tuning curves and acoustic distortion products,'' J. Acoust. Soc. Am. **92**, 1945–1952.

Maison, S. *et al.* (**1997**). Personal communication.

Maison, S., Micheyl, C., and Collet, L. (**1997**). ''Medial olivocochlear efferent system in humans studied with amplitude-modulated tones,'' J. Neurophysiol. **77**, 1759–1768.

Maison S., Micheyl, C., and Collet, L. (**1998a**). ''Contralateral frequency-modulated tones suppress transient-evoked otoacoustic emissions in humans,'' Hearing Res. **117**, 114–118.

Maison, S., Micheyl, C., and Collet, L. (**1998b**). ''Sinusoidal amplitude modulation alters contralateral noise suppression of evoked otoacoustic emissions,'' Neuroscience (in press).

Manley, G. A., and Gallo, L. (**1997**). ''Otoacoustic emissions, hair cells, and myosin motors,'' J. Acoust. Soc. Am. **102**, 1048–1055.

May, B. J., and McQuone, S. J. (**1995**). ''Effects of bilateral olivocochlear lesions on pure-tone intensity discrimination in noise,'' Aud. Neurosci. **1**, 385–400.

Micheyl, C., and Collet, L. (**1996**). ''Involvement of the olivocochlear bundle in the detection of tones in noise,'' J. Acoust. Soc. Am. **99**, 1604–1610.

Micheyl, C., Morlet, T., Giraud, A. L., Collet, L., and Morgon, A. (**1995**). ''Contralateral suppression of evoked otoacoustic emissions and detection of a multi-tone complex in noise,'' Acta Oto-Laryngol. **115**, 178–182.

Micheyl, C., Perrot, X., and Collet, L. (**1997**). ''Relationship between auditory intensity discrimination in noise and olivocochlear efferent system activity in humans,'' Behav. Neurosc. **111**, 801–807.

Nieder, P., and Nieder, I. (**1970**). ''Anti-masking effects of crossed olivocochlear bundle stimulation with loud clicks in guinea pig,'' Exp. Neurol. **28**, 179–188.

Norman, M., and Thornton, A. R. D. (**1993**). ''Frequency analysis of the contralateral suppression of evoked otoacoustic emissions by narrow-band noise,'' Br. J. Audiol. **27**, 281–289.

Rajan, R. (**1988a**). ''Effect of electrical stimulation of the crossed olivocochlear bundle on temporary threshold shifts in auditory sensitivity. I. Dependence on electrical stimulation parameters,'' J. Neurophysiol. **60**, 549–568.

Rajan, R. (**1988b**). ''Effect of electrical stimulation of the crossed olivoco-

chlear bundle on temporary threshold shifts in auditory sensitivity. II. Dependence on the level of temporary threshold shifts,'' J. Neurophysiol. **60**, 569–579.

Rasmussen, G. L. (**1946**). ''The olivary peduncle and other fiber projections of the superior olivary complex,'' J. Comp. Neurol. **84**, 141–218. .

Russell, I. J., and Murugasu, E. (**1997**). ''Medial efferent inhibition suppresses basilar membrane responses to near characteristic frequency tones of moderate to high intensities,'' J. Acoust. Soc. Am. **102**, 1734–1738.

Ryan, S., Kemp, D. T., and Hinchcliffe, R. (**1991**). ''The influence of contralateral auditory stimulation on otoacoustic emission responses in humans,'' Br. J. Audiol. **25**, 391–397.

Scharf, B., Magnan, J., and Chays, A. (**1997**). ''On the role of the olivocochlear bundle in hearing: 16 case studies,'' Hearing Res. **103**, 101–122.

Scharf, B., Magnan, J., Collet, L., Ulmer, E., and Chays, A. (**1994**). ''On the role of the olivocochlear bundle in hearing: a case study,'' Hearing Res. **75**, 11–26.

Schroeder, M. R. (**1970**). ''Synthesis of low-peak factor signals and binary sequences with low autocorrelation,'' IEEE Trans. Inf. Theory **16**, 85–89.

Smith, B. K., Sieben, U. K., Kohlrausch, A., and Schroeder, M. R. (**1986**). ''Phase effects in masking related to dispersion in the inner ear,'' J. Acoust. Soc. Am. **80**, 1631–1637.

Trahiotis, C., and Elliott, D. N. (**1970**). ''Behavioral investigation of some effects of sectioning the crossed olivocochlear bundle,'' J. Acoust. Soc. Am. **47**, 592–596.

Veuillet, E., Collet, L., and Duclaux, R. (**1991**). ''Effects of contralateral acoustic stimulation on active cochlear micromechanical properties in human subjects: dependence on stimulus variables,'' J. Neurophysiol. **65**, 724–735.

Warr, W. B., and Guinan, Jr., J. J. (**1979**). ''Efferent innervation of the organ of corti: two separate systems,'' Brain Res. **173**, 152–155.

Warren, E. H., and Liberman, M. C. (**1989**). ''Effects of contralateral sound on auditory-nerve responses. I. Contributions of cochlear efferents,'' Hearing Res. **37**, 89–104.

Wiederhold, M. L., and Kiang, N. Y. S. (**1970**). ''Effects of electrical stimulation of the crossed olivocochlear bundle on single auditory nerve fibers in cat,'' J. Acoust. Soc. Am. **48**, 950–965.

Winslow, R. L., and Sachs, M. B. (**1987**). ''Effect of electrical stimulation of the crossed olivocochlear bundle on auditory nerve response to tone in noise,'' J. Neurophysiol. **57**, 1002–1021.

Winslow, R. L., and Sachs, M. B. (**1988**). ''Single tone intensity discrimination based on auditory nerve rate responses in backgrounds of quite, noise and with stimulation of the crossed olivocochlear bundle,'' Hearing Res. **35**, 165–190.

Do click-evoked otoacoustic emissions have frequency specificity?

Hiromi Ueda
Department of Otolaryngology, Nagoya University, School of Medicine, Nagoya, Japan

(Received 26 June 1998; accepted for publication 21 September 1998)

Whether click-evoked otoacoustic emissions (CEOAEs) have frequency specificity is an issue still subject to debate. In order to resolve this issue, changes in the frequency components of the CEOAE power spectrum, together with changes in compound action potential (CAP) thresholds before and after pure-tone exposure in guinea pigs, were examined. Changes in CAP thresholds immediately before and 1 h after exposure were compared with changes in the frequency components in the CEOAE power spectrum before and 1 h after exposure. The ILO 88 was used for measurement of CEOAEs. Total echo energy in the CEOAE power spectrum was converted into frequency bands of 1000 Hz. Shifts in filtered echo power (FEP) levels correlated maximally with those in CAP thresholds at 0.5 kHz above the same frequency. Stepwise regression indicated that only one step could be entered in a linear regression model using the variable of CAP threshold shifts at 0.5 kHz above the same frequency for all FEP shifts except FEP4.5. The remaining variables played a negligible role, since variance no longer changed when they were included in the regression equation. From these results, it was concluded that CEOAEs display frequency specificity. Influence on CEOAEs from higher frequencies is negligible. © *1999 Acoustical Society of America.* [S0001-4966(99)01001-2]

PACS numbers: 43.64.Jb, 43.64.Nf, 43.64.Wn [BLM]

INTRODUCTION

Otoacoustic emissions (OAEs) are thought to be linked with the function of the outer hair cells, and to reflect the active process in the cochlea. If OAEs reflect the state of a specific region along the cochlea, they can be useful as a research or clinical tool for noninvasive assessment of cochlear function. Distortion product otoacoustic emission (DPOAE) is thought to be frequency specific in both clinical research (Avan and Bonfils, 1993) and animal studies (Schmiedt, 1986; Martin *et al.*, 1987). As for transiently evoked otoacoustic emissions, click-evoked otoacoustic emissions (CEOAEs) are generally measured in diagnostic settings. Kemp *et al.* (1990) and Norton (1993) suggest that a CEOAE's particular frequency component arises from the place in the cochlea tuned to that frequency in humans. On the other hand, Wilson (1980) and Avan *et al.* (1991a) assume that CEOAEs result from the total or partially summed contribution of mechanisms distributed along the basilar membrane, and had some doubts about the frequency specificity of CEOAEs. Avan *et al.* (1995) investigated relationships between CAP thresholds and CEOAEs before and after pure-tone exposure at relatively high frequencies, and reported that CEOAE components changed slightly at lower frequencies, at which CAP thresholds did not change. Recently, Ueda *et al.* (1997) found that the time course of recovery for component action potential (CAP) thresholds after acoustic overstimulation was similar to that of the CEOAE power spectrum's frequency components in guinea pigs. They also reported that changes in CAP thresholds were significantly correlated to those in components of the CEOAE power at the same frequencies. But the influence of other frequency sites could not be assessed, because any CAPS, except at a single frequency, were not measured in each experiment. Whether a CEOAE component reflects the state of a particular site of the basilar membrane is still questionable.

In this study, the changes of CEOAEs and CAP thresholds were measured at selected frequencies in guinea pigs after pure-tone acoustic overstimulation, which can cause a temporary local injury to the cochlea. Unlike the report of Avan *et al.* (1995), the exposure tones were the frequencies at which CEOAE components could be influenced. Whether a CEOAE component reflects the state of a particular site of the basilar membrane in guinea pigs was tested by comparing frequency-component shifts in the CEOAE's frequency power spectrum with CAP threshold shifts at selected frequencies before and after exposure.

I. METHODS

Healthy white guinea pigs, each weighing about 200 g ($N=22$), were anesthetized with ketamine (100 mg/kg), placed in a soundproof chamber, and restrained with a head holder. Tracheotomy was performed under spontaneous breathing control. After the cartilaginous external ear canal had been cut away, a customized metal tube was inserted into the ear canal. For measurement of CAPs and pure-tone exposure, a commercial earphone (Sony MDR-E 565, Tokyo) was attached to the metal tube. A silver electrode was placed on the auditory bulla near the styloid process as a negative input. A positive input was placed at the test ear mastoid. Calibration of the sound-pressure level was performed through the hole made in the external ear canal using the B & K probe microphone (type 4182). A tone burst of 1 ms in rise–fall time and 3 ms in duration time was delivered through the earphone at a rate of 10/s, and transient responses were averaged 100 times. CAPs at 1, 2, 3, 4, 6, and 8 kHz were measured, respectively. The visual detection-

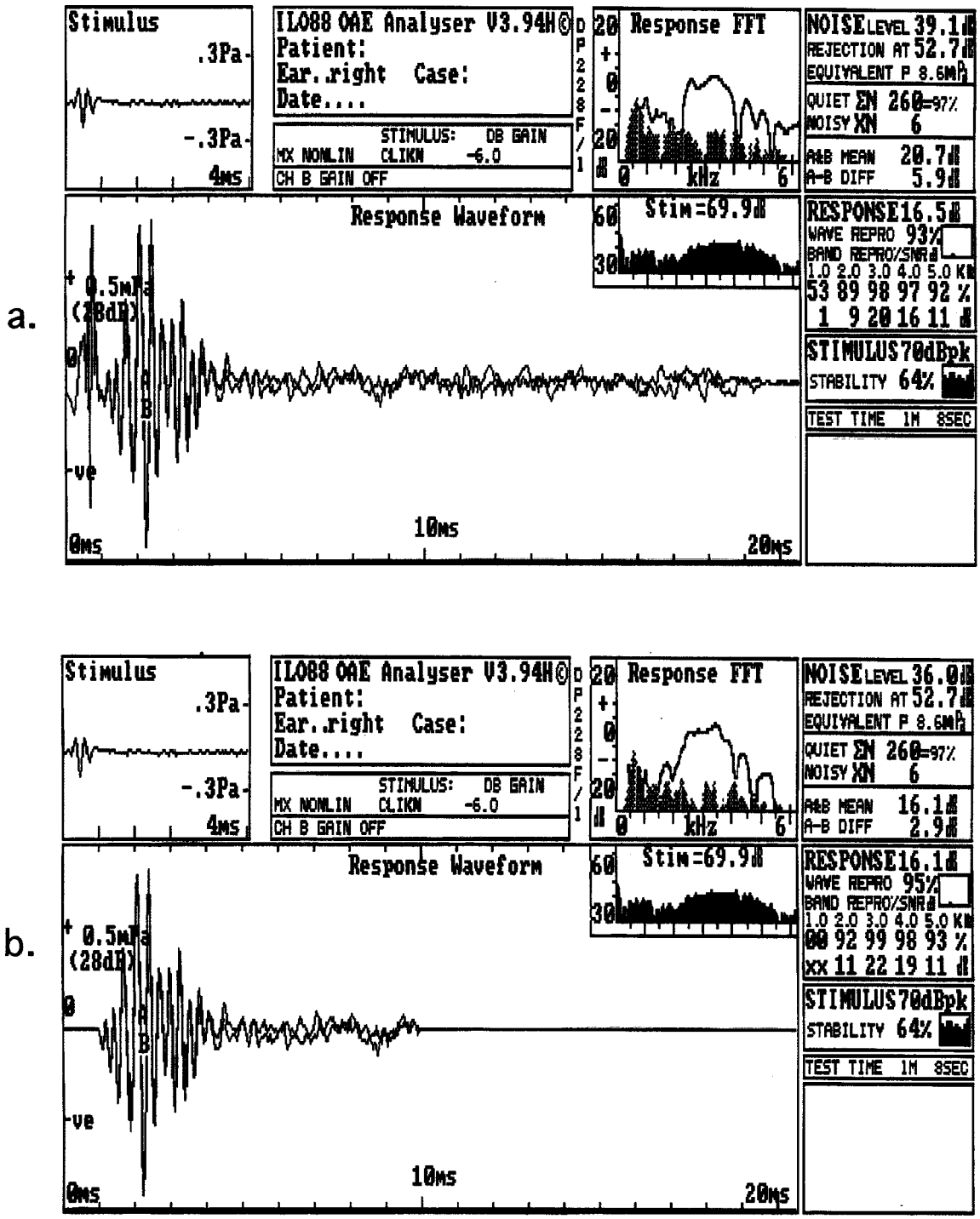

FIG. 1. One representative example of the acoustic waveform and power spectrum of the response and the stimulus. Upper figure (a) shows original waveform. Lower figure (b) shows the waveform after the time window was set from 1 to 10 ms after stimulus onset.

threshold level was measured via 5-dB decrements. Measurement of CEOAEs was made using an otodynamic analyzer ILO88 (Bray and Kemp, 1987; Ueda *et al.*, 1992). An E-type neonate OAE probe for the ILO88 was attached to the metal tube instead of to the earphone. Transient responses to nonlinear clicks at 72 ± 2 dB SPL were averaged 260 times. Generally, acoustic ringing in individual ear canals decreases in amplitude as time elapses and disappears after 1 ms at 70 dB SPL [Fig. 1(a)]. On the other hand, since CEOAEs increase in amplitude from 1 ms after stimulus onset, CEOAEs can easily be detected visually. After CEOAEs were distinguished from acoustic ringing in individual ear canals, the time window was then set from 1 to 10 ms after stimulus onset [Fig. 1(b)]. From total echo energy in the two independent echo responses' cross-power spectrum, a more precise analysis was conducted after conversion into frequency bands of 1000 Hz. Five frequency bands between 0.5 and 5.5 kHz were analyzed as follows: FEP (filtered echo power) 1=0.5–1.5 kHz, FEP2=1.5–2.5 kHz, FEP3=2.5–3.5 kHz, FEP4=3.5–4.5 kHz, and FEP5=4.5–5.5 kHz. In another

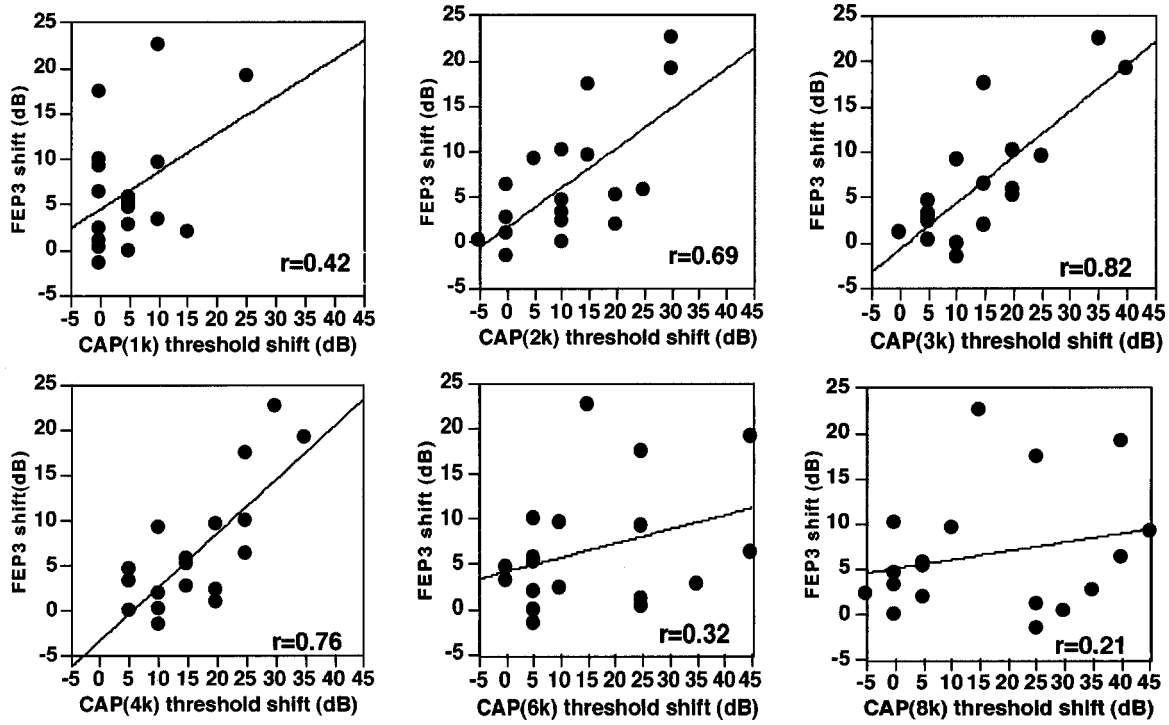

FIG. 2. Relationships between the shifts of FEP3 and those of each CAP threshold before and 1 h after exposure. Values indicate correlation coefficient.

analysis, other five-frequency bands between 1 and 6 kHz were used: FEP1.5=1–2 kHz, FEP2.5=2–3 kHz, FEP3.5 =3–4 kHz, FEP4.5=4–5 kHz, and FEP5.5=5–6 kHz.

First, CEOAEs and CAPs were measured, and then CEOAEs were observed every 10 min for 30 min. When the CEOAEs were considered stable, pure-tone stimuli were produced in a closed system for 3 or 6 min. Then the CEOAEs were measured every 10 min until 1 h after exposure. After 1 h, CAPs were measured. Then the CEOAEs were measured again in order to check their stability.

As a control, the CEOAEs without any exposure ($N=4$) were measured. Exposed pure tones were 0.5 kHz at 120 dB SPL for 3 min ($N=4$), 1 kHz at 120 dB SPL for 3 min ($N=4$), 2 kHz at 105 dB SPL for 3 min ($N=4$), 4 kHz at 115 dB SPL for 3 min ($N=4$), and 6 kHz at 105 dB SPL for 6 min ($N=2$). Each animal was exposed only once.

Correlation coefficients and step-wise regression analyses were calculated with Macintosh software (SUPER ANOVA ver. 1.11, Abacus Concepts, Inc., Berkeley, CA, USA).

II. RESULTS

Figure 1 shows one representative example for the acoustic waveform and power spectrum of the response and the stimulus. The response power spectrum showed no echo power above 5.5 kHz.

During control sessions, in which animals were kept unexposed for 1 h, the maximum difference in FEP level among those measurements was smaller than 2 dB.

A. Relationships between FEP and CAP threshold

Figure 2 shows the relationship between the FEP3 shifts and those of each CAP threshold before and 1 h after exposure. The correlation coefficient between FEP3 shift and CAP-threshold shift at 3 kHz was highest ($r=0.82$), followed by that between FEP3 shift and CAP-threshold shift at 4 kHz. On the other hand, the correlation coefficients between FEP3 and CAP-threshold shift at 1, 6, and 8 kHz were rather low. Table I shows the correlation coefficients between the FEP shifts and CAP thresholds before and after exposure.

TABLE I. Correlation coefficients between the shifts of FEP levels (1–5) and CAP thresholds before and after exposure. Values in parentheses indicate p values. Boldface values indicate $p<0.0001$.

ΔFEP / ΔCAP	FEP1	FEP2	FEP3	FEP4	FEP5
1 kHz	0.60(0.0078)	0.34(0.1768)	0.40(0.0967)	0.34(0.1774)	0.21(0.4037)
2 kHz	0.76(0.0001)	0.74(0.0002)	0.67(0.0018)	0.47(0.0488)	0.21(0.4014)
3 kHz	0.55(0.0156)	0.66(0.0023)	**0.80(<0.0001)**	0.63(0.0040)	0.47(0.0508)
4 kHz	0.20(0.4378)	0.59(0.0094)	0.76(0.0001)	**0.79(<0.0001)**	0.67(0.0019)
6 kHz	−0.08(0.7451)	−0.13(0.6184)	0.22(0.1815)	0.58(0.0100)	**0.78(<0.0001)**
8 kHz	−0.12(0.6417)	−0.31(0.2161)	0.23(0.3637)	0.44(0.0642)	0.70(0.0009)

TABLE II. Correlation coefficients between the shifts of FEP levels (1.5–5.5) and CAP thresholds before and after exposure. Values in parentheses indicate p values. Boldface values indicate $p<0.0001$.

ΔFEP / ΔCAP	FEP1.5	FEP2.5	FEP3.5	FEP4.5	FEP5.5
1 kHz	0.44(0.0656)	0.33(0.1812	0.42(0.0817)	0.33(0.1903)	0.27(0.2846)
2 kHz	**0.84(<0.0001)**	0.68(0.0014)	0.61(0.0057)	0.37(0.1288)	0.26(0.2964)
3 kHz	0.62(0.0047)	0.72(0.0004)	0.76(0.0001)	0.58(0.0108)	0.50(0.0332)
4 kHz	0.41(0.0890)	0.65(0.0026)	**0.81(<0.0001)**	**0.78(<0.0001)**	0.68(0.0013)
6 kHz	−0.20(0.4288)	−0.12(0.6494)	0.45(0.0630)	0.69(0.0100)	0.74(0.0002)
8 kHz	−0.31(0.2228)	−0.01(0.9656)	0.32(0.1984)	0.55(0.0162)	0.64(0.0032)

Shifts in FEP levels correlated maximally with those in CAP thresholds at, or 1 kHz above, the same frequency. Table II shows the correlation coefficients by using other FEP parameters. In this analysis, shifts in FEP levels correlated maximally with those in CAP thresholds at 0.5 kHz above the same frequency, except FEP4.5.

B. Step-wise regression analysis

Next we investigated how a CAP-threshold shift at one frequency can influence a shift in FEP. To study this, the step-wise regression method was used. If a variable of a CAP-threshold shift at one frequency could be improved in a linear regression model for an FEP shift at one frequency, the variable was adopted. If not, the variable was discarded. Finally, if the F values of the residual variables were under 4, the variables were not adopted. Table III shows linear regression equations for FEP using step-wise regression. One or two variables could be entered in a linear regression model with good correlation. The remaining variables played a negligible role, since variance no longer changed when they were included in the regression equation. For FEP1.5, FEP2.5, FEP3.5, and FEP5.5, the FEP level was strongly correlated with the CAP threshold at 0.5 kHz above the same frequency as each FEP. For FEB4.5, there was a shift in the multivariate correlation.

III. DISCUSSION

Kemp *et al.* (1990) and Norton (1993) have suggested that CEOAEs can be used to identify frequency ranges for normal hearing in impaired ears by measuring frequency components in the CEOAE spectrum. Collet *et al.* (1991) reported significant correlation between spectrum analysis of CEOAEs and hearing losses in pure-tone audiograms. Gorga *et al.* (1993) reported that CEOAEs were able to distinguish normal from impaired ears at 1, 2, and 4 kHz by analyzing frequency components in the CEOAE spectrum. Those reports suggest that analyzing frequency components in the CEOAE spectrum is useful for detecting local damaged area in the cochlea.

TABLE III. Step-wise regression model for FEP.

ΔFEP	Step-wise regression model	r
FEB1.5	0.29*ΔCAP(2k)	0.89
FEP2.5	0.37*ΔCAP(3k)	0.88
FEP3.5	0.48*ΔCAP(4k)	0.87
FEP4.5	0.20*ΔCAP(2k)+0.30*ΔCAP(6k)	0.85
FEP5.5	0.27*ΔCAP(6k)	0.81

Recently, Ueda *et al.* (1997) found that the time courses of compound action potential (CAP) thresholds after acoustic overstimulation was similar to those of the frequency components of the CEOAE power spectrum in guinea pigs, and reported that changes in CAP thresholds correlated significantly to those in the CEOAE power components at the same frequencies. This finding supports the above-mentioned reports. But our previous report (Ueda *et al.*, 1997) could not assess the influence of other frequency sites because we did not measure any CAPs, except at one frequency in each experiment. In the present study, CEOAEs and CAP thresholds at various frequencies at the same period before and after exposure were measured. The results showed that the change in each FEP level after exposure could be predicted based on that of the CAP threshold at 0.5 kHz above the same frequency as the FEP, except in FEP4.5. Even if changes in CAP thresholds at other frequencies were taken into account, the correlation coefficients of the step-wise regression model did not become greater.

Avan *et al.* (1991b) reported that CEOAEs after exposure to intense sounds could be reduced even if there was no CAP-threshold change at their frequencies. But in the present study, changes of CEOAEs were within 2 dB at the frequencies where CAP thresholds were unchanged after exposure, which is not significant. Hilger *et al.* (1995) investigated the relationship between CEOAEs and organ of Corti irregularities in the guinea pig. They concluded that there was no clear relationship between CEOAEs of specific frequencies and abnormalities at the corresponding cochleotopic location in the organ of Corti, and speculated that emissions arise as a result of irregularity producing variations in the reflection coefficient. But, they assessed CEOAEs in a normal state. In a pathological condition such as acoustic trauma, it is possible that local cochlear damage induces a decrease of CEOAE level at a restricted frequency. Recently, Avan *et al.* (1995) reported that CEOAE amplitude changes were linearly correlated with the percentage of cochlear base with unchanged CAP thresholds. So by using his proposed formula, the percentage of the basal cochlear length with unchanged CAP thresholds was calculated at any given frequency (f), abbreviated as RB(f):

$$\mathrm{RB}(f) = 1 - \log(f_{\max}/f_{\min})/\log(32/f)$$

(f in kHz, RB residual basal).

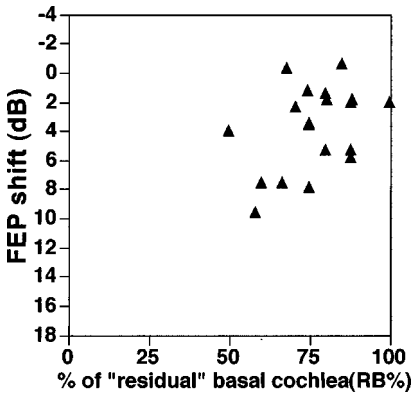

FIG. 3. Relationship between FEP shifts and RB% after exposure.

The f_{max} was defined as the highest frequency with which a temporal threshold shift (TTS) was 10 dB and over. Similarly, f_{min} was defined as the lowest frequency at which a TTS was 10 dB and over. If f was above f_{min}, RB(f) was given by the following formula:

$$\mathrm{RB}(f)=1-\log(f_{max}/f)/\log(32/f) \quad (f \text{ in kHz}).$$

In both cases, it was postulated that CAP thresholds above 8 kHz were unchanged if f_{max} was under 8 kHz. The result showed that correlation coefficients ($r=0.41$) between FEP shifts, and RB% after exposure were not significantly high (Fig. 3). The highest frequency measured in the present study was 8 kHz, so the correlation coefficients might get better or worse in CAPs were measured up to 32 kHz, as Avan *et al.* measured. In the present results, FEP shifts have better correlations with CAP thresholds at 0.5 kHz above the same frequency than the percentage of residual basal cochlea (RB). Clinically, Whitehead *et al.* (1996) observed changes of CEOAEs and DPOAEs before and after drug treatment with the antineoplastic agent cisplatin, while also measuring pure-tone audiometry. They reported that CEOAEs decreased at higher frequencies, where pure-tone thresholds increased, and that CEOAEs at lower frequencies, where pure-tone thresholds remained unchanged, were at the same level as before treatment. They concluded that both DPOAEs and CEOAEs effectively reflected the cisplatin-induced, frequency-specific decrease in hearing sensitivity. The present results show that higher frequencies may influence CEOAEs, because the change in each FEP level after exposure related to that of the CAP threshold at 0.5 kHz above the same frequency. But influence from other frequencies was negligible, because the correlation coefficients of the step-wise regression model did not improve.

The reason why changes in each FEP level after exposure paralleled those of the CAP threshold at 0.5 kHz above the same frequency, rather than those at the same frequency, is unknown. One possible explanation may lie in the difference of the stimulus intensity between the measurement of CAP thresholds and CEOAEs. The sound intensities in the measurement of CEOAEs were 72 ± 2 dB, and were higher compared to those in the measurement of CAP thresholds. The frequency of maximum amplitude of the basilar membrane is known to shift to a lower frequency as the sound intensity increases, even though the stimulus frequency is the same (Johnstone *et al.*, 1986). This may cause the 500-Hz shift between CAP thresholds and CEOAEs.

In conclusion, CEOAEs in guinea pigs display frequency specificity. The influence of higher frequencies in CEOAEs is negligible.

Avan, P., Bonfils, P., Loth, D., Narcy, P., and Trotoux, J. (**1991a**). ''Quantitative assessment of human cochlear function by evoked otoacoustic emissions,'' Hearing Res. **52**, 99–112.

Avan, P., Loth, D., Menguy, C., and Teyssou, M. (**1991b**). ''Frequency dependence of changes in guinea-pig cochlear emission after acoustic overstimulation,'' J. Acoust. **4**, 91–94.

Avan, P., and Bonfils, P. (**1993**). ''Frequency specificity of human distortion production otoacoustic emissions,'' Audiology **32**, 12–26.

Avan, P., Bonfils, P., Loth, D., Elbez, M., and Erminy, M. (**1995**). ''Transient-evoked otoacoustic emissions and high-frequency acoustic trauma in the guinea pig,'' J. Acoust. Soc. Am. **97**, 3012–3020.

Bray, P., and Kemp, D. T. (**1987**). ''An advanced cochlear echo technique suitable for infant screening,'' Br. J. Audiol. **21**, 191–204.

Collet, L., Veuillet, E., Chanal, J. M., and Morgan, A. (**1991**). ''Evoked otoacoustic emissions: Correlates between spectrum analysis and audiogram,'' Audiology **30**, 164–172.

Gorga, M. P., Neely, S. T., Bergman, B. M., Beauchaine, K. L., Kaminski, J. R., Peters, J., Schulte, L., and Jesteadt, W. (**1993**). ''A comparison of transient-evoked and distortion product otoacoustic emissions in normal-hearing and hearing-impaired subjects,'' J. Acoust. Soc. Am. **94**, 2639–2648.

Hilger, A. W., Furness, D. N., and Wilson, J. P. (**1995**). ''The possible relationship between transient evoked otoacoustic emissions and organ of Corti irregularities in the guinea pig,'' Hearing Res. **84**, 1–11.

Johnstone, B. M., Patuzzi, R., and Yates, G. K. (**1986**). ''Basilar membrane measurements and the travelling wave,'' Hearing Res. **22**, 147–153.

Kemp, D. T., Ryan, S., and Bray, P. (**1990**). ''A guide to the effective use of otoacoustic emissions,'' Ear Hear. **11**, 93–105.

Martin, G. K., Lonsbury-Martin, B. L., Probst, R., Scheinin, S. A., and Coats, A. C. (**1987**). ''Acoustic distortion products in rabbit ear canal. II. Sites of origin revealed by suppression contours and pure-tone exposures,'' Hearing Res. **28**, 191–208.

Norton, S. J. (**1993**). ''Application of transient evoked otoacoustic emissions to pediatric populations,'' Ear Hear. **14**, 64–73.

Schmiedt, R. A. (**1986**). ''Acoustic distortion in the ear canal. I. Cubic difference tones: Effects of acute noise injury,'' J. Acoust. Soc. Am. **79**, 1481–1490.

Ueda, H., Hattori, T., Sawaki, M., Niwa, H., and Yanagita, N. (**1992**). ''The effect of furosemide on evoked otoacoustic emissions in guinea pigs,'' Hearing Res. **62**, 199–205.

Ueda, H., Tsuge, H., and Hattori, T. (**1997**). ''Changes in evoked otoacoustic emission in the guinea pig after pure-tone acoustic overstimulation,'' J. Acoust. Soc. Am. **101**, 3577–3582.

Whitehead, M. L., Lonsbury-Martin, B. L., Martin, G. K., and McCoy, M. J. (**1996**). ''Otoacoustic emissions: Animal models and clinical observations,'' in *Clinical Aspects of Hearing*, edited by T. R. Van De Water, A. N. Popper, and R. R. Fay (Springer-Verlag, New York), pp. 199–257.

Wilson, J. P. (**1980**). ''Model for cochlear echoes and tinnitus based on an observed electrical correlate,'' Hearing Res. **2**, 527–532.

Discriminability of vowel representations in cat auditory-nerve fibers after acoustic trauma

Roger L. Miller,[a] Barbara M. Calhoun, and Eric D. Young
Department of Biomedical Engineering and Center for Hearing Sciences, Johns Hopkins University, Baltimore, Maryland 21205

(Received 9 February 1998; revised manuscript received 14 September 1998; accepted 17 September 1998)

This paper attempts to connect deficits seen in the neural representation of speech with perceptual deficits. Responses of auditory-nerve fibers were studied in cats exposed to acoustic trauma. Four synthetic steady-state vowels were used as test signals; these stimuli are identical, except that the second formant ($F2$) resonator in the synthesizer was set to 1.4, 1.5, 1.7, or 2 kHz, producing four spectra that differ mainly in the vicinity of the $F2$ frequency. These stimuli were presented to a large population (523) of auditory-nerve fibers in four cats with sloping high-frequency threshold shifts that reached 50–70 dB at 2–4 kHz. In normal animals, May *et al.* [Auditory Neurosci. **3**, 135–162 (1996)] showed previously that the discharge rates of fibers with best frequencies near the $F2$ frequencies provide enough information to allow discrimination of these stimuli at the performance levels shown by cats in behavioral experiments. Here it is shown that, after acoustic trauma, there is essentially no rate information which would allow the vowels with different $F2$ frequencies to be discriminated. However, information that could allow discrimination remains in the temporal (phase-locked) aspects of the responses. © *1999 Acoustical Society of America.* [S0001-4966(99)01501-5]

PACS numbers: 43.64.Pg, 43.64.Sj, 43.66.Ts [RDF]

INTRODUCTION

Analysis of the deficits produced by sensorineural hearing loss has generally been done using perceptual tests in human observers. This method provides direct data on the most important issues, which are the communication problems caused by hearing impairment. However, it can provide only indirect information on the underlying physiological deficits and their connections to the hearing problems. Previously, we have approached this question by directly analyzing the neural representation of a vowel (/ɛ/) in the auditory nerve following acoustic trauma (Miller *et al.*, 1997; Schilling *et al.*, 1998). These results show a striking degradation of the neural representation of the spectrum of the vowel. In particular, the normal tonotopic separation of responses to stimulus components of different frequencies is lost in the impaired preparation. The first and second formants ($F1$ and $F2$) normally produce responses at different places along the cochlear partition, consistent with their different frequencies. In an impaired animal, responses to $F1$ are seen across almost the whole cochlea and responses to $F2$ also spread widely away from the $F2$ place. As a result, the separation of stimulus components by frequency, which is the hallmark of normal cochlear processing, is significantly degraded in the impaired ear.

Although these results showed a reduction in the quality of the representation of the spectral shape of the vowel, the significance of the changes was unclear. In the degraded representation, there was still significant response to the formants; some optimized measures of response, such as the ALSR (average localized synchronized rate of Young and Sachs, 1979), show a remaining, weaker representation of the formant frequencies and of the general spectral shape of the vowel (Palmer and Moorjani, 1993; Schilling *et al.*, 1998). In order to refine the interpretation of the previous results, the representations of four variants of the vowel /ɛ/ were studied in cats with noise-induced hearing loss. The computer-generated vowels were identical except for the frequency placement of the second formant ($F2$) resonator. By considering the differences among the neural responses to these four stimuli, it is possible to directly estimate the sensitivity of the neural representation to the $F2$ frequency, and therefore also the quality of the representation of the second formant of this vowel in the presence of acoustic trauma.

Previous analyses had concluded that the $F2$'s of various vowels are robustly represented in terms of temporal (phase-locked) aspects of the neural responses (Young and Sachs, 1979; Sinex and Geisler, 1983; Delgutte and Kiang, 1984; Palmer *et al.*, 1986), but poorly represented by measures based on discharge rate alone (Sachs and Young, 1979). However, by analyzing the differences in neural firing rates to pairs of stimuli with slightly different $F2$ frequencies, Conley and Keilson (1995) showed a robust rate representation. The robustness of the rate-difference code, meaning a rate code for the difference between the spectral shapes of two stimuli, has been reported for other situations as well (Rice *et al.*, 1995; Le Prell *et al.*, 1996). In fact, May *et al.* (1996) used a signal-detection theory analysis to show that this rate-difference cue predicts behavioral performance that meets or exceeds the abilities of normal-hearing cats.

[a]Present address: Roger L. Miller Hearing Research Laboratories, Division of Otolaryngology-Head and Neck Surgery, Box 3550, Duke University Medical Center, Durham, NC 27710-0001, Electronic mail: rlmiller@duke.edu

TABLE I. Experimental conditions for the four cats. The sound levels of the four-h exposures and the recovery times between exposure and recording are given, along with the highest vowel sound levels used during recording. The fourth column gives the number of fibers included in the data sample from each cat.

Cat ID	Exposure level (dB SPL)	Recovery period (days)	Maximum vowel level (dB SPL)		Number of fibers isolated
201_17	107.5	54	117.8		119
201_65	108	125	116.2		72
201_81	107	139	117.6		129
201_101	108	173	117.1		203
Mean	108	123	117.2	Total	523

Here, we report that the rate differences between vowels differing in $F2$ frequency are lost after acoustic trauma; at the same time, a temporal representation of the differences between the vowels remains, even though the temporal representation is degraded. To the extent that the representations of these vowels in the cat and human auditory nerves are similar, these results suggest that the degree of loss following acoustic trauma depends on the observer's ability to use the information in the temporal representation of the stimuli.

I. METHODS

The results reported here were obtained in four healthy adult male cats purchased from Liberty Labs; they weighed about 3.5 kg each and showed no signs of middle or external ear pathology. Animal care and use procedures were approved by the Johns Hopkins Animal Care and Use Committee (protocol number CA96M302). The methods have been discussed in detail in previous publications (Miller *et al.*, 1997; Schilling *et al.*, 1998) and are described briefly below.

A. Acoustic trauma

For the sound exposure, cats were anesthetized with ketamine (200 mg im) mixed with acepromazine (2 mg im). Atropine was given (0.1 mg im) to control mucus secretions. Additional doses of acepromazine/ketamine were administered as needed to maintain the cat in an anesthetized state. The animal's head was restrained and positioned directly beneath two loudspeakers during a 4-h exposure to a noiseband of 50-Hz bandwidth, centered at 2 kHz. The parameters of the exposure are given in Table I. Note that the exposure level (≈108 dB) is lower than was used previously (110–115 dB; Miller *et al.*, 1997; Schilling *et al.*, 1998) and that the exposure duration is longer (4 instead of 2 h). These changes were made in order to decrease what was interpreted as inner hair cell damage in previous studies, which resulted in difficulty isolating fibers with best frequencies (BFs) in the octave above the exposure frequency. The animals were allowed to recover from the exposure for 54–173 days; in cats, there is little or no temporary threshold shift after about 30 days following an exposure (Miller *et al.*, 1963), so the deficits remaining at that time are permanent.

B. Single-fiber recording

Animals were anesthetized by an injection of xylazine (0.2 mg im) followed by ketamine (150–200 mg im); an areflexic state of anesthesia was maintained for the duration of the experiment with bolus injections of pentobarbital (≈12 mg/h iv). Physiological saline (≈1 ml/h iv) and lactated Ringer's (≈10 ml/24 h iv) were given to prevent dehydration. Atropine (0.1 mg im) was given every 24 h. A tracheotomy was performed to maintain an open airway and to minimize respiratory acoustic artifacts. The bulla was vented with a 40-cm length of polyethylene tubing (PE-90) to prevent the buildup of negative pressure in the middle ear (Guinan and Peake, 1967). Body temperature was maintained near 38.5 °C with a feedback-controlled heating pad.

Recordings were made in an electrically shielded, double-walled soundproof room (IAC-1204A). Micropipettes of 10–30 MΩ were filled with 3M KCl and placed in the auditory nerve under visual control after retraction of the cerebellum medially. Single fibers were isolated by driving the electrode in 1–2-μm steps with a piezoelectric microdrive (Burleigh) while presenting a broadband noise-search stimulus (spectrum level about 35 dB re: 20 μPa/Hz$^{1/2}$). Experiments usually lasted 2–3 days and were terminated by a lethal dose of pentobarbital. The state of the cochlea was monitored during experiments by plotting the thresholds of fibers with similar BFs versus time and looking for sudden shifts in the thresholds of the most sensitive fibers.

C. Stimulus protocol

Isolated fibers were first characterized by a tuning curve constructed by an automated program that tracks the sound level necessary to produce an increase in response of 1 spike during a 50-ms tone burst (Kiang *et al.*, 1970). Responses to the synthetic vowels described below were then obtained. In order to facilitate comparison of responses to different vowels, two vowels were presented in alternation. The vowels had a duration of 400 ms and were presented with an interstimulus interval of 600 ms. The vowels of a pair had approximately the same sound level and data from 30–50 repetitions were obtained. This process was repeated for two pairs of vowels (the pair V14 and V15 was usually followed by V17 and V20, defined below) at three sound levels (approximately 117, 97, and 77 dB, typically in that order). Vowel sound levels are given as the total power in the first 50 harmonics of the vowel. If the fiber remained well-isolated, a 10-s sample of spontaneous activity was taken to estimate the spontaneous firing rate (SR) and a tone was presented at the fiber's BF, 50 dB above threshold, to estimate the maximum firing rate. If the SR data were not ob-

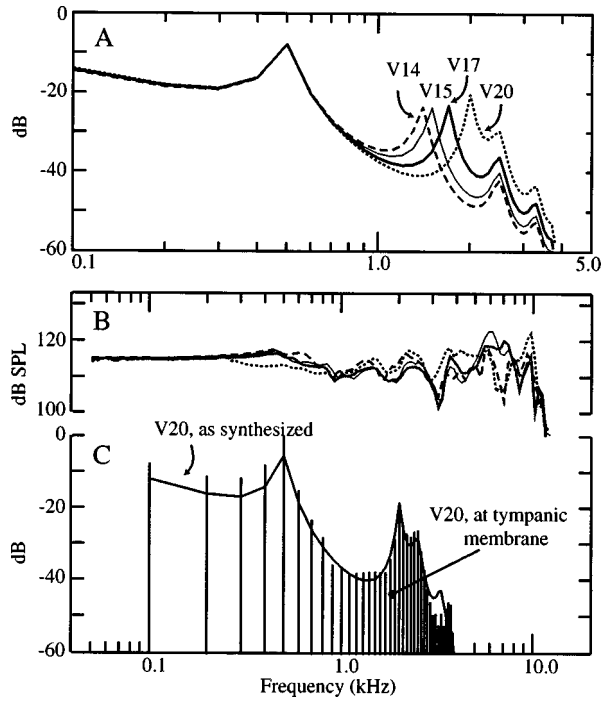

FIG. 1. Four variants of the synthetic vowel /ε/ were used to investigate the neural codes for discriminating second formant frequency; the power spectra of the vowels are shown in panel A. The vowels are periodic, so the spectra are actually harmonic line spectra, as shown in panel C, with a fundamental of 100 Hz. Placement of the resonator for $F2$ in the synthesizer software is indicated by the vowel name, e.g., V17 for 1700 Hz. All formants were placed at harmonics of 100 Hz. Acoustic calibration data taken from the four experimental animals are shown in panel B. Lines show the sound level at the tympanic membrane, for a constant electrical signal at the acoustic transducer input. The spectral envelope of the electrical signal of the vowel V20 is shown in panel C by the solid line, along with the spectral shape of the vowel corrected by the acoustic calibration from one experiment (vertical bars). Note that the frequency scales on the abscissae are different in A versus B/C.

tained because the fiber was lost, SR was estimated from the spike activity during the interstimulus intervals of trials with the vowel presented at the lowest level tested.

The vowels used are the same as those used previously for behavioral studies of vowel discrimination (Hienz *et al.*, 1996; May *et al.*, 1996) and for studies of the neural encoding of vowels in normal-hearing cats (Conley and Keilson, 1995; Le Prell *et al.*, 1996). The vowels were generated on a fundamental frequency of 100 Hz with a Klatt (1980) series-formant synthesizer; they all had first ($F1$) and third ($F3$) formants at 500 and 2500 Hz, respectively. The second formants ($F2$) were set at 1400 Hz (V14), 1500 Hz (V15), 1700 Hz, (V17), and 2000 Hz (V20) to generate four vowels with similar spectra except near $F2$. The envelopes of the spectra are shown in Fig. 1(A). The vowels were filtered with the human external-ear transfer function (Wiener and Ross, 1946) to make their spectral shapes at the cat's tympanic membrane approximate those at the human tympanic membrane.

Acoustic stimuli were delivered to the ear through a hollow earbar from a dynamic speaker (Schilling, 1995). The frequency response for this system is relatively flat (±6 dB) at frequencies below 10 kHz; Fig. 1(B) shows, for the four cats, the sound pressure at the eardrum with a fixed voltage input to the acoustic system. This system's upper cutoff frequency (10 kHz) was sufficient for tests with the vowels, since they contain little energy above 5 kHz. The acoustic system produced a maximum vowel level of about 117 dB at the cat's tympanic membrane. Figure 1(C) shows the spectral envelope of the electrical signal for the vowel V20 as the solid line, and the actual spectrum at the eardrum of one cat as the vertical bars.

D. Analysis

The responses to the four vowels were compared using both rate and temporal measures of response. For the rate measure, discharge rate was computed over the last 380 ms of the 400-ms vowel; the rate was averaged across the 30–50 repetitions of the vowel. Rate was converted to driven rate for Fig. 3 by subtracting SR. The population representation of the spectral differences between the vowels was studied as the change in discharge rate produced by changing the stimulus from one vowel to another. Rate difference was computed by subtracting the average discharge rate in response to one vowel from the rate in response to the other.

For the temporal analysis, a peristimulus time histogram (PSTH) with a bin width of 100 μs was computed from a fiber's spike trains and normalized to have units spikes/s. The fiber's frequency response was analyzed by applying a Hamming window $w(n)$ to the PSTH over latencies of 20 to 400 ms and taking the Fourier transform, giving the complex synchronization P where

$$P(kf_t)=\sum_{n=0}^{N-1} w(n)p(n)e^{-j2\pi kn/N} \Big/ \sqrt{N\sum_{n=0}^{N-1} w(n)^2}. \tag{1}$$

The $P(kf_t)$ are the complex synchronized rates at frequencies kf_t, where f_t is the frequency resolution of the analysis (1/380 ms=2.63 Hz). The term in the denominator is a correction for the attenuation of the signal by the window function $w(n)$. The synchronized rates $R(kf_t)$ are the magnitudes of the $P(kf_t)$; synchronized rate is interpreted in this paper as the component of the fiber's discharge rate that is responding to frequency kf_t.

For the discriminability analysis in Fig. 10, the statistics of $P(kf_t)$ were estimated by computing Eq. (1) separately for each of the 30–50 repetitions of the stimulus, yielding values $P_j(kf_t)$ for the synchronized rates of the responses to each tone burst. The mean and the standard deviation of these values were computed as follows (Miller *et al.*, 1987):

$$\overline{P}(kf_t)=\frac{1}{N}\sum_{j=1}^{N} P_j(kf_t)$$

and (2)

$$\sigma^2(kf_t)=\frac{1}{N-1}\sum_{j=1}^{N} |P_j(kf_t)-\overline{P}(kf_t)|^2.$$

II. RESULTS

A. Nature of the hearing loss

Data were taken from 523 fibers over the course of experiments on four impaired cats; these data were pooled together in order to obtain a dense sampling of fibers at different BFs. The noise exposure and recovery period for each animal are given in Table I. The thresholds, Q_{10}s and BF distribution of fibers included in the pool are shown in Fig. 2. Data are plotted as a function of BF, which was chosen as the frequency of the local minimum threshold nearest to the high-frequency slope portion of the tuning curve. Liberman (1984) has shown that this method gives a more reliable measure of the true BF, meaning the point of innervation of the basilar membrane, than the frequency at which the threshold is actually at a minimum. Fibers are grouped into the usual three SR groups, noted in the legend for Fig. 2(B); SR classification is indicated by symbol shape in this and subsequent plots.

Single-fiber thresholds are shown in comparison to the best thresholds in normal cats in Fig. 2(A). The line marked NBTC shows the best thresholds in unexposed cats from the same supplier (Miller *et al.*, 1997). The threshold shift induced by acoustic trauma was greatest for fibers with BFs in the range from 1 to 7 kHz. Figure 2(B) shows the Q_{10} measure of tuning-curve sharpness. The lines show the upper and lower boundaries of the Q_{10} values in unexposed cats (Miller *et al.*, 1997). Q_{10} distributions in the four individual cats were essentially the same (not shown) and, in all four cats, tuning is broadened in the frequency region showing the greatest threshold shift. Figure 2(C) shows a histogram of the distribution of BFs in the data sample. The peak in the distribution at 1.5–1.7 kHz reflects a sampling bias, in that we focused our efforts on finding fibers with BFs near $F2$. In previous studies, it was difficult to isolate fibers with BFs between 2–4 kHz (Miller *et al.*, 1997; Schilling *et al.*, 1998). However, in the four cats included in this study, it was relatively easy to find such fibers, except possibly for BFs between 3–4 kHz. This difference is probably a result of the change in exposure protocol, as discussed in Sec. I.

Figure 2(D) shows a comparison of the best thresholds of the fibers studied in the four cats. These contours were defined by passing a line through the lowest thresholds measured in each animal. The contours are similar in shape across animals, although they vary by up to 40 dB at some frequencies. Despite this variation, data from these four animals have been pooled for the population analyses described below. Pooling the data is justified, in the face of the differences shown in Fig. 2(D), because the measures of vowel response that are most important to the results in this paper, i.e., those shown in Figs. 4, 8, and 9, are very similar when analyzed in individual animals.

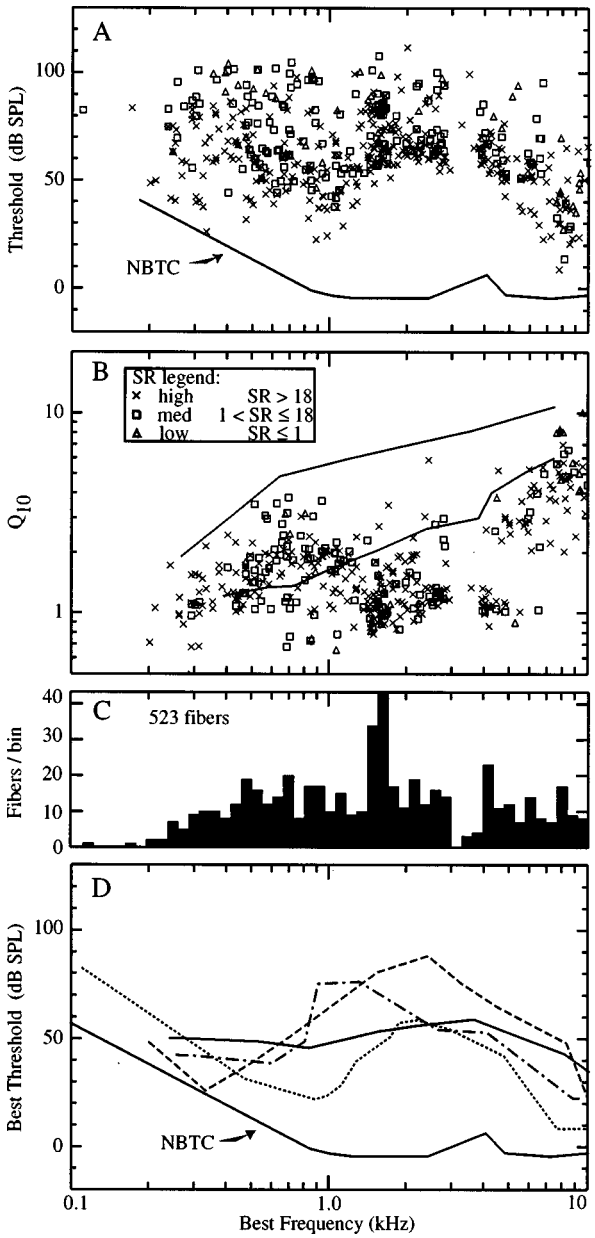

FIG. 2. (A) Threshold sound level at BF for all fibers in the four cats from which data were taken. Spontaneous firing rate (SR) is indicated by symbol shape, defined in the legend of B. The line marked NBTC indicates the best thresholds in normal animals (Miller *et al.*, 1997). Note the threshold shift of up to 50 dB over the frequency range 1–7 kHz. (B) Tuning-curve widths for all fibers, plotted as Q_{10}, which is BF divided by tuning-curve bandwidth 10 dB above threshold [the horizontal dashed lines in Fig. 5(A)]. Lines show the range of Q_{10}s in unexposed cats (Miller *et al.*, 1997). Fibers with BFs above 1 kHz were broadly tuned, as indicated by the symbols falling below the normal range of values. (C) Histogram showing the distribution of BFs of the fibers in panels A and B. (D) Best thresholds for each cat; these are lines passing through the minimum single-fiber thresholds in each population. Assuming that the fibers with the minimum threshold determine the cat's behavioral threshold, these plots correspond to audiograms for each cat. The thresholds in normal cats (NBTC) are also shown.

B. Rate representation of vowel spectra

The simplest neural representation of a complex stimulus is a rate profile, which plots the average firing rate to the stimulus as a function of fiber BF. Figure 3 shows rate profiles for two vowels, V14 [Fig. 3(A), (B), and (C)] and V20 [Fig. 3(D), (E), and (F)]. Data are shown at three levels for each vowel, as given in the legends. For reference, the first three formant frequencies are indicated by the vertical dashed lines. In normal animals, rate profiles give a good representation of the vowel's spectrum at lower stimulus levels, by exhibiting peaks of rate at the formant frequencies, but the rate profiles tend to become flat at higher levels (Sa-

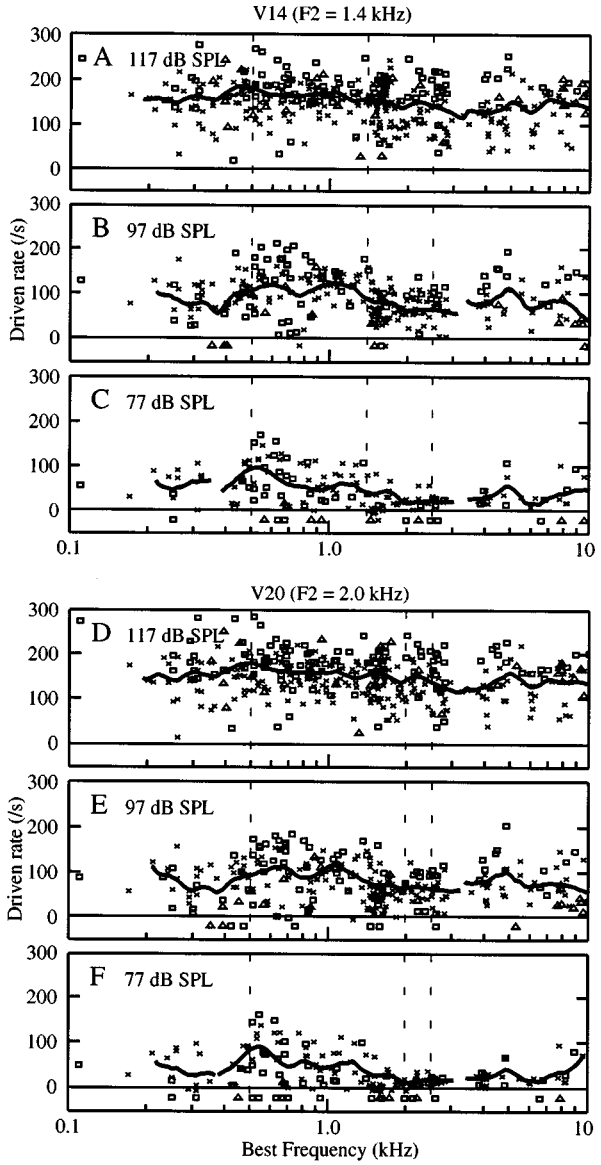

FIG. 3. Driven rate (rate-SR) is plotted as a function of fiber BF for the impaired fibers responding to vowels V14 (A, B, and C) and V20 (D, E, and F). The points show data for individual fibers and the heavy line is a log-triangular smoothed version of the data. The average at frequency f is computed from all fibers with BFs within 0.125 octaves of f. A fiber with BF b contributes to the average with weight $[1-|\log_2(b/f)/0.125|]$. The vertical dashed lines show the frequencies of the first three formants.

chs and Young, 1979; Conley and Keilson, 1995). The data in Fig. 3 show a much weaker rate representation in that there is not a clear representation of the vowels' spectra at any level. At the lowest level [77 dB, Fig. 3(C) and (F)], there is a peak of rate at BFs near $F1$, but this simply reflects a threshold effect because fibers with BFs around $F2$ and $F3$ are not responding to the vowel. As sound level increases, there is an increase in rate across BF, but rate peaks at the formants are not seen.

Unlike the situation in normal animals, the rate representation is not better in the subpopulation of fibers with low SRs; that is, these data scatter among the high spontaneous rate data with no evidence of peaks corresponding to the formants. Note, however, that the identification of a fiber with a particular SR group does not always survive acoustic trauma, in that the SRs of fibers decrease following acoustic trauma (Liberman and Dodds, 1984); thus, it is not clear that a difference between the representations in the low and the high SR populations is expected after acoustic trauma.

The rate profiles in Fig. 3 suggest that there is little or no information about the vowels' spectra encoded in discharge rates. However, previous investigations of the rate-place code have shown that the variability in rate profiles like Fig. 3 can obscure responses to the spectral features of the stimulus (Conley and Keilson, 1995; Rice *et al.*, 1995; Le Prell *et al.*, 1996). A significant component of the variability is differences between fibers, presumably differences in threshold or dynamic range properties. The interfiber variability can be controlled by changing the analysis to examine the differences in discharge rate between two stimuli, which effectively uses each fiber as its own control. Computation of rate differences can also serve as the basis for a signal-detection analysis of the discriminability of two vowels (Conley and Keilson, 1995; May *et al.*, 1996).

Figure 4 shows rate differences for four of the six possible vowel pairs in our stimulus set. The vowels are identified in column A, where the dB differences in their spectra are plotted versus frequency. Columns B and C show rate differences plotted versus BF for two sound levels, 97 and 117 dB. The data points show the rate differences for the population of impaired fibers and the dotted lines show average results from normal animals, for the same vowel pairs at 47-dB lower sound levels. The differences between the data in the normal and impaired animals are striking. Whereas the peaks and valleys in the difference spectra are clearly preserved in the rate-difference plots from normal animals, there is essentially no systematic rate change in the impaired animals. Occasional fibers show large rate changes in the impaired animals, but these differences are not systematically associated with the spectral differences in the stimuli and probably reflect random events. In addition, there is a small nonzero rate difference at frequencies below 2 kHz in the bottom two plots in column B. This difference resulted from a rate decrease when V20 was presented, which was caused by the fact that V20 was actually about 2.3 dB softer in level than the other three vowels. Again, this difference does not convey information about the formants. Finally, there are very small and systematic rate-difference changes near the formants for the V17–V20 and V14–V20 cases. The rate differences at the two formants are statistically significantly different ($P \approx 0.05$, 2-sided t test) for three of these cases (V17–V20 at the lower level and V14–V20 at both levels). However, these effects are small and the major effect shown in Fig. 4 remains the large difference between the data from normal and impaired animals.

A more direct measure of the usefulness of the rate differences in a discrimination task is d', defined below.

$$d' = \frac{R_{V1} - R_{V2}}{\sqrt{\sigma_{V1}^2 + \sigma_{V2}^2}} \tag{3}$$

R_{Vi} and σ_{Vi}^2 are the mean and standard deviation of the rate estimates derived from the 30–50 repeated presentations of vowel Vi. The resulting d' value is an index of the discrim-

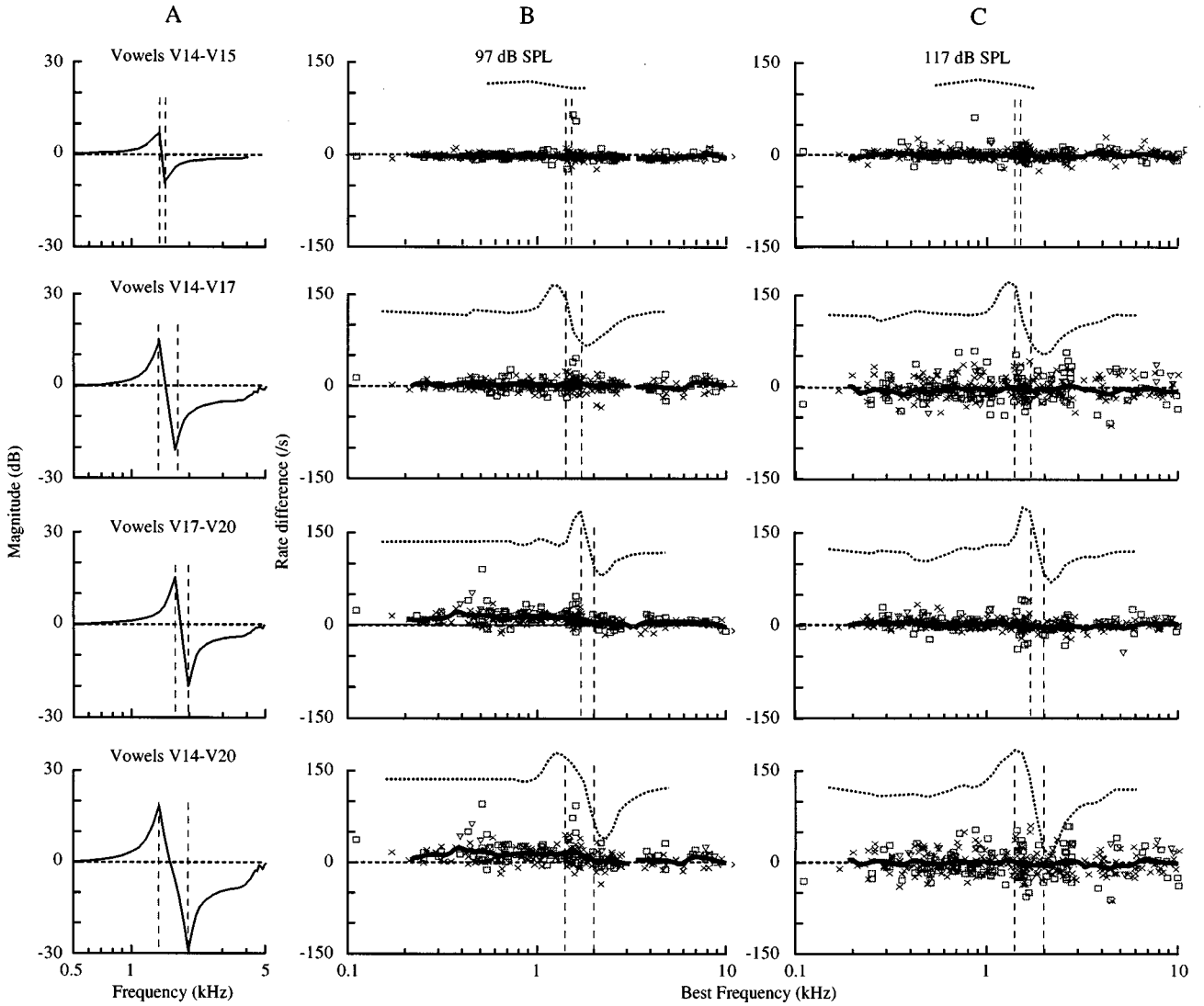

FIG. 4. The differences between vowel spectra are compared with the differences in discharge rate evoked by pairs of vowels. Column A shows the ratio of the magnitude spectra of four vowel pairs, identified in the legends. Data in the top row represent the vowel pair V14–V15, which has the weakest cue for discriminability ($F2$ change of 100 Hz) and data in the bottom row represent the vowel pair V14–V20 with the strongest cue tested ($F2$ change of 600 Hz). Columns B and C show differences in discharge rates in response to each of the four vowel pairs plotted against BF for two sound levels, 97 dB (column B) and 117 dB (column C). The points are data from individual fibers; heavy solid lines are log-triangular smoothed versions of the data points (see caption of Fig. 3). The dotted lines show log-triangular smoothed versions of data taken from fibers in normal-hearing cats, from Conley and Keilson (1995); the normal curves are displaced vertically to aid visualization. The normal-cat data were taken at 50 (column B) and 70 (column C) dB. Vertical dashed lines indicate the $F2$ frequencies of the two vowels of each pair.

inability of vowels V1 and V2 based on rate changes in a single fiber in response to a single presentation of each vowel. Generally, a d' of 1 corresponds to the behavioral threshold for discrimination. When this calculation is done for the data in Fig. 4, the resulting d' values scatter near zero, except for the systematic across-frequency rate difference discussed above. Scattered d' values larger than 1 are observed, but they are not systematically associated with the changes in formant frequency.

C. Temporal analysis of responses to the second formant

The basis for a peak in a rate-difference profile, such as those in the normal-animal data in Fig. 4, is a change in the strength of response to one or more stimulus harmonics when the stimulus changes. In order to analyze further the rate-difference data of Fig. 4, it is useful to know which stimulus harmonics are producing the responses. For vowels, this information can be gotten by analyzing the phase-locking patterns of the fibers. In a normal cat, fibers tend to phase-lock to the stimulus components at the formant frequencies; fibers with BFs near a formant show synchrony capture, meaning that the fiber's response is driven almost exclusively by the energy at that formant. In the hearing-impaired ear, however, this behavior is absent and broadband responses to multiple harmonics of the stimulus are seen instead (Miller *et al.*, 1997; Schilling *et al.*, 1998). The next five figures show data that support the idea that this difference in response properties between damaged and normal ears is the basis of the failure of the hearing-impaired cats to show a rate difference in response to the vowels.

Figure 5 shows the phase-locked responses of an im-

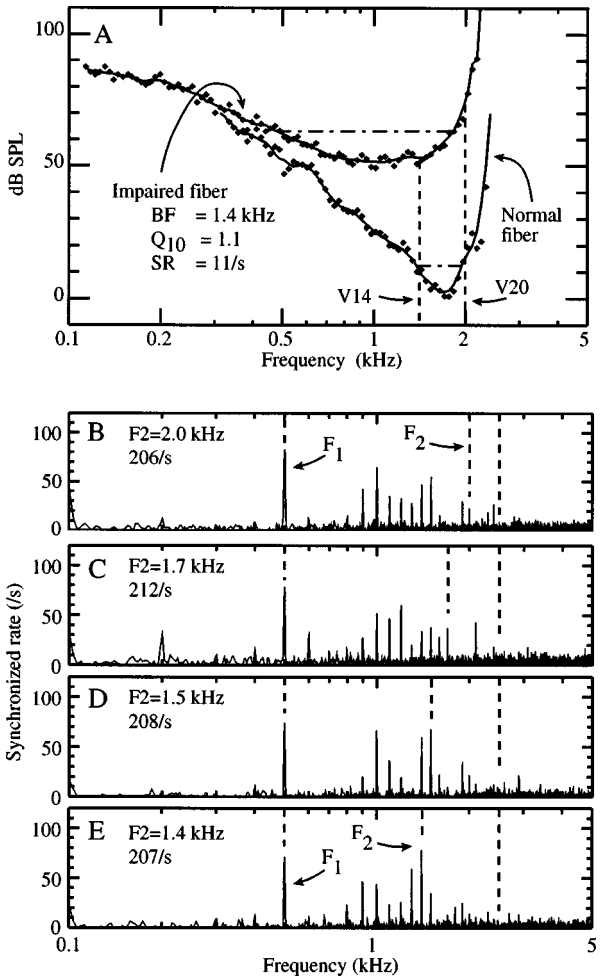

FIG. 5. (A) Tuning curves are shown for a normal and an impaired fiber with BFs near the $F2$ frequencies of the vowels. The lowest and highest $F2$ frequencies, 1.4 and 2.0 kHz, are indicated with vertical dashed lines. Horizontal dashed lines show the tuning-curve widths used to compute Q_{10}. Following Liberman (1984), BF is taken as the location of the first local minimum at a frequency below the steep-slope high-frequency part of the tuning curve. (B)–(E) Synchronized rates of the responses of the impaired fiber in A to the four vowels, i.e., $R(kf_t)$. The vowels contain energy only at harmonics of 100 Hz, so the peaks in these plots show the responses to the harmonic components of the stimulus; energy at intermediate frequencies is noise. The $F2$ frequencies of the vowels and the fiber's discharge rates are given in the legends. Vertical dashed lines show the frequencies of $F1$, $F2$, and $F3$. These data illustrate the broadband responses typically seen in impaired fibers and should be contrasted with data from normal animals (e.g., Figs. 9 and 10 of Miller *et al.*, 1997). Note that as the $F2$ frequency changes, the pattern of phase-locking is rearranged, but there is no change in overall response, as indicated by discharge rate.

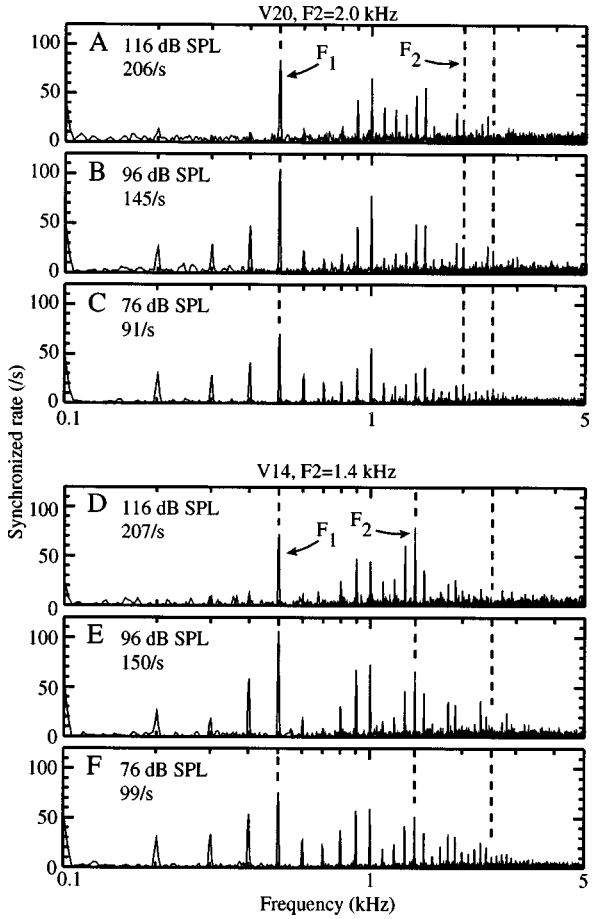

FIG. 6. Synchronized rates at three sound levels for the same impaired fiber as in Fig. 5, in response to V20 (panels A–C) and V14 (panels D–F). Vertical dashed lines show the first three formant frequencies. Legends give the vowel level and the fiber's average discharge rate to each stimulus. Note that the broadband pattern of phase-locking is seen at all sound levels tested.

paired fiber to the four vowels. The tuning curve of the fiber is shown in Fig. 5(A), along with the tuning curve of a normal fiber of similar BF. The impaired fiber shows a threshold shift of about 50 dB and a substantial increase in bandwidth; its Q_{10} of 1.1 places it in the middle of the population of impaired fibers in Fig. 2(B). The vertical dashed lines show the lowest (1.4 kHz) and highest (2 kHz) $F2$ frequencies among the vowel stimuli. The impaired fiber's threshold changes by about 10 dB over this frequency range and this difference might be sufficient to produce some differences in the fiber's responses to the four vowels. Figure 5(B)–(E) show synchronized rates $R(kf_t)$ for the fiber's responses to the four vowels at 116 dB. The legends identify the $F2$ frequencies and also give the fiber's discharge rates; note that the discharge rate did not change significantly with $F2$, which is consistent with Fig. 4.

Examination of the synchronized rate plots shows that the responses to the vowel did, in fact, change without changing discharge rate. The fiber responded strongly to $F1$ and to a broad range of stimulus harmonics at and below its BF, i.e., over the frequency range where the fiber's tuning curve had a broad minimum. Strong responses to $F2$ are seen for the lowest two $F2$ frequencies [Fig. 5(D) and (E)], but not for the upper two $F2$ frequencies. As $F2$ frequency changed, there was a change in the pattern of response, in that the relative size of responses to different harmonics changed, but the overall summed response did not change. Because its tuning was so broad, the fiber responded to stimulus harmonics over a wide frequency range, and therefore a small change in a few harmonics produced only a rearrangement in the pattern of response harmonics, not a net change in response. This pattern of response is typical of fibers with BFs in the region of threshold shift.

The response pattern shown in Fig. 5 does not change with stimulus level. Figure 6 shows responses of the same fiber to V14 and V20, which have the largest $F2$ separation in the stimulus set. Responses to each vowel are shown for

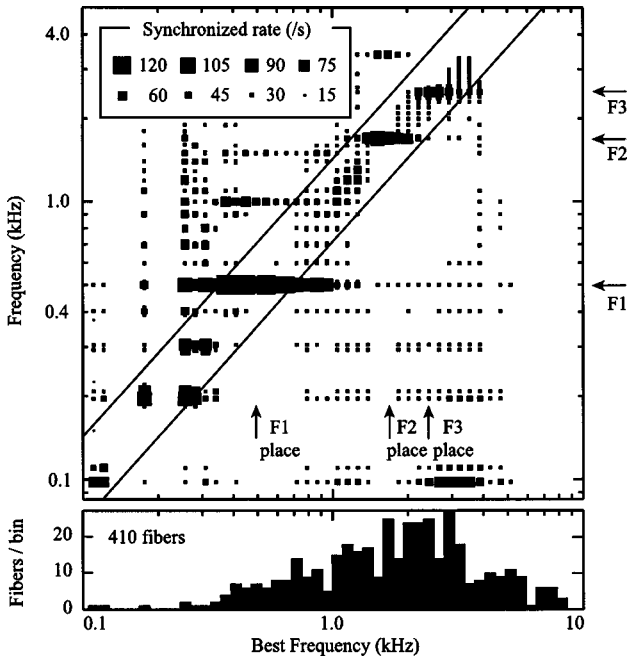

FIG. 7. Population distribution of synchronized rate to a vowel similar to V17 taken from normal animals; the sound level was 69 dB. The horizontal axis denotes fiber BF; the histogram at the bottom indicates the BF distribution of fibers in the plot. The column of squares above each bin shows the average synchronized rate, the average value of $R(kf_t)$, for all fibers within that bin (0.133 octave wide). The size of each square represents the rate, as defined in the legend; each square represents cases with synchronized rates within the range defined by the two numbers bordering the symbol; the largest squares are rates greater than 120 /s and response components less than 15 spikes/s are not plotted. Formant frequency positions are marked with arrows on the right, and points where BF equals formant frequency are shown by arrows at the bottom. Note that synchrony to the formants is centered on the diagonal band, which indicates frequencies within a half-octave of the fibers' BFs. (Same data as Fig. 6 of Schilling *et al.*, 1998.)

three sound levels, as given in the legends. The same broadband response patterns described in Fig. 5 remain evident, and $F1$ remains the dominant harmonic in the responses. Note that all three levels are well above threshold, as judged by the response rates, which are well above the SR of 11/s.

D. Population responses in synchronized rate profiles

The overall response to the vowels can be analyzed by looking at synchronized rate profiles. Figure 7 shows an example for a normal population of fibers (Schilling *et al.*, 1998). This three-dimensional plot shows the distribution of phase locking as a function of fiber BF. The synchronized rates of all fibers within a 0.133 octave bin are averaged together and plotted vertically along the ordinate, against synchronization frequency. The abscissa shows fiber BF, and the size of the box symbols shows the averaged synchronized rate to a particular frequency; the box scale is shown in the legend. The BF distribution of fibers contributing to the figure is shown by the histogram in the bottom panel.

The data in Fig. 7 illustrate the normal spread of synchrony to $F1$ and $F2$ for a vowel presented at 69 dB. Fibers with BFs near the $F1$ and $F2$ places (arrows at bottom) show strong synchrony (large squares) to that formant and its harmonics; little phase-locking to other frequencies is seen. This pattern is called synchrony capture and is typical of normal animals. The third formant frequency, 2.5 kHz, is also clearly indicated as a local maximum of synchrony, although synchrony capture does not occur at $F3$. Note that the largest squares are contained within the region bounded by the diagonal band, which indicates frequencies within a half-octave of a fiber's BF. In the normal animal, synchrony to the formants is centered on this band and the responses of most fibers contain significant components within this band, as is consistent with a tonotopic representation of the stimulus.

The synchronized rate profiles for all four vowels in the acoustically-traumatized cats are shown in Figs. 8 and 9. Data are shown for responses to the stimuli presented at 117 dB (Fig. 8) and 97 dB (Fig. 9). Given the threshold shift of 40–70 dB for BFs near $F2$ in the impaired animals [Fig. 2(A) and (D)], the higher level is comparable, in terms of dB *re*: threshold, to levels of 47–77 dB in normal ears. The dominant features of responses in the impaired ears have been described previously (Miller *et al.*, 1997; Schilling *et al.*, 1998); they include widespread synchrony to $F1$, indicated by the horizontal bar of boxes at 500 Hz, and broadband synchrony in the responses of all fibers, indicated by the abundance of small boxes at nonformant harmonics in each column. Synchrony capture by the formants is not observed, even at $F1$. The normal response pattern was not regained by lowering the vowel level 20 dB, as seen in Fig. 9. The synchronized rate profile for a particular vowel remained similar to those seen at the higher level. This is also consistent with previously described response properties of the ear after acoustic trauma (Miller *et al.*, 1997); synchrony capture by $F2$ fails to occur at levels ranging from near threshold to levels well above 100 dB.

The synchrony of fibers with BFs from 1 to 3 kHz has the greatest significance, because the responses of these fibers are the basis for the discriminability of the vowels in the normal cochlea (Fig. 4, Conley and Keilson, 1995). In both Figs. 8 and 9, the response profiles show a horizontal band of synchrony to the $F2$ frequency, which extends from the $F2$ place toward higher frequencies. This band moves vertically as the $F2$ frequency changes, while most other features of the response change little. This pattern of response in the population is similar to what was described for a single fiber in Fig. 5. Once again, it is clear why there is no rate change in the population data of Fig. 4. Fibers of all BFs are responding to a wide array of frequency components of the stimulus. When $F2$ moves, the band of phase-locking to $F2$ moves vertically in Figs. 8 and 9, with relatively little horizontal movement. The vertical movement does not change the fibers' rates, because response to one frequency component is just traded for response to another component. Because there is little horizontal movement, and because the response is divided among so many frequency components, there are no fibers for which substantial changes in response occur, and therefore no rate changes.

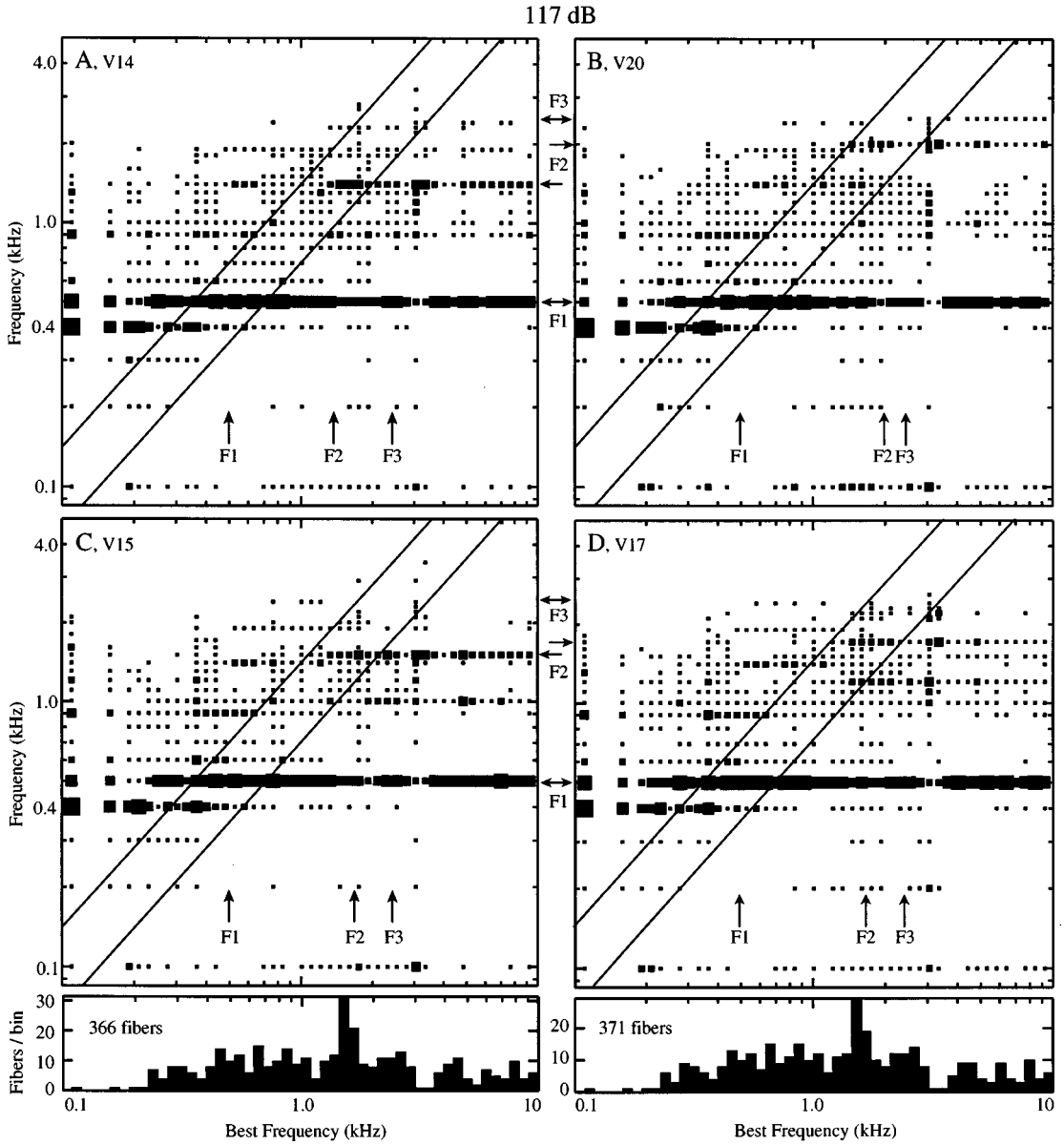

FIG. 8. Synchronized rate profiles for all four vowels presented at 117 dB SPL; vowels are identified in the legends. The layout of each part of the figure is like Fig. 7 and the box scale is the same. The distribution of fibers contributing to panels A and C is shown at bottom left (vowels V14 and V15 were presented together in alternating trials) and the distribution for panels B and D is shown at bottom right (vowels V17 and V20 were presented together). The dominant feature of the responses is synchrony to $F1$ at all BFs, which does not aid in distinguishing among these vowels. Synchrony to $F2$ is also seen, as the second horizontal line at the $F2$ frequency, pointed to by arrows in the middle of the figure. As $F2$ changes, the frequency of this line also changes, so that the vertical position of the line serves as a cue for discrimination of the vowels, but does not provide a rate cue.

E. Vowel discriminability based upon synchronized rate

The changes in phase-locking shown in Figs. 8 and 9 could conceivably provide a basis for discriminating the vowels. The issue of whether the central nervous system is capable of using such cues has been discussed but not resolved (Sachs, 1984). Regardless of that discussion, it is useful to evaluate how strong a cue the phase-locking could provide. The d' measure of signal detection theory can be written for differences in phase-locking as follows:

$$d'(kf_t)=\frac{|\overline{P}_1(kf_t)|-|\overline{P}_2(kf_t)|}{\sqrt{\sigma_1^2(kf_t)+\sigma_2^2(kf_t)}}, \tag{4}$$

where $\overline{P}_i(kf_t)$ and $\sigma_i^2(kf_t)$ are the mean and standard deviation of the synchronized rates to frequency kf_t for one vowel presentation [Eq. (2)] and the subscripts identify the two different stimuli. This definition of d' follows from the fact that the optimum decision rule for discrimination of frequency on the basis of phase-locking is based on the statistic $|P_1(kf_t)|-|P_2(kf_t)|$, i.e., the difference in the magnitudes of phase-locking to a frequency in two presentation intervals (Siebert, 1970; Miller *et al.*, 1987). Note that d' defined this way is a function of frequency, so that it measures the discriminability of the stimuli based on phase-locking to one particular frequency component. The overall discriminability of two vowels would depend on a combination of d' values across frequency.

Figure 10 shows the population distribution of discriminability for two of the vowel pairs (V17–V20 and V14–

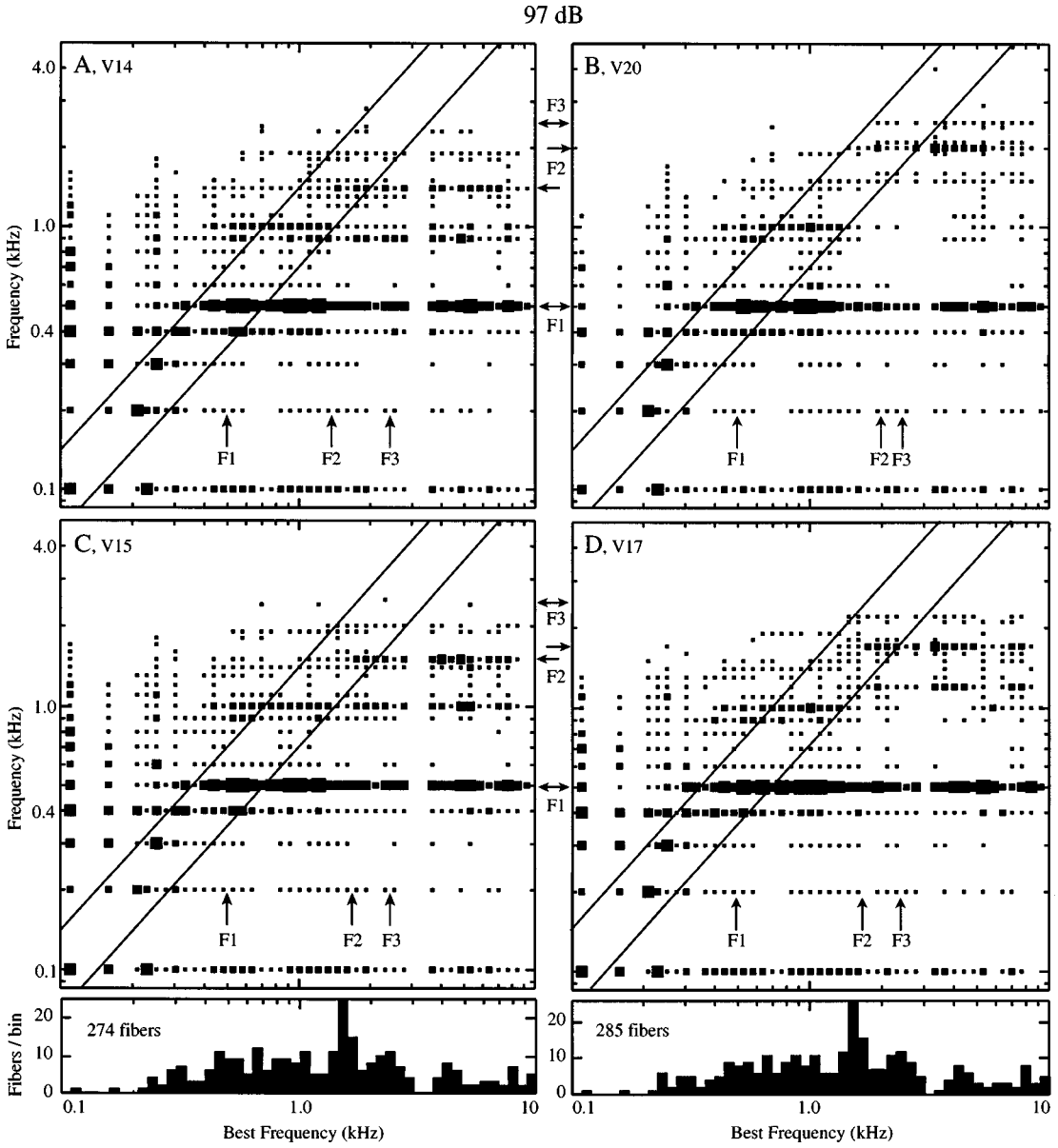

FIG. 9. Synchronized rate profiles for all four vowels presented at 97 dB SPL; the plot uses the same format as Fig. 8. Note that decreasing the level by 20 dB does not strengthen the representation of $F2$, nor does it diminish the response to $F1$ at all BFs.

V20) at two levels, as given in the legends. Discriminability d' was computed using Eq. (4), averaged across fibers in BF bins of 0.133 octave (abscissa) and plotted as in Figs. 7–9. The boxes indicate the size of d' using the scale in the legend of Fig. 10(A); note that d' can be positive (boxes) or negative (Xs). As expected from Figs. 8 and 9, the largest consistent differences between the responses to the two vowels of a pair are at the $F2$ frequencies, indicated by the arrows in the center of the figure. d' values as large as ± 1–2 are seen, which means that the vowels are theoretically discriminable on the basis of the phase-locking of a single, optimally chosen, auditory-nerve fiber. Note that the sign of the change in phase-locking correctly signals the direction of change of $F2$. Under these ideal listening conditions, optimal use of the phase-locked response to differentiate between these vowels would integrate d' values across frequencies of both the upper and lower $F2$, for fibers with BFs equal to 1 kHz and greater.

The only other consistently large difference between the responses in Fig. 10 are at the 12th harmonic in Fig. 10(C) and at the 9th harmonic in Fig. 10(D). These are probably $F2-F1$ rectifier distortion products (Young and Sachs, 1979) produced by the interaction of the formants of V17 in Fig. 10(C) ($F1=5$th, $F2=17$th harmonics, making $F2-F1$ the 12th harmonic) and V14 in Fig. 10(D) ($F1=5$th, $F2=14$th harmonics, making $F2-F1$ the 9th harmonic). In both cases the rectifier distortion product should be present with one vowel, but not present with the other. Similar effects of rectifier distortion are expected at $F2-F1$ for V20 (i.e., a negative d' at the 10th harmonic). This is not seen, probably because it coincides in frequency with the second harmonic of $F1$ (10th harmonic for all vowels), which is

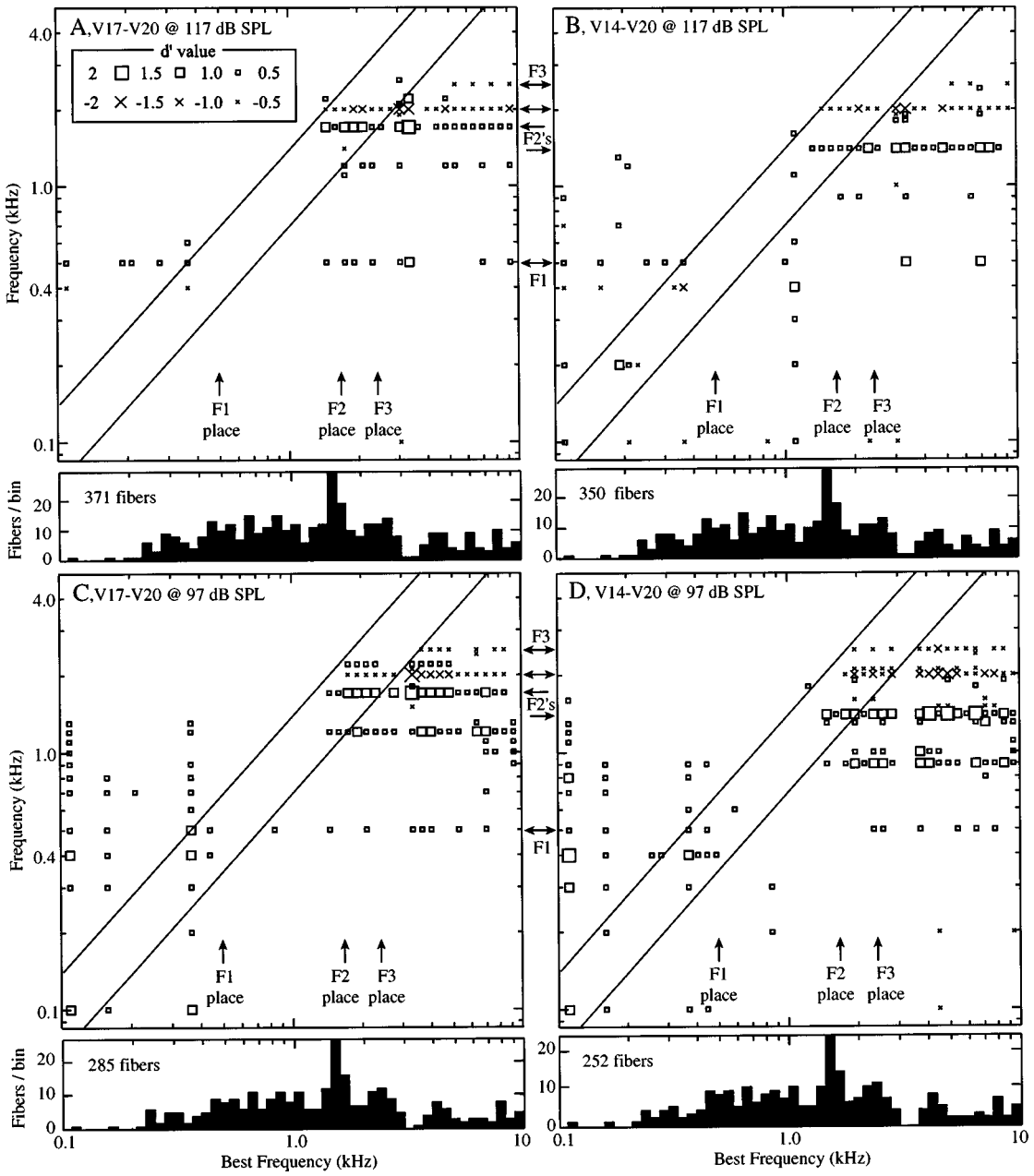

FIG. 10. Population distribution of discriminability based on phase-locking, as measured by $d'(kf_t)$ in Eq. (4). Frequency kf_t is shown on the ordinate. The plots are laid out as in Figs. 8 and 9, except it is d' that is plotted, not synchronized rate. The conventions for the scale are the same as in Figs. 7–9, except that boxes represent positive values of d' and Xs represent negative values.

present for both vowels of each comparison and should be larger.

III. DISCUSSION

A. Discriminability of the neural representations of the vowels

The results in Fig. 3 show that raising the level of the stimulus sufficiently, in this case to ≈97 dB, restores audibility, in the sense that fibers across the whole cochlea are responding to the stimulus. However, raising the level does not restore an adequate representation of the spectral shape of the stimulus, in that no clear representation of $F2$ can be seen at any level. In this paper, the quality of the neural representation of the stimulus was evaluated by looking at the representation of the differences between vowels differing in $F2$ frequency. This is a direct measure of the salience of $F2$ in the nervous system and should correlate with the animal's behavioral ability to discriminate $F2$ frequency. In fact, measurement of $F2$-frequency discrimination in normal cats shows that they are able to make this discrimination with a jnd that is comparable in size to that of humans (Hienz *et al.*, 1996). Comparison of behavioral jnds with the predictions of a signal-detection analysis of auditory-nerve responses in normal animals showed that the changes in discharge rate of the best auditory nerve fibers, i.e., those with BFs near the formants, are sufficient to support the behavioral discrimination (May *et al.*, 1996). Thus, the data in Fig. 4 are important in that they suggest little or no ability to discriminate $F2$ frequency on the basis of discharge-rate

changes after acoustic trauma. As discussed in Sec. II, the d' values for rate changes that signal changes in $F2$ are below 1 for almost all fibers. This result should be contrasted with the result for the same vowels in normal animals, where average d' values, among fibers with BFs near the $F2$ values, easily exceed 1 for $F2$ frequency changes as small as 50–100 Hz, depending on conditions (Conley and Keilson, 1995; May *et al.*, 1996).

Although the rate representation of the difference between stimuli is degraded, there are detectable differences in temporal measures of response, because of the rearrangement of the harmonic components in the response. This is shown in Fig. 10, where d' values for changes in phase-locking to the $F2$ frequencies exceed 1 among fibers with BFs at and above the $F2$ frequencies. Thus, the extent of the behavioral deficit caused by acoustic trauma will depend on the cues used by the CNS to discriminate the neural activity produced by two vowels. While the existence of both rate and temporal codes for spectral shape has long been recognized (Young and Sachs, 1979; Delgutte and Kiang, 1984; Palmer *et al.*, 1986), there is no direct evidence bearing on the question of which cues the CNS actually uses. The data in Figs. 4 and 10 predict that if the CNS uses only rate information, then cats should be essentially unable to discriminate these vowels after the kind of acoustic trauma used here; however, if the CNS can use some temporal information, then some ability to discriminate should survive.

In order to get a sufficient number of fibers to make population profiles, data were combined across four animals. At some frequencies, there were substantial threshold differences among these animals. Such threshold differences could conceivably degrade the quality of population representations since fibers were studied at different sound levels, relative to threshold. However, the two most important results of this paper, the lack of a rate difference representation and the presence of a weak temporal representation, could not be produced by such differences in relative sound level. In the case of the rate differences, no differences were seen in the whole population, so there cannot be differences in any subpopulation. By a similar argument, differences in temporal response that are present in the whole population must also be present in at least some subpopulations. In fact, plots like Figs. 8–10 made separately for each experiment (not shown) are just noisier versions of these figures.

B. Effects of errors in BF measurement

The tonotopic plots used to analyze the neural representations in this paper depend on obtaining an accurate measure of fiber BF. However, there are three well-known problems with determining BF following acoustic trauma (Robertson *et al.*, 1980; Liberman, 1984): (1) the tuning-curve program has a certain error, e.g., it does not return the same BF if it is run repeatedly on the same fiber (s.d.=0.022 octaves for normal fibers with our program, Calhoun *et al.*, 1998); (2) there is a shift in BF caused by acoustic trauma; and (3) the BFs of tuning curves in acoustically traumatized animals are ambiguous because of their broad, flat shape. The impaired-fiber tuning curve in Fig. 5(A), for example, could have a BF anywhere between about 0.8 and 1.4 kHz, if the minimum of the tuning curve is taken as the definition of BF. Obviously, using the minimum of such a tuning curve to define BF will lead to substantial errors with even small amounts of threshold noise. The definition of BF used here, the local minimum threshold nearest the high-frequency steep slope of the tuning curve, was chosen to minimize the ambiguity of BF in cases like this (Liberman, 1984). Liberman compared BF determined this way to the ''true'' BF determined from the fiber's point of innervation of the basilar membrane. Tuning-curve BFs were up to -0.6 octaves below the true BF, although the shifts were smaller (<0.2 octaves, about the standard deviation of BF shifts with this method in normal animals) for the majority of fibers, those which innervated points on the membrane that were at least 1 mm from regions of total destruction of the organ of Corti.

From the previous paragraph, it is clear that there is some uncertainty in BF determination in the data presented here, the question arises as to whether the poor quality of the neural representations described above results from this error. Three features of the data argue against this possibility. First, in the rate-difference analysis (Fig. 4), the vast majority of fibers show little or no rate difference. Any reasonable rearrangement of the data on the BF axis in Fig. 4 will not improve the representation. Extending this argument, if there are no rate differences between responses to different vowels, then the rate profiles in Fig. 3 cannot be substantially different for different vowels, implying that the poor quality of the absolute rate representation in Fig. 3 is not due to errors in BF. Second, although the synchronized responses to $F2$ in Figs. 8 and 9 spread over a wide range of cochlear locations, the low-BF end of the response is, in every case, located near the BF appropriate to the frequency of $F2$. That is, the spread in response to $F2$ is from the $F2$ place toward higher BFs. This result can only occur if the BFs of the fibers are generally correct. Third, when the spectral shape of the stimulus is modified to emphasize $F2$ and $F3$, a greatly improved tonotopic rate-difference representation of the vowels is seen (Miller *et al.*, 1996).

The uncertainties in determining BFs result from changes in the properties of the cochlea after acoustic trauma. These are real changes in fibers' BFs and in their tuning curves, which have functional consequences in terms of responses to complex stimuli. Given that the goal of this work is to analyze the perceptual consequences of changes in the neural representation of stimuli, it seems that the best definition of BF would be the one that the central nervous system uses. There are changes in the frequency organization of the central auditory system after cochlear damage (e.g., Leake *et al.*, 1995, Rajan and Irvine, 1998), although these have so far been analyzed only for much more severe damage than in the preparations used here. Because the nature and the extent of the central rewiring with hearing loss like that studied here are unknown, it is not possible to know with certainty how fibers should be placed on the BF axis in population plots like Figs. 3, 4, and 7–10. The definition of BF used here has the advantage that it corresponds roughly to the cochlear place map determined anatomically (Liberman, 1984). However, it has the disadvantage that it does not

take account of the activity-dependent processes that are usually thought to drive reorganization of sensory systems in the brain. For example, neurons over a wide range of BFs respond strongly to $F1$. This synchrony of response could drive a reorganization of the central frequency map in which fibers from a wide range of cochlear places project to the same point. Such a representation would be inferior to that shown here, in the sense that the weak tonotopic organization of $F2$ responses seen in phase-locking analyses (Figs. 8–10) would be lost. In that sense, the representations shown in this paper could be optimistic.

C. Impaired discriminability, loss of tuning, and nonlinear responses

The loss of the rate representation of $F2$ frequency derives from the degraded tuning of auditory-nerve fibers in the impaired animals. The nature of this change is apparent from the analyses of phase-locking in Figs. 5, 6, 8, and 9. Because fibers everywhere in the cochlea respond to a broad array of stimulus components (Figs. 8 and 9), there is no place in the cochlea where the discharge rate of a fiber is determined only, or even primarily, by the $F2$ component of the stimulus. The only fibers that will change rate significantly when $F2$ is altered are those responding primarily to $F2$; this can be seen by comparing response profiles in normal animals (e.g., Fig. 7) with rate-difference profiles in normal animals (dotted lines in Fig. 4). Because there are no fibers that respond primarily to $F2$ in the impaired animals, there are no fibers sensitive to $F2$ frequency changes in these animals. Thus, the broadband responses in impaired cochleas lead directly to a loss of sensitivity to $F2$ frequency.

Phase-locking to $F1$ is a significant component of the responses of impaired fibers with BFs near $F2$ (Figs. 8 and 9). The upward spread of response to $F1$ is therefore a major contributor to the degeneration of the representation of $F2$, in that the $F2$ fibers' rate responses are, to a significant degree, determined by their responses to $F1$. Spread of $F1$ can be controlled by high-pass amplification of the stimulus, which increases the level of $F2$ and $F3$ relative to $F1$ (Schilling *et al.*, 1998).

Part of the degradation of response in impaired animals may be attributable to the high sound levels that have to be used to exceed threshold following acoustic trauma. This possibility is suggested by the fact that fibers with BFs near $F2$ in normal animals show a response to $F1$ at high sound levels ($>$80 dB) that is similar to the upward spread of $F1$ observed in impaired animals (Wong *et al.*, 1998). However, even at high levels there are differences between the normal and impaired animals. In normal animals, the response of $F2$ fibers at high levels is almost exclusively to the stimulus components at $F1$, $F2$, and their harmonics and intermodulation products ($2F1$, $3F1$, $F2-F1$, etc.; Wong *et al.*, 1998). Such a response can be interpreted as being driven only by stimulus components at $F1$ and $F2$ (Young and Sachs, 1979), i.e., the response behaves as if the stimulus consisted only of two tones at the formant frequencies. By contrast, in the impaired animals a more diffuse phase-locking is seen to $F1$, $F2$, and most of the other frequency components of the stimulus (Miller *et al.*, 1997; Schilling *et al.*, 1998). This is apparent in the single-fiber data of Figs. 5 and 6, where responses to many stimulus components other than the formant harmonics and their intermodulation products are seen. It is also apparent in the population profiles of Figs. 8 and 9, where a broad distribution of phase-locking is seen in fibers of all BFs.

The differences in the nature of phase-locking between normal animals at high levels and impaired animals suggests that there are fundamental differences between the two preparations. In both cases, the large responses to $F1$ in fibers with BFs near $F2$ suggest a broadening of tuning. Previous studies, in normal animals, of basilar-membrane responses to tones and clicks (e.g., Ruggero *et al.*, 1992) show a broadening of the response area at high levels and a shift in BF which is consistent with a breakdown of the narrow tuning seen at lower sound levels. However, the fact that responses to a vowel in normal animals are seen only at $F1$ and $F2$ implies that energy at these formant frequencies is suppressing responses to other frequency components of the stimulus. That is, if it is assumed that the responses to $F1$ in the normal preparation at high levels and in the impaired preparation are both caused by broadening of the cochlear filters at the $F2$ place, then it follows that similar responses to intermediate frequency components of the vowel ought to be observed in the two preparations. The fact that they are not suggests that, in the normal preparation, the presence of nonlinear suppression allows the energy at $F1$ and $F2$ to suppress responses to other weaker components of the stimulus; this suppression is apparently weaker or not present in the impaired preparation. This conclusion is consistent with previous studies of two-tone suppression after acoustic trauma or ototoxic treatments (e.g., Dallos *et al.*, 1980; Schmiedt *et al.*, 1980; Salvi *et al.*, 1982; Miller *et al.*, 1997). Thus, there appear to be fundamental differences between normal responses at high sound levels and responses in impaired animals having to do with the lack of cochlear nonlinearities in the latter.

D. Implications for hearing impairment

To the extent that the neural representation in the cat is representative of results in humans, the results of this paper suggest that persons with sensorineural losses of the type studied here should show difficulties in speech perception related to perception of $F2$ and $F3$. Both rate and temporal representations of $F2$ and $F3$ are degraded, to different degrees. The difficulties should remain when amplification is provided to make the frequency components in the $F2/F3$ region audible (Schilling *et al.*, 1998). A component of the difficulties should be identifiable in perceptual terms as upward spread of masking of $F2$ and $F3$ by $F1$, but there may be additional difficulties associated with the general breakdown in cochlear filtering seen in these results. The data presented here, along with those from normal animals at high sound levels (Wong *et al.*, 1998), suggest that there should be some similarity in the deficits in hearing-impaired subjects and in normal subjects at high sound levels, particularly those associated with upward spread of masking, but that hearing-impaired listeners should show additional deficits related to the breakdown in cochlear nonlinearities.

Perceptual studies of hearing-impaired subjects are generally consistent with the expectations in the previous paragraph. Danaher and colleagues (Danaher *et al.*, 1973; Danaher and Pickett, 1975) showed that hearing-impaired subjects have increased thresholds, relative to normal subjects, for detection of changes in the $F2$ frequency of formant transitions in consonant–vowel (CV) syllables. A component of the deficit was upward-spread-of-masking by $F1$, because reducing the amplitude of $F1$, removing it, or moving it to the contralateral ear improved performance. A similar upward-spread-of-masking effect was seen in normal observers at high levels, although the effect was not as large as in hearing-impaired observers (Danaher *et al.*, 1973). Similar results were obtained for identification of stop consonants along a continuum that depended on $F2$ transitions (Hannley and Dorman, 1983); again, reducing the amplitude of $F1$ produced an improvement in performance, consistent with an upward-spread-of-masking effect. These results were obtained with CV transitions, not steady vowels, but the general nature of the phenomena should be similar for the two kinds of stimuli, based on previous studies of CV syllables in normal physiological preparations (Miller and Sachs, 1983). A possibly related result obtained with steady-state vowels is that the jnd for the amplitude of $F2$ is larger in hearing-impaired listeners than in normal listeners and performance is improved by high-pass filtering the stimuli, suggesting an upward-spread-of-masking effect (Turner and Holte, 1987). However, specific deficits of $F2$ perception have not been obtained in all studies (e.g., Van Tasell, 1980; Turner and Van Tasell, 1984) and in all conditions. Moreover, there are considerable differences among hearing-impaired observers; some of these differences are related to the nature of the hearing loss, so that observers having noise-induced or sloping high-frequency losses generally produce results most like the results shown here. Despite these reservations, the results from perceptual studies are generally consistent with the predictions from the data shown here.

The results in this paper suggest that insights into hearing-aid signal processing can be obtained by considering the neural representation of the stimulus at the level of the auditory nerve. Because the lesion in most cases of deafness is in the cochlea, auditory-nerve discharge patterns provide a direct measure of surviving function in an impaired cochlea. Auditory-nerve discharge patterns can be studied in animal models in which noise exposure or ototoxic drugs are used to induce a cochlear lesion. To the extent that the physiology is the same in these animal models and in humans with sensorineural loss, these auditory-nerve data provide a detailed direct view of the effects of the cochlear insult, the nature of the deficits in the impaired representation, and the effectiveness of various hearing-aid signal-processing strategies. By adding behavioral analysis of the discriminative capabilities of animals following acoustic trauma, the perceptual effects of particular lesions can be studied, because it is possible to experimentally characterize the auditory-nerve representation in experimental animals at the conclusion of the behavioral work. The effectiveness of particular cues can be studied in order to isolate the cues that are most important and then the effectiveness of particular hearing-aid processing strategies can be evaluated, in terms of their abilities to restore the cues that are most important. The data presented in this paper show that the normal tonotopic presentation of information to the central auditory system, in which responses to particular stimulus components are separated along the tonotopic axis, is degraded with moderate sensorineural loss of the type studied here. These data form a basis for considering how various hearing-aid signal-processing strategies could improve the representation of $F2$ and $F3$ in an impaired ear.

ACKNOWLEDGMENTS

The authors thank Kevin Davis, Patrick Kanold, Brad May, and Daniel Suta for helpful comments on the manuscript, Jane Yu for help in preliminary experiments, and Jeff Wong for participating in later experiments. The technical assistance of Ron Atkinson and Phyllis Taylor is also appreciated. This work was supported by NIDCD grant No. DC00109. Training support for R.L.M. was provided by grant No. DC00979 and support for B.M.C. was provided by fellowship No. DC00202.

Calhoun, B. M., Miller, R. L., Wong, J. C., and Young, E. D. (**1998**). ''Rate encoding of stimulus spectra by auditory nerve fibers,'' in *Psychophysical and Physiological Advances in Hearing*, edited by A. R. Palmer, A. Rees, A. Q. Summerfield, and R. Meddis (Whurr, London), pp. 170–177.

Conley, R. A., and Keilson, S. E. (**1995**). ''Rate representation and discriminability of second formant frequencies for /ε/-like steady-state vowels in cat auditory nerve,'' J. Acoust. Soc. Am. **98**, 3223–34.

Dallos, P., Harris, D. M., Relkin, E., and Cheatham, M. A. (**1980**). ''Two-tone suppression and intermodulation distortion in the cochlea: Effect of outer hair cell lesions,'' in *Psychophysical, Physiological and Behavioral Studies in Hearing*, edited by G. van den Brink and F. A. Bilsen (Delft U. P., Delft), pp. 242–252.

Danaher, E. M., Osberger, M. J., and Pickett, J. M. (**1973**). ''Discrimination of formant frequency transitions in synthetic vowels,'' J. Speech Hear. Res. **16**, 439–51.

Danaher, E. M., and Pickett, J. M. (**1975**). ''Some masking effects produced by low-frequency vowel formants in persons with sensorineural hearing loss,'' J. Speech Hear. Res. **18**, 261–271.

Delgutte, B., and Kiang, N. Y. (**1984**). ''Speech coding in the auditory nerve: I. Vowel-like sounds,'' J. Acoust. Soc. Am. **75**, 866–78.

Guinan, J. J., and Peake, W. T. (**1967**). ''Middle-ear characteristics of anesthetized cats,'' J. Acoust. Soc. Am. **41**, 1237–1261.

Hannley, M., and Dorman, M. F. (**1983**). ''Susceptibility to intraspeech spread of masking in listeners with sensorineural hearing loss,'' J. Acoust. Soc. Am. **74**, 40–51.

Hienz, R. D., Aleszczyk, C. M., and May, B. J. (**1996**). ''Vowel discrimination in cats: acquisition, effects of stimulus level, and performance in noise,'' J. Acoust. Soc. Am. **99**, 3656–68.

Klatt, D. H. (**1980**). ''Software for a cascade/parallel formant synthesizer,'' J. Acoust. Soc. Am. **67**, 971–995.

Kiang, N. Y., Moxon, E. C., and Levine, R. A. (**1970**). ''Auditory-nerve activity in cats with normal and abnormal cochleas,'' in *Sensorineural Hearing Loss*, edited by G. E. W. Wolstenholme and T. Knight (Churchill, London), pp. 241–273.

Leake, P. A., Snyder, R. L., Hradek, G. T., and Rebscher, S. J. (**1995**). ''Consequences of chronic extracochlear electrical stimulation in neonatally deafened cats,'' Hearing Res. **82**, 65–80.

Le Prell, G., Sachs, M. B., and May, B. J. (**1996**). ''Representation of vowel-like spectra by discharge rate responses of individual auditory-nerve fibers,'' Auditory Neurosci. **2**, 275–288.

Liberman, M. C. (**1984**). ''Single-neuron labeling and chronic cochlear pathology. I. Threshold shift and characteristic-frequency shift,'' Hearing Res. **16**, 33–41.

Liberman, M. C., and Dodds, L. W. (**1984**). ''Single-neuron labeling and chronic cochlear pathology. II. Stereocilia damage and alterations of spontaneous discharge rates,'' Hearing Res. **16**, 43–53.

May, B. J., Huang, A., Le Prell, G., and Hienz, R. D. (**1996**). ''Vowel formant frequency discrimination in cats: Comparison of auditory nerve representations and psychophysical thresholds,'' Auditory Neurosci. **3**, 135–162.
Miller, M. I., and Sachs, M. B. (**1983**). ''Representation of stop consonants in the discharge patterns of auditory-nerve fibers,'' J. Acoust. Soc. Am. **74**, 502–17.
Miller, J. D., Watson, C. S., and Covell, W. P. (**1963**). ''Deafening effects of noise on the cat,'' Acta Oto-Laryngol. **176**, 1–91.
Miller, M. I., Barta, P. E., and Sachs, M. B. (**1987**). ''Strategies for the representation of a tone in background noise in the temporal aspects of the discharge patterns of auditory-nerve fibers,'' J. Acoust. Soc. Am. **81**, 665–79.
Miller, R. L., Schilling, J. R., and Young, E. D. (**1996**). ''Effects of two amplification schemes on the representation of the vowel /ɛ/ in the auditory nerve of cats with a noise-induced hearing loss,'' ARO Abst. **19**, 79.
Miller, R. L., Schilling, J. R., Franck, K. R., and Young, E. D. (**1997**). ''Effects of acoustic trauma on the representation of the vowel /ɛ/ in cat auditory nerve fibers,'' J. Acoust. Soc. Am. **101**, 3602–3616.
Palmer, A. R., and Moorjani, P. A. (**1993**). ''Responses to speech signals in the normal and pathological peripheral auditory system,'' Prog. Brain Res. **97**, 107–115.
Palmer, A. R., Winter, I. M., and Darwin, C. J. (**1986**). ''The representation of steady-state vowel sounds in the temporal discharge patterns of the guinea pig cochlear nerve and primarylike cochlear nucleus neurons,'' J. Acoust. Soc. Am. **79**, 100–13.
Rajan, R., and Irvine, D. R. F. (**1998**). ''Neuronal responses across cortical field *A*1 in plasticity induced by peripheral auditory organ damage,'' Audiol. Neurootol. **3**, 123–144.
Rice, J. J., Young, E. D., and Spirou, G. A. (**1995**). ''Auditory-nerve encoding of pinna-based spectral cues: rate representation of high-frequency stimuli,'' J. Acoust. Soc. Am. **97**, 1764–76.
Robertson, D., Cody, A. R., Bredberg, G., and Johnstone, B. M. (**1980**). ''Response properties of spiral ganglion neurons in cochleas damaged by direct mechanical trauma,'' J. Acoust. Soc. Am. **67**, 1295–1303.
Ruggero, M. A., Robles, L., Rich, N. C., and Recio, A. (**1992**). ''Basilar membrane responses to two-tone and broadband stimuli,'' Philos. Trans. R. Soc. London, Ser. B **336**, 307–315.
Sachs, M. B. (**1984**). ''Speech encoding in the auditory nerve,'' in *Hearing Science Recent Advances*, edited by B. C. I. (College Hill, San Diego), pp. 263–307.
Sachs, M. B., and Young, E. D. (**1979**). ''Encoding of steady-state vowels in the auditory nerve: representation in terms of discharge rate,'' J. Acoust. Soc. Am. **66**, 470–9.
Salvi, R., Perry, J., Hamernik, R. P., and Henderson, D. (**1982**). ''Relationships between cochlear pathologies and auditory nerve and behavioral responses following acoustic trauma,'' in *New Perspectives on Noise-Induced Hearing Loss*, edited by R. P. Hamernik, D. Henderson, and R. Salvi (Raven, New York), pp. 165–188.
Schilling, J. R. (**1995**). ''The Effects of Acoustic Trauma and Hearing-aid Processing on the Encoding of Vowels in the Auditory Nerve,'' Master of Science in Engineering thesis, The Johns Hopkins University, Baltimore, MD.
Schilling, J. R., Miller, R. L., Sachs, M. B., and Young, E. D. (**1998**). ''Frequency shaping changes the neural representation of speech with noise-induced hearing loss,'' Hearing Res. **117**, 57–70.
Schmiedt, R. A., Zwislocki, J. J., and Hamernik, R. P. (**1980**). ''Effects of hair cell lesions on responses of cochlear nerve fibers. I. Lesions, tuning curves, two-tone inhibition, and responses to trapezoidal-wave patterns,'' J. Neurophysiol. **43**, 1367–1389.
Siebert, W. M. (**1970**). ''Frequency discrimination in the auditory system: Place or periodicity mechanisms?'' Proc. IEEE **58**, 723–30.
Sinex, D. G., and Geisler, C. D. (**1983**). ''Responses of auditory-nerve fibers to consonant–vowel syllables,'' J. Acoust. Soc. Am. **73**, 602–15.
Turner, C. W., and Holte, L. A. (**1987**). ''Discrimination of spectral-peak amplitude by normal and hearing-impaired subjects,'' J. Acoust. Soc. Am. **81**, 445–51.
Turner, C. W., and Van Tasell, D. J. (**1984**). ''Sensorineural hearing loss and the discrimination of vowel-like stimuli,'' J. Acoust. Soc. Am. **75**, 562–5.
Van Tasell, D. J. (**1980**). ''Perception of second-formant transitions by hearing-impaired persons,'' Ear Hearing **1**, 130–6.
Wiener, F. M., and Ross, D. A. (**1946**). ''The pressure distribution in the auditory canal in a progressive sound field,'' J. Acoust. Soc. Am. **18**, 401–408.
Wong, J., Miller, R. L., Calhoun, B. M., Sachs, M. B., and Young, E. D. (**1998**). ''Effects of high sound levels on responses to the vowel /ɛ/ in cat auditory nerve,'' Hearing Res. **123**, 61–77.
Young, E. D., and Sachs, M. B. (**1979**). ''Representation of steady-state vowels in the temporal aspects of the discharge patterns of populations of auditory-nerve fibers,'' J. Acoust. Soc. Am. **66**, 1381–1403.

Psychophysical measures of auditory nonlinearities as a function of frequency in individuals with normal hearing

Michelle L. Hicks and Sid P. Bacon
Psychoacoustics Laboratory, Department of Speech and Hearing Science, Arizona State University, Tempe, Arizona 85287-1908

(Received 16 March 1998; revised 19 August 1998; accepted 25 September 1998)

In order to gain a better understanding of how auditory nonlinear phenomena vary as a function of location along the cochlea, several psychophysical measures of nonlinearity were examined as a function of signal frequency. Six normal-hearing individuals completed three experiments, each designed to measure one aspect of nonlinear behavior: (1) the effects of level on frequency selectivity in simultaneous masking, measured using notched-noise maskers at spectrum levels of 30 and 50 dB, (2) two-tone suppression, measured using forward maskers at the signal frequency (f_s) and suppressor tones above f_s, and (3) growth of masking, measured using forward maskers below f_s at a signal/masker frequency ratio of 1.44. Four signal frequencies (375, 750, 1500, and 3000 Hz) were tested to sample the nonlinear behavior at different locations along the basilar membrane, in order to test the hypothesis that the apical (low-frequency) region of the cochlea behaves more linearly than the basal (high-frequency) region. In general, all three measures revealed a progressive increase in nonlinear behavior as signal frequency increased, with little or no nonlinearity at the lowest frequency, consistent with the hypothesis. © *1999 Acoustical Society of America.* [S0001-4966(99)03601-2]

PACS numbers: 43.66.Ba, 43.66.Dc [JWH]

INTRODUCTION

It is generally well known that the auditory system behaves in a nonlinear manner, with reports of otoacoustic emissions, distortion-product generation, suppression, and nonlinear growth of masking frequently being cited as evidence for the nonlinearity. This nonlinearity is believed to be responsible for high sensitivity and sharp frequency selectivity in the auditory system. The nonlinearity is often assumed to be the result of active processes inherent in the healthy cochlea, with the outer-hair cells believed to be the ''cochlear amplifiers'' responsible for the active, nonlinear behavior. It has been suggested (Wilson, 1992; Rosen and Stock, 1992) that the apical regions of the basilar membrane behave more linearly than the basal regions, although there are only a few studies that have addressed this idea (Cooper and Rhode, 1995; Cooper and Yates, 1994). Most previous physiological investigations have studied the mechanics and processing of the basal, or high-frequency, region of the basilar membrane, whereas relatively few studies have examined the apical, or low-frequency, region.

Several psychophysical investigations of nonlinear processing appear to support the idea of reduced nonlinearity at lower signal frequencies. Rosen and Stock (1992) measured auditory filter bandwidths in normal-hearing listeners using a notched-noise method. Simultaneous-masked thresholds were measured for signal frequencies (f_s) between 125 and 1000 Hz, and for masker spectrum levels of 40–70 dB. They found that the filter bandwidths generally increased with masker level, with the greatest effect of level at 1000 Hz, and little or no effect at 125 Hz. These results are similar to those of previous studies that have shown an effect of masker level for frequencies at and above 1000 Hz (Weber, 1977; Pick, 1980; Moore and Glasberg, 1987), as well as the results observed by Moore *et al.* (1990), where there was no effect of masker level at 100 and 200 Hz, but a significant effect at 800 Hz. Rosen and Stock suggested that the level-dependent changes in frequency selectivity only at higher signal frequencies may indicate less involvement of nonlinear processing at lower frequencies.

Psychophysical measurements of two-tone suppression also lend support for greater nonlinearity at high frequencies. Shannon (1976) measured two-tone suppression for signal frequencies from 500 to 6000 Hz using a forward-masking technique. He found that for signal frequencies from 1000–6000 Hz, the maximum amount of suppression was approximately equal, and occurred when the suppressor was at the same relative frequency (approximately $1.2f_s$). However, at 500 Hz, the maximum amount of suppression was smaller than that observed at higher signal frequencies, and occurred when the suppressor was at a higher relative frequency. Moreover, one of his five subjects only showed suppression for signal frequencies greater than 2000 Hz. More recently, Thibodeau and Fagelson (1993) and Lee and Bacon (1998) also found less suppression at low rather than at high frequencies, consistent with decreased nonlinear processing at low frequencies.

Another psychophysical measure that has been suggested as a technique for estimating basilar membrane nonlinearity is growth-of-masking functions for pure-tone signals and maskers, where f_s is greater than the masker frequency (f_m; Oxenham and Plack, 1997). This technique is based on physiological studies that have shown that the basilar membrane response to a tone at CF (the signal) is compressive at mid-stimulus levels, whereas the response to a tone below CF (the masker) is linear. Thus, if subjects monitor the place along the basilar membrane corresponding to f_s, a given increase in masker level requires a larger increase in signal level for detection (due to the compressive

basilar membrane response to the signal). The resulting growth-of-masking functions (signal level versus masker level) will be steeper than if the basilar membrane were responding linearly to both tones. Thus, a steep growth-of-masking function can be considered the reciprocal of a compressed basilar membrane input/output response. In studies that have examined growth of masking over a wide range of signal frequencies, including frequencies at or below 500 Hz, growth-of-masking functions ($f_m < f_s$) have typically been steeper (implying a greater nonlinearity) at higher frequencies than at lower frequencies (Kidd and Feth, 1981; Verschuure, 1981; Zwicker and Jaroszewski, 1982).

On the other hand, Schöne (1977) measured growth-of-masking functions in simultaneous masking for signal frequencies from 700 to 4800 Hz with maskers placed an equal number of barks below f_s, and found no differences in the slopes of the functions for the different signal frequencies. Oxenham and Plack (1997) also found no difference in slope across frequency when they measured growth-of-masking functions in forward masking for signal frequencies of 2000 and 6000 Hz. The lack of an effect of frequency is most likely due to not examining signal frequencies that were low enough.

Although most of the psychophysical literature to date seems to suggest that nonlinear processing is stronger at the basal, high-frequency region of the basilar membrane than at the apical, low-frequency region, there are few studies that have directly and systematically addressed this idea. Moreover, few studies have evaluated multiple measures of nonlinearity to determine whether these different phenomena are similarly affected by frequency, or have extended their investigations to signal frequencies below 500 Hz. It is important to evaluate a wide range of signal frequencies, to determine whether there is a gradual transition from nonlinear to linear processing as one proceeds from the base to the apex of the cochlea, or whether there is some critical frequency below which the nonlinearity disappears. Thus, the goal of this study was to further our understanding of how auditory nonlinear phenomena vary as a function of location along the cochlea by examining three psychophysical measures of nonlinearity as a function of frequency in normal-hearing individuals.

I. GENERAL METHODS

A. Subjects

Six normal-hearing subjects, ranging in age between 22 and 39 years, participated. All had absolute thresholds at or below 10 dB HL (ANSI, 1989) at the octave frequencies from 250–8000 Hz in the test ear. Subject S1 (the first author) had extensive experience in psychoacoustic tasks similar to those in the present study; subjects S4–S6 participated in experiments from Hicks and Bacon (1998), and had approximately 10 h of experience with conditions identical to those in the present study; and subjects S2 and S3 received approximately 1/2 h of practice with the forward-masking conditions (anticipated to be the most variable[1]) prior to data collection. Subjects S2–S6 were paid for their participation.

B. Apparatus and stimuli

The sinusoidal signals and maskers were digitally generated and produced at a 20-kHz sampling rate. The output of the digital-to-analog converter (TDT DA1) was low-pass filtered at 8 kHz (Kemo VBF 25.01; 135 dB/octave). The notched-noise maskers, which consisted of two bands of noise placed about f_s, were produced by low-pass filtering (Kemo VBF 25.01) random noise from two independent noise generators (GenRad 1381), and multiplying each low-pass noise by a different sinusoid (HP 8904 A synthesizer). The resultant noise masker consisted of two bands of noise, each with a bandwidth that was twice the cutoff frequency of the low-pass filter, and a center frequency that was equal to the frequency of the sinusoid. The bandwidth of each noise band was $0.4f_s$, and the frequencies of the sinusoids were chosen such that the bands were placed either symmetrically or asymmetrically about f_s. The spectrum level of the noise masker was calibrated using a Hewlett-Packard 3561 spectrum analyzer and controlled via manual attenuators. The level of the signal was varied adaptively via a programmable attenuator (Wilsonics PATT), and the signal and masker were added together prior to being presented monaurally through a TDH-49P headphone mounted in an MX/51 cushion. Specific stimuli and experimental conditions are described prior to each experiment.

C. Experimental procedure

Subjects were tested individually or in pairs in a double-walled, sound-attenuating booth. Thresholds were measured using an adaptive, two-interval forced-choice procedure with a decision rule that estimates 79% correct on the psychometric function (Levitt, 1971). Subjects responded by pushing one of two buttons on a response panel. Lights were used to indicate when the signal might occur and then to provide correct-response feedback. The two observation intervals were separated by 400 ms. The signal level began 10–15 dB above the estimated threshold; it was decreased following three correct responses and increased following one incorrect response. The step size was initially 4 dB, but was decreased to 2 dB following the second reversal. The first two reversals (or three, if the total number of reversals was odd) in each 50-trial block were discarded, and the signal levels at the remaining reversals were averaged to obtain the threshold for that run. A run was included only if the standard deviation (s.d.) of the signal levels at the reversals was 5 dB or less and if there were at least six signal levels in the average. Each threshold reported is the mean from at least three runs obtained over at least two days. If the s.d. of that mean was greater than 3 dB, additional runs were included (up to a maximum of six) until the s.d. was less than 3 dB.

II. EXPERIMENT 1: EFFECT OF LEVEL ON FREQUENCY SELECTIVITY AS A FUNCTION OF FREQUENCY

A. Rationale

The purpose of this experiment was to evaluate the effect of level on frequency selectivity over a wider range of

frequencies than has been previously examined within a single group of subjects to determine if the nonlinear increase in auditory filter bandwidth with increasing level would be greater at higher frequencies, as suggested by comparing across previous studies (Weber, 1977; Pick, 1980; Lutfi and Patterson, 1984; Moore *et al.*, 1990; Rosen and Stock, 1992). Masker spectrum levels of 30 and 50 dB were used, as a clear increase in auditory filter bandwidth has been demonstrated over this range of masker levels for signal frequencies greater than 1000 Hz (Weber, 1977; Lutfi and Patterson, 1984).

B. Stimuli and conditions

Simultaneous-masked thresholds were obtained for four signal frequencies (375, 750, 1500, and 3000 Hz) at two noise-masker spectrum levels (30 and 50 dB). The noise masker consisted of two bands of noise, each $0.4f_s$ wide, placed symmetrically or asymmetrically around f_s. In the symmetric conditions, the edge of the noise band closer to f_s was placed at 0.0, 0.2, and $0.4f_s$. In the asymmetric conditions, the closer edge of the noise band on the low- (or high-) frequency side was placed at 0.2 and $0.3f_s$, and the closer edge of the corresponding noise band on the high- (or low-) frequency side was placed at 0.4 and $0.5f_s$, respectively, for a total of three symmetric and four asymmetric notch conditions. The signal and masker were both 300 ms in duration (including their 10-ms $\cos^2$ rise/fall times).

The data from each combination of signal frequency and masker level were fitted with the roex(p,r) model (Patterson *et al.*, 1982) using a least-squares criterion to derive auditory filter shapes. The weighting function W that describes the upper skirt of the filter is

$$W(g)=(1-r)(1+p_u g)\exp(-p_u g)+r,$$

and the function that describes the lower skirt of the filter is

$$W(-g)=(1-r)(1+p_l g)\exp(-p_l g)+r,$$

where g is the deviation from the center (or signal) frequency and the near edge of the noise band, as a proportion of the center frequency, r is the dynamic range of the filter, and p_l and p_u represent the slopes of the lower and upper filter skirts, respectively, which determine the width of the passband of the filter. (Note that larger p values indicate steeper slopes.) These measures, as well as the Equivalent Rectangular Bandwidth (ERB) and the detector efficiency following the filter (K), were determined using a modified version of the computer program of Glasberg and Moore (1990). Only the measures of ERB, p_l, and p_u, will be discussed as the present study was concerned primarily with measures of filter shape and bandwidth. As suggested by Glasberg and Moore, correction for variations in absolute thresholds across frequencies was applied to the fitting procedure by implementing an equal-loudness-contour (ELC) weighting factor for the higher masker level.[2]

C. Results and discussion

The results for all subjects were similar, and thus their averaged data, and the filter shapes derived from the averaged data, are presented in Fig. 1. The masked thresholds are shown in the left-hand panels, and the derived filter shapes are shown in the right-hand panels. Results are shown for each signal frequency as a function of the deviation of the nearer noise band from the signal frequency, normalized to the signal frequency ($\Delta f/f_s$). Several measures related to the derived filter shapes (ERB, p_l, and p_u, and r) are given in Table I for the individual and mean data. (Note that the mean values represent the parameters of the filters fitted to the mean data, and not the mean of the parameter values across subjects.)

First consider the masked thresholds. As expected, for all signal frequencies, thresholds decreased as the noise bands were moved further away from f_s, and were higher for the 50-dB masker (filled symbols) than for the 30-dB masker (unfilled symbols). For the 375-Hz signal, thresholds for the two asymmetric notch conditions (right- and left-pointing triangles) essentially overlapped one another at both masker levels, indicating symmetric auditory filters at both masker levels. However, for the other signal frequencies, thresholds for the asymmetric notch conditions overlapped only at the lower masker level. At the higher masker level, thresholds were 5–10 dB higher for the conditions where the high-frequency noise band was further away from f_s (right-pointing triangles) than where the low-frequency noise band was further away (left-pointing triangles). Thus, at these three higher frequencies, the filters are symmetric only at the lower masker level. This effect of level on the shape of the auditory filters can be seen more easily by examining the derived auditory filter shapes. The filter shapes obtained from the average data with the 30-dB masker are shown by dashed lines, and those obtained with the 50-dB masker are shown by solid lines.

First consider the filter shapes obtained with a signal frequency of 375 Hz (top right). The filter shapes were very similar at the two levels, indicating that there was very little change in auditory filter shape over this 20-dB range of masker level. The ERB, p_l, and p_u values were similar at the two levels for all subjects except for S1 and S5, whose p_l values at the 30-dB masker level (indicated by asterisks in Table I) may have been overestimated by the fitting procedure: Glasberg and Moore (1990) have suggested that when the p value for one side of a filter is more than twice the value of the other side, then the larger value is poorly defined. The mean ERB, p_l, and p_u values at both masker-spectrum levels are similar to estimates obtained by Moore *et al.* (1990) for a signal frequency of 400 Hz and masker-spectrum levels of 52 and 62 dB SPL, and are consistent with the suggestion that auditory filter shape and bandwidth are independent of level at low signal frequencies (Rosen and Stock, 1992).

Now consider the filter shapes obtained with signal frequencies of 750, 1500, and 3000 Hz. For the most part, these frequencies can be considered together, as they exhibit the same general trend in terms of the effect of level, although to varying degrees. As f_s increased from 750 to 3000 Hz, there was an increasing difference between the filter shapes obtained at 30 and 50 dB, primarily on the low-frequency side. In particular, the effect of masker level was manifest as a

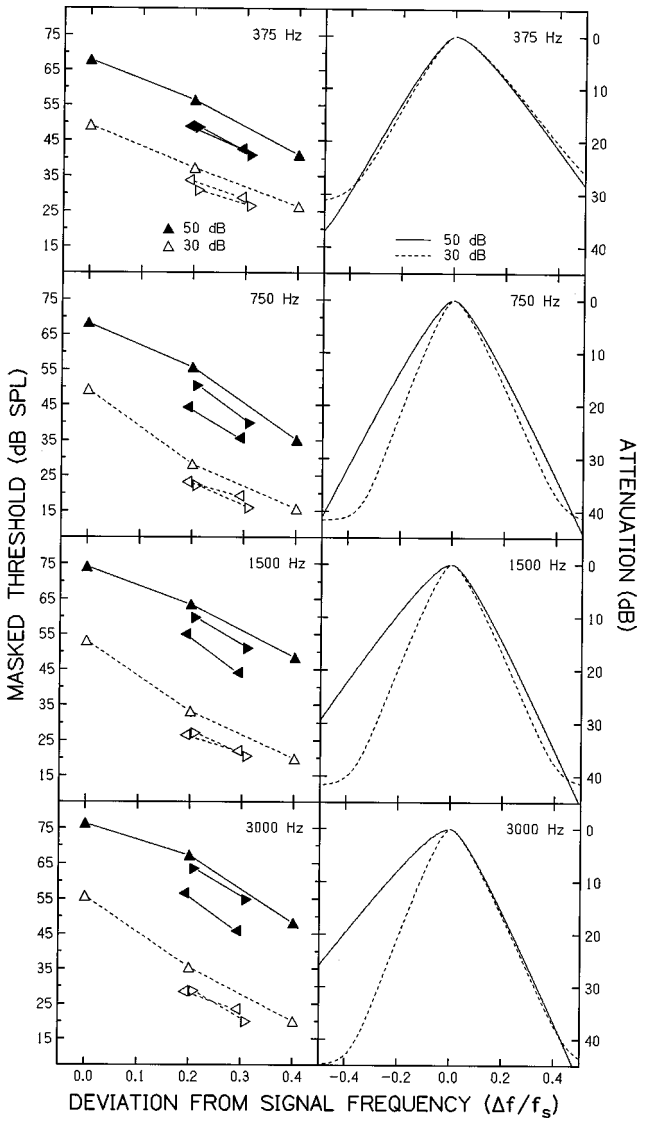

FIG. 1. In the left-hand panels, masked threshold is shown as a function of the deviation of the nearer noise band from the signal frequency, normalized to the signal frequency. Up-pointing triangles represent conditions where the noise bands were placed symmetrically about the signal frequency, and right- and left-pointing triangles represent conditions where the high- or low-frequency band was further away, respectively. Filled symbols are for the 50-dB masker, and unfilled symbols are for the 30-dB masker. The results were averaged across subjects S1–S6. The auditory filter shapes derived from the averaged data are shown in the right-hand panels. Filters obtained with the 30-dB masker are shown by dashed lines, and those obtained with the 50-dB masker are shown by solid lines.

shallower low-frequency slope at the higher masker level (indicated by smaller p_l values at the higher masker level), which became more pronounced as f_s increased. There was little or no change in the high-frequency slope. As a result, the filter bandwidths were wider at the 50-dB masker level than at the 30-dB masker level, and the difference between the two levels became greater as f_s increased. The filter bandwidths measured with the 50-dB masker were 26%, 44%, and 52% larger than those measured with the 30-dB masker for signal frequencies of 750, 1500, and 3000 Hz, respectively. These differences are similar to those observed by Weber (1977) over the same range of masker levels. The asymmetric broadening of the filters with increasing level also has been shown previously for high (typically greater than 1000-Hz) signal frequencies, and the mean ERB, p_l, and p_u values are generally close to estimates obtained by researchers using similar signal frequencies and masker levels (e.g., Moore and Glasberg, 1987; Moore, 1987; Wright, 1996).

When all of the signal frequencies are considered together, there is a clear trend in how level affects frequency selectivity as a function of f_s. In particular, there is essentially no effect of level (at least over the 20-dB range evaluated here) on the filter shape at 375 Hz, but there is an increasing effect of level on both the low-frequency slope (which most likely reflects the nonlinear nature of upward spread of masking) and the bandwidth of the auditory filters as f_s increases from 750 to 3000 Hz, consistent with greater nonlinear processing at higher frequencies. However, it is important to consider whether these results were influenced by differences in sensation level (SL) across frequency. If changes in frequency selectivity with level are smaller at lower SLs (as they are at lower masker SPLs: Weber, 1977; Lutfi and Patterson, 1984), it is possible that the absence of a level effect at low frequencies might not be due to an absence of a nonlinearity, but to a lower effective masker level. That is, the audibility of both noise bands at 375 Hz (and to a lesser extent, the audibility of the lower noise band at 750 Hz) may have reduced the effect of level on frequency selectivity at those lower frequencies. Quiet thresholds were higher at 375 Hz than at the other frequencies (see experiment 2, Fig. 2), and thus we cannot rule out the possible influence of SL. However, reduced SL cannot account for the overall progressive increase in apparent nonlinear processing as f_s increased beyond 750 Hz, as there was essentially no change in quiet thresholds over this range of frequencies.

III. EXPERIMENT 2: MEASURES OF TWO-TONE SUPPRESSION AS A FUNCTION OF FREQUENCY

A. Rationale

The purpose of this experiment was to measure two-tone suppression as a function of f_s to determine whether larger amounts of suppression would be obtained at higher rather than at lower signal frequencies. In general, Shannon (1976) found more suppression for signal frequencies at and above 1000 Hz than at 500 Hz. Unfortunately, Shannon decreased the signal duration with increasing frequency, making it difficult to determine whether the smaller amount of suppression at 500 Hz was due to the longer signal duration or to a decrease in nonlinear processing. Likewise, Thibodeau and Fagelson (1993) found more suppression at 2000 Hz than at 500 Hz, but by studying only two frequencies, it cannot be determined how suppression varies over a range of signal frequencies. Lee and Bacon (1998) measured suppression over a wider range of frequencies and found that suppression increased as f_s increased from 250 to 1000 Hz, with little or no additional increase in suppression as f_s increased to 4000 Hz. However, they observed, at most, only about 5 dB of two-tone suppression (measured as a change in threshold) at the highest frequencies, possibly because they used only a single masker (and suppressor) level and a single suppressor/

TABLE I. ERB, p_l, p_u, and r values for each signal frequency and masker level derived from the individual and mean data using the roex(p,r) filter model of Patterson *et al.* (1982). Asterisks (*) indicate values that may have been overestimated by the fitting procedure (see the text).

	Masker level							
	30 dB				50 dB			
Signal freq./subject	ERB	p_l	p_u	r	ERB	p_l	p_u	r
375 Hz								
S1	89	42.1*	10.6	−35.9	90	21.0	13.9	−59.2
S2	100	18.3	12.9	−31.3	89	19.7	14.9	−67.4
S3	60	28.2	22.8	−30.2	55	31.1	24.4	−38.5
S4	68	25.1	20.0	−31.2	70	24.9	18.7	−58.4
S5	73	34.2*	14.8	−34.4	78	24.9	15.9	−41.1
S6	61	25.2	24.1	−38.5	65	21.9	24.1	−40.6
mean	**75**	**24.5**	**17.2**	**−31.4**	**75**	**22.9**	**17.7**	**−41.5**
750 Hz								
S1	104	43.3	21.7	−39.3	133	26.9	19.3	−84.1
S2	90	40.6	28.2	−45.0	113	24.2	29.1	−45.4
S3	92	31.0	34.3	−43.1	126	22.2	25.8	−74.2
S4	95	35.2	28.7	−44.8	117	25.1	26.4	−73.9
S5	91	35.5	30.8	−41.5	107	26.3	30.0	−57.9
S6	95	29.1	34.4	−37.9	116	24.0	28.0	−47.4
mean	**95**	**34.8**	**28.9**	**−41.6**	**120**	**24.0**	**25.6**	**−64.3**
1500 Hz								
S1	316	22.9	16.2	−37.4	448	10.0	20.1	−64.6
S2	199	34.0	27.1	−42.2	214	26.5	29.5	−49.7
S3	187	31.9	32.1	−39.5	250	18.5	34.1	−43.5
S4	169	36.4	34.5	−48.8	249	21.1	28.0	−106.1
S5	198	31.4	29.4	−39.9	315	15.3	25.3	−66.3
S6	151	40.9	38.7	−47.4	235	21.4	31.4	−52.9
mean	**195**	**32.5**	**29.5**	**−41.7**	**281**	**18.1**	**26.4**	**−72.9**
3000 Hz								
S1	450	29.1	24.6	−46.0	648	13.4	30.3*	−76.3
S2	426	27.7	28.6	−40.3	474	19.0	37.8	−85.3
S3	324	45.1	31.6	−50.2	423	27.4	29.4	−87.7
S4	405	32.6	27.0	−52.7	792	12.6	19.1	−57.7
S5	339	47.7	28.3	−46.6	597	16.3	26.1	−65.9
S6	354	31.8	36.3	−39.3	717	12.4	25.8*	−38.6
mean	**387**	**34.1**	**28.3**	**−44.8**	**588**	**16.3**	**27.4**	**−86.1**

masker frequency ratio (although they did observe greater amounts of suppression with their noise maskers). If, however, the masker level and suppressor/masker frequency ratio for achieving maximum suppression are different at low and high frequencies, then their comparison may not have provided the best estimate of how this nonlinear phenomenon changes across frequency. To avoid this potential problem, masker level and suppressor/masker frequency ratio were varied in the present experiment at each f_s to optimize the chance of measuring the maximum amount of suppression at that frequency.

B. Stimuli and conditions

The same signal frequencies that were used in experiment 1 were used here. Forward-masked thresholds were obtained in the presence of either a single masker tone at f_s, or that masker tone plus a suppressor tone at a frequency of 1.1, 1.2, or 1.3f_s. The level of the masker was 40, 50, or 60 dB SPL, and the level of the suppressor was always 20 dB greater than that. The masker and suppressor (when present) were 200 ms in duration and immediately preceded the 15-ms signal (i.e., there was a 0-ms delay at the 0-voltage points). All stimulus durations included 5-ms $\cos^2$ rise/fall times.

C. Results and discussion

The results for all subjects were generally similar, and therefore only their mean data are shown in Fig. 2. Each panel represents a different masker level. The filled triangles represent conditions where the masker was presented alone (M), and the unfilled symbols (squares=suppressor/masker frequency ratio of 1.1; circles=1.2; diamonds=1.3) represent conditions where the masker and suppressor were presented simultaneously (M+S). The filled stars (bottom panel) represent the quiet thresholds (referenced to the right-hand axis).

First consider the thresholds obtained with the masker alone (filled triangles). For all masker levels, there was a modest decrease in masked threshold as f_s (and f_m) increased from 375 to 750 Hz; threshold increased slightly as f_s increased to 1500 Hz, and then remained essentially constant as frequency increased to 3000 Hz. This pattern of re-

sults is similar to that for the quiet thresholds. Now consider the effect of adding the suppressor tone (unfilled symbols). At 375 Hz, the suppressor increased threshold relative to that for the masker alone, indicating that the suppressor was producing significant amounts of masking; the thresholds decreased as the suppressor/masker frequency ratio increased. At 750 Hz, the suppressor either had no effect, or tended to increase thresholds somewhat. The results at 375 and 750 Hz are similar to those observed by Lee and Bacon (1998) for signal frequencies of 250 and 500 Hz, respectively. At 1500 Hz, and especially at 3000 Hz, the suppressor tended to decrease thresholds relative to those for the masker alone, indicating a certain amount of suppression.[3] In general, thresholds decreased as the suppressor/masker frequency ratio decreased.

The mean data in Fig. 2 have been replotted in terms of amount of suppression in Fig. 3. The amount of suppression was calculated by subtracting the threshold obtained in the M+S condition from the threshold obtained in the M condition. A positive value indicates that the suppressor reduced the masked threshold (hence suppression), whereas a negative value indicates that the suppressor increased the masked threshold. The horizontal dashed line in each panel is included as a visual reference for 0 dB of suppression. The bottom-right panel of Fig. 3 shows the maximum amount of suppression that was obtained at each f_s; the symbol and number in parentheses indicate the combination of frequency ratio and masker level that resulted in the largest amount of suppression at each frequency. In addition, Table II shows the amount of suppression (in dB) calculated for each subject, as well as for the mean across subjects.

In general, for all masker levels, the amount of suppression increased as f_s increased from 375 to 1500 Hz, the amount of suppression either remained about the same (ratios of 1.2 and 1.3) or increased (ratio of 1.1) as f_s increased to 3000 Hz. The increase in amount of suppression from 1500 to 3000 Hz was most obvious for four of the six subjects (S3–S6), whereas the amount of suppression tended to remain constant above 1500 Hz for two subjects (S1 and S2). When the results are combined across masker level and suppressor/masker frequency ratio (bottom right), the *maximum* amount of suppression increased with increasing f_s from 375 to 3000 Hz.

For a signal frequency of 375 Hz, the maximum amount of suppression was about −3 dB with a suppressor/masker frequency ratio of 1.3. Thus, even though the suppressor was in the most distal position relative to f_s, it continued to mask the signal. For a signal frequency of 750 Hz, the maximum amount of suppression was approximately 0 dB, also with a suppressor/masker frequency of 1.3. The fact that the maximum amount of suppression measured at the two lowest frequencies was obtained when the suppressor was furthest away from the signal may suggest that suppressor/masker frequency ratios greater than 1.3 may be necessary to obtain (positive values of) suppression at low frequencies. Pilot data reported in Lee and Bacon (1998), however, suggest that this may not be the case. For a signal frequency of 250 Hz, they increased the suppressor/masker frequency ratio from 1.1 to 1.7. As the suppressor was moved further away from the signal, it eventually stopped contributing to the masking of the signal, but it never caused suppression, suggesting that suppression may not exist (or at least may not be measurable) at these low frequencies. Therefore, it is likely that the results obtained here truly reflect an absence of measurable suppression at low frequencies. For signal frequencies of 1500 and 3000 Hz, the maximum amount of suppression increased to approximately 5 and 11 dB, respectively, with a suppressor/masker frequency ratio of 1.1. This ratio is consistent with the 1.15 ratio frequently reported as yielding the maximum amount of suppression (e.g., Houtgast, 1973; Shannon, 1976).

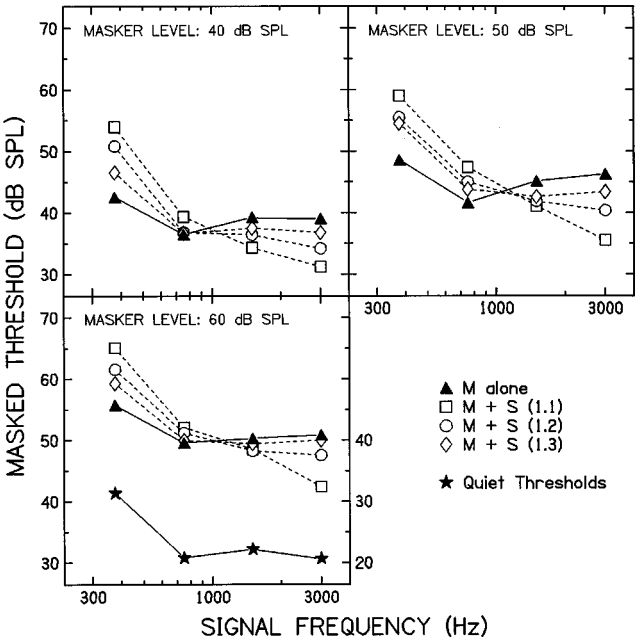

FIG. 2. Masked threshold as a function of signal frequency for two masking conditions: the masker alone (M, filled), and the masker plus suppressor (M+S, unfilled). Masker levels of 40, 50, and 60 dB SPL are shown across panels for three suppressor/masker frequency ratios: 1.1 (squares), 1.2 (circles), or 1.3 (diamonds). Quiet thresholds for the 15-ms signal (stars; bottom panel) are referenced to the right-hand axis. The results were averaged across subjects S1–S6.

In addition to considering suppression as the change in threshold between the M and M+S conditions, suppression can also be considered as a change in the effective level of the masker (ΔM). In this case, suppression is calculated by subtracting the threshold obtained in the M+S condition from the threshold in the M condition, divided by the slope of the growth-of-forward-masking function for the M condition (Moore and Glasberg, 1983; Lee and Bacon, 1998). Because the slope of the masking function in forward masking is typically less than 1.0, the second calculation yields larger estimates of suppression.

In order to calculate suppression as a change in the effective level of the masker, growth-of-masking functions for the masker alone were obtained for each signal frequency over a range of masker levels from 30 to 70 dB SPL. The slope values from the least-squares fits to the data for each subject are shown in the first column of Table III. In general, the slopes of the masking functions are similar to those observed in previous studies of tone-on-tone forward masking

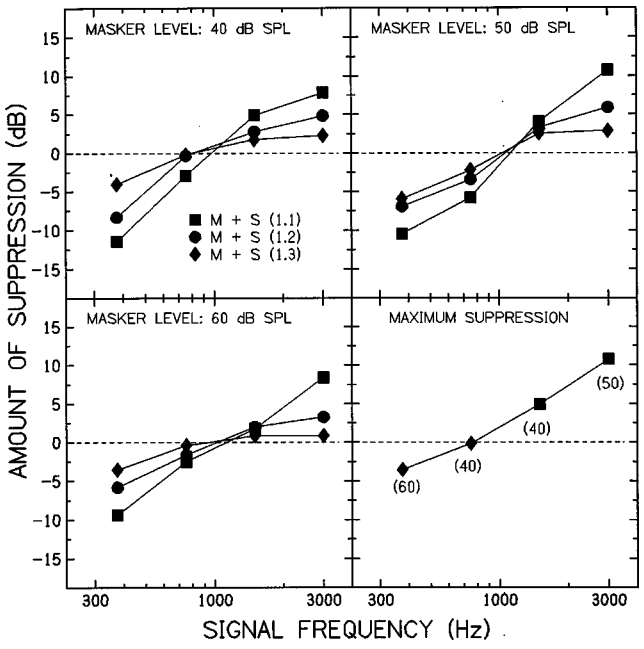

FIG. 3. Amount of suppression as a function of signal frequency for masker levels of 40, 50, and 60 dB SPL. Suppression was calculated by subtracting the threshold in the M+S condition from the threshold in the M condition. The suppressor/masker frequency ratio was either 1.1 (squares), 1.2 (circles), or 1.3 (diamonds). The horizontal dashed line is included as a visual reference for 0 dB of suppression. The symbols and numbers in the bottom-right panel indicate the combination of frequency ratio and masker level that resulted in the maximum amount of suppression at each signal frequency. The results were averaged across subjects S1–S6.

(Jesteadt *et al.*, 1982; Lee and Bacon, 1998), and indicate that there are no systematic changes in the slopes of the masking functions as a function of f_s. Thus, the effect of f_s on suppression calculated as a change in masker level is qualitatively similar to the effect of f_s on suppression calculated as a change in threshold, although the former yields larger values. The amount of suppression, defined as ΔM, is shown in Table III for each subject and for the average across subjects. The maximum amount of suppression (ΔM), averaged across subjects, increased from −6 dB at 375 Hz to 17 dB at 3000 Hz.

With either method of calculating suppression, there is a clear increase in the amount of suppression as f_s increases, at least over the range from 375 to 3000 Hz, although there are some subjects (S1 and S2) for whom suppression magnitude asymptotes at 1500 Hz. Overall, these results are consistent with greater nonlinearity at higher frequencies, although other explanations should be considered. The effects observed here are unlikely to reflect changes in SL with frequency. Results from Shannon (1976) and the present study indicate that the magnitude of suppression does not vary over a fairly wide range of masker levels (for a fixed level difference between the masker and suppressor). Other explanations also seem unlikely. In particular, recent results from Lee and Bacon (1998) appear to rule out the detection of spectral splatter and ringing in the auditory filters (which would be more likely at low frequencies) as explanations for changes in the magnitude of suppression across frequency. They reported similar effects of frequency with signal durations of 20 and 40 ms, where the effects of splatter would be minimal, and with a masker-signal delay of 20 ms, where the possibility of a temporal interaction between the suppressor and signal due to ringing would be reduced.

IV. EXPERIMENT 3: GROWTH OF FORWARD MASKING AS A FUNCTION OF FREQUENCY

A. Rationale

The purpose of this experiment was to measure growth-of-masking functions ($f_m < f_s$) in forward masking for a wide range of signal frequencies, to determine whether the masking functions become progressively steeper (implying a greater degree of compression) at higher frequencies.

B. Stimuli and conditions

The same signal frequencies that were used in experiments 1 and 2 were used here. Growth-of-masking functions were measured with a pure-tone forward masker where $f_s/f_m = 1.44$. Masked thresholds were measured over a range of masker levels from 40 to 95 dB SPL. The masker was 200 ms in duration and immediately preceded the 15-ms signal (i.e., there was a 0-ms delay at the 0-voltage points). All stimulus durations included 5-ms $\cos^2$ rise/fall times.

C. Results and discussion

Figure 4 shows the growth-of-masking functions (masked threshold as a function of masker level) for each subject and for the results averaged across subjects. Signal frequency is shown across panels. Table IV shows the individual and mean slope values of the functions, determined from least-squares fits to the data where there was at least 10 dB of masking. At 375 and 750 Hz, this included masker levels from about 60 to 95 dB, and at 1500 and 3000 Hz, it included levels from about 70 to 95 dB.

In general, the slopes of the functions for all subjects became steeper as f_s increased from 375 to 3000 Hz. The slopes fitted to the data averaged across subjects were 0.81, 0.90, 1.45, and 1.70 dB/dB for signal frequencies of 375, 750, 1500, and 3000 Hz, respectively. These slope values are generally similar or somewhat greater than those estimated from the results of Kidd and Feth (1981) for forward masking and Verschuure (1981) for pulsation threshold using similar signal frequencies, but are considerably less than the slope value of about 5–6 dB/dB obtained by plotting the data of Oxenham and Plack (1997) for a 3000-Hz masker and 6000-Hz signal on the same coordinates used here. Oxenham and Plack (1997) attributed their steeper slopes to their use of very brief (4-ms) signals and short (2-ms) masker-signal delays that allowed them to obtain masked thresholds at signal levels higher than 50 dB SPL, where they suggested the basilar membrane would be the most compressive. However, masked thresholds greater than 50 dB SPL were obtained in the present study. Their steeper slopes may be due, in part, to their use of a higher-frequency signal, if the slopes do in fact continue to increase with increasing f_s above 3000 Hz. The steeper slopes may also be due to their use of a high-pass noise to mask spread of excitation; when the noise was removed in a control condition in one subject, the slope of the

TABLE II. Individual and average amount of suppression (in dB) calculated for masker levels of 40, 50, and 60 dB SPL (the suppressor level was 20 dB greater than the masker level) for three suppressor/masker frequency ratios: 1.1, 1.2, and 1.3. Suppression was calculated by subtracting the threshold in the M+S condition from the threshold in the M condition.

	Masker level 40 dB SPL			50 dB SPL			60 dB SPL		
Signal freq./subject	1.1	1.2	1.3	1.1	1.2	1.3	1.1	1.2	1.3
375 Hz									
S1	−11.4	−8.1	−2.5	−9.7	−6.0	−4.8	−8.9	−4.1	0.1
S2	−11.6	−9.4	−6.7	−11.9	−10.5	−6.5	−10.5	−9.8	−7.9
S3	−11.6	−4.7	−4.5	−8.0	−2.4	−4.7	−12.0	−1.5	−2.6
S4	−15.1	−11.7	−4.9	−17.9	−10.6	−9.2	−17.6	−12.8	−6.4
S5	−7.1	−5.1	−1.9	−8.3	−8.1	−7.1	−4.5	−3.5	−1.1
S6	−11.5	−10.7	−3.5	−7.1	−3.8	−3.3	−2.4	−3.1	−3.2
mean	**−11.4**	**−8.3**	**−4.0**	**−10.5**	**−6.9**	**−5.9**	**−9.3**	**−5.8**	**−3.5**
750 Hz									
S1	−3.1	−3.7	−1.2	−2.0	−5.9	−5.0	0.9	−3.4	−2.4
S2	−1.6	0.5	−0.3	−10.2	−3.6	−0.8	−6.4	−1.2	−1.8
S3	0.1	1.0	1.6	−3.4	0.9	0.0	−1.1	−2.0	0.4
S4	−5.4	0.4	0.8	−9.1	−5.7	−3.5	−3.8	−3.7	−0.5
S5	0.4	1.1	1.2	−2.8	−2.0	−1.1	−2.8	−0.1	1.0
S6	−7.6	−1.4	−3.1	−7.4	−4.2	−2.9	−1.8	0.6	0.8
mean	**−2.9**	**−0.3**	**−0.2**	**−5.8**	**−3.4**	**−2.2**	**−2.5**	**−1.6**	**−0.4**
1500 Hz									
S1	6.9	2.7	0.8	7.4	3.6	3.7	−0.2	1.7	−0.8
S2	3.4	2.8	1.2	6.3	5.0	5.0	5.4	1.0	4.3
S3	0.3	0.9	2.5	−2.8	0.3	0.8	−5.0	−0.4	0.1
S4	6.9	4.3	1.8	6.4	6.9	3.7	7.4	4.9	0.4
S5	6.7	2.4	0.8	4.5	−0.2	0.6	2.8	4.2	0.9
S6	5.3	3.7	3.5	2.7	4.0	1.2	0.3	0.6	0.3
mean	**4.9**	**2.8**	**1.8**	**4.1**	**3.3**	**2.5**	**1.8**	**2.0**	**0.9**
3000 Hz									
S1	1.1	5.6	1.5	9.6	9.4	3.2	−0.2	3.9	0.5
S2	2.9	1.9	0.8	7.5	5.7	3.6	5.9	1.1	−0.4
S3	6.6	2.6	2.6	11.8	6.2	4.6	5.3	2.8	−0.3
S4	12.4	7.4	3.7	14.9	6.3	3.1	14.8	3.5	2.1
S5	15.1	5.5	2.1	12.3	6.0	2.4	13.2	5.0	1.9
S6	9.0	6.1	2.9	8.5	1.9	0.4	11.6	3.5	1.3
mean	**7.8**	**4.9**	**2.3**	**10.8**	**5.9**	**2.9**	**8.4**	**3.3**	**0.9**

masking function was reduced by a factor of 1.6. Even then, however, their slope was steeper than the steepest slope obtained here. Therefore, it is unclear why they obtained slope values that are so much greater than those reported here or in previous studies. The reciprocal of their slopes are, however, more consistent with typical values of compression (0.2 dB/dB) obtained from measures of basilar membrane and auditory nerve responses (Yates *et al.*, 1990; Ruggero, 1992).

It has been suggested that the amount of basilar-membrane compression at f_s can be estimated by taking the ratio of the slopes of the masking functions for a masker that is equal to f_s and a masker that is lower than f_s (Stelmachowicz *et al.*, 1987; Oxenham and Plack, 1997). Yates *et al.* (1990) and Cooper and Yates (1994) have used a similar method to estimate basilar membrane input–output responses from auditory nerve rate-intensity functions. This can be done here by taking the ratio of the slopes of the masking functions from this experiment (where $f_s/f_m = 1.44$) and the masking functions from experiment 2 (where $f_m = f_s$). These transformed slopes are shown in Table V. Because there were no systematic changes in the slopes of the masking functions (when $f_m = f_s$) as a function of f_s, the transformed slopes in Table V show the same effect of signal frequency as in Table IV. That is, the slopes become steeper as f_s increases from 375 to 3000 Hz. The transformed slope values, however, are larger than those in Table IV because the growth-of-masking functions when $f_m = f_s$ were less than 1.0 (left column, Table III). The transformed slopes of the averaged functions were 1.26, 1.46, 2.54, and 2.64 dB/dB for signal frequencies of 375, 750, 1500, and 3000 Hz, respectively. These values are still considerably less than the 5.0 dB/dB slopes that would be predicted based on a compression of 0.2 dB/dB observed physiologically from the basilar membrane, although the difference could be due to the fact that the physiological measures of basilar-membrane compression were obtained from relatively more basal recording sites (typically reflecting CFs greater than 8000 Hz), and thus they may reflect a greater compressive nonlinearity. Consistent with this possibility is the fact that the transformed slopes are very similar to the 2.0 dB/dB slopes pre-

TABLE III. Individual and average amount of suppression calculated for masker levels of 40, 50, and 60 dB SPL (the suppressor level was 20 dB greater than the masker level) for three suppressor/masker frequency ratios: 1.1, 1.2, and 1.3. Suppression was calculated by subtracting the threshold in the M+S condition from that in the M condition, divided by the slope (m, left column) of the masking function for the M condition.

	Slope	Masker level 40 dB SPL			50 dB SPL			60 dB SPL		
Signal freq./subject	m	1.1	1.2	1.3	1.1	1.2	1.3	1.1	1.2	1.3
375 Hz										
S1	0.670	−17.0	−12.1	−3.8	−14.5	−8.9	−7.2	−13.3	−6.1	0.1
S2	0.531	−21.9	−17.7	−12.6	−22.5	−19.8	−12.2	−19.8	−18.5	−14.9
S3	0.673	−17.3	−7.0	−6.7	−11.9	−3.6	−6.8	−17.9	−2.3	−3.9
S4	0.711	−21.2	−16.5	−6.8	−24.9	−14.9	−12.9	−24.8	−18.0	−9.1
S5	0.598	−11.9	−8.6	−3.2	−13.9	−13.6	−11.9	−7.6	−5.9	−1.9
S6	0.692	−16.6	−15.5	−5.1	−10.2	−5.5	−4.8	−3.5	−4.5	−4.7
mean	**0.646**	**−17.7**	**−12.8**	**−6.2**	**−16.2**	**−10.7**	**−9.2**	**−14.4**	**−9.0**	**−5.5**
750 Hz										
S1	0.740	−4.2	−5.0	−1.6	−2.6	−8.0	−6.8	1.3	−4.6	−3.2
S2	0.499	−3.3	1.1	−0.6	−20.4	−7.2	−1.6	−12.9	−2.3	−3.5
S3	0.593	0.1	1.7	2.7	−5.8	1.6	0.0	−1.9	−3.4	0.7
S4	0.669	−8.1	0.7	1.2	−13.5	−8.6	−5.2	−5.7	−5.5	−0.8
S5	0.568	0.7	2.0	2.1	−5.0	−3.5	−2.0	−5.0	−0.1	1.8
S6	0.636	−12.0	−2.2	−4.9	−11.6	−6.6	−4.6	−2.8	0.9	1.3
mean	**0.617**	**−4.7**	**−0.5**	**−0.3**	**−9.4**	**−5.5**	**−3.6**	**−4.1**	**−2.6**	**−0.6**
1500 Hz										
S1	0.596	11.6	4.5	1.4	12.5	6.0	6.3	−0.3	2.9	−1.3
S2	0.499	6.8	5.6	2.5	12.6	10.0	10.1	10.9	2.0	8.5
S3	0.661	0.4	1.3	3.8	−4.3	0.5	1.3	−7.5	−0.6	0.1
S4	0.762	9.1	5.6	2.3	8.4	9.0	4.8	9.7	6.5	0.5
S5	0.388	17.2	6.3	1.9	11.6	−0.4	1.6	7.1	10.7	2.4
S6	0.516	10.2	7.1	6.8	5.2	7.8	2.3	0.6	1.1	0.5
mean	**0.570**	**8.6**	**4.9**	**3.1**	**7.2**	**5.7**	**4.4**	**3.1**	**3.5**	**1.5**
3000 Hz										
S1	0.680	1.6	8.3	2.2	14.2	13.8	4.6	−0.2	5.7	0.8
S2	0.669	4.4	2.9	1.2	11.2	8.5	5.4	8.8	1.6	−0.6
S3	0.732	9.0	3.6	3.6	16.1	8.5	6.3	7.3	3.9	−0.4
S4	0.604	20.6	12.2	6.1	24.7	10.4	5.1	24.4	5.7	3.6
S5	0.585	25.8	9.4	3.6	21.0	10.3	4.0	22.5	8.5	3.2
S6	0.599	15.1	10.2	4.9	14.2	3.1	0.7	19.4	5.9	2.1
mean	**0.645**	**12.2**	**7.5**	**3.5**	**16.7**	**9.1**	**4.5**	**13.1**	**5.1**	**1.3**

dicted based on a compression of 0.5 dB/dB observed in the basilar membrane input–output functions derived from auditory nerve rate-intensity functions from fibers with CFs between 1800 and 2700 Hz (Cooper and Yates, 1994).

The results from this experiment are thus consistent with a greater compressive nonlinearity at the basal region of the basilar membrane, although it is worth considering to what extent other explanations might explain these differences across frequency. One possible explanation is based on differences in SL across frequency. If the effective level of a low-frequency signal is reduced relative to a higher-frequency signal, such that it is presented within the lower, more linear portion of the basilar-membrane response,[4] the slopes of the functions for a low-frequency signal may be reduced relative to those for a higher-frequency signal. However, differences in effective signal levels across frequency can be accounted for by recalculating the slopes of the masking functions in Fig. 4 over a fixed range of amount of masking (for example 20–40 dB), rather than over a fixed range of masker levels. The slopes of the functions calculated over this range are very similar to those in Table IV, suggesting that when the masking functions are compared over a range of signal levels that presumably reflect similar regions on the basilar membrane input–output function, the slopes are still greater at higher signal frequencies.

Two other factors that could influence the frequency effect observed here are ringing in the auditory filters and detection of signal splatter, both of which may be more prominent at low frequencies. To determine whether these factors might contribute to the results of experiment 3, pilot data that attempted to control for these effects were collected from subject S1. Two-point masking functions (70 and 95 dB SPL) were obtained for signal frequencies of 750 and 3000 Hz. A 10-ms delay between masker offset and the onset of the 10-ms signal was introduced to reduce any temporal interaction between the masker and signal due to ringing of the auditory filters. A low-level high-pass noise masker (spectrum level of 10 dB) with a cutoff frequency approximately 1.5 ERBs above f_s was presented continuously to minimize detection of spectral splatter. A high-pass, rather than a broadband or notched, noise masker was used as any detection of spectral splatter would occur primarily on the high-

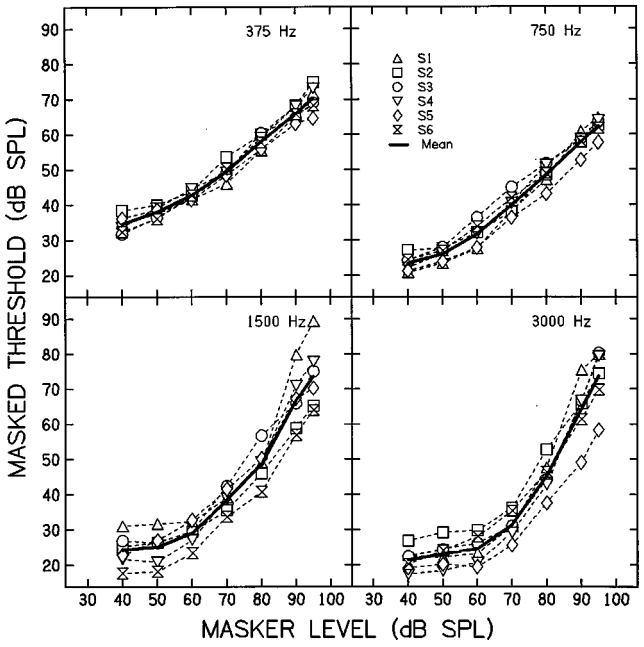

FIG. 4. Individual (unfilled symbols) and mean (solid line) growth-of-masking functions in forward masking for conditions where $f_s/f_m=1.44$. Results for each signal frequency are shown across panels.

frequency side of the signal away from the masker. The slopes of the masking functions obtained either with or without the high-pass noise were about 0.80 and 1.6 dB/dB, for signal frequencies of 750 and 3000 Hz, respectively. Therefore, it is very unlikely that either ringing of the auditory filters or off-frequency listening were influencing the growth-of-masking functions, at least over the range from 750 to 3000 Hz, suggesting that the effect of frequency in experiment 3 was most likely reflective of an increase in nonlinearity with frequency.

V. GENERAL DISCUSSION

A. Changes in nonlinearity as a function of frequency

When the results of all three experiments are taken together, and even if some of the results at 375 Hz (especially from experiment 1) must be treated with caution, the results clearly demonstrate that all three psychophysical measures of nonlinearity increased with increasing f_s. This increase in the apparent strength of the nonlinearity as frequency increases presumably reflects greater nonlinear processing in the more basal regions of the cochlea. These results are consistent with previous psychophysical studies; however, the present study is unique in that it evaluated all three measures in the same subjects, and that all of the measures demonstrated a *progressive* increase in nonlinear processing as f_s increases. Moreover, the results are generally consistent with various physiological studies of basilar membrane and auditory-nerve fiber responses that have shown greater nonlinearity for high-CF basilar-membrane regions or nerve fibers, but reduced or absent nonlinearity for low-CF regions or fibers (von Békésy, 1960; Schmiedt *et al.*, 1980; Khanna *et al.*, 1989; Ulfendahl *et al.*, 1989, 1991; Brundin, 1992; Gummer *et al.*, 1993; Cooper and Yates, 1994; Cooper and Rhode, 1995).

TABLE IV. Individual and mean slopes of the growth-of-masking functions for each signal frequency, where $f_s/f_m=1.44$. Slope values were determined from the least-squares fits to the data over the range of masker levels where at least 10 dB of masking occurred.

	Signal frequency			
Subject	375 Hz	750 Hz	1500 Hz	3000 Hz
S1	1.02	1.10	2.13	2.08
S2	0.83	0.98	1.19	1.50
S3	0.77	0.75	1.25	1.97
S4	0.84	0.92	1.63	2.03
S5	0.67	0.86	1.22	1.27
S6	0.74	0.79	1.25	1.38
mean	**0.81**	**0.90**	**1.45**	**1.70**

TABLE V. Individual and mean transformed slopes. The slope values were determined from the ratio of the masking function slopes for a masker below the signal frequency (from Table IV) to the slopes for a masker equal to the signal frequency (from Table III).

	Signal frequency			
Subject	375 Hz	750 Hz	1500 Hz	3000 Hz
S1	1.52	1.48	3.57	3.06
S2	1.56	1.97	2.39	2.24
S3	1.15	1.27	1.89	2.69
S4	1.18	1.37	2.14	3.36
S5	1.11	1.51	3.15	2.17
S6	1.07	1.25	2.42	2.30
mean	**1.26**	**1.46**	**2.54**	**2.64**

B. Nonlinear growth of forward masking

Recently, Oxenham and Moore (1995) and Plack and Oxenham (1998) have suggested that the compressive nonlinearity observed at the basilar membrane may be able to account for the nonlinear (slope <1.0 dB/dB) growth of forward masking when $f_s=f_m$. They argued that at moderate masker levels (>40 dB SPL), the masker is within the compressive region of the basilar-membrane response, whereas the signal level (which is typically lower than the masker level at masked threshold) is within the lower, more linear region (see footnote 4). Therefore, for a given increase in masker level, a smaller increase in signal level is required for detection, resulting in a masking function with a slope less than 1.0 dB/dB. Their hypothesis, then, would predict a two-part masking function, with a compressive slope at low levels, and an approximately linear slope at high levels where the masker level is increased to a range where the masker and signal are both within the compressive region of the basilar-membrane response (signal and masker levels greater than about 40 dB SPL). Plack and Oxenham (1998) report data that appear to fit fairly well with this hypothesis; however, the masking functions from experiment 2 in this study and from Jesteadt *et al.* (1982) and Widin and Viemeister (1979), among others, seem to be well described by a single straight line with a compressive slope (<1.0 dB/dB) over the entire range of signal and masker levels tested. Although for some studies the discrepancy may be due to measuring

masked thresholds that are too low to be within the compressive region of the response, the present study obtained thresholds over the range from 30 to 65 dB SPL, which should be well within the region where Plack and Oxenham (1998) suggest that linear growth of masking should be obtained. Moreover, it has been shown here and in previous studies (Jesteadt *et al.*, 1982; Lee and Bacon, 1998) that there are no systematic changes in the slopes of tone-on-tone masking functions as a function of f_s, as would be expected based on the changes in nonlinearity observed in the present study. Therefore, the nonlinearity in growth-of-forward masking when the signal and masker are equal in frequency may not solely be attributable to basilar-membrane compressive nonlinearity.

C. Individual differences in measures of nonlinearity

An interesting finding from the present study was that there appeared to be greater between-subject variability in thresholds and the psychophysical measures of nonlinearity at the higher signal frequencies. For signal frequencies of 375 and 750 Hz, the masked thresholds from experiment 1 and the masking functions from experiment 3 for the individual subjects were very similar to one another. The masked thresholds at any particular notchwidth (experiment 1) or masker level (experiment 3) generally did not vary by more than 10 dB, whereas the thresholds for either the 1500- or 3000-Hz signal varied across subjects by as much as 20 dB (see, for example, Fig. 4). Thus, in experiment 1, the ERB values, and in particular the change in ERB values with level, were similar across subjects at the lower frequencies, but varied over a wider range of values at the higher frequencies (see Table I). And, in experiment 3, the slopes of the individual masking functions were very similar to one another at the lower frequencies, but varied considerably at the higher frequencies (see Table IV). This trend was not observed in experiment 2; although some conditions tended to show less variability across subjects than others, there were no consistent patterns. It is not clear why measures of two-tone suppression would be different from the measures in experiments 1 and 2 with respect to this variability.

The larger individual variability at 1500 and 3000 Hz than at 375 and 750 Hz may reflect a greater contribution of nonlinear processing at higher signal frequencies than at lower signal frequencies. At low signal frequencies, if processing is mediated primarily by passive, linear cochlear mechanics, one might not expect large amounts of variability within a normal population, given minor differences in cochlear structures across subjects. However, at higher signal frequencies, if nonlinear processing is contributing significantly to auditory processing, then the active mechanism that is highly dependent on the status of the cochlea may be responsible for the large individual variability observed in the present study at high frequencies. This statement may seem unusual given that all the individuals in the present study exhibited normal absolute thresholds and thus all presumably had normal, healthy cochleae. However, Fagelson and Champlin (1997) have suggested that listeners that show normal absolute thresholds at discretely sampled test frequencies (typically octave frequencies) may have localized regions of damage (possibly due to noise trauma or ototoxic drugs) in which the active nonlinear processes are compromised. However, because threshold microstructure was not tested in the present study, it is not possible to determine whether minute variations in absolute thresholds can account for the individual variability at high frequencies.

If the individual variability is reflective of individual differences in the contribution of nonlinear processing, then one could expect that a particular individual would consistently show more or less nonlinearity across the different psychophysical measures than another individual, assuming that the measures reflect the same nonlinearity. This appears to be true in the present study. Although the relationship is far from perfect, those subjects that show the greatest nonlinear effect in one experiment also show the greatest nonlinear effects in the other experiments. For example, subjects S4, S5, and S6 tend to exhibit not only the largest effects of level on frequency selectivity, but also the greatest amount of suppression, and the steepest growth-of-masking functions. Subjects S1, S2, and S3 tend to show smaller effects across all three experiments. These differences in the degree of nonlinearity across individuals may also help explain the large individual differences observed in other studies that may reflect nonlinear auditory phenomena, such as overshoot and signal enhancement (e.g, McFadden and Wright, 1990; Wright, 1995).

VI. SUMMARY AND CONCLUSIONS

The primary goal of this project was to further our understanding of how auditory nonlinear phenomena vary as a function of location along the cochlea by examining three psychophysical measures of nonlinearity as a function of frequency. In particular, the hypothesis that the apical (low-frequency) region of the cochlea behaves more linearly than the basal (high-frequency) region was tested. The main findings can be summarized as follows: (1) All three psychophysical measures of nonlinearity revealed greater nonlinear effects as f_s increased from 750 to 3000 Hz, with no evidence of nonlinear processing at 375 Hz, consistent with the hypothesis. Moreover, it appeared to be a *progressive* increase in the degree of nonlinearity as f_s increased. (2) There appeared to be greater between-subject variability in thresholds and the psychophysical measures of nonlinearity at 1500 and 3000 Hz than at 375 and 750 Hz. The larger individual differences at the higher frequencies may reflect the larger (and more variable) contribution of nonlinear processing at those frequencies.

ACKNOWLEDGMENTS

This research was supported by NIDCD grant No. DC01376 and a research award from the American Academy of Audiology Research Award Program. Manuscript preparation was supported in part by NIDCD grant No. DC00187. This research is based on a doctoral dissertation submitted by the first author to the Graduate College at Arizona State University. We thank Marjorie Leek for her assistance with deriving the filter shapes in experiment 1, and Andrew Oxen-

ham, Chris Plack, Joseph Hall, and an anonymous reviewer for their helpful comments on an earlier version of this manuscript.

[1]Preliminary data from several subjects suggested that the forward-masking task (where $f_s = f_m$) was susceptible to ''confusion effects'' due to the very short (0-ms) masker-signal delay i.e., their signal thresholds were equal to the masker level). This confusion could be eliminated by providing the subjects practice with a longer (5–10 ms) masker-signal delay, and then gradually shortening the delay to 0 ms. Typically, less than 30 min of practice was required.

[2]Throughout, the data were fitted as though the masker level determines the shape of the auditory filter, even though some studies have suggested that auditory filter shapes are determined primarily by the level of the signal, rather than the level of the masker (Rosen *et al.*, 1992). The approach used here allows for comparisons with most previous notched-noise studies. Moreover, important here are accurate *comparisons* across signal frequencies and masker levels, which can be accomplished with fixed masker levels, assuming that any differences between filter shapes obtained with a fixed signal level versus a fixed masker level are essentially constant across frequency and level.

[3]Several studies have suggested that confusion effects, rather than suppression, may be influencing the larger thresholds in the M conditions, relative to those in the M+S conditions (Moore, 1981; Moore and Glasberg, 1982; Neff, 1985, 1986). They suggest that the threshold in the M condition may be artificially high due to the inability to discriminate between the offset of the forward masker and the onset of the signal when the two stimuli are perceptually similar; confusion effects tend to be greatest when the masker and signal level are equal (Neff, 1986). However, in the present study, the signal level at threshold in the M condition was generally lower than the level of the masker (either immediately, or with practice; see footnote 1) and the slope of the growth-of-masking function was less than 1.0 (see Neff, 1985), suggesting that confusion effects were not influencing thresholds in the M condition. Thus, the lower thresholds in the M+S condition most likely reflect true two-tone suppression, and not cueing by the addition of the suppressor tone.

[4]Previous studies (Ruggero *et al.*, 1992; Murugasu and Russell, 1995) have revealed two-part, basilar membrane input–output functions, with a linear slope at low levels, and a compressive, nonlinear slope at mid-to-high levels (50–80 dB SPL). However, more recent reports (Ruggero *et al.*, 1997; Nuttall and Dolan, 1996) suggest that the compressive region of the input–output function actually extends down to levels of around 20 dB SPL, which is similar to the threshold of auditory-nerve fibers (Ruggero *et al.*, 1997).

ANSI (**1989**). ANSI S3.6-1989, ''Specifications for Audiometers'' (American National Standards Institute, New York).

Békésy, G. von (**1960**). *Experiments in Hearing* (McGraw-Hill, New York), pp. 1–745.

Brundin, L., Flock, B., and Flock, A. (**1992**). ''Sound induced displacement response of the guinea pig hearing organ and its relation to the cochlear potentials,'' Hearing Res. **58**, 175–184.

Cooper, N. P., and Rhode, W. S. (**1995**). ''Nonlinear mechanics at the apex of the guinea-pig cochlea,'' Hearing Res. **82**, 225–243.

Cooper, N. P., and Yates, G. K. (**1994**). ''Nonlinear input–output functions derived from the responses of guinea-pig cochlear nerve fibres: Variations with characteristic frequency,'' Hearing Res. **78**, 221–234.

Fagelson, M. A., and Champlin, C. A. (**1997**). ''Auditory filters measured at neighboring center frequencies,'' J. Acoust. Soc. Am. **101**, 3658–3665.

Glasberg, B. R., and Moore, B. C. J. (**1990**). ''Derivation of auditory filter shapes from notched-noise data,'' Hearing Res. **47**, 103–138.

Gummer, A. W., Hemmert, W., Morioka, P., Ries, P., Reuter, G., and Zenner, H. P. (**1993**). ''Cellular motility measured in the guinea-pig cochlea,'' in *Biophysics of Hair Cell Sensory Systems*, edited by H. Diufhuis, J. W. Horst, P. van Dijk, and S. M. van Netten (World Scientific, Singapore), pp. 229–236.

Hicks, M. L., and Bacon, S. P. (**1998**). ''Psychophysical measures of frequency selectivity, two-tone suppression, and growth-of-masking in individuals with aspirin-induced hearing loss,'' J. Acoust. Soc. Am. (in preparation).

Houtgast, T. (**1973**). ''Psychophysical experiments on 'tuning curves' and 'two-tone inhibition','' Acustica **29**, 168–179.

Jesteadt, W., Bacon, S. P., and Lehman, J. R. (**1982**). ''Forward masking as a function of frequency, masker level, and signal delay,'' J. Acoust. Soc. Am. **71**, 950–962.

Khanna, S. M., Ulfendahl, M., and Flock, A. (**1989**). ''Comparison of the tuning of outer hair cells and the basilar membrane in the isolated cochlea,'' Acta Oto-Laryngol. Suppl. **467**, 151–156.

Kidd, G., and Feth, L. L. (**1981**). ''Patterns of residual masking,'' Hearing Res. **5**, 49–67.

Lee, J. M., and Bacon, S. P. (**1998**). ''Psychophysical suppression as a function of signal frequency: Noise and tonal maskers,'' J. Acoust. Soc. Am. **104**, 1013–1022.

Levitt, H. (**1971**). ''Transformed up–down methods in psychoacoustics,'' J. Acoust. Soc. Am. **49**, 467–477.

Lutfi, R. A., and Patterson, R. D. (**1984**). ''On the growth of masking asymmetry with stimulus intensity,'' J. Acoust. Soc. Am. **76**, 739–745.

McFadden, D., and Wright, B. A. (**1990**). ''Temporal decline of masking and comodulation detection differences,'' J. Acoust. Soc. Am. **88**, 711–724.

Moore, B. C. J. (**1981**). ''Interactions of masker bandwidth with signal duration and delay in forward masking,'' J. Acoust. Soc. Am. **70**, 62–68.

Moore, B. C. J. (**1987**). ''Distribution of auditory-filter bandwidths at 2 kHz in young normal listeners,'' J. Acoust. Soc. Am. **81**, 1633–1635.

Moore, B. C. J., and Glasberg, B. R. (**1982**). ''Contralateral and ipsilateral cueing in forward masking,'' J. Acoust. Soc. Am. **71**, 942–945.

Moore, B. C. J., and Glasberg, B. R. (**1983**). ''Growth of forward masking for sinusiodal and noise maskers as a function of signal delay; implications for suppression in noise,'' J. Acoust. Soc. Am. **73**, 1249–1259.

Moore, B. C. J., and Glasberg, B. R. (**1987**). ''Formulae describing frequency selectivity as a function of frequency and level, and their use in calculating excitation patterns,'' Hearing Res. **28**, 209–225.

Moore, B. C. J., Peters, R. W., and Glasberg, B. R. (**1990**). ''Auditory filter shapes at low center frequencies,'' J. Acoust. Soc. Am. **88**, 132–140.

Murugasu, E., and Russell, I. J. (**1995**). ''Salicylate ototoxicity: The effects of basilar membrane displacement, cochlear mechanics, and neural responses in the basal turn of the guinea pig cochlea,'' Aud. Neurosci. **1**, 139–150.

Neff, D. L. (**1985**). ''Stimulus parameters governing confusion effects in forward masking,'' J. Acoust. Soc. Am. **78**, 1966–1976.

Neff, D. L. (**1986**). ''Confusion effects with sinusoidal and narrow-band noise forward maskers,'' J. Acoust. Soc. Am. **79**, 1519–1529.

Nuttal, A. L., and Dolan, D. F. (**1996**). ''Steady-state sinusiodal velocity responses of the basilar membrane in guinea pig,'' J. Acoust. Soc. Am. **99**, 1556–1565.

Oxenham, A. J., and Moore, B. C. J. (**1995**). ''Additivity of masking in normally hearing and hearing-impaired subjects,'' J. Acoust. Soc. Am. **98**, 1921–1934.

Oxenham, A. J., and Plack, C. J. (**1997**). ''A behavioral measure of basilar-membrane nonlinearity in listeners with normal and impaired hearing,'' J. Acoust. Soc. Am. **101**, 3666–3675.

Patterson, R. D., Nimmo-Smith, I., Weber, D. L., and Milroy, R. (**1982**). ''The deterioration of hearing with age: Frequency selectivity, the critical ratio, the audiogram, and speech threshold,'' J. Acoust. Soc. Am. **72**, 1788–1803.

Pick, G. F. (**1980**). ''Level dependence of psychophysical frequency resolution and auditory filter shape,'' J. Acoust. Soc. Am. **68**, 1085–1095.

Plack, C. J., and Oxenham, A. J. (**1998**). ''Basilar-membrane nonlinearity and the growth of forward masking,'' J. Acoust. Soc. Am. **103**, 1598–1608.

Rosen, S., Baker, R. J., and Kramer, S. (**1992**). ''Characterizing changes in auditory filter bandwidth as a function of level,'' in *Auditory Physiology and Perception*, edited by Y. Cazals, K. Horner, and L. Demany (Pergamon, Oxford), pp. 171–177.

Rosen, S., and Stock, D. (**1992**). ''Auditory filter bandwidths as a function of level at low-frequencies (125 Hz–1 kHz),'' J. Acoust. Soc. Am. **92**, 773–781.

Ruggero, M. A. (**1992**). ''Responses to sound of the basilar membrane of the mammalian cochlea,'' Curr. Opin. Neurobiol. **2**, 449–456.

Ruggero, M. A., Robles, L., and Rich, N. C. (**1992a**). ''Two-tone suppression in the basilar membrane of the cochlea: Mechanical basis of auditory-nerve rate suppression,'' J. Neurophysiol. **68**, 1087–1099.

Ruggero, M. A., Robles, L., Rich, N. C., and Recio, A. (**1992b**). ''Basilar membrane responses to two-tone and broadband stimuli,'' Philos. Trans. R. Soc. London, Ser. B **336**, 307–314.

Ruggero, M. A., Rich, N. C., Recio, A., Narayan, S. S., and Robles, L.

(**1997**). ''Basilar-membrane responses to tones at the base of the chinchilla cochlea,'' J. Acoust. Soc. Am. **101**, 2151–2163.
Schmiedt, R. A., Zwislocki, J. J., and Hamernik, R. P. (**1980**). ''Effects of hair cell lesions on responses of cochlear nerve fibers. I. Lesions, tuning curves, two-tone inhibition, and responses to trapezoidal-wave patterns,'' J. Neurophysiol. **43**, 1367–1389.
Schöne, P. von (**1977**). ''Nichtlinearitäten im mithörschwellen-tonheitsmuster von sinustönen,'' Acustica **37**, 37–44.
Shannon, R. V. (**1976**). ''Two-tone unmasking and suppression in a forward-masking situation,'' J. Acoust. Soc. Am. **59**, 1460–1470.
Stelmachowicz, P. G., Lewis, D. E., Larson, L. L., and Jesteadt, W. (**1987**). ''Growth of masking as a measure of response growth in hearing-impaired listeners,'' J. Acoust. Soc. Am. **81**, 1881–1887.
Thibodeau, L. M., and Fagelson, M. A. (**1993**). ''Comparison of suppression across frequencies,'' J. Acoust. Soc. Am. **93**, 2314.
Ulfendahl, M., Flock, A., and Khanna, S. M. (**1989**). ''A temporal bone preparation for the study of cochlear micromechanics at the cellular level,'' Hearing Res. **40**, 55–64.
Ulfendahl, M., Khanna, S. M., and Flock, A. (**1991**). ''Effects of opening and resealing the cochlea on the mechanical response in the isolated temporal bone preparation,'' Hearing Res. **57**, 31–37.
Verschuure, J. (**1981**). ''Pulsation patterns and nonlinearity of auditory tuning. I. Psychophysical results,'' Acustica **49**, 288–295.
Weber, D. L. (**1977**). ''Growth of masking and the auditory filter shape,'' J. Acoust. Soc. Am. **62**, 4424–4429.
Widin, G. P., and Viemeister, N. F. (**1979**). ''Intensive and temporal effects in pure-tone forward masking,'' J. Acoust. Soc. Am. **66**, 388–395.
Wilson, P. (**1992**). ''Cochlear mechanics,'' in *Auditory Physiology and Perception*, edited by Y. Cazals, K. Horner, and L. Demany (Pergamon, Oxford), pp. 71–83.
Wright, B. A. (**1995**). ''Detectability of simultaneously masked signals as a function of signal bandwidth for different signal delays,'' J. Acoust. Soc. Am. **98**, 2493–2503.
Wright, B. A. (**1996**). ''Auditory filter asymmetry at 2000 Hz in 80 normal-hearing ears,'' J. Acoust. Soc. Am. **100**, 1717–1721.
Yates, G. K., Winter, I. M., and Robertson, D. (**1990**). ''Basilar membrane nonlinearity determines auditory nerve rate-intensity functions and cochlear dynamic range,'' Hearing Res. **45**, 203–220.
Zwicker, E., and Jaroszewski, A. (**1982**). ''Inverse frequency dependence of simultaneous tone-on-tone masking patterns at low levels,'' J. Acoust. Soc. Am. **71**, 1508–1512.

Sequential stream segregation in the absence of spectral cues

Joyce Vliegen[a] and Andrew J. Oxenham[b]
Institute for Perception Research (IPO), P.O. Box 513, 5600 MB Eindhoven, The Netherlands

(Received 8 October 1997; revised 24 September 1998; accepted 25 September 1998)

This paper investigates the cues used by the auditory system in the perceptual organization of sequential sounds. In particular, the ability to organize sounds in the absence of spectral cues is studied. In the first experiment listeners were presented with a tone sequence ABA ABA ..., where the fundamental frequency ($f0$) of tone A was fixed at 100 Hz and the $f0$ difference between tones A and B varied across trials between 1 and 11 semitones. Three spectral conditions were tested: pure tones, harmonic complexes filtered with a bandpass region between 500 and 2000 Hz, and harmonic complexes filtered with a bandpass region chosen so that only harmonics above the tenth would be passed by the filter, thus severely limiting spectral information. Listeners generally reported that they could segregate tones A and B into two separate perceptual streams when the $f0$ interval exceeded about four semitones. This was true for all conditions. The second experiment showed that most listeners were better able to recognize a short atonal melody interleaved with random distracting tones when the distracting tones were in an $f0$ region 11 semitones higher than the melody than when the distracting tones were in the same $f0$ region. The results were similar for both pure tones and complex tones comprising only high, unresolved harmonics. The results from both experiments show that spectral separation is not a necessary condition for perceptual stream segregation. This suggests that models of stream segregation that are based solely on spectral properties may require some revision. [S0001-4966(99)03501-8]

PACS numbers: 43.66.Ba, 43.66.Mk, 43.66.Hg [JWH]

INTRODUCTION

In the everyday acoustic environment the auditory system has the task of analyzing complex sounds and partitioning them into perceptual components to make the recognition of individual sound sources possible. The process whereby different sound elements are assigned to a single auditory object is known as ''auditory stream integration'' and, conversely, the process whereby sound elements are separated into different objects is known as ''auditory stream segregation'' (Bregman, 1990). One aspect of such auditory processing, known as ''sequential stream segregation,'' deals with the perceptual organization of sounds that do not overlap in time. This form of processing is important in, for instance, assigning consecutive speech segments to the same speaker, or following a melodic line in a background of other musical sounds.

A number of studies of sequential stream segregation have used pure-tone stimuli in rapidly alternating sequences (Miller and Heise, 1950; van Noorden, 1975; Rose and Moore, 1997). Figure 1 illustrates the stimuli typically used in such experiments. Using the type of sequence shown (ABA ABA ...), van Noorden (1975) found that with a small difference in frequency between the two tones, one coherent sequence with a galloping rhythm was heard (''temporal coherence'' or ''integration;'' upper panel). For larger frequency intervals the coherence was lost and two separate sequences were perceived, one consisting of low tones (A) and the other consisting of high tones (B), where the repetition rate of the low sequence was twice that of the high one (''fission'' or ''segregation;'' lower panel). At intermediate frequency intervals, either integration or segregation could be heard, depending on the attentional set of the listener. The largest frequency difference at which listeners are able to hear the sequence as a single stream is known as the integration boundary. The smallest frequency difference at which listeners can still segregate the two streams is termed the segregation boundary. The integration boundary increases dramatically with decreasing presentation rate of the tones, while the segregation boundary seems to be relatively independent of presentation rate (van Noorden, 1975).

The use of pure-tone stimuli makes it difficult to determine the mechanism(s) underlying sequential stream segregation. For instance, segregation may be determined by spectral distance, as represented by the frequency-to-place mapping within the cochlea. Alternatively, or in addition, cues based on temporal information may play a role. Two recent models of auditory stream segregation have assumed that sequential stream segregation is based solely on spectral differences (Beauvois and Meddis, 1996; McCabe and Denham, 1997). Essentially, in both models integration occurs if the two stimuli fall within a single auditory filter, and segregation occurs if the stimuli are processed primarily through different auditory filters. This view has some experimental support. For instance, van Noorden (1975) found that alternating a pure tone with a complex tone of the same fundamental frequency ($f0$) did not produce integration. Simi-

[a]Present address: Department of Experimental Psychology, University of Cambridge, Downing Street, Cambridge CB2 3EB, England.
[b]Corresponding author. Present address: Communication Research Laboratory (133 FR), Department of Speech-Language Pathology and Audiology, Northeastern University, 360 Huntington Avenue, Boston, MA 02115. Electronic mail: aoxenham@lynx.neu.edu

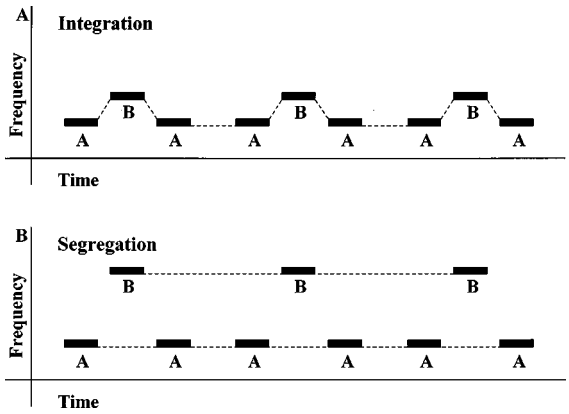

FIG. 1. Schematic diagram of auditory stream segregation. With a small frequency interval between tones A and B, one coherent sequence of tones with a galloping rhythm can be heard (upper panel). If the frequency interval is large, the two tones can be heard as two separate streams: a fast one with low tones (tone A) and a slower one with high tones (tone B) (lower panel).

larly, alternating two complex tones with the same $f0$ but comprising different harmonics also failed to result in integration. These results led van Noorden to conclude that contiguity ''at the level of the cochlear hair cells'' was a necessary (but not sufficient) condition for integration to occur. Hartmann and Johnson (1991) used the recognition of interleaved melodies (Dowling, 1973; Dowling *et al.*, 1987) to investigate whether factors other than spectral differences contributed to stream segregation. They concluded that ''peripheral channeling is of paramount importance'' in determining segregation. However, while their experiments included conditions in which timbre was altered independently of spectrum (e.g., by changing the temporal envelope of stimuli), their experiments did not include conditions in which pitch was altered independently of the spectral envelope. Work in that direction has been carried out by Singh (1987) and Bregman *et al.* (1990).

Singh (1987) used complex tones consisting of four consecutive harmonics and independently varied the harmonic number of the lowest harmonic and the $f0$. Bregman *et al.* (1990) used complex tones with spectra containing at least 13 harmonics and varied either the $f0$ or the location of a single spectral peak (formant) in the complex. Both experiments found that $f0$ and spectral shape can contribute independently to stream segregation. The interpretation of the results of Singh (1987) and Bregman *et al.* (1990) is, however, not clear cut. As both used resolved harmonics, it could be argued that streaming depended on changes in spectral information caused by the change in $f0$. Although the spectral envelope could be held constant, the place of excitation of each resolved harmonic changed with $f0$, resulting in a different spectral ''fine structure.'' It may therefore be that this change in spectral pattern was responsible for the changes in grouping with $f0$. In their present forms, the models of Beauvois and Meddis (1996) and McCabe and Denham (1997) could probably not account for results from experiments using complex stimuli. However, it is at least conceivable that an extension of the models, taking into account spectral patterns rather than just single components, could account for the data of Singh (1987) and Bregman *et al.* (1990).

Cochlear hearing loss is often characterized by broader auditory filters and, according to the models of Beauvois and Meddis (1996) and McCabe and Denham (1997), broader filters should result in a segregation boundary at a wider-than-normal frequency interval. This was investigated by Rose and Moore (1997). They examined the perceptual grouping of alternating tone sequences in normal-hearing and hearing-impaired listeners. Results for a group of unilaterally hearing-impaired listeners showed no clear difference in segregation boundary between the normal and the impaired ear. About half the bilaterally hearing-impaired listeners did show a segregation boundary at a wider frequency interval than normal, but the other half showed boundaries comparable to those of the normal-hearing listeners. These results seem not to be consistent with a wholly spectrally based account of sequential streaming.

From previous research we know that spectral information can be used, and probably plays a major role in auditory stream segregation (van Noorden, 1975; Hartmann and Johnson, 1991). The purpose of the present study is to investigate whether the auditory system is able to use only temporal cues to perform segregation. Spectral cues were eliminated in some conditions by using complex tones consisting only of harmonics with harmonic numbers of 10 or higher. Plomp (1964) has shown that listeners are generally not capable of resolving harmonics higher than the fifth to the eighth, depending on the $f0$. It has nevertheless been shown that complexes consisting only of high, unresolved harmonics can induce a pitch sensation which can be used to identify melodies and discriminate musical intervals (Moore and Rosen, 1979; Houtsma and Smurzynski, 1990). If it is found that segregation only occurs when resolvable components are present, providing spectral information, that would add support for spectrally based models of stream segregation. If, on the other hand, segregation occurs in the absence of such cues, additional processes based on temporal information would be implicated in the forming of auditory streams.

I. EXPERIMENT 1. STREAM SEGREGATION JUDGMENTS

A straightforward way to examine stream segregation is to present listeners with an alternating tone sequence in which the frequency difference between the tones is varied, and to ask them whether they hear one coherent sequence or two separate streams, or to let them adjust the frequency of one tone until they can just hear the sequence as integrated or segregated (depending on which boundary is to be measured). This method has been used often, for example, by Miller and Heise (1950), van Noorden (1975), Nooteboom *et al.* (1978), and Rose and Moore (1997). In the present experiment, as in some previous studies (van Noorden, 1975; Rose and Moore, 1997), a sequence of tone triplets (ABA ABA ABA ...) was used. This sequence produces the percept of a clear galloping rhythm when the tones are integrated. With segregation this rhythm is lost. The listeners' task was to report whether they could segregate the sequence and ''hear out'' tone B.

A. Stimuli

Each trial consisted of a sequence of tone triplets (ABA ABA ABA ...). Tone A had a constant $f0$ of 100 Hz. The $f0$ of tone B varied randomly across trials so that the $f0$ interval between tones A and B in a given trial could take the value of 1, 2, 3, 4, 5, 7, or 11 semitones (resulting in an $f0$ for tone B of 105.95, 112.25, 118.92, 125.99, 133.48, 149.83, or 188.77 Hz). Three sets of tone sequences were used: complex tones consisting of low (resolved) harmonics, complex tones consisting of high (unresolved) harmonics, and pure tones. The complex tones were generated by filtering harmonic complexes with equal-amplitude components, as follows. First, a broadband harmonic tone complex in sine phase was generated with the appropriate $f0$. Then, a fast Fourier transform (FFT) was performed and the amplitude spectrum was multiplied by a filter function. This filter consisted of a flat bandpass region, flanked by two raised-cosine ramps in the linear frequency domain. The midpoints (-6 dB points) of these ramps for the high-harmonic condition (2000 and 8000 Hz) were chosen so that only harmonics higher than the tenth would be at full amplitude, because it is assumed that these harmonics are unresolved (Plomp, 1964). For the low-harmonic condition the midpoint frequencies (500 and 2000 Hz) were chosen so as to keep the ratio between the midpoint frequencies for the two conditions the same. The width of each ramp was half the frequency of its midpoint. This resulted in -3 dB points of 535 and 1865 Hz for the low-harmonic condition and 2135 and 7455 Hz for the high-harmonic condition. An inverse FFT was then performed to produce the complex tones. The tones were presented at an overall level of 70 dB SPL. The perceived loudness of these tones seemed independent of $f0$. This is expected, as the overall level in each auditory filter remains roughly constant (Moore *et al.*, 1997). When the pure tones were presented at the same level, they sounded softer than the complex tones, and the low-frequency pure tones sounded softer than the high-frequency pure tones. Because of this the level of the pure tones was adjusted according to the loudness matching results of Suzuki *et al.* (1989). By drawing a straight line through their data points at 125 and 250 Hz for the 70 phon contour, the equation $L_p = -4.39 \log_2 f_p + 109.15$ was obtained, in which L_p is the level and f_p is the frequency of the pure tone. The total duration of each tone was 90 ms including 10-ms raised-cosine onset and offset ramps. The tone repetition time (TRT) between tones within a triplet was kept constant at 110 ms. One trial consisted of a sequence of 12 triplets, each separated by silent intervals of 110 ms. All stimuli were generated on a Silicon Graphics workstation and were played out at a sampling rate of 32 kHz using the built-in 16-bit D/A converters and antialiasing filters. Stimuli were then passed through a programmable attenuator (TDT PA4) and were presented diotically over Beyer DT 990 headphones in a sound-attenuating booth.

B. Listeners

The listeners were divided into two groups, depending on whether they were musically trained or not. This was done because musical listeners may be expected to show superior performance compared with nonmusical listeners, as musical training can involve ''hearing out'' certain patterns from within a more complex background (Beauvois and Meddis, 1997). Listeners were considered musical if they had received at least four years of formal instrumental training. Each group consisted of six listeners. All listeners were aged between 20 and 30 years and reported no history of hearing disorders or difficulties. Both authors participated as musically trained listeners.

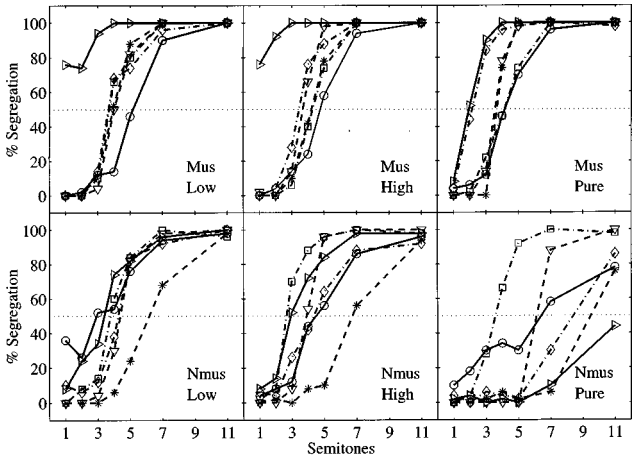

FIG. 2. Segregation judgments from the 12 individual listeners as a function of $f0$ separation in semitones. Results from the musically trained listeners are shown in the upper panels and the results from nonmusical listeners are shown in the lower panels. Low, High, and Pure denote the low-harmonic complex (resolved), high-harmonic complex (unresolved), and pure tones, respectively.

C. Procedure

With 7 different values for the $f0$ of tone B and 3 spectral conditions there were 21 different stimuli. In each trial, one stimulus was randomly chosen from this set and presented to a listener. Listeners were instructed to try to hear out tone B separately from tone A, and to press ''2'' if they could hear out tone B (segregation) or ''1'' if they could not (integration). After a response had been given, a new stimulus was randomly chosen and presented. Each stimulus was presented 5 times within one block, so with 21 different stimuli, each block consisted of 105 sequences. When all 105 sequences had been presented, the answers for that block were recorded and, after a short break, a new block was started. Before data were collected, listeners had a practice session consisting of a short block of only the low harmonic tones and a normal block of stimuli, in order to get used to the stimuli and the task. Excluding practice, the experiment consisted of ten blocks. Thus, each stimulus was presented to each listener a total of 50 times.

D. Results

The individual percentage segregation responses are shown in Fig. 2 as a function of the $f0$ interval between tones A and B. Results from the six musically trained listeners are shown in the upper panels and results from the listeners with no musical training are shown in the lower pan-

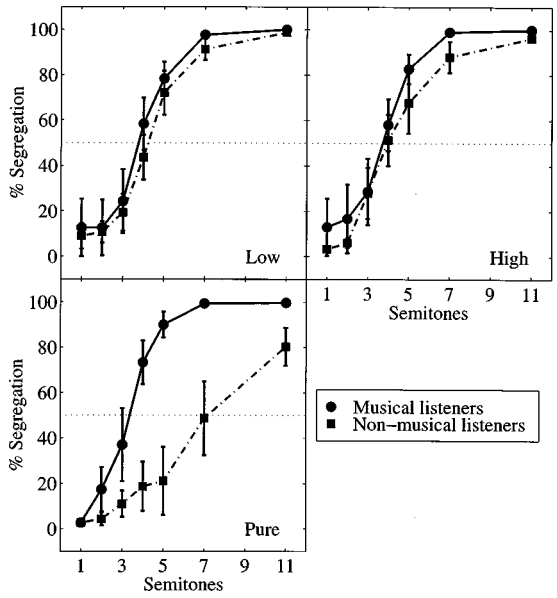

FIG. 3. As in Fig. 2, but averaged across listeners. The filled circles show the data for musical listeners and the filled squares show the data for nonmusical listeners. Error bars represent ±1 standard error of the mean across listeners.

els. The labels low, high, and pure denote the low-harmonic, high-harmonic, and pure-tone spectral conditions, respectively. The $f0$ interval at which the curve through the data crosses the 50% line is defined as the segregation boundary. The results from authors JV and AO are shown in the upper panel as diamonds and squares, respectively. The mean data for the two listener groups are shown in Fig. 3. Error bars denote ±1 standard error of the mean across listeners.

For both listener groups, the data generally show an increasing percentage of segregation responses with increasing $f0$ difference between tones A and B for all spectral conditions. These results indicate that for all three spectral conditions segregation occurs at large $f0$ intervals between tones A and B. Even in the high-harmonic condition the two tones were clearly segregated when there was a large $f0$ interval between them. This shows that in the absence of spectral cues, listeners seem to be able to segregate sequential sounds based solely on periodicity information.

On the whole the data from the musical listeners are rather homogenous. One exception is the listener shown as right-pointing triangles in the upper panels of Fig. 2. Unusually, this listener consistently reported hearing segregation for both sets of complex tones, even at the smallest $F0$ difference. The results from the nonmusical listeners seem more variable across listeners. This is especially true for the pure-tone condition, where a number of nonmusical listeners failed to reach 100% segregation even at the largest $f0$ separation. Many of these listeners reported having difficulty in hearing segregation with the pure tones. One nonmusical listener failed to hear segregation altogether. It is not quite clear what caused this difficulty. The tones had a rather low $f0$, in the range of 100 to 200 Hz. While it is very common for complex sounds to have an $f0$ in this range (for example, the human voice), spectral information in this frequency range is often not dominant in contributing to pitch perception. Musical listeners, who generally have more experience with listening in an analytical way to sounds, may have less difficulty in relating the $f0$ of a harmonic complex tone to the pure tone corresponding to that frequency.

In summary, listeners reported hearing segregation at large $f0$ differences in all three spectral conditions. For the musically trained listeners, the pattern of results was very similar across the three conditions. The results for the nonmusical listeners were similar for the two complex-tone conditions but showed somewhat *less* segregation for the pure-tone condition. The segregation boundary lies around four semitones for all conditions, except for the pure-tone condition for the nonmusical listeners. This is somewhat higher than was found in previous experiments by van Noorden (1975) and Rose and Moore (1997), who both found a segregation boundary around one semitone. This difference may be caused by differences in procedure. Both previous studies used a sweep-measurement task and van Noorden (1975) also used an adjustment task. With these tasks, the stimuli are presented to the listeners continuously while they make judgments rather than in short sequences. It is known that the bias towards segregation increases with presentation time (Bregman, 1978; Anstis and Saida, 1985). Additionally, the $f0$ of 100 Hz, used here, is lower than has previously been tested.

The results, which suggest that stream segregation can occur in the absence of spectral cues, seem not to be consistent with models based only on spectral information. However, while the physical stimulus in the high-harmonic condition contained only unresolved harmonics, it could be that nonlinear interactions between components produced lower, resolved distortion products which were used to segregate tones in the high-harmonic condition (Goldstein, 1967; Smoorenburg, 1970). For this reason a control experiment was set up with added noise to mask any possible combination tones.

II. EXPERIMENT 1A: EFFECT OF COMBINATION TONES

A. Preliminary experiment

The purpose of the preliminary experiment was to estimate the effective level of the combination tones produced by the high-harmonic tone complexes. The two authors served as listeners. The experiment consisted of two stages. The first stage estimated the masking produced by the combination tones; the second stage used these estimates to find the effective levels of the combination tones at various frequencies.

In the first stage, two 400-ms high-harmonic complex tones, as generated in experiment 1, with $f0$'s of 100 and 189 Hz and at a level of 70 dB SPL were used as maskers. Sinusoidal signals of 100-ms total duration, gated with 10-ms ramps, were temporally centered in the maskers and had a starting phase that was randomized from trial to trial. The frequencies of the signals corresponded to the $f0$ for both maskers, and to a number of randomly chosen harmonics with harmonic numbers between 3 and 8. Different harmonics were chosen for the two listeners and the two $f0$'s.

Signal thresholds were measured using a three-interval forced-choice method with a two-down one-up adaptive procedure. It was assumed that a signal was masked by the combination tone at the signal frequency.

In the second stage, the complex maskers were replaced by sinusoidal maskers at the same frequency as the sinusoidal signal, producing a tone-on-tone masking experiment with a randomized phase relationship between masker and signal. This was done to estimate the level of a sinusoidal masker needed to produce the same threshold as the complex masker of stage 1. This level should be equal to the effective level of a combination tone at that frequency.

This method established that the effective level of combination tones at the fundamental frequencies did not exceed 30 dB SPL, and that no other harmonic exceeded an effective level of 20 dB SPL for the two listeners tested. This enabled us to establish the level of a masking noise that was sufficient to ensure that any resolvable distortion products were at least 10 dB below masked threshold.

B. Method

Part of experiment 1 was repeated both with and without an added background noise. A pink noise (producing equal energy at the outputs of filters with a constant relative bandwidth, or Q value) was used with a spectrum level of 25 dB SPL at 1 kHz. Two of the three spectral conditions were tested here. For the high-harmonic condition, the noise was bandpass filtered with cutoff frequencies of 50 and 2000 Hz. For the sinusoidal condition, the cutoff frequencies were 300 and 4000 Hz. The noise was added to the sinusoidal condition in order to maintain some perceptual similarity between the two conditions and to control for any distracting effects of the noise not directly related to the masking of distortion products. The other stimuli were exactly the same as in experiment 1. They were generated with a Tucker-Davis System II, using a TDT DD1 16-bit digital-to-analog converter. Stimuli were then passed to a TDT PA4 programmable attenuator and a manual attenuator (Hatfield 2125) and were presented diotically over a Sennheiser HD 414 headphone in a sound-attenuating booth. The noise was presented continuously. Six listeners, with ages between 20 and 30 years and no reported hearing disorders or difficulties, took part. Three were musical and three were nonmusical, as defined in experiment 1. One musical listener was the author JV; all others had not participated in experiment 1. Four $f0$ intervals of 1, 4, 7, and 11 semitones were tested. The experiment consisted of four blocks, for the four different conditions: complex tones and pure tones, with and without added noise. The task was the same as in experiment 1. The order of presentation within a block was randomized, and each listener heard 25 presentations of each stimulus. Before data were collected, listeners were given a short (ca. 45 min) practice session using all four conditions to become accustomed to the stimuli and the task.

C. Results

The results from individual listeners are shown in Fig. 4. Open symbols joined by solid lines represent conditions without noise and filled symbols joined by dashed lines represent conditions with noise. Squares and circles represent pure-tone and complex-tone conditions, respectively. The results collected without noise are generally similar to the results from experiment 1. One difference is that the three new nonmusical listeners seem to have less difficulty in hearing segregation with the pure tones than did the listeners in experiment 1. This may simply be an illustration of the large intersubject variability in the task, especially for nonmusical listeners, as can also be seen in Fig. 2.

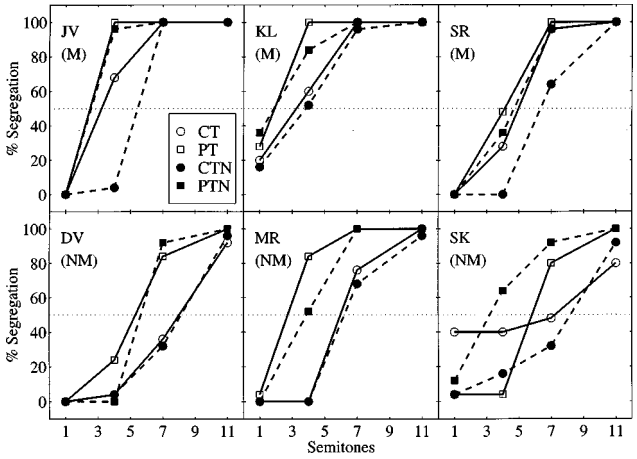

FIG. 4. Individual data from six listeners showing the effects of adding a background noise, designed to mask any audible distortion products. Open symbols with solid lines denote conditions with no noise (replication of experiment 1). Solid symbols with dashed lines denote conditions with added noise. Circles and squares represent the high-harmonic complex-tone (CT) and the pure-tone (PT) conditions, respectively.

Overall, the noise seems to have a small detrimental effect on segregation, although the amount seems to differ across listeners. This is true both for the complex-tone and the pure-tone conditions. All listeners show segregation at the highest $f0$ separation in both conditions, with and without added noise. This suggests that the segregation found for the complex-tone conditions in experiment 1 was probably not due to the audibility of lower, resolved distortion products.

III. EXPERIMENT 2: MELODY RECOGNITION

In experiment 1 listeners reported that they were able to perceptually segregate an alternating tone sequence with large $f0$ differences between the tones whether or not spectral cues were available. The effect was very strong and seemed not to depend on the spectral composition of the tones. However, the task used in that experiment is an introspective one in which listeners are free to set their own judgment criteria. In experiment 2 the more objective measure of melody recognition was used, in which performance is expected to depend on the degree of segregation. The study of Dowling (1973) was one of the first to use this method. He found that the recognition of two interleaved melodies improved with increasing frequency separation between the pitch ranges of the melodies, presumably as they begin to form separate streams. This effect occurred both for familiar melodies, consisting of about one phrase, and for unfamiliar, short melodies. Knowledge of which melody they were go-

ing to hear could help listeners to overcome the effect of interleaving. A melody recognition task was also used by Hartmann and Johnson (1991). Their stimuli consisted of interleaved familiar melodies, as in the first experiment of Dowling (1973), which were presented in twelve different conditions. The results of these experiments showed that the conditions for which the tones were expected to fall into widely separated frequency channels showed the greatest effects of streaming. However, a melody recognition task using tones covering the same spectral region, but different $f0$ regions, has not yet been tested. Such an experiment should help to clarify the role of temporal information in stream segregation.

For this experiment listeners judged whether an unfamiliar, atonal, five-tone melody, interleaved with random distracting tones, was the same as, or different from, a preceding melody presented without distracting tones. The distracting tones were either in the same $f0$ region as the melody tones, or in an $f0$ region 11 semitones higher than the melody. It was hypothesized that, if the melody and the distracting tones are in the same $f0$ region, the distracting tones should impede the recognition of the melody, whereas if they are in different $f0$ regions, they should form different streams, making the recognition of the melody easier.

A. Stimuli

For this experiment 17 pure tones and 17 complex tones were generated with $f0$'s ranging from 131 (C3) to 330 Hz (E4) at semitone intervals. The tones were generated in a similar way to that used in experiment 1. Only complex tones with high, unresolved harmonics and pure tones were tested in this experiment. As higher $f0$'s were used here than in experiment 1, the -3 dB points of the filter for the high-harmonic condition were placed at 4270 and 7455 Hz (-6 dB points at 4000 and 8000 Hz), to ensure that all the harmonics within the complex were unresolved. With these tones, reference (atonal) melodies were formed, consisting of five random tones within an $f0$ range of six semitones, from C3 to F3. The comparison melody was either the same as the reference melody or different, in which case the third and fourth tones of the reference melody were independently raised or lowered by two semitones. The random distracting tones also had an $f0$ range of six semitones and could be either in the same $f0$ region as the melody (see Fig. 5), or in an $f0$ region with a median 11 semitones higher than the melody.

The complex tones were presented at an overall level of 70 dB SPL. The level of the pure tones was adjusted to a level of 70 phon, as in experiment 1. The total duration of the tones was 100 ms, including 10-ms raised-cosine onset and offset ramps. The silent interval between succeeding melody tones was 120 ms, so that there was a silent interval of 10 ms between succeeding tones when distracting tones were present, giving a TRT of 110 ms. Stimuli were generated and presented in the same way as in experiment 1.

B. Listeners

The listeners were again divided into two groups, consisting of five musical and five nonmusical listeners, as defined in experiment 1. They were all between 20 and 30 years old and reported no hearing disorders or difficulties. All listeners except two (one musical and one nonmusical listener) had also participated in experiment 1.

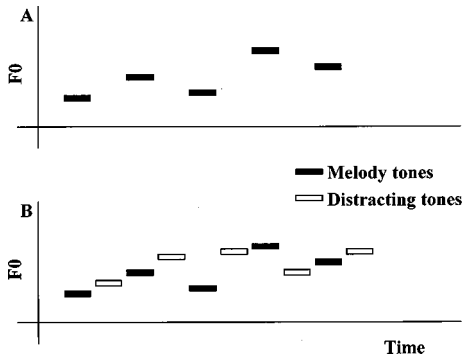

FIG. 5. A schematic diagram of the stimuli in the overlapping $f0$ condition of experiment 2. The reference melody (a) and the comparison melody (b) (here the same as the reference melody) are interleaved with distracting tones in the same $f0$ range as the melody.

C. Procedure

First, a randomly generated five-tone melody (the standard) was presented in isolation. After a silence of 2 s the comparison melody, interleaved with random distracting tones, was presented. Listeners were asked to indicate whether the two melodies were the same by pressing ''1'' (same) or ''2'' (different). They were given feedback on the computer screen in front of them. After an answer had been given, a new randomly generated melody was presented. The four conditions (two spectral conditions and two $f0$ ranges) occurred ten times in random order within each block. After each block the listener could take a short break. The experiment ended after seven blocks were completed. Before the experiment started, listeners were given about four blocks of training to get used to the task.

D. Results

Table I shows the percentages correct of the same/different responses for both $f0$ ranges of the distracting

TABLE I. Percentages correct for experiment 2 for each listener separately, with listener group in parentheses (M=Musical, N=Nonmusical) for both spectral conditions (complex and pure tones) and both $f0$ intervals between the melody tones and the distracting tones (1 and 11 semitones). Standard errors of the mean across blocks are given in parentheses.

	Complex tones		Pure tones	
Listener	1 semitone	11 semitones	1 semitone	11 semitones
AF (M)	65.7 (4.8)	97.1 (1.8)	58.6 (5.1)	91.4 (2.6)
AO (M)	65.7 (4.8)	94.3 (3.0)	60.0 (5.4)	95.7 (2.0)
JD (M)	65.7 (5.3)	95.7 (2.0)	57.1 (4.7)	85.7 (4.8)
JV (M)	71.4 (5.1)	98.6 (1.4)	71.4 (6.0)	80.0 (3.8)
SP (M)	48.6 (4.6)	77.1 (3.6)	50.0 (3.8)	70.0 (3.8)
AB (N)	54.3 (3.0)	60.0 (6.9)	50.0 (5.8)	50.0 (5.4)
EV (N)	61.4 (4.0)	62.9 (5.7)	60.0 (3.8)	52.9 (2.9)
JA (N)	47.1 (6.4)	81.4 (2.6)	54.3 (6.1)	77.1 (1.8)
MD (N)	55.7 (4.3)	54.3 (2.0)	55.7 (4.3)	65.7 (4.8)
PK (N)	50.0 (0.0)	61.4 (3.4)	50.0 (0.0)	75.7 (7.5)

tones, together with the standard errors across blocks, for each listener separately. All musical listeners and two of the nonmusical listeners (JA and PK) were able to perform the task after some practice, but the other three nonmusical listeners could not perform the task reliably in any condition. The results from one of them (AB) were not significantly above chance level in any condition. [Assuming binomial distribution, performance at 62% or higher is significantly above chance ($p<0.05$).]

The data show higher percentages correct for the conditions in which the distracting tones are in the $f0$ range 11 semitones above the $f0$ range of the melody tones. This suggests that the distracting tones are perceptually segregated from the melody tones, thereby facilitating the recognition of the melody. For the musical listeners this effect was highly significant both for the complex tones and the pure tones by the Friedman rank test [$\chi^2(1)=33.03$, $p<0.01$ and $\chi^2(1)=27.46$, $p<0.01$ respectively]. (A Friedman rank test was used as this does not rely on the assumptions of underlying normal distribution and equal variance: the data were found not to fulfill these criteria, even after various transformations.) For all nonmusical listeners combined, the difference between the two $f0$ ranges failed to reach significance. However, for the two nonmusical listeners who could do the task reliably in at least one condition (JA and PK), performance was significantly better with the 11-semitone difference than when the $f0$'s overlapped [$\chi^2(1)=13.76$, $p<0.01$ for the complex tones and $\chi^2(1)=12.19$, $p<0.01$ for the pure tones]. Performance in the high-harmonic condition was not poorer than in the pure-tone condition, suggesting again that spectral differences were not necessary to achieve segregation in this task. In fact, for the musical listeners and the 11-semitone interval, performance was significantly better in the high-harmonic condition than in the pure-tone condition [$\chi^2(1)=6.76$, $p<0.01$]. It is not immediately clear why this should be.

The task used in this experiment was selected after numerous pilot experiments. The main difficulty that arose was to find a task sufficiently difficult to avoid ceiling effects for the musically trained listeners, but not so difficult as to run into floor effects for listeners with no musical training. As can be seen in Table I, even with this rather difficult atonal task, musically trained listeners often performed above chance in at least one of the overlapping $f0$ conditions, primarily with the complex tones. This may have been because they learned to attend selectively to every second note in the melody (Dowling *et al.*, 1987). However, based on listeners' reports, it seems more likely that listeners were sometimes able to select the correct interval based on changes in the overall contour of the compound melody. For instance, if a change in the melody resulted in a note that was lower than any in the comparison interval, this might provide a cue. Note, however, that this is not a reliable cue: a low note in the distracting tones would provide a similar, but unreliable, cue. Also, the use of a contour cue should, if anything, improve performance in the overlapping $f0$ conditions, relative to the separated $f0$ conditions. Thus, the fact that significant differences were still found provides further support for the ability of listeners to use temporal cues in forming perceptual streams. Other studies have also reported performance well above chance in the condition where streaming is most limited. For instance, Hartmann and Johnson (1991) found performance of around 60% correct in their ''control condition'' in a task where chance performance would have been at approximately 1.5% correct. This highlights the difficulty of avoiding ceiling effects. On the other hand, most nonmusical listeners in the present study found difficulty performing the task reliably in any condition. It is possible that they would have found the task difficult even in the absence of the distracting tones. However, an easier task would have led to even better performance by the musically trained listeners, thereby leading to less easily discernible differences between the conditions.

Despite these difficulties, all listeners who could reliably perform the task in at least one condition showed a strong effect of distractor $f0$ region: performance was improved by introducing a large $f0$ difference between the melody and distractor tones, suggesting that stream segregation was possible. As in experiment 1, performance was not greatly affected by the presence or absence of spectral cues.

IV. GENERAL DISCUSSION

The results of both experiments show that perceptual stream segregation can occur with complex tones consisting of only high, unresolved harmonics. This indicates that stream segregation can be based solely on periodicity information in the absence of spectral information. These results are not consistent with purely spectral models of sequential stream segregation (Beauvois and Meddis, 1996; McCabe and Denham, 1997).

In both experiments the results for the different spectral conditions (pure tones, low-harmonic, and high-harmonic complexes in experiment 1 and pure tones and high-harmonic tones in experiment 2) were similar. This suggests that there may not be two different processes for segregation based on spectral content and based on periodicity information. It may be that segregation can be based on a pitch percept that is formed at a higher level of the auditory pathways, at which both spectral and temporal information are available. It should, however, be remembered that van Noorden (1975) found strong segregation for complexes with the same $f0$ but different spectral composition. Similarly, Bregman *et al.* (1990) and Singh (1987) found evidence for stream segregation based on spectral but not temporal cues. Thus, a more general conclusion may be that listeners are able to segregate into streams when sounds differ on *either* a spectral *or* a temporal dimension. It is interesting to note that the model of Beauvois and Meddis (1996) provides for the possibility of using periodicity information by retaining (but not currently using) fine-structure information.

As it is known that the pitch produced by a high, unresolved complex is less salient than for a low, resolved complex, it might have been expected that the effect of segregation based on pitch would be less strong in the high-harmonic condition than in either the low-harmonic or the pure-tone conditions. However, in both experiments the results across conditions were comparable. It has been shown that, although pitch is less salient for unresolved harmonics,

pitch intervals larger than about two semitones can still be identified correctly. Therefore, as segregation generally occurred only for intervals larger than four semitones, the reduced salience may not have played a large role.

The knowledge that periodicity information alone can influence segregation may be important in developing algorithms for cochlear implants. Coding algorithms for implants often use the rate of electrical impulses to code the $f0$ of incoming signals. An increase in the pulse rate generally leads to an increase in perceived pitch in implant patients (Busby and Clark, 1997), and there is some evidence that at least some patients can use this $f0$ information to identify musical intervals (McDermott and McKay, 1997) or recognize melodies (Moore and Rosen, 1979). The present results provide support for the preservation of $f0$ information in implant coding algorithms: under favorable conditions it may be possible for patients to use the rate information in the perceptual organization of incoming sounds.

ACKNOWLEDGMENTS

This work was supported in part by a Wellcome Trust Research Fellowship (0044215/Z/95/Z), awarded to AJO. The experiments presented here comprised part of a Master's thesis submitted by JV to the University of Utrecht, and supervised by AJO and Dr. Bert Schouten. We thank Dr. Brian C. J. Moore and two anonymous reviewers for helpful comments on an earlier version of this paper.

Anstis, S., and Saida, S. (**1985**). ''Adaptation to auditory streaming of frequency-modulated tones,'' J. Exp. Psychol. **11**, 257–271.

Beauvois, M. W., and Meddis, R. (**1996**). ''Computer simulation of auditory stream segregation in alternating-tone sequences,'' J. Acoust. Soc. Am. **99**, 2270–2280.

Beauvois, M. W., and Meddis, R. (**1997**). ''The decay of auditory stream biasing,'' Percept. Psychophys. **59**, 81–86.

Bregman, A. S. (**1978**). ''Auditory streaming is cumulative,'' J. Exp. Psychol. **4**, 380–387.

Bregman, A. S. (**1990**). *Auditory Scene Analysis: The Perceptual Organisation of Sound* (Bradford Books, MIT, Cambridge, MA).

Bregman, A. S., Liao, C., and Levitan, R. (**1990**). ''Auditory grouping based on fundamental frequency and formant peak frequency,'' Can. J. Psychol. **44**, 400–413.

Busby, P. A., and Clark, G. M. (**1997**). ''Pitch and loudness estimation for single and multiple pulse per period electric pulse rates by cochlear implant patients,'' J. Acoust. Soc. Am. **101**, 1687–1695.

Dowling, W. J. (**1973**). ''The perception of interleaved melodies,'' Cogn. Psychol. **5**, 322–337.

Dowling, W. J., Lung, K. M., and Herrbold, S. (**1987**). ''Aiming attention in pitch and time in the perception of interleaved melodies,'' Percept. Psychophys. **41**, 642–656.

Goldstein, J. L. (**1967**). ''Auditory nonlinearity,'' J. Acoust. Soc. Am. **41**, 676–689.

Hartmann, W. M., and Johnson, D. (**1991**). ''Stream segregation and peripheral channeling,'' Music Percept. **9**, 155–184.

Houtsma, A. J. M., and Smurzynski, J. (**1990**). ''Pitch identification and discrimination for complex tones with many harmonics,'' J. Acoust. Soc. Am. **87**, 304–310.

McCabe, S. L., and Denham, M. J. (**1997**). ''A model of auditory streaming,'' J. Acoust. Soc. Am. **101**, 1611–1621.

McDermott, H. J., and McKay, C. M. (**1997**). ''Musical pitch perception with electrical stimulation of the cochlea,'' J. Acoust. Soc. Am. **101**, 1622–1631.

Miller, G. A., and Heise, G. A. (**1950**). ''The trill threshold,'' J. Acoust. Soc. Am. **22**, 637–638.

Moore, B. C. J., and Rosen, S. M. (**1979**). ''Tune recognition with reduced pitch and interval information,'' Q. J. Exp. Psychol. **31**, 229–240.

Moore, B. C. J., Glasberg, B. R., and Baer, T. (**1997**). ''A model for the prediction of thresholds, loudness, and partial loudness,'' J. Aud. Eng. Soc. **45**, 224–240.

Nooteboom, S. G., Brokx, J. P. L., and de Rooij, J. J. (**1978**). ''Contributions of prosody to speech perception,'' in *Studies in the Perception of Language*, edited by W. J. M. Levelt and G. B. Flores d'Arcais (Wiley, New York).

Plomp, R. (**1964**). ''The ear as a frequency analyzer,'' J. Acoust. Soc. Am. **36**, 1628–1636.

Rose, M. M., and Moore, B. C. J. (**1997**). ''Perceptual grouping of tone sequences by normally hearing and hearing impaired listeners,'' J. Acoust. Soc. Am. **102**, 1768–1778.

Singh, P. G. (**1987**). ''Perceptual organization of complex-tone sequences: A trade off between pitch and timbre?'' J. Acoust. Soc. Am. **82**, 886–895.

Smoorenburg, G. F. (**1970**). ''Pitch perception of two-frequency stimuli,'' J. Acoust. Soc. Am. **48**, 924–942.

Suzuki, S., Suzuki, Y., Kono, S., Sone, T., Kumagai, M., Miura, H., and Kado, H. (**1989**). ''Equal-loudness contours for pure tone under free field listening conditions. I. Some data and considerations on experimental conditions,'' J. Acoust. Soc. Jpn. (E) **10**, 329–338.

van Noorden, L. P. A. S. (**1975**). ''Temporal coherence in the perception of tone sequences,'' Ph.D. thesis, Eindhoven University of Technology.

Dual temporal pitch percepts from acoustic and electric amplitude-modulated pulse trains

Colette M. McKay
Department of Otolaryngology, The University of Melbourne, Parkville 3052, Australia

Robert P. Carlyon
MRC Cognition and Brain Sciences Unit, 15 Chaucer Road, Cambridge CB2 2EF, England and Cochlear Implant Centre, Department of Audiology, Addenbrooke's Hospital, Hills Road, Cambridge CB2 2QQ, England

(Received 18 March 1998; accepted for publication 7 October 1998)

Two experiments examined the perception of unmodulated and amplitude-modulated pulse trains by normally hearing listeners and cochlear implantees. Four normally hearing subjects listened to acoustic pulse trains, which were band-pass filtered between 3.9 and 5.3 kHz. Four cochlear implantees, all postlinguistically deaf users of the Mini System 22 implant, listened to current pulse trains produced at a single electrode position. In the first experiment, a set of nine loudness-balanced unmodulated stimuli with rates between 60 and 300 Hz were presented in a multidimensional scaling task. The resultant stimulus spaces for both subject groups showed a single dimension associated with the rate of the stimuli. In the second experiment, a set of ten loudness-balanced modulated stimuli was constructed, with carrier rates between 140 and 300 Hz, and modulation rates between 60 and 150 Hz. The modulation rates were integer submultiples of the carrier rates, and each modulation period consisted of one higher-intensity pulse and one or more identical lower-intensity pulses. The modulation depth of each stimulus was adjusted so that its pitch was judged to be higher or lower 50% of the time than that of an unmodulated pulse train having a rate equal to the geometric mean of the carrier and modulation rates. A multidimensional scaling task with these ten stimuli resulted in two-dimensional stimulus spaces, with dimensions corresponding to carrier and modulation rates. A further investigation with one normally hearing subject showed that the perceptual weighting of the two dimensions varied systematically with modulation depth. It was concluded that, when filtered appropriately, acoustic pulse trains can be used to produce percepts in normal listeners that share common features with those experienced by subjects listening through one channel of a cochlear implant, and that the central auditory system can extract two temporal patterns arising from the same cochlear location.
[S0001-4966(99)05501-0]

PACS numbers: 43.66.Hg, 43.66.Mk, 43.66.Ts [JWH]

INTRODUCTION

The concept that pitch percepts are evoked by the periodicities in acoustic or electric signals has been well supported by experimental evidence. Early acoustic experiments showed that interrupted noise had a pitch which could be matched to that of a pure tone with a frequency equal to the interruption frequency (Miller and Taylor, 1948; Small, 1955). Similarly, sinusoidally amplitude-modulated (SAM) tones have a ''residue pitch'' which corresponds to the modulation or fundamental frequency, provided the individual components of the complex tone fall within certain regions (Ritsma, 1962, 1963), and the complex tone is harmonic (Schouten *et al.*, 1962). Although these types of stimuli could arguably provide some spectral cues for pitch perception, later experiments have demonstrated pitch percepts from purely temporal cues. For example, Burns and Viemeister (1976, 1981) showed that subjects listening to SAM noise stimuli (which had no spectral cues) could judge musical intervals for modulation rates between 80 and 300 Hz. It should be noted, however, that the pitch of SAM noise is less salient than that of deterministic stimuli such as pure tones or harmonic complexes.

Electrical stimulation of the auditory nerve via cochlear implants provides temporal information which is independent of the place of stimulation, and thus is ideal for studying pitch percepts which arise from purely temporal cues. Early experiments showed that the rate of pulsatile stimulation, or frequency of analog stimulation, evoked a pitch percept up to about 300 Hz (for example, Simmons, 1966; Eddington *et al.*, 1978; Tong *et al.*, 1979; Shannon, 1983), although there was some variability in the rate which defined the upper limit for the discriminability range (Tong and Clark, 1985; Townshend *et al.*, 1987). Amplitude modulation of current pulse trains also evokes a pitch percept which is dependent on the modulation frequency, provided that the carrier rate is sufficiently high, or is a multiple of the modulation frequency (McKay *et al.*, 1994), and provided that the modulation depth is sufficiently large (McKay *et al.*, 1995). Subjects have been shown to be able to judge musical intervals based on the pulse rate of unmodulated stimuli (Pijl and Schwarz, 1995; McDermott and McKay, 1997) and on the modulation rate of modulated pulse trains (McDermott and McKay, 1997). Although it has not been possible as yet to directly compare the salience of temporal pitches using co-

chlear implants to that of pitches evoked by normal acoustic hearing in the same subject, the variance of interval-estimation data and rate difference-limen data in implant subjects is of the same order of magnitude as shown in experiments with SAM noise (Burns and Viemeister, 1976, 1981), indicating that the pitch may be similarly weak.

The aim of the experiments reported here was to investigate the perception of pitch when there is more than one periodicity present simultaneously in the stimulus. A modulated pulse train is one such type of stimulus, in which both the carrier rate and the modulation rate can potentially evoke a pitch percept. McKay *et al.* (1995) studied the effect of modulation depth on pitch matching with cochlear implantees. In that experiment, each modulation period of the stimulus contained one high-current pulse followed by one or more identical lower-current pulses, and subjects were asked to compare the pitch of this stimulus (in a 2-interval forced-choice (2IFC) task) to that evoked by unmodulated pulse trains of various rates. The rate of the unmodulated stimulus for which the modulated stimulus was judged equal in pitch was found to vary systematically with modulation depth, being close to the carrier rate for small modulation depths, and falling smoothly to asymptote to the modulation rate for larger modulation depths. A model was proposed to explain the data, in which a weighted average of the two main neural interspike intervals (corresponding to modulation and carrier intervals) determined the pitch-comparison behavior of the subjects. The modulation depth determined the relative number of the two neural spike intervals and hence also the resultant matched-pitch.

Two questions arose from these results. First, considering the lack of reports in the acoustic literature on the pitch of modulated pulse trains, were the results peculiar to electric stimulation, perhaps as a consequence of greater neural synchrony or higher spike probabilities? Second, was the weighting of the two periodicities in the pitch-matching task performed precognitively by the auditory system, resulting in a unique pitch percept, or was the weighting performed cognitively by the subject when asked to compare the pitch of a stimulus containing two simultaneous pitches to that of a stimulus containing only one pitch? Although the first proposition may seem unlikely given the known existence of ambiguous pitch in stimuli such as inharmonic complexes, the response behavior of the subjects did not suggest that they were sometimes listening to the carrier and sometimes the modulation rate when comparing the pitch. In contrast to the above experiment, pitch-matching experiments with acoustic stimuli having ambiguous pitch generally result in more than one ''matched'' frequency (see, for example, Schouten *et al.*, 1962). Furthermore, acoustic stimuli which have been shown to have ambiguous pitch have, to date, not included stimuli differentiated only on the basis of temporal cues.

Arguments have been presented to support the idea that two periodicities cannot be extracted from the same cochlear location (or a single auditory filter). For example, Carlyon (1996) found that subjects could extract the fundamental frequencies ($F0$s) of two simultaneous groups of harmonics, bandpass filtered in the same spectral region, only when the harmonics were resolvable. He postulated that normal listeners could not segregate the $F0$s of two groups of harmonics in the absence of spectral cues. In a further experiment (Carlyon, 1997), he investigated listeners' ability to discriminate between a standard stimulus, consisting of two groups of pulse trains bandpass filtered into the same frequency region, and a signal which differed by one of the pulse trains, the ''target,'' having a higher $F0$. He found that listeners could do so only by exploiting the fact that the composite stimulus formed by the masker and target pulse trains had more pulses in the signal than in the standard intervals, rather than by extracting the $F0$ of the target from that of the masker. Listeners' dependence on this ''mean rate'' cue was demonstrated by an experiment in which a proportion of pulses was deleted from both the standard and signal stimuli. Performance dropped to chance when more pulses were deleted from the signal than from the standard, thereby removing the mean rate cue, whereas performance remained above chance in a control condition where more pulses were deleted from the standard than from the signal.

One difference between the electric experiments conducted by McKay and her colleagues and the acoustic experiments by Carlyon lies in the nature of the two periodicities present in each stimulus. In the electric experiments, each longer (''modulator'') period contained an integer number of shorter ''carrier'' periods. In contrast, Carlyon's acoustic pulse trains were formed by mixing two single pulse trains with close but unequal $F0$s, resulting in an irregular pattern of ''beating.''

The experiments reported below compare the perception of modulated pulse trains in electric and acoustic stimulation using analogous stimuli and procedures, and address the question of whether the central auditory system can extract two independent temporal patterns from a single cochlear location. Multidimensional scaling tasks were conducted with acoustic and electric modulated pulse trains which were constructed similarly to those of McKay *et al.* (1995), in which spectral cues were absent due, respectively, to bandpass filtering or constant electrode position. If the auditory system extracts both the carrier and modulation rates from the signal, the outcome is hypothesized to be a two-dimensional space with the dimensions corresponding to these two rates.

I. METHODS

A. Subjects and stimuli

Four normally hearing subjects (NC, NB, NR, and NT) and four cochlear implantees (CM, CA, CP, and CL) took part in the experiments. The normally hearing listeners were all adults whose hearing acuity was within 15 dB of the 1969 ANSI standard at all audiometric frequencies. Subjects NC and NB were the first and second authors, respectively; the others were paid for their services. The implantees were all postlinguistically deaf subjects who use the Mini System 22 implant, manufactured by Cochlear Ltd. Details of their etiology and the stimulation parameters for these experiments are contained in Table I.

The acoustic stimuli used in the experiments consisted of pulse trains (each pulse of duration 50 μs) which were

TABLE I. Details of the cochlear implantees who took part in the experiment. CSOM refers to chronic serious otisis media. The last three columns refer to the electrode and pulse duration used in the experiments, and the perceptual dynamic range for that electrode, measured with a 145-Hz pulse train. The numbers describing the electrode refer to the two rings comprising the bipolar pair used, or in the case of subject CP, the single ring in common-ground mode. The electrodes are numbered 1 to 22 in basal-to-apical direction.

Subject	Age (years)	Etiology	Length of profound deafness	Length of implant use	Electrode	Pulse width (μs)	Dynamic range (dB)
CM	20	Meningitis	9 months	12 months	[16,18]	100	6.85
CA	61	Menieres/CSOM	18 months	15 months	[19,21]	100	5.50
CP	50	Meningitis/CSOM	12 years	28 months	19	150	7.97
CL	57	unknown/progressive	6 years	17 months	[18,20]	150	4.62

generated at a sampling rate of 20 kHz (CED 1401 plus, 16-bit resolution), passed through antialiasing filters (Kemo VBF 25.01; attenuation rate 100 dB/octave), and then bandpass filtered between 3.9 and 5.3 kHz (Kemo VBF25.03; attenuation rate 48 dB/octave). The bandpass frequencies were chosen so that, for the pulse rates used (up to 300 Hz), adjacent harmonics would not be resolvable by the peripheral auditory system (Shackleton and Carlyon, 1994). The stimuli were presented against a continuous background of 10-kHz-wide pink noise having a spectrum level of 3.4 dB SPL at 4 kHz. For an unmodulated pulse train with an $F0$ of 145 Hz, the level of the pulses was set such that resulting harmonics had levels of 48 dB SPL each when in the filter passband. This level will be referred to henceforth as the ''48-dB reference level.'' The levels of the other stimuli varied across conditions and subjects, and will be described in Sec. I B. The noise and pulses were mixed by being fed to separate inputs of a headphone amplifier before being fed to one earpiece of a Sennheiser HD414 headset.

The electrical stimuli consisted of biphasic current pulse trains. A single apical electrode position was chosen since earlier studies have reported that rates on apical electrodes may produce a more ''pitchy'' sensation than those on basal electrodes (see McDermott and McKay, 1997, for example). The stimuli were generated and controlled by an IBM-compatible computer which was interfaced with a speech processor. The processor was used to encode the stimuli and transmit them to the implanted receiver–stimulator.

The duration of each pulse train stimulus was 500 ms.[1] Both unmodulated and amplitude-modulated stimuli were used. The unmodulated stimuli had rates between 60 and 300 Hz. The modulated stimuli had carrier rates between 140 and 300 Hz. In these stimuli, the modulation rate was always a submultiple of the carrier rate, so that each modulation period was identical. No modulation rate below 60 Hz was used, as rates below this tend to produce a buzz rather than a pitch. Each modulation period contained a single higher-intensity pulse followed by one or more identical lower-intensity pulses. Figure 1 shows 10-ms segments (one modulation period) of the acoustic and electric modulated stimuli with 300-Hz carrier rate and 100-Hz modulation rate.

B. Experimental procedures

1. Multidimensional scaling of unmodulated pulse trains

Nine unmodulated pulse trains with rates equal to 60, 80, 105, 125, 145, 170, 200, 240, and 300 Hz were constructed as described above and loudness balanced with the 145-Hz stimulus. For acoustic stimuli, the loudness-balance procedure was as follows. Each loudness-balancing run started with one of the two stimuli (either 145 Hz or the rate to be balanced) fixed in level followed, 500 ms later, by the second, variable-level, stimulus. The listener could then adjust the level of the variable stimulus by 2 or 4 dB up or down by pressing one of four buttons on a response box, after which the two stimuli were presented again, and the listener made a new adjustment. This procedure continued until he/she was satisfied that the two stimuli were equally

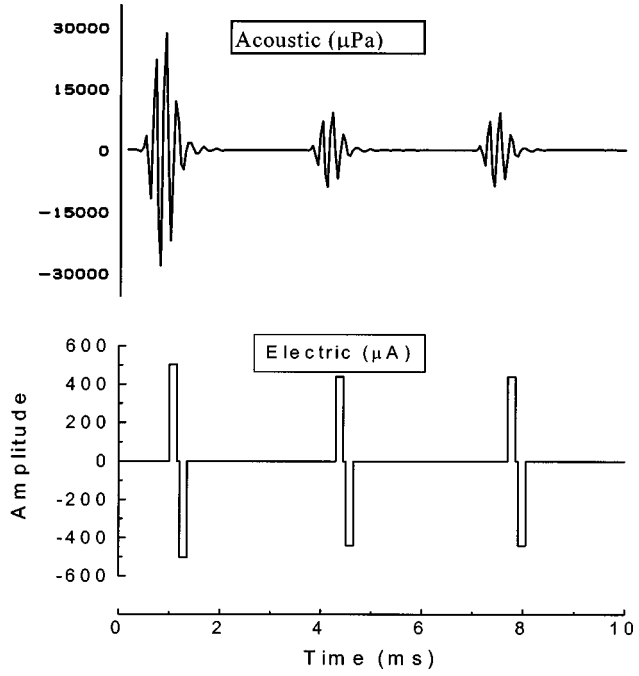

FIG. 1. Examples of acoustic and electric stimulus waveforms. Each panel shows a 10-ms segment (one modulation period) of the modulated pulse train of rate 300 Hz and modulation rate 100 Hz. The acoustic stimulus (top), shown after bandpass filtering but before transduction by the headphones, has a modulation depth of 10 dB. The electric stimulus (bottom) is that for subject CP, with modulation depth 1.2 dB.

loud. Six loudness matches were made for each stimulus pair: three with the 145-Hz stimulus varying and three with it fixed. When the 145-Hz stimulus was fixed, it was presented at the 48-dB reference level (see Sec. I A); when the other stimulus was fixed, its overall level was the same as that of the 145-Hz stimulus at the 48-dB reference level. The results of the six trials were averaged.

For electric stimuli, the current of the 145-Hz stimulus was first adjusted to produce a comfortable loudness. All other stimuli were then balanced to this stimulus in the following way. The 145-Hz stimulus and the other stimulus were presented continuously alternating with 500-ms silent intervals. The subject adjusted the current of the variable stimulus using an unmarked rotary knob until he/she was satisfied that the two stimuli were equally loud. The current of the adjusted stimulus was then fixed at the value set by the subject and the procedure repeated with the 145-Hz stimulus adjusted. The two procedures were repeated and the results of the four trials averaged.

The nine equally loud stimuli were then presented to the subjects in a multidimensional scaling task. The subjects were first familiarized with the stimulus set. All possible pairs of stimuli (in both orders) were presented to the subject in random order. After each pair of stimuli, the subject was required to respond with an estimate of their similarity. In both the acoustic and electric parts of the experiment, subjects responded using a 10-cm-long scale, on which one end represented stimuli which sounded exactly the same, and the other end represented the pair which was most dissimilar. The normally hearing subjects adjusted the position of a slider on a 10-cm-long potentiometer, thereby setting a voltage which was fed back to an analog-to-digital converter and scaled to a number between 0 and 400. The implantees pointed to a position along a ruled line, which was then converted to a number between 0 and 100. Three complete dissimilarity matrices were obtained for all subjects except NC and NB, who provided two matrices each.

The data were analyzed in two ways using the program ALSCAL (Young and Lewyckyj, 1979), which uses an iterative procedure developed from that of Kruskal (1964). The individual subject data were analyzed using repeated-measures nonmetric multidimensional scaling. The result of this analysis was a stimulus space in which the rank order of Euclidean distances between the stimuli represented, with the least error (*s*-stress), the rank order of perceptual dissimilarity of the stimuli. The appropriate number of dimensions for this stimulus space was obtained by comparing the stress in solutions of 1, 2, and 3 dimensions, and also by observing which solution had dimensions which could be described by stimulus parameters. The group data for each of the two subject groups were analyzed by first obtaining a summed matrix for each subject, and then performing individual-differences nonmetric multidimensional scaling. The output of this analysis was a single stimulus space which best described the stimulus dimensions perceived by the subject group as a whole. The individual-subject weight vectors obtained from the analysis represent the differences among subjects in how they perceived the sounds. The angles of the vectors represent the relative importance of the dimensions to the dissimilarity task for each subject; the lengths of the vectors represent the amount of variance for each subject explained by the stimulus space.

TABLE II. The carrier rates and modulation rates (in Hz) used for the ten modulated stimuli in the experiment. Also shown is the geometric mean of the carrier and modulation rates, which was the rate of the unmodulated stimulus used in the modulation-depth adjustment procedure.

	Carrier rate	Modulation rate	Geometric mean rate
1	300	150	212
2	300	100	173
3	300	75	150
4	300	60	134
5	252	126	178
6	252	84	145
7	252	63	126
8	198	99	140
9	198	66	114
10	140	70	99

2. Multidimensional scaling of modulated pulse trains

Ten modulated stimuli were constructed as described above. The carrier rates and modulation rates are shown in Table II. In order to minimize, as far as practical, the possible influence of stimuli differing by musical intervals, the carrier rates were chosen so as not to include octave relationships. However, the nature of the stimuli resulted in musical interval relationships between stimuli of the same carrier rate. The modulation depth was adjusted for each stimulus in the following way. The higher-amplitude pulses in the acoustic stimuli were initially set so that, at a modulation depth of zero, each stimulus had an overall (rms) level equal to the 145-Hz unmodulated pulse train at the 48-dB reference level. For the electric stimuli, these pulses (for a modulation depth of zero) were set to the current which provided equal loudness to the 145-Hz rate in experiment 1. A separate ''reference'' unmodulated pulse train, with rate equal to the geometric mean of the carrier and modulation rates (see Table II), was then loudness balanced to each modulated stimulus (with a modulation depth of zero) using the procedure described in Sec. I B1. The amplitude of the lower-amplitude pulse(s) in each modulated stimuli was then adjusted in a 2IFC, adaptive pitch-comparison procedure, using the corresponding reference unmodulated pulse train. The purpose of the adaptive procedure was to find the modulation depth where the pitch was judged to be higher or lower than that of the unmodulated reference stimulus 50% of the time.

In the adaptive pitch-matching procedure, the reference and modulated stimuli were presented in random order and the subjects were required to indicate which stimulus had the higher pitch. The first time the procedure was run in each condition, the modulation depth was zero (electric) or 2 dB (acoustic) for the first trial; at these small depths, the reference stimulus should be judged lower in pitch than the modulated stimulus. This was confirmed by obtaining at least three out of four reference-lower responses. The modulation depth was then increased by reducing the lower-amplitude pulse(s) by one step (2 dB for acoustic pulses, and two current steps (about 0.3 dB) for electric pulses), and the 2IFC

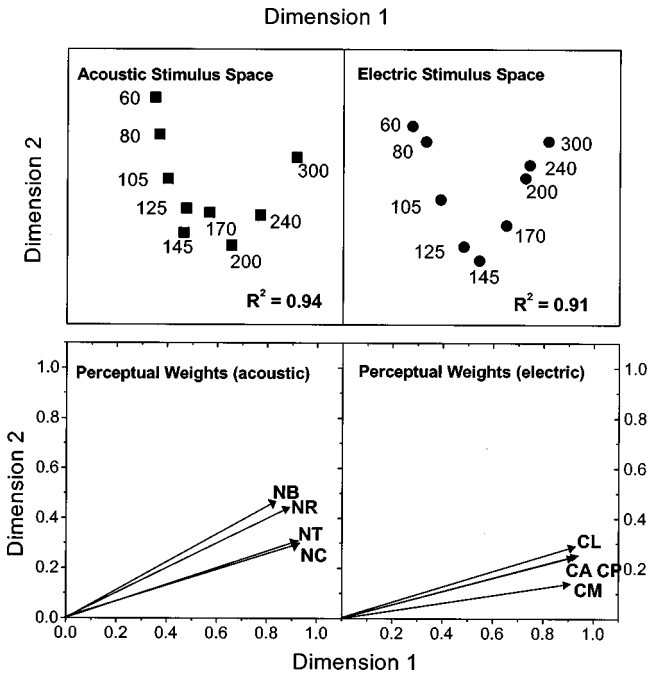

FIG. 2. The upper panels show the acoustic and electric stimulus spaces which best describe all the data from the normally hearing and cochlear-implantee subject groups, resulting from individual-difference scaling analysis in two dimensions. The rates (in Hz) are shown next to the appropriate symbols. The lower panels show the individual perceptual weight vectors for the two dimensions.

pitch comparison continued. The modulation depth was increased until at least three out of four responses were reference-higher responses (i.e., no more than one reference-lower response out of a group of four trials). The modulation depth was then decreased again until at least three out of four responses were reference-lower responses. The procedure continued
in this fashion until eight turning points had been obtained, and the modulation depths at the last six of these were averaged. A second run was performed starting with a modulation depth greater than the upper turning points of the first run (so that the pitch was definitely lower than the reference pitch). The starting modulation depth was chosen separately for each implantee, but was always 30 dB for the normal listeners. The two estimates of modulation depth were then averaged.

After adjusting the modulation depths as above, all ten modulated stimuli were loudness balanced to a 145-Hz unmodulated stimulus at the 48-dB reference level (acoustic) or at the comfortable listening level (electric). They were then presented to the subjects in the same multidimensional scaling task as they had performed for the unmodulated stimuli. Several complete dissimilarity matrices were obtained for each subject. Each implantee provided five matrices, and subjects NC, NB, NR, and NT provided four, six, six, and five matrices, respectively. The matrices were analyzed in the same way as the matrices for unmodulated rates, with individual-subject stimulus spaces being obtained, and two group stimulus spaces along with subject weight vectors.

II. RESULTS

A. Multidimensional scaling of unmodulated pulse trains

The individual-subject stimulus spaces for acoustic and electric unmodulated pulse trains were very similar for all subjects in both groups, with the rates of stimulation represented systematically along a single arc in a two-dimensional space. Because of the similarity of these stimulus spaces, only the two group stimulus spaces are shown (Fig. 2). This type of configuration is often seen with one-dimensional data. It was first described as the ''horseshoe effect'' by Kendall (1971), who used multidimensional scaling to study the structure of archeological artifact distribution with depth of digging. The mechanism which results in a curve instead of a straight line is still poorly understood, however. McKay *et al.* (1996) obtained similar curves when analyzing the perceptual dissimilarity of electrode positions within the cochlea.

Analysis of the way stress diminished with number of dimensions did not provide a clear ''knee-point'' at one or two dimensions. The one-dimensional (straight-line) solutions also showed the stimuli generally ranked along the rate dimension. However, they were not as evenly and systematically arranged as in the curves in the two-dimensional solutions shown in the figures. It is apparent, then, that the perception of nonmodulated stimuli varied along the single dimension of rate, and that the single dimension was best represented by a curve in a two-dimensional space. Given that the stimulus percept changes are really one-dimensional (along a single curve), the subject weights for the two dimensions should not be interpreted as the weighting for two independent perceptual dimensions. However, the fact that all subject weight vectors are clustered at the same angle is an indication that they perceived the stimuli in very similar ways.

B. Multidimensional scaling of modulated pulse trains

The adaptive pitch-comparison procedure to set the modulation depth of the ten modulated stimuli was successfully completed for all but one stimulus for one subject. Subject CM consistently ranked the stimulus with a 140-Hz carrier rate and a 70-Ha modulation rate as lower in pitch than the reference 99-Hz unmodulated stimulus, even when the modulation was set to zero (making the stimulus an unmodulated one with a 140-Hz rate). This was clearly an anomalous finding, considering the ordered perception of rates he exhibited in the first experiment. After ruling out software or hardware faults, it was conjectured that this subject may experience idiosyncratic percepts for particular stimuli. As his responses in the pitch-comparison procedure for the other nine stimuli were very consistent with those of the other implantees, it was decided to continue with his data collection using this reduced stimulus set.

The modulation depth for each modulated stimulus is shown separately for each subject in Fig. 3. The error bars span the average upper and lower turning points in the adaptive procedure (i.e., where the modulated stimulus was con-

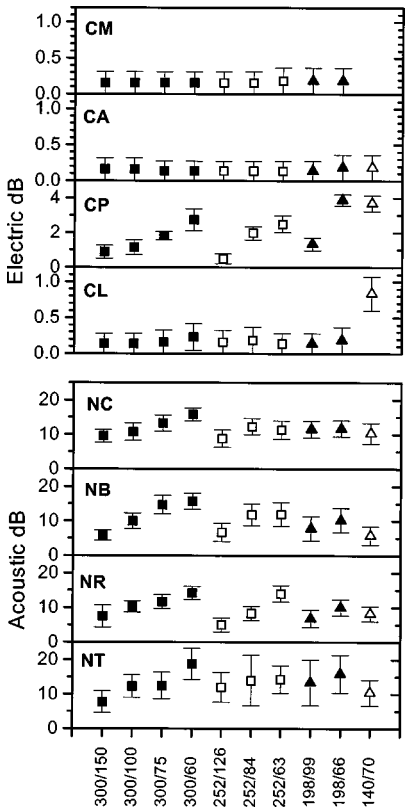

FIG. 3. The modulation depth for each modulated stimulus at which its pitch was rated higher or lower than that of the reference stimulus (see Table II) 50% of the time. The modulation depth is given as the dB difference (in current or sound pressure) between the high-intensity and low-intensity pulses in the pulse train. The error bars span the average upper and lower turning points in the adaptive procedure (where the modulated stimulus was considered higher or lower in pitch on three out of four trials). The carrier/modulation rates of each stimulus are noted on the horizontal axis, and each carrier rate is denoted by a different symbol for visual clarity.

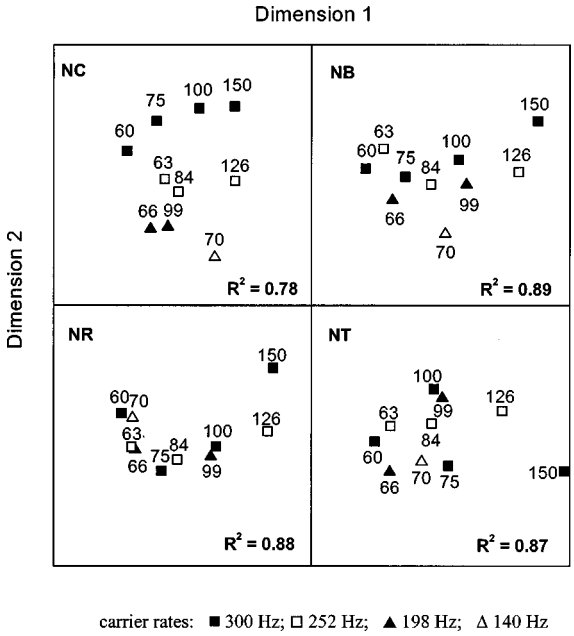

FIG. 4. Stimulus spaces for the four normally hearing subjects, resulting from nonmetric repeated-measures multidimensional scaling analysis of perceptual differences among amplitude-modulated acoustic pulse trains of differing carrier and modulation rates. The modulation rates (in Hz) are shown above or below the appropriate symbols, and the carrier rates are denoted by the symbol type.

sidered higher or lower in pitch than the reference stimulus in three out of four trials). The modulation depths for normally hearing subjects were generally in the range of 5 to 15 dB, with a tendency for a greater modulation depth to be required when the modulation frequency was a smaller submultiple of the carrier rate. Three out of the four cochlear implantees required very small modulation depths (usually one current step or about 0.15 dB) to match the pitch to the reference rate. The fourth implantee (CP) required larger modulation depths (up to 4 dB) and showed the same increase of modulation depth with smaller modulation submultiples as the normally hearing subjects. Although this subject had the largest dynamic range, there was no obvious correlation between dynamic range and modulation depth required; this was also true for the four other subjects in the former pitch-comparison study (McKay *et al.*, 1995).

The individual-subject stimulus spaces for acoustic and electric modulated pulse trains are shown in Figs. 4 and 5. In these figures, the carrier rate is coded by symbol type, and the modulation rate is labeled directly above or below the symbol. For subject NC (Fig. 4), the stimulus space is clearly two-dimensional, with the carrier rates ranked in the vertical direction (labeled dimension 2), and for each carrier rate, the modulation rates are ranked in the horizontal direction (dimension 1). For subject NB, a similar pattern is present, with the stimuli not as well ordered in the carrier-rate dimension. The stimulus space of subject NR is clearly similar to the one-dimensional unmodulated-rate stimulus space (Fig. 2), with modulation rate varying around the arc (only the 70-Hz modulation rate is out of order). Note that the position around the arc is not predicted well by the matched pitch of the stimuli (see Table II). For example, the stimulus with a

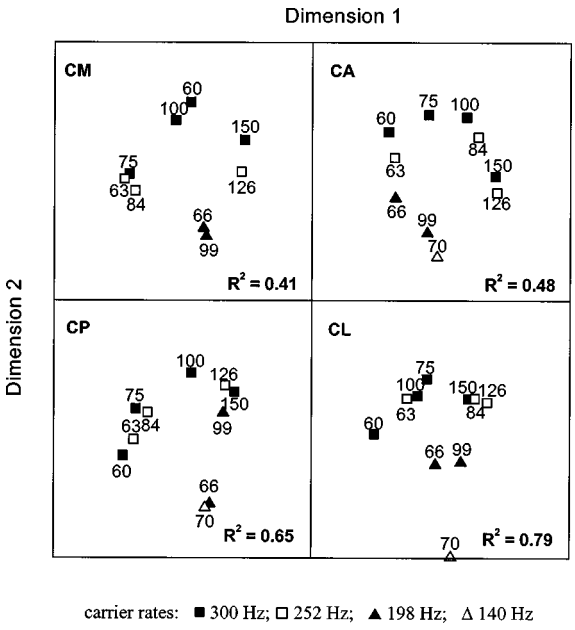

FIG. 5. Stimulus spaces for the four cochlear implantees, resulting from nonmetric repeated-measures multidimensional scaling analysis of perceptual differences among amplitude-modulated electric pulse trains of differing carrier and modulation rates. The carrier and modulation rates are denoted as in Fig. 4.

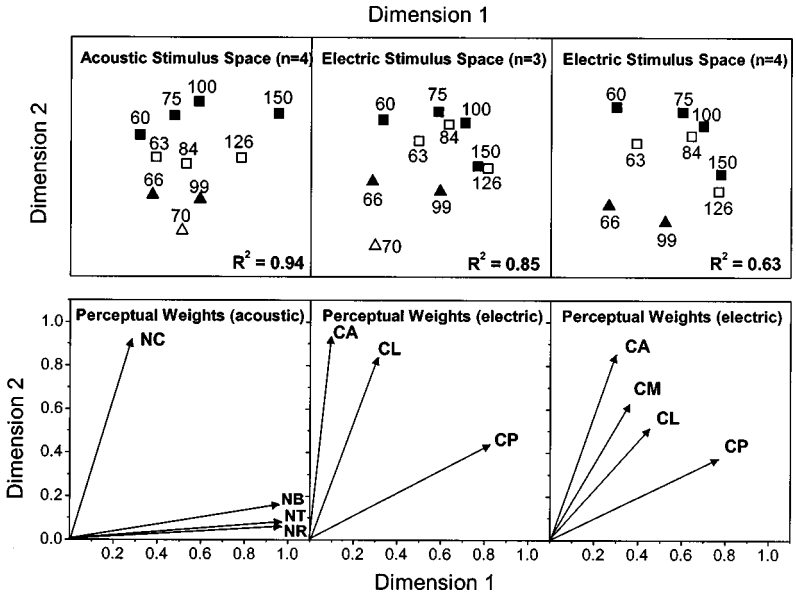

FIG. 6. The three upper panels show the stimulus spaces resulting from individual difference scaling analysis in two dimensions, and which best describe all the data from the normally hearing or cochlear-implantee subject groups. The middle panel represents the data from the three implantees (CA, CP, and CL) who listened to all ten stimuli. The right-hand panel represents the data for all four implantees for nine stimuli (excluding the one with carrier rate equal to 140 Hz (see the text)). The carrier and modulation rates are denoted as in Fig. 4. The lower panels show the individual perceptual weight vectors for the two dimensions.

99-Hz modulation rate would be ranked between the 60- and 75-Hz modulation rates, (being matched with a 140-Hz rate, compared to 134 and 150 Hz for the other two stimuli), and would not be close to the 100-Hz modulation rate stimulus (matched with a 173-Hz rate) as shown in Fig. 4. Subject NT's stimulus space has the stimuli ordered in modulation rate along dimension 1, but the stimuli were ordered irregularly in the second dimension. Analysis of the stress for different dimensions was consistent with two dimensions being most appropriate for stimulus spaces of subjects NC, NB, and NT (the average reduction in stress from one to two dimensions for these three subjects was 0.08, double the reduction from two to three dimensions, 0.04), whereas there was no knee-point in stress reduction for subject NR (with stress reductions of 0.02 and 0.03 between one and two dimensions and two and three dimensions, respectively).

The individual-subject stimulus spaces for the implantees (Fig. 5) account for less of the variance in their dissimilarity data (shown by lower R^2) than the normally hearing stimulus spaces. Analysis of the stress with number of dimensions was consistent, with two being the appropriate number of dimensions in each case. The average reduction in stress across the implantee subject group from one to two dimensions was 0.16, compared to 0.08 from two to three dimensions. In addition, the one-dimensional solutions could not be described by either of the stimulus parameters (carrier rate or modulation rate), or the matched-pitch rate. In all two-dimensional solutions (shown in Fig. 5), the carrier rate tends to increase along dimension 2, and the modulation rate along dimension 1.

The group analysis of the data was performed in two ways for the implant group to allow for the missing stimulus with subject CM, and the possibility that his other data might be corrupted in some way by anomalous percepts. First, the full set of data for the other three subjects was analyzed. Second, the dissimilarity matrices for the nine stimuli used for subject CM were extracted from the dissimilarity matrices of the other three subjects, and these data were analyzed across the four subjects. The normally hearing group stimulus space, as well as the two implantee stimulus spaces are shown in the top half of Fig. 6, along with the individual-subject weight vectors in the panels directly below. It can be seen that the same two-dimensional pattern of stimuli is apparent in each stimulus space. Carrier rate is represented in the vertical dimension, and modulation rate is represented in the horizontal dimension. The relative importance of the two dimensions for each individual subject is represented by the angle of the subject weight vector. A vector close to the horizontal axis (as for subjects NT and NR) means that these subjects mostly used the modulation rate to rank perceptual differences among the ten stimuli, as confirmed by their individual stimulus spaces (Fig. 4). A vector close to the vertical axis means that the subject was mostly using the carrier rate to rank the perceptual differences among the stimuli (for example, CA in the second panel). It is interesting to note that the importance of the carrier-rate dimension was reduced for subjects CA and CL, when the stimulus with a 140-Hz carrier rate was removed from the analysis (third panel). This effect may be due to the full stimulus set only containing one stimulus with that carrier rate. This stimulus might have had a ''uniqueness'' quality attributed to it, which may have increased its dissimilarity to the other stimuli, and hence increased the importance of the carrier-rate dimension.

It is important to note that the two-dimensional stimulus spaces obtained from the individual-differences scaling analysis did not arise from different subjects perceiving solely the modulation rate, or solely the carrier rate. In all cases except NR and NT, the individual stimulus spaces also reflect the dual nature of the perception of the modulated stimuli. Only in the case of NR did a clearly one-dimensional stimulus space result from the analysis. Even in this case, it would be incorrect to infer that modulation rate was the only stimulus parameter change that was perceivable for this subject. For example, the two closest modulation rates (99 and 100 Hz) are placed very near to each other on her individual stimulus space (Fig. 5), even though the two stimuli involved were matched in pitch to unmodulated stimuli with very different rates (140 and 173 Hz). A more plausible explanation

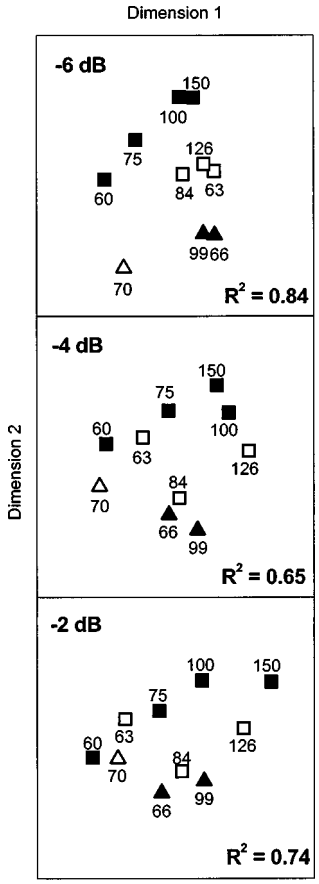

FIG. 7. The stimulus spaces for subject NR resulting from repeated-measures multidimensional analysis of perceptual differences among the modulated acoustic pulse trains, for the three reduced-modulation-depth conditions. The amount of reduction of the modulation depths (compared to the modulation depths in the original stimulus set) is shown in each panel. The carrier and modulation rates are denoted as in Fig. 4.

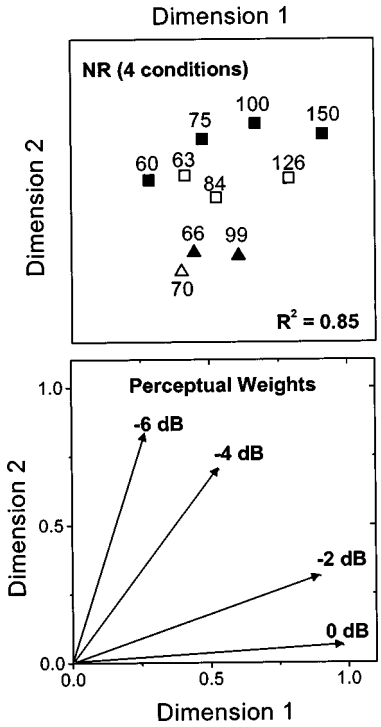

FIG. 8. The stimulus space and perceptual weights for four modulation-depth conditions for subject NR, obtained from individual-difference analysis. The carrier and modulation rates are denoted as in Fig. 4. In the lower panel, the four conditions are denoted as in Fig. 7. (The original modulation depths are denoted 0 dB.)

is that the modulation-rate differences were more salient than the carrier-rate differences for this subject, and that, when doing the multidimensional scaling task, she opted to base her responses solely on the most obvious differences, and to ignore the other differences.

It was hypothesized that the response behavior of subject NR would be altered if the carrier-rate percept was made more salient, and that the latter could be achieved by reducing the modulation depth. To test this hypothesis, three further conditions were tested with NR. The stimuli used in these conditions were the same as those in the original modulated-stimuli set, except that the modulation depths were all reduced by a fixed amount (2, 4, and 6 dB, respectively) relative to the modulation depths used initially (Fig. 3). Four dissimilarity matrices were obtained for each of the three modulation depths. For each of these conditions, repeated-measures analysis resulted in stimulus spaces which were best described in two dimensions (as indicated by a knee-point in the stress function at two dimensions, and the stimulus positions in the two-dimensional space being determined by carrier and modulation rates). These stimulus spaces are shown in Fig. 7. It can be seen that, although the stimulus with a 140-Hz carrier rate (open triangle) is displaced somewhat compared to the patterns in Fig. 6, there is the same tendency for modulation rate to increase along dimension 1 and carrier rate to increase along dimension 2. As modulation depth is reduced, the stimuli become more ordered in carrier rate (dimension 2), and less ordered in modulation rate (dimension 1).

Individual-differences analysis was used to examine the effect of modulation depth over the total of four conditions (including the original modulation depths). The results are shown in Fig. 8. The stimulus space is essentially the same two-dimensional one seen in Fig. 6. The weight vector for the original modulation-depth condition is also similar to that shown in Fig. 6, showing a weighting in favor of the modulation-rate dimension. In all three conditions with reduced modulation depth, the weight vector showed a significant influence of both carrier- and modulation-rate dimensions. There was a systematic shift of the dimension weights with reduction in modulation depth, towards more importance being given to the carrier-rate dimension, consistent with the individual spaces in Fig. 7.

III. DISCUSSION

The results of these experiments have shown that amplitude-modulated pulsatile stimuli, in which the modulation rate is a submultiple of the carrier rate, can evoke a percept with two independent percepts corresponding to the carrier and modulation rates. Since both the electric and the acoustic stimuli were constrained to stimulate nonvarying positions along the cochlea (and in the acoustic case, contained no resolvable harmonics to provide spectral cues), the conclusion can be drawn that the two percepts were derived solely from the temporal pattern of each stimulus.

The multidimensional scaling procedure involves the ranking of any perceptual differences among the stimuli, and therefore it cannot be directly inferred that the two percepts were pitch percepts. However, previous experiments have demonstrated that rates or modulation rates in the ranges used here do evoke pitches that can be assigned to musical intervals (for example, Burns and Viemeister, 1981; Pijl and Schwarz, 1995; McDermott and McKay, 1997), and this is consistent with the subjective reports of the normally hearing subjects in these experiments. The results will therefore be discussed in the context of current models of temporal pitch extraction in the auditory system. However, the significance of the finding of two percepts related to carrier and modulation rates is not dependent on the percepts being labeled specifically as pitch. The main conclusion, that the auditory system can extract and use two temporal patterns from the same cochlear region, would remain.

Licklider (1951) was the first to propose that pitch could be extracted from the neural firing patterns in the auditory nerve by an autocorrelation analysis performed by the central auditory system. There are a number of recent models which have refined this idea (for example, to include spectral analysis via cochlear mechanics) to account for temporal aspects of pitch extraction, frequency resolution, or separation of complex sounds. Srulovicz and Goldstein (1983) proposed a ''central spectrum model'' in which interval histograms of auditory-nerve fibers are passed through filters matched to the characteristic frequencies of the fibers. The central spectrum then determines frequency resolution and discrimination. Meddis and Hewitt (1991) proposed a model in which a running autocorrelation function (ACF) is obtained from all auditory channels (consisting of a histogram of all time intervals between spikes on any of the neurons in that channel) over a time window of 2.5 ms. These ACFs are then averaged to obtain a summary ACF from which inferences about pitch are made by selecting the highest peak. This model was recently modified by Meddis and O'Mard (1997), who proposed that stimuli were compared along the whole length of the summary ACF, and not at the position of the highest peak, in order to make judgments of similarity.

Summary ACFs for the acoustic stimuli used in this experiment were obtained using the Meddis and O'Mard model.[2] Examples of five ACFs for one stimulus (300-Hz pulse rate with 100-Hz modulation) at five different modulation depths are shown in Fig. 9. It can be seen that, in all cases, there are the expected peaks at the reciprocal of the modulation rate (10 ms), and, as modulation depth is decreased, peaks at multiples of the carrier interval (3.3 ms) increase in amplitude. Thus, if the ACF is viewed along its entire range of time intervals, it is possible to predict that, at intermediate modulation depths, pitches at both 300 and 100 Hz can be heard. It should be noted, however, that the modulation depths required by the model for the 10-ms interval to become prominent are larger (16–22 dB) than those actually used in the experiment (about 10 dB). This is not a serious failing, and it is probable that the model could be made to produce better predictions by decreasing the amount of peripheral compression, thereby increasing the effective modulation depth of the stimuli.

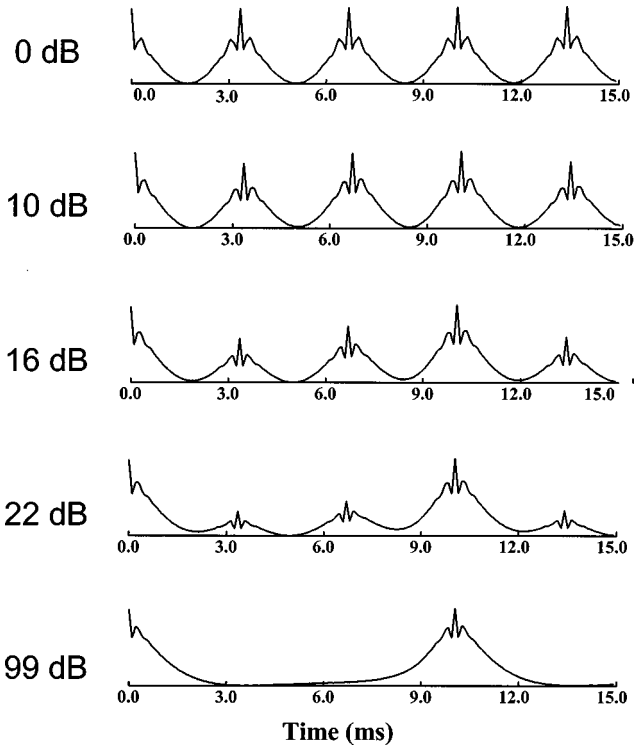

FIG. 9. Five summary autocorrelation functions for the acoustic stimulus with 300-Hz pulse rate and 100-Hz modulation obtained using the model of Meddis and O'Mard (1997). The modulation depth of the stimulus is marked to the left of each function.

It is uncertain, however, whether the actual physiological process which extracts these periodicities in the monaural acoustic-nerve firing patterns can be described accurately as an autocorrelation analysis, or whether some other process contributes. For example, some neural units in the inferior colliculus are activated preferentially by particular ranges of rates or modulation rates (Rees and Palmer, 1989; Langner, 1992). If these neurons are involved in the central encoding of temporal patterns, then our results would predict that two populations of these neurons would be activated by modulated pulse trains (those encoding the modulation and carrier rates). It should also be noted that the autocorrelation model proposed by Meddis and O'Mard fails to account for other important features of pitch perception, such as the different percepts elicited by stimuli containing resolved and unresolved harmonics (Carlyon, 1998).

The acoustic results of subject NR, along with the previous electrical pitch-ranking results obtained by McKay *et al.* (1995), suggest that the relative weighting of the percepts evoked by the carrier and modulation rates in pitch-comparison tasks, or dissimilarity-rating tasks, is systematically altered by the modulation depth. McKay *et al.* (1995) accounted for the pitch-ranking response behavior of implantees by assuming that the rates were weighted according to the number of neurons firing at the carrier or modulation intervals. The results of the experiments reported here suggest that, when comparing the pitch of a modulated pulse train to that of an unmodulated pulse train, subjects could perceive both the modulation and carrier rates in the modulated stimulus; to make a response decision (which sound

had the higher pitch?) the subject used a cognitive weighting of these two pitches, based on their relative salience, rather than using either carrier or modulation rate alone.

It is interesting to question whether the ability of the central auditory system to retain and use the whole temporal pattern of neural interspike intervals would be inconsistent with an inability to resolve two complex tones of close but different $F0$s presented in the same auditory channel (Carlyon, 1997). This type of stimulus would produce a different pattern of neural interspike intervals than that produced by the modulated stimuli used in this experiment. There would be many spurious intervals, not related to either $F0$, and these intervals would be constantly changing from one time frame to the next. These varying, spurious intervals might impair the resolution of a periodicity-detecting central neural processor.

IV. CONCLUSIONS

The modulated pulse trains used in these experiments evoked dual pitch percepts which were related to the carrier and modulation rates. Furthermore, the dual pitch percepts were evoked by stimuli which differed only in temporal features.

The similarity between the electrical and acoustic data suggests that, when filtered appropriately, acoustic pulse trains can be used to produce percepts in normal listeners that share common features with those experienced by deafened subjects listening through one channel of a cochlear implant. These similarities appear to be robust to any differences in neural activation patterns, such as the greater across-fiber synchrony observed with electrical stimulation, and to pathological processes such as poor nerve survival.

ACKNOWLEDGMENTS

This research was funded by the Australian National Health and Medical Research Council project grant ''Speech perception by cochlear implantees: perceptual and related psychophysical studies,'' the Human Communication Research Centre and the Co-operative Research Centre for Cochlear Implant, Speech and Hearing Research. The first author wishes to acknowledge sponsorship by the Australian Academy of Science Scientific Exchange Program with the Royal Society. We thank Hugh McDermott for programming support and Brian Moore, Hugh McDermott, and Peter Blamey for many useful discussions. Ian Nimmo-Smith helped in the interpretation of the stimulus spaces, and pointed us to previous work on the ''horseshoe effect.'' The Cochlear Implant Clinic at Addenbrookes hospital in Cambridge provided testing facilities and access to the cochlear-implant subjects. In particular, Zebunnisa Vanat (cochlear implant scientist) and David Baguley (head of department) provided invaluable assistance. Finally, we wish to thank all the subjects who cheerfully took part in the experiments, and Graeme Clark for his support.

[1]During the first experiment, a technical fault was discovered, which caused the electrical stimulus durations to randomly vary over a range of about 60 ms. This fault did not cause any significant effect in the data, because of its random nature and the long stimulus durations used. The variability was significantly reduced in the second experiment.

[2]Stimuli were generated and hardware filtered in exactly the same way as in the experiments, and captured using a 16-bit ADC (CED 1401 plus). The resulting waveforms (with same overall level as used experimentally) were then input to Meddis and O'Mard's model using their default parameters.

Burns, E. M., and Viemeister, N. F. (**1976**). ''Non-spectral pitch,'' J. Acoust. Soc. Am. **60**, 863–869.

Burns, E. M., and Viemeister, N. F. (**1981**). ''Played-again SAM: Further observations on the pitch of amplitude-modulated noise,'' J. Acoust. Soc. Am. **70**, 1655–1660.

Carlyon, R. P. (**1996**). ''Encoding the fundamental frequency of a complex tone in the presence of a spectrally overlapping masker,'' J. Acoust. Soc. Am. **99**, 517–524.

Carlyon, R. P. (**1997**). ''The effects of two temporal cues on pitch judgments,'' J. Acoust. Soc. Am. **102**, 1097–1105.

Carlyon, R. P. (**1998**). ''Comments on 'A unitary model of pitch perception' [J. Acoust. Soc. Am. 102, 1811–1820 (1997)],'' J. Acoust. Soc. Am. **104**, 1118–1121.

Eddington, D. K., Dobelle, W. H., Brackman, E. E., Brackman, D. E., Mladejovsky, M. G., and Parkin, J. L. (**1978**). ''Auditory prosthesis research with multiple channel intracochlear stimulation in man,'' Ann. Otol. Rhinol. Laryngol. **87**, Suppl. 53,5–39.

Kendall, D. G. (**1971**). ''Seriation from abundance matrices,'' in *Mathematics in the Archeological and Historical Sciences*, edited by F. R. Hodson, D. G. Kendall, and P. Tautu (Edinburgh U.P., Edinburgh), pp. 215–251.

Kruskal, J. B. (**1964**). ''Non-metric multidimensional scaling: a numerical method,'' Psychometrika **29**, 115–129.

Langner, G. (**1992**). ''Periodicity coding in the auditory system,'' Hearing Res. **60**, 128–133.

Licklider, J. C. R. (**1951**). ''A duplex theory of pitch perception,'' Experientia **7**, 128–133.

McDermott, H. J., and McKay, C. M. (**1997**). ''Musical pitch perception with electrical stimulation of the cochlea,'' J. Acoust. Soc. Am. **101**, 1622–1631.

McKay, C. M., McDermott, H. J., and Clark, G. M. (**1994**). ''Pitch percepts associated with amplitude-modulated current pulse trains in cochlear implantees,'' J. Acoust. Soc. Am. **96**, 2664–2673.

McKay, C. M., McDermott, H. J., and Clark, G. M. (**1995**). ''Pitch matching of amplitude modulated current pulse trains by cochlear implantees: the effect of modulation depth,'' J. Acoust. Soc. Am. **97**, 1777–1785.

McKay, C. M., McDermott, H. J., and Clark, G. M. (**1996**). ''The perceptual dimensions of single-electrode and non-simultaneous dual-electrode stimuli in cochlear implantees,'' J. Acoust. Soc. Am. **99**, 1079–1090.

Meddis, R., and Hewitt, M. J. (**1991**). ''Virtual pitch and phase sensitivity of a computer model of the auditory periphery. I: Pitch identification,'' J. Acoust. Soc. Am. **89**, 2866–2882.

Meddis, R., and O'Mard, L. (**1997**). ''A unitary model of pitch perception,'' J. Acoust. Soc. Am. **102**, 1811–1820.

Miller, G. A., and Taylor, W. G. (**1948**). ''The perception of repeated bursts of noise,'' J. Acoust. Soc. Am. **20**, 171–182.

Pijl, S., and Schwarz, D. W. (**1995**). ''Melody recognition and musical interval perception by deaf subjects stimulated with electrical pulse trains through single cochlear implant electrodes,'' J. Acoust. Soc. Am. **98**, 886–895.

Rees, A., and Palmer, A. R. (**1989**). ''Neuronal responses to amplitude modulated and pure-tone stimuli in the guinea pig inferior colliculus and their modification by broadband noise,'' J. Acoust. Soc. Am. **85**, 1978–1994.

Ritsma, R. J. (**1962**). ''Existence region of the tonal residue. I.,'' J. Acoust. Soc. Am. **34**, 1224–1229.

Ritsma, R. J. (**1963**). ''Existence region of the tonal residue. II.,'' J. Acoust. Soc. Am. **35**, 1241–1245.

Schouten, J. F., Ritsma, R. J., and Lopes Cardozo, B. (**1962**). ''Pitch of the residue,'' J. Acoust. Soc. Am. **34**, 1418–1424.

Simmons, F. B. (**1966**). ''Electrical stimulation of the auditory nerve in man,'' Arch. Otolaryngol. **84**, 24–76.

Shackleton, T. M., and Carlyon, R. P. (**1994**). ''The role of resolved and unresolved harmonics in pitch perception and frequency modulation discrimination,'' J. Acoust. Soc. Am. **95**, 3529–3540.

Shannon, R. V. (**1983**). ''Multichannel electrical stimulation of the auditory nerve in man: I. Basic psychophysics,'' Hearing Res. **11**, 157–189.

Small, A. M. (**1955**). ''Some parameters influencing the pitch of amplitude modulated signals,'' J. Acoust. Soc. Am. **27**, 751–760.
Srulovicz, P., and Goldstein, J. L. (**1983**). ''A central spectrum model: a synthesis of auditory-nerve timing and place cues in monoaural communication of frequency spectrum,'' J. Acoust. Soc. Am. **73**, 1266–1276.
Tong, Y. C., Black, R. C., Clark, G. M., Forster, I. C., Millar, J. B., O'Loughlin, B. J., and Patrick, J. F. (**1979**). ''A preliminary report on a multiple-channel cochlear implant operation,'' J. Laryngol. Otol. **93**, 679–695.
Tong, Y. C., and Clark, G. M. (**1985**). ''Absolute identification of electric pulse rates and electrode positions by cochlear implant patients,'' J. Acoust. Soc. Am. **77**, 1881–1888.
Townshend, B., Cotter, N., van Compernolle, D., and White, R. L. (**1987**). ''Pitch perception by cochlear implantees,'' J. Acoust. Soc. Am. **82**, 106–115.
Young, F. W., and Lewyckyj, R. (**1979**). ALSCAL-*4 User's Guide* (Data Analysis and Theory Associates, University of North Carolina, Chapel Hill, NC).

Effect of temporal position, proportional variance, and proportional duration on decision weights in temporal pattern discrimination[a)]

Toktam Sadralodabai[b)] and Robert D. Sorkin
Department of Psychology, University of Florida, Gainesville, Florida 32611

(Received 2 April 1997; revised 6 July 1998; accepted 22 September 1998)

Two experiments investigated how listeners allocate their attention to different segments of a temporal pattern. The experiments allowed a direct test of the predictions of the Proportion of Total Duration (PTD) rule and the Component Relative Entropy (CoRE) model. Listeners had to decide whether two sequences of nine tones had the same or different temporal patterns (tone duration=25 ms, tone frequency=1000 Hz). A sequence's temporal pattern was determined by the time intervals between each tone's offset and the next tone's onset. On *same* trials, the time intervals at corresponding temporal positions in the two sequences were identical. On *different* trials, the corresponding time intervals were randomly varied. Listener attention to different temporal positions within a sequence was assessed by calculating the decision weights at each position. The results supported the CoRE model and were inconsistent with the PTD rule. Manipulating the mean of the time intervals within the sequence had no consistent effect on the pattern of weights (or on overall performance), indicating that listener attention was not affected by either the proportion of total duration or the perceptual salience of a longer or shorter time interval. However, manipulating the variance of the time intervals had a significant effect: the highest weight was given to the highest variance segment. This weighting strategy leads to better performance because higher variance segments are more diagnostic of whether the sequences are the same or different. [S0001-4966(99)02001-9]

PACS numbers: 43.66.Mk, 43.66.Ba [RHD]

INTRODUCTION

Which segments of a temporal pattern will receive the most listener attention? Are the attended segments the best ones for discriminating between two different patterns? Recent experiments have attempted to specify how a listener allocates attention to different spectral components of an auditory pattern (e.g., Green *et al.*, 1983; Berg and Green, 1990; Kidd *et al.*, 1991; Zara *et al.*, 1993). In the present study, we apply similar techniques to determine the distribution of listener attention to the different temporal components of an auditory pattern.

In addition to improving our understanding of the basic auditory-processing mechanisms, specifying how attention is allocated to different portions of a temporal pattern may have practical implications for speech and music perception (e.g., Liberman *et al.*, 1967; Stevens and House, 1972; Klatt, 1976; Steedman, 1977; Vos and Rasch, 1981). For example, Collins *et al.* (1994) found a correlation between the discrimination of random temporal patterns and performance on standard speech-recognition tests. In music, a temporal pattern-recognition scheme appears to be used for the perception of the repetitive pattern of musical notes, both at a basic level and at more complex levels of rhythmicity (Martin and Struges, 1974; Deutsch, 1979; Fraisse, 1982).

The importance of specific factors in the discrimination of temporal patterns has been demonstrated in a series of studies conducted by Watson and colleagues (e.g., Watson *et al.*, 1975; Kidd and Watson, 1992). Watson *et al.* (1975) found that the ordinal position of the information was very important. A listener's performance was better when the change in the pattern occurred towards the end of the sequence (*recency* effect). Kidd and Watson (1992) and Kidd (1995) reported that the relative target duration was also important. Performance improved with an increase in the ratio of the target's duration to the total pattern's duration. They proposed the ''Proportion of the Total-pattern Duration (PTD)'' rule to describe this result. The rule states that each individual component of an unfamiliar tone sequence is resolved with an accuracy that is based on its proportion of the total duration of the sequence. The listener is assumed to evenly allocate attention over the pattern's duration; therefore, longer duration segments capture proportionally more attention (Kidd, 1995; Kidd and Watson, 1992). The PTD rule does not address the possible effect of variability in a segment's properties.

Lutfi (1993, 1995a, 1995b; Lutfi and Doherty, 1994) has suggested that Kidd and Watson's results can be accounted for by the Component Relative Entropy (CoRE) model. This model builds on Shannon's (1948) definition of entropy or variance, to determine the amount of information contained in a pattern. Unlike the PTD rule, the CoRE model (with assumptions about the nature of internal noise) allows explicit predictions to be made about performance. The CoRE

[a)]Portions of this research were presented at the 129th meeting of the Acoustical Society of America, Washington, DC, May 1995 [J. Acoust. Soc. Am. **97**, 3278(A) (1995)].

[b)]Current address: Boys Town National Research Hospital, 555 North 30th Street, Omaha, NE 68131; Electronic mail: sadra@boystown.org Reprint requests should be sent to the second author.

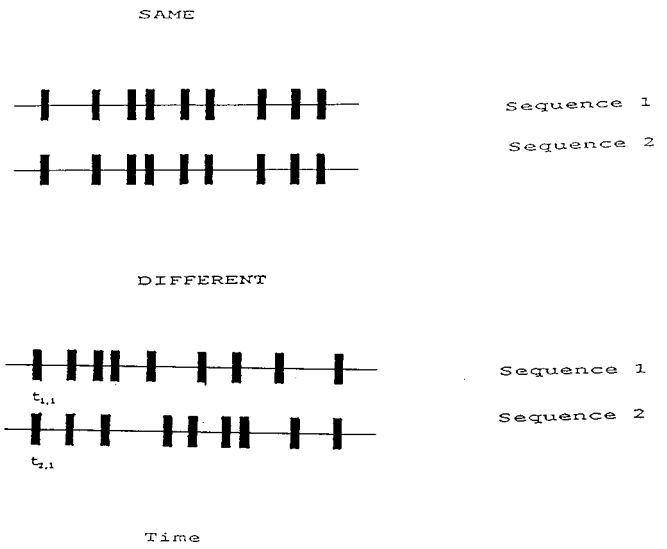

FIG. 1. The upper schematic illustrates a sample SAME trial for the two 9-tone sequences; the bottom schematic illustrates a sample DIFFERENT trial. Each tone in the sequence was 1000 Hz and 25 ms in duration. The pattern of a sequence was determined by the intertone–time intervals.

model has two basic premises. First, listeners try to adopt an ideal maximum-likelihood decision rule for the task. Second, listeners cannot ignore information that varies from trial to trial. Listeners are assumed to integrate information over a rectangular time–frequency window whose bandwidth and duration is equal to or exceeds the bandwidth and duration of the possible signals. One would, therefore, expect the relative variance of each time segment to have a significant effect on pattern-discrimination performance. In the present experiment, we manipulate both the duration and variance of elements within sequential patterns to examine PTD and CoRE predictions.

The present paradigm is an extension of one we have used previously (Sorkin, 1990; Sorkin and Montgomery, 1991; Sorkin *et al.*, 1994). The listener's task is to report whether two sequences of tones had the same or different temporal patterns. A sequence's temporal pattern is determined by the time intervals between the tones within each sequence. On *same* trials, the intertone–time intervals at corresponding temporal positions in the two sequences are identical (see Fig. 1). On *different* trials, the intertone–time intervals are randomized such that the intertone–time intervals are partially correlated or uncorrelated between the sequences. These studies showed that performance depends on the correlation between the sequences on *different* trials and also on the (uniform) mean and variance of the intertone–time intervals. These results are described by the Temporal Pattern Correlation model, which assumes that the listener attempts to estimate the correlation between the sequences on each trial, but is limited by a small internal jitter in time estimation of 10 to 20 ms (Sorkin, 1990; Sorkin and Montgomery, 1991).

A characteristic of the present experimental paradigm is that information about the difference between the pair of sequences being compared is distributed throughout the entire duration of the stimuli. A potential weakness of this approach is that it will not reveal whether some segments of the sequence have a much greater effect on performance than others. This problem would be eliminated if one could determine the relative contribution made by individual segments of the sequence to the listener's discrimination performance. Such a technique is provided by Berg's (1989) weight-estimation technique (Conditional-on-Single-Stimulus or COSS) and by Richards and Zhu's (1994) and Lutfi's (1995a) extension of this technique. These techniques examine the strength of the relationship, over trials, between the listener's response and the value of each stimulus component. One may infer from the resulting decision weights how much attention is given to different portions of the stimulus.

The main goal of the present study was to determine how attention is allocated to the different segments of each sequence in a temporal pattern-discrimination task. In experiment 1, the statistical properties of the intertone–time intervals were uniform within each sequence. That is, all intertone–time intervals had the same mean and standard deviation for duration. We anticipated that the greatest listener weights would be given to the final time intervals in the sequence, thereby replicating Watson *et al.*'s (1975) finding of best performance for a target that occupies the last temporal position.

In experiment 2, we used patterns with both uniform and nonuniform durations. In the nonuniform case, one segment of the patterns was made unique (and presumably more distinctive perceptually) by manipulating either the mean or the variance of its intertone–time interval. It is not clear, however, whether discrimination performance for nonuniform sequences would be better or worse than for uniform sequences. We can think of two possible consequences of this manipulation: Making one segment different from the others might make the entire pattern appear less random and more distinctive. Reducing the apparent randomness of a pattern might make it easier to store and recall information about that pattern, resulting in an improvement in discriminability. Alternately, the unique segment might capture more attention than the other segments. The resultant effect on performance could be positive or negative, depending on whether the unique segment was more or less informative about the correct discrimination response than the other segments.

The CoRE model and PTD hypothesis address these possibilities. Our interpretation of the PTD hypothesis is that the listener's attention will be spread evenly over the duration of the pattern to be discriminated, with the caveat that somewhat greater weighting may be given to the final portion of the pattern. It follows that increasing the mean duration of one segment will produce an effective increase in the listener's attention to that segment. If important, task-relevant information were contained in that segment, the result would be an increase in discrimination performance. The PTD hypothesis does not address the possible effect of manipulating the variance of an intertone–time interval.

The CoRE model, on the other hand, is primarily concerned with the informational aspects of the patterns to be discriminated. In the next section, we discuss a mechanism for temporal pattern discrimination that uses all of the information available in the two patterns to be discriminated. The mechanism's decision statistic considers the difference be-

tween the durations of the paired time segments in each pattern. We show that, although the variance of a segment can produce a large change in the decision statistic, the mean of a segment has no effect. The CoRE model makes the same prediction about the effect of segment variance, but it makes no additional assumptions about the effect of manipulating the mean duration of a pattern segment on the listener's decision weights. This is because the relative duration of these intervals is already given by the decision variable and cannot be used as its own weight.[1] Experiment 2 allows us to examine how well the CoRE model and the PTD rule account for the results of pattern discrimination based on changes in intertone–times.

A. Temporal pattern-discrimination mechanism

The sequence discrimination task requires the listener to compare the intertone–time intervals for two sequences and then make a judgment about whether they were the same or different. The set of intertone–time intervals for the first and second sequences are, respectively, $\{t_{1i}\}$ and $\{t_{2i}\}$; where the numbered index identifies the first and second sequence, and i identifies the intertone–time position (e.g., $i=1$ to M for a pattern of $M+1$ tones). We assume that the listener's decision variable is based on the sum of the weighted (absolute value of the) differences between the pair of intertone–time intervals in each sequence. That is, the decision variable is equal to $\Sigma a_i g_i$, where a_i is the decision weight for the ith temporal position and g_i is a random variable equal to $|t_{1i} - t_{2i}|$. The t_{1i} and t_{2i} are independent, normal random variables with equal means and variances equal to σ_t^2. The variance, σ_t^2, of t_{ij} is given by:

$$\sigma_t^2 = \sigma_{\text{internal}}^2 + \sigma_{\text{exp}}^2, \tag{1}$$

where $\sigma_{\text{internal}}^2$ is the variance due to the observer's jitter in estimating the time, and σ_{exp}^2 is the variance in the intertone–time interval that is set by the experimenter.

The listener's ability, d', to discriminate between the sequences depends on the mean and variance of the decision variable, $\Sigma a_i g_i$. Since the M time positions are independent, performance based on the decision variable can be computed from the discriminability, d_i', of each intertone–time segment difference, g_i. The segment discriminability depends on the mean and variance of g_i, given either the *same* or *different* sequences. The mean of g_i is an increasing function of the variance of the underlying time intervals, i.e., mean $(g_i) = f(\sigma_t^2)$. On *same* trials, the mean of g_i depends only on $\sigma_{\text{internal}}^2$, which is assumed to be constant.[2] On *different* trials, the mean of g_i increases with the value of σ_{exp}^2, the experimental variance.

Because the mean of g_i cannot be written in nonintegral form, we calculated an approximation for the mean and variance of g_i as a function of σ_t^2, based on a Monte Carlo simulation and on an assumed value for $\sigma_{\text{internal}}^2$. These statistics were then used to generate Receiver Operating Characteristics, from which equivalent values of d_i' were determined.[3] Note that an increase in σ_{exp}^2 is analogous to an increase in signal strength, because as the intertone–time intervals are made more variable they become more diagnostic of whether the intervals were drawn from the same or different patterns. According to the model, the mean segment duration has no effect on discrimination.

I. EXPERIMENT 1: EFFECT OF TEMPORAL POSITION ON LISTENER WEIGHTS

The goal of this experiment was to determine the effect of temporal position on listener attention when the statistics (mean and variance) of the intertone–time intervals were constant across the different ordinal positions of the sequence. A correlational weight-estimation technique (Richards and Zhu, 1994; Lutfi, 1995a) was used to determine the relative weight given to each position. That is, for each intertone–time interval, we calculated the correlation (over *different* trials) between the listener's response and the absolute difference between the corresponding intertone–time intervals in the two sequences, $|t_{1i} - t_{2i}|$. An assumption of this analysis is that the decision weight at each position is proportional to this normalized correlation. All weights were normalized to sum to unity ($\Sigma a_i = 1$).

A. Method

1. Listeners

One female and three male student volunteers, with normal hearing (as determined from self-report), participated in this experiment. One listener had prior experience with the task. All listeners were paid an hourly wage plus a bonus based on performance. Listeners were seated in a double-walled acoustically insulated chamber. The stimuli were presented monaurally via TDH-39 headphones.

2. Stimuli and procedure

On a given trial, listeners were presented with two sequences of tones, each composed of nine 1000-Hz tones presented at 71-dB sound-pressure level. The 25-ms tone bursts were generated by a T. T. Electronics system (precursor to Tucker Davis Technologies system I), at 20 000 16-bit samples per s. The tones were low-pass filtered at 7.5 kHz and gated with a TTE cosine switch. These tones were shaped by a 4-ms linear rise and decay envelope. All times are defined from the 0-voltage points on the envelope. Using procedures similar to those used in Sorkin (1990), the intertone–time intervals had a mean duration of 50 ms and a standard deviation of 35 ms. The minimum intertone–time interval was equal to either 2 ms or the mean intertone–time interval minus 2.5 times the s.d., whichever was larger. The maximum intertone–time interval was equal to either 300 ms or the mean intertone–time interval plus 2.5 times the s.d. of the intertone–time, whichever was smaller. Whenever an intertone–time interval smaller or larger than the allowed values was drawn, it was changed to the stated minimum and maximum.[4] An interval of 750 ms separated the two tone sequences. On each trial, the listeners indicated whether the temporal patterns of the sequences were the same or different. Correct-answer feedback was provided after each trial. The type of trial (*same* or *different*) was selected on a random basis (see Fig. 1). On *same* trials, the temporal patterns were perfectly correlated (sequence pattern correlation = 1.0).

TABLE I. Summary of the experimental conditions and average performance (d') for the listeners in the experiments.

	Unique position			Other positions		d'
Experiment	pos.	mean	σ_{exp}	mean	σ_{exp}	mean (standard error)
1		none		50	35	3.1 (0.22)
2		none		60	20	2.3 (0.23)
2(a)	2	20	20	60	20	2.8 (0.27)
	2	40	20	60	20	2.8 (0.29)
	2	80	20	60	20	2.7 (0.28)
	2	100	20	60	20	2.8 (0.40)
	6	20	20	60	20	2.8 (0.31)
	6	40	20	60	20	2.6 (0.37)
	6	80	20	60	20	2.6 (0.29)
	6	100	20	60	20	2.7 (0.17)
2(b)	2	60	40	60	20	2.7 (0.24)
	2	60	60	60	20	3.0 (0.23)
	2	100	100	100	20	2.5 (0.29)
	6	60	40	60	20	3.1 (0.29)
	6	60	60	60	20	3.5 (0.26)
	6	100	100	100	20	3.3 (0.28)

On *different* trials, the patterns were uncorrelated (sequence pattern correlation $=0$). Stimulus presentation and data collection were computer controlled.

Listeners participated in two or three 2-h sessions per week. Each session consisted of ten blocks of 100 trials.[5] Listeners completed 700–1000 trials of practice before data collection began. There was no notable effect of practice on performance. Each listener completed 20 blocks of 100 trials.

B. Results and discussion

The average d' of the four listeners for a mean intertone–time of 50 ms and an s.d. of 35 ms was 3.1 (first row of Table I). For this condition, and assuming an internal jitter of 9 ms, the model prediction was 4.1. The average relative weights across listeners are shown in Fig. 2 as a function of the temporal position of each intertone–time interval. The error bars indicate plus and minus one standard error of the mean. It is clear that the obtained weights were highest in the first and last temporal positions. The data for individuals resembled the average, except that for two listeners the highest weight was obtained in the first position, and for two listeners essentially equal weight was obtained for the first and last positions. An ANOVA (repeated-measures design with four listeners and eight temporal positions) confirmed a significant effect of temporal position [$F(3,7) = 5.27$, $p < 0.05$].

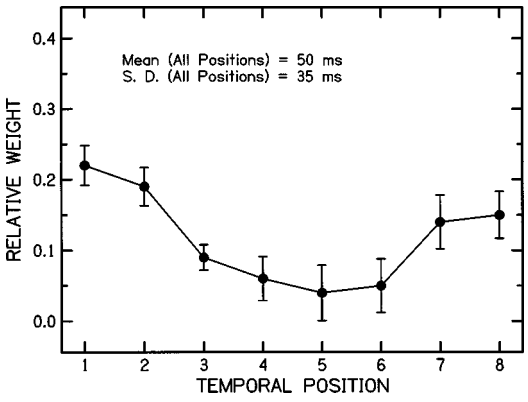

FIG. 2. The relative weights obtained in experiment 1, averaged over four listeners, are plotted as a function of temporal position. Error bars represent one standard error of the mean. See the text for the procedure for calculating weights.

II. EXPERIMENT 2: EFFECT OF SEGMENT MEAN AND VARIANCE ON LISTENERS' WEIGHTS

The results of experiment 1 suggested that listeners do not distribute their attention uniformly among intertone–time intervals of equal duration, but rather, allocate more weight to the early and late positions. However, the statistics of the intertone–time intervals were uniform across the sequence. Experiment 2 investigated whether a change in the properties of *one* of the intertone–time intervals would result in a change in the relative weights. The statistics of one of the intertone–time intervals was manipulated in two ways: In experiment 2(a), the average duration of one of the intervals was set to be either longer or shorter than all of the others (the others all had the same mean and s.d.). Recall that the PTD rule predicts that increasing the mean duration of a component will produce greater listener attention to that segment. The CoRE model predicts no effect for the manipulation of mean duration in this situation. In experiment 2(b), the s.d. of one of the intervals was set to be larger than the others. The CoRE model predicts that increasing the relative variance of the segment will increase the weight that the listener places on that segment. This prediction follows from the assumption that the decision variable is based on the weighted sum of the detectability of each segment, and the detectability of a segment increases with the segment's variance. The PTD rule makes no prediction about the effect of segment variances.

A. Method

1. Listeners

Four student volunteers, two males and two females with normal hearing, participated in both parts of experiment 2. Two listeners had participated in the first study and had prior experience with the task. All listeners were paid an hourly wage plus a bonus based on performance.

2. Stimuli and procedure

The procedure, tones comprising the sequences, and task were the same as in experiment 1. Across conditions, the duration and variance of intertone–time interval were varied. Table I summarizes the parameters of the different conditions run in experiment 2. In the control condition, the mean and s.d. of the intertone–time intervals were uniform across all temporal positions, as in experiment 1. The mean duration was 60 ms and the s.d. was 20 ms. The choice of these particular values was arbitrary, but allowed a simple and systematic manipulation of the relative duration of the means and standard deviations of the intertone–time intervals. In experiment 2(a), one of the intertone–time intervals had either a higher or lower mean duration than the other positions. This unique intertone–time interval occurred either at the 2nd or the 6th position in the sequence. The different values of mean intertone–time tested ranged from 20 to 100 ms, in steps of 20 ms. This mean value was fixed during a block of trials, as was the position of the unique intertone–time (2nd or 6th). The mean and s.d. for all other positions within the sequences were fixed at 60 and 20 ms, respectively (see Table I). For experiment 2(b), one of the intertone–time intervals had a higher standard deviation, which occurred at the 2nd or the 6th position in the sequence. The mean and s.d. for all other positions were set to 60 and 20 ms, respectively, except when the standard deviation value was 100 ms. In this case, the mean for all the positions was set to 100 ms. The different s.d. values tested were 40, 60, and 100 ms (see footnote 4). Listeners completed several h of practice before the data collection began and no subsequent practice effects were observed. All listeners completed 20 blocks of 100 trials for each condition in each experiment.

B. Results and discussion

The average d's for the four listeners is provided in Table I. The uniform (control) condition yielded a d' of 2.3. Figure 3 depicts the average relative weights from the four listeners in this condition. As in experiment 1 (see Fig. 2), the first and last positions were given the highest weight by these listeners, while the lowest weights are given to the intermediate positions. The large error bar for the final position is due to the relatively large weight given by one listener to this position.

Average performance in experiment 2(a), when the 2nd or the 6th position had a different mean value, are also shown in Table I. Performance was relatively constant over these eight conditions, with d' ranging between 2.6 and 2.8. The overall average d' of 2.7 for these conditions is somewhat higher than the 2.3 value obtained in the uniform condition. Assuming an internal jitter of 9 ms, our pattern-discrimination model predicted a d' of 2.7 for both the uniform condition and for the unique position conditions.

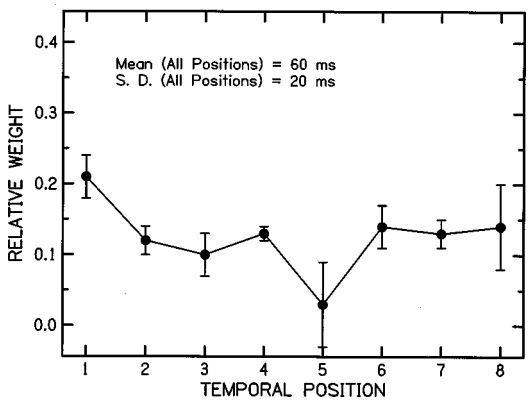

FIG. 3. The relative weights obtained in the uniform condition of experiment 2, plotted as in Fig. 2.

The relative weights averaged across the four listeners for this case are plotted in Fig. 4. Each panel presents data for one of the four mean intertone–time intervals of the unique segment. Filled and unfilled circles are for the 2nd and 6th temporal position, respectively. For these conditions, the standard deviations were all equal and fixed. The different mean durations of 20, 40, 80, and 100 ms correspond to 3, 5, 11, and 16 percent of the total pattern duration, while 60 ms for all the other intertone intervals corresponds to 8.5 percent. An ANOVA (repeated-measures design with four listeners and five mean values) showed no significant effect of mean intertone–time interval for either the 2nd position [$F(3,4)=2.2$, $p<0.05$] or the 6th position [$F(3,4)=1.0$, $p<0.05$]. However, the individual data in some cases showed a small tendency for a larger than usual weight given to the

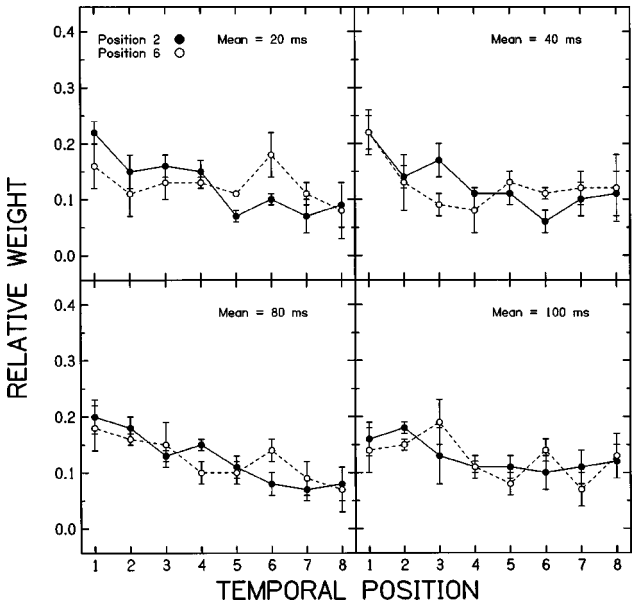

FIG. 4. The relative weights obtained in experiment 2, averaged over all listeners, are plotted as a function of temporal position for the case when the longer or shorter duration segment was in position 2 (filled circles) or position 6 (unfilled circles). Results for mean durations for the unique position of 20, 40, 80, and 100 ms are plotted across panels. The error bars represent one standard error of the mean.

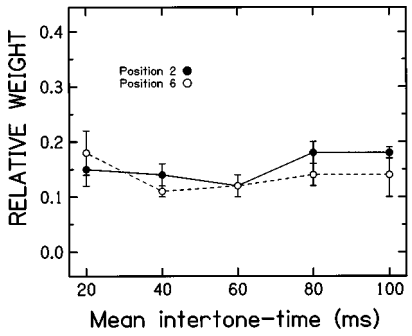

FIG. 5. The average relative weights for the 2nd (filled circles) and 6th (unfilled circles) positions are plotted as a function of the mean duration of the unique segment. The error bars represent one standard error of the mean.

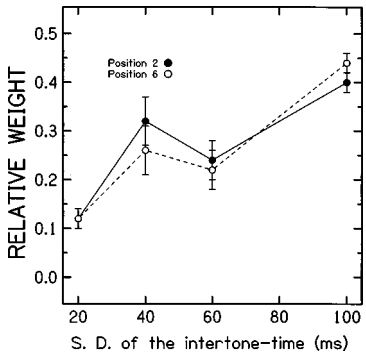

FIG. 7. The average relative weights for the 2nd (filled circles) and 6th (unfilled circles) position are plotted as a function of the s.d. of the unique segment. The error bars represent one standard error of the mean.

position with a different mean. To compare the effect of changing the mean duration of the unique segment, the average weights for the 2nd and 6th positions (see Fig. 4) were plotted as a function of the mean duration of that intertone–time interval in Fig. 5. The weights appear to be independent of the duration of the unique segment and, therefore, independent of the segment's proportion of the total pattern duration.

Table I shows that the average d' in experiment 2(b) (when the 2nd or 6th time had a higher s.d.) was somewhat higher than obtained in experiment 2(a) (when the 2nd or 6th time had a different mean value). When the higher variance intertone–time interval was assigned to position 2, the obtained d' values were essentially the same as those obtained in experiment 2(a) (2.5 to 3.0). However, when the different standard deviation was assigned to position 6, performance improved, with d's ranging between 3.1 and 3.5. Our model predicts d' values of 3.0, 3.2, and 3.4 for the σ_{exp} values of 40, 60, and 100 ms, respectively. The model makes no distinction between positions of the unique segment within the sequence.

The effect of changing the relative variance of the unique segment on weights is shown in Figs. 6 and 7. Figure 6 shows the average weight as a function of temporal position, with the three values of the variance of the unique segment plotted across panels. Filled and unfilled circles again represent data for the unique segment at the 2nd and 6th position, respectively. There are clear peaks in the weighting functions for the unique positions. Regardless of which position was assigned the higher s.d., either the 2nd or 6th, all listeners' weights were consistently highest for the unique position, and the magnitude of the other weights was essentially equal. Figure 7 shows the average weights for the 2nd and 6th positions (see Fig. 6) as a function of the s.d. of the unique position. In general, the higher the value of the standard deviation of the unique position, the larger the weight obtained for that position. The weights increase in direct proportion to the standard deviation, which would be predicted by a maximum-likelihood decision maker. An ANOVA (repeated-measures design with four listeners and four values for s.d.) showed a significant effect of standard deviation at position $2[F(3,3)=15.7, p<0.05]$ and $6[F(3,3)=16.8, p<0.01]$.

III. GENERAL DISCUSSION

Our model of sequence discrimination produced estimates of d' that were consistent with the performance obtained in both the uniform and unique sequence conditions. These estimates were based on an assumed value of 9 ms for the internal jitter. Smaller values for the magnitude of the assumed jitter predicted performance that was better than was obtained, and larger values predicted performance that was poorer than was obtained. In similar sequence experiments using uniform segments, Sorkin (1990) had estimated the magnitude of the internal jitter to be 15 ms. Sorkin's estimate was based on a condition in which there were 11 time intervals having a uniform mean interval of 50 ms. In other conditions, Sorkin reported that performance was affected by the number of intervals and the mean time interval. Thus, it is reasonable to conclude that the small discrepancy between the two estimates of internal jitter are attributable to differences between the specific conditions in Sorkin (1990) and the current experiment.

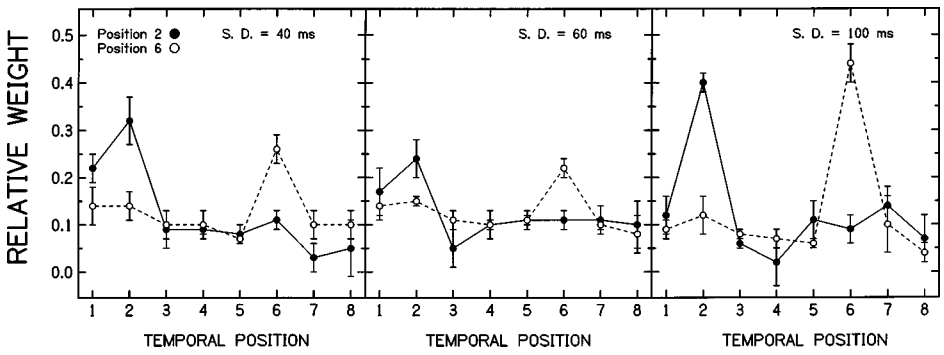

FIG. 6. Relative weights obtained in experiment 2, averaged over all listeners, are plotted as a function of temporal position for the case when the segment with the higher s.d. was in position 2 (filled circles) or position 6 (unfilled circles). Results for a standard deviation of the unique position of 40, 60, and 100 ms are plotted across panels. The error bars represent one standard error of the mean.

The present experiments suggest that listeners may allocate more attention to certain temporal positions of a stimulus pattern than to others. If the properties of segments within a sequence are uniform, most listener weight is typically assigned to the first and last segments, with less attention to the middle segments. One cannot therefore assume that a listener will allocate uniform attention over the duration of the stimulus. However, specific segments may be given substantially more weight when appropriate for a specific task.

These results can be compared with Watson *et al.* (1975), which found that best performance was obtained when a signal occurred in the last position within a temporal pattern. There are several important differences between this experiment and Watson *et al.* (1975) that may account for the apparently divergent results. In the Watson *et al.* experiments, the sequences consisted of ten tones of 40-ms duration that ranged from 256–1500 Hz. The listener's task was to detect changes in the frequency of only one tonal component in the pattern, using a same–different task. The frequency of these tones varied randomly within a sequence. In some conditions, the observer knew which component was the relevant one, and in other conditions the observer was uncertain about which was the signal component. In either type of condition, Watson *et al.* found that the best frequency resolution was obtained when the signal component was the last one. Of particular interest to our study, Watson and colleagues also investigated conditions in which a silent interval was inserted after an early-occurring component of the sequence. Provided the gap was greater than about 70 ms, detection of the change in frequency of the component that occurred just before the gap was as good as when that component was the final component. Apparently, a gap allowed the listener to retain information about a component that would otherwise have been disturbed by the subsequent components. Therefore, the presence of silent intervals, which in our task were the determining factor for temporal pattern discrimination, may provide the explanation for the disagreement between the two sets of results.

Experiment 2(a) showed that making one of the temporal positions noticeably longer or shorter in duration than the others did not cause the observers to assign more weight to that position. The first temporal position still received the largest weight. However, there was a small gain in overall performance when one of the positions was assigned a different mean value. Apparently, making one of the temporal positions in the pattern different from the others can make the entire pattern more discriminable from other patterns, but is not sufficient to change the amount of listener attention given to different portions of the pattern. Changing a segment's duration in our task did not cause it to carry more information than other segments, because a change in mean duration of a component does not affect the distribution of the differences (or absolute value of the differences) between the paired time intervals in the two sequences. Rather, allotting more attention to the unique segment could cause an observer to neglect relevant information from the other segments. For our patterns in which the properties of gaps or unfilled intervals were manipulated, the PTD hypothesis (Kidd and Watson, 1992) does not appear to describe the data.

Experiment 2(b) showed that when one of the temporal positions had a more variable intertone–time interval than the others, listeners allocated substantially more weight to that position. Contrary to the previous manipulation of mean duration, the variance manipulation does increase the information available to the listener from the unique component. That is, increasing the variance of the intertone–time interval provides the listener with additional diagnostic information about the pattern task because it increases that segment's signal-to-noise ratio. We observed a pronounced peak in the weighting function for the unique position, whether it was in the second or sixth position, a result fully consistent with the basic assumption of the CoRE model.

IV. SUMMARY AND CONCLUSIONS

The following conclusions can be drawn from our results:

(1) When all the temporal segments of a stimulus pattern have the same statistical properties, listeners allocate more attention to the first and last segments. These segments normally play the dominant role in the listener's judgment of the difference between patterns.
(2) Giving the 2nd or 6th temporal segments a noticeably longer or shorter duration than the others does not affect either the listeners' overall performance level or the pattern of decision weights given to each position. These results indicate that the PTD hypothesis, which assumes a proportional relationship between a segment's duration and its discrimination, does not provide a general description of temporal pattern-discrimination tasks. In addition, the weight analysis suggests that a listener's attention to different segment is not influenced by a segment's relative duration.
(3) Giving one of the temporal segments a higher variance than the others results in a pronounced peak in the weight assigned to that position. In this task, higher variance segments are more diagnostic of whether the patterns are the same or different, and it appears that listeners can use that information in their discrimination. These results are consistent with the CoRE model, which assumes that the relative variance of each segment has a significant effect on pattern-discrimination performance.

ACKNOWLEDGMENTS

This research was supported by grants from AFOSR. Portions of this research were reported in the doctoral dissertation of the first author submitted to the University of Florida. We would like to thank Dr. Kourosh Saberi for his assistance and very helpful comments on the earlier stages of this research. Our thanks are also extended to Dr. Donna Neff for the review of this work. A special thanks goes to the reviewers and the editor for helpful comments and suggestions.

[1]In other types of discrimination, such as when signal intensity is part of the decision statistic, the effect of the model's time window is to vary the

decision weight according to segment duration. In such cases, the model does predict an effect of proportional duration.

[2]Note that in the CoRE model, the internal error is assumed to be proportional to the experimental error.

[3]Receiver Operating Characteristic (ROC) curves were generated in the following manner: On *same* trials, the decision variable, g_i, was defined as the absolute value of the difference between two Gaussian random variables having zero means and a s.d. equal to the internal jitter, σ_{internal}. On *different* trials, the decision variable was defined as the absolute value of the difference between two Gaussian variables having zero mean and a s.d. equal to $(\sigma^2_{\text{internal}}+\sigma^2_{\text{exp}})^{1/2}$, where σ^2_{exp} is the variance introduced by the experimenter. A value for σ_{internal} was assumed and then, for each value of σ_{exp}, the area under the ROC was calculated and converted to an equivalent d_i' value. Different values for σ_{internal} were tried; a value of 9 ms produced overall d' values that were close to those obtained by the subject in our uniform segment conditions. An approximation for d_i' in terms of the perturbation σ_{exp} and an assumed value for σ_{internal} of 9 ms is given by

$$d_i'=0.233+0.0203\sigma_{\text{exp}}-0.000\,97\sigma^2_{\text{exp}}.$$

If the sequences consisted of eight segments with uniform statistics, and the listener assigned equal weights to each segment, it follows that d' would be $d_i'\sqrt{8}$. If the sequence had one unique segment, d' would be $[(d_i'\sqrt{7})^2+(d'_{\text{unique}})^2]^{1/2}$. A necessary assumption in the latter case is that a proportionately higher weight would be applied to the time difference obtained from the unique segment. A MATLAB program for evaluating the model is available from the authors.

[4]Instances when the intertone–time interval exceeded the maximum-allowed interval occurred less than 1% of the time. For intervals above the 2-ms minimum, the distribution appeared ''normal.'' However, for values at or less than 2 ms, there was a second peak in the distribution. That is, there were more tone bursts that were very close together than would have been expected based on a normal distribution of intertone–time intervals. In conditions where this occurred, the actual mean durations were longer and standard deviations smaller than the assigned values. We do not believe this had a significant effect on the results.

[5]Performance (d') was calculated based on a block of 100 trials. Hit rates of 100/100 and false alarm rates of 0/100 were arbitrarily converted to rates of 99/100 and 1/100, respectively, prior to d' calculation. Block d's were averaged to determine a listener's average performance in that condition.

Berg, B. G. (**1989**). ''Analysis of weights in multiple observation tasks,'' J. Acoust. Soc. Am. **86**, 1743–1746.

Berg, B. G., and Green, D. M. (**1990**). ''Spectral weights in profile listening,'' J. Acoust. Soc. Am. **88**, 758–766.

Collins, L. M., Wakefield, G. H., and Feinman, G. R. (**1994**). ''Temporal pattern discrimination and speech recognition under electrical stimulation,'' J. Acoust. Soc. Am. **96**, 2731–2737.

Deutsch, D. (**1979**). ''Binaural integration of melodic patterns,'' Percept. Psychophys. **25**, 399–405.

Fraisse, P. (**1982**). ''Rhythm and Tempo,'' in *The Psychology of Music*, edited by D. Deutsch (Academic, New York).

Green, D. M., Kidd, G., and Picardi, M. C. (**1983**). ''Successive versus simultaneous comparison in auditory intensity discrimination,'' J. Acoust. Soc. Am. **73**, 639–643.

Kidd, G., Mason, C. R., Uchanski, R. M., Brantley, M. A., and Shah, P. (**1991**). ''Evaluation of simple models of auditory profile analysis using random reference spectra,'' J. Acoust. Soc. Am. **90**, 1340–1354.

Kidd, G. R. (**1995**). ''Proportional duration and proportional variance as factors in auditory pattern discrimination,'' J. Acoust. Soc. Am. **97**, 1335–1338.

Kidd, G. R., and Watson, C. S. (**1992**). ''The 'proportion-of-the-total-duration-rule' for the discrimination of auditory patterns,'' J. Acoust. Soc. Am. **92**, 3109–3118.

Klatt, D. H. (**1976**). ''Linguistic uses of segmental duration in English: Acoustic and perceptual evidence,'' J. Acoust. Soc. Am. **59**, 1208–1221.

Liberman, A. M., Cooper, F. S., Shankweiler, D. P., and Studdert-Kennedy, M. (**1967**). ''Perception of speech code,'' Psychol. Rev. **74**, 431–461.

Lutfi, R. A. (**1993**). ''A model of auditory pattern analysis on component relative-entropy,'' J. Acoust. Soc. Am. **94**, 748–758.

Lutfi, R. A. (**1995a**). ''Correlation coefficients and correlation ratios as estimates of observer weights in multiple-observation tasks,'' J. Acoust. Soc. Am. **97**, 1333–1334.

Lutfi, R. A. (**1995b**). ''Further comments on proportional duration and proportional variance as factors in auditory pattern discrimination,'' J. Acoust. Soc. Am. **97**, 1339–1340.

Lutfi, R. A., and Doherty, K. A. (**1994**). ''Effect of component-relative-entropy on the discrimination of simultaneous tone complexes,'' J. Acoust. Soc. Am. **96**, 3443–3450.

Martin, J. G., and Struges, P. T. (**1974**). ''Rhythmic structures in auditory temporal pattern perception and immediate memory,'' J. Exp. Psychol. **102**, 377–383.

Richards, V. M., and Zhu, S. (**1994**). ''Relative estimates of combination weights, decision criteria, and internal noise based on correlation coefficients,'' J. Acoust. Soc. Am. **95**, 424–434.

Shannon, C. E. (**1948**). ''A mathematical theory of communication,'' Bell Syst. Tech. J. **27**, 379–423.

Sorkin, R. D. (**1990**). ''Perception of temporal patterns defined by tonal sequences,'' J. Acoust. Soc. Am. **87**, 1695–1701.

Sorkin, R. D., and Montgomery, D. A. (**1991**). ''Effect of time compression and expansion on the discrimination of tonal patterns,'' J. Acoust. Soc. Am. **90**, 846–857.

Sorkin, R. D., Montgomery, D. A., and Sadralodabai, T. (**1994**). ''Effect of sequence delay on the discrimination of tonal patterns,'' J. Acoust. Soc. Am. **96**, 2148–2155.

Steedman, M. J. (**1977**). ''The perception of musical rhythm and meter,'' Perception **6**, 555–569.

Stevens, K. N., and House, A. S. (**1972**). ''Speech perception,'' in *Foundations of Modern Auditory Theory*, edited by J. T. Tobias (Academic, New York).

Voss, J., and Rasch, R. (**1981**). ''The perceptual of musical tones,'' Percept. Psychophys. **29**, 323–335.

Watson, C. S., Wroton, H. W., Kelly, W. J., and Benbasset, C. A. (**1975**). ''Factors in the discrimination of tonal patterns. I. Component frequency, temporal position, and silent intervals,'' J. Acoust. Soc. Am. **57**, 1175–1185.

Zara, J., Onsan, Z. A., and Nguyen, Q. T. (**1993**). ''Auditory profile analysis of harmonic signals,'' J. Acoust. Soc. Am. **93**, 3431–3441.

Lateralization of a moving auditory image: Interrelation of interaural time and intensity differences

Jacob A. Altman,[a] Olga V. Variaguina, and Nikolay I. Nikitin
Laboratory of Hearing Physiology, I. P. Pavlov Institute of Physiology, Russian Academy of Sciences, Nab. Makarova 6, 199034, Saint Petersburg, Russia

Elena A. Radionova[b]
Laboratory of Functional Asymmetry of the Human Brain, I. M. Sechenov Institute of Comparative Physiology and Biochemistry, Russian Academy of Sciences, M. Torez Prospect 44, 194223, Saint Petersburg, Russia

(Received 10 November 1996; revised 3 August 1998; accepted 28 August 1998)

Lateralization of moving fused auditory images (FAIs) was studied under dichotic stimulation, with FAI movement from the right and left ears to midline. The movement was produced by the gradual change of interaural time delay (from ± 630 to 0 μs) in a binaurally presented click train in which a constant interaural intensity difference (IID) between ± 13 dB was also imposed. The task of the subjects was to show with her/his finger the point on the head surface where the FAI trajectory's ending or starting points were perceived. With IID change within ± 13 dB, the FAI movement trajectory shifted toward the ear receiving the more intense stimulus. The length of the movement trajectory shortened with IID increase. Functions relating the value of perceived lateral position (Y) of the movement trajectory's ending and starting points to IID value (X) were nearly linear: $Y = AX + B$. These functions differed in their characteristics whether the movement was to the right versus to the left of midline. They also differed from analogous functions for stationary FAI. At IID$=0$ the FAI movement trajectory's endpoint was shifted from midline in the direction of movement. Equivalence ratio for IID and ITD were estimated to be 51 and 29 μs/dB respectively for the trajectory's starting and ending points. The IID factor could be several times as effective in moving FAI lateralization as the ITD factor. © *1999 Acoustical Society of America.* [S0001-4966(98)02612-5]

PACS numbers: 43.66.Pn, 43.66.Qp, 43.66.Rq [RHD]

INTRODUCTION

Perception by humans of sound source motion is one of the most important features of sound source localization in space. However, up to the end of the 1960's there were only a few studies concerning perception of the sound source motion (Altman, 1968; Harris, 1972; a detailed historical review can be found in the comprehensive work by Perrott and Strybel, 1997). Starting in the late 1960's the number of publications connected with different aspects of perception of sound source motion increased nearly four times (Perrott and Strybel, 1997, Fig. 1). As follows from the above review, investigation of such a peculiar form of motion as autokinesis practically ceased beginning from the middle of the 1970's. Relatively few studies have been performed under real, free-field sound source motion (e.g., Perrott and Musicant, 1977, 1981; Mateeff and Hohnsbein, 1988), because of the serious methodical difficulties in such investigations. The greatest number of works were carried out using simulation of sound source motion—either with dichotic stimulation or with the help of a set of loudspeakers switched on successively. Just these two methodical approaches resulted in an increase in the number of works on perception of auditory image movement. It should be mentioned that simulation of sound source motion in different planes with the help of a set of loudspeakers or with dichotic stimulation has been widely used during recent years both for creating virtual acoustical reality and for analysis of special features of this reality perception (Wenzel, 1992; McKinley *et al.*, 1994). Results of investigations of sound source motion perception are considered in detail in a number of reviews in recently published books on hearing (Grantham, 1995, 1997; Perrott and Strybel, 1997; Saberi and Hafter, 1997).

Briefly, it can be noted that up to present a number of important characteristics is described concerning perception of the auditory image movement under dichotic stimulation with ITD and IID changing in time. In particular, limit conditions are established for forming movement of the auditory image (Blauert, 1972; Altman and Romanov, 1988; Grantham and Wightman, 1978); differential thresholds and subjective scales are measured for velocity perception of the auditory image movement (Altman and Romanov, 1988); characteristics of binaural release from masking for moving auditory image are also described (Altman *et al.*, 1982).

To extend our knowledge about perception of moving sound sources, further systematic study is necessary concerning perception of different (not yet investigated) parameters of moving sound sources. In particular, there are possible competitive relations between two main factors underlying moving sound source localization in the horizontal plane, namely between interaural differences in time and intensity.

[a]Electronic mail: altman@infran.ru
[b]Electronic mail: radionova@ief.spb.su

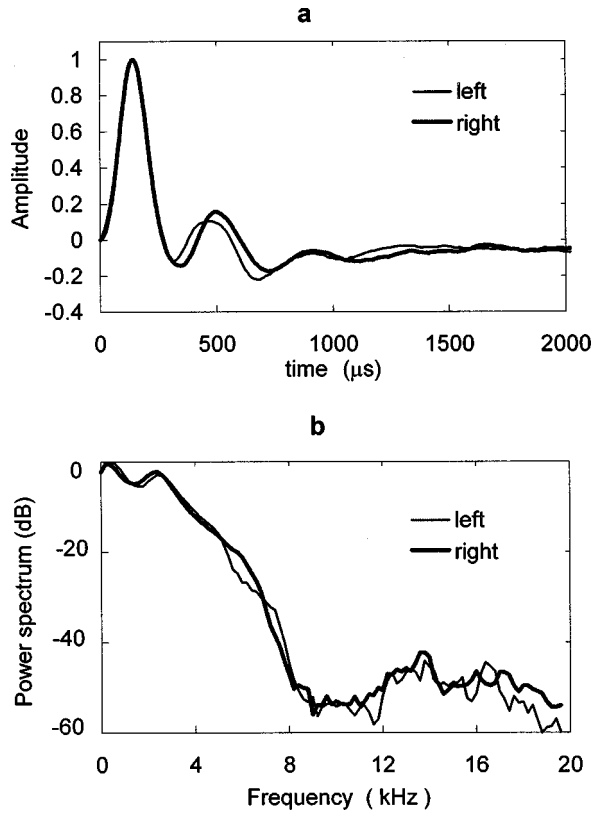

FIG. 1. Acoustic characteristics of the signals presented to the right and left ears. (a) Click waveform; (b) frequency spectra of the clicks.

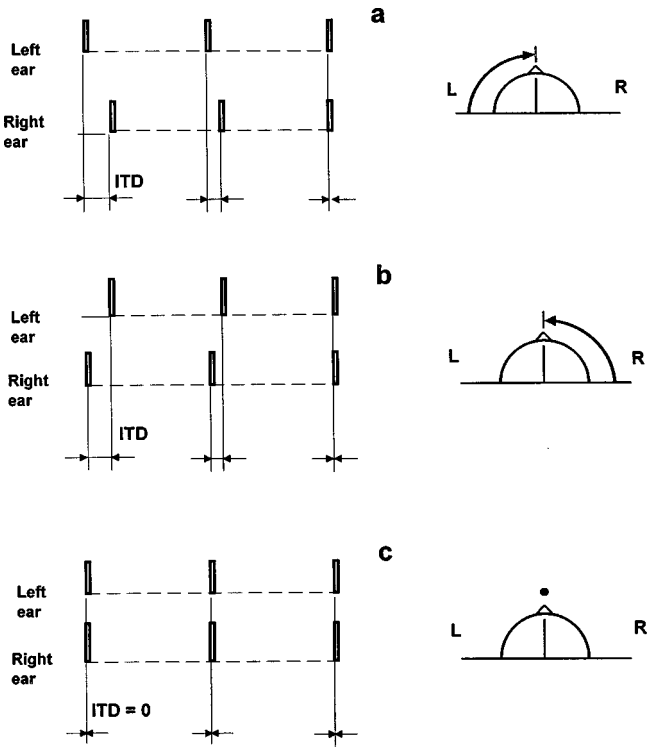

FIG. 2. Schematic representation of sound signals producing a sensation of fused auditory image (FAI) movement from left to right (a), from right to left (b), and of a stationary sound (c).

It is known that changes of interaural time or intensity differences during binaural presentation of the sound signal through head earphones result in auditory image movement over a certain trajectory (Altman and Viskov, 1977; Altman and Romanov, 1988). However, it still remains unknown how this illusion of sound source movement produced by one of the above factors (e.g., by interaural time differences, ITD, changing in time) can be influenced by the other localization factor (by interaural intensity differences, IID). In a number of earlier works (Harris, 1960; Hafter and Carrier, 1972; Yost and Hafter, 1987) it was shown that the spatial position of a stationary auditory image (lateralized by some value of ITD) could be changed by introducing an IID. Therefore a specific goal of the present work was to study the influence of IIDs on the trajectory of auditory image movement produced by changing ITDs. It seemed that estimation of this characteristic of directional hearing would be of importance also for such significant problems as masking in the process of sound source movement, localization of multiple sound sources, as well as for further possibilities in forming acoustical virtual reality.

I. METHODS

A. Subjects

The work was performed on ten subjects (six women and four men) with normal hearing and with small differences in threshold values for both ears. Nine of the subjects were aged 23–29 and one subject (male) was aged 42.

B. Sound signals

Sound signals were binaurally presented click trains which produced in listeners a sensation of a moving or stationary fused auditory image (FAI), depending on whether the interaural time delay was changing or constant. A two-channel generator of rectangular impulses was employed which allowed changing the value and sign of delay between the two channels of stimulation. Each impulse duration was 100 μs, and the click train duration was equal to 2 s. The click repetition rate was 25/s. Such a frequency was quite comfortable for listeners and enough to form in them a sensation of auditory image movement (Altman, 1981).

For acoustical stimulation two dynamic earphones (TDS-5, Russia) with identical characteristics were used. Their characteristics (Fig. 1) were measured with Brüel & Kjaer apparatus (condensor microphone 4131). Maximal intensity of the acoustical click trains, when measured monaurally, was about 60 dB above threshold. Signal intensity at the right and left ears was controlled separately (with attenuators graded in nepers) within ± 2 Np and converted to decibels (1 Np$=$8.67 dB). Click intensity was expressed in dB SPL as equivalent to the intensity of a 1-kHz tone signal of the same peak amplitude. The amplitude characteristics of the acoustic stimulation channels were linear within the range of 80 dB.

To produce a sensation of auditory image movement, the ITD between two channels was gradually decreased throughout signal presentation, as shown in Fig. 2. The initial interaural time delay was 630 μs; with equal intensities of stimulation at both ears, this should produce an auditory image located near the leading ear. The final delay was equal to

zero. Thus at the moment of signal cessation the auditory image should be located at the subject's midline. The sign of the initial delay determined the direction of auditory image movement, either from left to right or vice versa. As shown by direct measurements, the mean trajectory length at IID $=0$ was equal to 69 deg; thus with signal duration of 2 s the mean value of FAI movement velocity was 34.5 deg/s; at higher IID values it could be even lower depending on the direction of FAI movement. With synchronous stimulation of the right and left ears (when only one ITD was employed, namely equal to zero over the whole time of stimulus presentation) the sound signal was perceived as stationary and the auditory image was lateralized near midline.

C. Experimental conditions and procedure

The study was performed with two different instructions to the subjects: in the first part of the experiments (performed on ten subjects) the task was to estimate the position of the ending point of the FAI movement trajectory; in the second part of the experiments five of these subjects had to estimate position of the trajectory's starting point. Other conditions were the same in all the experimental sessions.

The measurements were performed in a quiet sound-attenuated room. On the subject's head a tape graded in centimeters and going from one ear to the other was fixed, its zero mark coinciding with the head midline. The tape position corresponded to the path through which FAI moved. In seven subjects the tape was fixed in the vertical (frontal) plane passing through the two ears. In three subjects the tape was fixed at the back of the head in the horizontal plane, with zero mark also at the midline. The average length of the arc going from one ear to the other in the frontal plane was 35.0 cm (from 33 to 36 cm in seven subjects); the length of the arc going around the back of the head was 31.0 cm (when averaged over three subjects).

The subjects were instructed to listen attentively to the sound, with his/her eyes closed, and to show with a finger (after stimulus cessation) the point on the head where the end or the start of the auditory image movement was perceived. The subject was free to show any point on the head where he/she perceived movement cessation or starting. The distance from these points to the head midline was measured in centimeters and converted to degrees, with the assumption that the length of the arc from one ear to the other was equal to 180 deg. Eight of ten subjects responded by pointing to a position of FAI on the tape itself, at any IID values used. In two others, at high IID values (of ± 13 and ± 17.3 dB) the indicated points deviated from the tape for 1–5 cm; in these cases, to measure the point position in relation to midline, an arc (whose center corresponded to the ear canal opening) was traced from the indicated point to the tape and thus the indicated point was projected to the tape. When stimulated with the click train which produced sensation of unmoving auditory image, the subject showed the place of its location; the distance between the unmoving FAI and the head midline was also expressed in centimeters and degrees. As it was established by repeated readings from the tape measure, in the great majority of cases (when the point indicated by the subject lay on the tape) accuracy of the response measure did not exceed 0.5 cm (of about 2.5–3 deg), i.e., half of the minimal division on the tape; in other cases this value could achieve about 5–10 deg.

Prior to the experiments the subjects were trained on estimating both the direction of auditory image movement, and its starting and ending location. A short training period was sufficient for all the subjects to estimate with confidence the end and start of trajectory of the auditory image movement as well as the position of the stationary FAI. Reliability of the pointing response was different in different subjects: some responded immediately after the first (of three) stimulus presentations and did not change their estimates, whereas others moved their finger back and forth over a certain distance (of about 1–3 cm) before giving their final response. This difference also manifested itself in different values of standard deviation of the mean estimates obtained in different subjects, as described in Sec. II.

Each session began with threshold measurements at the right and left ears separately with a stationary click train of 2-s duration as stimulus. The method of limits was used. Thresholds were measured with the step of 1.7 dB in the near-threshold intensity range. A signal intensity producing a 0.5 detection probability was used as the threshold. Threshold measurement took about 4–6 min and was not tiring for the listener. Then, under conditions of simultaneous binaural stimulation and eyes closed, the subject was asked to perform by himself/herself the task of centering the stationary auditory image, i.e., to place the auditory image at the head midline by varying sound signal intensity at one of the ears (at the left one) by controlling an attenuator. The initial level of the sound at this ear was about 40 dB above threshold. Signal intensity at the other ear (the right one) remained constant (about 40 dB above threshold); this intensity level was loud enough and quite comfortable for the subject at the same time. The signal intensity set by the subject at the left attenuator was evaluated. The centering procedure took about 1–2 min (a single adjustment was done).

Subsequently the main part of the experiment started: the estimation of the perceived starting or ending points of FAI movement trajectory. These experiments included four series with interaural intensity differences under conditions of FAI movement from right to left and from left to right. The series differed in the direction of FAI movement (from right to left or from left to right) and in the side (either the left or the right) at which sound intensity was varied. Each signal was presented three times with an interval of about 0.5 s. Immediately following the stimulus, the subject pointed to the starting or ending points of the FAI movement trajectory. When wanted, the signal was repeated. Before each signal presentation the subject was notified about it. Measurements were begun with signals of equal intensities at the right and left ears (about 40 dB SL) with one of the FAI movement directions. Next, the intensity at one of the ears was first reduced from 40 dB SL (in 4.3-dB steps) and then increased from 40 dB SL (in 4.3-dB steps), resulting in eight levels of IID within the range ± 17.3 dB. The series was ended with a final presentation of the signal of equal intensities (40 dB SL) at two ears. Thus during the whole series ten IIDs were presented in succession, each repeated three times (or more

in some cases). Duration of such experimental series was about 4–6 min. Then, after a short pause (of about 0.5–1 min, when the subject was offered a rest) the next series of measurements was performed, differing from the former only in direction of FAI movement. These two series were followed by two analogous series in which (also at two different directions of FAI movement) signal intensity was varied at the other ear. The session was ended by repeating the procedure of centering a stationary auditory image. Duration of the session as a whole was 30–40 min with no fatigue of the subjects. This procedure was repeated five or six times with each subject, the replications being completed on different days.

The above procedure was used in the experiments for estimation of both the ending and starting points of FAI movement trajectory. In addition, three of the subjects took part in control experiments in which the position of the earphones was changed (from the left ear to the right one and vice versa); results of these experiments did not differ from those described above.

The procedure for control experiments with stationary auditory images was the same. It included two series with interaural intensity differences at the left and right ears. Two such replications were performed on each subject.

D. Data processing

Results were averaged for each subject separately. Perceived positions of the FAI movement trajectory's ending or starting point (in degrees) at different IID values were estimated. Functions were constructed that were functions relating perceived position of the end (or of the start) of the trajectory to IID value. Results obtained with IID variation at the left and right ears were combined taking into consideration that IID increase at one ear and IID reduction at the other resulted in practically the same values of perceived lateral position of the end (and of the start) of FAI trajectory. Thus each point on the graphs related to FAI movement was the mean of 10 or 12 measurements for each of the subjects, except for the point at IID$=0$, which was the mean of 20 or 24 measurements on each subject. For each subject, the perceived lateral position of the FAI at stimulus offset or onset was plotted as a function of IID, and the data fitted by a linear function:

$$Y = AX + B,$$

where Y (the perceived lateral position of the offset or onset in degrees) is expressed as a function of X, the stimulus IID. The best-fitting straight lines were obtained using a linear least-squares criterion. In this equation, B represents the perceived lateral position when IID$=0$ (the intercept), and A represents the rate at which the perceived lateral position changes with IID (the slope of the function).

II. RESULTS

A. Thresholds

Hearing thresholds were similar in all subjects: in nine of ten persons (measurements on 18 ears) threshold values varied from 23 to 27 dB SPL; in the tenth subject thresholds were lower (19.5 dB SPL for both ears). The thresholds of the oldest subject practically did not differ from the younger ones. In all the subjects threshold variability was extremely low in different experimental sessions. Difference in threshold values for the left and right ears was also rather low in all the subjects: mean threshold values differed by 0.17–0.87 dB. The average of this difference was 0.37 dB (with the lower threshold for the right ear). As can be calculated from results presented below (Table II) this difference corresponded to an average change of stationary FAI position by 1.1 and 1.5 deg (for the left and right sides, respectively);[1] for moving FAI this change did not exceed 1.2 deg. Since these values were lower than possible error of measurements they are not reflected on the graphs below.

B. Centering of stationary FAIs

Experiments with centering stationary FAI (ten subjects) showed that in all subjects, stimulation of one of the ears was somewhat more effective in FAI centering than stimulation of the other ear. This difference was 0.3–4.2 dB. On the average, perceived position of FAI at midline in the centering experiment was achieved when left ear stimulation was slightly more intense (by an average of 0.78 dB); i.e., the right ear was slightly more effective (with threshold difference of the right and left ears taken into account).

C. Perception of moving FAIs

For IIDs within ± 13 dB the FAI movement trajectory (from left to right or from right to left) in seven subjects was located in the vertical (frontal) plane passing through the two ears, whereas in three others the auditory image moved in the horizontal plane around the back of the head. For IID exceeding 13 dB, trajectories moving in the vertical plane could deviate in the direction of the horizontal plane (although to a different extent in different subjects); for IID$=\pm 17.3$ dB trajectories often proved distorted, therefore these data will not be discussed further.

The FAI movement sensation was reported by all subjects at all IID values used in this work. The subjects did not notice any changes of signal duration at different IIDs. When asked, half of the subjects perceived a velocity decrease with an IID increase, although in all cases a shortening of the path covered by the moving FAI was observed.

With an IID increase, FAI movement trajectories were shifted toward the more intense sound. This shift value, when averaged, proved practically identical in cases when the stimulus intensity was increased at one ear and in cases when it was reduced at the other ear. Thus within the working range of intensities the FAI movement trajectory shift did not depend on summed loudness of the sound signal. Therefore it proved possible to average (for each direction of FAI movement) the data obtained in the experimental series with stimulus intensity variation at the right and left ears.

An example of FAI movement trajectory shift based on interaural intensity differences is shown in Fig. 3. It can be seen that with no interaural intensity differences (IID$=0$) FAI movement trajectories are placed asymmetrically in relation to midline for both directions of movement: the trajec-

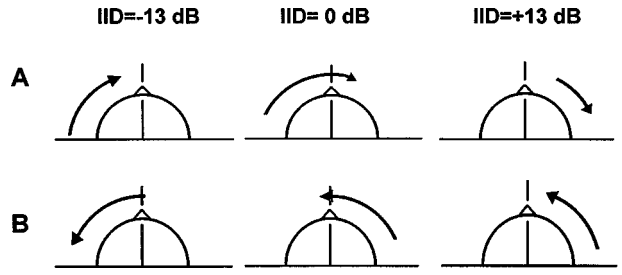

FIG. 3. Positions of trajectories of FAI movement (arrows) at different values of interaural intensity differences (IID, dB). Here and in all other cases positive values of IID mean that right ear stimulation is more intense than the left one, negative values correspond to more intense stimulation at the left ear. Mean data of subject *N* (Figs. 4–6, white squares).

tory endpoints are not at midline (although at the moment of movement cessation ITD=0), but are shifted in the direction of movement. It can be seen also that for both directions of FAI movement, an intensity increase at the right ear (or a decrease at the left) results in a shift of the trajectory to the right and shortening of the trajectory length. In contrast, an intensity decrease on the right (or an increase on the left), i.e., IID change from 0 to −13 dB, produces a trajectory shift to the left with a less pronounced change of the trajectory's length.

D. Lateralization of moving trajectory endpoints

To reveal the specificity of the movement effect, the results obtained for moving FAI were compared to those for the stationary one. For this purpose the experiments with estimation of the ending point of FAI movement trajectory were analyzed first. It was just the ending point which corresponded to ITD=0 as was the case also for the stationary FAI. In this part of the study ten subjects were investigated. These data are presented in Figs. 4–6 and in Tables I–III.

It was established that dependence of the trajectory's perceived ending point positions on IID value could be described by two lines (functions of the type $Y=AX+B$) fitted to the subject's judgements on the left and right sides, respectively (Figs. 4, 5). Since the above functions were of different steepness at positive and negative IIDs, their *A* and *B* values were estimated separately for +IID and −IID conditions. However, *B* values were rather close for +IIDs and −IIDs (the means differed by 1.3 and 1.5 deg, Table I) and therefore they were combined.

Characteristics of perceived positions of the end of FAI movement trajectory following interaural intensity differences were rather different in different subjects (Figs. 4, 5), both in curve slopes and in positions of the central point on these curves (corresponding to IID=0) in relation to midline. However, with left–right FAI movement, the perceived position of the endpoint was farther to the right of the midline than to the left of it (Fig. 4). With movement in the opposite direction (Fig. 5) lateralization of the trajectory's endpoint was greater to the left than to the right of midline.

It was also found that at IID=0 the perceived position of the trajectory's endpoint (*B* value) in most cases was shifted in the direction of movement: to the right in Fig. 4 and to the left in Fig. 5 (see also Table I). *B* values, when

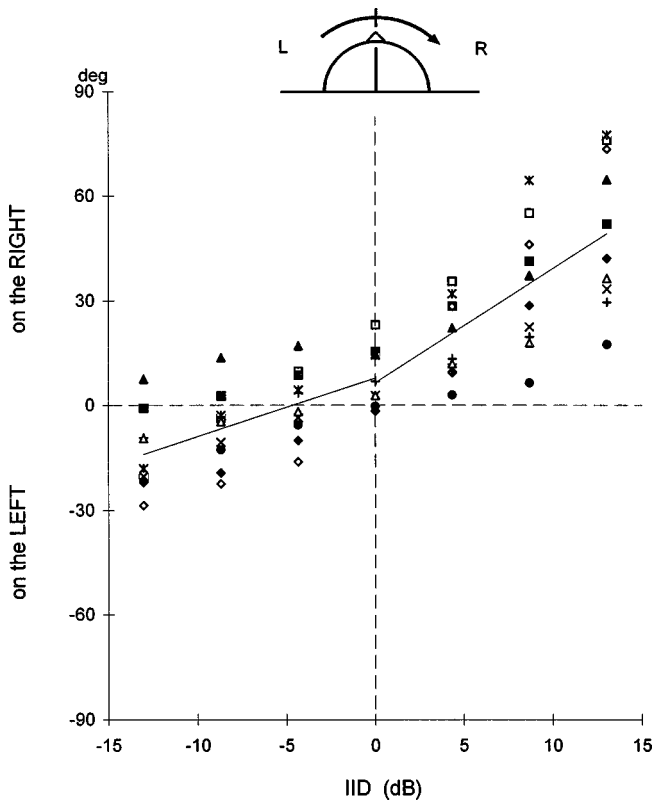

FIG. 4. Perceived position of the endpoint of FAI movement trajectory with FAI movement from left to right, depending on interaural intensity differences. Mean data for ten subjects (shown by different symbols) approximated by the straight line. On the abscissa: interaural intensity difference, IID, dB; positive values correspond to more intense stimulation at the right ear, negative values to that at the left ear. On the ordinate: perceived position of FAI movement trajectory endpoint in relation to midline, in degrees; positive values correspond to right-side position, negative values to the left-side position.

averaged for the left and right branches of the curves of Figs. 4–5, were +7.1 deg for rightward direction of FAI movement and −3.5 deg for the leftward direction. The difference in these *B* values was significant ($t=3.911$, $p<0.01$). Both values differed significantly also from the mean *B* value (+2.5 deg) obtained for stationary stimuli (Fig. 6): for movement from right to left $t=2.667$ ($p<0.05$) and for movement in the opposite direction (from left to right) $t=2.137$ ($0.01<p<0.05$).

Besides, in comparison with a stationary stimulus (Fig. 6) for moving stimuli (Figs. 4–5) greater absolute values of IID were required to cause the trajectory's endpoint to be lateralized at midline: Observing where the functions intersect the horizontal line (0 deg) in Figs. 4–5 indicates that on the average a −4.2 dB IID was required for left-to-right FAI movement (Fig. 4), and a +2.1 dB IID was required for movement in the opposite direction (Fig. 5); corresponding values for a stationary stimulus (Fig. 6) were about −1 dB.

In general, lateralization of the endpoint of the moving FAI was greatest when the direction of the IID factor was consistent with the direction of movement, suggesting that the effects of IID and ITD were summed, i.e., IID and ITD influences were coincident. When the direction of the IID did not coincide with FAI movement direction (i.e., with competitive relations of IID and ITD factors), the lateralization of

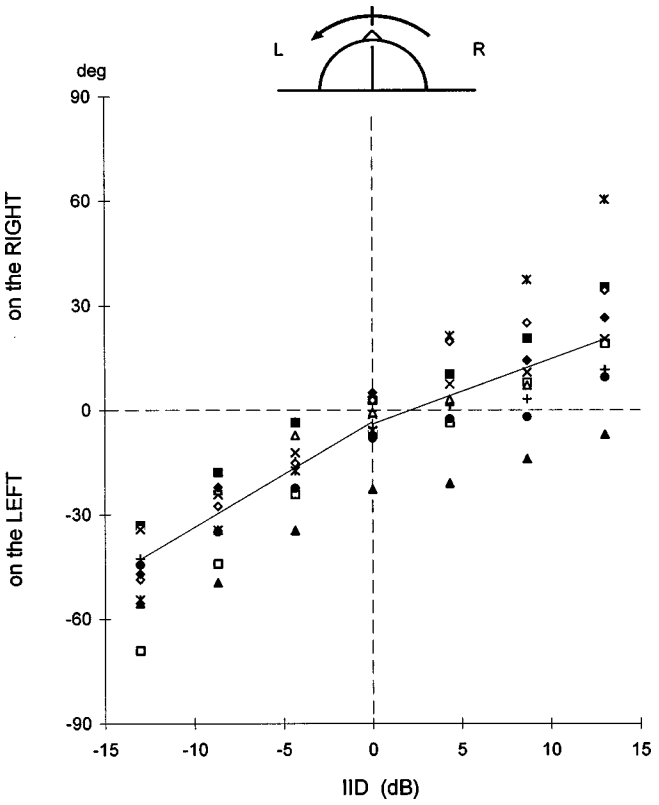

FIG. 5. Perceived position of the endpoint of FAI movement trajectory with FAI movement from right to left, depending on interaural intensity differences. Mean data for ten subjects (shown by different symbols) approximated by the straight line. Designations as in Fig. 4.

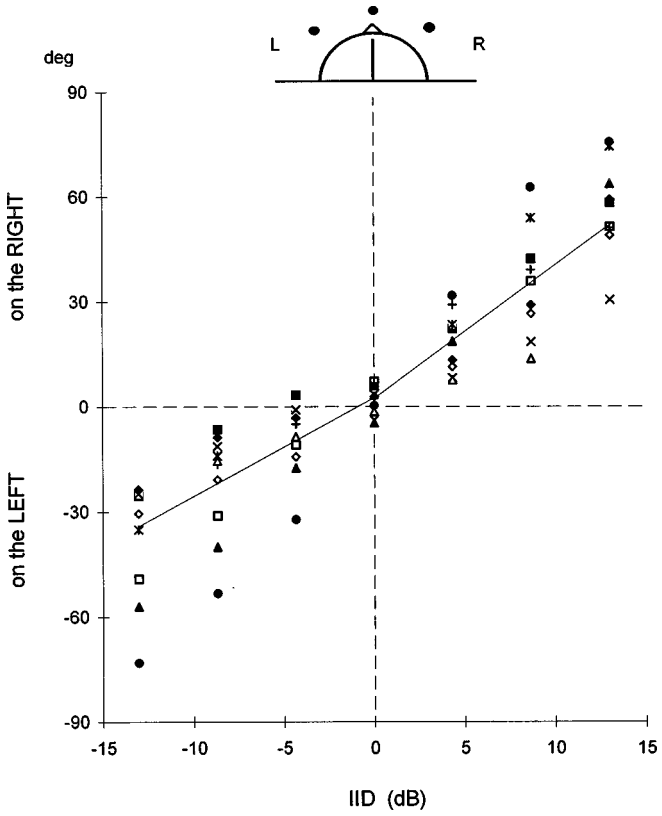

FIG. 6. Perceived position of the unmoving FAI with constant ITD (0 μs) throughout the click train. Mean data for ten subjects (shown by different symbols) approximated by straight line. Dots on the scheme at the top mean conventionally different positions of unmoving FAI. Designations as in Fig. 4.

trajectory's end point proved usually significantly lower (Figs. 4–5). Of 20 cases presented in Figs. 4–5, only two exceptions to this rule were observed (Fig. 4, filled circles; Fig. 5, asterisks).

The slope of the functions investigated (Figs. 4–5) determined by coefficient A in equation $Y=AX+B$, reflects the effectiveness of the IID factor in lateralization of the end point of FAI movement trajectory: It shows the value (in degrees) for which the trajectory's end point is shifted following IID change for a certain value (in decibels). Coefficient A values are presented in Table II. For comparison, analogous values are presented for the stationary FAI (see also Fig. 6). The difference in A values (Table II) evidences different effectiveness of IIDs on both sides of midline; this points to a certain asymmetry in organization of the lateralization process. As can be seen from Figs. 4, 5, and Table II, with FAI movement the slope of the functions was greater when the direction of trajectory shift produced by IID coincided with the direction of FAI movement.

Thus it proved characteristic that: (i) functions relating perceived ending point positions to IID, depended on movement direction; (ii) their slope (represented by the coefficient A) was different on the right and on the left of midline; (iii) at IID$=0$ the trajectory's end (when ITD$=0$ μs) was often shifted to the right or to the left of midline, i.e., the value B as a rule was not equal to zero; and (iv) maximal shift values of the trajectory's ending points (at IID$=\pm 13$ dB) depended on the FAI movement direction and on the side (the right or the left one) where these points of trajectory were.

E. Lateralization of moving trajectory start points

The position of the starting point was also described as a linear function of IID value. The mean starting location is presented on Fig. 7. At IID$=0$ dB, the mean values of the trajectory's starting position (at ITD$=630$ μs) were equal to -61 deg when FAI moved from left to right and to $+66$ deg with movement in the opposite direction; the difference between absolute values of these two means was not significant ($t=0.495$, $p>0.5$).

In Fig. 7(a) the functions for the starting and ending point positions are practically equal in slope only when the influence of the IID factor is opposite in its direction to the direction of FAI movement (i.e., within the IID range from 0 to -13 dB). In case of coincident action of IID and ITD factors [within the IID range from 0 to $+13$ dB in Fig. 7(a), and to -13 dB in Fig. 7(b)] the slopes of both functions become different: the mean values of coefficient A for the ending and starting points [Fig. 7(a) and (b) combined] were equal, respectively, to 3.3 and 5.6 deg/dB.

The data of Fig. 7 show a shortening of the trajectory's length (defined as the difference between perceived positions of the starting and ending points) with IID increase, due to the greater steepness of the functions obtained for the starting point position as compared to the corresponding functions for the ending point.

At IID$=0$ the mean trajectory length was about 68 deg [Fig. 7(a)] and 70 deg [Fig. 7(b)] with a mean of about 69

TABLE I. *B* values (intercepts), in degrees, for moving (arrows) and for stationary FAI (cross) to the left (L) and to the right (R) of midline. The data for the trajectory's endpoint, ten subjects.[a]

	B value (deg)					
	a →		*b* ←		*c* +	
	L	R	L	R	L	R
minimal	−4.1	−3.1	−23.5	−24.3	−3.6	−4.5
maximal	23.8	20.7	9.4	5.5	9.7	10.0
mean	7.8	6.5	−2.7	−4.2	3.0	1.9
averaged[b]	7.1		−3.5		2.5	
s.d.	8.6		8.6		4.9	

[a]Notes: *B* value in the equation $Y=AX+B$ for the experimental data (Figs. 4–5) corresponds to the perceived position of FAI movement trajectory's endpoint and of stationary FAI at IID=0. Minimal and maximal values are the limits of coefficient *B* observed in the experiments. L, R correspond to left and right branches of the functions. Arrows show directions of FAI movement (from left to right and from right to left), the cross corresponds to stationary FAI.
[b]L and R values are combined.

deg. At IID=+13 dB [in Fig. 7(a)] the mean trajectory length was about 27 deg, differing significantly from that at IID=0 dB ($p<0.01$). In the other case [Fig. 7(b), at −13 dB] changes of the trajectory length manifested themselves only as a tendency, being statistically not significant.[2]

With the above mean trajectory lengths of about 69 and 27 deg and constant signal duration of 2 s, calculated values of perceived movement velocity were 34.5 and and 13.5 deg/s for IID equal to 0 and +13 deg, respectively. With IID increase velocity decrease was actually reported by half of all subjects. Other subjects could not identify a certain change in sensation (at extreme IID values) with change in movement velocity.

Subjects differed to a certain extent in their accuracy of estimation of FAI movement position, both of its starting and ending points. (Accuracy of estimation was measured by standard deviation of the mean estimate.) Accuracy of estimation of the starting point position (at ITD=630 μs) was rather low: At IID=0 dB standard deviation of the mean estimate varied between 5 and 18 deg for different subjects. Meanwhile when judging trajectory endpoint position near the head midline (at equal intensities of stimulation at both ears and ITD=0, when the error was usually minimal), variability of estimates characterized by standard deviation varied between 2.3–9 deg and thus was about twice as low as variability of responses with determination of the starting point position. With increasing distance from midline following IID increase, variability of estimates usually became higher and in some cases reached 20 deg for endpoint estimates and 47 deg for estimation of the trajectory's starting point. As showed our supplementary experiments (reported in the Appendix) the higher accuracy of endpoint judgement than of start point judgement resulted not from the temporal position of the judged point (start or end), but rather from the fact that positions near midline are judged more accurately than those more lateral, whether they are start points or endpoints.

F. Equivalence ratios for IID and ITD

To evaluate equivalence ratio (*E*) for IID and ITD factors (in μs/dB) under conditions of FAI movement, positions of the trajectory ending and starting points (in degrees) were converted to equivalent values of interaural time delay (in microseconds), assuming that (a) FAI shift for 69 deg (the mean value of the trajectory's length at IID=0, as it was described above) corresponded to change of interaural time delay (ΔITD) for 630 μs (ITD change throughout the signal duration), and (b) both parameters (IID and ITD) were linearly interconnected (Blauert, 1974). Thus the FAI shift for 1 deg was equivalent to an ITD of about 9.1 μs (630 μs/69 deg; see also Blauert, 1974; Yost and Hafter, 1987). For the

TABLE II. Coefficient *A* (deg/dB) for moving (arrows) and for stationary FAI (cross) to the left (L) and to the right (R) of midline. The data for the trajectory's endpoint, ten subjects.[a]

	A-value (deg/dB)					
	a →		*b* ←		*c* +	
	L	R	L	R	L	R
minimal	0.6[b]	1.3	2.6	0.9[b]	1.6	1.7
maximal	3.3	5.6	4.7	4.9	5.6	5.9
mean	1.7	3.3	3.2	2.0	3.0	4.0
s.d.	0.78	1.40	0.77	1.17	1.28	1.39

[a]Notes: Coefficient *A* in equation $Y=AX+B$ determines the slope of the straight lines, as in Figs. 4–7. Minimal and maximal values are the limits of coefficient *A* observed in the experiments.
[b]Trajectory's endpoint does not go to the left side (Fig. 4 filled triangles, filled squares) and to the right side (Fig. 5, filled triangles).

TABLE III. Equivalence ratio, in μs/dB, for coincident and competitive relations of IID and ITD factors for moving FAI, at the movement trajectory length of 67 deg and FAI movement velocity of 34.5 deg/s.[a]

IID and ITD interrelation	Equivalence ratio, E (μs/dB)	
	Starting point	Ending point
Coincident	51	29
Competitive	13	17

[a]Notes: E-values are calculated from the data of Fig. 6 as $E=A(\Delta\text{ITD}/l)$. The data for both directions of FAI movement are combined. Other details are in the text.

trajectory length of 69 deg, values of equivalence ratio (in μs/dB) were calculated by multiplying values of coefficient A (deg/dB) by 9.1 μs/deg. Results of these calculations for trajectory's length of 69 deg are presented in Table III, the data for both directions of FAI movement being combined, separately for coincident and competitive effects of IID and ITD. Table III shows that E values varied considerably (within 13–51 μs/dB), depending on FAI perceived position (starting versus ending points) as well as on IID and ITD interrelation (coincident versus competitive). With changing trajectory's length following IID change (Fig. 7) the values of the equivalence ratio changed: e.g., at IID=+13 dB, E values were 2.6 times higher than presented in Table III. In general, in our experiments, the equivalence ratio for dynamic ITD and static IID factor could be described as $E=A(\Delta\text{ITD}/l)$.

As to equivalence ratio for the stationary signal, we assumed (in accordance with Blauert, 1974, Fig. 87) that at ITD=630 μs the FAI shift amounted to 72 deg, and thus 1-deg shift was equivalent to ITD=8.75 μs (630 μs/72 deg). Multiplying the value 8.75 μs/deg by coefficient A (deg/dB) gives an equivalence ratio of about 26 μs/dB to the left of midline and about 36 μs/dB to the right of it. These values are near to those in literature described for stationary signals (more often near 20–30 μs/dB according to different authors; Yost and Hafter, 1997; Saberi and Hafter, 1997); they are lower than E values for moving FAI with coincident effects of IID and ITD factors and higher than E values for moving FAI with competitive effects of both factors.

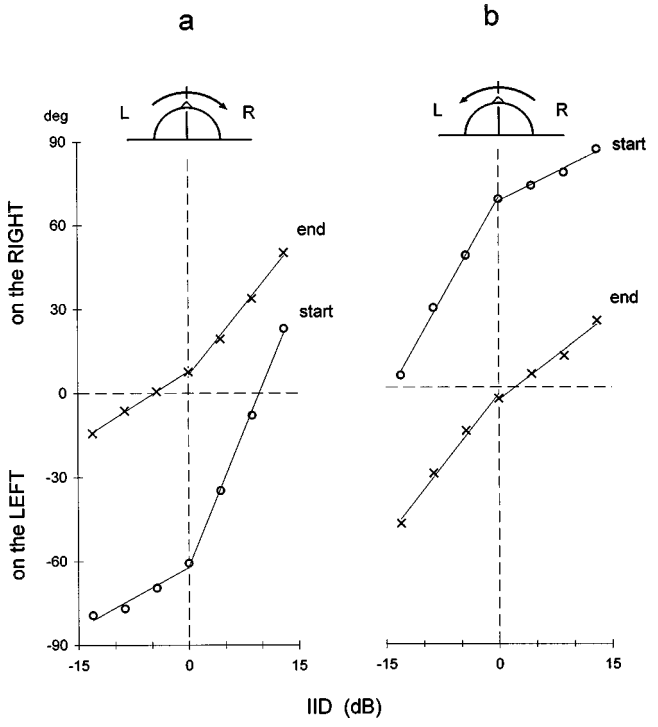

FIG. 7. Perceived positions of the starting and ending points of FAI movement trajectories depending on interaural intensity differences at different directions (a, b) of FAI movement. Function for the starting point presents mean data for five subjects. Function for the ending point is constructed from the mean B and A values for ten subjects presented in Tables I, II. Other designations as in Fig. 4.

III. DISCUSSION

As was shown, FAI movement trajectory shifted toward the ear receiving the more intense sound. The following aspects of moving auditory image lateralization will be considered: inertial property of the auditory system under moving FAI lateralization, functional asymmetry of the phenomena observed, and relative effectiveness of IID and ITD in lateralization of moving FAIs.

A. Inertial property

Inertia manifestation under conditions of coincident interaction of the main factors (IID, ITD) of sound source localization could be expected based on earlier works on lateralization and localization of moving auditory images (sound sources). Altman and Viskov (1977) and Altman and Romanov (1988), using dichotially presented click trains as stimuli, showed that to produce sensation of movement, a certain time interval (not longer than 100–150 ms) is needed between subsequent clicks in the train. This means that there is an inertia process which prolongates (within the time period of about 100–150 ms) the excitation state produced by each click in the train and thus secures a possibility of summation of subsequent excitations following subsequent clicks. The latter process seems necessary for sensation of uninterrupted movement. Perrott and Musicant (1977, 1981) and Mateeff and Hohnsbein (1988) working under free field conditions found that with a moving source, the locus of a perceived signal was shifted in the direction of motion.

This conclusion is confirmed by the data of the present work for FAI movement trajectory's endpoint at IID=0, in spite of the difference in experimental conditions in our work and especially in the above works by Perrott and Musicant (dichotic versus free-field stimulus presentation; signal onset near the ear versus near midline; click versus 0.5 kHz tone signal; signal duration of 2.0 s vs 50–300 ms).

As shown, in most of our subjects at IID=0, the end of FAI movement trajectory (at ITD=0 as well) was perceived as lateralized to the right of midline (by a 7.1 deg average) with FAI movement from left to right, and as lateralized to the left (by a 3.5 deg average) with FAI movement in the opposite direction (Table I; the difference being statistically significant). Thus with FAI movement, the position of the trajectory's end (as estimated by subjects) does not coincide with the head midline in spite of the fact that at this moment there are no interaural differences in stimulation (ITD=0, IID=0). It is typical that perceived shift of the movement

trajectory's end goes in the direction of FAI movement; this allows one to think about inertia of the physiological mechanisms underlying the processing of FAI movement and/or connected with forming an estimate and making a decision about FAI movement trajectory position.

In this connection it seems of interest that all subjects pointed with great accuracy to the position of the head midline; i.e., they oriented themselves quite well within the inner coordinate system determined by the body scheme.

B. Asymmetry

It was shown that trajectories of FAI movement differed in their characteristics depending on the side (the right or the left) where the movement occurred and on direction of FAI movement (Figs. 3–7, Tables I, II). These data evidence different significance of the right and left regions of subjective acoustical space in sound source localization. The data of earlier investigations performed on patients with functional deficit of the right or left hemispheres (Altman *et al.*, 1979, 1987) pointed to a certain specialization of the right hemisphere in relation to directional hearing. Results of the present work evidence that in healthy subjects the factor of either hemisphere involvement in moving FAI lateralization is even more distinctive.

As described above, the functions relating the value of perceived position of FAI movement trajectory's starting and ending points to IID, although rather different in different subjects (e.g., Figs. 4–5), were similar to each other in general tendency (Fig. 7). The slope of these functions (characterized by coefficient A in equation $Y=AX+B$), was different at the right- and left-sided positions of the trajectory's starting and ending points in relation to midline (Figs. 4–7, Table II), and depended on coincidence or noncoincidence of the direction of trajectory shift produced by IID with direction of FAI movement. With one direction of FAI movement [Fig. 7(a)] the movement trajectory's length also proved different to the right and to the left of midline.

To reveal more distinctly the difference between the right and left hemisphere involvement in lateralization of moving FAI, the data of Fig. 7 were presented in another way, with a different axis system (Fig. 8). Figure 8 shows that at both directions of FAI movement the rightward shift of the trajectory starting and ending points exceeds the leftward shift. For the starting point [Fig. 8(a)] the most difference between the rightward and leftward shifts is observed for the right branches of the functions which corresponds to coincident relations between ITD and IID. Meanwhile, for the ending point [Fig. 8(b)] the most difference corresponds to competitive relations between ITD and IID (the left branches of the functions). These data directly show to hemispheric asymmetry, with a certain prevalence of the right-side mechanisms of moving FAI lateralization in comparison with the left-side mechanisms.

Thus values of the term B (intercept), coefficient A (slope), and trajectory length evidence functional asymmetry of processes connected with lateralization of moving auditory image.

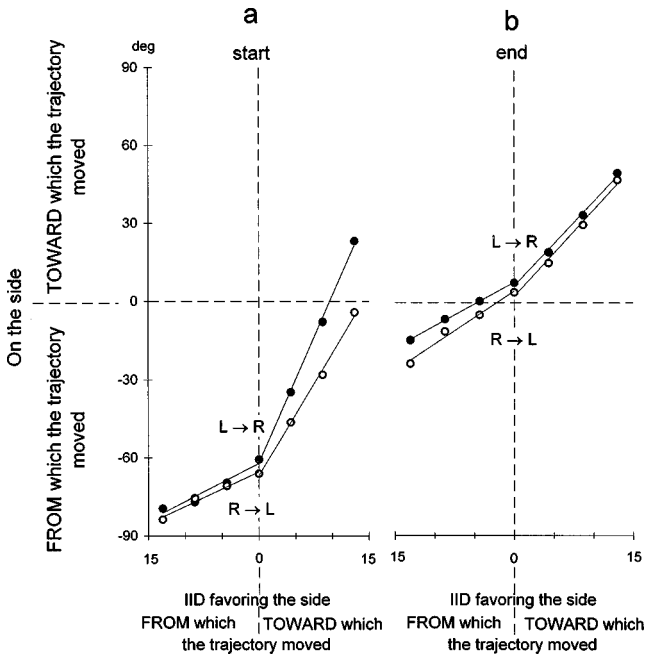

FIG. 8. Perceived positions of the starting and ending points (a, b, respectively) of FAI movement trajectories depending on interaural intensity differences. The data are replotted from Fig. 7. On the abscissa: IID, in dB, favoring the side from which the trajectory moved (on the left from zero; this corresponds to competitive relation of IID and ITD) and IID, in dB, favoring the side toward which the trajectory moved (on the right from zero; this corresponds to coincident relation of IID and ITD). On the ordinate: perceived positions (in degrees relative to midline) of the starting and ending points on the side toward which the trajectory moved (above zero) and on the side from which the trajectory moved (below zero). Arrows near the curves show movement direction (R→L or L→R).

C. Relative effectiveness of IID and ITD in lateralization of moving FAIs

To evaluate comparative effectiveness of IID and ITD factors in lateralization of moving FAI (under conditions when ITD was gradually changed throughout the stimulus presentation and IID was constant) the number of differential thresholds (DTs, for IID and ITD) was calculated which was covered by IID and ITD values necessary for 1-deg lateralization of moving FAI. For the ending point (Figs. 4–7, Table II), when ITD=0, a FAI shift of 1 deg corresponded to an IID change of about 0.31 dB on the average, with coincident relation of IID and ITD factors (with both directions of FAI movement combined). Assuming that the differential threshold for IID, with a click series as stimulus, is about 1.5 dB (Blauert, 1974) we determine (for coincident relation of IID and ITD factors) that 0.31/1.5=0.21; i.e., an IID equal to 0.21 DTs is needed for 1-deg lateralization of a moving FAI at ITD=0.

As to ITD factor, to shift the trajectory's endpoint by 1 deg at IID=0, an ITD change of 9.1 μs was needed on the average (as stated above). Taking the differential threshold for ITD as 11 μs (Blauert, 1974) it can be found that 9.1 μs includes 0.83 DTs (9.1/11=0.83). In comparison with IID indices this value is about four times higher: 0.83/0.21 $\approx$4.0. Thus using this method to quantify relative effectiveness, the IID is about four times more effective in lateralization of the moving FAI (at the ending point of movement) than ITD. FAI lateralization at its starting point (when

ITD=630 μs) shows even a greater effectiveness of the IID factor since the function relating FAI lateralization to IID value is about 1.7 times steeper for the starting point as compared to the ending point (Fig. 7, coincident relations of IID and ITD factors).

ACKNOWLEDGMENTS

The authors are grateful to Dr. G. L. Gerstein for his kind help with English language. Many thanks also to E. Josef and L. Zakharova for technical assistance throughout the work. We are also grateful to Dr. D. W. Grantham for critical remarks and editorial suggestions.

APPENDIX: INFLUENCE OF THE TRAJECTORY'S STARTING POINT POSITION

Some results were obtained also with a different starting position, namely with FAI movement from midline to the right and left ears. Two subjects (A, Figs. 4–6, white triangles, and V, Figs. 4–6, filled squares) were employed (six experiments on each, with the standard procedure described in Sec. I). Results for both subjects were rather near, and are shown in Fig. A1 for one of them. Of interest is the tendency for certain changes of the trajectory length [Fig. A1(a), (b)] which differ from those presented in Fig. 7 and are due to a greater steepness of the function for the ending point than for the starting one [unlike the data in Fig. 7(a)]. The feature common to that in Fig. 7 is that the function's steepness increase (when observed) is connected with that trajectory's characteristic [starting point as in Fig. 7(a) and ending point as in Fig. A1] which corresponds to ITD=630 μs.

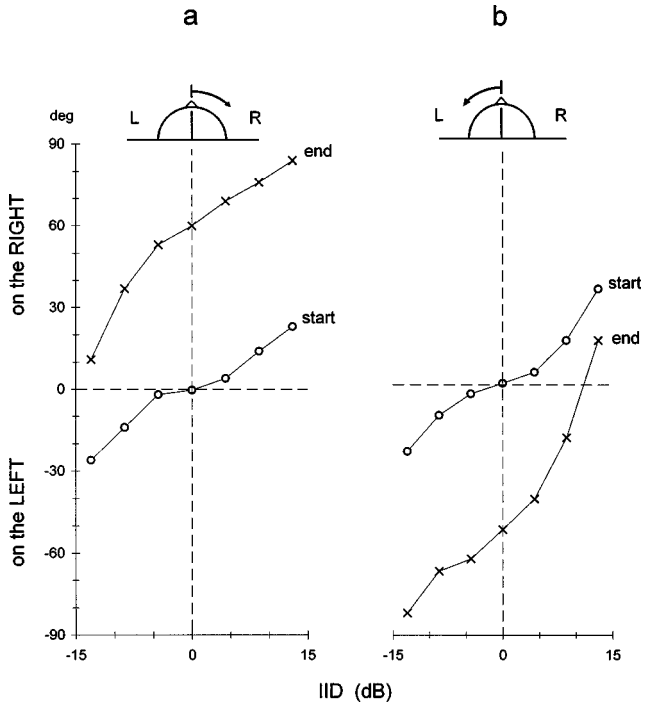

FIG. A1. Perceived positions of starting and ending points of FAI movement trajectories with changed positions of both the starting point (near the midline, at ITD=0 μs) and of the ending point (a: near the right ear at ITD=+630 μs, b: near the left ear at ITD=−630 μs), depending on interaural intensity differences. Mean data for subject A (Figs. 4–6, white triangles). Each point on the graphs are the means of 24 measurements (at IID=0) and of 12 measurements (at other IID values). Designations as in Fig. 4.

TABLE AI. Variability of estimation of perceived positions of trajectory starting and ending points (measured by standard deviation, s.d., of the mean estimate, in degrees) at different ITD values.[a]

	Variability of estimation, s.d. in degrees	
	near midline (ITD=0 μs)	near the ears (ITD=±630 μs)
Starting point	3.3	9.1
Ending point	3.7	10.0

[a]Notes: Mean data for two subjects. Results obtained with different starting positions (at ITD=0, +630, and −630 μs) and IID=0 are presented. The data for two sides of FAI movement (to the left and to the right of midline) are combined. Each figure for ITD=0 μs is the mean of 48 measurements; each figure for ITD=±630 μs is the mean of 24 measurements.

Accuracy of estimation (as measured by standard deviation of the mean estimate) of the starting point position in this experiment (at ITD=0 μs) was high and near that obtained in the same subjects for the ending point with FAI movement from the ear to midline (when ITD=0 μs as well): Mean values of standard deviation in both cases did not exceed 4 deg at IID=0 dB and did not depend on movement direction or on the side (to the left or to the right of midline) where the movement took place. It proved that ITD=±630 μs (positions near either of the ears) both for the starting and ending points resulted in nearly the same decrease in accuracy (increase in s.d.) of the estimate. Table AI allows one to compare results for the starting and ending points at different positions of starting points of FAI movement trajectories (at 0 and ±630 μs). Comparing these results with those by Perrott and Musicant obtained under free field stimulation and sound source onset at midline (1977, Fig. 2, Table II) it can be concluded, in agreement with the data by these authors, that it is position in relation to midline which determines the accuracy of estimation of perceived position of the moving FAI, both of its starting and ending points.

[1]The calculation was based on estimates from the data of Table II,c indicating that average slopes of the functions relating perceived lateral positions of the unmoved FAI to IID ranged from 3.0 to 4.0 deg/dB.

[2]It should be noticed that trajectory length was measured also in special experiments when subjects had to estimate both the ending and starting points; results obtained in these experiments were similar to those presented in Fig. 7.

Altman, J. A. (**1968**). ''Are there neurons detecting direction of sound source motion?'' Exp. Neurol. **22**, 13–25.

Altman, J. A. (**1981**). ''Psychophysical and neurophysiological data on the sound source motion perception,'' in *Neural Mechanisms of Hearing*, edited by J. Syka and Br. Masterton (Plenum, New York), pp. 289–299.

Altman, J. A., and Romanov, V. P. (**1988**). ''Psychophysical characteristics of the auditory image movement perception during dichotic stimulation,'' J. Int. Neurosci. **38**, 369–379.

Altman, J. A., and Viskov, O. V. (**1977**). ''Discrimination of perceived movement velocity for fused auditory image in dichotic stimulation,'' J. Acoust. Soc. Am. **61**, 816–819.

Altman, J. A., Balonov, L. Ya., and Deglin, V. L. (**1979**). ''Effects of unilateral suppression of the brain hemisphere function in man on directional hearing,'' Neuropsychologia **17**, 295–301.

Altman, J. A., Rosenblum, A. S., and Lvova, V. G. (**1987**). ''Lateralization

of a moving auditory image in patients with focal damages in brain hemispheres,'' Neuropsychologia **25**, 435–442.
Altman, J. A., Romanov, V. P., and Shakhshayev, S. A. (**1982**). ''Special features of binaural release from masking for a moving auditory image,'' Human Physiology **8**, 537–541 (translation from Russian, Plenum Press).
Blauert, J. (**1972**). ''On the lag of lateralization caused by interaural time and intensity differences,'' Audiology **11**, 265–270.
Blauert, J. (**1974**). *Raümliches Hören* (Hirzel Verlag, Stuttgart).
Grantham, D. W. (**1995**). ''Spatial hearing and related phenomena,'' in *Hearing* (Academic, New York), Chap. 9, pp. 297–346.
Grantham, D. W. (**1997**). ''Auditory motion perception: Snapshots revisited,'' in *Binaural and Spatial Hearing in Real and Virtual Environments* (Elbaum, Hillsdale, NJ), Chap. 15, pp. 295–313.
Grantham, D. W., and Wightman, F. L. (**1978**). ''Detectability of varying interaural temporal differences,'' J. Acoust. Soc. Am. **63**, 511–523.
Hafter, E. R., and Carrier, S. C. (**1972**). ''Binaural interaction in low frequency stimuli: The inability to trade time and intensity completely,'' J. Acoust. Soc. Am. **51**, 1852–1862.
Harris, G. G. (**1960**). ''Binaural interactions of impulsive stimuli and pure tones,'' J. Acoust. Soc. Am. **32**, 685–692.
Harris, J. D. (**1972**). ''A florilegium of experiments on directional hearing,'' Acta Oto-Laryngol. Suppl. **208**, 1–26.
Mateeff, S., and Hohnbein, J. (**1988**). ''Dynamic auditory localization: Perceived position of a moving sound source,'' Acta Physiol. Pharmacol. Bulg. **14**, 32–38.
McKinley, R. L., Erickson, M. A., and D'Angelo, W. R. (**1994**). ''3-dimensional auditory displays: Development, applications, and performance,'' Aviat., Space Environ. Med. **65**, (5 Suppl.), A31–A38.
Perrott, D. R., and Musicant, A. D. (**1977**). ''Minimum auditory movement angle: Binaural localization of moving sound sources,'' J. Acoust. Soc. Am. **62**, 1463–1466.
Perrott, D. R., and Musicant, A. D. (**1981**). ''Dynamic minimum audible angle: Binaural spatial acuity with moving sound sources,'' J. Aud. Res. **21**, 287–295.
Perrott, D. R., and Strybel, T. Z. (**1997**). ''Some observations regarding motion without direction,'' in *Binaural and Spatial Hearing in Real and Virtual Environments* (Erlbaum, Hillsdale, NJ), Chap. 14, pp. 275–294.
Saberi, K., and Hafter, E. R. (**1997**). ''Experiments in auditory motion discrimination,'' in *Binaural and Spatial Hearing in Real and Virtual Environments* (Erlbaum, Hillsdale, NJ), Chap. 16, pp. 315–327.
Wenzel, E. M. (**1992**). ''Localization in virtual acoustic displays,'' Presence **1**, 80–106.
Yost, W. A., and Hafter, E. R. (**1987**). ''Lateralization,'' in *Directional Hearing*, edited by W. A. Yost and G. Gourevich (Springer-Verlag, New York), pp. 49–84.

Observer weighting of interaural delays in source and echo clicks[a)]

Mark A. Stellmack
Department of Psychology, University of Minnesota, Minneapolis, Minnesota 55455

Raymond H. Dye, Jr. and Sandra J. Guzman
Department of Psychology and Parmly Hearing Institute, Loyola University, Chicago, Illinois 60626

(Received 22 December 1997; revised 18 May 1998; accepted 19 September 1998)

A correlational analysis was used to assess the relative weight given to the interaural differences of time (IDTs) of source and echo clicks for echo delays ranging from 1–256 ms. In three different experimental conditions, listeners were instructed to discriminate the IDT of the source, the IDT of the echo, or the difference between the IDTs of the source and echo. The IDT of the target click was chosen randomly and independently from trial-to-trial from a Gaussian distribution ($\mu = 0$ μs, $\sigma = 100$ μs). The IDT of the nontarget click was either fixed at 0 μs or varied in the same manner as the IDT of the target. The data show that for echo delays of 8 ms or less, greater weight was given to the IDT of the source than to that of the echo in all experimental conditions. For echo delays from 16–64 ms, the IDT of the echo was weighted slightly more than that of the source and the weights accounted for a greater proportion of the responses when the echo was the target, indicating that the binaural information in the echo was dominant over the binaural information in the source. The data suggested the possibility that for echo delays from 8–32 ms, listeners were unable to resolve the temporal order of the source and echo IDTs. Listeners were able to weight the binaural information in the source and echo appropriately for a given task only when the echo delay was 128 ms or greater. © *1999 Acoustical Society of America.* [S0001-4966(99)01601-X]

PACS numbers: 43.66.Pn [DWG]

INTRODUCTION

A. Suppression of binaural information in echoes

When an auditory event is followed, after a very brief delay, by an identical or similar auditory event, such as an echo, spatial information carried by the second event often is suppressed. That is, for a small range of delays between the onsets of the leading and lagging events, localization judgments are dominated by the spatial information in the leading source, and in some cases it might appear that spatial information in the lagging source, or echo, is completely unavailable to the listener. (Note that although the directional information of the echo might be suppressed, the echo can still contribute to the loudness, timbre, or overall spaciousness of the auditory event.) The range of echo delays over which the suppression of spatial information occurs depends upon the type of stimulus, with the shortest range of echo delays for clicks (less than about 4 ms; Gaskell, 1983; Saberi and Perrott, 1990) and a longer range of echo delays for more complex stimuli, such as noise (less than about 20 ms, Zurek, 1980) and speech (also less than about 20 ms; Haas, 1951; Cherry and Taylor, 1954). This dominance of spatial information of the leading source can be demonstrated both in the free-field and in lateralization paradigms (in which stimuli are presented over headphones). At the heart of the ''precedence effect,'' or the ''law of the first wavefront,'' is the basic idea that over some range of short echo delays the binaural information in the leading event appears to be dominant over the binaural information in the lagging event. More recently, dominance of the spatial information of a leading source also has been observed for leading and lagging sources in the median sagittal plane, where interaural differences are minimal (Rakerd and Hartmann, 1992, 1994; Litovsky, Rakerd, Yin, and Hartmann, 1997). (General reviews of the precedence effect may be found in Blauert, 1983 and Zurek, 1987.)

The present paper addresses the relative weight that listeners give to the binaural information in leading and lagging click stimuli that are presented over headphones. In this paper, the leading sound is identified simply as the ''source'' while the lagging sound is identified as the ''echo,'' following the terminology of Yost and Guzman (1996). These experiments examine the artificial situation in which one source and one echo carrying only interaural differences of time are presented to listeners. In separate experimental conditions, listeners are instructed to indicate whether the apparent lateral position of the source or the echo was to the left or right of the midline, or to indicate whether the apparent lateral position of the echo was to the left or right of the source.

B. Weighting of binaural information in noise bursts and trains of clicks

Inherent in any headphone study in which the relative directional strengths of the leading and lagging clicks are assessed by the ''trading'' of information from the two interaural differences of time (IDTs) is the assumption that judgments are based upon single, fused intracranial images

[a)]A portion of these data were presented at the 133rd meeting of the Acoustical Society of America [M. A. Stellmack, R. H. Dye, Jr., and S. J. Guzman, J. Acoust. Soc. Am. **101**, 3083(A) (1997)].

(e.g., Wallach, Newman, and Rosenzweig, 1949; but see the cautionary note in Yost and Soderquist, 1984). The relative magnitudes of the IDTs of the source and echo bursts that produce centered intracranial images (or 50% left/50% right laterality judgments relative to the midline) provide a measure of the weighting given to the source and echo. This idea has been expressed formally in a model by Shinn-Cunningham and her colleagues (Shinn-Cunningham, Zurek, and Durlach, 1993; Shinn-Cunningham, Zurek, Durlach, and Clifton, 1995) for headphone-presented noise bursts and was adopted by Litovsky and Macmillan (1994) for loudspeaker-presented noise bursts. Shinn-Cunningham *et al.* (1993) determined the relative weights given to the binaural information in each of two noise bursts (a source and echo, as the terms are used in this paper) by way of a pointer task in which listeners adjusted the IDT of a noise burst (the pointer) such that its apparent position matched the presumed single intracranial position of the source and echo. Their model assumed that the intracranial image associated with the source and echo occupied a single lateral intracranial position that could be equated to a single effective interaural delay. Shinn-Cunningham *et al.* went on to show that weights estimated in this manner were able to predict the results of a discrimination task reasonably well. However, they also point out that their model is valid only for stimuli that yield single, fused intracranial images.

A number of researchers have looked at the relative influence of binaural information in the individual clicks of a click train. Saberi and Perrott (1995) presented to listeners a click train in which the first click was interaurally delayed to one ear and the remaining clicks were interaurally delayed by the same amount to the other ear. Listeners were instructed to indicate whether the click train appeared to occupy an intracranial position to the left or right of a diotic reference stimulus. In general, for interaural delays from 100–600 μs, listeners' responses were consistent with the interaural delay of the onset click for interclick intervals less than 2 ms, and responses were consistent with the interaural delay of the ongoing train for interclick intervals greater than 4 ms. For interclick intervals between 2 and 4 ms, listeners often reported perceiving two intracranial images related to the interaural delay of the onset and ongoing portions of the click train.

Building upon the study of Saberi and Perrott, Freyman and his colleagues (Freyman *et al.*, 1997) also examined the relative influence of the IDTs in the onset and ongoing portions of pulse trains. In this subjective task, listeners were instructed to position an acoustic pointer at the same intracranial position as that of a pulse train in which the IDT of the onset click differed from those of the remaining clicks in the train. If two intracranial images were perceived, listeners were instructed to point to the ''strongest'' image. In general, the IDT of the onset click had a greater influence on the apparent intracranial position of the click train when the ongoing portion of the train contained conflicting or ambiguous IDTs. The authors note that the binaural information in the ongoing portion of the click train was never completely lost because the configuration of the ongoing portion was critical in determining the extent of onset dominance.

Using a COSS (conditional on a single stimulus) analysis (Berg, 1989), Saberi (1996) estimated the weight given to each click in a train of clicks by assuming that a listener's lateralization judgments are based upon a weighted combination of the IDTs of the individual clicks. Saberi selected the IDTs of all clicks in a train independently from one of two Gaussian distributions that differed in their mean IDT, and listeners were instructed to indicate which distribution was sampled. For all interclick intervals (ICIs) used (1.8, 3, and 12 ms), greatest weight was given to the initial click, but the relative weight given to the initial click decreased as ICI increased. In addition, some listeners gave small but significant weight to one or more clicks after the onset click, even for the shortest ICI. In Saberi's experiments, all clicks in the train were equally informative with respect to the experimental task, and the optimal weighting strategy was one in which the listener weighted all components equally; in effect, using the average IDT of the click train as the decision statistic.

The present paper applies a correlational analysis (Richards and Zhu, 1994; Lutfi, 1995) in order to obtain the relative weights given to source and echo clicks in a lateralization paradigm. One advantage over procedures in which weights are based on the position of the composite image of the source and echo (e.g., Shinn-Cunningham *et al.*, 1993) is that no assumptions need to be made as to the number of intracranial images that might be present. Rather, the IDTs of the source and echo simply are considered to be independent sources of information which the listener weights in some manner to compute a decision statistic upon which responses are based. (This was also true of the COSS analysis performed by Saberi, 1996.) In the present set of experiments, this property of the correlational analysis allows for computation of relative weights in a number of objective tasks that require the listener to weight the binaural information in the source and echo in various ways. In one set of conditions, either the source or echo is identified as the target and the listener is instructed to indicate the direction of the IDT of the target relative to the midline (0-μs IDT) while ignoring the other click. In another set of conditions, the listener is instructed to indicate the direction of the IDT of the echo relative to the IDT of the source. In all conditions, feedback is given that is consistent with the particular task.

I. METHODS

The experimental conditions and data analysis were similar to those of Stellmack and Lutfi (1996), but in this experiment, source and echo clicks (instead of tones of different frequencies) were used as targets and distractors. In addition, in the present experiments, IDTs of the target and distractor were selected from a Gaussian distribution (instead of a rectangular distribution, as in Stellmack and Lutfi, 1996).

Each trial consisted of two intervals, an example of which is shown in Fig. 1. In the first interval, a single diotic click, the cue, was presented. This was intended to mark the intracranial position associated with an IDT of 0 μs. The second interval consisted of a source click and an echo click, which were separated by the echo delay. The echo delay was the time between the onset of the leading click of the source

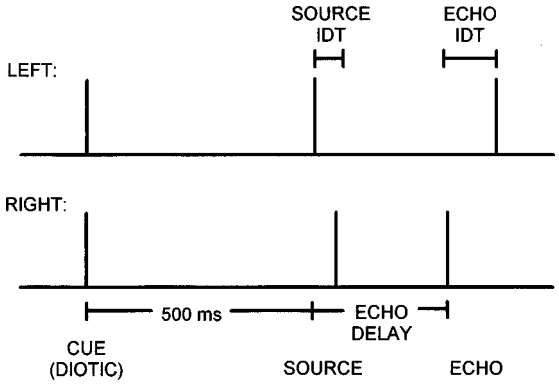

FIG. 1. A representation of a trial in which both the source and echo IDTs were varied. The first interval consisted of a diotic cue, followed by the listening interval, which consisted of a source and echo click with randomly and independently chosen IDTs. The echo delay was fixed for an entire block of trials. In this example, the source leads to the left ear while the echo leads to the right ear. Because the IDTs of the clicks were selected randomly and independently from trial to trial in certain experimental conditions, the directions of the IDTs might be consistent with or opposite to one another on any given trial in those conditions.

and the onset of the leading click of the echo. Data were collected for echo delays of 1, 2, 4, 8, 16, 32, 64, 128, and 256 ms. In addition, the source and echo clicks carried IDTs that were randomly and independently chosen or fixed at 0 μs on each trial, depending on the particular experimental condition. When the IDTs were randomly chosen, they were chosen from a Gaussian distribution with a mean of 0 μs (as described below). Thus, when both the source and echo IDTs were randomly chosen, the clicks might lead to the same ear or opposite ears on a trial-by-trial basis. The cue and listening interval of each trial were separated by 500 ms of silence. All clicks were 50-μs rectangular pulses. The level of a continuous train of clicks (100/s) was calibrated to 52 dB SPL using a digital rms voltmeter (Fluke PM 2525 multimeter). The echo delay and instructions to the listener (described below) were fixed during each 50-trial block. Twenty blocks were presented to listeners for every echo delay in each experimental condition, so that 1000 responses were obtained for each. In all of the conditions described below, feedback that was consistent with the particular experimental condition was given to the listener after each trial.

Listeners were instructed to use the information in the source and echo clicks in a particular way in each experimental condition. In one set of conditions, the source was identified as the target. In this case, the listener was instructed to indicate whether the source click appeared to be to the left or right of the position of the diotic cue by pressing one of two keys on a computer keyboard. The listener was instructed to ignore the apparent position of the second click (echo) when the source was the target. In one condition, the echo IDT was fixed at 0 μs, and in a separate condition the echo IDT was selected randomly from a Gaussian distribution with the same parameters as that of the source. In this latter condition, the source and echo IDTs were selected independently. For convenience, these separate conditions were called ''target-*S*/fixed-*E*'' and ''target-*S*/variable-*E*.''

In another set of conditions, the echo was identified as the target and the listener was instructed to indicate its apparent left/right position relative to the diotic cue while ignoring the apparent position of the first click of the listening interval. As above, the nontarget (source) IDT was fixed at 0 μs in one condition (target-*E*/fixed-*S*), and in a separate condition (target-*E*/variable-*S*) the nontarget IDT was selected from a Gaussian distribution with the same parameters as that of the target.

In another condition, the ''difference'' condition, listeners were instructed to indicate the apparent position of the echo relative to the apparent position of the source. This task was described to listeners in a number of ways. They were instructed to indicate whether the source and echo combination (in the second interval) appeared to move from left to right or right to left, or, equivalently, they were instructed to indicate whether the echo appeared to be to the left or right of the source. Above all, listeners were instructed to use the feedback and to attempt to maximize percent correct. In this condition, the diotic cue may not have been relevant or useful, but it still was presented so that the stimuli were essentially identical to those in the target-*S*/variable-*E* and target-*E*/variable-*S* conditions.

In all conditions, when a click's IDT varied from trial to trial, the IDT was selected randomly from a Gaussian distribution with a mean of 0 μs and a standard deviation of 100 μs, where positive IDTs corresponded to right-ear leading stimuli and negative IDTs corresponded to left-ear leading stimuli. For conditions in which the IDTs of both the source and echo were variable, they were sampled independently from the Gaussian distribution. The IDTs were limited to a range of ± 2.5 standard deviations from the mean (± 250 μs) in order to avoid excessively large IDTs (in order to remain well within the range of IDTs that would be produced by external sound sources due to the geometry of the head, generally ± 600 μs or so). The IDTs were rounded to the nearest multiple of 5 μs so that the IDTs would correspond to integer numbers of digital samples, given the 200-kHz sampling rate that was used. If the randomly chosen IDTs produced a stimulus for which a correct response was undefined (0-μs IDT for the target when the source or echo was defined as the target, or a difference between the IDTs of 0 μs in the difference condition), new IDTs were randomly chosen for the clicks.

As a baseline measure of performance, percent correct was also measured for a single click. In this case, the cue was presented in the first interval of each trial, followed by a single click with its IDT selected in the same manner as those in the variable IDT conditions described above. Listeners were instructed to indicate whether the second click appeared to be to the left or right of the position of the cue.

Stimuli were generated digitally and converted to analog signals by an IBM-compatible PC interfaced with 16-bit digital-to-analog converters (TDT DD1), the output rates of which were set to 200 kHz per channel. The levels of the clicks were adjusted by TDT attenuators (PFA4), and the clicks were low-pass filtered at 7.5 kHz (PF1). The clicks were presented over Sony MDR-V6 headphones to listeners seated in an IAC sound-attenuating chamber.

Before each block of trials, listeners were allowed to listen to practice trials which were like those to be presented during the experimental run. Listeners were instructed to adjust the headphones during the practice trials so that the diotic cue appeared to be centered. When ready, listeners initiated a set of experimental trials by pressing a key on a computer keyboard. Listeners were run during 2-h sessions during which approximately 10–15 50-trial blocks were completed. As stated previously, 1000 trials were run for each echo delay in each condition. All trials of a particular condition were run before trials of another type were presented.

There were 12 listeners in the target-*S* and target-*E* conditions and seven listeners in the difference condition. Due to the unavailability of some listeners, the first author was the only listener common to both groups. All remaining listeners were undergraduate volunteers who were paid to participate in the experiment. The first author was experienced in listening to these types of stimuli and required little training in order to become familiar with the task. The remaining 17 listeners had little or no experience in these types of listening tasks and were run for several thousand trials before data collection began. In addition, listeners were run in one or more blocks of practice trials in each condition before data was collected. Of the 12 listeners who participated in the target-*S* and target-*E* conditions, half of the listeners ran the conditions in the following order: target-*S*/fixed-*E*, target-*S*/variable-*E*, target-*E*/fixed-*S*, and target-*E*/variable-*S*. The remaining listeners ran the conditions as follows: target-*E*/fixed-*S*, target-*E*/variable-*S*, target-*S*/fixed-*E*, and target-*S*/variable-*E*. Within each condition, stimuli were presented from the longest echo delay to the shortest echo delay. The difference condition was run last.

II. RESULTS

A. Computation of observer weights

The data in the present experiments were analyzed by way of the model described by Stellmack and Lutfi (1996) in which the listener's responses are based on a decision variable that is the weighted sum of the IDTs of the individual components (in this case, the source and echo):

$$D = w_S \mathrm{IDT}_S + w_E \mathrm{IDT}_E + \epsilon, \tag{1}$$

where the *w*'s are the observer's weights for the source and echo IDTs (as indicated by the *S* and *E* subscripts), and ϵ is an additive error term encompassing all variability unaccounted for by the weighted IDTs. Responses are assumed to be based on the value of *D* such that listeners respond

$$\text{``left''} \text{ if } D<0; \quad \text{``right''} \text{ if } D>0;$$

$$\text{``left''} \text{ or } \text{``right''} \text{ randomly if } D=0. \tag{2}$$

The relative weight given to the binaural information of a given component [in Eq. (1)] is proportional to the correlation between the trial-by-trial IDTs for that component and the listener's left–right responses. (See Stellmack and Lutfi, 1996.)

In the results reported here, the *magnitudes* (absolute values) of the correlation coefficients were normalized to sum to 1.00 rather than the actual correlation coefficients, and the *sign* of each original correlation coefficient was retained. This was done in order to deal with situations in which negative correlations were obtained. When negative correlations are obtained, normalizing the actual correlation coefficients produces weights beyond the range of -1.00 to $+1.00$. Normalizing the magnitudes of the correlation coefficients more accurately reflects the relative weight given to each component across conditions. The sign of each weight then simply indicates whether the listener's responses were consistent with $(+)$ or opposite to $(-)$ the direction of the IDT of that component.

B. Interpretation of observer weights

In the results that follow, one can consider the weighting strategy used by an ideal observer that performs the task optimally, that is, a ''noiseless'' observer that maximizes percent correct (as in Stellmack and Lutfi, 1996). In the experimental tasks used here, every trial has an unambiguously correct response based on either the IDT of the target or the difference between the IDTs of the source and echo. Thus, an ideal observer that weights the information optimally for a given task will achieve 100% correct. When a human observer fails to achieve 100% correct, one can evaluate the extent to which imperfect performance results from (1) inappropriate weighting of the interaural delays of the source and echo or (2) sources of variability other than the sum of the weighted IDTs.

The listener is said to use an inefficient or nonoptimal weighting strategy when the relative weights for that listener differ from the ideal weighting strategy for a given condition. Given the method of normalizing the observer weights that is used here, the weights will fall in the range from -1.00 to $+1.00$. When the source or echo is identified as the target and the listener is instructed to ignore the nontarget click, the ideal weighting strategy (which maximizes percent correct) is one in which the observer gives the target click a weight of $+1.00$ and the nontarget click a weight of 0.00. Such a weighting strategy will produce 100% correct for the ideal noiseless observer [from Eqs. (1) and (2)]. To the extent that weight is given to the nontarget click, performance will fall below 100% correct. When the listener is instructed to respond to the IDT of the echo relative to that of the source (the difference condition), the ideal weighting strategy is one in which the source and echo are weighted equally but with opposite signs; that is, the echo weight is $+0.50$ and the source weight is -0.50. This weighting strategy will produce 100% correct for an ideal observer in the difference condition. In general, for tasks in which listeners must make comparisons between stimulus elements in order to determine the correct response, the optimal weighting strategy for a particular task includes weights of opposite sign for the relevant parameters of the stimulus components that must be compared.[1]

Even if the human observer uses the optimal weighting strategy, performance (percent correct) will be adversely affected by the presence of other sources of variability [ϵ in Eq. (1)] that are unrelated to the sum of the weighted IDTs. In other words, the relative influence of ϵ in Eq. (1) indicates how well the weighted combination of IDTs alone accounts for the listener's responses. The error term cannot be computed directly, but its influence can be estimated by computing the percentage of the listener's responses that can be predicted by the listener's weights. In order to calculate this percentage, the computed weights were inserted into Eq. (1) and ϵ was set to zero. Simulated responses were obtained by inserting into Eq. (1) the actual IDTs that were presented to the listener on each trial and using Eq. (2) to generate a response. The percentage of simulated responses that agreed with the listener's actual responses (the percentage of responses predicted by the weights) was then computed. This value is inversely related to the relative contribution of ϵ in the decision process. If $\epsilon = 0$, then 100% of the responses can be predicted by the weights. As ϵ becomes large, the percentage of responses predicted by the weights will drop to a lower limit of 50%. Furthermore, the particular weighting strategy that is adopted by the listener becomes irrelevant when the weights predict a very low percentage (near 50%) of the responses. In such cases, the weights have essentially no predictive value (responses are uncorrelated with both the IDT of the source and echo). A comparison of the influence of ϵ across conditions indicates which conditions are influenced to a greater or lesser extent by factors other than the weighted IDTs.

The focus of the present paper is on the relative weight placed on the IDTs of the source and echo. Given that the presence of additive internal noise has essentially no effect on the estimated weights except when the variance of the noise is very large (Richards and Zhu, 1994), little attention is devoted in this paper to the noise term of Eq. (1) other than as an estimate of the predictive value of the weights, as described above. In this paper, the proportion of responses predicted by the weights simply is used as an estimate of the relative influence of factors other than the weighted sum of the interaural delays. One might choose to undertake a more elaborate analysis of the noise in the decision process, such as estimating the magnitude of an additive noise process that would yield results similar to those of the actual listeners. Such an analysis would require additional assumptions, such as the form of the noise process and where the noise is added (e.g., to the interaural delays before weighting, or to the weighted sum of the interaural delays, or both). A detailed analysis of the noise would not change the conclusions of the present paper regarding the relative weight given to the IDTs of the source and echo.

The rationale behind the present analysis is similar to that of multiple linear regression. The variability in the data can be partitioned into that which is attributable to the sum of the weighted IDTs and residual variance that is due to other factors. The main question of the present paper is: Can some portion of the variability in the listener's responses be attributed to the manner in which the listener weights the IDTs of the source and echo clicks? That is, in situations in which a listener performs a task imperfectly (in terms of percent correct), can a greater-than-chance proportion of the listener's responses be predicted by weighting the source and echo IDTs in some nonoptimal manner? Percent correct is the percentage of responses that can be predicted by the optimal weighting strategy for a particular task (for example, giving no weight to the echo when the source is the target). The correlational method used here produces weights that predict a maximal percentage of the listener's responses. Thus, percent correct can never be higher than the percentage of responses predicted by the weights as computed here.

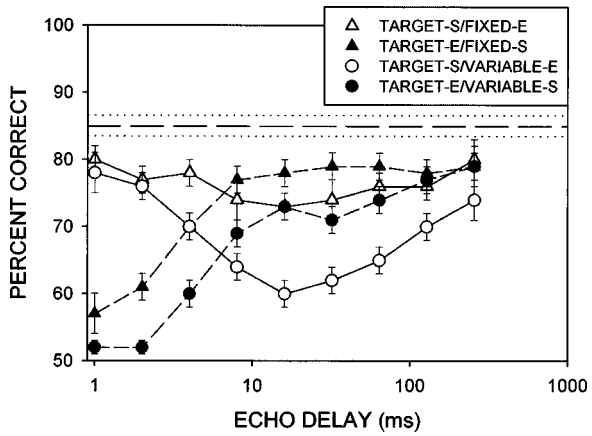

FIG. 2. Percent correct as a function of echo delay in the two target-*S* conditions and the two target-*E* conditions. Percentages have been averaged across 12 listeners. Error bars represent standard errors of the mean. The dashed line at the top of the figure represents mean percent correct for the same 12 listeners in the single-click condition. The dotted lines above and below the dashed line represent ± 1 standard error of the mean.

C. Target-*S* and target-*E* conditions

Because the patterns of results for the 12 listeners were remarkably similar in the target-*S* and target-*E* conditions, the results were averaged across listeners. Figure 2 shows percent correct as a function of echo delay in all of the target-*S* conditions (open symbols) and target-*E* conditions (filled symbols). Triangles represent the conditions in which the nontarget IDT was fixed at 0 μs, and circles represent the conditions in which the nontarget IDT varied. The error bars indicate standard errors of the mean. The dashed and dotted horizontal lines near the top of the panel indicate the average percent correct and ± 1 standard error of the mean, respectively, for these listeners for the single-click condition, in which only the source and no echo was presented during the listening interval of each trial.

The conditions in which the nontarget IDT was fixed at 0 μs are represented by triangles in Fig. 2. In the target-*S*/fixed-*E* condition (open triangles), there is very little effect of echo delay on performance. Percent correct is highest at the longest and shortest echo delays and is approximately 6–7 percent lower in the middle range of echo delays (8–32 ms). There is a much larger effect of echo delay on performance in the target-*E*/fixed-*S* condition (filled triangles). Percent correct is over 20 percent lower at the shortest echo delay than at the longest echo delay. For echo delays of 8 ms and lower, percent correct in the target-*S*/fixed-*E* condition is

much higher than that in the target-*E*/fixed-*S* condition, suggesting that binaural information in the echo is suppressed in these conditions. In these data, the range of delays over which one might conclude that the precedence effect operates (approximately 1–4 ms) is comparable to the range reported elsewhere for click stimuli (e.g., Gaskell, 1983; Saberi and Perrott, 1990).

In the target-*S* and target-*E* conditions, performance was generally poorer when the nontarget IDT varied than when it was fixed at 0 μs. For the target-*S* conditions (open symbols), percent correct was 6–13 percentage points lower when the nontarget IDT varied (circles) than when it was fixed (triangles) for all but the two smallest echo delays. The largest decrement in performance occurred at an echo delay of 16 ms. There was a slightly smaller effect of varying the nontarget IDT in the target-*E* conditions (filled symbols). For all but the two largest echo delays, percent correct in the target-*E* conditions when the nontarget IDT varied (circles) is 5–10 percentage points lower than when the nontarget IDT was fixed (triangles).

The percent correct scores for all conditions containing both a source and echo were lower than that for a single click in isolation. This is true even for conditions in which the nontarget IDT was fixed at 0 μs. All data points in Fig. 2 fall below the horizontal dashed line representing percent correct for a single click. Even at the shortest delay, the mere presence of the echo click had a deleterious effect on performance when listeners made judgments about the source.

In the top panel of Fig. 3, percent-correct scores from the target-*S*/variable-*E* condition (open symbols) and target-*E*/variable-*S* condition (filled symbols) have been replotted from Fig. 2. The middle panel of Fig. 3 shows the average normalized *echo* weights as a function of echo delay for the target-*S*/variable-*E* condition (open symbols) and the target-*E*/variable-*S* condition (filled symbols). (For the conditions in which the nontarget IDT is *fixed*, the relative weights are undefined.) Because the weights were normalized to sum to 1.00, the source weights are simply 1.00 minus the echo weights that are plotted in the middle panel of Fig. 3. Although negative weights are possible, all average weights for both the target and nontarget clicks were positive in these conditions. The bottom panel of Fig. 3 shows the percentage of responses predicted by the weights for the same conditions. The ordinate in the bottom panel has been inverted to reflect the inverse relationship between the percentage of responses predicted by the weights and the relative influence of variance due to factors other than the weighted sum of the IDTs. Thus, higher levels of unexplained variance are represented toward the upper portion of the panel.

As shown in the middle panel of Fig. 3, the relative weight given to the echo (and source) was nearly the same regardless of whether the source or echo was identified as the target for echo delays of 1–32 ms. Very little weight was given to the echo at the shortest echo delay, and the echo weight increases with increasing echo delay. Because the echo weight was independent of which click was identified as the target for echo delays up to 32 ms, it appears that the listeners had little control over the relative weight that was given to the source and echo. For this range of echo delays,

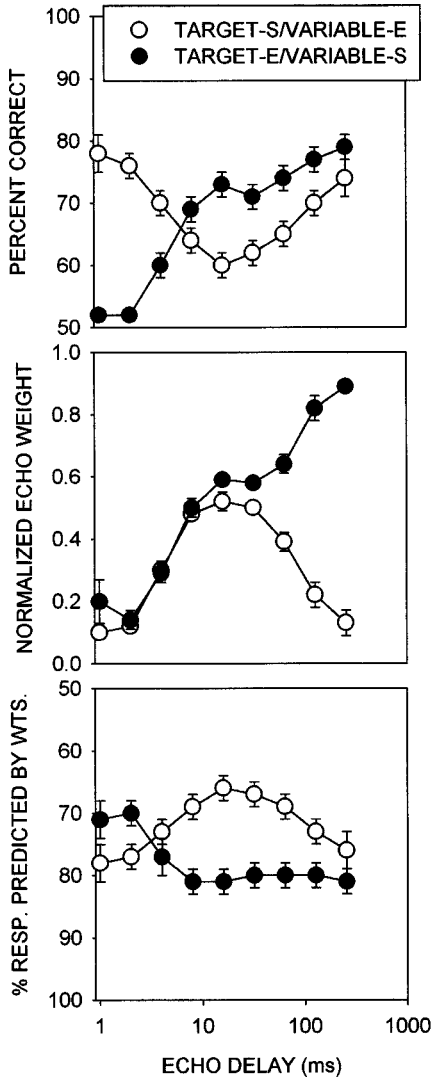

FIG. 3. In the top panel, percent correct is replotted from Fig. 2 for the target-*S*/variable-*E* and target-*E*/variable-*S* conditions. For the same conditions, the middle panel shows the *echo* weight and the bottom panel shows the percentage of responses predicted by the weights, both as a function of echo delay. All data are averaged across 12 listeners. Error bars represent standard errors of the mean.

the listeners approached the optimal weighting strategy only at echo delays of 1 and 2 ms when the source was the target.

For echo delays of 64 ms and larger, the listeners adjusted their weighting strategies appropriately, depending upon which click was the target. At these longer echo delays, the target click was given greater weight than the nontarget click. The relative weight given to the target increased as echo delay increased. However, even at the longest echo delay, 256 ms, small but significant weight was given to the nontarget click.

The percentage of responses predicted by the weights (shown in the bottom panel of Fig. 3) is not constant, which indicates the extent to which responses were based upon the weighted combination of IDTs; that is, the extent to which the amount of unexplained variance in the decision process varied across conditions. For conditions in which the echo was the target (filled symbols), the unexplained variance was greatest at the shortest two echo delays, it decreased to a

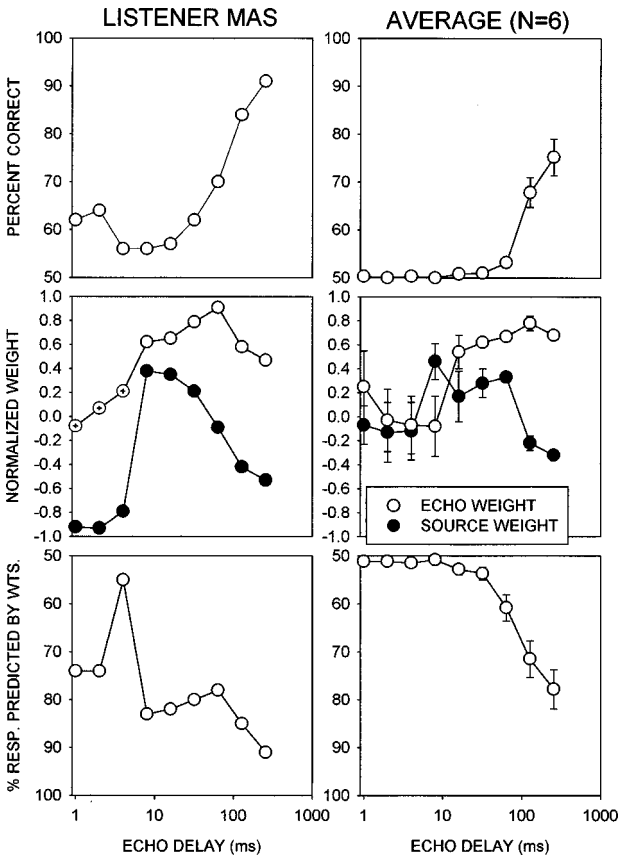

FIG. 4. The results of the difference condition, plotted in the same format as Fig. 3. Results are shown for listener MAS (in the left-hand column) and average data are shown for the remaining six listeners whose results were similar to one another (in the right-hand column). In the middle panel of both columns, open and filled symbols represent echo and source weights, respectively. In the middle panel of the left-hand column, symbols filled with a + represent weights that are not significantly different from zero. In the right-hand column, error bars represent standard errors of the mean.

roughly constant level for echo delays of 8 ms and above. In contrast, in the conditions in which the source was the target (open symbols), the amount of unexplained variance was lowest for the shortest echo delay. The influence of the unexplained variance increased as echo delay increased, and reached a maximum for an echo delay of 16 ms. The influence of the unexplained variance decreased as the echo delay increased above 16 ms.

The fact that performance was only partially affected by the weighting strategy can be seen by comparing the three panels of Fig. 3. For the target-*S* condition (open symbols), percent correct is clearly inversely related to both the echo weight and the amount of additional unexplained variance. Both the echo weight and error variance are at their maximum values where percent correct is at its minimum (echo delay=16 ms). Similarly, percent correct for the target-*E* condition (filled symbols) is directly related to the echo weight and approximately inversely related to the error variance. The increase in percent correct as echo delay increases, with a slight plateau for echo delays of 16–32 ms, is accompanied by a similar increase and plateau in the echo weight. The large increase in percent correct for echo delays from 2–8 ms corresponds to a decrease in the error variance, as well as an increase in the echo weight over the same range of echo delay. Although the echo weight increases sharply for echo delays from 32–256 ms, percent correct increases less rapidly over this range of echo delays than at the shorter echo delays because the level of unexplained variance is approximately constant.

D. Difference condition

The results for the difference condition were somewhat less consistent across listeners. Data for listener MAS (the first author) were qualitatively different than those for the other six listeners, whose data were fairly similar to one another. As a result, data are presented separately for listener MAS in the left-hand column of Fig. 4, while average data are shown for the remaining listeners in the right-hand column of the same figure. The data are presented in the same format as Fig. 3. The magnitudes of the source and echo weights shown in the right-hand column of Fig. 4 do not sum to 1.0 in all cases because the weights have been averaged across listeners, and in several cases some listeners produced positive weights while the remaining listeners produced negative weights. (The magnitudes of the weights for each individual listener first were normalized to sum to 1.0.)

Listener MAS performed above chance at all echo delays in the difference task. Percent correct was lowest for echo delays from 4–16 ms and increased to a maximum as echo delay increased to 256 ms. The percentage of responses predicted by the weights, shown in the bottom panel of the left-hand column of Fig. 4, is greater than chance at all echo delays, and substantially so at all but one echo delay, indicating that performance can be attributed in part to the weighting strategy adopted by this listener.

The weights shown in the middle panel of the left-hand column of Fig. 4 indicate that MAS gave large negative weight to the source IDT and no weight to the echo IDT at echo delays from 1–4 ms. (Symbols filled with a plus sign indicate weights that are not significantly different from 0.00.[2]) In the difference condition, recall that the ideal weighting strategy is one in which the echo and source are given equal weight but with opposite signs, with the source given negative weight. If the binaural information due to the echo IDT is weak or unavailable, it is still possible to perform above chance by simply giving negative weight to the source IDT; that is, by making a left/right response opposite to the direction of the apparent intracranial position of the source. This is because the ''correct'' response is partially (and negatively) correlated with the IDT of the source. It appears that MAS adopted such a strategy for echo delays of 1, 2, and 4 ms, which allowed him to perform above chance even though he gave no weight to the echo IDT.

For echo delays from 8–32 ms, MAS gave significant positive weight to both the source and echo, with slightly greater weight given to the echo. This pattern of weights is somewhat similar to the pattern obtained for the same range of echo delays in the target-*S* and target-*E* conditions shown in Fig. 3. The possibility that the listener was able to resolve the IDTs of the source and echo and was merely confused as to the order of the IDTs is considered in the discussion section below.

MAS weighted the IDTs of the source and echo with the optimal, opposite signs for echo delays of 64 ms and greater, with the magnitudes of the weights nearly equal for echo delays of 128 and 256 ms. The average data from the remaining six listeners (right-hand column of Fig. 4) show the same pattern for the two longest echo delays. In the target-*S* and target-*E* conditions (Fig. 3), the optimal weighting strategy was also most closely approximated for echo delays of 128 and 256 ms. Thus across all of the listening tasks presented here, the source and echo IDTs were weighted optimally and listeners adjusted their weighting strategies appropriately only for echo delays greater than or equal to 128 ms.

The six listeners whose data are averaged in the right-hand column of Fig. 4 experienced much more difficulty in performing the difference task as indicated by both their data and their obvious frustration during the experiment. For echo delays from 1–8 ms, these listeners were unable to perform above chance and their responses were essentially random. The weights accounted for only a chance proportion of the responses, indicating that the responses were uncorrelated with both the source and echo IDTs. For echo delays from 16–64 ms, although these listeners still performed near chance, the weights began to account for an increasing proportion of their responses as echo delay increased. Positive weight was given to both the source and echo IDTs, with slightly greater weight given to the echo IDT, as was the case for MAS. As indicated earlier, the average weighting strategy approached the optimal strategy for the two longest echo delays.

It is possible that the data of MAS were qualitatively different from those of the remaining six listeners in the difference condition due to MAS's previous participation in the target-*S* and target-*E* conditions. However, it is more likely that MAS's performance in the more difficult difference task was due to his extensive experience in listening tasks of this sort. This same listener also showed a greater ability to hear out the IDTs of tones of different frequencies and to adjust his weighting of those IDTs in the results of Stellmack and Lutfi (1996).

III. DISCUSSION

A. Dominance of the source at short echo delays

Generally, for the conditions in the present study that are most similar to conditions in previous studies of the precedence effect (i.e., fixed nontarget click, and echo delays of 8 ms or less), the results are consistent with those of the previous studies. Binaural information in the source click was given vastly greater weight than that of the echo click. Inspection of percent-correct scores seems to suggest that binaural information in the echo click was almost completely suppressed at these short echo delays. However, echo IDTs still had a small effect even at the shortest echo delays. Performance in the target-*E* conditions was significantly better when the source did not vary, indicating that the binaural information in the echo was accessible to some small extent, although clearly the information in the source was dominant.

In the present series of experiments, it was not completely surprising that the echo click had a small influence on lateralization judgments even at the shortest echo delays. Wallach *et al.* (1949) found that lateralization of a source click was influenced by the presence of an echo click for an echo delay of 2 ms, while Gaskell (1983) observed the same effect for echo delays from 50 μs to 2 ms. Shinn-Cunningham *et al.* (1993) observed in many cases that some small weight was given to the binaural information in a lagging noise burst for echo delays of 1 and 10 ms. Litovsky and Macmillan (1994) also showed that a small amount of weight was given to binaural information in a lagging noise burst with an echo delay of 4 ms. Saberi (1996) found that significant weight sometimes was given to the second click in a train of clicks when the time between clicks was as small as 1.8 ms. Freyman *et al.* (1997) showed that the degree of interaural ambiguity in the ongoing portion of a click train affects the extent to which the initial click in a click train dominates lateralization. As stated earlier, the authors pointed out that later-arriving binaural information in their click trains must not have been completely lost because lateralization judgments for the entire click train were partially dependent on the binaural configuration of the ongoing portion. Saberi and Perrott (1990) showed that the precedence effect almost completely disappears with practice for some subjects, indicating that the binaural information in the echo clicks must be available to listeners. The evidence suggests that binaural information in echoes is available to the auditory system to some extent even at very short echo delays. In addition, the shortest echo delay used in the present experiments (1 ms) is approximately the upper limit of the range of delays at which summing localization is observed (e.g., Blauert, 1983), so this effect may have resulted in weight being given to the echo at the 1-ms echo delay.

For source and echo click pairs at very short echo delays, there is evidence that listeners' left–right responses are based upon interaural spectral differences that are produced when the source and echo click carry different interaural delays (Gaskell, 1983; Tollin and Henning, 1998). For such stimuli, differences between the spectra of the left–and right-ear signals result simply because the temporal gap between the source and echo clicks is different in the two ears (due to the different interaural delays of the source and echo). It has been shown that for very short echo delays (less than about 2 ms), the interaural spectral differences produced by interaurally delaying either the source or echo click (rather than the interaural delay itself) can account for listeners' responses to source and echo clicks. These results provide additional evidence that the directional information in echoes is not suppressed at echo delays as small as 1–2 ms.

B. Identification of temporal order at longer echo delays

While the results obtained at very short echo delays were consistent with the results of previous studies of the precedence effect, the large amount of interference between the source and echo clicks was unexpected at the longer echo delays. Most often, studies of the precedence effect utilize stimuli in which the binaural information of the nontarget (either the source or echo) is fixed and listeners must detect a change in the binaural information of the target. (Shinn-

Cunningham *et al.*, 1993, and Saberi, 1996, are two exceptions.) Rarely is the binaural information of both the source and echo varied within the same block of trials, and it is necessary to do so in order to observe the type of interference seen in the present experiment. Although percent correct is lower when the nontarget IDT is fixed (as in the target-*S*/fixed-*E* and target-*E*/fixed-*S* conditions) relative to percent correct for a single click, an additional large decrement in performance occurs when the nontarget IDT varies from trial-to-trial (as in the target-*S*/variable-*E* and target-*E*/variable-*S* conditions).

Interestingly, Shinn-Cunningham *et al.* (1993) estimated source and echo weights based on the data of Zurek (1980), and showed results that might predict interference between the source and echo for echo delays as long as 80 ms. In the original experiments (Zurek, 1980), listeners positioned an acoustic pointer at the same apparent intracranial position as a source–echo combination of continuous noise low-pass filtered at 2 kHz. The source (leading noise) had an interaural delay of 330 μs to one ear and the echo (lagging noise) had an interaural delay of 330 μs to the opposite ear. (There was no interaural delay of the onset or offset in Zurek's stimuli.) The subsequent analysis (Shinn-Cunningham *et al.*, 1993, Fig. 8) suggests that substantial weight was given to the echo IDT for all echo delays up to 80 ms. However, such interference was not evident in the pointer adjustments at these long echo delays in the original data and this issue was not pursued. The analysis of Zurek's data never indicated that the echo was given greater weight than the source while the present data did show greater echo weights for comparable echo delays, but it must be emphasized that different stimuli were used in the two experiments.

In the target-*S* and target-*E* conditions, for echo delays from 16–64 ms, the subjective impressions of the listeners suggested the possibility that the IDTs of the source and echo were resolved, but that there was confusion as to the order in which the IDTs occurred; that is, there was trial-by-trial confusion as to which click was the target. This would be evidenced in the data of both the target-*S*/variable-*E* and target-*E*/variable-*S* conditions by (1) equal weights for the two clicks, (2) a relatively large amount of unexplained variance, and (3) relatively low percent correct. In the present data, these three trends were observed in the target-*S*/variable-*E* condition for the middle range of echo delays. However, for the target-*E*/variable-*S* condition for the same range of delays, slightly greater weight was given to the echo, there was minimal error variance, and percent correct was substantially higher than in the target-*S*/variable-*E* condition. These results suggest that the binaural information in the echo is, in fact, dominant over that in the source at the middle range of echo delays.

In the difference condition, in order to perform optimally, listeners needed to resolve the IDTs of the source and echo and to determine their correct temporal order. The data show that the listeners did not weight the IDTs of the source and echo optimally for the middle range of delays. Once again, one can consider the possibility that the information due to the IDTs of the clicks was separable but that the listeners could not determine the correct temporal order of the IDTs for this range of delays. One way in which the listeners might handle such confusion is to randomly give one IDT positive weight and the other IDT negative weight on a trial-by-trial basis. If that were the case, the data computed over all trials would show (1) zero weight for the source and echo, (2) a large amount of unexplained variance (which is necessarily the case when both weights are zero), and (3) chance performance. In fact, in the present data, MAS gave significant positive weight to both the source and echo, and exhibited a very small amount of error variance for echo delays from 8–32 ms. The remaining listeners displayed poor performance and large amounts of unexplained variance over the same range of delays, but they also gave positive weight to both the source and echo IDTs. This is not consistent with the notion that the listeners gave positive and negative weight to the two IDTs in a random fashion from trial to trial.

Considering further the data for the middle range of echo delays, if listeners were confused as to the temporal order of the IDTs in the difference condition, suppose that rather than randomly weighting one IDT positively and the other negatively, listeners made responses consistent with the IDT of only one click and disregarded the IDT of the other click. Furthermore, if each response was based upon the IDT with the larger magnitude on a particular trial, this would result in (1) nearly equal positive weights for both the source and echo and (2) small amounts of error variance, when computed over all trials. The data for MAS in Fig. 4 are somewhat consistent with such a strategy but, even so, the echo IDT was given greater weight overall than the source IDT in the middle range of echo delays.

Note that in the target-*S*/variable-*E*, target-*E*/variable-*S*, and difference conditions, the stimuli were statistically identical. The conditions differed only in the instructions given to the listeners. Therefore, listeners would have attained maximum performance in all of these conditions (for a given level of additional unexplained variance) only if they adjusted their weighting strategy so that it was optimal for each experimental condition. A description of the ability of listeners to change their strategies for using the source and echo IDTs in different tasks (e.g., to change weights to the optimal weights for a given task, as discussed above) illustrates the extent to which the binaural information in the two clicks is truly separable. Only at the two longest echo delays, 128 and 256 ms, were the listeners able to approximate the ideal weighting strategy in all of the listening tasks. For echo delays of 64 ms and less, there was substantial interaction between the source and echo in all conditions, such that listeners appeared to be unable to adjust their weighting strategy to the task demands. The source was generally dominant for echo delays of 1–8 ms, but the binaural information in the echo had slightly greater influence for echo delays from 16–64 ms regardless of the instructions and feedback given to listeners.

The present results, which show that listeners might have difficulty in judging the temporal order of interaural delays of a source and echo click for an intermediate range of echo delays, are consistent with an observation made by Wallach *et al.* (1949, experiment 5). Their listeners could

separately lateralize a source and echo click for an echo delay of 10 ms, but the listeners often had difficulty in telling which sound was heard first. The experimenters did not follow up on this observation because their primary interest was in conditions in which the source and echo were perceptually fused into a single auditory event (i.e., an echo delay of 2 ms).

One might suspect that judgments of temporal order of binaural information require larger temporal separations than judgments of temporal order for monaural sources of information, due to the apparent ''sluggishness'' of the binaural system (e.g., Grantham and Wightman, 1978). However, the sluggishness of the binaural system most likely influences the *detection* of a nonzero IDT of one click in the presence of another (as in the fixed nontarget conditions) when their temporal separation is small. In the present experiments, the judgment of temporal order (as in the variable nontarget and difference conditions) is poor even when the IDT of either the source or echo can be detected (as indicated by relatively better performance in the fixed nontarget conditions), so it would seem that binaural sluggishness is not the sole determinant of the ability to judge the temporal order of binaural information.

More likely, the present results are related to the effects of the spatial separation of auditory streams on perceptual segregation of those streams (Bregman, 1990). For example, it has been observed that when sequences of 100-ms tones are perceptually segregated on the basis of the ear to which they are presented, listeners have great difficulty in making judgments of the temporal order of events across the segregated streams (Judd, 1979). (In contrast, the temporal order of monaurally presented tones can be identified correctly for durations less than 10 ms in some cases, e.g., Divenyi and Hirsh, 1974.) On the basis of these previous observations, one might predict that listeners in the present experiments would be unable to identify the temporal order of the interaural delays of two clicks at echo delays up to 100 ms even though the interaural delays are perceptually separable. In fact, the results of Judd (1979) would suggest that listeners would have even greater difficulty in judging the temporal order of a source and echo click as the apparent spatial separation of the clicks increases (for example, if their mean IDTs were unequal). The method used in the present paper essentially produces weights that are averaged over the range of possible IDTs for each click. In order to determine if the relative weights vary with changes in the relative IDTs of the clicks, it would be necessary to compute weights for conditions in which the mean IDT of the source differs from that of the echo. (Recall that in the present experiment, the mean IDTs of the source and echo were always 0 μs.)

Although nonoptimal performance in the target-*S*/variable-*E*, target-*E*/variable-*S*, and difference conditions may have been partially due to confusion as to the temporal order of the IDTs of the clicks, it should be noted once again that performance was also worse in the conditions in which the nontarget click was fixed (target-*S*/fixed-*E* and target-*E*/fixed-*S*) relative to the baseline condition in which a single click was presented in each trial. It is difficult to attribute such a decrement in performance to confusion as to the temporal order of the IDTs in the two-click conditions because one of the IDTs was always fixed at 0 μs. If the IDTs of both clicks were resolved and separable in the target/fixed conditions, the listener merely had to respond to the nonzero IDT without regard to the temporal order of the IDTs. This suggests that at all echo delays studied in this experiment, there is interference or interaction between the source and echo IDTs beyond that due to confusion as to their temporal order.

C. Possible cues for reducing temporal order confusion

The precedence effect generally is posited as a mechanism which allows the auditory system to localize sound sources accurately in reverberant environments by suppressing the potentially conflicting cues that can be present in echoes. The data of this paper and those discussed in the introduction show that for click stimuli, the influence of binaural information in echoes is severely reduced when the echo follows the source by less than about 8 ms. However, the present data also show that there is substantial interference produced by the simulated echo in a lateralization task over a range of longer delays of approximately 16–64 ms. Over this range of delays, the binaural information of the echo appears to be slightly dominant over the binaural information of the source. This interference had not been seen previously because of the type of stimuli used in other experiments studying the precedence effect (stimuli containing small echo delays and/or fixed nontarget stimuli). Reverberation times of 16–64 ms are not uncommon in real environments, and the directions of reverberations are usually unpredictable or change as the listener or source moves. Thus, the ability to suppress binaural information in echoes at short echo delays might be a useful mechanism by which sound sources can be localized in small spaces, but there appears to be a much larger range of echo delays over which the echo might interfere substantially with the ability to localize the source, particularly when the direction of the echo is unexpected or unpredictable. (Although the present paper deals with binaural information, accurate localization of a source in the presence of echoes would require the listener to suppress the directional information associated with the echoes in general, regardless of whether that directional information is binaural or monaural in origin.)

In real-world listening situations, certain monaural aspects of the source and echo, such as differences between their intensities and spectra, might provide additional cues for segregating the binaural information in the source and echo. Echoes often arrive at a listener's ear at a lower level than the source due to the longer distance traveled by the echo. In addition, high frequencies in echoes may be attenuated relative to the source due to absorption by air, or high and low frequencies in the echo might be attenuated differentially depending on the absorptive properties or physical dimensions of the reflecting surface. It is possible that these additional cues for segregating sources from echoes would reduce the interference that was observed over an intermediate range of echo delays, in the same way that Freyman *et al.* (1997) showed that spectral differences between onset and ongoing noise bursts can reduce the dominance of the onset

noise burst. It remains to be seen whether interference effects such as those observed in the present results occur in the localization of sources and echoes in free-field listening situations where these potential cues for segregation are naturally present.

ACKNOWLEDGMENTS

This work was supported by a program project grant from the National Institute on Deafness and Communication Disorders (P01 DC00293) and a grant from AFOSR, both to the Parmly Hearing Institute. This work was also supported by research grant No. R01 DC 00683 from the National Institute on Deafness and Communication Disorders, National Institutes of Health. The authors would like to thank Dr. Robert Lutfi, Dr. Ewan Macpherson, and Dr. Pavel Zahorik for their helpful discussions related to the material herein. The authors would also like to thank Dr. Wes Grantham, Dr. Daniel J. Tollin, and an anonymous reviewer for making critical comments that resulted in a stronger and clearer manuscript.

[1]It is possible that the actual weights used by the listener vary in some way that is dependent upon the IDTs presented in each trial. For example, Shinn-Cunningham *et al.* (1993) found evidence in some conditions that the weights for some listeners varied with the difference between the IDTs of the source and echo. The present correlational analysis would ''average over'' such variation, providing a single pair of weights for the entire of range of IDTs applied to the source and echo. There are several reasons to suspect that variation of the weights with the difference between the IDTs plays little if any role in the present data: (1) If the weights vary with the difference between the IDTs, this would produce a nonlinear decision boundary through the matrix of responses (such as the matrices shown in Stellmack and Lutfi, 1996, Fig. 1). In no condition of the present experiment was any such nonlinearity evident in visual inspections of the response matrices. (2) In the present experiments, the range of IDTs was half that used by Shinn-Cunningham *et al.* (1993), so any dependence of the weights on the difference between the IDTs would most likely have a smaller effect than that observed by Shinn-Cunningham *et al.* (3) The same range of IDTs was applied to the source and echo in all conditions of the present experiments, so any IDT-dependent variation in weights would presumably be present in all conditions. Therefore, if a larger weight is computed for the echo (for example) in certain conditions, then this truly reflects a greater influence of the echo IDT in these conditions.

[2]The statistical significance of individual weights can be tested given the fact that the standard error of the correlation coefficient, ρ, is $1/\sqrt{n}$, where n is the number of trials. Here, tests of the statistical significance of individual weights are based upon the 0.05 level of significance.

Berg, B. G. (**1989**). ''Analysis of weights in multiple observation tasks,'' J. Acoust. Soc. Am. **86**, 1743–1746.

Bregman, A. S. (**1990**). Auditory Scene Analysis (MIT, Cambridge, MA).

Blauert, J. (**1983**). Spatial Hearing (MIT, Cambridge, MA).

Cherry, E. C., and Taylor, W. K. (**1954**). ''Some further experiments upon recognition of speech with one and with two ears,'' J. Acoust. Soc. Am. **26**, 554–559.

Divenyi, P. L., and Hirsh, I. J. (**1974**). ''Identification of temporal order in three-tone sequences,'' J. Acoust. Soc. Am. **56**, 144–151.

Freyman, R. L., Zurek, P. M., Balakrishnan, U., and Chiang, Y.-C. (**1997**). ''Onset dominance in lateralization,'' J. Acoust. Soc. Am. **101**, 1649–1659.

Gaskell, H. (**1983**). ''The precedence effect,'' Hearing Res. **11**, 277–303.

Grantham, D. W., and Wightman, F. L. (**1978**). ''Detectability of varying interaural temporal differences,'' J. Acoust. Soc. Am. **63**, 511–523.

Haas, H. (**1951**). ''The influence of a single echo on the audibility of speech,'' Journal of the Audio Engineering Society **20**, 146–159.

Judd, T. (**1979**). ''Comments on Deutsch's musical scale illusion,'' Percept. Psychophys. **26**, 85–92.

Litovsky, R. Y., and Macmillan, N. A. (**1994**). ''Sound localization precision under conditions of the precedence effect: Effects of azimuth and standard stimuli,'' J. Acoust. Soc. Am. **96**, 752–758.

Litovsky, R. Y., Rakerd, B., Yin, T. C. T., and Hartmann, W. M. (**1997**). ''Psychophysical and physiological evidence for a precedence effect in the median sagittal plane,'' J. Neurophysiol. **77**, 2223–2226.

Lutfi, R. A. (**1995**). ''Correlation coefficients and correlation ratios as estimates of observer weights in multiple-observation tasks,'' J. Acoust. Soc. Am. **97**, 1333–1334.

Rakerd, B., and Hartmann, W. M. (**1992**). ''Precedence effect with and without interaural differences—Sound localization in three planes,'' J. Acoust. Soc. Am. **92**, 2296.

Rakerd, B., and Hartmann, W. M. (**1994**). ''More on the precedence effect in three planes,'' J. Acoust. Soc. Am. **95**, 2917.

Richards, V. M., and Zhu, S. (**1994**). ''Relative estimates of combination weights, decision criteria, and internal noise based on correlation coefficients,'' J. Acoust. Soc. Am. **95**, 423–434.

Saberi, K. (**1996**). ''Observer weighting of interaural delays in filtered impulses,'' Percept. Psychophys. **58**, 1037–1046.

Saberi, K., and Perrott, D. R. (**1990**). ''Lateralization thresholds obtained under conditions in which the precedence effect is assumed to operate,'' J. Acoust. Soc. Am. **87**, 1732–1737.

Saberi, K., and Perrott, D. R. (**1995**). ''Lateralization of click-trains with opposing onset and ongoing interaural delays,'' Acustica **81**, 272–275.

Shinn-Cunningham, B. G., Zurek, P. M., and Durlach, N. I. (**1993**). ''Adjustment and discrimination measurements of the precedence effect,'' J. Acoust. Soc. Am. **93**, 2923–2932.

Shinn-Cunningham, B. G., Zurek, P. M., Durlach, N. I., and Clifton, R. K. (**1995**). ''Cross-frequency interactions in the precedence effect,'' J. Acoust. Soc. Am. **98**, 164–171.

Stellmack, M. A., and Lutfi, R. A. (**1996**). ''Observer weighting of concurrent binaural information,'' J. Acoust. Soc. Am. **99**, 579–587.

Tollin, D. J., and Henning, G. B. (**1998**). ''Some aspects of the lateralization of echoed sound in man. II: The role of the stimulus spectrum,'' J. Acoust. Soc. Am. **104**, 3030–3038.

Wallach, H., Newman, E. B., and Rosenzweig, M. R. (**1949**). ''The precedence effect in sound localization,'' Am. J. Psychol. **52**, 314–336.

Yost, W. A., and Guzman, S. J. (**1996**). ''Auditory processing of sound sources: Is there an echo in here?,'' Current Directions in Psychological Science **5**, 125–131.

Yost, W. A., and Soderquist, D. R. (**1984**). ''The precedence effect: Revisited,'' J. Acoust. Soc. Am. **76**, 1377–1383.

Zurek, P. M. (**1980**). ''The precedence effect and its possible role in the avoidance of interaural ambiguities,'' J. Acoust. Soc. Am. **67**, 952–964.

Zurek, P. M. (**1987**). ''The precedence effect,'' in *Directional Hearing*, edited by W. A. Yost and G. Gourevitch (Springer, New York).

Masking with interaurally delayed stimuli: The use of "internal" delays in binaural detection

Marcel van der Heijden and Constantine Trahiotis
Surgical Research Center, Department of Surgery (Otolaryngology) and Center for Neurological Sciences, University of Connecticut Health Center, Farmington, Connecticut 06030

(Received 12 December 1997; revised 19 May 1998; accepted 26 September 1998)

Detectability of 500-Hz tones was measured in the presence of broadband masking noise using three types of binaural conditions. In the first, the masker was presented diotically and the tone was interaurally delayed. In the second, the masker was interaurally delayed and the 500-Hz tone was presented either in phase (S0) or out of phase ($S\pi$). In the third, the masker consisted of the sum of two independent noises having interaural delays of equal magnitude and opposite sign. The signal was, once more, presented either in phase (S0) or out of phase ($S\pi$). Comparisons among the data and quantitative analyses assuming the use of compensatory ''internal delays'' suggested that internal delays are operative and compensate accurately for external delays of up to approximately 750 μs. The analyses also indicated that larger internal delays (i.e., up to 2 to 3 ms) are probably also operative. However, performance using such large internal delays appears to be degraded in accord with the hypothesis that their application introduces ''noise'' in the internal representation of the stimuli. [S0001-4966(99)03001-5]

PACS numbers: 43.66.Pn, 43.66.Dc, 43.66.Ba [DWG]

INTRODUCTION

Numerous investigations of the auditory system have validated Jeffress' postulation (Jeffress, 1948) of an internal delay mechanism that allows for the processing of stimulus-imposed, external, interaural delays. Currently, there are anatomical and physiological data that confirm the existence of neural elements within the central auditory system that appear to provide a functional implementation of Jeffress' conception (Kuwada *et al.*, 1997). Further, a stage of processing involving internal delays is an integral part of modern models of binaural hearing dealing with localization, lateralization, and detection based on binaural information (e.g., Colburn and Durlach, 1978; Durlach *et al.*, 1982; Stern and Trahiotis, 1992). Of particular interest for this investigation is Durlach's equalization-cancellation (Durlach, 1963, 1972) model of binaural detection. Within that model, stimuli containing external delays are ''equalized'' by internal delays.

The purpose of this study was to investigate the contribution of internal delays to binaural detection. In order to do so, we compared performance using three types of stimulus conditions containing an external interaural delay. In one type of condition (termed N0Sτ), a tonal *signal* was interaurally delayed and a broadband masking noise was presented diotically. For this stimulus configuration, internal delays are expected to play no role. In another type of condition, the *masker* was interaurally delayed and the signal was presented either interaurally in phase (NτS0) or interaurally out of phase (NτSπ). For this type of stimulus configuration, internal delays could play a role. Both of these stimulus conditions have been used in the past (e.g., Jeffress *et al.*, 1962; Langford and Jeffress, 1964).

In a third, novel, type of condition, we employed two simultaneous, independent sources of masking noise having identical magnitudes of interaural delay that were opposite in sign. That is, in this type of condition, which we will refer to as the ''double-delay'' condition, one source led in the left ear and the other source led in the right ear. As was true in the former ''single-delay'' conditions, the signal was presented either interaurally in phase or interaurally out of phase. An important characteristic of the double-delay conditions is that, because *two independent* noises are simultaneously present, internal delays cannot be used to compensate for external delays. In order to understand why this is so, assume that an internal delay is applied to equalize and subsequently cancel *one* of the independent noise components of the double-delay stimulus. Doing so, however, results in the interaural delay of the other, independent, noise component being *doubled* rather than being compensated. Subsequent subtraction of the two channels will lead to complete elimination of the first component of noise. However, this apparent advantage will be counteracted by the effect of the subtraction on the power of the second component of noise. Depending on the magnitude of the double delay applied to the stimulus, the power of the second noise component might be reduced or increased. In some cases, a net reduction in the power of the combined components may result from the equalization of one of the components. However, a detailed analysis of the cross-correlation functions of double-delayed maskers revealed that, in *all cases that lead to an appreciable binaural advantage*, this advantage is smaller than that obtained by a direct subtraction or summation of the two channels without the imposition of any ''compensating'' internal delay. Such direct subtraction or summation without the imposition of any internal delay always results in *both* noise components being partially reduced, if not fully eliminated. Thus, maximizing the binaural release from masking in the double-delay conditions necessitates that no internal delay be applied.

Although it is not necessarily intuitively obvious, it is the case that the interaural correlation of maskers in the

single- and double-delay conditions is identical for any particular magnitude of interaural delay. Thus, predictions of detection performance based strictly on binaural correlation *coefficients* would be identical for these two types of stimuli. However, if compensatory internal delays are utilized (and perhaps if the cross-correlation function rather than the correlation coefficient is relevant for detection), then detection in the single-delay condition would be better than in the corresponding double-delay condition.

A comparison of data obtained when the *signal* was delayed ($N0S\tau$) with data obtained when the *noise* was delayed in the single-delay conditions ($N\tau S0$ and $N\tau S\pi$) also sheds light on the use of internal delays. To the degree that internal delays precisely compensate for external delays, performance should be equivalent for these two types of stimuli because internal delays would transform the differing types of stimuli into effectively identical internal representations. However, if performance when the noise is delayed is *inferior* to performance when the signal is delayed by the same amount, then we would have rather direct evidence that delays of such magnitude cannot be internally compensated.

It will be seen that comparisons among the data suggest that binaural detection is mediated by a limited range of internal delays. Although internal delays smaller than 750 μs or so appear to be used without appreciable processing errors, quantitative analyses suggest that utilization of larger internal delays entails inaccuracies that degrade binaural processing.

I. EXPERIMENT

A. Procedure

Detection of 500-Hz tones was measured in the presence of 900-Hz-wide Gaussian noise that was centered at 500 Hz and presented at an overall level of 75 dB SPL (spectrum level equivalent to 45.5 dB SPL). The total duration of the noise was 300 ms (including 10-ms, cosine-squared, rise/decay times). The signals were 280 ms long (including 10-ms, cosine-squared, rise/decay times) and were temporally centered within the maskers. All stimuli were generated digitally with a sampling rate of 20 kHz via an array processor (Tucker-Davis Technologies AP2). The noises were constructed as follows. Amplitudes of the spectral components within the passband were drawn from a Raleigh distribution; phases were choosen from a uniform distribution. Inverse fast Fourier transforms (FFTs) yielded 32 768 points in the time domain. This yielded 1.64-s-long buffers of noise from which segments were randomly chosen in a manner that provided essentially independent waveforms in each interval of the psychophysical task. New, independent buffers were generated for each experimental run.

The tonal signals were generated in the time domain and added to the noise waveforms prior to D/A conversion. All stimuli were low-pass filtered at 8.5 kHz (TDT FLT2) and presented via TDH-39 earphones (mounted in MX/41-AR cushions) to listeners seated in single-walled, IAC booths. Three young adults, two male and one female, with no evidence or history of hearing loss served as listeners. All listeners received extensive practice before the collection of data began.

The stimuli were presented in a two-cue, two-alternative, forced-choice task. Each trial consisted of a warning interval (300 ms) and four 300-ms observation intervals separated by 400 ms. Intervals were marked by a visual display on a computer monitor. The first and fourth intervals contained only the masker. The signal was presented with equal *a priori* probability in either the second or the third interval. The remaining interval, like the first and fourth intervals, contained only the masker. Masker waveforms were randomly chosen both within and across trials. Correct-answer feedback was provided after each response.

The level of the signal was varied adaptively in order to estimate 70.7% correct (Levitt, 1971). The initial step size of the adaptive track was 4 dB and was reduced to 2 dB and to 1 dB after two reversals occurred at each of the former step sizes. A run was terminated after 12 reversals using the 1-dB step size and estimates of threshold were calculated using the average level of the signal across the last 10 reversals. Final thresholds were calculated by averaging three estimates of threshold for each listener and for each stimulus condition.

As mentioned in the Introduction, three types of conditions, differing in the binaural presentation of the stimuli, were employed. In the first type of condition (termed $N0S\tau$), the *signal* was interaurally delayed from 0 to 1000 μs in steps of 125 μs and the masker was presented diotically. In the second type of condition, the *masker* was interaurally delayed from 0 to 4125 μs in steps of 125 μs and the signal was presented either interaurally in phase ($N\tau S0$) or interaurally out of phase ($N\tau S\pi$). This will be referred to as the ''single-delay'' condition. In the third type of condition, we mixed two simultaneous, independent sources of masking noise having identical magnitudes of interaural delay of opposite sign. This will be referred to as the ''double-delay'' condition. Once more the magnitudes of interaural delays ranged from 0 to 4125 μs in steps of 125 μs and the signal was presented either interaurally in phase or interaurally out of phase.

All possible combinations of type of condition, interaural phase of the signal, and magnitude of interaural delay were tested once in random order. Then, the strategy of visiting all of the conditions once exhaustively was used twice more utilizing two new random orders.

B. Results and discussion

We proceed in the following way. First, we present detection thresholds obtained when the *signal* was interaurally delayed. Then we show that these thresholds are very well accounted for by using a noise-cancellation approach similar to that of Durlach (1963). Next, we present detection thresholds obtained when the *noise* was interaurally delayed in the single-delay conditions. We then compare those thresholds to the thresholds obtained when the *signal* was delayed in order to assess how efficiently internal delays could have been utilized in the single-delay conditions. Next, we present detection thresholds obtained in the double-delay conditions. We then compare those thresholds to the thresholds obtained in the single-delay conditions in order to assess how effi-

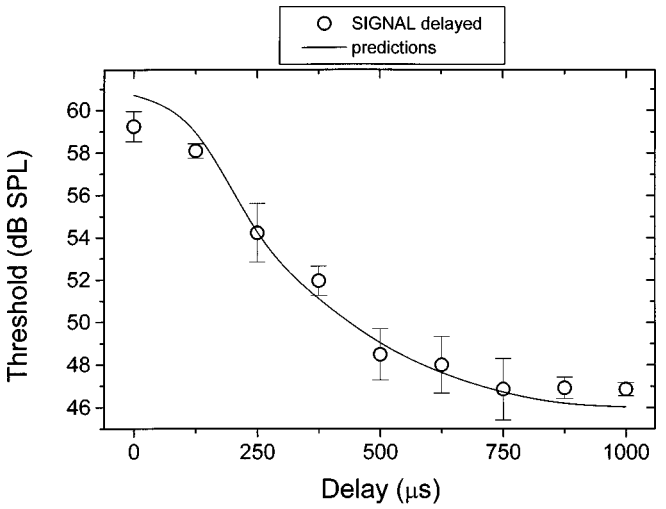

FIG. 1. Average thresholds of the three listeners in the N0Sτ condition (circles). Error bars indicate across-listener standard errors. The solid line shows thresholds predicted by a cancellation model (see text).

ciency of detection changes when internal delays *cannot* be utilized to compensate for external delays. After the data have been analyzed in this manner, we address quantitatively how efficiently internal delays can be used, as a function of external delay. Finally, we show that all of our data can be accounted for by an equalization-cancellation model that takes into account the processing bandwidth of the listener and the limited accuracy with which internal delays can be applied. We wish to emphasize that all of the modeling presented in this paper represents a general approach pioneered by Durlach (1963) that has been augmented by the postulation of a ''noisy'' internal delay mechanism.

The thresholds obtained when the noise was diotic and the signal was interaurally delayed (N0Sτ thresholds) are plotted in Fig. 1. The data points represent the mean of the thresholds of three listeners. Error bars indicate ± one standard error of the mean. The highest threshold was found when the delay was 0 μs. This was expected because that stimulus condition is diotic (N0S0) and provides no binaural information. The lowest thresholds occurred for delays approaching a value of 1000 μs. This was also expected because a delay of 1000 μs of the 500-Hz signal results in an N0Sπ condition for which listeners are commonly found to have the lowest threshold. The differences between N0S0 and N0Sπ thresholds (i.e., the masking level difference, or MLD) was 13 dB. This is a value commonly found in studies employing a low-frequency tone masked by a broadband noise (e.g., Durlach and Colburn, 1978) and a MLD of that size indicates that our listeners were adept at performing the tasks.

The data indicate that the thresholds decrease sharply as increasing interaural delays of the signal are imposed and that thresholds appear to level off for the larger interaural delays. This patterning of thresholds is in agreement with the findings of earlier studies that also employed an N0Sτ condition (Jeffress *et al.*, 1952). No data were obtained for delays larger than 1000 μs because, as shown by Jeffress *et al.* (1962), interaural phase differences of equal magnitude but different sign produce equivalent thresholds.

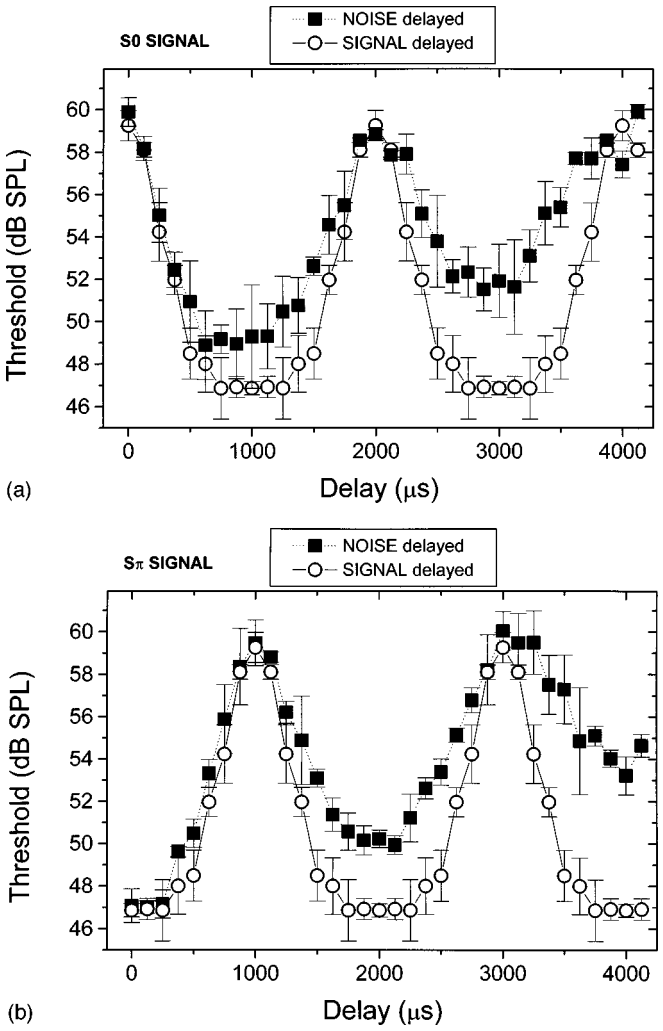

FIG. 2. Average thresholds of the three listeners in the single-delay conditions (squares). Error bars indicate across-listener standard errors. Panel (a) shows the NτS0 thresholds. Panel (b) shows the NτSπ thresholds. In both panels, the corresponding N0Sτ thresholds were replotted from Fig. 1 as circles. Note that, in the case of an Sπ signal [panel (b)], the phase inversion of the signal is accounted for by an effective 1000-μs offset (half the period of the signal) of the N0Sτ data.

The solid line in Fig. 1 shows predictions of N0Sτ thresholds computed utilizing a simple noise-cancellation scheme *a la* Durlach (1963) that does not include internal delays. Details are presented later in a section devoted to the modeling of the data. The model accounted for 95% of the variance in the data. It is important to note that the putative internal delay line *played no role* in the derivation of the predictions.

We now turn to a description of the data obtained when the *noise* was interaurally delayed and the tonal signal was either presented in phase (NτS0) or out of phase (NτSπ). The NτS0 and NτSπ thresholds are plotted as closed squares in Fig. 2(a) and (b), respectively. As before, data points represent the mean of the thresholds of three listeners and error bars indicate standard errors of the mean. To facilitate a direct comparison with the N0Sτ thresholds shown in Fig. 1, those thresholds are replotted in Fig. 2 as open circles.[1]

The patterning of NτS0 thresholds in of Fig. 2(a) shows ''damped oscillations'' having a 2000-μs periodicity. The

periodicity is evident in local maxima at delays of the noise of 0, 2000, and 4000 μs and in local minima at delays of 1000 and 3000 μs. The ''damping'' is evident in MLDs (*re*: N0S0) of 11 and 8 dB for delays of the noise of 1000 μs (half a period of the signal) and 3000 μs (3/2 periods of the signal), respectively.

The NτSπ thresholds in of Fig. 2(b) show a similar, but opposite, patterning. For these data, thresholds have local minima at delays of 0, 2000, and 4000 μs; local maxima occur at delays of 1000 and 3000 μs. A decline of the MLD with increasing interaural delay of the noise occurred once more, with values of MLD being 13, 9, and 6 dB for delays near 0, 2000, and 4000 μs, respectively.

The declining size of the MLD with increasing interaural delay agrees with earlier findings of Langford and Jeffress (1964) and Rabiner *et al.* (1966). Such a patterning of NτS0 and NτSπ data has often been associated with effects due the damping of the cross-correlation function of the narrow, or ''critical,'' band of noise assumed to be responsible for the masking. This type of explanation will be evaluated in detail later.

The NτS0 thresholds [squares in Fig. 2(a)] practically coincide with their replotted N0Sτ counterparts (circles) for delays of up to about 750 μs. Note that, however, for delays between 750 and 1500 μs or so, NτS0 thresholds are higher (i.e., performance is worse) as compared to the corresponding N0Sτ thresholds. A similar difference between N0Sτ and NτS0 thresholds for delays larger than about 700 μs was reported by van der Heijden *et al.* (1998).

In order to interpret these data, let us make the following general observation. If a perfect internal delay line were employed, then *independent of the actual mechanisms mediating detection*, detection of the tone should be the same whether the interaural delay is conveyed by the tonal signal or the masking noise. This is so because, by assumption, internal delays would always be available to compensate for the external delay, regardless of whether the delay is conveyed by the signal or the masker. By imposing a compensatory internal delay, one effectively transforms a NτS0 stimulus condition into a N0Sτ stimulus condition and vice versa. Consequently, N0Sτ and NτS0 conditions would be equivalent insofar as detectability of the signal is concerned.

Our finding that N0Sτ and NτS0 thresholds are practically equivalent for values of interaural delay up to 750 μs suggests, in view of the argument presented above, that (1) internal delays of up to 750 μs are used to compensate for external delays and (2) the utilization of these internal delays does not result in significant inaccuracies of processing. On the other hand, our finding that N0Sτ and NτS0 thresholds are *different* for larger values of interaural delay is direct evidence that the delay line, if it exists, is not perfect for these larger delays. The efficient processing of external delays in the human of up to 750 μs or so is accord with the range of interaural delays produced by external sources of sound. Of course, the similarity may be merely coincidental.

The thresholds obtained when the masking noise contained a double delay are presented in Fig. 3. Data obtained when the signal was presented in phase are plotted in Fig. 3(a) and data obtained when the signal was presented out of phase are plotted in Fig. 3(b). The diamonds in Fig. 3 indicate the mean thresholds of the three listeners and error bars indicate ± one standard error of the mean. For comparison, we have also replotted the data obtained with a single delay of the noise from Fig. 2.

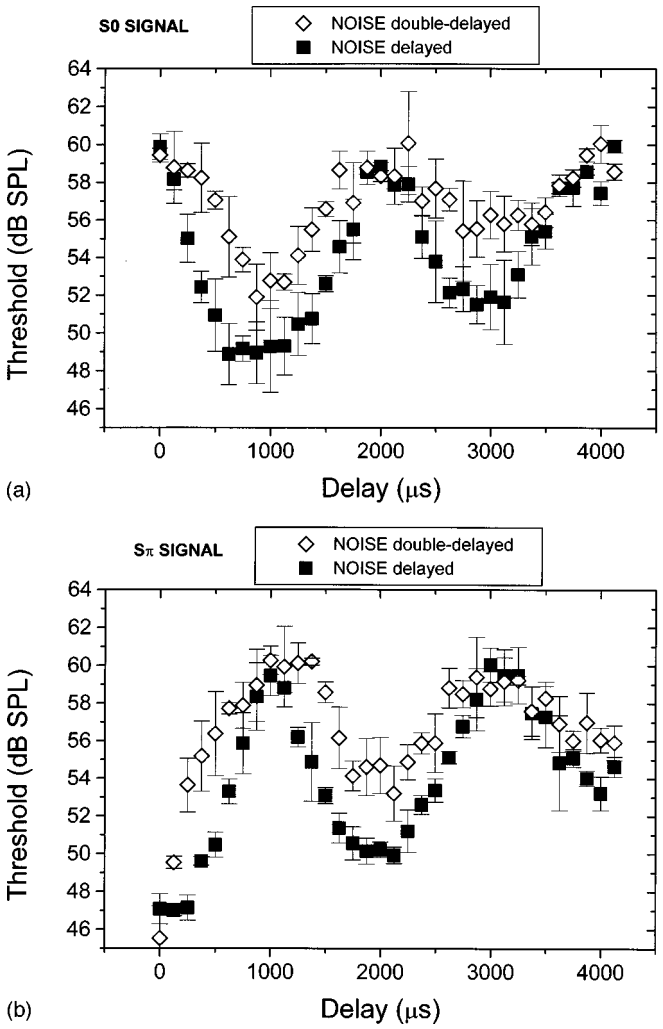

FIG. 3. Average thresholds of the three listeners in the double-delay conditions (diamonds). Error bars indicate across-listener standard errors. Panel (a) shows the thresholds obtained with an S0 signal. Panel (b) shows the thresholds obtained with an Sπ signal. In both panels, the corresponding single-delay thresholds are replotted from Fig. 2 as squares.

For both in-phase signals [Fig. 3(a)] and out-of-phase signals [Fig. 3(b)], the general patterning of the thresholds obtained in the double-delay conditions is similar to the patterning of thresholds obtained in single-delay conditions. Thresholds vary more or less periodically with a period of about 2000 μs and damping is evident in thresholds obtained with larger values of interaural delay.

Note, however, that there is a systematic difference between the thresholds obtained in the double-delay condition as compared to the thresholds obtained in the single-delay condition. Thresholds obtained with a double delay are generally higher than their single-delay counterparts (compare diamonds and squares in Fig. 3). The only delays for which the two conditions result in comparable thresholds are those for which there is no binaural advantage. Of course, comparable thresholds also occurred when the delay was zero and

an Sπ signal was utilized; in this case, the single- and double-delay stimulus conditions constitute one and the same N0Sπ condition.

Of particular importance for the purposes of this investigation are the substantial (up to 7 dB) differences in threshold found between thresholds obtained in single- and double-delay conditions for delays of less than 750 μs. These differences in thresholds are important because they occurred even though the maskers in both types of conditions have the same interaural correlation for the same magnitude of delay. Therefore, this observation provides direct evidence that the interaural correlation of the masker is *not* the *only* variable determining binaural detection performance. Moreover, the finding for external delays of less than 750 μs that performance in single-delay conditions is *better* than performance in double-delay conditions is consistent with, and supports, our earlier suggestion that such values of delay are effectively internally compensated. Discussion of thresholds obtained with delays larger than 750 μs is postponed until thresholds obtained in the double-delay conditions are treated quantitatively.

C. Modeling the data

Having these results in hand allowed us to attempt to model the data while taking advantage of the fact that for some of our stimulus conditions the use of compensatory internal delays could improve performance while, for other stimulus conditions, performance would not be improved if internal delays were utilized. As alluded to earlier, our general approach follows the equalization-cancellation (E-C) model of Durlach (1963). We proceed as follows. First, we show how such a scheme can account for data obtained when the signal was delayed in the N0Sτ condition. The salient features of this analysis are that no assumptions are necessary regarding either the processing bandwidth of the listener or the existence or utilization of compensatory internal delays. In essence, the success of this type of model demonstrates that a ''black-box'' E-C model (or its equivalent cast in terms of cross-correlation) is sufficient when only the signal is delayed.

Next, we apply the very same model to the data obtained in the double-delay condition. The reader is reminded that, as was true for delays of the signal, the application of internal delays provides no advantage to detection, thereby making any internal delay mechanism irrelevant. This allows one to use the variation of thresholds with external delay in the double-delay condition in order to estimate the processing bandwidth of the listener without the confounding effects of internal delays.

Finally, we use this estimate of the processing bandwidth in conjunction with a new assumption that the application of internal delays is ''noisy'' in order to model the thresholds obtained in the single-delay condition. Thus, in summary, we show how the design of our experimental conditions permits one to disentangle and to analyze separately two factors which determine binaural detection performance: spectral resolution and the application of internal delays.

1. Delays of the signal

We derived the predictions of the N0Sτ thresholds (solid line in Fig. 1) while utilizing a simplified version of Durlach's equalization-cancellation model (Durlach, 1963). We assumed that binaural detection is limited by inaccuracies within the internal representation of the stimulus and that the inaccuracies can be adequately modeled by an additive ''internal noise.'' We also assumed that the characteristics of the internal noise are *independent of the binaural parameters of the stimuli* (see van der Heijden and Trahiotis, 1997, for a fuller discussion).

Computational details of the derivation can be found in Sec. 2 of the Appendix. As was stated earlier, the model was quite successful in that it accounts for 95% of the variance in the data.

2. Double delays of the masker

We modeled the data obtained in the double-delay conditions using the same E-C approach as before, but this time cast the model in terms of the interaural correlation (coefficient) of the masker evaluated at a stage following peripheral filtering (e.g., Durlach, 1972; Langford and Jeffress, 1964). Here we present the modeling in general form; details of how the computations were made can be found in Sec. 3 of the Appendix.

We began with the observation that the interaural correlation of the noise effective in masking the signal, as a function of interaural delay, depends on its power spectrum. Because we used relatively broadband noise in all of our conditions, the relevant power spectrum is equivalent to the frequency response function of the peripheral filters used for detection. Our strategy was to compute the interaural correlation as a function of interaural delay while assuming a particular form or shape of the peripheral filter. We then used those values of correlation to make predictions of thresholds for our S0 and Sπ signals. The predictions were obtained using a procedure recently described by van der Heijden and Trahiotis (1997) and shown to account successfully for the effect of interaural correlation on the detectability of tones masked by broadband noise.

We used a variety of filter types, including rectangular, Gaussian, trapezoidal (Kohlrausch, 1988), RoEx, RoEx2 (Patterson and Nimmo-Smith, 1980), and gamma-tone. We adjusted the parameters of each type of filter in order to minimize the mean-square difference between predicted and obtained thresholds. We found that all of the types of filters, except the rectangular, enabled predictions that accounted for, at most, 89%–92% of the variance in the behavioral thresholds. A rectangular filter accounted for, at most, only 81% of the variance in the data. In addition, we found that the 3-dB-down bandwidths of these filters were very similar. The bandwidths of the best fitting filters ranged from 90 Hz for the trapezoidal and gammatone filters to 170 Hz for the Gaussian filter. The equivalent rectangular bandwidths of the filters ranged from 130 to 180 Hz.

We were gratified that several types of filters having 3-dB bandwidths that differed by a factor of just less than 2 provided essentially equivalent and relatively accurate fits to

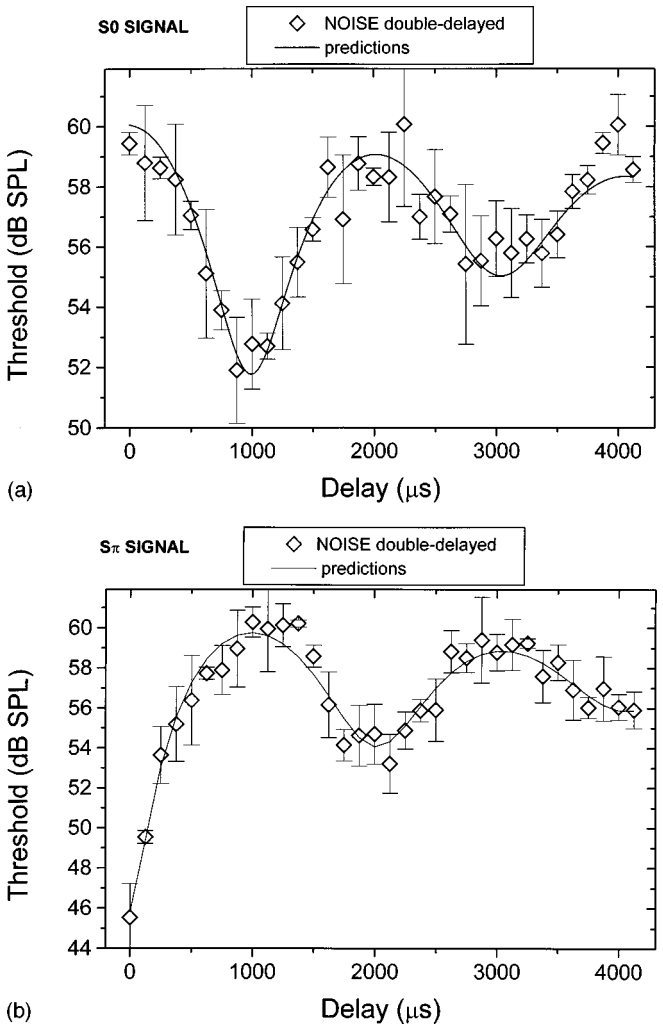

FIG. 4. Comparison between data and predictions for the double-delay condition. Behavioral thresholds (diamonds) were replotted from Fig. 3 and predicted thresholds (solid lines) were derived from the interaural correlation of the noise masker (see text). Panel (a) shows the thresholds obtained with an S0 signal. Panel (b) shows the thresholds obtained with an Sπ signal.

the thresholds obtained in the double-delay conditions. We conclude from this analysis that minor details concerning the frequency selectivity assumed to underlie detection are unimportant and that variations of the data are well captured assuming an internal filter (critical band) having a bandwidth in the range of 90 to 170 Hz. These values of *binaural* critical bandwidth are noteworthy because they are not unlike estimates of critical bandwidth derived from *monaural* stimulus conditions where binaural cues are precluded (see van der Heijden and Trahiotis, 1998).

To illustrate fits to the data based on our procedure, we have plotted in Fig. 4 predictions of thresholds for the double-delay conditions that were computed using a 90-Hz-wide gammatone filter. That type of filter provided for 92% of the variance in the data. Note that, consistent with the large amount of variance accounted for, the line depicting the predictions captures well the complexities in the patterning of the data.

In summary, the data obtained in the double-delay condition, where compensatory internal delays are ineffective, can be explained or accounted for by assuming that detection is determined by the interaural correlation of the masker. The reader is reminded that the interaural correlation is mathematically equivalent to the cross-correlation function at lag zero. This is tantamount to saying that detection performance in double-delay conditions was not mediated by internal delays.

3. Single delays of the masker

As explained in the Introduction, a major concern of this investigation is to compare detection performance in the double-delay condition with detection performance in single- and signal-delay conditions. The availability of data obtained in the double-delay condition enables us to eliminate potentially confounding effects due to auditory filtering while assessing the contribution of internal delays in the single-delay condition.

Because of the importance of the arguments and their complexity, let us review our findings. The N0Sτ thresholds are modeled successfully by a simple cancellation-of-noise algorithm. The double-delay thresholds are well described by a similar approach taking into account both critical-band filtering and interaural correlation of the noise masker. It is important to note that *neither* of those two explanations of the data involves the use of internal delays.

The single-delay (NτS0 and NτSπ) thresholds are not so easily explained. For delays *smaller* than 750 μs, the single-delay thresholds practically coincide with the N0Sτ thresholds. This finding is in accord with there being internal delays that permit a virtually perfect compensation of external delays smaller than 750 μs. For delays *larger* than 750 μs, however, the single-delay thresholds are *higher* than their corresponding N0Sτ thresholds. This implies that there is no ''perfect'' delay line that can cancel these larger delays. Finally, for almost all delays employed in this study, the single-delay thresholds are *lower* than their corresponding double-delay thresholds. This implies that detection performance in the *single-delay* case cannot be accounted for solely in terms of the interaural correlation.

From these observations, it is clear that an explanation of the single-delay data (Fig. 2) requires a different approach than that used to explain the data obtained in the N0Sτ and double-delay conditions (Figs. 1 and 4). We now consider a straightforward extension, based on internal delays, of the cancellation algorithm. Specifically, we begin by assuming that the auditory system has a wide repertoire of internal interaural delays and that it uses those values of internal delay perfectly in a manner that optimizes detection based on interaural correlation. In a subsequent analysis, we will replace the assumption that the internal delay mechanism is ''perfect'' with the assumption that it is ''noisy:'' its operation introduces an internal noise that grows with increasing internal delays. This type of noisy delay mechanism is not unreasonable and has been suggested by Jeffress *et al.* (1956, p. 425) who state that ''increased delays will be accompanied by a decrease in precision and a correspondingly increased threshold for interaural time shift.'' It will be seen that, in both noise cases (i.e., the noiseless and the noisy delay mechanisms), our analysis leads to the conclusion that

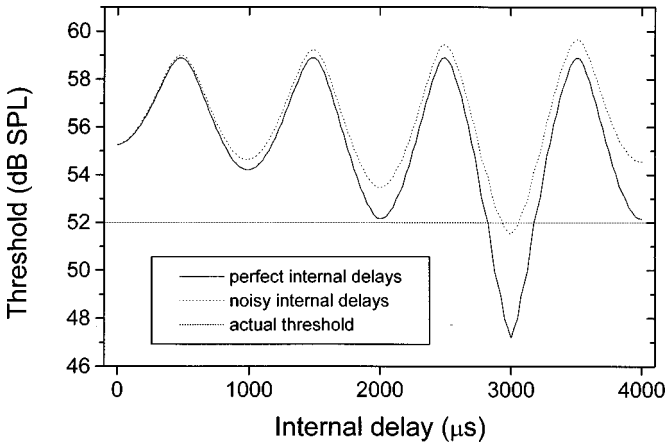

FIG. 5. Illustration of the effect of internal delays on predicted thresholds of an S0 signal in the presence of a noise having a 3000-μs interaural delay. Both curves show predicted threshold as a function of the internal delay applied to the stimulus prior to noise cancellation. The solid line shows predictions obtained with a noiseless delay mechanism; the dashed line shows predictions obtained with a noisy delay mechanism (see text).

internal delays as large as 2000 μs must have been available for the processing of the stimuli presented in the single-delay conditions.

The following discussion will be restricted to the basic ideas and will focus on an especially illuminating portion of the data. A detailed account of the modeling of the single-delay data is presented in Sec. 4 of the Appendix.

In Fig. 3(a), it can be seen that a *single* delay of about 3000 μs results in thresholds of about 52 dB, while the corresponding *double* delay results in thresholds of about 56 dB. In order to account quantitatively for the superior performance in the *single*-delay conditions, we incorporated internal delays to see how specific values of internal delay affected predictions of threshold. The reader is reminded that, in general, the application of an internal delay changes the *effective* interaural delay of both the masker and the signal. Application of the previously successful noise-cancellation algorithm to the ''effective'' stimulus (owing to the internal delay) led to the predictions of threshold. This was done for a wide range of values of internal delays in order to see which, if any, values of internal delay accounted for performance.

Figure 5 contains predictions for our example: an NτS0 stimulus condition with a signal frequency of 500 Hz and an external delay of 3000 μs. It is crucial to note that the thresholds are plotted as a function of *internal* delay. This means that *each* predicted threshold reflects performance based on the assumption that the cancellation algorithm operates *after* the application of solely that value of internal delay indicated on the abscissa.

The solid line with several maxima and minima shows the predicted thresholds. The dashed horizontal line indicates the actual threshold obtained for the stimulus condition which serves as our example [see Fig. 2(a)].

The predictions of threshold appear to ''oscillate'' with a period of about 1000 μs. This can be understood as follows. The band of noise producing the masking is centered on the 500-Hz signal frequency and, therefore, its cross-correlation function has a periodicity of 2000 μs. The efficiency of the cancellation stage is maximal when the internally delayed noise has a correlation close to either $+1$ (in which case the effective stimulus condition approximates the N0Sπ condition) or -1 (in which case the effective stimulus condition approximates the NπS0 condition). In the former case, a *subtraction* of the two channels cancels most of the noise; in the latter case, a *summation* does the job. This results in the occurrence of *two* locally optimally effective internal delays per 2000-μs-long period of the cross-correlation function of the noise. The separation between consecutive locally optimal internal delays is thus 1000 μs.

For our example, the internal delay that optimizes detection is the one that matches the 3000-μs external delay in the noise. On the other hand, the internal delay that leads to the best prediction of threshold is roughly 2000 μs. We neglect the 4000-μs threshold that simply reflects the ''mirror imaging'' of the cross-correlation function about the external delay of 3000 μs.

From a comparison between the predictions and the actual threshold in our example, it is clear that internal delays less than 2000 μs result in predictions of threshold that consistently underestimate performance. Therefore, it appears that internal delays of *at least 2000 μs* are needed in order to account for the measured threshold. A parallel analysis (not illustrated here for purposes of brevity) of thresholds obtained in the single-delay condition using an Sπ signal and an external delay of about 2000 μs (which led to a large MLD) led to the same conclusion: internal delays of at least 2000 μs are needed in order to account for the actual thresholds.

Now, it is the case that the general conclusion that internal delays of up to 2000 μs mediate detection performance is unaffected by the subsequent introduction of a ''noisy'' delay line, regardless of the exact nature of this noisiness. To understand why this is true, note that any errors introduced by the application of internal delays could only degrade predicted performance. That is, such errors could only lead to *higher* predicted thresholds. In Fig. 5, an upward displacement of the predicted thresholds will only move the predictions mediated by internal delays smaller than 2000 μs *further away* from the measured threshold. In general, the introduction of noise associated with the use of internal delays can only lead to the need for even larger internal delays than those already necessary in the case of a ''perfect'' delay mechanism.

At this point, we present an analysis while making the assumption that the application of internal delays is ''noisy.'' This assumption is necessary to explain why NτS0 thresholds and N0Sτ thresholds are different for delays larger than about 750 μs. We modeled the noisy character of the delay line by adding to each monaural channel an interaurally uncorrelated noise that was independent of the external stimulus. We made the reasonable assumption that the power of this additive ''internal'' noise increases exponentially with the internal delay imposed on the stimulus. The parameter describing the rate of growth of the internal noise with internal delay was determined (see Sec. 4 of the Appendix) by

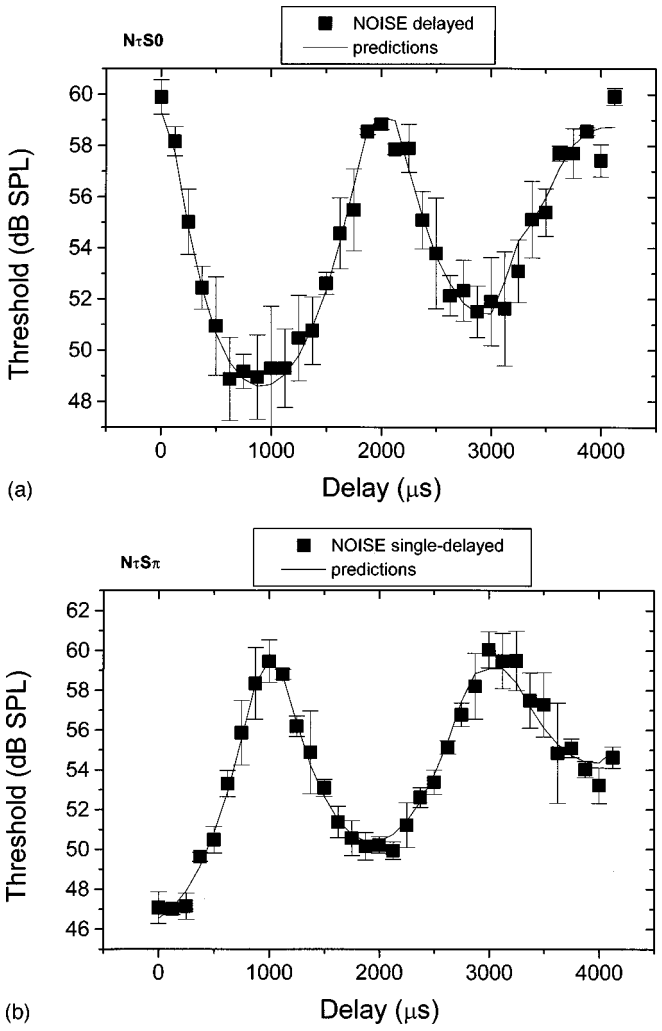

FIG. 6. Comparison between data and predictions for the single-delay condition. Behavioral thresholds (squares) were replotted from Fig. 2 and predicted thresholds (solid lines) were derived from cancellation model including a noisy internal-delay mechanism (see text). Panel (a) shows the thresholds obtained with an S0 signal. Panel (b) shows the thresholds obtained with an Sπ signal.

fitting the NτS0 and NτSπ data to the predictions obtained with the noisy delay line.

Predictions of threshold for our exemplifying stimulus condition that include this type of internal noise are shown by the dotted line in Fig. 5. Consistent with our assumptions concerning the growth of internal noise with internal delay, predicted performance is degraded in such a way that larger internal delays result in increasingly poorer detection, as compared to the predictions obtained with the perfect (noiseless) delay line. As a result, a 2000-μs internal delay is no longer ''good enough'' to account for the actual NτS0 thresholds obtained with delays of the noise on the order of 3000 μs. In order to account for those behavioral thresholds, internal delays of at least 3000 μs must be assumed to operate.

We are now in a position to present predictions of thresholds that incorporate ''noisy'' processing of internal delays for the single-delay conditions. Figure 6 contains the relevant thresholds replotted from Fig. 2. The predictions are represented by the solid lines in Fig. 6. Figure 6(a) and (b) displays predictions and thresholds obtained in the NτS0 and NτSπ conditions, respectively. The range of internal delays used to generate the predictions was 3000 μs. The same parameter governing the growth of noise with internal delay was used for predicting both sets of data. Its value was determined by minimizing the mean-square error between the data and the predictions, in their totality. As indicated by visual inspection, the predictions provide an excellent fit. The predictions account for 96% of the variance in the NτS0 data and for 97% of the variance of the NτSπ data.

II. SUMMARY AND CONCLUSIONS

In summary, the data suggest that internal delays are operative and compensate quite accurately for magnitudes of external delay of up to approximately 750 μs. Those values of delay are important for hearing by humans because they are produced by naturally occurring sources of sound (Kuhn, 1987). Quantitative analyses of the data suggest that larger magnitudes of internal delay, including those of up to 2 to 3 ms, are probably also operative. However, performance using those larger delays is degraded in accord with the hypothesis that their application introduces substantial ''noise'' in the internal representation of the stimuli. Both findings appear to be consistent with anatomical/physiological evidence suggesting a reduced density of neural elements available for the processing of larger delays (Kuwada *et al.*, 1997).

These conclusions stem from a relatively small number of general assumptions regarding binaural detection. First, we made the common assumption that the spectral portion of the noise surrounding the signal dominates masking. Second, we, like others, assumed that a parsimonious model like Durlach's equalization-cancellation model, which can also be cast in terms of interaural correlation, contains the necessary ingredients to account for or to characterize binaural detection performance (Durlach, 1972; Domnitz and Colburn, 1976; Durlach *et al.*, 1982). Third, we assumed that detectability was determined by the information stemming from that value of internal delay that maximizes detection performance.[2] Overall, it is gratifying that our binaural detection data can be quantitatively well accounted for using only these general assumptions.

ACKNOWLEDGMENTS

The authors wish to thank Dr. Les Bernstein for his many positive and insightful suggestions and the editor and reviewers for their helpful comments. This research was supported by Research Grant No. NIH DC-00234 from the National Institute on Deafness and Other Communication Disorders, National Institutes of Health.

APPENDIX

1. Proof that the interaural correlation (cross correlation coefficients) of our single and double-delay noises are identical

We denote the time average of a waveform $x(t)$ by $\overline{x}$:

$$\overline{x} = 1/T \int_0^T x(t)dt. \tag{A1}$$

Assuming that the waveform is mean zero, the power P_x of a stimulus x is given by

$$P_x = \overline{x^2}. \tag{A2}$$

The normalized cross correlation, ρ, between two stimuli x and y is given by

$$\rho = \overline{xy}/\sqrt{P_x P_y}. \tag{A3}$$

Now, consider two binaural stimuli, a and b, and denote the waveforms presented to the left ear by $a_L(t)$ and $b_L(t)$ and the waveforms presented to the right ear by $a_R(t)$ and $b_R(t)$. Assume: (1) that the power of all of these waveforms is identical:

$$\overline{a_L^2} = \overline{a_R^2} = \overline{b_L^2} = \overline{b_R^2} = P, \tag{A4}$$

(2) that a and b have identical interaural correlation:

$$\overline{a_L a_R}/P = \overline{b_L b_R}/P = \rho, \tag{A5}$$

and (3) that a and b are generated by independent processes. Then, the binaural stimulus $a+b$, obtained by adding the respective channels of a and b, has the same interaural correlation ρ of either of the components a and b:

$$\begin{aligned}\overline{(a_L+b_L)(a_R+b_R)}/(P+P) &= a_L a_R/(2P) + b_L b_R/(2P) \\ &= \tfrac{1}{2}\rho + \tfrac{1}{2}\rho = \rho.\end{aligned} \tag{A6}$$

The cross products are zero because a and b are independent, thus uncorrelated.

The double-delay stimulus provides a special case of this identity. In this case, the two independent binaural stimuli a and b are interaurally delayed noises, delayed by τ and $-\tau$, respectively. The interaural correlation coefficient $\rho(\tau)$ of an interaurally (single) delayed stimulus, as a function of interaural delay τ, is equal to the (normalized) autocorrelation function of the noise waveform presented to each ear. Due to the symmetry of the autocorrelation function (Haykin, 1983), we have $\rho(\tau) = \rho(-\tau)$ and the identity (A6) applies.

As a consequence of this identity, the interaural correlation coefficient $\rho(\tau)$ of the double-delayed noise as a function of the stimulus parameter τ is equal to the autocorrelation function of the masker waveform presented to each ear. This fact is used in Sec. A 3 on modeling the double-delay thresholds. Note that the function $\rho(\tau)$ is *not* the cross-correlation function of the double-delay stimulus (the stimulus parameter τ is not an ordinary, ''single'' delay).

It is also true that passing the double-delay noises in each ear through identical linear filters does not affect these results because the filtered stimulus can also be written as the sum of two independent stimuli, each having opposite interaural delay.

2. Modeling of the N0Sτ thresholds

In the case of an N0Sτ stimulus, cancellation results from a subtraction of the stimuli presented to the two ears. In order to calculate the predictions, we have to evaluate the stimulus parameters of the *effective* stimulus after the cancellation of the noise.

The signal is a tone presented with interaural phase difference ϕ:

$$x_L(t) = A\ \cos(2\pi f t + \phi/2), \tag{A7a}$$

$$x_R(t) = A\ \cos(2\pi f t - \phi/2), \tag{A7b}$$

where $x_L(t)$ and $x_R(t)$ denote the waveforms presented to the left and right ears, A is the amplitude, and f is the frequency of the signal. At the output of the subtractor, the waveform of the signal is

$$d(t) = x_L(t) - x_R(t) = 2A\ \sin(\phi/2)\ \cos(2\pi f t). \tag{A8}$$

Note that the subtraction results in a change of amplitude, *re* the stimulus amplitude, by a factor $2\sin(\phi/2)$. This corresponds to a change of signal power by a factor $4\sin^2(\phi/2)$.

The subtraction completely eliminates the *external* noise. Therefore, detection performance is limited by the residual *internal* noise. We express the power of this residual noise, R, as the ratio of its power *re* the power of the external noise. This ratio is assumed to be independent of the binaural parameters of the stimulus and, therefore, has the same value for all of the N0Sτ conditions.

After combining the effects of the subtraction on the powers of both the signal and the noise, we arrive at the gain, G, in the S/N ratio accomplished by the cancellation:

$$G = 4\ \sin^2(\phi/2)/R. \tag{A9}$$

Assuming linearity of masking, this gain in S/N ratio directly corresponds to the advantage of binaural processing over monaural processing:

$$T_b = T_m/G, \tag{A10}$$

where T_m is the signal power at threshold based on monaural processing and T_b is the signal power at threshold on the basis of the binaural cancellation process.

Now, if ϕ is close to, or equal to, zero, the effective monaural stimulus can lead to a poorer detection as compared to monaural processing of the external stimulus. That is, $G<1$ leads to ''negative MLDs.'' To avoid this situation, we assume that the information at the output of the binaural processor is *combined* with the information obtained from the monaural mode of processing. Then, assuming that monaural and binaural processing are independent and that the information from the two processors is combined in an optimal way, the predicted threshold is expressed by the following formula [see van der Heijden and Trahiotis, 1998, formula (A4), with $k=1$]:

$$1/T_c^2 = 1/T_m^2 + 1/T_b^2, \tag{A11}$$

where T_c is the signal power at threshold.

Combining the foregoing and converting the interaural phase difference, ϕ, to an interaural time difference, τ, we arrive at the following expression for the predicted N0Sτ thresholds, $P_{\mathrm{N0S}\tau}(\tau)$, expressed in dB, as a function of τ:

$$P_{N0S_T}(\tau) = 10 \log T_c(\tau)$$
$$= 10 \log T_m - 5 \log[1 + 16 \sin^2(\pi f \tau)/R^2]. \quad \text{(A12)}$$

Predictions were made by simultaneously varying $10 \log T_m$ and $10 \log R$ so as to minimize the sum of the squared error between the predictions and obtained thresholds, both of which are plotted in Fig. 1. The squared error was minimal for $10 \log T_m = 60.7\ dB$ and $10 \log R = -8.7\ dB$.

3. Modeling of the double-delay thresholds

The basic assumption underlying the predictions of the double-delay data (curves in Fig. 4) is that detection performance is determined by the interaural correlation of the spectral portion of the noise producing the masking (the critical band of noise). The derivation consists of two steps which are outlined before they are presented in detail. First, we calculated the interaural correlation, $\rho(\tau)$, of the critical band of noise, for a given value of the interaural delay of the noise, τ. Second, we used the value of $\rho(\tau)$ to obtain predicted thresholds by utilizing a method recently described by van der Heijden and Trahiotis (1997).

Let the peripheral auditory frequency selectivity be described by a linear filter whose frequency response is $H(f)$, where f denotes frequency. In the case of a noise with a flat power spectrum (as in our experiments), the power spectrum density at the output of the filter is proportional to $H^2(f)$, where f ranges from $f_{\min}$ to $f_{\max}$, the cutoff frequencies of the external noise.

First, recall that $\rho(\tau)$, the interaural correlation as a function of the value of double delay of the noise stimulus, is equal to the autocorrelation function of the noise (see Sec. A 1). Now, the autocorrelation function is equal to the Fourier transform of the power spectrum (e.g., Haykin, 1983), from which it follows that

$$\rho(\tau) = N \int_{f_{\min}}^{f_{\max}} \cos(2\pi f \tau) H^2(f)\, df, \quad \text{(A13)}$$

where N is a normalization constant ensuring that $\rho(0) = 1$. For a number of filter types (see main text), we approximated $\rho(\tau)$ by computing a 8096-point discrete Fourier transform of the respective filter's frequency response function.

Using Eq. (1) of van der Heijden and Trahiotis (1997), the signal power at threshold is given by

$$T_{S0}(\rho) = \tfrac{1}{2}(1+\rho) T_{S0}(1) + \tfrac{1}{2}(1-\rho) T_{S0}(-1), \quad \text{(A14a)}$$

$$T_{S\pi}(\rho) = \tfrac{1}{2}(1+\rho) T_{S\pi}(1) + \tfrac{1}{2}(1-\rho) T_{S\pi}(-1), \quad \text{(A14b)}$$

where $T_{S0}(\rho)$ and $T_{S\pi}(\rho)$ denote the signal power at threshold for S0 and Sπ signals, respectively, in the presence of masking noise having an interaural correlation ρ. The "special cases," $T_{S0}(1)$, $T_{S0}(-1)$, and $T_{S\pi}(-1)$, which appear within the right-hand side of this equation correspond to N0S0, NπS0, N0Sπ, and NπSπ stimulus conditions, respectively. Strictly speaking, all four of the special cases are free parameters of the cancellation model. However, in order to prevent an unnecessary (and numerically burdensome) amount of free parameters, we reduced their number to two by simply postulating

$$T_{S0}(1) = T_{S\pi}(-1); \quad \text{(A15a)}$$

$$T_{S0}(-1) = 1.6\, T_{S\pi}(1). \quad \text{(A15b)}$$

The first line expresses equivalent performance in N0S0 and NπSπ stimulus conditions (Jeffress *et al.*, 1956); the second line states that N0Sπ thresholds are smaller by 2 dB than their NπS0 counterparts (e.g., Robinson and Jeffress, 1963).

The fits to the double-delay data were generated as follows. First a filter type was selected (see main text). The free parameters of the fit were $T_{S0}(1)$, $T_{S\pi}(1)$, and the parameters of the filter under consideration (the number of filter parameters depends on the type of filter but in each case this number was at least two, allowing the center frequency and bandwidth of the filter to vary). The parameters were independently varied so as to minimize the mean-square error between the predictions and *all* of the double-delay thresholds (i.e., taking together data obtained in S0 and Sπ conditions). Thresholds were cast in dB; as was the mean-square error between the predictions and the actual data.

As discussed in the body of the paper, the best fit of the double-delay data was obtained with a 90-Hz-wide gammatone filter centered at 495 Hz. However, also as discussed in the body of the paper, the predictions were robust with respect to the type of filter assumed.

4. Modeling the single-delay thresholds

The modeling of the single-delay (NτS0 and NτSπ) thresholds involved an equalization stage prior to cancellation. We begin by considering the use of *noiseless* internal delays (see main text).

Internal delays applied to an NτS0 or NτSπ stimulus result in a new, effective, stimulus condition. The cancellation scheme described above was applied to the effective stimuli while using the parameters calculated in Sec. A 3 that led to the best fit of the double-delay thresholds. Each effective stimulus condition was characterized by the interaural correlation of the noise (calculated as described in Sec. A 3) and the interaural phase of the signal. The cancellation stage of binaural processing consisted of either summing or subtracting the channels of the effective stimulus. To explain, for each effective stimulus condition, we calculated the effects of summation and subtraction on the S/N ratio of the effective stimulus. The strategy was to evaluate separately the amount of noise reduction due to the summation/subtraction (van der Heijden and Trahiotis, 1997) and the effect of summation/subtraction on the power of the signal (see Sec. A 2).

The S/N ratios of the effective stimuli lead to preliminary estimates of threshold resulting from both types of cancellation. We assumed that both strategies (summation and

subtraction) were simultaneously available to the binaural system and we combined the predictions from each strategy by using an equation analogous to Eq. (A11) to obtain the predictions of threshold such as those shown in Fig. 5. As described in the main text, final predictions were obtained by assuming a certain range of available internal delays and by selecting the optimal internal delay within that range. The optimal internal delay was the one that led to the lowest threshold.

However, as explained in the main text, a noiseless internal delay mechanism does not lead to satisfactory predictions: on the one hand, delays of at least 2000 μs must be available to account for NτS0 thresholds with τ=3000 μs, on the other hand, such large internal delays, when assumed to operate without a loss of processing accuracy, are in conflict with the differences between N0Sτ and NτS0 thresholds for τ>750 μs.

Therefore, we investigated the utility of assuming ''noisy'' internal delays, which we modeled in the following way. We considered the ''delay line'' as consisting of a large number of small ''links.'' Each link was assumed to add an amount of internal noise, the power of which was proportional to the power of the stimulus at the input of the link. This type of delay line contains an ''accumulation'' of internal noise along its entire length that results in the power, P_N, of the internal noise growing exponentially with the magnitude of the total internal delay, τ_i (τ_i is assumed to be proportional to the ''number of links''):

$$P_N(\tau_i) = P \cdot (\exp(\alpha|\tau_i|) - 1), \tag{A16}$$

where P is the power of the external stimulus and α is a parameter describing the rate of growth of the internal noise with internal delay (specified in reciprocal units of the units in which τ_i is specified).

The addition of internal noise has two effects on the effective stimulus (the stimulus after the application of the internal delay). First, it increases the power of the effective stimulus P_E:

$$P_E = P \cdot \exp(\alpha|\tau_i|). \tag{A17}$$

Second, it changes the interaural correlation of the effective stimulus. To evaluate this change, we assumed that the internal noise was uncorrelated with the stimulus and was interaurally uncorrelated. Using these assumptions, we applied the formula of Jeffress and Robinson (1962) and obtained the interaural correlation, ρ_E, of the effective stimulus:

$$\rho_E = P/P_E = \rho \ \exp(-\alpha|\tau_i|), \tag{A18}$$

where ρ is the correlation that would result from a noiseless internal delay.

After taking into account the effects of internal noise on the parameters of the effective stimulus, we generated predictions of thresholds in the manner described above. The effect of this type of internal noise on the predictions is illustrated in Fig. 5.

The parameters used to fit the double-delay thresholds (Sec. A 3) were retained and the only new free parameters used to provide fits to the single-delay thresholds were the maximum magnitude of available internal delays, τ_{max} and the rate of growth of the internal noise, α. Best fits were obtained when τ_{max} was at least 3000 μs and α was 4.8 ms^{-1}.

[1]Data points for delays of the signal between 1000 and 2000 μs are the mirror images of the data points obtained with delays of the signal from 0 to 1000 μs. Data points with delays larger 2000 μs are extrapolations based on the periodicity of the 500-Hz signal. Note that there is a 1000-μs offset between the signal-delayed thresholds (circles) in panels a and b which was imposed in order to ''line up'' properly data obtained with the S0 and Sπ signals.

[2]An alternative approach which assumes a more ''multi-channel'' mode of processing is beyond the scope of this investigation. However, preliminary analyses suggest that such an approach would not alter the fundamental character of the predicted thresholds and, therefore, would not affect the general conclusions offered in this study. We also considered the alternative of interpreting our data in terms of the interaural envelope- and phase-distributions of our stimuli (e.g., Zurek, 1991; Bernstein and Trahiotis, 1995). Using our exemplifying stimulus condition, we calculated both types of distributions for our single- and double-delay stimulus conditions. We discovered that single- and double-delay stimuli were indistinguishable in terms of those distributions, even though the behavioral thresholds for each stimulus condition differed by about 4 dB. We conclude that considering envelope- and phase-distributions cannot provide an alternative account of our data.

Bernstein, L. R., and Trahiotis, C. (**1995**). ''Binaural interference effects measured with masking-level difference and with ITD- and IID-discrimination paradigms,'' J. Acoust. Soc. Am. **98**, 155–163.

Colburn, H. S., and N. I. (**1978**). ''Models of binaural interaction,'' in *Handbook of Perception, Vol. IV, Hearing*, edited by E. C. Carterette and M. P. Freedman (Academic, New York), pp. 467–518.

Domnitz, R. H., and Colburn, H. S. (**1976**). ''Analysis of binaural detection models for dependencies of interaural target parameters,'' J. Acoust. Soc. Am. **59**, 598–601.

Durlach, N. I. (**1963**). ''Equalization and cancellation theory of binaural masking differences,'' J. Acoust. Soc. Am. **35**, 1206–1218.

Durlach, N. I. (**1972**). ''Binaural signal detection: Equalization and cancellation theory,'' in *Foundations of Modern Auditory Theory*, edited by J. V. Tobias (Academic, New York).

Durlach, N. I., and Colburn, H. S. (**1978**). ''Binaural phenomena,'' in *Handbook of Perception, Vol. IV, Hearing*, edited by E. C. Carterette and M. P. Friedman (Academic, New York).

Durlach, N. I., Gabriel, K. J., Colburn, H. S., and Trahiotis, C. (**1982**). ''Interaural correlation discrimination: II. Relation to binaural unmasking,'' J. Acoust. Soc. Am. **79**, 1548–1557.

Haykin, S. (**1983**). *Communication Systems* (Wiley, New York).

Heijden, M. L. van der, and Trahiotis, C. (**1997**). ''A new way to account for binaural detection as a function of interaural noise correlation,'' J. Acoust. Soc. Am. **101**, 1019–1022.

Heijden, M. van der, and Trahiotis, C. (**1998**). ''Binaural detection as a function of interaural correlation and bandwidth of masking noise: Implications for estimates of spectral resolution,'' J. Acoust. Soc. Am. **103**, 1609–1614.

Heijden, M. L. van der, Trahiotis, C., Kohlrausch, A., and Par, S. van de (**1998**). ''Binaural detection with spectrally non-overlapping signals and maskers: Evidence for masking by aural distortion products,'' J. Acoust. Soc. Am. **102**, 2966–2972.

Jeffress, L. A. (**1948**). ''A place theory of sound localization.'' J. Comp. Physiol. Psychol. **41**, 35–49.

Jeffress, L. A., and Robinson, D. E. (**1962**). ''Formulas for the coefficient of interaural correlation for noise,'' J. Acoust. Soc. Am. **34**, 1658–1659.

Jeffress, L. A., Blodgett, H. C., and Deatherage, B. H. (**1952**). ''The masking of tones by white noise as a function of interaural phases of both components,'' J. Acoust. Soc. Am. **24**, 523–527.

Jeffress, L. A., Blodgett, H. C., and Deatherage, B. H. (**1962**). ''Masking and interaural phase. II. 167 cycles,'' J. Acoust. Soc. Am. **34**, 1124–1126.

Jeffress, L. A., Blodgett, H. C., Sandel, T. T., and Wood, C. L. III (**1956**). ''Masking of tonal signals,'' J. Acoust. Soc. Am. **28**, 416–426.
Kohlrausch, A. (**1988**). ''Auditory filter shape derived from binaural masking patterns,'' J. Acoust. Soc. Am. **84**, 573–583.
Kuhn, G. (**1987**). ''Physical acoustics and measurements pertaining to directional hearing,'' in *Directional Hearing*, edited by W. A. Yost and G. Gourevitch (Springer-Verlag, New York).
Kuwada, S., Batra, R., and Fitzpatrick, D. C. (**1997**). ''Neural processing of binaural temporal cues,'' in *Binaural and Spatial Hearing in Real and Virtual Environments*, edited by R. H. Gilkey and T. R. Anderson (Erlbaum, Mahwah, NJ), pp. 399–425.
Langford, T. L., and Jeffress, L. A. (**1964**). ''Effect of noise crosscorrelation on binaural signal detection,'' J. Acoust. Soc. Am. **36**, 1455–1458.
Levitt, H. (**1971**). ''Transformed up–down methods in psychoacoustics,'' J. Acoust. Soc. Am. **49**, 467–477.
Patterson, R. D., and Nimmo-Smith, I. (**1980**). ''Off-frequency listening and auditory-filter asymmetry,'' J. Acoust. Soc. Am. **67**, 229–245.
Rabiner, L. R., Laurence, C. L., and Durlach, N. I. (**1966**). ''Further results on binaural unmasking and the EC model.'' J. Acoust. Soc. Am. **40**, 62–70.
Robinson, D. E., and Jeffress, L. A. (**1963**). ''Effect of varying the interaural noise correlation on the detectability of tonal signals,'' J. Acoust. Soc. Am. **35**, 1947–1952.
Stern, R. M., and Trahiotis, C. (**1992**). ''The role of consistency of interaural timing over frequency in binaural lateralization,'' in *Auditory Physiology and Perception*, edited by Y. Cazals, L. Demany, and K. Horner (Pergamon, New York), pp. 547–554.
Zurek, P. M. (**1991**). ''Probability distributions of interaural phase and level differences in binaural detection stimuli,'' J. Acoust. Soc. Am. **90**, 1927–1932.

Benefits of linear amplification and multichannel compression for speech comprehension in backgrounds with spectral and temporal dips

Brian C. J. Moore
Department of Experimental Psychology, University of Cambridge, Downing Street, Cambridge CB2 3EB, England

Robert W. Peters
Division of Speech and Hearing Sciences, Department of Medical Allied Health Professions, The School of Medicine, and Department of Psychology, The University of North Carolina at Chapel Hill, North Carolina 27599-7190

Michael A. Stone
Department of Experimental Psychology, University of Cambridge, Downing Street, Cambridge CB2 3EB, England

(Received 30 April 1998; revised 6 October 1998; accepted 7 October 1998)

People with cochlear hearing loss have markedly higher speech-receptions thresholds (SRTs) than normal for speech presented in background sounds with spectral and/or temporal dips. This article examines the extent to which SRTs can be improved by linear amplification with appropriate frequency-response shaping, and by fast-acting wide-dynamic-range compression amplification with one, two, four, or eight channels. Eighteen elderly subjects with moderate to severe hearing loss were tested. SRTs for sentences were measured for four background sounds, presented at a nominal level (prior to amplification) of 65 dB SPL: (1) A single female talker, digitally filtered so that the long-term average spectrum matched that of the target speech; (2) a noise with the same average spectrum as the target speech, but with the temporal envelope of the single talker; (3) a noise with the same overall spectral shape as the target speech, but filtered so as to have 4 equivalent-rectangular-bandwidth (ERB) wide spectral notches at several frequencies; (4) a noise with both spectral and temporal dips obtained by applying the temporal envelope of a single talker to speech-shaped noise [as in (2)] and then filtering that noise [as in (3)]. Mean SRTs were 5–6 dB lower (better) in all of the conditions with amplification than for unaided listening. SRTs were significantly lower for the systems with one-, four-, and eight-channel compression than for linear amplification, although the benefit, averaged across subjects, was typically only 0.5 to 0.9 dB. The lowest mean SRT (−9.9 dB, expressed as a speech-to-background ratio) was obtained for noise (4) and the system with eight-channel compression. This is about 6 dB worse than for elderly subjects with near-normal hearing, when tested without amplification. It is concluded that amplification, and especially fast-acting compression amplification, can improve the ability to understand speech in background sounds with spectral and temporal dips, but it does not restore performance to normal.
 [S0001-4966(99)05401-6]

PACS numbers: 43.66.Ts, 43.66.Dc, 43.71.Gv, 43.71.Ky [JWH]

INTRODUCTION

Relative to normally hearing people, people with cochlear hearing impairment have particular difficulty understanding speech in the presence of background sounds with spectral and/or temporal dips. This problem is often quantified in the laboratory by estimating the speech-to-background ratio required to achieve a given level of intelligibility, such as 50%-correct identification of sentences or words. We will refer to this ratio as the speech reception threshold (SRT), and will express it in decibels (dB); both speech and background levels are specified in terms of their long-term rms values. When the background is a single competing talker (Carhart and Tillman, 1970; Duquesnoy, 1983; Hygge *et al.*, 1992; Moore *et al.*, 1995; Peters *et al.*, 1998), a time-reversed talker (Duquesnoy, 1983), or an amplitude-modulated noise (Duquesnoy, 1983; Takahashi and Bacon, 1992; Eisenberg *et al.*, 1995; Peters *et al.*, 1998), the difference in SRT between normal and hearing-impaired people can be as large as 15 dB. When the background is a steady speech-shaped noise, without distinct spectral or temporal dips, the difference is usually much less, typically being 2–5 dB (Glasberg and Moore, 1989; Plomp, 1994; Peters *et al.*, 1998).

In a previous study (Peters *et al.*, 1998), we measured SRTs for sentences in several background sounds for four groups of subjects: (a) young with normal hearing; (b) elderly with near-normal hearing; (c) young with moderate to severe cochlear hearing loss; and (c) elderly with moderate to severe cochlear hearing loss. The background sounds varied in the extent to which they contained temporal and/or spectral dips. The results indicated that both spectral and temporal dips allowed normally hearing subjects to achieve

much lower SRTs than for a noise without such dips. Hearing-impaired subjects gained less benefit from the presence of the dips. In a background that contained both spectral and temporal dips, groups (c) and (d) performed much more poorly than group (a). The signal-to-background ratio required for 50% intelligibility was about 19 dB higher for group (d) than for group (a). Young hearing-impaired subjects showed a slightly smaller, though still substantial, deficit.

Peters *et al.* also investigated the effect of linear amplification combined with frequency-response shaping as prescribed by the NAL(*R*) formula (Byrne and Dillon, 1986). They found that this only partially compensated for the higher SRTs in background sounds with spectral and temporal dips. For example, group (d) still required a speech-to-background ratio that was 15 dB higher than for group (a). Calculations of the articulation index indicated that NAL(*R*) amplification did not restore audibility of the whole of the speech spectrum when the speech-to-background ratio was low. Thus, the ability of the hearing-impaired subjects to understand speech in the backgrounds with spectral and temporal dips was limited by part of the speech spectrum being inaudible, even if the background sounds had been removed.

In principle, it is possible to increase audibility by increasing the amount of linear gain applied. However, this can only be done to a limited extent because of loudness recruitment, which is nearly always associated with cochlear hearing loss (Dix *et al.*, 1948; Hood, 1972). The threshold for detecting sounds is higher than normal, but once the sound level is increased above the absolute threshold, the rate of growth of loudness level with increasing level is greater than normal. At a sound level of 90–100 dB SPL, the loudness in an impaired ear often ''catches up'' with that in a normal ear (Fowler, 1936; Steinberg and Gardner, 1937; Miskolczy-Fodor, 1960; Moore and Glasberg, 1997). As a consequence, the range of sound levels over which sounds are both audible and comfortable (the dynamic range) is much smaller for hearing-impaired than for normally hearing people.

Most rules for prescribing the gain of a linear aid are appropriate for speech inputs with a moderate level. However, when listening to speech in background sounds with spectral and temporal dips, it may be impossible to apply sufficient linear gain to ensure that all of the target speech spectrum is above absolute threshold while preventing the background or the more intense parts of the speech from becoming unpleasantly loud.

One way of compensating for the effects of loudness recruitment is to use hearing aids with fast-acting compression or automatic gain control (AGC). Such aids can increase the available dynamic range and make it possible for the hearing-impaired person to deal with sounds covering a wide range of levels without needing to adjust the volume control on the aid (Villchur, 1973; Lippmann *et al.*, 1981; Moore *et al.*, 1992). In principle, such aids can also improve the ability to listen in dips of a competing sound, by increasing the gain for signals in the dips, thus improving the intelligibility of the speech. However, laboratory studies of systems using fast-acting compression have given mixed results, with some studies showing no benefit or even a worsening in comparison to linear amplification, and others showing moderate benefits (Villchur, 1973; Lippmann *et al.*, 1981; Villchur, 1982; Moore and Glasberg, 1988a; Moore *et al.*, 1992; Hickson, 1994; Moore, 1995; Dillon, 1996).

The laboratory studies have generally used test materials covering a much smaller range of sound levels than would be encountered in everyday life. Also, when background sounds have been used, the most common sound has been steady speech-shaped noise. This may not be the most effective background for revealing benefits of fast-acting compression; backgrounds with spectral and temporal dips might provide a more sensitive test.

In the present study, we compare the effectiveness of linear amplification and of fast-acting wide-dynamic-range compression amplification with one, two, four, or eight channels, by measuring SRTs for sentences in background sounds with spectral and/or temporal dips. We expected that the number of channels would not be of great importance when the background sound contained temporal, but not spectral, dips. An example of such a background sound is speech-shaped noise amplitude modulated with the envelope of a single talker. The main role of the fast-acting compression with such a background would be to amplify low-level portions of the target speech falling in the temporal dips in the background. However, when the background contained spectral dips, we anticipated that there might be some benefit of having multiple channels. This would allow low-level portions of the target speech falling in the spectral dips of the background to be selectively amplified. Such selective amplification is only possible if the widths of the channels are comparable to or less than the widths of the spectral dips in the background. This was the case with our eight-channel system, but not with the two- and four-channel systems. However, the channel edges of the eight-channel system were *not* chosen so as to coincide with the edges of the spectral dips in the background; this might have revealed a benefit that would not be realizable in practice.

In summary, our hypotheses were that when the background sound contains temporal dips, compression should provide better performance than linear amplification, and when the background contains spectral dips, multichannel compression should provide better performance than single-channel compression.

I. STIMULI AND METHODS

A. Subjects

Eighteen elderly subjects (mean age 77.9 years, s.d. 5.6 years) with moderate to severe cochlear hearing loss were tested. Their ages, SRTs in quiet, and audiograms are given in Table I. The subjects were all alert, able to follow instructions, and able to concentrate.

B. Stimuli

The speech materials used were the sentence lists recorded at the House Ear Institute in Los Angeles (the hearing

TABLE I. Ages, SRTs in quiet in equivalent free-field dB SPL, and absolute thresholds in dB HL for the 18 subjects.

		Frequency, kHz							
Age	SRT in quiet	0.25	0.5	1.0	2.0	3.0	4.0	5.0	6.0
86	57.4	35	35	40	50	55	55	57	60
83	63.2	25	50	50	60	65	70	75	80
78	39.8	10	10	15	32	40	45	50	55
74	62.2	35	35	45	60	65	70	72	75
77	60.2	30	35	38	62	80	80	82	85
77	57.0	30	30	55	55	60	60	60	60
75	59.0	50	35	40	50	55	55	57	60
66	62.2	35	50	55	55	57	60	65	67
73	52.7	35	35	35	55	65	70	75	80
75	62.6	15	35	50	65	65	60	62	65
80	47.8	20	15	30	55	75	80	82	85
78	51.5	25	35	35	40	60	70	67	65
84	52.6	40	35	40	45	55	60	60	60
76	51.8	30	30	35	40	60	60	62	65
76	63.8	30	30	40	50	55	65	70	75
77	48.2	20	20	30	45	65	75	70	65
84	60.2	30	30	35	40	45	60	62	65
65	27.8	15	15	20	35	55	65	65	65

in noise test—HINT) (Nilsson *et al.*, 1994). The background sounds were a subset of those used by Peters *et al.* (1998). They were:

(1) A single competing female talker. This sound was taken from a compact disc (CD) of test sounds recorded by ReSound Corporation. The passage lasts approximately 1 min. For our tests, the sample was recycled, to give a continuous sample about 7 min in length. This background has both spectral and temporal dips. The speech was digitally filtered so that its long-term average spectrum matched that of the HINT sentences.

(2) A noise with the same spectrum as the HINT sentences, but with the overall temporal fluctuations of the single female talker. This was achieved by extracting the envelope of the speech of the single talker, and imposing that envelope on the HINT noise. The envelope was extracted by calculating the root-mean-square amplitude of the speech in a 10-ms long sliding temporal window. We refer to this noise as ''modulated noise.''

(3) Steady noise filtered so as to have the same long-term average spectrum as the HINT sentences and then filtered again to introduce spectral dips in several frequency regions. The additional filtering was based on the equivalent-rectangular-bandwidth (ERB) scale derived from the auditory-filter bandwidths for normally hearing subjects (Glasberg and Moore, 1990). Each ERB represents one auditory-filter bandwidth. The relationship between ERB number and frequency is

$$\text{ERB number} = 21.4 \log_{10}(4.37F + 1), \quad (1)$$

where F is frequency in kHz.

The noise was filtered with an alternating pattern of four ERBs present and four ERBs removed, as described in Peters *et al.* (1998). The characteristics of the digital filter used are illustrated in Fig. 1. The figure also shows the channel edges of the eight-channel compression system, which is described later.

(4) A noise with both spectral and temporal dips obtained by applying the temporal envelope of the single talker to speech-shaped noise [as in (2)] and then filtering that noise [as in (3)].

The overall level of backgrounds (1) and (2) was 65 dB SPL, prior to any amplification. For backgrounds (3) and (4), the spectrum level of the noise in the passbands of the digital filters was left the same as for the other backgrounds. Thus, the overall level of the noise was slightly reduced by the filtering (by about 3 dB). This was done so that we could examine benefits of removing part of the background spectrum without the confounding effect of increases in level of the remaining part of the spectrum.

The background sounds were produced by digital processing using a Silicon Graphics Indy computer. All processing was done using a 16-kHz sampling rate and floating-point arithmetic. When processing was complete, samples were converted to 16-bit integers and up-sampled to a 44.1-

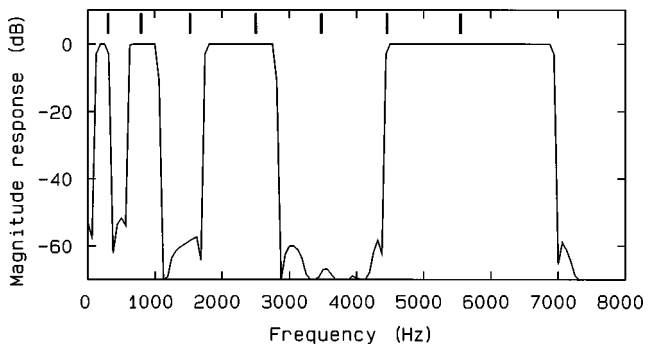

FIG. 1. Characteristic of the digital filter used to produce the noises with multiple spectral notches. The bold lines at the top indicate the crossover frequencies for the eight-channel compression system.

TABLE II. Values of the intercept (INT) in the Cambridge formula for each audiometric frequency (kHz).

Frequency	0.125	0.25	0.5	0.75	1.0	1.5	2.0	3.0	4.0	5.0
INT	−11	−10	−8	−6	0	−1	1	−1	0	1

kHz rate. They were transferred digitally to recordable compact disc (CDR) for use in the experiment. The speech was played back from digital audio tape (DAT). The target speech and background sounds were independently amplified and their levels were controlled by independent manual attenuators. The outputs of the attenuators were mixed using an active mixer. The stimuli were then passed through a digital signal-processing system (described below) and an amplifier before presentation to the better-hearing ear, or to the left ear if the audiograms were very similar for the two ears, using Sennheiser HD424 earphones, which have a ''diffuse field'' response; the response at the eardrum is similar to what would be produced by a free-field presentation averaged over many directions of incidence.

C. Procedure and design

We used a Latin square design to counterbalance the order of testing both for the six signal-processing conditions (see below for details) and for the four background sounds. As there were 18 subjects, three Latin squares were used for the processing conditions. For the background sounds, 16 subjects were tested using four complete Latin squares, and an incomplete Latin square was used for the remaining two subjects.

An adaptive procedure was used to estimate the SRT for each processing condition in each background noise. The procedure was as recommended for use with the HINT materials (Nilsson *et al.*, 1994). Two sentence lists were used for each condition. The first was a training sentence list to provide experience under a particular listening condition; this was either list 25, 26, 27, or 28 (used repeatedly and in this order). The second was one of lists 1 to 24. These lists were used in sequence for testing the 24 conditions. Prior to testing, practice was given with each background sound, using lists 25–28. The SRT for speech in quiet (unaided listening) was measured immediately prior to the SRTs for the unaided condition; the SRTs in quiet are shown in Table I. For this test, a list was chosen randomly from lists 1–24. Subjects were seated in a single-walled sound-attenuating chamber situated within the testing room. Subjects communicated with the tester via a microphone located in the sound-attenuating chamber.

II. SIGNAL PROCESSING

A. Processing conditions

There were six conditions:

(1) Unaided listening.
(2) Frequency-dependent linear amplification. This was based on the ''Cambridge'' formula (Moore and Glasberg, 1998), which is intended to give a flat specific-loudness pattern (equal loudness per ERB) over the range of center frequencies from 500 to 4000 Hz when the signal is speech with an overall level of 65 dB SPL. The formula is

$$\mathrm{IG}=\mathrm{HL}\times 0.48+\mathrm{INT}, \tag{2}$$

where IG is insertion gain in dB, HL is the absolute threshold in dB HL, and INT is a frequency-dependent intercept. The value of INT is given in Table II for each audiometric frequency. Above 5 kHz, gains are limited to the value at 5 kHz. This formula prescribes slightly less gain than the NAL(R) formula (Byrne and Dillon, 1986) for frequencies around 750 Hz, and slightly more gain for frequencies of 2000 Hz and above. For a given (calculated) overall loudness, the Cambridge formula usually leads to a higher articulation index than the NAL(R) formula (Moore and Glasberg, 1998). This might be expected to lead to greater speech intelligibility for listeners with mild or moderate losses, although greater audibility often does not produce greater intelligibility for those with severe or profound losses.
(3) Frequency-response shaping combined with single-channel ''fast-acting wide-dynamic-range compression,'' hereafter referred to simply as compression.
(4) Frequency-response shaping combined with two-channel compression. The crossover frequency between the two channels was 2501 Hz.
(5) Frequency-response shaping combined with four-channel compression. The crossover frequencies between the channels were 793, 2501, and 4453 Hz.
(6) Frequency-response shaping combined with eight-channel compression. The crossover frequencies between the channels were 305, 793, 1525, 2501, 3477, 4453, and 5551 Hz.

The crossover frequencies for the eight-channel system are shown as the bold lines at the top of Fig. 1. More details of the frequency-response shaping and the fitting of the compression systems are given below.

B. Implementation

Both linear amplification and multichannel compression were implemented using a real-time digital signal-processing (DSP) system. The stimuli for the unaided listening condition were also passed through this system, but the processing was set up to give an insertion gain of zero dB for all frequencies up to 7 kHz. The system was based on an Audallion digital hearing aid manufactured by Audiologic, which contains a Motorola DSP56009 DSP chip. For the purpose of this experiment, the microphone of the aid was disconnected and the signal was applied via a direct electrical connection. The internal analog-to-digital converter (ADC, 12-bit resolution, 15 625-Hz sampling rate) was used. Analog circuitry within the aid performed high-frequency emphasis prior to

the ADC, to flatten the speech spectrum and give better coding of the higher-frequency portions of the input. The voltages of the input stimuli were adjusted so that the highest values used were just below the clipping point of the ADC. The output transducer (receiver) of the aid was also disconnected and the electrical output from the internal digital-to-analog converter (DAC, 16-bit resolution) was used to drive the final amplifier.

Every 4.1 ms, the aid operating system delivered a time ''frame'' (a waveform segment) to be processed. This frame contained 128 samples with a 50% overlap with the preceding frame. The data were windowed (using the positive half-cycle of a sine function) and subjected to a fast Fourier transform (FFT) to produce 64 complex values, spaced 122 Hz apart. The effects of the analog high-frequency emphasis used prior to the ADC were compensated for at this stage so as to give a flat frequency response between 125 and 7000 Hz. This also had the effect of reducing quantization noise introduced by the ADC.

In what follows, *bands* refers to frequency ranges used for frequency-response shaping, while *channels* refers to frequency ranges used for compression. The bands had nominal center frequencies (CFs) of 250, 500, 1000, 2000, 3000, 4000, 5000, and 6000 Hz. Frequency ''bins'' resulting from the FFT occurred at intervals of 122 Hz. Bands were achieved by combining bins as follows:

Band 1, CF=250 Hz: dc term, + bins up to 244 Hz (3 bins),
Band 2, CF=500 Hz: Bins from 366 to 732 Hz (4 bins),
Band 3, CF=1000 Hz: Bins from 854 to 1464 Hz (6 bins),
Band 4, CF=2000 Hz: Bins from 1586 to 2440 Hz (8 bins),
Band 5, CF=3000 Hz: Bins from 2562 to 3416 Hz (8 bins),
Band 6, CF=4000 Hz: Bins from 3538 to 4392 Hz (8 bins),
Band 7, CF=5000 Hz: Bins from 4514 to 5490 Hz (9 bins),
Band 8, CF=6000 Hz: Bins from 5612 to 7686 Hz (18 bins).

For the eight-channel compression system, the channels covered the same frequency ranges as the bands. For the four-channel system, bands were combined as follows:

Channel 1: bands 1 and 2,
Channel 2: bands 3 and 4,
Channel 3: bands 5 and 6,
Channel 4: bands 7 and 8.

For the two-channel system, bands were combined as follows:

Channel 1: bands 1, 2, 3, and 4,
Channel 2: bands 5, 6, 7, and 8.

For the single-channel system, all eight bands were combined.

For each compression channel, the signal power was summed across all bins included in that channel; the square root of the power was taken to give an rms value. The logarithm of the channel rms value was calculated in a pseudo-floating point format. By means of a look-up table the logarithm was represented by two components, an integer corresponding to an index of position in the table and a fractional part corresponding to an interpolation between the bracketing index points. The two components were combined into a representation on which linear algebra could be performed on the fixed-point format processor. The log value was low-pass filtered with a two-pole, Bessel-derived filter. The step response of the filter showed no over- or undershoot for either positive or negative steps. The cutoff frequency was 20 Hz, giving a step-response delay (time to 50% of final value) corresponding to two frames (8.2 ms).

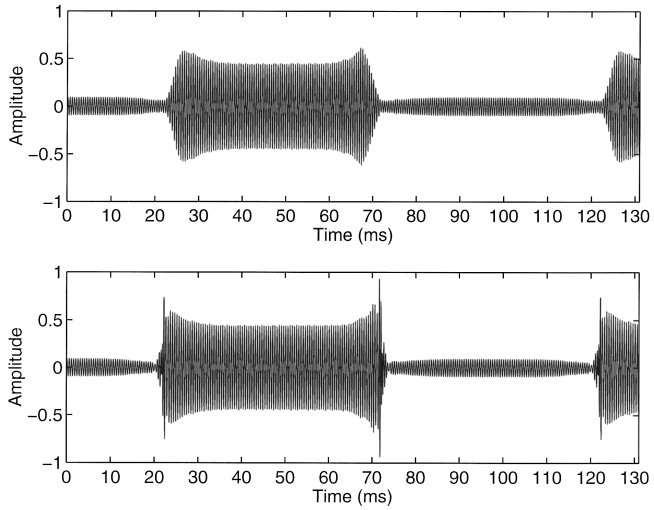

FIG. 2. The response of one channel of the four-channel compression system to a 2000-Hz sinusoid with abrupt 25-dB increases and decreases in level. For the lower panel, the increases and decreases in level were instantaneous. For the upper panel, 5-ms raised-cosine ramps were used between the two levels.

The filtered-envelope value for a given channel was used to calculate the gain value for that channel, as described in the next section. The gain values for the channels were used to calculate gain values at the center frequencies of the eight bands, as described in the next section. Gains at the frequencies corresponding to the 64 bins in the FFT were calculated by interpolation and extrapolation from the eight band values. The interpolation removed step changes in gain values which would otherwise have given rise to excessive oscillatory time-domain responses. As only a 50% overlap was used between successive frames, such oscillations would have led to distortion (time-domain aliasing).

The gain signals so derived were applied to the FFT of an earlier frame stored in a delay line. The delay line introduced a delay to the audio signal that matched the delay associated with the step response of the two-pole envelope filter. This ensured that the audio and gain signals were synchronized, reducing the signal overshoot normally associated with the response of compression systems to abrupt increases in level. A potential problem with this system is that, just before an abrupt decrease in level, the output increases (''preshoot''). However, the two-pole filter had an asymmetric step response which reduced this problem. An inverse FFT was performed on the modified frame and the resulting time frame was windowed (same function as before) and returned to the operating system, where successive frames were combined with 50% overlap. The resultant waveform was fed to the DAC.

Figure 2 shows the response of the second channel in a

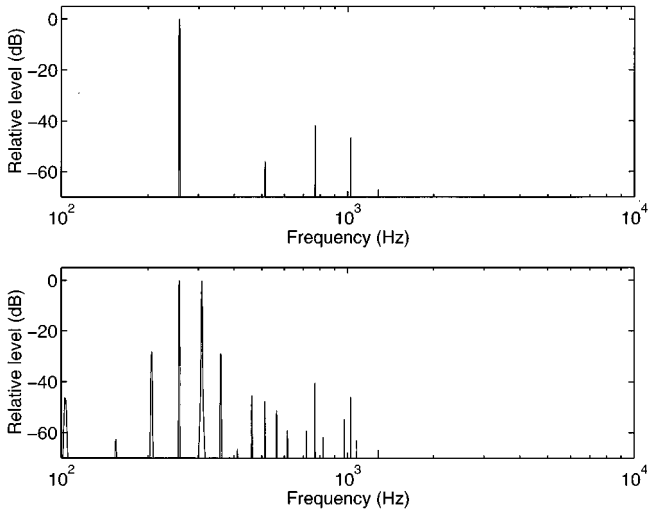

FIG. 3. The spectrum of the output of the lowest channel in the four-channel compression system in response to a 256-Hz sinusoid (upper panel) and the sum of a 256-Hz and a 307-Hz sinusoid (lower panel). The compression ratio was 2.

four-channel system to a 2000-Hz sinusoid with abrupt 25-dB increases and decreases in level. For the lower panel, the increases and decreases in level were instantaneous. For the upper panel, 5-ms raised-cosine ramps were used between the two levels; this is more representative of the rise times typically found for speech signals. The overshoot in response to the increase in level was small, as were the preshoot and the undershoot in response to the decrease in level. The effective attack and release times, after allowing for the delay of the audio signal, were both 7 ms. The compression ratio was 2, so the amplitude ratio between the high-level and low-level portions of the signal was reduced from 17.8 to 4.2.

Fast-acting compression can introduce harmonic and intermodulation distortion, especially at low frequencies, where the gain can change significantly during one cycle of the stimulus. That is one reason why compression circuits in commercial hearing aids typically avoid release times shorter than about 50 ms. However, the fast-acting compression implemented here introduced only moderate distortion for frequencies in the range of typical speech fundamental frequencies, because the envelope filter, with its 20-Hz cutoff frequency, did not significantly distort the envelope of signals with frequencies above about 100 Hz. This is illustrated in Fig. 3. The upper panel shows the spectrum of the response of the lowest channel of the four-channel system (compression ratio=2) to a 256-Hz sinusoid. All harmonic distortion products have levels 40 dB or more below that of the primary tone. The lower panel shows the spectrum of the response of the same channel to the sum of two sinusoids with frequencies of 256 and 307 Hz. The largest intermodulation-distortion products, at 205 and 358 Hz, have levels about 30 dB below the level of the primary tones. These distortion products would be masked by the primary tones, even for normally hearing subjects. Informal listening tests, using normally hearing subjects, confirmed that the harmonic and intermodulation distortion in response to single-tone and two-tone inputs, was not readily audible; the output could not be distinguished from the input when the input and output levels were matched.

III. FITTING OF THE LINEAR AND COMPRESSION SYSTEMS

A. Fitting procedure for the linear system

Target insertion gains were calculated from the audiogram, using the Cambridge formula, as described above. Where gains would be negative, they were set to zero. The gain in each band was set to give the Cambridge target insertion gains as closely as possible. As the earphone had a ''diffuse-field'' response, it was assumed that insertion gains corresponded to programmed gains. The gains at the center frequencies of the bands, i.e., 250, 500, 1000, 2000, 3000, 4000, 5000, and 6000 Hz, are called Glin(1), Glin(2),...,Glin(8).

B. Fitting the compression systems

Two constraints were imposed for all of the compression systems:

(1) The response for a speech-shaped noise input with an overall level of 65 dB SPL should be the same as for the linear system.
(2) As far as possible, speech should be audible over its entire dynamic range in each frequency band when the overall speech level is 45 dB SPL (this corresponds to the case where the speech is presented in a background sound at 65 dB SPL with a speech-to-background ratio of −20 dB. We have shown that normally hearing subjects have SRTs as low as this when the background contains both spectral and temporal dips; see Peters *et al.*, 1998. We wanted to allow for the possibility that multiband compression would restore performance to almost ''normal''). In each frequency band, the dynamic range of the speech was assumed to extend from 18 dB below the rms level to 12 dB above it.

The steps to fulfill these two constraints required the following preliminary calculations:

(1) The absolute thresholds in dB HL at the center frequencies of the bands, ABSHL(i), were converted to equivalent free-field dB SPL. To achieve this, the following conversion factors in dB were added to the values of ABSHL(i): 13, 5, 4, 0, −4, −5, 0, and 4, for the frequencies 0.25, 0.5, 1, 2, 3, 4, 5, and 6 kHz, respectively. These conversion factors, Conv(i), were derived from the free-field absolute threshold values specified in ISO 389-7 (1996), except that 2 dB was added to each threshold value to allow for the average difference between monaural and binaural thresholds (Moore *et al.*, 1997).
(2) For a speech-shaped noise input with an overall (free-field) level of 65 dB SPL, the input levels, I$n(i)$ for each channel in the n-channel compression systems were calculated using the average speech-spectrum shape published in Byrne *et al.* (1994). The resulting values, for

the eight-, four-, two-, and one-channel systems, respectively, were

$$\mathrm{I8}(i) = 60.3,\ 62.6,\ 54.1,\ 47.5,\ 43.8,\ 40.5,\ 38.4,\ 39.8 \text{ dB SPL, for } i = 1 \text{ to } 8, \quad (3)$$

$$\mathrm{I4}(i) = 64.4,\ 54.9,\ 45.3,\ 42.2 \text{ dB SPL, for } i = 1 \text{ to } 4, \quad (4)$$

$$\mathrm{I2}(i) = 64.9,\ 47.0 \text{ dB SPL, for } i = 1 \text{ to } 2, \quad (5)$$

$$\mathrm{I1}(i) = 65.0 \text{ dB SPL, for } i = 1. \quad (6)$$

1. Fitting the eight-channel system

The gains, compression ratios, and compression thresholds for the eight-channel system were calculated in the following way. The subject-dependent gains Glin(1)···Glin(8) should be achieved for speech with an overall input level of 65 dB SPL, corresponding to input levels to the individual channels of I8(1)···I8(8). When speech with an overall input level of 45 dB is applied, the speech minima in the ith channel have a level of $\mathrm{I8}(i) - (65 - 45) - 18$. The gain in the ith channel for that input level should be such that the input of $[\mathrm{I8}(i) - 38]$ is amplified to the absolute threshold. The absolute threshold in dB SPL in the ith channel is $\mathrm{ABSHL}(i) + \mathrm{Conv}(i)$. Therefore, the gain required for speech with an overall input level of 45 dB SPL is

$$G(i) = \mathrm{ABSHL}(i) + \mathrm{Conv}(i) - \mathrm{I8}(i) + 38. \quad (7)$$

For an input of $\mathrm{I8}(i) - 38$, the output is

$$\mathrm{I8}(i) - 38 + \mathrm{ABSHL}(i) + \mathrm{Conv}(i) - \mathrm{I8}(i) + 38 = \mathrm{ABSHL}(i) + \mathrm{Conv}(i). \quad (8)$$

For an input of $\mathrm{I8}(i)$, the output is $\mathrm{I8}(i) + \mathrm{Glin}(i)$. Therefore, over an input range of 38 dB [from $\mathrm{I8}(i) - 38$ to $\mathrm{I8}(i)$], the output changes by $\mathrm{I8}(i) + \mathrm{Glin}(i) - \mathrm{ABSHL}(i) - \mathrm{Conv}(i)$. Therefore, the compression ratio for the ith channel is

$$\mathrm{CR8}(i) = 38/\{\mathrm{I8}(i) + \mathrm{Glin}(i) - \mathrm{ABSHL}(i) - \mathrm{Conv}(i)\}. \quad (9)$$

For example, at 3 kHz, if I8(5)=43.8 dB, Glin(5)=23 dB, ABSHL(5)=50 dB and Conv(5)=−4 dB, the compression ratio is $\mathrm{CR8}(5) = 38/(43.8 + 23 - 50 + 4) = 1.83$. In practice, a limitation has to be placed on the amount of low-level gain. Since previous research suggests that high compression ratios (greater than 2–3) have deleterious effects (Plomp, 1994; Goedegebure *et al.*, 1996; Verschuure and Dreschler, 1996), it seemed reasonable to apply the following constraint: if the denominator of Eq. (9) <13, then this quantity was set to 13. This gave a maximum compression ratio of 2.92. This limited the ability to apply constraint (2)—that speech with a level of 45 dB SPL should be audible over its entire dynamic range—for frequencies above 2 kHz. For the fifth channel (centered at 3 kHz), the constraint could not be met for four subjects out of 18. For the sixth channel (centered at 4 kHz) the constraint could not be met for one-half of the subjects. For the seventh and eighth channels, the constraint could not be met for the great majority of subjects. For a small hearing loss, Eq. (9) can call for a compression ratio less than 1. In this case, the ratio was set to 1.

It was desired to apply the appropriate amplification for levels in the ith channel down to $\mathrm{I8}(i) - 38$ dB SPL, in order to restore audibility of the minima in speech with an overall level of 45 dB SPL. The compression threshold in the ith channel, $\mathrm{CT8}(i)$, was therefore set to $\mathrm{I8}(i) - 38$ dB SPL. However, owing to the limited input dynamic range of the system, if this called for a value of $\mathrm{CT8}(i)$ less than 7 dB SPL, the value was set to 7 dB SPL. In practice, this meant that the compression thresholds for channels five to eight were set to 7 dB SPL. The noise floor imposed by the ADC was equivalent to less than 5 dB SPL in each channel.

2. Fitting the four-channel system

When fitting the four-channel system, it was desired to retain the same degree of flexibility and accuracy in shaping the frequency response as was used with the eight-channel system. This was achieved in the following way. For a 65-dB speech-shaped noise input (i.e., for an input to the first channel of 64.4 dB SPL), the gain in channel 1, $G(\mathrm{ch1})$ was initially set to the mean of Glin(1) and Glin(2). To preserve the appropriate frequency-response shaping, the relative gains in bands 1 and 2 should be the same as for the eight-channel system. Therefore for band 1, the gain was increased by $\{\mathrm{Glin}(1) - \mathrm{Glin}(2)\}/2$ and for band 2, the gain was decreased by $\{\mathrm{Glin}(1) - \mathrm{Glin}(2)\}/2$. A similar procedure was applied for calculating the gains in the other channels and bands for a 65-dB speech-shaped noise input. For a speech-shaped noise with an overall input level of 65 dB SPL, this gave the same output as for the eight-channel system.

The compression ratio for channel n was set to be the mean of the compression ratios $2n-1$ and $2n$ in the eight-channel system. The compression thresholds, $\mathrm{CT4}(i)$, were calculated as for the eight-channel system: $\mathrm{CT4}(i) = \mathrm{I4}(i) - 38$ dB SPL. Note that the values $\mathrm{I4}(i)$ here are those appropriate for the four-channel system, i.e., 64.4, 54.9, 45.3, and 42.2 dB, for $i = 1$ to 4. If this called for a value of $\mathrm{CT4}(i)$ less than 7 dB SPL, the value was set to 7 dB SPL.

3. Fitting the two-channel system

For a 65-dB speech-shaped noise input, the gain in channel 1, $G(\mathrm{ch1})$ was set to the mean of Glin(1), Glin(2), Glin(3), and Glin(4) and the gain in channel 2 was set to the mean of Glin(5), Glin(6), Glin(7), and Glin(8). In a similar way to that described for the four-channel system, the relative gains in the eight bands were adjusted so that, for a speech-shaped noise with an overall input level of 65 dB SPL, the output was the same as for the eight-channel system; the gain in each band was equal to the gain in each channel centered on the same frequency for the eight-channel system.

The compression ratio for channel 1 was set to the mean of the compression ratios for channels 1, 2, 3, and 4 in the eight-channel system. The compression ratio for channel 2 was set to the mean of the compression ratios for channels 5, 6, 7, and 8 in the eight-channel system. The compression thresholds, $\mathrm{CT2}(i)$, were calculated as for the eight-channel

TABLE III. Mean SRTs expressed as speech-to-background ratios, in dB. Results are shown for each type of background sound (single talker, speech-shaped noise amplitude modulated with the envelope of a single talker, speech-shaped noise with 4-ERB wide spectral gaps, and speech-shaped noise with the envelope of a single talker and with 4-ERB wide spectral gaps) and each processing condition. A smaller number indicates better performance. Numbers in parentheses are standard deviations across subjects.

Condition	Type of background			
	Single talker	Modulated noise	4-ERB gaps	Modulated, 4-ERB
Unaided	0.5 (2.9)	0.5 (2.2)	−1.6 (2.4)	−3.0 (2.0)
Linear	−2.0 (2.6)	−1.7 (1.8)	−6.3 (1.9)	−8.0 (2.3)
One-channel compression	−2.3 (2.1)	−3.6 (2.9)	−5.6 (2.3)	−8.8 (2.1)
Two-channel compression	−2.7 (1.7)	−2.7 (2.0)	−5.2 (1.9)	−8.9 (2.4)
Four-channel compression	−3.0 (3.0)	−2.7 (2.0)	−5.7 (2.3)	−8.9 (2.6)
Eight-channel compression	−2.9 (2.6)	−2.9 (1.7)	−6.0 (2.5)	−9.9 (2.9)

system: $CT2(i) = I2(i) - 38$ dB SPL. Note that the values $I2(i)$ here are those appropriate for the two-channel system, i.e., 64.9 and 47 dB.

4. Fitting the one-channel system

The gain, $G(\mathrm{ch1})$ was set to the mean of Glin(1), Glin(2), Glin(3), Glin(4), Glin(5), Glin(6), Glin(7), and Glin(8) for an overall input level of 65 dB. To preserve frequency-response shaping, the relative gains in the eight bands were adjusted so that, for a speech-shaped noise with an overall input level of 65 dB SPL, the output was the same as for the eight-channel system; the gain in each band was equal to the gain in each channel centered on the same frequency for the eight-channel system. The compression ratio was set to the mean of the compression ratios for channels one to eight in the eight-channel system. The compression threshold was set to $65 - 38 = 27$ dB SPL.

IV. RESULTS

The mean results for the 18 subjects are given in Table III. For all four types of background sound, SRTs were highest (poorest) for the unaided condition. Both linear amplification according to the Cambridge formula and compression amplification resulted in lower SRTs. Overall, the conditions with compression gave slightly lower SRTs than the condition with linear amplification. SRTs averaged across type of background were −0.9 dB for the unaided condition, −4.5 dB for linear amplification, −5.1 dB for single-channel compression, −4.9 dB for two-channel compression, −5.1 dB for four-channel compression, and −5.4 dB for eight-channel compression.

A within-subjects analysis of variance (ANOVA) was conducted on the SRTs, with the factors type of background and signal-processing condition. The main effect of type of background was highly significant; $F(3,51) = 195.5$, $p < 0.001$. Mean SRTs were −2.1, −2.2, −5.1, and −7.9 dB, for the single talker, modulated noise, noise with four-ERB gaps, and modulated noise with four-ERB gaps, respectively. *Post hoc* comparisons based on the least-significant-difference test (Snedecor and Cochran, 1967) indicated that the noise with both spectral and temporal dips gave lower SRTs than any of the other noises ($p < 0.001$). The main effect of signal-processing condition was also highly significant; $F(5,85) = 47.24$, $p < 0.001$. Averaged across backgrounds, all five aided conditions gave significantly lower SRTs than the unaided condition ($p < 0.001$). The interaction term was also significant; $F(15,255) = 4.06$, $p < 0.001$. This partly reflects the fact that the change in SRT with type of background was greater for the aided conditions than for the unaided conditions. In particular, the improvement in SRT produced by spectral gaps was greater for the aided conditions than for the unaided condition. For each of the backgrounds considered separately, all of the aided conditions gave significantly lower SRTs than the unaided condition ($p < 0.001$).

A second ANOVA was conducted including only the SRTs for the aided conditions. The main effect of type of background was highly significant; $F(3,51) = 191.7$, $p < 0.001$. Mean SRTs were −2.6, −2.7, −5.8, and −8.9 dB, for the single talker, modulated noise, noise with four-ERB gaps, and modulated noise with four-ERB gaps, respectively. *Post hoc* comparisons indicated that the noise with both spectral and temporal dips gave lower SRTs than any of the other noises ($p < 0.001$). The main effect of signal-processing condition was also highly significant; $F(4,68) = 3.46$, $p = 0.012$. *Post hoc* comparisons showed that the condition with eight-channel compression gave a significantly lower mean SRT than the condition with linear amplification ($p < 0.001$) and than the condition with two-channel compression ($p < 0.05$). The conditions with one- and four-channel compression also gave significantly lower mean SRTs than the linear condition (both $p < 0.05$). Other differences across compression conditions were not significant.

The interaction term was also significant; $F(12,204) = 2.29$, $p = 0.009$. This reflects the fact that the effect of processing condition varied with the type of background. For the single-talker background, the conditions with four-channel and eight-channel compression gave significantly lower mean SRTs than the linear condition ($p < 0.05$). The other conditions did not differ significantly from one another. For the modulated-noise background, the mean SRT was significantly lower for all compression conditions than for linear amplification ($p < 0.05$ or less). The SRTs did not differ significantly across compression systems. For the steady noise with four-ERB spectral gaps, none of the aided conditions differed significantly from one another. For the modulated noise with four-ERB spectral gaps, the mean SRT was

significantly lower for the eight-channel compression system than for the linear condition ($p<0.001$). Also, the mean SRT was significantly lower for the eight-channel system than for the one-, two-, or four-channel compression systems (all $p<0.05$).

The mean SRTs for the unaided condition are similar to those reported by Peters *et al.* (1998) for ten elderly hearing-impaired subjects. The conditions and methods of that experiment were very similar to those of the present experiment. They reported mean SRTs of 0.8, 1.5, −2.1, and −3.1 dB, for the single talker, modulated noise, noise with four-ERB gaps, and modulated noise with four-ERB gaps, respectively, whereas we obtained mean SRTs of 0.5, 0.5, −1.6, and −3.0 dB. Peters *et al.* also reported SRTs using linear amplification as prescribed by the NAL(*R*) formula. Their mean SRTs were close to, but consistently slightly higher (worse) than, those found by us using linear amplification according to the Cambridge formula. Their mean SRTs were −1.9, −1.4, −4.9, and −7.2 dB, for the four types of background, while our mean SRTs were −2.0, −1.7, −6.3, and −8.0 dB. The slightly better SRTs for amplification using the Cambridge formula might reflect the slightly higher gains prescribed by the Cambridge formula for frequencies of 2 kHz and above. However, based on *t*-tests, these differences are not statistically significant.

To examine the relationship of the SRTs to the audiometric thresholds, we calculated Pearson correlations between the SRTs and the mean absolute threshold over a wide frequency range (0.5, 1, 2, and 4 kHz; we will call this ABS_{WB}) and the mean absolute threshold at high frequencies (2, 3, 4, and 5 kHz; we will call this ABS_{HF}). For 18 subjects, the correlation needs to exceed 0.44 to be significant at the 0.05 level, and must exceed 0.56 to be significant at the 0.01 level. For the unaided condition, the correlations for the different types of backgrounds ranged from 0.50 to 0.57 for ABS_{WB} and from 0.4 to 0.6 for ABS_{HF}. For the condition with linear amplification, the correlations were lower, ranging from 0.21 to 0.38 for ABS_{WB} and from 0.004 to 0.30 for ABS_{HF}. For the compression conditions, the SRTs were also only weakly associated with ABS_{WB} and ABS_{HF}, although the correlations were positive in all cases except one. Averaged across types of background, the correlations for the one-, two-, four-, and eight-channel systems were 0.46, 0.41, 0.38, and 0.33 for ABS_{WB} and 0.26, 0.26, 0.15, and 0.21 for ABS_{HF}. Thus, when the reduced audibility of the speech stimuli was partially compensated by linear or compression amplification, the SRTs were only weakly and nonsignificantly associated with the absolute thresholds.

We also assessed whether the improvements produced by compression relative to linear amplification were related to the absolute thresholds. To do this, we calculated correlations between the absolute threshold measures, ABS_{WB} and ABS_{HF}, and the differences in SRTs for the condition with linear amplification and each of the compression conditions. The correlations were nearly all small (typically in the range −0.25 to 0.25) and nonsignificant. We conclude that there is no clear relationship between the absolute thresholds and the benefit from compression.

V. DISCUSSION

Even with amplification, the SRTs of our elderly hearing-impaired subjects were well above (i.e., poorer than) those reported by Peters *et al.* (1998) for elderly subjects with near-normal hearing listening to unamplified stimuli. For example, for the modulated noise with four-ERB gaps, Peters *et al.* reported a mean SRT for the elderly normal-hearing subjects of −16.5 dB, while our SRTs for aided listening ranged from −8.0 dB for linear amplification to −9.9 dB for eight-channel compression. Peters *et al.* presented calculations of the articulation index which suggested that, for hearing-impaired subjects listening to speech in a background with spectral and/or temporal dips, performance would have been limited by part of the target speech spectrum being below absolute threshold. Linear amplification increased the audibility of the target speech, but did not fully restore it. We anticipated that fast-acting compression amplification would improve still further the audibility of the low-level parts of the target speech, and that this would lead to lower SRTs in background noise with spectral and/or temporal dips. The results provide some support for this idea. All of the conditions with compression gave, on average, slightly lower SRTs than the condition with linear amplification. Also, for the modulated noise with four-ERB spectral gaps, the eight-band compression system gave a mean SRT that was 1.9 dB lower than that for linear amplification, and this difference was statistically significant ($p<0.001$). However, the differences in the SRTs between linear amplification and compression were disappointingly small. For the background of a single talker, the multichannel compression conditions gave SRTs that were only about 1 dB lower than that for the linear condition.

One possible reason for the small benefit of compression is that subjects did not have sufficient opportunity to get used to the compression amplification. It may take weeks or even months of listening experience for the benefit of amplification to be revealed, even for linear amplification (Gatehouse, 1992). It is quite possible that, if our subjects had received more practice, preferably with wearable aids, the benefits of compression would have been larger. On the other hand, it should be noted that our stimuli were chosen to have rather extreme temporal and spectral dips, larger than those that would typically be available in everyday life. With less extreme dips, the benefits of compression might be even smaller.

Another possible reason for the small benefits of compression is connected with the effects of cochlear hearing loss on suprathreshold processing. It seems likely that the relatively poor ability of hearing-impaired subjects to understand speech in background sounds with spectral and/or temporal dips arises partly from deficits in the processing of sounds that are above the absolute threshold. Such deficits include reduced frequency selectivity (Pick *et al.*, 1977; Glasberg and Moore, 1986; Tyler, 1986; Moore, 1995; Moore, 1998), reduced temporal resolution for sounds with fluctuating envelopes (Fitzgibbons and Wightman, 1982; Glasberg *et al.*, 1987; Moore, 1995), slow recovery from forward masking (Glasberg *et al.*, 1987), and impaired frequency discrimination for pure tones (Gengel, 1973; Tyler

et al., 1983; Hall and Wood, 1984; Freyman and Nelson, 1986, 1987, 1991; Moore and Glasberg, 1986; Moore and Peters, 1992; Simon and Yund, 1993), and complex tones (Hoekstra and Ritsma, 1977; Rosen, 1987; Moore and Glasberg, 1988b, 1990; Moore and Peters, 1992; Arehart, 1994). Amplification, especially compression amplification, can help to restore audibility, but it compensates only partially, if at all, for these suprathreshold deficits.

We hoped that the effects of reduced frequency selectivity might be partly overcome by the use of multichannel compression with a reasonably large number of bands. For background noises with spectral dips, portions of the target speech falling in the dips may be masked by the surrounding noise. In principle, multichannel compression can alleviate this situation by amplifying the speech in the dips relative to the surrounding noise. Such an effect might have been expected to occur for our two background noises with four-ERB wide dips. In fact, the mean SRT for speech in the modulated background with four-ERB dips was significantly lower for eight-channel compression than for any of the other compression conditions, but the difference was only about 1 dB. For the unmodulated noise with four-ERB gaps, there were no significant differences between compression conditions.

It should be noted, however, that multichannel compression would only be expected to have a beneficial effect if the channels in the compression system cover frequency ranges that correspond mainly to one or more of the dips in the noise. As pointed out in the Introduction, the frequency ranges covered by the compression channels were chosen independently of the frequency ranges of the spectral dips in the background noises. In fact, as can be seen from Fig. 1, only one of the channels of the eight-channel compression system, that with cutoff frequencies of 3477 and 4453 Hz, coincided reasonably well with a spectral notch in the noise. Thus, it is not surprising that increasing the number of compression channels from one to eight had only a small beneficial effect. In principle, further increases in the number of compression channels, with corresponding reductions in the bandwidth of each channel, might lead to a system that was more effective in improving the detectability of portions of the target speech falling in the spectral dips in a background sound. However, such a system has the potential disadvantage of reduced spectral contrasts, which might make it more difficult for the hearing-impaired person to identify speech sounds. Yund and Buckles (1995) investigated the effect of varying the number of channels in a multiband compression system, but they used a steady speech-shaped noise as the background, rather than a noise with spectral or temporal dips. They found that the intelligibility of nonsense syllables in the noise was slightly but significantly improved as the number of channels was increased from four to eight. A further increase to 16 produced no significant change.

It should be emphasized that, in our experiment, while compression amplification gave only modest improvements in the mean SRTs relative to linear amplification, the conditions of the experiment were close to optimal for the linear condition; the Cambridge formula used to derive the frequency-gain characteristic for the linear condition is intended to give a comfortable loudness for speech-shaped noise with a level of 65 dB SPL and to give a specific loudness pattern for such a noise that is almost flat (equal loudness per ERB) over the frequency range 500 to 4000 Hz (Moore and Glasberg, 1998). This usually leads to a high value of the articulation index for speech with a level of 65 dB SPL (Moore and Glasberg, 1998). If the level of the background had been increased to about 75 dB SPL, then in the condition with linear amplification the stimuli would have become uncomfortably loud for many of the subjects. If the level of the background had been decreased, then much of the speech spectrum would have fallen below the absolute threshold.

In everyday life, the level of speech and of background noises can vary over a considerable range (Pearsons *et al.*, 1976; Killion, 1997). With linear amplification, it is very difficult for hearing-impaired people to deal with such a range, except by frequent adjustment of the volume control. This is a major reason why compression amplification is often preferred to linear amplification (Killion, 1997). In our experiment, the conditions with compression would have allowed presentation of speech at levels up to at least 85 dB SPL without any discomfort. Similarly, if the input level had been decreased, the audibility of the target speech would have decreased much less in the compression conditions than in the linear condition. Compression can allow speech in quiet to be understood over a wide range of levels without discomfort, while linear amplification provides comfort and intelligibility only over a limited range of levels (Laurence *et al.*, 1983; Moore *et al.*, 1992). Compression can also improve the intelligibility of speech in background noise when the overall level of the speech and background noise is low, simply because it gives more amplification for low-level sounds. It should be noted that improvements of this type can be produced by slow-acting, single-channel compression (Moore and Glasberg, 1988a; Moore *et al.*, 1991), as well as by fast-acting compression as used in the present experiment. It should also be noted that the fast-acting compression used in the present study differs from that used in many earlier studies. With our method of compression, the depth of modulation for amplitude-modulated signals is decreased uniformly for all modulation rates within the passband of the envelope filter (i.e., rates up to 20 Hz). With simpler compression systems using asymmetric attack and release times (Villchur, 1973; Braida *et al.*, 1982), the reduction of modulation depth (i.e., the effective amount of compression), decreases progressively with increasing modulation rate (Stone and Moore, 1992).

In summary, while our results have shown only a modest benefit for fast-acting compression in comparison to linear amplification, we believe that compression amplification is much more effective than linear amplification in dealing with the wide range of speech levels that occur in everyday life. The (small) benefit of compression under conditions which are optimal for linear amplification might be regarded as a ''bonus.'' Multichannel compression may be slightly better than single-channel compression when background sounds contain both spectral and temporal dips.

ACKNOWLEDGMENTS

We thank Tom Baer for preparing the recording of the background sounds, Brian Glasberg for writing some of the software for fitting the amplification systems, William Irwin for help in collecting and organizing data, Joseph Alcántara and Harry Levitt and an anonymous reviewer for comments on an earlier version of this paper, and Audiologic for the donation of the Audallion digital hearing aid. We also thank our subjects, especially those from the Carol Woods Retirement Community. This project was supported by the American Hearing Research Foundation, the Medical Research Council (UK), Defeating Deafness, and the European Union (SPACE project).

Arehart, K. H. (**1994**). ''Effects of harmonic content on complex-tone fundamental-frequency discrimination in hearing-impaired listeners,'' J. Acoust. Soc. Am. **95**, 3574–3585.

Braida, L. D., Durlach, N. I., De Gennaro, S. V., Peterson, P. M., and Bustamante, D. K. (**1982**). ''Review of recent research on multiband amplitude compression for the hearing impaired,'' in *The Vanderbilt Hearing-Aid Report*, edited by G. A. Studebaker and F. H. Bess (Monographs in Contemporary Audiology, Upper Darby, PA).

Byrne, D., and Dillon, H. (**1986**). ''The National Acoustic Laboratories' (NAL) new procedure for selecting the gain and frequency response of a hearing aid,'' Ear Hear. **7**, 257–265.

Byrne, D., Dillon, H., Tran, K., Arlinger, S., Wilbraham, K., Cox, C., *et al.* (**1994**). ''An international comparison of long-term average speech spectra,'' J. Acoust. Soc. Am. **96**, 2108–2120.

Carhart, R. C., and Tillman, T. W. (**1970**). ''Interaction of competing speech signals with hearing losses,'' Arch. Otolaryngol. **91**, 273–279.

Dillon, H. (**1996**). ''Compression? Yes, but for low or high frequencies, for low or high intensities, and with what response times?,'' Ear Hear. **17**, 287–307.

Dix, M., Hallpike, C., and Hood, J. (**1948**). ''Observations upon the loudness recruitment phenomenon with especial reference to the differential diagnosis of disorders of the internal ear and VIIIth nerve,'' J. Laryngol. Otol. **62**, 671–686.

Duquesnoy, A. J. (**1983**). ''Effect of a single interfering noise or speech source on the binaural sentence intelligibility of aged persons,'' J. Acoust. Soc. Am. **74**, 739–743.

Eisenberg, L. S., Dirks, D. D., and Bell, T. S. (**1995**). ''Speech recognition in amplitude-modulated noise of listeners with normal and listeners with impaired hearing,'' J. Speech Hear. Res. **38**, 222–233.

Fitzgibbons, P. J., and Wightman, F. L. (**1982**). ''Gap detection in normal and hearing-impaired listeners,'' J. Acoust. Soc. Am. **72**, 761–765.

Fowler, E. P. (**1936**). ''A method for the early detection of otosclerosis,'' Arch. Otolaryngol. **24**, 731–741.

Freyman, R. L., and Nelson, D. A. (**1986**). ''Frequency discrimination as a function of tonal duration and excitation-pattern slopes in normal and hearing-impaired listeners,'' J. Acoust. Soc. Am. **79**, 1034–1044.

Freyman, R. L., and Nelson, D. A. (**1987**). ''Frequency discrimination of short-versus long-duration tones by normal and hearing-impaired listeners,'' J. Speech Hear. Res. **30**, 28–36.

Freyman, R. L., and Nelson, D. A. (**1991**). ''Frequency discrimination as a function of signal frequency and level in normal-hearing and hearing-impaired listeners,'' J. Speech Hear. Res. **34**, 1371–1386.

Gatehouse, S. (**1992**). ''The time course and magnitude of perceptual acclimatization to frequency responses: Evidence from monaural fitting of hearing aids,'' J. Acoust. Soc. Am. **92**, 1258–1268.

Gengel, R. W. (**1973**). ''Temporal effects on frequency discrimination by hearing-impaired listeners,'' J. Acoust. Soc. Am. **54**, 11–15.

Glasberg, B. R., and Moore, B. C. J. (**1986**). ''Auditory filter shapes in subjects with unilateral and bilateral cochlear impairments,'' J. Acoust. Soc. Am. **79**, 1020–1033.

Glasberg, B. R., and Moore, B. C. J. (**1989**). ''Psychoacoustic abilities of subjects with unilateral and bilateral cochlear impairments and their relationship to the ability to understand speech,'' Scand. Audiol. Suppl. **32**, 1–25.

Glasberg, B. R., and Moore, B. C. J. (**1990**). ''Derivation of auditory filter shapes from notched-noise data,'' Hearing Res. **47**, 103–138.

Glasberg, B. R., Moore, B. C. J., and Bacon, S. P. (**1987**). ''Gap detection and masking in hearing-impaired and normal-hearing subjects,'' J. Acoust. Soc. Am. **81**, 1546–1556.

Goedegebure, A., Hulshof, M., Maas, A. J. J., and Verschuure, J. (**1996**). ''The effects of syllabic compression on speech intelligibility in hearing impaired,'' in *Psychoacoustics, Speech and Hearing Aids*, edited by B. Kollmeier (World Scientific, Singapore).

Hall, J. W., and Wood, E. J. (**1984**). ''Stimulus duration and frequency discrimination for normal-hearing and hearing-impaired subjects,'' J. Speech Hear. Res. **27**, 252–256.

Hickson, L. M. H. (**1994**). ''Compression amplification in hearing aids,'' Am. J. Audiol. **3**, 51–65.

Hoekstra, A., and Ritsma, R. J. (**1977**). ''Perceptive hearing loss and frequency selectivity,'' in *Psychophysics and Physiology of Hearing*, edited by E. F. Evans and J. P. Wilson (Academic, London).

Hood, J. D. (**1972**). ''Fundamentals of identification of sensorineural hearing loss,'' Sound **6**, 21–26.

Hygge, S., Rönnberg, J., Larsby, B., and Arlinger, S. (**1992**). ''Normal-hearing and hearing-impaired subjects' ability to just follow conversation in competing speech, reversed speech, and noise backgrounds,'' J. Speech Hear. Res. **35**, 208–215.

ISO 389-7 (**1996**). Acoustics—Reference Zero for the Calibration of Audiometric Equipment. Part 7: Reference Threshold of Hearing under Free-field and Diffuse-field Listening Conditions (International Organization for Standardization, Geneva).

Killion, M. C. (**1997**). ''Hearing aids: Past, present and future: Moving toward normal conversations in noise,'' Br. J. Audiol. **31**, 141–148.

Laurence, R. F., Moore, B. C. J., and Glasberg, B. R. (**1983**). ''A comparison of behind-the-ear high-fidelity linear aids and two-channel compression hearing aids in the laboratory and in everyday life,'' Br. J. Audiol. **17**, 31–48.

Lippmann, R. P., Braida, L. D., and Durlach, N. I. (**1981**). ''Study of multichannel amplitude compression and linear amplification for persons with sensorineural hearing loss,'' J. Acoust. Soc. Am. **69**, 524–534.

Miskolczy-Fodor, F. (**1960**). ''Relation between loudness and duration of tonal pulses. III. Response in cases of abnormal loudness function,'' J. Acoust. Soc. Am. **32**, 486–492.

Moore, B. C. J. (**1995**). *Perceptual Consequences of Cochlear Damage* (Oxford U.P., Oxford).

Moore, B. C. J. (**1998**). *Cochlear Hearing Loss* (Whurr, London).

Moore, B. C. J., and Glasberg, B. R. (**1986**). ''The relationship between frequency selectivity and frequency discrimination for subjects with unilateral and bilateral cochlear impairments,'' in *Auditory Frequency Selectivity*, edited by B. C. J. Moore and R. D. Patterson (Plenum, New York).

Moore, B. C. J., and Glasberg, B. R. (**1988a**). ''A comparison of four methods of implementing automatic gain control (AGC) in hearing aids,'' Br. J. Audiol. **22**, 93–104.

Moore, B. C. J., and Glasberg, B. R. (**1988b**). ''Pitch perception and phase sensitivity for subjects with unilateral and bilateral cochlear hearing impairments,'' in *Clinical Audiology*, edited by A. Quaranta (Laterza, Bari, Italy).

Moore, B. C. J., and Glasberg, B. R. (**1990**). ''Frequency selectivity in subjects with cochlear loss and its effects on pitch discrimination and phase sensitivity,'' in *Advances in Audiology*, edited by F. Grandori, G. Cianfrone, and D. T. Kemp (Karger, Basel).

Moore, B. C. J., and Glasberg, B. R. (**1997**). ''A model of loudness perception applied to cochlear hearing loss,'' Aud. Neurosci. **3**, 289–311.

Moore, B. C. J., and Glasberg, B. R. (**1998**). ''Use of a loudness model for hearing aid fitting. I. Linear hearing aids,'' Br. J. Audiol. **32**, 301–319.

Moore, B. C. J., Glasberg, B. R., and Baer, T. (**1997**). ''A model for the prediction of thresholds, loudness and partial loudness,'' J. Audio Eng. Soc. **45**, 224–240.

Moore, B. C. J., Glasberg, B. R., and Stone, M. A. (**1991**). ''Optimization of a slow-acting automatic gain control system for use in hearing aids,'' Br. J. Audiol. **25**, 171–182.

Moore, B. C. J., Glasberg, B. R., and Vickers, D. A. (**1995**). ''Simulation of the effects of loudness recruitment on the intelligibility of speech in noise,'' Br. J. Audiol. **29**, 131–143.

Moore, B. C. J., Johnson, J. S., Clark, T. M., and Pluvinage, V. (**1992**). ''Evaluation of a dual-channel full dynamic range compression system for people with sensorineural hearing loss,'' Ear Hear. **13**, 349–370.

Moore, B. C. J., and Peters, R. W. (**1992**). ''Pitch discrimination and phase sensitivity in young and elderly subjects and its relationship to frequency selectivity,'' J. Acoust. Soc. Am. **91**, 2881–2893.
Nilsson, M., Soli, S. D., and Sullivan, J. A. (**1994**). ''Development of the Hearing in Noise Test for the measurement of speech reception thresholds in quiet and in noise,'' J. Acoust. Soc. Am. **95**, 1085–1099.
Pearsons, K. S., Bennett, R. L., and Fidell, S. (**1976**). *Speech Levels in Various Environments. Report No. 3281* (Bolt, Beranek, and Newman, Cambridge, MA).
Peters, R. W., Moore, B. C. J., and Baer, T. (**1998**). ''Speech reception thresholds in noise with and without spectral and temporal dips for hearing-impaired and normally hearing people,'' J. Acoust. Soc. Am. **103**, 577–587.
Pick, G., Evans, E. F., and Wilson, J. P. (**1977**). ''Frequency resolution in patients with hearing loss of cochlear origin,'' in *Psychophysics and Physiology of Hearing*, edited by E. F. Evans and J. P. Wilson (Academic, London).
Plomp, R. (**1994**). ''Noise, amplification, and compression: Considerations of three main issues in hearing aid design,'' Ear Hear. **15**, 2–12.
Rosen, S. (**1987**). ''Phase and the hearing impaired,'' in *The Psychophysics of Speech Perception*, edited by M. E. H. Schouten (Martinus Nijhoff, Dordrecht).
Simon, H. J., and Yund, E. W. (**1993**). ''Frequency discrimination in listeners with sensorineural hearing loss,'' Ear Hear. **14**, 190–199.
Snedecor, G. W., and Cochran, W. G. (**1967**). *Statistical Methods* (Iowa U.P., Ames, IA).
Steinberg, J. C., and Gardner, M. B. (**1937**). ''The dependency of hearing impairment on sound intensity,'' J. Acoust. Soc. Am. **9**, 11–23.
Stone, M. A., and Moore, B. C. J. (**1992**). ''Syllabic compression: Effective compression ratios for signals modulated at different rates,'' Br. J. Audiol. **26**, 351–361.
Takahashi, G. A., and Bacon, S. P. (**1992**). ''Modulation detection, modulation masking, and speech understanding in noise in the elderly,'' J. Speech Hear. Res. **35**, 1410–1421.
Tyler, R. S. (**1986**). ''Frequency resolution in hearing-impaired listeners,'' in *Frequency Selectivity in Hearing*, edited by B. C. J. Moore (Academic, London).
Tyler, R. S., Wood, E. J., and Fernandes, M. A. (**1983**). ''Frequency resolution and discrimination of constant and dynamic tones in normal and hearing-impaired listeners,'' J. Acoust. Soc. Am. **74**, 1190–1199.
Verschuure, J., and Dreschler, W. A. (**1996**). ''Dynamic compression in hearing aids,'' in *Psychoacoustics, Speech and Hearing Aids*, edited by B. Kollmeier (World Scientific, Singapore).
Villchur, E. (**1973**). ''Signal processing to improve speech intelligibility in perceptive deafness,'' J. Acoust. Soc. Am. **53**, 1646–1657.
Villchur, E. (**1982**). ''The evaluation of amplitude-compression processing for hearing aids,'' in *The Vanderbilt Hearing-Aid Report*, edited by G. A. Studebaker and F. H. Bess (Monographs in Contemporary Audiology, Upper Darby, PA).
Yund, E. W., and Buckles, K. M. (**1995**). ''Multichannel compression hearing aids: Effect of number of channels on speech discrimination in noise,'' J. Acoust. Soc. Am. **97**, 1206–1223.

Subjective effects of peak clipping and compression limiting in normal and hearing-impaired children and adults

P. G. Stelmachowicz, D. E. Lewis, B. Hoover, and D. H. Keefe
Boys Town National Research Hospital, 555 North 30 Street, Omaha, Nebraska 68131

(Received 15 January 1998; accepted for publication 18 September 1998)

Despite many advances in hearing-aid signal processing, compression limiting and peak clipping are still used. To date, perceptual studies have been conducted only with adults. The current study was designed to investigate the clarity of peak-clipped and compressed speech for both adults and children. Subjects were 30 normal-hearing and 30 hearing-impaired individuals in three age ranges (7–9, 10–12, and 16–50 years). Stimuli were processed at 60, 70, 75, and 80 dB SPL using peak clipping and at 80 dB SPL using compression limiting. Paired-comparison measures were used to assess the clarity of sentences, and a signal-to-distortion ratio (SDR) based on a measure of coherence between input and output was computed for each condition. For the peak-clipping conditions, there was a decrease in perceived clarity as the input increased from 60 to 80 dB SPL. This perceptual continuum was most apparent for the normal-hearing adults. The normal-hearing 10–12 year olds and the hearing-impaired adults showed a similar, but less pronounced, pattern. In contrast, the remaining three subject groups showed minimal differences in perceived clarity across conditions. Surprisingly, only the two oldest normal-hearing groups showed a clear preference for compression limiting over peak clipping at the highest input level, and only their results were consistent with the pattern of coherence across stimuli. Judgments of clarity by the normal-hearing subjects correlated best with the SDR in the 500–2000-Hz range, while clarity judgments of the hearing-impaired subjects correlated best with the SDR below 1000 Hz. © *1999 Acoustical Society of America.* [S0001-4966(99)01701-4]

PACS numbers: 43.66.Ts [JWH]

INTRODUCTION

In recent years, there has been a proliferation of advanced signal-processing circuitry for hearing aids. Various forms of nonlinear processing are now widely available in both programmable and nonprogrammable hearing aids. Compression limiting is still widely used, however, to minimize distortion for high-level input signals, and many manufacturers still utilize peak clipping in certain instruments. Many high-gain hearing aids allow the option of either compression limiting or peak clipping. There is evidence that some listeners with severe–profound hearing loss either perform better with peak clipping than with compression limiting or express a preference for peak clipping (Boothroyd *et al.*, 1988; Dawson *et al.*, 1990). For individuals with mild–moderate hearing loss, field studies with both linear and nonlinear processors prompted one hearing-aid manufacturer to incorporate wide dynamic range compression in the low frequencies and linear peak clipping in the high frequencies (Brunved, 1994).

From a purely acoustic standpoint, the negative consequences of peak clipping have been clearly established. If the input stimulus level plus the hearing-aid gain exceed the saturation sound-pressure level (SSPL), then some degree of clipping will occur. When the input signal is speech, it is necessary to consider the overall level as well as the peak-to-rms ratio of speech (usually estimated as 12 dB on average). That is, when the rms level of hearing-aid-processed speech is within 12 dB of the SSPL at any frequency, clipping will occur. Compared to adult hearing-aid users, this situation is likely to occur more often for infants and young children fitted with hearing aids for two reasons. First, because young children demonstrate larger real-ear-to-coupler differences than older children or adults (Feigin *et al.*, 1989; Nelson Barlow *et al.*, 1988; Westwood and Bamford, 1992, 1995), it is often necessary to reduce the SSPL90 of the hearing aid for safety purposes. In some cases (e.g., severe–profound hearing loss) this may limit the available distance (in dB) between the peaks of speech and the maximum output as a function of frequency (Preves and Newton, 1989). Second, for infants and young children, communication often occurs at a reduced speaker–listener distance (e.g., while the child is held by a parent or sitting on a parent's lap). Under these circumstances, the input levels can be 15–20 dB higher than average conversation at a distance of 1 m (Stelmachowicz *et al.*, 1993). It is also the case that self-generated speech is one of the most common inputs to the hearing-aid microphone. Cornelisse, Gagne, and Seewald (1991) have shown that the overall level of a child's own voice measured at ear level is approximately 13 dB higher than at a 1 m, 0 deg azimuth position. These high-level input signals can result in nonlinear operation of a hearing aid and have implications for the method of output limitation to be used with this population.

A. Intelligibility

Despite the known acoustic drawbacks to hearing-aid circuits which utilize peak clipping, studies of the effects of this type of processing on the intelligibility of speech have produced varying results. Some of the earliest studies suggested that peak clipping was not detrimental to intelligibil-

ity (Martin, 1950; Licklider, 1964; Pollack, 1952). This effect was probably related to the fact that the two types of stimuli were equated in terms of peak level. When the reduced peak-to-rms ratio associated with peak clipping is taken into account during calibration (by equating rms levels), however, most studies show a slight reduction in intelligibility as the magnitude of clipping is increased. Direct comparisons between peak clipping and compression limiting have been made only in a small number of studies. Using a phoneme identification task, Dreschler (1988) found a mean advantage of approximately 12% for compression limiting. Using a word-recognition task in both quiet and noise, May, Dillon, and Battaglia (1989) compared compression limiting to peak clipping for both normal-hearing subjects and subjects with mild–moderate hearing loss. They found a statistically significant advantage for compression limiting over peak clipping only for the hearing-impaired subjects in the noise condition. Crain and Van Tasell (1994) measured speech-reception thresholds for spondees and found that significant threshold shifts occurred only when clipping exceeded 18 dB. Using both sentence and phoneme test materials, Dawson, Dillon, and Battaglia (1990) found no significant differences in speech intelligibility between peak-clipped and compressed speech for subjects with severe–profound hearing loss. Although a peak-clipping condition was not used as the reference, in a study of individuals with profound hearing loss, Boothroyd *et al.* (1988) found a significant reduction in speech perception for some subjects when compression limiting was used. The pattern of errors was consistent with the notion that compression degraded normal amplitude envelope cues that were critical for perception in this population.

B. Quality of speech

The effects of peak clipping and compression limiting on the perceived quality of speech also have been studied. Hawkins and Naidoo (1993) compared asymmetrical peak clipping with compression limiting for subjects with mild–moderate hearing loss. Their subjects were asked to rate the quality of hearing-aid-processed speech (in both quiet and noise) and music. They found a statistically significant preference for compression limiting which became more pronounced as the magnitude of saturation increased. In contrast, May, Dillon, and Battaglia (1989) found no significant differences in sound quality between peak clipping and compression circuits for 12 subjects with mild–moderate hearing loss. For subjects with severe–profound hearing loss, Lyregaard (1986) found that 50% of the group preferred peak clipping and 50% preferred compression limiting. Dawson, Dillon, and Battaglia (1990) used two types of questionnaires to assess hearing-aid benefit and satisfaction for 14 subjects with severe–profound hearing loss. No significant differences were observed for the two types of processing.

C. Coherence measures

Recently, there have been attempts to relate a physical measure of the distortion produced by hearing aids to the distortion perceived by listeners (Crain and Van Tasell, 1994; Fortune and Preves, 1992a, b; Hawkins and Naidoo, 1993; Kates, 1992; Kates and Kozma-Spytek, 1994; Kozma-Spytek *et al.*, 1996; Preves and Newton, 1989). Kates (1992) has formulated coherence and signal-to-distortion ratio (SDR) as a tool to measure nonlinearities in hearing aids excited using broadband-noise stimuli. This measure has potential as an objective predictor of subjective responses to various nonlinear processing algorithms used in hearing aids, but it is limited in its formulation to broadband noise. The temporal aspects of speech are complex, and the time-varying nonlinear processing algorithms cope with these complexities by the use of various compression thresholds and attack and release times to control the transition from linear to nonlinear processing. The physical performance of any such algorithm, let alone its subjective influences, for a speech stimulus cannot be predicted solely by a physical measurement using random noise as an input.

A number of previous researchers have used speech stimuli to measure the coherence of various types of hearing-aid processing (Dyrlund, 1992; Dyrlund *et al.*, 1994; Fortune and Preves, 1992b; Crain and Van Tasell, 1994). Dyrlund (1992) and Dyrlund *et al.* (1994) measured coherence and SDR using speech and other signals as stimuli to hearing aids, and found that the SDR was significantly reduced for hearing aids with nonlinear signal processing. They pointed out that both a short-term and long-term coherence can be defined, and that these are only identical for a linear system. Because the short-term coherence fluctuates with the automatic gain-control characteristics of the device, the long-term and short-term coherence are unequal for a nonlinear system. They concluded that coherence analysis is only valid for linear hearing aids because it is impossible to separate the distortion due to intentional nonlinear signal processing from other sources of nonlinear distortion or additive noise. In the Dyrlund (1992) and Dyrlund *et al.* (1994) studies, coherence was measured as that quantity conventionally output by a two-channel spectrum analyzer, and thus represented only the long-term coherence. Fortune and Preves (1992b) measured coherence using continuous discourse and speech-shaped noise presented at various levels. As part of their analysis, they averaged the coherence responses obtained in each frequency bin across the entire frequency range to obtain a single value for coherence, which was used to characterize a given hearing-aid processing condition. They concluded that the distortion produced by a saturating hearing aid contributes to the perceived discomfort of the hearing aid at high output levels. Crain and Van Tasell (1994) calculated coherence for spondees processed by both peak clipping and compression limiting. They also averaged the coherence across the frequency range of interest to obtain a single mean coherence that characterized the hearing-aid processing. This mean coherence was used to predict degradations in speech intelligibility.

The results of these studies support the view that the (magnitude-squared) coherence $\gamma^2(f)$, defined in the Appendix, is reduced relative to a linear hearing aid by the types of processing algorithms used in nonlinear hearing aids. One can operationally define a ratio in terms of this coherence by $\gamma^2/[1-\gamma^2]$. In a linear system, this ratio is precisely equal

TABLE I. Mean pure-tone thresholds (in dB HL) and standard deviation (in parentheses) for each subgroup of hearing-impaired subjects. Also shown is the percentage of individuals that is aided within each group and the circuit type of their personal hearing aids (PC=peak clipping, CL=compression limiting, WDRC=wide dynamic range compression).

	Frequency (Hz)							
Group	250	500	1000	2000	4000	8000	% Aided	Circuit type
7–9 years	35.0	37.0	47.0	52.5	47.0	47.0	90%	5 PC, 1 CL,
$N=10$	(15.0)	(11.7)	(11.2)	(7.5)	(12.9)	(18.2)		3 WDRC
10–12 years	29.4	37.2	48.9	52.2	47.2	51.7	70%	4 PC, 3 CL
$N=10$	(14.0)	(14.6)	(14.9)	(16.3)	(15.7)	(16.0)		
16–50 years	35.5	35.5	41.0	51.5	49.0	63.5	50%	3 PC,
$N=10$	(15.2)	(13.9)	(12.6)	(12.9)	(13.9)	(18.3)		2 WDRC

to the ratio of the coherent output signal power to the noise power (i.e., incoherent power). In a nonlinear system using a random input stimulus, this ratio is equal to the ratio of the coherent signal power to the sum of the noise power and the distortion power. The noise in a high-quality nonlinear hearing aid is usually small compared to the distortion produced by the nonlinearities, and can therefore be neglected, so that the ratio simplifies to an SDR. It is complicated to compare the coherence of linear and nonlinear hearing aids, because the linear algorithm is controlled by system noise (which has a relatively constant envelope) and the nonlinear algorithm is controlled by system distortion (which fluctuates with signal level).

Because speech stimuli influence the temporal behavior of a nonlinear hearing aid in a much different manner than random noise, the measurement of coherence using random noise may not be indicative of the coherence measured using speech. There are reasons to use speech stimuli for distortion measurements, but there are gaps in our knowledge and problems to be overcome. No studies on coherence in hearing aids using speech stimuli have controlled for bias error due to group delay by the hearing aid (Kates, 1992). No studies have measured the short-term coherence or short-term SDR during continuous discourse, so it is unknown how the time-varying nature of speech influences the short-term transfer functions. Finally, it is necessary to formulate nonlinear coherence measurements using speech stimuli in a manner that can be related to the SDR, and there are subtle aspects involved in averaging responses across frequency. An approach addressing these issues is described in the Appendix.

D. Statement of the problem

To date, the studies in which a comparison was made between compression limiting and peak clipping were conducted with adult subjects. Since both forms of processing are in widespread clinical use, it is important to understand the perceptual consequences of peak clipping and compression limiting for young children who are in the process of speech and language development. The primary goal of the present study was to investigate the perceived clarity of peak-clipped vs compressed speech for both adults and children. A secondary goal was to examine the relationship between the perceived clarity of speech and a physical measure of hearing-aid distortion.

I. METHODS

A. Subjects

Sixty subjects participated in this experiment. Thirty subjects had normal hearing and 30 had mild–moderate sensorineural hearing losses. Within each group, subjects were divided into three age ranges with ten in each subgroup: 7–9 years, 10–12 years, and 16–50 years. All normal-hearing subjects had thresholds $\leqslant$20 dB HL from 250–8000 Hz. The mean thresholds of the hearing-impaired subjects are shown in Table I along with the percentage of subjects that was aided in each group and the circuit types. Across these subjects, scores on an age-appropriate test of word recognition (PBK-50 or NU-6) ranged from 66%–100%.

B. Hearing aid

In this study, all stimuli were processed by a Phonak PICS (Sonoforte 332X) hearing aid. Two different conditions of output limiting were included: compression limiting with adaptive release time and peak clipping.[1] For the compression-limiting mode, the attack time was 8 ms and the release time varied from 80 to 1000 ms depending upon the length of time that the signal exceeded the compression threshold. We elected to use the adaptive release time because this type of processing is used by at least three different manufacturers in their compression-limiting circuits. Using target values based on the desired sensation level approach (Seewald, 1988), this hearing aid was adjusted to provide recommended gain and maximum output for a hypothetical listener with a moderate hearing loss. The frequency/gain characteristics and SSPL90 curves for both the peak-clipping and compression-limiting conditions are shown in Fig. 1. Many previous studies have used large amounts of peak clipping. Our goal was to provide realistic levels of peak clipping, comparable to what one might actually encounter under typical conditions with a well-fit hearing aid. As such, we assumed that the most common high-level input to the hearing-aid microphone during actual use would be the wearer's own voice, which we assumed would occur at an overall level of 75–80 dB SPL. With this frequency response and maximum output, an 80 dB SPL pure-tone signal at 1000 Hz would be clipped by approximately 3 dB. Obviously, speech would be clipped to a greater extent because of the high peak-to-rms ratio.

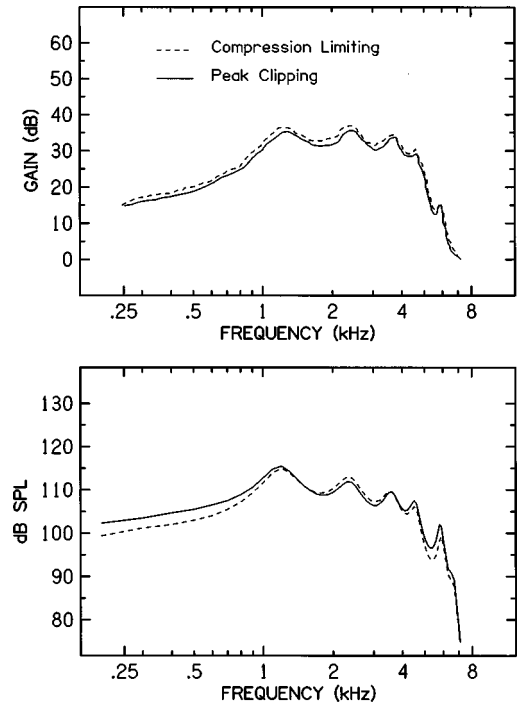

FIG. 1. Top panel: 2-cm^3 coupler gain (measured with a 60-dB SPL speech-weighted signal) as a function of frequency for the compression-limiting and peak-clipping circuits. Lower panel: 2-cm^3 coupler saturation sound-pressure level as a function of frequency (measured with a 90-dB SPL swept pure-tone signal) for the compression-limiting and peak-clipping circuits.

C. Stimuli

Test stimuli were five sentences from the connected sentence test (Cox *et al.*, 1987, 1988). The long-term rms level of the unprocessed sentences was measured using the following procedure. Each sentence was presented to a loudspeaker located within a hearing-aid test box and the output of a 1/2-in. microphone was low-pass filtered at 9500 Hz, digitized at a 20-kHz rate, and stored digitally. An overlapping (50%) 120-ms Hanning window was applied and the rms level of the entire sentence (including pauses) was measured. With the hearing aid attached to a 2-cm^3 coupler, these sentences were presented to the hearing aid at 60, 70, 75, and 80 dB SPL in the peak-clipping condition (PC60, PC70, PC75, and PC80). These levels were selected to provide a condition of near-linear operation (60 dB) and a range of nonlinear operation of the hearing aid. For the compression-limiting condition (CL80), test stimuli were presented at a single level of 80 dB SPL. The processed stimuli were low-pass filtered and stored digitally. Minor adjustments were made in the amplitude of the stored waveforms to produce equivalent rms levels across all test stimuli.

D. Procedure

The goal of this experiment was to determine how peak clipping and compression limiting affected judgments of clarity of speech. Pilot data with children in the 7–9-year age range revealed that many of these children had difficulty with a rating task. Specifically, the children rarely judged any of the sentences as ''clear,'' presumably because all signals had been processed by a hearing aid. Furthermore, the perceptual differences between conditions were often very subtle because a large amount of peak clipping was not occurring. Eisenberg, Dirks, and Gornbein (1997) have shown that a paired-comparison task is more sensitive to differences in clarity than a category-rating task. Therefore, a paired-comparison procedure was used for this experiment.

Although the test stimuli were initially processed with different input levels (thus creating varying levels of distortion), test stimuli were presented at each subject's most comfortable loudness level (based on running speech) to minimize the influence of loudness on judgments of clarity. Following processing, it was noted that the perceived loudness of the sentences varied across the five processing conditions. Equating neither the rms level nor the peak level of these sentences produced ''equal loudness'' across conditions. We chose to equate the rms level across all stimuli, but to vary the level over a 5-dB range during stimulus presentation in order to remove the influence of loudness differences from the judgments of clarity. Each stimulus pair was preceded by a 1000-Hz warning signal. For each trial, the subject listened to the same sentence processed in two different ways (e.g., PC60 vs PC70), and was instructed to indicate which of the two sentences sounded clearer.[2] The paired-comparison task utilized a round-robin tournament in which every condition was paired with every other condition to form ten pairs. The order of presentation was counterbalanced, producing 20 pairs for each of the five sentences (100 pairs). Prior to testing, subjects were given a short training session using highly divergent conditions.

Data for both experiments were collected in 1–2 sessions which lasted approximately 90–120 min. Frequent breaks were provided as needed during data collection.

E. Coherence measures

Since any coherence function is biased by the presence of a time delay between the input and output signals, this bias error was removed prior to the calculation of coherence using a slight modification in the algorithm described by Kates (1992). In this study, the unbias filtering and coherence calculations were implemented on a laboratory computer using MATLAB. Each 50-ms window of speech input and hearing-aid output was multiplied by a Hanning window and the discrete Fourier transforms were calculated (sample rate 20 kHz and frequency bin width of approximately 20 Hz). An SDR function was calculated for each window of data and the set of SDR functions over the entire waveform formed an SDR waveform. Because there was a 2:1 overlapping of analysis windows, the short-term SDR waveform had a sample period of 25 ms. Octave averages were calculated, and the outputs were SDR waveforms in the 500-, 1000-, 2000-, and 4000-Hz octaves. By averaging across all four octaves, a single SDR waveform also was calculated.

Each SDR waveform obtained was a short-term transfer function, the fine structure of which varied for each sentence used. For time intervals when the hearing aid was behaving linearly, the SDR value tended to be large, since it was constrained only by noise (i.e., the SDR) behaved near its peak values like a signal-to-noise ratio. When the hearing aid was clipping or limited by compression, the corresponding SDR

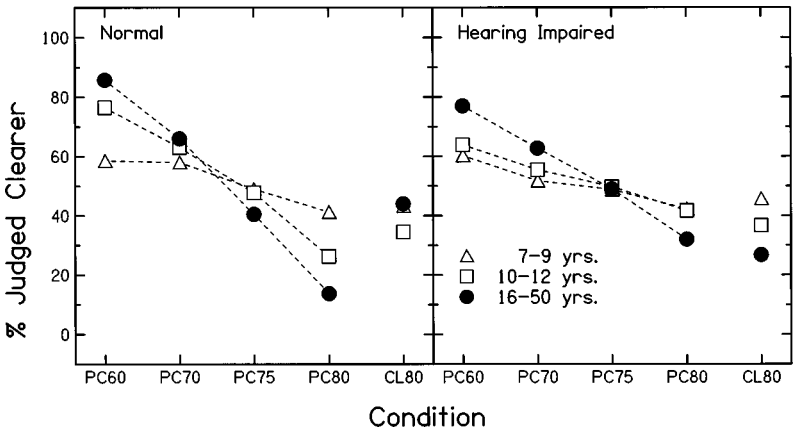

FIG. 2. Percent judged clearer as a function of test condition. The left and right panels show data for the normal- and hearing-impaired subjects, respectively. The parameter in each panel is age group.

value was much lower due to the influence of distortion. For time intervals when the input signal power was small, the SDR was also small. Thus, the SDR waveform for speech was characterized by peaks and broad dips during continuous speech, and by nulls during silent portions.

Since the intent was to use the SDR to account for the subjective quality of hearing aids, it was necessary to reduce the SDR waveforms to a manageably small number of variables. The mean and standard deviation of the SDR in each octave band (or over the entire bandwidth) for each sentence was calculated after discarding the transient onset of SDR at the beginning of the utterance and the transient decay of SDR at the end of the utterance. The criterion was that the SDR in time windows at the beginning and end of the utterance had to exceed 25% of the median value of SDR over the entire waveform to be included in the calculation of the mean and standard deviation. The SDR mean was a measure of the typical SDR of the hearing-aid algorithm during continuous speech, and the SDR standard deviation was a measure of the fluctuations in the SDR during continuous speech. The grand average of the SDR mean and standard deviations were calculated over the five sentences used in the subjective study. Thus, each hearing-aid processing condition was quantified within each frequency band by two values, the SDR mean and standard deviation.

II. RESULTS AND DISCUSSION

For all subjects, the number of times each condition was selected as clearer was divided by the total number of paired presentations (100) to derive the selection rate for each condition. Figure 2 presents the mean data showing the percent judged clearer as a function of condition for the ten subjects in each group. Table II presents the standard deviations (s.d.) and the range associated with these mean data. In general, the s.d.s do not appear to be markedly different as a function of age group, test condition, or the presence or absence of hearing loss. From Fig. 2, it can be seen that there is a decrease in selection rate as the input level is increased from 60 dB SPL (PC60) to 80 dB SPL (PC80). This perceptual continuum is most apparent for the normal-hearing 16–50-year-old group. The normal-hearing 10–12 year olds and the 16–50 year old hearing-impaired subjects showed a clear, but less pronounced, decrease in selection rate across conditions. In contrast, the slope of the function for the youngest normal-hearing subjects and the two youngest hearing-impaired groups was quite shallow, suggesting that these subjects may have been unable to differentiate between many of these conditions.

A small number of studies has been reported in which a paired-comparison procedure has been used with children to determine the preferred frequency response of a hearing aid

TABLE II. Standard deviation and range (in parentheses) associated with the selection rates reported in Fig. 2.

	Condition				
	PC60	PC70	PC75	PC80	CL80
Normal hearing	0.14	0.09	0.09	0.15	0.11
7–9 years	(0.40–0.85)	(0.45–0.75)	(0.38–0.60)	(0.18–0.68)	(0.20–0.58)
	0.10	0.09	0.10	0.10	0.10
10–12 years	(0.58–0.88)	(0.45–0.75)	(0.25–0.60)	(0.10–0.45)	(0.28–0.58)
	0.11	0.05	0.10	0.09	0.15
16–50 years	(0.63–0.95)	(0.55–0.75)	(0.23–0.50)	(0.05–0.35)	(0.15–0.68)
Hearing impaired	0.17	0.08	0.10	0.12	0.08
7–9 years	(0.40–0.90)	(0.35–0.63)	(0.28–0.65)	(0.20–0.58)	(0.28–0.63)
	0.08	0.06	0.05	0.08	0.08
10–12 years	(0.48–0.78)	(0.47–0.65)	(0.45–0.63)	(0.30–0.53)	(0.25–0.50)
	0.15	0.11	0.07	0.12	0.15
16–50 years	(0.50–0.93)	(0.43–0.78)	(0.33–0.55)	(0.18–0.52)	(0.08–0.52)

(Ching *et al.*, 1994, 1995; Eisenberg and Dirks, 1995; Eisenberg and Levitt, 1991). Eisenberg and Dirks (1995) asked normal-hearing children in four age groups between 4 and 8 years to judge the clarity of filtered speech. The 4-year-old children demonstrated poorer test–retest reliability and were less sensitive to the differences in filter settings than the older children. They concluded that paired-comparison procedures can be used reliably in children as young as 5 years of age provided that they have normal language skills. In the present study, however, both the normal-hearing and hearing-impaired 7–9 year olds were less sensitive to the distortion associated with signal processing than the older subjects. It is likely that the lower age limit for reliable and valid measures is related to the magnitude of differences between test stimuli. The differences in lower age limit between the two studies may be related to the fact that the degree of peak clipping in the current study produced only subtle differences between stimuli.

It also appears that for the two older groups, the functions in Fig. 2 are slightly more shallow for the hearing-impaired than for the normal-hearing subjects. This result is consistent with the findings of Kozma-Spytek, Kates, and Revoile (1996). In their study, subjects with moderate–profound hearing losses rated the quality of sentence materials that had been peak-clipped at 0, 4, 8, and 12 dB above the rms level of sentences. Compared to normal-hearing subjects from an earlier study (Kates and Kozma-Spytek, 1994), the listeners with impaired hearing were less sensitive to the acoustic differences across peak-clipping conditions. Lawson and Chial (1982) also found that subjects with moderate hearing losses were less sensitive to distortion of speech produced by linear rectification than were normal-hearing subjects.

It is also of interest to look at the selection rate for the CL80 condition. For the normal-hearing 10–12 and 16–50 year olds, CL80 showed a higher selection rate than PC80. For the youngest normal-hearing group and all three hearing-impaired groups, the selection rate for CL80 was similar to or less than the selection rate for PC80.

A three-way analysis of variance (ANOVA) was performed. A significant three-way interaction (condition by hearing status by age) was observed [$F(8,102)=2.30$, $p=0.036$]. Since the slopes of the functions in Fig. 2 appear to suggest an interaction between age and hearing status, simple effects tests were performed for each age category independently. For the 7–9 year olds, there was a significant effect of condition [$F(4,216)=6.86$, $p<0.001$] but no hearing status effect or condition by hearing status interaction. For the 10–12 year olds, there was a significant effect of condition [$F(4,216)=29.52$, $p<0.001$], a significant condition by hearing status interaction [$F(4,216)=3.54$, $p=0.008$], but no hearing status effect. For the oldest group, there was a significant effect of condition [$F(4,216)=70.38$, $p<0.001$], a significant condition by hearing status interaction [$F(4,216)=6.40$, $p<0.001$], but no hearing status effect.

The results discussed thus far were analyzed in terms of the overall selection rate for each condition. Figure 3 shows a direct comparison between the PC80 and CL80 conditions, excluding all other comparisons. This figure shows the percentage of time that CL80 was judged to be clearer than PC80 as a function of age for both the normal-hearing and hearing-impaired groups. For both groups of 7–9 year olds, the percentages were slightly above chance level, suggesting that these youngest children could not distinguish the two conditions. The pattern of results for the remaining groups is unexpected. The normal-hearing 10–12 year olds demonstrate chance performance just like the younger children. The normal-hearing 16–50 year olds, however, show a clear preference for compression limiting with an average selection rate of 74%. In contrast, the 10–12 and 16–50 year old hearing-impaired subjects judge CL80 to be clearer than PC80 only about 40% of the time. As would be expected, a two-way ANOVA revealed a significant hearing status by age interaction [$F(2,54)=5.91$, $p<0.005$]. These findings suggest that, for the 80-dB SPL conditions, subjects in the two oldest hearing-impaired groups preferred peak clipping to compression limiting. This particular trend has been observed previously in subjects with severe–profound hearing loss (Dawson *et al.*, 1990; Lyregaard, 1986). For subjects with mild–moderate losses, however, previous studies have yielded conflicting results. Hawkins and Naidoo (1993) found a statistically significant preference for compression limiting (even with only 5 dB of clipping) while May (1988) found no significant differences in perceived intelligibility between compression-limiting- and peak-clipped speech. It is possible that the magnitude of distortion by peak clipping in the Hawkins and Naidoo (1993) study may have been greater than in the May (1988) study and the current investigation. Unfortunately, different methods were used to quantify distortion in these studies, so it is not possible to verify this hypothesis.

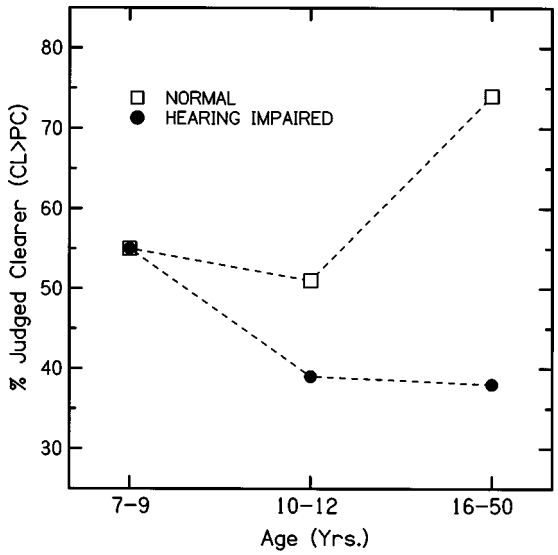

FIG. 3. Percentage of time that compression limiting was judged clearer than peak clipping as a function of age group for both the normal and hearing-impaired groups.

A. Coherence measures

It is of interest to ask how the physical measures of distortion for these test stimuli might relate to the perceptual data. Figure 4 shows the SDR as a function of time for the

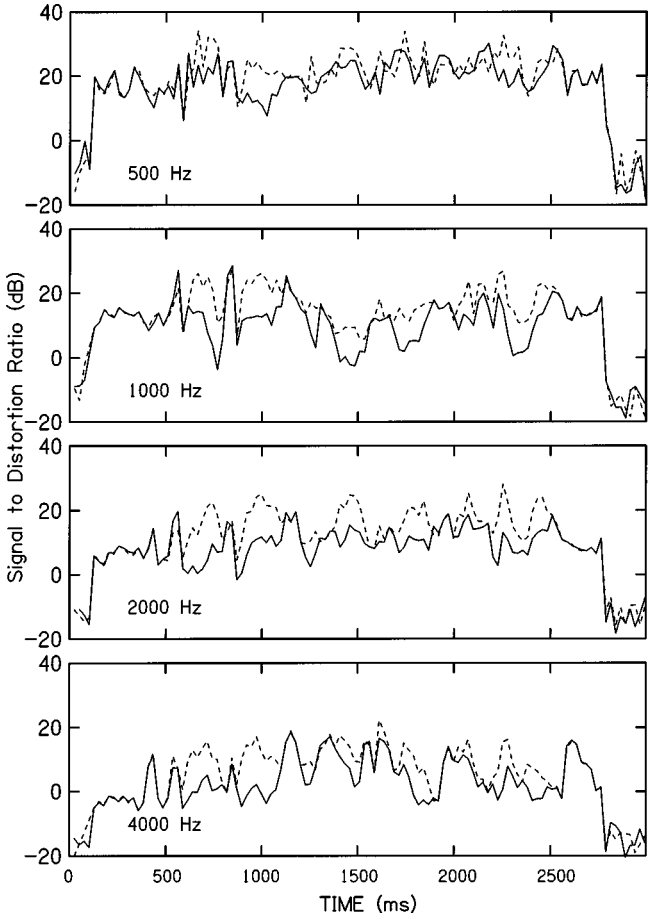

FIG. 4. SDR as a function of time for a single sentence processed by either peak clipping (solid line) or compression limiting (dashed line). Each panel represents a different octave band.

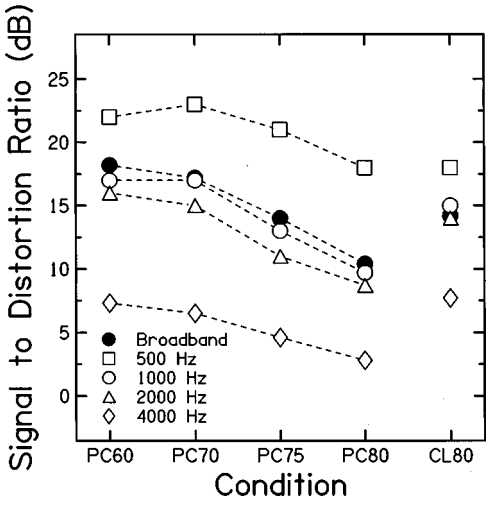

FIG. 5. Signal-to-distortion ratio as a function of test condition. The filled circles illustrate results of the broadband analysis and the various open symbols depict the octave-band analyses.

sentence, ''Colored glass was used in European windows.'' Each panel represents a different octave band, the solid line represents the PC80 condition while the dashed line shows the CL80 condition. In general, the SDR is greater for compression limiting compared to peak clipping. However, the differences between the two conditions vary throughout the sentence and are greatest at 1000 Hz and above. To obtain SDR values that could be used to compare conditions easily, values were collapsed across both time and frequency to create a broadband SDR for each sentence. These values were then averaged across the five sentences. In a similar fashion, SDRs were collapsed across time and averaged across the five sentences to create mean SDRs in each octave band.

In Fig. 5, the mean SDR for the five sentences is plotted as a function of the test condition. The filled circles represent the SDR when the analysis was performed on the entire signal (350–5660 Hz) and the open symbols depict the SDR for octave bands from 500 to 4000 Hz. In general, the SDR is highest at 500 Hz and lowest at 4000 Hz (where the hearing-aid gain is low). The broadband analysis is most similar to the octave-band analysis at 1000 Hz. For all functions, the SDR decreases from PC60 to PC80. With the exception of the 500-Hz-band analysis, the SDRs for the CL80 condition increase markedly relative to PC80. For the broadband analysis, as well as 1000 and 2000 Hz, the SDR for the CL80 condition is roughly equivalent to SDRs in the PC70 to PC75 range. At 500 Hz, however, the SDRs for PC80 and CL80 are nearly identical.

The patterns observed in this figure can be compared to the data in Fig. 2. For the normal-hearing 10–12 and 16–50 year olds, the perceptual pattern is quite similar to that shown for the broadband, 1000-Hz, and 2000-Hz analyses. That is, there is a monotonic decrease from PC60 to PC80 with a marked increase for the CL80 condition. In contrast, the youngest normal-hearing group and all three hearing-impaired groups show a minimal difference or a slight decrease in CL80 relative to PC80. It is possible that perceptual judgments of the hearing-impaired listeners may have been weighted more heavily by the low-frequency components of the signal than was the case for the normal-hearing listeners.

To investigate this possibility, correlation coefficients relating selection rate to the SDR at each octave frequency were computed for each of the three age groups of normal and hearing-impaired subjects. Regardless of hearing status, the correlation coefficients for the youngest subjects were low (0.26–0.50). Thus, additional analyses were designed to investigate the oldest two subject groups only, and a 0.05 level of significance was adopted for all tests. For each subject, the normalized correlation coefficients between the five clarity scores and the five SDR scores were calculated. Separate two-way ANOVA were conducted for each of the five analysis bands. Results revealed a significant main effect for hearing status for all analysis bands except 500 Hz. In all cases, there was no effect of age and no age by hearing status interaction. Because age was not significant in this analysis, the older children and adults were combined into a single group ($N=40$) for all subsequent analyses. Figure 6 shows the mean correlation coefficients as a function of the analysis band for both the normal and hearing-impaired subjects. For the normal-hearing subjects, the correlation coefficients were relatively high for all analysis bands except 4000 Hz. In contrast, the hearing-impaired group showed the highest correlation at 500 Hz, followed closely by the broadband condition. Above 500 Hz, there was a steady decrease in correlation as a function of frequency.

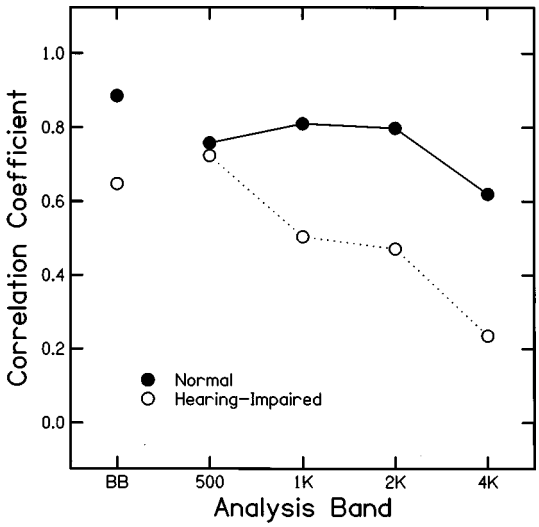

FIG. 6. Correlation coefficient as a function of analysis band for both the normal (filled circle) and hearing-impaired (open circles) subjects (>10 years of age).

A repeated-measures ANOVA was conducted to determine if significant differences in the correlation coefficients existed across the two groups (normal vs hearing impaired) or across the analysis frequencies. Results revealed a significant main effect for hearing status and analysis frequency and a significant hearing status by analysis frequency interaction. These findings support the notion that the normal-hearing and hearing-impaired subjects in this study used different cues to judge signal quality. To investigate this further, contrasts between the correlation coefficients were examined across analysis frequency and hearing status. For the hearing-impaired group, the correlation at 500 Hz was significantly higher than the correlations at 1000, 2000, and 4000 Hz, and the correlations at 1000 and 2000 Hz were significantly higher than at 4000 Hz. For the normal-hearing group, the correlations at 500, 1000, and 2000 Hz were similar, but the correlations at 1000 and 2000 Hz were significantly higher than at 4000 Hz.

These findings are partially consistent with the results of an investigation reported by Kozma-Spytek, Kates, and Revoile (1996). They studied the relation between quality judgments of peak-clipped speech and coherence measured with a speech-shaped noise test signal for both normal-hearing and hearing-impaired listeners. For each group, they derived distortion index weights similar to those used in the computation of the articulation index (French and Steinberg, 1947; Kryter, 1962). In general, the listeners with impaired hearing appeared to base their quality judgments on the perceived distortion below 1000 Hz and ignore distortion in the higher-frequency regions, as did the listeners in the current study. In contrast, the normal-hearing listeners in their study appeared to base their judgments on distortion in the high frequencies (above 1000 Hz). While both studies revealed differences between the normal and hearing-impaired groups, the normal-hearing subjects in the current study appeared to rely more on the 500–2000-Hz region. Kozma-Spytek *et al.* (1996) offered three possible reasons for the inability of the hearing-impaired listeners to perceive high-frequency distortion products: (1) upward spread of masking, (2) elevated high-frequency thresholds, and/or (3) inadequate real-ear gain at high frequencies. Interestingly, the hearing-impaired subjects in the Kozma-Spytek study were primarily listeners with moderate-to-severe hearing losses whose thresholds were approximately 20 dB poorer than the subjects in the current study. It is somewhat surprising to find this same result in subjects with mild–moderate hearing losses.

III. SUMMARY AND CONCLUSIONS

In general, there was a decrease in perceived clarity for the peak-clipping conditions as the input increased from 60 to 80 dB SPL. This decline in clarity was most apparent for the normal-hearing adults. The normal-hearing 10–12-year olds and the hearing-impaired 16–50 year olds showed a similar, but less pronounced, pattern. In contrast, the youngest normal-hearing subjects and both groups of hearing-impaired children showed minimal differences in perceived clarity across conditions.

Based on quality judgments, the hearing-impaired listeners in this study preferred peak clipping when the input level was high. While this result has been reported previously for listeners with severe–profound hearing loss, it is an unexpected finding for listeners with mild-to-moderate hearing loss. The broadband SDRs observed for the five processing conditions resulted in a pattern that closely followed the preference judgments for the two oldest normal-hearing groups only. When the coherence measures were analyzed in octave bands, it appears that judgments of clarity for the normal-hearing listeners were most closely related to the SDR in the 500–2000-Hz range. In contrast, our results are consistent with the theory that hearing-impaired subjects focused more on the SDR below 1000 Hz and less on the SDR at higher frequencies. These results raise the question of whether it is appropriate to rely on normal-hearing listeners in the development of signal-processing algorithms for hearing aids. The current findings also suggest that SDRs can be calculated in a straightforward manner as a function of both frequency and time using processed speech signals as input. The resultant SDRs describe aspects of the hearing-aid processing that are perceptually significant in accounting for the differing listening strategies of normal and hearing-impaired listeners.

From a clinical perspective, the results of this study raise an interesting question. If one assumes equivocal performance in terms of speech recognition, should peak clipping be used in lieu of compression limiting based on the listener's subjective judgments? In the design of the present study, it was assumed that the highest input level typically encountered in daily activities would be speech at an overall level of 80 dB SPL. It is possible that inclusion of higher-level stimuli or different types of signals (e.g., transients, music) would have produced different results. Furthermore, in the current study, all of the testing was performed in quiet. In the presence of noise, intermodulation between the speech and noise would be expected to have a marked effect upon quality judgments and the SDR for both types of processing.

Additional studies are needed to determine if the pattern of listener preferences observed in this study also is observed under different stimulus conditions.

ACKNOWLEDGMENTS

This work was supported by NIH-NIDCD Grant No. P-60 DC00982, Center for Hearing Loss in Children, and partially supported by NIH-NIDCD Grant No. P01 DC00520. The authors wish to thank Harvey Dillon for helpful discussions regarding signal processing and Michael Gorga, Steve Neely, and Susan Nittrouer for many helpful comments on an earlier version of this manuscript. We also wish to thank Arthur Boothroyd for constructive comments and suggestions during the review process.

APPENDIX: COHERENCE MEASURES

Kates derived an overdetermined matrix equation for the set of unbiased filter coefficients, the solution of which depended on the calculation of the pseudoinverse matrix. He solved it using a truncated singular value decomposition (TSVD). An important step in TSVD is that all singular values less than some threshold are set to zero. This regularizes the calculation of the pseudoinverse and stabilizes the resulting solution for the filter coefficients. The TSVD technique has no criterion by which to choose the threshold singular value at which to truncate the pseudoinverse; the threshold must be chosen arbitrarily, and may not be optimum. Our implementation adopts the criterion that the threshold should be chosen so that the associated generalized cross-validation function is minimized, using an implementation from the library described in Hansen (1992). Since the input signal is continuous speech discourse, this unbiased filtering is calculated for each 50-ms window of data. Windows are overlapped by 50% so that the short-term processing is updated every 25 ms. Regularization of the pseudoinverse is needed, because some data windows contain only background noise, while others contain different portions of the speech signal. To use a fixed threshold in TSVD might be problematic for time-varying signals such as speech.

Suppose, for the moment, that these input and output spectra are measured in K different measurements, resulting in input spectrum $X_i(f)$ and output spectrum $Y_i(f)$, respectively, such that i ranges over the independent measurements 1,...,K. For example, one might use random noise and obtain K measurements of the system response, but we can equally well choose $K=1$ if a particular speech segment is measured and analyzed. The input and output power spectral densities, denoted by $G_{xx}(f)$ and $G_{yy}(f)$, respectively, are calculated by an ensemble average over the K independent measurements:

$$G_{xx}(f)=(1/K)\sum_{i=1}^{K} X_i^*(f)X_i(f),$$
$$G_{yy}(f)=(1/K)\sum_{i=1}^{K} Y_i^*(f)Y_i(f), \tag{A1}$$

where the asterisk denotes complex conjugation. Similarly, a cross-spectral density $G_{xy}(f)$ is defined as an ensemble average by

$$G_{xy}(f)=(1/K)\sum_{i=1}^{K} X_i^*(f)Y_i(f). \tag{A2}$$

The cross-spectral density involves both the input and output signals and is a complex quantity, in contrast to the power spectral densities which are each real and non-negative.

The (magnitude-squared) coherence $\gamma^2(f)$ is defined in terms of these spectral densities by

$$\gamma_{xy}^2(f)=\frac{|G_{xy}|^2}{G_{xx}G_{yy}}. \tag{A3}$$

This is the operational definition of coherence, which is calculated in terms of the measurements of the input and output signals.

The interpretation of the nonlinear coherence is considered next. The output spectrum is modeled as the sum of three components: the linear response of the hearing aid $H(f)X(f)$, such that the linear hearing-aid transfer function is $H(f)$, a distortion spectrum $D(f)$, and random noise $R(f)$, which is uncorrelated with the input spectrum, the output linear response, and the output distortion response. For a pseudorandom signal such as speech, the coherence function between $X(f)$ and $Y(f)$ is well known (Delavault and Saumon, 1982; Maki, 1986):

$$\gamma_{xy}^2(f)=\frac{1+|G_{xd}/(HG_{xx})|^2+2\,\mathrm{Re}[G_{xd}/(HG_{xx})]}{1+(G_{dd}+G_{rr})/(|H|^2G_{xx})+2\,\mathrm{Re}[G_{xd}/(HG_{xx})]}. \tag{A4}$$

Each of the power spectral densities and cross-spectral densities are defined in an analogous manner to Eqs. (A1) and (A2). In particular, $G_{dd}(f)$ is the power spectral density of the distortion spectrum, $G_{rr}(f)$ is the power spectral density of the random-noise spectrum, $G_{xd}(f)$ is the cross-spectral density of the input and distortion spectra, and Re $[\cdots]$ denotes the real part of the complex quantity within the square brackets.

In a linear system, $G_{dd}=G_{xd}=0$ (because there is no distortion), and a signal-to-noise ratio is well defined. For a nonlinear system with a *stochastic* input signal, as considered by Kates (1992), $G_{xd}=0$, and a signal-to-distortion ratio is well defined. In either case, the coherence in Eq. (A4) simplifies considerably.

The concept of ensemble averaging applies to averaging across frequency, because the noise spectral densities in adjacent frequency bins are uncorrelated with the input and with each other. A similar situation exists, in approximate form, for the distortion spectral densities in adjacent frequency bins. Because the transformation of the input into the output distortion is so complicated, averaging across adjacent frequencies will tend to reduce the correlation of these signals within any particular frequency band. It follows that the cross-spectrum G_{xd} tends towards zero as the number of frequency bins comprising the average becomes larger. The resulting coherence in the limit that G_{xd} approaches zero simplifies from Eq. (A4) to

$$\gamma_{xy}^2(f) = \frac{1}{1+(G_{dd}+G_{rr})/G_{yy}^0}, \tag{A5}$$

where the coherent output power spectral density $G_{yy}^0(f)$ is defined by

$$G_{yy}^0 = |H(f)|^2 G_{xx}. \tag{A6}$$

This expression for coherence is precisely the same as that obtained using a stochastic input.

This allows the introduction of the signal-to-distortion ratio SDR by the standard relation:

$$\text{SDR} = \frac{\gamma_{xy}^2(f)}{1-\gamma_{xy}^2(f)} = \frac{G_{yy}^0}{G_{dd}+G_{rr}} \approx \frac{G_{yy}^0}{G_{dd}}, \tag{A7}$$

the latter approximate equality representing the typical case in hearing-aid algorithms for which the noise autospectrum is small relative to the distortion autospectrum.

For octave averaging, the number of elements K in the sums in Eqs. (A1) and (A2) is the number of frequency bins per octave. This allows the calculation of SDR waveforms for each frequency bandwidth used in the coherence analysis. This averaging of power spectra and cross-spectra is contrasted with the averaging of coherence used in some previous research. Alternatively, when coherence is averaged across frequency, as in past studies, the influence of G_{xd} is retained in Eq. (A4) and may not be eliminated. The ensemble averaging of power spectra and cross-spectra adopted in this report is based upon the conventional definition of coherence in Eq. (A3); this allows for the transformation of coherence into an SDR.

[1]In the hearing aid used, the signal was peak clipped by an instantaneous nonlinearity prior to the final power amplifier stage. The instantaneous input–output function of the peak clipper was symmetrical and had a rounded shape in the clipping region so that the onset of clipping was gradual as level increased. The clipper was designed to minimize transistor saturation in the power amplifier, which often occurs in many peak-clipping circuits and leads to excessive distortions (Bachler, personal communication, 1997).

[2]Pilot data with 7–9 year olds revealed that the instructions needed to be explicit in a number of areas. The following instructions were developed to avoid confusion with this youngest group and were subsequently used for all subjects: ''You will hear a beep followed by a woman saying the same sentence two times. You should have no trouble understanding the sentences, but you may not know all of the words. One sentence will be a little clearer than the other (live voice example given). Some sentences will be louder than others. Sometimes the soft one will be clearer and other times the loud one will be clearer. Your job is to tell which sentence (1 or 2) is clearer. Sometimes they may sound the same to you. If they do, it is okay to guess. Sometimes you can guess #1 and sometimes you can guess #2.''

Bachler, H. (**1997**). Personal communication.

Boothroyd, A., Springer, N., Smith, L., and Schulman, J. (**1988**). ''Compression amplification and profound hearing loss,'' J. Speech Hear. Res. **31**, 362–376.

Brunved, P. B. (**1994**). ''How studying loudness growth led to the development of Multi Focus,'' Hear. Instr. **45**(3), 8–10.

Ching, T., Newall, P., and Wigney, D. (**1994**). ''Audio-visual and auditory paired comparison judgments by severely and profoundly hearing impaired children: Reliability and frequency response preferences,'' Aust. J. Audiol. **16**, 99–106.

Ching, T., Newall, P., and Wigney, D. (**1995**). ''Reliability and sensitivity of intelligibility judgments by severely and profoundly hearing-impaired children,'' Ann. Otol. Rhinol. Laryngol. **166**, 151–153.

Cornelisse, L. E., Gagné, J. P., and Seewald, R. (**1991**). ''Ear level recordings of the long-term average spectrum of speech,'' Ear Hear. **12**, 47–54.

Cox, R. M., Alexander, G. C., and Gilmore, C. (**1987**). ''Development of the connected speech test (CST),'' Ear Hear. **8**, 119S–126S.

Cox, R. M., Alexander, G. C., Gilmore, C., and Pusakulich, K. M. (**1988**). ''Use of the connected speech test (CST) with hearing-impaired listeners,'' Ear Hear. **9**(4), 198–207.

Crain, T. R., and Van Tasell, D. J. (**1994**). ''Effect of peak clipping on speech recognition threshold,'' Ear Hear. **15**, 443–453.

Dawson, P., Dillon, H., and Battaglia, J. (**1990**). ''Output limiting compression for the severe–profoundly deaf,'' Aust. J. Audiol. **13**, 1–12.

Delavault, E., and Saumon, G. (**1982**). ''Fourier analysis of nonlinear fluid systems,'' IEEE Trans. Biomed. Eng. **29**, 215–219.

Dreschler, W. (**1988**). ''Dynamic-range reduction by peak clipping or compression and its effects on phoneme perception in hearing-impaired subjects,'' Scand. Audiol. **17**, 45–51.

Dyrlund, O. (**1992**). ''Coherence measurements in hearing instruments, using different broad-band signals,'' Scand. Audiol. **21**, 73–78.

Dyrlund, O., Ludvigsen, C., Olofsson, A., and Poulsen, T. (**1994**). ''Hearing aid measurements with speech and noise signals,'' Scand. Audiol. **23**(3), 153–157.

Eisenberg, L. S., and Dirks, D. D. (**1995**). ''Reliability and sensitivity of paired comparisons and category rating in children,'' J. Speech Hear. Res. **38**(5), 1157–1167.

Eisenberg, L. S., and Levitt, H. (**1991**). ''Paired comparison judgments for hearing aid selection in children,'' Ear Hear. **12**, 417–430.

Eisenberg, L. S., Dirks, D. D., and Gornbein, J. A. (**1997**). ''Subjective judgments of speech clarity measured by paired comparison comparisons and category rating,'' Ear Hear. **18**, 294–306.

Feigin, J. A., Kopun, J. G., Stelmachowicz, P. G., and Gorga, M. P. (**1989**). ''Probe-tube microphone measures of ear-canal sound pressure levels in infants and children,'' Ear Hear. **10**(4), 254–258.

Fortune, T. W., and Preves, D. A. (**1992a**). ''Hearing aid saturation and aided loudness discomfort,'' J. Speech Hear. Res. **35**(1), 175–185.

Fortune, T. W., and Preves, D. A. (**1992b**). ''Hearing aid saturation, coherence, and aided loudness discomfort,'' J. Am. Acad. Audiol. **3**(2), 81–93.

French, N. R., and Steinberg, J. C. (**1947**). ''Factors governing the intelligibility of speech sounds,'' J. Acoust. Soc. Am. **19**, 90–119.

Hansen, P. C. (**1992**). ''Regularization tools: A MATLAB package for analysis and solution of discrete ill-posed problems.'' Danish Computing Center for Research and Education, Technical University of Denmark, Lyngby, Version 2.0 for MATLAB 4.0 edition.

Hawkins, D. B., and Naidoo, S. V. (**1993**). ''Comparison of sound quality and clarity with asymmetrical peak clipping and output limiting compression,'' J. Am. Acad. Audiol. **4**(4), 221–228.

Kates, J. M. (**1992**). ''On using coherence to measure distortion in hearing aids,'' J. Acoust. Soc. Am. **91**, 2236–2244.

Kates, J. M., and Kozma-Spytek, L. (**1994**). ''Quality ratings for frequency-shaped peak-clipped speech,'' J. Acoust. Soc. Am. **95**, 3586–3594.

Kozma-Spytek, L., Kates, J. M., and Revoile, S. G. (**1996**). ''Quality ratings for frequency-shaped peak-clipped speech: Results for listeners with hearing loss,'' J. Speech Hear. Res. **39**(6), 1115–1123.

Kryter, K. D. (**1962**). ''Methods for calculation and use of the articulation index,'' J. Acoust. Soc. Am. **34**, 1689–1697.

Lawson, G. D., and Chial, M. R. (**1982**). ''Magnitude estimation of degraded speech quality by normal- and impaired-hearing listeners,'' J. Acoust. Soc. Am. **72**, 1781–1787.

Licklider, J. C. R. (**1964**). ''Effects of amplitude distortion upon the intelligibility of speech,'' J. Acoust. Soc. Am. **18**, 429–434.

Lyregaard, P. (**1986**). ''On the psychoacoustical implications of a sensorineural hearing loss, loudness perception,'' paper presented at the Seventh National Conference of the Audiological Society of Australia, Ballarat, Victoria.

Maki, B. (**1986**). ''Interpretation of the coherence function when using pseudorandom inputs to identify nonlinear systems,'' IEEE Trans. Biomed. Eng. **33**, 775–779.

Martin, D. W. (**1950**). ''Uniform speech-peak clipping in a uniform signal-to-noise spectrum ratio,'' J. Acoust. Soc. Am. **22**, 614–621.

May, A. E. (**1988**). ''Reducing the SSPL of hearing aids: The effect on the intelligibility and pleasantness of the signal,'' MA Thesis, Macquarie University, Australia, p. 143.

May, A., Dillon, H., and Battaglia, J. (**1989**). ''Compression vs peak clipping: Intelligibility and quality in saturation,'' presented at the 1989 American Speech Language Hearing Association Meeting, St. Louis, MO.

Nelson Barlow, N. L., Auslander, M. C., Rines, D., and Stelmachowicz, P.

G. (**1988**). ''Probe-tube microphone measures in hearing-impaired children and adults,'' Ear Hear. **9**, 243–247.
Pollack, I. (**1952**). ''On the effect of frequency and amplitude distortion on the intelligibility of speech in noise,'' J. Acoust. Soc. Am. **24**, 538–540.
Preves, D., and Newton, J. R. (**1989**). ''The headroom problem and hearing aid performance,'' Hearing J. **42**, 1–5.
Seewald, R. C. (**1988**). ''The Desired Sensation Level approach for children: Selection and verification,'' Hear. Instr. **39**(7), 18–22.
Stelmachowicz, P. G., Mace, A. L., Kopun, J. G., and Carney, E. (**1993**). ''Long-term and short-term characteristics of speech: Implications for hearing aid selection for young children,'' J. Speech Hear. Res. **36**(3), 609–620.
Westwood, G. F., and Bamford, J. M. (**1992**). ''Probe-tube microphone measurements with very young infants,'' Brit. J. Aud. **26**, 143–151.
Westwood, G. F. S., and Bamford, J. M. (**1995**). ''Probe-tube microphone measures with very young infants: Real ear to coupler differences and longitudinal changes in real ear unaided responses,'' Ear Hear. **16**(3), 63–273.

Editor's note: *The following four papers were originally presented at the First International Conference on Voice Physiology and Biomechanics, Evanston, IL, 28–31 May 1997. Anders Löfqvist*

A theoretical study of the hysteresis phenomenon at vocal fold oscillation onset–offset

Jorge C. Lucero[a)]
Departamento de Matemática, Universidade de Brasília, 70910-900 Brasília DF, Brazil

(Received 4 August 1997; accepted for publication 24 September 1998)

This paper presents a theoretical study on the differences in the biomechanical parameters of the vocal folds between oscillation onset and offset. The dynamics of the oscillation is analyzed from the perspective of the theory of nonlinear dynamical systems, using a mucosal wave model of the vocal folds with the subglottal pressure and the vocal fold half-width as control parameters. It is shown that the oscillation onset occurs through a Hopf bifurcation of the subcritical type, at which an unstable limit cycle is generated. Also, the oscillation offset occurs at a cyclic fold bifurcation, at which the unstable limit cycle and a stable limit cycle (the actual vocal fold oscillation) coalesce and cancel each other. Both bifurcations combine to form an ''oscillation hysteresis'' phenomenon, common in cases of flow-induced oscillations. An analytical expression for the onset/offset ratio of parameters is derived. The onset/offset ratio is in the range of 0.5–1, in agreement with the experimental evidence. This value depends on the phase delay in motion of the upper edge of the vocal folds versus the lower edge, and on the particular model adopted for airflow separation within the glottis. [S0001-4966(99)00201-5]

PACS numbers: 43.70.Aj, 43.70.Bk, 43.40.At, 43.40.Ga [AL]

INTRODUCTION

It is known that the biomechanical configuration of the vocal folds at oscillation onset is different from their configuration at oscillation offset. This difference has been observed for various parameters related to the vocal fold oscillation and under various experimental settings. For example, studies of excised larynges (Baer, 1981; Berry *et al.*, 1995) and physical models of the vocal fold mucosa (Titze *et al.*, 1995; Chan *et al.*, 1997) have shown that the subglottal pressure is lower at oscillation offset than at oscillation onset, when other biomechanical parameters (e.g., glottal width) are kept constant. Similar onset–offset differences have been also observed during the production of speech. Studies with subjects uttering vowel–voiceless consonant–vowel sequences have shown that the intraoral pressure is lower at the voice onset of the second vowel compared to the voice offset of the first vowel (Munhall *et al.*, 1994), the airflow is lower (Koenig and McGowan, 1996), the transglottal pressures is higher (Hirose and Niimi, 1987), and the glottal width is smaller (Hirose and Niimi, 1987).

According to this experimental evidence, the vocal fold configuration at oscillation onset seems to be always more restricted than the configuration at offset. When the geometry and other biomechanical parameters are fixed, as in the excised larynx experiments, then a larger subglottal pressure is required to start the oscillation. In the speech production experiments, if we assume that the subglottal pressure is approximately constant during the vowel–consonant–vowel sequence, then the experimental results indicate a larger vocal fold adduction at oscillation onset. Note that a smaller glottal width will increase the glottal aerodynamic resistance and therefore cause the observed larger transglottal pressure, smaller intraoral pressure, and lower airflow.

Why does this phenomenon occur? In this paper, we will look for its origin by examining the generation of the vocal fold oscillation from the perspective of the theory of nonlinear dynamical systems. In a previous work (Lucero, 1995), a describing function method (Siljak, 1969) was used to analyze the onset–offset difference in the subglottal pressure. The present work intends to offer an improved and more general description of this phenomenon, which might provide a theoretical basis for further studies. Considering that this paper is directed mainly to readers in the speech field, the mathematical techniques used in the paper which might be not familiar to some readers will be presented in detail.

I. VOCAL FOLD MODEL

Analysis will be based on a version of Titze's mucosal wave model (Titze, 1988) for the vocal fold oscillation. As shown in Fig. 1, we assume that during the oscillation the cover (epithelium and superficial layers of the vocal ligament) of the vocal folds propagates a surface mucosal wave in the direction of the airflow, and the body (deep layer of the vocal ligament and muscle) is stationary.

The cross-sectional areas at glottal entry a_1 and exit a_2 are approximated by

$$a_1 = 2L(x_0 + x + \tau\dot{x}), \tag{1}$$

$$a_2 = 2L(x_0 + x - \tau\dot{x}), \tag{2}$$

a)Electronic mail: lucero@mat.unb.br

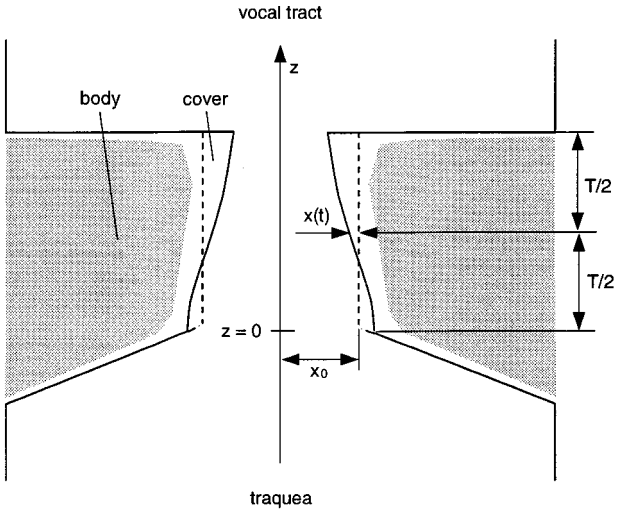

FIG. 1. Mucosal wave model (Titze, 1988).

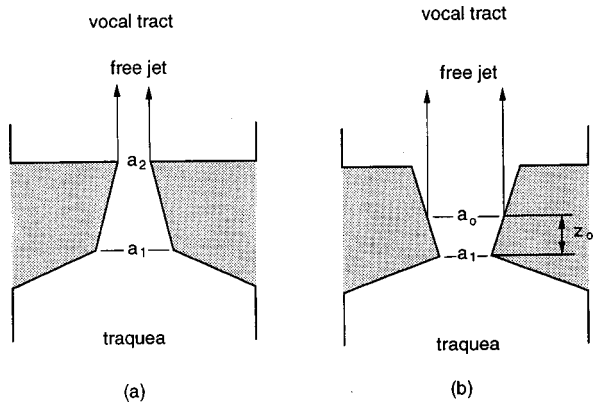

FIG. 2. Airflow separation from the glottis. (a) Convergent glottis, (b) divergent glottis.

where L is the length of the vocal fold in the antero–posterior direction, and τ is the time delay for the mucosal wave in traveling half the glottal width T (length of the glottal channel in the direction of the airflow). The motion of the vocal fold is described by the differential equation

$$m\ddot{x}+r\dot{x}+kx+P_g, \tag{3}$$

where x is the lateral displacement of the vocal fold at the midpoint of the glottis, m, r, and k, are the mass, damping, and stiffness of the oscillating portion of the vocal fold tissue per unit area of the medial surface of the vocal folds (LT), and P_g is the intraglottal pressure, equal to the mean of the glottal pressure $P(z)$ along the direction of the airflow (z axis in Fig. 1)

$$P_g=\frac{1}{T}\int_0^T P(z)dz. \tag{4}$$

Details on the derivation of the above equations may be found in Titze's paper (Titze, 1988).

For simplicity, we assume further that the supraglottal pressure is equal to the atmospheric pressure, the subglottal pressure P_s is constant, and the prephonatory glottal shape is rectangular (dashed line in Fig. 1).

The glottal aerodynamics is described following the boundary layer model by Pelorson and co-workers (Pelorson *et al.*, 1994, 1995) for high Reynolds numbers. This model appears to be valid for the range of typical values for the glottal flow (Re in the order of 3000), except when the glottis is narrow and near closure (in this case, a viscous model should be used).

The glottal flow is considered quasisteady and incompressible. The bulk of the flow is frictionless and laminar, except in the vicinity of the glottal walls (boundary layer) where viscous forces are large. Due to the abrupt area expansion at the glottal exit, the boundary layer separates from the glottal wall and causes a free jet stream downstream the glottis (Fig. 2). The point at which the flow detaches from the glottal wall is located at the exit of the glottis, in the case of a convergent glottis [Fig. 2(a)], or may move within the glottis, as it becomes divergent [Fig. 2(b)].

According to Pelorson *et al.*'s results (1994), in a divergent glottis the ratio between the glottal area a_0 at the point of airflow separation [see Fig. 2(b)] and the minimum glottal area (a_1) becomes asymptotically constant at high Reynolds numbers ($a_0/a_1\approx k_0$). In measurements on a physical model of the larynx with a cylindrical profile for the vocal folds, they obtained the approximate relation $a_0/a_1\approx 1.1$. For the present analysis, their equations (as they appear in Pelorson *et al.*, 1994) were solved assuming a linear variation of the glottal area along the glottis (z-axis in Fig. 1), and an approximate relation $a_0/a_1\approx 1.3$ was obtained. Hence, we assume as a first approximation that airflow separation occurs at the point where the glottal area is

$$a_0=\begin{cases} k_0a_1, & \text{if } a_2>k_0a_1, \\ a_2, & \text{if } a_2\leqslant k_0a_1, \end{cases} \tag{5}$$

where $k_0=1.3$. Coordinate z at the point of airflow separation has the value $z=z_0$, with

$$z_0=\frac{a_0-a_1}{a_2-a_1}\,T. \tag{6}$$

Downstream from the point of airflow separation, the air exits the glottis in a free jet and becomes turbulent. The turbulence dissipates all the kinetic energy of the flow and no pressure is recovered. Thus the pressure at the point of airflow separation is zero.

Upstream from the point of airflow separation, friction in the bulk of the flow may be neglected, and the flow described with the energy equation

$$P_s=\frac{\rho u^2}{2a_0^2}, \tag{7}$$

where P_s is the subglottal pressure, ρ is the air density, and u is the air flow volume velocity.

Finally, applying the energy equation between the point of coordinate z and the point of airflow separation z_0 to evaluate the pressure $P(z)$ (Titze, 1988) and integrating Eq. (4), we obtain

TABLE I. Parameter values of the mucosal wave model (Titze, 1988).

Parameter	Value
m	4.76 kg m^{-2}
r	1000 N s m^{-3}
k	2×10^6 N m^{-3}
L	1.4 cm
T	0.3 cm
$\omega=\sqrt{k/m}$	648.2 s^{-1}
δ	60°
$\tau=\delta/(2\omega)$	0.81 ms
ρ	1.15 kg m^{-3}

$$P_g = P_s \frac{z_0}{T}\left(1-\frac{a_0}{a_1}\right). \tag{8}$$

The dynamics of the model is then completely described by Eqs. (1), (2), (3), (5), (6), and (8). As standard values for the parameters, we adopt the values shown in Table I. In the table, $\delta=2\omega\tau$ is the phase delay in motion of the upper edge of the vocal folds in relation to the lower edge. These values will be used throughout the analysis, except where indicated otherwise.

We must be aware that this model contains gross simplifications of the vocal fold dynamics. Particularly, it neglects three factors consistent with the quasi-steady flow assumption: (1) viscous losses, which may become significant when the glottis is narrow and the glottal flow is low (note that the boundary layer model contains the assumption of a high Reynolds number); (2) glottal exit rounding effects on the pressure distribution in the glottis (Guo and Scherer, 1993); and (3) the actual point of action of the resultant glottal pressure (P_g), which should be lower than the glottal midpoint (Guo and Scherer, 1993). Preliminary analyses including viscous losses [following Pelorson *et al.*'s model (1994)] have shown no significant variation of the present results for the range of parameters considered here, e.g., a wide open glottis at the prephonatory position. This fact is consistent with a previous analysis on the optimal glottal configuration (Lucero, 1997), which shows that in a wide glottis airflow separation effects are much larger than viscous losses, and hence the later may be neglected as approximation. However, the situation may be different in a glottis near closure (as in the case of a pressed voice onset). The above simplifications are intended to reduce the model to the basic oscillatory dynamics, neglecting details not relevant to the present study.

II. EQUILIBRIUM POSITION AND STABILITY (PREVIOUS RESULTS)

The first step in the analysis is to determine the equilibrium positions of the vocal folds and their stability. Setting to zero the time derivatives, from Eqs. (1) and (2) we obtain $a_1=a_2$. Since the glottis is rectangular, there is no airflow separation within the glottis, hence $a_0=a_2$ and $z_0=T$. Solving the resultant equations for x, we find that there is only one equilibrium position and it is located at the initial position $x=0$.

The stability of the equilibrium position may be next analyzed taking only the linear part of the equation of motion in the neighborhood of the equilibrium position (Minorsky, 1962; Guckenheimer and Holmes, 1983). Since the oscillation has a small amplitude in that neighborhood and hence the glottis is near rectangular, there is no airflow separation within the glottis and the glottal pressure simplifies to

$$P_g = P_s\left(1-\frac{a_2}{a_1}\right)=\frac{2\tau P_s\dot{x}}{x_0+x+\tau\dot{x}}. \tag{9}$$

Expanding this equation in a Taylor series and keeping only the linear terms, we obtain

$$P_g = r_g\dot{x}, \tag{10}$$

where

$$r_g=\frac{2\tau P_s}{x_0}. \tag{11}$$

We can see that the glottal pressure is proportional to the vocal fold velocity, and hence it acts as an aerodynamic damping with the coefficient r_g. Replacing in Eq. (3), we obtain the linearized equation of motion

$$m\ddot{x}+(r-r_g)\dot{x}+kx=0. \tag{12}$$

The roots of the characteristic equation are

$$s=-\frac{r-r_g}{2m}\pm\sqrt{\left(\frac{r-r_g}{2m}\right)^2-\frac{k}{m}}. \tag{13}$$

The real part of the roots are zero at

$$r-r_g=0. \tag{14}$$

For $r_g>r$ the roots have positive real parts and the equilibrium position is unstable. Note that under this condition, the total damping [coefficient for the $\dot{x}$ term in Eq. (12)] becomes negative. This negative sign implies a net transfer of energy from the airflow to the vocal folds, and so oscillation may start, as it will be shown later in Sec. IV A.

The condition expressed by Eq. (14) is the threshold condition for oscillation onset, at which the equilibrium position of the vocal folds becomes unstable and the oscillation is generated. Replacing Eq. (11) and solving, we may compute for example the oscillation threshold subglottal pressure

$$P_{s\text{-onset}}=\frac{rx_0}{2\tau}, \tag{15}$$

which is the minimum subglottal pressure required to start the oscillation. Similarly, we can consider an oscillation threshold glottal half-width

$$x_{0\text{-onset}}=\frac{2\tau P_s}{r}, \tag{16}$$

which is the maximum glottal half-width to start the oscillation.

This same stability analysis has been done in previous works using a variety of models and techniques (e.g., Ishizaka, 1981; Ishizaka and Matsudaira, 1972; Lucero, 1993, 1995; Steinecke and Herzel, 1995; Titze, 1988). However, analysis only shows that at threshold the equilibrium position

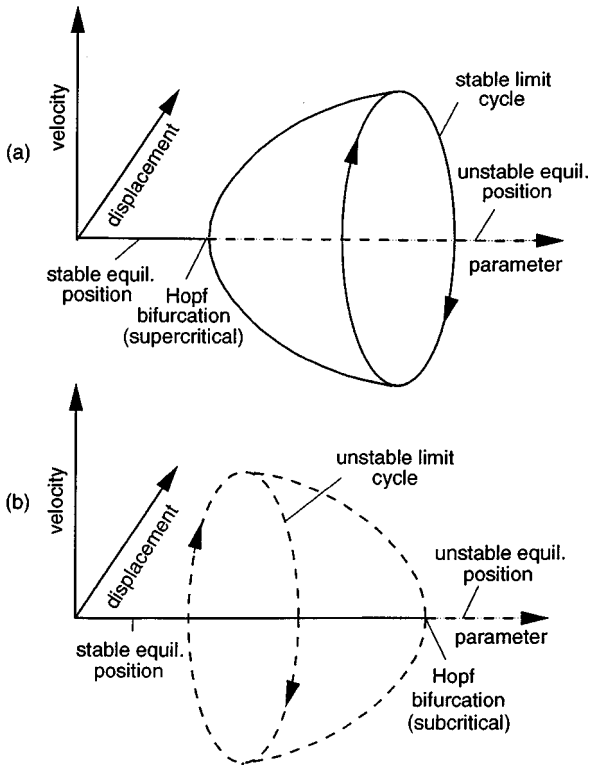

FIG. 3. The Hopf bifurcation. (a) Supercritical, (b) subcritical (Thompson and Stewart, 1986).

becomes unstable, and it says nothing about the generation of an oscillation. It is clear that an oscillation appears at threshold, as it can be shown by solving numerically the equations of motion. But exactly how is it generated? This issue is important in understanding the oscillation onset–offset dynamics, and will be considered in the following sections.

III. OSCILLATION ONSET: SUBCRITICAL HOPF BIFURCATION

A. The Hopf bifurcation

Let us briefly review how an oscillation may be generated from an equilibrium position. In the theory of nonlinear dynamical systems (Guckenheimer and Holmes, 1983; Minorsky, 1962; Thompson and Stewart, 1986), the qualitative change of dynamical behavior at a critical value of a parameter is called a bifurcation. At a Hopf bifurcation, an equilibrium position changes its stability and an oscillation (limit cycle) is generated.

Two types of Hopf bifurcations are possible. We illustrate them in Fig. 3, where we represent the dynamical behavior as a function of a control parameter (in the case of the vocal fold model, this parameter would be, e.g., the subglottal pressure or the glottal half-width). In the figures, a solid line represents stable equilibrium (a position or a limit cycle), and a dashed line represents unstable equilibrium. At the supercritical Hopf bifurcation [Fig. 3(a)], as the parameter increases a stable equilibrium position bifurcates into an unstable position and a stable limit cycle. This is the simplest case, and corresponds, e.g., to the well-known van der Pol oscillator. In the subcritical Hopf bifurcation [Fig. 3(b)], as the parameter increases a stable equilibrium position and an unstable limit cycle coalesce into an unstable equilibrium position. This case is more complex and appears in combination with other bifurcation phenomena. It is common in the flow-induced oscillation of structures, such as wind-induced oscillation of bridges (Thompson, 1982; Thompson and Stewart, 1986).

B. Hopf's theorem

To show the existence of a Hopf bifurcation at the oscillation onset threshold and determine its type, we may use Hopf's Theorem (Guckenheimer and Holmes, 1983). According to this theorem, first we have to verify that at the bifurcation, the system has a pair of pure imaginary roots and no other roots with zero real parts. This was done in the previous section. Next, we have to verify that, as the control parameter (e.g., the subglottal pressure) varies and passes the bifurcation value (i.e., the oscillation onset threshold), these roots cross the imaginary axes transversely. In mathematical terms,

$$\frac{d}{dP_s}\left[\mathrm{Re}\ s(P_s)\right]\Big|_{P_s=P_{s\text{-onset}}} \neq 0\,. \tag{17}$$

Introducing Eqs. (13) and (11), we obtain

$$\frac{d}{dP_s}\left[\mathrm{Re}\ s(P_s)\right]\Big|_{P_s=P_{s\text{-onset}}} = \frac{\tau}{mx_0} \neq 0. \tag{18}$$

Finally, we have to rewrite the equations of motion in the form

$$\begin{pmatrix}\dot{u}\\ \dot{v}\end{pmatrix} = \begin{pmatrix}0 & -\omega\\ \omega & 0\end{pmatrix}\begin{pmatrix}u\\ v\end{pmatrix} + \begin{pmatrix}f(u,v)\\ g(u,v)\end{pmatrix}, \tag{19}$$

where ω is a constant, $f(0,0)=g(0,0)=0$ (i.e., there is an equilibrium position at $u=0$, $v=0$), and $(\partial f/\partial u)(0,0)=(\partial f/\partial v)(0,0)=(\partial g/\partial u)(0,0)=(\partial g/\partial v)(0,0)=0$, and compute the parameter

$$K=\frac{1}{16}\left(f_{uuu}+f_{uvv}+g_{uuv}+g_{vvv}\right)+\frac{1}{16\omega}\left[f_{uv}\left(f_{uu}+f_{vv}\right)\right.$$
$$\left.-g_{uv}\left(g_{uu}+g_{vv}\right)-f_{uu}g_{uu}+f_{vv}g_{vv}\right], \tag{20}$$

where f_{uv} denotes $(\partial^2 f/\partial x\,\partial y)(0,0)$, etc. If $K\neq 0$ then the bifurcation is of the Hopf type, and a limit cycle is generated at the bifurcation. Further, if $K>0$ the bifurcation is subcritical, and if $K<0$ it is supercritical.

We can write the equations of motion in the form shown in Eq. (19) with the change of variables

$$u=-\omega x, \tag{21}$$

$$v=\dot{x}, \tag{22}$$

where $\omega=\sqrt{k/m}$, and letting

$$f(u,v)=0, \tag{23}$$

$$g(u,v)=-\frac{r}{m}\,v+\frac{2\tau P_s v}{m(-u/\omega+x_0+\tau v)}. \tag{24}$$

Note that $f(0,0)=g(0,0)=0$ as required by the theorem.

Next, we compute all the derivatives required by the theorem, and evaluate them at the equilibrium position $u=0$, $v=0$ and at the bifurcation condition $P_s=P_s-\text{onset}$. All of the derivatives of $f(u,v)$ are identically zero. The derivatives of $g(u,v)$ are

$$g_u=g_v=g_{uu}=0, \tag{25}$$

$$g_{uv}=\frac{r}{mx_0\omega}, \tag{26}$$

$$g_{vv}=-\frac{2\tau r}{mx_0}, \tag{27}$$

$$g_{uuv}=\frac{2r}{m\omega^2x_0^2}, \tag{28}$$

$$g_{vvv}=\frac{6\tau^2 r}{mx_0^2}, \tag{29}$$

and replacing in Eq. (20) we obtain finally

$$K=\frac{r}{8mx_0^2}\left(3\tau^2+\frac{1}{\omega^2}+\frac{\tau r}{m\omega^2}\right)>0. \tag{30}$$

The above result shows that oscillation onset is a subcritical Hopf's bifurcation, at which an unstable limit cycle is generated. This same conclusion will be reached repeating the same analysis with the glottal half-width x_0 as the control parameter

IV. HYSTERESIS AT OSCILLATION ONSET–OFFSET

A. Energy balance

In the previous section we found that the limit cycle generated at the oscillation onset bifurcation is unstable. An unstable limit cycle cannot be observed physically; if we could put the vocal folds exactly on the trajectory of this limit cycle, any infinitesimal perturbation would take them out of it. However, we know that the vocal folds are capable of a stable steady state oscillation. Moreover, if we solve the equations of motion numerically with a subglottal pressure just above the onset threshold value (as will be done later), we will find a stable limit cycle. We conclude then that the observed oscillation of the vocal folds (stable limit cycle) is not the same limit cycle generated at the Hopf bifurcation of the equilibrium position. Then, where does this stable limit cycle come from?

To answer this question, we have to study the system at large amplitude oscillations. Unfortunately, the vocal fold model is still complex and we cannot obtain a closed-form solution for the limit cycles. We will take then a more indirect approach, considering the exchange of energy between the glottal airflow and the vocal folds.

A criterion by Lièenard states that an oscillator reaches a steady state oscillation when the energies absorbed and dissipated in one cycle cancel out (Minorsky, 1983). In their oscillation, the vocal folds absorb energy from the airflow and dissipate energy in the tissues (Titze, 1988, 1994). Let us compute those energies.

The energy dissipated in the tissues is the work done by the damping force

$$W_r=\oint_{\text{cycle}} r\dot{x}\,dx=\int_0^{2\pi/\omega} r\dot{x}^2\,dt. \tag{31}$$

To compute this integral, we need an expression for $x(t)$. Let us assume as an approximation that the oscillation may be described by the sinusoid

$$x=A\sin\omega t. \tag{32}$$

Replacing into Eq. (31) and integrating, we obtain

$$W_r=\pi A^2\omega r. \tag{33}$$

The energy absorbed from the airflow is the work done by the glottal pressure

$$W_g=\oint_{\text{cycle}} P_g(x)dx=\int_0^{2\pi/\omega} P_g(t)\dot{x}\,dt. \tag{34}$$

Using again Eq. (32) for $x(t)$, we obtain

$$W_g=A\omega\int_0^{2\pi/\omega} P_g(t)\cos\omega t\,dt. \tag{35}$$

We can rewrite this equation in a similar form to Eq. (33)

$$W_g=\pi A^2\omega r_g, \tag{36}$$

where

$$r_g=\frac{1}{\pi A}\int_0^{2\pi/\omega} P_g(t)\cos\omega t\,dt \tag{37}$$

is an aerodynamic damping factor. This aerodynamic damping is equivalent to the one derived for the stability analysis of the equilibrium position [Eq. (11)], and we use the same symbol to denote it. Equation (37) is the general expression function of the oscillation amplitude, and it reduces to Eq. (11) when A tends to zero. [For small A, there is no airflow separation and P_g is given by Eq. (9). Introducing Eq. (32) and letting $A\to 0$, we obtain $P_g=(2P_s\omega\tau A\cos\omega t)/x_0$, and replacing in Eq. (37) and integrating we obtain Eq. (11).]

We will use r and r_g as normalized measures of the energies dissipated in the tissues and absorbed from the airflow, respectively, in one oscillation cycle. Lièenard's criterion will be then satisfied when $r=r_g$.

Figure 4 shows a numerical example of the normalized absorbed energy versus the oscillation amplitude, at various values of the airflow separation coefficient k_0. The solid line represents results using the above equations, and the dashed line represents results neglecting airflow separation in the glottis (i.e., setting $a_0=a_2$). The dashed line shows that the absorbed energy increases as the oscillation amplitude grows larger. This fact may be understood by considering that the transfer of energy from the airflow to the vocal folds is caused by the oscillation itself, so as the oscillation grows in amplitude, more energy can be transferred. However, for physical constraints the absorbed energy cannot grow to infinity. We see in the solid line that when airflow separation in the glottis is included, the slope of the curve changes at a certain oscillation amplitude. This amplitude is precisely the amplitude at which the point of airflow separation moves within the glottis. Airflow separation reduces the vocal fold surface through which the airflow transfers energy to the vocal folds, causing the decrease in the absorbed energy. If a

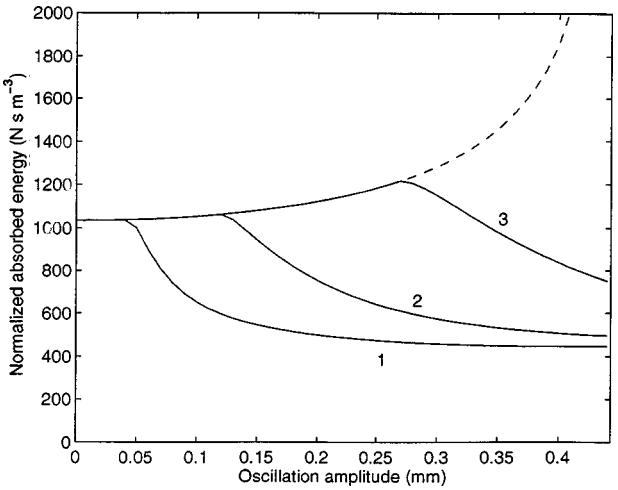

FIG. 4. Normalized absorbed energy versus oscillation amplitude, for $P_s = 320$ Pa, $x_0 = 0.5$ mm, and $k_0 = 1.1$ (1), 1.3 (2), 2 (3). At the right, the curves stop at the glottal closure.

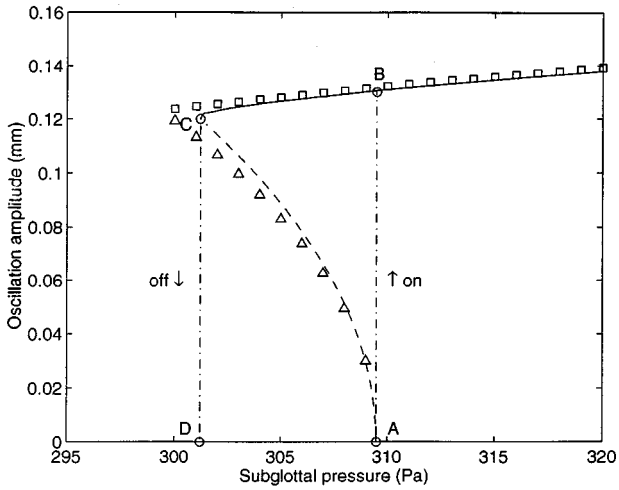

FIG. 6. Oscillation amplitude versus subglottal pressure for $x_0 = 0.5$ mm. Solid line: stable limit cycle, dashed line: unstable limit cycle. Point A: subcritical Hopf bifurcation, point C: cyclic fold bifurcation. A-B-C-D: oscillation hysteresis loop. Squares (stable limit cycle) and triangles (unstable limit cycle): results from direct solution of the equations of motion.

larger value of k_0 is adopted, then airflow separation within the glottis starts at a larger glottal divergence angle. In this case, the change of slope of the energy curve occurs at a larger oscillation amplitude, and the difference between the energy absorbed at zero amplitude and the maximum absorbed energy increases.

B. Oscillation hysteresis

Based on the previous results, we will examine the oscillation dynamics through numerical examples.

Figure 5 shows curves of normalized absorbed energy versus oscillation amplitude at various values of lung pressure. The normalized dissipated energy is $r = 1000$ N s m^{-3}, indicated in the plot with a dashed line.

Let us consider how the oscillation starts and stops. Assume that the vocal folds are initially at rest at the equilibrium position and hence the oscillation amplitude is zero. To start the oscillation, the absorbed energy has to be increased to a value above the dissipated energy. This will be accomplished increasing the lung pressure, for example, to 315 Pa (curve 4). Since the absorbed energy at zero amplitude is larger than the dissipated energy, the oscillation amplitude will grow following curve 4 until reaching a point of balance, at point A. This point represents a stable oscillation, or stable limit cycle. If a perturbation increases the oscillation amplitude, the absorbed energy becomes smaller than the dissipated energy, and the oscillation amplitude will return to the balance point. The opposite will happen if the perturbation decreases the oscillation amplitude. In this case, the absorbed energy becomes larger than the dissipated energy, and the oscillation amplitude will grow.

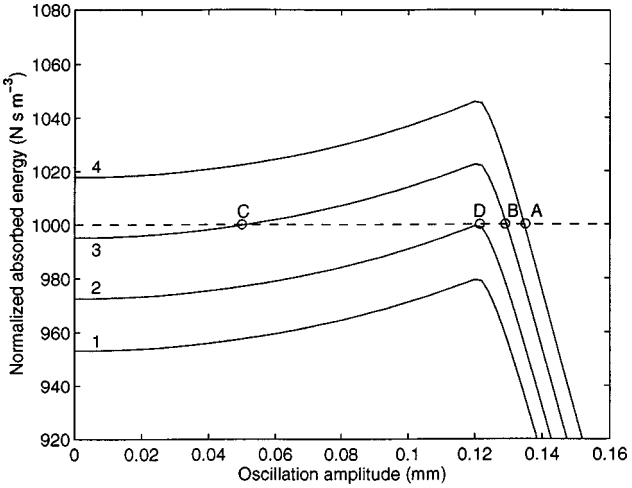

FIG. 5. Normalized absorbed energy versus oscillation amplitude, for $x_0 = 0.5$ mm and $P_s = 295$ Pa (1), 301 Pa (2), 308 Pa (3), 315 Pa (4). Dashed line: normalized dissipated energy. Points A and B: stable limit cycle, point C: unstable limit cycle, point D: cyclic fold bifurcation.

We can now decrease the subglottal pressure to a value lower than the value required to start the oscillation. For example, 308 Pa (curve 3). The oscillation amplitude will decrease to the new point of balance B. Note that there is also a second point of balance, point C. However, this is an unstable point. If a perturbation increases the oscillation amplitude, the absorbed energy becomes larger than the dissipated energy, and the oscillation will continue growing to point B. If the perturbation decreases the oscillation amplitude, the absorbed energy becomes smaller than the dissipated energy, and the oscillation will continue decreasing to the equilibrium point at zero amplitude. Point C represents then an unstable limit cycle, which is the limit cycle generated at the subcritical Hopf bifurcation.

At a subglottal pressure equal to 301 Pa (curve 2), both limit cycles coalesce at point D. Below this pressure (curve 1), there is no point of balance between the dissipated and absorbed energies, and hence no oscillation is possible. Point D is a bifurcation called cyclic fold, at which the unstable and stable limit cycles coalesce and canceled each other.

We can plot the points of energy balance taking the oscillation amplitude versus the lung pressure, as shown in Fig. 6. In this figure, the stable points (stable limit cycle) are plotted with solid line, and the unstable points (unstable limit cycle) with dashed line. The square and triangle symbols indicate results obtained by direct numerical solution of the

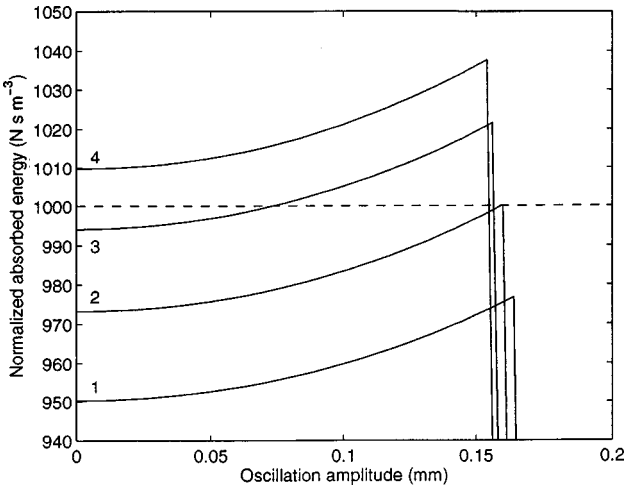

FIG. 7. Normalized absorbed energy versus oscillation amplitude, for $P_s = 400$ Pa and $x_0 = 0.68$ mm (1), 0.66 mm (2), 0.65 mm (3), 0.64 mm (4). Dashed line: normalized dissipated energy.

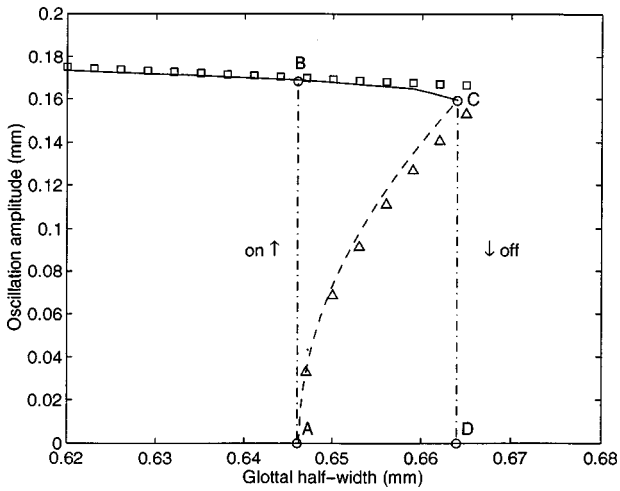

FIG. 8. Oscillation amplitude versus glottal half-width for $P_s = 400$ Pa. Solid line: stable limit cycle, dashed line: unstable limit cycle. Point A: subcritical Hopf bifurcation, point C: cyclic fold bifurcation. A-B-C-D: oscillation hysteresis loop. Squares (stable limit cycle) and triangles (unstable limit cycle): results from direct solution of the equations of motion.

equations of motion. The square is the amplitude of a stable limit cycle [the maximum value of $x(t)$] and the triangle is the amplitude of an unstable limit cycle. We can see no significant difference between the analysis and the numerical results, which validates the sinusoidal approximation for $x(t)$ [Eq. (32)] used in the energy analysis.

Increasing the subglottal pressure from zero, we need to reach point A to start the oscillation. Point A is the subcritical Hopf bifurcation found in Sec. III; at this point, the unstable limit cycle is generated and the equilibrium position becomes unstable. The subglottal pressure at this point is the oscillation onset threshold. As explained above, at this point the energy absorbed from the airflow becomes large enough to overcome the energy dissipated in the tissues. The oscillation will then start jumping to point B in the curve corresponding to the stable limit cycle. If we now reduce the lung pressure, the oscillation amplitude will decrease following the curve, until we reach point C. At this point, the stable and unstable limit cycles coalesce and disappear in a cyclic fold bifurcation. The oscillation will then vanish abruptly. The subglottal pressure at point D is then the oscillation offset threshold, and it is lower than the onset threshold. During this process, the oscillation amplitude follows a hysteresis loop A-B-C-D. The oscillatory behavior shown in the figure is the phenomenon called ''oscillation hysteresis'' by Appleton and Van der Pol (1922).

Note that according to Fig. 6, oscillation offset (i.e., the cyclic fold bifurcation) occurs at an oscillation amplitude at which there is a change in the slope of the curve absorbed energy versus oscillation amplitude, and recall that at this amplitude the point of airflow separation moves within the glottis (see explanation for Fig. 4). Hence, the analysis predicts that airflow separation within the glottis will occur in general during the oscillation cycle, except at the precise condition of offset threshold.

We can also consider the glottal half-width as control parameter. Figure 7 shows curves of normalized absorbed energy at various values of glottal widths. We can see a pattern for the curves similar to Fig. 5. In this case, to start the oscillation we have to decrease the glottal width, so that the absorbed energy at zero oscillation amplitude becomes larger than the dissipated energy. This will be accomplished at, for example, $x_0 = 0.64$ mm (curve 4). This curve has only one point of balance between the absorbed and dissipated energies, and it represents a stable limit cycle. The curve for $x_0 = 0.65$ mm (curve 3) has two points of balance, the left point represents an unstable limit cycle and the right point is a stable limit cycle. The curve for $x_0 = 0.66$ mm (curve 2) shows a cyclic fold bifurcation, at which both limit cycles coalesce. For larger glottal widths (curve 1) there is no point of energy balance and hence no oscillation is possible.

Figure 8 shows the points of energy balance taking the oscillation amplitude versus the glottal half-width. We can see also here a hysteresis loop A-B-C-D, similar to Fig. 6.

C. Onset–offset ratio

We will derive an analytical expression for the onset–offset ratio, to examine its relation to vocal fold parameters. Recall from Figs. 5 and 7 that the onset threshold corresponds to an oscillation amplitude $A = 0$, and the offset threshold corresponds to an oscillation amplitude at which the point of airflow separation moves within the glottis.

At this amplitude

$$a_2 = k_0 a_1 . \tag{38}$$

Using Eqs. (1), (2), and the sinusoidal approximation for $x(t)$ [Eq. (32)], and solving for the value of A such that there is a unique solution to Eq. (38), we obtain

$$a = \frac{k_0 - 1}{\sqrt{(k_0 - 1)^2 + \omega^2 \tau^2 (k_0 + 1)^2}}, \tag{39}$$

where $a = A/x_0$ is the normalized oscillation amplitude. Next, we compute the normalized absorbed energy at this oscillation amplitude. At this amplitude, there is no airflow separation within the glottis throughout the oscillation cycle, except at the point where the glottal divergence is maximum.

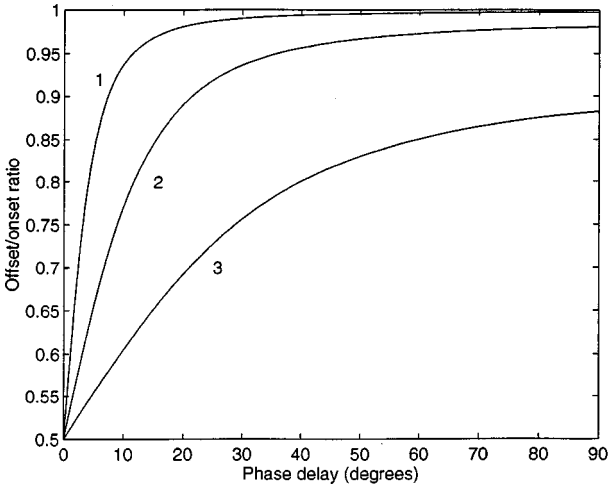

FIG. 9. Oscillation offset/onset ratio [Eq. (42)] versus phase delay, and $k_0 = 1.1$ (1), 1.3 (2), 2 (3).

Hence, we can use Eq. (9) for $P_g(t)$ (expression for no airflow separation in the glottis). Replacing in Eq. (37), and letting $\delta = 2\omega\tau$ be the phase delay of the upper edge of the vocal fold in relation to the lower edge, and $\theta = \omega t$, we obtain

$$r_g = \frac{2P_s\tau}{x_0}\,\Phi(\delta), \tag{40}$$

where

$$\Phi(\delta) = \frac{1}{\pi}\int_0^{2\pi} \frac{\cos^2\theta}{1 + a\,\sin\theta + 2\delta a\,\cos\theta}\,d\theta. \tag{41}$$

In the above equations, letting $r = r_g$, we obtain the point of balance between the absorbed and dissipated energies. Further, letting $a = 0$ we obtain the oscillation onset condition, and letting a equal to the value given by Eq. (39) we obtain the offset condition. Considering only the subglottal pressure and the glottal half-width as control parameters, we obtain the relation

$$\frac{(P_s/x_0)|_{\text{offset}}}{(P_s/x_0)|_{\text{onset}}} = \frac{1}{\Phi(\delta)}. \tag{42}$$

Figure 9 shows values of the offset/onset ratio versus the phase delay δ, and various values of the airflow separation coefficient k_0. Note that according to the above equations, the offset/onset ratio is only a function of these two parameters. In general, the offset/onset ratio varies between 0.5 and 1. This range is in agreement with experimental values (Baer, 1981; Berry *et al.*, 1995; Chan *et al.*, 1997; Hirose and Niimi, 1987; Koenig and McGowan, 1996; Munhall *et al.*, 1994; Titze *et al.*, 1995).

We see that at a given phase delay, the offset/onset ratio decreases (that is, the difference between onset and offset increases) as the airflow separation coefficient k_0 increases. Recall here the relation between coefficient k_0 and the glottal divergence angle at which airflow separation in the glottis starts, discussed for Fig. 4. Considering this result, we must note that previous models of the vocal fold oscillation (e.g., Herzel *et al.*, 1995; Steinecke and Herzel, 1995; Story and Titze, 1995) have assumed for simplicity that airflow separation in the glottis starts at zero degree of glottal divergence angle. This assumption is equivalent to a separation coefficient $k_0 = 1$, which leads to an offset/onset ratio equal to 1. Thus the present analysis predicts that those models should not be able to simulate the oscillation hysteresis phenomenon.

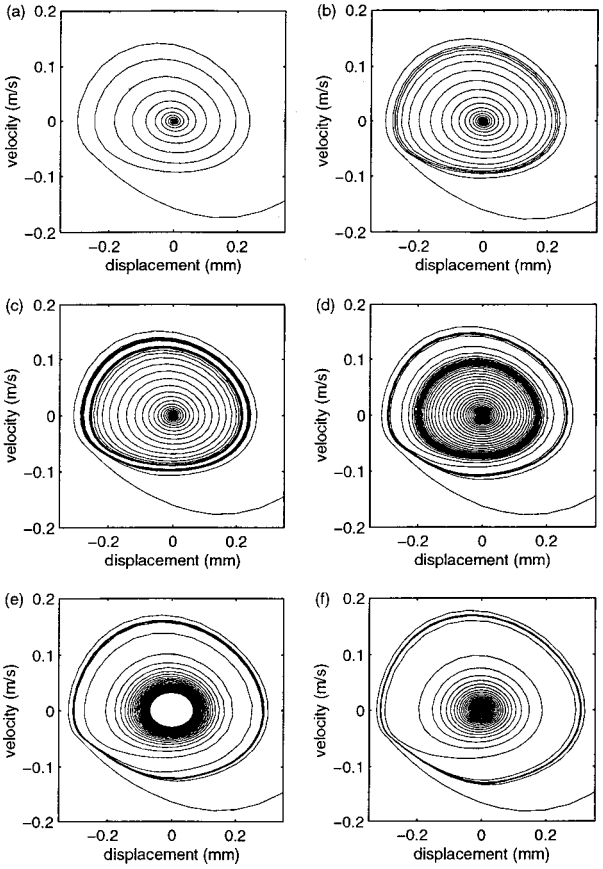

FIG. 10. Phase plane plots, for $x_0 = 0.5$ mm, $\delta = 30°$, $r = 2000$ N s m^{-3}, $k = 1\times10^6$ N m^{-3}, and $P_s = 750$ Pa (a), 786 Pa (b), 800 Pa (c), 830 Pa (d), 870 Pa (e), and 900 Pa (f). For clarity in the plots, no trajectory was plotted between the limits cycles in plot (c), and inside the internal limit cycle in plot (e).

D. Phase plane plots

The phase plane plots in Fig. 10 illustrate the dynamical behavior of the vocal folds, as the subglottal pressure is varied. They were obtained by direct solution of the equations of motion with numerical algorithms, and with parameter values selected to provide a clear plot. Plot (a) corresponds to a subglottal pressure below both thresholds, and shows a stable equilibrium position at the origin. In plot (b), we see that as the subglottal pressure increases and becomes near the offset threshold, the trajectory curves become closer together in a region around the equilibrium position, anticipating the cyclic fold bifurcation. Plot (c) corresponds to a subglottal pressure just above the offset threshold. We see that two limit cycles have appeared from a cyclic fold bifurcation. The internal limit cycle is unstable, and the external is stable. As the subglottal pressure continues to increase, we see in plots (d) and (e) that the internal unstable limit cycle becomes smaller and closes around the stable equilibrium

position at the origin. Finally, as the subglottal pressure passes the subcritical Hopf bifurcation at the onset threshold, unstable limit cycle and the stable equilibrium position coalesce and the equilibrium position becomes unstable. Plot (f) corresponds to a subglottal pressure above the onset threshold, we can see the unstable equilibrium position at the origin, surrounded by the stable limit cycle.

V. CONCLUSIONS

This analysis has shown that the differences observed at vocal fold oscillation onset versus offset may be described through the phenomenon of oscillation hysteresis (Appleton and van der Pol, 1922). This phenomenon is produced by a combination of two bifurcations: a subcritical Hopf bifurcation at oscillation onset and a cyclic fold bifurcation at oscillation offset, which occur at different values of the control parameters (e.g., glottal half-width or subglottal pressure). It is a consequence of the flow-induced nature of the vocal fold oscillation; in fact, it appears commonly in other cases of flow-induced oscillations (Thompson, 1982; Thompson and Stewart, 1986).

According to this analysis, the oscillation offset–onset ratio of vocal fold parameters is determined by the airflow separation from a divergent glottis. Airflow separation seems to be a central issue to understand the vocal fold oscillation dynamics. Pelorson *et al.* (1994, 1995) have already pointed out that airflow separation is the main mechanism for the airflow control by the movement of the vocal folds. Also, it seems to determine the optimal glottal angle for ease of phonation (Lucero, 1998). These results indicate the importance of an accurate modeling of the airflow separation, which should be a subject for further research efforts.

ACKNOWLEDGMENTS

These results were presented in partial form at the First International Conference in Voice Physiology and Biomechanics, in Evanston, IL, 29–31 May 1997. I am grateful to Kevin G. Munhall for his interest and support to this work, Ingo R. Titze for inspiring discussions on the vocal fold oscillation dynamics, Xavier Pelorson for his explanations on the airflow separation models, and Laura L. Koenig for discussions on her airflow measurements. This research was done while I was at the Speech Perception and Production Laboratory of the Department of Psychology, Queen's University at Kingston, and it was funded by NIH Grant No. DC-00594 from the National Institute of Deafness and other Communications Disorders and NSERC.

Appleton, E. V., and van der Pol, B. (**1922**). ''On a type of oscillation-hysteresis in a simple triode generator,'' Philos. Mag. **43**, 177–193.

Baer, T. (**1981**). ''Observation of vocal fold vibration: Measurement of excised larynges,'' in *Vocal Fold Physiology*, edited by K. N. Stevens and M. Hirano (University of Tokyo, Tokyo), pp. 119–133.

Berry, D., Herzel, H., Titze, I. R., and Story, B. (**1995**). ''Bifurcations in excised larynx experiments,'' NCVS Status and Progress Report **8**, 15–24.

Chan, R. W., Titze, I. R., and Titze, M. R. (**1997**). ''Glottal geometry and phonation threshold pressure in a vocal fold physical model,'' J. Acoust. Soc. Am. **101**, 3722–3727.

Guckenheimer, J., and Holmes, P. (**1983**). *Nonlinear Oscillations, Dynamical Systems, and Bifurcations of Vector Fields* (Springer-Verlag, New York), pp. 151–157.

Guo, C. G., and Scherer, R. C. (**1993**). ''Finite element simulation of glottal flow and pressure,'' J. Acoust. Soc. Am. **94**, 688–700.

Herzel, H., Berry, D., Titze, I., and Steinecke, I. (**1995**). ''Nonlinear dynamics of the voice: Signal analysis and biomechanical modeling,'' Chaos **5**, 30–34.

Hirose, H., and Niimi, S. (**1987**). ''The relationship between glottal opening and the transglottal pressure differences during consonant production,'' in *Laryngeal Function in Phonation and Respiration*, edited by T. Baer, C. Sasaki, and K. Harris (College-Hill, Boston), pp. 381–390.

Ishizaka, K. (**1981**). ''Equivalent lumped-mass models of vocal fold vibration,'' in *Vocal Fold Physiology*, edited by K. N. Stevens and M. Hirano (University of Tokyo, Tokyo), pp. 231–244.

Ishizaka, K., and Matsudaira, M. (**1972**). ''Theory of vocal cord vibration,'' Rep. Univ. Electro-Comm. Sci. Tech. Sect. **23**, 107–136.

Koenig, L. L., and McGowan, R. S. (**1996**). ''Voicing and aerodynamics of /h/ produced by men, women and children,'' J. Acoust. Soc. Am. **100**, 2689(A).

Lucero, J. C. (**1993**). ''Dynamics of the two-mass model of the vocal folds: Equilibria, bifurcations, and oscillation region,'' J. Acoust. Soc. Am. **94**, 3104–3111.

Lucero, J. C. (**1995**). ''The minimum lung pressure to sustain vocal fold oscillation,'' J. Acoust. Soc. Am. **98**, 779–784.

Lucero, J. C. (**1998**). ''Optimal glottal configuration for ease of phonation,'' J. Voice **12**(2), 151–158.

Minorsky, N. (**1962**). *Nonlinear Oscillations* (Krieger, Malabar), pp. 101–102 and 163–189.

Munhall, K. G., Löfqvist, A., and Scott Kelso, J. A. (**1994**). ''Lip-larynx coordination in speech: Effects of mechanical perturbations to the lower lip,'' J. Acoust. Soc. Am. **95**, 3605–3616.

Pelorson, X., Hirschberg, A., van Hassel, R. R., Wijnands, A. P. J., and Auregan, Y. (**1994**). ''Theoretical and experimental study of quasisteady-flow separation within the glottis during phonation. Application to a modified two-mass model,'' J. Acoust. Soc. Am. **96**, 3416–3431.

Pelorson, X., Hirschberg, A., Wijnands, A. P. J., and Bailliet, H. (**1995**). ''Description of the flow through *in-vitro* models of the glottis during phonation,'' Acta Acust. (China) **3**, 191–202.

Siljak, D. D. (**1969**). *Nonlinear Systems* (Wiley, New York), pp. 121–151.

Steinecke, I., and Herzel, H. (**1995**). ''Bifurcations in an asymmetric vocal fold model,'' J. Acoust. Soc. Am. **97**, 1874–1884.

Story, B. H., and Titze, I. R. (**1995**). ''Voice simulation with a body-cover model of the vocal folds,'' J. Acoust. Soc. Am. **97**, 1249–1260.

Thompson, J. M. T. (**1982**). *Instabilities and Catastrophes in Science and Engineering* (Wiley, New York), pp. 155–178.

Thompson, J. M. T., and Stewart, H. B. (**1986**). *Nonlinear Dynamics and Chaos* (Wiley, New York), pp. 108–131.

Titze, I. R. (**1988**). ''The physics of small-amplitude oscillation of the vocal folds,'' J. Acoust. Soc. Am. **83**, 1536–1552.

Titze, I. R. (**1994**). *Principles of Voice Production* (Prentice-Hall, Englewood Cliffs, NJ), pp. 81–105.

Titze, I. R., Schmidt, S. S., and Titze, M. R. (**1995**). ''Phonation threshold pressure in a physical model of the vocal fold mucosa,'' J. Acoust. Soc. Am. **97**, 3080–3084.

Global and local dimensions of vocal dynamics

Alison Behrman
Voice and Laryngeal Center, Department of Otolaryngology and Communicative Disorders, Long Island Jewish Medical Center, 270-05 76th Avenue, New Hyde Park, New York 11040

(Received 18 November 1997; accepted for publication 24 September 1998)

The global embedding dimension (d_E) and the local dynamical dimension (d_L) are calculated from the microphone and electroglottographic (EGG) signals elicited from five healthy subjects and seven dysphonic subjects with laryngeal pathology during phonation of sustained/a/. The data from each pathologic subject contain at least one bifurcation and are divided into periodic and irregular segments for analysis. The d_E values from both the microphone and EGG signals elicited from the healthy subjects indicate that a relatively small coordinate space can be used to reconstruct the attractor, with little residual noise. Consistent across all healthy subjects, three dominant degrees of freedom (d_L) are found to govern local dynamics of the trajectories on the attractor. From the pathologic subjects, many of the d_E values suggest the presence of a high-dimensional component in the signals. However, the noise does not completely obscure the deterministic dynamics of the source signal or prevent extraction of an optimal global embedding dimension. The data do not reveal consistent differences in degrees of freedom between healthy and pathologic phonation, or between different modes of pathologic phonation. However, the d_L values suggest that the pathologic vocal fold vibration of these subjects, even highly irregular vibration, is governed locally by a low number of dominant degrees of freedom, sometimes no greater than those calculated from the signals of healthy subjects. Only in the cases of severe breathiness are the microphone and EGG signals sufficiently contaminated by noise to obscure any deterministic component. [S0001-4966(99)00301-X]

PACS numbers: 43.70.Aj, 43.70.Bk [AL]

INTRODUCTION

Voice production may be conceptualized as a multidimensional array of nonlinearly coupled oscillators (Fletcher, 1996; Titze, 1995). Many of these oscillators, such as the respiratory system (Porter *et al.*, 1995) and even the distantly related cardiac system (Orlikoff and Baken, 1989), are themselves capable of complex and even chaotic dynamics (Paydarfar and Buerkel, 1995; Peng *et al.*, 1995). Analysis of voice production is made more complex by the fact that the vocal folds are not easily accessible, and the relevant signal is often only an indirect measure of the event under study. The larynx resides in close proximity to major blood vessels and muscles that have the potential to contaminate that signal with high-dimensional noise. Typically, in analyzing the voice, the signal is obtained with its accompanying measurement and dynamical noise, and Fourier analysis is used to extract its periodic composition. The signal is classified based on the location and sharpness of the spectral peaks, and the resonant frequencies of the system. The problem, of course, is that it is difficult to distinguish between random events, high-dimensional broadband noise, and chaos—deterministic aperiodicities.

Determination of the sources of irregular vibratory behavior guides the theoretical model and the research methodologies used to understand, and ultimately control, abnormal vocal fold behavior. Even given a wholly deterministic vocal system, a large number of active degrees of freedom would best be characterized using stochastic, probabilistic models. This is the reason for the emphasis upon the determination of whether the dynamics can be described as a low-dimensional chaotic system—that is, does it have a tractable number of degrees of freedom. Much research suggests that it does (Baken, 1990; Behrman and Baken, 1997; Hertrich *et al.*, 1997; Herzel, 1993; Herzel *et al.*, 1994; Kumar and Mullick, 1996; Narayanan and Alwan, 1995; Titze *et al.*, 1993).

In characterizing vocal fold vibratory behavior as synchronized modes of oscillation, Titze (1994, 1976) models healthy vibration as a coupled 11 mode. This corresponds to one degree of freedom in the antero-posterior plane, and one degree of freedom in the inferior-to-superior plane. Increasing the mode of the antero-posterior plane by only one degree of freedom (21 mode) generates two half-wavelengths along the horizontal axis and results in abnormal vocal fold vibration and potentially, a highly dysphonic voice. Modal analyses of computationally generated signals that bifurcate from periodic to chaotic regimes (Berry *et al.*, 1994; Herzel, 1996; Steinecke and Herzel, 1995) have generated evidence of low-dimensional determinism. These data support a model of dysphonia as the disentrainment of only a few principal vibratory modes. These models have shown that studying the output of a system which transitions to different states has the potential to reveal information about how that system functions. Dimensional analysis of real voice signals which similarly bifurcate from periodic to aperiodic regimes might well provide important data to compare with those generated from the models.

It is quite a leap, however, from computational model to physiology. Nonstationarity, finite data sets, limited observation of the dynamics, and the inherent high dimensionality of the system inhibit observation of deterministic sources

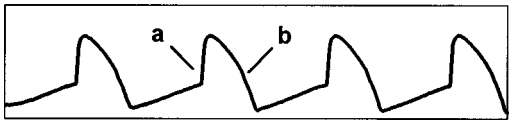

FIG. 1. Four cycles of a typical EGG waveform from a healthy subject, showing (a) increasing and (b) decreasing relative vocal fold contact.

(Glass and Kaplan, 1993; Kantz and Schreiber, 1995). Nonlinear dynamical analyses are based, not upon Fourier methods, but rather upon recreation of a state space, where the value of a single observed variable at a given point in time is lagged against itself, using a fixed time delay, and so the lagged scalars are used as vectors coordinates in *d*-dimensional state space. This refers, of course, to embedding theorem (Takens, 1981). Yet the selection of the scalar in a high-dimensional and spatially extended system such as the voice production system is problematic. It is unlikely that all of the effective degrees of freedom of the system will be strongly coupled to, and equally expressed in, the observed scalar variable (Kantz and Olbrich, 1997). Certainly there is no one signal that wholly represents the complexity of the voice production system. Therefore, the determination of the most relevant signal to embed in state space should be made carefully. The microphone signal captures the end product of the voice production system, the complex acoustic spectrum which is ultimately perceived by the listener. It would therefore seem an appropriate selection.

There is a drawback to using the microphone signal, however. The source energy of the acoustic spectrum is substantially defined by the temporal and geometric characteristics of the changing vocal fold contact area throughout each vibratory cycle. Typically, the presence of vocal irregularities can arise from turbulent airflow caused by incomplete vocal fold closure, from irregular oscillatory movement of the vocal fold tissue, or from both types of events. Therefore, exploration of the dynamics of abnormal voice production might best include both sources. The electroglottographic (EGG) signal is an easy and noninvasive means of isolating vocal fold vibratory behavior, free of the resonant characteristics of the vocal tract. Potentially, it could provide information not easily accessible in the microphone signal. Based on the principle of Ohm's law, the EGG measures the change in electrical conductance across the neck in the region of the vocal folds, and the resulting output reflects the change in impedance due to changes in relative vocal fold contact area during phonation (Fig. 1) (Baken, 1992; Childers *et al.*, 1987; Fourcin, 1981). Salient characteristics of the EGG waveform of healthy, modal phonation produced at comfortable intensity include uniformity of successive periods and cycle amplitudes, a relatively sharper increase than decrease in vocal fold contact, and a relatively long maximal contact duration (Fourcin, 1981).

Various statistics can be used to capture different aspects of the complexity of a nonlinear system. Perhaps the most popular has been the correlation dimension (Grassberger and Procaccia, 1983). Behrman and Baken (1997), however, found considerable difficulties in scale interpretation of correlation dimension from vocal signals. Specifically, it was found that nonstationarity, short data sets, and the presence of noise (characteristics common to all physiologic data) preclude the meaningful application of correlation dimension to analysis of the voice production system. Previous dimension analyses have relied heavily on estimation of the correlation dimension (Hertrich *et al.*, 1997; Herzel, 1993; Herzel *et al.*, 1994; Kumar and Mullick, 1996; Narayanan and Alwan, 1995; Titze *et al.*, 1993). Therefore, this study uses the more robust methods of global and local false nearest neighbors (Abarbanel, 1996) to characterize the embedding dimension of the reconstructed attractor, and the dominant degrees of freedom of the local trajectories, respectively. These measures are developed more fully in the following section. There is no literature documenting the application of either of these statistics to vocal dynamics.

The broad purpose of this research was to provide initial exploration of the hypothesis that vocal dynamical dimension during sustained /a/ phonation is a function of vibratory mode, that is, the dynamical dimension of abnormal yet regular phonation would differ from abnormal, irregular phonation or normal phonation. Such a finding could then potentially form the basis for classification of vibratory mode. Toward that end, the specific aims of this study were to determine whether: (i) there is evidence to support the theory of low-dimensional dynamics in healthy and abnormal voice production, using the measures of global and local false nearest neighbors; (ii) the values of global and local false nearest neighbors obtained from one segment of phonation are different from those values obtained from another segment across a point of bifurcation; and (iii) the presence of any low-dimensional dynamics is more likely to be expressed in either the EGG or microphone signal.

I. METHODS

A. Data collection

Seven dysphonic subjects and five healthy young adult individuals served as subjects. The dysphonic subjects were chosen from a database of over 200 voice patients in the Department of Otolaryngology at the New York Hospital–Cornell Medical Center. Selection criteria required that complete data files be available for review. This included a good quality videostroboscopy tape recording, and microphone and EGG signals of sustained /a/. The waveforms and corresponding narrow-band spectrograms were reviewed, and only signals with good signal-to-noise levels that contained no amplitude saturation or artifact were retained. Signals were then selected which contained an abrupt alteration in amplitude and or frequency with accompanying change in vocal quality, suggesting a bifurcation in vibratory mode (less than half of all files examined). Each vibratory mode had to be a minimum of 0.5 s in duration, so that a sufficient number of data points would be available for analysis. This length requirement resulted in the elimination of most patient files, because many transitions were of very short duration, or the bifurcation resulted in cessation of oscillation or transition to a highly breathy mode of phonation which typically yielded a poor EGG signal.

All EGG signals were transduced with a Kay Elemetrics Fourcin-type electroglottograph. The EGG and microphone

TABLE I. Description of the segments extracted from the EGG and microphone signals elicited from the pathologic subjects. Vocal fold closure is based upon videostroboscopy examination. The presence of a small posterior glottal chink was ignored. Segments labeled periodic refer only to regularity of the signals.

Pathologic Subject (age, sex)	Primary laryngeal pathology	Segment type	Vocal fold closure	Vocal quality
P1 (35, F)	right intra-cordal cyst			
		periodic	complete	unremarkable
		period-4	complete	diplophonic
		period-6	complete	diplophonic and rough
P2 (61, F)	Reinke's edema			
		periodic	incomplete	moderately breathy
		irregular	incomplete	severely breathy
P3 (29, F)	bilateral nodules			
		periodic	complete	mildly rough
		period-4	complete	moderately rough
P4 (38, M)	right sessile polyp+left small nodularity			
		periodic	incomplete	mildly breathy
		irregular	incomplete	moderately breathy and rough
P5 (46, F)	bilateral nodules			
		periodic	incomplete	unremarkable
		irregular	incomplete	mildly breathy and rough
P6 (83, M)	bilateral bowing			
		periodic	spindle-shaped	mildly breathy
		irregular	posterior contact only	moderately breathy and ''pulsed''
P7 (52, F)	bilateral keratosis			
		irregular	complete	rough + diplophonic
		irregular	incomplete	severely hoarse

signals in the database had all been obtained using the Kay Elemetrics A/D conversion hardware and software, with 16 bit resolution, at a sampling rate of 20.0 k samples/s/channel with appropriate low-pass filtering to prevent signal aliasing. For the present study, the EGG signals were refiltered and downsampled to 10k samples/s. From each subject file, a sample of approximately 0.4 s (4096 data points from the EGG signals, and 8192 data points from the microphone signals) was selected from the most stationary-appearing portion of the waveform before and after every bifurcation. Segments were labeled ''periodic'' if the cycles were largely regular, and there was an absence of noise and subharmonic structure in the narrow-band spectrograms. Two segments were extracted from the data of each of the five healthy subjects. However, no bifurcations were present in these waveforms, and therefore both segments appeared similar in waveform morphology and in vocal quality. Table I specifies the number of segments extracted from each of the pathologic subjects' data files, along with information about the nature of the laryngeal pathology and dysphonia.

B. Data analysis

1. State space embeddings

All nonlinear analyses were performed on a Pentium-based PC using Tools For Dynamics Software. The EGG data were embedded in state space following the methods of Takens (1981), in which reconstruction of the attractor was accomplished using the method of lag variables. In such a representation, the value of a variable ν at time (x) is lagged against itself, using a fixed time delay T, to create a vector time series of the form

$$\mathbf{y}(x)=[\nu(x),\nu(x+T),\nu(x+2T),\ldots,\nu(x+(d-1)T)], \tag{1}$$

where each lagged time series is a d-dimensional embedding. The optimal delay is found by the minimum of the mutual information function (Fraser and Swinney, 1986). The resulting vectors are used as coordinates in d-dimensional state space. Included in Tables II and III are the delay values for each of the data sets.

TABLE II. The delay values (T) calculated from the average mutual information function, used to create the state space embeddings, and the d_E and d_L values derived from the microphone and EGG signals of healthy subjects.

Healthy subject (age, sex)	Segment type	Delay value (Mic:EGG)	Mic d_E	Mic d_L	EGG d_E	EGG d_L
H1 (42, F)						
	periodic	(12:6)	6	3	8	3
	periodic	(12:6)	5	3	6	3
H2 (51, F)						
	periodic	(11:5)	6	3	6	3
	periodic	(11:5)	6	3	6	3
H3 (39, M)						
	periodic	(21:10)	5	3	5	3
	periodic	(21:10)	4	3	5	3
H4 (47, M)						
	periodic	(20:10)	5	3	7	3
	periodic	(20:10)	5	3	8	3
H5 (28, F)	periodic	(10:5)	5	3	6	3
	periodic	(10:5)	5	3	5	3

2. Global embedding dimension

The calculation of the global embedding dimension is based on the concept that the dynamical attractor is a compact and complex structure due to the stretching and folding properties of the attractor (Baker and Gollub, 1990). The stretching (unstable) motion of the trajectories tends to amplify differences, errors, and noise. The folding motion keeps the system in a bounded region of state space. Folding, however, also places points into near neighborhoods of one another when they are not necessarily close in a dynamical sense. The purpose of embedding the reconstructed dynamics in a multi-dimensional state space is to unfold the attractor. A point in the data set that is a neighbor solely because the orbit is viewed in too small an embedding space is a false neighbor. The concept of testing for false nearest neighbors has been discussed as a means of identifying an optimal embedding dimension (Cellucci *et al.*, 1997; Gao and Zheng, 1993; Kennel *et al.*, 1992). If the trajectories are projected into a dimensional space that is too small—that is, contains too few coordinates—then points which appear close to one another in state space might actually be quite far apart. In effect, trajectories will appear to intersect one another when they really do not. The presence of false neighbors appears as random behavior, because the location of a given point along a trajectory would not be due to deterministic dynamics. Dynamical analyses that rely on following a given tra-

TABLE III. The delay values (T), and the d_E and d_L values derived from the microphone and EGG signals of pathologic subjects. A dash means that the noise in the signal prevented estimation of the relevant dimension. An asterisk means that the dimension could be estimated, but that a noise floor was observed.

Pathologic subject	Segment type	Delay value (Mic:EGG)	Mic d_E	Mic d_L	EGG d_E	EGG d_L
P1	periodic	(10:5)	7	3	8	3
	period-4	(12:6)	6	5	6	4
	period-6	(14:8)	6	3	6	5
P2	periodic	(8:4)	4	3	5	3
	irregular	(11:6)	8*	-	9*	-
P3	periodic	(10:5)	4	4	5	3
	period-4	(12:6)	5	4	6	3
P4	periodic	(20:10)	8	5	8	5
	irregular	(18:11)	9*	-	9*	-
P5	periodic	(9:4)	5	4	6	4
	irregular	(9:3)	5	4	6*	4
P6	periodic	(19:9)	10	6	5	4
	irregular	(17:10)	8*	-	5*	4
P7	irregular	(11:6)	6	5	8	6
	irregular	(6:4)	6*	-	8*	-

jectory for a specified period of time, on encountering a false intersection, would not distinguish between the true and false path of the trajectory; each would have an equal probability of being the correct path. Therefore, it is absolutely necessary to establish the number of delay coordinates required to unfold the system over the entire set of data. This is referred to as the global embedding dimension (d_E)—the number of geometric dimensions that are required to fully reconstruct the attractor.

In theory, working in a dimension higher than the true or minimum embedding should not be a problem. Once the attractor is unfolded, embedding it in higher dimensions should be of no consequence. In practice, however, all signals derived from the voice system contain noise. Most dynamical analyses rely on the geometry of the data within small Euclidean distances. It is primarily within these small spaces that noise most contaminates the dynamics. The result is that the higher dimensions are populated more dominantly by noise. So not only do calculations carried out in higher dimensions add unnecessary computational burden due to the exponential increase in data requirements with increasing dimension, but those higher-dimensional computations are corrupted by noise.

The presentation of the calculation of d_E is drawn from Abarbanel (1996), Frison *et al.* (1996), and Kennel *et al.* (1992). The interested reader is encouraged to review these sources (especially the first) for a more thorough treatment. First, the nearest neighbor to $\mathbf{y}(x)$ is described by the vector

$$\mathbf{y}^{NN}(x)=[\,\nu^{NN}(x),\nu^{NN}(x+T),\nu^{NN}(x+2T),\ldots,\nu^{NN}(x+(d-1)T)]. \tag{2}$$

Moving from dimension d to dimension $d+1$ requires adding a $\nu(x+dT)$ coordinate onto $\mathbf{y}(x)$ and adding a $\nu^{NN}(x+dT)$ coordinate onto $\mathbf{y}^{NN}(x)$. Therefore, assessing the distance between the neighbors can be found by evaluating $|\nu^{NN}(x+(d-1)T)-\nu(x+(d-1)T)|$ as compared with the Euclidean distance $|\mathbf{y}^{NN}(x)-\mathbf{y}(x)|$ in dimension d. Taking the square of the Euclidean distance between the vector $\mathbf{y}^{NN}(x)$ and $\mathbf{y}(x)$ in dimension d as

$$R_d(x)^2=\sum_{m=1}^{d}[\,\nu(x+(m-1)T)-\nu^{NN}(x+(m-1)T)]^2, \tag{3}$$

and adding the $\nu^{NN}(x+dT)$ coordinate onto $\mathbf{y}^{NN}(x)$ in dimension $d+1$, one obtains

$$R_{d+1}(x)^2=R_d(x)^2+|\nu(x+dT)-\nu^{NN}(x+dT)|^2. \tag{4}$$

Therefore, the distance between the neighbors in dimension $d+1$ as compared to the distance in dimension d is evaluated and nearest neighbors are found to be false if

$$\sqrt{\frac{R_{d+1}(x)^2-R_d(x)^2}{R_d(x)^2}}=\frac{|\nu(x+dT)-\nu^{NN}(x+dT)|}{R_d(x)}>R_{\text{Criterion 1}}, \tag{5}$$

where $R_{\text{Criterion 1}}$ is determined in a data-driven manner, although Abarbanel (1996) notes that for many dynamical systems examined, the threshold is approximately 15.

Equation (5) is not sufficient by itself, however, to make the determination of false neighbors. It is not possible to have an infinite amount of physiologic data, and so the vectors will be less densely populated in the higher embeddings. Because of the sparsity of data points, the vector $\mathbf{y}^{NN}(x)$ may be a true neighbor of $\mathbf{y}(x)$, but they may appear far apart. Therefore, a second criteria is necessary which takes into consideration the Euclidean distance between neighbors relative to the volume of the attractor. If $\mathbf{y}^{NN}(x)$ is not close to $\mathbf{y}(x)$, then

$$R_d(x)\approx R_A, \tag{6}$$

where R_A is the rms value of the data about the mean, indicating the nominal radius of the attractor. Further, if nearest neighbors are false, then

$$R_{d+1}(x)\approx 2R_A. \tag{7}$$

Therefore, the second criterion for establishing the presence of false near neighbors is

$$\frac{R_{d+1}(x)^2}{R_A}>R_{\text{Criterion 2}}. \tag{8}$$

In this way, the additional distance which results from increasing the dimension by one is not larger than the nominal diameter of the attractor.

Figure 2 shows the d_E for the Lorenz equations (Lorenz, 1963) and for a computer-generated random number data set. The Lorenz equations are a set of three ordinary differential equations obtained as a model of convection fluid flow. The temperature and velocity parameter values used here, $\sigma=16$, $b=4$, and $r=45.92$, are the typical values used to model chaotic flow. The fractal dimension of the attractor d_A is 2.06. For this ideal (noiseless) chaotic system, the percentage of false nearest neighbors (d_E) drops to zero at dimension three. A three-coordinate system is required to completely unfold the attractor, which is one integer greater than its fractal dimension, as expected. For the random numbers, noise expands to fill each additional embedding, and so there is no coordinate space that will completely unfold the attractor. The percentage of false near neighbors increases with higher embeddings. The significance of Fig. 2 is that it suggests how the d_E can provide an indication of the presence of high-dimensional noise. If the source of the signal is low-dimensional chaos with a small amount of high-dimensional contaminating noise, then the d_E should allow one to distinguish between them. The percentage of false nearest neighbors should drop close to zero at the optimal embedding dimension, and then begin to increase with higher embeddings as the high dimensionality of the noise begins to dominate the state space.

3. Local dynamical dimension

Abarbanel (1996), Frison *et al.* (1996), and Kennel *et al.* (1992) point out that the dynamical degrees of freedom which specify the evolution of the system along local areas of the attractor will likely be less than the dimension which is sufficient to unfold the attractor. The 2-torus is a commonly used example; it is composed of two incommensurate

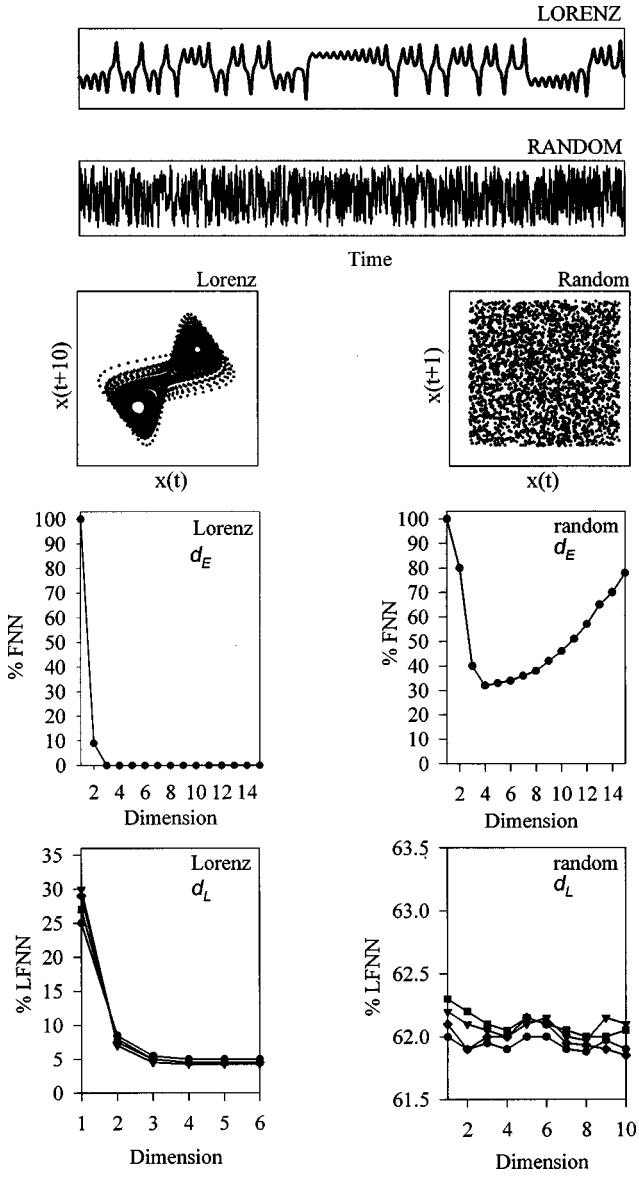

FIG. 2. The state-space plots and global (d_E) and local (d_L) false nearest neighbors for the Lorenz equations (Lorenz, 1963) and for a computer-generated random number data seta set. Legend for d_L plots: circle: $N_B=40$; square: $N_B=60$; triangle: $N_B=80$; diamond: $N_B=100$.

frequencies, but requires a global embedding dimension of three for complete unfolding of the geometry.

Abarbanel and Kennel (1993) developed an approximation of the dominant degrees of freedom by calculation of the local false nearest neighbors. For local regions of the unfolded attractor, the algorithm assesses the accuracy with which the evolution of nearest neighbors can be predicted. When nearest neighbors are located close to one another due to similar dynamics, they will remain close to one another for short predictions, even when the trajectories diverge exponentially and contain a positive Lyapunov exponent (Eckmann and Ruelle, 1985). When the neighbors are false, trajectories will move apart more quickly than expected, and so the ability to predict the evolution of those points will be poor. Establishing the dynamical dimension, therefore, is based on defining a criteria for how trajectories within d_E evolve in one time step from the local neighborhood near $\mathbf{y}(x)$ into the local neighborhood near $\mathbf{y}(x+1)$, and then testing numerous neighborhoods using that criteria.

The algorithm of local false nearest neighbors defines a local coordinate system of dimension d_L within d_E using local principal component decomposition by forming the sample covariance matrix among the number of neighbors N_B of $\mathbf{y}(x)$, and then selecting the eigendirections associated with the largest eigenvalues of the matrix. In this way, local coordinates are established in the appropriate direction of the trajectories, and then the nearest neighbors in the local coordinate system are chosen. A local polynomial prediction map is constructed and the distance between all pairs of points in the neighborhood are assessed. Local neighbors are considered false if the prediction map fails within Δ time steps, which is defined as some finite size relative to R_A as referenced in Eq. (6). The prediction map is then tested in repeatedly larger local dimensions. To determine the dynamical dimension of a system, the ability to predict short-time evolution (based on the percentage of local false nearest neighbors) must become independent of both the local dimension and N_B. Frison *et al.* (1996) comment that it is this independence of the local predictions, rather than the quality of the predictions themselves, which contributes to the elegance of this algorithm.

Figure 2 shows that, as expected, there are three degrees of freedom (d_L) of the Lorenz system. For the random numbers, a lack of low dimensionality is reflected in the featureless contour of the d_L plot, in which the percentage of local false nearest neighbors does not decrease substantially with higher embeddings. In this random set, neighbors that are false due to folding of the attractor are no different from the stochastic process itself.

II. RESULTS AND DISCUSSION

A. Healthy subjects

The values of the global and local embedding dimensions from the microphone and EGG signals elicited from the healthy subjects are shown in Table II. The percentage of global false nearest neighbors fell to zero for all of the microphone and EGG data sets obtained from the five healthy subjects, similar to the d_E plots shown in Fig. 3. This is consistent with the low noise levels observed in the qualitative inspection of the waveforms and spectrographic data, and in the perceptual analysis of good vocal quality of the subjects. These results suggest that six to eight embedding dimensions (sometimes less) are required in which to model the healthy voice production system and capture its essential determinism.

The microphone-derived d_E values were consistently either equal to or less than the EGG-derived d_E values. This may be an artifact of the small number of subjects, however, and so interpretation must be limited. Nevertheless, this characteristic was also demonstrated in the pathologic subject group (with the exception of one subject). This suggests that the embedding space is dependent on the type of signal used to characterize the system. This is consistent with the theoretical basis of the global embedding dimension, which specifies that the global coordinate system will not necessar-

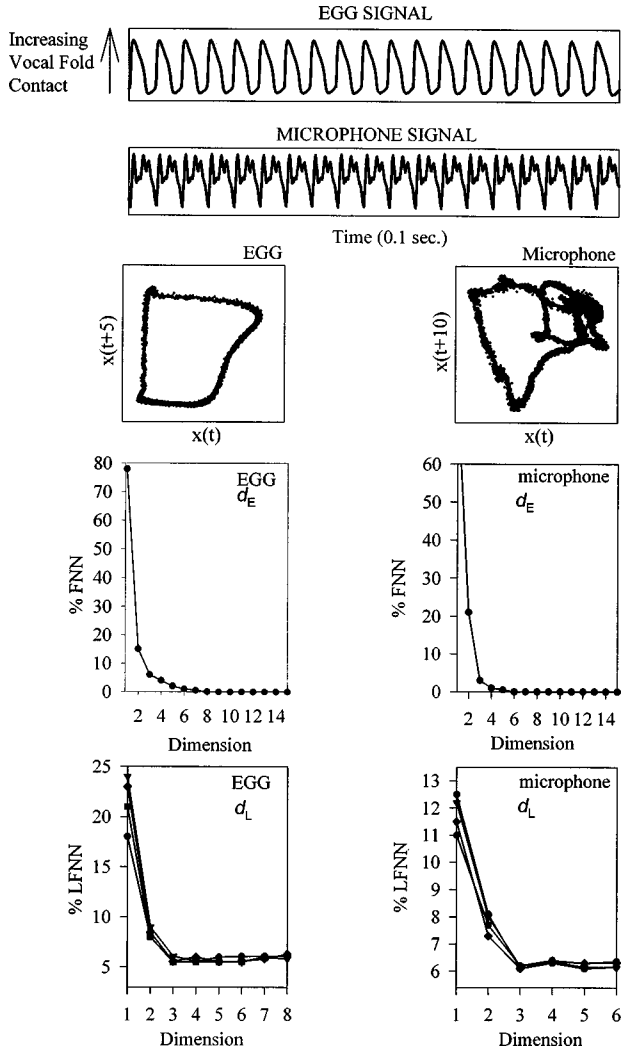

FIG. 3. The state-space plots and global (d_E) and local (d_L) false nearest neighbors from one of the periodic segments of the EGG and microphone signals elicited from healthy subject H1. Legend for d_L plots: circle: $N_B = 40$; square: $N_B = 60$; triangle: $N_B = 80$; diamond: $N_B = 100$.

ily be equivalent across different types of measurements, or even different samples of the same signal type (Abarbanel, 1996). The variable d_E values suggest that the coordinate space required to completely unfold the reconstructed attractor is generally smaller when the voice production system is captured from the acoustic signal than from the EGG signal. This is somewhat counterintuitive, in that the EGG signal is typically conceived of as ''simpler'' than the microphone signal, because it is free of vocal tract resonant influences. It was expected that the EGG waveform, with its simpler morphology, would be geometrically represented in fewer dimensions than the more complex-appearing microphone signal. The d_E values suggest that this is not true.

The d_L values derived from the healthy subjects (Table II and lowest plots of Fig. 3) imply that there are three dominant degrees of freedom that determine the evolution of the trajectories on the attractor. The fact that the d_L values were the same within and across all healthy subjects is consistent with the theoretical basis of nearest neighbors. The number of degrees of freedom which capture the essential deterministic features of the system should be independent of separate realizations of the system. Even across different subjects, the healthy voice production system of young adults phonating a sustained vowel should be quite similar functionally. The equivalent values of d_L derived from the EGG and microphone signals suggests that, in healthy phonation, the largely passive resonatory oscillator does not add to the effective degrees of freedom of the voice source.

B. Pathologic subjects

The d_E values obtained from the pathologic subjects are listed in Table III. There was considerable dispersion of the values. This is unsurprising, considering that the subject grouping was not homogeneous in vocal pathology or type of dysphonia. And again, the global coordinate system is not expected to be the same across different samples. This would be especially true when the systems are pathologic and typically demonstrate instability and irregularities both within and across phonatory samples. Unlike the data from the healthy subjects, however, many of the d_E values derived from this pathologic group suggested the presence of noise in the signals, which increased in dominance as the embedding dimension increased. A clear example of this is found in subject P6, as follows.

Two segments of the EGG waveforms and d_E and d_L plots from pathologic subject $P6$ are shown in Fig. 4. The corresponding microphone data are shown in Fig. 5. Stroboscopically, the subject was observed to have a spindle-shaped closure of the airway during oscillation, so that the anterior and posterior portions of the vocal folds adducted, and the center portion did not contact. There was, however, a mucosal wave present along the entire length of the folds. Vocal quality was (a bit surprisingly) only very mildly breathy. This type of vibration represents the segment of the microphone and EGG signals labeled ''periodic.'' (This label is used only to characterize the vibration as possessing a certain regularity. The vibration is clearly abnormal.) Intermittently, the anterior contact would fail briefly, and closure was then achieved only along the posterior portion of the folds. The voice was moderately breathy and had a ''pulsed'' quality. (The breathiness was due to the likely large dc airflow. The pulsed quality was likely due to the low frequency ac component caused by the intermittent anterior closure.) This type of vibration represents the waveform segments labeled ''irregular.'' Comparing the d_E plots of the EGG and microphone signals from the periodic and irregular segments provides an excellent illustration of the effect of noise on the embedding dimension. For the ''periodic'' segment of the EGG signal, the change in tissue contact produced a sufficiently large impedance change to yield a clean signal. The noise level observed in the microphone signal of the periodic portion, as indicated by the percentage of false nearest neighbors in the d_E plot, is so low at the optimal embedding dimension as to be inconsequential for most purposes. In the irregular portion of both the microphone and EGG signals, although the noise level increases in the higher dimensions, an optimal embedding dimension can still be selected in which the substantial portion of the determinism of the system has been captured. Frison *et al.* (1996) suggest that when the d_E values drop below 1%, or even 2%, from a practical

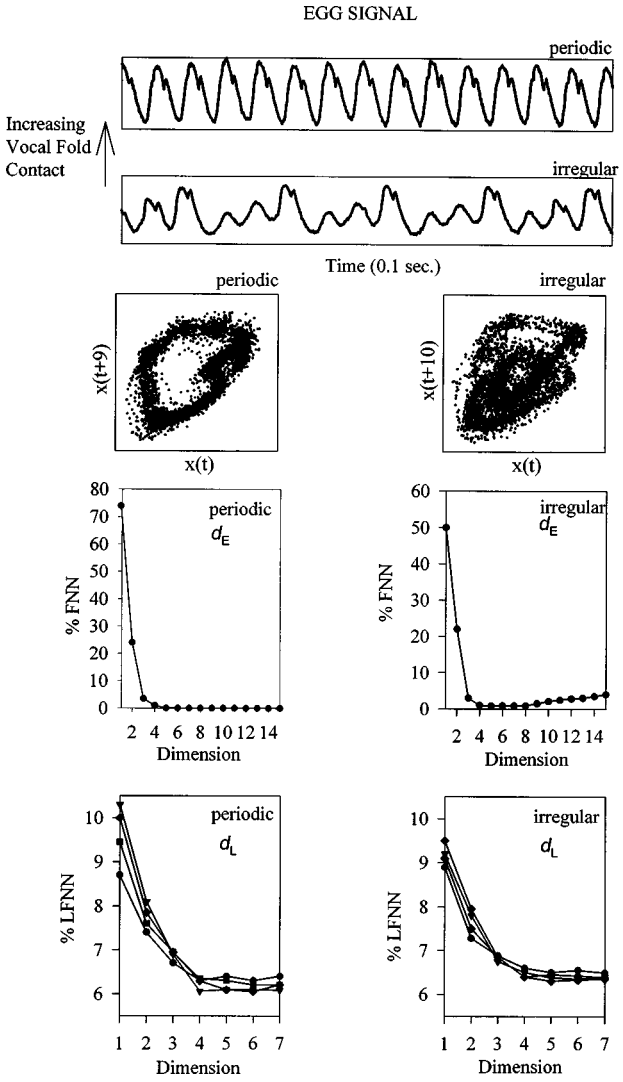

FIG. 4. The ''periodic'' and ''irregular'' segments of the EGG signal, and corresponding state-space plots and global (d_E) and local (d_L) false nearest neighbors, from dysphonic subject P6. Legend for d_L plots: circle: $N_B=40$; square: $N_B=60$; triangle: $N_B=80$; diamond: $N_B=100$.

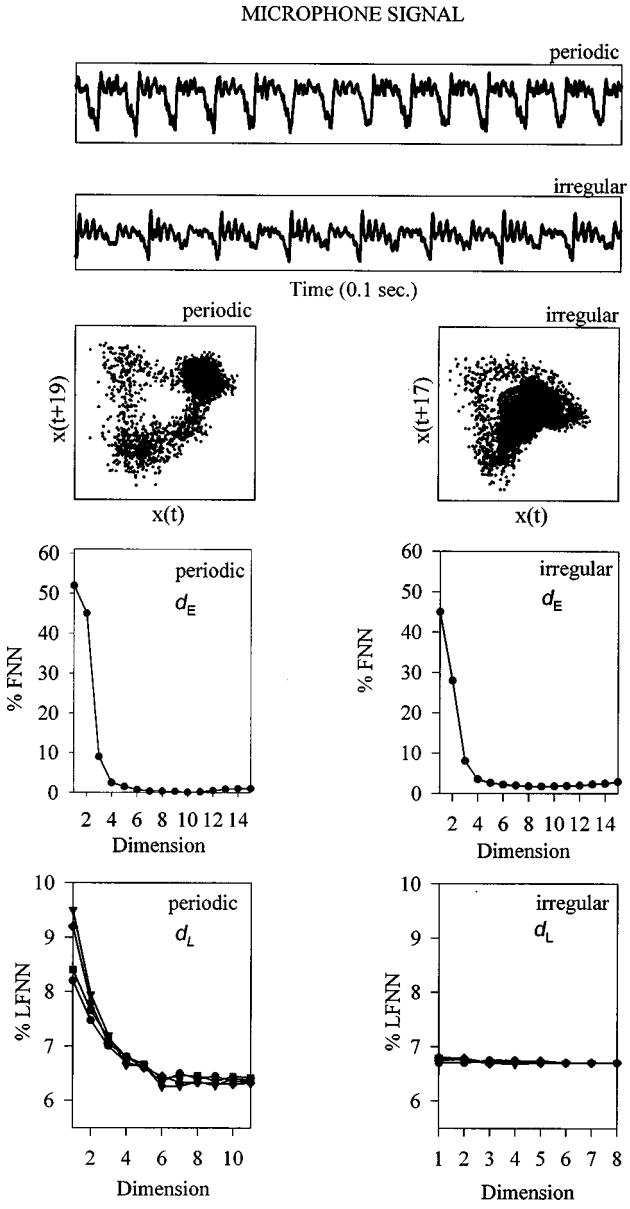

FIG. 5. The ''periodic'' and ''irregular'' segments of the microphone signal, and corresponding state-space plots and global (d_E) and local (d_L) false nearest neighbors, from dysphonic subject P6. Legend for d_L plots: circle: $N_B=40$; square: $N_B=0$; triangle: $N_B=80$; diamond: $N_B=100$.

standpoint the minimum embedding dimension has been obtained. Schreiber (1993) reports a similar criterion above which noise obscures the scaling of the correlation integral. This irregular microphone signal closely approaches that criterion level. From all of the pathologic subjects, the greatest noise level at the optimal global embedding dimension was approximately 2.5% false nearest neighbors, which was found in the ''irregular'' segment of subject P2.

There are clearly four dominant degrees of freedom (d_L) in the periodic segment of the EGG signal (Fig. 4), and six degrees of freedom in the corresponding microphone signal (Fig. 5). The d_L extracted from the irregular portion of the EGG signal similarly suggests a low number of degrees of freedom. However, the turbulent airflow noise in the corresponding microphone signal dominates all embedding dimensions, effectively obscuring the deterministic component (i.e., the vibrating vocal folds), and suggests a random signal.

In examining the data from the seven pathologic subjects, it was found that the apparent ''randomness'' of the signal did not correspond to the effective degrees of freedom. This can be observed in the d_L plots of Fig. 4, and even more dramatically in the data from subject P7 (Fig. 6). Stroboscopically, the vibratory characteristics of the vocal folds of subject P7 were difficult to observe, because the lack of a single, consistent fundamental frequency resulted in a blurring of the image. The vocal folds did appear to completely close, however. Vocal quality was rough and diplophonic. Although the movement of the vocal folds appeared to have a strong random component, the d_E and d_L data suggest that an eight-dimensional coordinate space is sufficient to completely unfold the reconstructed attractor, and that approximately six effective degrees of freedom determine the movement of the trajectories on the attractor. The corresponding microphone signal also suggests a low-noise, deterministic

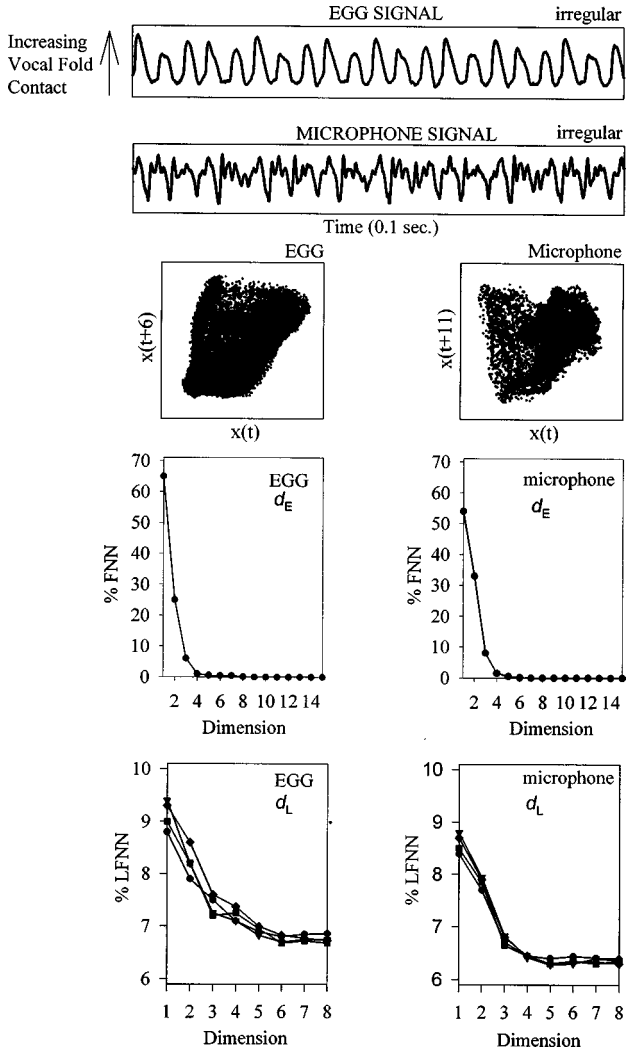

FIG. 6. The ''irregular'' segment of the EGG and microphone signals and corresponding state-space plots from a dysphonic subject (P7). The global (d_E) and local (d_L) false nearest neighbors, suggest low-dimensional dynamics. Legend for d_L plots: circle: $N_B=40$; square: $N_B=60$; triangle: $N_B=80$; diamond: $N_B=100$.

system with five essential degrees of freedom that can be embedded in a six-dimensional state space.

Based on these results, and similarly from all of the other subjects, the following statements can be made regarding the comparison between the EGG and microphone signals. Irrespective of degree of actual glottal closure or periodicity of the oscillation, when there was sufficient change in relative vocal fold contact to yield an embeddable EGG signal with less than approximately 2% noise (as indicated by the d_E), then a low number of dominant degrees of freedom (d_L) were demonstrated. However, when vocal quality contained a moderate amount of breathiness, the microphone signal was typically not embeddable and low-dimensional dynamics were not evidenced.

Oftentimes, abnormal voice production is characterized by period doubling and the presence of subharmonic structure, rather than by random behavior or noise. The waveform segments from pathologic subject P1 (Fig. 7) show rather dramatic bifurcations from periodic (period-2) to period-4 and then period-6 oscillation. Vocal quality changed from normal and unremarkable to diplophonic, and then bifurcated again to diplophonic with associated roughness. All d_E data suggest a lack of noise in the signals. Interestingly, the periodic portion of both the EGG and microphone signals require a higher-dimensional coordinate space (d_E) to unfold the attractor than do the abnormal segments. It would be tempting to infer that this suggests an instability which predicts the bifurcation to period-4 and period-6 oscillation. There is simply insufficient data to support that hypothesis. The d_L values, in turn, suggest low-dimensional determinism. Although the d_L values increased by one degree of freedom with period doubling in this case (subject P1), in another example of period doubling (subject P3) such an increase was not demonstrated.

III. CONCLUSIONS

There are three important conclusions to be drawn from these data. First, evidence has been provided to support the theory of low-dimensional dynamics in healthy and abnormal voice production, using the measures of global and local false nearest neighbors. The multidimensional array of coupled oscillators that comprise the healthy voice production system are expressed in the microphone and EGG signals during sustained /a/ by a low number of dominant degrees of freedom. The dynamics of the pathologic system during a sustained /a/ task can sometimes, but not always, also be represented in the microphone and EGG signals as low dimensional. These abnormal signals do not necessarily require a larger coordinate space for unfolding their complex geometry, nor are they necessarily described by a greater number of dominant degrees of freedom than signals from healthy systems. The second conclusion to be drawn from these data is that there is no evidence that the values of global and local false nearest neighbors obtained from one segment of abnormal phonation differ consistently from those values obtained from another segment across a point of bifurcation, or from healthy phonation. And third, in comparing the EGG and microphone signals, the presence of low-dimensional dynamics is no more likely to be expressed in one signal than in the other.

For all pathologic subjects, a clear indication of optimal global embedding dimension was found. In some cases there was a persistent noise floor, but in all of these instances the d_E values from the microphone and EGG signals still suggested an optimal embedding dimension which would retain the deterministic component of the signals with the least amount of noise. For all cases in which no local embedding dimension could be found for the microphone or EGG signals, the corresponding voice was highly breathy, and stroboscopy revealed incomplete glottal closure. Even in those cases where vocal fold vibratory behavior was highly irregular, if glottal closure was achieved, then the d_L values identified low-dimensional dynamics.

One could conclude that the movement of the vocal fold masses, even at their most irregular, represent low-dimensional dynamics, and that it is the complex aerodynamics generated from incompletely adducted vocal folds that are high-dimensional or stochastic. Herzel (1996) commented that a nonlinear dynamics' framework can be applied

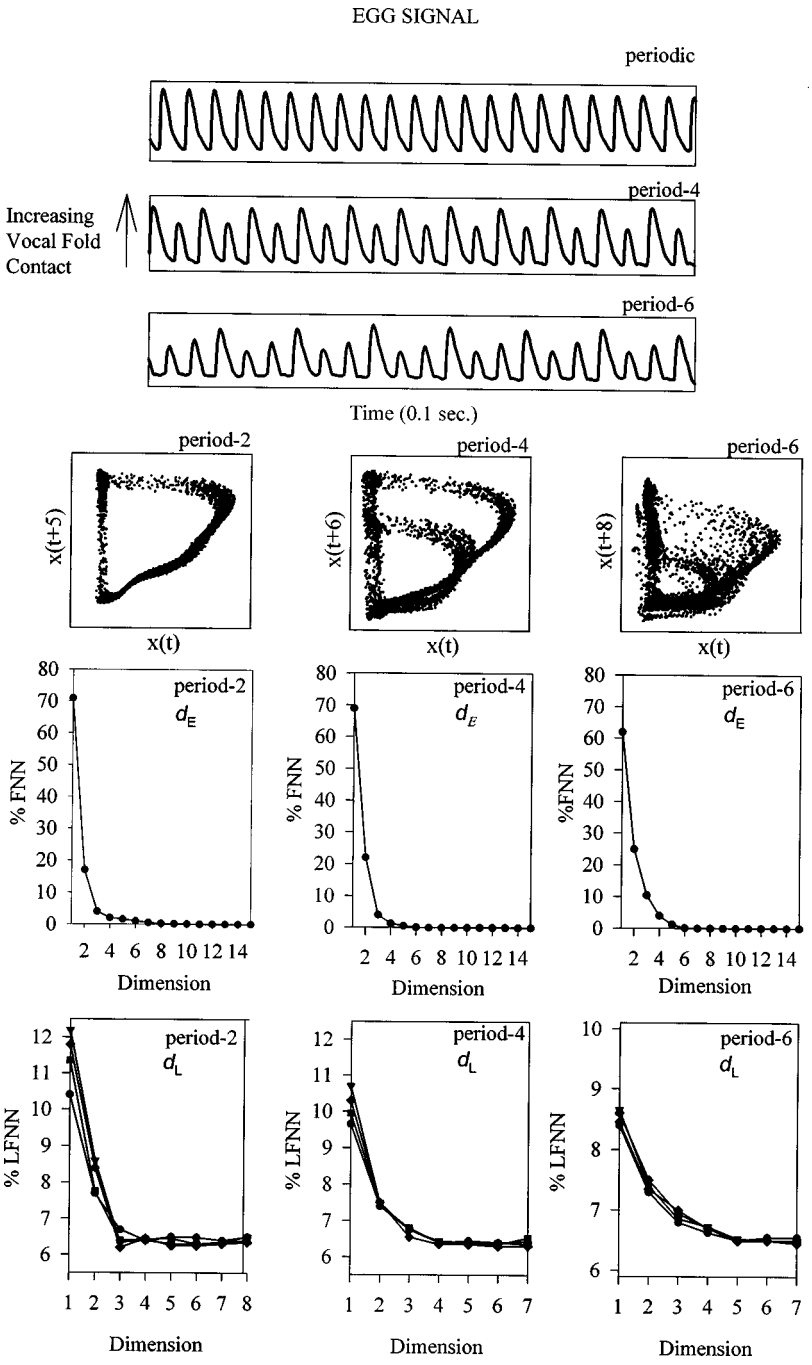

FIG. 7. The ''periodic'' and ''period-4'' and ''period-6'' segments of the EGG signal, and corresponding state-space plots, and global (d_E) and local (l_E) false nearest neighbors from dysphonic subject P1. Legend for d_L plots: circle: $N_B=40$; square: $N_B=60$; triangle: $N_B=80$; diamond: $N_B=100$.

to the analysis of rough voices (irregular vocal fold vibration), but not breathy voices (incomplete airway closure). This conclusion is only partially supported by the d_E and d_L values from the signals elicited from the pathologic subjects. Other data which provide additional conflicting evidence are presented by Narayanan and Alwan (1995). Using the correlation integral estimated from the microphone signal, they found evidence of low-dimensional chaotic dynamics in 44% of all unvoiced fricative productions studied, and in 59% of all voiced fricatives sampled. These data need to be interpreted cautiously, however, because the scaling regions were quite small in many instances. Dynamical analyses of the chaotic and turbulent states of fluid systems in general is challenging, and data suggest a certain level of determinism (Cheng, 1987; Khurana, 1988; Levy, 1987). Brandstater and Swinney (1987), for example, found a correlation dimension of four in a weakly turbulent Couette–Taylor flow at a Reynolds number 50% above the onset of turbulence. It is possible that the complex airflow of the breathy voice is not high dimensional but rather, the breathy voice generates a high-dimensional acoustic signal. In other words, the determinism of the aerodynamics is poorly coupled to, or weakly expressed in, the microphone signal. The EGG signal is already acknowledged to provide no information about aerodynamics (Baken, 1992). Perhaps measures which more directly assess aerodynamics would be revealing. Although no definitive conclusions regarding vocal tract aerodynamics can be made, there appears to be sufficient conflicting evidence to warrant further investigation.

The d_L results provide an interesting comparison to the

data from Berry *et al.* (1994), who found that the first two empirical orthogonal eigenfunctions extracted from the vocal output of a biomechanical model simulating a healthy vocal fold system accounted for approximately 97.7% of the variance in regenerating the nodal trajectories. The third eigenfunction accounted for an additional 1.5% of the variance. This compares favorably with the three degrees of freedom expressed in the signals from the healthy subjects. When the model parameters were changed to simulate a lax cover, the output bifurcated to irregular phonation, and then to period-4 oscillations. For the irregular output, the authors found that six spatio-temporal eigenfunctions accounted for 95% of the variance. For the period-4 oscillations, four eigenfunctions accounted for 98% of the variance. Again, this compares favorably with the increase in degrees of freedom found for many of the abnormal signals. Differences in actual degrees of freedom are attributable to a number of factors, not the least of which is the fact that the computational model only simulates actual laryngeal dynamics. In addition, only the Reinke's edema of subject P2 likely increased the laxity of the mucosal cover of the vocal folds. For most of the other subjects, the pathology most likely increased the stiffness of the cover. This may alter the expression of the dominant modes of vibration.

It is certainly reasonable to hypothesize that the nature of the laryngeal pathology could alter the modes of vocal fold vibration in predictable ways. The dimensionality of unilateral paralysis, for example, may be different from that of antero-posterior desynchronization, as hypothesized by Berry *et al.* (1994), Herzel (1996), and Steinecke and Herzel (1995). The subject pool was simply too small to even begin to address this type of categorization. It is doubtful at this point, though, that given a low-dimensional pathologic system, the number of degrees of freedom would have any diagnostic value regarding actual vibratory behavior of the vocal folds. The d_L does not define tissue movement trajectories. One could always hope that the dominant degrees of freedom in the ''periodic'' portion of a signal from an abnormal larynx are different in number from the periodic signal of a healthy larynx; that this could somehow presage a bifurcation to aberrant oscillation. Unfortunately, the data did not reveal anything so dramatic.

The results show that the d_E provides an indication of the relative amounts of low- and high-dimensional processes in a signal. Whether those high-dimensional dynamics are properly described as chaotic or stochastic cannot be known within the limitations of current analyses. But that difference is not important for any practical purposes. In this group of abnormal waveforms preselected for good signal-to-noise levels, neither the EGG nor the microphone signal provided a superior measure of determinism. In those cases in which the microphone signal was contaminated by airflow noise, the corresponding EGG signal was contaminated by measurement noise. Unfortunately, even with appropriate signal conditioning, it can be quite difficult to acquire impedance changes due solely to vocal fold movement and not those due to other conditions, such as mucous movement or vertical laryngeal movement. In the presence of a large glottal gap, detecting vibratory movement with the EGG is often impossible. In general, however, the d_E values suggest that overembedding of voice data from healthy individuals should not corrupt results because of a lack of residual noise in the higher embeddings. For pathologic systems, however, the careful selection of embedding dimension can be critical. The fact that, for some signals, noise increased with higher embeddings, suggests that overembedding could seriously affect calculations.

Further research in dimensional analysis might include larger subject groups, greater homogeneity of pathology, and other types of measures, especially aerodynamic, as previously suggested. The selection criteria for the abnormal data presented here was that a minimum of 0.5 s of each segment of phonation had to be sustained. This means that the only types of dynamical behavior assessed were those modes of phonation for which self-sustained oscillation could be supported. It would be interesting to know whether vibratory behavior which cannot be sustained as long, or which repeatedly bifurcates, is characterized by a different level of dimensionality.

ACKNOWLEDGMENTS

The assistance of Dr. Henry D. I. Abarbanel is gratefully acknowledged. The commentaries of Dr. Anders Löfqvist and three anonymous reviewers are also appreciated. Portions of this paper were presented at the First International Vocal Physiology and Biomechanics Conference in Evanston, Illinois in May 1997.

Abarbanel, H. D. I. (**1996**). *Analysis of Observed Chaotic Data* (Springer-Verlag, New York), p. 74.

Abarbanel, H. D. I., and Kennel, M. B. (**1993**). ''Local false nearest neighbors and dynamical dimensions from observed chaotic data,'' Phys. Rev. E **47**, 3057–3068.

Baken, R. J. (**1990**). ''Irregularity of vocal period and amplitude: A first approach to the fractal analysis of voice,'' J. Voice **4**, 185–197.

Baken, R. J. (**1992**). ''Electroglottography,'' J. Voice **6**, 98–110.

Baker, G. L., and Gollub, J. P. (**1990**). *Chaotic Dynamics: An Introduction* (Cambridge U.P., New York), pp. 111–132.

Behrman, A., and Baken, R. J. (**1997**). ''Correlation dimension of electroglottographic data from healthy and pathologic subjects,'' J. Acoust. Soc. Am. **102**, 2371–2379.

Berry, D. A., Herzel, H., Titze, I. R., and Krischer, K. (**1994**). ''Interpretation of biomechanical simulations of normal and chaotic vocal fold oscillations with empirical eigenfunctions,'' J. Acoust. Soc. Am. **95**, 3595–3604.

Brandstater, A., and Swinney, H. (**1987**). ''Strange attractors in weakly turbulent Couette-Taylor flow,'' Phys. Rev. Lett. **66**, 2207.

Cellucci, C. J., Albano, A. M., Rapp, P. E., Pittenger, R. A., and Josiassen, R. C. (**1997**). ''Detecting noise in a time series,'' Chaos **7**, 414–422.

Cheng, S.-I. (**1987**). ''A deterministic view of sheer turbulence,'' Comput. Methods Appl. Mech. Eng. **64**, 5–19.

Childers, D. G., Alsaka, Y., Hicks, D., and Moore, G. P. (**1987**). ''Vocal fold vibrations: An EGG model,'' in *Laryngeal Function in Phonation and Respiration*, edited by T. Baer, C. Sasaki, and K. Harris (College-Hill, Boston), pp. 181–202.

Eckmann, J. P., and Ruelle, D. (**1985**). ''Ergodic theory of chaos and strange attractors,'' Rev. Mod. Phys. **57**, 617–656.

Fletcher, N. H. (**1996**). ''Nonlinearity, complexity, and control in vocal systems,'' in *Vocal Fold Physiology: Controlling Complexity and Chaos*, edited by P. J. David and N. H. Fletcher (Singular, San Diego, CA), pp. 3–16.

Fourcin, A. J. (**1981**). ''Laryngographic assessment of phonatory function,'' in *Proceedings of the Conference on the Assessment of Vocal Pathology. ASHA Reports No. 11*, edited by C. Ludlow and M. Hart (American Speech-Language-Hearing Assoc., Rockville, MD), pp. 116–127.

Fraser, A. M., and Swinney, H. L. (**1986**). ''Independent coordinates for strange attractors from mutual information,'' Phys. Rev. A **33**, 1134–1146.
Frison, T. W., Abarbanel, H. D. I., Cembrola, J., and Neales, B. (**1996**). ''Chaos in ocean ambient ''noise'','' J. Acoust. Soc. Am. **99**, 1527–1539.
Gao, J., and Zheng, Z. (**1993**). ''Local exponential divergence plot and optimal embedding of a chaotic time series,'' Phys. Lett. A **181**, 153–158.
Glass, L., and Kaplan, D. (**1993**). ''Complex dynamics in physiology and medicine,'' in *Time Series Prediction: Forecasting the Future and Understanding the Past*, edited by A. S. Weigend and N. A. Gershenfeld (Addison-Wesley, Reading, MA), pp. 513–527.
Grassberger, P., and Procaccia, I. (**1983**). ''Measuring the strangeness of a strange attractor,'' Physica D **9**, 189–208.
Herzel, H. (**1993**). ''Bifurcations and chaos in voice signals,'' Appl. Mater. Res. **46**, 399–413.
Herzel, H. (**1996**). ''Possible mechanisms of vocal instabilities,'' in *Vocal Fold Physiology: Controlling Complexity and Chaos*, edited by P. J. David and N. H. Fletcher (Singular, San Diego, CA), pp. 63–75.
Herzel, H., Berry, D., Titze, I. R., and Saleh, M. (**1994**). ''Analysis of vocal disorders with methods from nonlinear dynamics,'' J. Speech Hear. Disorders **37**, 1008–1019.
Hertrich, I., Lutzenberger, W., Spieker, S., and Ackermann, H. (**1997**). ''Fractal dimension of sustained vowel productions in neurological dysphonias: An acoustic and electroglottographic analysis,'' J. Acoust. Soc. Am. **102**, 652–654.
Kantz, H., and Olbrich, E. (**1997**). ''Scalar observations from a class of high-dimensional chaotic systems: Limitations of the time delay embedding,'' Chaos **7**, 423–429.
Kantz, H., and Schreiber, T. (**1995**). ''Dimension estimates and physiological data,'' Chaos **5**, 143–154.
Kennel, M. B., Brown, R., and Abarbanel, H. D. I. (**1992**). ''Determining embedding dimension for phase-space reconstruction using a geometrical construction,'' Phys. Rev. A **45**, 3403–3411.
Kumar, A., and Mullick, S. K. (**1996**). ''Nonlinear dynamical analysis of speech,'' J. Acoust. Soc. Am. **100**, 615–629.
Khurana, A. (**1988**). ''Rayleigh-Bénard experiment probes transition from chaos to turbulence,'' Phys. Today **41**(6), 17–21.
Levy, B. G. (**1986**). ''New global fractal formalism describes paths to turbulence,'' Phys. Today **39**(4), 17–18.
Lorenz, E. N. (**1963**). ''Deterministic nonperiodic flow,'' J. Atmos. Sci. **20**, 130–141.
Narayanan, S. S., and Alwan, A. (**1995**). ''A nonlinear dynamical systems analysis of fricative consonants,'' J. Acoust. Soc. Am. **97**, 2511–2524.
Orlikoff, R. F., and Baken, R. J. (**1989**). ''The effect of the heartbeat on vocal fundamental frequency perturbation,'' J. Speech Hear. Res. **32**, 576–582.
Paydarfar, D., and Buerkel, D. M. (**1995**). Dysrhythmias of the respiratory oscillator,'' Chaos **5**, 18–29.
Peng, C.-K., Havlin, S., Stanley, H. E., and Goldberger, A. L. (**1995**). ''Quantification of scaling exponents and crossover phenomena in nonstationary heartbeat time series,'' Chaos **5**, 82–87.
Porter, R. J., Hogue, D. M., and Tobey, E. A. (**1995**). ''Dynamic analysis of speech and nonspeech respiration,'' in *Producing Speech: Contemporary Issues*, edited by F. Bell-Berti and L. J. Raphael (American Institute of Physics, New York), pp. 169–185.
Schreiber, T. (**1993**). ''Determination of the noise level of chaotic time series,'' Phys. Rev. E **48**, R13–R16.
Steinecke, I., and Herzel, H. (**1995**). ''Bifurcations in an asymmetric vocal-fold model,'' J. Acoust. Soc. Am. **97**, 1874–1884.
Takens, F. (**1981**). ''Detecting strange attractors in turbulence,'' in *Lecture Notes in Mathematics*, Vol. 898, edited by D. Rand and L. Young (Springer-Verlag, Berlin), p. 366.
Titze, I. R. (**1995**). *Workshop on Acoustic Voice Analysis: Summary Statement* (National Center for Voice and Speech, Iowa City, IA), p. 5.
Titze, I. R. (**1994**). *Principles of Voice Production* (Prentice-Hall, Englewood Cliffs, NJ), pp. 97–100.
Titze, I. R., Baken, R. J., and Herzel, H. (**1993**). ''Evidence of chaos in vocal fold vibration,'' in *Vocal Fold Physiology: New Frontiers in Basic Science*, edited by I. R. Titze (Singular, San Diego), pp. 143–188.
Titze, I. R. (**1976**). ''On the mechanics of vocal-fold vibration,'' J. Acoust. Soc. Am. **60**, 1366–1380.

Fluid flow in a dynamic mechanical model of the vocal folds and tract. I. Measurements and theory

Anna Barney
Faculty of Engineering and Applied Science, University of Southampton, Highfield, Southampton SO17 1BJ, United Kingdom

Christine H. Shadle
Department of Electronics and Computer Science, University of Southampton, Highfield, Southampton SO17 1BJ, United Kingdom

P. O. A. L. Davies
Institute of Sound and Vibration Research, University of Southampton, Highfield, Southampton SO17 1BJ, United Kingdom

(Received 6 December 1997; accepted for publication 24 September 1998)

In this study, aerodynamic and acoustic measurements were obtained in a dynamic mechanical model of the larynx and vocal tract. The model consisted of a uniform duct, intersected by a pair of sinusoidally oscillating shutters. A controlled airflow along the duct was periodically disturbed by the action of the shutters and pressure, and flow velocity measurements were obtained in the region downstream. The velocity field in the duct could be decomposed into three distinct components: a mean flow, a fluctuating acoustic particle velocity, and a fluctuating nonacoustic velocity associated with the transport of vortices along the duct at the local mean flow velocity. Two theoretical models for sound radiation from the duct exit were investigated. The first was based on the in-duct acoustic field alone and was unable to provide a realistic prediction of the measured, radiated sound field except at the first formant of the duct. In the second a simple description of sound generation due to the interaction of vortices with the duct exit was added. In this case much closer prediction of the measured values was achieved, leading to the conclusion that the interaction of the nonacoustic velocity fluctuation with the duct boundaries results in a significant additional source of acoustic energy located in the region of the duct exit.
[S0001-4966(99)00401-4]

PACS numbers: 43.70.Aj, 43.70.Bk, 43.28.Ra [AL]

INTRODUCTION

Realistic models of the aerodynamic and acoustic events occurring in and around the larynx during the production of vowel sounds are an important prerequisite for natural sounding articulatory speech synthesis. Furthermore, understanding how changes in these events affect the radiated speech signal may allow diagnosis of speech pathologies without recourse to intrusive and potentially dangerous surgical procedures.

Generally, current models of voiced speech production are developed from the basis of the Acoustic Theory of Speech Production (Fant, 1960). This is a one-dimensional plane-wave acoustic model which proposes that the fluctuating volume velocity at the glottal exit constitutes an acoustic source, and that the vocal tract acts as a passive acoustic filter such that the output speech wave is a convolution of the source waveform and the filter response. All acoustic excitation is assumed to occur at the glottal exit and only fluctuating velocity associated with the acoustic disturbance is considered in the model.

To obtain information regarding physiologically realistic values for fluid velocity and pressure within the glottis and around its inlet and outlet, static modeling studies have frequently been used (e.g., Scherer *et al.*, 1983, 1990; Binh and Gauffin, 1983). However, such models can give little information about the location and nature of the acoustic sources present in the tract, or about unsteady fluid motion.

Latterly, Teager and Teager (1983, 1990) and Kaiser (1983) have called for the rejection of the linear one-dimensional model in its entirety, prompted by apparent anomalies observed in fluid velocity measurements which Teager and Teager obtained in the mouth during the phonation of sustained vowels. These anomalies led them to believe that the fluid motion they were measuring was not solely associated with an irrotational, plane-wave, acoustic particle velocity. They suggested that the separation of the flow from the tract walls, leading to the presence of vortices, could result in additional acoustic sources throughout the vocal tract.

McGowan (1988) and Hirschberg (1992), perhaps prompted by the questions raised by Teager and Teager, have made theoretical studies of the fluid motion in the vocal tract using an aeroacoustic analysis. They suggest that the fluid motion in the vocal tract may, in part, be associated with a nonacoustic velocity component due to the generation of vortices at the glottal exit. Although such a nonacoustic velocity field will not, itself, radiate sound, it may result in additional acoustic sources in the vocal tract due to interaction with the tract boundaries at area discontinuities.

Two-dimensional theoretical models of the fluid motion

at the glottal exit (e.g., Liljencrants, 1989; Thomas, 1986; Hergel and Höge, 1991) suggest that the flow in this region consists of an unsteady jet due to the glottal efflux each cycle, together with its associated shear layer. Thus a mechanism for the production of ordered vortical structures in the flow downstream of the glottal exit is predicted by these computational models.

Calibrated *in vivo* measurements of the time-varying supra- and sub-glottal pressure within the vocal tract close to the larynx were obtained by Cranen and Boves (1985). However, to obtain corresponding fluid velocity measurements seems both hazardous and impracticable, especially when it is noted that a single measurement per plane, as used for the pressure, is unlikely to be representative of the complicated three-dimensional flow pattern expected in this region.

Experiments using excised canine larynges (e.g., Alipour *et al.*, 1996) show some promise for flow measurements, but the complexity of the geometry provides perhaps too much richness of detail for the underlying mechanisms to be easily identified.

Dynamic mechanical models with, initially, simplified geometries offer the opportunity to investigate unsteady fluid motions while maintaining controllability and repeatability of experimental conditions. Shadle *et al.* (1991) report flow visualization experiments in a model with a single oscillating shutter representing the vocal fold motion and a square duct representing the vocal tract. They observed the development of a jet at the shutter exit for each cycle of the oscillation. Kiritani *et al.* (1987) investigated the flow through a driven slit in a rubber sheet using hot wires, noting that the flow close to the slit was confined to a region with roughly the same area as the slit, but that further downstream the region of fluid disturbance had expanded. More recently, Mongeau *et al.* (1997) used a driven, rubber model with a symmetrical oscillation to investigate the validity of the quasi-static assumption.

In this study a Dynamic Mechanical Model (DMM) has been designed to study the acoustic and aerodynamic effects of periodically interrupting a steady airflow (Barney, 1995). The DMM has similar dimensions to the human male vocal tract. It consists of a cylindrical duct (the vocal tract), open at one end, and supplied with a regulated air flow at the other. The flow is modulated by the motion of a pair of electromechanically driven shutters (the vocal folds). In the first instance the simplest possible representative duct geometry was adopted. In-duct pressure and velocity measurements, together with radiated sound measurements, have been used to investigate the nature of the fluid and acoustic fields within the duct.

The model and its instrumentation are described in Sec. I. In Sec. II the far-field radiated sound spectrum outside the model is presented and in Sec. III the acoustic field within the duct is estimated. It will be shown that the acoustic field within the duct cannot alone provide a realistic estimate for the radiated sound field. Section IV details further study of the in-duct velocity field. It will be deduced from hot wire measurements of the fluid velocity within the duct that in addition to an acoustic field, a nonacoustic flow field is also present, dominated by an ordered train of vortices that convect along the duct at the local mean flow velocity. In Sec. V a simplified model for the scaling of the sound generated by the vortices at the duct exit will be developed. It will be shown that predictions of the radiated sound field that incorporate the contribution of both the acoustic *and* nonacoustic velocity fluctuation provide closest agreement with the measured values.

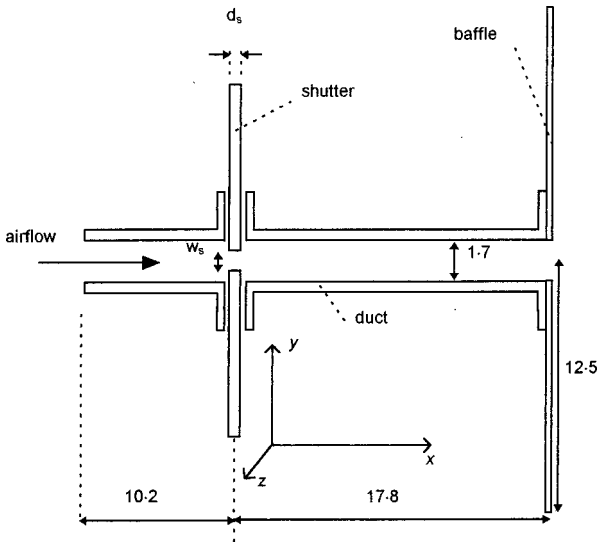

FIG. 1. Plan view of the Dynamic Mechanical Model showing reference axes and dimensions in centimeters (not to scale).

I. THE MODEL

The DMM is shown schematically in Fig. 1. It is made from a clear plastic, cylindrical duct 28 cm in length, with an interior diameter of 1.7 cm. The duct is intersected 17.8 cm from the open end by a pair of shutters. The shutters are made of a rigid plastic and can slide across the duct such that they meet each other, dividing the duct into two separate sections. The rectangular channel between the shutters has a length l_s of 1.7 cm, a depth d_s of 0.3 cm and a width w_s that is variable according to the degree of opening. At the open end, the duct terminates in a plane circular baffle 12.5 cm in radius.

Instrumentation can be inserted into the duct at any point, both upstream and downstream of the shutters, via a slot of width 0.5 cm extending the entire length of the duct. The slot can be sealed, with modelling clay, along its length and round the measuring instruments to prevent air leakage. The entire duct can be rotated about its axis, allowing the position of the slot relative to the shutters to be varied. This allows measurements to be obtained at any point in the duct.

Each shutter of the DMM is driven by a Ling Dynamic Systems LD202 vibration generator. The seal between the perspex block and the shutters is not airtight. The amount of air leakage around the shutters can be gauged from the reduction of mean flow velocity downstream of the shutters compared to upstream. For all flow rates used, the reduction was found to be of the order of 10%. The effect of this leakage on the pressure and velocity measurements made in the duct is discussed in the companion paper (Shadle *et al.*, 1999).

The amplitude and driver waveform of each shutter may be individually controlled. However, for the measurements reported here, each vibration generator was driven by an identical sinusoidal waveform with a frequency of 80 Hz.

The shutter position during vibration was monitored by a B&K 4367 accelerometer attached to each shutter. The maximum channel width w_s for all measurements was 2 mm.

Initially, the shutters were constructed of the same hard plastic material throughout. It was found that setting the shutters so as to obtain complete closure across the duct resulted in their meeting with such force that they bounced apart. This was expected to be reflected in the measured pressure and velocity signals and was thus undesirable. A closed-cell foam strip 1 mm thick was attached to the edge of each shutter allowing closure to occur without bounce. As a result, closure was not instantaneous but could be estimated from the pressure measurements (see Sec. III) to last approximately 1/5 of a shutter cycle (2.5 ms).

Air passed along the duct in the direction shown in Fig. 1. The air was supplied by a compressor remote from the model and could be controlled locally by a pressure regulating valve. The air passed from the valve, via a plastic tube, to a Platon rotameter with a range of 33–416 $\mathrm{cm^3\,s^{-1}}$ and a measurement error of $\pm 8\ \mathrm{cm^3\,s^{-1}}$. A valve at the rotameter allowed fine tuning of the flow rate passing through the model. Pressure at the upstream side of the shutters was not directly controlled, but was allowed to develop as a result of the chosen flow rate. The air passed from the rotameter through a flexible hose to the entrance of the duct.

At the entrance to the duct, the air passed through a gently diverging nozzle to allow expansion of the flow without separation from the duct walls. Three volume flow rates were used: 200, 300, and 400 $\mathrm{cm^3\,s^{-1}}$. Note that where volume flow rate is quoted in this paper, the value given is that measured at the rotameter and takes no account of leakage around the shutters. The volume flow rate is used only as a parameter to distinguish the three flow speeds investigated.

All transducer signals were stored on a 386 PC and were acquired via a four-channel ADC with 12 bits per sample and a voltage range of ± 1 V. The sampling error was equivalent to ± 0.5 mV. Acquisition was controlled by Hvlab software which had a simultaneous sample-and-hold method for A-to-D conversion. A sampling frequency of 5015 Hz was used unless otherwise indicated. Hvlab includes software controlled anti-aliasing filters which were used for signal conditioning prior to sampling. The in-duct pressure analysis method described in Sec. III placed a limitation on the bandwidth of the measurements. In accordance with this limitation, the cutoff frequency of the anti-aliasing filters was set to 1 kHz for all measurements except where indicated. The sampling time for each data set was of the order of 10 s.

II. RADIATED SOUND MEASUREMENTS

A. Method

The sound radiated from the open end of the duct of the DMM was measured using a B&K 4134 $\frac{1}{2}$-in. condenser microphone connected to a B&K 4230 amplifier, and placed level with the duct exit at a distance $r = 60$ cm from the duct exit plane such that a line connecting the duct exit plane to the microphone position made an angle of 45° to the long axis of the duct. Measurements were made in a semi-anechoic room with a background noise level, measured using a B&K 2203 sound level meter, of less than 10 dB SPL (*re:* 20 μPa).

In addition to the aeroacoustically generated sound, the DMM made large amounts of mechanically generated noise due to the shutter driver mechanism. In order to minimize the contribution of the mechanical acoustic sources to the measured radiated sound, two strategies were adopted. The DMM was placed in a separate room from the microphone. A hole the size of the duct was drilled in the wall between the rooms and the DMM was placed so that the duct passed through the hole with the duct exit lying flush with the wall of the measurement room. The circular baffle was removed and the wall, which was sealed round the duct, acted as an ''infinite'' baffle at the duct termination. All measurements in this paper, with the exception of one set of hot wire measurements (see Fig. 5), were obtained using the ''infinite'' baffle. The isolation of the mechanical parts of the DMM from the measurement room reduced the mechanically generated contribution to the radiated sound to a large degree, but it was found that some mechanically generated sound traveled down the duct. An estimate of this small contribution was obtained by measuring the sound radiated from the duct exit with no air flow through the model. For all with-flow measurements of radiated sound, the time domain estimate of zero-flow radiated noise was subtracted from the measured radiated sound. The shutter accelerometer trace was used to determine the appropriate relative phase for the signals prior to subtraction. A more detailed description of the analysis and implementation of the noise reduction procedure may be found in Barney (1995). With the contributions to the radiated spectrum due to mechanical noise sources minimized, the resulting spectral level for each harmonic of the shutter frequency is considered to be primarily that associated with the aeroacoustic sound generation in the duct.

The far-field microphone measurements (see Figs. 2, 4, and 8) are spectral envelopes in dB *re:* 20 μPa plotted against nondimensional shutter frequency f/f_0, where f is the frequency of the harmonic and f_0 is the fundamental shutter frequency. All spectral envelopes were calculated from an average of 13 4096-point power spectra with an overlap between time windows of 15%. The data were Hanning-windowed prior to the DFT.

B. Results

Figure 2 shows far-field sound pressures for all three volume flow rates. All spectral components were at least 20 dB above the background noise level except for the 7th harmonic where the SPL was at least 9 dB above the background noise. It is clear that, with the exception of the 7th, 8th, 9th, and 12th harmonics, the SPL increases with increasing volume flow rate U. The highest level for each volume flow rate occurs at the first harmonic and decreases until the 5th harmonic, where there is evidence of a resonance peak. A second, higher amplitude resonance spanning the 9th, 10th,

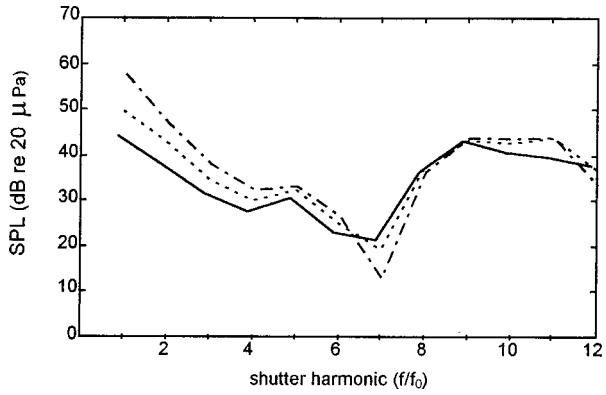

FIG. 2. Spectral envelope for the radiated sound pressure measured at 60 cm from the duct exit at an angle of 45° to the long axis of the duct for shutter frequency 80 Hz and three mean flow rates: $U=200\ \mathrm{cm^3\,s^{-1}}$ (solid), 300 $\mathrm{cm^3\,s^{-1}}$ (dotted), 400 $\mathrm{cm^3\,s^{-1}}$ (dash-dot).

and 11th harmonics can be observed for all volume flow rates. A minimum occurs at the 7th harmonic, which becomes lower as the volume flow rate increases.

It is of interest to investigate the velocity and pressure fields within the duct and to determine their relationship to the radiated sound spectrum.

III. THE ACOUSTIC FIELD WITHIN THE DUCT

A. Theory

The transport of acoustic energy within the duct is modeled according to the theory described by Davies (1988, 1992). The theory is a linear, plane-wave model of acoustic wave motion within a duct with a mean flow, v, of Mach number $M=v/c$, where c is the speed of sound.

A plane-wave acoustic theory is valid within the duct for waves with wave number k such that the Helmholtz number ka is less than $1.84(1-M^2)^{0.5}$ (where a is the radius of the duct). For ka greater than this value the first circumferential mode will propagate. For the duct of the DMM the Mach number M is of the order of 10^{-3} and a is 8.5 mm leading to a cut-on frequency for the first circumferential mode of around 12 kHz, which is well above the frequency range of this study.

For a uniform duct of finite length, terminating in an open end, the fluctuating pressure at any point in the duct will be a superposition of two waves, one, an incident wave, traveling outward from an acoustic source, and the other a wave reflected from the open end. Thus the time varying pressure $p(x,t)$ and acoustic particle velocity $u_a(x,t)$ at any distance x along the duct axis for each propagating mode, will be given by

$$p(x,t)=p^+(x,t)+p^-(x,t), \tag{1a}$$

$$u_a(x,t)=u_a^+(x,t)+u_a^-(x,t), \tag{1b}$$

where the superscript ''+'' identifies a wave traveling in the positive x direction and the superscript ''−'' identifies a wave traveling in the negative x direction.

In the presence of mean flow, for each spectral component of a periodic disturbance

$$p^+(x,t)=p_x^+=p_0^+e^{j(\omega t-k^+x)}, \tag{2a}$$

$$u_a^+(x,t)=u_{ax}^+=u_{a0}^+e^{j(\omega t-k^+x)}, \tag{2b}$$

$$p^-(x,t)=p_x^-=p_0^-e^{j(\omega t+k^-x)}, \tag{2c}$$

$$u_a^-(x,t)=u_{ax}^-=u_{a0}^-e^{j(\omega t+k^-x)}, \tag{2d}$$

where p_0^+ and p_0^- are the component pressure wave amplitudes at the $x=0$ plane, u_{a0}^+ and u_{a0}^- are the component particle velocity wave amplitudes at the $x=0$ plane, and $k^+=\omega/(c_0+v)$ and $k^-=\omega/(c_0-v)$ are the wave numbers for the positive- and negative-going wave components in the presence of mean flow v.

From Euler's equation and Newton's second law it may be shown (Davies, 1988) that the acoustic particle velocity u_{ax} and pressure p_x are described by

$$\rho_0c_0u_{ax}=p_x^+-p_x^-, \tag{3a}$$

$$p_x=p_x^++p_x^-, \tag{3b}$$

where ρ_0 is the ambient fluid density and c_0 is the local sound speed of the fluid.

Given two pressure time histories $p_{x1}(t)$ and $p_{x2}(t)$ at the duct wall at positions x_1 and x_2, respectively, then the wave components for each frequency in the spectrum may be written (Davies *et al.*, 1980)

$$p_{x1}=p_0^+e^{-jkx_1}+p_0^-e^{jkx_1}, \tag{4}$$

$$p_{x2}=p_0^+e^{-jkx_2}+p_0^-e^{jkx_2}, \tag{5}$$

forming a set of linear simultaneous equations which can be solved for p_0^+ and p_0^-. Then using Eqs. (2) and (3), the fluctuating pressure and acoustic particle velocity can be estimated for any position within the duct.

B. Method

In the DMM, the pressure within the duct was measured using $\frac{1}{4}$-in. omni-directional electret condenser microphones inserted through the slot in the duct so that they were flush with the duct wall. The microphones have a bandwidth of 20–20 000 Hz with a linear amplitude response for SPLs up to 120 dB (Harrison, 1994). The microphones were calibrated for amplitude and phase in a known acoustic field. Each microphone was connected to one channel of an ISVR four-channel solid state amplifier.

For this acoustic analysis, pressure time histories were obtained at the wall of the duct for two positions, $x=4$ and $x=14$ cm, where the $x=0$ plane corresponds to the downstream face of the shutters and the positive x direction is the direction of mean air flow. In order to carry out the decomposition of the measured pressure into its component pressure amplitudes, it is important that the downstream transducer not be placed overly close to the duct exit, where the pressure is expected to be close to zero. Furthermore, preliminary hot wire measurements (using the system described in Sec. IV) showed that the velocity disturbance within the first three centimeters of the duct downstream of the shutters was extremely complicated and it was deemed best to place the upstream transducer away from this region. Positioning

the microphones at $x=4$ cm and $x=14$ cm gave the largest possible spacing given the above constraints. Harrison (1994) has shown that the low frequency reliability of component pressure amplitude estimates made from pairs of pressure measurements increases as the separation of the transducers is increased. However, the estimates become unrealistic at frequencies where the half-wavelength is of the order of the transducer separation. For a transducer spacing of 10 cm, as used in this study, this gives a band of unreliable estimates for frequencies between 1.5 and 1.9 kHz. With this in mind, a conservative estimate for the useable bandwidth of the pressure measurements was adopted with an upper frequency limit of 1 kHz.

Examination of the spectra of the pressure signals, obtained from a DFT, showed that most of the energy in the spectrum was contained in the harmonics of the shutter frequency. A set of software bandpass filters with center frequency equal to each of the harmonics of the shutter frequency and bandwidth of 20 Hz was designed. The filters were third-order Butterworth filters and a zero-phase distortion filtering algorithm was adopted. The filters were used to break the pressure signal down into its constituent frequency bands.

For each frequency band, Eqs. (4) and (5) were solved to give the component pressure waves for each frequency at the $x=0$ plane. Pressures at other points in the duct were found for each frequency component using Eqs. (2). The total fluctuating pressure prediction at any point is given by the sum of the predictions for each spectral component of the pressure. Similarly the total acoustic particle velocity at any point is given by the sum of the acoustic particle velocity estimates for each spectral component. To minimize the contribution due to mechanically generated noise sources, a similar method to that adopted for the radiated pressure measurements was used. The pressure fluctuation with zero flow was measured at the duct wall for each measurement location and subtracted from the with-flow measurement at the same location.

C. Results

The pressure fluctuation measured at the duct wall for $x=4$ and $x=14$ cm can be seen in Fig. 3(a) for a volume flow rate of 200 $\mathrm{cm}^3\,\mathrm{s}^{-1}$. Here 0° shutter phase is taken as the mid-point of the closed period of the shutters.

The measurements show large, strongly damped pressure oscillations about a depressed mean during shutter closure, followed by smaller, less strongly damped oscillations about a raised mean while the shutter is open. The amplitude of the oscillations at $x=4$ cm is about twice that at $x=14$ cm, which corresponds to the well-established fluctuating pressure distribution in a tube open at one end. For larger volume flow rates the amplitude of the fluctuations is greater, but the overall pattern throughout the shutter cycle shows the same features.

The acoustic particle velocity estimate derived from the pressure measurements is shown in Fig. 3(b) for all three volume flow rates at $x=14$ cm. The amplitude of the fluctuating acoustic particle velocity increases with increasing volume flow rate and is positive during shutter closure, becoming negative as the shutters open and remaining so until they close again.

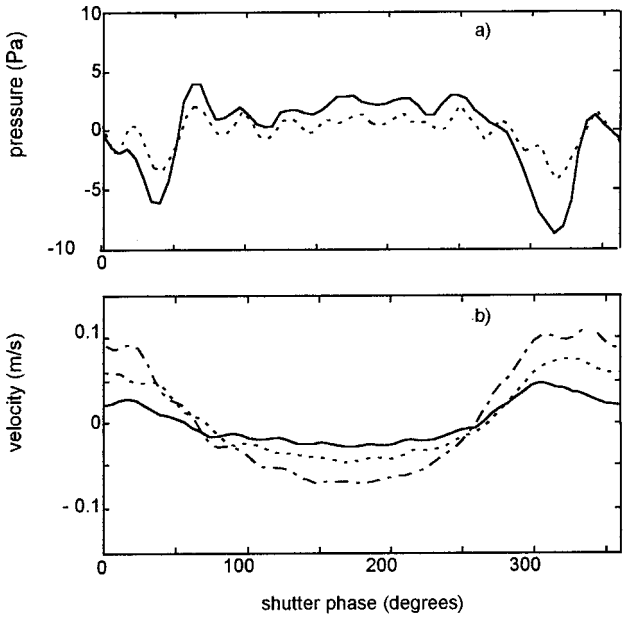

FIG. 3. (a) Average of five shutter cycles of measured in-duct pressure, low-pass filtered at 1 kHz with microphones at $x=4$ cm (solid) and $x=14$ cm (dotted). $U=200\ \mathrm{cm}^3\,\mathrm{s}^{-1}$. (b) Average of five shutter cycles of the acoustic particle velocity estimated as described in Sec. III A at $x=14$ cm for $U=200\ \mathrm{cm}^3\,\mathrm{s}^{-1}$ (solid), $300\ \mathrm{cm}^3\,\mathrm{s}^{-1}$ (dotted), and $400\ \mathrm{cm}^3\,\mathrm{s}^{-1}$ (dash-dot).

The acoustic power, $W(u_a)$, radiated from the open end of the duct due to the acoustic field within, may be predicted for each frequency component by the well known piston-in-a-plane-baffle model (e.g., Kinsler *et al.*, 1982). The acoustic power at the duct exit is related to the mean square pressure $\overline{p_r^2}$ in the hemispherical acoustic far field a distance r from the duct exit by

$$W(u_a)=2\pi r^2\,\frac{\overline{p_r^2}}{\rho_0 c_0}=\rho_0 c_0\overline{\{u_a(17.8,\,t)\}^2}\pi a^2\sigma, \qquad (6)$$

where a is the duct radius, $\sigma=(ka)^2/2$ is the asymptotic value of the radiation efficiency of the duct exit, $ka\to 0$, and $\overline{\{u_a(17.8,t)\}^2}$ is the time-averaged acoustic particle velocity at the duct exit plane, which may be obtained by using the acoustic particle velocity estimates for the $x=0$ plane together with Eqs. (2) to obtain an acoustic particle velocity estimate for $x=17.8$ cm and then taking a time average. For a far-field position not on the duct axis, a directivity factor $2J_1(ka\,\sin\theta)/(ka\,\sin\theta)$ must be included on the right hand side of Eq. (6), where $J_1(ka\,\sin\theta)$ is a Bessel function of the first kind of order 1 for cylindrical coordinates and θ is the angle between the duct axis and the line from the duct exit to the point at which p_r is measured.

Equation (6) was used to make a prediction for each spectral component of the far-field radiated pressure a distance of 60 cm from the duct exit at an angle of 45° to the duct axis. In Fig. 4, this prediction is compared to the mea-

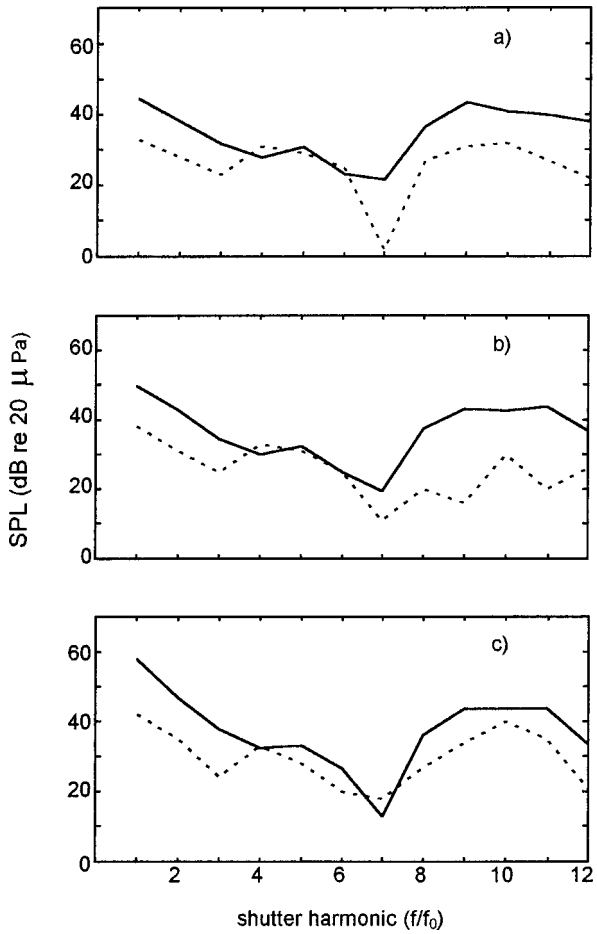

FIG. 4. Radiated far-field sound pressure, measured at 60 cm from the duct exit plane at an angle of 45° to the long axis of the duct; measured (solid) and predicted (dotted) using the acoustic particle velocity estimate at the duct exit plane, for (a) $U=200\ \mathrm{cm^3\,s^{-1}}$, (b) $U=300\ \mathrm{cm^3\,s^{-1}}$, (c) $U=400\ \mathrm{cm^3\,s^{-1}}$.

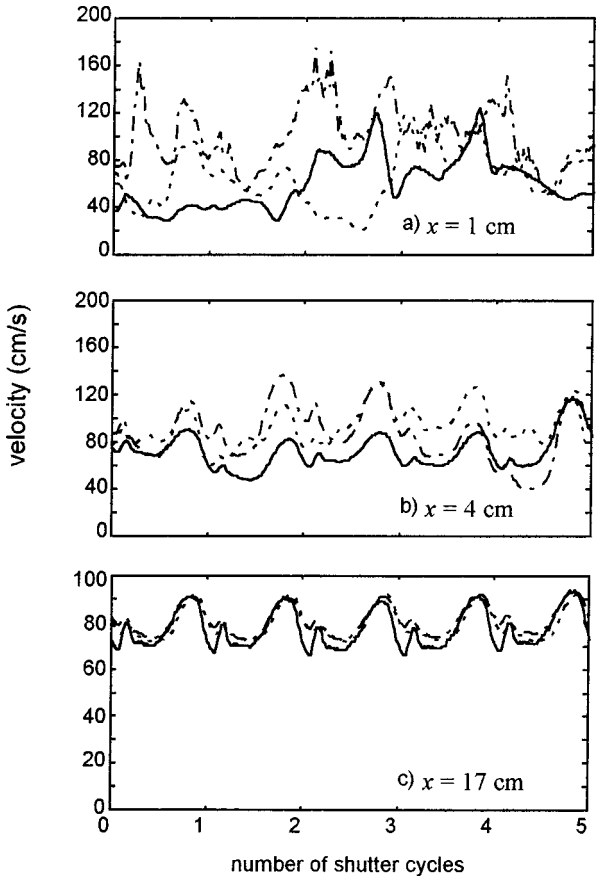

FIG. 5. Fluctuating velocity measured in-duct with a hot wire for $U=200\ \mathrm{cm^3\,s^{-1}}$ at (a) $x=1$ cm, (b) $x=4$ cm, and (c) $x=17$ cm for $y=0$, $z=0$ (solid); $y=0$, $z=0.6$ cm (dotted); $y=0.6$ cm, $z=0$ (dash–dot). For these measurements only, the finite baffle shown in Fig. 1 was used.

sured radiated pressure obtained at the same location for each volume flow rate.

It is clear that while the predicted and measured values are similar for the 4th, 5th, and 6th shutter harmonics, elsewhere the measured signal is underpredicted by at least 10 dB.

The acoustic field within the duct presumably had significant contributions from one or more acoustic source mechanisms (McGowan, 1998) in the region of the shutters. However, a prediction based on this acoustic field alone was unable to account for the far-field measured spectrum. To investigate further, a more detailed picture of the velocity field within the duct of the DMM was required.

IV. HOT WIRE MEASUREMENTS IN THE DUCT

A. Method

The velocity field at a sequence of selected points in the duct was measured using an ISVR constant temperature hot wire anemometer system (Davies and Mason, 1974), which had a measurement bandwidth of approximately 0–17 kHz. The prongs of the hot wire were 0.5 cm apart with an active wire length of 0.2 cm. The hot wire was calibrated in the duct of the DMM in the following way: The wire was located parallel to the y axis at $x=14$, $y=0$, $z=0$ and the shutters were opened to a width of 1 cm. The rotameter was used to supply volume flow rates measured as 0–416 $\mathrm{cm^3\,s^{-1}}$ in steps of 16 $\mathrm{cm^3\,s^{-1}}$. For each volume flow rate the output voltage of the hot wire was recorded and then paired with the flow velocity calculated from the dynamic pressure measured by a 2-mm pitot-static tube attached to a manometer. The pitot-static tube was located with its tip 1 cm downstream of the hot wire. The voltage recorded by the hot wire was found to be insensitive to the presence or otherwise of the pitot-static tube and, similarly, the dynamic pressure recorded by the pitot-static tube was found to be insensitive to the presence or otherwise of the hot wire. A least-mean-squares fit of a cubic curve was made to the voltage-velocity data pairs to give a calibration curve for the hot wire. A software calibration program applied the calibration curve to each time history recorded by the hot wire. Note that generation of the calibration curve relies only on measurements made in the duct and is thus independent of any error in the volume flow rate as measured at the rotameter due to leakage around the shutters.

B. Results

In Fig. 5 typical velocity time histories are plotted for the lowest volume flow rate for $x=1$, 4, and 17 cm downstream of the shutters for three positions on each plane as

indicated in the figure. For the measurements in Fig. 5 only, the sampling frequency was 5 kHz and the anti-aliasing filter cutoff frequency was 2 kHz; also the finite baffle of Fig. 1 was used to facilitate access of the hot wire to locations close to the duct termination. When examining the velocity time histories it is important to remember that none of the time histories was acquired simultaneously, but were later aligned with reference to the observed shutter phase using the shutter accelerometer trace. For the $x=1$ cm plane, the flow pattern varies greatly with time and position across the duct. At $x=4$ cm, the signals are almost periodic for all positions and by $x=17$ cm, the three signals have settled down to an effectively periodic fluctuation superimposed on an almost one-dimensional mean flow. The same general pattern of an approximately uniform flow was observed for the higher volume flow rates although the mean and fluctuating amplitudes were proportionately larger.

Positions $y=0, z=0$ and $y=0, z=0.6$ are directly downstream of the opening between the shutters. At $x=1$ cm a symmetric jet exiting the shutters might thus be expected to impinge on the hot wire during every cycle resulting in a periodic hot wire signal. However, shear layers tend to roll up to form vortices which can be expected to develop just downstream of the shutter exit (e.g., Davies, 1981). The vorticity is seldom uniformly distributed and symmetric about the plane of the opening at any instant and thus the jet may be expected to flap (like the flapping waves seen in a flag). The observed lack of uniformity of the hot-wire signal over the $x=1$ plane seems to correspond to this flow regime.

By 20 jet-widths downstream, it is known from the literature (e.g., Davies, 1981) that a shear layer will have rolled up into a succession of well-formed vortices which, as they move further downstream, will become progressively more diffuse and regularly spaced. This is in accordance with the observed development in both the uniformity and periodicity of the hot wire signals with increasing distance downstream from the shutters (Davies *et al.*, 1995). The observed vorticity distribution corresponds to the field obtained by the appropriate superposition of a one-dimensional acoustic field with that produced by a succession of axially symmetric vortices with their images (Davies, 1996).

It is apparent from the measurements shown in Fig. 5 that a mean flow is always present at all positions, including those at the plane $x=1$. The observations show that the instantaneous velocity at any radial position seldom falls below (and normally remains well above) half its mean value, even when the shutters are closed.

In Fig. 6(a), the amplitude of the measured velocity fluctuation is compared with the acoustic particle velocity estimate for $x=14$ cm for a volume flow rate of $U=200\ \mathrm{cm^3\,s^{-1}}$. For these measurements, the ''infinite'' baffle was once again in place. The time histories for the acoustic velocity and the velocity measured with the hot wire, although not acquired simultaneously, were aligned with reference to the observed shutter phase using the shutter accelerometer trace. It is evident that the hot wire measurements and the acoustic particle velocity estimate are dissimilar in both amplitude and phase, suggesting that the acoustic

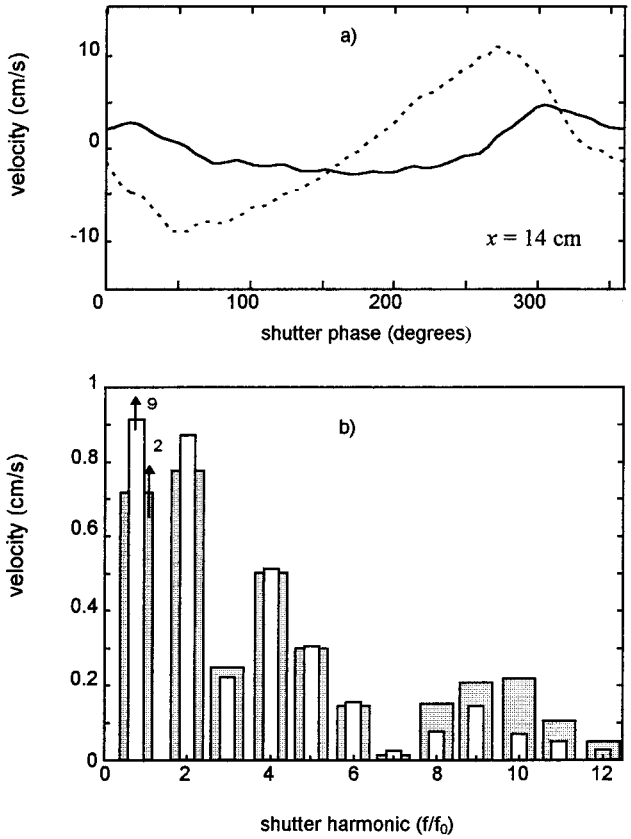

FIG. 6. (a) Average of five shutter cycles of velocity at $x=14$ cm for $U=200\ \mathrm{cm^3\,s^{-1}}$: acoustic particle velocity estimate (solid line); velocity measured with a hot wire at $y=0$, $z=0$ (dotted line). (b) Harmonic-by-harmonic comparison of fluctuating velocity amplitudes at $x=14$ cm for $U=200\ \mathrm{cm^3\,s^{-1}}$, acoustic particle velocity estimate (shaded bars), hot wire measurement (empty bars). (Note: graph not to scale for first harmonic.)

particle velocity may be only one contribution to the total measured velocity fluctuation. A corresponding discrepancy in amplitude and phase was observable in the higher volume flow rate cases.

In Fig. 6(b), the amplitude of the total velocity fluctuation is compared with that of the acoustic particle velocity estimate on a harmonic-by-harmonic basis for a volume flow rate of $200\ \mathrm{cm^3\,s^{-1}}$. At the 4th, 5th, and 6th harmonics, the two have approximately equal amplitude and, furthermore, were found to be in phase. Thus for these frequencies the total fluctuating velocity is dominated by the contribution from the acoustic particle velocity. This corresponds to the frequencies where the measured radiated pressure field outside the duct was well predicted using the acoustic field within the duct. Elsewhere the amplitudes (and phases) differ, with the greatest difference in amplitude being at the first harmonic [as can be seen from Fig. 6(a)]. For harmonics 8–12 the acoustic particle velocity is larger than the total measured velocity, but here the total fluctuation was in antiphase with the acoustic particle velocity estimate. Thus for all harmonics with the exception of the 4th, 5th, and 6th, there appears to be a fluctuating velocity component in addition to the acoustic field within the duct.

It seemed reasonable to assume that this additional fluctuating component might be associated with vortices, generated at the shutter exit and propagating along the duct. To

determine whether this was the case it was necessary to find the convection velocity for this fluctuating contribution. Acoustic disturbances propagate at the local sound speed in the duct, but vortices may be convected at speeds of the order of the local mean flow speed. In the DMM, the local mean flow speeds, determined from the hot wire measurements, were 80 and 120 cm s^{-1} for volume flow rates measured at the rotameter of 200 and 300 $cm^3\ s^{-1}$, respectively.

C. Determination of convection velocity

Velocity measurements obtained using a single hot wire at a fixed position x within the duct of the DMM may contain components due to the convection of spatial variations past the measuring point, and further components due to temporal variations at that fixed measuring point. If two velocity measurements can be obtained with a spatial separation Δx between the measurement positions, then the general dependence of each on the other may be estimated by finding their cross-correlation function. Their cross-correlation coefficient, R, is defined as

$$R(\Delta x,\tau)=\lim_{T\to\infty}\frac{1}{T}\int_0^T \frac{u_A(t)u_B(t+\tau)}{\left(\overline{u_A^2}\ \overline{u_B^2}\right)^{1/2}}\,dt, \tag{7}$$

where the subscripts A and B denote measurements at positions A and B, respectively, and the overbar denotes a time average. One useful attribute of this function is that it can be used to find the average convection velocity of flow disturbances over the path Δx (Davies and Bose, 1968).

In the duct of the DMM, the velocity was measured simultaneously at two points using two hot wire systems. Note that these measurements were made using the ''infinite'' baffle. Two volume flow rates were investigated: $U=200\ cm^3\ s^{-1}$ and $U=300\ cm^3\ s^{-1}$. Hot wire A was placed at $x=14$ cm and hot wire B was placed at $x=14.7$, 14.9, 15.1, and 15.3 cm successively to give four different separation values of Δx: 7, 9, 11, and 13 mm, respectively. The spacing between the wires was maintained by a series of shims corresponding to the spacings Δx, which were clamped between the two probes.

A hot wire loses heat to the air passing by it and thus for some distance downstream of it there exists a thermal wake. If two wires are placed directly behind each other, the downstream wire (hot wire B) will lie in the thermal wake of the upstream wire (hot wire A) and its measurements will be contaminated by the presence of the upstream wire. To reduce the cross-talk between the wires during this study, hot wire B was offset in the z direction with respect to hot wire A, by a distance $\Delta z=5$ mm. The hot wires were inserted into the duct such that hot wire A was at $x=14$, $y=0$, $z=0.25$. Hot wire B was thus at $x=14+\Delta x$, $y=0$, $z=-0.25$. Both the spacings Δx and the offset Δz were measured using a traveling microscope.

If one assumes a ''smoke ring'' vortex traveling down the duct such that it is axially symmetric, then the offset between the wires Δz, being itself axially symmetric, should cause no error in the measurement of the time-of-flight of such a vortex from hot wire A to hot wire B. Unfortunately, vortices are seldom so symmetrically distributed and thus errors may be introduced into the convection velocity estimates. It can be argued that the presence of the duct boundaries in the DMM, with the resultant image vortices, would encourage the migration of vorticity toward an axially symmetric distribution, minimizing such errors. Examination of Fig. 5 suggests that an axially symmetric assumption may be valid from about 4 cm downstream of the shutters onward. Any discrepancies in the relative axial displacements of the hot wires would similarly introduce errors. However, Davies and Bose (1968) have shown that for convection velocity measurements in a nonacoustic flow, the estimates of the convection velocity, u_E, converge to the convection velocity, u_c, as the wire separation, Δx, increases in part because the discrepancies due to positioning of the wires becomes less significant as the overall separation increases. Hence, by taking successive spacings one will arrive at a good estimate of the true convection velocity.

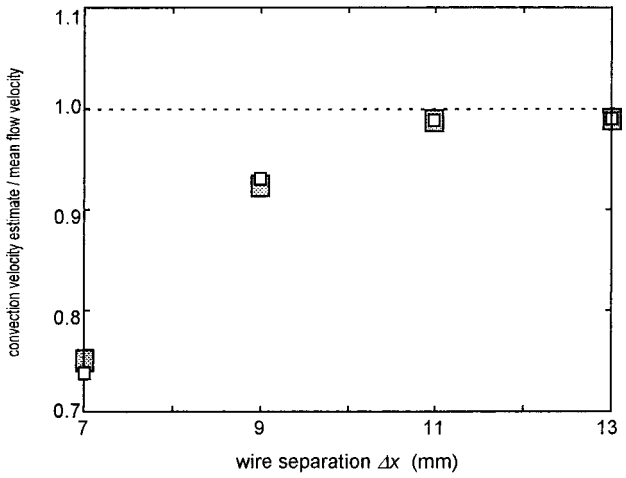

FIG. 7. Ratio of the convection velocity estimated from the cross-correlation functions, u_E, to the mean flow velocity measured in the duct, v, for successive hot wire spacings Δx; $U=200\ cm^3\ s^{-1}$ (empty squares), $U=300\ cm^3\ s^{-1}$ (shaded squares).

It is possible that different harmonic components in the flow will have different convection velocities. Thus cross-correlation analysis was performed for each successive harmonic component of the fluctuating signals after the corresponding local contribution from the estimated acoustic field had been subtracted from the total measured velocity fluctuation, taking due account of the relative phase between the signals.

For all measurements for the cross correlation, the sampling rate was raised to 10 kHz to provide greater time resolution, while the anti-aliasing filter cutoff frequency was maintained at 1 kHz. The resulting time history extended over 20 shutter cycles for each measurement location.

Figure 7 shows the ratio of the convection velocity estimate u_E for each hot wire spacing to the mean flow velocity within the duct for the fundamental frequency. It may be seen from Fig. 7 that as the hot wire separation increased, the convection velocity estimate tended toward the mean flow speed, indicating that the component of the measured fluctuating velocity not associated with the estimated acoustic field was likely to be due to nonacoustic disturbances or vortex transport along the duct.

A corresponding analysis at the other harmonics of the shutter frequency gave results for the convection velocity estimates which did not differ significantly from those reported for 80 Hz, with the exception of the 4th, 5th, and 6th harmonics where the residual velocity waveforms, after subtracting the acoustic particle velocity estimate, were too small to obtain realistic cross-correlation functions. Care had to be taken to ensure the correlations always referred to an individual disturbance.

V. VORTEX SOUND GENERATION

A. Theory

A picture emerges of the field within the duct consisting of an acoustic standing wave field, presumably generated by some combination of sources due to the fluctuating mass and fluctuating aerodynamic force at the exit to the shutters (and possibly the open end), together with a train of vortices, one generated during each shutter cycle, drifting down the duct at the mean flow speed. Thus an expression for the total velocity disturbance within the duct may be written

$$u = v + u_a + u_n, \tag{8}$$

where u is the total velocity, v is the mean flow velocity, u_a is the fluctuating acoustic particle velocity for which $\nabla \times u_a = 0$, and u_n is the fluctuating nonacoustic velocity due to vortex transport along the duct for which $\nabla \cdot u_n = 0$.

For a mean flow rate v of 80 cm s^{-1}, a vortex generated at the shutters at time t_0 travels a distance of 1 cm in time t_s, where t_s is equal to the period of the shutter cycle. Similarly, for a mean flow velocity of 120 cm s^{-1}, a vortex will travel 1.5 cm over a shutter cycle. Hence for a mean flow velocity of 80 cm s^{-1} there will be within the duct at any instant, approximately 17 vortices, each with a length of approximately 1 cm. For a mean flow velocity of 120 cm s^{-1} there will be approximately 11 vortices within the duct, each with a length of approximately 1.5 cm.

Periodically generated vortices are not themselves good radiators of sound. However, it is well known that where they interact with solid boundaries they provide significant acoustic sources and in particular can excite resonators very strongly, as in wind instruments (Davies, 1981). A fluctuating nonacoustic flow generated at an area expansion can thus provide a source of acoustic excitation for a duct. In the DMM where the duct geometry is uniform along its length, the first major area expansion after the shutters is at the open end.

For the DMM it has been demonstrated that the measured fluctuating velocity has contributions from both acoustic and nonacoustic flow fields. The nonacoustic part of the velocity disturbance, incident at an area discontinuity, will cause pressure and velocity fluctuations which will be transported in the acoustic flow field as sound and thus may be expected to contribute to the radiated spectrum. The mechanism by which the nonacoustic flow produces sound is, in general, rather complicated as is the interaction of the two velocity fields; however, a simplified model of the appropriate scaling for vortex noise generation at a duct area discontinuity (e.g., the open end) may be developed (Davies, 1996).

Consider, for simplicity, the vortex motion in the duct to be comprised of an axially symmetric vortex of radius R, where $R = a/2$ and a is the radius of the duct. The circulation Γ of each vortex is given by

$$\Gamma = \oint u_n \cdot R \, d\theta = 2\pi R u_n, \tag{9}$$

with a corresponding vorticity of

$$\Omega = \frac{\Gamma}{\pi R^2} = \frac{2u_n}{R}. \tag{10}$$

According to Doak (1995), who described the source in terms of the total fluctuating enthalpy [see also Powell (1964), Howe (1975), and McGowan (1988)], the relationship between the acoustic mean intensity vector $\overline{\mathbf{J}}$ and the nonacoustic fluid motion at the boundary discontinuity may be expressed, for the case of small amplitude, adiabatic fluctuations, in an otherwise static and uniform fluid where the convection velocity of the vortices $v \ll c_0$, as

$$\nabla \cdot \overline{\mathbf{J}} = -\rho_0 c_0 \overline{(\Omega \times u_n)}, \tag{11}$$

where the overbar indicates a time average, and which for the duct becomes

$$\nabla \cdot \overline{\mathbf{J}} = -\rho_0 c_0 \left(\frac{2\overline{u_n^2}}{R} \right) = -\rho_0 c_0 \left(\frac{4\overline{u_n^2}}{a} \right). \tag{12}$$

The generated acoustic power associated with the vortices is then

$$\int_{V_S} \nabla \cdot \overline{\mathbf{J}} \, dV_S = 4\pi a^2 \rho_0 c_0 \overline{u_n^2}, \tag{13}$$

where V_S is the volume enclosing each vortex and the vorticity is assumed to be uniformly distributed through V_S.

From conservation of energy considerations an expression relating the radiated acoustic power at the duct exit to the mean square pressure in the acoustic far field, which is analogous to Eq. (6), may be written for a source in an ''infinite'' baffle

$$W(u_n) = 2\pi r^2 \frac{\overline{p_r^2}}{\rho_0 c_0} = 4\rho_0 c_0 \overline{\{u_n(17.8, t)\}^2} \pi a^2 \sigma, \tag{14}$$

where the radiation efficiency $\sigma = (ka)^2/2$ was defined with Eq. (6).

One should be cautious about the application of Eq. (14); while it will be valid for the simplified geometry of the DMM, it cannot be strictly relevant for the vocal tract *in vivo*.

B. Predictions from theory

The same method used for the cross-correlation measurements in Sec. IV was used to estimate the fluctuating nonacoustic fluid velocity amplitude for each harmonic. The acoustic velocity for each harmonic, as predicted from pressure measurements, was subtracted from each harmonic of the total velocity measured by the hot wire, taking due account of the relative phase of the two signals in each case. Since the acoustic velocity is associated with plane-wave

propagation in the duct and the measured velocity close to the open end of the duct was found to be approximately uniform across the duct area, u_n will also be approximately uniform across the duct area. Thus a value for u_n obtained at a single measurement position within the duct may be used to estimate the net volume flux over any plane close to the duct exit. The nonacoustic velocity was estimated at the $x=14$ plane. To obtain the nonacoustic velocity estimate at the open end ($x=17.8$), each harmonic component must be translated along the duct in the positive x direction. This is achieved using an appropriate time shift for the fluctuation at $x=14$. It was shown in Sec. IV that the nonacoustic velocity fluctuation convected along the duct in the positive x direction at approximately the mean flow velocity v. Consequently, an appropriate time shift to translate the disturbance estimated at $x=14$ cm the short distance to the open end is

$$u_n(17.8,\, t)=u_n\left(14,\, t-\frac{x_1}{v}\right), \tag{15}$$

where $x_1=3.8$ cm is the distance between the $x=14$ plane and the open end.

A prediction of the far-field sound pressure level for each spectral component at a distance of 60 cm from the duct exit and an angle of 45° due to the contributions to the radiated sound from both the acoustic and the nonacoustic fields is shown in Fig. 8. The contributions from the two velocity fields have been treated as independent since analysis of the relative amplitudes and phases of each harmonic of the two velocity disturbances indicated that contributions from the cross terms $(u_a \cdot u_n)$ were negligible.

The predictions of Fig. 8 demonstrate that combining the contribution associated with the nonacoustic field with the acoustic contribution to the pressure results in much improved agreement between the measured SPL and the predicted SPL. When $U=200\ \mathrm{cm^3\,s^{-1}}$, the two curves are closely similar except at the 3rd harmonic where the new prediction is 9 dB lower, and at the 10th harmonic where the prediction is 4 dB higher. When $U=300\ \mathrm{cm^3\,s^{-1}}$ the prediction is closely similar to the measurement except at the seventh harmonic where it is 12 dB higher. When $U=400\ \mathrm{cm^3\,s^{-1}}$ the predicted levels lie around the measured levels except at the 7th harmonic where the prediction is 14 dB above the measurement. The discrepancies between the measured and predicted levels may be primarily attributable to a combination of the neglect of the cross terms as noted previously and the assumption in the vortex sound model of an axially symmetric vortex with neglect of the effect of any nonuniformity of flow local to the core region. Additionally, implicit in Eq. (15) is the assumption that the vorticity convects in a nondispersive manner. In general such convection will be dispersive; however, comparison of the hotwire measurements at $x=14$ cm (Fig. 6) and $x=17$ cm (Fig. 5) together with the evidence of the cross-correlation analysis suggests that, far from the shutters and over short distances at least, this assumption of nondispersive convection will lead to a reasonable estimate for the rms value of the nonacoustic velocity fluctuation at the duct exit plane. Clearly there is much better agreement between the measured and predicted SPLs in Fig. 8 than was found for the prediction based on the acoustic velocity component acting in isolation. Thus one concludes that the nonacoustic velocity field within the duct constitutes a significant part of the sound generation mechanism, providing the dominant sound source except at the 4th, 5th, and 6th harmonics, where the acoustic field was dominant.

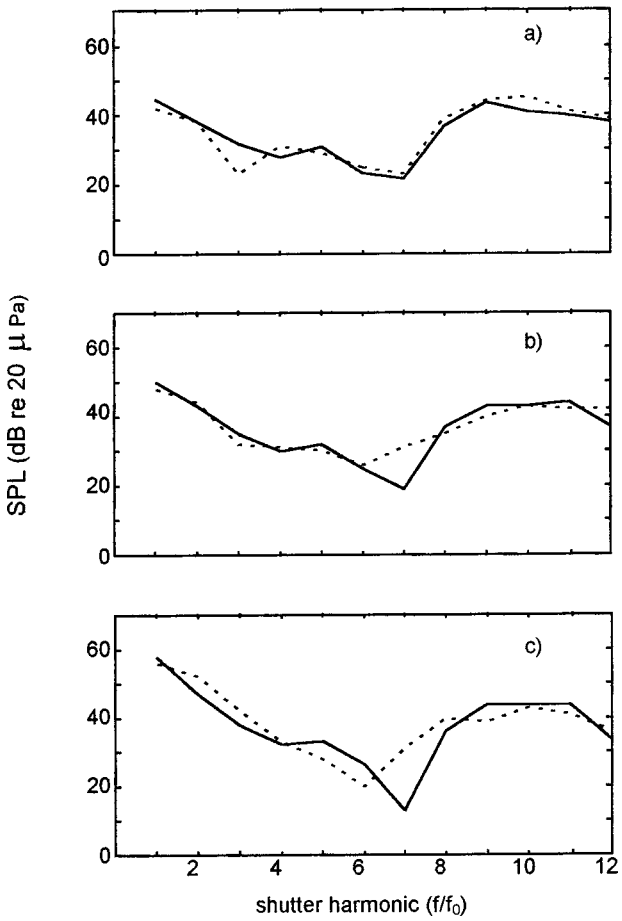

FIG. 8. Radiated far-field sound pressure, measured at 60 cm from the duct exit plane at an angle of 45° to the long axis of the duct; measured (solid) and predicted (dotted) using both the acoustic particle velocity estimate and the nonacoustic velocity estimate at the duct exit plane for (a) $U=200\ \mathrm{cm^3\,s^{-1}}$, (b) $U=300\ \mathrm{cm^3\,s^{-1}}$, (c) $U=400\ \mathrm{cm^3\,s^{-1}}$.

VI. CONCLUSIONS

We have described a simple Dynamic Mechanical Model (DMM) of the vocal folds and tract, where the folds are represented by a pair of driven, sinusoidally oscillating shutters.

Measurements of the fluctuating pressure at two points along the duct wall of the DMM, downstream of the shutters, were found to exhibit the characteristic amplitude distribution of an acoustic standing wave field. The energy in these pressure fluctuations was found to be predominantly concentrated at the harmonics of the shutter oscillation frequency, and thus a time domain, plane-wave, harmonic analysis allowed an estimate of the fluctuating acoustic particle velocity field within the duct to be obtained.

Measurements of the velocity field within the duct using hotwire anemometry showed a pattern characteristic of an unsteady jet downstream of the shutters due to the passage of

air through the shutter channel. Over the first 4 cm or so the jet became more diffuse and mixed with the air in the downstream duct. The velocity field was highly three-dimensional at 1 cm downstream of the shutter exit and became gradually more uniform as distance from the shutters increased.

At no position within the three-dimensional flow field close to the shutter exit or the more uniform flow field further downstream did the acoustic particle velocity estimate compare well either in amplitude or in phase-relationship-to-the-shutter-cycle to the measured velocity fluctuation. This is unsurprising, since to assume that the entire fluctuating velocity field within the duct is associated with the fluctuating acoustic field is to assume an acoustic source distribution at the shutter exit with unrealistically high efficiency. It is well known that the shear layer associated with an unsteady jet is inclined to roll up, eventually forming ordered vortical structures in the flow. It seemed probable that the measured velocity fluctuation was the resultant of contributions from both the acoustic particle velocity and from a fluctuating nonacoustic velocity field.

Cross-correlation analysis of dual hot wire measurements confirmed that the component of the measured velocity fluctuation not associated with the acoustic particle velocity estimates had a propagation velocity comparable to the mean flow speed in the duct. Such a nonacoustic, fluctuating velocity field is characteristic of the convection of a train of vortices along the duct.

McGowan (1988) has proposed that the generation of acoustic energy at the glottal exit may be due to two mechanisms: the fluctuating volume flow through the glottal channel as modeled by Fant (1960), and the fluctuating force due to the interaction of the vorticity with the fluid velocity. In the DMM, no information as to the type or number of acoustic source mechanisms, close to the shutter exit or elsewhere, which contribute to the acoustic field within the duct can be obtained from the pressure measurements made at the duct wall. In McGowan's model, the vorticity is assumed to decay downstream of the glottis. In general, in the absence of strong damping mechanisms, vorticity is known to persist for large distances. Hirschberg (1992) and Teager and Teager (e.g., 1990) have noted that the interaction of a nonacoustic velocity with abrupt expansions in a duct area function may result in the transfer of energy from the nonacoustic velocity field to the irrotational acoustic field. In the vocal tract this could occur at the epiglottis, palate, teeth, and lips. In the DMM the only abrupt area expansion downstream of the shutters is the duct exit.

For the DMM, a model of the sound radiation at the duct exit based on the irrotational acoustic particle velocity fluctuation in the duct cannot alone account for the measured radiated pressure field except at the first formant of the duct. A model that includes additional contributions to the radiated sound field due to the interaction of the nonacoustic flow field with the area change at the duct exit is much more successful at predicting the observed sound field despite the simplicity of the model of the vorticity distribution and its relation to the acoustic field. One is led to conclude that the nonacoustic flow field within the duct provides a significant additional source of acoustic energy located in the region of the duct exit.

The spectral distribution of a nonacoustic velocity field depends strongly on the geometry of the region where it is generated. The spectral distribution of sound from any acoustic sources due to the interaction of the nonacoustic velocity field with the duct boundaries will also be geometry dependent. One should not therefore expect that the results obtained in the DMM will map directly to the vocal tract. A companion paper (Shadle *et al.*, 1999) compares measurements made in the DMM to *in vivo* measurements made during voiced speech production and considers the implications of including a nonacoustic velocity field in speech production models.

ACKNOWLEDGMENTS

This article is based on a paper given at the May 1997 International Conference on Voice Physiology and Biomechanics. The authors would like to thank Dr. T. Baer and Professors P. Nelson and P. Doak for helpful discussions and also the three anonymous reviewers for their extensive comments on an earlier version of this manuscript. A Leverhulme Emeritus Fellowship awarded to the third author provided partial support for this research.

Alipour, F., Scherer, R., and Patel, V. (**1996**). ''An experimental study of pulsatile flow in canine larynges,'' NCVS Status and Progress Report 9, 47–52.

Barney, A. (**1995**). ''Fluid flow in a dynamic mechanical model of the larynx,'' Ph.D. thesis, Dept. Electronics and Computer Science, University of Southampton, England.

Binh, N., and Gauffin, J. (**1983**). ''Aerodynamic measurements in an enlarged static laryngeal model,'' STL-QPSR **2-3**/1983, 36–45.

Cranen, B., and Boves, L. (**1985**). ''Pressure measurements during speech production using semiconductor miniature pressure transducers: Impact on models for speech production,'' J. Acoust. Soc. Am. **77**, 1543–1551.

Davies, P. O. A. L. (**1981**). ''Flow-acoustic coupling in ducts,'' J. Sound Vib. **77**, 191–209.

Davies, P. O. A. L. (**1988**). ''Practical flow duct acoustics,'' J. Sound Vib. **124**, 91–115.

Davies, P. O. A. L. (**1992**). ''Intake and exhaust noise,'' ISVR Technical Report No. 207.

Davies, P. O. A. L. (**1996**). ''Aeroacoustics and time varying systems,'' J. Sound Vib. **190**, 345–362.

Davies, P. O. A. L., and Bose, B. (**1968**). ''The convection of dispersive waves,'' Proceedings of the International Congress on Acoustics, Tokyo, Japan, F-133–F-136.

Davies, P. O. A. L., and Mason, J. (**1974**). ''The ISVR constant temperature hot wire anemometer,'' ISVR Technical Report No. 66, University of Southampton, England.

Davies, P. O. A. L., Bhattacharya, M., and Bento Coelho, J. L. (**1980**). ''Measurement of plane wave acoustic fields in flow ducts,'' J. Sound Vib. **72**, 539–542.

Davies, P. O. A. L., Barney, A., and Shadle, C. H. (**1995**). ''Aeroacoustic sources in a vocal tract model,'' Proceedings of the 15th ICA **3**, 23–26.

Doak, P. E. (**1995**). ''Fluctuating total enthalpy as a generalised acoustic field,'' Acoust. Phys. **41**, 769–778.

Fant, G. (**1960**). *The Acoustic Theory of Speech Production* (Mouton, The Hague).

Harrison, M. F. (**1994**). ''Time and frequency domain modelling of vehicle intake and exhaust systems,'' Ph.D. Thesis, I.S.V.R, University of Southampton, England.

Hergel, G. C., and Höge, H. (**1991**). ''Numerical simulation of the glottal flow by a model based on the compressible Navier–Stokes equations,'' Proc. ICASSP '90, Toronto, Canada, Vol. 1, 477–480.

Hirschberg, A. (**1992**). ''Some fluid dynamic aspects of speech,'' Bulletin de la Communication Parlée, No. 2, 7–30.

Howe, M. S. (**1975**). ''Contributions to the theory of aerodynamic noise with applications to excess jet engine noise and the theory of the flute,'' J. Fluid Mech. **71**, 625–673.

Kaiser, J. F. (**1983**). ''Some observations on vocal tract operation from a fluid flow point of view'' in *Vocal Fold Physiology: Biomechanics, Acoustics and Phonatory Control*, edited by I. R. Titze and R. C. Scherer (Denver Center for the Performing Arts, Denver, CO), pp. 358–386.

Kinsler, L. E., Frey, A. R., Coppens, A. B., and Sanders, J. V. (**1982**). *Fundamentals of Acoustics* (Wiley, New York), 3rd ed.

Kiritani, S., Fukawa, H., Imagawa, H., Imaizumi, S., and Saito, S. (**1987**). ''Measurement of air flow pattern through a mechanically driven oscillating slit—A preliminary report,'' Annual Bulletin of the Research Institute of Logopedics and Phoniatrics **21**, 1–8.

Liljencrants, J. (**1989**). ''Numerical simulations of glottal flow,'' in *Vocal Fold Physiology: Acoustic, Perceptual and Physiological Aspects of Voice Mechanics*, edited by J. Gauffin and B. Hammarberg (Singular, San Diego), pp. 99–104.

McGowan, R. S. (**1988**). ''An aeroacoustic approach to phonation,'' J. Acoust. Soc. Am. **83**, 696–704.

Mongeau, L., Franchek, N., Coker, C. H., and Kubli, R. A. (**1997**). ''Characteristics of a pulsating jet through a small modulated orifice, with application to voice production,'' J. Acoust. Soc. Am. **102**, 1121–1133.

Powell, A. (**1964**). ''Theory of vortex sound,'' J. Acoust. Soc. Am. **36**, 177–195.

Scherer, R. C., and Guo, C. G. (**1990**). ''Laryngeal modelling: Translaryngeal pressure for a model with many glottal shapes,'' Proc. ICSLP 90, Kobe, Japan, 57–60.

Scherer, R. C., Titze, I. R., and Curtis, J. F. (**1983**). ''Pressure-flow relationships in two models of the larynx having rectangular glottal shapes,'' J. Acoust. Soc. Am. **73**, 668–676.

Shadle, C. H., Barney, A., and Davies, P. O. A. L. (**1999**). ''Fluid flow in a dynamic mechanical model of the vocal folds and tract. II. Implications for speech production studies,'' J. Acoust. Soc. Am. **105**, 456–466.

Shadle, C. H., Barney, A., and Thomas, D. W. (**1991**). ''An investigation into the acoustics and aerodynamics of the larynx,'' in *Vocal Fold Physiology*, edited by J. Gauffin and B. Hammarberg (Singular, San Diego, CA), pp. 73–82.

Teager, H. M., and Teager, S. M. (**1983**). ''A phenomenological model for vowel production on the vocal tract,'' in *Speech Sciences: Recent Advances*, edited by R. G. Daniloff (College-Hill, San Diego, CA), pp. 73–109.

Teager, H. M., and Teager, S. M. (**1990**). ''Evidence for nonlinear sound production mechanisms in the vocal tract,'' in *Speech Production and Speech Modeling*, edited by W. J. Hardcastle and A. Marchal (Kluwer Academic, London), pp. 241–262.

Thomas, T. J. (**1986**). ''A finite element model of fluid flow in the vocal tract,'' Comput. Speech Lang. **1**, 131–151.

Fluid flow in a dynamic mechanical model of the vocal folds and tract. II. Implications for speech production studies

Christine H. Shadle
Department of Electronics and Computer Science, University of Southampton, Southampton SO17 1BJ, United Kingdom

Anna Barney
Faculty of Engineering and Applied Science, University of Southampton, Southampton SO17 1BJ, United Kingdom

P. O. A. L. Davies
Institute of Sound and Vibration Research, University of Southampton, Southampton SO17 1BJ, United Kingdom

(Received 6 December 1997; accepted for publication 24 September 1998)

A companion paper [Barney *et al.*, J. Acoust. Soc. Am. **105**, 444–455 (1999)] presents measurements in a dynamic mechanical model (the DMM) of the vocal folds and vocal tract: It was shown that closer prediction of the radiated sound pressure was possible when nonacoustic (vortical) as well as acoustic components of the velocity in the duct were included. In this paper, using such a simple geometry to model the vocal tract is justified by comparing acoustic and aerodynamic measurements in the DMM to those made *in vivo*: sub- and supraglottal pressures, radiated pressure, and hot wire velocities. The DMM produces sound equivalent to weak, low-frequency falsetto. A Rothenberg mask was then placed on the end of the DMM, and two estimates of the glottal waveform were compared to velocities measured near the ''glottis.'' The results show that the glottal waveform does not resemble any hot wire velocities measured near the shutters; travel times for acoustic and nonacoustic components of the velocity field differ significantly, which may cause problems when using the Rothenberg mask to analyze transients; the mask itself alters the acoustic field in the duct, and the radiated pressure, significantly. The evidence points toward the existence of a vortex train during and caused by phonation, and significant sound generation due to the interaction of that train with tract boundaries; these findings indicate that the models on which inverse filtering are based have been overgeneralized. [S0001-4966(99)00501-9]

PACS numbers: 43.70.Aj, 43.70.Bk, 43.70.Jt [AL]

INTRODUCTION

In the companion paper (Barney *et al.*, 1999) the Dynamic Mechanical Model (DMM) of the vocal folds and vocal tract was described. Measurements of its acoustic and aerodynamic behavior were presented, and it was shown that the velocity field in the duct could be described in terms of a mean flow, an acoustic velocity field, and a nonacoustic fluctuating velocity field. A model for the radiation of sound from the duct that included contributions associated with acoustic as well as nonacoustic components of the velocity in the duct led to closer prediction of the measured, radiated sound field than did predictions based on the acoustic field alone. These observations suggest that at least two different acoustic source mechanisms may exist in the duct, each of which has a different spectral characteristic and location.

Numerous studies using a wide variety of approaches support these conclusions and their application to speech. Development of vorticity has been observed in simulations (Liljencrants, 1991, 1995; Iijima *et al.*, 1992; Alipour *et al.*, 1996). The development of vorticity, and in some cases evidence of convecting vortices, has been observed using flow visualization on mechanical models of the vocal tract (Shadle *et al.*, 1991; Pelorson *et al.*, 1994; Hirschberg *et al.*, 1996) and on a human subject releasing a bilabial plosive (Pelorson *et al.*, 1994). Hot wire anemometry signals consistent with the development of vorticity have been measured in mechanical models (Kiritani *et al.*, 1987; Mongeau *et al.*, 1997), in excised canine larynges (Berke *et al.*, 1989; Smith *et al.*, 1991; Alipour and Scherer, 1995; Alipour *et al.*, 1996), and in a human subject (Teager, 1980).

In the speech literature it is typically assumed that normal phonation results in one type of sound source, which is classically modeled as a volume velocity source, located at the glottis, and assumed to represent a spatial average of the velocities across the exit plane. This ''glottal waveform'' is considered to be closely related but not identical to the periodic area function of the glottis. In some phonemes, such as voiced stops or voiced fricatives, other sources are assumed, but these are noise sources located supralaryngeally (Flanagan, 1972).

However, more recently speech researchers have tried to reconcile theories of speech production with experimental results, such as those cited above, consistent with vorticity in the vocal tract. Teager's first observations that his hot wire measurements demonstrated separated, nonlaminar flow in the oral cavity, and that this made it appear that there was

active sound generation in the front cavity (Teager, 1980) were elaborated in later papers. Whistle studies were cited, and a ''jet-cavity interaction'' was proposed (Teager and Teager, 1983a, b). Kaiser was somewhat more specific, stating (1983) that ''source-filter theory...implicitly assumes irrotational flow in the tract, that is, that vortices are not possible or present.'' Later in the same paper, he proposed that there was a ''complex interaction of sheetlike jet flows throughout the tract...surface conditions do markedly affect the behavior of the attached flows.'' Later papers described various mechanisms by which separated flows and standing vortices could generate sound, although the descriptions were never expressed mathematically (Teager and Teager, 1985, 1990).

McGowan (1988) applied fluid mechanical theory to the simple geometry of a single contraction in a cylindrical tube. He showed that the classic volume-velocity source could be characterized as a flow monopole, but that a flow dipole source was also necessary, and corresponded to the vorticity-velocity interaction force. He assumed that the rotational motion decayed rapidly downstream of the glottis. However, once generated, vorticity is known to persist with little change for relatively large distances downstream. In this case, he pointed out, in a realistic vocal tract geometry the interaction between such rotational motion and the epiglottis, palate and lips may produce acoustic sources, in addition to those located close to the glottal exit.

Hirschberg (1992) continued in this vein, adding quadrupole sources to the list in order to model frication. Later experiments with starting transients applied to glottal models showed that turbulence occurred in the jet exiting the glottis, although with some delay; thus the quadrupole source was needed to model phonation also (Hirschberg *et al.*, 1996).

In 1995 we first described the theory (Davies *et al.*, 1995) that explains the experimental results of the DMM given in the companion paper (Barney *et al.*, 1999). Davies (1996) used that as one of a variety of examples of an aeroacoustic system to which source-filter modeling could be applied. By source-filter modeling, though, he does not imply a restriction to electrical circuit analogues. He concludes, ''The distinctive role of vortex sound sources... in this example goes some way toward confirming McGowan's suggestion that they should be included in all realistic models of phonation, including the open vowels.''

A variety of inverse-filtering methods have been described that estimate the glottal waveform from some form of the external speech signal, either the radiated sound pressure or pressure difference across the Rothenberg mask. The Rothenberg mask has certain advantages (described by Rothenberg, 1973, and summarized in Sec. II) and, as a result, has been used extensively to derive glottal waveforms for different voice types performing different vocal tasks. In some cases the derived waveforms are used to describe different sources for speech synthesis (see, e.g., Fant *et al.*, 1985; Karlsson, 1992); in other cases they are used together with other measures of vocal fold motion to deduce the relationship between the motion and the phonation source (e.g., Sundberg and Gauffin, 1978; Rothenberg, 1987; Holmberg *et al.*, 1988). Yet these uses, particularly the latter, are based on a model that assumes there is no significant sound generation by any vortical flow, nor at locations different from the glottal exit plane. We have already shown in the companion paper that such a model does not work for the DMM. The crucial question, though, is: how much do these assumptions matter for the human vocal tract, for speech? Further, what implications does a vortical flow have for the use of the Rothenberg mask?

The DMM was constructed with dimensions typical of the human vocal tract and folds; experiments were conducted with volume velocities typical of phonation (200–400 cm^3/s) and a forced frequency of the shutters, analogous to the vocal folds, of 80 Hz. However, the simplicity of the DMM's flow channel geometry (a cylindrical duct bisected by rectangular shutters) and the hardness of its walls are dissimilar to the vocal tract. In this paper we first compare the acoustic and aerodynamic behavior of the DMM to that of the vocal tract during phonation in order to decide to what extent the DMM results, and source modeling for the DMM, can be applied to the vocal tract. We then describe some experiments conducted using a Rothenberg mask on the DMM in an effort to clarify the meaning of the waveforms obtained through inverse filtering.

I. COMPARISON OF DMM AND VOCAL TRACT MEASUREMENTS

Methodological details about the DMM already presented in the companion paper (Barney *et al.*, 1999) will not be repeated here. These include the design and construction of the DMM, specification and method of calibration of the hot wire anemometers, recording and analysis of the hot wire signals, method of removal of mechanical shutter noise from the sound pressure measurements, and recording and analysis of sound pressure and accelerometer signals. Where signals are estimated by different methods the relevant equations are repeated here, but the complete derivation and justification of each estimation procedure is omitted. Experiments reported only in this paper are, of course, described in full here.

A. Transglottal pressure comparisons

The first comparison was made between pressures recorded across the shutters of the DMM, and pressures recorded across the vocal folds by Cranen and Boves (1985a). In the DMM, the time trace of the pressure during a shutter cycle was recorded 4 cm downstream and 3 cm upstream of the oscillating shutters. This was measured for three volume velocities, $U=200$, 300, and 400 cm^3/s. Cranen and Boves' measurements involved inserting a set of four microphones mounted at 5-cm intervals on a wire through the glottis, and recording the pressure signals while the subjects phonated the vowels [a] and [i]. Two microphones were above, two below the glottis, which meant that the glottis-microphone distance could never exceed 5 cm; however, that distance could not be determined more accurately, nor held constant during speech, owing to the movement of the larynx. The two microphones nearest to the glottis were used to compute the transglottal pressure drop. The EGG and PGG signals

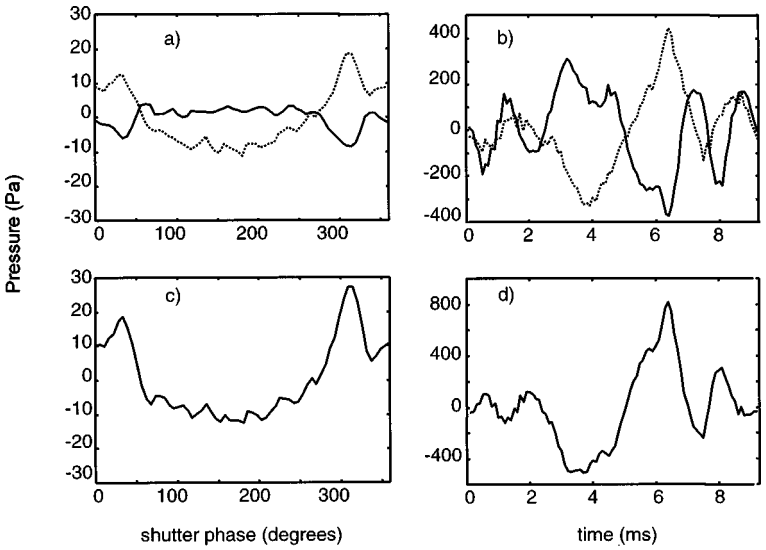

FIG. 1. Left: Pressure across shutters of DMM, compared to Right: pressures measured in vocal tract of subject BC saying /a/ (Cranen and Boves, 1985a). Upper graphs: solid trace $=P_{\text{sup}}$, dotted $=P_{\text{sub}}$. Lower graphs: P_{trans}. In the DMM P_{sup} is measured 4 cm downstream, P_{sub} 3 cm upstream of the shutters, at $U=200$ cm^3/s.

were recorded simultaneously, which allowed them to identify closed and open phase on the pressure waveforms. The radiated sound pressure was also recorded.

Figure 1 shows a comparison of one set of such signals recorded by Cranen and Boves (subject BC saying [a]; total volume velocity is unknown), and corresponding measurements in the DMM (for $U=200$ cm^3/s). The individual sub- and supraglottal pressure traces, with means removed, are shown in graphs (a) and (b), and their differences, P_{trans}, in graphs (c) and (d). The Cranen and Boves signals have been arranged so that they begin at the midpoint of one closed phase, as originally identified using EGG and PGG signals, and end at the midpoint of the next closed phase. This effectively aligns these signals with those of the DMM, for which 0 degrees is the midpoint of the closed phase.

The shape of the waveforms is roughly the same: the two pressures alternate during a cycle, with P_{sup} higher in amplitude during the open phase, P_{sub} higher in closed phase. One-fifth of the shutter cycle is closed phase due to the foam attached to the edges of the shutters. P_{trans} is low during the open phase. Note that both cases show significant formant ripple during the open phase.

The magnitude of the pressure fluctuations, on the other hand, differs greatly between people and the DMM, being much smaller in the DMM signals. Higher volume velocities produced pressures in the DMM one order of magnitude smaller than in the subject; lower ones, two orders of magnitude smaller.

These comparisons hold for the other examples given by Cranen and Boves, and for other studies in the literature, insofar as they can be compared [e.g., Koike and Hirano (1973), Koike (1981), and Koike *et al.* (1983) present similar but uncalibrated pressure measurements, allowing comparison of shape but not magnitude. Hirose and Niimi (1987) made calibrated measurements, but present means and standard deviations corresponding to consonants only].

B. Velocity field in tract comparisons

Numerous hot wire signals were recorded at various points in the DMM, and under varying conditions. Some hot wire signals have been recorded in phonating human subjects and described in the literature, and we compare our measurements in the DMM to these signals later on in this section. However, we chose to make our own recordings in human subjects as well so that we could ensure the same hot wires and the same hot wire calibration was used on both cases.

Four male subjects were used for this experiment. A hot wire was inserted 1 cm behind their front teeth and centrally located with respect to the palate. They phonated [ʌ] steadily, and approximately 2 s of the hot wire signal was recorded. The neutral vowel was chosen because the tract shape should be most similar to the uniform tube of the DMM; male subjects were chosen because their tract length, and F_0, should be most similar to that of the DMM. The signals were low-pass filtered at 2 kHz and sampled at 5 kHz. The central 5 or 6 cycles of the filtered signals are displayed for each subject in Fig. 2(a), and are contrasted in Fig. 2(b) with a hot wire velocity measured in the DMM at $x=17$ cm, 1.8 cm from the open end of the duct, where x is the longitudinal axis of the duct and $x=0$ is located at the shutters.

The magnitude of the mean flow is comparable, although it clearly varies during these 5 or 6 cycles in humans much more than in the DMM. The fluctuating flow is also comparable: approximately 50 cm/s peak-to-peak in humans, and approximately 30 cm/s peak-to-peak in the DMM. The wave shape is also comparable: skewed to the right in all cases, and with small ripples in addition to the larger ones. The fluctuations in the DMM were shown to have contributions from convecting vortices. Because of the similarities noted above, we could make an assumption that in the human vocal tract the underlying mechanisms are the same as in the DMM, i.e., that convecting vortices contribute to the hot wire signals measured in the human subjects.

Teager (1980) and Teager and Teager (1983a, b, 1985, 1990) also reported hot wire traces measured in the mouth. Their signals exhibit similar wave shapes but differ in magnitude from ours. They observed a main pulse followed by small pulses during one pitch period, with the velocity signal never reaching zero. The fluctuations, however, are of the order of 145 cm/s about a mean flow of approximately 150

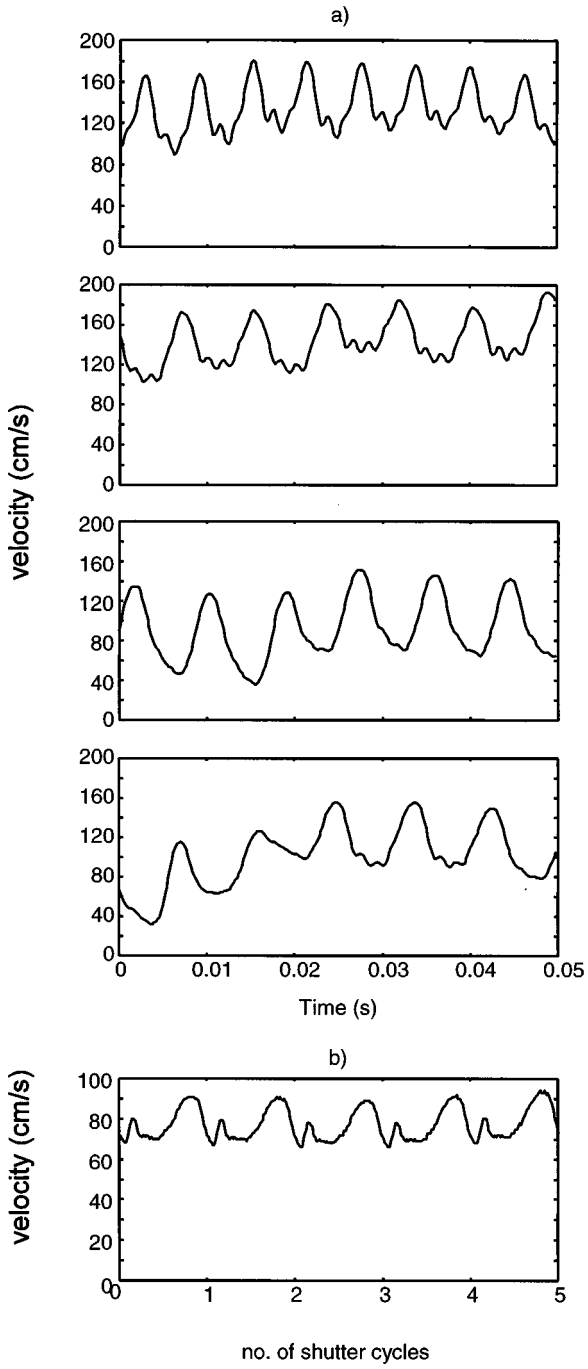

FIG. 2. (a) Hot wire velocity measured midsagittally 1 cm behind front teeth in four adult male subjects during steady phonation of vowel [ʌ]. (b) Hot wire velocity measured 1.8 cm from open end of DMM ($x=17$ cm) at center of duct. $U=200$ cm^3/s.

cm/s, and thus somewhat larger than the amplitudes we observed for our four subjects. Their calibration system differed from ours, which may explain these differences in part. It is also possible that their subject was simply speaking louder than ours. Neither Teager and Teager nor we measured the absolute sound pressure in the far field while making the hot wire measurements.

C. Radiated pressure comparisons

The radiated sound pressure, measured at 60 cm, 45 deg off-axis, was used to compute a total SPL value, which ranged from 50 to 60 dB depending on which of the three volume flow rates was considered. Beranek gives a long-term average value for a ''raised man's voice'' at 1 m of 69 dB, and notes that normal voice will be 6 dB less, shouting 12 dB more (Beranek, 1954, pp. 408–410). Clearly the DMM produces a weaker radiated pressure, even at its highest flow rate, than a normal man's voice.

D. Discussion

The results of comparing three different kinds of signals measured in the DMM and in phonating humans can be summarized as follows. Pressure fluctuations across the glottis are much smaller in the DMM but exhibit a similar waveform shape during the glottal cycle. Hot wire velocities are roughly similar in shape and order of magnitude in the DMM and our subjects; in shape, for Teager's subject. The radiated sound pressure is 10–20 dB lower for the DMM.

What are differences between the model and the human vocal tract that could account for these pressure magnitude differences? The shutter area function is sinusoidal, whereas in humans it is generally more sawtooth in shape (except for falsetto). Since, for an acoustic source associated with fluctuating volume velocity, source strength is proportional to the time derivative of the velocity, a sawtooth wave should imply a stronger acoustic source. This explains in part why the DMM pressure is lower.

The shutters of the DMM leaked air (10% of the volume flow), decreasing the maximum possible pressure drop across the shutters.

In the DMM the closed phase was approximately one-fifth of the shutter cycle, whereas in humans it is never less than one-third of a cycle, even for falsetto, and two-fifths to one-half for normal phonation (Sundberg and Gauffin, 1978; Cranen and Boves, 1985a). This difference would predict that for the same mean volume flow, a longer closed phase (as in humans) implies that the peak velocity during the open phase will be bigger, and the peak pressure drop, proportional to the peak value of u^2, will therefore also be bigger.

We conclude that the DMM does behave in many respects like a phonating vocal tract, and is most similar to a low-frequency falsetto-style phonation. The two main results for the DMM were the analysis of its velocity field, where one contribution was shown to consist of a vortex train convecting at the mean flow velocity; and evidence supporting significant sound generation by the vortex train at all frequencies except that of the first formant.

The similarities in amplitude and shape of the fluctuating velocity measurements made in the vocal tract and the DMM suggest that a vortex train exists in the vocal tract during, and caused by, phonation. If so, this vortex train may generate sound at area discontinuities in the vocal tract. As noted in the Introduction, this conclusion is supported by a wide variety of studies.

Note that the spectral distribution and amplitude of a nonacoustic field is highly geometry dependent; we cannot therefore expect the DMM's nonacoustic field (hypothesized to be due to axisymmetric vortices) to map directly to the bilaterally symmetric vocal tract. Likewise, sound generation by the interaction of a vortex train with the tract boundary

could occur at any area discontinuity in the vocal tract, such as at the lips or teeth; the DMM has no discontinuity between shutters and the open end of the duct.

II. ROTHENBERG MASK EXPERIMENTS

The picture painted by the DMM of the in-duct velocity field and the acoustic source location is at variance with the assumptions underlying estimation of the glottal waveform by inverse filtering, and subsequent use of that glottal waveform as the sole phonation source. When the Rothenberg-mask pressure gradient is inverse filtered, what is obtained, and how does that waveform relate to measurable parameters? With the DMM we can investigate this.

Before the advent of the Rothenberg mask, either the radiated pressure signal or the velocity measured by a pneumotachograph mounted in a solid mask were inverse filtered to obtain an estimate of the glottal volume-velocity waveform. Using the radiated pressure had the disadvantage that the mean flow could not be recovered. Using the pneumotachograph had the disadvantage that the mask it was mounted in distorted the speech markedly.

The Rothenberg mask uses circumferentially mounted screening of known resistance to lessen the distortion while allowing measurement of the mean flow through the mask. Rothenberg calibrated and tested the mask in several ways in order to validate its use on speech. These included measuring the pressure developed across the mask as a function of flow through it, measuring the transmission characteristic for a sinusoidal loudspeaker input, measuring the rise time of the inverse-filtering circuit, and measuring formant frequencies of ten vowels produced with and without the mask. In addition, he tested the mask aeroacoustically, using as a source air passing through a rotating disk with slots in it; this source was first directly fed through the mask, and then fed into a simulated vocal tract. He measured a mask antiresonance at approximately 2 kHz, but reported that apart from a slight lowering of formant frequencies, the mask appeared to have no other distorting properties, and indeed, exhibited virtues compared to inverse filtering using only an external pressure signal: ambient noise made the pressure-derived waveform more noisy, and when both were used on a vowel onset, ''only the waveform derived from volume velocity shows clearly the nature of the onset of voicing'' (Rothenberg, 1973).

Two more recent studies have investigated the acoustic effects of various models of the Rothenberg mask. The mask was mounted on a loudspeaker and a sweep tone was used to generate a transmission characteristic. Both studies found a pronounced spectral dip, at either 1.5 kHz (Badin *et al.*, 1990) or 1.9 kHz (Hertegård and Gauffin, 1992), and other less pronounced peaks and dips at higher frequencies. These dips were shown to be caused by the mask. Badin *et al.* also recorded the long-term-averaged spectrum of a 10-s sentence with and without the mask, and compared /a, i/ productions. They concluded that the mask did not distort speech up to 1 kHz (Badin *et al.*, 1990) and 1.6 kHz (Hertegård and Gauffin, 1992). At the time the experiments in this study were first reported (Barney, 1995), only Rothenberg had tested the masks aeroacoustically as well as acoustically.

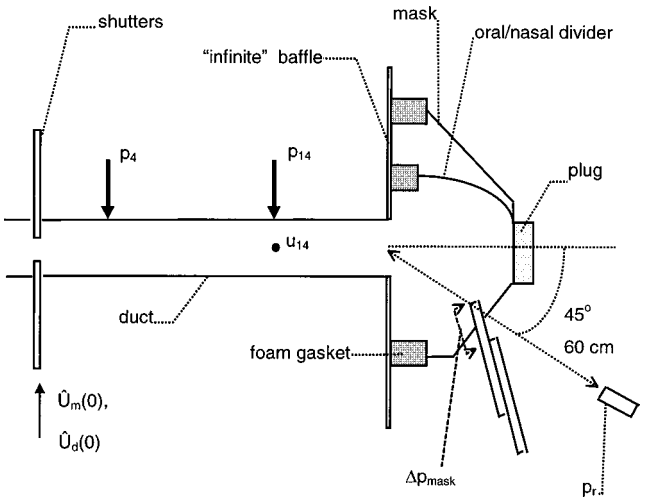

FIG. 3. Diagram showing the DMM with Rothenberg mask attached, and various measurement points. p_4, p_{14} are measured by pressure transducers placed flush with the duct walls at locations shown. u_{14} indicates the location of a hot wire anemometer. $\hat{U}_d(0)$, $\hat{U}_m(0)$ represent two predictions of volume velocity at $x=0$; see text. Δp_{mask} is the pressure drop across the mask measured by the two pressure transducers shown. p_r is the pressure measured at the distance ($r=60$ cm) and angle shown. Diagram not to scale.

After Rothenberg's initial methodological paper (1973), he and other researchers proceeded to use the mask to investigate a wide range of voices and vocal behaviors. Reviewing these studies is beyond the scope of this paper. However, one aspect has been noted from the beginning and is relevant to our findings, the striking fact that the glottal waveform derived from inverse filtering tends to be much more skewed than the corresponding glottal area function. Variation in the skewing and other aspects of the waveform shape were studied by Sundberg and Gauffin (1978) for their relation to voice register, pitch, vocal effort, and the consequences in the shape of the glottal source spectrum were derived. Rothenberg (1981) showed that the amount of skewing could be theoretically related to the inertive loading of the tract, though this mechanism did not apply to the soprano voice (Rothenberg, 1987). Others have used skewing to discuss source-tract interaction (e.g., Guérin, 1983; Cranen and Boves, 1985b). By using the Rothenberg mask with the DMM it seemed possible to shed more light on the physical mechanism resulting in the skewing.

A. Method

Figure 3 shows a diagram of the Rothenberg mask, model MA-1D, mounted on the baffle at the open end of the DMM. The foam gasket supplied with the mask and silicone sealant were used to seal the mask to the flat baffle. Electret microphones, used to measure the pressure gradient across the mask, Δp_{mask}, were 1 cm apart, with the mask midway between them. (Note: the same microphones were used on either side of the mask as were used to make the in-duct pressure-probe measurements. Details of these microphones are given in Barney *et al.*, 1999.) Another microphone, located at 45 deg, $r=60$ cm, recorded the radiated pressure signal, p_r. For all experiments the volume flow rate, measured by rotameter, and the accelerometer trace on one shut-

ter were recorded. Zero-flow recordings (in which the shutters were driven at 80 Hz but the air compressor was off so that no air flowed through the model) were used to remove shutter noise from signals, as described in Barney *et al.* (1999), Sec. II A, and Barney (1995). The signals for a given experimental setup were acquired simultaneously on all four channels of an analog-to-digital converter, that is, with no multiplexing. In setup 1, $\Delta p_{\text{mask}}, p_r$ were measured in addition to one accelerometer trace. In setup 2, two pressures were measured along the wall of the duct, at $x=4$ and $x=14$ cm from the shutters; in addition to p_4, p_{14}, the radiated pressure p_r and one accelerometer trace were measured. In setup 3, the hot wire anemometer was inserted into the center of the duct at $x=14$ cm, and u_{14}, as well as p_r and both accelerometer traces, were measured.

These measurements were then used to obtain two estimates of the volume velocity at the shutters, referred to as $\hat{U}_m(0)$ and $\hat{U}_d(0)$, where the subscript denotes the method of estimation and the argument denotes the x coordinate of the estimate. The first estimate, $\hat{U}_m(0)$, was made using classical inverse filtering. First, five cycles of Δp_{mask} were averaged and scaled by the mask screen resistance to obtain U_{mask}. Then U_{mask} was filtered using second-order Bessel filters; they were used twice (with the signal going forward and then backward) to eliminate phase distortion and therefore effectively formed a fourth-order filter. [The solid line in Fig. 7 (top graph) shows the amplitude of each harmonic of the radiated pressure measured with the mask in place, for one flow rate. Two formants can be seen, centered at the 5th harmonic (corresponding to 400 Hz) and the 10th harmonic (800 Hz). Please see Barney *et al.* (1999) for plots of the radiated pressure at the other flow rates.]

By setting the center frequency of the filters to 400 Hz and then 800 Hz, the first and then second formant were removed, resulting in the first estimate of the volume velocity at $x=0$, $\hat{U}_m(0)$. From p_4, p_{14}, u_{14}, the ''in-duct'' measurements, we derived the second estimate of the volume velocity, referred to as $\hat{U}_d(0)$. A detailed derivation is given in the companion paper (Sec. III A) and summarized here. First, u_{14} measured with the hot wire is the total velocity at $x=14$ cm, consisting of three components:

$$u_{14}=v+u_a(14)+u_n(14), \tag{1}$$

where $v=$mean flow velocity, and is derived from the hot wire measurements; $u_a(14)=$the fluctuating acoustic particle velocity, and is derived from p_4 and p_{14}; and $u_n(14)=$the fluctuating nonacoustic velocity, and is computed using Eq. (1) once v and $u_a(14)$ have been derived. These components are then separately used to estimate the corresponding components at the shutters ($x=0$). The mean flow velocity remains the same since the duct has uniform area. Acoustic components propagate at the speed of sound adjusted by the mean flow rate, resulting in the estimate at each harmonic frequency of $\hat{u}_a(0,t)$. Nonacoustic components convect at the mean flow velocity:

$$\hat{u}_n(0,\,t)=u_n\left(14,\,t+\frac{14}{v}\right). \tag{2}$$

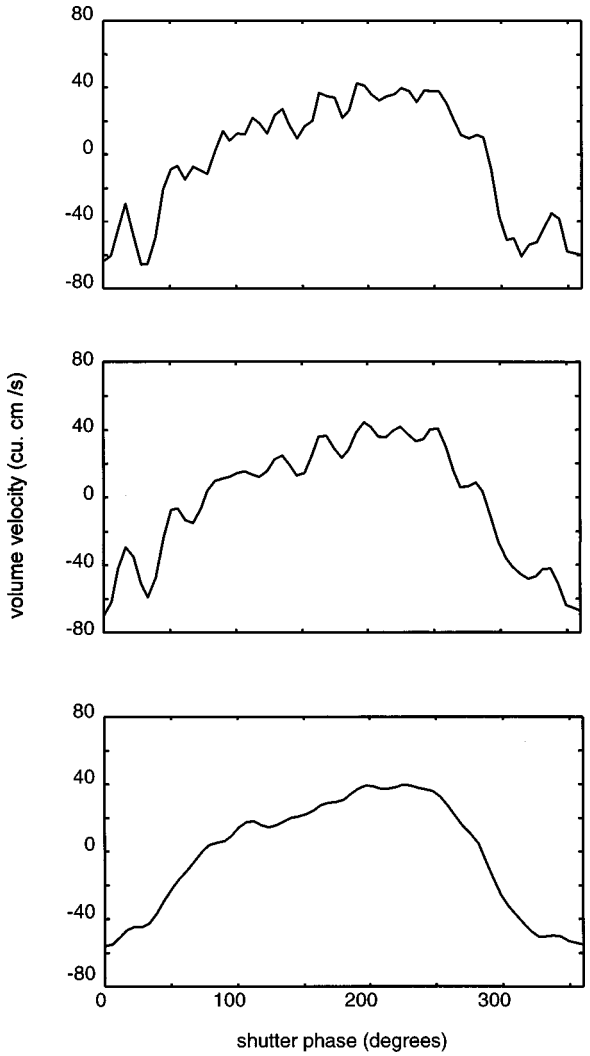

FIG. 4. One averaged cycle of volume velocity shown for two stages of inverse filtering. Top: volume velocity U_{mask} derived from average of five cycles of pressure difference at the mask. $U=400$ cm^3/s. Middle: U_{mask} with F_1 filtered out. Bottom: U_{mask} with F_1, F_2 filtered out.

Note that this equation implies an assumption of frozen vorticity, i.e., the nonacoustic components of the velocity do not change in amplitude or phase as they are convected by the mean flow. The validity of this assumption will be discussed in Sec. II C. Thus the desired estimate of the volume velocity at the shutter exit plane is:

$$\hat{U}_d(0)=A_{\text{duct}}[v+\hat{u}_a(0,\,t)+\hat{u}_n(0,\,t)]. \tag{3}$$

The same set of measurements was used to investigate the effect of the mask by comparing the in-duct measurements made with and without the mask in place, and to estimate the measured radiated pressure, p_r, in two ways. For the acoustic prediction, p_4 and p_{14}, measured with the mask in place, were used, and for the acoustic and nonacoustic prediction, p_4, p_{14}, u_{14}, measured with the mask in place, were used. The methods are described in Secs. III C and V B of Barney *et al.* (1999).

B. Results

Figure 4 demonstrates the result of inverse filtering at one mean volume flow, $U=400$ cm^3/s. The volume velocity

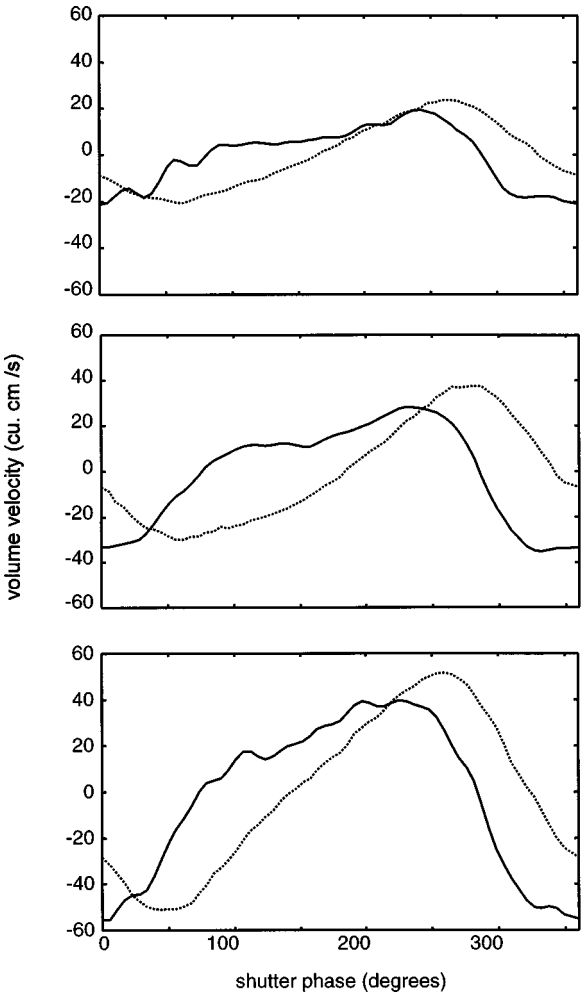

FIG. 5. Volume velocity at $x=0$ cm, estimated by two means: solid line: $\hat{U}_m(0)$, the inverse filtered mask velocity, as demonstrated in Fig. 4. Dotted line: $\hat{U}_d(0)$, predicted from in-duct measurements p_4, p_{14}, u_{14}. Top, mid, bottom graphs correspond, respectively, to $U=200,\ 300,\ 400$ cm^3/s.

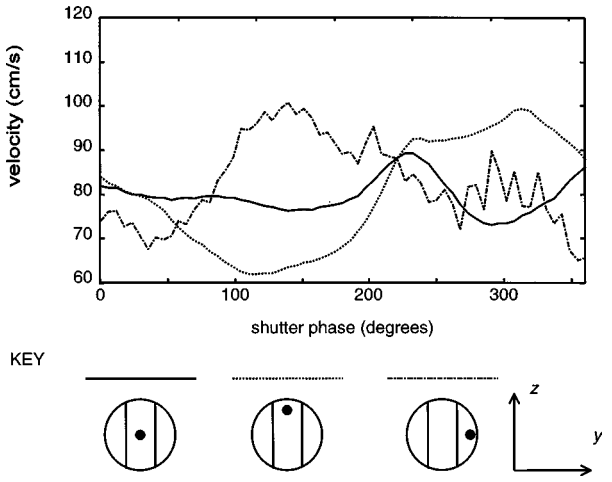

FIG. 6. Hot wire velocities at $x=1$ cm, three positions within tract, as a function of shutter phase. Each signal is averaged over five shutter cycles. Positions in the plane relative to opening between shutters indicated diagrammatically below. Exact coordinates, given in terms of indicated y, z axes (x axis is out of the page), are, in cm: solid trace, $y,z=(0,0)$; dotted, (0,0.6); dash-dotted, (0.6,0). Duct diameter is 1.7 cm. $U=200$ cm^3/s.

derived from the pressure drop across the mask is shown together with the result when just the first formant, and then the first two formants, are filtered out. With the first two formants removed the signal looks smooth, fitting the ripple minimization criterion normally used in inverse filtering. Note the mean value is 0, since the frequency range of the electret microphones does not extend to 0 Hz.

Figure 5 shows $\hat{U}_m(0)$ and $\hat{U}_d(0)$ contrasted for each of three volume velocities. In all three cases the main difference is in the amount of skewing of the pulse. The prediction from the in-duct measurements, $\hat{U}_d(0)$, is more skewed than the prediction from the mask measurements, $\hat{U}_m(0)$.

We have expressed the in-duct estimate $\hat{U}_d(0)$ as a volume, not particle velocity, to facilitate comparison with the mask estimate $\hat{U}_m(0)$. We would ideally like to compare both estimates with the measured volume velocity at $x=0$, according to the definition of the glottal waveform: a spatial average of all particle velocities at the glottal exit plane, multiplied by the area of the duct. The three hot wire velocities we have measured at $x=1$ cm are the closest we have come to that ideal. However, we could not measure them simultaneously without distorting the flow, and thus we cannot meaningfully combine them to form a single ''glottal'' volume velocity. Let us take a close look at these signals and consider some methodological aspects before we return to this point.

Figure 6 shows hot wire velocities obtained by averaging five cycles of the signal measured by a hot wire positioned at $x=1$ cm, at three locations in that plane, shown at the bottom of the figure with respect to the gap between the shutters. Note that the Rothenberg mask was not in place when these signals were measured; later on we will present a direct comparison of hot wire signals measured with and without the mask. For the present, we note that *if* there is a difference between velocity signals measured near the shutters with or without the mask, we would ideally like to be able to use the signals measured at the mask to predict the signals present near (or at) the shutters *without* the mask.

The velocities shown were averaged because of the large cycle-to-cycle variation observed at locations near the shutters. (Remember that five shutter cycles of the mask pressure drop were averaged before the inverse filtering was performed.) Of the three signals shown here, that measured at $x,y,z=(1.0,\ 0.6,\ 0)$, that is, not in line with the ''glottis,'' had more random variation prior to averaging; that measured in the center of the duct showed the most variation between successive averages, consistent with the idea of a flapping jet.

It is clear that these three hotwire signals are highly dissimilar. As already discussed, we cannot combine them to form a volume velocity. And, while we can convert the volume velocities $\hat{U}_m(0)$ and $\hat{U}_d(0)$ to signals with dimensions of particle velocity (by dividing by the duct area), we cannot decompose them into individual particle velocities at particular points within the duct. Clearly, none of the hot wire velocities is similar in shape to the estimated volume velocities

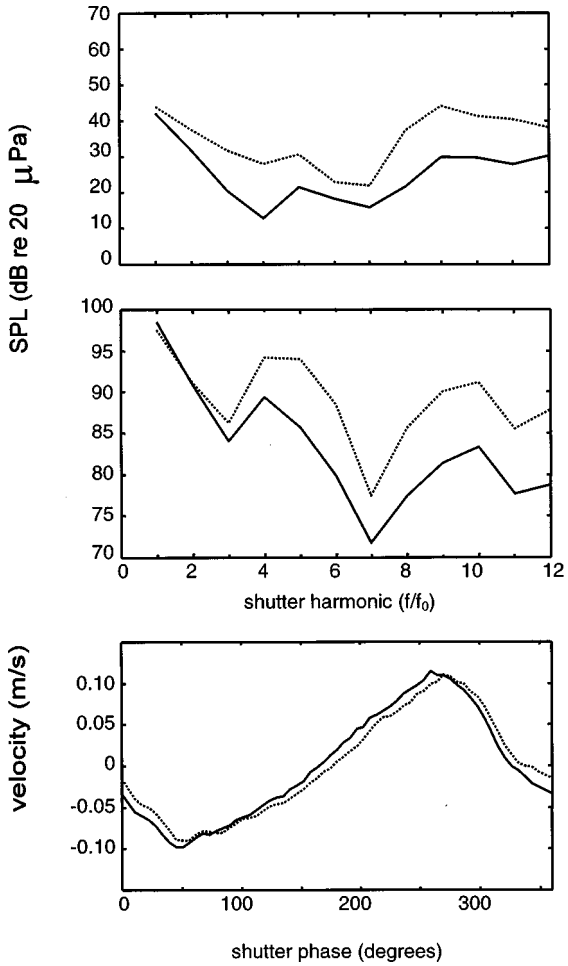

FIG. 7. Signals measured with (solid line) and without (dotted) Rothenberg mask. $U=200$ cm^3/s. Top: radiated pressure; middle: pressure at $x=14$ cm; bottom: hotwire velocity at $x=14$ cm.

of Fig. 5. $\hat{U}_m(0)$ and $\hat{U}_d(0)$ are both more similar to a skewed glottal area function.

Figure 7 shows three signals measured with and without the Rothenberg mask: the radiated pressure, the in-duct pressure p_{14}, and the hot wire velocity u_{14}. For both the radiated and in-duct pressures, sound pressure levels are lower with the mask in place; the amount varies with the harmonic, but at some harmonics the difference is as much as 20 dB. First formant frequency is lower with the mask for the in-duct pressure, consistent with Rothenberg's observations. The in-duct particle velocity is changed much less; the shutter phase of the maximum amplitude is advanced with the mask by approximately 10 deg. We can thus be somewhat reassured on the point raised with regard to Fig. 6; the hot wire signals at $x=1$ cm may vary with the mask in place, but certainly not enough to make them similar to either estimated glottal waveform. We do note, however, that the direction of the phase shift induced at $x=14$ cm by the mask is consistent with that observed by flow visualization when a long impedance tube was added to the duct (Shadle *et al.*, 1991).

Figure 8 compares the predicted with measured radiated sound pressure, p_{rad}, using both predictions, with and without the mask. The acoustic-only prediction underpredicts in the vicinity of $F2$ both with and without the mask. The

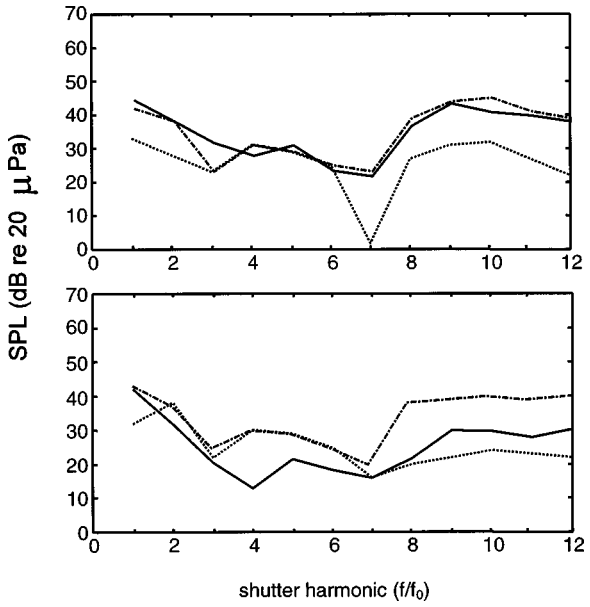

FIG. 8. Measured and predicted radiated sound pressure vs shutter harmonic, without (top) and with (bottom) Rothenberg mask on the DMM, $U=200$ cm^3/s. Solid line: measured p_r. Dotted line: $\hat{p}_r$, acoustic prediction. Dashed line: $\hat{p}_r$, acoustic and nonacoustic prediction.

acoustic plus nonacoustic prediction predicts well without the mask, but overpredicts at all harmonics with the mask.

C. Discussion

The actual flow at 1 cm, very near the shutters, varies across the duct and is not periodic at any position in the plane. Inverse filtering the signal recorded at the Rothenberg mask results in a signal more related to the area function of the shutters, and somewhat resembling glottal waveforms derived for human subjects, than it does any of the signals at 1 cm.

The mask affects the pressure field in the duct and the radiated pressure. The component of the radiated sound associated with vortical flow at the duct exit is reduced. The phase delay of the estimated glottal volume velocity relative to A_g differs if derived from p only (as from the mask pressures) or from p,u (in-duct measurements). This difference affects the skewing of the estimated waveform significantly, and its amplitude slightly.

These differences have been borne out by a recent study by Fahas (1997), who used a mechanical model to evaluate the accuracy of estimates of the flow through the glottis or any tract constriction. The model incorporated different glottal shapes, including driven ''vocal folds,'' false folds, and a supraglottal constriction. They put a Rothenberg mask on the model and used its output plus the orifice equation to evaluate estimates of constriction areas so derived. However, they found that the mask changed the airflow slightly and the pressure upstream of any constriction significantly.

It could be argued that one of the inverse-filtered estimates of the volume velocity at $x=0$ is equivalent to the classic glottal waveform. We cannot directly measure enough velocities to estimate such a glottal waveform without destroying the flow pattern at the shutters. However, the clear differences between the hot wire velocities at x

$=1$ cm suggest that the flow in that plane is complicated in a way that lends support to the flow dipole source proposed by McGowan (1988). Yet no information about the flow mechanism underlying such a source can be obtained from either of the one-dimensional prediction methods investigated here.

At the open end of the duct, we know that the mask changes the reflection coefficient, because the in-duct acoustic field is changed. We know that the mask affects the radiation of the acoustic component because we can no longer correctly predict p_r in the vicinity of the first formant, and we have no evidence that the nonacoustic field is suddenly playing a part in that frequency range. It is known that screens attenuate acoustic and nonacoustic fields, especially in the presence of mean flow (Taylor and Batchelor, 1949). It is probable that the mask transfers some of the energy in the acoustic field to heat.

We also know that the mask affects the nonacoustic field, because p_r differs in the region where that field dominated, $8\,f_0 \leqslant f \leqslant 12\,f_0$. The mask must be attenuating the nonacoustic field, presumably by destroying vortices, since p_r is overpredicted with the mask in place; this attenuation must contribute to the pressure drop across the mask, since the estimates of volume velocity at the shutters agree except for skewing.

The estimates $\hat{U}_m(0)$ and $\hat{U}_d(0)$, the hot wire velocity measured mid-duct at $x=1$ cm, and the flow visualization results of Shadle *et al.* (1991) all indicate that the pulse of flow through the shutters is delayed with respect to $A_g(t)$. Since each prediction or estimate suggests a different amount of skewing, it appears that the mask could be used to estimate the direction of change in skewing (but not absolute amount of skewing) as a result of change in voice parameters.

Our estimate $\hat{U}_d(0)$ was based on a frozen vorticity assumption which Fig. 5 in Barney *et al.* (1999) suggests to be invalid, at least from $x=0$ to 4 cm. This may explain in part the mismatch between $\hat{U}_d(0)$ and the hot wire velocities at $x=1$ cm. On the other hand, the estimate $\hat{U}_m(0)$ treats any vorticity that has contributed to Δp_{mask} as an acoustic signal, transfering it to $x=0$ at the speed of sound rather than at the convection velocity. This may be a more problematic assumption when inverse-filtering speech with its time-varying mean flow rate than when dealing with the static flow rate signals analyzed here.

Why were these differences caused by the mask not noted in the earlier mask calibration studies? As noted above, Rothenberg (1973) used a mechanical tract model, with a ''glottal pulse'' generator (a siren) at one end and a Rothenberg mask at the other, to check on the effect of the mask. He reported that the presence of the mask had little effect on the radiated sound. However, he measured the volume velocity output by the siren by placing a screen of known resistance between the siren and the entrance to the tract. The screen was thus ideally placed to reduce vorticity throughout his model tract. This seems a plausible explanation for the difference in our results.

In our studies using the mask with the DMM the microphones used to measure the pressure gradient across the mask were not sensitive down to 0 Hz. One advantage claimed for the Rothenberg mask has been that, by collecting all of the flow out of the mouth, and measuring the dc component, one thereby is able to measure the amount of glottal leakage. But, as has been pointed out before (Davies *et al.*, 1993; Barney, 1995), it is fundamental to our model of flow in the duct that the acoustic and nonacoustic components travel from glottis to mask with a significant difference in propagation velocity. Any steady flow ''leaking'' through the glottis, and any vortices, will travel at the local mean flow velocity; the acoustic disturbance will travel at the speed of sound. For volume velocities and tract area functions typical of vowel phonation, the difference is considerable: glottis-to-lip travel time when $U=200$ cm^3/s and average tract area$=2$ cm^2 is 170 ms at the local mean flow velocity, and 0.5 ms at the speed of sound. In the DMM, the range of mean flows used gives travel times for vortices of between 100 and 200 ms. Mean and vortical flow and sound generated near the glottis simultaneously do not arrive at the mask at the same time. This discrepancy is likely to be most discernible when inverse filtering is used on transients.

III. CONCLUSION

Comparison of the Dynamic Mechanical Model (DMM) to the human vocal tract during phonation has revealed that the DMM is similar to a human vocal tract phonating in a very weak low-frequency falsetto. Behavior of the air in the tract seems roughly the same as in the DMM.

The DMM provides evidence of the existence of a vortex train, and significant sound generation by the interaction of that vortex train with the duct boundaries, especially away from the first formant. The consistency between velocity field measurements in the vocal tract and the DMM suggest that it would be wise to investigate whether such a nonacoustic field has significant effect on sound generation during phonation. Note that the absence of vortical flow contributions to the radiated field at the first formant in the DMM does not necessarily mean that such contributions will be absent from the radiated field of the vocal tract's first formant.

In the DMM contributions to the radiated pressure generated by the vortical flow at the open end of the duct were identified; in the human vocal tract, such contributions could occur at any abrupt area change.

The Rothenberg mask attenuates both acoustic and nonacoustic fields, and thereby significantly reduces the sound generated by vortical flow.

The pressure difference measured at the mask at one time, and the volume velocity derived from it, probably contain a number of contributions, not all of which started at the glottis simultaneously.

What can we conclude about inverse filtering? The glottal waveform obtained differs greatly from actual velocities measurable near the glottis, but provided a consistent method is used, changes in the glottal waveform are related to changes in the glottal area function and therefore to changes in signals such as the EGG. It is more problematic, however, to relate the glottal waveform obtained by use of the Rothenberg mask to the radiated pressure, since the mask changes

the acoustic field and the radiated pressure significantly. Further, to attempt to relate the glottal waveform directly to detailed vocal fold motion, or to explain its shape by referring to parameters physically measurable near the glottis, seems to be overgeneralizing the model on which it is based. In particular, the whole issue of skewing of glottal pulses should be looked at further. Finally, analysis of transients with the Rothenberg mask should be approached with care because of the significant differences in glottis-to-mask travel time for mean flow and nonacoustic components, on the one hand, and acoustic components, on the other.

And finally, it can be said that Teager's work has generated discussion and experiment. It appears to be correct that vortices are generated in the vocal tract as a result of phonation, and that they do generate significant sound. They do not appear to be the only, nor the principal source, of sound, however. Further, Teager proposed standing vortices, whereas in the DMM it appears that the vortices convect along the duct. These details are less important than the main conclusion, which is that one needs an underlying theoretical aeroacoustic model in order to interpret measurements, and in particular, to assess the degree to which the vorticity may contribute to the radiated sound field.

ACKNOWLEDGMENTS

This article is based on a paper given at the May 1997 International Conference on Voice Physiology and Biomechanics. The authors would like to thank Dr. Martin Rothenberg for helpful discussions concerning his calibration experiments, Dr. Xavier Pelorson for helpful discussions and in particular bringing the Fahas thesis to our attention, and Dr. Bert Cranen for providing permission to generate Fig. 1 from his and Dr. Lou Boves' original data. The authors would also like to thank Professor Phil Doak and three anonymous reviewers for extensive comments on an earlier version of this manuscript. A Leverhulme Emeritus Fellowship to the third author provided partial support for this research.

Alipour, F., and Scherer, R. C. (**1995**). ''Pulsatile airflow during phonation: An excised larynx model,'' J. Acoust. Soc. Am. **97**, 1241–1248.

Alipour, F., Fan, C., and Scherer, R. C. (**1996**). ''A numerical simulation of laryngeal flow in a forced-oscillation glottal model,'' Comput. Speech Lang. **10**, 75–93.

Badin, P., Karlsson, I., and Hertegård, S. (**1990**). ''Notes on the Rothenberg mask,'' STL-QPSR **1**, 1–7.

Barney, A. (**1995**). ''Fluid flow in a dynamic mechanical model of the larynx,'' Ph.D. thesis, Department of Electronics and Computer Science, University of Southampton.

Barney, A., Shadle, C. H., and Davies, P. O. A. L. (**1999**). ''Fluid flow in a dynamic mechanical model of the vocal folds and tract. I. Measurements and theory,'' J. Acoust. Soc. Am. **105**, 444–455.

Beranek, L. (**1954**). *Acoustics* (McGraw-Hill, New York).

Berke, G. S., Moore, D. M., Monkewitz, P. A., Hanson, D. G., and Gerratt, B. R. (**1989**). ''A preliminary study of particle velocity during phonation in an in vivo canine model,'' J. Voice **3**, 306–313.

Cranen, B., and Boves, L. (**1985a**). ''Pressure measurements during speech production using semiconductor miniature pressure transducers: Impact on models for speech production,'' J. Acoust. Soc. Am. **77**, 1543–1551.

Cranen, B., and Boves L. (**1985b**). ''The acoustic impedance of the glottis-modeling and measurements,'' in *Vocal Fold Physiology*, edited by T. Baer, C. Sasaki, and K. Harris (College-Hill, San Diego), pp. 203–218.

Davies, P. O. A. L. (**1996**). ''Aeroacoustics and time varying systems,'' J. Sound Vib. **190**, 345–362.

Davies, P. O. A. L., Barney, A. M., and Shadle, C. H. (**1995**). ''Aeroacoustic sources in a vocal tract model,'' Proc. 15th ICA **3**, 23–26.

Davies, P. O. A. L., McGowan, R. S., and Shadle, C. H. (**1993**). ''Practical duct-flow acoustics applied to the vocal tract,'' in *Vocal Fold Physiology*, edited by I. Titze (Singular, San Diego), pp. 93–142.

Fahas, S. (**1997**). ''Mésures aérodynamiques sur des maquettes du conduit vocal: Application au masque de Rothenberg,'' Master's thesis, Ecole de Physique de Grenoble, Univ. J. Fourier.

Fant, C. G. M., Liljencrants, J., and Lin, Q. (**1985**). ''A four-parameter model of glottal flow,'' STL-QPSR **4**, 1–13.

Flanagan, J. L. (**1972**). *Speech Analysis Synthesis and Perception* (Springer-Verlag, Berlin).

Guérin, B. (**1983**). ''Effects of the source-tract interaction using vocal fold models,'' in *Vocal Fold Physiology*, edited by I. Titze and R. C. Scherer (Denver Center for the Performing Arts, Denver), pp. 482–489.

Hertegård, S., and Gauffin, J. (**1992**). ''Acoustic properties of the Rothenberg mask,'' STL-QPSR **2-3**, 9–18.

Hirose, H., and Niimi, S. (**1987**). ''The relationship between glottal opening and the transglottal pressure differences during consonant production,'' in *Vocal Fold Physiology*, edited by T. Baer, C. Sasaki, and K. Harris (College-Hill, San Diego), pp. 381–390.

Hirschberg, A. (**1992**). ''Some fluid dynamic aspects of speech,'' Bull. Communication Parlée **2**, 7–30.

Hirschberg, A., Pelorson, X., Hofmans, G. C. J., van Hassel, R. R., and Wijnands, A. P. J. (**1996**). ''Starting transient of the flow through an in-vitro model of the vocal folds,'' in *Vocal Fold Physiology*, edited by P. Davis and N. Fletcher (Singular, San Diego), pp. 31–46.

Holmberg, E. B., Hillman, R. E., and Perkell, J. S. (**1988**). ''Glottal airflow and transglottal air pressure measurements for male and female speakers in soft, normal, and loud voice,'' J. Acoust. Soc. Am. **84**, 511–529.

Iijima, H., Miki, N., and Nagai, N. (**1992**). ''Glottal impedance based on a finite element analysis of two-dimensional unsteady viscous flow in a static glottis,'' IEEE Trans. Signal Process. **40**, 2125–2135.

Kaiser, J. F. (**1983**). ''Some observations on vocal tract observation from a fluid flow point of view,'' in *Vocal Fold Physiology*, edited by I. Titze and R. Scherer (Denver Center for the Performing Arts, Denver), pp. 358–386.

Karlsson, I. (**1992**). ''Analysis and synthesis of different voices with emphasis on female speech,'' Dissertation, Department of Speech Communication and Music Acoustics, Royal Institute of Technology, Stockholm, Sweden.

Kiritani, S., Fukawa, H., Imagawa, H., Imaizumi, S., and Saito, S. (**1987**). ''Measurement of air flow pattern through a mechanically driven oscillating slit: A preliminary report,'' Ann. Bull. RILP **21**, 1–8.

Koike, Y. (**1981**). ''Sub-land supraglottal pressure variation during phonation,'' in *Vocal Fold Physiology*, edited by K. N. Stevens and M. Hirano (University of Tokyo, Tokyo), pp. 181–191.

Koike, Y., and Hirano, M. (**1973**). ''Glottal-area time function and subglottal-pressure variation,'' J. Acoust. Soc. Am. **54**, 1618–1627.

Koike, Y., Imaizumi, S., Kitano, Y., Kawasaki, H., and Hirano, M. (**1983**). ''Glottal area time function and supraglottal pressure variation,'' in *Vocal Fold Physiology*, edited by D. M. Bless and J. H. Abbs (College-Hill, San Diego), pp. 300–306.

Liljencrants, J. (**1991**). ''Numerical simulations of glottal flow,'' in *Vocal Fold Physiology: Acoustic, Perceptual and Physiological Aspects of Voice Mechanics*, edited by J. Gauffin and B. Hammarberg (Singular, San Diego), pp. 99–104.

Liljencrants, J. (**1995**). ''Airflow visualizations in a model of the glottal passage,'' in Speech MAPS Year 3 Report, Vol. 2, WP1-From speech signal to acoustic sources, edited by C. H. Shadle, Del 26, pp. 26–35.

McGowan, R. S. (**1988**). ''An aeroacoustic approach to phonation,'' J. Acoust. Soc. Am. **83**, 696–704.

Mongeau, L., Franchek, N., Coker, C. H., and Kubli, R. A. (**1997**). ''Characteristics of a pulsating jet through a small modulated orifice, with application to voice production,'' J. Acoust. Soc. Am. **102**, 1121–1133.

Pelorson, X., Hirschberg, A., van Hasssel, R. R., and Wijnands, A. P. J. (**1994**). ''Theoretical and experimental study of quasisteady-flow separation within the glottis during phonation. Application to a modified two-mass model,'' J. Acoust. Soc. Am. **96**, 3416–3431.

Rothenberg, M. (**1973**). ''A new inverse-filtering technique for deriving the glottal airflow waveform during voicing,'' J. Acoust. Soc. Am. **53**, 1632–1645.

Rothenberg, M. (**1981**). ''Acoustic interaction between the glottal source

and the vocal tract,'' in *Vocal Fold Physiology*, edited by K. N. Stevens and M. Hirano (University of Tokyo, Tokyo), pp. 305–328.
Rothenberg, M. (**1987**). ''Cosi fan tutte and what it means, or Nonlinear source-tract acoustic interaction in the soprano voice and some implications for the definition of vocal efficiency,'' in *Vocal Fold Physiology*, edited by T. Baer, C. Sasaki, and K. Harris (College-Hill, San Diego), pp. 254–269.
Shadle, C. H., Barney, A. M., and Thomas, D. W. (**1991**). ''An investigation into the acoustics and aerodynamics of the larynx,'' in *Vocal Fold Physiology*, edited by J. Gauffin and B. Hammarberg (Singular, San Diego), pp. 73–82.
Smith, M. E., Green, D. C., and Berke, G. S. (**1991**). ''Pressure-flow relationships during phonation in the canine larynx,'' J. Voice **5**, 10–17.
Sundberg, J., and Gauffin, J. (**1978**). ''Waveform and spectrum of the glottal voice source,'' STL-QPSR **2-3**, 35–50.
Taylor, G. I., and Batchelor, G. K. (**1949**). ''The effect of a wire gauze on small disturbances in a uniform stream,'' Q. J. Mech. Appl. Math. **2**, 1–29.
Teager, H. M. (**1980**). ''Some observations on oral air flow during phonation,'' IEEE Trans. Acoust., Speech, Signal Process. **25**, 599–601.
Teager, H. M., and Teager, S. M. (**1983a**). ''The effects of separated air flow on vocalization,'' in *Vocal Fold Physiology*, edited by D. M. Bless and J. H. Abbs (College-Hill, San Diego), pp. 124–143.
Teager, H. M., and Teager, S. M. (**1983b**). ''Active fluid dynamic voice production models, or there is a unicorn in the garden,'' in *Vocal Fold Physiology*, edited by I. Titze and R. Scherer (Denver Center for the Performing Arts, Denver), pp. 387–401. [Note: copyright date is 1983, printing date is 1985.]
Teager, H. M., and Teager, S. M. (**1985**). ''A phenomenological model for vowel production in the vocal tract,'' in *Speech Science: Recent Advances*, edited by R. G. Daniloff (College-Hill, San Diego), pp. 73–109.
Teager, H. M., and Teager, S. (**1990**) ''Evidence for nonlinear sound production mechanisms in the vocal tract,'' in *Speech Production and Speech Modelling*, edited by W. J. Hardcastle and A. Marchal (Kluwer Academic, London), pp. 241–262.

The impact of early onset otitis media on babbling and early language development

Susan Rvachew[a)]
Speech-Language Pathology, Alberta Children's Hospital, Calgary, Alberta, Canada

Elzbieta B. Slawinski
Department of Psychology, University of Calgary, Calgary, Alberta, Canada

Megan Williams and Carol L. Green
Audiology, Alberta Children's Hospital, Calgary, Alberta, Canada

(Received 23 April 1998; accepted for publication 11 September 1998)

Numerous studies have shown that otitis media (OM) during infancy has a negative impact on language development later in life. Few studies have examined the effect of OM on linguistic and prelinguistic behavior during infancy. The purpose of this study was to investigate the impact of OM on the development of canonical babble in children who experienced at least one episode during the period birth through 6 months of age, in comparison with children who did not experience OM during this period. The results show a consistently lower rate of canonical syllable production among children with early onset OM, when compared to children with later onset OM, during the period 6 through 18 months of age. In addition, a relationship between canonical babbling ability and expressive vocabulary size was observed at 18 months of age. © *1999 Acoustical Society of America.* [S0001-4966(99)00601-3]

PACS numbers: 43.70.Ep, 43.71.Ft [AL]

INTRODUCTION

The term *otitis media* (OM) covers a variety of conditions that involve the presence of fluid within the middle-ear space. Each episode of acute otitis media is accompanied by a period of effusion which may last weeks or months. Klein (1983) found that effusion persisted for a month following identification of an acute infection in 40% of cases. Mild to moderate hearing loss may occur during any of the possible acute and nonacute phases of the disease (Fria *et al.*, 1985).

OM places children at risk for a number of developmental and behavioral sequels that may persist long past the resolution of the middle-ear condition. Many studies have found relatively poor performance on tests of speech perception and central auditory processing among children with OM histories, in comparison with children who have not experienced recurrent or chronic OM (Menyuk, 1986; Clarkson *et al.*, 1989; Gravel and Wallace, 1992; Welsh *et al.*, 1983). Children with positive OM histories have particular difficulty with the discrimination of speech stimuli under noise conditions. Difficulties with the perception of speech sounds are correlated with speech production disorders for some children (Broen *et al.*, 1983; Rvachew and Jamieson, 1995). Between-group differences with respect to phonological abilities are consistently found for children older than age 3 years who do or do not have histories of early OM (Chalmers *et al.*, 1989; Roberts *et al.*, 1988). Many studies have identified an effect of OM on other aspects of language development such as vocabulary, morphology, syntax, and narrative abilities (e.g., Feagans *et al.*, 1987; Klein *et al.*, 1988).

Although many studies indicate a negative relationship between OM and language skills, these findings are not unequivocal, as a significant body of contrary research findings exists. For example, Webster *et al.* (1989) assessed school-age children and found no relationship between chronic OM and measures of brainstem-evoked responses, speech perception in noise, reading, spelling, phonics, or behavior. Grievink *et al.* (1993) found no significant effect of OM history on preschool children's performance on a broad battery of speech and language tests. In the past, the degree of confusion in the research findings was attributed to poor research methodology (Ventry, 1980; Paradise, 1983), but research regarding OM outcomes has become increasingly sophisticated in recent years.

It is becoming clear that the differences in findings across studies can be attributed to the complexity of the relationships among the relevant variables. Some of these variables are assumed to play a causal role while other variables help to explain some of the variation in the observed relationship between OM and outcomes. A number of intervening variables have been identified, including the following: degree of hearing impairment (Friel-Patti and Finitzo, 1990); the illness experience (Roberts and Schuele, 1990); mother–child interaction (Black *et al.*, 1988; Freeark *et al.*, 1992; Wallace *et al.*, 1996); socioeconomic status of the child's family (Teele *et al.*, 1984); and medical management of OM (Hubbard *et al.*, 1985). Two additional intervening variables are of particular relevance to the research reported here and will be discussed in more depth below.

Friel-Patti (1990) suggests that the relationship between OM, hearing, and language changes over time. Most studies that administer the same battery of tests to the same sample at different ages find age effects in the pattern of performance of the OM group. Changes in performance and pat-

a)Electronic mail: rvachew@acs.ucalgary.ca

tern of deficit over time can be expected as a consequence of the changing expectations for language performance with age. For example, Roberts *et al.* (1988) found a relationship between OM history during the first three years of life and phonological development; however, this relationship was observed only for older children, aged 4.5 to 8 years. Intersubject variation in phonological skills among 3-year-olds appeared to mask the relationship between OM and phonological development for the younger children. This finding highlights the importance of matching outcome measures to the developmental challenges that are important to the age group represented by the research subjects.

The final intervening variable to be considered here is age of onset of OM. Prospective studies have found that the risk of negative speech and language outcomes increases with earlier age of onset and a greater number of episodes of middle-ear effusion (Feagans *et al.*, 1987; Friel-Patti and Finitzo, 1990; Gravel and Wallace, 1992; Klein *et al.*, 1988; Menyuk, 1986; Roberts *et al.*, 1988). For example, Teele *et al.* (1984) found that time spent with OM during the first 12 months of life was strongly correlated with language performance at age three years; in contrast, the amount of OM during later years did not explain the variance in language outcomes. A recent study also shows that the presence of OM during the period two through four years of age does not place children at risk for language deficits (Grievink *et al.*, 1993).

Otitis media during infancy may interfere with certain prelinguistic skills that are critical to the normal development of linguistic abilities at later ages. Recent research indicates that there are dramatic changes in speech perception abilities during the prelinguistic period, as the infant moves from language-general to language-specific processing of speech. These developmental changes in speech perception abilities are fully dependent upon appropriate auditory input (e.g., Jusczyk, 1992; Kuhl *et al.*, 1992; Polka and Werker, 1994). During the same period, the infant moves through a predictable series of stages to gain considerable skill in the production of speech sounds (e.g., Oller, 1980; Roug *et al.*, 1989). These changes in speech production ability are also dependent upon auditory input, as evidenced by cross-language studies (de Boysson-Bardies *et al.*, 1989), and by studies of children with severe hearing losses (Kent *et al.*, 1987; Eilers and Oller, 1994; Stoel-Gammon and Otomo, 1986). Specifically, severe hearing impairment leads to significant delays in the emergence of canonical babble and a markedly restricted vowel repertoire.

Two recent case studies suggest a relationship between early onset OM, babbling, and early language development. Donahue (1993) reported a diary study of a child who demonstrated delays in both phonological and expressive language skills, secondary to chronic otitis media during the first year of life. Another case study documented phonetic inventories for a boy who underwent bilateral tympanoplasty tube insertion before 11 months of age for treatment of chronic OM (Robb *et al.*, 1993). Assessments conducted at monthly intervals revealed a progressive reduction of his phonetic repertoire over time, and an unusually low consonant–vowel ratio throughout the course of the study.

The preceding review indicates that early-onset OM can have a negative impact on speech and language development. This effect may have its origin in infancy by disrupting the acquisition of certain prelinguistic skills that are critical to the normal development of linguistic abilities at later ages. During the first year of life, normal-hearing infants develop a language-specific set of perceptual categories. With the emergence of canonical babble, these perceptual categories are linked to the articulatory movements required to produce language-specific speech sounds in a variety of phonetic contexts. This system of perceptual–articulatory phonetic categories is largely developed prior to the infant's expressive use of true words and provides part of the foundation for language development.

The hypothesis underlying the research to be reported here is that early-onset OM disrupts the normal course of phonetic development. It is expected that such a disruption to phonetic development will be evident in the quality of the child's speech and speech-like productions during the period 6 through 18 months of age. This study improves on the case studies described above by using a larger sample of children and systematic assessment techniques applied at regular intervals in a prospective, longitudinal design. It is expected that speech samples recorded from infants with early-onset OM will be characterized by smaller canonical syllable ratios relative to the samples recorded from infants who did not experience OM during the first six months of life.

I. METHOD

A. Subjects

Eighteen children were referred by family physicians and community health nurses. Nine infants were reported to have had no known ear infections before age six months (although many of them experienced ear infections at a later age). The remaining 9 infants had received antibiotic treatment for at least one ear infection at or before the age of 6 months. These two groups of children will be referred to as the ''late onset (LO)'' and ''early onset (EO)'' groups, respectively. The LO group consisted of five boys and four girls, while the EO group consisted of six boys and three girls. All of the infants had unremarkable birth, developmental, and family histories at the time of referral.

All of the infants lived in two-parent homes with at least one employed parent. All parents were native speakers of Canadian English. The mean number of years of education for the mothers was 15.11 and 13.77 for the LO and EO groups, respectively. The mean number of years of education for the fathers was 14.9 and 14 for the LO and EO groups, respectively. The range across groups was 12 to 16 years of education for the mothers and 10 to 20 years of education for the fathers. These differences in years of education between groups were not found to be statistically significant [$t(1,16)=1.81$, $p=0.09$, for mothers; $t(1,16)=0.61$, $p=0.55$, for fathers].

The results of the ''general development'' subscale of the *Child Development Inventory* (Ireton, 1992) showed that all of the children were developing normally at 18 months of age.

B. Procedure

1. General procedures

All the children visited the audiology department at the Alberta Children's Hospital for approximately 1 hour at 3 month intervals between six and 18 months of age. All assessments were conducted within two weeks of the exact chronological birthdate of 6, 9, 12, 15, and 18 months, except for three instances where the assessment occurred three weeks after the birthdate (these exceptions occurred for children in the early onset group, two at 6 months and one at 12 months of age).

In most cases, the hearing and impedance measures were obtained first and a taped speech sample was obtained immediately thereafter. At each assessment the parents were asked to complete a word production checklist as a means to estimate expressive vocabulary size. Formal assessments of expressive and receptive language development were conducted during the 18-month visit. The infant's performance with respect to other areas of development was also screened during the final assessment.

The audiology assessments were conducted by the third and fourth authors, who are certified pediatric audiologists. The speech and language assessments and analysis of the speech samples were completed by the first author, a CASLPA certified speech-language pathologist.

2. Audiology assessment

Sound-field threshold testing was accomplished in an Ekoustic double-walled sound chamber with the following equipment: Interacoustics clinical audiometer (model AC 30) and DALI speakers. The infants were seated between two loudspeakers positioned at 90 deg relative to midline. Visual reinforcement audiometry (VRA) was used to assess auditory sensitivity to live voice and to warbled tones presented at 250, 500, 1000, 2000, and 4000 Hz. Lighted toys with animation were used as visual reinforcers. A response was considered positive when the subject localized toward the signal source upon presentation of the stimulus. Criterion for a threshold was met at the lowest intensity level which elicited two or more reliable head-turning responses. Middle-ear impedance measures were obtained with a GSI-33 middle ear analyzer. Tympanometry was performed using a 226-Hz probe tone. Two values produced by the instrument were recorded: peak pressure in decaPascals and tympanic membrane compliance in milliliters. At each visit, ipsilateral reflexes were attempted at 500, 1000, 2000, and 4000 Hz at the previously recorded peak pressure value.

3. Language assessments

During each assessment, the parent was asked to complete one of the five forms of the word production checklist described by Reznick and Goldsmith (1989). These checklists are equivalent forms, each containing a list of 123 words covering 20 different categories including nouns, verbs, prepositions, pronouns, and modifiers.

At the age of 18 months, the *Receptive-Expressive Emergent Language Test* (REEL-2; Bzoch and League, 1991) was administered. Although this is an interview scale, most receptive items were administered directly to the child to confirm the parent's report. The parent's report of the child's expressive language abilities was also verified through direct observation where possible.

4. Speech sample collection

The speech samples were recorded in an Ekoustic sound-treated chamber using a Sony Walkman Professional tape recorder and a Crown PZM-6D microphone. The mother was instructed to interact with her child in the usual manner. The mother and child were provided with the same set of quiet toys during each assessment (e.g., soft blocks, cloth books, pop beads, stuffed toys, a ball, and puppets). No effort was made to restrict the child's movements during recording sessions; rather, the microphone was moved when necessary so that it was within 1 to 2 ft of the child, preferably positioned with the child facing the microphone (the pressure-zone microphone used was capable of capturing almost all speech produced within the sound chamber, even when whispered). The recording session continued until the child produced at least 60 utterances that were perceived to meet the utterance selection criteria discussed below. These recording sessions typically lasted between 10 and 30 min. The infants' mothers would not consent to recording sessions longer than 30 min; consequently, infants were scheduled for a second recording session if 60 utterances could not be obtained in this time frame. This happened infrequently, usually because the infant was distressed by the tympanometric assessment procedure that always preceded the recording session.

5. Speech sample analysis procedures

a. Acoustic analyses. The speech samples were digitized using the Computerized Speech Research Environment (CSRE; Jamieson *et al.*, 1989) and the following hardware: an AST Premium 386C computer, DT2821 D/A, A/D board (12 bit), and a TTE 411 AFS amplifier and antialiasing filter. The utterances were digitized at a sampling frequency of 20 kHz and low-pass filtered at 10 kHz. These utterances were then submitted to autoregression spectral analyses using a 6.4-ms analysis window, 78-Hz frequency bands, preemphasis, and a Hanning window.

b. Utterance selection. For the purpose of this research, it was considered necessary to differentiate reflexive and nonreflexive utterance types only. Therefore, cries, grunts, burps, and other vegetative noises were excluded from analysis. The hypothesis to be considered here predicts that early-onset OM will impact on the phonetic characteristics of the infant's nonreflexive utterances with no predicted difference for babble compared with meaningful speech. In addition, previous researchers have demonstrated the phonetic similarity of meaningful and nonmeaningful speech-like utterances (Vihman *et al.*, 1985). Therefore, it was not considered necessary to differentiate these utterance types. Furthermore, the term ''speech'' will be used to refer to both meaningful and babbled speech-like utterances. Fifty consecutive utterances were selected from the tape, each meeting the following criteria: the utterance was bounded by 1 s of silence, an audible

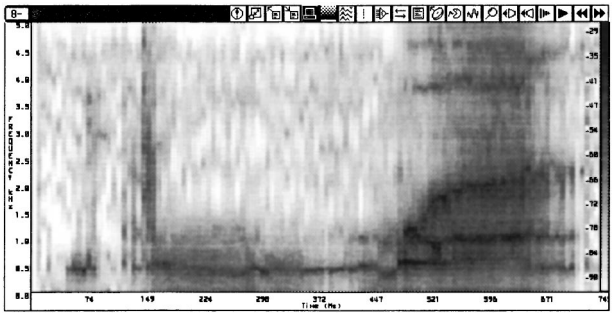

FIG. 1. Spectrogram of a two-syllable utterance ([buwa]) produced by a 6-month-old infant. The first utterance is perceived as a consonant–vowel combination but is coded as marginal syllable because the nucleus is quasiresonant. This syllable was produced with the mouth closed or almost closed throughout its articulation and thus there is little energy over 1200 Hz. The second syllable is produced with full resonance, as indicated by the strong upper-frequency formants. A smoothly changing formant transition, 92 ms in duration, is also visible and therefore this syllable is coded as canonical syllable The entire utterance would be coded as a canonical utterance.

inspiration, or adult speech; the utterance was perceived to have a ''unifying pitch contour'' (a criterion which overrode the first criterion in some instances so that two utterances were coded with less than a 1-s separation); the utterance was produced and recorded with sufficient loudness for coding; and the utterance was not so obscured by adult speech or other noise as to prevent accurate coding. In total, 4500 utterances were selected and submitted to the analyses described below.

c. Infraphonological analysis. Each utterance was coded using the criteria described in detail by Oller (1986) and in brief as follows: The OTHER category includes squeals, raspberries, growls, and yells; quasiresonant nuclei (QRN) are syllabic nasals or nasalized vowels that contain little energy over 1200 Hz; fully resonant nuclei (FRN) are vowel-like utterances with at least two measurable formants and with resonances above 1200 Hz in addition to resonances in the lower frequency range; marginal syllables (MS) are transcribed as consisting of consonant–vowel (CV) or vowel–consonant (VC) syllables, but do not meet the criteria for a canonical syllable; canonical syllables (CS) contain at least one consonant (excluding glottal stops and fricatives) joined with at least one fully resonant vowel by formant transitions between 25- and 120-ms duration.

Utterances coded as OTHER, QRN, or FRN could generally be identified by listening to the tape. All utterances that were transcribed as containing a C and V were digitized and submitted to acoustic analysis in order to differentiate MS and CS utterances and syllables. An example spectrogram of an utterance containing both an MS and CS syllable is shown in Fig. 1.

There are a number of different ways to calculate the canonical syllable ratio (CSR). The most recent studies define the CSR as the ratio of canonical syllables to total number of syllables (Eilers *et al.*, 1993). This procedure creates some problems in the coding of essentially nonsyllabic utterances, however, especially when such utterances involve the combination of more than one OTHER-type utterance. In order to avoid this problem, the two methods that involve the utterance as the basic unit of analysis were selected. This analysis yielded two outcomes for each sample: (1) a frequency count for each of the five utterance types, similar to the procedure used by Carney (1996); and (2) a canonical syllable ratio calculated by dividing the number of canonical *syllables* contained in the sample by the number of utterances, as in Oller and Eilers (1988). Any utterance that combined elements from different categories was coded as the highest utterance type represented. Therefore, any utterance containing at least one canonical syllable was coded as a CS utterance, thus, multisyllable canonical utterances might contain both canonical and noncanonical syllables. These two measures are related in that the canonical syllable ratio will increase with both the number and length of canonical utterances contained in the sample.

d. Reliability of coding for speech sample analyses. Two speech–language pathologists (SLPs) were trained to transcribe and code infant speech samples on the basis of both perceptual and acoustic analyses. The reliability coders were unaware of the investigator's judgments regarding the utterances and were blind to the subject's history of middle-ear function; however, they were aware of the infant's age at the time of recording. The samples used for reliability coding were selected at random. Two hundred and fifty utterances were transcribed and then coded using the infraphonological analysis procedures. Point-by-point agreement between the investigator and the SLP who conducted the reliability analysis was calculated for two different judgments: (1) the infraphonological classification of each utterance using all possible categories, including the individual categories grouped as OTHER (agreement=86%); and (2) the number of CS syllables when coding all MS and CS utterances (agreement=86%).

II. RESULTS

A. Audiology assessments

The age of onset of OM (as reported by the parent and confirmed by a physician) varied from 1 to 6 months for the early onset group. Four children in the late onset group experienced no identified episodes of OM during the course of the study. The remaining children in the LO group were treated for their first known ear infection between 9 and 12 months of age.

Three infants in the EO group were referred to an otolaryngologist at approximately 12 months of age, and two of these infants received bilateral myringotomies with insertion of ventilating tubes between the ages of 15 and 18 months.

Parents reported the number of times the child's physician prescribed a course of antibiotics for treatment of OM. At 6 months, the number of prescriptions was counted for the 6-month period since birth. At 9, 12, 15, and 18 months, the number of prescriptions was counted for the 3-month period since the last audiometric assessment. Parents were instructed to ask their physician to check the child's ears via otoscopy at all office visits, including well-baby checkups. They were also instructed to visit the doctor whenever they had any concerns regarding the child's ears or hearing, and to return for a checkup when a course of antibiotics was

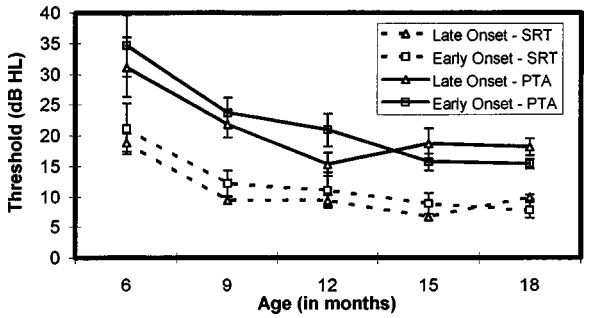

FIG. 2. Mean speech reception thresholds (SRT) and mean pure tone average (PTA) thresholds for the late onset and early onset groups (with standard error bars).

completed. They were advised not to wait for the scheduled audiometric assessment before requesting a medical assessment of middle-ear function, in the event that they had concerns immediately prior to the scheduled assessment. All nine early onset infants, but no late onset infants, were treated for OM at or before 6 months of age. All nine EO infants and five LO infants experienced at least one ear infection between 6 and 18 months of age. The LO group received a total of nine prescriptions while the EO group received a total of 55 prescriptions for the period birth through 18 months of age, indicating a significant between-groups difference in the occurrence of OM [$t(16)=4.26$, $p=0.0003$].

Parents were asked to attend the scheduled audiometric assessment even when their infants were ill or experiencing an ear infection, but typically parents would reschedule these appointments until after antibiotic treatment was started in the case of an ear infection coinciding with the scheduled assessment. In addition, most of the reported ear infections occurred in between assessment dates, which is not surprising, given the long (i.e., 3-month) assessment interval. Therefore, the tympanometric assessments do not provide a good picture of each child's middle-ear history during the period of study. The results of the tympanometric assessments were interpreted using the criteria suggested by Silman and Silverman (1991). A flat tympanogram (i.e., type B) or peak pressure below -100 dPa, combined with an absent ipsilateral acoustic reflex at 1 kHz indicated abnormal middle-ear function. In total (i.e., across infants and assessments), seven abnormal ears were observed for the late onset group while 14 abnormal ears were observed for the early onset group. This between-group difference is not statistically significant [$t(1,17)=1.61$, $p=0.12$].

Analysis of variance (ANOVA) revealed that both speech reception thresholds (SRT) and pure-tone average (PTA) thresholds decreased with age [$F(4,64)=11.88$, $p=0.0001$, for SRTs; $F(4,64)=20.67$, $p=0.0001$, for PTAs]. The between-group differences in mean thresholds are not statistically significant [$F(1,16)=0.74$, $p=0.59$, for SRTs; $F(1,16)=0.18$, $p=0.68$, for PTAs]. Mean SRTs and PTAs are shown in Fig. 2.

B. Infraphonological analysis

Figure 3 shows the mean frequency of occurrence of each of the five infraphonological utterance types at each

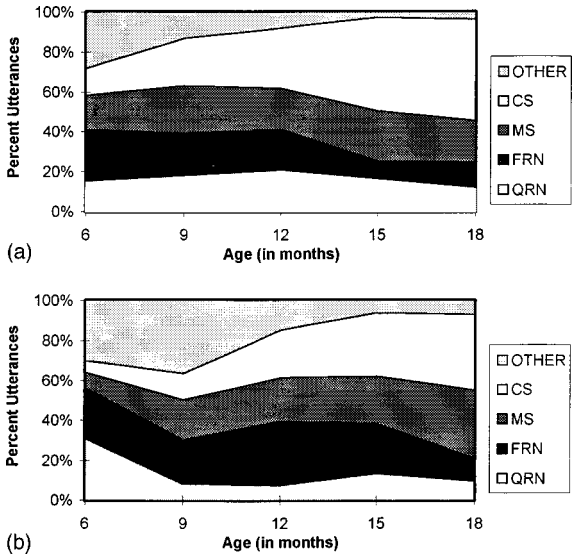

FIG. 3. Profile of mean frequency of occurrences of five different utterance types as a function of age for the late onset (panel A) and early onset (panel B) groups. The utterance types shown are QRN (quasiresonant nucleus), FRN (fully resonant nucleus), MS (marginal syllable), CS (canonical syllable), and OTHER (raspberries, squeals, growls, etc.).

assessment. The top panel represents the 2250 utterances produced by the LO infants and shows that the LO group demonstrated a steady increase in CS utterances and a corresponding decrease in OTHER-type utterances with age. The bottom panel represents the 2225 utterances produced by the EO infants. Comparison with the top panel shows that the EO group produced fewer CS utterances and more OTHER-type utterances than the LO group at all age levels. QRNs were unusually frequent at 6 months of age for this group. These results suggest that the early onset infants showed a similar course of development to the late onset infants, but with a 3- to 6-month delay.

Figure 4 shows that the early onset group obtained a lower mean CSR at each age level in comparison with the late onset group. The ANOVA revealed significant main effects for both age [$F(4,64)=16.75$, $p=0.0001$] and group [$F(1,16)=10.89$, $p=0.0046$]. The effect size for the between-group difference in CSR was calculated, using the eta statistic as described by Meline and Schmitt (1997); $\eta^2=0.41$, greater than the standard of $\eta^2=0.138$, indicating a

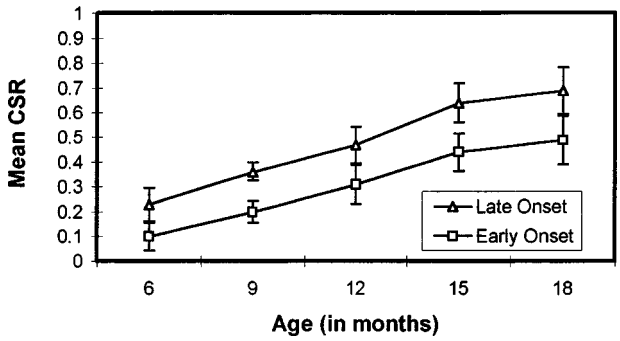

FIG. 4. Mean canonical syllable ratio (CSR) for the late onset group (triangles) and for the early onset group (squares) as a function of age. Standard errors are indicated by error bars.

large effect size for the impact of early-onset OM on the development of babbling.

Previous research with normally developing and profoundly hearing-impaired infants shows that all normally developing children attain the canonical babbling stage between the ages of 6 and 11 months, and typically by 7 months of age (Oller and Eilers, 1988; Eilers and Oller, 1994), when this stage is indicated by a canonical syllable ratio of 0.2 or higher. For the LO group, this level of canonical babbling was demonstrated by four infants at age 6 months, eight infants at 9 months, and all nine infants at 12 months. For the early onset group, the canonical stage was indicated for one infant at 6 months, four infants at 9 months, and all nine infants at 12 months.

Some infants in the EO group showed remarkable fluctuations in their canonical syllable ratio over time. For example, one infant's score fell from 0.44 at 6 months to 0.12 at 9 months, rising only to 0.24 at 12 months. Another infant in this group obtained scores of 0.1, 0.42, 0.24, 0.16, and 0.14 at the five observation points. A similar downward shift in the canonical syllable ratio was observed for one child in the LO group after he began to experience recurring middle-ear effusion at the age of 9 months: this subject obtained CSRs of 0.48, 0.49, 0.22, 0.58, and 0.28 at ages 6, 9, 12, 15, and 18 months, respectively. Note that these shifts to lower canonical syllable ratios were not necessarily associated with the presence of acute infection or elevated thresholds. In most cases the children had normal hearing and middle-ear function on the day that the speech samples were recorded. The mean CSR for samples recorded when abnormal middle-ear status was observed ($M=0.33$) was not significantly different from the mean CSR for samples recorded when middle-ear function was normal ($M=0.40$) [$t(89)=0.98$, $p=0.16$, one-tailed]. Thus, the results of this study do not reflect temporary fluctuations in vocal output or quality that are associated with illness or conductive hearing loss. Rather, early-onset infants demonstrate a persistent difference in CSR over a 1-year period, even after resolution of the middle-ear problem.

C. Assessment of language skills

Table I shows the mean standard scores obtained by the late onset and early onset groups for the receptive and expressive subscales of the REEL-R at 18 months of age. The mean scores are above average for both groups, reflecting individual scores that were typically above average or within normal limits, although four infants obtained at least one subscale score that was below 85. These data were submitted to a 2×2 ANOVA, where OM onset was the between-groups factor with two levels (late onset and early onset) and REEL-R performance was the within-groups factor with two levels (receptive and expressive subscale scores). This analysis revealed no significant difference in performance between groups [$F(1,16)=0.663$, $p=0.56$]. In addition, there was no significant difference in performance for the two subscales [$F(1,16)=0.99$, $p=0.66$] and no significant interaction of group with subscale [$F(1,16)=0.86$, $p=0.63$].

Table I also shows the mean word production checklist scores at ages 6 through 18 months for both the late onset and early onset groups. Although the mean score for the LO group was higher than the mean score for the EO group at each assessment, this difference between groups was not statistically significant [$F(1,16)=0.642$, $p=0.56$]. A significant increase in word production scores was observed with age [$F(3,48)=18.229$, $p=0.001$] (the 6-month assessment was excluded from this analysis because none of the babies was using real words at this age). Considerable variability within groups and overlap in scores between groups was observed. For example, if the scores are summed for the year 6 through 18 months, the range in total numbers of words for the late onset group was 4 to 151; the range for the early onset group was 0 to 71 words for this same period.

TABLE I. Mean REEL-R scores and word production checklist scores for the late onset and early onset groups.

Test	Late onset	Early onset
REEL-R scores[a]		
Receptive	114	107
Expressive	118	105
Word production checklist scores[b]		
6 months	0.00	0.00
9 months	0.33	0.22
12 months	3.11	1.67
15 months	9.22	4.89
18 months	29.89	21.00

[a]These are expressed as standard scores with a mean of 100 and a standard deviation of 15.

[b]These scores represent the mean number of words checked by the parents on each of the five different equivalent forms of this checklist. The scores *do not* represent the child's total expressive vocabulary size.

Although there was no significant between-groups difference in word production scores (WPS), expressive vocabulary ability was related to the children's canonical babbling ratio. This is shown in Fig. 5, which plots the CSRs against WPSs for each of the 18 infants at 18 months of age along with the associated regression line and regression equation. Regression analysis shows that there is a trend toward a linear relationship ($r=0.46$) between these variables [$F(1,16)=4.34$, $p=0.05$], with the canonical syllable ratio accounting for 21 percent of the variance in word production checklist scores. This figure suggests a threshold effect,

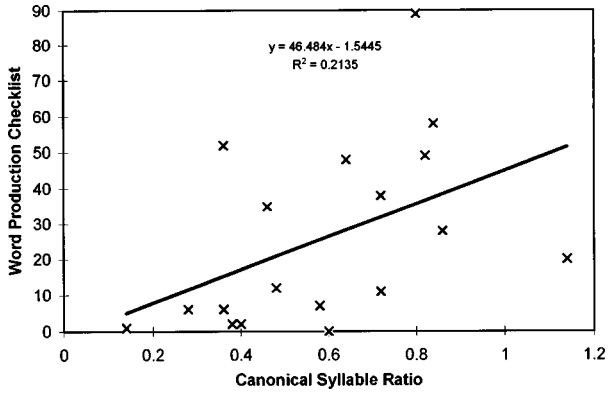

FIG. 5. Canonical syllable ratios (CSR) for 18-month speech samples are plotted against word production checklist (WPC) scores at 18 months for each of the 18 infants. The associated regression line, regression equation, and the proportion of predictable variance are also shown.

whereby a CSR greater than 0.4 is required for the ''naming explosion'' to occur, a finding consistent with results reported by Oller and Eilers (1988) and Whitehurst *et al.* (1991).

III. DISCUSSION

The purpose of the research reported here was to assess the hypothesis that infants with early-onset OM would demonstrate less mature phonetic development in comparison with infants who experienced no OM during the first 6 months of life. In support of the hypothesis, the EO infants obtained consistently and significantly lower canonical syllable ratios (CSR), in comparison with the LO group, throughout the period of study. The EO group also produced a greater frequency of less-speech-like utterances, such as growls, squeals, and raspberries.

We have previously reported that early-onset OM is associated with a restricted vowel space at 18 months of age (Rvachew *et al.*, 1996). Our findings for vowels and the results reported here for the CSR parallel those for children with severe–profound sensory neural hearing loss (Carney, 1996; Kent *et al.*, 1987; Eilers and Oller, 1994; Oller and Eilers, 1988). Taken together, these studies highlight the importance of the auditory environment to early phonetic development and are consistent with the model of early phonetic development described recently by Kuhl and Meltzoff (1996). It has been demonstrated that infants' vowel categories become increasingly differentiated in both perception and production with age, and that this process is dependent upon auditory input (e.g., de Boysson-Bardies *et al.*, 1989; Kuhl *et al.*, 1992). Kuhl and Meltzoff propose that the infants' processing of auditory input from the ambient environment leads to the formation of memory representations for individual speech-sound categories. The infants then work to progressively match their vocal output to their developing system of memory representations for language-specific speech sound categories. According to this model, ''both hearing the sound patterns of ambient language (auditory exteroception) and the ability to hear one's own attempts at speech (auditory proprioception) are critical to determining the course of vocal development (p. 2436).''

We propose that the fluctuating conductive hearing loss that is associated with OM impairs both auditory exteroception and auditory proprioception, thus leading to a delayed course of phonetic development during infancy. The hypothesis that OM impairs the infant's ability to process speech input from the ambient environment is controversial because OM-related hearing loss is very mild, with average thresholds being 23 dB during an episode of middle-ear effusion (Fria *et al.*, 1985). However, performance versus intensity functions for speech discrimination by adults and infants show that a 10- to 20-dB hearing loss would not impact on adult performance, but would lower infant performance to chance-level responding (Nozza, 1988). Therefore, it seems fully credible that a mild hearing loss could impact on auditory exteroception during the first year of life.

OM-related hearing loss is frequently unilateral, another characteristic that may impact on the child's reception of speech input from the external environment. Pillsbury *et al.* (1991) speculate that fluctuating unilateral losses interfere with the normal development of binaural processing abilities, thus accounting for the smaller binaural masking level differences observed in children with OM histories. Children with OM histories have been observed to have difficulty with binaural processing even when middle-ear function and hearing acuity is normal (Moore *et al.*, 1991). Persistent abnormalities in auditory brainstem response have also been reported in both retrospective and prospective studies of children with and without histories of recurrent OM (e.g., Gunnarson and Finitzo, 1991). Binaural processing is important to the child's ability to localize sound and to process speech in the presence of competing noise. Children with a history of OM in infancy have been found to have difficulty with both of these skills relative to children who have not experienced chronic or recurring OM (e.g., Gravel and Wallace, 1992).

With respect to auditory proprioception, OM may disrupt the child's access to his or her own speech, given that infant-produced upper formants tend to be very high frequency and low in energy. For example, Kent and Murray (1982) found that the first three formants of infant-produced vowels averaged $F1 = 1000$ Hz, $F2 = 3000$ Hz, and $F3 = 5000$ Hz. Infant-produced fricative noises have primary spectral components at very high frequencies, up to and above 14 kHz (Bauer and Kent, 1987). OM-related hearing loss is minimal at 2 kHz but significant at lower and higher frequencies (Fria *et al.*, 1985). The intersection of the hearing profile during an episode of OM and the acoustic characteristics of infant-produced speech may explain the preponderance of quasiresonant nuclei, produced both in isolation and within the context of consonant–vowel syllables by the infants with early-onset OM.

As noted earlier, the relationship between OM and outcomes is complex, and there are several important mediating variables that have not been addressed by this study. One such variable is the socioeconomic status (SES) of the infant's family. Eilers *et al.* (1993) have shown that SES does not impact on age of onset of the canonical babbling stage. However, SES does mediate the relationship between OM and language development (Teele *et al.*, 1984); thus, further study of the impact of SES on early phonetic development is required. A related issue is the effect of the mother's style of interaction with the infant. Black *et al.* (1988) found poorer-quality social interactions between mothers and infants with OM compared to the control group of mother–infant pairs. Other studies have shown that good language stimulation and cognitive growth-fostering skills on the part of parents may protect the child from the potential negative impact of OM on language development (Black and Sonnenschein, 1993; Freeark *et al.*, 1992; Wallace *et al.*, 1996). Finally, the illness experience itself may have effects that are independent of OM-related hearing loss. There is some evidence that illness impacts on attachment processes and on mother–infant interactions (Wille, 1991; Jarvis *et al.*, 1989). The canonical syllable ratio could be a useful tool in the investigation of the complex relationships between these variables, OM, and long-term outcomes.

A further issue not addressed by this study is the predic-

tive validity of the canonical syllable ratio. In this study, the canonical syllable ratio was positively correlated with expressive vocabulary size at 18 months. Other studies have also found an association between early phonetic abilities and the emergence of early vocabulary skills (Paul and Jennings, 1992; Stoel-Gammon, 1989; Whitehurst *et al.*, 1991). It is not clear that infants with delayed onset of canonical babble are at risk for phonological or language difficulties at later ages. One EO child who had not reached the canonical babble stage by 18 months of age was followed for an additional 2 years. His receptive and expressive language skills were found to be below normal limits at 18 months, but well within the normal limits at 22 and 31 months of age. At the age of 39 months his language skills were again below normal limits, largely due to problems with the comprehension and expressive use of grammatical morphemes. His phonological skills were also clearly below average as he scored at the seventh percentile on the Goldman–Fristoe Test of Articulation, resulting in a referral for speech therapy. Menyuk *et al.* (1995), in their study of premature infants, observed a similar developmental course for some children with delayed onset of ''structured'' babble. More study directed specifically at this question is required. If a predictive relationship between the CSR (either by itself or in combination with other variables) and later language development is confirmed, earlier identification and earlier intervention may be possible. Normal limits for the attainment of the babbling stage are between seven and nine months of age (Oller and Eilers, 1988); however, normal limits for expressive vocabulary development cannot be established prior to 24 months of age due to the extreme intersubject variability observed for vocabulary size during infancy (Thal *et al.*, 1997). If risk factors for language delay could be identified during infancy, preventative treatments could be directed at the middle-ear effusion itself, the infant's hearing acuity, auditory attention and speech perception skills, the quality of the infant's auditory environment, or the infant–parent relationship.

IV. SUMMARY AND CONCLUSIONS

This study found that infants with early-onset OM had consistently smaller canonical syllable ratios throughout the period 6 through 18 months of age, in comparison with children who had no ear infections before 6 months of age. This study demonstrates that early-onset OM has an impact on phonetic development during infancy. Further study is required to determine if delayed development of canonical babbling skills is correlated with difficulties with phonological and morphological development at later ages.

ACKNOWLEDGMENTS

This research was supported by the Medical Research Council of Canada. We are grateful to the infants and their families for their participation in this study. We are also thankful to the audiology and speech-language sections of the Alberta Children's Hospital for their support of this project. In particular, we appreciate the assistance of Naida Feldman and Linda Hornsberger, who conducted the reliability analyses.

Bauer, H. R., and Kent, R. D. (**1987**). ''Acoustic analyses of infant fricative and trill vocalization,'' J. Acoust. Soc. Am. **81**, 505–511.

Black, M. M., Gerson, L. R., Freeland, C. A. B., Nair, P., Rubin, J. S., and Hutcheson, J. J. (**1998**). ''Language screening for infants prone to otitis media,'' J. Pediatric Psychol. **13**, 423–433.

Black, M. M., and Sonnenschein, S. (**1993**). ''Early exposure to otitis media: A preliminary investigation of behavioral outcome,'' Develop. Behav. Pediatrics **14**, 150–155.

de Boysson-Bardies, B., Halle, P., Sagart, L., and Durand, C. (**1989**). ''A crosslinguistic investigation of vowel formants in babbling,'' J. Child Lang. **16**, 1–17.

Broen, P., Strange, W., Doyle, S., and Heller, J. H. (**1983**). ''Perception and production of approximant consonants by normal and articulation delayed preschool children,'' J. Speech Hear. Res. **26**, 601–608.

Bzoch, K. R., and League, R. (**1991**). *Receptive-Expressive Emergent Language Test*, 2nd ed. (Pro-Ed, Austin, TX).

Carney, A. E. (**1996**). ''Audition and the development of oral communication competency,'' in *Amplification for Children with Auditory Deficits*, edited by F. Bess (Bill Wilkerson Center Press, Nashville, TN).

Chalmers, D., Stewart, I., Silva, P., and Mulvena, A. (**1989**). *Otitis Media with Effusion in Children-The Dunedin Study* (MacKeith, Oxford).

Clarkson, R. L., Eimas, P. D., and Marean, G. C. (**1989**). ''Speech perception in children with histories of recurrent otitis media,'' J. Acoust. Soc. Am. **85**, 926–933.

Donahue, M. L. (**1993**). ''Early phonological and lexical development and otitis media: A diary study,'' J. Child Lang. **20**, 489–501.

Eilers, R. E., and Oller, D. K. (**1994**). ''Infant vocalizations and the early diagnosis of severe hearing impairment,'' J. Pediatr. (St. Louis) **124**, 199–203.

Eilers, R. E., Oller, D. K., Levine, S., Basinger, D., Lynch, M. P., and Urbano, R. (**1993**). ''The role of prematurity and socioeconomic status in the onset of canonical babbling in infants,'' Infant Behav. Develop. **16**, 297–315.

Feagans, L., Sanyal, M., Henderson, F., Collier, A., and Appelbaum, M. (**1987**). ''Relationship of middle ear disease in early childhood to later narrative and attention skills,'' J. Pediatric Psychol. **12**, 581–595.

Freeark, K., Frank, S. J., Wagner, A. E., Lopez, M., Olmsted, C., and Girard, R. (**1992**). ''Otitis media, language development, and parental verbal stimulation,'' J. Pediatric Psychol. **17**, 173–185.

Fria, T. J., Cantekin, E. I., and Eichler, J. A. (**1985**). ''Hearing acuity of children with otitis media with effusion,'' Arch. Otolaryngol. (Chicago) **111**, 10–16.

Friel-Patti, S. (**1990**). ''Otitis media with effusion and the development of language: A review of the evidence,'' Topics Lang. Disord. **11**, 11–22.

Friel-Patti, S., and Finitzo, T. (**1990**). ''Language learning in a prospective study of otits media with effusion in the first two years of life,'' J. Speech Hear. Res. **33**, 188–194.

Gravel, J. S., and Wallace, I. F. (**1992**). ''Listening and language at 4 years of age: Effects of early otitis media,'' J. Speech Hear. Res. **35**, 588–595.

Grievink, E. H., Peters, S. A. F., van Bon, W. H. J., and Schilder, A. G. M. (**1993**). ''The effects of early bilateral otitis media with effusion on language ability: A prospective cohort study,'' J. Speech Hear. Res. **36**, 1004–1012.

Gunnarson, A. D., and Finitzo, T. (**1991**). ''Conductive hearing loss during infancy: Effects on later auditory brain stem electrophysiology,'' J. Speech Hear. Res. **34**, 1207–1215.

Hubbard, T. W., Paradise, J. L., McWilliams, B. J., Elster, B. A., and Taylor, F. H. (**1985**). ''Consequences of unremitting middle ear disease in early life,'' N. Engl. J. Med. **312**, 1529–1534.

Ireton, H. (**1992**). *Child Development Inventory* (Behavioral Science Systems, Inc., Minneapolis, MN).

Jamieson, D. G., Nearey, T. M., and Ramji, K. (**1989**). ''CSRE: A speech research environment,'' Can. Acoust. **17**, 23–35.

Jarvis, P. A., Myers, B. J., and Creasey, G. W. (**1989**). ''The effects of infants' illness on mother's interactions with prematures at 4 and 8 months,'' Infant Behav. Develop. **12**, 25–35.

Jusczyk, P. W. (**1992**). ''Developing phonological categories from the speech signal,'' in *Phonological Development: Models, Research, Implications*, edited by C. A. Ferguson, L. Menn, and C. Stoel-Gammon (York, Timonium, MD), pp. 17–65.

Kent, R., and Murray, S. (**1982**). ''Acoustic features of infant vocalic utterances at 3, 6, and 9, months,'' J. Acoust. Soc. Am. **72**, 353–365.

Kent, R. D., Osberger, M. J., Netsell, R., and Hustedde, C. G. (**1987**).

''Phonetic development in identical twins differing in auditory function,'' J. Speech Hear. Disord. **52**, 64–75.
Klein, J. O. (**1983**). ''Epidemiology and natural history of otitis media,'' Pediatrics **71**, 639–640.
Klein, J. O., Chase, C., Teele, D. W., Menyuk, P., and Rosner, B. A. (**1988**). ''Otitis media and the development of speech, language, and cognitive abilities at seven years of age,'' in *Recent Advances in Otitis Media*, edited by D. J. Lim (B. C. Decker, Toronto, Canada), pp. 396–397.
Kuhl, P. K., and Meltzoff, A. N. (**1996**). ''Infant vocalizations in response to speech: Vocal imitation and developmental change,'' J. Acoust. Soc. Am. **100**, 2425–2438.
Kuhl, P. K., Williams, K. A., Lacerda, F., Stevens, K. N., and Lindblom, B. (**1992**). ''Linguistic experience alters phonetic perception in infants by 6 months of age,'' Science **255**, 606–608.
Meline, T., and Schmitt, J. F. (**1997**). ''Case studies for evaluating statistical significance in group designs,'' Am. J. Speech-Language Pathol. **6**, 33–41.
Menyuk, P. (**1986**). ''Predicting speech and language problems with persistent otitis media,'' in *Otitis Media and Child Development*, edited by J. F. Kavanaugh (York, Parkton, MD), pp. 83–96.
Menyuk, P., Liebergott, J. W., and Schultz, M. C. (**1995**). *Early Language Development in Full-term and Premature Infants* (Erlbaum, Hillsdale, NJ).
Moore, D. R., Hutchings, M. E., and Meyer, S. E. (**1991**). ''Binaural masking level differences in children with a history of otitis media,'' Audiology **30**, 91–101.
Nozza, R. J. (**1988**). ''Auditory deficit in infants with otitis media with effusion: More than a 'mild' hearing loss,'' *Recent Advances in Otitis Media*, edited by D. J. Lim (B. C. Decker, Toronto, Canada), pp. 376–379.
Oller, D. K. (**1980**). ''The emergence of the sounds of speech in infancy,'' in *Child Phonology*, edited by G. H. Yeni-Komshian, J. F. Kavanaugh, and C. A. Ferguson (Academic, NY), Vol. 1, pp. 93–112.
Oller, D. K. (**1986**). ''Metaphonology and infant vocalizations,'' in *Precursors of Early Speech*, edited by B. Lindblom and R. Zetterstrom (Stockton, NY), pp. 21–36.
Oller, D. K., and Eilers, R. E. (**1988**). ''The role of audition in infant babbling,'' Child Dev. **59**, 441–449.
Paradise, J. L. (**1983**). ''Long-term effects of short-term hearing loss-menace or myth?'' Pediatrics **71**, 647.
Paul, R., and Jennings, P. (**1992**). ''Phonological behavior in toddlers with slow expressive language development,'' J. Speech Hear. Res. **35**, 99–107.
Pillsbury, H. C., Grose, J. H., and Hall, J. W. (**1991**). ''Otitis media with effusion in children,'' Arch. Otolaryngol. (Chicago) **117**, 718–723.
Polka, L., and Werker, J. F. (**1994**). ''Developmental changes in perception of nonnative vowel contrasts,'' J. Exp. Psychol. **20**, 421–435.
Reznick, J. S., and Goldsmith, L. (**1989**). ''A multiple form word production checklist for assessing early language,'' J. Child Lang. **16**, 91–100.
Robb, M. P., Psak, J. L., and Pang-Ching, G. K. (**1993**). ''Chronic otitis media and early speech development: a case study,'' Int. J. Pediatr. Otorhinolaryngol. **26**, 117–127.
Roberts, J. E., Burchinal, M. R., Koch, M. A., Footo, M. M., and Henderson, F. W. (**1988**). ''Otitis media in early childhood and its relationship to later phonological development,'' J. Speech Hear. Disord. **53**, 424–432.
Roberts, J. E., and Schuele, C. M. (**1990**). ''Otitis media and later academic performance: The linkage and implications for intervention,'' Topics Lang. Disord. **11**, 43–62.
Roug, L., Landberg, I., and Lundberg, L.-J. (**1989**). ''Phonetic development in early infancy: A study of four Swedish children during the first eighteen months of life,'' J. Child Lang. **16**, 19–40.
Rvachew, S., and Jamieson, D. G. (**1995**). ''Learning new speech contrasts: Evidence from adults learning a second language and children with speech disorders,'' in *Speech Perception and Linguistic Experience: Theoretical and Methodological Issues in Cross-language Speech Research*, edited by W. Strange (York, Timonium, MD), pp. 411–432.
Rvachew, S., Slawinski, E. B., Williams, M., and Green, C. L. (**1996**). ''Formant frequencies of vowels produced by infants with and without early onset otitis media,'' Can. Acoust. **24**, 19–28.
Silman, S., and Silverman, C. A. (**1991**). *Auditory Diagnosis: Principles and Applications* (Academic, San Diego, CA).
Stoel-Gammon, C. (**1989**). ''Prespeech and early speech development of two late talkers,'' First Lang. **9**, 207–224.
Stoel-Gammon, C., and Otomo, K. (**1986**). ''Babbling development of hearing-impaired and normally hearing subjects,'' J. Speech Hear. Disord. **51**, 33–41.
Teele, D. W., Klein, J. O., and Rosner, B. A., and the Greater Boston Otitis Media Study Group (**1984**). ''Otitis media with effusion during the first three years of life and development of speech and language,'' Pediatrics **74**, 282–287.
Thal, D. J., Bates, E., Goodman, J., and Jahn-Samilo, J. (**1997**). ''Continuity of language abilities: An exploratory study of late- and early-talking toddlers,'' Develop. Neuropsychol. **13**, 239–273.
Ventry, I. M. (**1980**). ''Effects of conductive hearing loss: Fact or fiction?'' J. Speech Hear. Disord. **45**, 143–156.
Vihman, M. M., Macken, M., Miller, R., Simmons, H., and Miller, J. (**1985**). ''From babbling to speech: A reassessment of the continuity issue,'' Language **61**, 397–445.
Wallace, I. F., Gravel, J. S., Schwartz, R. G., and Ruben, R. J. (**1996**). ''Otitis media, communication style of primary caregivers, and language skills of 2 year olds: A preliminary report,'' Developmental and Behavioral Pediatrics , 27–35.
Webster, A., Bamford, J. M., Thyer, N. J., and Ayles, R. (**1989**). ''The psychological, educational and auditory sequelae of early, persistent secretory otitis media,'' J. Child Psychol. Psychiatry **30**, 529–546.
Welsh, L. W., Welsh, J. J., and Healy, M. P. (**1983**). ''Effect of sound deprivation on central hearing,'' Laryngoscope **93**, 1569–1575.
Whitehurst, G. J., Smith, M., Fischel, J. E., Arnold, D. S., and Lonigan, C. J. (**1991**). ''The continuity of babble and speech in children with specific expressive language delay,'' J. Speech Hear. Res. **34**, 1121–1129.
Wille, D. (**1991**). ''Relation of preterm birth with quality of infant-mother attachment at one year,'' Infant Behav. Develop. **14**, 227–240.

Some lengthening factors in English speech combine additively at most rates

Fred Cummins
Department of Linguistics, 2016 Sheridan Road, Northwestern University, Evanston, Illinois 60208

(Received 14 May 1998; accepted for publication 16 September 1998)

The known lengthening effects of phrase-final position and of contrastive emphasis have been predicted by Klatt to combine superadditively. In a new experiment, texts elicited at a wide range of speaking rates were measured and the separate and combined effects of these lengthening factors were found to combine approximately additively at all rates studied. The proportion of lengthening attributable to each factor was found to be relatively invariant except at the fastest speaking rates, where lengthening was eventually eliminated. The results support the interpretation of absolute speaking rate as an inessential variable for characterizing speech at a range of moderate rates. © *1999 Acoustical Society of America.* [S0001-4966(99)00801-2]

PACS numbers: 43.70.Fq, 43.70.Bk [AL]

INTRODUCTION

This paper deals with the individual and combined effects of three of the best known factors which influence macroscopic speech timing: speech rate, phrase-final lengthening, and contrastive emphasis.

Phase-final lengthening (hereafter, PFL) refers to the relatively longer durations observed within a syllable which lies at the right edge of a major prosodic constituent, such as an intonational phrase. PFL effects are largely restricted to the rhyme of the final syllable (Klatt, 1976). This distinguishes PFL from utterance final lengthening, which is characterized by global deceleration and a reduction in articulatory effort distributed over several syllables. Estimates of lengthening due to PFL vary from 30% (Klatt, 1975) to as much as 120% for long stressed vowels in V# position (Crystal and House, 1988).

Contrastive emphasis (CE) is a form of accenting used to highlight a particular syllable or word. An accented syllable will bear the nuclear accent of a phrase, often with an exaggerated pitch excursion. Lengthening is frequently associated with CE, and unlike PFL, all parts of the syllable are found to be affected (Beckman *et al.*, 1992; Turk and Sawusch, 1997). In English, if a syllable bearing CE is followed by an unstressed syllable, the latter may also show some lengthening. Accenting due to CE may be considered an extreme form of phrasal, or nuclear, accenting, especially when the elicitation form suggests a previous misunderstanding (e.g., ''I said BEEF arm, not REEF arm,'' from Turk and Sawusch, 1997). No reliable estimates of the degree of lengthening due to CE are available.

In an early study (Klatt, 1973), Klatt examined the combined effect of two factors, each of which has a shortening effect on vowels in stressed syllables: voiceless coda consonants (relative to voiced), and the addition of an unstressed syllable after the stressed syllable but within the same word. He found that their combined effect was considerably less than a simple additive model would predict. Thus, he proposed that vowel duration be computed based on an inherent (relatively long) duration D_i, which is analyzable as an incompressible part $D_{\min}$ and a compressible part which is multiplied by a constant:

$$D_o = k(D_i - D_{\min}) + D_{\min}. \tag{1}$$

The serial application of shortening rules of this sort will produce a subadditive modification of the overall duration. In his well-known review, Klatt (1976) lists many factors which can influence segmental durations. Each, he suggests, can be associated with a different constant k, with $0<k<1$ for shortening rules and $k>1$ for lengthening rules. This approach to combining factors has found practical application in speech-synthesis algorithms. In the present context, Klatt's model predicts that two lengthening factors, such as PFL and CE, will combine superadditively.

The combination of utterance-final lengthening and CE was examined in a study by Cooper *et al.* (1985). They had subjects read isolated sentences with contrastive emphasis on specific key words, as induced by a preceding question (e.g., ''Did Chuck like the letter or the present that Shirley sent to her sister?''). They found that the placement of CE on sentence final words resulted in much less durational increase than an additive model would predict. This suggests that there might be an expandability constraint, analogous to the compressibility constraint. A similar expandability constraint has been independently proposed by Berkovits (1991).

The present study examines the separate and combined durational effects of PFL and CE at a range of rates. Rate is seen as a possible lengthening or shortening factor which can take on values over a continuous range, and which combines

TABLE I. Words used in the *X* and *Y* slots of the first and second sentences for each condition. Capitalization was used to highlight the required contrastive emphases. The labels PFL and CE refer to the target syllable /pe͡ɪn/.

	−PFL	+PFL
−CE	*X*: painful SHOT *Y*: painful BLOW	*X*: WINdowpane *Y*: COUNTerpane
+CE	*X*: ARTfully *Y*: PAINfully	*X*: cancer PILL *Y*: cancer PAIN

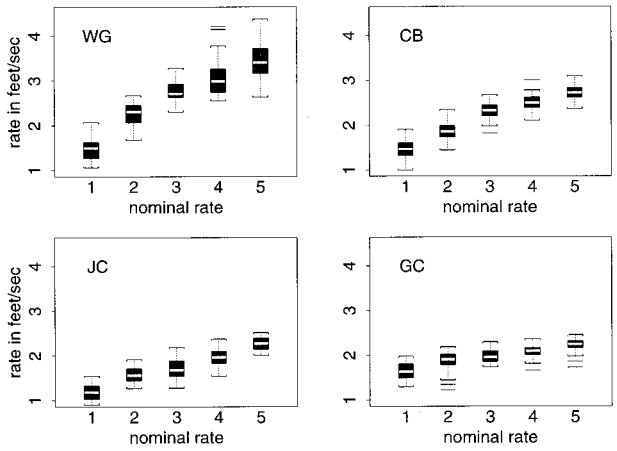

FIG. 1. Distribution of the reciprocal of the duration of the words *message was*, shown as a function of nominal rate. White horizontal bars show the median, filled bars delimit the interquartile range, and the whiskers mark the range of values lying within 1.5*interquartile range. Points outside this range are shown individually.

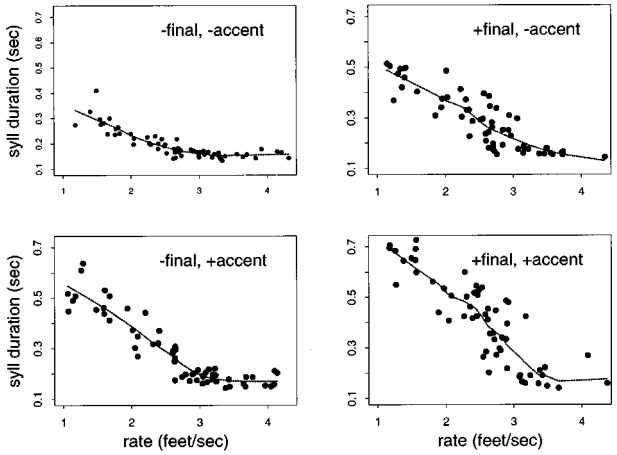

FIG. 2. Syllable durations as a function of (continuously valued) speech rate, fast rates to the right. Only subject W.G. is shown here. Each dataset has been fitted with a smooth curve based on locally weighted least-squares linear regression.

with the two factors of PFL and CE to influence the final duration of segments and syllables. Careful indexing of rate should allow separation of the relative contributions of these three factors to observed acoustic durations. This approach should also reveal any possible interaction between rate of speech and lengthening due to CE or PFL.

I. METHOD

A. Sentence materials

Four short texts consisting of three sentences were devices. Each was of the form *Didn't he say X? The message was Y. Surely that's not what he said.*, where *X* and *Y* differ minimally in one syllable, so that contrastive emphasis is placed on that syllable in *Y*. All measurements are taken from the second sentence, where *Y* is phrase final but not utterance final. The *X/Y* pairs used were chosen so that a target syllable /peɪn/ was or was not phrase final (±PFL), and received or did not receive contrastive emphasis (±CE). Table I lists *X*/*Y* pairs for each condition.

B. Subjects and recording conditions

Four subjects (three female, one, J.C., male) were paid a flat rate for their participation. Three were undergraduates at Northwestern University, W.G. was a full-time mother. Subjects J.C., G.C., and C.B. had lived exclusively in the American upper Midwest (Wisconsin, Michigan, Northern Illinois); W. G. was a native of Connecticut who had lived 6 years in Southern Indiana. All were monolingual native speakers of American English. None had any known speech or hearing defects.

Subjects were seated at a computer screen and used a mouse to control the succession of trials. In each trial they were presented with one of the four three-sentence texts. They were also given a nominal speech rate which was one of ''slow,'' comfortable,'' ''medium,'' ''fast,'' and ''very fast,'' together with a graphic which had an arrow pointing to the appropriate point on a five-point scale from slow to very fast. To further ensure that they would attempt to vary rate across trials, they were asked to repeat the nominal rate aloud before reading the text. Once they were ready to repeat the text, they initiated recording and read the text at their best estimate of the nominal rate. Subjects were given several practice runs, and they were instructed to place contrastive emphasis on the capitalized syllable (see Table I). No subject had overt difficulty with the required task or with producing the required prosody. Trials were self-paced, and after every block of 20 trials a computer message encouraged subjects to take a break.

The four conditions were crossed with five nominal rates to yield blocks of 20 trials which were randomized within blocks. Each subject completed 12 such blocks in a single session, providing 240 trials in all. Recordings were done in a quiet but not soundproofed room using a Shure SM10A head-mounted microphone. Speech was captured directly onto disk via a ProPort D/A unit which digitized at 11 025 Hz, with 16-bit linear resolution.

C. Acoustical measurement

Segmentation was done by hand using Entropics XWAVES software. Of the points measured from the waveform and with simultaneous spectrographic control, the following are relevant here: the onset of a nasal formant pattern for /m/ in ''message was,'' the offset of frication in ''was,'' which coincided with the abrupt drop in energy at the /p/ or /k/ closure of the following word, the onset of the syllable *pane/pain*, and the offset of the syllable.

A randomly generated subset of 10% of the utterances was selected and remeasured. Means and standard deviations for the differences between the two measurements showed that all points were reliably measured (mean discrepancy <5 ms) with the exception of the onset of the final /n/ in ''cancer PAIN'' and ''COUNTerpane,'' which was occasionally uncertain from the acoustic record due to phrase-final weakening (mean discrepancy: 11 ms, s.d. 30 ms). All measurements were done by the author.

In addition to the remeasurement described above, interval distributions were examined and all obvious outliers

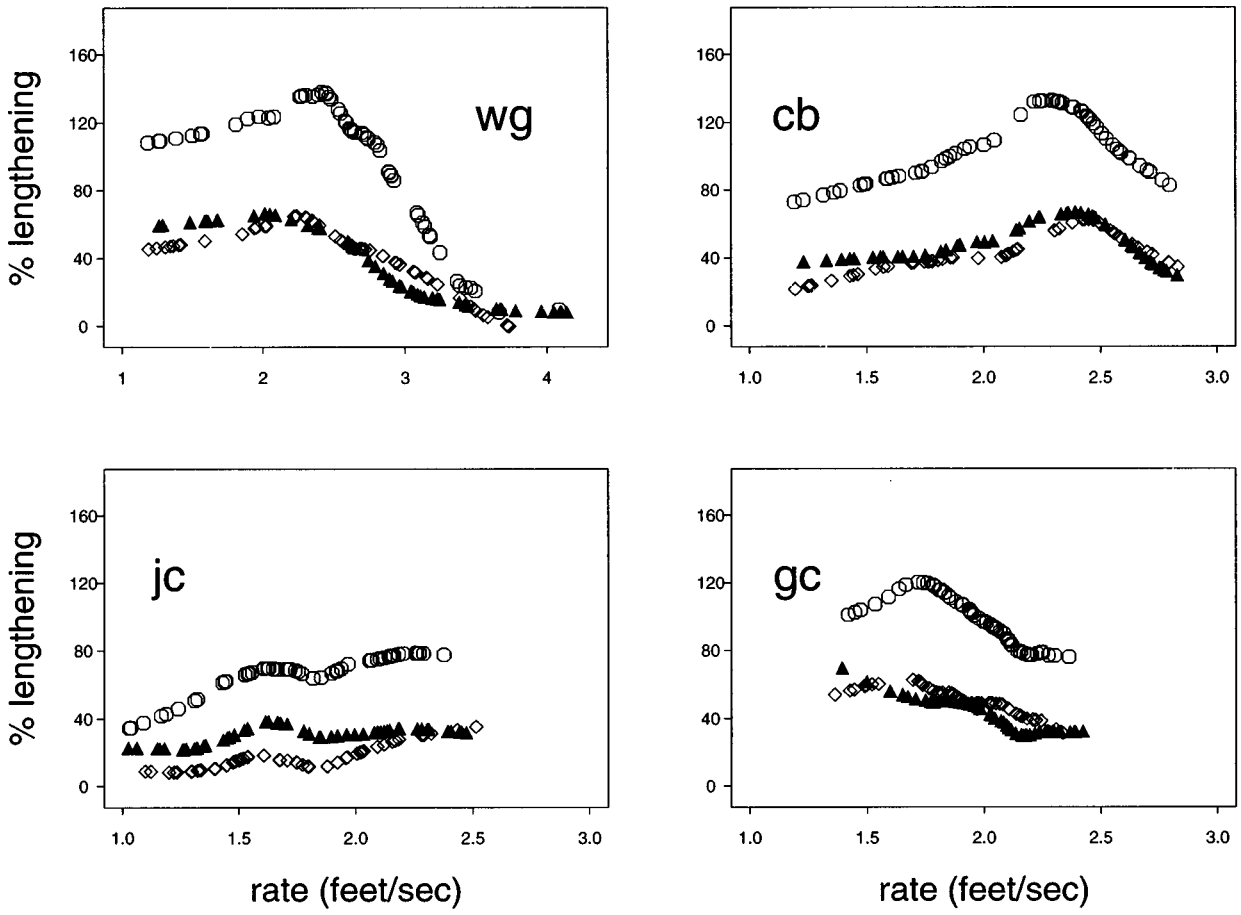

FIG. 3. Lengthening ascribable to [+PFL] (open diamonds), [+CE] (closed triangles), and both (open circles). The proportion of lengthening is based on an estimate of the unlengthened [−PFL,−CE] condition.

were remeasured. A few measurement errors were easily detected in this manner.

D. Indexing speech rate

Several recent kinematic studies of rate have opted to treat speech rate as a continuous variable, rather than the categorical division into two or three self-selected rates, which has been more usually employed (Byrd and Tan, 1996; Shaiman *et al.*, 1995). In the present study, the duration of a common stretch of speech provided a starting point for computing a rate measure. All texts contain the words *message was* in the second sentence, i.e., within the same intonational phase as the target syllable. These three syllables constitute a single prosodic foot. The reciprocal of the duration of this foot was used as a continuous measure of rate, which thus has the units feet/s. This measure served to make the variance across nominal-rate conditions approximately equal, and there was an approximately linear increase in median rate across nominal values. The measure does not take into account any phonological reorganization which may underlie production at fast rates.

II. RESULTS

A. Rate variation

From Fig. 1 it can be seen that subject W.G. produced a much greater variety of rates than the remaining subjects. Given that there are three syllables in the reference foot *message was*, her fastest rates corresponding to about 12 syll/s, which is very fast indeed. Subjects C.B. and J.C. each produced a wide variety of rates with clear separation across nominal-rate classes, while subject G.C. produced very little rate variation from the slowest to the fastest.

B. Syllable durations

Figure 2 shows syllable durations as a function of speech rate for subject W.G. only. Note that rate is a continuous variable (feet/s), and not merely nominal. The relationship between syllable duration and rate appears to be nonlinear. As W.G. speaks more rapidly, there comes a point at which the nonfinal syllable /peɪ̯n/ does not compress further while the trisyllabic foot *message was* is still getting shorter. This effect is less obvious when the syllable is in final position (right-hand panels).

While the nonlinearity is not as obvious in the data for the other subjects, nothing in the following analysis depends on linearity in this relationship between rate and syllable duration.

For statistical analysis of the data from all four subjects, syllable durations were rank ordered by rate and then binned into four bins with 15 tokens per bin. Inhomogeneity of variance, as evidenced by Levine's test (Snedecor and Cochran, 1989) was corrected for by taking a log transform of the

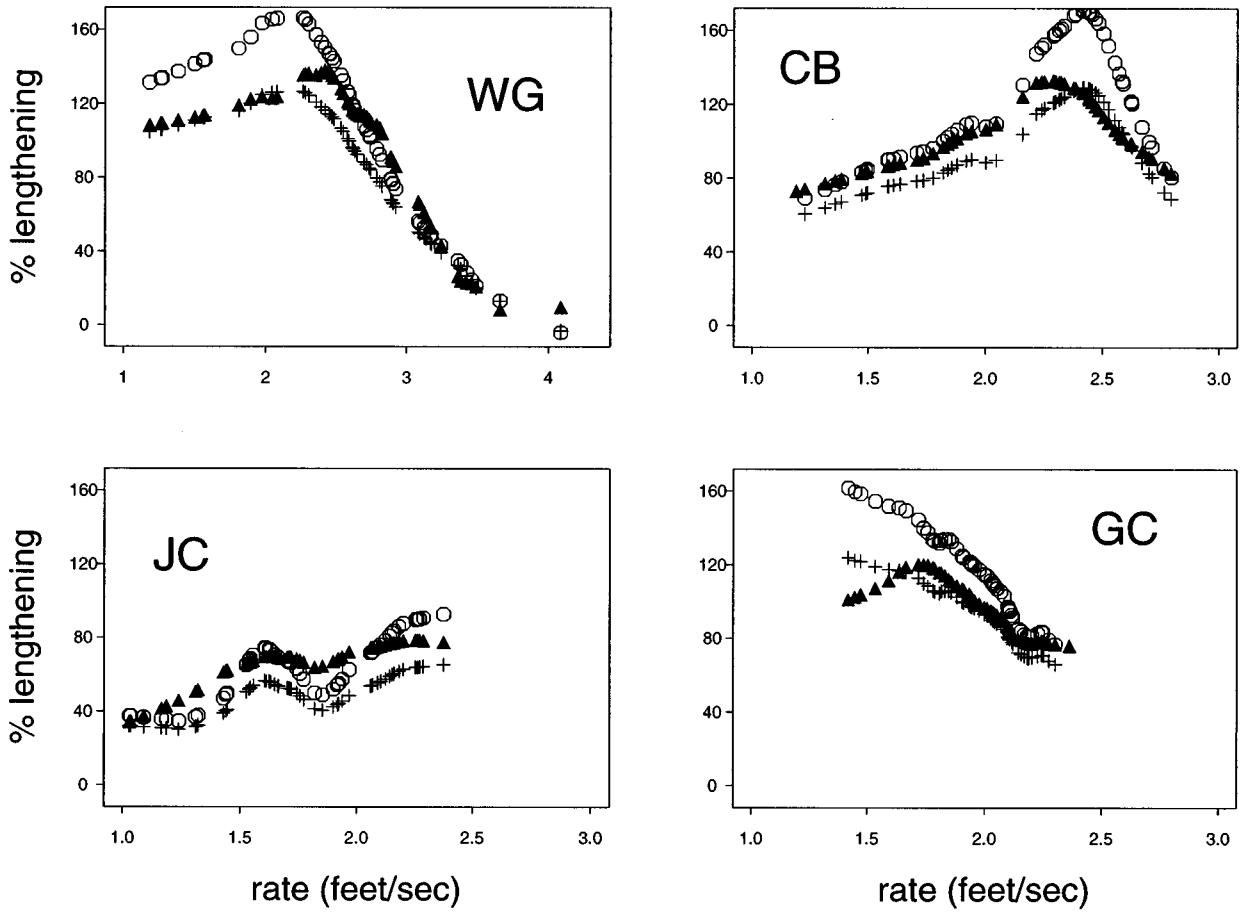

FIG. 4. Comparison of predictions from a simple additive model (crosses), Klatt's 1975 model with best fit $D_{\min}$ (open circles), and actual data (filled triangles) in the [+PFL,+CE] condition.

duration data. A 224 (PFL*CE*RATE) factorial analysis with repeated measures on all factors was then carried out. The main effects associated with PFL [$F(1,3)=89.24$, $p<0.01$] CE[$F(1,3)=916.6$, $p<0.001$], and rate [$F(1,3)=12.26$, $p<0.05$] were all significant at $\alpha=0.05$. The rate effect was evaluated after the conservative Geisser–Greenhouse adjustment to the degrees of freedom to allow for noncircularity (Hayes, 1988). All two-way interactions and the three-way interaction were not significant at $\alpha=0.05$.

C. Estimating the degree of lengthening

In order to estimate the degree of lengthening of an individual token y_i which is directly attributable to the factor PFL and/or CE, a prediction of the duration of that token in the baseline [−PFL,−CE] condition, $\hat{y}_0$, based on its measured rate, is required. As shown in Fig. 2, the relationship between rate and target syllable duration is nonlinear, precluding a simple linear model of the form $\hat{y}_0=mx+c$. However, a more general additive model of the form $\hat{y}_0=f(x)$ is possible, where the function $f(x)$ is estimated using a locally linear smooth fit to the data. For a given token y_i in the [+PFL,−CE] condition, the proportion of its duration attributable to the factor [+PFL] is $y_i-\hat{y}_0$.

The Splus function ''lo,'' which fits a locally weighted least-squares linear regression, was used for all smoothing (Statistical Sciences, 1995). This fit was used as a predictor in a generalized additive model. The dashed lines in Fig. 2 illustrate the local fits computed for each condition for subject W.G.

Figure 3 shows the proportion of total syllable duration attributable to condition-specific factors for the [+PFL], [+CE] and [+PFL,+CE] conditions. From this figure, it is evident that PFL and CE contribute approximately the same amount of total syllable lengthening when each is present alone. Only subject J.C. shows a consistent difference, with [+CE] occasioning greater lengthening than [+PFL].

Because the estimates of lengthening are based on a smooth fit to the data, rather than on the raw data directly, lengthening estimates are not independent from token to token, and rate effects cannot be estimated using classical methods. However, one main effect of rate stands out: the disappearance of any lengthening for either prosodic effect at the fastest rates for subjects W.G. No other subject approaches these extremely fast production rates. Within the range of rates produced by all speakers (approximately 1.2–2.5 feet/s), there is no obvious systematic effect of rate on the proportion of duration attributable to lengthening. It also appears that the proportion of lengthening which is due to each of the two factors changes in similar fashion as rate changes. The lengthening due to [+PFL] thus seems to be

directly comparable to that due to [+CE], irrespective of speaking rate.

D. Comparison with model-based predictions

Klatt's model given in Eq. (1) was originally intended to account for the lengthening or shortening of segments, and in fact, Klatt applies it to compute shortened durations only. The model extends directly to the prediction of lengthening ($k>1$) and for estimating durational changes in units larger than the segment. Given two factors, each of which adds l_i, $i \in \{1,2\}$ to a baseline duration, a simple additive model predicts that the combined effect will add l_1+l_2 to the baseline. Klatt's model predicts a superadditive effect equal to $l_1+l_2+[1/(D_0-D_{\min})]l_1l_2$. The magnitude of the superadditive term $[1/(D_0-D_{\min})]l_1l_2$ depends on the size of the hypothesized incompressible portion (estimated by Klatt to be about 0.45 for vowels. See Klatt, 1975), and is minimized for $D_{\min}=0$.[1]

Figure 4 shows the predicted length of the target syllable in the [+PFL,+CE] condition as generated by a simple additive model and by Klatt's model, where the incompressible portion $D_{\min}$ has been fitted for each subject separately. The actual data have been included in the plot. For W.G., C.B., and G.C., the simple additive model provides a better fit as estimated from the sum of the squared residuals, and in each case, the best fit using Klatt's model requires $D_{\min}=0$. For J.C., Klatt's model is the better fit and $D_{\min}=0.61$.

III. DISCUSSION

This study examined the combination of lengthening effects over a range of (continuously measured) speaking rates. Although previous studies of durational modifiers in combination have suggested that there are limits to both expansion and compression of syllable duration, a simple additive model was found to provide a good fit over a wide range of rates. An algorithmic approach to computing durations could conceivably accommodate limits on both expandability and compressibility by treating the segment (or syllable) as a hard spring with a neutral or preferred duration. Over some medial range, factors which influence duration combine in simple additive fashion, while beyond that range, little compression or stretching is effected.

This simple interpretation is premised on the assumption that timing factors all behave in approximately the same manner. Port (1981) raised the possibility that factors which instantiate phonological features may combine by constant ratios, while other factors (tempo, number of syllables in a word) may be more likely to exhibit subadditive combination. This accords well with the present data, where both PFL and CE can be seen as phonologically specified, and both are manifested by lengthening of constant proportion. The influence of tempo on durations was more complex, but for all but the fastest rates, relative proportions were essentially unaffected by tempo. Models of constant proportion of duration have not fared well as predictors of timing in speech movement (Löfqvist, 1991). They may, however, be appropriate in the acoustic domain for specific factors over a wide range of rates.

Much work remains to be done in examining the edges of the range within which simple timing effects are found. Fast-speech studies need to take into account the existence of a continuum of rates, with the likelihood of a discontinuity or reorganization in articulation at some fast rate, beyond which timing is likely to be heavily influenced by the biomechanical limitations of the production system and less obviously dictated by linguistic factors. Slow speech (as opposed to clear speech, see, e.g., Uchanski *et al.*, 1996) has attracted less attention to date, but merits closer scrutiny not least because it serves to demarcate a range of ''normal'' operation of speech production.

ACKNOWLEDGMENTS

The present work has benefitted from discussions with Janet Pierrehumbert, Art Kovitz, Bob Port, and Ken de Jong. Funding came from a postdoctoral fellowship from the Andrew W. Mellon Foundation and SNF Grant No. 21-49144.96 (Long Short-Term Memory).

[1]Although näive as a production model, Klatt's model still finds application in synthesis algorithms and its has the inestimal virtue of making numerically testable predictions.

Beckman, M. E., Edwards, J., and Fletcher, J. (**1992**). ''Prosodic structure and tempo in a sonority model of articulatory dynamics,'' in *Gesture, Segment, Prosody: Papers in Laboratory Phonology II*, edited by G. J. Docherty and D. R. Ladd (Cambridge U.P., Cambridge), pp. 68–86.

Berkovits, R. (**1991**). ''The effect of speaking rate on evidence for utterance-final lengthening,'' Phonetica **48**, 57–66.

Byrd, D., and Tan, C. C. (**1996**). ''Saying consonant clusters quickly,'' J. Phon. **24**, 263–282.

Cooper, W. E., Eady, S. J., and Mueller, P. R. (**1985**). ''Acoustical aspects of contrastive stress in question–answer contexts,'' J. Acoust. Soc. Am. **77**, 2142–2156.

Crystal, T. H., and House, A. S. (**1988**). ''The duration of American-English vowels: an overview,'' J. Phon. **16**, 263.

Hays, W. L. (**1988**). *Statistics* (Harcourt Brace, Orlando, FL), 4th ed.

Klatt, D. H. (**1973**). ''Interaction between two factors that influence vowel duration,'' J. Acoust. Soc. Am. **54**, 1102–1104.

Klatt, D. H. (**1975**). ''Vowel lengthening is syntactically determined in a connected discourse,'' J. Phon. **3**, 129–140.

Klatt, D. H. (**1976**). ''Linguistic use of segmental duration in English: Acoustic and perceptual evidence,'' J. Acoust. Soc. Am. **59**, 1208–1221.

Löfqvist, A. (**1991**). ''Proportional timing in speech motor control,'' J. Phon. **19**, 343–350.

Port, R. F. (**1981**). ''Linguistic timing factors in combination,'' J. Acoust. Soc. Am. **69**, 262–274.

Shaiman, S., Adams, S. G., and Kimelman, M. D. Z. (**1995**). ''Timing relationships of the upper lip and jaw across changes in speaking rate,'' J. Phon. **23**, 119–128.

Snedecor, G. W., and Cochran, W. G. (**1989**). *Statistical Methods* (Iowa State U.P., Ames, IA).

Statistical Sciences (**1995**). *S-PLUS Guide to Statistical and Mathematical Analysis, Version 3.3* (StatSci, a division of MathSoft, Inc., Seattle, WA).

Turk, A. E., and Sawusch, J. R. (**1997**). ''The domain of accentual lengthening in American English,'' J. Phon. **25**, 25–41.

Uchanski, R. M., Choi, S. S., Braida, L. D., Reed, C. M., and Durlach, N. I. (**1996**). ''Speaking clearly for the hard of hearing IV: Further studies of the role of speaking rate,'' J. Speech Hear. Res. **39**, 494–509.

Utterance rate and linguistic properties as determinants of lexical dysfluencies in children who stutter

Peter Howell, James Au-Yeung, and Lesley Pilgrim
Department of Psychology, University College London, Gower Street, London WC1E 6BT, England

(Received 19 May 1998; accepted for publication 15 September 1998)

Two important determinants of variation in stuttering frequency are utterance rate and the linguistic properties of the words being spoken. Little is known how these determinants interrelate. It is hypothesized that those linguistic factors that lead to change in word duration, alter utterance rate locally within an utterance that then gives rise to an increase in stuttering frequency. According to the hypothesis, utterance rate variation should occur locally within the linguistic segments in an utterance that is known to increase the likelihood of stuttering. The hypothesis is tested using length of tone unit as the linguistic factor. Three predictions are confirmed: Utterance rate varies locally within the tone units and this local variation affects stuttering frequency; stuttering frequency is positively related to the length of tone units; variations in utterance rate are correlated with tone unit length. Alternative theoretical formulations of these findings are considered. © *1999 Acoustical Society of America.* [S0001-4966(99)00901-7]

PACS numbers: 43.70.Fq, 43.70.Gr [AL]

INTRODUCTION

Traditionally, calculation of speech rate has included pauses and stuttering events in their measurement of the total speech time, and speech rate has been expressed as the number of words or syllables uttered in that period of time divided by the total speech time. Recent researchers have advocated the use of articulation rate (see Kalinowski *et al.*, 1993, 1995, 1996; Kelly and Conture, 1992; Logan and Conture, 1995; Yaruss and Conture, 1995). This rate excludes dysfluent words or syllables from the rate calculations and time spent pausing is left out of the total speech time. These two methods of calculation of rate are termed here ''global speech rate'' and ''global articulatory rate,'' respectively.

Rate measures may need further refinement to establish the relationship between speech rate and stuttering. One reason is that speakers vary rate at different points in time. One aim of this article is to investigate whether such ''local'' variations occur and to see if such local measurement of articulation rate is appropriate in elucidating the relationship between speech rate and stuttering. The local rate is measured by calculating the articulation rate of speech material that is grouped together prosodically (within a tone unit) which often only spans a few words. The second reason for employing local rate measures is in order to allow the relationship between speech rate and linguistic factors to be studied (for the reasons described below).

When global speech rate measures have been made, researchers have been in almost unanimous agreement that reducing speech rate decreases stuttering frequency. Johnson and Rosen (1937), for example, found that the amount of stuttering decreased during slow speech compared with normal speech rate. Other authorities who concur with this conclusion include Perkins *et al.* (1991), Starkweather (1985), and Wingate (1976). However, a qualifying rider has been made by Kalinowski and his colleagues concerning articulatory rate. They have reported results employing altered auditory feedback that led them to question whether a slow articulatory rate is always necessary for fluency to improve (Kalinowski *et al.*, 1993, 1995, 1996). It is frequently reported that increased global speech rate has a complementary effect on stuttering frequency. Thus Johnson and Rosen found that subjects had greater difficulty in speaking at fast rates compared to slower rates. Bloodstein (1987) also noted that high speaking rates can result in stuttering. In an experiment on the effects of speech rate on stuttering frequency, Kalinowski *et al.* (1993) found that when reading at a faster than normal articulatory rate, seven out of nine subjects showed an increase in stuttering frequency. In a later study, however, Kalinowski *et al.* (1995) found no difference in stuttering frequency between normal and fast rates. In the light of this discrepancy, Kalinowski *et al.* (1995) concluded that an increase in articulatory rate does not determine stuttering frequency with the same consistency as does a decrease in rate.

The other established determinants of frequency of stuttering are those associated with the linguistic properties of the words. Identification of the linguistic factors that are indicative of the likelihood of stuttering on particular words started with the work of Brown (reviewed in Brown, 1945). In this review, he concluded that four linguistic factors were paramount: (a) Words occurring in early positions in sentences are more likely to be stuttered than those nearer the end. (b) Content words are more likely to be stuttered than function words. (c) Long words are more prone to be stuttered than short ones. (d) Words starting with consonants are stuttered more often than those starting with vowels. There have been three main areas of investigation on linguistic determinants of stuttering since Brown's seminal work: (a) Differences between the way these factors operate in children who stutter compared with adults. (b) Identification of additional factors that need to be added to Brown's list. (c) Attempts to provide a unifying theoretical framework to explain the operation of some or all of the linguistic factors that affect the frequency of stuttering (Au-Yeung *et al.*, 1998;

Brown, 1945; Howell *et al.*, in press; Wingate, 1988).

The best documented linguistic indicator that is sensitive to speakers' age is word type. Bloodstein and Gantwerk (1967) and Bloodstein and Grossman (1981) have found that children who stutter experience more difficulty on function words than on content words. Recently, Howell *et al.* (in press) compared frequency of stuttering directly for different age groups. They found that frequency of stuttering of function words was significantly higher than on content words for age groups up to nine years but not for older age groups.

One of the additional linguistic factors that has been investigated in detail since Brown's work is sentence length (Gaines *et al.*, 1991; Logan and Conture, 1995; Tornick and Bloodstein, 1976; Weiss and Zebrowski, 1992). Logan and Conture (1995), for example, have investigated this factor in children who stutter. They found that frequency of stuttering was higher on long sentences than on short ones. This factor was noted to occur for adults who stutter in an early study by Brown and Moren (1942) but did not appear in his 1945 list of principal determinants.

Previous attempts at supplying a unifying framework have concentrated on explaining the linguistic determinants listed by Brown (1945). Brown himself considered that the four linguistic factors he identified were all associated with semantic difficulty. Wingate (1988) argued that stress could explain how all these same factors operate in these speakers. Although these two explanations may account for stuttering in adults, it is less clear how they would apply to children who stutter. Thus Brown's argument for a semantic association cannot explain why children have difficulties on the semantically simpler function words observed in these speakers. Similarly, Wingate's emphasis on the role of stress is less applicable to children's speech due to the prevalence of dysfluency on function words which are rarely stressed.

The principle reason why speech rate has not been considered along with linguistic determinants within such unifying frameworks is that analyses of the influence of rate have usually been made globally whereas linguistic determinants are assessed at a local level in an utterance. Thus the greatest extent investigated in Brown's (1945) work was when he examined word position effects using sentences as the unit of analysis. Restricting attention to short linguistic segments has the advantage that it allows the words or linguistic contexts that lead to stuttering to be specified with precision. Increased precision would be a sufficient reason on its own to motivate investigating whether speech rate influences occur at a local level within extended utterances. However, there are also reasons to suppose that it is misleading to base conclusions about how rate affects stuttering frequency on long utterances, even utterances the length of a sentence. The grounds for this follow.

As stated earlier, in continuous spontaneous speech, rate variations occur between constituent stretches even though speakers receive no instructions to do this. There is surprisingly little information how such local rate variations are made in speech. One thing tested in the below experiment is whether words within fast spoken groups have the highest tendency to be stuttered. When speakers make global rate changes, this might or might not be expected to lead to changes in frequency of stuttering. This can be illustrated by considering two ways which contrast in what happens to stuttering frequency depending on how global rate increases are effected at a local level. The first possibility is that a speaker increases rate proportionately for all the utterance. The parts of the utterance that are spoken at fast, medium, and slow rates would tend to change with slow local stretches becoming medium rate, medium rate local stretches becoming fast, and fast stretches becoming faster still. In this case, the global rate increase would be expected to increase the frequency of stuttering due to the increased number of the problematic fast local stretches. The second possibility arises if speakers only have flexibility to increase rate in local stretches that are spoken at a slow rate. When the rate of these slow stretches is increased, they would become medium rate. In this situation, there would be no increase in frequency of stuttering with increased speech rate as no additional local stretches are spoken sufficiently fast. The different findings about the effects of speech rate increases on stuttering frequency noted in the studies of Kalinowski *et al.* (1993, 1995) may have occurred because speakers in the two studies used these different ways of speeding speech up. It is possible that, by chance, the speakers in Kalinowski *et al.* (1993), who showed an increase in stuttering frequency with rate, may have increased rate proportionately throughout the utterance, while the subjects in Kalinowski *et al.* (1995) may have just accelerated the slow stretches.

Alternative ways of changing speech rate are not investigated in the current study but they do have methodological implications for the way the study was conducted. They show that it is necessary to investigate the association between stuttering frequency and rate changes at local levels in utterances as misleading conclusions can be drawn if only global measures are investigated. That is, global rate changes can occur without affecting stuttering frequency even though local rate changes influence the frequency of stuttering. The current experiment shows that the variations in stuttering frequency that occur in groups of words within the same utterance depend on local speech rate.

In the experimental procedure adopted below, the recorded speech is segmented into regions spoken at different rates. The segmental unit that is employed is the tone unit. These segments, by definition, reflect the prosodic grouping imposed on an utterance by a speaker whether the material is read or spoken spontaneously (Crystal, 1969, 1987). Tone units consist of a minimum of one syllable and its boundaries are marked by the prosodic properties of a change in pitch and a junctural feature (usually a very slight pause). Every tone unit has a coherent intonation and one accented nucleus syllable (Kreidler, 1997). An example of tone unit segmentation within a sentence would be, ''If the delivery man comes ‖ give me a shout'' (where ‖ marks the boundary between tone units). A typical reading of this sentence would be to speak the words in the first tone unit relatively rapidly and those in the second more slowly which a speaker might adopt so as to emphasize the instruction. This example shows that tone units can be produced at different rates from one unit to the next. It was assumed in the preceding paragraph that words grouped together prosodically that are spo-

ken at a fast rate would be the ones prone to contain stutterings. To establish this, tone units are classified into different rates and examined to see whether the groups of tone units spoken at different rates have any influence on frequency of stuttering.

Spontaneous speech was used in the current study while most previous studies on speech rate employed read material. Choice of this type of material may appear surprising as read material is more convenient to deal with experimentally. For example, it is straightforward to get speakers to change their speech rate by telling them to read faster. Read speech also has the advantage that it allows sentences to be used which are also commonly employed in studies of linguistic factors. Consequently, comparisons between rate and linguistic factors could be made directly if sentences were used. A procedure which involved reading sentences was avoided here for the primary reason that the rate changes that occur in read material are unnatural. The reason for this is that reading does not involve certain on-going processes like utterance formulation which are likely to have important roles in determining speech rate. Thus it is not clear whether variation in speech rate enforced by an experimenter has similarities to the mechanisms of rate variation that speakers use spontaneously in everyday speaking situations. It is also known from empirical evidence that the two modes of delivery (read and spontaneous) lead to differences in prosodic organization. For instance, Howell and Kadi-Hanifi (1991) showed speakers do not produce the same tone unit boundaries in speech they produced spontaneously compared with those they produce where they were required to read the same material at a later date.

The speech of children around nine years old is used in the analyses. Nine years was chosen for two reasons. First, children who are stuttering at this age are more likely to persist than younger ones (Andrews and Harris, 1964). Thus at this age, it has been more definitely established that these speakers have a stuttering problem. Second, secondary idiosyncratic influences characteristic of long-term persistent stuttering that may affect utterance rate measures at older ages are less likely to have appeared in speakers of this age. The types of stuttering incidents that are counted are what Howell *et al.* (1997) refer to as lexical dysfluencies. These consist of word and part-word repetitions, prolongations, and broken words (the latter category is referred to by the more neutral term ''other'' dysfluencies). Supralexical dysfluencies that extend over groups of words (such as phrase repetitions) can be split up over more than one tone unit.

The hypothesis about how rate changes within spontaneous speech and how these rate changes are associated with the linguistic determinants that affect the likelihood of stuttering is as follows. The linguistic characteristics associated with stuttering change speech rate. When speech rate increases, stuttering is more likely to occur. In the current experiment, the length of tone units is the linguistic property under investigation which would affect the utterance rate. As noted earlier, it has been reported previously that stuttering frequency increases when sentence length increases (Brown and Moren, 1942; Gaines *et al.*, 1991; Logan and Conture, 1995; Tornick and Bloodstein, 1976; Weiss and Zebrowski, 1992). In addition, it is known that utterance rate increases when utterance length increases in fluent speakers (Ferreira, 1993; Levelt, 1989). A check is first made as to whether utterance rate and stuttering frequency covary within tone units in spontaneous speech in the same way that they do in sentences in read speech. Next, analyses are made to ascertain whether tone unit length in spontaneous speech influences stuttering frequency in a similar way to that which occurs in sentences in read speech. The two preceding analyses do not rule out the possibility that utterance rate and tone unit length operate independently. Therefore, the data are examined in the final analysis to assess whether there is a correlation between tone unit length and utterance rate. To obtain a satisfactory measure of utterance rate for this purpose, rate is measured only on nonstuttered syllables in a tone unit (Hargrave *et al.*, 1994).

TABLE I. Speaker information including speaker initials, age, gender, overall stuttering rate, and the number of words uttered by individual speakers and used in this study.

Speaker	Age	Gender	Stuttering rate	Number of words
cn	10	M	15.08	166
dc	10	M	4.92	230
dm	9	M	12.07	246
jg	9	M	7.69	98
mt	10	M	25.00	199
pm	9	M	20.35	200
rp	11	M	35.83	145
sh	11	F	23.27	164

I. METHOD

A. Subjects

The data used for speech assessments are from eight children who stutter. The children ranged in age from 9 to 11 years old. There were seven boys and one girl. The children had been assessed by therapists and admitted to a 2 week intensive therapy course. Detailed information on individual speakers is provided in Table I.

B. Materials and apparatus

Recordings were made at the commencement of the intensive therapy course (i.e., before they received treatment). The children were asked to speak in monologue for about 2 min on any topics they liked, for example, hobbies, friends, holidays. The children talked continuously during this period, which is probably due to them having free choice about topic. Recordings of the children were made in an Amplisilence sound-attenuated booth (Howell *et al.*, 1998). The speech was transduced with a Sennheiser K6 microphone positioned 6 in. in front of the speaker in direct line with the mouth. The speech was recorded on DAT tape and transferred digitally to computer for further processing. The speech from the DAT tapes was down-sampled to 20 kHz.

C. Transcription and segmentation procedures

The speech was first transcribed in orthographic form with lexical dysfluencies not marked. These were made in-

dependently by two judges. The experimental judge had eight years experience transcribing stuttered speech. The second judge was used for assessing the reliability of this and all other aspects of assessment and had two years experience transcribing stuttered speech but was naive as to the purpose of the experiment. Agreement between the two judges for the orthographic transcriptions was high at 96%, giving a Kappa coefficient of 0.92 which is much higher than chance (Fleiss, 1971). The version of the transcription produced by the more experienced judge was used in the next stages of the procedure.

The end-points of the words in this transcription were located. Using end-points ensured that any pauses or word-initiation attempts were included at the start of the subsequent word (for the purpose of this experiment, word repetitions were also treated as word-initiation attempts). The position where each word ended was located with the aid of two traveling cursors that were superimposed on the oscillographic display of the speech waveform. Each cursor position was independently adjusted with a mouse. The first cursor was initially placed at the start of the speech. The second cursor was positioned slightly before where the end of the first word was thought to be located. The section of speech between the first and second cursors was then played and listened to over an RS 250-924 headset, to check whether the end of the word had been correctly located. The second cursor was then adjusted further forward and the word replayed again. Once the judge had adjusted past the end of the word, he adjusted the second cursor back in time into the file until the end of the word was not heard. By continually crossing backward and forward across the boundary at the end of the word, he became satisfied that he had located it accurately. This marker was stored and the subject proceeded to locate the boundary between the next words in the sequence in the same way (this procedure is similar to that used by Osberger and Levitt, 1979). Once the judge was happy about the position of the end-point cursor, this marker was stored and the boundary between the next words in the sequence was located in the same way. Silent pauses not associated with stuttered words were located using the same procedure. Filled pauses were treated as words both here and when the words were categorized. Both the experimental judge and the judge used for assessing reliability worked independently through the recordings of each speaker sequentially. Judge 1 was about as likely to place his marker in advance of Judge 2 (49.2%) as the reverse (48.7%). When this happened, the differences were small (3.9% of the duration of a fluent word and 4.6% of a dysfluent word). Thus the placement of the word end-point markers is consistent between judges and, therefore, the markers of the experienced judge were used in the next phase of the procedure.

In this next phase, the two judges used a similar procedure to that employed to locate word end-points to establish words at tone unit boundaries. The inter-judge agreement about tone unit boundaries was calculated as the average of tone units identified by the first judge and agreed by the second, and vice versa. Agreement about tone-unit segmentation was 83% and the Kappa coefficient was 0.66 which is considered as a good reproducibility (Fleiss, 1971).

D. Assessment procedures for dysfluencies

Fluency assessments were made using words as defined previously (that is, extending from the interval from the end of one word to the end of the next) using the word end-point markers produced by the more experienced judge again. Each word in the speech of all eight subjects was assessed. A randomized presentation order was used so that the global context in which all judgments were made was as constant as possible (thus minimizing range effects; Parducci, 1965). The random sequence was obtained computationally. The first randomly selected word was heard in isolation. After a short pause the test word was heard along with the word that had preceded it (the two words had the same timing and were in the same order as in the original recording). Consequently, pauses were apparent when they occurred between the context and test word. The test word alone and this word with the word that preceded it could be heard as often as the judge required by hitting the return key on the computer keyboard. Thus presentation of the test and context words was initiated by the judge, and the current trial ended and the next trial commenced after the judge entered his responses (detailed in the following paragraph). The full context was not available at the beginning of the recording (in these cases, the word to be judged was still played in isolation beforehand).

Assessments obtained about each word were a rating about how comfortably the word ''flowed'' and a categorization of the word as fluent, prolongation, repetition of word or part-word, or other dysfluency. The flow judgments were included as a classificatory response does not allow a judge to indicate anything about the relative fluency or dysfluency within a category. The flow judgments were made after the categorization on a 5-point scale. The 5-point scale employed a Likert scale format (Likert, 1932) in which the judge indicated the extent to which he agreed with the statement that ''the speech is flowing smoothly'' (1 = agree, 5 = disagree with intermediate values showing levels of agreement). Thus it represents a judge's assessment of the speaker's ability or inability to proceed with speech (Perkins, 1990). It was stressed that the rating scale was not a finer-grained indication of whether a word is fluent or dysfluent: A word high in ''flow'' might nevertheless be categorized as fluent or vice versa. Howell *et al.* (1997) have shown that inter-judge agreement is high for repetitions. Agreement about prolongations is also satisfactory provided that words called prolongation and given ratings of 4 or 5 are selected (as in the below analyses). The inter-judge agreement level for location of dysfluent words where both judges agreed that a word was dysfluent was 85.6% out of all words identified dysfluent by either judge (Kappa's coefficient is 0.71 which is considered as a good level of agreement).

E. Classification of utterance rate of each tone unit

As just described, fluency assessments were based on words. Utterance rate measures, on the other hand, were always made on syllables as they are less variable in duration than words. First, the duration of each tone unit was computed by removing all dysfluent words and pauses between words (Hargrave *et al.*, 1994). The number of syllables in all

fluent words in a tone unit was then divided by the duration of the tone unit after dysfluent words had been removed to produce the stutter-free utterance rate (syllables/second) of that tone unit. Utterance rates of 4–5 syllables/s were classified as medium [based on fluent speakers' speech rate found by Pickett (1980) and concurred by Kalinowski and his colleagues]. Utterance rates above and below the 4–5 syllables/s were classified as fast and slow, respectively. In a second analysis, the utterance rate was classified as fast, medium, or slow depending on the individual speaker's utterance rate. The mean and s.d. of utterance rate of all words were calculated for each speaker. The fast rate was defined as the utterance rate more than one s.d. above the mean rate while the slow rate was defined as lower than one s.d. below the mean utterance rate. The rest were classified as medium rate.

II. RESULTS

The hypothesis that there is a greater likelihood of stuttering on tone units which are spoken fast compared to those spoken at a medium or slow rate was tested. In the first analysis, the division of utterance rate was carried out using the 4–5 syllables/s criteria. For each speaker, all the tone units at a selected rate were located and the number of words across all these tone units was calculated. The number of these words that were stuttered was then determined. Stuttering rate was expressed as the percentage of the number of stuttered words out of the total number of words in tone units of a particular utterance rate. This provides a measure of the per word stuttering rate of words in that rate division of tone units. It is unaffected by differences in tone unit length between the utterance rate divisions. A one-way ANOVA was performed on the stuttering rates at different utterance rate (with the overall stuttering rate of the speakers taken out as covariate) to see if there was a relationship between utterance rate divisions and, the dependent variable, stuttering rate. Words in fast tone units had a significantly higher chance of being stuttered than tone units at slower utterance rates, $F(2,20)=4.36$, $p<0.05$. The adjusted stuttering rates are plotted as boxplots for each utterance rate in Fig. 1 (the caption to the figure describes the convention used in boxplots). *Post hoc* Tukey test showed that the tone units of fast utterance rate had significantly higher stuttering rate than those of the slow utterance rate.

In order to test if fast speech rate alone increased the likelihood of stuttering, the medium and slow tone units were grouped together and tested against the fast tone units. Words in the fast tone units were found to be stuttered more when the stuttering rate of individual speakers were taken out as covariate, $F(1,13)=15.03$, $p<0.005$, in a one-way ANOVA test with speech rate as the independent variable. This confirmed that fast speech rate did have higher level of stuttering than the remaining rate divisions.

In the second analysis, the utterance rate was defined for individual speakers using the mean and s.d. of utterance rate of all words as described above. A one-way ANOVA was performed on the stuttering rates at different utterance rates (with the overall stuttering rate of the speakers taken out as covariate). Words which were classified as fast had a significantly higher chance of being stuttered than tone units at slower utterance rates, $F(2,20)=4.07$, $p<0.05$. The adjusted stuttering rates are plotted as boxplots for each utterance rate in Fig. 2. A *post hoc* Tukey test showed that the tone units of fast utterance rate has significantly higher stuttering rate than those of the medium utterance rate. Once again, the medium and slow tone units were grouped together to test against the fast tone units similar to the first analysis. Words in the fast tone units were found to be stuttered more when the stuttering rate of individual speakers was taken out as covariate, $F(1,13)=6.58$, $p<0.05$, in a one-way ANOVA test with speech rate as the independent variable. This again con-

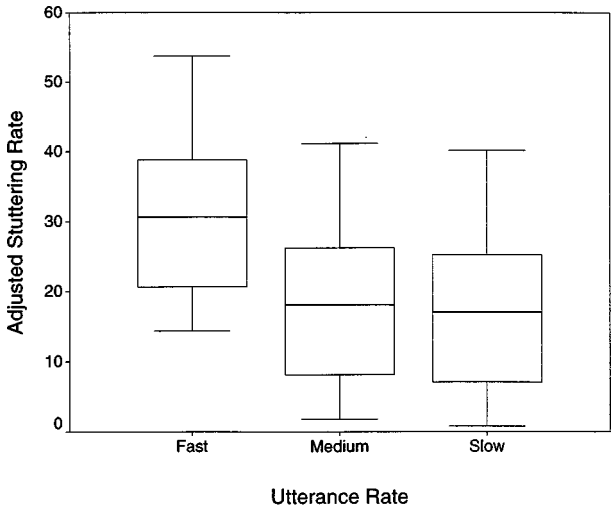

FIG. 1. Boxplots of the adjusted stuttering rates on words (ordinate) for the three utterance rate divisions based on syllables. Fast, medium, and slow utterance rates are labeled on the abscissa. Fast is any rate above 5 syllable per second; medium as between 4 and 5 syllable per second; slow as under 4 syllable per second. The boxes at each rate indicate the inter-quartile range of stuttering rates and the mean is shown by the solid horizontal line within the box. The full range of stuttering rates is shown by the whiskers.

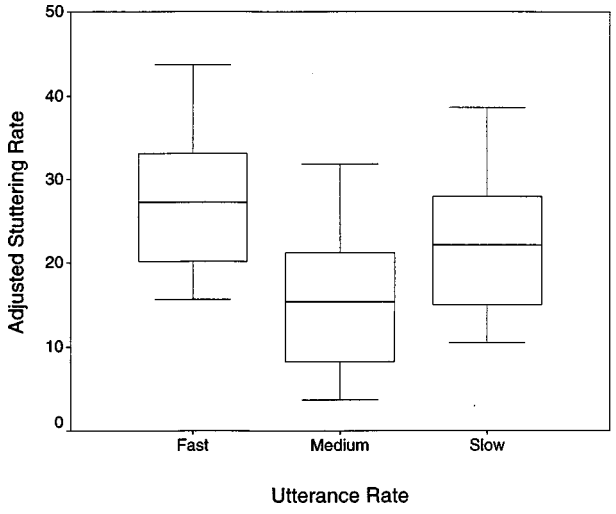

FIG. 2. Boxplots (formatted as in Fig. 1) of the adjusted stuttering rates on words (ordinate) for the three utterance rate divisions based on the speech rate of individual speaker. Fast, medium and slow utterance rates are labeled on the abscissa. Fast is defined as speech rate higher that the level at one s.d. above the mean speech rate of all fluent words. Slow rate is defined as less than one s.d. below the mean rate. Medium is the rate in between $+1$ and -1 s.d. levels.

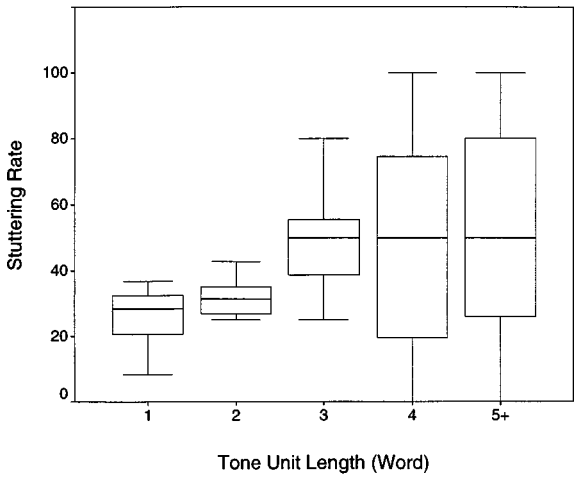

FIG. 3. Boxplots (formatted as in Fig. 1) of stuttering rates on words (ordinate) for different tone unit lengths measured in words (abscissa).

firmed that fast speech rate had a higher level of stuttering.

Next, the hypothesis that words in longer tone units have a higher chance of being stuttered was tested. Tone unit length was measured both in words and syllables. The first step in obtaining the length of tone units in words was to divide tone units into those that contained one, two, three, four, and more than four words. For each speaker, all the tone units of a given length were located and the words in them summed to obtain the total. The number of words out of this total that were stuttered was then determined. The stuttering rate for tone units of the specified length was expressed as the percentage of stuttered words out of the total number of words for the tone units of that particular length. A one-way ANOVA (with the overall stuttering rate of the speakers taken out as covariate) showed that stuttering rate differed significantly over tone units of different word lengths $[F(4,34)=3.04,\ p<0.05]$. The stuttering rates against tone unit length in words are presented as boxplots in Fig. 3. Tone unit length was measured on syllables in a similar way as with words. Stuttering rate varied across tone units of different length measured in syllables, in a similar

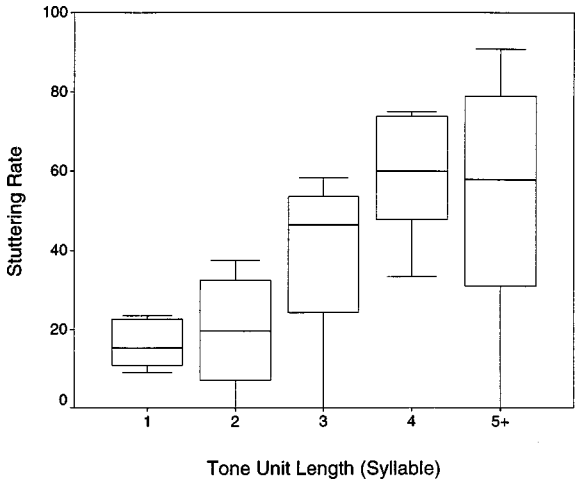

FIG. 4. Boxplots (formatted as in Fig. 1) of stuttering rates on words (ordinate) for different tone unit lengths measured in syllables (abscissa).

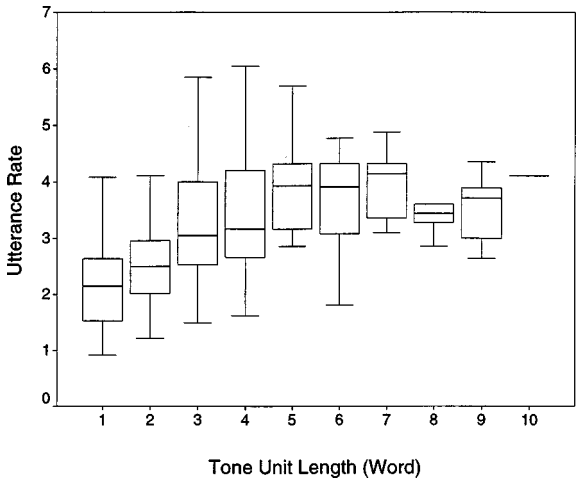

FIG. 5. Boxplots (formatted as in Fig. 1) showing the correlation between utterance rate (ordinate) measured on syllables and utterance length measured in number of words (abscissa).

way to that found with words $[F(4,34)=8.00,\ p<0.001]$. These data are plotted in Fig. 4 in the same way as the word data (which appeared in Fig. 3).

The third analysis examined whether utterance rate and tone unit length were correlated. Tone unit length and utterance rate correlated (linearly) significantly both when tone unit length was measured in words ($r=0.500$, $p<0.001$) and in syllables ($r=0.568$, $p<0.001$). The quadratic correlations were also significant ($r=0.557$, $p<0.001$ and $r=0.633$, $p<0.001$, respectively). Cubic regressions were also carried out and not much improvement was found from the quadratic ones, $r=0.558$, $p<0.001$, and $r=0.643$, $p<0.001$, respectively. This suggests that rate asymptotes in long tone units. Boxplots showing the correlation between raw tone unit length and utterance rate scores are given for the case where tone unit length was measured in words in Fig. 5 and when measured on syllables in Fig. 6.

III. DISCUSSION

In the analysis using fixed criteria for dividing utterances into fast, medium, and slow rate, the fast rate produced

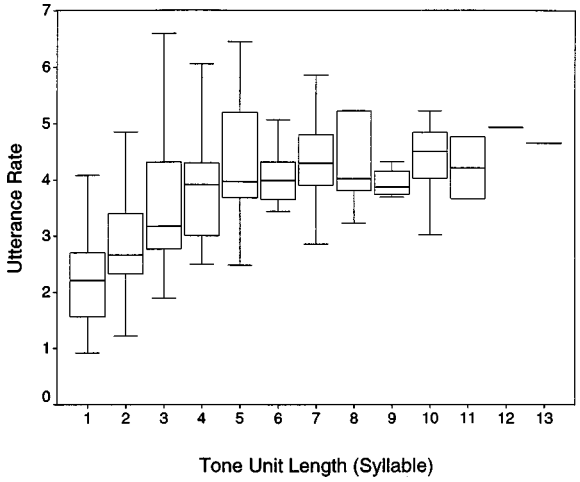

FIG. 6. Boxplots (formatted as in Fig. 1) showing the correlation between utterance rate (ordinate) measured on syllables and utterance length also measured in number of syllables (abscissa).

a higher stuttering rate than the slow rate. Medium rate utterances had lower frequency of stuttering than fast rates, but not significantly so. When criteria based on the individual's speech rate were employed, fast rate speech produced a significantly higher rate of stuttering than medium rate speech. Slow rate speech had lower rates of stuttering than fast rate, although not significantly so. The common factors in these different rate analyses are: (a) The significant effect in these analyses both involve the fast rate division which produced higher rates of stutterings than other rate partitions. (b) In rate partitions that do not differ significantly in frequency of stuttering from the fast one, stuttering rates were always lower. We conclude, therefore that the hypothesis that there is a greater likelihood of stuttering on tone units which are spoken rapidly was supported. These tone units are interspersed with other tone units spoken at different rates. The findings suggest that not all stretches of speech in an utterance are equally problematic for speakers. A local utterance rate measure allows the stretches that are likely to be difficult to be specified in part. The two subsequent analyses addressed the question whether linguistic factors, known from previous studies to operate at a local level in an utterance, bring about rate changes that then lead to stuttering. One linguistic factor that could change utterance rate is utterance length. It was first shown that long tone units have a greater likelihood of stuttering than short ones, as has been reported to occur in speech read by children (Logan and Conture, 1995). It was then shown that the length of nonstuttered tone units was correlated with speech rate. A similar correlation has been established between speech rate and tone unit length for fluent speakers of English (Ferreira, 1993). Two questions need considering with respect to these findings. (a) Why should utterance rate increases lead speakers to be dysfluent? (b) Why should long utterances be spoken more rapidly than short ones? Some proposed answers to these questions will be developed dealing, in particular, with the level at which the effects arise. This will be followed by an attempt at specifying how utterance length and utterance rate interact leading to dysfluency.

First, two potential ways of explaining why utterance rate increases frequency of stuttering are considered. In both these accounts, a distinction is drawn between planning a sound and its execution (Levelt, 1989). The two views are differentiated by whether rate-dependent speech dysfluencies occur through the operation of the planning or the execution processes. The first possibility is a development of Postma and Kolk's (Kolk and Postma, 1997; Postma, 1997; Postma and Kolk, 1992, 1993) Covert Repair Hypothesis (CRH). CRH is a model that maintains stuttering arises out of repair processes (Levelt, 1983) that occur in fluent speakers' speech as well as in the speech of people who stutter. Repairing appears to be taking place in an utterance like ''turn left at the, no, turn right at the crossroads'' where the speech indicates that the speaker realizes he or she has given the wrong direction and alters it. CRH maintains that stuttering is a by-product of repairing covert, rather than such overt, phonemic errors in the speech plan before it is executed. CRH proposes that the errors occur as a result of a defect in the phonological planning process. In Postma and Kolk's account, speakers replan the speech when they detect that such an error has occurred. Such a replanning process is hypothesized by Postma and Kolk and remains to be proven. The model could be applied to the rate data reported in the current experiment. It would simply be necessary to make the reasonable assumption that the covert errors that require replanning are more likely to occur when utterance rate is high.

Blackmer and Mitton (1991) have questioned whether dysfluencies that fluent speakers produce during self-repairs allow sufficient time for replanning. Their data were from recordings of speech errors and repairs made by adults to late night radio shows. They found that speakers were able to interrupt themselves extremely rapidly and would then repeat words they had spoken immediately prior to the interruption. Elsewhere, Clark and Clark (1977) have proposed that interruptions and repetitions, similar to those in the examples Blackmer and Mitton give, occur because the plan for a subsequent word or words is not ready. Speakers have the plan for words spoken previously and these can be automatically re-executed (i.e., without replanning them). The time during which the repetition occurs allows further time for planning to be completed. It would be expected that the process just described would be prone to happen more when speech rate is high, as rapid rates would increase the chance that the plan for the next word is unavailable. Note that the role of repetition is to allow time for completing the plan of a later word and is a stalling tactic, not a malfunction in central nervous system structures responsible for planning speech. Also, an erroneous plan has not been produced for the word that initiates the stalling, more time to complete the plan is just needed. Thus neither the sequence of repetitions nor the later word involve planning errors. The occurrence of dysfluencies arises out of strategic responses speakers make during execution. Blackmer and Mitton's (1991) account offers a critique of the notion that replanning takes place during rapidly produced repetitions associated with speech repairs produced by fluent speakers. As well as the critical side of their argument, they propose an execution level strategy to explain the surface form of rapid repetitions. Au-Yeung and Howell (1998), Au-Yeung *et al.* (1998), and Howell *et al.* (in press) have shown how a process based on Blackmer and Mitton (1991) and Clark and Clark (1977) could explain features of stuttering behavior.

Two further comments about the execution level account of rate-induced dysfluencies are necessary: First, when applied as an account of all classes of dysfluency, the execution level explanations make predictions about activity in different sites in the brain. The execution level account proposes that there are no fundamental planning-level differences between fluent speakers and people who stutter though there would be at the levels involved in execution. Consequently, this view would predict that activity differences between fluency groups are more likely to be seen in the motor centers than in the areas attributed a role in language formulation. Even in the strong form of the execution level account, errors during planning would be allowed to occur in the speech of people who stutter. However, the prediction that there are no brain process differences between speaker groups due to replanning utterances would still apply providing that the pro-

pensity for errors that require replanning, occurs equally often between the speaker groups. The second comment concerns what descriptors are appropriate to account for difficulties arising from plan unavailability. CRH was developed from a linguistic perspective and describes difficulty at an abstract phonological level. The execution level account has continued this tradition using, for example, terminology from the repair literature and linguistic-based typologies of stuttered dysfluencies. However, since the problem of stuttering is deemed to be tied up with execution-level strategies, motoric descriptions would be more appropriate. The translation is straightforward as linguistic characterizations which specify phonological difficulty are directly related to motoric descriptions.

The second question mentioned was why should long utterances be spoken faster than short ones? The more specific question will be addressed about the level at which utterance length dependencies on stuttering arise. One possibility is that all the linguistic factors that lead to variations in frequency of stuttering emerge during planning. Since, as argued above, rate variations associated with stuttering appear through the operation of execution levels, linguistic factors that appear during planning would have supremacy. According to this account, the first step in utterance formulation is to decide on the words that will appear in a tone unit. Once the lexical content of a tone unit has been decided, the duration of individual words and syllables could arise through contextual influences operating in the tone unit. Empirical evidence suggests that planning that leads to long tone units being produced changes the duration of the constituent syllables. Thus if the stressed syllable duration in a word list is taken as the normal (or baseline) duration for a syllable in that particular word, compression of the syllable occurs when the syllable is uttered in the same word in connected speech (referred to by Levelt, 1989, as the word-in-isolation effect). Rate changes and an increase in frequency of stuttering would then follow from the change in duration.

A factor that commends this account (referred to as duration compression theory) is that it could also account for how some of Brown's (1945) other linguistic factors operate. A circumstantial interpretation can be made that duration compression occurs for different word positions in tone units. Thus Nakatani *et al.* (1981) have shown that, in fluent speakers, word durations are shortened when a stressed syllable occurs in tone unit-initial position than when it appears at later positions (Nakatani *et al.*, 1981). Syllable compression could also potentially explain the word length effect. Thus Lehiste (1970) has reported that the duration of a syllable in a long word is significantly shorter than when the same syllable occurs in a shorter word in fluent speakers' speech. Nooteboom (1972; cited by Levelt, 1989) showed that the duration of a syllable decreases the more syllables that follow it in a word. This could potentially explain why stuttering occurs almost exclusively on phones in early positions in words (Wingate, 1988). There does not seem any easy way of accounting for the word-initial consonant effect by duration compression. If this theory is correct, this factor may have a different basis to the others discussed probably because difficulty arises due to words having this factor being phonologically more difficult.

The duration compression account developed above has the major drawbacks that it relies on observational data and circumstantial arguments to account for the relationship between linguistic factors, speech rate and frequency of stuttering. Saying that the effects of duration are planned has little explanatory value. Moreover, the durational effects could well arise during the execution of the plan rather than being inherent specifications of the plan itself. The duration-compression approach would be more convincing if some superordinate factor could be found which explains why duration compression is associated with the different linguistic characteristics where the level at which it operates (planning or execution) can be deduced. One possibility is that duration compression factors in the plan could be mediated by longer lexical access time (time to retrieve the mental lexicon) in people who stutter (Prins *et al.*, 1997) and that lexical access time is influenced by Brown's factors. Thus lexical access would have to take longer when words are in, for instance, long tone units than short ones. This view can be contrasted with one in which duration compression is mediated by latency differences attributed to lexical access time but which derive from different times required to execute words with different forms and in different contexts known to affect frequency of stuttering.

Data to support the point of view that people who stutter show differences in lexical access time are not extensive and there are no data of speakers at the ages of 9–11 we tested (Prins *et al.*, 1997; Van Lieshout *et al.*, 1996a, 1996b). Furthermore, there is disagreement between the two principal groups of researchers about how to interpret these results. The main dispute between the groups is whether lexical access time differences can be accounted for at central (Prins *et al.*, 1997) or peripheral levels (Van Lieshout *et al.*, 1996a, 1996b). We have examined Prins *et al.*'s study elsewhere and shown that the latency differences interpreted as revealing differences in lexical access time of verbs between fluent speakers and people who stutter, could occur during speech-execution rather than while these words are being planned (Au-Yeung and Howell, submitted). The latency differences may reflect, then, more about execution times of phonologically difficult words rather than lexical access time per se.

Considering the evidence on these two questions together, some tentative conclusions can be drawn about how speech rate and linguistic factors interact. First, increases in stuttering frequency associated with increased utterance rate appear to arise during execution rather than planning. Although it is possible that duration differences associated with Brown's factors occur during planning, there is no compelling reason for this conclusion unless the process through which these effects arise can be specified. Lexical access time differences associated with words with these linguistic characteristics is one possible way of supplying such a process. Although latency differences that are supposed to indicate that people who stutter have slow access to verbs (instances of content words) and conceivably also for words that have other of Brown's factors, the latency differences between fluency groups can be explained by differences aris-

ing during execution of these word forms. Taking all this evidence together, it appears that people who stutter can be differentiated from fluent speakers in the way they execute speech, in particular, because they speak too fast in specified contexts this then precipitates stuttering. The contexts that are likely to be stuttered when spoken too fast are those in which the linguistic or motor load is high. At present, no metric has been definitively established to measure this. EMG work on fluent speakers (Van Lieshout *et al.*, 1995) and work identifying phonological properties indicating high motor load in people who stutter (Howell *et al.*, submitted) may provide such indices in the future. Linguistic factors and utterance rate operate interactively at the execution level leading to dysfluencies. This interaction is strategic rather than hard-wired as shown by the fact that fluency is reversible in various ways for a time when speech rate is artificially controlled. Two important question that remain to be answered are why does fluency not stick when it is induced and why do some children stay dysfluent if dysfluent speech patterns are merely strategic?

In this study, only two factors were considered that trigger stuttering: local utterance rate and tone unit length. There are other linguistic factors that interact with tone unit length such as syntactic, prosodic, phonetic structures. The interaction of these factors with utterance length will be investigated in further studies. These observations mean that the explanation offered here is by no mean exhaustive. We consider we have supplied a possible way that the linguistic utterance being planned leads to a high motor load at the execution/motor level. Further work is needed to separate between the motor/execution account versus accounts that maintain the problem arises in speech planning processes (such as the proposal that stuttering arises out when covert repairs to plans are made).

ACKNOWLEDGMENTS

We wish to express our thanks to the reviewers, Dr. Joe Kalinowski, Dr. Pascal van Lieshout, and Dr. Anders Lofqvist, the associate editor of JASA, for their comments on this paper. This research was supported by a grant from the Wellcome Trust.

Andrews, G., and Harris, M. (**1964**). *The Syndrome of Stuttering* (Heinemann, London).

Au-Yeung, J., and Howell, P. (**1998**). ''Lexical and syntactic context and stuttering,'' Clinical Linguistics and Phonetics **12**, 67–78.

Au-Yeung, J., and Howell, P. (**submitted**). ''Lexicalization and stuttering: Comments on Prins. Main and Wampler (1997).''

Au-Yeung, J., Howell, P., and Pilgrim, L. (**1998**). ''Phonological words and stuttering on function words,'' J. Speech, Language and Hearing Research **41**, 1019–1030.

Blackmer, E. R., and Mitton, J. L. (**1991**). ''Theories of monitoring and the timing of repairs in spontaneous speech,'' Cognition **39**, 173–194.

Bloodstein, O. (**1987**). *A Handbook on Stuttering* (National Easter Seal Society, Chicago), 4th ed.

Bloodstein, O., and Gantwerk, B. F. (**1967**). ''Grammatical function in relation to stuttering in young children,'' J. Speech Hear. Res. **10**, 786–789.

Bloodstein, O., and Grossman, M. (**1981**). ''Early stutterings: Some aspects of their form and distribution,'' J. Speech Hear. Res. **24**, 298–302.

Brown, S. F. (**1945**). ''The loci of stutterings in the speech sequence,'' J. Speech Disorders **10**, 182–192.

Brown, S. F., and Moren, A. (**1942**). ''The frequency of stuttering with relation to word length during oral reading,'' J. Speech Disorders **7**, 153–159.

Clark, H. H., and Clark, E. (**1977**). *Psychology and Language. An Introduction to Psycholinguistics* (Harcourt, New York).

Crystal, D. (**1969**). *Prosodic Systems and Intonation in English* (Cambridge U.P., Cambridge, MA).

Crystal, D. (**1987**). *Clinical Linguistics* (Edward Arnold, London).

Ferreira, F. (**1993**). ''Effects of length and syntactic complexity on initiation times for prepared utterances,'' Journal of Memory Language, **30**, 210–233.

Fleiss, J. L. (**1971**). ''Measuring nominal scale agreement among many raters,'' Psychol. Bull. **76**, 378–382.

Gaines, N., Runyan, C. M., and Meyers, S. C. (**1991**). ''A comparison of young stutterers' fluent versus stuttered utterances on measures of length and complexity,'' J. Speech Hear. Res. **34**, 37–42.

Hargrave, S., Kalinowski, J., Stuart, A., Armson, J., and Jones, K. (**1994**). ''Effect of frequency-altered feedback on stuttering frequency at normal and fast rates,'' J. Speech Hear. Res. **37**, 1313–1319.

Howell, P., Au-Yeung, J., and Sackin, S. (**in press**). ''Exchange of stuttering from function words to content words with age,'' Journal of Speech, Language and Hearing Research.

Howell, P., Au-Yeung, J., and Sackin, S. (**submitted**). ''Internal structure of content words leading to lifespan differences in phonological difficulty in stuttering.''

Howell, P., and Kadi-Hanifi, K. (**1991**). ''Comparison of prosodic properties between read and spontaneous speech,'' Speech Commun. **10**, 163–169.

Howell, P., Sackin, S., and Glenn, K. (**1997**). ''Development of a two-stage procedure for the automatic recognition of dysfluencies in the speech of children who stutter. I. Psychometric procedures appropriate for selection of training material for lexical dysfluency classifiers,'' Journal of Speech, Language and Hearing Research **40**, 1073–1084.

Howell, P., Staveley, A., Sackin, S., and Rustin, L. (**1998**). ''Methods of interval selection, presence of noise and their effects on detectability of repetitions and prolongations,'' J. Acoust. Soc. Am. **104**, 3558–3567.

Johnson, W., and Rosen, L. (**1937**). ''Effect of certain changes in speech pattern upon frequency of stuttering,'' Journal of Speech Disorders **2**, 105–109.

Kalinowski, J., Armson, J., Mieszkowski, M., Stuart, A., and Gracco, V. L. (**1993**). ''Effects of alterations in auditory feedback and speech rate on stuttering frequency,'' Language and Speech **36**, 1–16.

Kalinowski, J., Armson, J., and Stuart, A. (**1995**). ''Effect of normal and fast articulatory rates on stuttering frequency,'' Journal of Fluency Disorders **20**, 293–302.

Kalinowski, J., Stuart, A., Sark, S., and Armson, J. (**1996**). ''Stuttering amelioration at various auditory feedback delays and speech rates,'' European Journal of Disorders of Communication **31**, 259–269.

Kelly, E. M., and Conture, E. G. (**1992**). ''Speaking rates, response time latencies, and interrupting behaviors of young stutterers, nonstutterers, and their mothers,'' J. Speech Hear. Res. **35**, 1256–1267.

Kolk, H., and Postma, A. (**1997**). ''Stuttering as a covert repair phenomenon,'' in *The Nature and Treatment of Stuttering: New Directions*, 2nd ed., edited by R. F. Curlee and G. M. Siegel (Allyn & Bacon, New York).

Kreidler, C. W. (**1997**). *Describing Spoken English: An Introduction* (Routledge, London).

Lehiste, I. (**1970**). *Suprasegmentals* (MIT, Cambridge, MA).

Levelt, W. J. M. (**1983**). ''Monitoring and self-repair in speech,'' Cognition **14**, 41–104.

Levelt, W. J. M. (**1989**). *Speaking: From Intention to Articulation* (MIT, Cambridge, MA).

Likert, R. (**1932**). ''A technique for the measurement of attitudes,'' Archives of Psychology, Number 140.

Logan, K. J., and Conture, E. G. (**1995**). ''Length, grammatical complexity, and rate differences in stuttered and fluent conversational utterances of children who stutter,'' Journal of Fluency Disorders **20**, 36–61.

Nakatani, L. H., O'Connor, J. D., and Aston, C. H. (**1981**). ''Prosodic aspects of American English speech rhythm,'' Phonetica **38**, 84–106.

Nooteboom, S. (**1972**). ''Production and perception of vowel duration,'' Unpublished doctoral dissertation, Utrecht University.

Osberger, M. J., and Levitt, H. (**1979**). ''The effect of timing errors on the intelligibility of deaf children's speech,'' J. Acoust. Soc. Am. **66**, 1316–1324.

Parducci, A. (**1965**). ''Category judgement: a range-frequency model,'' Psychol. Rev. **17**, 9–16.

Perkins, W. H. (**1990**). ''What is stuttering?'' J. Speech Hear. Res. **55**, 370–382.

Perkins, W. H., Kent, R., and Curlee, R. (**1991**). ''A theory of neuropsycholinguistic function in stuttering,'' J. Speech Hear. Res. **34**, 734–752.

Pickett, J. M. (**1980**). *The Sounds of Speech Communication: A Primer of Acoustic Phonetics and Speech Perception* (University Park, Baltimore).

Postma, A. (**1997**) ''On the mechanisms of speech monitoring,'' in *Speech Production: Motor Control, Brain Research and Fluency Disorders*, edited by W. Hulstijn, H. F. M. Peters, and P. H. H. M. van Lieshout (Elsevier Science, New York).

Postma, A., and Kolk, H. (**1992**). ''Error monitoring in people who stutter: Evidence against auditory feedback defect theories,'' J. Speech Hear. Res. **35**, 1024–1032.

Postma, A., and Kolk, H. (**1993**). ''The Covert Repair Hypothesis: Prearticulatory repair processes in normal and stuttered disfluencies,'' J. Speech Hear. Res. **36**, 472–487.

Prins, D., Main, V., and Wampler, S. (**1997**). ''Lexicalization in adults who stutter,'' Journal of Speech, Language and Hearing Research **40**, 373–384.

Starkweather, C. (**1985**). ''The development of fluency in normal children,'' in *Stuttering Therapy: Prevention and Intervention with Children*, edited by H. Gregory (Speech Foundation of America, Memphis, TN), pp. 9–42.

Tornick, G. B., and Bloodstein, O. (**1976**). ''Stuttering and sentence length,'' J. Speech Hear. Res. **19**, 631–654.

Van Lieshout, P. H. H. M., Hulstijn, W., and Peters, H. F. M. (**1996a**). ''Speech production in people who stutter: Testing the motor plan assembly hypothesis,'' J. Speech Hear. Res. **39**, 76–92.

Van Lieshout, P. H. H. M., Hulstijn, W., and Peters, H. F. M. (**1996b**). ''From planning to articulation in speech production: What differentiates a person who stutters from a person who does not stutter,'' J. Speech Hear. Res. **39**, 546–564.

Van Lieshout, P. H. H. M., Starkweather, C. W., Hulstijn, W., and Peters, H. (**1995**). ''Effects of linguistic correlates of stuttering on EMG activity in nonstuttering speakers,'' J. Speech Hear. Res. **38**, 360–372.

Weiss, A. L., and Zebrowski, P. M. (**1992**). ''Dysfluencies in the conversations of young children who stutter: Some answers about questions,'' J. Speech Hear. Res. **35**, 1230–1238.

Wingate, M. E. (**1976**). *Stuttering: Theory and Treatment* (Irvington-Wiley, New York).

Wingate, M. E. (**1988**). *The Structure of Stuttering: A Psycholinguistic Analysis* (Springer-Verlag, New York).

Yaruss, J. S., and Conture, E. G. (**1995**). ''Mother and child speaking rates and utterance lengths in adjacent fluent utterances: Preliminary observations,'' Journal of Fluency Disorders **20**, 257–278.

Neuronal response to cochlear distortion products in the anteroventral cochlear nucleus of the gerbil

Michael Faulstich[a] and Manfred Kössl
Zoologisches Institut der LMU, Luisenstrasse 14, 80333 München, Germany

(Received 21 April 1998; accepted for publication 16 September 1998)

To receive information on the intracochlear magnitude and propagation properties of cochlear distortion products, the neuronal response of AVCN cells to distortion stimuli and the acoustical correlates in the ear canal (DPOAE) were measured for frequencies between 0.7 and 45.3 kHz. Comparison of the growth of neuronal response to a distortion stimulus and the neuronal rate-versus-level function for an externally applied pure tone of equal frequency allowed for an assessment of the intracochlear magnitude of the distortions. AVCN neurons with a characteristic frequency (CF) >1.8 kHz started to respond to the intracochlear distortion stimulus, at primary levels for which the ear-canal level of the corresponding DPOAE was close to the pure-tone threshold of the units. This finding suggests that transmission of sound energy is comparable in the forward and reverse direction, and that mechanical distortions of the cochlea are fully encoded by neurons in the AVCN. For neurons with a CF <1.8 kHz, the intracochlear magnitude of the distortion stimulus appeared to be about 15 to 30 dB higher than the corresponding DPOAE, at the threshold of neuronal response. This discrepancy between intracochlear magnitude of cochlear distortions and their acoustical expression may be explained by high-pass filter action of the middle ear during DPOAE re-emission from the cochlea. A contribution to the observed discrepancy of the type of distortion (cubic versus quadratic) used as stimulus, and possible differences in mechanical frequency processing between the apex and base of the gerbil cochlea, are also discussed. The delay of the neuronal response to an intracochlear distortion stimulus was on average 1.1 ms longer than the neuronal delay to an external pure tone of equal frequency and intensity, most likely stemming from the activation delay of the DPOAE generating mechanisms. [S0001-4966(99)01301-6]

PACS numbers: 43.70.Hs, 43.70.Jt, 43.71.−k [BLM]

INTRODUCTION

Mechanical preprocessing in the cochlea enables the hearing system to act at very high sensitivity and frequency selectivity. In addition to the passive properties of the basilar membrane (BM) and the tectorial membrane (TM), active force production by electromotile outer hair cells (OHC) is critical for shaping the mechanical response of the cochlea (Dallos and Corey, 1991). This amplification system is characterized by a distinct mechanical nonlinearity which results in making the system subject to mechanical distortions. After stimulation of the cochlea with two primary tones of the frequencies $f1$ and $f2$ ($f2>f1$), cochlear distortion product otoacoustic emissions (DPOAE) can be measured in the ear canal with a sensitive microphone. The frequencies of these two-tone distortion products are defined by combinations of the primary frequencies $f1$ and $f2$ at $(n+1)f1-nf2$, $(n+1)f2-nf1$, and $n(f2-f1)$. Of these DPOAEs, the $2f1-f2$ distortion is usually the most prominent and is therefore best studied (for reviews see Probst *et al.*, 1991; Whitehead *et al.*, 1996). The level of the $2f1-f2$ distortion is correlated with cochlear sensitivity (Gaskill and Brown, 1990) and has been used to describe the action of the cochlear amplifier (Mills and Rubel, 1996). The level of the difference tone of the frequency $f2-f1$ has been associated with the position of the operating point of the cochlear amplifier (Brown, 1994; Frank and Kössl, 1996).

The primary tones evoke the formation of traveling waves on the BM and it is likely that in the region of overlap of the primary traveling waves, nonlinear OHC properties will generate the DPOAEs. This has been derived from iso-suppression tuning curves (STC), whose minimum can usually be found around the primary frequencies (Brown and Kemp, 1984; Martin *et al.*, 1987). The distortion sound-energy travels bidirectionally to the cochlear frequency place that corresponds to its frequency and to the middle and outer ear, where it can be measured acoustically. It is not fully understood how the DPOAEs are transmitted inside the cochlea, especially during re-emission to the middle and outer ear. A possible loss of energy due to reverse transfer characteristics of the middle-ear ossicles has been controversially discussed. While some groups report little or no loss of energy (Fahey and Allen, 1985; Rübsamen *et al.*, 1995), others have found evidence for an energy loss of up to 30 dB (Powers *et al.*, 1995; Magnan *et al.*, 1997). Furthermore, reflections and cancellations inside the cochlea may also influence the DPOAE measured in the ear canal. Another problem is how neuronal processing deals with cochlear distortion products which are byproducts of the distinct mechanical nonlinearity and supposedly serve no purpose but rather make signal processing more ambiguous. Psychoacoustical measure-

[a]Author to whom correspondence should be addressed. Electronic mail: brueck@zi.biologie.uni-muenchen.de

ments have shown that cochlear distortions are, in fact, neuronally encoded and can be perceived by the subject (Zwicker, 1981).

To address these open questions, in the present study we have combined measurement of DPOAEs and neurophysiological recordings in anteroventral cochlear nucleus (AVCN). Cells in the AVCN presumably reflect relatively direct input from the sensory inner hair cells (IHC), and therefore can be used to assess cochlear output to the auditory brainstem (Rose *et al.*, 1974). After characterization of an AVCN cell's response to externally applied stimuli of known frequency and intensity, the same cell was stimulated indirectly with an intracochlear stimulus in the form of a distortion product, generated by two simultaneously applied pure-tone stimuli. By comparing acoustically measured DPOAEs to the neuronal reaction of an AVCN cell to the corresponding distortion, it should be possible to derive information on the re-emission characteristics of DPOAE, as well as on properties of the transmission within the cochlea. The Mongolian gerbil (*Meriones unguiculatus*) is an ideal subject for such a study, as it is an animal with a hearing range that covers almost the entire human hearing range but extends into the ultrasonic range as well (from about 100 Hz up to 65 kHz: Ryan, 1976; Müller, 1996). This should allow for a distinction between general features of a mammalian cochlea and specializations for the processing of either low or high frequencies.

I. MATERIAL AND METHODS

Sixteen pigmented (black and agouti) Mongolian gerbils of both sexes, between 7 and 40 weeks old, from our own breeding colony, were used for this study. Body weight was between 48 and 81 g. Before each experiment, the ear canal of the animal was checked for signs of abnormalities such as choleasteatomata or a damaged eardrum. All experiments were conducted in a sound-shielded chamber. The animals were anesthetized using a 10:1 combination of ketamine (50 mg/ml, Parke-Davis) and rompun (2%, Bayer). About 30–40 min after an initial dose of 3 ml/kg of this mixture, injected subcutaneously (s.c.) between the hind legs, a continuous anesthetic infusion at a flow rate of 75 μl/h was administered (s.c.) between the shoulders using a Harvard Apparatus infusion syringe pump 22. Depth of anesthesia was verified at regular intervals by checking the foot pinch reflex. During the initial preparation, the skin over the skull was opened and the bone was exposed and cleaned. A small metal rod was glued to the skull in the midline, just rostral of the Bregma point, using dental cement and superglue. A 500-μm-diam hole was drilled into the skull with an electronic microdrill in the midline, 2500 μm caudal of the λ-point. The metal rod was clamped in a stereotactic holder and the occipital plate was oriented horizontally. From this position, the AVCN could be approached at a lateral angle of 31° ($\pm$4) and a rostrocaudal angle between -2 and 12° (positive values indicating caudal and lateral from vertical). During all experiments, the animal was lying on a heating mat at a constant temperature of 38 °C. Recording sessions usually lasted about 4 h.

An acoustic coupler system was introduced into the ear canal under visual control, at a distance of about 0.2 to 0.5 mm from the eardrum. The coupler system was custom made from two conically shaped plastic tubes to fit the ear canal of the animal. One of the tubes connected to either a 1/2-in. B & K 4133 microphone, for frequencies below 40 kHz, or to a 1/4-in. B & K 4135 microphone, for higher frequencies. The other tube connected to the output of two reverse-driven 1/2-in. B & K 4133 microphones, used as loudspeakers for the primary frequencies ($f1$ and $f2$). Sinusoidal stimuli were generated by an HP 8904 A synthesizer. The closed sound system was calibrated *in situ* for a constant sound-pressure level at the microphone membrane, using white noise. Microphone response was amplified by a B & K 2610 measuring amplifier and fed into an HP 3561 A spectrum analyzer. The entire system was computer controlled by a fast Pentium PC using programs written in ASYST (Keithley). A more detailed description of the equipment and the calibration procedure can be found elsewhere (Kössl, 1992; Frank and Kössl, 1995). With different animals and in the different recording sessions, care was taken to achieve a similar position and distance of the coupler tip in relation to the tympanum. At the beginning of the first session for each animal, the cochlear response was controlled by recording so-called ''distortion audiograms.'' For these audiograms, $f1$ and $f2$ were kept at a constant ratio ($f2/f1$) and constant levels of 40/30 dB SPL, respectively, and then $f2$ was advanced from 2 to 40 kHz in 1-kHz steps. For each step, the resulting level of $2f1\text{-}f2$ was measured. Separate measurements were made for primary ratios of 1.10, 1.15, 1.20, 1.25, 1.30, and 1.35. In this way the mechanical integrity of the cochlea was verified, and the range of the optimum primary-frequency combination for the $2f1-f2$ DPOAE for different primary frequencies was determined for later use. At the beginning of each consecutive session, control runs were made for a ratio of 1.25, which usually resulted in more or less pronounced $2f1-f2$ for all $f2$ frequencies from 2–40 kHz. The coupler was repositioned when the difference to the control measurements was greater than 5 dB for a wider frequency range (>5 kHz). The range of optimum primary ratio for other order DPOAE investigated in this study ($f2-f1$, $3f1-2f2$), was known from previous measurements (unpublished data) or determined during the experiment.

Extracellular neuronal recordings were made with glass microelectrodes filled with 3 M KCl, resulting in a resistance *in situ* of 3 to 20 MΩ. The AVCN was approached in 10-μm steps with a remote-controlled piezo stepper; step size was reduced to 0.5–2 μm inside the AVCN. An Ag/AgCl wire was inserted into the forebrain through a small hole and used as an indifferent electrode. Neuronal response was picked up by a custom-made amplifier (Jim Hartley, University of Sussex, England). Search stimulus was a 50-ms noise burst with a rise/fall time of 5 ms. When a single or multi unit (maximum number of distinguishable different spikes 3–4) was isolated, the frequency tuning curve was determined using 50-ms pure-tone bursts (5-ms rise/fall time) presented once every 500 ms. For measurement of the tuning curve, either the response area of the neuron was determined automatically by random presentation of frequency/level combina-

tions, or frequency and intensity of the stimulus were changed manually until acoustical responses disappeared. The primary frequencies $f1$ and $f2$ were chosen in a way that the frequency of the resulting DPOAE under investigation would be at a unit's CF. Neuronal response to cochlear distortion products was typically measured by simultaneous presentation of $f1$ and $f2$ as fully overlapping 50-ms pulses. In cases where the neuron responded to one of the primary frequencies ($f1$), additional measurements were made using partially overlapping primary tone pulses. In these measurements, the $f1$ pulse was 80 ms long and a 50-ms $f2$ pulse was added 30 ms after onset of the $f1$ pulse. Neuronal rate versus level functions were determined by increasing primary levels in 5-dB steps; the response to each stimulus was averaged 20 times. Acoustical rate versus level functions were determined immediately after a successful neuronal stimulation with a distortion product for the identical primary frequencies. In some cases, the level of the DPOAE was measured simultaneously with the neuronal data acquisition by averaging the acoustical signal on the spectrum analyzer. The recording site was verified during the last experiment by a small horse radish peroxidase (HRP) injection ($\varnothing = 50–100\ \mu$m).

II. RESULTS

A. General characteristics of AVCN units

Seventeen single units and 58 multi units were isolated in the AVCN with their characteristic frequency (CF) ranging from 0.7 to 45.3 kHz. The full measurement required stable recording conditions for a minimum of 30 min and could therefore be performed on only about half ($n = 39$) of all isolated units. The number of units available for the individual tests is indicated in the respective figure legends. Units with a low threshold were preferred and with one exception, units with a pure-tone threshold >20 dB SPL were discarded. The one unit with a threshold of 30 dB was stimulated only with the $f2-f1$ distortion, allowing the use of high-level primary tones without influence on the unit's response. Relative distribution of thresholds fits well with the published audiograms by Ryan (1976) and Müller (1996), with a broad minimum in thresholds around 7 kHz. A second, much sharper minimum in threshold could be found for CFs around 30 kHz. Minimum threshold was -20 dB SPL for a single unit with a CF of 6.45 kHz. Figure 1 shows the distribution of CFs and thresholds of the units recorded from the AVCN. There did not appear to be a significant difference between pure-tone thresholds of the single and multi units. Tuning sharpness was low to moderate, with a maximum Q10dB value (CF of the unit divided by the bandwidth 10 dB above the pure-tone threshold) of 9.62. The frequency tuning curves measured in the AVCN resemble curves measured in other unspecialized mammals, displaying an asymmetrical shape with a steeper high-frequency flank and a more- or less-pronounced low-frequency tail (Fig. 2). Units with a low CF (<3 kHz) display more symmetrical tuning curves and the steep high-frequency flank becomes increasingly more shallow with decreasing CF. The latency of neuronal response ranged from 0.8 to 3 ms, with low-CF units usually displaying longer latencies than high-CF units.

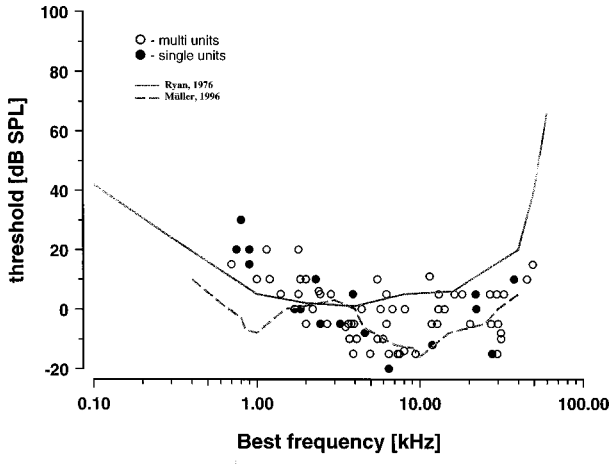

FIG. 1. Distribution of the pure-tone thresholds of all the AVCN units isolated in this study as a function of CF. Open symbols mark multiunit ($n = 58$) and solid symbols mark single unit ($n = 17$) recordings. For comparison, the behavioral audiogram by Ryan (1976), solid line, and the neuronal audiogram determined from single auditory nerve fiber recordings by Müller (1996), dashed line, are shown.

B. Neuronal correlates of cochlear distortion products

The neuronal response area to randomly presented level/frequency combinations was assessed either by using a single tone ($f1$) or by presenting two fully overlapping tone pulses in a fixed-frequency combination ($f2/f1$). Neuronal response to cochlear distortion products becomes obvious when these response areas are compared. In Fig. 3(A), the high-frequency portion of the response area for a unit with a CF of 3.7 kHz and a pure-tone threshold of -10 dB SPL to single-tone stimulation is given. For each level/frequency combination, peristimulus time histograms (PSTHs) are shown. In Fig. 3(B), the neuronal response of the same neuron to simultaneous presentation of two tones at a ratio $f2/f1$ of 1.3 extends into frequency regions where either the $2f1-f2$ or the $3f1-2f2$ distortion stimulate the neuron. For these frequencies (>5 kHz), none of the primary tones alone acts excitatory.

To be able to compare neuronal and acoustical distortion

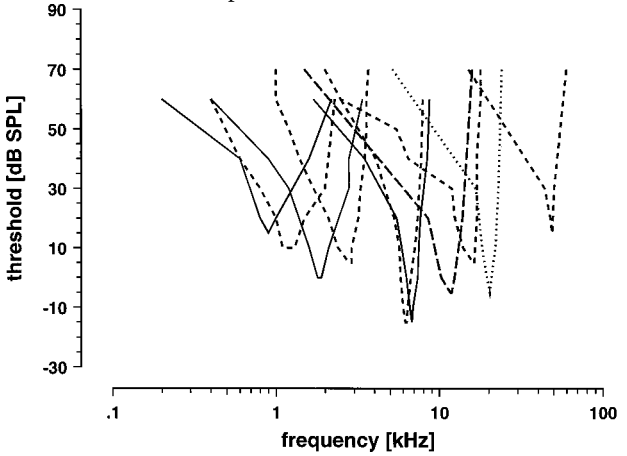

FIG. 2. A number of representative frequency tuning curves of AVCN units. Solid lines indicate tuning curves measured for single units, dashed and dotted lines mark multi unit recordings. Note the increasing symmetry for low-CF units.

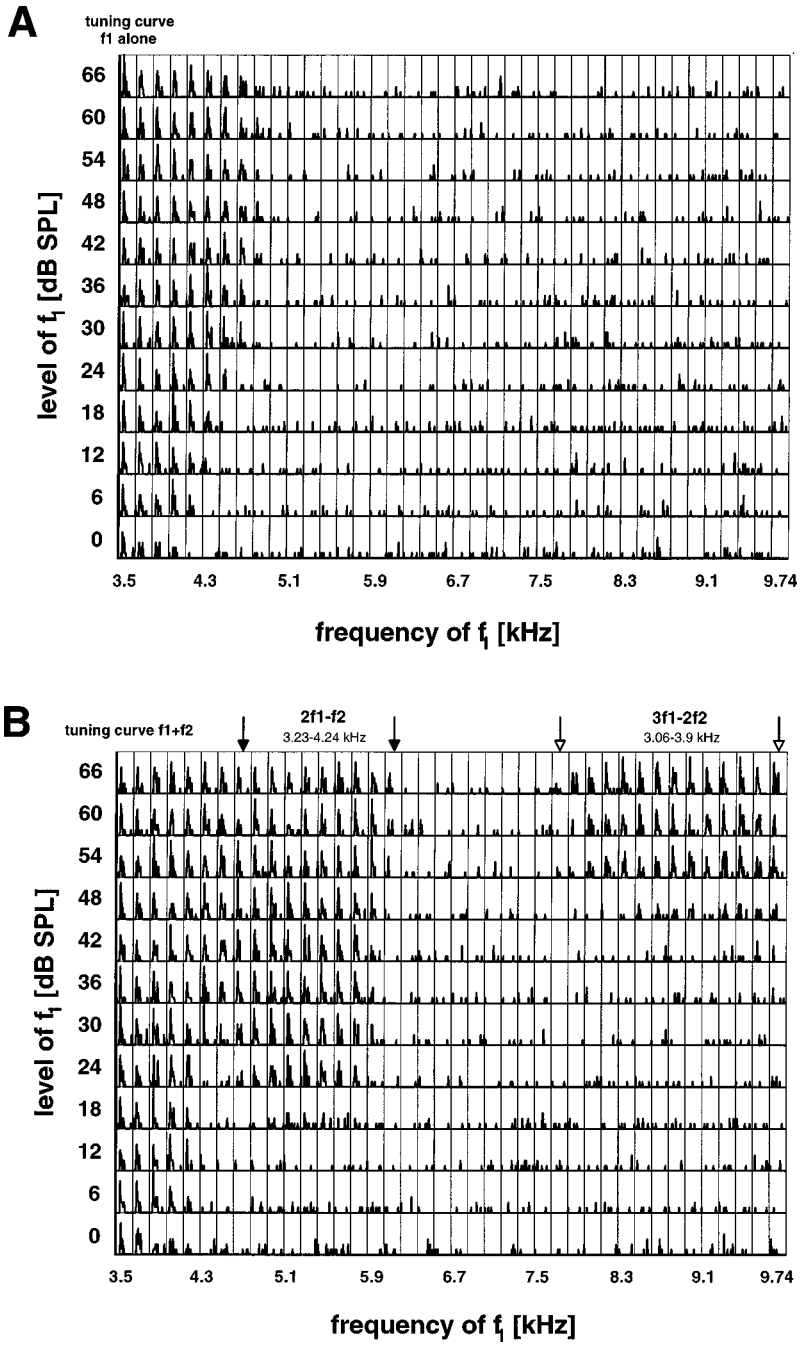

FIG. 3. (A) PST histograms for a multi unit with a CF of 3.7 kHz and a pure-tone threshold of −10 dB SPL, after random presentation of a single 50 ms pure-tone pulse at frequencies from 3.5 to 9.74 kHz (step size 160 Hz) and intensities from 0 to 66 dB SPL (step size 6 dB). Each box represents two averages of neuronal activity measured over 150 ms (stimulus from 30 to 80 ms) for each frequency/level combination. PSTH bin width is 6 ms, maximum spike number (height of box) is 8 per bin. (B) PST histograms for the same unit but for random stimulation with two simultaneous pure-tone pulses ($f1$ and $f2$, from 30 to 80 ms). For each $f1$, an $f2$ was presented resulting in a $f2/f1$ ratio of 1.3. Note the neuronal response to cochlear distortions induced by simultaneous presentation of $f1$ and $f2$, for stimulus frequencies where a single-tone pulse was outside the excitatory tuning curve, as determined in A. The range and the order of the cochlear distortion product responsible for the neuronal response is marked by the arrows.

product response, the following paradigm was used: After the CF and threshold of a unit had been determined, primary frequencies were chosen in a way that, in all but 16 cases, there was no reaction to $f1$ and $f2$ for stimulus levels <60 dB SPL. In most cases, the primary stimuli were completely outside the excitatory tuning curve of the unit. The frequency ratio $f2/f1$ was adjusted approximately to the optimum value resulting in maximum acoustic DPOAE levels, and the frequency of the resulting DPOAE was matched to the unit's CF. The level of $f1$ was always 10 dB above the level of $f2$. Only for some control measurements, in which the difference tone $f2-f1$ was used as intracochlear stimulus, additional runs were made with both primaries at equal intensity. For each primary frequency, a rate-versus-level function was determined before neuronal reaction to both stimuli was measured. During simultaneous presentation of $f1$ and $f2$, the unit would respond at primary levels where no reaction to each primary frequency alone could be measured. Figure 4(A) shows the neuronal response of a single unit with a CF of 6.8 kHz to presentation of two primaries at frequencies of 9.07 and 11.33 kHz. In this case, presentation of $f1$ starts 30 ms before presentation of $f2$, and then both tones overlap for 50 ms. There is no response to $f1$ alone, but starting at an $f1$-level between 30 and 35 dB SPL ($f2$ level=20–25 dB SPL), the neuron responds. The resulting growth function of discharge rate versus primary level is shown in Fig. 4(C). The corresponding acoustical growth function of DPOAE level versus primary level reveals that the neuron starts to respond when the level of $2f1-f2$ measured in the ear canal reaches the range of the CF threshold level of the unit [Fig. 4(B)].

Similar curves could be determined for all units with

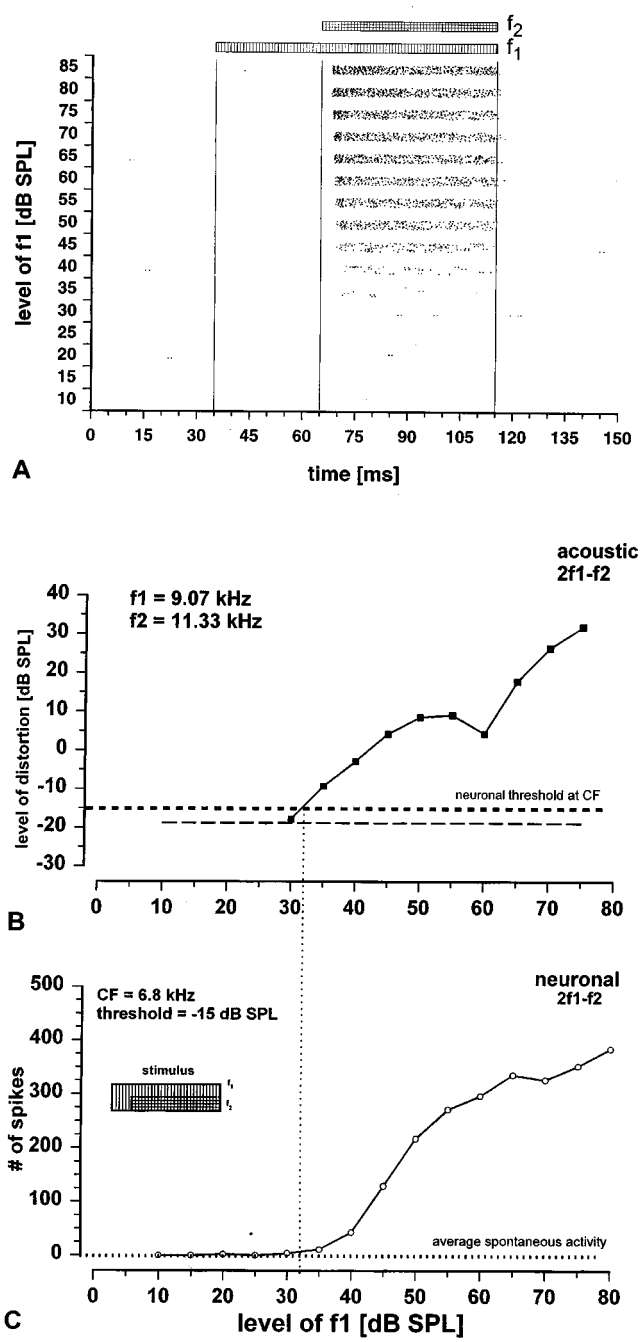

FIG. 4. (A) Dot display of neuronal activity as a function of stimulus intensity ($l1 = l2 + 10$ dB) for one multi unit (CF=6.8 kHz). Vertical lines mark the beginning and the end of primary tone presentation. $F1$ (9.07 kHz) was presented from 35 to 115 ms, $f2$ (11.33 kHz) was presented from 65 to 115 ms. Each stimulus level was presented 20 times. (B) Dependence of the level of the $2f1-f2$ DPOAE measured in the ear canal on the level of the $f1$ primary (level of $f2$ is 10 dB less). The thin dashed line indicates the average noise floor of the acoustical measurement. Only the part of the growth function where the level of the DPOAE raises above the average noise floor is plotted. The thick dashed line indicates the pure-tone threshold of the AVCN unit for which a neuronal response to the same distortion product was measured. (C) Dependence of the discharge rate of an AVCN unit with a CF of 6.8 kHz and a pure-tone threshold of -15 dB on the level of $f1$, at simultaneous presentation of two pure tones $f1$ and $f2$ at the same frequencies as in (A). Discharge rate was averaged over 20 presentations from 65 to 115 ms. Hatched boxes indicate the stimulus paradigm with $f1$ louder and longer than $f2$. The horizontal dotted line marks the average spontaneous activity of the unit (in this case, 0.12 spikes/s). The vertical dotted line marks the level of $f1$ where the ear-canal level of $2f1-f2$ reaches the unit's pure-tone threshold.

CFs >1.8 kHz, and the neurons always started responding when the level of DPOAE in the ear canal was close to the pure-tone threshold level of the unit as demonstrated by the examples given in Fig. 5(A)–(D). For higher stimulus levels, the shape of growth functions of neuronal versus acoustical DPOAE response could differ significantly (Fig. 5). Here, neuronal saturation, possible phase cancellations between different DPOAE sources (Mills and Rubel, 1997), and suppression phenomena could occur. Such effects should be minimal for lowest primary-tone levels.

To quantify the acoustical and neuronal DPOAE responses, the acoustical distortion threshold (ADT) was defined as the level of $f1$ for which the DPOAE level, measured at the tympanum, reached the unit's pure-tone threshold level at CF. The ADT was calculated from an interpolation of the acoustic DPOAE growth function. The neuronal distortion threshold (NDT) was defined as the $f1$-level at which the unit started to respond to the intracochlear distortion stimulus. It was calculated by extrapolating the intersection between the tone-evoked neuronal response and the level of average spontaneous activity from the first two data points of the neuronal discharge growth function that had values greater than the mean spontaneous rate $+2$ s.d. Figure 6(A) shows the difference between the level of $f1$ at ADT versus the level of $f1$ at the NDT of a unit. Positive values indicate that the neuronal response started before the level of the DPOAE in the ear canal reached the unit's pure-tone threshold level. The mean value for this difference is $+0.6$ dB for units with a CF above 1.8 kHz, indicating that, on average, the neurons start to respond to the intracochlear distortions when the DPOAE level at the tympanum is 0.6 dB below the unit's pure-tone threshold. The corresponding 95% confidence interval (lower dotted lines) indicates that the scatter of the difference between ADT and NDT ranges from about -7 to about $+8$ dB. Only units with a CF below 1.8 kHz display a different behavior; the threshold difference is well above $+8$ dB. These units are described in more detail later. An alternative measure of the acoustical versus neuronal distortion magnitude was applied to obtain data for primary tone combinations for which the DPOAE amplitude in the ear canal did not reach the unit's pure-tone threshold, or which resulted in strongly nonmonotonic growth functions. The alternative measure was calculated by determining or extrapolating the actual DPOAE magnitude for the level of $f1$ at NDT and calculating the difference between this magnitude and the unit's pure-tone threshold in dB, representing the theoretical magnitude necessary to drive the unit. This alternative analysis resulted in very similar results to the ADT–NDT measurement [Fig. 6(B)]. A significant difference was present only for the scatter of data for units with a CF below 1.8 kHz (95% confidence interval from about $+4$ to about $+53$ dB). For 20 units, neuronal and acoustical growth functions were determined not only for $2f1-f2$, but also for one or two different order distortions of the frequencies $3f1-2f2$ and $4f1-3f2$, as well as for the difference tone $f2-f1$. Again, units with a CF above 1.8 kHz started responding when the acoustic level of the DPOAE in the ear canal was close to the pure-tone threshold of the unit. Figure 7(A) and (B) show the neuronal response of one unit to the

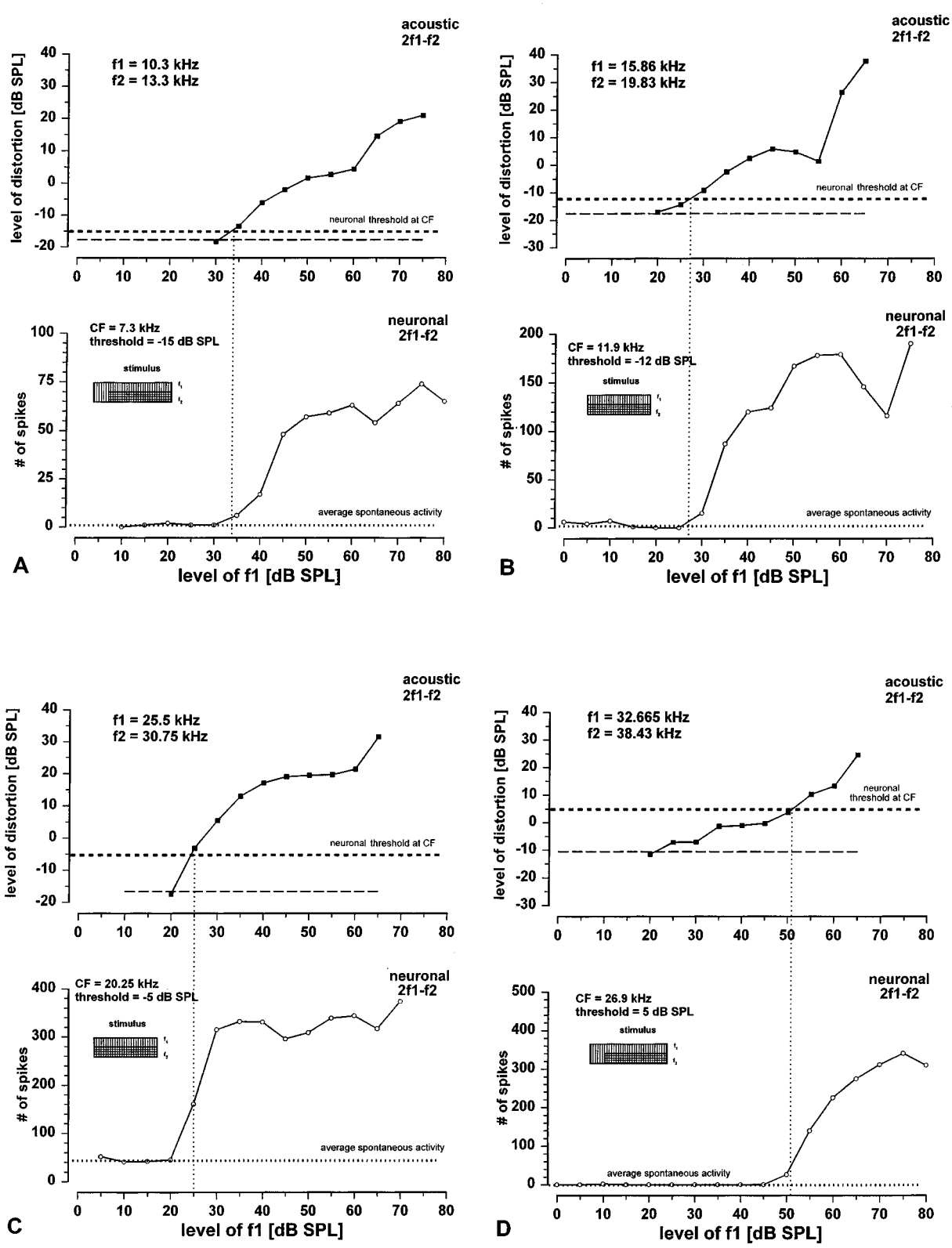

FIG. 5. DPOAE level growth functions (upper panels) and corresponding neuronal rate-versus-level functions (lower panels) in response to the intracochlear distortion stimulus, for four AVCN units. Hatched boxes indicate the stimulus paradigm with either total (B and C) or partial (A and D) overlapping of $f1$ and $f2$. The CF and pure-tone threshold of the respective unit, as well as the primary frequencies, are displayed for each figure. All other descriptions as in Fig. 4(B) and (C).

$2f1-f2$ and the $3f1-2f2$ distortion product. Figure 7(C) represents the acoustical and neuronal growth functions for another unit, using the difference tone $f2-f1$ as intracochlear stimulus.

In five units, the $f1$ frequency itself became excitatory at a higher stimulus level (>60 dB SPL) and in four of these cases, a suppression of the neuronal response to the intracochlear distortion stimulus could also be observed. This sup-

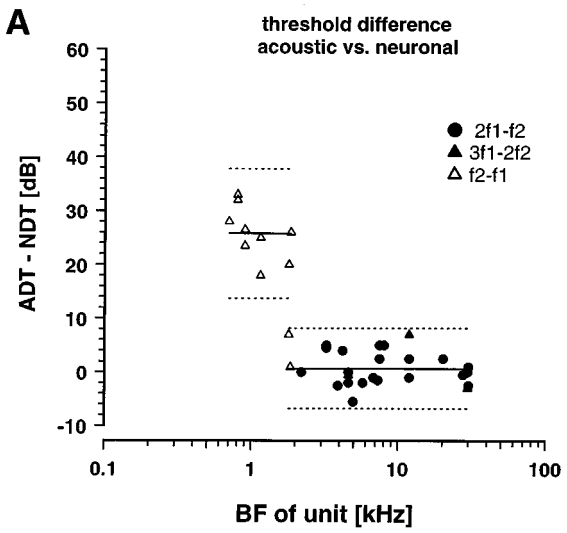

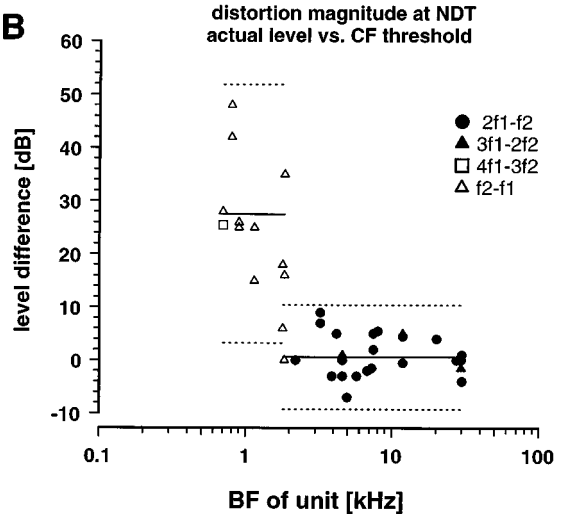

FIG. 6. (A) Difference between the level of $f1$ when the ear-canal level of the DPOAE reaches the corresponding unit's pure-tone threshold (ADT) and the level of $f1$ where the unit starts to respond to the intracochlear distortion stimulus (NDT) in dB, as a function of CF of the unit and the order of distortion used for stimulation. (B) Alternative quantification of the difference between acoustic and neuronal distortion magnitude. Data points represent the difference between the actual ear-canal level of a DPOAE (in dB SPL) for an $f1$ level at NDT and the unit's pure-tone threshold. Data are plotted as a function of CF of the unit and the order of distortion used for stimulation. Positive values in both figures indicate that the neuron started to respond to the distortion stimulus before the corresponding DPOAE had reached the level of the unit's pure-tone threshold. Solid lines mark the mean value ($n_A=36$; $n_B=38$), dotted lines mark the 95% confidence band. Note the two different groups of data for CFs below and above 1.8 kHz.

pression, however, was only observable at higher primary levels (level of $f1>50$ dB SPL), and the value of ADT–NDT was within the 95% confidence interval of the data given in Fig. 6 for either type of analysis. Figure 8 shows an example where $f1$ itself becomes excitatory at 65 dB SPL and also has a suppressive effect on the neuron's response to $2f1-f2$, starting at about 55 dB SPL.

In three cases, the acoustic distortion threshold was more than 7 dB below the neuronal threshold and clearly outside the 95% confidence interval for both methods of analysis [Fig. 6(A) and (B)]. These cases were excluded from Fig. 6 since it became obvious that the $f1$-stimulus lay within the inhibitory sideband at the high-frequency slope of the tuning curve and suppressed the unit's response to the distortion stimuli at low sound-pressure levels. The example in Fig. 9 shows that when the frequency ratio $f2/f1$ was increased, in this case from 1.25 to 1.35, the difference between ADT and NDT decreased from -9 to -3 dB. For the higher frequency ratio, both primary frequencies were probably well outside the inhibitory sideband. This suggests that the initial threshold difference for the smaller ratio is not due to a decrease in the neuronal response to the distortion stimulus compared to the other units in this study.

For units with a CF below 1.8 kHz, a clear increase of the ADT–NDT difference value, as well as for the alternative measure, could be observed. The units from this frequency range started to respond to the intracochlear distortion stimulus before the acoustical level of the corresponding DPOAE, measured in the ear canal, reached the pure-tone threshold of the neuron. Or, as expressed by the alternative measure, the acoustic magnitude of the DPOAE at the onset of neuronal response was smaller than the magnitude theoretically necessary to drive the unit. The neurons responded as if the intracochlear distortion magnitude were 15–33 dB above the acoustic level in the ear canal (Fig. 10). The mean difference in threshold between ADT and NDT is +25.65 dB with the 95% confidence band between +15 and +37 dB, not overlapping with the confidence band of the mean for the units with a CF above 1.8 kHz. For the alternative analysis, the mean difference was only slightly higher at +27.5 dB but had a significantly greater scatter (see above), resulting in an overlap of the 95% confidence bands for the two groups of data for CFs above and below 1.8 kHz. The abrupt frequency-dependent change between the two groups of data is evident in Fig. 6. The increase of the value of ADT–NDT started at CFs around 1.8 kHz, but for this frequency, units with a normal behavior could be found as well [see Figs. 6 and 7(C)]. For units with CF<1.5 kHz, the discrepancy between ADT and NDT was always present (Fig. 6). However, to avoid neuronal response to the primary frequencies, these low-frequency units (which have a broad tuning curve) had to be stimulated with the difference tone $(f2-f1)$ for which the primary frequencies could be chosen well outside the unit's response area. Only in one case stimulation was possible with the $4f1-3f2$ distortion, but in this measurement the acoustic growth function of the DPOAE never reached the unit's pure-tone threshold and analysis was possible only with the alternative method [Fig. 6(B)].

C. Latency of neuronal response

In units for which a complete rate-versus-level function for both the distortion stimulus and an externally applied pure tone of the same frequency could be obtained, the response latency about 10–15 dB above the threshold of response was determined. Growth functions for which a precise onset latency could not be determined, due to a low spike number or influence of the primary tones at two-tone stimulation, were omitted from this analysis, resulting in a total of 28 data points. The response latency of a unit to the

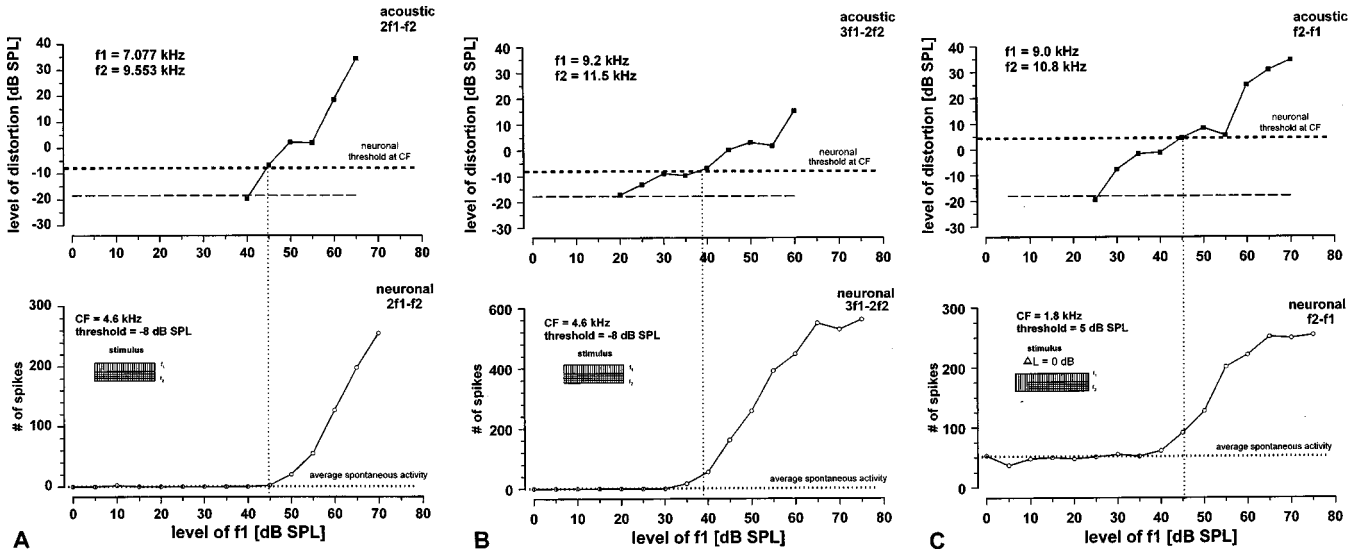

FIG. 7. DPOAE level growth functions (upper panels) and corresponding neuronal rate-versus-level functions (lower panels), for two different AVCN units, using either $2f1-f2$, $3f1-2f2$, or $f2-f1$ as intracochlear stimulus. Hatched boxes indicate the stimulus paradigm with either total (A and B) or partial (C) overlapping of $f1$ and $f2$. In contrast to A and B, the level of the primary tones in C is equal. The CF and pure-tone threshold of the respective units, as well as the primary frequencies, are displayed for each figure. All other descriptions as in Fig. 4(B) and (C).

external tone of CF was shorter than the latency of response to the intracochlear distortion stimulus of similar level. The magnitude of the intracochlear distortion stimulus was approximated by the discharge rate and its acoustical level in the ear canal. The response to the distortion stimulus was about 1.1 ms (mean 1.11 ms; s.d.$=0.22$; $n=28$) delayed compared to the response to the externally applied tone. This difference in latency was independent of CF and of the order of distortion under investigation ($2f1-f2$, $3f1-2f2$, $4f1-3f2$, and $f2-f1$). Figure 11 shows the distribution of the difference in latency between neuronal response to an intracochlear distortion stimulus and an externally applied tone as a function of CF for different order distortions. To investigate a possible influence of the primary tone rise/fall time on the onset latency of the neuronal distortion response, in six units the rise/fall times were varied between 1 and 10 ms. Again, for stimuli about 10–15 dB above pure-tone threshold, the difference in latency to the externally applied stimulus was within the standard deviation, around 1.1 ms.

III. DISCUSSION

A. General properties of AVCN units

The relative distribution of thresholds in relation to the CF of our units fits well with the published audiograms for the Mongolian gerbil (Ryan, 1976; Müller, 1996). There is a broad minimum in thresholds around 7 kHz, thresholds increase below about 1 kHz and above about 40 kHz. Because we have deliberately omitted units with high thresholds (>20 dB SPL, with one exception), the low- and high-frequency flanks of the hearing range of Meriones are not fully reflected by our data. The bias for low-threshold units rather reflects the course of the absolute threshold of hearing. The thresholds of the most sensitive units were slightly lower than those reported for single auditory nerve fibers by Müller (1996). In comparison to Müller, we could not find a second broad-threshold minimum for units with a CF around 1 kHz, and the relative course of the audiogram in our study resembles more the behavioral audiogram of Ryan (1976).

B. Neuronal correlates of cochlear distortion products

For most of the units studied, it was possible to choose primary frequencies which did not have any excitatory or suppressive effect on the neurons themselves at low to medium sound-pressure levels (<40–50 dB SPL). But when two primaries were presented simultaneously, they would evoke the generation of a distortion product inside the cochlea at the unit's CF; for certain primary levels, this intracochlear stimulus would be able to evoke a neuronal response (Fig. 3). We have used this intracochlear stimulus as a probe to gain information on the re-emission characteristics of DPOAE to the ear canal.

One recent study by Magnan *et al.* (1997), who have measured the re-emission characteristics of the middle ear of the guinea pig by comparing intracochlear pressure to acoustical DPOAE measurement in the ear canal, have found a significant loss of distortion sound energy of up to 30 dB for a wide frequency range from 1.5 to 8 kHz. If this were the case in the gerbil, the actual distortion levels inside the cochlea would exceed the primary levels by far, since, under optimum conditions, we are able to measure $2f1-f2$ levels approaching the level of $f2$. If there were a loss of that magnitude during re-emission, the neuronal response to the intracochlear distortion stimulus should also set in for much lower primary levels than those necessary to measure a threshold level of DPOAE in the ear canal. Powers *et al.* (1995) have measured the cochlear microphonic corresponding to spontaneous otoacoustic emissions (SOAEs) between 4 and 5 kHz in the chinchilla, and found that its magnitude was equivalent to that generated by an external stimulation with a 61-dB SPL tone of equal frequency. The level of the SOAE measured in the ear canal, however, was 30 dB less,

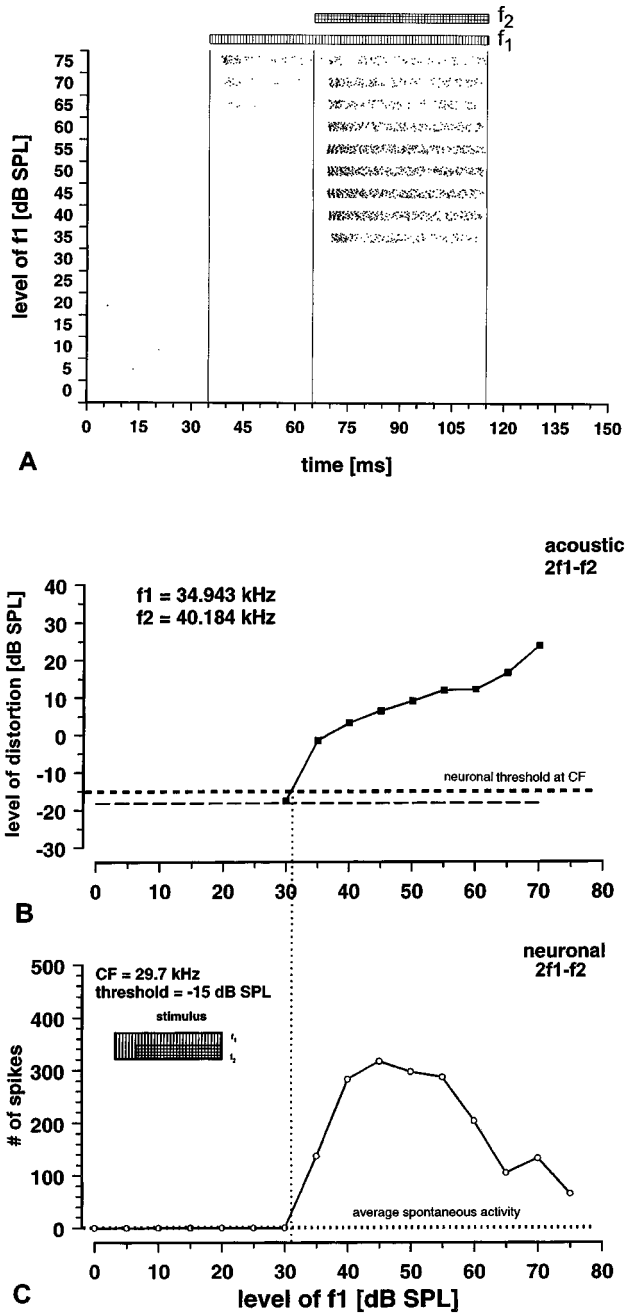

FIG. 8. Dot display of neuronal activity (A) and the corresponding growth functions of acoustical ear-canal level (B), and neuronal response (C) for one unit displaying inhibitory and excitatory effects of the primary stimuli. All descriptions as in Fig. 4. (A) Neuronal response to $2f1-f2$ begins at an $f1$ level of 35 dB SPL, saturates for an $f1$ level of 45 dB SPL, and is suppressed for $f1$ levels >55 dB SPL. $F1$ itself stimulates the unit at levels above 60 dB SPL.

so they also attribute a 30-dB loss to re-emission of the SOAE energy. Studies of the neuronal representation of cochlear distortions in both the AVCN of the cat (Fahey and Allen, 1985; CF$<$13 kHz) and the gerbil (Rübsamen *et al.*, 1995; CF$=$1.4–7.5 kHz) in comparison to the corresponding DPOAE in the ear canal find no significant difference between intracochlear and acoustical magnitude due to reverse middle-ear transfer, similar to our findings for units with CFs from about 2 to 45.3 kHz and for a number of different order DPOAEs. Since the primary level at the threshold of neuronal response to the distortion stimulus (NDT) was always within the range of the primary level sufficient to generate an acoustical DPOAE level in the ear canal equivalent to the unit's pure-tone threshold (ADT), the re-emission of the DPOAE from their generation site (presumably in the region of overlap of the two primary-tone traveling waves), through the cochlear-fluid spaces and via the middle-ear ossicles probably happens without a significant loss of sound energy. Sound transmission through middle-and inner-ear appears to be completely bidirectional without an energetically directional preference. Of course, this can only be seen within the scatter of our data (about ± 7 dB, see the 95% confidence bands in Fig. 6) and loss of sound energy during passage of the middle ear, within this magnitude, is certainly to be expected. Reflections at impedance boundaries like the oval window, and energy loss due to resistive elements in the middle ear reduce the power transmission efficiency of the middle ear (Rosowski, 1991). Our findings and the studies of the cat by Fahey and Allen (1985) and of the gerbil by Rübsamen *et al.* (1995) make us believe that the cochlear DPOAEs we have measured in the ear canal of the gerbil are a direct reflection of the output of nonlinear cochlear mechanics. If there were a significant loss or gain of sound energy of cochlear distortions on their way to the microphone in the ear canal, due to a difference in the efficiency of sound transmission through the middle ear, the NDT should not coincide with the ADT as closely as we have found.

One exception, however, is the frequency range below 2 kHz. All of the AVCN units with a CF$<$1.5 kHz and some units with a CF between 1.5 and 2 kHz respond to the intracochlear distortion stimulus generated by two external tones $f1$ and $f2$, as if either their pure-tone threshold was 10–30 dB lower than determined with an externally applied single tone, or as if the intracochlear magnitude of the distortion were 10–30 dB greater than the acoustical magnitude in the ear canal. When taking the alternative measurement from Fig. 6(B), this discrepancy is even greater with values up to 48 dB. Controls in one animal were made, where in the same recording session, low-frequency units (CF between 0.7 and 1.3 kHz) and high-frequency units (CF between 5.6 and 7.8 kHz) were tested for acoustical versus neuronal DPOAE level. Whereas the low-frequency units all displayed the discrepancy between ADT and NDT, the high-frequency units reacted as described for the majority of units above. So, the difference in DPOAE level cannot be attributed to placement of the coupler or other systematic artifacts. This would mean that the intracochlear magnitude of DPOAEs with a frequency $<$1.8 would have to be 10–30 dB greater than in the ear canal, and is probably attenuated during re-emission via the middle ear, or that the distortions would be amplified by the same amount on their way to the cochlear representation site. Cochlear distortions are most probably generated within a small cochlear region close to the frequency place of $f2$, although evidence for this has only been provided by suppression tuning curves for the $2f1-f2$ DPOAE. For the low-CF units in our study, to have the primary frequencies outside the excitatory tuning curve of the neurons, we have used the difference tone $f2-f1$ and, in one case, the $4f1-3f2$ distortion product, as stimuli. For most of the

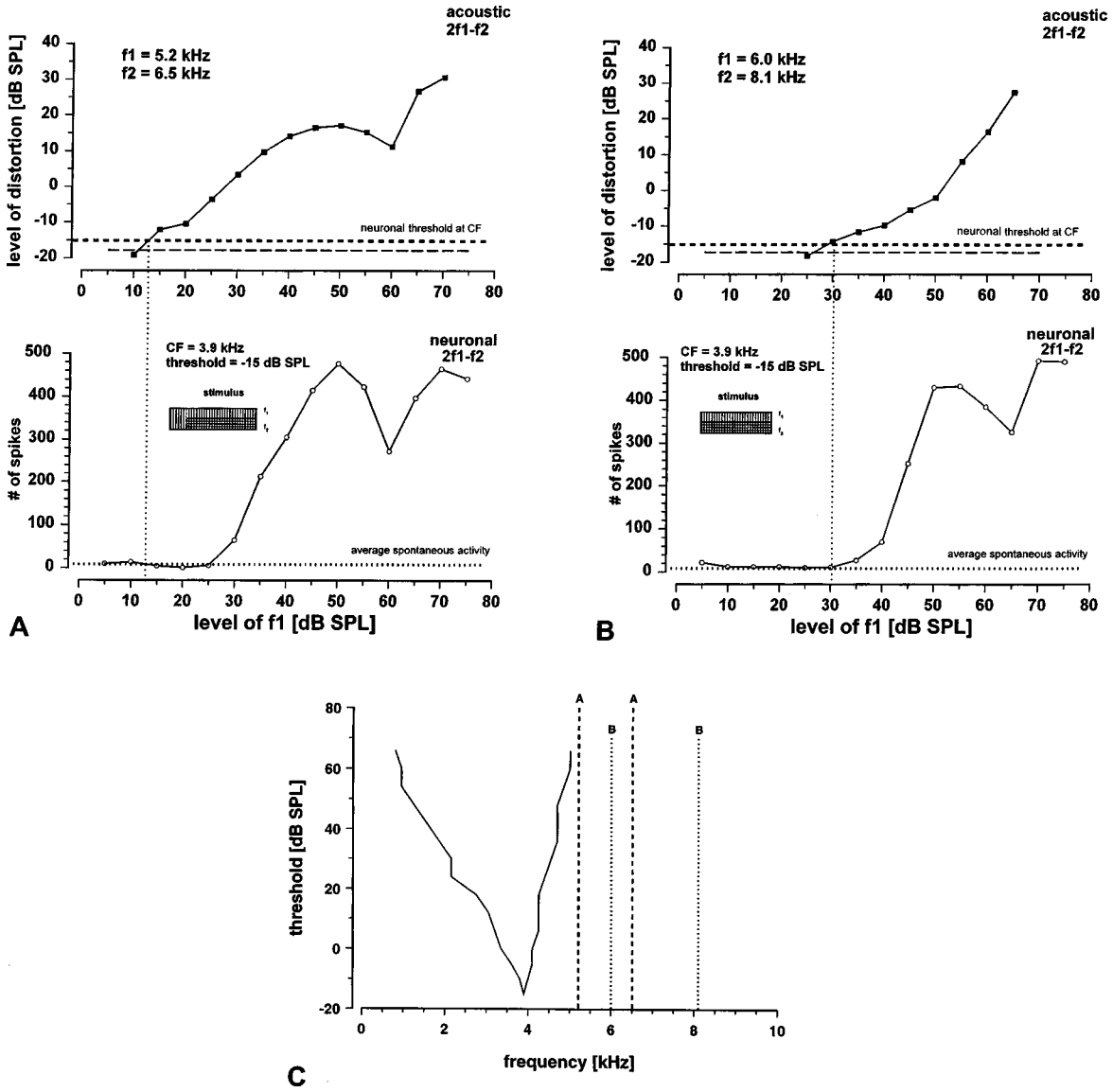

FIG. 9. Influence of primary ratio on the course of growth functions of acoustical ear-canal level and neuronal response to the intracochlear $2f1-f2$. Hatched boxes indicate the stimulus paradigm with either total (B) or partial (A) overlapping of $f1$ and $f2$. The CF and pure-tone threshold of the unit, as well as the primary frequencies, are displayed for each figure. All other descriptions as in Fig. 4(B) and (C). Note how in A ($f2/f1=1.25$) neuronal response to the $2f1-f2$ stimulus begins for an $f1$ level about 15 dB higher than the $f1$ level sufficient to evoke an ear-canal level $2f1-f2$ of the unit's pure-tone threshold level, −15 dB SPL (ADT−NDT=15 dB). With increasing primary ratio ($B=1.35$), the difference between ADT and NDT is reduced to 3 dB. (C) Excitatory tuning curve of the corresponding unit and position of the primary frequencies (vertical lines) used as stimuli in A (dashed) and B (dotted).

units, this would mean that the actual generation site in the cochlea would lie between the 4.5 and 8.1 kHz place in the cochlea. Since, for a large number of units with a CF between about 3 and 7 kHz, stimulated with $2f1-f2$, the primary frequencies were also from the 4–8-kHz frequency range but the equivalence of forward and reverse transmission was obvious in the acoustical growth functions, it seems plausible that the observed behavior may be attributed to frequency-dependent processes acting on the distortions rather than to mechanisms at their generation place. The reverse-sound transmission via the middle ear may be involved in attenuating frequencies below 2 kHz, similar to the findings presented by Powers *et al.* (1995) and by Magnan *et al.* (1997). This would mean that, in contrast to the situation in the chinchilla and the guinea pig, reverse-transfer characteristics of the middle ear in the gerbil is significantly different for frequencies below and above 2 kHz. Another possible contribution to the observed discrepancy may be attributed to the use of cubic versus quadratic distortions. To evoke neuronal responses at lowest frequencies, we have almost exclusively used the $f2-f1$ difference tone as intracochlear stimulus; however, $f2-f1$ was also used as stimulus for higher frequencies where the data are comparable to those obtained with $2f1-f2$ (Fig. 6). Only in one case the cubic $4f1-3f2$ distortion product served as stimulus for a low-CF unit, though the acoustic growth function required the application of the alternative analysis method [Fig. 6(B)]. For this example, a large discrepancy between actual magnitude and theoretically required magnitude, as for stimulation with $f2-f1$, was present. Clearly, more data for higher-order distortion stimuli at low CF are needed to prove the equivalence of the difference tone and the cubic distortions as

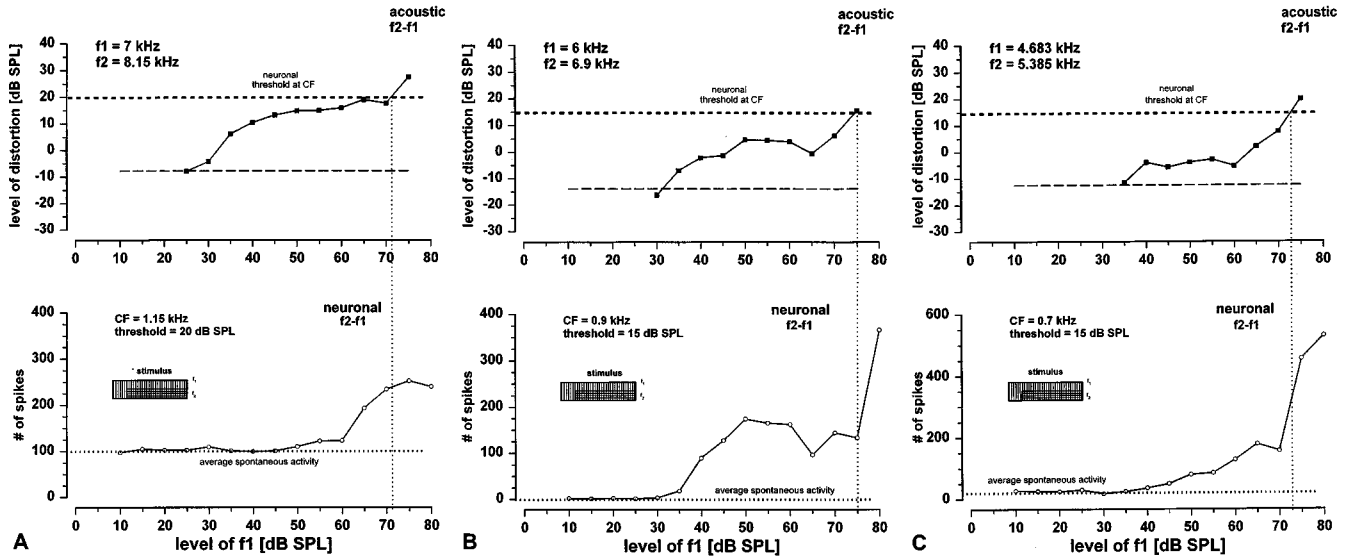

FIG. 10. DPOAE level growth functions (upper panels) and corresponding neuronal rate-versus-level functions (lower panels) in response to the intracochlear distortion stimulus, for two AVCN units. Hatched boxes indicate the stimulus paradigm with partial overlapping of $f1$ and $f2$. The CF and pure-tone threshold of the respective unit, as well as the primary frequencies, are displayed for each figure. All other descriptions as in Fig. 4(B) and (C). Note how the neuronal response to the distortion stimulus begins for $f1$ levels where the ear-canal level of the DPOAE is significantly lower than the unit's pure-tone thresholds.

probes in our experiment. However, we deem it unlikely that the large discrepancy between intracochlear and acoustic magnitude of the distortions is a result of differences in the generation and propagation properties between even-and odd-order distortions. Rather, we would conclude that there is a selective attenuation by the middle ear of low-frequency DPOAE sound energy during re-emission from the cochlear frequency place of the primaries. In a study of the transmission properties of the isolated gerbil middle ear, Ravicz *et al.* (1996) have shown that frequencies below 1.5 kHz are strongly attenuated. Thus, the middle ear of the gerbil would act like a high-pass filter. Assuming the equivalence of forward and reverse transmission evident from our higher-frequency data is valid also at low frequencies, the observed discrepancy between ADT and NDT may be attributed mainly to the filtering properties of the middle ear. The situation around 1.8 kHz, where some units did show the large discrepancy and others did not, may reflect individual variations in the transfer characteristics among different animals. Another possible contribution to the findings at CFs below 1.8 kHz may be a change in the way sound energy is mechanically processed and encoded in the apex of the gerbil cochlea. Here, sensitivity seems to depend mostly on passive processes rather than on active mechanical energy input by OHC motility. This is supported by a number of other studies which have also discussed the possibility of less compressive apical cochlear mechanics in the guinea pig (Cooper and Yates, 1994), the cat (Sewell, 1984), and the gerbil (Müller, 1996). In the cat, Sewell (1984) has demonstrated that cochlear sensitivity and frequency tuning of the low-frequency range (<3 kHz) are much less vulnerable to inactivation of the OHC after furosemide application. These findings suggest that part of the difference between units with CF above and below 1.8 kHz may also stem from baso–apical changes in the way sound energy is processed in the cochlea.

C. Latency of neuronal response

When comparing the response of an AVCN unit to an external stimulus tone at CF to the neuronal response of the same unit to an intracochlear stimulus in the form of a cochlear distortion product of equal level and frequency, the latency to the external stimulus is about 1.1 ms shorter. This latency difference is widely independent of CF and of the order of distortion used for stimulation of the neuron (Fig. 11). The major factors contributing to the observed delay in neuronal response to an intracochlear stimulus should be the travel time of the distortion within the cochlea and delay

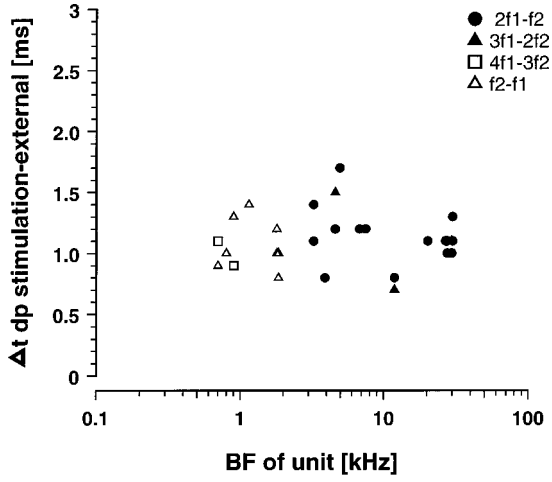

FIG. 11. Difference in the latency of the neuronal response to an intracochlear distortion stimulus about 15 dB above pure-tone threshold and the neuronal response to an externally applied tone of equal frequency and intensity plotted as a function of CF of the unit. Different symbols indicate different order distortion products used as intracochlear stimulus. Response to the intracochlear stimulus is, on average, 1.11 ms (s.d.$=0.22$ ms, $n=28$) slower than to a comparable extracochlear stimulus, independent of the order of distortion.

during the generation of distortion products. The latency difference seems to be independent of CF and the order of distortion used for stimulation. This could indicate that the position of the primary frequencies and, consequently the place of DPOAE generation in relation to the units corresponding frequency place, does not play a major role in producing the latency difference. Consequently, the 1.1 ms of additional delay, observed when the neurons are stimulated with a distortion product, seem to be made up mostly of the time constants of the nonlinear cochlear mechanisms at the representation place of the primaries that are responsible for the generation of distortion products.

ACKNOWLEDGMENTS

We would like to thank E. Covey, G. Neuweiler, I.J. Russell, and M. Vater for critical comments on earlier versions of this manuscript. This study was supported by the DFG, SFB 204.

Brown, A. M., and Kemp, D. T. (**1984**). ''Suppressibility of the $2f1$-$f2$ stimulated acoustic emissions in gerbil and man,'' Hearing Res. **13**, 29–37.

Brown, A. M. (**1994**). ''Modulation of the hair cell motor: A possible source of odd-order distortion [see comments],'' J. Acoust. Soc. Am. **96**, 2210–2215.

Cooper, N. P., and Yates, G. K. (**1994**). ''Nonlinear input–output functions derived from the responses of guinea-pig cochlear nerve fibres: Variations with characteristic frequency,'' Hearing Res. **78**, 221–234.

Dallos, P., and Corey, M. E. (**1991**). ''The role of outer hair cell motility in cochlear tuning,'' Curr. Opin. Neurobiol. **1**, 215–220.

Fahey, P. F., and Allen, J. B. (**1985**). ''Nonlinear phenomena as observed in the ear canal and at the auditory nerve,'' J. Acoust. Soc. Am. **77**, 599–612.

Frank, G., and Kössl, M. (**1995**). ''The shape of $2f1-f2$ suppression tuning curves reflects basilar membrane specializations in the mustached bat, pteronotus parnellii,'' Hearing Res. **83**, 151–160.

Frank, G., and Kössl, M. (**1996**). ''The acoustic two-tone distortions $2f1-f2$ and $f2-f1$ and their possible relation to changes in the operating point of the cochlear amplifier,'' Hearing Res. **98**, 104–115.

Gaskill, S. A., and Brown, A. M. (**1990**). ''The behavior of the acoustic distortion product, $2f1-f2$, from the human ear and its relation to auditory sensitivity,'' J. Acoust. Soc. Am. **88**, 821–839.

Kössl, M. (**1992**). ''High frequency distortion products from the ears of two bat species, megaderma lyra and carollia perspicillata,'' Hearing Res. **60**, 156–164.

Magnan, P., Avan, P., Dancer, A., Smurzynski, J., and Probst, R. (**1997**). ''Reverse middle-ear transfer function in the guinea pig measured with cubic difference tones,'' Hearing Res. **107**, 41–45.

Martin, G. K., Lonsbury Martin, B. L., Probst, R., Scheinin, S. A., and Coats, A. C. (**1987**). ''Acoustic distortion products in rabbit ear canal. II. Sites of origin revealed by suppression contours and pure-tone exposures,'' Hearing Res. **28**, 191–208.

Mills, D. M., and Rubel, E. W. (**1996**). ''Development of the cochlear amplifier,'' J. Acoust. Soc. Am. **100**, 428–441.

Mills, D. M., and Rubel, E. W. (**1997**). ''Development of distortion product emissions in the gerbil: 'filter' response and signal delay,'' J. Acoust. Soc. Am. **101**, 395–411.

Müller, M. (**1996**). ''The cochlear place-frequency map of the adult and developing mongolian gerbil,'' Hearing Res. **94**, 148–156.

Powers, N. L., Salvi, R. J., Wang, J., Spongr, V., and Qiu, C. X. (**1995**). ''Elevation of auditory thresholds by spontaneous cochlear oscillations,'' Nature (London) **375**, 585–587.

Probst, R., Lonsbury Martin, B. L., and Martin, G. K. (**1991**). ''A review of otoacoustic emissions,'' J. Acoust. Soc. Am. **89**, 2027–2067.

Ravicz, M. E., Rosowski, J. J., and Voigt, H. F. (**1996**). ''Sound-power collection by the auditory periphery of the mongolian gerbil meriones unguiculatus. II. External-ear radiation impedance and power collection,'' J. Acoust. Soc. Am. **99**, 3044–3063.

Rose, J. E., Kitzes, L. M., Gibson, M. M., and Hind, J. E. (**1974**). ''Observations on phase-sensitive neurons of anteroventral cochlear nucleus of the cat: nonlinearity of cochlear output,'' J. Neurophysiol. **37**, 218–253.

Rosowski, J. J. (**1991**). ''The effects of external- and middle-ear filtering on auditory threshold and noise-induced hearing loss,'' J. Acoust. Soc. Am. **90**, 124–135.

Rübsamen, R., Mills, D. M., and Rubel, E. W. (**1995**). ''Effects of furosemide on distortion product otoacoustic emissions and on neuronal responses in the anteroventral cochlear nucleus,'' J. Neurophysiol. **74**, 1628–1638.

Ryan, A. (**1976**). ''Hearing sensitivity of the mongolian gerbil, *meriones unguiculatis*,'' J. Acoust. Soc. Am. **59**, 1222–1226.

Sewell, W. F. (**1984**). ''The effects of furosemide on the endocochlear potential and auditory-nerve fiber tuning curves in cats,'' Hearing Res. **14**, 305–314.

Whitehead, M. L., Lonsbury Martin, B. L., Martin, G. K., and McCoy, M. J. (**1996**). ''Otoacoustic emissions: Animal models and clinical observations,'' in *Clinical Aspects of Hearing*, edited by T. R. Van De Water, A. N. Popper, and R. R. Fay (Springer-Verlag, New York).

Zwicker, E. (**1981**). ''Dependence of the level and phase of the $(2f1-f2)$-cancellation tone on frequency range, frequency difference, level of primaries and subject,'' J. Acoust. Soc. Am. **1**, 1277–1288.

Virtues and perils of an empiricist approach to speech perception

Keith R. Kluender[a)]
Department of Psychology, University of Wisconsin, 1202 West Johnson Street, Madison, Wisconsin 53706

Andrew J. Lotto
Department of Psychology, Parmly Hearing Institute, Loyola University Chicago, 6525 North Sheridan Road, Chicago, Illinois 60626

(Received 2 January 1997; revised 20 August 1998; accepted 6 October 1998)

Nearey's ''double-weak'' approach [J. Acoust. Soc. Am. **102**, 3241–3254 (1997)] advocates a pattern-recognition model in answer to fundamental problems of speech perception. Both theoretically and empirically, there is much to recommend double-weak. However, there is some question whether this approach avoids long-standing disagreement with respect to the objects of speech perception. In addition, the descriptive power of even relatively simple empiricist models such as Nearey's can mislead with respect to fundamental articulatory and auditory processes underlying speech perception. Here, the positive contributions are celebrated, and several cautionary observations—germane to broader questions of experience and learning—are offered. © *1999 Acoustical Society of America.* [S0001-4966(99)04601-9]

PACS numbers: 43.71.An, 43.71.Es [WS]

INTRODUCTION

Nearey (1997) presents an approach to understanding phonetics and speech perception, which he labels ''double-weak.'' This approach, in some ways new and in some ways familiar, provides the motivation for this commentary. Nearey suggests the name ''double-weak'' because, in contrast to some previous theorization concerning speech perception, his approach assumes relatively weak constraints on both articulatory and auditory processes. In place of substantial demands upon articulation or audition, Nearey argues that relatively simple pattern-recognition processes may be adequate to yield phonological units from patterns in the acoustic signal. He suggests, however, that talkers do control their productions in a fashion that permits these pattern-recognition processes to be successful. Nearey simulates simple pattern recognition using logistic regression analysis, which shares characteristics of several other modeling approaches, and he demonstrates the efficacy of this approach with old and new data from perception studies. Each of these major points will be considered in what follows. A number of positive contributions will be celebrated, and several cautionary observations will be offered.

I. OBJECTS OF PERCEPTION

Nearey begins with some reflection upon the tension among theories with respect to whether objects of speech perception are articulatory gestures or acoustic patterns typically produced by vocal tracts. Describing this division as one of mere ''tension'' may be an understatement. Together with issues concerning whether perception of speech requires special mechanisms (specific to humans and separate from processes responsible for perception of other events or complex sounds), polemics concerning the primacy of gestures versus acoustics have been longstanding.

Over the past 40 years and across evolving versions of motor theory, perception of gestures lies at the heart of the matter. Liberman and Mattingly asserted that ''the objects of speech perception are the intended phonetic gestures of the speaker'' (1985, p. 1). In recent versions of motor theory (e.g., Liberman and Mattingly, 1985, 1989), this specialization takes the form of a ''phonetic module.'' Although this hypothesized module shares duties of production and perception, the emphasis has been upon how such a module is exquisitely adapted for recovering the intended gesture when its existence is considerably obscured as portrayed in the acoustic signal. The force of this gestural approach[1] has been to accept articulation and its seemingly inscrutable acoustic products as part of the problem and to rely upon specialized perceptual processes as the solution.

In contrast, other researchers and theorists have emphasized the acoustic signal and its auditory impression as most clearly defining the phonetic message. Liberman refers to such approaches as ''conventional'' because, for better or worse, these views rest most comfortably within traditions of perception and cognition. Pastore (1981), for example, draws attention to psychoacoustic factors and similarities between perception of speech and perception of other complex sounds. Arguments supporting acoustic objects of speech perception are not based solely upon general similarities. Diehl and Kluender (1989a, b) argue that acoustic patterns and their auditory consequences are the appropriate objects of speech perception on the basis of an array of phonetic regularities across languages and a number of empirical findings (e.g., Diehl, 1987; Diehl *et al.*, 1990; Kluender *et al.*, 1987).

Diehl and others (e.g., Diehl and Kluender, 1989a, b; Kingston and Diehl, 1994, 1995; Lotto *et al.*, 1997a) have

a)Electronic mail: kluender@macc.wisc.edu

extended this approach to suggest that talkers actively manage articulation to produce acoustic patterns most congenial to general operating characteristics of auditory systems. In this case, one may be able to conceptualize the perceptual side of the equation as more general or tractable, but at the expense of increased flexibility and control of articulation (e.g., Kingston and Diehl, 1994).

Nearey (1997) attempts to distinguish his approach from more polarized perspectives. In a field he presents as being cleaved by theories that are ''strong gestural'' versus those that are ''strong auditory,'' [2] Nearey (1997) proposes an alternative approach which he labels ''double-weak.'' He describes his position as double-weak because he envisions relatively loose constraints both on production and perception. By this account, much of speech perception is achieved through simple pattern-recognition processes which map acoustic attributes onto symbolic phonemic labels. Although Nearey adopts acoustic patterns to be the objects of perception, he assumes relatively weak constraints to be imposed by audition. Instead, the theory suggests that acoustic covariation is the product of real-time demands on articulation, but only up to a point. Nearey does not suggest that pattern recognition operates upon whatever acoustic patterns happen to arise from gestures. Instead, he suggests that talkers find ways to accommodate processing capabilities of pattern recognizers such as those he proposes through ''stylized output patterns.''

Avoidance of strong claims, as Nearey attempts to do, does not necessarily result in a model that is less parsimonious. This is because, in some cases, parsimony on one side of the communication channel can incur costs on the other side. Based upon the conclusion that more general processes are inadequate, motor theorists (e.g., Liberman and Mattingly, 1985) posit specialized perceptual processes in the form of a speech module.[3] On the other hand, a strong auditorist may have confidence in the power of default perceptual processes so long as the talker takes on the burden of added articulatory planning and control. Parsimony may suffer no more by a double-weak approach than by either a strong gesturalist or strong auditorist approach.

To the extent that Nearey (1997) assumes some middle ground, however, it bears note that the middle ground is not virgin territory. As Nearey notes, for even the most ardent gestural and auditory theorists, positions have not been exclusively one-sided. Gesturalists (e.g., Fowler, 1989) note the importance of perceptual constraints in development of phonetic inventories, and auditorists admit the importance of minimizing articulatory effort (e.g., Kingston and Diehl, 1994). Further, a good many researchers make progress without expressing any strong commitment to gestures or acoustics; although, assumptions typically are implicit in designs of experiments and the questions they address.

It is unlikely that the double-weak approach will provide a harmonious midpoint between gestures and acoustics. In large part, this is because from the start, Nearey adopts auditory patterns as the objects of speech perception. In fact, it may be inescapable that researchers explicitly or implicitly embrace some sense of what it is that is perceived, be it gestural or auditory.

Further, although Nearey does not emphasize control of production for auditory effect, he looks favorably upon articulation being actively managed to be more amenable to pattern-recognition models such as his own. In particular, he suggests that speech is decodable via simple pattern recognition because talkers adhere to ''orderly output constraints'' such as those proposed by Sussman and his colleagues (Sussman *et al.*, 1995, 1998).[4] Given the embracing of acoustic/auditory patterns as objects of speech perception and acceptance of articulation organized to facilitate perception, Nearey's approach tilts clearly away from gestural approaches. Relative to other approaches, double-weak bridges the divide between auditory and gestural approaches modestly if at all.

II. THE MODEL

One way that the double-weak approach *does* distinguish itself from other contemporary psychological approaches is that it can be viewed as ''a crassly empirical approach to phonological contrast'' (Nearey, 1997, p. 3252). Nearey's approach simply is to model the mapping between individual acoustic attributes of the signal and phonological elements. Using logistic regression analysis, Nearey generates *territorial maps* depicting regions in space corresponding to particular percepts with boundaries separating these regions. The essential feature is not logistic regression analysis *per se*. The framework is one of general linear analysis; there are strong commonalities between Nearey's models and analysis of covariance. Similarly, the models are closely related to fuzzy logical models (Massaro, 1987; Massaro and Oden, 1980; Oden and Massaro, 1978). The force of logistic regression models is generality and simplicity.

In the simplest form of the logistic regression model presented by Nearey, the *primary cue model*, a particular property of the signal (cue) contributes solely and independently to define a phonetic distinction. In Nearey's (1997) example, the attribute ''vocoid duration'' (vowel duration) in VCs varying in tenseness–laxness[5] of the vowel (/æ/–/ɛ/) and voicing of the consonant (/d/–/t/) could contribute to identification of the vowel or the consonant, but not both. Nearey uses this model to set a lower bound on simplicity, for such a model is at odds with perceptual data because a single acoustic property can contribute simultaneously to perception of more than one phonetic unit (e.g., Mermelstein, 1978; Repp *et al.*, 1978).

Slightly more complex is what Nearey refers to as a *secondary cue model* in which a given auditory property can contribute to defining more than one phonetic distinction. For Nearey's VC example, vowel length can contribute to distinguishing both vowel (longer→/æ/) and consonant (longer→/d/). The term *secondary* refers to the notion that one acoustic attribute may be weighted less heavily than another. Hence, the same attribute may be weighted heavily for one distinction (*primary*) and be weighted less heavily (*secondary*) for another distinction. Although these distinctions may be helpful in understanding particular applications, the terms *primary*, *secondary*, *tertiary*, etc., relate to *territorial maps* only to the extent that they reflect relative magnitude of coefficients of the logistic regression model. Formally, if

not in practice, two attributes could have exactly the same coefficients. As a general linear model, there also is nothing that constrains logistic regression analysis to include no more than two attributes. However, it is easier to visualize results on a plane, and it is more practical to study perception of stimuli when only two attributes simultaneously covary.

To the *secondary cue model*, Nearey (1990, 1992) adds a final term which he refers to as a *diphone bias*. This term permits interaction between the identity of adjacent phonemes. What this term does is permit some diphones (/æt/ and /ɛd/ in Nearey's example) to be more probable outputs (relative to /ɛd/ and /æt/). In this example, more lax+voiceless also results in more tense+voiced VCs. In a *territorial map, diphone bias* permits regions to be translated along a dimension such that the areas of two diphones are larger at the expense of the areas for the other two phoneme combinations.

Nearey (1997) speculates about why listeners may behave as if such bias effects exist. He considers the possibilities that they represent phonotactic constraints (some VC sequences are more common than others), or they could reflect underlying lexical biases (e.g., some VCs occurs in more words or in words that are heard more often.) Recent studies with infant listeners (Aslin *et al.*, 1998; Saffran *et al.*, 1996) are consistent with this approach.

Overall, the *diphone-biased secondary-cue* model does an admirable job accommodating the variance in listeners responses to VCs varying in two dimensions. In either case, experience with probabilities of co-occurrences could serve to induce *diphone bias*, thus maintaining Nearey's empirical commitment. It may prove important that this bias must be symmetric in Nearey's models to the extent that symmetrical bias effects do or do not generally coincide with actual frequencies of co-occurrence.

Nearey's models are admirably frugal when it comes to computational power. He considers how the fit of the model could be improved by adding additional terms. While more free parameters always will improve performance, Nearey demonstrates not only that the limited *diphone-biased secondary-cue* logistic regression provides quite accurate description of the data, but also that additional variables do not account for sufficient variance to justify their inclusion. The models embody welcome elegance and tractability. Unlike, for example, multi-layer connectionist simulations in which ''hidden units'' permit nonlinear mapping and render difficult or impossible the task of understanding how a network succeeds if and when it does, logistic regression models and their general linear relatives are simple and understandable. In the cases Nearey presents, these models work and one knows why they work. As Nearey himself shows (Nearey and Shammass, 1987; Nearey, 1997), there likely will be cases when they do not work and linearity must be violated. These failures will be the kind of useful failures upon which good science prospers. For now, these models are simple and general, and it will be possible to add power prudently to these models as required by the data.

III. LEARNING AND EXPERIENCE

Nearey's empiricist approach also implies a welcome emphasis upon learning, or more accurately, learnability. Although Nearey mostly describes his modeling efforts as investigations of processes of pattern recognition, he makes the point that his modeling should be taken, at least for now, as a simple case of auditory-perceptual learning.[6] Most speech perception theorists acknowledge the importance of learning, and most appeal to experience in a language environment as explanation. One lapse in Nearey's depiction of strong gesturalists and strong auditorists is the fact that he does not acknowledge that they, too, appreciate the importance of learning. Best (1995), as a strong gesturalist and proponent of direct realism, focuses upon the role of experience. Diehl and Kluender (1989a, b; Kluender and Diehl, 1987; Kluender *et al.*, 1987), among the strong auditorists Nearey notes, clearly embrace the role of experience and learning in shaping perception of speech.

In the last decade, investigators have been keenly interested in studies demonstrating changes in how infants respond to speech sounds as they have increasing amounts of experience in a language environment (e.g., Best *et al.*, 1988; Greiser and Kuhl, 1989; Kluender *et al.*, 1998; Kuhl, 1991; Kuhl *et al.*, 1992; Werker and Lalonde, 1988; Werker and Tees, 1984a, b). What is lacking, however, is sufficient modeling concerning how experience brings the perceptual system to behave in a manner that respects distributional properties of speech sound attributes.

Nearey's (1997) major contribution is making explicit some of the characteristics that he sees to be embodied by a model for how language-users are capable of exploiting correlations between multiple stimulus attributes and linguistically significant units. To the extent to which Nearey constrains his models to use as little computational power as possible, he has something in common with gesturalists[7] and auditorists. While they work to require relatively less from speech production and speech perception, respectively, Nearey's models require relatively little computational (brain) power. Nearey's models of pattern recognition are constrained to be linear and he argues for the preeminence of the segment as an economical unit of phonetic perception. Although the present authors are not sanguine regarding the role of phonetic segments *per se*, if one were to develop a language system that is easily learnable by most members of a group, a perceptron-like process like Nearey's may be about as simple as one could desire. If the architecture of phonetic perception can be so elegant, effects of experience evidenced in six-month-old infants probably ought not be surprising.

Nearey's approach also can be viewed as being constrained by ecology in as much as processes are tuned by distributional properties encountered through experience. In many ways, his empirical approach has a precedent in the theory of Egon Brunswik over 50 years ago (Brunswik, 1937, 1940, 1944, 1955; Postman and Tolman, 1959). For Brunswik, too, no single stimulus attribute is necessary and sufficient for perception of an object or event. Multiple stimulus attributes are used, each weighted to reflect probability and manner of occurrence in the world.[8] In this re-

gard, perception of multiply-specified phonetic units would be much the same as for other objects and events (Kluender, 1994).

It has been demonstrated that quite simple processes may be adequate to account for perceptual learning of multiply-specified phonetic equivalence classes such as that for alveolar stops (e.g., Kluender, 1998). Kluender *et al.* (1987) found that Japanese quail (*Coturnix coturnix japonica*) could learn the ostensibly complex mapping between multiple acoustic attributes and a response that maps onto alveolar stop consonants. Despite arguably feeble mental capacity, quail learning generalized accurately to novel syllables beginning with /d/.

Kluender and Diehl (1987) proceeded to explore ways in which multiple acoustic properties could be used by explicitly training quail to learn functional mappings without benefit of any single necessary or sufficient property. They used syllables produced by ten different talkers that varied on three dimensions: initial-consonant type (voiced versus voiceless, velar versus nonvelar), vowel type (front versus back, high versus low), and sex of talker. Two quail learned different equivalence classes based upon these dimensions. For one bird, the positive-class properties were voiced stop, front vowel, and male talker, while for a second bird, positive properties were velar stop, high vowel, and female talker. During training, birds were reinforced for pecking when hearing stimuli that were positive on exactly two of the three dimensions, and were not reinforced when hearing stimuli that were negative on two of the dimensions.

As formidable a task as this may appear, both quail learned to use all three constituent dimensions in mastering the task. Each quail generalized to novel instances of its equivalence class, pecking significantly more to novel positive stimuli than to novel negative ones. This happened when novel stimuli were positive on only two of three dimensions, and the highest level of responding occurred when the novel stimulus was positive on all three dimensions (a situation never encountered during training). Such behavior is consistent with theories of human categorization that account for the fact that certain category instances seem more representative than others and are generally easier to learn and remember, even when they have never been directly experienced (Posner and Keele, 1968; Rosch, 1978). With the exception of triple-positive stimuli, quail responded more strongly to stimuli used in training than to novel tokens, consistent with accounts of human category formation that emphasize experience with individual exemplars (Medin and Schaffer, 1978).

More recent data imply that relatively simple learning processes may account for the fact that some acoustic instances of vowel sounds are phonemically more compelling than others. Kluender *et al.* (1998) trained eight European starlings (*Sturnus vulgaris*) to respond differentially to vowel tokens drawn from stylized distributions for the English vowels /i/ and /ɪ/, or from two distributions of vowel sounds (approximate to /y/ and /ʉ/) that were orthogonal in the $F1-F2$ plane. Following training, starlings' responses to novel stimuli drawn from these distributions could be predicted well on the bases of frequencies of the first two formants as well as by distance from the centroid of these distributions of vowel sounds. Graded responses relative to the centroid were much like those often taken to imply the existence of category prototypes.[9] Starling responses corresponded closely to adult human judgments of ''goodness'' for English vowel sounds. Most germane to Nearey's efforts, a simple linear association network model trained with vowels drawn from the birds' training set captured 95% of the variance in birds' response rates for novel vowel tokens. Nearey's logistic models can successfully accommodate all of these avian response patterns because these are problems that require linear combinations of stimulus attributes.

Another virtue of Nearey's logistic models lies in what they cannot do. Following the successful Kluender and Diehl (1987) experiments in which quail conquered the simultaneously introduced complexities of vowel frontness/backness, consonantal voicing and place of articulation, and sex of talker, it was questioned whether a nonperceptron or XOR-like problem was beyond the pale of quail performance. In this study, in order for a syllable to be positive, it must **either** have a labial [b,p] stop and a high [i,u] vowel, **or** have a nonlabial stop [d,t,g,k] and a low [æ,ɔ] vowel. Despite training for a full year (the average lifespan for the species), performance on training stimuli never approximated avian performance for any of the forementioned tasks, and there was no positive transfer of performance to novel stimuli that obeyed the rule.

Nearey's linear logistic models would do no better than quail at this task. This is good. Despite the potential power of logistic or quail models of learning, there exist principled constraints upon the sorts of processes these models can accommodate. In the case of Nearey's logistic model, one reason this XOR problem cannot be accommodated is that the solution would require the functions for dimensions of voicing and of vowel height to be nonmonotonic. Such ''failures'' can be taken as encouraging in as much as Nearey's models have an elegance that constrains the domain of solutions in a principled and informative manner.

One may view as a potential weakness of Nearey's and similar empiricist approaches the fact that few predictions can be made beyond maintaining that these models ought to reflect distributional properties of the input. It then becomes critical that, as simple learning models, one can predict that models will fail when the task exceeds certain computational bounds. And, very significantly, Nearey has done admirable job of demonstrating how one may be able to account for the vast majority of perceptual data with a nicely constrained segment-based model. Moreover, perceptron-like linear logistic models may have some biological plausibility, as analogous processes apparently can be embodied in the neural substrate of an animal with presumably quite limited intellect. These are important contributions, but they are only a part of the story.

IV. PERILS

A. What cannot be explained

Is there any reason one may be reluctant to be fully satisfied with what Nearey calls a ''crassly empiricist ap-

proach''? For example, why might one continue to search for constraints on auditory perception with concomitant demands upon articulation?

Purely empiricist models are quite silent regarding why linguistic sound inventories are structured as they are. Why, for example, are vowels longer before voiced consonants in all or almost all languages (see, e.g., Kluender *et al.*, 1988)? What logistic models will do is describe response patterns that are sensitive to the fact that such covariation exists. These models do not explain **why** covariation exists. To better appreciate why searching for articulatory and auditory explanations continues to be pivotal, imagine what would happen if, contrary to covariation typical of sound systems, [ɛ] was typically produced with longer duration than [æ]. In this revised bæd–bet perceptual study, listeners should perceive more long vowels as [ɛ] and more short vowels as [æ]. And, the logistic model will fit the data exactly as well, accounting for the same amount of variance. This is not to say that there is no virtue in a model of perceptual learning by which lawful variance in the world is reflected in lawful perception and behavior. But, a model that, for the most part, reflects probabilities in an inverted imaginary world as well as it does in a real world cannot be taken as fully explanatory. Nearey appears to be appropriately cautious about this general problem when he suggests that real-time demands upon articulation constrain the range of realized covariation. Nearey also portrays some regularities as products of articulation ''stylized'' to accommodate pattern recognition; however, pattern recognition would work exactly as well if vowel duration and voicing were stylized in reverse.

B. What may be missed

A related concern is that, sometimes, the success of such an empiricist model can clearly mislead. Kluender (1991) conducted a series of perceptual studies with quail that were designed to investigate the role of $F1$ transitions on perception of voicing for syllable-initial stops. When $F1$-onset frequency is lower, a longer $F1$ cutback (one of the acoustic products of voice onset time) is required for human listeners to perceive synthesized stop consonants as voiceless. He synthesized CVs with four types of natural-like rising $F1$ transitions that varied in duration of $F1$ cutback. Thus, endpoint training stimuli (with 5- or 65-ms $F1$ cutback) always differed in onset frequency of $F1$ because a longer cutback resulted in a higher $F1$ onset. (See Fig. 1.) Comparable effects of $F1$-onset frequency across the four $F1$ types were found for human and avian listeners. Lower $F1$-onset frequency shifted the boundary to higher values of $F1$ cutback (more ''voiced'' responses).

These data can be interpreted as evidence of quail and humans responding to simple covariations in the input and, thus, are amenable to Nearey's logistic model approach. The $F1$-onset frequency covaried with $F1$-cutback for all the series in the Kluender (1991) study, and earlier work had demonstrated the ability of quail to learn covariations between acoustic attributes (Kluender and Diehl, 1987; Kluender *et al.*, 1987). As is the case for data from these previous studies, Nearey's models would seamlessly incorporate this covariance with no reference to auditory processes and the model would provide a reasonable fit.

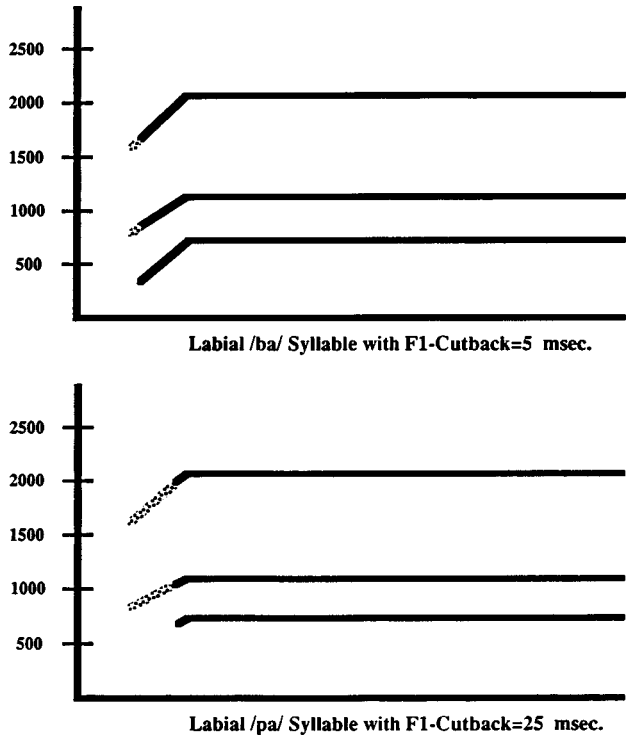

FIG. 1. During release of an initial stop consonant (in this case labial), the frequency of $F1$ increases. Prior to voice onset, there is little or no energy in the region of $F1$. Consequently, when delay in voice onset is longer, the onset frequency of $F1$ is higher.

However, a simple pattern-recognition approach would fail to discover that auditory processes were at least in part responsible for the shift in birds' responses (and, by extension, humans' responses). Another quail experiment was conducted with synthetic continua having either a relatively low (375 Hz) or high (750 Hz) constant-frequency $F1$ (Kluender and Lotto, 1994). Because $F1$ did not vary in frequency, there was no opportunity for birds to use covariation of $F1$-onset frequency and $F1$ cutback. Despite this, quail exhibited reliably shorter ''labeling'' boundaries (more voiceless stops) for intermediate stimuli of continua when $F1$ frequency was higher. Human performance with the same stimuli was like that for birds.

Essentially the same effect was observed for human and quail whether or not there was any possibility to use covariation between $F1$-onset frequency and $F1$-cutback. Absent the opportunity for learning the natural relationship between $F1$-cutback and $F1$-onset frequency, these results suggest that the effect of $F1$-onset frequency is due to quite general auditory processes common to humans and quail. The problem is that an empiricist model would have fit the original data very well, and there would have been little reason to suspect what was true all along; the effect is of general auditory—not learning—origins (see also Parker, 1988). Without denying the likely event that experienced covariance can play a role as well, it appears that modeling these data solely as an empiricist process of simple pattern recognition would have been misleading.

In other cases as well, one may find that, despite the fact

that a logistic model will accommodate labeling data with near-perfect accuracy, such empiricist models may be misleading. Worse is that these mistakes can deprive one's model of economy if multiple acoustic attributes collapse onto a smaller number of auditory properties. This argument does not depend upon constructs such as Kingston and Diehl's (1994) putative ''intermediate perceptual properties.'' Simpler more obvious instances exist. For example, at relatively short durations (<200 ms), loudness is the product of both physical time and intensity (e.g., Blodgett *et al.*, 1958; Zwicker and Wright, 1963; Zwislocki, 1960). The fact that auditory systems ''summate energy'' in this fashion may well account for the existence of trading relations between duration and amplitude of aspiration energy for English stops (Repp, 1979). Similarly, loudness integration likely explains the finding that identification of heavily aspirated stops by Korean listeners is predicted by both duration and amplitude of aspiration energy (Kim *et al.*, 1994).

Nearey does anticipate the virtue of limiting the inventory of attributes and, thus, decreasing the degrees of freedom; although, he expresses concern about what he calls ''a premature commitment to a limited set of properties.'' His caution is well taken. However, even if one embraces the empiricist strategy in general, the empiricist approach should probably be the less attractive default condition invoked only after one has wrenched all the explanation one can from lawful constraints upon speech production and auditory perception.

Nearey's computational austerity is laudable with respect to virtues of good scientific theory, but it is questionable whether these models will be able to scale up gracefully from single-syllable examples to longer strings of fluent speech. Effects of coarticulation can be long lasting and quite varied, and the number of acoustic attributes that will have to be placed in the model will become large. Some coarticulatory effects cross-syllable boundaries. For example, the acoustic realization of [d] in the disyllable [alda] is quite different from [d] in [arda] (Dianora *et al.*, 1996). Labeling tasks have demonstrated that humans' identifications of /d/ in these syllables are sensitive to the characteristics of the preceding liquids (Mann, 1980). To account for these data, Nearey's models would need to include acoustic variables measured in the preceding syllable. *Diphone-bias* terms would have to operate across both preceding and following phonemes at a minimum. The number of attributes could increase dramatically to account for all coarticulatory and suprasegmental effects which may affect phonemic identification. As noted before, the logistic regression model can scale up easily to accommodate additional variables. However, such explosion of learned attributes may not be necessary.

Lotto and Kluender (1998) have described similar effects of preceding acoustic energy for nonspeech/speech hybrid stimuli, and Lotto *et al.* (1997b) have demonstrated that quail respond in the same pattern as humans for [alda] and [arda] stimuli, despite never having experience with coarticulatory covariation. It appears that many effects of covariation, even those occurring across syllables, can be accounted for by general auditory mechanisms. The problem is not simply that Nearey's model downplays the importance of these general mechanisms, but that claims of learnability and simplicity are unnecessarily compromised as a result of failure to recognize the role of the auditory system. An approach that includes **both** aspects of auditory function and learning (e.g., Diehl and Kluender, 1987) would be more complete and has a realistic chance of accounting for most phenomena of speech perception. As noted above,[6] separating auditory processes and effects of experience may not even be possible.

C. Audition and learning

With the suggestion that a complete model include both auditory and learning processes, a legitimate fear is that falsifiability becomes at risk. One way to characterize the foregoing is that part of the explanation of speech perception falls out of general auditory processes, and the remaining variance can be ''mopped up'' by learning processes. If the auditory hypothesis fails under test, the default position becomes the appeal to learning. In fact, Nearey describes his approach as having the potential to be viewed as a ''fallback theoretical position'' (1997, p. 3243). Stated this way, an auditory/learning model could be tough to falsify; however, it also could be true.

The response to concerns about falsifiability must be found in more specific definition of processes of audition and learning. What can be falsified are specific hypotheses about these processes. The occasional demonstration of similar patterns of response data for speech and nonspeech analogs (or, human and nonhuman subjects) may no longer be sufficient. Instead, hypotheses about specific auditory processes must be generated, and experiments that test specific predictions must be conducted. Instead of placing gestural theories at risk via analogy, specific auditory hypotheses must be placed at risk.

With respect to experience and learning, the same can be said. It is not very useful to hypothesize that learning plays some role. Of course it does. One type of information that will be critically important in the development of adequate models for perceptual experience with speech will be richer characterization of the input to the process. In this way, one's model can be constrained by ecology as well as computation. Next, learning processes must be given greater definition. Nearey (1997) demonstrates the power of one approach to this challenge, and he provides a fine example by making his model explicit and computationally simple. The model will be falsified and modified (likely by Nearey himself), and therein lies part of its strength.

V. AUXILIARY ISSUES

Before conclusion, it may be useful to express some concerns with regard to attempts to reveal the processes through which a young child comes to exploit experienced regularities in becoming a proficient language user. Two seminal issues arise concerning learning and learnability. First, what is it that infants really learn? Do they learn about phonetic segments, syllables, or morphemes? It is beyond the present focus to explore each possibility. However, without

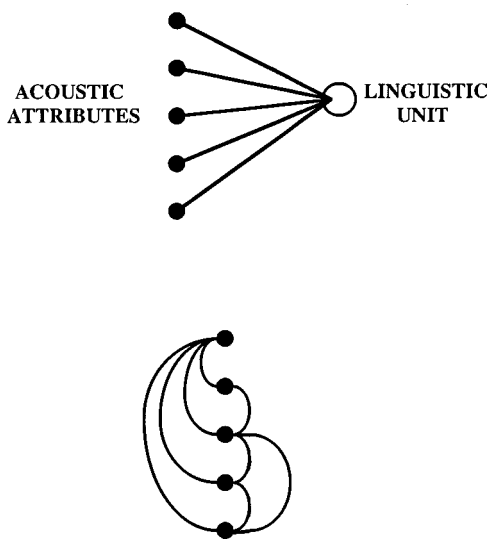

FIG. 2. The top figure illustrates multiple stimulus attributes each being correlated more or less with a particular phonetic unit. The bottom figure illustrates the concept of phonetic units defined as covariance between stimulus attributes.

dismissing phonetic units, one can imagine that something akin to phonetic dimensions come to play an increasingly important role as infants learn more functionally significant units such as morphemes. The traditional linguistic definition of phonemes is that they serve to efficiently distinguish morphemes. Because phonemes provide efficient descriptors of lexical space, could they emerge as dimensions of the developing lexical space instead of being taken as primitives (see, e.g., Lindblom *et al.*, 1984)?

The alternative, learning phonetic units per se, may require suggesting that lexical space begins its organization only after phonetic segments have been defined. Many reports concerning development of speech perception seem to portray the infant's task as one of learning phonemes as early functional units of language; however, explicit treatment of this question is rare. It is possible that neither lexical items nor phonetic units serve exclusively to structure the developing lexicon, and simultaneous organization seizing upon both sources of input regularities is not beyond possibility. In any case, this question is seminal for any computational or learning model aspiring to describe the use of experienced covariation in speech pattern recognition.

A closely related concern is that one could be misled by models that rely upon the correlation between particular stimulus attributes and putative phonetic units or symbols (Fig. 2, top). Nearey's linear logistic models seize precisely upon these correlations. Unless one is prepared to posit the innate existence of every phoneme from every language, and over 800 phonetic units is a lot (Kluender, 1994; Maddieson, 1984), one must consider an alternative. One alternative, favored here, is that correlations among stimulus attributes convey information (Fig. 2, bottom).[10] As a first approximation, one could characterize phonemes more as vectors through a covariance space. Studies of infant categorization of objects and events suggest that infants use correlated attributes to learn categories (Cohen and Strauss, 1979; Husaim and Cohen, 1981; Younger, 1985; Younger and Cohen, 1983, 1985, 1986).

VI. CONCLUSIONS

These questions concerning development extend beyond Nearey's present empiricist efforts, but they are central issues that should be of concern to all who find virtue in the empiricist approach to speech perception. Following the more circumspect nature of the second half of this commentary, the virtues of the double-weak approach merit brief repeat. Although there is some question regarding the degree to which Nearey has established novel middle ground between gestures and acoustics, there may be virtues to sidestepping a contentious issue about which efforts have shed more heat than light. Nearey has encouraged a balanced theory that may be more inclusive rather than exclusive. His approach implicitly employs constraints of ecology in as much as experienced probability distributions of attributes play a central role, and he encourages a welcome focus upon learnability, if not learning *per se*. Within the linear logistic framework, Nearey has constrained his models to embody admirable elegance and parsimony. Finally, Nearey's efforts may serve to illuminate seminal issues of ontogeny of phonetic perception.

ACKNOWLEDGMENTS

The authors are grateful to Carol Fowler and Terrance Nearey for comments on an earlier version of this paper. This effort was supported by NSF Young Investigator Award DBS-9258482 to the first author.

[1]Not all theories that accept gestures to be the objects of speech perception require unique perceptual processes. Within the Gibsonian tradition, direct realism (e.g., Fowler, 1986) holds the objects of perception to be actual objects and events in the world. As a general theory of perception in force across modalities, direct realism takes gestures to be the objects of speech perception just as the theory would take physical structures (and not arrays of light of varying wavelengths and luminences) to be the proper objects of visual perception. In the broader view, direct realism deserves more attention than will be provided in this commentary. This is because Nearey (1997) does not consider direct realism to any great extent.

[2]Nearey (1997) briefly considers what he refers to as a ''double-strong'' theory of speech perception with strong relations between phonetic symbols and gestures and between phonetic symbols and auditory processes. Because Nearey argues that each of these putatively strong relations is relatively weak, this approach is doubly discouraged.

[3]Because one module is hypothesized to be responsible for both producing and perceiving speech, one may ask how one task could be more complex or special than the other. One way would be for one part, production of speech, to be much like motor control generally while the other part, perception of speech, is remarkable in that it is not accomplished in a fashion similar to perception of other objects and events in the world, instead hewing closely to motor control. Certainly, the emphasis of motor theory has been to distinguish perception of speech from more general models of perception.

[4]Because very recently there has been extended commentary upon Sussman's theorization (Sussman *et al.*, 1998), this aspect of Nearey's approach will not be considered in greater depth here.

[5]Describing vowels, particularly low vowels, as tense or lax is not unambiguous; however, for this discussion, the longer vowel /æ/ will be referred to as tense and the shorter vowel /ɛ/ as lax.

[6]In this commentary, auditory factors will be contrasted with experience and learning. This division of labor is too simplistic, and it is hoped that it is not misleading. Experience, particularly early in life, plays a considerable role in the development of sensory systems. Absent experience, nonpathological

perception does not exist. In addition, when something is the product of auditory-perceptual learning, it does not cease to be auditory because learning has occurred. Throughout this contribution, ''auditory'' can be taken to suggest general operating characteristics of auditory systems without consideration of experience within a particular domain (speech). ''Learning'' will refer to the processes by which performance comes to be in accord with systematic properties in the environment.

[7]Again, direct realism is distinct for other gesturalist approaches. This theory holds that perception of gestures is direct and no more complex or burdensome than perception of other objects or events.

[8]Brunswick did allow ''psychological weights'' to deviate somewhat from strict ecological validity.

[9]No inference is being made here with regard to the putative existence of prototypes. The present authors have argued elsewhere (Kluender *et al.*, 1998) that the theoretical construct of prototypes is unnecessary (see, e.g., Knapp and Anderson, 1984; Medin and Schaffer, 1978).

[10]These alternatives are rarely easy to distinguish for real-world objects and events such as speech because attributes that are relatively highly correlated with a category (perhaps phonetic) also tend to be correlated with one another.

Aslin, R. N., Saffran, J. R., and Newport, E. L. (**1998**). ''Computation of conditional probability statistics by 8-month-old infants,'' Psych. Sci. **9**, 321–324.

Best, C. T. (**1995**). ''A direct realist view of cross-language speech perception,'' in *Speech Perception and Linguistic Experience*, edited by W. Strange (York, Timonium, MD), pp. 171–204.

Best, C. T., McRoberts, G. W., and Sithole, N. M. (**1988**). ''Examination of perceptual reorganization for nonnative speech contrasts: Zulu click discrimination by English speaking adults and infants.'' J. Exp. Psychol. **14**, 345–360.

Blodgett, H. C., Jeffress, L. A., and Taylor, R. W. (**1958**). ''Relation of masked threshold to signal-duration for various phase-combinations,'' Am. J. Psychol. **71**, 283–290.

Brunswik, E. (**1937**). ''Psychology as a science of objective relations,'' Philos. Sci. **4**, 227–260.

Brunswik, E. (**1940**). ''Thing constancy as measured by correlation coefficients,'' Psychol. Rev. **47**, 69–78.

Brunswik, E. (**1944**). ''Distal focussing of perception: Size constancy in a representative sample of situations,'' Psych. Mono. **254**.

Brunswik, E. (**1955**). ''Representative design and probabilistic functionalism: A reply.'' Psychol. Rev. **62**, 236–242.

Cohen, L. B., and Strauss, M. S. (**1979**). ''Concept acquisition in the human infant,'' Child Dev. **7**, 419–424.

Dianora, A., Hemphill, R., Hirata, Y., and Olson, K. (**1996**). ''Effects of context and speaking rate on liquid-stop sequences: A reassessment of traditional acoustic cues,'' J. Acoust. Soc. Am. **100**, 2601.

Diehl, R. L. (**1987**). ''Auditory constraints on speech perception,'' in *The Psychophysics of Speech Perception*, edited by M. E. H. Schouten, NATO ASI series, Series D, Behavioral and Social Sciences, No. 39 (Martimus-Nijhoff, Dordrecht, The Netherlands), pp. 210–219.

Diehl, R. L., and Kluender, K. R. (**1989a**). ''On the objects of speech perception,'' Ecol. Psych. **1**, 121–144.

Diehl, R. L., and Kluender, K. R. (**1989b**). ''Reply to the commentators,'' Ecol. Psych. **1**, 195–225.

Diehl, R. L., Kluender, K. R., and Walsh, M. A. (**1990**). ''Some auditory bases of speech perception and production,'' in *Advances in Speech, Hearing and Language Processing*, edited by W. A. Ainsworth (JAI, London), pp. 243–268.

Fowler, C. A. (**1986**). ''An event approach to the study of speech perception from a direct-realist perspective,'' J. Phon. **14**, 3–28.

Fowler, C. A. (**1989**). ''Real objects of speech perception: A commentary on Diehl and Kluender,'' Ecol. Psych. **1**, 145–160.

Greiser, D., and Kuhl, P. K. (**1989**). ''Categorization of speech by infants: Support for speech-sound prototypes,'' Dev. Psych. **25**, 577–588.

Husaim, J. S., and Cohen, L. B. (**1981**). ''Infant learning of ill-defined categories,'' Merrill-Palmer Quart. **27**, 443–456.

Kim, M-R., Kluender, K. R., Lotto, A. J., and Read, C. (**1994**). ''Perception of syllable-initial English stops by native Korean listeners,'' J. Acoust. Soc. Am. **95**, 2977.

Kingston, J., and Diehl, R. L. (**1994**). ''Phonetic knowledge,'' Language **70**, 419–454.

Kingston, J., and Diehl, R. L. (**1995**). ''Intermediate properties in the perception of distinctive feature values,'' in *Phonology and Phonetic Evidence: Papers in Laboratory Phonology IV*, edited by B. Connell and A. Arvanti (Cambridge U.P., Cambridge), pp. 7–27.

Kluender, K. R. (**1991**). ''Effects of first formant onset properties on voicing judgments result from processes not specific to humans,'' J. Acoust. Soc. Am. **90**, 83–96.

Kluender, K. R. (**1994**). ''Speech perception as a tractable problem in cognitive science,'' in *Handbook of Psycholinguistics*, edited by M. A. Gernsbacher (Academic, New York), pp. 173–217.

Kluender, K. R. (**1998**). ''Locus equations reveal learnability,'' Behav. Brain Sci. **21**, 273.

Kluender, K. R., and Diehl, R. L. (**1987**). ''Use of multiple speech dimensions in concept formation by Japanese quail,'' J. Acoust. Soc. Am. Suppl. 1 **82**, S84.

Kluender, K. R., and Lotto, A. J. (**1994**). ''Effects of first formant onset frequency on [-voice] judgments result from auditory processes not specific to speech,'' J. Acoust. Soc. Am. **95**, 1044–1052.

Kluender, K. R., Diehl, R. L., and Killeen, P. R. (**1987**). ''Japanese Quail can learn phonetic categories,'' Science **237**, 1195–1197.

Kluender, K. R., Diehl, R. L., and Wright, B. A. (**1988**). ''Vowel-length differences before voiced and voiceless consonants: An auditory explanation,'' J. Phon. **16**, 153–169.

Kluender, K. R., Lotto, A. J., Holt, L. A., and Bloedel, S. L. (**1998**). ''Role of experience for language-specific functional mappings of vowel sounds,'' J. Acoust. Soc. Am. **104**, 3568–3582.

Knapp, A. G., and Anderson, J. A. (**1984**). ''Theory of categorization based on distributed memory storage,'' J. Exp. Psychol. **10**, 616–637.

Kuhl, P. K. (**1991**). ''Human adults and human infants show a 'perceptual magnet effect' for the prototypes of speech categories; Monkeys do not,'' Percept. Psychophys. **50**, 93–107.

Kuhl, P. K., Williams, K. A., Lacerda, F., Stevens, K. N., and Lindblom, B. (**1992**). ''Linguistic experience alters phonetic perception in infants six-months of age,'' Science **255**, 606–608.

Liberman, A. M., and Mattingly, I. G. (**1985**). ''The motor theory of speech perception revised,'' Cognition **21**, 1–36.

Liberman, A. M., and Mattingly, I. G. (**1989**). ''A specialization for speech perception,'' Science **243**, 489–494.

Lindblom, B., MacNeilage, P., and Studdert-Kennedy, M. (**1984**). ''Self-organizing processes and the explanation of phonological universals,'' in *Explanations of Phonetic Universals*, edited by B. Butterworth, B. Comrie, and O. Dahl (Mouton, The Hague, The Netherlands).

Lotto, A. J., and Kluender, K. R. (**1998**). ''General contrast effects in speech perception: Effect of preceding liquid on stop consonant identification,'' Percept. Psychophys. **60**, 602–619.

Lotto, A. J., Kluender, K. R., and Holt, L. L. (**1997a**). ''Perceptual compensation for coarticulation by Japanese quail (*Coturnix coturnix japonica*),'' J. Acoust. Soc. Am. **102**, 1134–1140.

Lotto, A. J., Kluender, K. R., and Holt, L. L. (**1997b**). ''Effect of voice quality on the tense/lax distinction for English vowels,'' Phonetica **54**, 76–93.

Maddieson, I. (**1984**). *Patterns of Sound* (Cambridge U.P., Cambridge).

Mann, V. A. (**1980**). ''Influence of preceding liquid on stop-consonant perception,'' Percept. Psychophys. **28**, 407–412.

Massaro, D. W. (**1987**). *Speech Perception by Ear and Eye—A Paradigm for Psychological Inquiry* (Erlbaum, Hillsdale, NJ).

Massaro, D. W., and Oden, G. C. (**1980**). ''Evaluation and integration of acoustic features in speech perception,'' J. Acoust. Soc. Am. **67**, 996–1013.

Medin, D. L., and Schaffer, M. M. (**1978**). ''A context theory of classification learning,'' Psychol. Rev. **85**, 207–238.

Mermelstein, P. (**1978**). ''On the relationship between vowel and consonant identification when cued by the same acoustic information,'' Percept. Psychophys. **23**, 331–335.

Nearey, T. M. (**1990**). ''The segment as a unit of speech perception,'' J. Phon. **18**, 347–373.

Nearey, T. M. (**1992**). ''Context effects in a double-weak view of trading relations: Comments on Kingston and Diehl,'' in *Phonology and Phonetic Evidence: Papers in Laboratory Phonology IV*, edited by B. Connell and A. Arvanti (Cambridge U.P., Cambridge), pp. 28–40.

Nearey, T. M. (**1997**). ''Speech perception as pattern recognition,'' J. Acoust. Soc. Am. **101**, 3241–3254.

Nearey, T. M., and Shammass, S. (**1987**). ''Formant transitions as partly distinctive invariant properties in the identification of voiced stops,'' Can. Acoust. **15**, 17–24.

Oden, G. C., and Massaro, D. W. (**1978**). ''Integration of featural informa-

tion in speech perception,'' Psychol. Rev. **85**, 172–191.
Parker, E. M. (**1988**). ''Auditory constraints on the perception of stop voicing: The influence of lower-tone frequency on judgements of tone-onset simultaneity,'' J. Acoust. Soc. Am. **83**, 1597–1607.
Pastore, R. E. (**1981**). ''Possible psychoacoustic factors in speech perception,'' in *Perspectives on the Study of Speech Perception*, edited by P. D. Eimas and J. L. Miller (Erlbaum, Hillsdale, NJ), pp. 165–205.
Posner, M. I., and Keele, S. W. (**1968**). ''On the genesis of abstract ideas,'' J. Exp. Psychol. **73**, 28–38.
Postman, L., and Tolman, E. C. (**1959**). ''Brunswik's probabilistic functionalism,'' in *Psychology: A Study of a Science. Volume 1. Sensory, Perceptual, and Physiological Formulations*, edited by S. Koch (McGraw-Hill, New York).
Repp, B. H. (**1979**). ''Relative amplitude of aspiration noise as a voicing cue for syllable-initial stop consonants,'' Lang. Speech **22**, 173–189.
Repp, B. H., Liberman, A. M., Eccardt, T., and Pesetsky, D. (**1978**). ''Perceptual integration of acoustic cues for stop, fricative, and affricate manner,'' J. Exp. Psychol. **4**, 621–637.
Rosch, E. H. (**1978**). ''Principles of categorization,'' in *Cognition and Categorization*, edited by E. Rosch and B. Lloyd (Erlbaum, Hillsdale, NJ).
Saffran, J. R., Aslin, R. N., and Newport, E. L. (**1996**). ''Statistical learning by 8-month-olds,'' Science **274**, 1926–1928.
Sussman, H. M., Fruchter, D., and Cable, A. (**1995**). ''Locus equations derived from compensatory articulation,'' J. Acoust. Soc. Am. **97**, 3112–3124.
Sussman, H. M., Fruchter, D., Hilbert, J., and Sirosh (**1998**). ''Linear correlates in the speech signal: The orderly output constraint,'' Behav. Brain Sci. **21**, 241–299.
Werker, J. F., and Lalonde, C. E. (**1988**). ''Cross-language speech perception: Initial capabilities and developmental change,'' Dev. Psych. **24**, 672–683.
Werker, J. F., and Tees, R. C. (**1984a**). ''Cross-language speech perception: Evidence for perceptual reorganization during the first year of life,'' Inf. Behav. Dev. **7**, 49–63.
Werker, J. F., and Tees, R. C. (**1984b**). ''Phonemic and phonetic factors in adult cross-language speech perception,'' J. Acoust. Soc. Am. **75**, 1866–1878.
Younger, B. A. (**1985**). ''The segregation of items into categories by 10-month-old infants,'' Child Dev. **56**, 1574–1583.
Younger, B. A., and Cohen, L. B. (**1983**). ''Infant perception of correlations among attributes,'' Child Dev. **54**, 858–867.
Younger, B. A., and Cohen, L. B. (**1985**). ''How infants form categories,'' in *The Psychology of Learning and Motivation: Advances in Research and Theory*, edited by G. Bower (Academic, New York), Vol. 19, pp. 211–247.
Younger, B. A., and Cohen, L. B. (**1986**). ''Developmental changes in infants' perception of correlations among attributes,'' Child Dev. **57**, 803–815.
Zwicker, E., and Wright, H. N. (**1963**). ''Temporal summation for tones in narrow-band noise,'' J. Acoust. Soc. Am. **35**, 691–695.
Zwislocki, J. (**1960**). ''Theory of temporal auditory summation,'' J. Acoust. Soc. Am. **32**, 1046–1060.

Language identification with suprasegmental cues: A study based on speech resynthesis

Franck Ramus and Jacques Mehler
Laboratoire de Sciences Cognitives et Psycholinguistique (EHESS/CNRS), 54 boulevard Raspail, 75006 Paris, France

(Received 4 April 1997; revised 30 June 1998; accepted 8 September 1998)

This paper proposes a new experimental paradigm to explore the discriminability of languages, a question which is crucial to the child born in a bilingual environment. This paradigm employs the speech resynthesis technique, enabling the experimenter to preserve or degrade acoustic cues such as phonotactics, syllabic rhythm, or intonation from natural utterances. English and Japanese sentences were resynthesized, preserving broad phonotactics, rhythm, and intonation (condition 1), rhythm and intonation (condition 2), intonation only (condition 3), or rhythm only (condition 4). The findings support the notion that syllabic rhythm is a necessary and sufficient cue for French adult subjects to discriminate English from Japanese sentences. The results are consistent with previous research using low-pass filtered speech, as well as with phonological theories predicting rhythmic differences between languages. Thus, the new methodology proposed appears to be well suited to study language discrimination. Applications for other domains of psycholinguistic research and for automatic language identification are considered. [S0001-4966(98)04512-3]

PACS numbers: 43.71.Hw [WS]

INTRODUCTION

The predicament of the newborn having to learn a language seems quite difficult by itself. But things become even more complicated when the infant is raised in a bilingual or multilingual environment. If the child has no means to separate input utterances according to source languages, great confusion ought to arise. Such confusion, however, is not supported by informal observation. We will explore one possible strategy that infants may adopt to organize their linguistic environment.

To begin with, let us emphasize that bilingual environments are more than a remote possibility. Bilingualism is, in fact, more widespread than is usually acknowledged. Bilinguals may represent more than half the world's population (Hakuta, 1985; MacKey, 1967). Moreover, bilingual children do not show any significant language-learning impairment or retardation due to possible confusion between languages. What is interpreted as confusion by monolingual parents is usually code-switching, a common feature of the bilingual's linguistic system (see Grosjean, 1982, 1989).

Children's proficiency at learning multiple languages simultaneously suggests that they should have some way to discriminate languages, prior to learning any of them. Early language discrimination has indeed been demonstrated by a growing number of researchers. Mehler *et al.* (1986, 1988), Bahrick and Pickens (1988), Jusczyk *et al.* (1993), Moon *et al.* (1993), Bosch and Sebastián-Gallés (1997), and Dehaene-Lambertz and Houston (1998) have found that very young children, including newborns, are able to discriminate native from non-native utterances. Moreover, Nazzi *et al.* (1998) recently demonstrated that newborns also discriminate utterances from two unknown languages, e.g., English and Japanese for French subjects (see also Mehler *et al.*, 1988 as reanalyzed by Mehler and Christophe, 1995). However, this result does not extend to any pair of languages, which will be discussed below.

What cues are available to achieve such precocious discrimination? The adult bilingual may rely upon lexical knowledge, but such information is not available to infants. Therefore, the speech signal must contain some prelexical cues that enable language discrimination. The most obvious cues that can be thought of are the following:

(i) Phonetic repertoire. It is well-known that different languages use different sets of phonemes (see Maddieson, 1984 for an inventory). For example, an English speaker should have no trouble discriminating between French and Arabic, since Arabic makes use of very characteristic pharyngeal consonants, which don't exist in French.

(ii) Phonotactic constraints. In every language, there are constraints on the structural distribution of phonemes. In Japanese, for instance, a liquid (r) can never follow a stop consonant (p,b,k...), unlike in English or French.

(iii) Prosody. The term prosody collectively refers to the suprasegmental features of speech, mostly captured by the notions of rhythm and intonation. Since Pike (1945) and Abercrombie (1967), it has been acknowledged that languages can have different rhythms. English, as with all Germanic languages, has been described as stress-timed, while French and other Romance languages have been described as syllable-timed. Furthermore, Ladefoged (1975) has proposed a third rhythmic class consisting of mora-timed languages, such as Japanese. Although Nespor (1990) warns that these rhythmic differences might be better described as a continuum than as classes, they certainly can serve as reliable cues for language discrimi-

nation (Nazzi *et al.*, 1998). Finally, let us note that languages can also have different melodic properties, and therefore, intonation can be expected to play a role in language discrimination as well, as suggested by Maidment (1976, 1983), Ohala and Gilbert (1979), Willems (1982), and de Pijper (1983).

Obviously, all of these prelexical cues could be of interest for language discrimination. However, they may not all be relevant for discrimination by newborns. Mehler *et al.* (1988) and Nazzi *et al.* (1998) have shown that language discrimination is not hindered when utterances are filtered (low-pass, 400 Hz): newborns can perform the task equally well when segmental cues are removed. This led these authors to favor the *rhythm hypothesis*, i.e., that newborns can discriminate two languages if, and only if, they belong to different rhythmic classes, as defined above. In order to clarify the *rhythm hypothesis*, we reformulate it as follows:

(1) There are groups of languages that share a number of phonological properties.
(2) Rhythm is one these phonological properties, or alternatively, it is the outcome of some of them.
(3) By paying attention to rhythm, newborns are able to discriminate languages which have different phonological properties.

This hypothesis has been tested and confirmed by Nazzi *et al.* (1998) by showing that French newborns can discriminate filtered English and Japanese sentences (stress- versus mora-timed), but not English and Dutch ones (both stress-timed) under the same conditions. Moreover, infants can discriminate groups of languages, but only if these groups are congruent with rhythmic classes, e.g., they can discriminate English+Dutch from Spanish+Italian (stress- versus syllable-timed), but not English+Italian from Spanish +Dutch (incoherent groups). Thus, Nazzi *et al.*'s findings are in perfect agreement with the *rhythm hypothesis*.

However, we feel that the case for the *rhythm hypothesis* still needs to be bolstered for at least two reasons:

(1) The range of languages explored is insufficient. For example, Nespor (1990) questions the dichotomy between syllable-timed and stress-timed languages by presenting languages that share phonological properties of both types (Polish, Catalan, Portuguese). For such languages, one would like to know whether they can be discriminated from syllable-timed languages, or stress-timed languages, or both, or neither. The *rhythm hypothesis*, in its current formulation, would hold only if they clustered along with one or the other language group. Recent work by Bosch and Sebastián-Gallés (1997) suggests that Catalan is discriminable from Spanish (with low-pass filtered speech). Thus, either Catalan should not be considered as a syllable-timed language, as it has often been, or the *rhythm hypothesis* is wrong.
(2) Low-pass filtering is not an ideal way to degrade utterances with the aim of deleting segmental information and preserving prosody. Basically, filtering does not allow one to know which properties of the signal are eliminated and which are preserved. As a first approximation, segmental information should be eliminated because it is mainly contained in the higher formants of speech, and pitch should be preserved because it rarely rises higher than 400 Hz. But this is only an approximation. Listening to filtered speech makes it obvious that *some* segmental information is preserved (sometimes words can even be recognized), and pitch *does* sometimes rise higher than 400 Hz, especially for female voices.[1] The proportion of energy preserved is also problematic because it differs from phoneme to phoneme: for example, an /a/ vowel has a lot more energy in the low frequencies than an /i/ vowel, not to mention other segments like stop consonants. Low-pass filtering thus gives an unwarranted amplification to /a/. Consequently, there is no guarantee that filtered speech really preserves rhythm, at least from an acoustical point of view. From a perceptual point of view, it seems that the alternation between consonants and vowels is essential to the notion of syllabic rhythm, and there is no reason to believe that this is preserved either. Finally, Mehler *et al.*'s and Nazzi *et al.*'s results leave open another interpretation, one that we could call the *intonation hypothesis*: the idea being that discrimination may have been performed on the basis of intonation and not rhythm. Filtering, once again, does not make any distinction between intonation and rhythm, and much information would be gained by separating these two components of the speech signal.

In the remainder of this paper, we will concentrate on this second point by putting forward a new experimental paradigm to better assess the relative importance of the different components of prosody. The first point will not be addressed here, but it is quite clear that if one is to investigate the discrimination of more language pairs, one would first want to control more precisely the acoustic cues made available to subjects.

I. SPEECH RESYNTHESIS

A. General principles

The difficulties with low-pass filtering we mentioned above indicate that speech rhythm is an ill-defined concept. The cues that make us perceive rhythm in the speech signal are not well understood. Perceived speech rhythm could emerge from the succession of syllables, vowels, stresses, pitch excursions, energy bursts within a certain range of frequencies, or whatever occurs repeatedly in speech that the human ear can perceive. In this paper, we propose a methodology that can be used to explore the perception of rhythm under most of the above interpretations.

The main hypotheses that guided our search for better controlled stimuli can be stated as follows:

(i) what the newborn actually perceives and analyzes is a sequence of vowels or syllables, where the syllables are signaled by the energetic and spectral prominence of vowels.
(ii) if rhythm can be said to be a cue to language discrimi-

nation, it is in the sense that rhythm is the perceptual outcome of the succession of syllables and their organization.

(iii) if one wants to test rhythm as a potential cue to discriminate between two languages, one should have stimuli that preserve as much as possible the organization of sequences of syllables and degrade as much as possible all alternative cues.

To this end, we explored a new technique, namely *speech resynthesis*, to determine the perceptual cues relevant to language discrimination and to test the *rhythm hypothesis*. Speech resynthesis was first developed at IPO at Eindhoven, and it has been used for delexicalization purposes by Pagel *et al.* (1996) and Guasti *et al.* (1998). It amounts to:

(i) measuring all relevant acoustic components of the speech signal;

(ii) using these measures and an appropriate algorithm to resynthesize the spoken material.

The distinctiveness of our approach rests in the selection of the acoustic components used for resynthesis. This allows us to eliminate or preserve at will different dimensions of the speech signal, such as the nature of phonemes, rhythm, or intonation. See below for a description of signal treatment.

In order to explore the validity and usefulness of this technique, we limited the present study to adult subjects and to two languages whose discrimination was highly predictable: English and Japanese. Sentences were recorded by native speakers of each language and resynthesized in order to preserve various levels of information. In a first condition, intonation, rhythm, and broad phonetic categories were preserved in order to evaluate the technique with a maximum amount of information for discrimination. In a second condition, only intonation and rhythm were preserved. In a third condition, only intonation, and in a fourth condition, only rhythm was preserved. In all the experiments, French native speakers were trained and tested on a language categorization task.

B. Construction of the stimuli[2]

1. Source sentences

The stimuli used were taken from the set of sentences recorded by Nazzi *et al.* (1998). They consisted of 20 sentences in Japanese and 20 sentences in English (see list in Appendix) read by four female native speakers per language, and digitized at 16 kHz. Sentences were all declarative, and speakers read them as adult-directed utterances. They were matched in mean number of syllables (16.2 syllables per sentence in both languages), and in mean-fundamental frequency (229 Hz (s.d. 15.3) for English, 233 Hz (s.d. 15.9) for Japanese). However, the mean length of the sentences was not perfectly matched between the two languages: 2752 ms (s.d. 219) for English, 2627 ms (s.d. 122) for Japanese. It will be argued later that this difference had no consequence on the results observed.

2. General treatment

The following treatment was applied to each sentence:

(1) The fundamental frequency was extracted every 5 ms, using the Bliss software, by John Mertus;

(2) The beginning and end of each phoneme was marked by an experimenter, using both auditory and visual cues;

(3) The two types of information were merged into a text file including, for each phoneme of the sentence, its duration, and its pitch contour points;

(4) In this text file, a transformation was applied to the phonemes and/or to the pitch contour points, depending on the condition (see below).

(5) The resulting file was fed into the MBROLA software (Dutoit *et al.*, 1996) for synthesis by concatenation of diphones, using a French diphone database. The French (rather than Japanese or English) diphone database was chosen in order to remain neutral with respect to the language discrimination task.

3. Transformations applied

(i) The first kind of transformation, which we named ''*saltanaj*,'' consisted of replacing all fricatives with the phoneme /s/, all stop consonants with /t/, all liquids with /l/, all nasals with /n/, all glides[3] with /j/, and all vowels with /a/. These phonemes were chosen because they were the most universal in their respective categories (Maddieson, 1984; Crystal, 1987). Thus new sentences were synthesized, preserving the following features of the original ones:

(1) Global intonation;
(2) Syllabic rhythm;
(3) Broad phonotactics.

However, all nonprosodic lexical and syntactic information was lost. Exact phonetic and phonotactic information was lost as well, both because of the substitution of the phonemes before synthesis, and because the phonemes used by the software were French.

(ii) The second kind of transformation, named ''*sasasa*,'' consisted of replacing all consonants with /s/, and all vowels with /a/. The consonant /s/ was selected because its continuant character enabled transformation of consonant clusters into something sounding like a single (but long) consonant. Thus, in this condition, only syllabic rhythm and intonation were preserved.

(iii) The third kind of transformation, named ''*aaaa*,'' consisted of replacing all phonemes with /a/. It was ensured that the synthesized sentences did not sound like a weird succession of /a/s with noticeable onsets. Instead, they sounded like one long /a/, varying continuously in pitch (fundamental frequency was interpolated over unvoiced portions of the sentences). Here, only the intonation of the original sentences was preserved.

(iv) As for the fourth kind of transformation, named ''*flat sasasa*,'' the phonemes were substituted as in the *sasasa* transformation, but all sentences were synthesized with a constant fundamental frequency at 230 Hz (i.e., approximately the mean $F0$ measurement of

the original sentences). Thus, the only cue for language discrimination was syllabic rhythm.

II. EXPERIMENTAL TEST OF RESYNTHESIZED STIMULI

A. Method

The experimental protocol was programmed on an IBM-compatible computer using the EXPE language (Pallier *et al.*, 1997). Subjects read instructions indicating that they would be trained to recognize ''acoustically modified'' sentences of two languages, Sahatu and Moltec. The instructions were written in such a way as to make the subjects believe that the sentences belonged to two real and exotic languages, rather than to languages that they might know. Subjects heard the sentences through headphones. After the experiment, they were asked to explain which strategies they had used to perform the task.[4]

The 40 sentences were divided into two arbitrary sets of 20 sentences, each containing 10 sentences in each language, pronounced by two different speakers per language. They were called the training set and the test set. This was done to assess if what the subjects learned in the training phase was due only to particular sentences' or speakers' characteristics, or to more general properties of the two languages.

At the beginning of the training phase, one sentence of each language was selected at random from the training set, and served as a preliminary example. Then, all the sentences from the training set were presented in random order. After each sentence, the subject was required to enter S or M on the keyboard for Sahatu and Moltec and was given immediate feedback on the answer. After hearing the 20 sentences, the subjects who scored 70% or more correct responses went on to the test phase, while the others went through another training session with the same 20 sentences. Subjects were allowed to undergo a maximum of three training sessions, after which they were given the test session irrespective of their scores.

In the test phase, subjects heard the 20 sentences of the test set in a random order and answered as in the training phase. They were given feedback as well.

B. Participants

Sixty-four students participated voluntarily, without payment. They were all French native speakers with a mean age of 22 years. They were tested in their own rooms with a portable PC. There were four experimental conditions, corresponding to the four types of transformations mentioned above. They were run sequentially with the first 16 participants in the *saltanaj* condition, the next 16 in the *sasasa* condition, then the *aaaa* condition, and finally, the *flat sasasa* condition. Participants in the four experiments were drawn from the same pool of students, and the order in which they were tested was random. Besides the nature of the stimuli, the only thing that differed among the conditions was the minimum training score required to switch directly to the test phase: originally it was 75% for the *saltanaj* condition, but it was then lowered to 70% for the other conditions to allow more successful subjects to complete the experiment quickly.

TABLE I. Mean-percent scores during the different sessions of each condition (chance is 50%). In parentheses: number of subjects.

	Training 1	Training 2	Training 3	Test
saltanaj	61.8(16)	59.6 (14)	61.2(12)	66.9 (16)
sasasa	54.2(16)	63.1 (13)	66.1 (9)	65.0 (16)
aaaa	49.7(16)	55 (14)	54.1(11)	50.9 (16)
flat sasasa	62.5(16)	55.5 (10)	55.6 (8)	68.1 (16)

C. Results

A summary of the raw data, session by session, is presented in Table I. As can be seen, the number of subjects decreases during the training phase due to the fact that the most successful ones are allowed to skip training sessions 2 or 3. The scores correspond to total hit rates of all the answers.

In order to assess which general properties of the two languages the subjects have learned, independently of the characteristics of particular sentences or speakers, we restricted the statistical analyses to the test session. Indeed, scores during the test session measure the ability of subjects to generalize what they have learned during training sessions to novel sentences produced by new speakers. Therefore, it would be very difficult to interpret the results as showing that the subjects have learned individual characteristics of certain sentences or speakers. Test-session scores thus represent a conservative measure of language discrimination.

Moreover, we converted our test-session scores into hit rates and false-alarm rates (in the sense of signal detection theory) in order to perform an analysis of discrimination, taking into account any response biases that subjects may have had. We used as hit rates the percentage of Japanese sentences correctly recognized, and as false alarms, the percentage of English sentences incorrectly labeled as Japanese. Table II presents, for each condition, mean hit rates, false-alarm rates, discrimination scores (A') and response bias measures (B''_D)[5] (see Donaldson, 1992).

A Kolmogorov test for normality ensured that the distributions of A' scores could be considered as normal (all p values >0.36). A t-test was computed to compare A' scores to chance level (0.5). Discrimination scores were found to be significantly above chance in the *saltanaj* [$t(15)=4.47$, p

TABLE II. Mean-hit rates, false-alarm rates, discrimination scores, and response bias measures, in each condition during test session. A' is compared to 0.5 (chance level) and B''_D to 0 (no bias).

	Hit rates	False alarms	A'	B''_D
saltanaj	0.69	0.35	0.71[a]	−0.11
sasasa	0.65	0.35	0.68[b]	−0.02
aaaa	0.56	0.54	0.52	−0.18[c]
flat sasasa	0.70	0.34	0.72[a]	−0.18

[a] $p<0.001$.
[b] $p<0.01$.
[c] $p<0.05$.

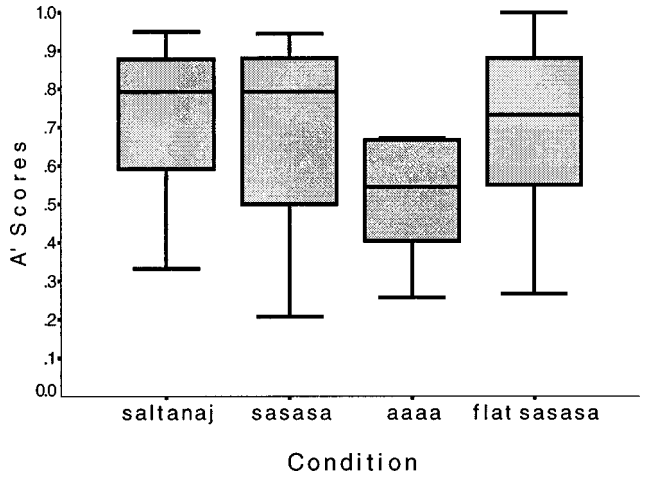

FIG. 1. Distribution of A' scores in each condition. Horizontal bars represent the medians, boxes the central half of the data, and whiskers the whole range of the data.

$=0.000\,4]$, *sasasa* $[t(15)=3,\ p=0.009]$, and *flat sasasa* $[t(15)=4.15,\ p=0.000\,9]$ conditions, but not in the *aaaa* condition $[t(15)<1]$.

The results presented in Table II seem to be quite clear-cut: the two sets of sentences were discriminable in all but the *aaaa* condition. To further evaluate the four conditions, the distribution of A' scores in each condition is shown in Fig. 1. Multiple comparisons of the four conditions with a Bonferroni correction showed that the *aaaa* condition was significantly different from both the *saltanaj* ($p=0.002$) and *flat sasasa* ($p=0.004$) conditions. No other differences showed significance, but there was a tendency for the *aaaa* condition to be different from the *sasasa* condition as well ($p=0.026$), which was offset by the Bonferroni correction. It is thus reasonable to say that the *aaaa* condition was different from all the others.

Finally, B''_D scores show that the subjects did not have any particular bias, except in the *aaaa* condition, where they were slightly liberal ($p=0.046$); that is, they tended to answer ''Japanese'' more often than ''English.'' This isolated and modest effect does not seem to us to require any particular interpretation or attention.

D. Discussion

1. Acoustic cues available to the subjects

In the *saltanaj* condition, the manner of articulation, the duration, and the place of each phoneme was preserved. Since the overall structure and organization of the syllables was preserved, syllabic rhythm certainly was as well. In addition, global intonation was also preserved. Thus, subjects had many available cues for discriminating utterances. Possibly the most salient one was the presence of numerous consonant clusters in English, with almost none in Japanese.

In the *sasasa* condition, in contrast, the identity of the phoneme classes, their respective distributions, and their arrangement was lost. Only the intonation and gross syllabic information was preserved. More precisely:

(i) the consonant/vowel distinction and temporal ratio were preserved;

(ii) the weight of the syllables was also preserved, since consonant clusters of the original stimuli were converted into long consonants (indeed, /s/ of the same duration as the corresponding clusters);

(iii) the broad temporal organization of the syllables was preserved as well;

(iv) finally, the rendering of the fundamental frequency conveyed information about both the global intonation of the sentences and, more locally, stress and pitch-accent, i.e., stressed or accented syllables were detectable, at least with partial cues (intensity cues were not available, for instance).

The subjects' ability to discriminate the two sets of *sasasa* sentences has an interesting implication, namely that suprasegmental cues are sufficient to allow for discrimination of the two languages. In this respect, our results are quite similar to those of Ohala and Gilbert (1979), who showed discrimination between several languages with stimuli that also preserved rhythm and intonation (although in their experiment, rhythm was that of the envelope of the signal, rather than of the syllables).

In the *aaaa* condition, the only remaining cue was the global intonation of the sentences, as resynthesized from the $F0$ data. Local intonational cues were probably of little use since they were not aligned with any syllable. Therefore, this condition simply explored whether melody could serve to discriminate English from Japanese. It seems that it cannot, as subjects behaved in a way that looked like guessing.

This result can be viewed as being at odds with some of the few previous studies on the role of intonation in language discrimination (Maidment, 1976, 1983; Willems, 1982; de Pijper, 1983). However, these experiments differ from ours in at least two respects: first, they compared English with Dutch and French, but not with Japanese; second, the native language of the subjects was always pitted against another language, and the subjects were aware of this fact. This must have made the task considerably easier. Indeed, when hearing a sentence, the subjects had to judge whether it met the intonational pattern of their native language, and did not have to forge new categories from scratch. This strategy would not be possible for an infant who has not yet acquired a native language. Given that one of our aims was to explore language acquisition, we wanted to place the adult subjects in a similar situation. Thus, our findings are not in contradiction with previous studies. However, it is not yet clear whether our subjects failed because English and Japanese intonations are not different enough, or because our stimuli were too degraded, or because the subjects were not native speakers of either of the two languages presented.

To further explore this question, we recruited 16 native English speakers (ten Americans, four English, one other, and one unknown), with a mean age of 29 years. Most of them were paid for their participation. They were tested on the *aaaa* stimuli under the same conditions as the French subjects, except that they were told that the languages were English and Sahatu, and that they were to recognize them by their intonation. The task thus was as close as possible to the previous studies cited above. The average A' score was 0.61

(s.d. 0.14), which was significantly above chance [$t(15) = 3.25$, $p = 0.005$]. There was no response bias [$B''_D = 0.09$, $t(15) < 1$]. Thus, it seems that English and Japanese intonations are sufficiently dissimilar to be differentiated, and that the *aaaa* stimuli are not too degraded or uninteresting for the task to be performed. However, the task seems to be feasible only when subjects have a certain knowledge of one of the languages and of the task itself.

Finally, the success of our subjects in discriminating between the two sets of sentences in the *flat sasasa* condition shows that they could easily do without any intonation, and that syllabic rhythm was a robust cue for discrimination. Indeed, this finding seems surprising, given the disembodied nature of speech uttered with a flat intonation. But at the same time, this points out the remarkable robustness of the cues present in the *flat sasasa* stimuli. As we mentioned above, these cues are related to the temporal organization of consonants and vowels within the sentence. Since there are very few consonant clusters in Japanese and many in English, large differences may persist between the two languages. *Flat sasasa* English sentences were characterized by longer consonants, heavier syllables, a greater variety of syllable types, weights, and durations, and thus a more irregular temporal organization of syllables than Japanese sentences. These cues are indeed thought to be the main constituents of syllabic rhythm (see Dauer, 1983, 1987; Nespor, 1990).

In conclusion, syllabic rhythm was shown to be both necessary and sufficient for the discrimination task. Indeed, its presence was sufficient in the *flat sasasa* condition, and its absence was an obstacle in the *aaaa* condition. This is not to say that this is always the case; as we mentioned above, intonation can be of greater interest to native speakers. It could also be a crucial cue for other pairs of languages, like tonal languages. Conversely, one can also imagine situations where rhythm may not be sufficient, possibly English and Dutch, or Spanish and Italian. This is a matter for future research, where speech resynthesis methodology should be of further use.

2. Possible problems and improvements

Before drawing more general conclusions, we will now turn to more methodological questions concerning this particular study and the general procedure.

First, one might be concerned with the fact that, in this study, the length of the sentences was not perfectly matched between the two languages. Indeed, as the English sentences were on average about 5% longer than the Japanese ones, it could be argued that the discrimination observed had nothing to do with rhythm, but rather with a strategy relying on sentence length. If this were the case, then we would expect a similar result in the *aaaa* condition, where the sentences were exactly the same length as in the other conditions. The results obtained in the *aaaa* condition clearly show that subjects were unable to use average sentence length to perform the task, and therefore this interpretation must be ruled out, unless one is prepared to argue that the length information was unusable only in the *aaaa* condition.

As regards the methodology itself, one might want to argue that the discriminability of the two sets of resynthesized sentences could be an artefact of the synthesis itself. However, since all the stages in the resynthesis process were performed in a similar fashion for both languages, it seems unlikely that some artefact or artificial difference was introduced for one language and not the other. At any rate, as we have already noted, there are differences between English and Japanese that we expected subjects to use in the task.

An aspect of our results that can seem surprising is the relatively low level of average discrimination scores (68%–72%), when the two languages studied seem so different. Doesn't this suggest that the technique lacks sensitivity? This would be consistent with the fact that scores are not higher in the *saltanaj* than in the *sasasa* condition, despite the additional information provided to perform the task. Indeed, a more sensitive task that would allow us to detect more subtle effects would be desirable. However, we have several reasons to think that discrimination scores would not be dramatically higher. As the stimuli are quite impoverished, they are not particularly interesting for the subjects. In addition, since they unfold over three seconds, the task demands sustained attention and an unusual effort to extract regularities. Likewise, the source sentences themselves show great variability, and the acoustic cues do not allow for a definite determination of their origin, i.e., what is true of the prosody of English sentences in general is not necessarily true of the prosody of every English sentence, and there can be an overlap between the prosodies of English and Japanese sentences.

To confirm this intuition, we ran an item analysis on the *sasasa* sentences used in the test phase. Scores for individual sentence recognition ranged from 38% to 88% (chance = 50%), and an ANOVA (analysis of variance) using the logistic generalized linear model (Hosmer and Lemeshow, 1989) showed a significant effect of the sentence factor, i.e., some sentences yielded scores that were significantly different from others. In brief, some sentences were not very good exemplars of their language, at least in the sense of the acoustic cues preserved under the different conditions. For instance, the three sentences yielding the worst scores (38%, 44%, and 50%) were English sentences (respectively #20, 16, 17, see Appendix) that have few consonant clusters. Indeed, they were found to have a higher vowel/consonant temporal ratio (respectively, 0.49, 0.44, 0.45) than most other English sentences (average 0.4 over our 20 sentences, s.d. = 0.05), thus getting closer to the Japanese prototype (average 0.53, s.d. = 0.03). This confirms that syllabic complexity is a critical cue in the English/Japanese discrimination. This might also explain why subjects tended to respond slightly more ''Japanese'' than ''English'' overall: English sentences can occasionally have mostly simple syllables like Japanese ones, but the phonology of Japanese forbids the reverse situation. As infants are confronted with similarly noisy input, it seems only fair to test adults under the same conditions, rather than with sentences selected for their prototypicality. Lower discrimination scores are thus to be expected.

The great complexity of the stimuli and their variability within one language may also explain why more information does not seem to improve necessarily our subjects' perfor-

mance. In the *flat sasasa* condition, we claim that subjects are provided with the most reliable cue, i.e., syllabic rhythm. If intonation is irrelevant to the task, or at least if it is a less reliable cue than rhythm, then the presence of intonation in the *sasasa* and *saltanaj* conditions may not necessarily help subjects; it could even disturb them by distracting them from the most relevant cue. The same can be said of broad phonotactics.

Finally, a possible way to improve the subjects' scores might be to incorporate a measure of amplitude in the synthesis. This has not been done in the present work simply because the MBROLA software doesn't take amplitude as a possible input. Thus, in our resynthesized stimuli, stress was signaled only by pitch excursions and duration, not by amplitude. As there is reason to think that stress is an important component of rhythm, adding a cue such as amplitude could make the perception of rhythm more accurate, and would furthermore make it possible to analyze separately the respective roles of rhythm due to the succession of syllables and rhythm due to amplitude.

How dependent are our results on the maternal language of our subjects, and on the language chosen as a diphone database (French)? As mentioned above, being a native speaker of one of the target languages helps, at least when one is aware of it. More generally, the subjects' native language may influence performance in the tasks we proposed. Indeed, speech perception is often said to be biased by one's maternal language. This is particularly true for phonemic perception, but also for more abstract phonological processing. For instance, French native speakers are quite poor at perceiving stress (Dupoux *et al.*, 1997; see also Dupoux *et al.*, 1999, for another example). Granting that English has stress and Japanese has pitch-accent, and if one accepts that these cues remained present in the resynthesized stimuli (possibly in the *saltanaj* and *sasasa* conditions), it is possible that French subjects were unable to detect this type of information. If so, this could actually account for the lack of a difference in performance between the intonated and *flat sasasa* conditions, in which the presence or absence of intonation seemed to make no difference to the subjects. We hope to test speakers of other languages in order to assess whether they do better in the *sasasa* condition. Nonetheless, considering performance in the *flat sasasa* condition, we find no similar reason to believe that the perception of syllabic rhythm alone would be any better or worse for speakers of languages other than French. Therefore, we think that our main conclusion, that syllabic rhythm is enough to allow for discrimination of English and Japanese, should hold across speakers of any other languages.

Another point worth mentioning is that our subjects were much more familiar with English than with Japanese. English is learned at school in France, not Japanese. However, subjects were told that the languages were Sahatu and Moltec. Moreover, sentences were delexicalized, providing subjects with no obvious way to detect the presence of English. As a matter of fact, *a posteriori* reports revealed that none of them guessed that Moltec was English. Moreover, no response asymmetries were observed (such as a tendency to recognize Moltec sentences more often), so there is no reason to believe that the subjects' greater familiarity with English had an influence on the results.

Finally, the influence of the French diphone database could be relevant for the *saltanaj* condition only, as *sasasa* or *aaaa* sentences would hardly have sounded any different if we had used another diphone database. For the *saltanaj* condition, the number of phonemes used was low, and the chosen phonemes (s, a, l, t, n, j) exist in both Japanese and English. We checked that the transposition of the phonemes did not produce illegal sequences in either language. All the resulting diphones were legal in French, which enabled a correct diphone synthesis. Occasionally the phoneme transposition led to a slight change of syllabification. For example, the English phrase ''the truck'' was transformed into /satlat/. /tl/ is a legal phoneme sequence in English, but only across a syllable boundary (as in ''butler''). The same is true for French. Thus, the transformation of ''the truck'' into /satlat/ shifted the perceived syllable boundary to fall between /t/ and /l/. If one is concerned with the precise contribution of phonotactics for language discrimination, such effects could indeed be a problem, and one should then choose the phonemes accordingly. In the present case, where the discrimination was made possible by massive differences in syllable weight and the presence or absence of consonant clusters, such minor effects must have been negligible.

III. GENERAL DISCUSSION

In this study, we have put forward a new method, speech resynthesis, to explore the discrimination of languages on the basis of prosodic cues. We used this method to construct stimuli that preserved different possible levels of prosodic information in both English and Japanese sentences, and we tested discrimination of these two sets of stimuli by French subjects. Our results show that syllabic rhythm is clearly sufficient to allow for discrimination between English and Japanese.

This finding is consistent with both phonological theories and past experimental studies. Indeed, the contrasting rhythmic patterns of languages such as English and Japanese have been noticed by linguists (Pike, 1945; Abercrombie, 1967; Ladefoged, 1975), leading them to classify languages into different rhythmic classes. Mehler *et al.* (1996) and Nazzi *et al.* (1998) have, moreover, hypothesized that discrimination should be possible between languages belonging to different rhythmic classes. Our results not only confirm that this is true of English and Japanese, but also demonstrate that syllabic rhythm is, as predicted, a relevant parameter.

In this respect, we think that the scope of our work goes beyond past studies upholding the role of prosody for language discrimination. Indeed, previous studies have relied on only one type of degradation of the speech signal at any one time. Ohala and Gilbert (1979), for instance, explored the joint role of intonation and rhythm, whereas Maidment (1976, 1983), Willems (1982) and de Pijper (1983) explored the role of intonation alone. Likewise, in their studies on infants, Mehler *et al.* (1988), Nazzi *et al.* (1998), Bosch and Sebastián-Gallés (1997) and Dehaene-Lambertz and Houston (1998) relied on low-pass filtering to isolate gross prosodic

cues. In all those studies, however, the different levels of prosodic information were not separated and compared.

We thus view our main contribution as having (1) provided a methodology allowing to separate and analyze different components of prosody in a systematic fashion, (2) isolated the prosodic component of interest to the *rhythm hypothesis*, that is, syllabic rhythm, (3) shown that this component is, as expected, an excellent and possibly the best prosodic cue for the discrimination of languages that are said to differ in rhythm.

Let us now turn to the possible future applications of this new methodology. To further test the *rhythm hypothesis*, the *flat sasasa* stimuli provide a better tool than low-pass filtering. For example, a replication of Nazzi *et al.*'s (1998) experiments with such stimuli would allow us to rule out the alternative-intonation hypothesis. Indeed, even though our present results on adults strongly suggest that their rhythm-based interpretation was right, extrapolation of results from the adult state to the initial state is not warranted.

More language discrimination experiments on adults and infants using *flat sasasa* stimuli would also be needed to evaluate whether languages actually tend to congregate into rhythmic classes, or whether, as Nespor (1990) suggests, they form a rhythmic continuum.

Studying the prosodic properties of languages using speech resynthesis may also influence research on automatic language identification. Indeed, much of the research in this domain has concentrated on modeling the short-term acoustics of the speech signal. Prosodic features have rarely been taken into account, and with relatively low success (for a review, see Muthusamy *et al.*, 1994). Even though one should not expect to discriminate all pairs of languages using prosodic cues only, prosody could still be used as a first-order classifier, thus restraining the problem space for analysis with other cues. In this respect, we feel that language-discrimination studies using speech resynthesis might be a practical way to establish a taxonomy of the world languages along different prosodic dimensions, and such a taxonomy could be a first step towards the elaboration of a prosodic classifier.

Outside the range of the *rhythm hypothesis*, one can imagine various applications of the speech resynthesis paradigm. When studying the perception of prosody, it is often desirable to cancel possible lexical and/or segmental influences. This has sometimes been done in the past by using reiterant speech, that is, by asking speakers to produce nonsense syllables (like ''mamama'') while imitating the prosody of a natural sentence (Larkey, 1983; Liberman and Streeter, 1978). In our view, resynthesis provides a way to create such reiterant stimuli in a more controlled and systematic manner, without having to rely on speakers producing nonspeech, which is quite an unnatural task.

A possible application is the study of prosodic correlates of word boundaries. For instance, de Pijper and Sanderman (1994) delexicalized whole sentences and asked subjects to judge word and phrase boundaries. In the authors' opinions, their stimuli proved quite painful to listen to, so similar work would benefit from using speech resynthesis (see Pagel *et al.*, 1996 for a first approach).

Finally, higher-level prosodic cues can also be studied using speech resynthesis. For instance, the head-direction parameter in syntax is said to have a prosodic correlate, namely prosodic phrase prominence (Nespor *et al.*, 1996). By carefully resynthesizing their sentences to control the acoustic cues preserved, Guasti *et al.* (1998) showed that such prominence is perceived by adults and infants, and could thus serve to set the head-direction parameter early on.

To conclude, we think that the use of speech resynthesis goes beyond the need, evident in the above studies, for a practical delexicalization tool. Its flexibility authorizes countless ways to selectively preserve or eliminate cues, of which the present paper has proposed only a few. For other purposes yet to be defined, one could also decide to preserve the place rather than the manner of articulation of phonemes, or to blur function words while preserving content words and prosody, or vice versa. We leave it to the reader's imagination to invent other interesting manners to manipulate speech resynthesis.

ACKNOWLEDGMENTS

This work was supported by the Délégation Générale pour l'Armement and the Human Frontiers Science Program. We would like to thank Emmanuel Dupoux and Anne Christophe for their help and suggestions, and Peter Jusczyk and Thierry Nazzi for comments on a previous version of this paper.

APPENDIX

English sentences

Speaker 1

1. The next local elections will take place during the winter.
2. A hurricane was announced this afternoon on the TV.
3. The committee will meet this afternoon for a special debate.
4. This rugby season promises to be a very exciting one.
5. Artists have always been attracted by the life in the capital.

Speaker 2

6. My grandparents' neighbor is the most charming person I know.
7. The art gallery in this street was opened only last week.
8. The parents quietly crossed the dark room and approached the boy's bed.
9. Nobody noticed when the children slipped away just after dinner.
10. Science has acquired an important place in western society.

Speaker 3

11. Much more money will be needed to make this project succeed.
12. This supermarket had to close due to economic problems.

13. The first flowers have bloomed due to the exceptional warmth of March.
14. The last concert given at the opera was a tremendous success.
15. Finding a job is difficult in the present economic climate.

Speaker 4

16. The local train left the station more than five minutes ago.
17. In this famous coffee shop you will eat the best donuts in town.
18. The young boy got up quite early in order to watch the sunrise.
19. In this case, the easiest solution seems to appeal to the high court.
20. The library is opened every day from eight A.M. to six P.M.

Japanese sentences

Speaker 1

1. Oono shigo ni machi no saiken ga hajimatta.
2. Noomin no sonchoo ni taisuru fuman ga tamatta.
3 Totemo kichoona kaiga ga saikin nusumareta.
4. Kochira no kata wa keiseigeka no senmonka desu.
5. Tsugino chihoosenkyo wa kondo no harugoro deshoo.

Speaker 2

6. Monku wa shihainin ni iuno ga tettoribayai.
7. Nihon no tabemononara mazu teni hairu.
8. Operaza no saigo no konsaato wa seikoodatta.
9. Kaikakusuishinha ga kenchoomae de demokooshinshita.
10. Bakayooki no seide hayakumo hana ga saiteiru.

Speaker 3

11. Noomin no sonchoo ni taisuru fuman ga tamatta.
12. Haru no koozui de zuibun ookina higaiga deta.
13. Konshuu mo terebibangumi o mirujikan ga nai.
14. Tsugino chihoosenkyo wa kondo no harugoro deshoo.
15. Tsugi no gekijooshiizun wa totemo kyoomibukaidaroo.

Speaker 4

16. Hachiji no nyuusu de jiken ga hoodoosareta.
17. Kinyoobi no gogo wa ginkooga hayaku shimaru.
18. Konopanya no keiki wa konokaiwai de hyoobanda.
19. Bakayooki no seide hayakumo hana ga saiteiru.
20. Kusuriya no kamisan wa moosugu kaimononi deru.

[1]In experiments on infants, female voices are used almost exclusively.
[2]Samples of all the types of stimuli described in this article can be heard on http://www.ehess.fr/centres/lscp/persons/ramus/resynth/ecoute.htm
[3]At this point, the ambiguous status of glides should be mentioned. The following rule was applied: pre- and inter-vocalic glides were marked as consonants, post-vocalic glides (in diphthongs) were marked as vowels. Therefore, pre- and inter-vocalic glides were transformed into /j/ in the *saltanaj* condition and /s/ in the *sasasa* condition, whereas postvocalic glides were transformed into /a/ in both conditions.
[4]Subjects' reports were not found to be consistent nor informative and are therefore not reported here.
[5]We are grateful to Dr. Strange for suggesting this type of analysis.

Abercrombie, D. (**1967**). *Elements of General Phonetics* (Aldine, Chicago).
Bahrick, L. E., and Pickens, J. N. (**1988**). ''Classification of bimodal English and Spanish language passages by infants,'' Infant Behav. Dev. **11**, 277–296.
Bosch, L., and Sebastián-Gallés, N. (**1997**). ''Native language recognition abilities in 4-month-old infants from monolingual and bilingual environments,'' Cognition **65**, 33–69.
Crystal, D. (**1987**). *The Cambridge Encyclopedia of Language* (Cambridge U.P., Cambridge).
Dauer, R. M. (**1983**). ''Stress-timing and syllable-timing reanalyzed,'' J. Phon. **11**, 51–62.
Dauer, R. M. (**1987**). ''Phonetic and phonological components of language rhythm,'' in *XIth International Congress of Phonetic Sciences* (Tallinn), pp. 447–450.
de Pijper, J. R. (**1983**). *Modelling British English Intonation* (Foris, Dordrecht).
de Pijper, J. R., and Sanderman, A. A. (**1994**). ''On the perceptual strength of prosodic boundaries and its relation to suprasegmental cues,'' J. Acoust. Soc. Am. **96**, 2037–2047.
Dehaene-Lambertz, G., and Houston, D. (**1998**). ''Faster orientation latency toward native language in two-month old infants,'' Language Speech **41**, 21–43.
Donaldson, W. (**1992**). ''Measuring recognition memory,'' J. Exp. Psychol. **121**, 275–277.
Dupoux, E., Kakehi, K., Hirose, Y., Pallier, C., Fitneva, S., and Mehler, J. (**1999**). ''Epenthetic vowels in Japanese: a perceptual illusion?'' J. Exp. Psychol. Hum. Percept. Perform. (to be published).
Dupoux, E., Pallier, C., Sebastian, N., and Mehler, J. (**1997**). ''A destressing 'deafness' in French?'' J. Memory Lang. **36**, 406–421.
Dutoit, T., Pagel, V., Pierret, N., Bataille, F., and van der Vrecken, O. (**1996**). ''The MBROLA Project: Towards a set of high-quality speech synthesizers free of use for non-commercial purposes,'' in *ICSLP'96* (Philadelphia, PA), pp. 1393–1396.
Grosjean, F. (**1982**). *Life With Two Languages: An Introduction to Bilingualism* (Harvard U.P., Cambridge, MA).
Grosjean, F. (**1989**). ''Neurolinguists, beware! The bilingual is not two monolinguals in one person,'' Brain and Language **36**, 3–15.
Guasti, M. T., Nespor, M., Christophe, A., and van Ooyen, B. (**1998**). ''Prelexical setting of the head-complement parameter through prosody,'' in *Signal to Syntax II*, edited by J. Weissenborn and B. Höhle (to be published).
Hakuta, K. (**1985**). *Mirror of Language: The Debate on Bilingualism* (Basic Books, New York).
Hosmer, D. W., and Lemeshow, S. (**1989**). *Applied Logistic Regression* (Wiley, New York).
Jusczyk, P. W., Friederici, A., Wessels, J., Svenkerud, V., and Jusczyk, A. (**1993**). ''Infants' sensitivity to the sound pattern of native language words,'' J. Memory Lang. **32**, 402–420.
Ladefoged, P. (**1975**). *A Course in Phonetics* (Harcourt Brace Jovanovich, New York).
Larkey, L. S. (**1983**). ''Reiterant speech: An acoustic and perceptual validation,'' J. Acoust. Soc. Am. **73**, 1337–1345.
Liberman, M. Y., and Streeter, L. A. (**1978**). ''Use of nonsense-syllable mimicry in the study of prosodic phenomena,'' J. Acoust. Soc. Am. **63**, 231–233.
MacKey, W. F. (**1967**). *Bilingualism as a World Problem/Le Bilinguisme: Phénomène Mondial* (Harvest House, Montreal).
Maddieson, I. (**1984**). *Patterns of Sounds* (Cambridge U.P., Cambridge).
Maidment, J. A. (**1976**). ''Voice fundamental frequency characteristics as language differentiators,'' Speech and hearing: Work in progress, University College London, 74–93.
Maidment, J. A. (**1983**). ''Language recognition and prosody: further evidence,'' Speech, hearing and language: Work in progress, University College London **1**, 133–141.
Mehler, J., and Christophe, A. (**1995**). ''Maturation and learning of language during the first year of life,'' in *The Cognitive Neurosciences*, edited by M. S. Gazzaniga (Bradford Books/MIT, Cambridge, MA), pp. 943–954.
Mehler, J., Dupoux, E., Nazzi, T., and Dehaene-Lambertz, G. (**1996**). ''Cop-

ing with linguistic diversity: The infant's viewpoint,'' in *Signal to Syntax: Bootstrapping from Speech to Grammar in Early Acquisition*, edited by J. L. Morgan and K. Demuth (Erlbaum, Mahwah, NJ), pp. 101–116.
Mehler, J., Jusczyk, P., Lambertz, G., Halsted, N., Bertoncini, J., and Amiel-Tison, C. (**1988**). ''A precursor of language acquisition in young infants,'' Cognition **29**, 143–178.
Mehler, J., Lambertz, G., Jusczyk, P., and Amiel-Tison, C. (**1986**). ''Discrimination de la langue maternelle par le nouveau-né,'' Comptes-rendus de l'Académie des Sciences de Paris **303**, **Série III**, 637–640.
Moon, C., Cooper, R. P., and Fifer, W. P. (**1993**). ''Two-day-olds prefer their native language,'' Infant Behav. Dev. **16**, 495–500.
Muthusamy, Y. K., Barnard, E., and Cole, R. A. (**1994**). ''Reviewing automatic language identification,'' IEEE Signal Process. Mag., 33–41 (Oct. 1994).
Nazzi, T., Bertoncini, J., and Mehler, J. (**1998**). ''Language discrimination by newborns: towards an understanding of the role of rhythm,'' J. Exp. Psychol. Hum. Percept. Perform. **24**, 756–766.
Nespor, M. (**1990**). ''On the rhythm parameter in phonology,'' in *Logical Issues in Language Acquisition*, edited by I. M. Roca (Foris, Dordrecht), pp. 157–175.
Nespor, M., Guasti, M. T., and Christophe, A. (**1996**). ''Selecting word order: The rhythmic activation principle,'' in *Interfaces in Phonology*, edited by U. Kleinhenz (Akademie, Berlin), pp. 1–26.
Ohala, J. J., and Gilbert, J. B. (**1979**). ''Listeners' ability to identify languages by their prosody,'' in *Problèmes de Prosodie*, edited by P. Léon and M. Rossi (Didier, Ottawa), pp. 123–131.
Pagel, V., Carbonell, N., and Laprie, Y. (**1996**). ''A new method for speech delexicalization, and its application to the perception of French prosody,'' in *ICSLP'96* (Philadelphia, PA).
Pallier, C., Dupoux, E., and Jeannin, X. (**1997**). ''EXPE: An expandable programming language for on-line psychological experiments,'' Behav. Res. Methods Instrum. Comput. **29**, 322–327.
Pike, K. L. (**1945**). *The Intonation of American English* (University of Michigan Press, Ann Arbor, Michigan).
Willems, N. (**1982**). *English Intonation from a Dutch Point of View* (Foris, Dordrecht).

Psychoacoustical evaluation of PSOLA. II. Double-formant stimuli and the role of vocal perturbation

Reinier W. L. Kortekaas[a)]
IPO—Center for Research on User-System Interaction, P.O. Box 513, 5600 MB Eindhoven, The Netherlands

Armin Kohlrausch[b)]
IPO—Center for Research on User-System Interaction, P.O. Box 513, 5600 MB Eindhoven, The Netherlands and Philips Research Laboratories Eindhoven, Prof. Holstlaan 4, 5656 AA Eindhoven, The Netherlands

(Received 15 July 1997; accepted for publication 9 October 1998)

This article presents the results of listening experiments and psychoacoustical modeling aimed at evaluating the pitch synchronous overlap-and-add (PSOLA) technique. This technique can be used for simultaneous modification of pitch and duration of natural speech, using simple and efficient time-domain operations on the speech waveform. The first set of experiments tested the ability of subjects to discriminate double-formant stimuli, modified in fundamental frequency using PSOLA, from unmodified stimuli. Of the potential auditory discrimination cues induced by PSOLA, cues from the first formant were found to generally dominate discrimination performance. In the second set of experiments the influence of vocal perturbation, i.e., jitter and shimmer, on discriminability of PSOLA-modified single-formant stimuli was determined. The data show that discriminability deteriorates at most modestly in the presence of jitter and shimmer. With the exception of a few conditions, the trends in these data could be replicated by either using a modulation-discrimination or an intensity-discrimination model, dependent on the formant frequency. As a baseline experiment detection thresholds for jitter and shimmer were measured. Thresholds for jitter could be replicated by using either the modulation-discrimination or the intensity-discrimination model, dependent on the (mean) fundamental frequency of stimuli. The thresholds for shimmer could be accurately predicted for stimuli with a 250-Hz fundamental, but less accurately in the case of a 100-Hz fundamental. [S0001-4966(99)05201-7]

PACS numbers: 43.72.Ja, 43.66.Fe, 43.66.Ba [JLH]

INTRODUCTION

For speech modification and speech synthesis purposes, high computational efficiency can be achieved using techniques that are based on speech-waveform operations in the time domain. For instance, Roucos and Wilgus (1985) presented speech-waveform modification schemes within the overlap-and-add (OLA) framework. A pitch-synchronous OLA model (PSOLA) in which all overlap-and-add operations are aligned to the ''local'' pitch period was proposed in Hamon *et al.* (1989) and Moulines and Charpentier (1990). The PSOLA technique was developed for the (simultaneous and independent) modification of duration and pitch of natural speech.[1] PSOLA has proven to be a practical method for speech modification and synthesis (e.g., Moulines and Laroche, 1995; Klaus *et al.*, 1997).

In our previous paper (Kortekaas and Kohlrausch, 1997), we argued that despite the widespread application of PSOLA, the perceptual consequences of speech-waveform modification were not well understood. This lack of knowledge was, for instance, reflected in the unpredictable occurrence of annoying artifacts such as roughness when using PSOLA. We presented results of a psychoacoustical evaluation of PSOLA aimed at determining the auditory sensitivity to the ''basic distortions'' introduced by PSOLA. Basic distortions referred to spectro-temporal changes of the speech signal that result from the overlap-and-add operations *per se*, and not from ''improper'' PSOLA application such as erroneous estimation of the local pitch periods. By measuring the sensitivity of the human auditory system to these basic distortions, the study was aimed at understanding the perceptual consequences of speech-waveform modification, rather than at explaining the occurrence of the artifacts mentioned above.

The auditory sensitivity was investigated through listening experiments in which single-formant stimuli (Klatt, 1980) were modified in fundamental frequency ($F0$). The subjects' task was to discriminate PSOLA-modified signals from unmodified references as a function of ΔF, the percentage shift in $F0$. Spectral consequences of such an $F0$ modification are most prominent in the formant region, where changes in both levels and relative phases of the harmonics occur (''formant broadening;'' Moulines and Charpentier, 1990). Discriminability was typically found to vary nonmonotonically with ΔF, indicating an interaction between ΔF and the formant frequency. This discrimination performance could be modeled reasonably well by detection of changes in an auditory excitation pattern (''profile analysis;''

a)Present address: Boys Town National Research Hospital, 555 North 30th Street, Omaha, NE 68131.
b)Corresponding author. Electronic mail: kohlraus@ipo.tue.nl

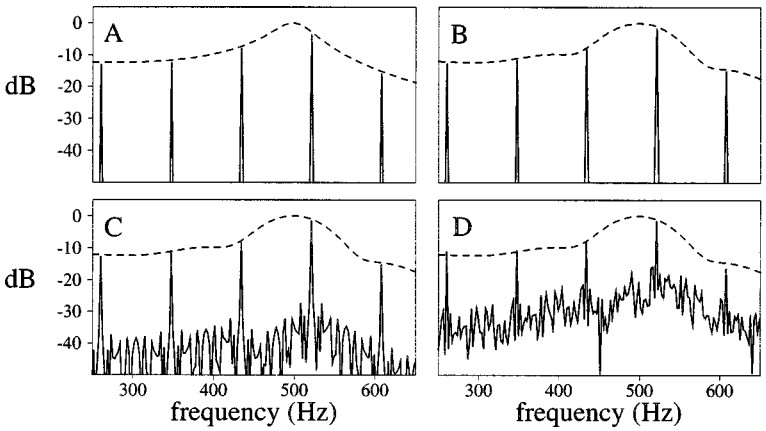

FIG. 1. Illustration of PSOLA-induced spectral changes. (A) Magnitude spectrum of the impulse response of a formant filter at 500 Hz with 50-Hz bandwidth (dashed lines), and line spectrum of a 500-Hz formant signal with an *F*0 of 87 Hz. (B) Magnitude spectrum of a PSOLA-decomposed signal segment of a 500-Hz formant signal (dashed line), and line spectrum of a signal obtained by overlap-adding segments at a rate of $F_{ws}=87$ Hz. Power spectra of a signal as in panel (B), but with shimmer or jitter perturbation are shown in panels (C) and (D), respectively.

Gagné and Zurek, 1988), provided the harmonics around the formant frequency were resolved by auditory filtering. Such a model only takes (power) spectral cues into account. In the case of unresolved harmonics, the data could be best explained on the basis of detection of changes in modulation depth at the output of a simulated auditory filter (Wakefield and Viemeister, 1990). In that case, changes in relative harmonic phases may affect discriminability.

The present study extends these results to more natural and, consequently, more complex stimuli. The aim of the study was to determine whether the auditory discrimination cues for the single-formant stimuli are also available if stimulus complexity increases. Two separate aspects of natural speech were dealt with. First, discrimination sensitivity was measured for double-formant stimuli because natural vowels are characterized by at least two formants. If the available information from both formant regions is processed optimally, we expect discriminability of double-formant PSOLA-modified stimuli to be higher than in the case of single-formant stimuli. Because vowels vary in length and intensity in natural speech, the influence on discriminability of presentation level and stimulus duration was investigated additionally.

Second, the extent to which discrimination performance is influenced by perturbations of either amplitude or *F*0 was investigated. These two perturbation types are usually referred to as shimmer and jitter (Pinto and Titze, 1990). If such perturbations reduce discriminability of PSOLA-induced spectro-temporal changes, then their presence in natural speech could at least partly explain the success of PSOLA. Shimmer and jitter are often conceived of as characteristics of natural speech (Lieberman, 1961) and have been proposed as criteria to classify certain types of pathological voices (e.g., Askenfelt and Hammarberg, 1986). In the present study shimmer and jitter were simulated by introducing random fluctuations in the pulses exciting the formant filter (cf. Hillenbrand, 1987, 1988; Rozsypal and Millar, 1979). Even though this way of simulating shimmer and jitter may be consistent with quantitative measures based on the analysis of the speech waveform (Horii, 1980), the relevance of such measures is still under debate because of, e.g., interactions between vocal tract and glottis (Klatt and Klatt, 1990; Cranen, 1997; Schoentgen and De Guchteneere, 1997). Therefore, these shimmer and jitter simulations should be conceived of as a means to investigate in a controlled manner the role of perturbations in perceiving PSOLA-modified stimuli, rather than as a true-to-nature simulation of speech production. As a baseline experiment to the discrimination experiments, detection thresholds were measured for jitter and shimmer in single-formant stimuli, without any PSOLA modification.

I. GENERAL METHODS

A. The PSOLA technique and terminology

The terminology used in the present paper is consistent with that in our previous paper (Kortekaas and Kohlrausch, 1997). PSOLA-modified stimuli were obtained by (1) decomposing a single- or double-formant signal into signal segments by pitch-synchronous windowing, and (2) recombining these decomposed signal segments by means of overlap-and-add. The decomposition was performed with Hanning (raised-cosine) windows which had a length of two pitch periods. The window maxima coincided with the ''glottal pulses'' that excited the formant filters (see Sec. II A). In this way, the signal was regularly decomposed at an ''analysis window rate'' F_{wa} Hz. By means of overlap-add, the decomposed signal segments were recombined at a ''synthesis window rate'' F_{ws} Hz, yielding a signal with an *F*0 of F_{ws} Hz. Discrimination performance was measured as a function of the shift in *F*0 expressed as a Weber fraction: $\Delta F=[(F_{ws}-F_{wa})/F_{wa}]\times 100\%$. For a detailed description of the PSOLA technique and its signal-processing aspects, the reader is referred to Moulines and Laroche (1995).

B. Spectral consequences of PSOLA application

Figure 1 illustrates the spectral consequences of PSOLA applications to synthetic formant signals. Panel A shows the magnitude spectrum (dashed line) of the impulse response of a formant filter with a formant frequency of 500 Hz, and a bandwidth of 50 Hz. The solid vertical lines show the harmonics of a periodic signal having this formant frequency and an *F*0 of 87 Hz. In the experiments, such a signal was used as reference. Panel B shows the magnitude spectrum (dashed line) of a single segment decomposed by PSOLA windowing a 500-Hz formant signal, having an *F*0 of 100 Hz ($F_{wa}=100$ Hz). Clearly, the spectral envelope in panel B

shows the effect of ''formant widening'' due to windowing (Moulines and Charpentier, 1990). The vertical lines in panel B show the harmonics of a signal obtained after overlap-adding of the decomposed signal segments at a rate of $F_{ws}=87$ Hz. In addition to the harmonic level differences between panels A and B, the harmonics around the formant frequency in panel B are phase shifted by approximately $\pi/4$ rad (the phase spectrum is not shown).

These spectral changes were found to be detectable by listening to excitation-pattern differences in the case of low formants, and by listening to modulation-depth differences in the case of high formants (Kortekaas and Kohlrausch, 1997). Intuitively, the presence of shimmer and jitter may be expected to affect the use of both spectral and temporal discrimination cues. In the case of temporal (modulation-depth) cues, jitter and shimmer introduce additional modulations and may therefore hamper discrimination. The use of spectral discrimination cues might also be hampered because shimmer and jitter introduce ''noise'' components between the harmonics in the spectrum (Klingholz and Martin, 1985), thereby possibly obscuring excitation-pattern differences. This is illustrated in panels C and D. Panel C shows the power spectrum of a PSOLA-modified signal similar to that in panel B, but perturbed by additional shimmer ($\sigma_A=20\%$; see Sec. III). Similarly, panel D shows the power spectrum of such a signal, but perturbed by jitter ($\sigma_P=2.5\%$; see Sec. III also). In both panels, the noise components between the harmonics are 20–30 dB below the harmonic levels.

II. EXPERIMENT 1: DOUBLE-FORMANT STIMULI

A. Method

1. Stimuli

The stimuli were generated by filtering a ''glottal-pulse train'' by two second-order formant filters $F1$ and $F2$ connected in series (Klatt, 1980). The glottal-pulse train was a preemphasized Dirac-impulse train having low-pass characteristics of natural voicing and high-pass characteristics of radiation at the mouth opening (Klatt, 1980). The test signal was first generated at $F0=F_{wa}=100$ Hz and subsequently PSOLA modified to accomplish a shift in $F0$ to F_{ws} Hz. The reference signals were directly generated with an $F0$ of F_{ws} Hz.

Stimuli will be labeled as $[F1,F2]$ in the case of fixed formant frequencies (expressed in Hz): the stimuli under investigation were [500,1000], [500,2000], and [1000,2000]. The -3-dB bandwidths were 50, 50, and 100 Hz for the 500-, 1000-, and 2000-Hz formant filters, respectively. Because formant frequencies vary in natural speech, conditions in which $F1$ was roved while $F2$ was fixed were additionally investigated. These will be labeled as $[F1R,F2]$. Under these conditions, $F1$ was fixed for the duration of each stimulus, but varied randomly between stimuli. The formant-frequency rove was uniformly distributed over a range of $\pm 2\ \Delta F1$, where $\Delta F1$ denotes one just-noticeable difference (jnd) in $F1$ and amounts to $0.079\ F1/\sqrt{Q}$ (Gagné and Zurek, 1988). Q denotes the Q-factor of the formant filter. The mean overall level L of the stimuli was set to 70 dB SPL, except for the experiment addressing the influence of level where L was also set to 30 and 50 dB SPL. In all conditions, L was roved uniformly in the range ± 5 dB in order to make probable that discrimination was based on difference in timbre, but not loudness.

The spectral level difference between $F1$ and $F2$ can become rather large: the difference is approximately 12 dB for [500,1000], 30 dB for [500,2000], and 16 dB for [1000,2000]. Cues associated with the $F1$ region may therefore dominate the discrimination performance. By applying an additional formant filter, having the same resonance frequency and bandwidth as $F2$, the level difference is reduced to within a few dB, at the cost of somewhat reducing the bandwidth of $F2$. In a limited set of conditions, which will be labeled as $[F1,F2D]$, the importance of equalizing the formant levels was investigated. In a pilot experiment it was verified that the general shape of the psychometric function for discriminating a PSOLA-modified single-formant signal was not affected by using the formant filter twice.

Stimulus duration was 300 ms, with raised-cosine ramps of 25 ms at the beginning and end of the signal. In the experiment addressing the influence of duration, the duration was additionally set to 37.5, 75, and 150 ms. For the shortest duration, ramp durations were set to 18.75 ms. Stimulus intervals were separated by 200 ms. All signals were generated at a sample rate of 32 kHz.[2]

2. Procedure

The experimental procedure was similar to the procedure described in Kortekaas and Kohlrausch (1997). Psychometric functions were measured using a 3I-3AFC procedure with a fixed value of ΔF in each run. A run consisted of 15 trials and the subject's task was to indicate, for each of these trials, which interval contained the odd-ball, i.e., the PSOLA-modified stimulus. The psychometric functions were only measured for positive values of ΔF by varying F_{ws} in the following fashion: $F_{ws}=1/(T_a-n/4)$ [Hz], where $T_a=1/F_{wa}$ and $n=1,2,3,\ldots$ ms.

Because most subjects had not participated in the previous experiments, psychometric functions were remeasured for the single-formant condition first for three subjects. For all combinations of formant frequency ([500], [1000], and [2000]) and ΔF, each subject performed five runs each consisting of 15 trials. In the double-formant experiment, six runs were performed. In the experiment addressing the influence of level and duration, three subjects each performed five runs. In all experiments, the first run of each condition was regarded as learning phase and thus not included in the analysis. The means and standard errors of the means shown in the figures below thus represent 60 or 75 trials, respectively. These figures will display discrimination sensitivity d' as a function of ΔF which was obtained by means of a percentage correct to d' conversion table (Macmillan and Creelman, 1991).

All signals were software generated on a Silicon Graphics Indigo workstation, D/A converted using the built-in board, and attenuated using TDT PA4 modules to have the appropriate sound pressure level. The signals were presented diotically to the subjects over Beyer 990 headphones while they were seated in a soundproof booth. The subjects re-

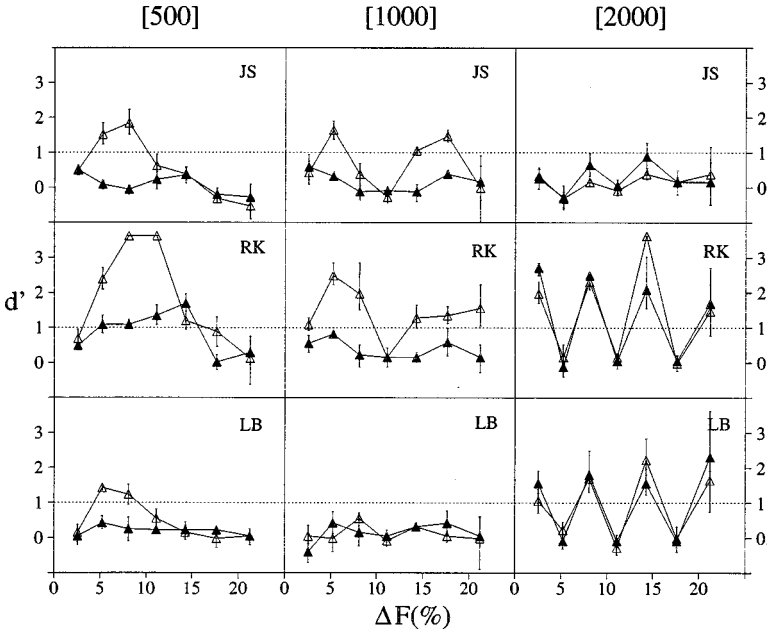

FIG. 2. Psychometric functions for discrimination of PSOLA-manipulated and unmanipulated single-formant signals, with $F_{wa}=100$ Hz. Formant frequencies are indicated above each column. Open symbols indicate conditions with constant first formant frequencies, closed symbols conditions with $F1$ roving. Standard errors of the mean are shown by vertical lines.

sponded via a keyboard and received immediate feedback after each trial.

3. Subjects

Four subjects, aged between 23 and 28, participated in the experiments. All subjects had normal pure-tone thresholds in quiet for the frequencies 500, 1000, and 2000 Hz. All subjects had experience in other psychoacoustic listening experiments. Except for subject RK (the first author), subjects were paid an hourly wage for their participation.

B. Results

1. Single-formant stimuli

Psychometric functions obtained for the single-formant stimuli are shown in Fig. 2. The open symbols indicate conditions where the first formant was fixed, closed symbols indicate roved-$F1$ conditions. The alternating patterns of discrimination sensitivity as a function of ΔF, most easily observable for the 2000-Hz formant for subjects LB and RK, can be explained as follows. To a first approximation, each decomposed signal segment can be thought of as a modulated carrier having a frequency equal to the formant-frequency. The maxima of the discrimination-sensitivity patterns shown in Fig. 2 correspond to values of F_{ws} at which the carriers of adjacent decomposed segments are added incoherently in the synthesis phase. Conversely, the minima in the patterns correspond to F_{ws} values at which coherent addition of adjacent segments occurs.

The psychometric functions for subject RK correspond reasonably well with those reported previously (Figs. 4–6 in Kortekaas and Kohlrausch, 1997), but appear to be more pronounced in their variations than the functions for subjects JS and LB. This is probably due to the fact that subject RK was much more familiar with the stimuli and that subjects JS and LB were only presented with stimuli that were roved in level. In our previous experiments, level roving did preserve the general pattern of the psychometric function but decreased discrimination sensitivity compared to fixed-levels conditions.

The results for all three subjects for the $F1=500$ Hz (fixed and roving) conditions show similar patterns. In the case of fixed formant frequency, subject JS seems to be able to use discrimination cues for $F1=1000$ Hz, but for $F1=2000$ Hz this subject's performance is generally below the threshold of $d'=1$. Interestingly, subject LB shows the opposite discrimination performance. Differences between subjects in the ability to attend to cues were also reported in Kortekaas and Kohlrausch (1997).

2. Double-formant stimuli

In Fig. 3 the psychometric functions for the double-formant stimuli are shown. Open and filled symbols indicate experimental data for the $[F1,F2]$ and $[F1R,F2]$ conditions, respectively. The dashed curves indicate the discrimination performance predicted for $[F1,F2]$ on the basis of the sensitivities determined for the single-formant stimuli with fixed $F1$. These predictions are based on the mean d' values shown in Fig. 2, under the assumption that the sensitivities for $F1$ and $F2$ are independent and that they are optimally combined so that $d'=\sqrt{(d'_{F1})^2+(d'_{F2})^2}$. They should be thought of as first-order estimates due to the rather large variances. Because discrimination sensitivity in the case of roving the 500- or 1000-Hz formant was below $d'=1$ with just a few exceptions, the expected sensitivities under the $[F1R,F2]$ condition are expected to be practically identical to the performance for $F2$ alone (not shown in Fig. 3).

As a general trend, discrimination performance seems to be predominantly determined by the first formant. For instance, the psychometric function for subject JS for the [500,1000] condition seems to show just a single maximum as for the [500] condition, even though this subject's discrimination performance showed two maxima for the

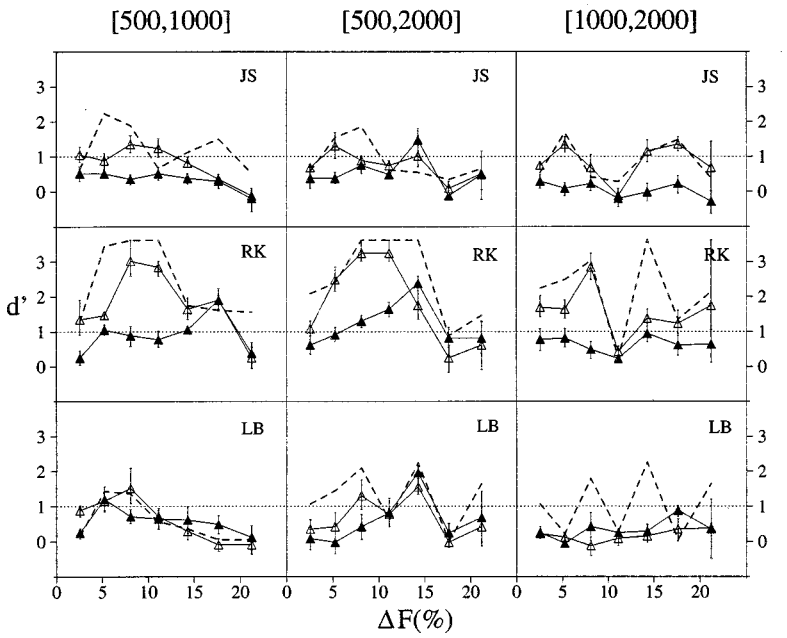

FIG. 3. Psychometric functions for discrimination of PSOLA-manipulated and unmanipulated double-formant signals, with $F_{wa}=100$ Hz. Formant-frequencies pairs are indicated above each column. Open symbols indicate conditions with constant $F1$, closed symbols conditions with roved $F1$. The dashed lines indicate the d' values predicted on the basis of an optimal combination of the d' values of the nonroved, single-formant condition. Standard errors of the mean are shown by vertical lines.

1000-Hz single-formant condition. The contribution of the second formant of 2000 Hz (as in [1000,2000]) is expected to be minimal on the basis of this subject's psychometric functions shown in Fig. 2. Another example for the minor role of the higher formant are the data for the [1000,2000] condition for subject LB where the predicted sensitivities show a clear alternating pattern while the observed d' values are essentially close to zero. Further evidence for $F1$ dominance can be inferred from the d' values for the $[F1R,F2]$ condition; for all subjects, these are generally comparable to the roved single-$F1$ condition.

3. Influence of level of F2

The dominance of the $F1$ region observed in Fig. 3 may have its origin in the difference in levels of $F1$ and $F2$. Psychometric functions obtained for the $[F1,F2D]$ condition with ''enhanced $F2$'' are shown in Fig. 4. As in Fig. 3, the dashed lines indicate expected (optimal) sensitivities. Subjects RK and LB performed the experiment for the [500,2000D] condition. They seem to benefit from the higher level of $F2$ for the higher ΔF shifts only. Because subject JS apparently could not use the auditory cues arising from changes in the 2000-Hz region (see Fig. 2), this subject participated for the [500,1000D] condition. Equalization of the formant levels tends to introduce two maxima in this subject's psychometric function, indicating a contribution of $F2$ of 1000 Hz, although the effect is rather weak.

4. Influence of duration and presentation level

The left panels in Fig. 5 show discriminability as a function of stimulus duration for the [500,2000D] condition. The squares represent ΔF values for which subjects primarily attend to the information from the $F2$ region, the triangles from the $F1$ region (see figure caption for specific ΔF values). The ΔF values under investigation corresponded to maximum discrimination performance for a duration of 300 ms. For subject JG the ΔF values were determined separately. The presentation level was 70 dB SPL.

For subjects LB and RK, the discriminability sensitivity at most decreases by about 1 d' unit if stimulus duration is reduced from 300 to 75 ms. A further reduction to 37.5 ms leads to another decrease in sensitivity by about 1 d' unit. For subject JG, discrimination performance only seems to show a clear drop if duration is reduced from 300 to 150 ms, especially in the ''$F2$ cue'' condition (squares). For shorter durations, discrimination performance remains around threshold.

The same ΔF values were used for testing the influence of presentation level (the stimulus duration was 300 ms). These data are shown in the right panels in Fig. 5. Discrimination sensitivity can decrease by about 2 d' units by decreasing the presentation level, either by 20 dB (''$F2$ cue'' condition for subject LB, and both conditions for subject JG), or by 40 dB (remaining cases). Surprisingly, subject JG

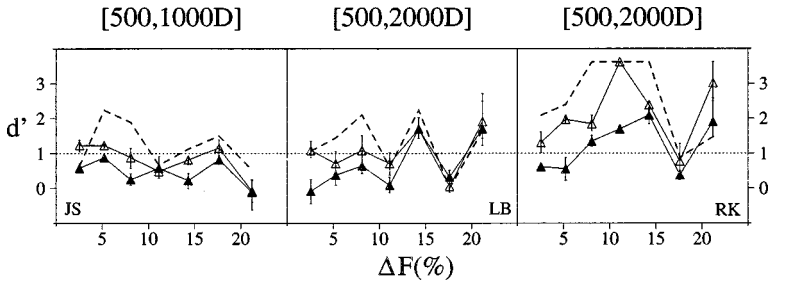

FIG. 4. Psychometric functions for discrimination of PSOLA-manipulated and unmanipulated double-formant signals, with $F_{wa}=100$ Hz. The $F2$ filter is applied twice. Formant–frequencies pairs are indicated in each panel separately. Symbols are used as in Fig. 2.

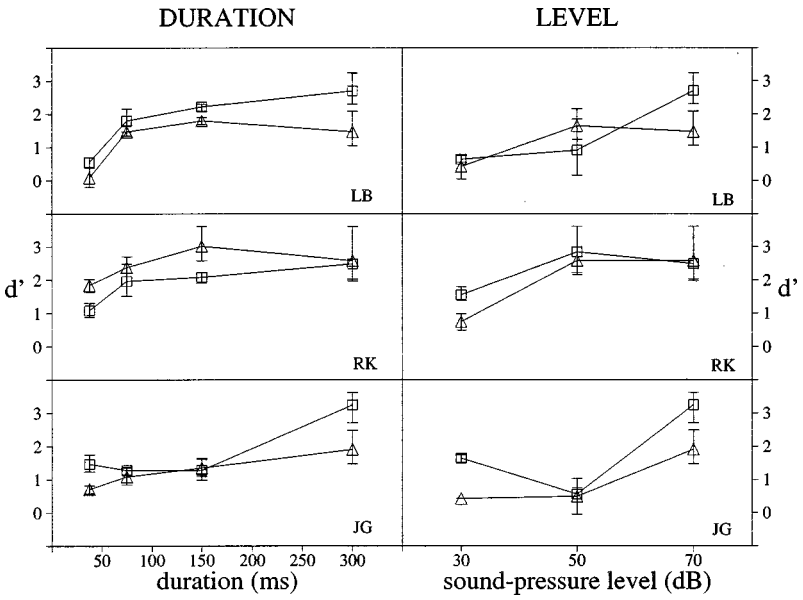

FIG. 5. Psychometric functions showing the influence of duration and presentation level on discrimination. Triangles represent ΔF conditions for which subjects predominantly used information from the low $F1$ region ($\Delta F = 5.3\%$ for subjects LB and JG, 11.1% for subject RK). Squares represent conditions for which the high $F2$ region information is used ($\Delta F = 22.2\%$ for subjects LB and RK, and 14.3% for subject JG).

seems to perform better at 30 dB SPL presentation level than at 50 dB SPL in the ''*F2* cue'' condition.

C. Discussion

As a general trend, auditory cues from the $F1$ region seem to dominate the discrimination process if both formant frequencies are fixed. If the first formant of 500 or 1000 Hz is roved, the general finding is that subjects can no longer discriminate between PSOLA-modified and reference signals despite the fact that, in principle, subjects could use cues from the $F2$ region. If the levels of both formants are more or less balanced, two out of three subjects seem to be able to focus on information from the $F2$ region for the high but not the low ΔF shifts. It is unclear at present from where this dependency on ΔF may stem.

1. Spectral and temporal cues

Lyzenga and Horst (1997) studied formant-frequency jnd's of single-formant synthetic stimuli having, among other conditions, a spectral envelope that was identical to the amplitude transfer-function of Klatt formant filters. Most of their data could be explained by using a model based on comparison of excitation patterns (''profile analysis''). At least part of the remaining data could be explained using a model based on detection of changes in the temporal envelope. Lyzenga extended these results to double-formant signals by measuring jnd's for both single and combined formant-frequency changes (Chap. 5 in Lyzenga, 1997). In the case of combined changes, Lyzenga proposed a model in which jnd's of both formant regions were assumed to be independent and to be combined in an optimal fashion. This model could accurately predict thresholds for combined changes.

Those conditions for which the single-formant jnd's were in good agreement with predictions of a temporal model could be described better by the excitation-pattern model after introduction of an additional low formant. Under such conditions, jnd's of the second formant were generally higher than the corresponding jnd's in isolation. These findings are in line with the trend in the discrimination data observed here for the $[F1,F2]$ conditions, which demonstrated an $F1$ dominance. Lyzenga hypothesized that, due to the increase in stimulus complexity, listeners are no longer able to attend to the temporal cues if spectral cues are available. It is uncertain whether this means that temporal cues are always inferior to spectral cues or whether the human auditory system is not able to combine both types of cues. The discrimination data for the high ΔF values in the $[500,2000D]$ condition suggest that the temporal cues are not necessarily inferior.

In order to study the effectiveness of cues from the $F2$ region, it is necessary that the roving of $F1$ does not distort the spectrum around $F2$. Because the phase transfer function of the Klatt formant filter is essentially linear for frequencies far from its resonance frequency, roving of $F1$ is not expected to alter the relative phases of neighboring harmonics around $F2$. Moreover, roving of $F1$ can be thought of as shifting the spectral envelope of the single formant along the frequency axis. This means that level changes of neighboring harmonics around $F2$ should be strongly coherent under $F1$ roving, which was confirmed by inspection of amplitude line spectra. Because such coherent level changes are overall-level changes rather than changes of spectral shape, roving of $F1$ was not expected to affect discrimination performance. This expectation is supported by the results of a study of Sommers and Kewley-Port (1996) who measured formant-frequency jnd's in $F1$ or $F2$ in the presence of three other formants, as a function of the number of harmonics varied in level (in accordance with the Klatt transfer function). Their results showed that level differences of only two to three harmonics in the formant region play a role in formant-frequency discrimination, even though many more harmonics undergo level changes.

2. Natural vowels

The data shown above contribute to the understanding of why PSOLA can often be applied to pitch shifting natural

vowels, and presumably voiced consonants, without conspicuous perceptual consequences. The dominating auditory cues associated with changes in the low $F1$ region vanish if the formant is roved, even if the roving range is relatively small, such as two jnd's. It is highly likely that this amount of variability is also present in steady parts of natural vowels (Pisoni, 1980). The formant frequency may also fluctuate in time, implying that differences in instantaneous harmonic levels may be of the same order as the instantaneous spectral changes introduced by PSOLA. If the PSOLA-induced differences are greater, then discrimination may still be hampered by the rate of the formant fluctuations; if the rate is too high, the auditory system may not be able to reliably integrate PSOLA-induced spectral information. In contrast, temporal cues associated with changes in the high $F2$ formant region were found to be much less affected by formant roving. These cues, however, are also less likely attended to due to the $F1$ dominance.

Natural vowels often have ''steady states'' considerably shorter than 300 ms, but this does not mean that the cues reported here are not available when modifying natural speech; for stimuli as short as 75 ms, two out of three subjects could still use PSOLA-induced discrimination cues. The effect of presentation level was somewhat stronger: some subjects showed considerable decrease in discrimination sensitivity even if the presentation level was reduced in such a way that it still was within the level range of normal conversation [about 50–70 dB SPL at 30 cm from the mouth; Dunn and White (1940)].

When modifying natural speech, a reference often is not available so that PSOLA-induced spectro-temporal changes may be difficult to identify. In such cases, changes may be more conspicuous if they elicit phonetically rather than psychophysically different perceptions (cf. Klatt, 1982). For instance, some subjects in our experiments reported changes in ''vowel quality'' as the cue for discriminating PSOLA-modified and unmodified 500-Hz single-formant stimuli. Darwin (1984) studied /ɪ/–/ɛ/ classification boundaries for five-formant synthetic vowels. An increase of 3 dB of an harmonic near $F1$ was found to be sufficient for shifting the classification boundary. Comparable PSOLA-induced harmonic level changes occur for the 500-Hz formant (Kortekaas and Kohlrausch, 1997). PSOLA-synthesized speech, however, is generally highly intelligible (Klaus *et al.*, 1997).

III. EXPERIMENT 2: JITTER AND SHIMMER

A. Method

1. Stimuli

Jitter and shimmer were introduced by randomly varying either the temporal positions or the amplitudes of the pulses in the glottal pulse train (see Sec. II A). The temporal position of the ith pulse was given by $P_i = i \cdot T + J_{P,i}$, where T is the mean period duration. The jitter process J_P had a Gaussian distribution with zero mean and standard deviation σ_P which will be expressed as a percentage of T. In a similar fashion the (linear) amplitude of the ith pulse was determined according to $A_i = A + J_{A,i}$, where A is the mean pulse amplitude. J_A denotes a zero-mean, Gaussian process with standard deviation σ_A expressed as a percentage of A.

The above way of generating jitter is consistent with a number of other studies (e.g., Cardozo and Ritsma, 1968; Rozsypal and Millar, 1979). In these studies, perturbation values $J_{P,i}$ within a realization of the jitter process were uncorrelated. In other words, such a sequence of perturbation values is expected to have an autocorrelation function which is only nonzero for zero lag. Hillenbrand (1988) studied the influence of jitter and shimmer, simulated in synthetic vowels, on perceived roughness. To this end, Hillenbrand first measured autocorrelation functions for period duration and voice amplitude in natural sustained vowels. Instead of a single peak at zero lag, the measured autocorrelation functions had an exponential decay which indicates that the perturbation values in the sequences were correlated [for a recent review, see Schoentgen and De Guchteneere (1997)]. In spectral terms, the uncorrelated sequences have a white (flat) power spectrum, whereas the correlated sequences described in Hillenbrand (1988) have a low-pass (LP) characteristic. Hillenbrand argued that the power spectra ''were similar, but not identical to $1/f$ spectra.'' Because the exact nature of $1/f$ processes is still unknown, Hillenbrand proposed an algorithm that yielded autocorrelation functions *approximating* the functions measured for sustained vowels.

In the present study, spectrally white and LP perturbation sequences were generated in a slightly different way. Gaussian noise buffers were generated whose samples indicated the instantaneous jitter values $J_{P,i}$ or shimmer values $J_{A,i}$ in the case of *uncorrelated* sequences. By filtering these sequences using a LP filter, correlated sequences were obtained. The cutoff frequencies of the filters were derived from the autocorrelation functions shown in Fig. 2 in Hillenbrand (1988). More details of this procedure are given in the Appendix.

For shimmer, the method of introducing perturbation by modulating pulse amplitudes is consistent with the procedure described in Hillenbrand (1988). For jitter, however, both methods differ in the sense that Hillenbrand introduced perturbation to *period durations* rather than to pulse positions. Hillenbrand's procedure likely results in large deviations with respect to regular pulse positioning (at positions given by $i \cdot T$); because the process is a random walk with respect to pulse positioning, deviations are bound to accumulate. This means that the shift of the PSOLA windows, regularly spaced at a rate of F_{wa} Hz, relative to the excitation pulses has a certain probability to steadily increase or decrease. Because our main interest was the influence of small irregularities in $F0$, *pulse positions* were jittered which has a limited effect on this ''mismatch.'' The power spectrum of the corresponding perturbations in terms of *period duration*, however, is rather flat so that, strictly speaking, our simulations are not compatible with those of Hillenbrand.

First, for the baseline detection-threshold measurements, (single-) formant frequencies of 500, 1000, and 2000 Hz were used, with bandwidths of 50, 50, and 100 Hz, respectively. The $F0$ of all signals (i.e., without jitter) was 100 Hz, yielding a mean period duration T of 10 ms. For the 1000-Hz formant an additional condition was measured in which $F0$

was 250 Hz ($\overline{T}=4$ ms). Thresholds were obtained for both the LP and the spectrally white perturbation conditions. The presentation sound-pressure level, range of level roving, and stimulus duration were the same as in experiment I. The sample rate was set to 48 kHz, yielding the highest resolution given the specifications of our hardware.[3]

Second, for the experiments dealing with discrimination of perturbed PSOLA-modified stimuli, formant frequencies of 500 and 2000 Hz were used with bandwidths as given above. For the 500-Hz formant, ΔF was either 8.1%, yielding above-threshold to almost perfect discrimination in the absence of perturbation, or 17.7%, yielding performance at chance level or close to threshold (see Fig. 2). For the 2000-Hz formant, the respective ΔF values were 14.3% and 11.1%. The test signal was first generated with an $F0$ of F_{wa} Hz including perturbation, and subsequently shifted in $F0$ using PSOLA. Reference signals were directly synthesized with an $F0$ of F_{ws} Hz, including (independent realizations of) perturbation. Note that in the case of jitter, the PSOLA analysis-window positions corresponded to the unjittered instants of excitation $i\cdot\overline{T}$, meaning that window maxima and filter excitations were no longer exactly aligned. In the context of PSOLA modification of natural speech, this may translate to making small estimation errors in the local $F0$.

2. Procedure

In the (baseline) detection experiments, thresholds of jitter and shimmer were measured using an adaptive 3I-3AFC paradigm. Two of the intervals contained strictly periodic single-formant signals. The odd-ball interval contained a signal whose perturbation level, in terms of σ_P or σ_A, was adaptively varied. In each trial, a new realization of the perturbation process was applied to the odd-ball interval (''running jitter or shimmer''). The initial perturbation level of each adaptive measurement was sufficiently high to facilitate easy detection. After two consecutive correct responses, the perturbation level was decreased. After each incorrect response, the level was increased again so that the 70.7% correct level was tracked [''two-down, one-up,'' Levitt (1971)]. At each reversal from increasing to decreasing perturbation level, the step size was halved. For jitter, the initial step size was 0.8% and 0.4% for LP and white jitter, respectively. The minimum step sizes were 0.1% and 0.05%, respectively. For shimmer, the initial step sizes were 4.5% and 2.0% for LP and white shimmer, with minimal step sizes of 0.5625% and 0.25%, respectively. After having reached the minimal step size, the perturbation levels at eight subsequent reversals were recorded. The median of these levels was taken as a threshold data point. For each condition, each subject performed five threshold measurements of which the first measurement was regarded as a practice run. The data shown below are the means and standard deviations of the four remaining measurements.

In the discrimination experiment, psychometric functions were only measured for LP perturbation. Perturbation levels for jitter, in terms of σ_P, were 1.2%, 2.4%, 4.8%, and 9.6%, and for shimmer, in terms of σ_A, 6.75%, 13.5%, 27%, and 54%. The unrealistically high σ_A values could lead to changes of sign of the pulse amplitude and the subjects described these stimuli correspondingly as very rough and irregular (cf. Hillenbrand, 1988). These stimuli reminded one of the subjects of recordings of the first contact with Neil Armstrong on the moon. The same 3I-3AFC experimental procedure as described for experiment I was used. Each subject performed five runs, each consisting of 15 trials, of which the first was regarded as a practice run.

3. Subjects

Four subjects, including the first author, participated in the experiments. They were aged between 23 and 29 and all had at least some experience in psychoacoustic listening experiments. Except for subject RK, the subjects were paid an hourly wage for their services.

B. Jitter and shimmer detection thresholds

1. Results

Detection thresholds for jitter perturbation are shown in Fig. 6 for the LP jitter (squares) and the white jitter condition (triangles). Open symbols are data obtained for $F0=100$ Hz, closed symbols for $F0=250$ Hz (1000-Hz formant only). Model predictions (''SIM''), which are displayed in the lower right panel, will be discussed below. For the LP and white jitter conditions separately, a low-to-high ranking of the thresholds would be: 1000 ($F0=250$ Hz), 1000 (100 Hz), 500, and 2000 Hz. Thresholds for the spectrally white jitter condition are about a factor of 2 lower than the thresholds for LP jitter. Moreover, the standard deviations for the LP-jitter threshold data tend to be larger, which is presumably a consequence of the larger variability across realizations of the LP-jitter process.

Figure 7 shows detection thresholds for shimmer perturbation using the same symbols as in Fig. 6. Thresholds for the 2000-Hz formant again tend to be highest, although the effect is less pronounced than for jitter. Comparable to jitter perturbation, thresholds for the white perturbation condition are lower than for the LP condition, and standard deviations tend to be larger for the latter condition. The high 250-Hz $F0$ condition yields the lowest thresholds, which is a clear trend in the data of all subjects.

2. Models

a. Modulation discrimination model. Kortekaas and Kohlrausch (1997) described a modulation-discrimination model that estimated perceptual distances between PSOLA-modified and reference single-formant signals in terms of differences in their ''effective modulation depth.'' The signals were filtered by a single Gammatone filter (Patterson *et al.*, 1987) centered at or near the formant frequency. Subsequently, the temporal envelope of the filtered signal was calculated by a discrete Hilbert transform. Then, the effective modulation depth M was defined as $M=\sqrt{2}\cdot\sigma_e/m_e$, where σ_e is the standard deviation of the envelope, and m_e its mean. As a distance measure between a reference and a test signal, we defined $D_{\mathrm{mod}}=|M^2_{\mathrm{ref}}-M^2_{\mathrm{sig}}|$.

The same model was used here to predict detection thresholds for σ_P and σ_A. In the case of jitter detection, M^2_{sig}

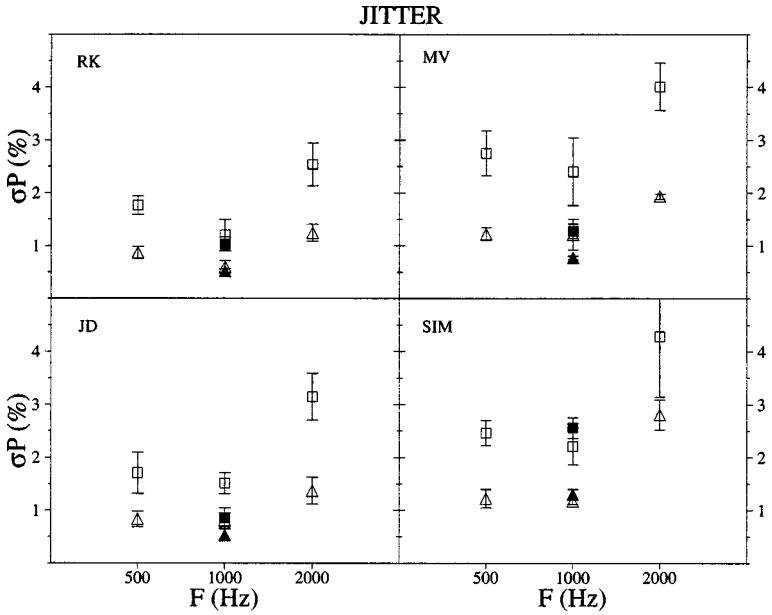

FIG. 6. Jitter detection thresholds for σ_P as a function of formant frequency. Open symbols indicate the $F0 = 100$ Hz condition, closed symbols the 250-Hz condition. Squares indicate data for LP jitter, triangles for white jitter. Standard deviations are shown by vertical lines. Model predicted thresholds, using the modulation-discrimination model, are shown in the lower right panel.

of a perturbed test signal may be larger than M^2_{ref} of a strictly periodic reference due to the interaction of the (varying) instantaneous $F0$ and the formant structure in the spectral envelope (cf. Neelen, 1969). This resembles an FM-to-AM conversion (Zwicker, 1952). As for shimmer thresholds, M^2_{sig} is expected to be larger because shimmer introduces amplitude modulation to the pulse train.

The ''SIM'' data in the lower right panels of Figs. 6 and 7 were obtained by letting the model take the role of ''listener.'' At each trial, the model calculated M^2 for each of the three intervals. In order to limit the detection sensitivity, an independent ''internal noise'' value was added to each of these M^2 values. This internal noise had a Gaussian distribution with zero mean and standard deviation σ_{int}. The interval that deviated most in terms of M^2 from both orders was regarded as the odd-ball. For determination of σ_{int}, we can assume detection sensitivity to obey $d' = D_{\text{mod}}/\sigma_{\text{int}}$ (Green and Swets, 1966). In our previous study, we reported detection thresholds ($d' = 1$) for D_{mod} of 0.14 for 1000 Hz, and of 0.25 for 2000 Hz. In simulating the present detection experiments, however, setting σ_{int} to these values resulted in thresholds that were too high. Instead, the ''SIM'' data were run with $\sigma_{\text{int}} = 0.03$ for the 2000-Hz formant, and 0.02 in the other conditions. This conspicuous difference in sensitivity will be discussed in Sec. III C 3. Further details of the adaptive procedure were the same as for the ''real'' experiment.

The jitter detection thresholds shown in Fig. 6 replicate the general trends observed in the data of the subjects, at least for a fundamental of 100 Hz. Simulation thresholds for $F0 = 250$ Hz are too high, although the ranking of the thresholds is in line with the experimental data. The simulated thresholds for shimmer shown in Fig. 7, however, match the experimental data to a lesser extent, although the simulated thresholds do show an independence of formant frequency, probably even to greater extent than the experimental data.

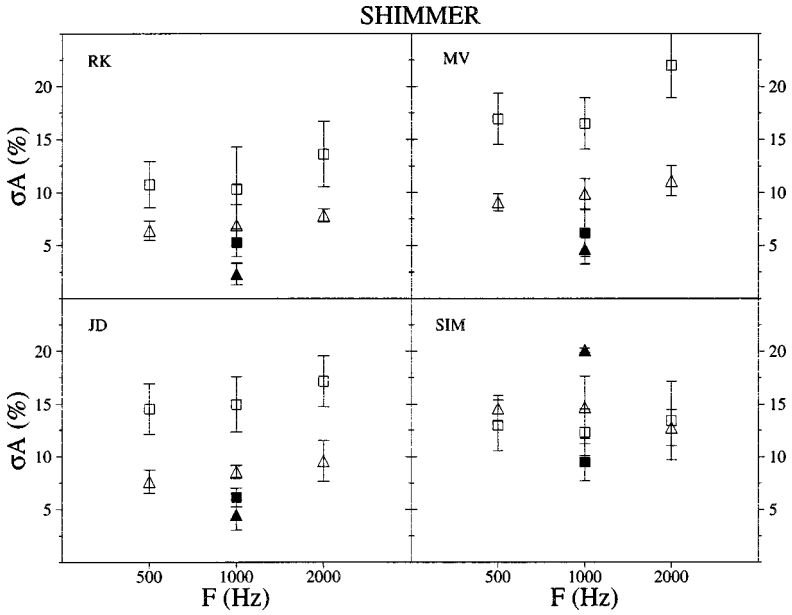

FIG. 7. Shimmer detection thresholds for σ_A as a function of formant frequency. Symbols are used as in Fig. 6. Model predicted thresholds, using the modulation-discrimination model, are shown in the lower right panel.

Thresholds for the LP and white-shimmer condition lie much closer to each other than in the experimental data. The thresholds for the high 250-Hz $F0$ condition are much too high and in addition show the wrong ranking.

b. Intensity-discrimination model. An alternative model would be an intensity-discrimination model (Florentine and Buus, 1981; Gagné and Zurek, 1988) that only takes (power) spectral differences into account. In our previous study we used a model in which stimuli were critical-band analyzed by a Gammatone filterbank. Subsequently the power in each band is determined over the duration of the stimulus, yielding an ''excitation pattern.'' The distance measure between two stimuli was the optimal combination of level differences in each channel of the excitation pattern: $D_{\text{sum}} = (\Sigma_{i=1}^{N} \Delta L_{E,i}^2)^{1/2}$, where $\Delta L_{E,i}$ is the level difference in channel i. Here the channels are assumed to be independent. For simulation of the present detection experiments, the excitation patterns of the three intervals were compared. The pair of stimuli yielding the lowest D_{sum} were regarded as the reference. D_{sum} was corrupted by an internal noise with $\sigma_{\text{int}} = 1$ dB, a value which was found to correspond to threshold in our previous study.

Pollack (1971b) argued that jitter detection for stimuli with short pulse-to-pulse intervals relies on spectral cues, rather than on temporal cues. The intensity-discrimination model yielded the following thresholds for $F0 = 250$ Hz: thresholds for σ_P for white jitter of 0.8% (standard deviation 0.07%) and for LP jitter of 1.6% (1.17%), and for σ_A thresholds for white shimmer of 5.4% (0.1%) and for LP shimmer of 4.4% (1.32%). In all four cases predicted thresholds are in better agreement with the experimental data, although the prediction for LP jitter is somewhat higher than expected. The order of the thresholds for LP and white shimmer seems to be wrong, albeit that the thresholds appear to lie closer to each other in the experimental data as well (especially for subjects MV and JD).

3. Discussion

Cardozo and Ritsma (1968) reported jitter detection thresholds for band-pass-filtered pulse trains using a filter with a Q-factor of 3 and slopes of 34 dB per octave. The sequences of pulse-position perturbations had a white spectrum. Thresholds were found to decrease with increasing stimulus duration up to approximately 100 ms, and to remain constant for longer durations. In the latter case, Cardozo and Ritsma reported thresholds for pulse sequences with a (mean) $F0$ of 100 Hz and filtered at 1000-Hz center frequency of $\sigma_P = 0.5\%$. For a higher center frequency of 1400 Hz the threshold was about 0.7%. These two results are in line with the thresholds reported here: for 1000- and 2000-Hz formants thresholds are in the range 0.5%–1.0% and 1.2%–2.0%, respectively. For high $F0$ levels of 333 Hz Cardozo and Ritsma (1968) reported thresholds for a ''formant'' at 1400 Hz of about 0.2%, which is a factor of 2–3 lower than the present thresholds of 0.4%–0.6% for a 1000-Hz formant with a 250-Hz fundamental. Neelen (1969) measured thresholds for a center frequency of 500 Hz (of a band-pass filter with 50-Hz bandwidth) of 0.5%. This value is also a factor of 2 lower than the present range of 0.8%–1.1%. Pollack (1971a) also measured shimmer thresholds by randomly varying the amplitudes of the rectangular pulses by $\pm \Delta A$. For stimulus $F0$ and durations comparable to the present study, detection thresholds were 10%–20% which is a factor of 2 higher than the range of 5%–10% reported here.

The fact that the jitter thresholds presented here generally are a factor of 2 higher may be due to differences in paradigms: for instance, Cardozo and Ritsma (1968) used an adaptive 2IFC paradigm tracking the 72% correct level, which corresponds to $d' \simeq 1$. In the present study, the 70.7% correct level in a 3IFC paradigm corresponds to $d' \simeq 1.28$ (Macmillan and Creelman, 1991). Additionally, the difference in thresholds may have been caused by the limited temporal resolution of the digital signal representation, relative to the analog signal generation of the older studies.

C. PSOLA-modified perturbed signals

1. Results

Figure 8 shows psychometric functions for subjects MV, AK, and RK for discrimination of a PSOLA-modified single-formant signal from an unmodified comparison as a function of perturbation level σ_P. Model predictions, shown by the filled symbols, will be treated in detail below.

For the 500-Hz formant (lower panels) and the baseline condition of $\sigma_P = 0\%$, all three subjects show above-threshold performance if $\Delta F = 8.1\%$ (lower left panel), and near-threshold performance if $\Delta F = 17.7\%$ (lower right panel). For the corresponding stimulus conditions in experiment I, subjects JS and LB performed reasonably above threshold and at chance level, respectively. Linear regression analysis for $\Delta F = 8.1\%$ yielded estimated slopes of the psychometric functions which were not significantly different from zero ($p > 0.15$) for all subjects. This means either that jitter does not seriously hamper the use of the PSOLA-induced spectral discrimination cues around the 500-Hz formant, or that new cues become available at higher perturbation levels. An example of the latter explanation appears to occur for $\Delta F = 17.7\%$ where the psychometric functions for subjects AF and RK increase from $d' \simeq 1$ for no jitter to $d' \simeq 2$ for maximal jitter. The corresponding slopes of the psychometric functions were found to be significantly different from zero at the $p < 0.05$ and $p < 0.005$ level, respectively. For subject MV the function remains essentially flat around $d' = 1$ ($p > 0.08$).

The discrimination performance for the 2000-Hz formant condition (upper panels) seems to be even more independent of jitter perturbation. None of the psychometric functions have linear regression slopes significantly different from zero at the $p < 0.1$ level. These findings suggest that temporal discrimination cues remain intact under jitter perturbation for this high $F2$ condition, and that an increase of perturbation level does not result in new PSOLA-induced discrimination cues. The variability in sensitivity among the three subjects is large, both for the 500- and 2000-Hz formants.

Psychometric functions of discrimination performance under influence of shimmer perturbation are shown in Fig. 9. The data for $\sigma_A = 0\%$ are the same as those shown in Fig. 8

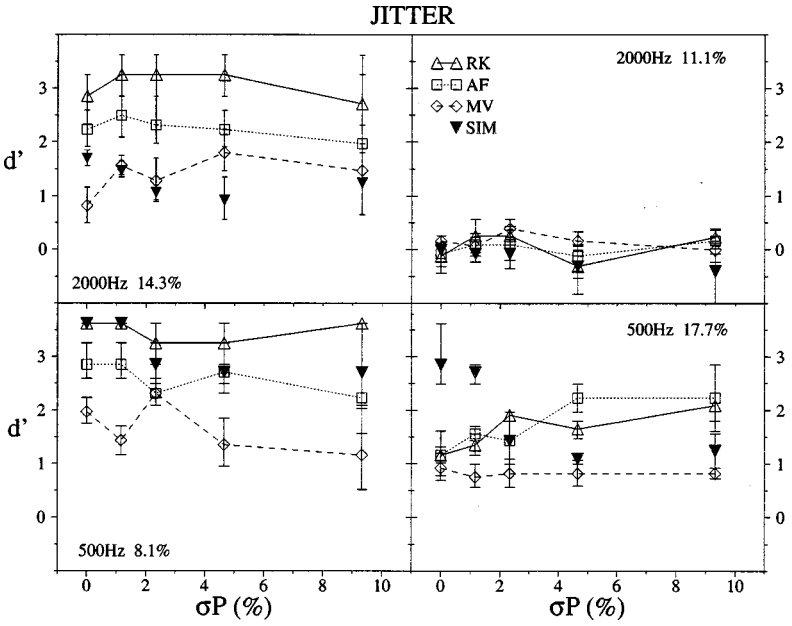

FIG. 8. Psychometric functions for discrimination of PSOLA-manipulated and unmanipulated single-formant signals, with $F_{wa}=100$ Hz, as a function of the jitter perturbation level σ_P. Closed symbols indicate model predicted sensitivities (see text for details). Standard errors of the mean are shown by vertical lines.

for $\sigma_P=0\%$. As a general trend, performance for $\Delta F=8.1\%$ under the 500-Hz formant condition (lower left panel) decreases by about one to two d' units as a result of increasing σ_A from 0% to 54%. Linear regression slopes for subjects AF and MV were about -0.02 (d' units per percent of σ_A) and were significantly different from zero at the $p<0.01$ level. The slope for subject RK was not found to be significantly different from zero, although there may be a difference between the data for $\sigma_A=0\%$ and 6.5%, and the higher shimmer levels (not tested). Performance for $\Delta F=17.7\%$ (lower right panel) remains either more or less constant near threshold (for subjects MV and RK; $p>0.5$), or tends to decrease (subject AF; slope of -0.02, $p<0.05$).

For the 2000-Hz formant and $\Delta F=14.3\%$ (upper left panel) slopes of -0.02 and -0.03 were found for subjects AF and RK ($p<0.05$ and $p<0.005$, respectively), and an insignificant slope ($p>0.25$) for subject MV. No significant effect of σ_A was found for $\Delta F=11.1\%$ shown in the upper right panel ($p>0.75$). In general, the discrimination sensitivities for subjects AF and RK agree better than under the jitter condition. For both perturbation conditions, subject MV showed a discrimination performance about one to two d' units lower in sensitivity compared to the other subjects.

2. Models

Discrimination of a PSOLA-modified 2000-Hz formant signal could be modeled on the basis of modulation discrimination in our previous study, where a threshold of $D_{\text{mod}}=0.25$ was found. Psychometric functions were simulated using the modulation-discrimination model, with σ_{int} set to 0.25 accordingly. The simulation results are shown as the closed symbols in the top panels of Figs. 8 and 9.

The simulated psychometric functions for jitter (upper panels in Fig. 8) capture the general trend in the experimental data: discrimination varies within about one d' unit as a function of σ_P. In absolute terms, discrimination sensitivity

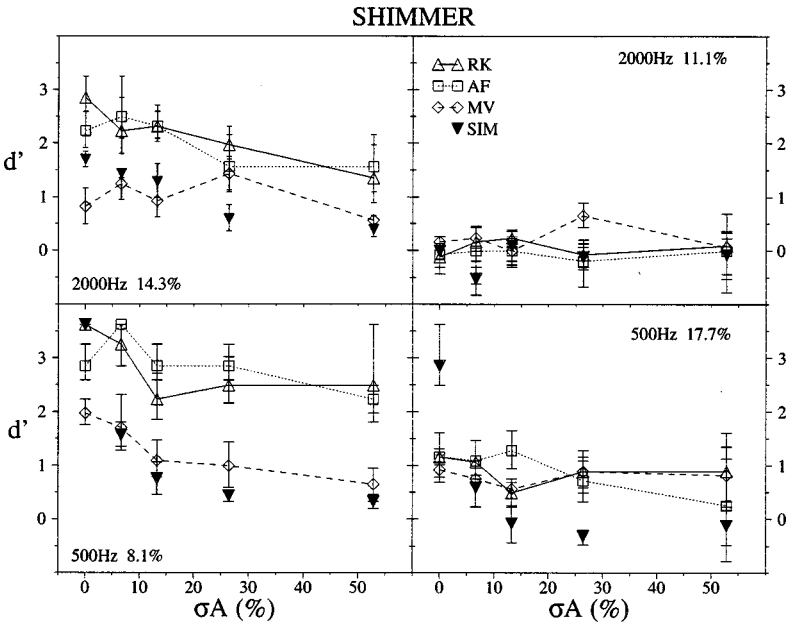

FIG. 9. Psychometric functions for discrimination of PSOLA-manipulated and unmanipulated single-formant signals, with $F_{wa}=100$ Hz, as a function of the shimmer perturbation level σ_A. Closed symbols indicate model predicted sensitivities (see text for details). Standard errors of the mean are shown by vertical lines.

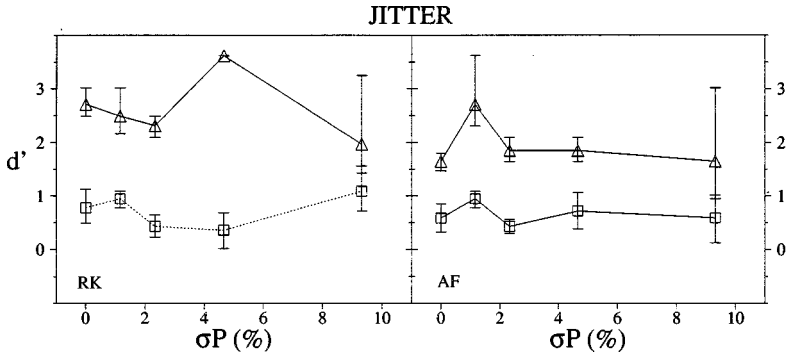

FIG. 10. Psychometric functions for discrimination of PSOLA-manipulated and unmanipulated single-formant signals, with $F_{wa}=100$ Hz, as a function of the shimmer perturbation level σ_A and under formant roving. Triangles indicate data for the 2000-Hz formant ($\Delta F=14.3\%$), squares for the 500-Hz formant ($\Delta F=17.6\%$). Standard errors of the mean are shown by vertical lines.

for $\Delta F=14.3\%$ (upper left panel in Fig. 8) is rather low compared to the data of the subjects, although they also show large variation in sensitivity. The predicted psychometric functions for the shimmered 2000-Hz formant, displayed in the upper panels of Fig. 9, are in line with the experimental observations for shimmer described above.

Model-predicted psychometric functions for the 500-Hz formant using the intensity-discrimination model are shown as the closed symbols in the lower panel of Figs. 8 and 9 ($\sigma_{\text{int}}=1$ dB). For jitter (lower panels in Fig. 8), simulated discrimination sensitivities display only a moderate influence of increasing σ_P for $\Delta F=8.1\%$. Remarkably, the sensitivity in the case of $\Delta F=17.7\%$ drops from $d'>2$ for the two lowest σ_P values to just above threshold, which is not in agreement with the experimental data. More or less in contrast, the model psychometric functions for shimmer (lower panels in Fig. 9) do show the ''correct'' trend, at least for $\sigma_A>0\%$, but suggest that the model sensitivity is too low.

3. Discussion

The initial hypothesis in the discrimination experiments was that the introduction of jitter and shimmer in the single-formant signals would severely affect the subjects' discrimination performance. The psychometric functions shown in Figs. 8 and 9 do not support this hypothesis: even though performance tends to deteriorate for larger values of σ_P and σ_A for $\Delta F=14.3\%$ (2000 Hz) and $\Delta F=8.1\%$ (500 Hz), the size of this effect is limited to approximately one d' unit. In other words, the PSOLA-modified signals remain discriminable. Moreover, the same models as applied in our previous study for strictly periodic signals capture the general trends in the experimental data, with the exception of some conditions.

a. FM-to-AM conversion. For the $\Delta F=17.7\%$ (500 Hz) condition, larger σ_P values led to an unexpected increase in sensitivity for subjects AF and RK. The jitter perturbation might have introduced additional discrimination cues, due to the interaction between harmonics and the (formant) spectral envelope (Neelen, 1969). Under jitter, ''harmonics'' of the signal will be shifted randomly ''under'' the spectral envelope. In the case of the test signal prior to PSOLA-modification, the strong fifth harmonic of the 100-Hz $F0$ coincides with the 500-Hz formant frequency. Roving of $F0$ thus results only in moderate AM at the output of the auditory filter, because side harmonics remain relatively weak, provided the fluctuations in $F0$ are small compared to the bandwidth of the formant. If $\Delta F=17.7\%$ (500 Hz) in the absence of jitter, there is a strong harmonic at about 470 Hz and a somewhat weaker harmonic at 590 Hz. In this case, random fluctuations of $F0$ influence the relative levels of these harmonics significantly so that considerable AM in the output of an auditory filter can be expected. The difference in AM in the auditory filter output may have been an unforeseen cue.

This explanation can be tested by *roving* the formant frequency; this alters the relative levels of harmonics, also for the test-signal interval. In the case of roving the 500-Hz formant for $\Delta F=17.7\%$, the expected performance is close to threshold (see Fig. 2) and should be independent of σ_P. If this explanation holds for the 500-Hz formant case, then it may be questioned whether discrimination for large σ_P for the 2000-Hz formant and $\Delta F=14.3\%$ was also based on perturbation-induced cues, rather than on PSOLA-induced cues. If PSOLA-induced cues were used, performance is expected to remain above threshold independently of σ_P.

Figure 10 shows the psychometric functions obtained for roving the formant by $\pm 3\,\Delta F1$ (Gagné and Zurek, 1988). As predicted, the psychometric function for the 500-Hz formant, indicated by squares, remains flat around $d'\simeq 0.5$ ($p>0.75$ for AF, and $p>0.5$ for RK). For the 2000-Hz formant the functions indicated by triangles have more or less the same shape as those in Fig. 8, and the corresponding linear regression slopes for both subjects are not significantly different from zero ($p>0.75$). In general, discrimination performance is well above threshold, suggesting that discrimination was not based on additional cues in the fixed-formant condition.

b. Modulation-discrimination model. The modulation-discrimination model was based on two assumptions: (1) jitter and shimmer detection essentially is a one-channel process, and (2) the decision variable solely depends on first- and second-order statistics of the temporal envelope within that channel. The first assumption might explain the observed difference in internal noise required to yield satisfactory threshold predictions in the present study, and good linear fits to discrimination performance in our previous study. In the absence of perturbation, the spectral changes due to PSOLA are essentially restricted to the formant area, making it likely that a limited number of auditory filters will be attended to. Jitter and shimmer perturbation, however, are wideband processes which (coherently) affect all harmonics of the glottal source. Under the assumption that the internal noises in different channels are uncorrelated, the differences in effective modulation depths may be optimally combined

across channels. This means that, in order to achieve the same discrimination sensitivity, the internal noises per individual channel may be larger. Combination of modulation information across auditory filters seems to be present in detecting sinusoidal modulation of broadband noises (Eddins, 1993; Dau *et al.*, 1997).

As for the second assumption, the use of merely first- and second-order envelope statistics, there is growing evidence that the human auditory system is able to perform an analysis of the distribution of modulation frequencies within auditory channels (e.g., Houtgast, 1989). In order to simulate such processing, Dau *et al.* (1997) proposed a modulation filterbank acting on the output of simulated auditory filters. For the detection of jitter and shimmer, such a spectral decomposition might separate the intrinsic modulation around *F*0 of the (quasi-)harmonic formant signal, and the modulation probably lower in frequency due to the random perturbations. This may be a topic for future investigations.

c. Jitter and shimmer in natural speech. Pinto and Titze (1990) advocated the use of standardized perturbation measures. For jitter, one can adopt the mean rectified jitter measure[4] (Horii, 1980) according to which the jitter levels applied in the discrimination experiments were approximately 0, 0.75, 1.5, 3.0, and 6.0%. Likewise, according to the mean rectified shimmer measure, the shimmer perturbation levels were 0, 0.3, 0.6, 1.2, and 2.4 dB. Both the jitter and shimmer ranges are comparable to the range of investigation in Hillenbrand (1988). The *detection thresholds* for the 500- and 1000-Hz formants shown in Figs. 6 and 7 correspond to MR (*J*) values of 0.5%–0.8% for LP and white jitter, and MR (*S*) values of 0.75–1 dB for white shimmer and 0.2–0.3 dB for LP shimmer.

Horii (1980) measured jitter and shimmer in three natural sustained vowels uttered by 31 speakers and found MR (*J*) and MR (*S*) values of 0.6%–0.7% and 0.3–0.4 dB, respectively. According to our threshold measurements, these perturbation levels would be at detection threshold, questioning the role of perturbation in natural speech of healthy voices (cf. Klatt and Klatt, 1990). The perturbation levels used in determining the influence of jitter and shimmer of discriminating PSOLA-induced changes would range from close to, to far above the levels measured in healthy voices. This suggests that vocal perturbation, as a source of variation present in natural speech, presumably does not contribute to the success of PSOLA by possibly hampering the use of auditory cues.

IV. CONCLUSIONS

(1) Discrimination of PSOLA-modified double-formant stimuli is predominately determined by the availability of cues in the region of *F*1. If the level differences in *F*1 and *F*2 due to the spectral tilt are canceled, cues from the *F*2 region can be used in a restricted number of conditions. Differences in discrimination sensitivity between subjects are rather large.

(2) Stimulus duration has only a moderate influence on discrimination performance, except for the shortest (37.5 ms) duration. Reduction of the presentation level from 50 to 70 dB SPL decreases sensitivity considerably for some subjects.

(3) The detection thresholds for LP jitter or shimmer are generally higher than the thresholds measured for spectrally white perturbation. Thresholds are found to depend on formant frequency to a somewhat greater extent for jitter than for shimmer. In agreement with data reported in the literature, thresholds for the high *F*0 conditions are generally lowest.

(4) The detection thresholds for jitter perturbation of single-formant signals can be modeled reasonably well by analyzing the effective modulation depth at the output of simulated auditory filters. For shimmer, thresholds are moderately well predicted in quantitative terms, although differences between the LP and white shimmer conditions are not replicated. For high *F*0 conditions, jitter and shimmer detection thresholds can be accurately predicted by applying an intensity-discrimination model.

(5) Although jitter and shimmer perturbations do influence discrimination sensitivity, the general pattern of discrimination performance of PSOLA-modified stimuli is maintained under influence of jitter and shimmer.

(6) In discriminating PSOLA-modified from unmodified stimuli, additional modulation cues can be introduced as a result of the interaction between the formant frequency and the harmonics of the signal subjected to PSOLA modification.

ACKNOWLEDGMENTS

The authors greatly appreciated the comments of Dik Hermes, Adrian Houtsma, Andrew Oxenham, Rob Maher, and two anonymous reviewers on an earlier version of this paper.

APPENDIX: JITTER AND SHIMMER CHARACTERISTICS

Sequences of instantaneous perturbation values $J_{P,i}$ or $J_{A,i}$ were obtained by (1) generating Gaussian noise buffers, and (2) LP filtering these buffers in the case of correlated sequences. To determine the parameters of LP filtering, the autocorrelation functions in Fig. 2 of Hillenbrand (1988) were parametrized by the function $R_{nn}[l]=e^{-\beta|l|}$, where l is the lag (in periods) and $|.|$ denotes absolute value. R_{nn} denotes the *normalized* autocorrelation. A close fit to the measured functions was obtained by setting parameter β to 0.23 for the synthesis of jitter, and to 0.046 for the synthesis of shimmer. The corresponding power spectra have a LP shape similar to the power spectrum of a noise filtered by a second-order LP filter with a cut-off frequency of 4 and 1 Hz, respectively.[5] Note that for white jitter and shimmer perturbation parameter β has to be set to ∞ resulting in a single peak at $R_{nn}[0]$.

The relation between *pulse-position* and *period-duration* perturbation can be described as follows. The *i*th period duration is by definition equal to

$$\begin{aligned} D_i &= P_i - P_{i-1} \\ &= \overline{T} + J_{P,i} - J_{P,i-1} \\ &= \overline{T} + J_{D,i}, \end{aligned}$$

where P_i is the ith pulse position and $J_{P,i}$ is the ith perturbation value. The mean of J_D is zero and its standard deviation can be related to the standard deviation of J_P as follows: $\sigma_{J_D} = \sqrt{2(1-e^{-\beta})}\sigma_{J_P}$, which reduces to $\sqrt{2}\sigma_{J_P}$ in the case of white jitter. Because J_D is based on a difference of adjacent samples in a J_P sequence, its power spectrum is expected to be a high-pass-filtered version of the power spectrum of J_P. Therefore, if J_P has a low-pass spectrum, the power spectrum of J_D is essentially flat.

[1]The present study is restricted to the time-domain implementation (TD-PSOLA), although a frequency-domain variant was also proposed (FD-PSOLA; Charpentier and Moulines, 1989). PSOLA/TD is a registered trademark of France Telecom.

[2]Klatt (1980) proposed an implementation of the formant filters for a 10-kHz sample rate. Using higher sample rates, 32 kHz in experiment I and 48 kHz in experiment II, results in a stronger rolloff of the spectrum to higher frequencies, due to the periodic nature of the discrete spectrum. This rolloff was compensated for by applying a ''correction formant filter'' twice (center frequency 5 kHz, bandwidth 2.2 kHz), for both sample rates. In this way, the magnitude of the transfer functions for the 10-kHz and the 32-(48-) kHz implementations differed by no more than 1 dB. Because the phase-transfer function of a Klatt formant filter is approximately linear for frequencies remote from the resonance frequency, the phase characteristic in the region of the ''true'' formants is preserved.

[3]By using a sampling rate of 48 kHz, the sampling interval is approximately 21 μs, which corresponds to approximately 0.21% of the period for an $F0$ of 100 Hz.

[4]Horii (1980) defined mean rectified jitter as

$$\mathrm{MR}(J) = \frac{1}{N-1}\sum_{i=1}^{N-1} |T_i - T_{i-1}|,$$

where T_i is the ith period duration. Mean rectified shimmer was defined as

$$\mathrm{MR}(S) = \frac{20}{N-1}\sum_{i=1}^{N-1} \left|\log_{10}\frac{A_i}{A_{i-1}}\right|,$$

where A_i denotes the waveform peak in the ith period.

[5]The sample rate of the perturbation sequence is assumed to correspond to $F0$.

Askenfelt, A., and Hammarberg, B. (**1986**). ''Speech waveform perturbation analysis: a perceptual-acoustical comparison of seven measures,'' J. Speech Hear. Res. **29**, 50–64.

Cardozo, B. L., and Ritsma, R. J. (**1968**). ''On the perception of imperfect periodicity,'' IEEE Trans. Audio Electroacoust. **16**, 159–164.

Charpentier, F., and Moulines, E. (**1989**). ''Pitch-synchronous waveform processing techniques for text-to-speech synthesis using diphones,'' in *EUROSPEECH'89, Paris*, Vol. 2, pp. 13–19.

Cranen, B. (**1997**). Personal communication.

Darwin, C. J. (**1984**). ''Perceiving vowels in the presence of another sound: Constraints on formant perception,'' J. Acoust. Soc. Am. **76**, 1636–1647.

Dau, T., Kollmeier, B., and Kohlrausch, A. (**1997**). ''Modeling auditory processing of amplitude modulation. II. Spectral and temporal integration,'' J. Acoust. Soc. Am. **102**, 2906–2919.

Dunn, H. K., and White, S. D. (**1940**). ''Statistical measurements on conversational speech,'' J. Acoust. Soc. Am. **11**, 278–288.

Eddins, D. A. (**1993**). ''Amplitude modulation detection of narrow-band noise: Effects of absolute bandwidth and frequency region,'' J. Acoust. Soc. Am. **93**, 470–479.

Florentine, M., and Buus, S. (**1981**). ''An excitation-pattern model for intensity discrimination,'' J. Acoust. Soc. Am. **70**, 1646–1654.

Gagné, J., and Zurek, P. M. (**1988**). ''Resonance-frequency discrimination,'' J. Acoust. Soc. Am. **70**, 1646–1654.

Green, D. M., and Swets, J. A. (**1966**). *Signal Detection Theory and Psychophysics* (Wiley, New York).

Hamon, C., Moulines, E., and Charpentier, F. (**1989**). ''A diphone synthesis system based on time-domain prosodic modifications of speech,'' in *Proceedings of the IEEE International Conference on Acoustics Speech and Signal Processing*, Glasgow (IEEE, New York), Vol. 3, pp. 238–241.

Hillenbrand, J. (**1987**). ''A methodological study of perturbation and additive noise in synthetically generated voice signals,'' J. Speech Hear. Res. **30**, 448–461.

Hillenbrand, J. (**1988**). ''Perception of aperiodicities in synthetically generated voices,'' J. Acoust. Soc. Am. **83**, 2361–2371.

Horii, Y. (**1980**). ''Vocal shimmer in sustained phonation,'' J. Speech Hear. Res. **23**, 202–209.

Houtgast, T. (**1989**). ''Frequency selectivity in amplitude-modulation detection,'' J. Acoust. Soc. Am. **85**, 1676–1686.

Klatt, D. H. (**1980**). ''Software for a cascade/parallel formant synthesizer,'' J. Acoust. Soc. Am. **67**, 971–995.

Klatt, D. H. (**1982**). ''Prediction of perceived phonetic distance from critical-band spectra: a first step,'' in *Proc. IEEE ICASSP-82*, Vol. 2, pp. 1278–1281.

Klatt, D. H., and Klatt, L. C. (**1990**). ''Analysis, synthesis, and perception of voice quality variations among female and male talkers,'' J. Acoust. Soc. Am. **87**, 820–857.

Klaus, H., Fellbaum, K., and Sotscheck, J. (**1997**). ''Auditive Bestimmung und Vergleich der Sprachqualität von Sprachsynthesesystemen für die deutsche Sprache,'' Acust. Acta Acust. **83**, 124–136.

Klingholz, F., and Martin, F. (**1985**). ''Quantitative spectral evaluation of shimmer and jitter,'' J. Speech Hear. Res. **28**, 169–174.

Kortekaas, R. W. L., and Kohlrausch, A. (**1997**). ''Psychoacoustical evaluation of the pitch-synchronous overlap-and-add speech-waveform manipulation technique using single-formant stimuli,'' J. Acoust. Soc. Am. **101**, 2202–2213.

Levitt, H. (**1971**). ''Transformed up-down methods in psychoacoustics,'' J. Acoust. Soc. Am. **49**, 467–477.

Lieberman, P. (**1961**). ''Perturbation in vocal pitch,'' J. Acoust. Soc. Am. **33**, 597–603.

Lyzenga, J. (**1997**). ''Discrimination of simplified vowel spectra,'' Ph.D. thesis, Rijksuniversiteit Groningen, Groningen, The Netherlands.

Lyzenga, J., and Horst, J. W. (**1997**). ''Frequency discrimination of stylized synthetic vowels with a single formant,'' J. Acoust. Soc. Am. **102**, 1755–1767.

Macmillan, N. A., and Creelman, C. D. (**1991**). *Detection Theory: A Users Guide* (Cambridge U.P., Cambridge).

Moulines, E., and Charpentier, F. (**1990**). ''Pitch-synchronous waveform processing techniques for text-to-speech synthesis using diphones,'' Speech Commun. **9**, 453–467.

Moulines, E., and Laroche, J. (**1995**). ''Non-parametric techniques for pitch-scale and time-scale modification of speech,'' Speech Commun. **16**, 175–205.

Neelen, J. J. M. (**1969**). ''Audibility of jitter in pulse trains as affected by filtering—II,'' in *IPO Annual Progress Report*, Vol. 4, pp. 23–29.

Patterson, R. D., Nimmo-Smith, I., Holdsworth, J., and Rice, P. (**1987**). ''An efficient auditory filterbank based on the gammatone function,'' in *Appendix B of SVOS Final Report: The Auditory Filterbank*, Vol. APU, report 2341.

Pinto, N. B., and Titze, I. R. (**1990**). ''Unification of perturbation measures in speech signals,'' J. Acoust. Soc. Am. **87**, 1278–1289.

Pisoni, D. B. (**1980**). ''Variability of vowel formant frequencies and the quantal theory of speech: a first report,'' Phonetica **37**, 285–305.

Pollack, I. (**1971a**). ''Amplitude and time jitter thresholds for rectangular-wave trains,'' J. Acoust. Soc. Am. **50**, 1133–1142.

Pollack, I. (**1971b**). ''Spectral basis of auditory 'jitter' detection,'' J. Acoust. Soc. Am. **50**, 556–558.

Roucos, W., and Wilgus, A. M. (**1985**). ''High quality time-scale modification for speech,'' in *Proc. IEEE ICASSP-85*, Vol. 2, pp. 493–496.

Rozsypal, J., and Millar, B. M. (**1979**). ''Perception of jitter and shimmer in synthetic vowels,'' Journal of Phonetics **7**, 343–355.

Schoentgen, J., and De Guchteneere, R. (**1997**). ''Predictable and random components of jitter,'' Speech Commun. **21**, 255–272.

Sommers, M. S., and Kewley-Port, D. (**1996**). ''Modeling formant frequency discrimination of female words,'' J. Acoust. Soc. Am. **99**, 3770–3781.

Wakefield, G. H., and Viemeister, N. F. (**1990**). ''Discrimination of modulation depth of sinusoidal amplitude modulation (SAM) noise,'' J. Acoust. Soc. Am. **88**, 1367–1373.

Zwicker, E. (**1952**). ''Die Grenzen der Hörbarkeit der Amplitudenmodulation und der Frequenzmodulation eines Tones,'' Acustica **2**, AB125–AB133.

Generation of partials due to nonlinear mixing in a stringed instrument

Harold A. Conklin, Jr.
P.O. Box 1915, Dunedin, Florida 34697

(Received 15 April 1997; revised 8 June 1998; accepted 29 September 1998)

Nonlinear mixing appears to account for the production of ''phantom partials'' in piano tones. ''Phantom partials'' are those that appear at frequencies exactly harmonic to normal inharmonic string partials, and at frequencies equal to the sums of the frequencies of normal inharmonic partials. Nonlinear mixing can occur because tension varies during transverse vibration. This produces longitudinal string forces of phantom-partial frequency that appear at the soundboard bridge and are coupled to the soundboard. ''Phantom partials'' were found in piano tones, in the motion of a piano bridge, in the longitudinal vibrations of a monochord string, in the acoustical output of a soundboard coupled to a monochord string, and in the acoustical output of a guitar. Any plucked-string or struck-string instrument having appreciable acoustical response to longitudinal string forces could be expected to produce phantom partials. The relation in frequency between phantom partials and normal partials, which varies with inharmonicity, may play a part in differentiating the timbre of tones at the same fundamental frequency in pianos of different size and design. © *1999 Acoustical Society of America.* [S0001-4966(99)03401-3]

PACS numbers: 43.75.Mn [WJS]

INTRODUCTION

The author has reported finding unexpected partials, which he called ''phantoms,'' in the acoustical spectra of piano tones.[1] Reference 1 includes a 2.1–2.9 kHz spectrum, showing normal partials 13-17 of the tone E3 from a 1.32-m vertical piano. Phantom partials appear slightly below the frequencies of the normal partials. ''Even'' phantoms occurred at frequencies exactly equal to twice the frequency of a normal inharmonic partial. ''Odd'' phantoms were found at frequencies equal to the sum of the frequencies of a pair of normal inharmonic partials. Phantom partials were found in other stringed instruments. Figure 1 is a 1–2. 6-kHz acoustical spectrum showing normal inharmonic partials 13 through 29 from a six-string acoustic guitar. The open E2 string was plucked. Eight phantom partials, identified by dots, appear. Figure 2 is a 1.5–3.1-kHz spectrum showing normal partials 20–38 of the tone D#2 from a compact disc acoustical recording of an orchestral harp.[2] Four partials, tentatively identified as ''even'' phantoms, are shown with dots. Phantom partials appear plainly in a piano tone spectrum recently published in the Journal of the Acoustical Society of America,[3] though the authors of the paper did not comment about them.

I. MONOCHORD TEST I

A monochord was used to search for phantoms in a simple system. The string was a steel piano wire 1.24 mm in diameter. A strip of softwood 38×6 cm, 3.9 mm thick served as a soundboard. A pianolike maple bridge piece 6×4×3.7 cm was glued to the soundboard at 11.7 cm from one end. Each end of the soundboard was glued to a 2×4×14-cm maple cross member that was clamped to the monochord frame rails. The bridge/soundboard assembly was positioned to establish a speaking length of 1.047 m, about the same as for the E3 string of the 1.32-m piano. The string continued about 1 m beyond the bridge to a hitch pin. The section between the bridge and the hitch pin was muted. A condenser microphone was placed approximately 1 cm over the soundboard. A PCB model 303A03 miniature accelerometer was glued to the side of the bridge, 1 cm below the string, and oriented for sensitivity to bridge motion in the direction of the string. A velocity-responsive electrostatic pickup was located 8.4 cm from the end of the speaking length opposite the bridge and was oriented for maximum sensitivity to transverse string motion normal to the soundboard. The string was tuned to 100 Hz at a tension of about 414 N. The first mode of the bridge–soundboard assembly was at 72 Hz.

Spectra (880–1280 Hz) were taken from the microphone, the accelerometer, and the electrostatic pickup, as the string was plucked at 15.2 cm (L/7) from the speaking length end opposite the bridge. Figure 3 shows microphone output. Normal partials 9 through 12 (numbered) appear with accompanying phantom partials. The accelerometer output showed normal partials and prominent phantoms at the same frequencies but at different relative amplitudes. Peak longitudinal bridge acceleration in this range was 0.49 g, for partial 12 at 1.231 kHz. The spectrum from the electrostatic pickup (Fig. 4), simultaneous with Fig. 3, has normal partials at the same frequencies, but only a small response to phantom partials. These results showed that phantom partials can occur in a simple system, and indicated that they are transmitted to the bridge and soundboard primarily by longitudinal rather than by transverse string forces.

II. MONOCHORD TEST II

In a test to simulate the production of ''even'' phantoms, a 1.24-mm steel piano wire of 1.177-m speaking length, resonant at 75 Hz at about 295 N static tension, was driven transversely at its center at 10 Hz. Figure 5 shows the

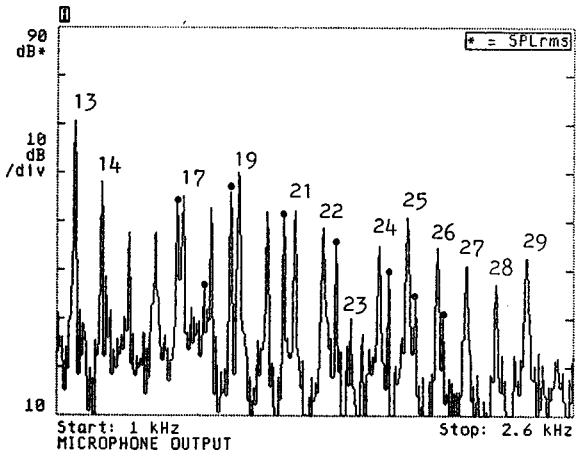

FIG. 1. Acoustical spectrum, 1–2.6 kHz, showing normal partials 13–29 of the tone E2 from a six-string acoustic guitar. Eight phantom partials are shown with dots.

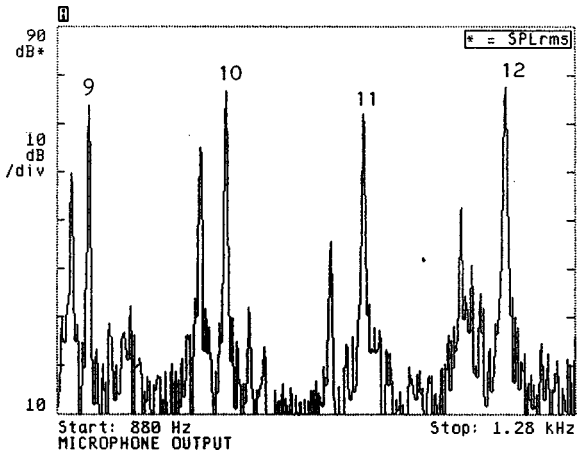

FIG. 3. Microphone output spectrum (880–1280 Hz) showing normal partials 9–12 (numbered) and accompanying phantom partials for the monochord string. String was plucked at L/7.

setup. Peak center displacement was measured with a special micrometer. A force pickup at the hitch-pin end sensed the corresponding tension variation. The string was driven at frequencies far below its first transverse mode so as not to excite normal string modes. The driver (*V*) was an MB model C11-D electrodynamic vibration exciter equipped with an independent velocity sensing coil (VS) that allowed the waveform of string motion to be monitored and its distortion measured. The driver was connected to the string at the center of its speaking length via a maple dowel (DR), 0.8 m long and 9.3 mm in diameter. At one end of its speaking length, the string was attached with three 2.1-mm-diam steel bridge pins to a maple bridge piece (*B*), 58 mm wide, 38 mm deep, and 37 mm high. There was no soundboard. The bridge was constrained longitudinally and laterally only by the string itself. To prevent vertical bridge motion as the string was driven transversely in a vertical plane at its center, a maple dowel (CR) 12.7 mm in diameter and 1.3 m long was glued into the bottom of the bridge piece and attached at its lower end to a 3-kg steel mass (*W*) that rested on the floor.

The string continued 0.9 m beyond the bridge to a PCB model 086B01 quartz force sensor (FS) that supported the static string tension and provided an output voltage directly proportional to varying string tension. The force sensor was bolted to a steel block attached to the monochord frame. The span of string between the bridge and the force sensor was heavily damped to prevent random transverse excitation of this segment so that only longitudinal string forces would be transmitted to the force sensor. An electrostatic pickup (EP), 2.5 cm from the end of the speaking length opposite the bridge piece, having an electrode 19 mm in diameter, spaced approximately 6 mm from the string and polarized at 200 V dc, monitored transverse string displacement to insure that there were no extraneous modes.

Center displacement and end force were measured at several different vibration levels as the string was driven sinusoidally at 10 Hz. The result can be described by

$$f_t = 0.0972 d^2, \tag{1}$$

where f_t is the tension end force in Newtons and d is the center displacement in mm. Simultaneous ''input'' and ''output'' waveforms are shown in Fig. 6. At the top is the waveform of 10-Hz string center motion (from the shaker velocity coil). Total distortion measured less than 0.5%. Be-

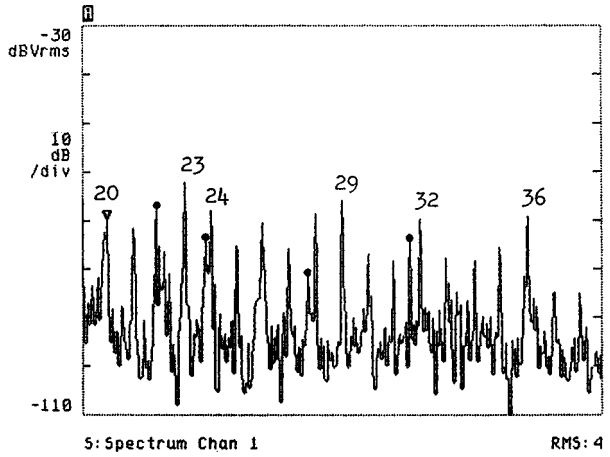

FIG. 2. Spectrum, 1.5–3.1 kHz, showing normal partials 20–38 of the tone D#2 from a compact disc recording of an orchestral harp. Four phantom partials are shown with dots.

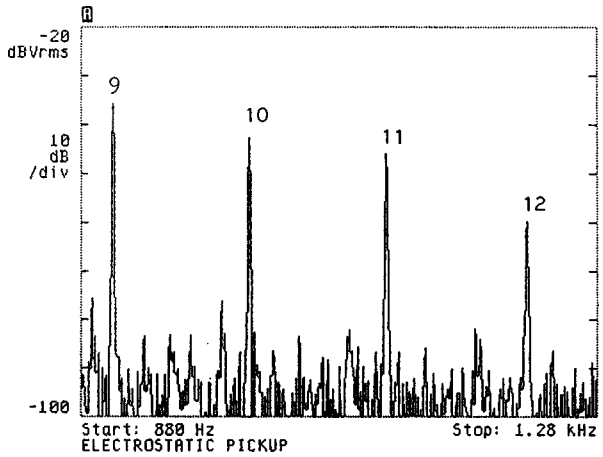

FIG. 4. Electrostatic pickup output spectrum (880–1280 Hz), simultaneous with Fig. 3. Pickup responds to transverse string motion, has low response to phantom partials.

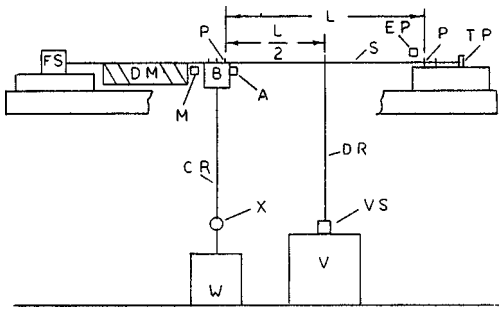

FIG. 5. Setup for monochord tests II, III, and IV. A=accelerometer. B=bridge piece. CR=connecting rod. DM=damping material. DR=drive rod. EP=electrostatic string pickup. FS=tension-force sensor. L=speaking length, 1.177 m. Hitch length=0.9 m. (M)=microphone. P=speaking length terminating points. S=string, 1.24 mm in diameter. TP=tuning pin. (V) =driver. VS=velocity sensing coil. W=3 kg mass. (X)=disconnect point.

low is the tension end force waveform, a rather good sine wave at 20 Hz. (The 10-Hz component was 26.2 dB below the 20-Hz component.) Peak end force was 1.26 N for a peak center displacement of 3.6 mm. (Force sensor sensitivity was 10.2 mv/N.) Frequency doubling, simulating the production of even phantoms, occurred because deflection of the center of the string from its rest position, whether up or down, produced an increase in string tension. If, with the driver turned off, the string did not rest precisely at its neutral position, then the output from the end-force sensor, when the string was driven sinusoidally, contained a component at the driving frequency.

III. NONLINEAR MIXING

If the string in Monochord Test II is considered to be an unknown device that receives an input motion $d=(A\ \sin \omega t)$, produces an output force $f(t)$ at a frequency $2\omega t$, and has a square-law transfer curve, it evidently operates according to Eq. (2) to produce frequency doubling:

$$f(t)=kd^2=k(A\ \sin\ \omega t)^2=k(A^2/2)(1-\cos 2\omega t). \quad (2)$$

If the input sine wave decayed exponentially, the output force would be given by Eq. (3), showing that the decay rate

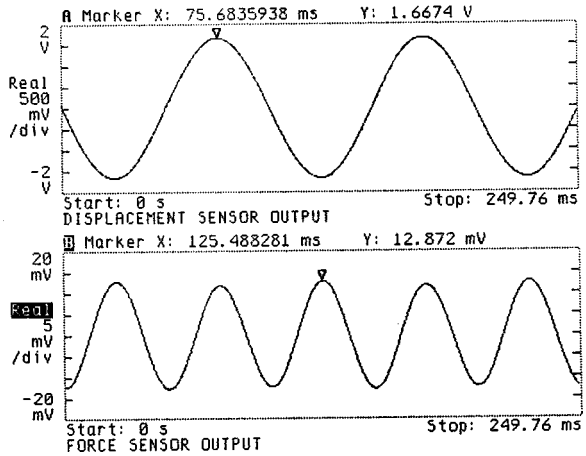

FIG. 6. Top: Waveform of 10-Hz string center-motion, 3.6-mm peak. Distortion measured less than 0.5%. Bottom: Simultaneous tension-force waveform at hitch pin end, 1.26-N peak, essentially sinusoidal at 20 Hz.

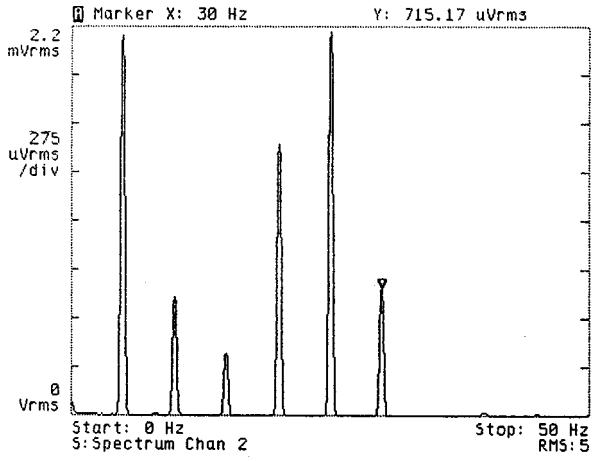

FIG. 7. Spectrum of tension end force with center of string driven simultaneously at 10 and 15 Hz. Displacement at 15 Hz was 0.694 times displacement at 10 Hz. Components at 5, 20, 25, and 30 Hz conform closely to Eq. (4). Following are values in rms millivolts from Fig. 8, followed by values predicted by Eq. (4): 5 Hz: 2.14, 2.13; 10 Hz: 0.668, 0; 15 Hz: 0.350, 0; 20 Hz: 1.53, 1.53; 25 Hz: 2.17, 2.13; 30 Hz: 0.715, 0.738.

of an ''even'' phantom will be twice that of the parent partial:

$$f(t)=k(Ae^{-at}\ \sin\ \omega t)^2=k(A^2e^{-2at}/2)(1-\cos 2\omega t). \quad (3)$$

When two frequencies are put into such a device, generation of harmonics and also sum and difference frequencies will occur according to Eq. (4):

$$\begin{aligned} f(t)=kd^2&=k(A\ \sin\ \omega_1 t+B\ \sin\ \omega_2 t)^2 \\ &=k[A^2\ \sin^2\ \omega_1 t+2AB(\sin\ \omega_1 t\ \sin\ \omega_2 t) \\ &\quad +B^2\ \sin^2\ \omega_2 t] \\ &=k\{(A^2/2)(1-\cos 2\omega_1 t)+[AB(\cos\ \omega_1-\omega_2)t \\ &\quad -\cos(\omega_1+\omega_2)t]+(B^2/2)(1-\cos 2\omega_2 t)\}. \end{aligned} \quad (4)$$

IV. MONOCHORD TEST III

To simulate the production of ''odd'' phantoms, the string was driven simultaneously at its midpoint at 10 and 15 Hz. (The velocity at 15 Hz measured 4.1% greater than that at 10 Hz, making displacement at 15 Hz equal 0.694 times that at 10 Hz.) Figure 7 is the resulting tension end-force spectrum. The relative amplitudes at 5, 20, 25, and 30 Hz agree with those predicted from Eq. (4) with a maximum error (at 30 Hz) of 3.19%. The string and its associated elements appear to function as a mechanical analog of electronic circuits known as mixers,[4] thereby acting nonlinearly to generate tension forces not only at twice the input frequencies but also an at frequencies equal to their sum and difference. The fact that 10- and 15-Hz energy appeared in the tension force though not in Eq. (4) indicates that the string did not rest exactly at its neutral position with zero excitation.

Equation (5) gives the result of mixing nonlinearly two parent partials having independent decay rates. The resulting ''odd'' phantom partials will have decay rates equal to the sums of the decay rates of the parents:

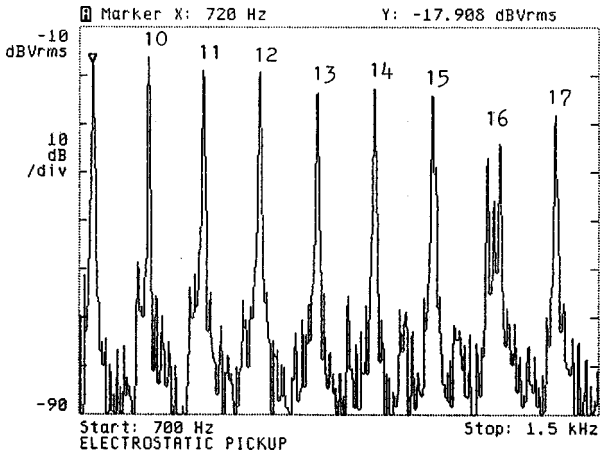

FIG. 8. Spectrum (700–1500 Hz) from electrostatic pickup showing normal partials 9–17. Phantom partials are nearly absent. String plucked at 5.5 cm.

$$f(t)=k\{(A^2/2)(e^{-2at})(1-\cos 2\omega_1 t)+ABe^{-(a+b)}\times[\cos(\omega_1-\omega_2)t-\cos(\omega_1+\omega_2)t]+(B^2/2)(e^{-2bt})(1-\cos 2\omega_2 t)\}. \quad (5)$$

With the noted exception due to neutral position imbalance, and with accuracy in decay rate measurement limited, test results appeared to confirm the predictions of Eqs. (2) through (5).

V. OTHER MONOCHORD TESTS

Tests were made to confirm that a plucked string in the setup of Fig. 5. would produce phantom partials. A miniature microphone (M) was mounted 5 mm behind the bridge for monitoring acoustical output due to bridge motion. A PCB model 303A03 accelerometer (A) was glued to the side of the bridge, 1 cm below the string, and oriented for sensitivity to bridge motion in the direction of the string. The string was tuned approximately to D#2 (77.8 Hz, static tension about 317 N). Drive rod (DR) was removed. Connecting rod (CR) was disconnected from the 3-kg weight, giving a vertical system resonance at about 12 Hz. Plucking, at 5.5 cm from the end of the speaking length, was controlled to keep the output of the electrostatic pickup constant within ±0.5 dB.

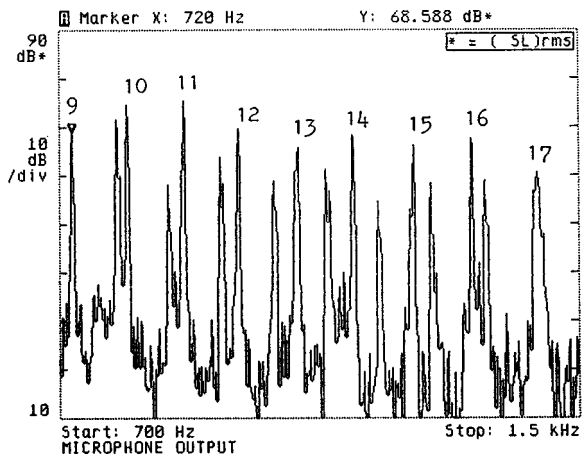

FIG. 9. Spectrum (700–1500 Hz) from microphone showing normal partials 9–17 (numbered). Phantom partials are prominent. String plucked at 5.5 cm.

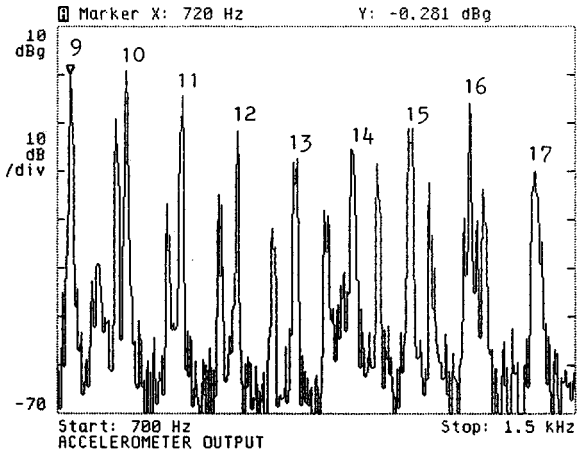

FIG. 10. Spectrum (700–1500 Hz) from accelerometer showing normal partials 9–17. Phantom partials are prominent. Accelerometer was oriented for response to bridge motion in direction of string. String plucked at 5.5 cm.

Figures 8 through 11 show spectra in the range 700–1500 Hz from the electrostatic pickup, the microphone, the accelerometer, and the force sensor. Normal partials 9–17 are numbered. All sensors but the electrostatic pickup show prominent phantom partials. The electrostatic pickup was nearly insensitive to phantom partials because it responded primarily only to transverse string motion.

Figures 12 and 13 show the outputs of the electrostatic pickup and the force sensor in the range 20 Hz to 6.42 kHz. Attenuation of partials 8, 16, 24, etc., can be seen in both figures because the string was plucked at L/8. Despite this, the tension end-force output shows *peaking* near partial 24, in the 2-kHz region, around the frequency of the first longitudinal mode of the speaking length. In pianos, response to longitudinal string forces is known to exist and is evidenced by a tonal accentuation at the frequencies of the longitudinal modes.[5–10] In Fig. 13, the peak near partial 4, around 300 Hz, was due to a flexural resonance of connecting rod (CR), which was free at its lower end during this test.

To confirm the nonlinear amplitude relation of phantom partials to normal partials, the monochord string was excited to different vibration levels by plucking at 5.5 cm (L/21). A

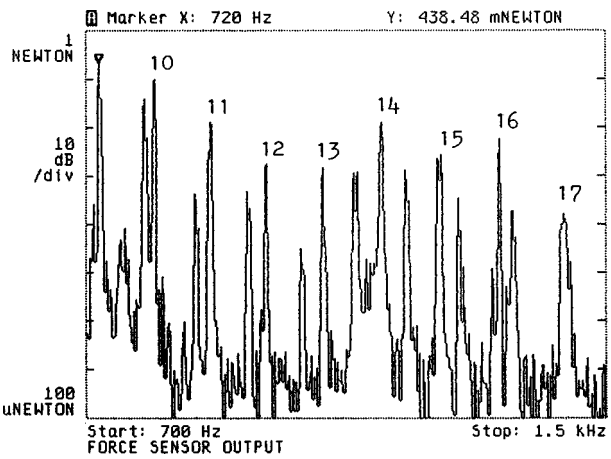

FIG. 11. Spectrum (700–1500 Hz) from end-force sensor showing normal partials 9–17 and phantom partials. String plucked at 5.5 cm.

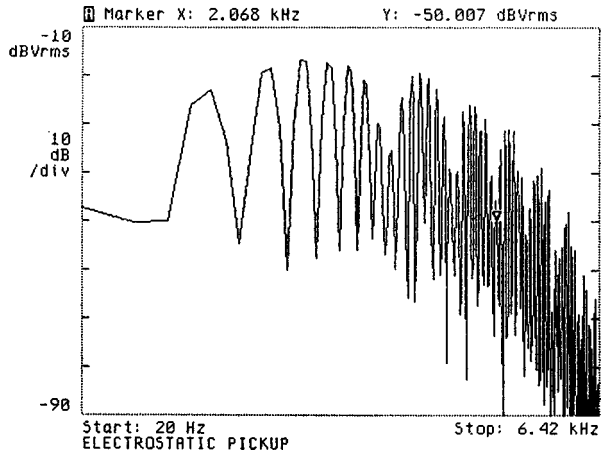

FIG. 12. Spectrum (20 Hz–6.42 kHz) from electrostatic pickup. String plucked at L/8.

microphone output spectrum (380–1180 Hz) was recorded at each level. Normal partial 5 was used as a reference. Figure 14 shows the initial sound-pressure level in dB of each of several phantom partials, plotted versus the initial sound-pressure level of normal partial 5. The phantom partials are identified with the number of the normal partial nearest each one. The top line in Fig. 14 shows the slope for linear response. The bottom line shows the slope for $y=x^2$.

An ''even'' phantom partial could be eliminated or greatly attenuated if the string was plucked at a nodal point for the parent partial. An ''odd'' phantom partial could be eliminated or greatly attenuated if the string was plucked at a nodal point for either parent partial. This appears consistent with generation by nonlinear mixing.

VI. BASEBAND SPECTRA FOR 1.32-m PIANO

Figure 15 is a 0–3.2-kHz acoustical spectrum showing normal partials 1–18 of the tone E3 from the 1.32-m piano. Full scale corresponds approximately to 89-dB sound level. Figure 16 shows acceleration on the bass bridge, normal to the soundboard, near the strings of E3. Figure 17 shows acceleration at the same point but in the direction of the strings. The piano, with normal felt hammers, was played with a

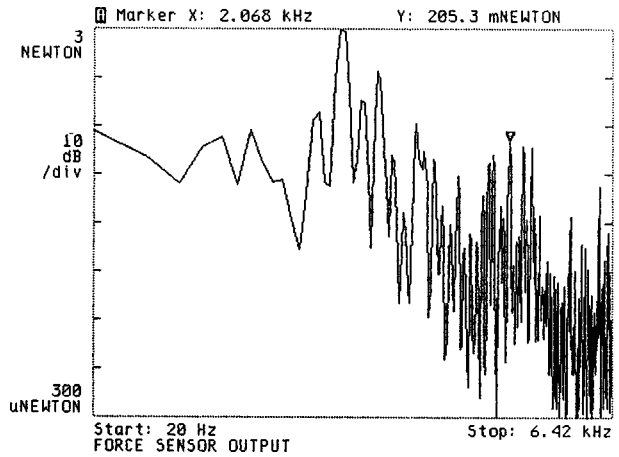

FIG. 13. Spectrum (20 Hz–6.42 kHz) from tension-force sensor. String plucked at L/8. Peaks around 2 kHz occurred in vicinity of longitudinal mode of speaking length.

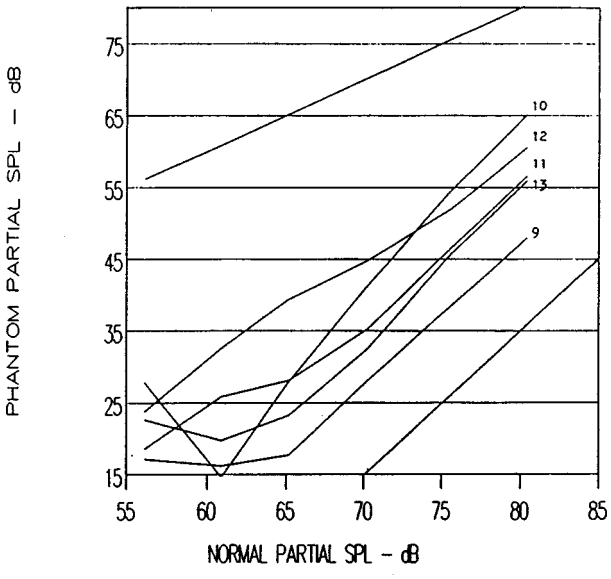

FIG. 14. Amplitude nonlinearity of phantom partials from D#2 monochord string. Sound-pressure level in dB of phantom partials versus sound-pressure level in dB of normal partial 5. Top line shows slope for linear response, bottom line slope for $y=x^2$. Numbers identify normal partial nearest to phantom.

mechanical finger at the same forte level for all three figures. A prominent ''odd'' phantom at 2.488 kHz accompanies normal partial 15 in each. Full scale in Figs. 16 and 17 corresponds approximately to 2.3-g peak. Peak acceleration in the direction of the strings (Fig. 17) was 1.74 g at 2.488 kHz, (near the frequency of the first longitudinal mode, which was at about 2.4 kHz), and occurred for a sum phantom larger in amplitude than the adjacent normal partial. Peak acceleration at the same frequency but normal to the soundboard (Fig. 16) was 0.035 g, 33.8 dB less. Phantoms accompanying lower-numbered normal partials were not separately resolvable at this bandwidth.

Multiple phantoms accompanying a low-numbered normal partial will be closely spaced in frequency and may appear in a test spectrum to be a single phantom. The following are computed frequencies for phantoms between partials 10

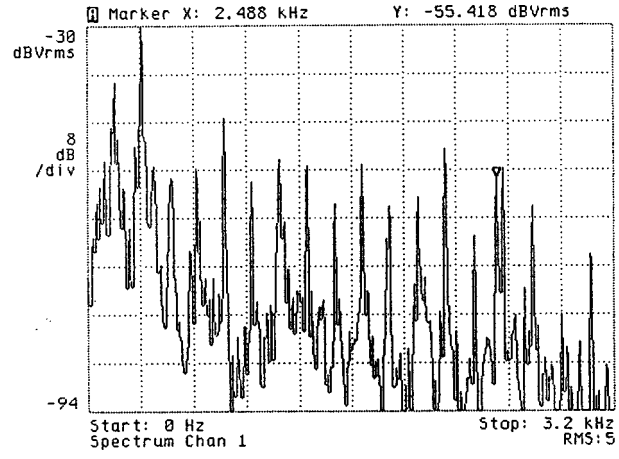

FIG. 15. Acoustical spectrum (0–3.2 kHz) showing normal partials 1–18 of tone E3 from a 1.32-vertical piano. Note large phantom partial at 2.488 kHz. Full scale corresponds to about 89 dB sound-pressure level. Key was played ''forte'' with a mechanical finger.

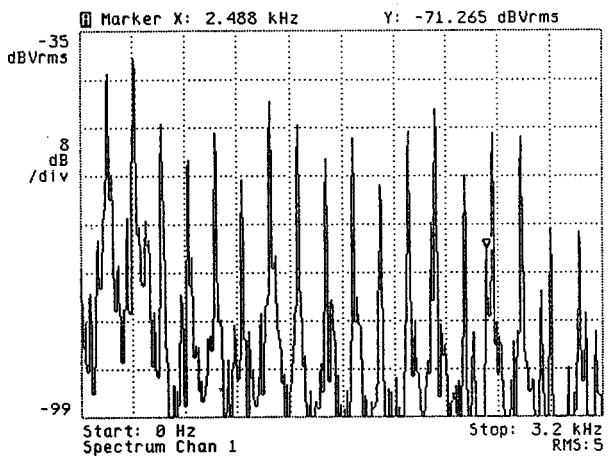

FIG. 16. Spectrum (0–3.2 kHz) from accelerometer on bridge of 1.32-m vertical piano near strings of E3. Accelerometer was oriented for sensitivity to bridge motion normal to soundboard. Key was played with mechanical finger as for Fig. 15. Note low level of phantom partials. Full scale = 2.3 g peak. Peak acceleration at 2.488 kHz was 0.035 g.

and 11 of E3 of the 1.32-m piano: Par. 10: 1664.27 Hz; Pars. 5+6: 1818.47; Pars. 4+7: 1819.53; Pars. 3+8: 1821.66; Pars. 2+9: 1824.86; Pars. 1+10: 1829.08; Par. 11: 1834.40. All five cluster in a 10.61-Hz band, the most distant, 15.93 Hz below partial 11, the nearest, 5.32 Hz below. Cluster width and distance increase with inharmonicity. (E3 had strings of 1.24-mm diameter, 1.044-m speaking length, and about 1120-N tension.)

VII. SPECTRAL EFFECTS—SMEARING

It is well known that piano tones are somewhat inharmonic due to the finite stiffness of the strings,[11,12] and that the frequency f_n of the nth transverse partial can be predicted by

$$f_n = n f_0 (1 + B n^2)^{0.5}, \tag{6}$$

where f_0 would be the fundamental frequency of a string without stiffness and (B) is a coefficient of inharmonicity.[13]

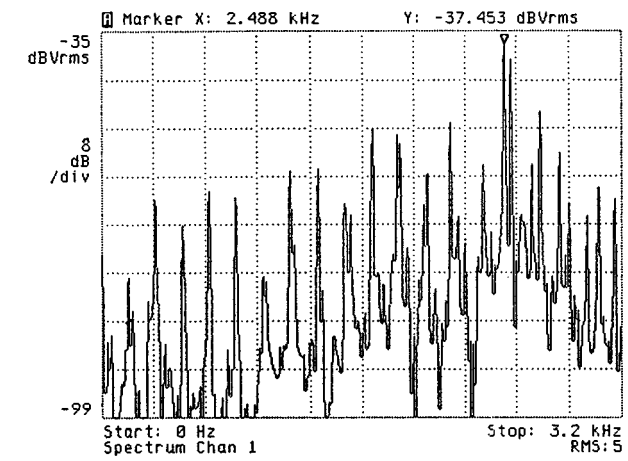

FIG. 17. Spectrum (0–3.2 kHz) from accelerometer on bridge of 1.32-m vertical piano near strings of E3. Accelerometer was oriented for sensitivity to bridge motion in direction of strings. Note prominent phantom partials. Key was played with mechanical finger as for Figs. 15 and 16. Full scale =2.3 g peak. Peak acceleration at 2.488 kHz was 1.74 g.

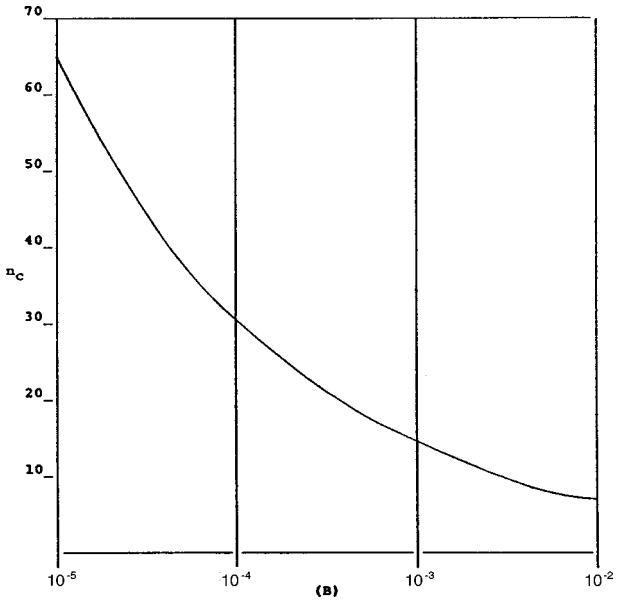

FIG. 18. Curve showing (n_c) in relation to inharmonicity coefficient (B). (n_c) is the smallest numbered normal transverse partial at which frequency coincidence with a phantom partial can occur.

Accordingly, the frequency space between adjacent normal partials increases with both mode number and (B). As defined by Fletcher *et al.*,

$$B = \pi^3 E d^4 / 64 L^2 T, \tag{7}$$

where T is the tension, d the diameter, L the length, and E the Young's modulus of the material.[14]

For a given string, phantom-to-normal-partial frequency separation increases with transverse mode number until a phantom lies equidistant between two normal partials. For still higher modes, separation *decreases* and phantom partials approach frequency coincidence with the normal partial next lower in frequency. The value of (B) determines the number (n_c), of the least-numbered normal partial at which coincidence with a phantom can occur. Figure 18 shows the relation between (B) and (n_c). Above (n_c), phantoms may appear throughout the interpartial frequency space. Phantom partials cause spectral smearing. The degree of smearing increases with both (B) and (n).

Figures 19 and 20, simultaneous spectra from accelerometer (A) and electrostatic pickup (EP), illustrate spectral smearing in the monochord setup of Sec. V. Accelerometer (A) was sensitive to phantom partials. Electrostatic pickup (EP), responsive primarily only to transverse string motion, had little sensitivity to phantoms. The string was tuned to D#2 and plucked at 5.5 cm (L/21). (B) was 5.47×10^{-4}, giving n_c near partial 18. The figures show the range 2.03–2.43 kHz, with normal partials numbered 23–26. Output from the accelerometer shows severe smearing. This could be expected to have an audible counterpart.

VIII. DISCUSSION

Previous papers have considered nonlinearity in stretched strings. Oplinger[15] studied the forced vibration of an elastic string theoretically and experimentally. He found tension variation during vibration to be an important source

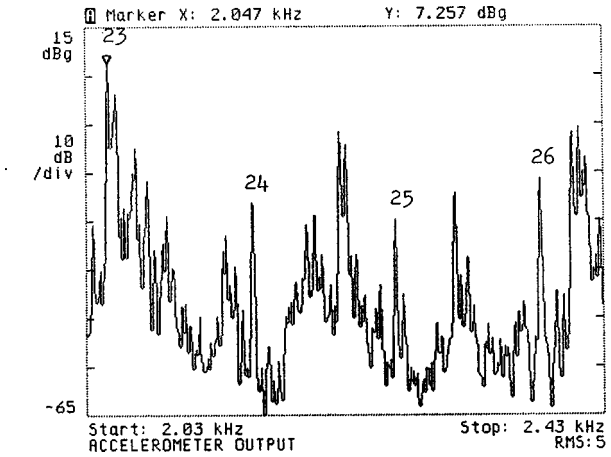

FIG. 19. Spectrum (2.03–2.43 kHz) from bridge accelerometer, illustrating spectral smearing due to phantom partials. Normal partials 23–26 are numbered. (B) was 5.47×10^{-4}.

of nonlinearity. He drove a nylon string at one end with a variable-frequency vibration generator and found that the tension variation took on large values as the system approached resonance.

Legge and Fletcher[16] studied, theoretically and experimentally, the nonlinear transfer of energy among modes of different frequencies on a vibrating string. They found that energy could be transferred from existing normal modes to an initially missing normal mode provided that at least one of the end supports had finite mechanical admittance. They conclude as follows: ''Two different situations emerge from the analysis. If the non-rigid bridge has zero admittance parallel to the string length and if the string is fixed simply to it, then the only nonlinear processes tending to mix modes or to generate missing modes are of third order.''[17] (Author's comment: In pianos, a condition of zero bridge admittance in the direction of the string would be anomalous. However, if phantom partials are generated by nonlinear mixing, it would seem that they could exist with zero bridge admittance in the direction of the strings, even though transmission to the soundboard might be negligible.) ''On the other hand, if the bridge is a non-rigid support over which the string passes at an angle as in many musical instruments, then there is an additional second-order nonlinearity which provides driving forces at frequencies that are twice those of any modes present on the string.'' This second conclusion supports the production of ''even'' phantoms, but only in cases where the string crosses the bridge at an angle. It does not appear to support the production of ''odd'' phantoms. The existence of oscillatory components of the tension is noted by Legge and Fletcher, but their analysis appears to consider only bridge forces that would be normal to the soundboard in a piano. However, a referee extended the calculations of Legge and Fletcher to conclude that any sum and difference frequency components in the tension would be 80 dB lower than the octave components. These conclusions appear at odds with the results reported herein: *Tension* forces at twice modal frequencies were found in the absence of a ''bearing'' angle, ''odd'' phantoms were found at amplitudes equal to or greater than those of ''even'' phantoms, and Fig. 11 shows measured sum tension components *similar* in amplitude to octave components. Though the described monochord systems simulate only crudely the conditions in pianos, it is believed that a probable mechanism for the generation of phantom partials has been demonstrated.

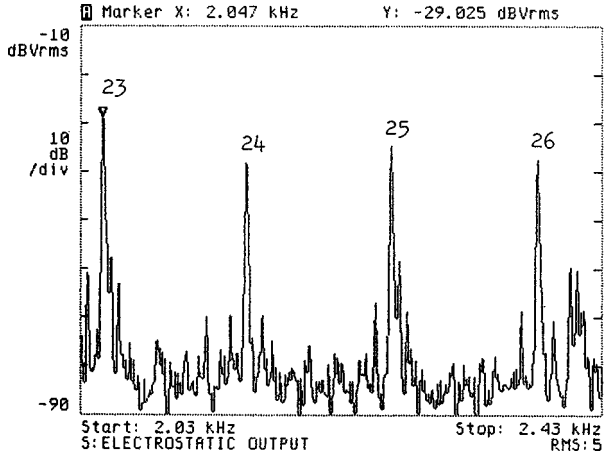

FIG. 20. Spectrum (2.03–2.43 kHz) from electrostatic pickup, simultaneous with Fig. 19. Spectral smearing is minimal because primary response of pickup was to transverse string motion only. Normal partials 23–26 are numbered.

A. Tonal effects

Nonlinear mixing in audio amplifiers causes undesirable intermodulation distortion.[18–20] It is of interest to discover whether phantom partials contribute significantly to the perceived quality of piano tones; to find whether they cause tonal degradation, tonal enhancement, or neither; to find if they are significant to identifying a tone as a piano tone; and to learn how their audible effect, if any, varies with the size, design, and hammer condition of pianos.

Because of their amplitude nonlinearity in relation to normal partials, phantom partials will be most prominent at the onset of a piano tone. It is well known that, with increasing hammer velocity, the high-frequency partials of piano tones become more prominent in relation to the low-frequency partials, causing the tone to become brighter as well as louder. This is due to the nonlinear properties of felt piano hammers[21–28] which, because of their hardness gradient (softer on the outside, harder within[29]) become effectively harder as the velocity at impact with the strings increases. Phantom partials, due to *their* amplitude nonlinearity, may contribute audibly to the onset transient and may augment the brightness increase due to the felt.

An assured effect of phantom partials is the production of beats. Beat rates between normal partials and phantom partials, and between phantom partials of different parentage, will be determined by inharmonicity, which is a function of piano size and scale design, and by fundamental frequency. Under most conditions, beats cause a ''roughened'' tone quality. In some conditions beats may enhance a tone. The audibility of beats due to phantom partials will depend on their amplitude, frequency, and duration, in relation to the other tonal components.

The effect of inharmonicity on the *tuning* of pianos is

TABLE I. Typical values of inharmonicity coefficient (B), least numbered partial (n_c) for coincidence with a phantom partial, and first longitudinal mode frequency, for selected keys of 2.74- and 0.91-m pianos.

Key	Piano	(B)	n_c	Freq.	L.M. freq.	Nearest partial	Par. freq.
A0	2.74-m	1.02×10^{-4}	31	893	440	16	446
	0.91-m	5.64×10^{-4}	18	538	577	19	573
C2	2.74-m	4.91×10^{-5}	39	2644	929	14	920
	0.91-m	2.13×10^{-4}	24	1663	977	15	1004
D#2	Monochrd	5.47×10^{-4}	18	1519	2152	24	2141
E3	2.74-m	1.51×10^{-4}	27	4688	2430	15	2514
	1.32-m	1.97×10^{-4}	25	4366	2432	14	2351
	0.91-m	1.49×10^{-4}	27	4686	2064	12	1999
G3	2.74-m	2.15×10^{-4}	24	4986	2894	14	2801
	0.91-m	6.15×10^{-4}	17	3616	3679	17	3616
C4	2.74-m	3.39×10^{-4}	21	5891	3839	14	3783
	0.91-m	5.11×10^{-4}	18	5084	4252	15	4141
A4	2.74-m	7.20×10^{-4}	17	8222	6161	13	6058
	0.91-m	7.58×10^{-4}	16	7693	6406	14	6602
A7	2.74-m	1.67×10^{-2}	7	33 211			
	0.91-m	1.37×10^{-2}	7	31 853			

well established.[30,31] The questions of whether inharmonicity influences the *quality* of piano tones and, if so, how, presently have contrary answers. In 1943, Schuck and Young suggested that inharmonicity is undesirable because the subjective fundamentals derived from the differences in frequency between successive inharmonic partials do not have the same frequency, resulting in ''confusion in the ear.''[32] In 1952, Young[33] proposed as an ''attractive hypothesis'' that ''Those pianos are 'best' in which the inharmonicity is least and in which it changes smoothly.'' In 1962, Fletcher *et al.* concluded that inharmonicity is responsible for a ''warmth'' of piano tones that is pleasing to the listener, and that ''the partials below middle C must be inharmonic in frequency to be piano-like.''[34] In 1987, Reinholdt, Janssen, and Askenfelt presented computer-generated tones having constant fundamental frequency but continuously varying inharmonicity.[35] The perception of this listener was that the apparent pitch of the tones clearly increased with increasing inharmonicity but that the quality did not otherwise greatly change. In 1997, Galembo and Cuddy reported that varying the inharmonicity of computer-generated piano tones through the range normally found in real pianos produced only marginal audible difference in tone quality as judged by a panel of listeners.[36] During a subsequent ASA paper[37] they presented recorded A0 tones from a small vertical piano having $(B)=5.6 \times 10^{-4}$ in comparison with a computer-generated A0 piano tone having a similar spectral formant but $(B)=1.6\times 10^{-4}$. A third recorded tone was A0 from a 2.74-m Steinway grand having $(B)=1.6\times 10^{-4}$. The real and synthesized small vertical piano tones, from a tape recording lent by them to this author, sound nearly alike. The tone from the 2.74-m grand sounds unmistakably different.

The author's experience indicates that inharmonicity plays a significant part in defining the timbre of piano tones. Small pianos of any manufacture usually have a quality of tone clearly different in the lower third of the compass from that of large pianos. One important reason for this is that larger pianos normally have more output and more uniform response at low and medium frequencies due to their greater soundboard size. The tonal differences that appear related to inharmonicity seem to lie at higher frequencies. That the shorter bass strings of small pianos usually have greater inharmonicity than the longer strings of large pianos is indisputable. The question is whether the inharmonicity differences have an audible effect, and whether the effect, if any, is due to inharmonicity alone.

Real piano tones from the lower half of the keyboard seem to become less agreeable with increasing inharmonicity. Convincing demonstrations of this require that strings of differing inharmonicity but the same fundamental frequency be installed in the same scale region of the same piano and compared. Other factors being equal, the string with the lowest inharmonicity usually sounds best. The author, though not an advocate of zero inharmonicity in pianos, found this result repeatedly in designing and testing piano strings.

Table I gives values of (B) and n_c, and frequencies for n_c and for the first longitudinal mode (LM), computed for the same keys of a 2.74-m concert grand and a 0.91-m spinet piano, for E3 of the 1.32-m vertical, and for the D#2 string as used in the monochord tests. Though at E3 the inharmonicity of the 0.91-m spinet is slightly less than that of the concert grand, few of sound musical ear would judge, on comparing the tones, that the spinet sounds as good as the concert grand: the spinet is less loud and has less energy in low- and medium-frequency partials.

For the 0.91-m spinet, it is seen that the inharmonicity of G3 is more than four times that of E3. Though G3 and E3 had strings on the same bridge, only a few cm apart, and did not differ widely in loudness, a timbre difference was obvious. Note that for G3 the coincidence partial (n_c) and the

longitudinal mode coincide in frequency, placing the peak-producing longitudinal mode in a region of potentially high spectral smearing. Listeners usually agreed that E3 sounded noticeably better than G3. (E3 had two wrapped strings with smaller core wire at higher tension, while G3 had three plain strings that were larger in diameter and 18.7 cm shorter than those in the 2.74-m grand.) In a second example, D2 strings of a 2.82-m grand having 1.88-m speaking length and $(B)=9.6\times10^{-5}$ were replaced by strings having $(B)=4.39\times10^{-5}$. The tone was judged to be significantly improved.

Using the setup of Sec. V, a realistic sounding reference tone derived from a digitally sampled concert grand piano was compared with the tone from electrostatic pickup (EP), the tone from tension-force sensor (FS), and the tone from accelerometer (A). Fundamental frequencies were at D#2. (B) for the tone from the large grand piano was about 4.9×10^{-5}. (B) for the monochord string was 5.47×10^{-4}. All three identically inharmonic tones from the monochord sounded different from the piano tone and had slightly higher apparent pitch. Though it did not sound at all like the piano, the tone from the electrostatic pickup did not have the expected ''less agreeable'' quality. Its spectrum showed no phantom partials of significant amplitude. The tones from tension-force sensor (FS) and from accelerometer (A) did contain phantom partials, and did have a less agreeable quality.

IX. CONCLUSION

It is suggested that any struck- or plucked-stringed instrument having appreciable acoustical response to longitudinal string forces may be expected to produce phantom partials. It is suggested that phantom partials, coacting with inharmonicity and with the peaking of both phantom and normal partials at and around the frequencies of longitudinal string modes, may produce some of the timbral differences that distinguish pianos of different design. It is suggested that phantom partials may be responsible in part for a less agreeable quality in the bass tones from small pianos.

ACKNOWLEDGMENTS

The author is most grateful for helpful discussions in correspondence with Alexander Galembo, and for helpful comments from Gabriel Weinreich.

APPENDIX: DETERMINING PARENTAGE

''Odd'' phantom partials seemed to come predominantly from parent normal partials having consecutive mode numbers (e.g., 5+6 rather than 3+8). Lower-numbered partials would normally be associated with larger string deflections. In pianos, partial 8 and its multiples may be attenuated because hammers in the lower compass normally strike the strings at around one-eighth of the speaking length. The frequencies of all partials decrease slightly from beginning to end of a piano tone due to the small gradual reduction of average tension, creating an additional measurement difficulty.

Two narrow-band tunable filters (wave analyzers) were used to verify the double-frequency exactness of ''even'' phantoms. The first filter was tuned to the phantom at frequency f. The second filter was tuned to the suspected parent normal partial at $f/2$. The output of each filter was sent to a different input of a two-channel oscilloscope whose sweep was triggered from $f/2$. Exact frequency doubling was confirmed if both waveforms appeared stationary on the oscilloscope screen. This method compensated for frequency drift of partials due to changes in average string tension. The first filter, if tuned slightly sharp, could respond to the nearest normal inharmonic partial, whose waveform would appear to precess.

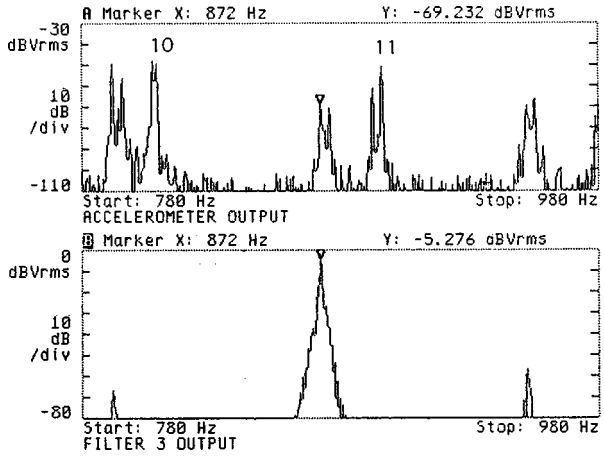

FIG. A1. Spectra (780–980 Hz) illustrating use of a two-channel digital analyzer plus three analog filters to identify the parents of close-spaced phantom partials. Top: Channel 1 shows two phantoms (872 and 875.5 Hz) below partial 11. Bottom: Channel 2 shows output of a filter (see text) tuned to the sum of partials (5+6). Partials (3+8) were the parents of the phantom at 975.5 Hz.

Sum-frequency exactness was tested with four narrow-band filters. Filter (1) was tuned to the frequency of one suspected parent partial and filter (2) to the other. Their outputs were combined linearly and sent to a diode distortion-generating circuit (D) that produced sum and difference frequencies. Output from (D) was sent to filter (3), which was tuned to select that distortion product at the sum frequency of the suspected parent partials. Output from (3) was applied to one channel of the two-channel oscilloscope and used to trigger its sweep. Filter (4) was tuned to the phantom in question and its output applied to the second oscilloscope channel. Confirmation that the partials from filters (1) and (2) were the parents of the phantom from filter (4) was obtained if the output waveform from (4), as well as that from (3), appeared stationary.

The 3-Hz minimum bandwidth of analog filters limited the usefulness of the above method for determining the parents of multiple phantoms close in frequency. An alternate method used a two-channel digital analyzer, adjusted for 0.5-Hz frequency increments, to supplement filters (1), (2), and (3). Figure A1 (top) shows normal partials 10 and 11 from a monochord string. Prominent phantoms appear below partial 11 at 872 and 875.5 Hz. Figure A1 (bottom) shows the simultaneous output of filter (3), which was tuned to the sum frequency of partials 5 and 6. This sum is shown to coincide in frequency with the 872-Hz phantom, confirming that partials 5 and 6 are the parents. Partials 3 and 8 were found to be the parents of the phantom at 875.5 Hz.

[1] H. A. Conklin, Jr., ''Piano strings and 'phantom' partials,'' J. Acoust. Soc. Am. **102**, 659 (1997).
[2] K. Allvin (harpist) (Woodland Music CD 40012, 1995), Bach Suite in E-flat Major, opening E-flat.
[3] N. Giordano and A. J. Korty, ''Motion of a piano string: Longitudinal vibrations and the role of the bridge,'' J. Acoust. Soc. Am. **100**, 3899–3908 (1996). See Fig. 9, p. 3906, the spectrum from the microphone.
[4] See, for example, P. Horowitz and W. Hill, *The Art of Electronics* (Cambridge U.P., New York, 1989), pp. 885–886.
[5] A. F. Knoblaugh, ''The clang tone of the pianoforte,'' J. Acoust. Soc. Am. **16**, 102 (1944).
[6] H. A. Conklin, Jr., U.S. Patent No. 3,532,480, ''Longitudinal Mode Tuning of Stringed Instruments'' (1970).
[7] T. Kanagisawa, K. Nakamura, and I. Shirayanagi, ''Longitudinal vibration and inharmonic tone of piano string—vibration analysis of piano string and sound board by finite element method (II),'' J. Acoust. Soc. Jpn. **33**, 412–416 (1977) (in Japanese with English abstract).
[8] H. A. Conklin, Jr., ''Tuning the longitudinal mode of piano strings,'' J. Acoust. Soc. Am. Suppl. 1 **73**, S84 (1983).
[9] M. Podelsak and A. R. Lee, ''Longitudinal vibrations in piano strings,'' J. Acoust. Soc. Am. Suppl. 1 **81**, S61 (1987).
[10] M. Podelsak, ''Dispersion of waves in piano strings,'' J. Acoust. Soc. Am. **83**, 305–317 (1988) (see pp. 313–316).
[11] R. S. Shankland and J. W. Coltman, ''The departure of the overtones of a vibrating wire from a true harmonic series,'' J. Acoust. Soc. Am. **10**, 161–166 (1939).
[12] P. M. Morse, *Vibration and Sound* (McGraw-Hill, New York, 1948), 2nd ed., Chap. IV, pp. 166–170.
[13] H. Fletcher, E. D. Blackham, and R. Stratton, ''Quality of piano tones,'' J. Acoust. Soc. Am. **34**, 749–761 (1962).
[14] P. M. Morse, *Vibration and Sound* (McGraw-Hill, New York, 1948), 2nd. ed., p. 757.
[15] D. W. Oplinger, ''Frequency response of a nonlinear stretched string,'' J. Acoust. Soc. Am. **32**, 1529–1538 (1960).
[16] K. A. Legge and N. H. Fletcher, ''Nonlinear generation of missing modes on a vibrating string,'' J. Acoust. Soc. Am. **76**, 5–17 (1984).
[17] D. W. Oplinger, ''Frequency response of a nonlinear stretched string,'' J. Acoust. Soc. Am. **32**, 12 (1960).
[18] J. K. Hilliard, ''Distortion tests by the intermodulation method,'' Proc. IRE **29**, 614–620 (1941).
[19] W. J. Warren and W. R. Hewlett, ''An analysis of the intermodulation method of distortion measurement,'' Proc. IRE **36**, 457–466 (1948).
[20] S. J. Aagard, ''An improved method for the measurement of nonlinear audio distortion,'' IRE Trans. Audio **AU-6**, 121 (1958).
[21] T. Yanagisawa and K. Nakamura, ''Dynamic compression characteristics of piano felt,'' J. Acoust. Soc. Jpn. **40**, 725–729 (1984) (in Japanese).
[22] D. E. Hall, ''Piano string excitation in the case of small hammer mass,'' J. Acoust. Soc. Am. **79**, 141–147 (1986).
[23] D. E. Hall, ''Piano string excitation II: General solution for a hard narrow hammer,'' J. Acoust. Soc. Am. **81**, 535–546 (1987).
[24] D. E. Hall, ''Piano string excitation III: General solution for a soft narrow hammer,'' J. Acoust. Soc. Am. **81**, 547–555 (1987).
[25] D. E. Hall and A. Askenfelt, ''Piano string excitation V: Spectra for real hammers and strings,'' J. Acoust. Soc. Am. **83**, 1627–1638 (1988).
[26] A. Askenfelt and E. Jansson, ''From touch to string vibrations,'' in *Five Lectures on the Acoustics of the Piano*, edited by A. Askenfelt (Royal Swedish Academy of Music, Stockholm, 1990).
[27] D. E. Hall, ''The hammer and the string,'' in *Five Lectures on the Acoustics of the Piano*, edited by A. Askenfelt (Royal Swedish Academy of Music, Stockholm, 1990).
[28] A. Askenfelt and E. Jansson, ''From touch to string vibrations. I: Timing in the grand piano action,'' J. Acoust. Soc. Am. **88**, 52–62 (1990); **90**, 2383–2393 (1991); **93**, 1–16 (1993).
[29] H. A. Conklin, Jr., ''Design and tone in the mechanoacoustic piano. Part I: Piano hammers and tonal effects,'' J. Acoust. Soc. Am. **99**, 3286–3296 (1996).
[30] O. L. Railsback, J. Acoust. Soc. Am. **9**, 274 (1938); **10**, 86 (1938).
[31] O. H. Schuck and R. W. Young, ''Observations on the vibrations of piano strings,'' J. Acoust. Soc. Am. **15**, 1–11 (1943).
[32] O. L. Railsback, J. Acoust. Soc. Am. **9**, 7 (1938).
[33] R. W. Young, ''Inharmonicity of plain wire piano strings,'' J. Acoust. Soc. Am. **23**, 267–273 (1952).
[34] P. M. Morse, *Vibration and Sound* (McGraw-Hill, New York, 1948), 2nd ed., pp. 749, 758, 761.
[35] A. Reinholdt, E. Jansson, and A. Askenfelt, ''Analysis and synthesis of piano tone,'' J. Acoust. Soc. Am. Suppl. 1 **81**, S61 (1987).
[36] A. Galembo and L. Cuddy, ''String inharmonicity and the timbral quality of piano bass tones: Fletcher, Blackham and Stratton (1962) revisited,'' paper given 1 Aug. 1997 at the 3rd U.S. Conference on Music Perception and Cognition, Cambridge, MA, 31 July–3 Aug. (1997).
[37] A. Galembo and L. Cuddy, ''Large grand versus small upright pianos: Factors of timbral difference,'' J. Acoust. Soc. Am. **102**, 3107(A) (1997).

Acoustic behavior of chimney pipes

Servaas J. J. M. F. Kokkelmans
Technische Universiteit Eindhoven, W & S 0.54, Postbus 513, 5600 MB Eindhoven, The Netherlands

Marc-Pierre Verge[a)]
Laboratoire d'Acoustique Musicale CNRS, Université de Paris VI, Ministère de la Culture, 4, Place Jussieu, case 161, 75252 Paris Cedex 05, France

A. Hirschberg, A. P. J. Wijnands, and R. L. M. Schoffelen
Technische Universiteit Eindhoven, W & S 0.54, Postbus 513, 5600 MB Eindhoven, The Netherlands

(Received 6 October 1997; accepted for publication 16 September 1998)

The objective of this work is to study the acoustic behavior of chimney organ pipes. The working hypothesis is that its role is to reinforce the fifth harmonic of the tone of a stopped pipe. According to Helmholtz, the chimney should have the length of an open pipe resonating at the frequency of the fifth harmonic. This design appears to be the least favorable one, except if the chimney is placed half inside and half outside the main pipe, and should therefore be avoided. The ratio of the modulus of the admittance of the different harmonics appears to describe, for the chimney pipe used in this study, the dependency of the ratio of the measured amplitude of the fifth, third, and first harmonic with the geometry of the chimney. The admittance curve can therefore be used to determine the effects of the geometry of the chimney on the timbre of the organ pipe. This result is used in order to determine the optimal diameter of the chimney as a function of its length. © *1999 Acoustical Society of America.* [S0001-4966(99)01401-0]

PACS numbers: 43.75.Np [WJS]

INTRODUCTION

A chimney pipe or ''rohrflöte,'' illustrated in Fig. 1, is obtained by inserting in the cover of a stopped organ pipe a small cylindrical tube or ''chimney'' open at both of its extremities. The length L_c, the diameter D_c, and the position of the chimney may vary, giving the organ builder a wide range of parameters in order to adjust the timbre of the instrument. This is well described by Dom Bedos[1] who writes: ''One observes that the proportions of the chimney pipes are exactly the same as that of stopped pipes; hence it is very easy to transform them in chimney pipes; one only has to add a chimney on the cover. The wider the chimney the taller it should be; and the narrower it is the shorter it must be. The widest have a diameter equal to half of that of the main pipe. In these cases it must be almost as tall as the main pipe. Some organ makers give them a diameter equal to only a quarter or an eighth of that of the main pipe, they are then proportionally much smaller. The wider and taller the chimney is, the more the harmony approaches that of an open pipe; the narrower and shorter it is, the more the harmony approaches that of a closed pipe. Hence in the choice of a stopped or open pipes, one can obtained the desired tone.''

In a survey of rohrflöte registers Oosterhof and Bouman[2] describe an evolution from the XVth to the XIXth century toward pipe proportions, both for the body and the chimney, which we found to correspond to an optimization of the quality factor of these pipes as stand-alone resonators. Bouman also observes a richer sound due to the reinforcement of the third and fifth harmonics in comparison with a stopped pipe. According to these authors, the chimneys are usually placed outside the main pipe and have a length L_c varying between 1/5 and 2/5 of the length L_p of the main pipe. They consider these data on the length of the chimney to constitute an upper bound, since the chimneys are usually cut down during intonation. These rules remain, however, rather general and discussions with craftsmen indicate that they feel uncertain about the design of the chimney, which calls for some research on this topic.

Scientific investigation on the role of chimneys was initiated by Bernoulli.[3] Helmholtz[4] confirms that the role of chimneys is to reinforce the fifth harmonic and therefore concludes that the optimal design should be that of an open pipe resonating at that frequency. This leads to a chimney having a length $L_c = 2L_p/5$, where the length of the chimney should include an end correction, as will be discussed later. Audsley[5] quotes theoretical works by Gerhardt,[6] which for narrow chimneys confirm the design rule of Helmholtz and suggests a ratio $D_c/D_p = 1/4$. Audsley further notes that chimneys can be placed quite indifferently either outside on the top of the cover or totally inside the main pipe, implying that the position of the chimney should affect neither the harmony of the pipe nor its tuning.

Of course Bouasse[7] disagrees with Helmholtz and states that the chimney causes polyphony, the simultaneous emis-

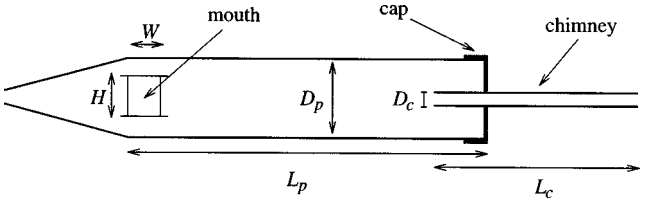

FIG. 1. Geometry of a typical chimney-flue organ pipe.

[a)]Electronic mail: mpv@ccr.jussieu.fr

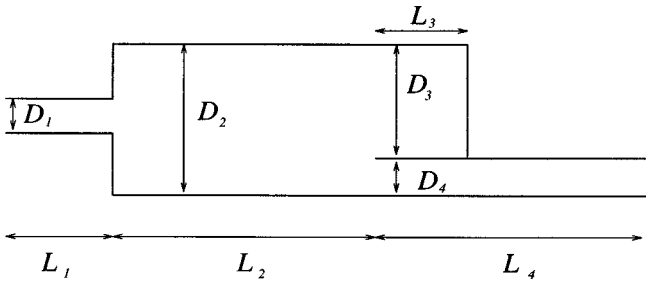

FIG. 2. One-dimensional acoustic model of a chimney pipe.

sion of nonharmonic tones. Castellengo[8] did extensive experimental work on chimney pipes and proposes an analysis of the influence of the different parameters of the chimney geometry on the fundamental oscillation frequency and partials of the system. Her measurements contradict the conclusions of Bouasse. She states that polyphony can be obtained for very specific excitation conditions, but never observed it in organ making. She confirms that the main role of the chimney is to influence the timbre of the pipe by varying the relative amplitude of the different harmonics, both during steady state and the attack transient, and that, as stated by Dom Bedos[1] and Oosterhof and Bouman,[2] the choice is a matter of taste. In addition to the classical design, she also considered the effect of placing the chimney partially inside and outside the main pipe, and observed important timbre variations.

The working hypothesis will be that the role of the chimney is to enhance the amplitude of the fifth harmonic in the spectrum of a stopped pipe. A simple analysis indicates that, for this purpose, the only design which should be avoided is that proposed by Helmholtz[4] and Gerhardt.[6] We will explain this by considering the admittance experienced by the sound source in the mouth of the instrument. We will use a simple low-frequency approximation of the steady-sound field for the calculation of this admittance. Some results can already be understood, however, in terms of standing-wave patterns of frictionless nonradiating pipes. Measurements obtained from two pipes provided by different organ makers confirm the theoretical analysis. Some preliminary results concerning an optimal choice of the diameter of the chimney and on the attack transient will also be presented.

I. EXPERIMENTAL PIPE

The measurements presented in this paper were performed on a typical Dutch C_2 sharp (138 Hz) chimney pipe having a length $L_p = 607$ mm, a diameter $D_p = 58.3$ mm, and terminated by an adjustable cap in order to test chimneys of various geometries. The mouth width H and the distance W between the flue exit and the labium are 46.0 and 17.6 mm, respectively. Ears, 14-mm high, are placed on each side of the mouth. The original chimney has a length $L_c = 124.7$ mm, a diameter $D_c = 14.1$ mm, and is placed completely inside the main pipe. For this particular pipe, the craftsman used a driving pressure $p_f = 54$ mm H_2O. The measurements were obtained from a 1/4-inch B&K microphone placed 20 cm in front of the mouth and connected to a spectrum analyzer. Radiation from the chimney appears to contribute usually less than 30% of the sound production from the pipe, and it radiates at most as much as the mouth.

II. AN ACOUSTICAL MODEL OF CHIMNEY PIPES

Assuming plane-wave propagation, the chimney pipe illustrated in Fig. 1 can be modeled by means of the simplified configuration shown in Fig. 2. The chimney is a tube of length L_4 and cross section $S_4 = \pi D_c^2/4$ inserted in the main pipe of length $L_2 + L_3$, where L_3 varies depending on the position of the chimney ($L_4 \geqslant L_3 \geqslant 0$). The tube L_3 is closed by the cap at its extremity and has a cross section $S_3 = S_2 - S_4$, where $S_2 = \pi D_2^2/4$ is the cross section of the main pipe. The mouth of the pipe is represented by a pipe segment of length L_1 with a cross section S_1 equal to that of the mouth. This length L_1 is determined by a contribution associated with sound radiation, a second associated with the effects of the constriction of the mouth, and a third one due to the presence of ears around the mouth. The value of L_1 is

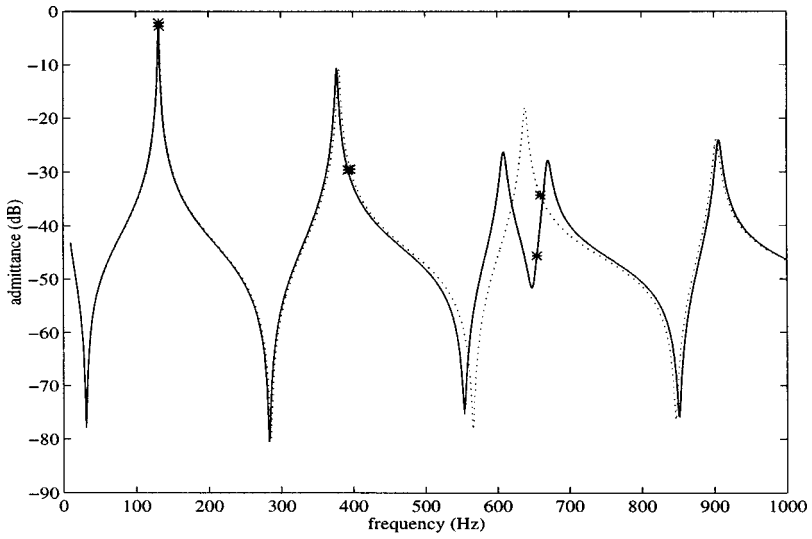

FIG. 3. Calculated admittance of a chimney pipe having a chimney made according to Helmholtz's rule ($L_c = \lambda_0/10 = 266$ mm $D_c = 14.0$ mm, $D_p = 58.3$ mm) for two different positions of the chimney (chimney completely out of the main pipe: bold line, chimney in the halfway position: dotted line). The stars indicate the position of the different harmonics ($f_0, 3f_0, 5f_0$) where the fundamental f_0 is assumed to be determined by the maximum of the admittance curve. (This is Fig. 2 from Verge *et al.*, 1997. Reproduced with the permission of the authors.)

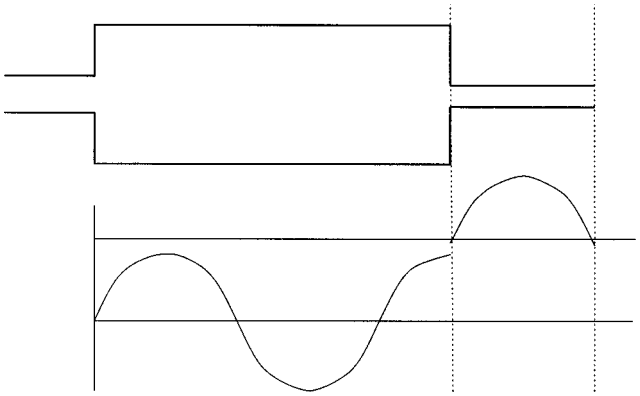

FIG. 4. Standing-wave pattern for a chimney placed completely outside the main pipe.

chosen so that the first resonance peak of the admittance curve, calculated with the geometry of the original pipe and chimney, coincides with the nominal fundamental frequency of the pipe. In the rest of this study, when varying the geometry of the system, the fundamental frequency f_0 will also be assumed to coincide with the maximum of the admittance curve. This of course implies, when comparing with measurements performed in playing conditions, that the driving pressure is reasonably well adjusted. Finally, volume flow and pressure continuity is assumed at the different interfaces.

Visco-thermic dissipation in the different tubes is taken into account by the use of a complex wave number k[9]

$$k^{\pm}=\frac{\omega}{c_0}\pm\sqrt{\frac{\omega}{2}}\frac{\alpha}{r_p}(1-i), \tag{1}$$

with α a damping coefficient given by

$$\alpha=\frac{\sqrt{l_v}+(\gamma-1)\sqrt{l_t}}{\sqrt{c_0}}, \tag{2}$$

where ω is the angular frequency, c_0 is the speed of sound, r_p is the radius of the tube, l_v, and l_t are the viscous and thermal characteristic lengths (in air at 20 °C, $l_v=4.0\times10^{-8}$ m, and $l_t=5.6\times10^{-8}$ m) and γ is the Poisson constant, i.e, the ratio of specific heats at constant pressure and volume, respectively ($\gamma=1.4$). Sound radiation at both open extremities of the system is estimated by using the following expression of the radiation impedance Z_r[10]

$$Z_r=\rho_0 c_0\left(\tfrac{1}{4}(kr_p)^2+ik\Delta l\right), \tag{3}$$

where $\Delta l=0.6D_4/2$ is an end correction. In the calculations, the pipe of length L_4 was assumed to include an end correction only at its extremity radiating toward the exterior of the system. At the other extremity, due to continuity of flow and pressure, there is no distortion of the acoustic streamlines unless the acoustic field has a much larger amplitude in the chimney than in the main pipe. We will see further that in common designs, the standing wave in the chimney has the same amplitude for the fifth harmonic in the chimney and in the main pipe.

III. THE HELMHOLTZ DESIGN

According to Helmholtz, the role of the chimney is to reinforce the fifth harmonic. He consequently proposes to use a chimney having its first resonance on the fifth harmonic of the system oscillating with a wavelength $\lambda_0=c_0/f_0$. This leads to a chimney length L_c given by[4]

$$2L_c=\frac{\lambda_0}{5}. \tag{4}$$

The position of the chimney relative to the cap is, however, not specified by Helmholtz. Common practice is to place the chimney either completely outside or inside the main pipe. This is confirmed by Audsley[5] as discussed in the Introduction.

It appeared from our initial measurements on an ($L_p=607$ mm and $D_p=58.3$ mm) pipe that such a design ($L_c=266$ mm, $D_c=14$ mm) does not reinforce the fifth harmonic in comparison with a closed-pipe configuration. In fact, a chimney with such a length would reinforce the fifth

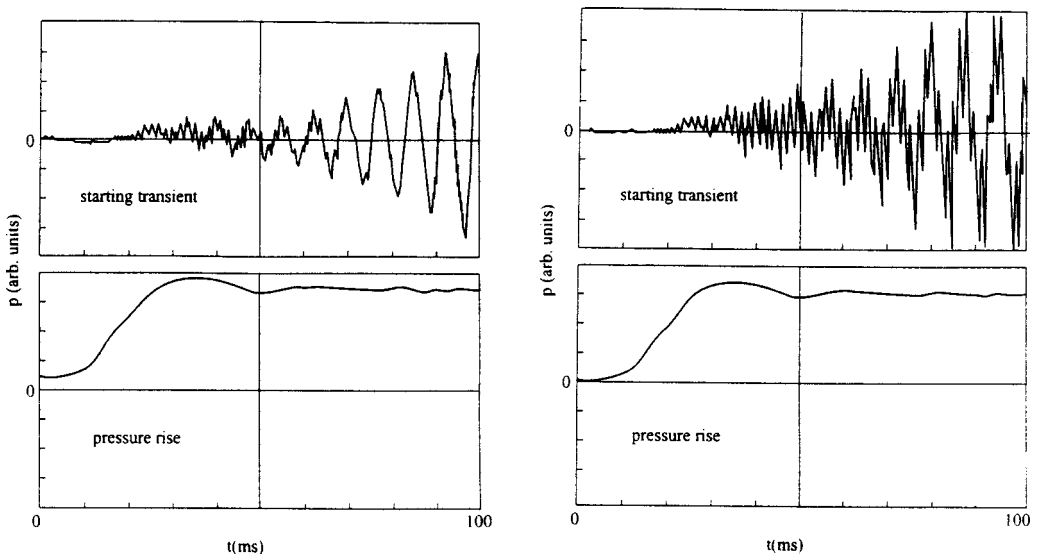

FIG. 5. Attack transient of a chimney pipe having a length $L_c=2/5L_p$: (a) chimney placed completely outside the main pipe; (b) chimney placed halfway outside the main pipe.

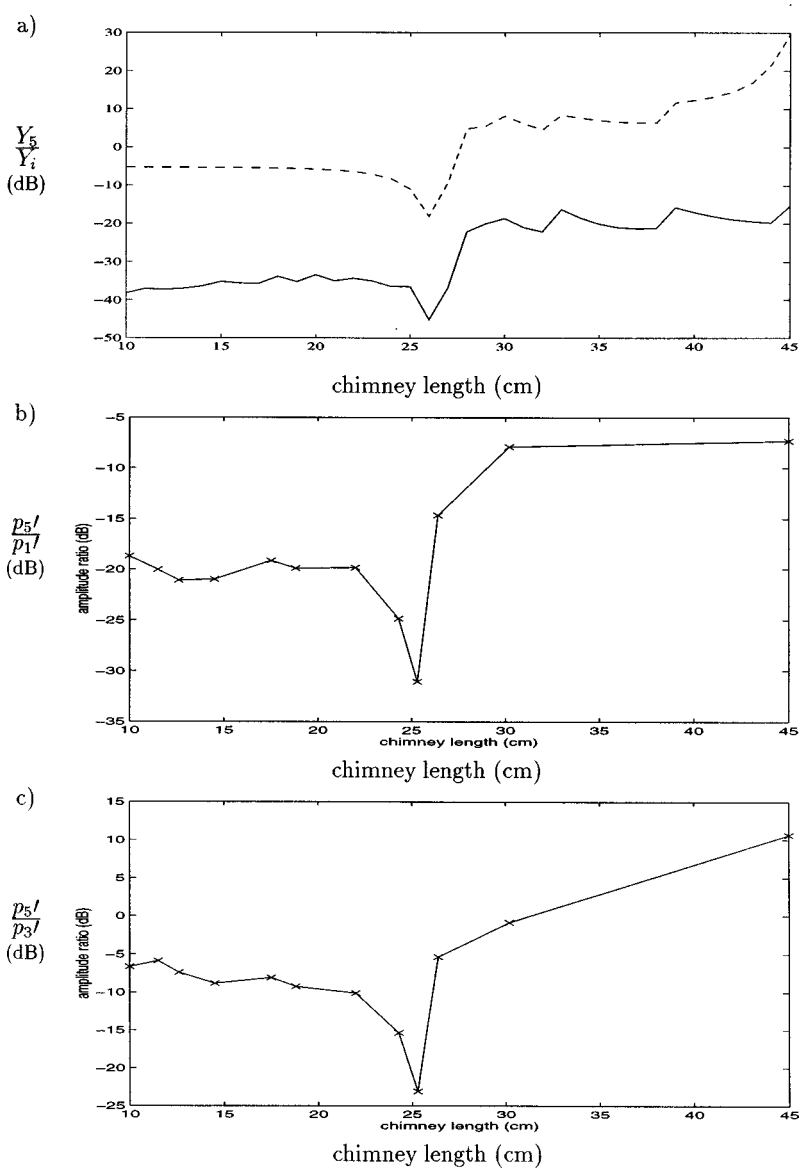

FIG. 6. (a) Ratio of the modulus of the calculated admittance of the fifth with the third and first harmonic of a chimney pipe as a function of the chimney length for a chimney placed completely outside the main pipe and having a diameter of 14 mm (Y_5/Y_1: bold line, Y_5/Y_3: dotted line) and comparison with the ratio of measured harmonic amplitudes: (b) $p_{5'}/p_{1'}$; (c) $p_{5'}/p_{3'}$ for a driving pressure $p_f=40(x)$ mm H_2O. (Adapted from Fig. 3 of Verge *et al.*, 1997. Reproduced with the permission of the authors.)

harmonic only when placed halfway inside and halfway outside the main pipe. This position and chimney length provided a significant enhancement of the fifth harmonic in comparison with the original design ($L_c=125$ mm, $D_c=14$ mm, and the chimney placed completely outside the main pipe).

Improvements of the chimney performance when $L_c=\lambda_0/10$ and when it is placed in the intermediate position can be explained by the calculated impedance curve of the system shown in Fig. 3. In the intermediate position, a strong third pipe mode is observed at a frequency close to $5f_0$. When the chimney is placed either entirely inside or outside the pipe, this peak is split into two low resonances, thereby strongly decreasing the value of the admittance for the fifth harmonic ($5f_0$). This effect can easily be understood in terms of the compatibility of the standing-wave patterns in the main pipe and in the chimney, as shown in Fig. 4. When it is placed entirely inside or outside the main pipe, a ''resonating'' chimney ($L_c=\lambda_0/10$) imposes at the ''closed end'' of the main pipe a pressure node, where the main pipe would like to see a pressure antinode. The chimney thereby ''kills'' the standing-wave pattern of the corresponding stopped pipe for the fifth harmonic. Placing the chimney halfway inside or outside the main pipe clearly solves this conflict. A similar effect would be obtained by placing a chimney of length $L_c=\lambda_0/20$ (half Helmholtz's rule) entirely outside the main pipe or a closed chimney of length $\lambda_0/10$ entirely outside the main pipe. These configurations do not conflict with the standing-wave pattern of the main pipe, but do not provide an increase of the amplitude of the third peak of the admittance curve. Furthermore, this compatibility of the wave patterns implies, by continuity of pressure and acoustic flux, that the standing wave in the chimney will have the same amplitude as that in the main pipe. Under such conditions, the contribution of the chimney to the radiation of the fifth harmonic is only a fraction $[S_4/(S_4+S_2)]$ of the total radiated power.

A similar effect of the position of a resonating chimney is observed during the attack transient, as shown in Fig. 5. It appears that with a chimney having a length $L_c=\lambda_0/10$ adjusted in the intermediate position, the attack transient is dominated by a precursor burst on the fifth harmonic. This

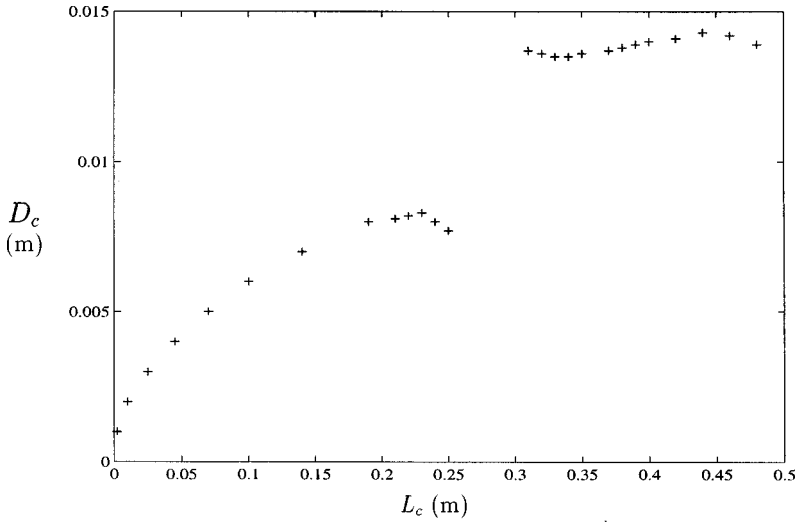

FIG. 7. Optimal diameter D_c of a chimney as a function of its length L_c when the chimney is placed completely outside the main pipe. The geometry of the experimental pipe was used in the calculations.

effect disappears when the chimney is placed entirely inside or outside the pipe. As the attack transient is very important perceptually, this confirms the importance of the chimney design.

These observations seem to indicate that the actual role of the chimney is not to amplify the fifth harmonic by ''resonance,'' but rather to place the fifth harmonic at a favorable location on the admittance curve. This can be obtained with a resonating chimney, but only if it is placed halfway inside and outside the main pipe. For this given length and position of chimney, it is even possible to find a diameter which enables one to match the location of the fifth harmonic with that of the third peak of the admittance curve. It is also possible, however, as will be discussed in the next section, to obtain a similar effect for a wide range of chimney lengths regardless of the chimney position.

IV. OPTIMIZATION OF THE CHIMNEY DESIGN

The discussion of the previous section suggests that, rather than a resonating device, the chimney can be viewed as an instrument enabling one to match the fifth harmonic $(5f_0)$ with a point of high admittance $Y_5=Y(f_5)$ or, in other words, to reduce the inharmonicity of the modes of the system.

This is confirmed by measurements which show that the ratio of the modulus of the admittance Y_i for different harmonics $f_i=if_0$ is a good indicator of the relative amplitude $p_{i'}$ of these harmonics in measured spectra. Comparison between simulation results obtained from the simple acoustic model and measurements presented in Fig. 6 shows indeed that, for our organ pipe, the ratio of the calculated admittance qualitatively accounts for variations of the ratios $p_{5'}/p_{1'}$ and $p_{5'}/p_{3'}$ of the amplitude of the fundamental, third, and fifth harmonic for chimney diameter $D_c=14$ mm. In this example, the chimney was placed completely outside the main pipe. The absolute value of the amplitude $p_{i'}$ of the different harmonics can not, of course, be determined by this admittance ratio; it is determined by the amplitude of the source associated with the jet oscillations. This ratio characterizes, however, the dependency of the amplitude of the different harmonics with the chimney geometry. This result also indicates that the source associated with the jet motion is not very sensitive to feedback from higher harmonics, which implies that the jet oscillations must mainly be determined by the fundamental (and eventually the second harmonic).

The measurements of Fig. 6 show that the relative amplitude of the different harmonics appears to be rather independent of the length of the chimney, except around the region corresponding to Helmholtz's design, where a minimum is observed. Note that this minimum disappears when the resonating chimney is shifted halfway into the main pipe. This indicates that a wide range of chimney lengths can be used. Similar results were previously presented.[11]

The advantage of using a ''nonresonating'' chimney is that the resulting timbre is not very sensitive to the chimney position. In particular, placing the chimney completely inside or outside the main pipe is more convenient from the point of view of organ making. Furthermore, the chimney length can then easily be adjusted for tuning purposes without affecting the timbre too much. For chimneys having a length smaller than $\lambda_0/10$, as is commonly used,[2] the fifth harmonic is always located on the right of the third peak of the admittance curve, a position where the admittance is fairly high and does not vary rapidly. For chimney lengths greater than Helmholtz's design, the pipe becomes more harmonic and the effects of the resonance of the chimney are shifted towards lower frequencies. This brings the fifth harmonic near the third peak of the admittance curve, while the amplitude around the second peak decreases. This results, in certain cases, in a spectrum where the fifth harmonic has a greater amplitude than the third. It is not obvious to us why such a design is not commonly used in practice. This might be related to the behavior of the system during the attack transient.

The previous results show that by using the admittance curve, one can try to optimize the amplitude of the fifth harmonic by making the resonator harmonic and fitting the fifth harmonic on the third peak of the admittance curve. For a given chimney length, this can be achieved by adjusting the diameter of the chimney. Figure 7 shows the optimal diameter of the chimney as a function of its length, obtained with

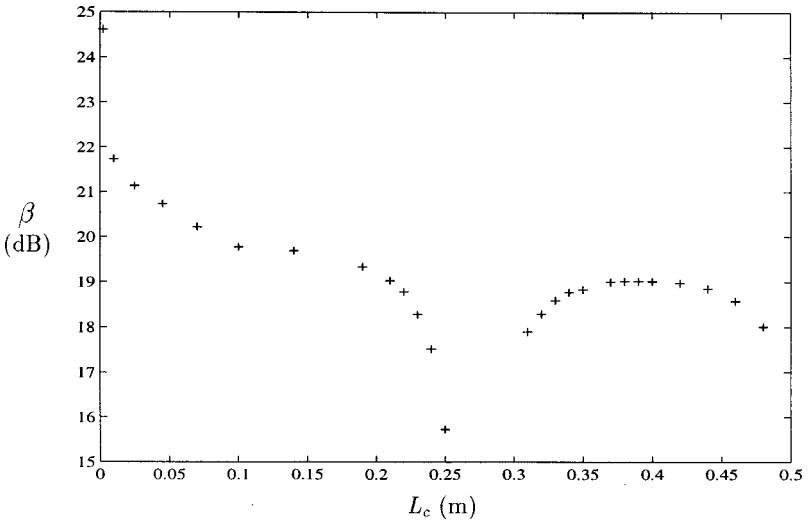

FIG. 8. Enhancement β of the ratio Y_5/Y_1 of the modulus of the admittance of the fifth harmonic and the fundamental with respect to a stopped-pipe configuration as a function of the length L_c of a chimney having an optimal diameter. The geometry of the experimental pipe was used in the calculations.

the geometry of our experimental pipe with the chimney placed completely outside. The corresponding enhancement β of the ratio Y_5/Y_1 of the admittance of the fifth harmonic and fundamental, with respect to the stopped-pipe geometry, is shown in Fig. 8. These results clearly show that a significant reinforcement of the fifth harmonic relative to the fundamental can be expected with a good choice of chimney geometry. In these examples, the fundamental frequency varied slightly but could be kept constant by adjusting the cap position. Globally, the optimal diameter of the chimney increases with the length of the chimney, while the ratio Y_5/Y_1 decreases as the diameter of the chimney is increased because of greater radiation losses. Around the region corresponding to a length $L_c=\lambda_0/10$, the third peak of the admittance curve is split and the pipe cannot be made harmonic. As expected, the efficiency of the chimney then strongly decreases. In Fig. 7, the length corresponding to a chimney diameter $D_c=14$ mm, as used in the measurements of Fig. 6, is approximately 40 cm, which coincides with the maximum of the ratio of the amplitudes $p_{5'}/p_{1'}$ in these measurements.

V. CONCLUSION

Using a simple acoustic model, we have investigated the behavior of chimney organ pipes. It appears that the admittance curve gives a good estimate of the effect of the chimney geometry on the tone produced by the pipe during steady state. Measurements show that the ratio of the amplitude of the different harmonics is well correlated with the modulus of the pipe admittance for these harmonics. This indicates that the source associated with the jet oscillations is not very sensitive to feedback from high harmonics. One of the purpose of chimneys is to enhance the fifth harmonic. In this case, the design rule proposed by Helmholtz, consisting of using a chimney having a length such that it resonates at that frequency, appears to be the least favorable one. Indeed, unless the chimney is placed half inside and half outside the main pipe, which is not very convenient from the viewpoint of instrument making, it will tend to attenuate the standing-wave pattern corresponding to the fifth harmonic in the main pipe. In this study, we have limited ourselves to the study of the steady-state tone of chimney pipes. Preliminary measurements show, however, that the chimney also strongly affects the attack transient. Because of the importance of transients on tone perception, further work on this topic should include a study of this regime, since it may strongly influence the choice of particular geometries by instrument makers.

[1] Dom Bedos de Celles, *L'Art du Facteur d'Orque* (Bärenreitel Kassel, 1958, Basel), p. 1766.
[2] A. P. Oosterhof and A. Bouman, *Orgelbouwkunde* (Spruyt, van Mantgen and de Does, Leiden, The Netherlands, 1971).
[3] D. Bernoulli, ''Sur le son et sur les tons des tuyaux d'orgue différemment construits,'' *Mémoires de l'Académie Royale des Sciences*, p. 1762.
[4] H. Helmholtz, *On the Sensation of Tone* (Dover, New York, 1954, 1885).
[5] G. E. Audsley, *The Art of Organ Building* (Dover, New York, 1965).
[6] R. Gerhardt, ''Die Rohrflöte, ein Pfeifenregister der Orgel,'' *Nova Acta de Ksl. Leop.-Carol.-Deutschen Akademie der Naturforscher* (1884), Vol. XLVII, No. I.
[7] H. Bouasse, *Instruments à Vent* (Librairie Delagrave, Paris, 1930).
[8] M. Castellengo, ''Contribution à l'etude expérimentale des tuyaux à bouche,'' Ph.D. thesis, Université de Paris VI, Paris, France, 1976.
[9] J. D. Polack, X. Menial, J. Kergomard, C. Cosnard, and M. Bruneau, ''Reflection function of a plane wave in a cylindrical tube,'' Rev. Phys. Appl. **22**, 331–337 (1987).
[10] Lord Rayleigh, *The Theory of Sound* (Dover, New York, 1995), p. 1894.
[11] M. P. Verge, R. L. M. Schoffelen, A. P. J. Wijnands, A. Hirschberg, and C. Box, ''Acoustic behavior of chimney pipes,'' in *ISMA-97*, Vol. 19 Part (5), pp. 309–314 (Institute of Acoustics, September 1997).

Dynamic programming matching as a simulation of budgerigar contact-call discrimination

Ken Ito[a)]
Department of Otolaryngology, Faculty of Medicine, University of Tokyo, 7-3-1 Hongo, Bunkyo-ku, Tokyo 113, Japan

Koichi Mori
Department of Sensory and Communicative Disorders, Research Institute of National Rehabilitation for the Disabled, 4-1 Namiki, Tokorozawa, Saitama 359-8555, Japan

(Received 17 November 1997; revised 9 February 1998; accepted 19 September 1998)

Dynamic programming (DP) matching has been successfully used to classify budgerigar contact calls into natural groups (Ito *et al.*, J. Acoust. Soc. Am. **100**, 3947–3956 (1996)]. In this paper, the biological relevance of the DP-matching algorithm was further investigated with an enlarged test set and using psychophysical test results from actual birds. Five call comparison methods (CCMs), including an improved DP-matching method, were used to quantify the dissimilarity or similarity between the contact calls of different budgerigars. Peak–time matrices, consisting of the three most intense peak frequencies in the respective time bins of given calls, formed the common input to the CCMs. The CCMs were compared in terms of (1) efficiency for classification (cluster analysis) of very similar cagemate contact calls into natural groups, i.e., by individual, and (2) correlation to the birds' own perception as inferred from psychophysical tests. The DP-matching method, which chose two representative peak frequencies out of the three for the best match, proved to be the most effective in the classification of cagemate calls and the most correlated with bird perception. Its performance was comparable to that of individual birds. The use of two prominent peak frequencies, time warping, and sequential matching in contrast to correlational computation were found to be important factors not only in classifying calls into natural groups, but also in simulating the perceptual discrimination of budgerigars. Possible counterparts in the bird's brain, such as those responsible for sequential processing, which could serve as the mechanisms of call recognition, were discussed in connection with the above results.
[S0001-4966(99)01901-3]

PACS numbers: 43.80.Lb, 43.66.Gf, 43.66.Mk [FD]

INTRODUCTION

Since the invention of the sonagraph (sound spectrograph), the study of animal vocalization has been able to advance from limited descriptions of relative pitch and duration of sounds to more complex analyses (Catchpole, 1979; Williams and Slater, 1991), because the sonagram can represent visually the time–frequency structure of sounds. Since its invention, classifying animal sounds by a visual inspection of sonagrams has become the common first step in analyzing vocalization (Lemon, 1965; Marler and Peters, 1982). This method of classification using the human eye can be reliable. However, it is not always perfectly objective or practical. Results can vary between observers, and there always remains the possibility that visually subtle but biologically important differences in sound characteristics may be missed. Moreover, it is quite demanding to consistently sort hundreds of sonagrams by eye. However, the complexity of the time–frequency representation, the visualization of which is the sonagram, has stood up well against objective comparison methods.

The attempts at objective comparison methods started by using relatively simple characteristics of animal vocalizations, such as duration and pitch, in multivariate analyses (Clark, 1982; Symmes *et al.*, 1979). Discriminant function analysis was employed in discriminating the *P*-songs of short-toed treecreepers (Bauer and Nagl, 1992), and in classifying budgerigar contact calls (Brown *et al.*, 1988). Bradley and Bradley (1983) applied sequence matching with time warping to the classification of Savannah sparrow songs, which are composed of sequences of notes separated by silence. Their method was a mixture of a visual classification of elemental notes and an objective evaluation of the sequences of the notes.

Increases in computer power and sophistication have enabled objective comparison within a practical time using time–frequency representations. A two-dimensional cross correlation has been applied to the classification of swamp sparrow notes (Clark *et al.*, 1987). Farabaugh *et al.* (1994) have developed a method to compare the peak-frequency contours of different budgerigar contact calls. The dynamic programming (DP) matching method (Sakoe and Chiba, 1978), which was first used in automatic human speech recognition, has been found to be effective in contour comparisons of dolphin whistles (Buck and Tyack, 1993). A practical method using one-stage DP-matching has recently been reported (Anderson *et al.*, 1996) which automatically recognizes birdsong syllables of indigo buntings and zebra finches.

a)Electronic mail: itoken-tky@umin.ac.jp

DP-matching with dynamic time warping using two frequency tracks (DP2peak) has been shown capable of classifying cagemate budgerigar contact calls into natural call groups (Ito *et al.*, 1996). Among the large repertoire of budgerigar vocalizations (Brockway, 1964), the contact call has a particularly complex structure characterized by rapid frequency and amplitude modulations, in spite of its short duration of 100 to 200 ms. Although cagemate contact calls gradually become very similar to one another through learning (Farabaugh *et al.*, 1994), cagemate budgerigars do discriminate contact calls from different individuals (Brown *et al.*, 1988).

These efforts to objectively analyze animal vocalizations, especially bird songs or calls, achieved a certain success. However, their biological relevance was usually assumed rather than measured. So far, there has been no attempt to develop a method that could simulate the psychoacoustical discrimination of the animals themselves. No study has compared the efficiencies of different methods in terms of their similarities to birds' perception of calls. There is a chance, for example, that some of the methods in our previous paper (Ito *et al.*, 1996) could have discriminated contact calls in a way that was different from the bird's own by attending to cues that the birds themselves ignore (i.e., ''technically'' or ''artifactually'' good results).

The aim of the present study was to evaluate the biological, rather than technical, relevance of our computational methods. In the process, we have improved upon the most successful DP-matching method in our previous report to better simulate bird performance. Our evaluation was based on two parameters: (1) Efficiency in classifying an extended data set of cagemate contact calls closely resembling one another, in order to lower the rate of technical success. (2) Correlation with behavioral perception, as inferred from psychophysical tests of the budgerigars.

Finding a method that classifies calls as closely as birds do would allow us to sort animal vocalizations in more biologically significant ways, would help us better understand the cues that birds attend to in call discrimination, and eventually would provide clues about which processes in the bird brain are involved in call recognition.

I. METHODS

A. Recording of contact calls

The contact calls of four adult cagemate budgerigars, three males and one female, were recorded. Details of the recording procedures appear elsewhere (Ito *et al.*, 1996). The contact calls of the four budgerigars had become very similar to one another from their being kept together. For the present study, 20 similar contact calls, five calls from each budgerigar, were extracted from the pool of recorded calls. Their sound spectrograms, or sonagrams, are shown in Fig. 1.

B. Preparation of data by extracting features from each call

Serial power spectra (SPS), or the representation of the calls in terms of frequency–time matrices, were calculated from each of the 20 contact calls with frequency and time resolutions of 78.1 Hz and 2.0 ms, respectively (Ito *et al.*, 1996). The frequencies of the most intense ($f1$), the second most intense ($f2$), and the third most intense ($f3$) peaks were extracted from each time bin of the SPS in order to make peak-time matrices (PTM).

C. Call comparison methods (CCMs)

The calculation method (CCM) for the dissimilarity (distance) or similarity between any two calls used the PTM. Four of the five CCMs in this study (DP1peak, DP2peak, Lin2peak and Corr2shift) have already been described by Ito *et al.* (1996). Here we introduce another DP-matching algorithm, improved over DP2peak, that utilizes the third frequency as well and seeks a best match by choosing two frequencies out of the three most intense peak frequencies (DP2of3).

D. DP-matching and linear matching methods

Appendix A of our previous article (Ito *et al.*, 1996) describes in detail the DP-matching algorithm employed again here. In brief, two calls are aligned along a comparison path which permits time warping; the total distance between the calls is calculated by adding up the regional distances (intervector distances) at each point along the path and then dividing this sum by the path length for normalization. The call distance was defined as the minimum normalized distance among all possible warping paths. For the intervector distance, each set of the three most intense frequencies in the PTM in a time bin was used to make up a feature vector representing the time segment. The intervector distance was defined as the difference in feature vectors from given time bins for two different calls.

The formulas for calculating the intervector distances are given in the Appendix. The discrete scoring function (S) gives the tolerance in the frequency comparison, to a certain extent. DP1peak uses only $f1$. DP2peak uses $f1$ and $f2$. DP2of3 uses three frequencies ($f1$, $f2$, and $f3$), but picks the two that match best. DP2of3 is an improvement in DP2peak designed to cope with rapid alternations between $f2$ and $f3$, which are sometimes observed in time segments where the intensities of $f2$ and $f3$ are similar. Figure 2 shows an example of one such rapid alternation. Although the $f1$ track is stable [Fig. 2(a)], $f2$ and $f3$ rapidly alternate with each other in certain time segments [Fig. 2(b) and (c)]. Therefore, while using three peak frequencies ($f1$, $f2$, and $f3$) overall, DP2of3 uses only two frequencies at a time in comparing two calls (see the Appendix).

The linear matching method, Lin2peak, is identical to DP2peak, except for the lack of dynamic time warping.

E. Correlation method

Similarities between two calls were calculated by the cross-correlation method (Corr2shift), which uses $f1$ and $f2$ (Ito *et al.*, 1996). This algorithm permits no time warping, but is tolerant of frequency differences to a certain extent.

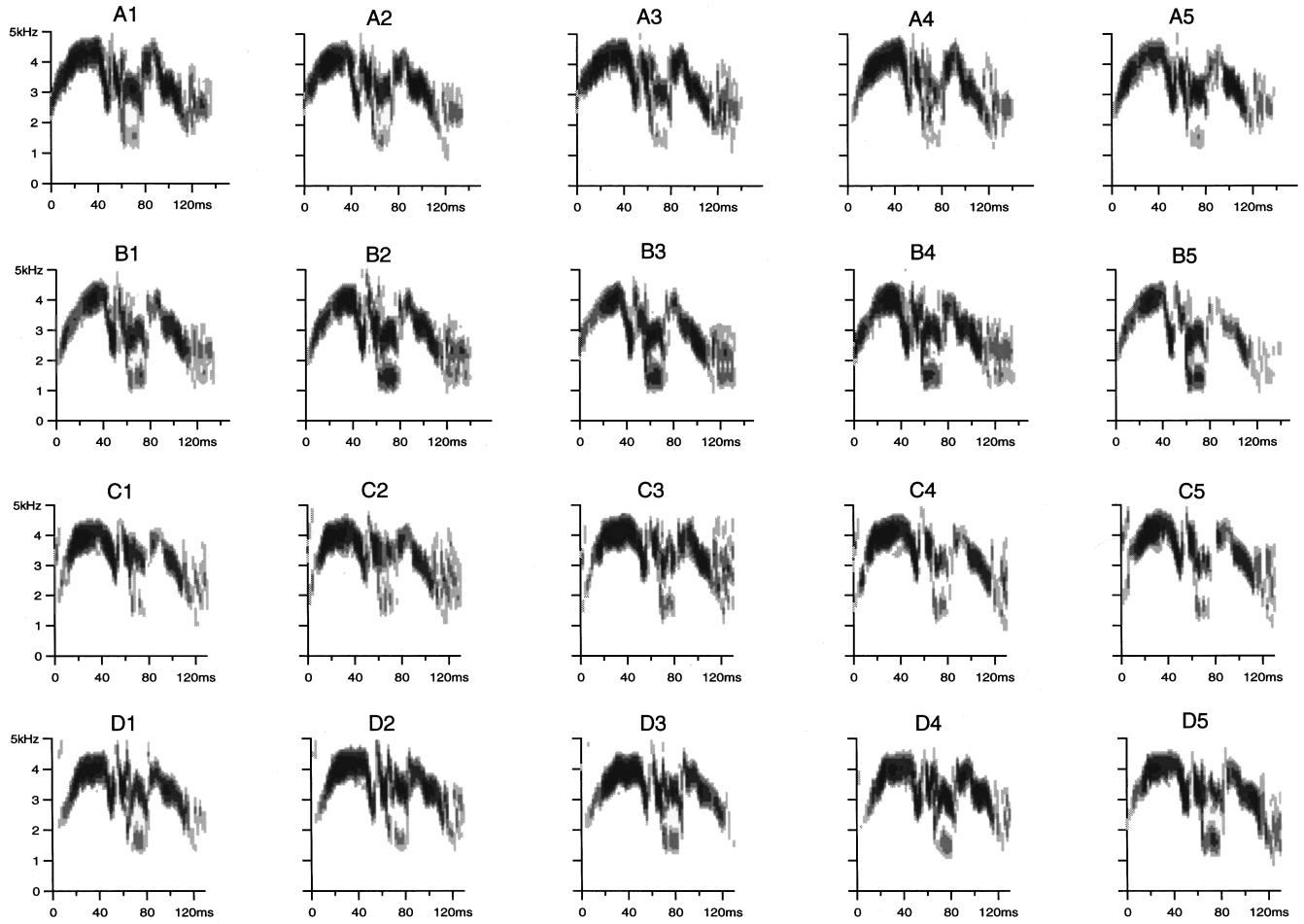

FIG. 1. Sonagrams of contact calls in groups A through D. Numbers appended to the group letter denote individual calls. Degree of shading represents intensity. The ordinate and the abscissa represent frequency and time, respectively.

F. Psychophysical call-discrimination task

The birds were trained and tested according to the method of Dooling *et al.* (1987a, 1987b). Briefly, the four budgerigars whose contact calls were recorded (A1 to D5) underwent a Go–NoGo (same–different) call-discrimination task after reaching the criterion of 90%-correct responses to a set of training calls. Each bird was put in a small cage placed in a sound-attenuated room. On one wall of the cage were two keys, an observation key on the left and a report key on the right, and a small opening to a grain hopper. The two keys could be illuminated by means of light-emitting diodes. All events in the experiment, including sound delivery, the illumination of the keys, and the response latency data collection were controlled by a personal computer. The illumination of the two keys started a trial. A peck at the left key initiated a sequence of playbacks of a background call at 500-ms intervals. An alternating sequence of a test call and a background call was delivered after a randomized number of background call playbacks. If the two calls were different, the bird was required to peck at the right key within 2 s in order to gain access to grain as a reward. Responding to two ''identical'' calls (a false alarm) when the target call and the background call were the same (sham trials), was punished by a time-out of 20 s, during which all the lights in the room were turned off. Each bird went through one or two sessions per day, five days a week. Each session was self-paced and comprised about 100 trials. The birds were monitored with an infrared video camera during each session. Their body weights were measured before and after every session. They had free access to food on weekends. Access to water was allowed all the time. Throughout the experiments they were treated with care and were in good health.

Response times in the same–different task were taken as psychophysical indices of call similarity (Brown *et al.*, 1988; Dooling *et al.*, 1987a, 1987b). The psychophysical similarity index (PSI) for two sound stimuli was calculated from the response time rt in ms as, $\mathrm{PSI}=\log_{10}(2000/\mathrm{rt})$, which gave smaller values for greater similarity. PSI was always zero or a positive value because the time-out occurred at 2000 ms (rt did not exceed 2000).

G. Experiment 1 (classification of contact calls)

Either dissimilarity (distance) or similarity between the members of every pair in a set of calls was calculated by each CCM. Cluster trees were drawn as in our previous article (Ito *et al.*, 1996). Twenty calls of groups A, B, C, and D were classified by a cluster analysis of the dissimilarities or similarities calculated by the five CCMs.

The efficacy of the classification by each CCM was determined by the following grading criteria. A ''correct''

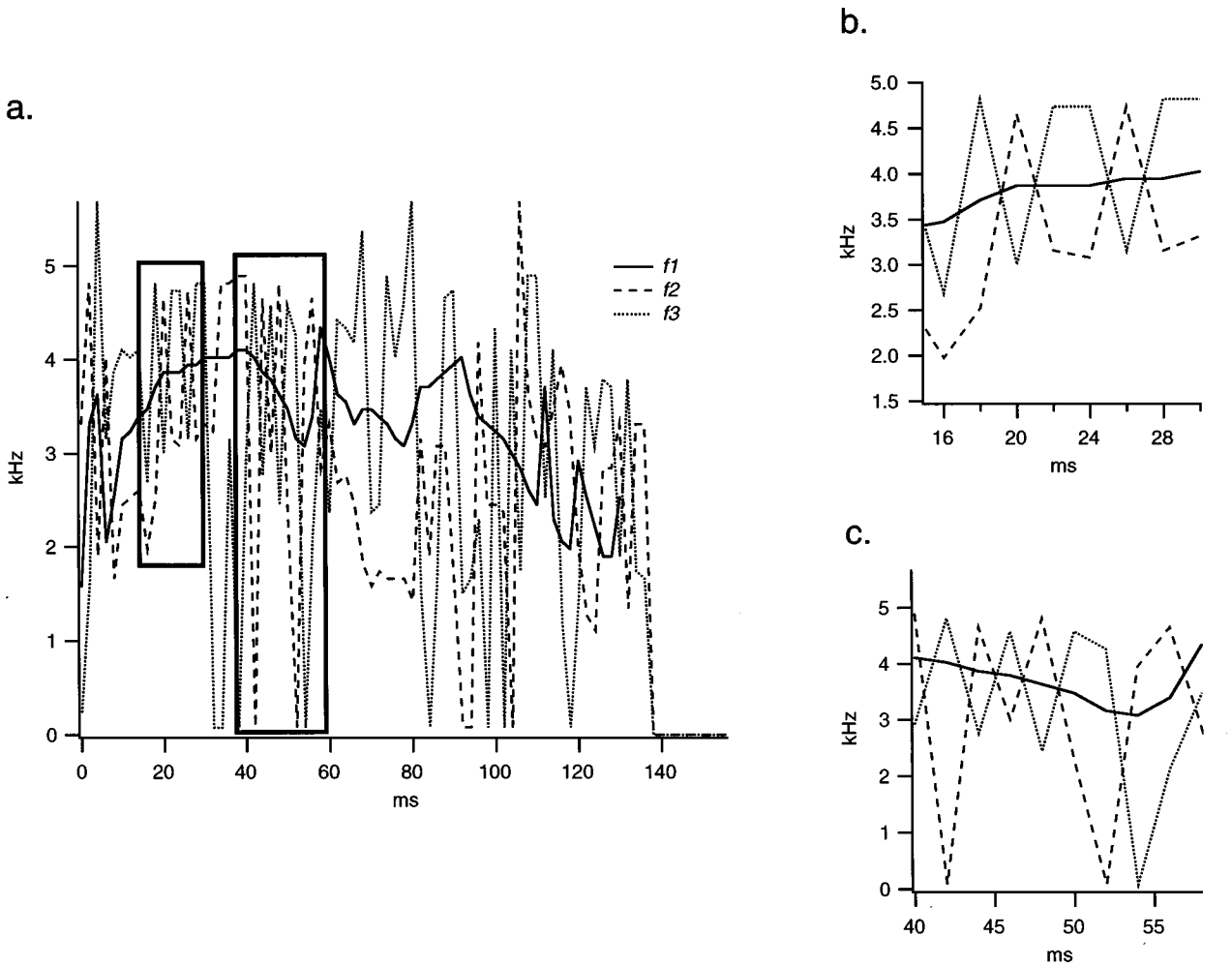

FIG. 2. Peak frequency tracks of a budgerigar contact call (a). Time segments around 20 and 50 ms (bordered) are expanded in (b) and (c), respectively.

grouping was defined as the grouping of all five calls in a predefined group within a branch of the cluster tree. Similarly, a ''fair'' grouping was defined as the grouping of four calls in a predefined group within a branch of the cluster tree.

''Good'' classification stood for the correct grouping of all four groups, A to D. ''Partial'' classification meant that at least one fair grouping was attained. In partial classification, the number of fair or correct groupings was also reported. ''Poor'' classification meant that no correct or fair grouping was seen.

H. Experiment 2 (similarity to the birds' perceptions)

The four cagemate budgerigars underwent psychophysical tests (same–different tasks) in which they were to discriminate calls in all possible pairwise combinations, presented in random order, of the 20 different calls (190 pairs in all), the sonagrams of which are shown in Fig. 1. As with the CCMs, a 20×20 halfmatrix of PSIs was obtained for each budgerigar. Each bird went through each pairwise comparison block of 90 trials six times, three times with one call as the target and the other as the background call, and the other three times with the target and background calls exchanged. Half were sham trials with identical target and background calls. The median reaction times (rt) for the respective three responses before and after the target/background exchange were averaged to produce an rt for a given call pair. Data from the four birds were averaged to produce the final PSI half matrix.

The nonparametric rank-correlation Spearman coefficients (Brown and Benedetti, 1977) and the p values of the correlations were calculated between the set of 190 pairwise dissimilarities (distances) or similarities, calculated by each CCM, and the 190 pairwise psychophysical distances in the PSI.

II. RESULTS

A. Experiment 1 (classification of contact calls)

The results are summarized in Table I. DP2of3 grouped the calls correctly [Fig. 3(a)]. DP2peak clustered group A and B calls correctly, but group C and D calls were grouped imperfectly, with one call of group C straying into the other. DP1peak also clustered group A and B calls correctly and group D calls fairly, but group C calls poorly. Lin2peak classified group A, B, and D calls fairly. Corr2shift gave no pertinent grouping [Fig. 3(b)].

B. Experiment 2 (similarity to the birds' perceptions)

The results are shown in Fig. 4 ($n=190$). DP2of3 had the largest correlation coefficient (0.423) to the birds' psy-

TABLE I. The grading of call classifications (experiment 1). The numbers in parentheses for ''partial'' classifications indicate the number of ''fair'' or ''correct'' groupings. (See the text for definitions.)

CCM	Classification
DP matching	
DP2of3	Good
DP2peak	Partial (4)
DP1peak	Partial (3)
Linear matching	
Lin2peak	Partial (3)
Correlation	
Corr2shift	Poor

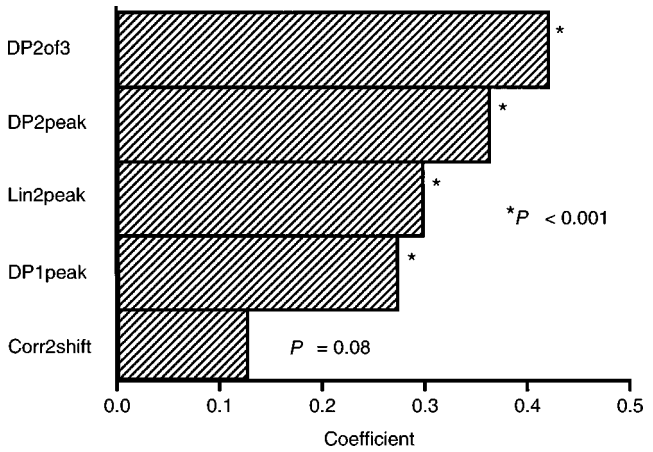

FIG. 4. Spearman's correlation coefficients between call distances calculated by various CCMs and those obtained from the psychophysical tests. The abscissa represents the coefficients for the CCMs denoted on the ordinate. *P*-values are also indicated.

chophysical perceptions. DP2peak had the second largest value (0.365), and Lin2peak ranked after them. DP1peak had the smallest coefficient among the DP- and linear-matching methods. All CCMs using DP and linear matching had a significant correlation with the bird perceptions ($p < 0.001$). Corr2shift had the smallest correlation coefficient (0.129), and failed to reach statistical significance ($p = 0.08$).

Next, we compared the performance of DP2of3 to those of individual birds. The Spearman's correlation coefficients between the pairs from the psychophysical test results for the four birds ranged from 0.297 to 0.546 (mean, 0.444). The range of the coefficients between the DP2of3 distance matrix and the individual bird perceptions (0.262 to 0.504) almost overlapped with these values. There was no significant difference between the interbird correlation coefficients and the correlation coefficients between DP2of3 and individual birds.

We also compared the bird perceptions and the perfor-

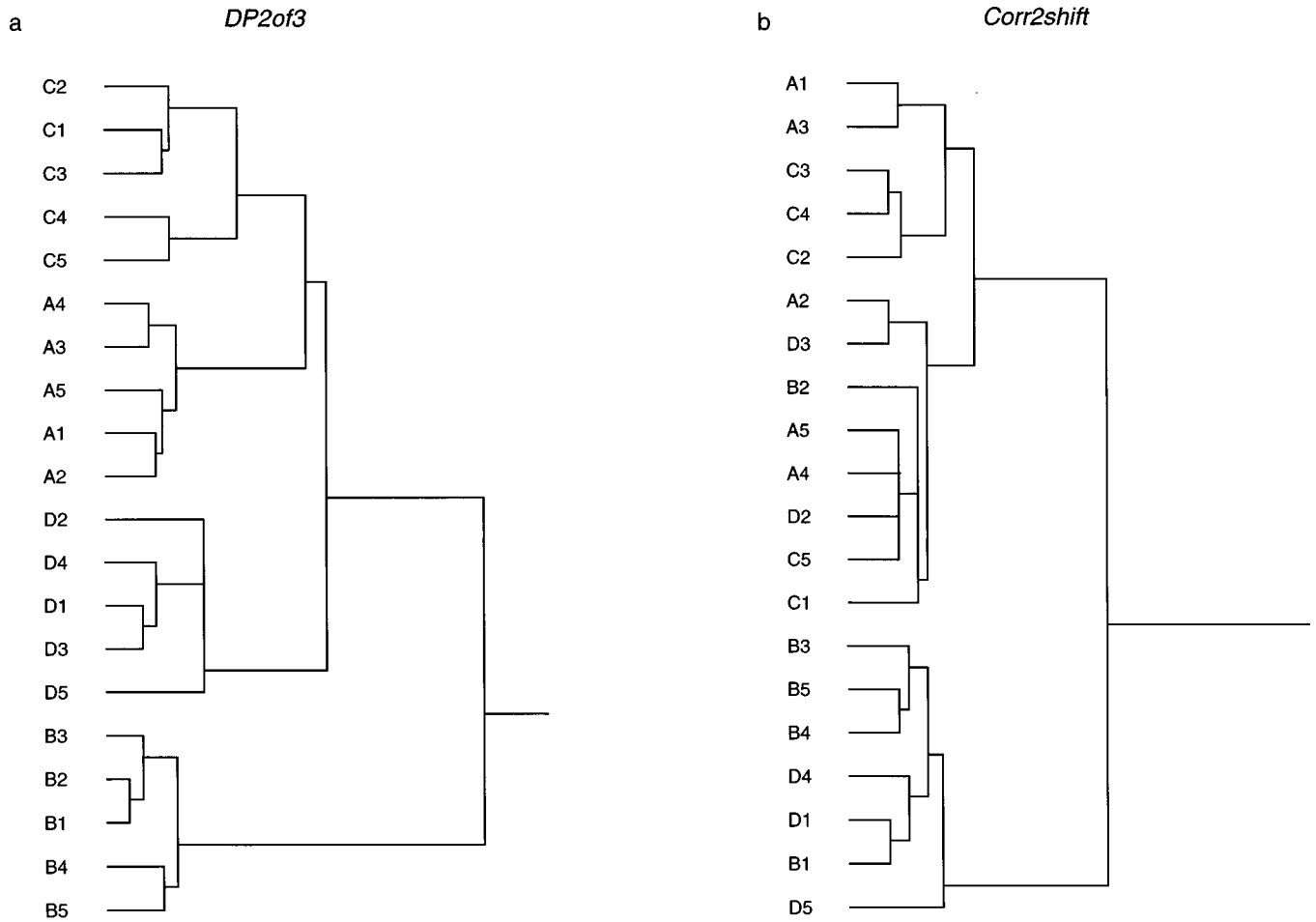

FIG. 3. Classification of calls by CCMs, seen as tree diagrams from a cluster analysis. (a) DP2of3; (b) Corr2shift.

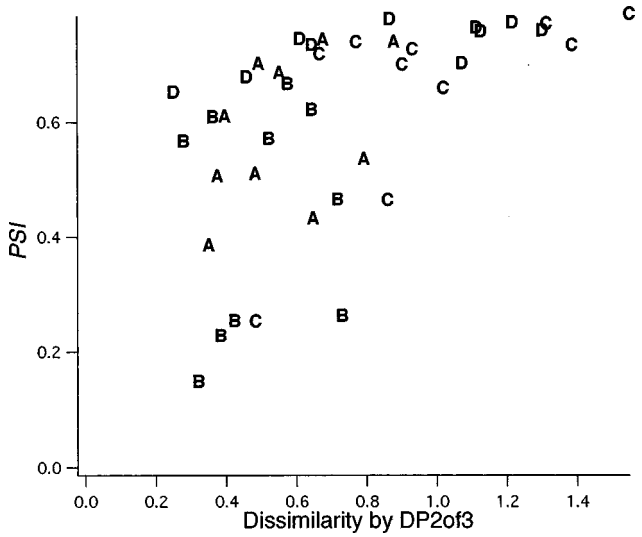

FIG. 5. A scatterplot to show the relationship between bird perception (PSI, ordinate) and dissimilarity as calculated by DP2of3 (abscissa). The 40 pairs within each group (A to D), such as A1–A2 and C3–C4, are depicted using the group characters (A to D).

mance of DP2of3 in terms of call discrimination within respective groups (A to D), such as A1–A2 and C3–C4 (Fig. 5). Pairs from groups A and C showed near-diagonal distributions, i.e., good correlational patterns. (Please note that data points would not fall on a line even if the correlation was perfect, because the data values were not normalized.) Group D pairs stayed in a very limited range in terms of PSI, whereas they were widely scattered in the dissimilarity calculated by DP2of3. The distribution of group B pairs was opposite to those of group D. The overall correlation among these 40 pairs reached significance ($p<0.001$).

III. DISCUSSION

The goal of developing a CCM is to create one that behaves like a bird. Its purpose is twofold: such a CCM could provide a means of classifying animal vocalizations in a biologically relevant way, and it might give us insight into how birds perceive and process species-specific vocalizations. Therefore, CCMs have been evaluated by their correlation to birds' perceptual discrimination, as well as by their efficacy in classifying calls into the natural groups which they are assumed to produce by researchers (Brown *et al.*, 1988; Ito *et al.*, 1996).

The main point of our paper lies in the quantitative comparison between the computed results (classification by mathematical calculation) and the psychophysical test results (classification by cagemate birds) in experiment 2. No report of such a comparison has yet been made for bird song/call analysis. Such a comparison is essential to minimize the chance of a technically good classification of calls resulting when a method attends to cues that the birds themselves ignore. In our previous paper (Ito *et al.*, 1996), cross-correlational methods classified different kinds of contact calls correctly, but failed to classify similar cagemate calls.

One problem, however, with this kind of comparison is how to evaluate the strength and consistency of the correlation between data obtained through totally different modalities. DP2of3 was judged to have a meaningful correlation with bird perception because of the following results: (1) With Spearman's nonparametric evaluation, DP- and linear-matching methods reached the significant level ($p<0.01$), whereas the correlation method did not. (2) The results of experiment 2 were consistent with the results from the qualitative evaluation in experiment 1. (3) The correlation coefficients between the distance matrices of DP2of3 and each bird perception were almost indistinguishable from those between individual birds.

DP matching has been successfully applied to the classification not only of budgerigar contact calls, but also to the vocalizations of other species (Anderson *et al.*, 1996; Buck and Tyack, 1993). In contrast to previous studies with DP matching which used fixed vectors such as the fundamental frequency (Buck and Tyack, 1993) and the log-magnitude FFT bins (Anderson *et al.*, 1996), our methods make vector comparison algorithms exchangeable. This enables the examination of the influence of various factors, such as the number of frequencies, and linear vs time warping. Using only one frequency in DP matching (DP1peak) considerably lowered the correlation coefficient with the psychophysical tests. Disabling the time-warping feature (Lin2peak) also lowered the correlation coefficient with the birds' perceptions. The correlation method (Corr2shift) turned out to be incapable of simulating the birds' perceptions. Adding the third frequency in DP matching produced somewhat unexpected results. The method (DP3peak) that simply used the three most intense peak frequencies made no improvement over DP2peak (coefficient: 0.358, not shown in Fig. 4), as well as in the classification of contact calls (Ito *et al.*, 1996). However, the DP-matching method (DP2of3), which chooses the two best-matching peaks out of the three, produced better results than DP2peak. In other words, DP2of3 adopted tolerance in the selection of the two most important peaks. In summary, the use of two prominent peak frequencies, dynamic time warping, and sequential matching in contrast to correlational computation proved to be important in terms of obtaining a closer similarity to the birds' perceptual discrimination.

The exact acoustic parameters that budgerigars attend to in call discrimination are not yet known, nor are the brain processes involved in their sound or call recognition. However, the properties of CCMs that contribute to better correlation to the bird perception as well as to correct classification may have some counterparts in the bird's call recognition mechanisms. These properties include the three factors itemized above. Our results suggest that the correlation method (Corr2shift) has little in common with the brain processes for budgerigar call discrimination. On the other hand, it is not likely that the exact same computation as the DP-matching method is performed in the bird's brain; DP matching can backtrack sounds, which may not be physiologically possible. However, the consistent improvement in the correlation with bird perception by adding dynamic time warping suggests that there is a mechanism in the bird's brain that adjusts the time axis in comparing two calls.

The advantage of using two frequencies instead of one or three in call classification suggests that budgerigars may

make use of two representative frequencies simultaneously when discriminating contact calls, although a counterpart to this in the brain remains to be found. Potential counterparts in the bird's brain to sequential matching have been reported; in the forebrain nuclei of the white-crowned sparrow, song-specific units respond to a particular sequence of two frequencies (Margoliash, 1983). Such combination-sensitive (CS) neurons were also found in zebra finches (Doupe and Konishi, 1991; Margoliash and Fortune, 1992). The existence of CS neurons underscores the importance of temporal as well as spectral parameters for the perception of calls. However, these CS neurons seem to have response properties that are hard-coded during development. It remains to be clarified whether a similar sequential processing is performed when the brain tries to compare an ongoing call with a call trace memorized a few seconds before. Further investigation using various methods to simulate birds' behavior will contribute not only to the development of methods for classifying bird vocalization, but also to the elucidation of bird-call recognition processes, hand-in-hand with the basic physiological research.

The most successful method so far, DP2of3, has a good but not perfect correlation with averaged bird perception. Because the difference between two calls within one group is usually much smaller, and therefore more difficult to discriminate than those between calls in different groups, within-group data sets are best for critically testing the discrimination power of a CCM. As shown in Fig. 5, DP2of3 simulated bird perception fairly well in discriminating A and C within-group calls. In group D calls, DP2of3 may have attended to certain factors that the birds themselves ignored, and *vice versa* in group B calls. This result, together with the similar correlation coefficients between the performance of this CCM and that of the individual birds, suggests that DP2of3 discriminates budgerigar contact calls in a way similar to a cagemate.

IV. SUMMARY

Of the five call-comparison methods (CCMs) including DP-matching, linear-matching, and correlation methods, the DP-matching method which chose two representative peak frequencies out of three for the best match (DP2of3) proved the most effective in terms of (1) classification of very similar cagemate contact calls into natural groups, and (2) correlation with the birds' own perception as inferred from psychophysical tests. Use of two prominent peak frequencies, time warping, and sequential matching in contrast to correlational computation were important in simulating the birds' perceptual discrimination.

ACKNOWLEDGMENTS

The present study was supported in part by a fellowship from the Kawai Sound Technology Promotion Foundation (STPF), and the Japanese Ministry of Education, Science, Sports, and Culture.

APPENDIX: CALCULATION OF INTERVECTOR DISTANCES FOR DP- AND LINEAR-MATCHING METHODS

Here we represent the most intense, the second most intense, and the third most intense peak frequencies of a feature vector v in a given time bin of a PTM as $v\text{-}f1$, $v\text{-}f2$, and $v\text{-}f3$, respectively. The intervector distance d between two feature vectors $v1$ and $v2$ from respective PTMs is calculated by the formulas described below. S represents a discrete scoring function for frequency comparison, which gives smaller values for better matches with a certain frequency tolerance (Ito *et al.*, 1996).

DP1peak: Only the most intense peaks ($f1$) of $v1$ and $v2$ are used as the following.

$$d(v1,v2)=S(v1\text{-}f1,v2\text{-}f1).$$

DP2peak and Lin2peak: $f1$ and $f2$ are used in the calculation as,

$$d(v1,v2)=\min(S(v1\text{-}f1,v2\text{-}f1)+S(v1\text{-}f2,v2\text{-}f2),\\ S(v1\text{-}f1,v2\text{-}f2)+S(v1\text{-}f2,v2\text{-}f1)),$$

where $\min(a,b)$ represents the smaller of a and b. As seen from this equation, the two most intense peak frequencies are interchangeable.

DP2of3: This method chooses two frequencies out of the three most intense ($f1$, $f2$, and $f3$) in the following manner. The most intense peak frequency ($f1$) is given a preference and is always used. When diagonal matching of $f1$ and $f2$ ($f1$ to $f2$, $f2$ to $f1$) is better than parallel matching ($f1$ to $f1$, $f2$ to $f2$), the diagonal matching is adopted. Otherwise, $f1$ is matched to $f1$, and the better of the parallel and diagonal matchings of the other two frequencies ($f2$ and $f3$) is adopted.

If $S(v1\text{-}f1,v2\text{-}f1)+S(v1\text{-}f2,v2\text{-}f2)$

$$\geqslant S(v1\text{-}f1,v2\text{-}f2)+S(v1\text{-}f2,v2\text{-}f1),$$

$$d(v1,v2)=S(v1\text{-}f1,v2\text{-}f2)+S(v1\text{-}f2,v2\text{-}f1).$$

Otherwise

$$d(v1,v2)=S(v1\text{-}f1,v2\text{-}f1)\\ +\min[S(v1\text{-}f2,v2\text{-}f2),S(v1\text{-}f2,v2\text{-}f3),\\ S(v1\text{-}f3,v2\text{-}f2)].$$

Anderson, S. E., Dave, A. S., and Margoliash, D. (**1996**). ''Template-based automatic recognition of birdsong syllables from continuous recordings,'' J. Acoust. Soc. Am. **100**, 1209–1219.

Bauer, H. G., and Nagl, W. (**1992**). ''Individual distinctiveness and possible function of song parts of short-toed treecreepers (*Certhia brachydactyla*). Evidence from multivariate song analysis,'' Ethology **91**, 108–121.

Bradley, D. W., and Bradley, R. A. (**1983**). ''Application of sequence comparison to the study of bird songs,'' in *Time Warps, String Edits, and Macromolecules: The Theory and Practice of Sequence Comparison*, edited by D. Sankoff and J. B. Kruskal (Addison Wesley, Reading, PA), pp. 189–207.

Brockway, B. F. (**1964**). ''Ethological Studies of the budgerigar (*Melopsittacus undulatus*): non-reproductive behavior,'' Behaviour **22**, 193–222.

Brown, M. B., and Benedetti, J. K. (**1977**). ''Sampling behavior of tests for correlation in two-way contingency tables,'' J. Am. Stat. Assoc. **72**, 309–315.

Brown, S. D., Dooling, R. J., and O'Grady, K. (**1988**). ''Perceptual organization of acoustic stimuli by budgerigars (*Melopsittacus undulatus*): III. Contact calls,'' J. Comp. Psych. **102**, 236–247.

Buck, J. R., and Tyack, P. L. (**1993**). ''A quantitative measure of similarity for *Tursiops truncatus* signature whistles,'' J. Acoust. Soc. Am. **94**, 2497–2506.

Catchpole, C. K. (**1979**). *Vocal Communication in Birds* (Edward Arnold, London).

Clark, C. W. (**1982**). ''The acoustic repertoire of the southern right whale, a quantitative analysis,'' Anim. Behav. **30**, 1060–1071.

Clark, C. W., Marler, P., and Beeman, K. (**1987**). ''Quantitative analysis of animal vocal phonology: an application to swamp sparrow song,'' Ethology **76**, 101–115.

Dooling, R. J., Brown, S. D., Park, T. J., Okanoya, K., and Soli, S. D. (**1987a**). ''Perceptual organization of acoustic stimuli by budgerigars (*Melopsittacus undulatus*): I. Pure tones,'' J. Comp. Psych. **101**, 139–149.

Dooling, R. J., Park, T. J., Brown, S. D., Okanoya, K., and Soli, S. D. (**1987b**). ''Perceptual organization of acoustic stimuli by budgerigars (*Melopsittacus undulatus*): II. Vocal signals,'' J. Comp. Psych. **101**, 367–381.

Doupe, A. J., and Konishi, M. (**1991**). ''Song-selective auditory circuits in the vocal control system of the zebra finch,'' Proc. Natl. Acad. Sci. USA **88**, 11339–11343.

Farabaugh, S. M., Linzenbold, A., and Dooling, R. J. (**1994**). ''Vocal plasticity in budgerigars (*Melopsittacus undulatus*): evidence for social factors in the learning of contact calls,'' J. Comp. Psych. **108**, 81–92.

Ito, K., Mori, K., and Iwasaki, S. (**1996**). ''Application of dynamic programming matching to classification of budgerigar contact calls,'' J. Acoust. Soc. Am. **100**, 3947–3956.

Lemon, R. E. (**1965**). ''Geographic variation in the song of cardinals,'' J. Zool. **44**, 413–428.

Margoliash, D. (**1983**). ''Acoustic parameters underlying the response of song-specific neurons in the white-crowned sparrow,'' J. Neurosci. **3**, 1039–1057.

Margoliash, D., and Fortune, E. S. (**1992**). ''Temporal and harmonic combination-sensitive neurons in the zebra finch's HVc,'' J. Neurosci. **12**, 4309–4326.

Marler, P., and Peters, S. (**1982**). ''Developmental overproduction and selective attrition: new processes in the epigenesis of birdsong,'' Dev. Psychobio. **15**, 369–378.

Sakoe, H., and Chiba, S. (**1978**). ''Dynamic programming algorithm optimization for spoken word recognition,'' IEEE Trans. Acoust., Speech, Signal Process. **ASSP-26**, 43–49.

Symmes, D., Newman, J. D., Talmage-Riggs, G., and Lieblich, A. K. (**1979**). ''Individuality and stability of isolation peeps in squirrel monkeys,'' Anim. Behav. **27**, 1142–1152.

Williams, J. M., and Slater, P. J. B. (**1991**). ''Computer analysis of bird sounds: a guide to current methods,'' Bioacoustics **3**, 121–128.

LETTERS TO THE EDITOR

This Letters section is for publishing (a) brief acoustical research or applied acoustical reports, (b) comments on articles or letters previously published in this Journal, and (c) a reply by the article author to criticism by the Letter author in (b). Extensive reports should be submitted as articles, not in a letter series. Letters are peer-reviewed on the same basis as articles, but usually require less review time before acceptance. Letters cannot exceed four printed pages (approximately 3000–4000 words) including figures, tables, references, and a required abstract of about 100 words.

A third note on the prediction of sound intensity

J. Pan
Department of Mechanical and Materials Engineering, The University of Western Australia, Nedlands, Western Australia 6907, Australia

(Received 3 June 1998; revised 28 September 1998; accepted 5 October 1998)

The modal expansion of the sound field in an enclosure often employs rigid-wall modes of the enclosure as base functions. Simple analytical expressions of the modal amplitudes can be obtained if the specific acoustic-impedance ratio of the enclosure boundary is large and the modal coupling among the rigid-wall modes is negligible. It has been demonstrated that the analytical expressions fail to give a correct prediction of sound intensity [J. Pan, J. Acoust. Soc. Am. **93**, 1641–1644 (1993)]. Even including the modal coupling, prediction error still exists as a result of the poor convergence inherited in the use of the rigid-wall mode [J. Pan, J. Acoust. Soc. Am. **97**, 691–694 (1995)]. This note discusses a new approach of using the extended mode shape functions for the expansion of sound pressure. The new approach significantly improves the accuracy in the prediction of sound pressure and sound intensity in enclosures. © *1999 Acoustical Society of America.* [S0001-4966(99)04901-2]

PACS numbers: 43.55.Br, 43.20.Ks [JDQ]

INTRODUCTION

The modal expansion of sound pressure in an enclosure often uses rigid-wall modes of the enclosure as base functions. With absorptive boundaries, the modal amplitudes are coupled. Ignoring the coupling among the rigid-wall modes gives rise to a simple analytical sound-pressure expression (uncoupled model) which has reasonable prediction accuracy when the specific acoustic-impedance ratio ($Z/\rho_0 c_0$) of the boundary is sufficiently large.[1] However, the uncoupled model fails to deliver correct prediction of the distributed sound intensity, although $Z/\rho_0 c_0$ is large.[2] Although including the modal coupling (the coupled model) may improve the accuracy in the predicted sound pressure,[3] further investigation[4] indicates that even with a large number of rigid-wall modes, the coupled model still has insufficient accuracy for the prediction of particle velocity and sound intensity in the vicinity of boundaries.

It was recognized that the coupled model is also an approximate description in the sense that only finite number of the rigid-wall modes can be used in practical calculation.[3] Many more terms are needed in the expansion series of particle velocity (for the calculation of sound intensity) in order to achieve a comparable precision with the predicted sound pressure.

The requirement of a large number of rigid-wall modes implies a poor convergence property in the expansion of the particle velocity in terms of the rigid-wall modes. In this note, the sound pressure is expanded by base functions corresponding to the extended rigid-wall modes. In this extended mode shape model, the previously used rigid-wall mode shape functions $\cos(n\pi x/L)$ are replaced by $\cos[n\pi x/(L+\Delta L)]$. The new base functions allows the nonzero-velocity condition at the boundary $x=L$ to be satisfied. As a result, the convergence property of the sound pressure and sound intensity is significantly improved.

I. METHOD OF EXTENDED MODE SHAPE FUNCTIONS

The Lagrangian function of sound field in an enclosure can be expressed as:[5]

$$\mathbf{L}=\frac{1}{2}\int_V\left[\frac{p^2}{\rho_0 c_0^2}-\frac{(\nabla p)^2}{\rho_0\omega^2}\right]d\nu \tag{1}$$

where p is the sound pressure, $\rho_0 c_0$ is the characteristic impedance for free plane waves in air, and ∇p is the gradient of the sound pressure.

The work done at the boundary and acoustic source are, respectively:

$$\mathbf{W}_B=-\frac{1}{2}\int_S\frac{p^2}{j\omega Z}\,dx, \tag{2}$$

and

$$\mathbf{W}_S=-\frac{1}{2}\int_V\frac{pQ}{j\omega}\,d\nu, \tag{3}$$

where Z is the specific acoustic impedance of the boundary and Q is the source strength.

The sound pressure is expanded as

$$p=\sum_n P_n\phi_n, \tag{4}$$

where ϕ_n is a set of base functions. For the sound field in a one-dimensional pipe of length L, the base functions may be selected as:

$$\phi_n=\cos\frac{n\pi x}{L+\Delta L}. \tag{5}$$

The selected base functions are the rigid-wall mode shape functions for a pipe of length $L+\Delta L$. The advantage of selecting such base functions is that they allow for non-zero gradient of the sound pressure at the actual boundary $x=L$. The Lagrangian equations use Eqs. (1), (2), and (3) and give rise to the following modal equations:

$$\sum_{n=0}^{N}\left(k^2\int_V\phi_n\phi_m\,d\nu-\int_V\phi_n'\phi_m'\,d\nu+j\,\frac{\rho_0c_0}{Z}\,k\int_S\phi_n\phi_m\,ds\right)P_n=-\frac{j\rho_0c_0k}{2}\int_V Q\phi_m\,d\nu, \tag{6}$$

where $k=\omega/c_0$. For the one-dimensional sound field with a point sound source at $x=x_0$, a rigid surface at $x=0$, and specific acoustic impedance Z at $x=L$, the integrations in Eq. (6) can be solved analytically:

$$\frac{1}{S}\int_V\phi_n\phi_m\,d\nu=\int_0^L\cos k_nx\cos k_mx\,dx=\begin{cases}L, & n=m=0\\ \dfrac{\sin k_mL}{k_m}, & n=0,\ m\neq0\\ \dfrac{\sin k_nL}{k_n}, & n\neq0,\ m=0\\ \dfrac{L}{2}+\dfrac{\sin 2k_nL}{4k_n}, & m=n\\ \dfrac{\sin(k_n+k_m)L}{2(k_n+k_m)}+\dfrac{\sin(k_n-k_m)L}{2(k_n-k_m)}, & m\neq n\end{cases} \tag{7}$$

$$\frac{1}{S}\int_V\phi_n'\phi_m\,d\nu=k_nk_m\int_0^L\sin k_nx\sin k_mx\,dx=k_nk_m\begin{cases}\dfrac{L}{2}-\dfrac{\sin 2k_nL}{4k_n}, & m=n\\ 0, & n,m=0\\ -\dfrac{\sin(k_n+k_m)L}{2(k_n+k_m)}+\dfrac{\sin(k_n-k_m)L}{2(k_n-k_m)}, & m\neq n\end{cases} \tag{8}$$

and

$$\frac{1}{S}\int_V Q\phi_m\,d\nu=Q_0\cos k_mx_0, \tag{9}$$

where $k_n=n\pi/(L+\Delta L)$, S is the cross-section area of the pipe and Q_0 is the volume velocity of the sound source. When $\Delta L=0$, Eq. (6) describes the coupled model.[3,4]

II. RESULTS AND DISCUSSION

The same physical system used in Refs. 2, 3, and 4 is used here. The length of the one-dimensional pipe is 1 m ($L=1$ m) and the volume velocity of the sound source is $Q_0=0.2\ \mathrm{m}^3/\mathrm{s}$. The coupled model and the extended mode shape method are used to predict the sound-pressure response at $x=0.3$ m to the excitation of a sound source at $x_0=0$. The accuracy of the two methods are examined by comparing their predictions with the exact solution.[2] A pressure-released boundary impedance of $Z/\rho_0c_0=(0.5,0.1j)$ is considered. The first 16 base functions are used in the two predictions and the frequency range of examination is 1000 Hz (note $f_{16}=2580$ Hz). Figure 1(a) shows the exact sound-pressure response at $x=0.3$ m. Figure 1(b) shows the prediction error which is defined by the level difference between the predicted sound-pressure level (from the two approximate methods) and the exact sound-pressure level. Comparing the prediction errors, the extended mode shape method provides high accuracy in the prediction of sound pressure in a pipe with a pressure-released boundary throughout the frequency range of interest. In other words,

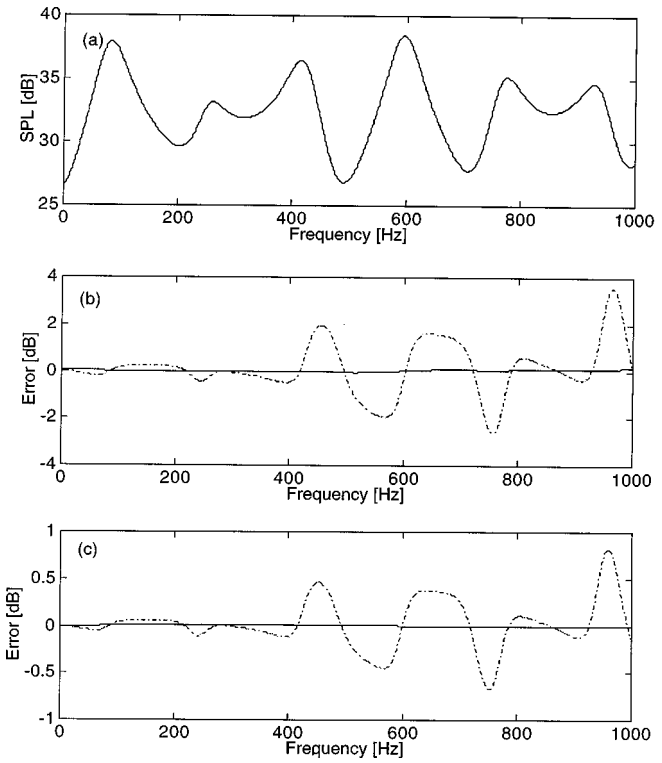

FIG. 1. (a) Sound pressure at $x=0.3$ m due to $Q_0=0.2\ \mathrm{m}^3/\mathrm{s}$ at $x_0=0$, for $N=16$ and $Z_L/\rho_0c_0=(0.5,j0.1)$; (b) prediction error ($N=16$), (- - -): coupled model, (———): extended mode shape method ($\Delta L=0.1$ m); (c) prediction error ($N=64$), (- · - · -): coupled model, (———): extended mode shape method ($\Delta L=0.1$ m).

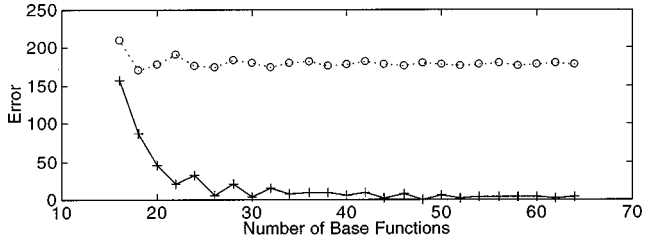

FIG. 2. Comparison of convergence rates in the prediction of sound pressure described in Fig. 1. (···○···): coupled model, (—+—): extended mode shape method.

the expansion of sound pressure using the extended mode shape functions exhibits improved convergence property. Figure 1(c) corresponds to the prediction errors when $N=64$. The results show that with such a large number of modes, the prediction by the coupled model still has obvious error, while that by the extended mode shape method is very close to the exact sound-pressure response.

The convergence rates of the two approximated methods are compared and shown in Fig. 2. The overall prediction errors corresponding to the pressure shown in Fig. 1 are estimated using the following definition

$$\text{Error}=\int_0^{1000}|\text{SPL}_{\text{ex}}-\text{SPL}_{\text{app}}|df, \tag{10}$$

while the number of modes (N) increases from 16 to 64. Although increasing N reduces the error, the coupled model converges very slowly. On the other hand, the extended mode shape method demonstrates a very fast convergence rate. For this case, when $N\geqslant 32$ the error becomes negligible.

The two approximated methods are also used to predict the distributed sound intensity in the pipe at 500 Hz. The sound source is now located at $x_0=0.3$ m. Figure 3 includes the exact sound intensity (dotted line) and sound intensity predicted by the two methods ($N=16$). It is shown that the prediction using the coupled model (dash-dotted curve) has significant error in the vicinity of the boundary. The large prediction error is due to the poor convergence property of the base functions used in the coupled model. The solid curve in Fig. 3 is the prediction using the extended mode shape method. Improved prediction accuracy, in particular in the vicinity of the boundary $x=L$, is observed.

Increasing the number of the base functions used for the modal expansion improves the prediction accuracy as shown

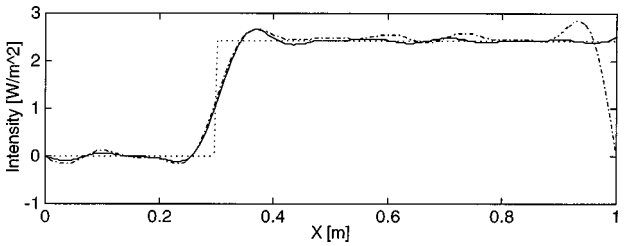

FIG. 3. Sound-intensity prediction at 500 Hz and for $Z_L/\rho_0 c_0=(5,j)$, $N=16$ and $x_0=0.3$ m. (···): exact solution, (-·-): coupled model, (———): extended mode shape method ($\Delta L=0.1$ m).

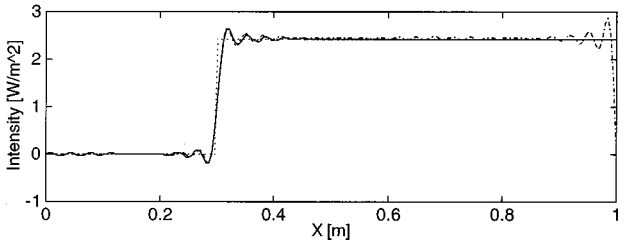

FIG. 4. Sound-intensity prediction at 500 Hz and for $Z_L/\rho_0 c_0=(5,j)$, $N=64$ and $x_0=0.3$ m. (···): exact solution, (-·-): coupled model, (———): extended mode shape method ($\Delta L=0.1$ m).

in Fig. 4 ($N=64$). The prediction using the extended mode shape method has achieved a high accuracy, while the coupled model still shows a significant error near $x=L$. The two methods have similar prediction errors at the sound-source location $x_0=0.3$ m. This indicates that both sets of base function have similar convergence property near the discontinuity of the sound-source location.

Although in this analysis a specific value of $\Delta L=0.1$ m is used, it has been found that a range of values for ΔL may be used to give the same convergence rate.[6] Reference 6 demonstrated that the range for ΔL corresponding to highly accurate predictions is related to the orthogonal properties of the base functions in $0\leqslant x\leqslant L$.

III. CONCLUSIONS

Following the previous two notes[2,4] on the problems in the prediction of sound intensity using the rigid-wall mode expansion, this third note presents an extended mode shape method. Using the extended mode shape functions as the base functions for the modal expansion of sound pressure, the nonzero boundary condition of the sound field can be satisfied with improved convergence property. The sound pressure and sound intensity in a one-dimensional pipe are predicted using the coupled model and the extended mode shape method. The predictions are compared with the exact solution. The comparison results demonstrate the advantage of using the extended mode shapes for the modal expansion. Further effort is required to improve the convergence rate of the sound intensity near the sound-source location and to extend the proposed method to the prediction of sound-intensity field in two- and three-dimensional enclosures.

[1] E. H. Dowell, ''Reverberation time, absorption and impedance,'' J. Acoust. Soc. Am. **64**, 181–191 (1978).
[2] J. Pan, ''A note on the prediction of sound intensity,'' J. Acoust. Soc. Am. **93**, 1641–1644 (1993).
[3] L. P. Franzoni and E. H. Dowell, ''On the accuracy of modal analysis in reverberant acoustical systems with damping,'' J. Acoust. Soc. Am. **97**, 687–690 (1995).
[4] J. Pan, ''A second note on the prediction of sound intensity,'' J. Acoust. Soc. Am. **97**, 691–694 (1995).
[5] D. G. Crighton, A. P. Dowling, J. E. Ffowces Williams, M. Heckle, and F. G. Leppington, *Modern Methods in Analytical Acoustics* (Springer-Verlag, Berlin, 1992).
[6] J. Pan, ''Approximating eigensolutions of distributed structures using the adjustable quasi comparison functions,'' *Proceedings of the 5th International Congress on Sound and Vibration*, Adelaide, December 1997, pp. 2411–2418.

Additivity of perceptual channel-crossing effects in auditory gap detection

T. L. Taylor
Vision Research Center, Department of Psychology, Wilson Hall, Vanderbilt University, Nashville, Tennessee 37240

S. E. Hall, S. E. Boehnke, and D. P. Phillips[a)]
Department of Psychology, Dalhousie University, Halifax, Nova Scotia B3H 4J1, Canada

(Received 8 July 1998; accepted for publication 25 September 1998)

Five normal listeners were tested in detail for their auditory gap-detection thresholds, using stimuli in which the narrow-band noise markers of the gap differed in one or both of two auditory dimensions (frequency composition and ear stimulated). Gap thresholds for stimuli in which the markers differed along either single dimension averaged about 18 ms, while thresholds for markers differing across both dimensions were closer to 28 ms. These data suggest that the perceptual relative-timing operation that mediates between-channel gap detection is shared across auditory dimensions. © *1999 Acoustical Society of America.* [S0001-4966(99)03301-9]

PACS numbers: 43.66.Ba, 43.66.Mk, 43.66.Pn [JWH]

INTRODUCTION

Gap detection is a measure of auditory temporal acuity. It is typically studied by requiring a listener to specify which of two streams of otherwise homogeneous sound contains a brief silent period (''gap'') at its temporal midpoint; an adaptive tracking procedure is then used to determine the minimum detectable gap, or ''gap threshold.'' Recently, a distinction has been made, on both theoretical and empirical grounds, between the perceptual processes involved in the detection of gaps bounded by identical sounds and the detection of gaps bounded by different sounds (Phillips *et al.*, 1997, 1998). Briefly, in the former (''within-channel'') case, the perceptual operation is construed as a *discontinuity detection* performed on the activity in the neural or perceptual channel representing the stimulus (see also Grose, 1991). Depending on the stimulus, this process can have an acuity in the order of a few milliseconds (Eddins *et al.*, 1992; Moore *et al.*, 1993; Penner, 1977; Plomp, 1964). In the latter (''between-channel'') case, the perceptual operation is thought to be a *relative timing* of the offset of activity in the perceptual channel representing the leading marker and the onset of activity in the perceptual channel representing the trailing marker of the gap. Under these conditions, gap discrimination (Divenyi and Danner, 1977) and gap detection (Neff *et al.*, 1982; Formby *et al.*, 1993, 1996, 1998; Phillips *et al.*, 1997,1998) have poorer acuity, and gap detection has a dependence on the brevity of the leading marker, which is rarely seen in within-channel tasks (Phillips *et al.*, 1997, 1998).

The effect on gap threshold of introducing a channel disparity between the leading and trailing markers is certainly qualitatively, and perhaps quantitatively, similar across stimuli whose markers differ in frequency composition, ear stimulated, or free-field location (Phillips *et al.*, 1997, 1998; Formby *et al.*, 1998). This similarity suggests that the perceptual machinery engaged to execute the relative-timing operation might be shared or common across those perceptual dimensions. An alternative interpretation is that this similarity is coincidental, and that the mechanisms or resources engaged in the execution of relative timing across differences in one dimension (e.g., frequency region) are independent of those engaged in between-channel gap detection across another dimension (e.g., ear stimulated).

One way to differentiate these hypotheses may be based on additive factors logic, originally intended for reaction-time data (Sternberg, 1969), but also used to advantage in studies of perceptual accuracy (e.g., Enns and Shore, 1997). The experiment is to compare gap-detection performance in a single set of listeners for stimuli in which the markers differ across either or both of two auditory dimensions. If the mechanisms mediating between-channel gap detection within one dimension are independent of those mediating between-channel gap detection in a second dimension, then gap markers differing across both dimensions should reveal an additivity of the between-channel temporal acuity disadvantage. On the other hand, if a single relative-timing mechanism operates over multidimensional perceptual or representational space, then the temporal acuity disadvantage will not be linearly additive. The purpose of the present study was to address this general question.

I. METHODS

Five listeners, all with absolute auditory sensitivities within laboratory norms, and all with extensive experience in auditory gap detection, participated in the study.

The stimuli were narrow-band (0.25 octave, 48 dB/octave rolloff) noise signals with center frequencies of 4.0 and 1.0 kHz (after Phillips *et al.*, 1997). Sample waveforms generated by analog equipment were captured by Deck II™ software, and were edited into stimulus ''resource files'' by SOUNDEDIT™ software on a Power Macintosh 8600 computer. The experiment was then programmed in Hyper-

[a)]Electronic mail: ears@is.dal.ca

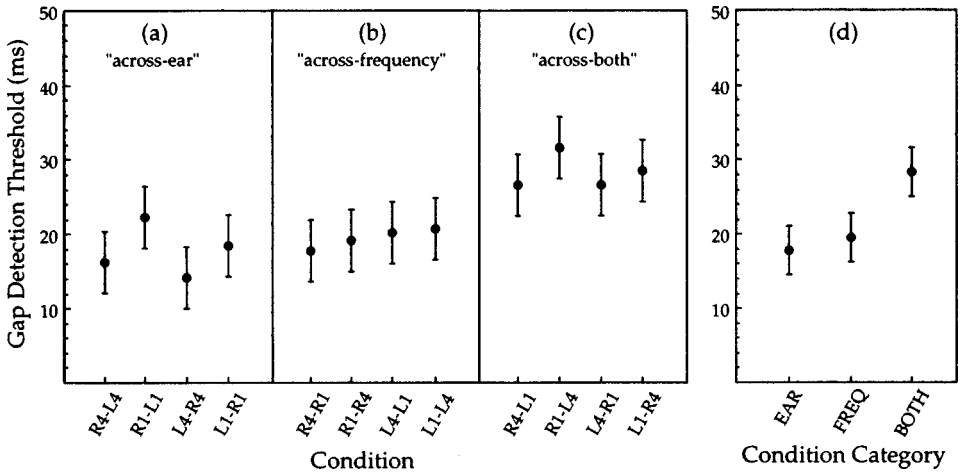

FIG. 1. Gap thresholds, averaged across the five listeners, are plotted separately for the four across-ear, the four across-frequency, and the four across-both stimulus conditions in panels (a), (b), and (c), respectively. The 95% confidence interval, calculated with the subject variance removed (after Loftus and Masson, 1994) is shown as the error bars. (d) Shows the three group-mean gap thresholds, averaged across both listeners and condition for the data in panels (a), (b), and (c), respectively. Error bars in (d) are the 95% confidence interval. Abbreviations: R (right), L (left), 4 (4.0 kHz), 1 (1.0 kHz), FREQ (frequency).

Card™, which called up the resource files as needed. Stimuli were delivered to the listener via Koss Pro/466 earphones at a comfortable listening level (approximately 30–35 dB sensation level), and all listener responses were executed as ''mouse clicks.'' This mode of stimulus generation used the same noise samples in each stimulus presentation. Two lines of evidence suggest that the use of ''frozen'' noise was inconsequential to the gap thresholds we obtained. First, in ongoing studies of some of the same listeners, we are drawing on different noise samples for each stimulus presentation, but the within-channel gap thresholds are the same as those reported here. Second, the within-channel gap thresholds in this study are similar or identical to those obtained in our earlier study using analog signals.

Every listener was tested with 16 stimulus conditions. Within-channel gap detection for 1.0 and 4.0 kHz noise was tested separately in each ear (a total of four conditions). These were essentially control conditions to ensure that the listeners had normal acuity for conventional gap-detection tasks. There were 12 between-channel conditions. In the following, the leading and trailing markers are identified with letters (specifying ear stimulated) and numbers (specifying stimulus center frequency in kHz) and are separated by a hyphen. Between-channel gap detection ''across frequency'' was studied factorially in both ears (four conditions, i.e., 4–1 kHz and 1–4 kHz in the left [L] ear, and right [R] ear, separately). Between-channel gap detection ''across ear'' was studied factorially for both frequencies (four conditions, i.e., R–L and L–R at the two frequencies, separately). Finally, each listener was tested with gap stimuli whose markers differed across both dimensions (four conditions: R4–L1, R1–L4, L4–R1, and L1–R4). For all 16 stimulus conditions, the leading marker duration was 10 ms, including 1.0 ms rise–fall times, and the trailing marker duration was 300 ms (same rise–fall times). The relatively short duration of the leading marker was selected to ensure the experimental detection of the relative-timing operation, because this is expressed behaviorally as elevated gap thresholds, and gap thresholds are most elevated in the between-channel case when the leading marker is brief (Phillips *et al.*, 1997, 1998).

The general design of the study was otherwise as described in our previous reports (Phillips *et al.*, 1997, 1998). Listeners were tested individually. Gap thresholds for every stimulus condition were tested using a two-down/one-up adaptive tracking method (Levitt, 1971). Each stimulus trial consisted of the presentation of two gap-detection stimuli: one in which there was no audible silent period (nominally 2.0 ms, including 1.0 ms rise–fall times), and one in which there was a detectable silent period. These were presented in random order. The task of the listener was to specify by mouse click which stimulus contained the gap. After two successive correct responses, the computer decreased the gap duration by a factor of 1.2; following any single incorrect response, the gap duration was increased by the same factor. The adaptive tracking method was continued, without trial-by-trial feedback, until there there had been 14 reversals in the direction of change of gap size, and the gap durations associated with the last ten such reversals were then averaged to calculate the gap threshold for that block of trials for that stimulus condition. Commonly, between 50 and 80 trials per stimulus condition were needed to obtain a single gap threshold.

Each listener was tested on every stimulus condition until gap thresholds were relatively stable (up to eight threshold determinations/condition). Data entered into the statistical analyses for each listener were the means of the last four gap thresholds obtained for each of the 16 stimulus conditions. Gap durations (and therefore gap thresholds) are specified as the durations of silent intervals, excluding the stimulus rise–fall times.

II. RESULTS

Averaged across both ears in each the five listeners, mean within-channel gap thresholds were 2.29 ms for the 4.0-kHz noise, and 5.48 ms for the 1.0-kHz noise. These values are similar or identical to those previously reported from this laboratory (Phillips *et al.*, 1997). The difference in thresholds for the two noises probably reflects differences in absolute stimulus bandwidth (after Eddins *et al.*, 1992).

Figure 1(a)–(c) shows the mean gap thresholds for each of the 12 between-channel conditions. For the four across-ear conditions [Fig. 1(a)], mean gap thresholds were in the range from about 14 to 22.5 ms (mean for that category of conditions=17.86 ms). For the four across-frequency conditions [Fig. 1(b)], mean gap thresholds were in the range from

18 to 20 ms (category mean=19.49 ms). Finally, for the stimulus conditions in which the leading and trailing markers differed in both dimensions [Fig. 1(c)], mean gap-detection thresholds were in the range from 26.5 to 32 ms (category mean=28.36 ms).

As in our previous studies, individual listeners differed markedly (up to a factor of four) in their absolute gap thresholds for the between-channel conditions, but relatively little in the pattern of gap thresholds across the stimulus conditions (Phillips *et al.*, 1997, 1998). Because our interest was in differences in gap thresholds across stimulus conditions, and not in differences in absolute thresholds between listeners, the subject variance was partitioned out, and a 95% confidence interval (4.29 ms) was based on the listener-by-condition interaction (pooled error, after Loftus and Masson, 1994). This confidence interval is shown in Fig. 1(a)–(c), and it applies to all 12 means plotted in Fig. 1(a)–(c). It is apparent that the mean gap thresholds for most of the eight conditions in which the markers differed across a single dimension were within a 95% confidence interval of each other [Fig. 1(a) and (b)]. In contrast, the mean gap thresholds for ''across-both'' conditions, while mostly within a 95% confidence interval of each other, fell outside of a 95% confidence interval around the across-ear and across-frequency means.

The foregoing data suggest that the temporal acuities of the between-ear and between-frequency gap-detection mechanisms are very similar, but that listeners have poorer thresholds if the markers differ across both dimensions. The mean thresholds for the four across-ear, the four across-frequency, and the four across-both conditions were averaged separately and the means for these three categories of conditions are shown in Fig. 1(d). A new 95% confidence interval (3.31 ms) was calculated, and this is shown as the error bars in Fig. 1(d). The mean gap thresholds in Fig. 1(d) were subjected to an analysis of variance (based on a new pooled error; see Loftus and Masson, 1994). This confirmed that there were statistically significant differences between the three groups [$F(2,8)=15.45$, $p<0.01$]. *Post hoc* (*t*-test) comparisons confirmed that the group mean thresholds for the across-ear and across-frequency conditions did not differ ($p>0.05$), but that the group mean threshold for the across-both conditions was higher than either of the others ($p<0.01$).

Finally, the data suggest that the effects on gap threshold of using markers that differ across different dimensions were not linearly additive. In none of the individual listeners (nor in the mean data: Fig. 1), was the mean across-both gap threshold particularly close to the sum of the mean across-ear and mean across-frequency gap thresholds. The mean across-both gap thresholds were always less than the sum of the mean across-ear and across-frequency gap thresholds.

III. DISCUSSION

The general purpose of the present study was to determine whether gap thresholds for stimuli in which the leading and trailing markers differed across two dimensions (frequency composition and ear stimulated) were higher than those for stimuli in which the markers differed in only one dimension. The within-channel gap thresholds of the present listeners were similar to previous published accounts (Penner, 1977; Plomp, 1964; Phillips *et al.*, 1997). Between-channel gap thresholds have been studied less extensively, but the gap thresholds seen here were within range of those published by at least two laboratories (Formby *et al.*, 1996, 1998; Phillips *et al.*, 1997). Our main findings were that, for the stimuli in this study, the between-channel gap-detection acuity was comparable for the cases in which markers differed in one dimension (either frequency composition or ear), and that acuity was poorer when the markers differed across both of those dimensions.

The further question concerns the additivity of these ''channel-crossing'' effects. A strict linear additivity would suggest independence of the processing of ''ear'' from the processing of ''frequency.'' This view is not without precedent in either the auditory neurophysiological (Evans, 1974; Knudsen and Konishi, 1978) or psychophysical literature (Deutsch and Roll, 1976 but see Bregman and Steiger, 1980). We found that gap thresholds in the across-both conditions were systematically shorter than the linear sum of those seen in conditions in which the markers differed only along a single dimension. We take this to mean that the mechanisms or resources mediating the two kinds of between-channel gap-detection tasks are partially shared. Our data depart from those presented by Formby *et al.* (1998) who, using sinusoidal markers, found that dichotic (across-ear) temporal gap-detection thresholds were relatively insensitive to variations in the spectral composition of the markers. The reasons for this apparent disagreement are unclear, but might reflect that we used short leading markers to optimize the visibility of the between-channel process (after Phillips *et al.*, 1997, 1998).

We are concerned, however, about the usefulness of conceptualizing auditory function in the additive factors framework, despite the success of that model in early reaction-time studies of cognitive processes (e.g., Sternberg, 1969). From the neurological standpoint, the architecture of the mammalian auditory nervous system, while demonstrably containing circuits with identifiable and separable functions (e.g., encoding of interaural phase delays and interaural intensity differences), is tonotopically constrained throughout, so that much, if not all, low-level sensory processing is done on a frequency-specific basis. This means that the ''representation'' of frequency information is probably never completely isolated from (''independent of'') the processing or representation of other stimulus dimensions (e.g., Phillips *et al.*, 1994). This conclusion is compatible with that drawn previously by Bregman and Steiger (1980) on purely psychophysical grounds. The modularity envisaged by the additive factors logic may therefore be misplaced in this level of perceptual analysis. In this light, the intended quantitative meaning of ''additivity'' becomes unclear.

In this regard, there is a different way of thinking about this issue (P. J. Fitzgibbons, personal communication). One could construe the mean gap thresholds for the across-ear (17.9 ms) and across-frequency (19.5 ms) conditions as the magnitudes of orthogonal vectors, in which case, their vector sum would be 26.4 ms—a value very close to (within a 95% confidence interval of) that we obtained for the across-both

condition (28.4 ms). Whether this similarity is coincidental can be determined by future experiments. The conceptually important point is that this vector addition, as opposed to the linear addition implied by the additive factors logic, is consistent with the existence of a single relative-timing mechanism that operates over different, independent channels in multidimensional perceptual space.

This leads us to return to our (qualitative) account of how the within- and between-channel processes contribute to gap-detection performance. The leading and trailing gap markers have representations that occupy channels defined by frequency and/or ear. The acuity of gap-detection performance depends on the extent to which those representations overlap, and thus on the amount of substrate available for (high-resolution) discontinuity detection in the channels activated by the markers. The alternative mechanism, between-channel relative timing, has inherently poor acuity (Phillips *et al.*, 1997; Formby *et al.*, 1998). In previous studies, decreasing the overlap of the spectral contents of leading and trailing markers increased gap-detection or gap-discrimination thresholds (Divenyi and Danner, 1977; Neff *et al.*, 1982; Formby *et al.*, 1993, 1996, 1998; Phillips *et al.*, 1997). In the present experiment, the imposition of both ear and frequency differences in the markers for the across-both conditions further reduced the representational overlap of the markers, and so resulted in a still poorer medium on which the within-channel process could operate. This, in turn, resulted in poorer temporal acuity than that seen in conditions in which the markers differed along a single dimension. In cases of nonoptimal representational overlap between the markers, it remains to be determined whether it is solely the sparser substrate available to the discontinuity detector, or some interaction between the outputs of concurrently activated within- and between-channel processes, which results in the gap-threshold elevations.

Finally, in a recent study of cochlear implant patients, Chatterjee *et al.* (1998) reported gap thresholds obtained using dissimilar (electrical) markers applied to a single cochlear-implant electrode pair. The markers differed in either pulse rate or pulse amplitude. Chatterjee *et al.* suggested that between-channel gap thresholds thus reflected the *perceptual* discontinuity between the markers (cf. our use of the more neurophysiological term ''representational overlap''). However, we know independently that tones of the same frequency but different amplitudes activate different central neurons (Phillips, 1990; Phillips *et al.*, 1994), and the same might apply to periodicities (Schreiner and Urbas, 1988). This means that Chatterjee *et al.*'s (1998) conclusion may be in keeping with our own.

ACKNOWLEDGMENTS

This research was supported by grants from NSERC of Canada to D.P.P. Special thanks are due to Dr. P.J. Fitzgibbons and Dr. P.L. Divenyi for thoughtful and helpful commentaries on a previous version of this manuscript.

Bregman, A. S., and Steiger, H. (**1980**). ''Auditory streaming and vertical localization: Interdependence of 'what' and 'where' decisions in audition,'' Percept. Psychophys. **28**, 539–546.

Chatterjee, M., Fu, Q-J., and Shannon, R. V. (**1998**). ''Within-channel gap detection using dissimilar markers in cochlear implant users,'' J. Acoust. Soc. Am. **103**, 2515–2519.

Deutsch, D., and Roll, P. (**1976**). ''Separate 'what' and 'where' decision mechanisms in processing a dichotic tonal sequence,'' J. Exp. Psychol. Hum. Percept. Perf. **2**, 23–29.

Divenyi, P. L., and Danner, W. F. (**1977**). ''Discrimination of time intervals marked by brief acoustic pulses of various intensities and spectra,'' Percept. Psychophys. **21**, 12–142.

Eddins, D. A., Hall, J. W., and Grose, J. H. (**1992**). ''The detection of gaps as a function of frequency region and absolute noise bandwidth,'' J. Acoust. Soc. Am. **91**, 1069–1077.

Enns, J. T., and Shore, D. I. (**1997**). ''Separate influences of orientation and lighting in the inverted-face effect,'' Percept. Psychophys. **59**, 23–31.

Evans, E. F. (**1974**). ''Neural processes for the detection of acoustic patterns and for sound localization,'' in *The Neurosciences. Third Study Program*, edited by F. O. Schmitt and F. T. Worden (MIT, Cambridge, MA), pp. 131–145.

Fitzgibbons, P. J. (**1998**). (Personal communication).

Formby, C., Barker, C., Abbey, H., and Raney, J. J. (**1993**). ''Detection of silent temporal gaps between narrow-band noise markers having second-formantlike properties of voiceless stop/vowel combinations,'' J. Acoust. Soc. Am. **93**, 1023–1027.

Formby, C., Gerber, M. J., Sherlock, L. P., and Magder, L. S. (**1998**). ''Evidence for an across-frequency, between-channel process in asymptotic monaural temporal gap detection,'' J. Acoust. Soc. Am. **103**, 3554–3560.

Formby, C., Sherlock, L. P., and Forrest, T. G. (**1996**). ''An asymmetric Roex filter model for describing detection of silent temporal gaps in sinusoidal markers,'' Aud. Neurosci. **3**, 1–20.

Grose, J. H. (**1991**). ''Gap detection in multiple narrow bands of noise as a function of spectral configuration,'' J. Acoust. Soc. Am. **90**, 3061–3068.

Knudsen, E. I., and Konishi, M. (**1978**). ''Space and frequency are represented separately in auditory midbrain of the owl,'' J. Neurophysiol. **41**, 870–884.

Levitt, H. (**1971**). ''Transformed up-down methods in psychoacoustics,'' J. Acoust. Soc. Am. **49**, 467–477.

Loftus, G. R., and Masson, M. E. J. (**1994**). ''Using confidence intervals in within-subjects designs,'' Psychonom. Bull. Rev. **1**, 476–490.

Moore, B. C. J., Peters, R. W., and Glasberg, B. R. (**1993**). ''Detection of temporal gaps in sinusoids: Effects of frequency and level,'' J. Acoust. Soc. Am. **93**, 1563–1570.

Neff, D. L., Jesteadt, W., and Brown, E. L. (**1982**). ''The relation between gap discrimination and auditory stream segregation,'' Percept. Psychophys. **31**, 493–501.

Penner, M. J. (**1977**). ''Detection of temporal gaps in noise as a measure of the decay of auditory sensation,'' J. Acoust. Soc. Am. **61**, 552–557.

Phillips, D. P. (**1990**). ''Neural representation of sound amplitude in the auditory cortex: Effects of noise masking,'' Behav. Brain Res. **37**, 197–214.

Phillips, D. P., Hall, S. E., Harrington, I. A., and Taylor, T. L. (**1998**). '''Central' auditory gap detection: A spatial case,'' J. Acoust. Soc. Am. **103**, 2064–2068.

Phillips, D. P., Semple, M. N., Calford, M. B., and Kitzes, L. M. (**1994**). ''Level-dependent representation of stimulus frequency in cat primary auditory cortex,'' Exp. Brain Res. **102**, 210–226.

Phillips, D. P., Taylor, T. L., Hall, S. E., Carr, M. M., and Mossop, J. E. (**1997**). ''Detection of silent intervals between noises activating different perceptual channels: Some properties of 'central' auditory gap detection'', J. Acoust. Soc. Am. **101**, 3694–3705.

Plomp, R. (**1964**). ''Rate of decay of auditory sensation,'' J. Acoust. Soc. Am. **36**, 277–282.

Schreiner, C. E., and Urbas, J. V. (**1988**). ''Representation of amplitude modulation in the auditory cortex of the cat. II. Comparison between cortical fields,'' Hearing Res. **32**, 49–64.

Sternberg, S. (**1969**). ''The discovery of processing stages: Extensions of Donders' method,'' Acta Psychol. **30**, Attention and Performance II, 276–315.

Erratum: "Time-average temperature distribution in a thermoacoustic stack" [J. Acoust. Soc. Am. 103, 380–388 (1998)]

George Mozurkewich
Ford Motor Company Research Laboratory, Mail Drop 3028, P.O. Box 2053, Dearborn, Michigan 48121-2053

(Received 5 August 1998; accepted for publication 16 September 1998)

[S0001-4966(99)00701-8]

PACS numbers: 43.35.Cg, 43.10.Vx [HEB]

A hyperbolic function was omitted from the denominator of the first term in Eq. (10). The equation should read:

$$T_g(z,\boldsymbol{\rho}) = \sum_m \frac{\boldsymbol{\nabla} T_m}{s_m} \frac{\sinh(s_m z)}{\cosh(s_m L/2)} \Theta_m(\boldsymbol{\rho}) + \sum_{n\ \mathrm{odd}} B_n \sin\left(n\pi \frac{z}{L}\right) \frac{\Psi_n(\boldsymbol{\rho})}{\Psi_n(\mathrm{wall})}.$$

In the second line on page 386, s_w^{-i} should read s_w^{-1}.

 0001-4966/99/105(1)/567/1/$15.00